Transactions of the ASME®

Transactions of the ASME, Journal of Heat Transfer (ISSN 0022-1481) is published quarterly (Feb., May, Aug., Nov.) for $150 per year by The American Society of Mechanical Engineers, 345 East 47th Street, New York, NY 10017. Second class postage paid at New York, NY and additional mailing offices. POSTMASTER: Send address changes to The Journal of Heat Transfer, c/o THE AMERICAN SOCIETY OF MECHANICAL ENGINEERS, 22 Law Drive, Box 2300, Fairfield, NJ 07007-2300.

CHANGES OF ADDRESS must be received at Society headquarters seven weeks before they are to be effective. Please send old label and new address.

PRICES: To members, $27.00, annually; to nonmembers, $150.00. Add $12.00 for postage to countries outside the United States and Canada.

INDEXED by Applied Mechanics Reviews and Engineering Information, Inc.

Journal of Heat Transfer

Published Quarterly by The American Society of Mechanical Engineers

VOLUME 110 • NUMBER 3 • AUGUST 1988

ANNOUNCEMENTS

561 Change of address form for subscribers

810 Call for papers: 26th National Heat Transfer Conference

812 International Conference on Mechanics of Two-Phase Flows

Inside back cover Information for authors

TECHNICAL PAPERS

544 Shape Optimization and Identification of Solid Geometries Considering Discontinuities
R. A. Meriç

551 Conduction Heating of Objects of Simple Shape in a Fluid With Finite Heat Capacity
Q. T. Pham

554 An Analysis of Inverse Heat Transfer Problems With Phase Changes Using an Integral Method
N. Zabaras, S. Mukherjee, and O. Richmond

562 On Numerical Methods Used in Mathematical Modeling of Phase Change in Liquid Metals
D. Poirier and M. Salcudean

571 Forced Convection Heat Transfer in a Finitely Conducting Externally Finned Pipe
F. Moukalled and S. Acharya

577 Boundary Layer Analysis for Two-Dimensional Slot Jet Impingement on Inclined Plates
V. K. Garg and S. Jayaraj

583 A Two-Equation Model for Heat Transport in Wall Turbulent Shear Flows
Y. Nagano and C. Kim

590 Three-Dimensional Unsteady Flow With Heat and Mass Transfer Over a Continuous Stretching Surface
K. N. Lakshmisha, S. Venkateswaran, and G. Nath

596 Buoyancy Effects on Forced Convection Heat Transfer in the Transition Regime of a Horizontal Boundary Layer Heated From Below
K. C. Cheng, T. Obata, and R. R. Gilpin

604 Transient Free Convection of a Non-Newtonian Fluid Along a Vertical Wall
S. Haq, C. Kleinstreuer, and J. C. Mulligan

608 Flow Visualization Studies on Vortex Instability of Natural Convection Flow Over Horizontal and Slightly Inclined Constant-Temperature Plates (86-WA/HT-85)
K. C. Cheng and Y. W. Kim

616 An Experimental Study of Natural Convection in a Vertical Cavity With Discrete Heat Sources
M. Keyhani, V. Prasad, and R. Cox

625 Natural Convection in Shallow Enclosures With Differentially Heated Endwalls
S. Paolucci and D. R. Chenoweth

635 An Effective Equation Governing Convective Transport in Porous Media
J. G. Georgiadis and I. Catton

642 Natural Convection Around a Heated Cylinder in a Saturated Porous Medium
B. Farouk and H. Shayer

649 Thermal Convection Around a Heat Source Embedded in a Box Containing a Saturated Porous Medium
K. Himasekhar and H. H. Bau

655 Fluid Flow and Mixed Convection Transport From a Moving Plate in Rolling and Extrusion Processes
M. V. Karwe and Y. Jaluria

662 The Influence of Secondary Convection on Axial Segregation in a Floating Zone
J. Y. Murthy

670 Modeling of Hot Fragment Conductive Ignition of Solid Propellants With Applications to Melting and Evaporation of Solids
K. K. Kuo, W. H. Hsieh, K. C. Hsieh, and M. S. Miller

680 Measurements of the Spectral and Directional Emission From Microgrooved Silicon Surfaces
P. J. Hesketh, B. Gebhart, and J. N. Zemel

687 Heat Transfer Characteristics From a Flat Plate to a Gas-Solid Two-Phase Flow Downstream of a Slit Injection
S. Obi, K. Hishida, and M. Maeda

(Contents continued)

695 Electrically Induced Shape Oscillation of Drops as a Means of Direct-Contact Heat Transfer Enhancement: Part 1—Drop Dynamics
N. Kaji, Y. H. Mori, and Y. Tochitani

700 Electrically Induced Shape Oscillation of Drops as a Means of Direct-Contact Heat Transfer Enhancement: Part 2—Heat Transfer
N. Kaji, Y. H. Mori, and Y. Tochitani

705 Transition Boiling Models in Heat Exchangers
D. M. France, S. K. Shin, M. Azimi, and A. Shafiei

710 Application of a Multifield Model to Reflooding of a Hot Vertical Tube: Part II—Analysis of Experimental Results
M. Kawaji and S. Banerjee

721 Parametric Trends for Post-CHF Heat Transfer in Rod Bundles
C. Unal, K. Tuzla, O. Badr, S. Neti, and J. Chen

728 Effects of Size of Simulated Microelectronic Chips on Boiling and Critical Heat Flux
K.-A. Park and A. E. Bergles

735 Stability of Single-Phase Natural Circulation With Inverted U-Tube Steam Generators
J. Sanders

743 Gas-Concentration Measurements and Analysis for Gas-Loaded Thermosyphons
P. F. Peterson and C. L. Tien

748 Predicting the Performance of an Evaporative Condenser
D. Peterson, D. Glasser, D. Williams, and R. Ramsden

754 Similarity Analysis of Condensing Flow in a Fluid-Driven Fracture
S. K. Griffiths and R. H. Nilson

763 The Properties of Steam: Current Status
P. G. Hill and R. D. C. MacMillan

TECHNICAL NOTES

778 Steady Conduction With Space-Dependent Conductivity
A. V. Munoz and L. C. Burmeister

780 Two-Dimensional Fin Performance: Bi (top surface) ≥ Bi (bottom surface)
D. C. Look, Jr.

782 Multipass Heat Exchangers With a Single Well-Mixed Shell Pass
R. A. Seban

785 Methods for Rapid Calculation of the Operation of Asymmetric Counterflow Regenerators
F. E. Romie and B. S. Baclic

789 Heat Transport Along an Oscillating Flat Plate
U. H. Kurzweg and J. Chen

790 Transient Forced Convection in Fluids With Vanishing Prandtl Number
R. W. Lycans and B. T. F. Chung

793 Free Convection on a Horizontal Plate With Blowing and Suction
Hsiao-Tsung Lin and Wen-Shing Yu

796 Low Peclet Number Heat Transfer in a Laminar Tube Flow Subjected to Axially Varying Wall Heat Flux
A. J. Pearlstein and B. P. Dempsey

798 Convective Heat Transfer in a Circular Annulus With Variable Heat Generation
M. A. Ebadian, H. C. Topakoglu, and O. A. Arnas

801 Heat Transfer Correlation for Flow in a Parallel-Plate Channel With Staggered Fins
A. Lazaridis

802 Predicting Temperatures of Stacked Heat Sinks With a Shroud
T. W. Petrie, A. A. Bajabir, D. J. Petrie, and J. W. Kroll

807 A Coordinate Transformation Method for Radiation Heat Transfer Prediction in Soot-Laden Combustion Products
S. L. Chang and K. T. Rhee

Shape Optimization and Identification of Solid Geometries Considering Discontinuities

R. A. Meriç
Department of Applied Mathematics,
Research Institute for Basic Sciences,
TUBITAK,
Gebze, Kocaeli, Turkey

Shape sensitivity analysis of heat-conducting bodies is performed in general terms incorporating interface conditions and boundary singularities. Adjoint variables and the material derivative concept are utilized to obtain the material derivatives of volume and surface integrals of temperature and heat flux. Two illustrative examples are then analyzed by iterative numerical techniques incorporating the boundary element method of discretization. In the first problem, the interface position in a nonhomogeneous material is optimized for a minimum of total surface heat flow. The second problem involves the determination of the solidification interface shape in the so-called steady-state one-phase Stefan problem. Numerical results, checked by exact solutions, where available, indicate that the proposed solution procedure is suitable for free boundary problems in heat transfer.

1 Introduction

Shape optimization, identification, Stefan, and other free or moving boundary problems may be thought of as shape inverse problems (SIP), in which the positions of free boundaries or interfaces are determined along with the solutions of field variables. In such problems the missing data (i.e., the position of free boundaries) are compensated for by the presence of the so-called inverse problem conditions (IPC). If such a condition is composed of the minimization of an objective function (subject to any constraints), then the corresponding SIP may be considered as an optimal SIP (compare shape optimization). On the other hand, an exact SIP requires the satisfaction of a functional equation (i.e., the IPC) exactly (compare shape identification). It may be noted that for solution purposes exact SIPs may be recast as optimal SIPs, or vice versa.

In the case of shape optimization problems, Barone and Caulk (1982) analyzed optimal thermal design of compression molds by boundary element methods. The rate of heat loss from a body surrounded by a layer of homogeneous insulation was minimized by Curtis (1983) employing a perturbation technique. Much literature is available on the optimization of extended surfaces (see, for example, a recent study by Hyrmak et al., 1985). However, most of the optimization studies on fins are simplified by the fact that the shape parameters are directly incorporated into the field equations. In a study of this type Meriç (1986) has optimized the insulation thickness distribution over a heat-conducting body by utilizing boundary element methods. It is also noted that vast literature is available on structural (i.e., nonthermal) shape optimization problems (e.g., see the recently published NATO ASI Series Book, edited by Mota Soares (1987) and references cited therein). In fact, the present analysis can be regarded as an extension of formulations in structural optimization problems.

In some of the exact SIPs, for example, Stefan (melting/solidification) problems (see Crank, 1981), the IPC is an explicit condition, that is, the function (or its time derivative) characterizing the unknown (free or moving) boundary can be solved directly in terms of the field variables. The SIPs with implicit IPCs, on the other hand, find by far most applications in the so-called shape identification problems. Such problems appear in, for example, nondestructive testing of flaws and cavities in bodies, as studied by Hsieh et al. (1982) and Hsieh and Kassab (1986). Boundary element methods (BEM) were utilized for some SIPs governed by Navier's equations of elasticity and Laplace's equation by Tanaka and Masuda (1986), Mota Soares et al. (1987), Kwak and Choi (1987), and Meric (1987, 1988). Murai and Kagawa (1986) and Kagawa et al. (1983) employed the BEM and finite element methods for determining the interface between Laplace and Poisson domains. For such free boundary problems analytical methods, for example, conformal mapping (Siegel, 1982) and inverse formulation (Siegel, 1986; Bell, 1985) techniques, proved sometimes to be effective in two-dimensional problems, while numerical methods using the BEM, finite element methods, and integrated penalty methods with finite differencing (Natori and Kawarada, 1981) have the advantage of generality.

In the present analysis, a shape sensitivity analysis (SSA) of a general integral functional of temperature and heat flux is first performed by borrowing techniques from structural optimization. Namely, the adjoint variable method and the material derivative (MD) concept (Haug et al., 1986; Dems and Mroz, 1984) are utilized in order to find the total variation of the integral functional with respect to variations of the domain geometry. Discontinuities in the boundary data, piecewise regular boundary surfaces, and interface conditions in the domain are all accommodated in the SSA.

Two two-dimensional example problems are than analyzed by utilizing the general SSA expressions. A material interface position in a nonhomogeneous hollow solid body is optimized in the first problem. A steady-state one-phase Stefan problem, involving a solidification free boundary with discontinuities, is then investigated as the second example problem. For both problems iterative numerical methods are proposed employing the BEM of discretization.

2 Primary Problem

Consider a three-dimensional isotropic solid body with temperature-independent material properties. Under steady-state conditions, the heat conduction equation may be written in V–σ as

$$\nabla \cdot (k \nabla T) + Q = 0 \tag{1}$$

where V is the volume of the solid body containing a discontinuity surface σ across which the thermal conductivity k may undergo a finite jump (refer to Fig. 1); T is the temperature. The discontinuity surface σ has its bounding curve γ_σ on the

Contributed by the Heat Transfer Division for publication in the JOURNAL OF HEAT TRANSFER. Manuscript received by the Heat Transfer Division February 3, 1987. Keywords: Conduction, Moving Boundaries, Phase-Change Phenomena.

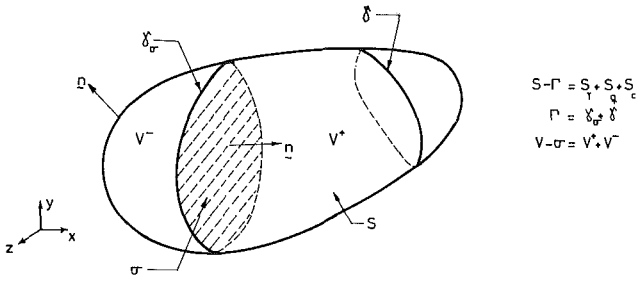

Fig. 1 Schematic of a solid body with a discontinuity surface σ and a discontinuity line γ

surface S of V, as shown in Fig. 1. However, σ may be a closed surface with γ_σ being a null set.

Mixed boundary conditions are imposed on S, where any discontinuities of the boundary data are assumed to occur, representatively across the surface curve γ of S. Thus,

$$\text{on } S_T \ : \ T = T^0 \tag{2}$$

$$\text{on } S_q \ : \ q_n = q^0 \tag{3}$$

$$\text{on } S_c \ : \ q_n = h(T - T_\infty) \tag{4}$$

where $S_T + S_q + S_c = S - \Gamma$; $\Gamma = \gamma_\sigma + \gamma$; T^0, q^0, h, and T_∞ are given quantities of space; $q_n = -k \nabla T \cdot \mathbf{n}$ is the normal heat flux, $\mathbf{n}$ is the unit vector normal to S.

The following "jump" conditions must also be satisfied on σ:

$$[\![T]\!] = 0 \text{ and } [\![q_n]\!] = 0 \tag{5}$$

where the quantities enclosed by the symbol $[\![\ ]\!]$ indicate the jump, that is, the difference between their values from the negative and positive sides of σ, for example

$$[\![T]\!] = T^- - T^+ \tag{6}$$

The unit normal vector $\mathbf{n}$ on σ is directed into V^+, where $V - \sigma = V^+ + V^-$. It is noted that equation $(5)_2$ may easily be extended to incorporate discontinuous normal heat fluxes, as in a two-phase Stefan problem, by taking a nonzero value (i.e., latent heat effect term) on the right-hand side of the equation.

3 Shape Sensitivity Analysis (SSA)

Assuming that the system's response of interest in a SIP may be written as an integral functional, a general performance criterion I may be defined as follows:

$$I = \int_{V-\sigma} f(T, \nabla T) dV + \int_{S-\Gamma} g(T, q_n) dS \tag{7}$$

where f and g are continuous and differentiable functions with respect to their arguments, except at a discontinuity surface σ and surface line Γ, respectively. It is noted that I may represent either an objective function to be minimized or an integral behavioral constraint to be satisfied.

3.1 Material Derivative Concept. The shape of the physical domain (and hence S and σ) is not fixed, but varied in the SSA. This variation of V under a transformation, characterized by a timelike parameter τ, may be regarded as a dynamic deformation of a continuous medium, with τ playing the role of time. Following Haug et al. (1984) this domain deformation is given by a deformation velocity $\mathbf{V}$ defined in the domain. The MD of functions and integrals may thus be defined by using the material velocity $\mathbf{V}$. In fact, the MD of a continuously differentiable function w is defined as

$$\dot{w} = w' + \nabla w \cdot \mathbf{V} \tag{8}$$

where $(\cdot)$ and $(\,)'$ denote the material and partial derivatives of $(\,)$, respectively, with respect to τ.

The MD of a general volume integral is given as follows:

$$\psi = \int_{V-\sigma} w dV \tag{9}$$

$$\dot{\psi} = \int_{V-\sigma} w' dV + \int_{S-\Gamma} w V_n dS + \int_\sigma [\![w]\!] V_n dA \tag{10}$$

where w may have discontinuities across $\sigma \epsilon V$ and $\Gamma \epsilon S$, and $V_n = \mathbf{V} \cdot \mathbf{n}$.

Nomenclature

a = width of the problem geometry in Example II
A = cross-sectional area of V^-
b^i = decision variable
f, g = integrands of I
h = heat transfer coefficient
H = boundary curvature
I = general performance criterion
J_1, J_2 = objective functions
k = thermal conductivity
m = amplitude of spatial variation of heat flux
$\mathbf{n}$ = unit vector normal to boundary (or interface)
n_x, n_y = Cartesian components of $\mathbf{n}$
q_n = normal boundary heat flux
q_n^* = adjoint normal boundary heat flux
q^0 = prescribed boundary heat flux
Q = distributed heat source
S = boundary surface
S_T, S_q, S_c = boundary segments
$\mathbf{t}$ = unit vector tangent to boundary
T = temperature
T^0 = prescribed temperature
T^* = adjoint temperature
T_∞ = ambient temperature
V = volume
$\mathbf{V}$ = deformation velocity
V_n = component of $\mathbf{V}$ normal to boundary (or interface)
V_μ = component of $\mathbf{V}$, tangent to boundary and normal to discontinuity line
w = general function
x, y, z = Cartesian coordinates
α^i = angle between b^i and the x axis
γ = discontinuity line on boundary surface S
γ_σ = bounding curve of σ on S
Γ = sum of γ_σ and γ
η = vertical distance of free boundary S_q^1 in Example II
θ^i = included angle between b^i and b^{i+1}
σ = discontinuity surface in volume
τ = timelike parameter characterizing shape variations
ψ = constraint function

Subscripts

$(\,)_{,n}$ = normal derivative of $(\,)$
$(\,)_{,s}$ = circumferential derivative of $(\,)$

Superscripts

$(\,)'$ = derivative of $(\,)$ with respect to τ
$(\cdot)$ = material (total) derivative of $(\,)$
$(\,)^-$, $(\,)^+$ = $(\,)$, evaluated on the negative and positive sides of σ, respectively

The MD of a general surface integral defined over a piecewise regular surface S, having a discontinuity line Γ, may be written in the following form:

$$\psi = \int_{S-\Gamma} w dS \tag{11}$$

$$\dot{\psi} = \int_{S-\Gamma} [w' + (w_{,n} + Hw) V_n] dS + \int_{\Gamma} [\![w]\!] V_\mu d\Gamma + \sum_j \int_{\Gamma_j} (w^+ V_{\mu^+} + w^- V_{\mu^-}) d\Gamma_j \tag{12}$$

where $(\ )_{,n}$ represents the normal derivative of $(\ )$; H is the mean surface curvature; V_μ is the component of $\mathbf{V}$ on S, normal to Γ and tangent to S; the summation is taken over the intersection lines Γ_j of piecewise regular surface sections; V_{μ^+}, and V_{μ^-} represent V_μ for the positive and negative sides of Γ_j (Mroz, 1987).

3.2 Outline of Procedure. The general performance criterion I is first augmented by incorporating the equilibrium equation (1) by using an adjoint function T^* (i.e., a Lagrange multiplier function). After using generalized Green's first identity, the MD of the augmented functional can be taken by employing equations (9)–(12). Green's first identity is again utilized, this time to increase the order of differentiation. Taking the MDs of the boundary and jump conditions (2)–(5) results in the following expressions of partial derivative (with respect to τ) forms on S and σ:

$$\text{on } S_T : T' = (\nabla T^0 - \nabla T) \cdot \mathbf{V} \tag{13}$$

$$\text{on } S_q : q_n' = (\nabla q^0 - \nabla q) \cdot \mathbf{V} \tag{14}$$

$$\text{on } S_c : q_n' = -[\nabla (hT_\infty) + \nabla (q_n - hT)] \cdot \mathbf{V} + hT' \tag{15}$$

$$\text{on } \sigma : [\![T']\!] = -[\![\nabla T \cdot \mathbf{n}]\!] V_n \tag{16}$$

$$\text{on } \sigma : [\![q_n']\!] = -[\![q_{n,n}]\!] V_n \tag{17}$$

Equations (13)–(17) are inserted into the SSA expression of the augmented functional.

In order to get rid of the local variations of the state variables, the adjoint temperature T^* is required to satisfy the following adjoint problem:

$$\text{in } V\text{-}\sigma : \nabla \cdot (k \nabla T^*) + \frac{\partial f}{\partial T} - \nabla \cdot \frac{\partial f}{\partial \nabla T} = 0 \tag{18}$$

$$\text{on } S_T : T^* = \frac{\partial g}{\partial q_n} \tag{19}$$

$$\text{on } S_q : q_n^* = -\frac{\partial g}{\partial T} - \frac{\partial f}{\partial \nabla T} \cdot \mathbf{n} \tag{20}$$

$$\text{on } S_c : q_n^* = hT^* - \frac{\partial g}{\partial T} - \frac{\partial f}{\partial \nabla T} \cdot \mathbf{n} - h \frac{\partial g}{\partial q_n} \tag{21}$$

$$\text{on } \sigma : [\![T^*]\!] = 0 \text{ and } [\![q_n^*]\!] = -\left[\!\left[\frac{\partial f}{\partial \nabla T} \right]\!\right] \cdot \mathbf{n} \tag{22}$$

where the adjoint normal heat flux is given by $q_n^* = -k \nabla T^* \cdot \mathbf{n}$.

3.3 Material Derivative of I. When the primary and adjoint problems are satisfied, the MD of I can finally be expressed as follows:

$$\begin{aligned} \dot{I} = & \int_{S-\Gamma} [f - k \nabla T \cdot \nabla T^* + QT^* + (g - q_n T^*)_{,n} \\ & + H(g - q_n T^*)] V_n dS \\ & + \int_{S_T} \left(\frac{\partial g}{\partial T} + \frac{\partial f}{\partial \nabla T} \cdot \mathbf{n} + q_n^* \right) (\nabla T^0 - \nabla T) \cdot \mathbf{V} dS \\ & + \int_{S_q} \left(\frac{\partial g}{\partial q_n} - T^* \right) (\nabla q^0 - \nabla q_n) \cdot \mathbf{V} dS \\ & - \int_{S_c} \left(\frac{\partial g}{\partial q_n} - T^* \right) [\nabla (hT_\infty) + \nabla (q_n - hT)] \cdot \mathbf{V} dS \\ & + \int_\sigma \left[\!\left[f - k \nabla T \cdot \nabla T^* + QT^* \right.\right. \\ & \left.\left. - \left(q_n^* + \frac{\partial f}{\partial \nabla T} \cdot \mathbf{n} \right) \nabla T \cdot \mathbf{n} - q_n T_{,n}^* \right]\!\right] V_n dA \\ & + \int_\Gamma [\![g - q_n T^*]\!] V_\mu d\Gamma + \sum_j \int_{\Gamma_j} [(g - q_n T^*)^+ V_{\mu^+} \\ & + (g - q_n T^*)^- V_{\mu^-}] d\Gamma_j \end{aligned} \tag{23}$$

It is noted that no domain integrals are present and that $\dot{I}$ is given in terms of boundary and interface perturbations only in the above equation. The outlined SSA must be performed for each objective function and/or constraint present in a shape inverse problem.

4 Example I: Interface Shape Optimization Problem

Consider an infinitely long hollow solid body composed of two dissimilar materials with thermal conductivities k^- and k^+ where the interface σ is assumed to be a closed surface (see Fig. 2). Assuming that the inner and outer boundary surfaces, S_T, and S_c, respectively, are known (i.e., fixed), the optimal shape configuration of the interface σ is sought corresponding to a minimum amount of total heat inflow through S_T, while holding the volume V^- fixed. Thus, the objective is to minimize

$$J_1 = -\int_{S_T} q_n dS \tag{24}$$

while the following equality constraint is satisfied:

$$\psi = \int_{V^-} dV - A = 0 \tag{25}$$

where J_1 is the objective function of Example I, ψ is the constraint function, and A is a problem parameter. Taking no heat sources, and prescribed temperature T^0 on S_T, and con-

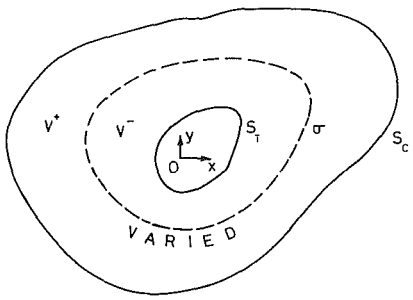

Fig. 2 Schematic of the interface shape optimization problem—Example I

vective condition with $T_\infty = 0$ on S_c, the MD of J_1 can directly be found from the general SSA given in the last section as

$$\dot{J}_1 = \int_\sigma \left(T_{,s} T^*_{,s} + \frac{q_n q_n^*}{k^- k^+} \right) (k^+ - k^-) V_n dA \tag{26}$$

where the circumferential derivative of a quantity along σ (compare a two-dimensional problem) is indicated by $(\ )_{,s}$. The primary problem and the adjoint problem corresponding to J_1 are given by the following equations:

$$\text{in } V\text{-}\sigma \ : \ \nabla \cdot (k \nabla T) = 0 \text{ and } \nabla \cdot (k \nabla T^*) = 0 \tag{27}$$

$$\text{on } S_T \ : \ T = T^0 \text{ and } T^* = -1 \tag{28}$$

$$\text{on } S_c \ : \ q_n = hT \text{ and } q_n^* = hT^* \tag{29}$$

$$\text{on } \sigma \ : \ [\![T]\!] = [\![T^*]\!] = [\![q_n]\!] = [\![q_n^*]\!] = 0 \tag{30}$$

Since the constraint ψ, equation (25), is explicit, no adjoint variables need be defined, and the MD of ψ simply follows from (9) and (10), i.e.,

$$\dot{\psi} = \int_\sigma V_n dA \tag{31}$$

5 Example II: Steady-State Solidification Problem

Siegel, in a series of papers (see, for example, 1982, 1986), has analyzed the solidification interface shapes in connection with continuous casting processes by using exact (i.e., analytical) methods. In a steady-state process, it has been assumed that the net amount of energy being locally removed from the freezing interface is equal to zero at all locations along the interface, which is kept at the freezing temperature. Example II of the present study consists of the same steady-state one-phase solidification (or Stefan) problem, as analyzed by Siegel (1982), with a generalization of one of the boundary conditions in order to introduce an extra boundary discontinuity. It is understood that this problem is only a simplified version of the time-dependent two-phase Stefan problems with moving boundaries (Crank, 1981).

The problem geometry of Example II is illustrated in Fig. 3, where the solidification interface S_q^1 is given by $\eta = \eta(x)$, on which the heat transfer from the liquid to the interface varies in a sinusoidal manner in the x direction. The primary problem is thus defined by the following equations:

$$\text{in } V \ : \ \nabla^2 T = 0 \tag{32}$$

$$\text{on } S_q^1 \ : \ q_n = -\left(1 + m\cos\frac{\pi x}{a}\right) \tag{33}$$

$$\text{on } S_q^2 \ : \ q_n = 0 \tag{34}$$

$$\text{on } S_T \ : \ T = 0 \tag{35}$$

$$\text{on } S_c \ : \ q_n = hT \tag{36}$$

where m and a denote the amplitude of the spatial variation of heat flux on S_q^1 and the width of the problem geometry, respectively. The IPC for the determination of the free boundary S_q^1, which is varied between the $x=0$ and $x=a$ vertical lines, is given by the freezing temperature condition, i.e.,

$$\text{on } S_q^1 : T = 1 \tag{37}$$

It is noted that all the quantities have been nondimensionalized exactly as in Siegel's (1982) analysis. When the heat transfer coefficient h in equation (36) is equal to zero, Example II becomes the same as Siegel's problem.

Using equation (37), the exact SIP may be converted into an optimal SIP by minimizing the objective function J_2 defined by

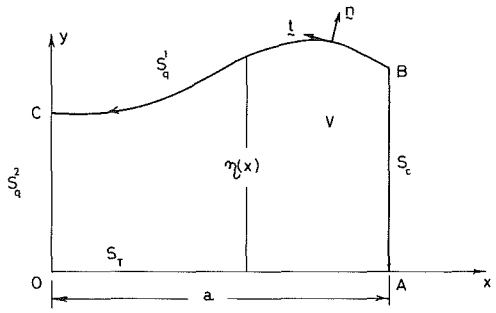

Fig. 3 Schematic of the steady-state one-phase Stefan problem—Example II

$$J_2 = \frac{1}{2}\int_{S_q^1} (T-1)^2 dS \tag{38}$$

subject to the system's equations (32)–(37), but without any isoperimetric constraints as in Example I. It may also be noted that the present problem is slightly different from shape identification problems, in which the IPCs are usually given on accessible (i.e., known) boundaries.

Using the general SSA expression (23), the MD of J_2 is obtained, including the discontinuity terms at the corners B and C, as follows:

$$\dot{J}_2 = \int_{S_q^1} \left\{ \left[(u-1)u_{,n} - u_{,s}\, u^*_{,s} + H u_{,n} u^* + \frac{H}{2}(u-1)^2 \right] n_2 - \frac{m a n_x n_y}{\pi} u^* \sin\frac{\pi x}{a} \right\} \delta\eta dS$$

$$+ [(u_{,n}u^*)_{B^-} - (n_x u_{,n} u^*)_{B^+}]\delta\eta_B + (n_x u_{,n} u^*)_{C^-}\delta\eta_c \tag{39}$$

In the above equation, since the variation of the boundary S_q^1 is constrained to lie in the y direction, the normal and circumferential components of $\mathbf{V}$ have been taken as $V_n = n_y \delta\eta$ and $V_s = n_x \delta\eta$, respectively, where $\delta\eta$ represents the vertical variation in S_q^1; n_x and n_y are the x and y components of $\mathbf{n}$. It is noted that the coefficient of $\delta\eta_B$ in equation (39) would be equal to zero if $h \to 0$, while that of $\delta\eta_c$ is expected to be zero anyhow, since S_q^1 will be horizontally located near the corner point C (see Fig. 3). The solution of the adjoint temperature T^*, which is needed for $\dot{J}_2$ calculations, is obtained through the following adjoint problem:

$$\text{on } V \ : \ \nabla^2 T^* = 0 \tag{40}$$

$$\text{on } S_q^1 \ : \ q_n^* = 1 - u \tag{41}$$

$$\text{on } S_q^2 \ : \ q_n^* = 0 \tag{42}$$

$$\text{on } S_T \ : \ T^* = 0 \tag{43}$$

$$\text{on } S_c \ : \ q_n^* = hT^* \tag{44}$$

6 Numerical Method of Solution

The interface σ and the free boundary segment S_q^1 in Examples I and II, respectively, are approximated by piecewise linear elements. In each example problem, different types of decision variables are utilized. In Example I, the radial lengths b^i between the ith vertex of the interface line element (see Fig. 4) and the origin are chosen as the decision variables which are varied. The angle that each of the decision variables, called the ray functions, makes with the x axis is denoted by α^i, and is held fixed. Hence, as the variation of σ proceeds in an iterative

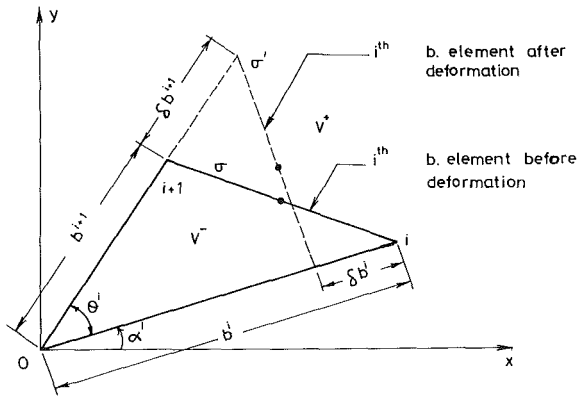

Fig. 4 Perturbation of the interface, σ, and the ray functions b^i, and $b^{i=1}$ in Example I

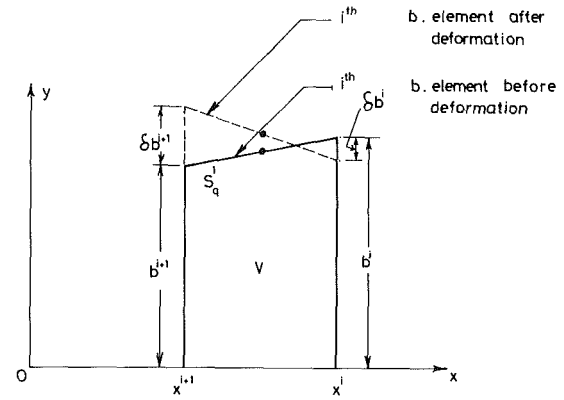

Fig. 5 Perturbation of the free boundary S_q^1, and the height functions b^i, and $b^{i=1}$ in Example II

solution scheme, the vertices of the interface line elements will always move along the lines of the ray functions. The angle between the ray functions b^i and b^{i+1} is thus a constant, and is denoted by θ^i.

The normal component of the interface deformation V_n on σ must be expressed in terms of the variations of b^i, i.e., δb^i. Referring to Fig. 4, the integral of V_n over an interface (boundary) element σ^e is thus given by the following first-order approximation (Mota Soares et al., 1984):

$$\int_{\sigma^e} V_n dA = \frac{1}{2}\sin\theta^i (b^{i+1}\delta b^i + b^i \delta b^{i+1}) \tag{45}$$

The volumetric (or area) constraint (25) can be converted into a surface (or line) integral by taking

$$\psi = \frac{1}{2}\sum_i |x^i y^{i+1} - x^{i+1} y^i| - A = 0 \tag{46}$$

where the summation is taken over the vertices of all the line elements of the surface of V^-, i.e., on S_T and σ, with an opposite numbering scheme on each segment.

In Example II, since the free boundary S_q^1 is forced to stay within the interval $0 \le x \le a$, the y coordinates of the extreme points of the line elements on S_q^1, called the height functions, are taken as the decision variables b^i (see Fig. 5). Thus, the vertices of the boundary line elements will always move in the vertical direction, and the horizontal distances between the height functions remain constant.

The curvature H needed in equation (39) is calculated from the relation $H = \mathbf{t} \cdot d\mathbf{n}/ds$ (Goetz, 1970), where $\mathbf{t}$ represents the unit tangential vector to S_q^1. The circumferential derivative of

Table 1 Comparison of exact and numerical solutions for Example I with uniform conditions

Solution Method	b_{opt} (error, percent)	J_1 (error, percent)	∇J_1 (error, percent)	$\nabla\psi$ (error, percent)	T_σ (error, percent)	T_c (error, percent)	q_{nT} (error, percent)
Present method, 48 boundary elements	0.4857 (1.06)	0.3399 (0.06)	0.3400 (1.39)	2.9744 (1.50)	0.9520 (0.50)	0.6813 (0.69)	−0.2722 (0.59)
Present method, 96 boundary elements	0.4818 (0.25)	0.3400 (0.03)	0.3435 (0.38)	3.0084 (0.37)	0.9524 (0.01)	0.6778 (0.18)	−0.2710 (0.15)
Exact Solution	0.4806	0.3401	0.3448	3.0197	0.9525	0.6766	−0.2706

Table 2 Numerical results for Example II using 40 and 64 boundary elements, with percentage errors indicated, as compared to Siegel's (1982) exact solutions, for $h=0$ and $m=0.3$

a	y_B (error, percent)	y_c (error, percent)	$(y_B-y_c)/2m$ (error, percent)
0.25	1.0148 (1.32)	0.9760 (0.32)	0.0647 (21.19)
	1.0256 (0.27)	0.9781 (0.10)	0.0792 (3.53)
0.50	1.0468 (0.95)	0.9543 (0.40)	0.1540 (6.21)
	1.0513 (0.52)	*0.9577 (0.05)*	*0.1560 (4.99)*
1.0	1.0971 (1.47)	0.9086 (0.93)	0.3142 (3.97)
	1.1099 (0.32)	0.9139 (0.35)	0.3267 (0.15)
2.0	1.1918 (2.01)	0.8431 (1.18)	0.5811 (3.95)
	1.2128 (0.29)	0.8509 (0.27)	0.6032 (0.30)
4.0	1.3018 (2.25)	0.7948 (0.81)	0.8450 (4.43)
	1.3268 (0.38)	0.7989 (0.30)	0.8798 (0.50)
8.0	1.3710 (1.90)	0.7797 (0.13)	0.9855 (4.46)
	1.3921 (0.40)	0.7781 (0.08)	1.0233 (0.79)

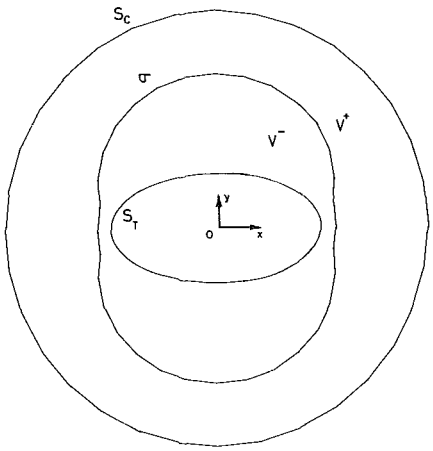

Fig. 6 Optimal interface σ configuration in Example I

$\mathbf{n}$ is approximated by a simple finite difference scheme, employing averaged normal directions at the vertices of the line elements. The integral of $\delta\eta$, i.e., the vertical variation of S_q^1, over a boundary line element can also easily be found in terms of δb^i, the variations in the height functions.

The BEM with constant elements (Banerjee and Butterfield, 1981; Brebbia, 1978) are chosen for the space discretization of the primary and adjoint problems in both Example I and II. No internal cells are needed, and the required normal temperature gradients are directly available from the BEM solutions. It is noted that a "zoned inhomogeneous body" formulation of BEM is necessary for Example I, while Example II deals with a single homogeneous body.

In an iterative solution procedure, starting from an initial guess for b^i, i.e., b^{i0}, it is possible to minimize the relevant objective function (i.e., J_1 or J_2) subject to ($\psi=0$ or nil) constraint by using, for example, a sequential quadratic programming algorithm (NAG, 1984). At each iteration step, the primary and adjoint problems are solved by the BEM, whose solutions are then substituted into the integral functionals and their MDs for the purpose of updating the decision variables b^i in both example problems.

7 Numerical Results and Discussion

For Example I, numerical results by the proposed procedure were first checked by exact solutions when the surfaces S_T, S_c, and σ (see Fig. 2) were of circular shape in a practically one-dimensional case. For this, the S_T and S_c boundary surfaces (i.e., lines) were set as circles with radii of 0.2 and 0.8, respectively. Some of the other problem parameters were prescribed as $h=0.1$, $T^0=1$, and $A=0.6$. The piecewise uniform thermal conductivities across the interface σ were also given as $k^-=1.0$ and $k^+=0.1$. Numerical results, obtained within five iterations starting from $b^{i0}=0.6$, are tabulated in Table 1. The numerical solutions for optimal values of the ray functions, b_{opt}, the gradients of J_1 and ψ with respect to b_{opt}, ∇J_1 and $\nabla\psi$, respectively, the temperatures on S_σ and S_c, T_σ and T_c, respectively, and the normal heat flux on S_T, q_{nT}, are shown in the table using a total of 48 and 96 boundary elements on the surfaces, along with their percentage errors as compared to their exact (i.e., analytical) solutions. It is seen that more accurate results are obtained employing a higher number of boundary elements (and also of ray functions). The reason for this is that with higher degrees of freedom the circles are more closely approximated and that the truncation errors in the potential solutions by the BEM are also diminished.

Figure 6 depicts the optimal solution for the interface σ in Example I when the inner surfce S_T was prescribed as an ellipse with semimajor and semiminor axis lengths of 0.4 and 0.2, respectively. All the other problem parameters were fixed as before. However, the lower and upper bounds for the ray functions were such that $0.45\le b^i\le 0.60$. Convergence within a tolerance of 10^{-4} was achieved within ten iterations in this case. The optimal σ distribution is seen to be situated in such a way that there is less contribution of material with the higher $k^-=1.0$ conductivity to V^- in regions of higher temperature gradients, as dictated by the minimization of J_1, equation (24), while holding the area of V^- constant.

In Example II, numerical results by the present procedure were first compared with the exact (i.e., analytical) solutions obtained by Siegel (1982), when the heat transfer coefficients h on S_c was taken as zero. Denoting the y coordinates of the points B and C (see Fig. 3) by y_B and y_C, respectively, the present numerical solutions by employing 40 and 64 boundary elements are tabulated in Table 2, along with their percentage errors (written in parentheses) as compared to Siegel's exact results, for $m=0.3$. It is noted that an average of nine iterations were needed for convergence (with a tolerance of 10^{-6}) for this steady-state one-phase Stefan problem.

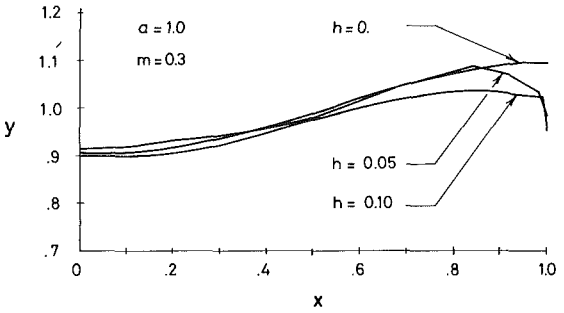

Fig. 7 Free boundary S_q^1 shapes for various h values in Example II

Lastly, Fig. 7 depicts the free boundary shape of S_q^1 for Example II for various values of h, when $a=1.0$ and $m=0.3$. It is seen from the figure that the boundary is horizontal near $x=0$ and 1 for $h=0$, as expected, while it deviates from zero slope at $x=1$ with nonzero h values on S_c. It is also noted that finer boundary elements have been used near $x=1$ in order to take care of the boundary singularity present at corner B (Fig. 3).

8 Conclusions

The proposed numerical solution scheme for shape optimization and identification problems seems to be very promising in view of the close agreement of the numerical results with exact solutions. However, as all inverse problems are ill-posed (Beck et al., 1985), care should always be exercised in the implementation of the method. For especially exact inverse problems (e.g., identification or Stefan problems), with no constraints present on the decision variables, a good initial guess for the free boundaries is in order (compare "infinitesimal inverse" problem). A priori knowledge of the location of boundary discontinuities, which may not be available in every inverse problem, helps for correctly evaluating the sensitivity expressions of integral functionals. Finally, it may be said that the present study does not pretend to treat fully the extensive and difficult subject of inverse problems, but only proposes a possible numerical solution scheme for free boundary problems in heat transfer.

References

Banerjee, P. K., and Butterfield, R., 1981, *Boundary Element Methods in Engineering Science*, McGraw-Hill, New York.

Barone, M. R., and Caulk, D. A., 1982, "Optimal Arrangement of Holes in a Two-Dimensional Heat Conductor by a Special Boundary Integral Method," *Int. J. Numer. Meth. Eng'g.*, Vol. 18, pp. 675-685.

Beck, J. V., Blackwell, B., and St. Clair, C. R., Jr., 1985, *Inverse Heat Conduction: Ill-Posed Problems*, Wiley, New York.

Bell, G. E., 1985, "Inverse Formulations as a Method for Solving Certain Melting and Freezing Problems," *Numerical Methods in Heat Transfer*, R. W. Lewis, ed., Wiley, New York, Vol. III, pp. 59-78.

Brebbia, C. A., 1978, *The Boundary Element Method for Engineers*, Pentech Press, London.

Crank, J., 1981, "How to Deal with Moving Boundaries in Thermal Problems," *Numerical Methods in Heat Transfer*, R. W. Lewis, ed., Wiley, New York, Vol. III, pp. 177-200.

Curtis, J. P., 1983, "Optimization of Homogeneous Thermal Insulation Layers," *Int. J. Solids Structures*, Vol. 19, pp. 813-823.

Dems, K., 1987, "Sensitivity Analysis in Thermoelasticity Problems," *Computer Aided Optimal Design: Structural and Mechanical Systems*, C. A. Mota Soares, ed., NATO ASI Series, Springer-Verlag, Berlin, Vol. F27, pp. 563-572.

Dems, K., and Mroz, Z., 1984, "Variational Approach by Means of Adjoint Systems to Structural Optimization and Sensitivity Analysis. II—Structure Shape Variation," *Int. J. Solids Structures*, Vol. 20, pp. 527-552.

Goetz, A., 1970, *Introduction to Differential Geometry*, Addison Wesley, London.

Haug, E. J., Choi, K. K., and Komkov, V., 1986, *Design Sensitivity Analysis of Structural Systems*, Academic Press, New York.

Hrymak, A. N., McRae, G. J., and Westerberg, A. W., 1985, "Combined Analysis and Optimization of Extended Heat Transfer Surfaces," ASME JOURNAL OF HEAT TRANSFER, Vol. 107, pp. 527-532.

Hsieh, C. K., and Kassab, A. J., 1986, "A General Method for the Solution of Inverse Heat Conduction Problems With Partially Unknown System Geometries," *Int. J. Heat Mass Transfer*, Vol. 29, pp. 47-58.

Hsieh, C. K., Wang, X. A., and Yang, S. L., 1982, "Infrared Scanning Thermography for a Quantitative Detection of Cavities in a Plane Slab and a Rectangular Prism," *J. Nondestructive Evaluation*, Vol. 3, pp. 64-74.

Kagawa, Y., Murai, T., and Matsumoto, O., 1983, "Finite Element Iterative Techniques for Determining the Interface Boundary Between Laplace and Poisson Domains—Characteristic Analysis of a Field Effect Transistor," *Int. J. Numer. Meth. Eng'g.*, Vol. 19, pp. 315-325.

Meric, R. A., 1986, "Optimal Thermal Insulation by the Boundary Element Method," *Numerical Heat Transfer*, Vol. 9, pp. 163-182.

Meric, R. A., 1987, "Boundary Elements in Shape Optimization of Thermoelastic Solids," *Computer Aided Optimal Design: Structural and Mechanical Systems*, C. A. Mota Soares, ed., NATO ASI Series, Springer-Verlag, Berlin, Vol. F27, pp. 643-652.

Meric, R. A., 1988, "Shape Design Sensitivity Analysis for Nonlinear and Anisotropic Heat Conducting Solids and Shape Optimization by the BEM," *Int. J. Numer. Meth. Eng'g.*, Vol. 26, pp. 109-120.

Mota Soares, C. A., Rodrigues, H. C., Oliveria Faria, L. M., and Haug, E. J., 1984, "Optimization of the Geometry of Shafts Using Boundary Elements," ASME *Journal of Mech. Transmission Automation in Design*, Vol. 106, pp. 199-202.

Mota Soares, C. A., 1987, *Computer Aided Optimal Design: Structural and Mechanical Systems*, NATO ASI Series, Springer-Verlag, Berlin, Vol. F27.

Mroz, Z., 1987, "Sensitivity Analysis and Optimal Design With Account for Varying Shape and Support Conditions," *Computer Aided Optimal Design: Structural and Mechanical Systems*, C. A. Mota Soares, ed., NATO ASI Series, Springer-Verlag, Berlin, Vol. F27, pp. 407-438.

Murai, T., and Kagawa, Y., 1986, "Boundary Element Iterative Techniques for Determining the Interface Boundary Between Two Laplace Domains—A Basic Study of Impedance Plethysmography as an Inverse Problem," *Int. J. Numer. Meth. Eng'g.*, Vol. 23, pp. 35-47.

NAG Library, 1984, Mark 11, The Numerical Algorithms Group, Oxford, United Kingdom.

Natori, M., and Kawarada, H., 1981, "An Application of the Integrated Penalty Method to Free Boundary Problems of Laplace Equation," *Numer. Funct. Analy. and Optimiz.*, Vol. 3, pp. 1-17.

Siegel, R., 1986, "Free Boundary Shape of a Convectively Cooled Solidified Region," *Int. J. Heat Mass Transfer*, Vol. 29, pp. 309-315.

Siegel, R., 1982, "Analysis of Solidification Interface Shape Resulting From Applied Sinusoidal Heating," ASME JOURNAL OF HEAT TRANSFER, Vol. 104, pp. 13-18.

Tanaka, M., and Masuda, Y., 1986, "Boundary Element Method Applied to Some Inverse Problems," *Engineering Analysis*, Vol. 3, pp. 138-143.

Conduction Heating of Objects of Simple Shape in a Fluid With Finite Heat Capacity

Q. T. Pham
Meat Industry Research Institute of New Zealand (Inc.), Hamilton, New Zealand

A unified analytical solution and an approximate method are presented for calculating the time to cool or heat an object of simple shape to a given mean temperature, using a fluid with finite heat capacity in batch, parallel-flow, or counterflow modes. In the approximate method, an equivalent constant fluid temperature is calculated, which would give the same log-mean temperature difference. The cooling time at this equivalent temperature is found by conventional methods, then multiplied by a correction factor calculated from a simple regression equation.

Introduction

The conduction heating or cooling without phase change of homogeneous objects of simple shape has been extensively analyzed (Carslaw and Jaeger, 1959). In most cases considered, the boundary conditions are either constant or predetermined functions of time. In many cases of industrial importance, however, the environmental temperature depends on the heat released or absorbed by the objects. This happens in the counterflow, parallel-flow, or batchwise heating/cooling of products using noncondensing, nonevaporating fluids. This paper presents a unified solution to these problems and introduces simple approximate methods to take into account the temperature change in the environment due to product heating or cooling.

Analysis

Consider a solid object of simple shape (slab of infinite area, infinite cylinder, or sphere) immersed in a well-mixed fluid with mass M_f. Heat is transferred between the fluid and the solid by convection at the surface and by conduction inside the solid.

On the solid side the following equations apply:

$$\partial T/\partial t = \alpha\left[\partial^2 T/\partial r^2 + \left(\frac{n-1}{r}\right)\partial T/\partial r\right] \tag{1}$$

with initial and boundary conditions

$$T = T_1 \qquad \text{at } t = 0 \tag{2}$$

$$T_f = T_{f1} \qquad \text{at } t = 0 \tag{3}$$

$$k(\partial T/\partial r) = h(T_f - T) \qquad \text{at } r = R \tag{4}$$

On the fluid side:

$$Ak(\partial T/\partial r) + c_f M_f(dT_f/dt) = 0 \qquad \text{at } r = R \tag{5}$$

For continuous operations such as in a moving-bed type heat exchanger, the same equation applies if t is replaced by x/v_s, where x is the distance from the solids' inlet and v_s is the velocity of the solid. For this case, A would then be the surface area of the solids that move through the equipment in unit time, and M_f the mass of fluid moving through in the same time interval.

If the fluid flows in the opposite direction to the solid (counterflow situation), then as one moves along x, the temperatures of the solid and fluid vary in the same direction. The solid "sees" a fluid that becomes cooler as heat is given up to it: This is taken into account by assigning a negative sign to $c_f M_f/A$.

Thus, the same set of equations applies to batch, parallel-flow, or counterflow heat (or mass) transfer processes.

In dimensionless form, equations (1)–(5) become:

$$\partial\theta/\partial\tau = \partial^2\theta/\partial\xi^2 + \left(\frac{n-1}{\xi}\right)\cdot\partial\theta/\partial\xi \tag{6}$$

$$\theta = 0 \qquad \text{at } \tau = 0 \tag{7}$$

$$\theta_f = 1 \qquad \text{at } \tau = 0 \tag{8}$$

$$\partial\theta/\partial\xi + \mathrm{Bi}(\theta - \theta_f) = 0 \qquad \text{at } \xi = 1 \tag{9}$$

$$nK(\partial\theta/\partial\xi) + d\theta_f/d\tau = 0 \qquad \text{at } \xi = 1 \tag{10}$$

The dimensionless temperature θ is defined as (change in solid temperature)/(temperature difference between solid and fluid at time 0, or at solid inlet). In counterflow situations, the solid inlet is the fluid *outlet* and the fluid temperature at that point is not known beforehand, so users prefer to work in terms of ϕ = (change in solid temperature)/(temperature difference between entering solid and liquid). It can readily be shown that

$$\phi = \theta \text{ for batch or parallel flow} \tag{11}$$

$$\phi = \theta/(1 - K\theta_m) \text{ for counterflow} \tag{12}$$

Equations (6)–(10) can be solved using Laplace transforms. Solutions for a variety of cases have been presented in various papers (Carslaw and Jaeger, 1959; Jaeger, 1945; Goldfarb, 1954; Mikhailov, 1966, 1970; Farritor and Tao, 1972), but these solutions are rather unwieldy and incomplete or shape-specific. A solution covering the whole range of K is not available. Therefore the complete solution is given below.

Mean Temperature of Solids

(*a*) $K > -1$:

$$\theta_m = 1/(1+K) - \sum_{j=1}^{\infty} A_{mj}\exp(-\delta_j^2\tau) \tag{13}$$

(*b*) $K = -1$:

$$\theta_m = \frac{n(n+2)\mathrm{Bi}\tau}{\mathrm{Bi}+n+2} + \frac{n\mathrm{Bi}^2}{(n+4)(\mathrm{Bi}+n+2)^2} - \sum_{j=1}^{\infty} A_{mj}\exp(-\delta_j^2\tau) \tag{14}$$

Contributed by the Heat Transfer Division for publication in the JOURNAL OF HEAT TRANSFER. Manuscript received by the Heat Transfer Division April 24, 1987. Keywords: Conduction, Materials Processing and Manufacturing Processes, Transient and Unsteady Heat Transfer.

Table 1 Functions used in calculating the roots δ_j, γ

	Slab	Cylinder	Sphere
$g_1(x)$	$\cos x$	$J_0(x)$	$\sin(x)/x$
$g_2(x)$	$\sin x$	$J_1(x)$	$\sin(x)/x^2 - \cos(x)/x$
$g_3(x)$	$\cosh x$	$I_0(x)$	$\sinh(x)/x$
$g_4(x)$	$\sinh x$	$I_1(x)$	$\cosh(x)/x - \sinh(x)/x^2$

Note: I_0, I_1 are modified Bessel functions of order 0 and 1.

(c) $K < -1$:

$$\theta_m = 1/(1+K) + D_m \exp(\gamma^2\tau) - \sum_{j=1}^{\infty} A_{mj}\exp(-\delta_j^2\tau) \quad (15)$$

where

$$A_{mj} = 2n/[(\mathrm{Bi}+2-n)\delta_j^2/\mathrm{Bi} + n^2K + (nK-\delta_j^2/\mathrm{Bi})^2] \quad (16)$$

$$D_m = 2n/[(\mathrm{Bi}+2-n)\gamma^2/\mathrm{Bi} - n^2K - (nK+\gamma^2/\mathrm{Bi})^2] \quad (17)$$

δ_j is the jth root of

$$g_1(\delta)/g_2(\delta) = \delta/\mathrm{Bi} - nK/\delta \quad (18)$$

γ is the root of

$$g_3(\gamma)/g_4(\gamma) = -\gamma/\mathrm{Bi} - nK/\gamma \quad (19)$$

and g_1 to g_4 are shape-dependent functions given in Table 1.

Local Temperature in Solid

(a) $K > -1$:

$$\theta = 1/(1+K) - \sum_{j=1}^{\infty} A_j \exp(-\delta_j^2\tau) \quad (20)$$

(b) $K = -1$:

$$\theta = \frac{\xi^2/2 + n\tau}{1/(n+2) + 1/\mathrm{Bi}} - \frac{n/(n+4) + n/\mathrm{Bi}}{2(n+2)[1/(n+2)+1/\mathrm{Bi}]^2} - \sum_{j=1}^{\infty} A_j \exp(-\delta_j^2\tau) \quad (21)$$

(c) $K < -1$:

$$\theta = 1/(1+K) + D\cdot\exp(\gamma^2\tau) - \sum_{j=1}^{\infty} A_j \exp(-\delta_j^2\tau) \quad (22)$$

where

$$A_j = A_{mj}\cdot\delta_j g_1(\delta_j\xi)/[n\, g_2(\delta_j)] \quad (23)$$

$$D = D_m\cdot\gamma g_3(\gamma\xi)/[n\, g_4(\gamma)] \quad (24)$$

Equations (13)–(15) and (20)–(22) indicate that for $K > -1$ [i.e., for batch or parallel flow ($K > 0$), or counterflow where the thermal capacity of the fluid is greater than that of the solid ($-1 < K < 0$)] the solution tends to a finite value $1/(1+K)$. This is because the fluid either tends to the solid's temperature (for batch or parallel flow), or cools/heats more slowly than the solid, so that the temperature difference between the two eventually vanishes.

$K < -1$ represents counterflow with the solid thermal capacity being greater. This is an unstable situation since the liquid cools or heats faster than the solid, so that the temperature difference between the two, and hence the temperature of each, increases exponentially, as shown by the presence of the term $\exp(\gamma^2\tau)$ in equations (15) and (22).

In a real-life situation, the process would not continue indefinitely but would stop at a finite time, so the exponential increase poses no problem. When $K = -1$, there is

Nomenclature

A = surface area, m^2
A_j, A_{mj} = coefficients, equations (16) and (23)
Bi = hR/k_s = Biot number
c = specific heat, J/kg K
D, D_m = coefficients, equations (17) and (24)
E = parameter defined in equation (29)
g_1, g_2, g_3, g_4 = functions defined in Table 1
h = heat transfer coefficient, W/m^{2}K
k = thermal conductivity, W/m K
K = $M_s c_s/M_f c_f$
M = mass, kg
n = shape index (1 for slab, 2 for cylinder, 3 for sphere)
r = space coordinate, m
R = half-thickness or radius of object, m
t = time, s
t_c = time to cool object from T_1 to T_2, s
t_e = time to cool object from T_1 to T_2 when fluid temperature is T_e, s
T = temperature of object, K
T_f = fluid temperature, K
T_{f1}, T_{f2} = temperature of fluid at start (or inlet) and finish (or outlet), K
T_e = equivalent fluid temperature, i.e., constant temperature that would yield the same log-mean temperature difference, K
T_m = mean object temperature, K
T_1, T_2 = initial (inlet) and final (outlet) mean object temperature, K
ΔT_M = log-mean temperature difference, equation (25) or (26), K ($\Delta T_m > 0$ for solid cooling, < 0 for solid heating)
U = value of ϕ_m at solid outlet, i.e., change in mean solid temperature/temperature difference between entering solids and fluid
x = distance from solid inlet, m
Y = t_c/t_e = time correction factor
α = thermal diffusivity of solid, m^2/s
γ = root of equation (19)
δ_j = jth root of equation (18)
θ = dimensionless temperature based on temperature difference between fluid and solid at solid inlet; $\theta = \phi$ for parallel flow or batch; $\theta = (T - T_1)/(T_{f2} - T_1)$ for counterflow
ξ = r/R
τ = $\alpha t/R^2$ = dimensionless time
ϕ = $(T - T_1)/(T_{f1} - T_1)$ = dimensionless temperature

Subscripts

f = fluid
m = mean (object temperature)
s = solid object

counterflow with a constant difference between the mean solid temperature and the fluid temperature. Therefore, after an initial period, the temperature varies linearly with time, equations (14) and (21). Putting $K = 0$ leads to the familiar case of constant fluid temperature.

Approximate Method

The full solutions, equations (13)–(24), are of use only to those who have access to and can program computers. In this section, a simple approximate approach is proposed, which can be used if only the fluid or mean solid temperature is wanted.

The starting point of the method is the well-known fact that for Bi = 0 (external resistance controlling) the cooling time t_c from a given temperature T_1 to a given (mean) temperature T_2 is a function of the log-mean temperature difference (LMTD) ΔT_M, where

$$\Delta T_M = \frac{(T_{f1} - T_1) - (T_{f2} - T_2)}{\ln[(T_{f1} - T_1)/(T_{f2} - T_2)]} \tag{25}$$

for batch or parallel-flow processes, and

$$\Delta T_M = \frac{(T_{f1} - T_2) - (T_{f2} - T_1)}{\ln[(T_{f1} - T_2)/(T_{f2} - T_1)]} \tag{26}$$

for counterflow processes.

Thus, the cooling time for Bi = 0 is unchanged when $K = 0$ (i.e., $T_f = T_e$, a constant), provided that the LMTD remains the same

$$\frac{(T_2 - T_e) - (T_1 - T_e)}{\ln[(T_2 - T_e)/(T_1 - T_e)]} = \Delta T_M \tag{27}$$

[ΔT_M given by equation (25) or (26)]. Solution of equation (27) gives the equivalent temperature

$$T_e = (E\,T_2 - T_1)/(E - 1) \tag{28}$$

where

$$E = \exp[(T_1 - T_2)/\Delta T_M] \tag{29}$$

($\Delta T_M > 0$ for cooling, $\Delta T_M < 0$ for heating of solid).

In the general case (Bi > 0), the cooling time from $T_m = T_1$ to $T_m = T_2$ in an environmental temperature of T_e is t_e. The ratio $Y = t_c/t_e$ depends on Bi, K, and U. The procedure suggested is to calculate t_e from existing equations, tables, or charts and apply a correction factor Y to obtain t_c.

Using equations (13)–(19) the correction factor Y was calculated over the following range of parameters: Bi = 0 to 1000; $K = -2$ to $+2$; $U = 0$ to $0.9U_{\max}$, where

$$\begin{aligned} U_{\max} &= 1 \text{ for counterflow with } K > -1 \\ &= -1/K \text{ for counterflow with } K < -1 \\ &= 1/(1+K) \text{ for parallel flow or batch} \end{aligned}$$

To correlate the results, an approximate equation is sought that would correctly predict that $Y \to 1$ as Bi $\to 0$, $U \to 0$, or $K \to 0$. The following equation was chosen:

$$Y = 1 + a[1 - \exp(bU^c)]\exp(d\mathrm{Bi}^e)/(1/|K| + f) \tag{30}$$

The parameters a to f were found by a procedure that minimizes the sum of square errors in Y over the ranges of variables Bi, U, K given earlier. Their values are shown in Table 2. In the range specified earlier, the equation agrees with analytical results to within ± 5 percent.

Table 2 Parameters for equation (30)

Physical situation	a	b	c	d	e	f
Counterflow						
Slab	−0.186	−7.20	1.42	−3.18	−0.77	+0.01
Cylinder	−0.294	−4.12	1.49	−3.66	−0.75	−0.03
Sphere	−0.377	−2.99	1.53	−4.12	−0.75	−0.06
Parallel flow or batch						
Slab	0.192	−10.22	1.69	−3.27	−0.72	−0.18
Cylinder	0.346	−7.47	2.06	−3.80	−0.67	−0.27
Sphere	0.442	−7.86	2.32	−4.24	−0.64	−0.30

Example

A sphere is cooled from 100°C in a well-stirred fluid at 0°C. The fluid-to-solid heat capacity ratio is $K = 1.0$. The sphere's thermal diffusivity, specific heat, and radius are all unity, and the heat transfer coefficient is such that Bi = 10.0. Calculate the time for the mean temperature of the sphere to fall to 52.1°C.

Solution: When the sphere is at 52.1°C, the fluid temperature is at $100 - 52.1 = 47.9$°C.

$$\Delta T_M = \frac{(100 - 0) - (52.1 - 47.9)}{\ln[(100 - 0)/(52.1 - 47.9)]} = 30.2\text{°C}.$$

From equation (29), $E = \exp[47.9/30.2] = 4.89$.

From equation (28), the equivalent fluid temperature is

$$T_e = (4.89 \times 52.1 - 100)/(4.89 - 1) = 39.8\text{°C}.$$

The dimensionless time to cool from 100°C to 52.1°C in a fluid at a constant temperature of 39.8°C for Bi = 10 can be found from charts or tables in standard texts (e.g., Kreith, 1965), or by using an exponential approximation (Ramaswamy and Tung, 1982) and is $\tau = 0.164$.

The correction factor Y is found from equation (30) using Bi = 10, $U = 0.479$, $K = 1$ and a to f from the last line of Table 2. The value $Y = 1.18$ is obtained.

Hence the cooling time required (in any consistent system of units) is

$$t_c = \tau \times Y = 0.164 \times 1.18 = 0.194$$

The analytical result is $t_c = 0.200$ [6].

References

Carslaw, H. S., and Jaeger, J. C., 1959, *Conduction of Heat in Solids*, 2nd ed., Oxford University Press, United Kingdom.

Farritor, R. E., and Tao, L. C., 1972, "Transient Mass Transport Between a finite Volume of Homogenized Fluid and a Sphere With Finite Interfacial Transport Coefficients," *Int. J. Heat Mass Transfer*, Vol. 15, pp. 1179–1183.

Goldfarb, E. M., 1954, "Heat Transfer to an Object in Parallel and Counterflow Gas Stream" [in Russian], *Zh. Teknich. Fiziki*, Vol. 24, pp. 1012–1019.

Jaeger, J. C., 1945, "Conduction of Heat in a Slab in Contact With Well Stirred Fluid," *Proc. Cambridge Phil. Soc.*, Vol. 41, pp. 43–49.

Kreith, F., 1965, *Principles of Heat Transfer*, Internat. Textbook Co., London; 4th ed. revised by M. Bohn, Harper & Row, London, 1986.

Mikhailov, M. D., 1966, "Warme- oder Stoffubertragung an eifachen Korper in einem begrentzen Flussigkeitstraum," *Forsch. Ingenieur*, Vol. 32, pp. 101–110, 147–150.

Mikhailov, M. D., 1970, "Body Heating in Bounded Volume of Finely Mixed Liquid," *J. Engng. Phys.*, Vol. 13, pp. 401–405.

Ramaswamy, K. V., Lo and Tung, M. A., 1982, "Simplified Equations for Transient Temperatures in Conductive Foods With Convective Heat Transfer at the Surface," *J. Food Sci.*, Vol. 47, pp. 2042–2047.

N. Zabaras
Assistant Professor,
Department of Mechanical Engineering,
University of Minnesota,
Minneapolis, MN 55455
Assoc. Mem. ASME

S. Mukherjee
Professor,
Department of Theoretical and Applied Mechanics,
Cornell University,
Ithaca, NY 14853
Mem. ASME

O. Richmond
ALCOA Laboratories,
Alcoa Center, PA 15069
Mem. ASME

An Analysis of Inverse Heat Transfer Problems With Phase Changes Using an Integral Method

This paper provides a methodology for the solution of certain inverse heat transfer problems with phase changes. It is aimed particularly at the design of casting processes. The idea is to use the inverse method to calculate the boundary flux history that will achieve the velocities and fluxes at the freezing front that are needed to control liquid feeding to the front, as well as yield the desired cast structure. The proposed method also can be applied to predict the freezing front motion using temperature measurements at internal points. A boundary element analysis with constant elements is used here in conjunction with Beck's sensitivity analysis. The accuracy of the method is illustrated through one-dimensional numerical examples. It is demonstrated that, by using an integral formulation, one can extend all of the current methods for solving inverse heat conduction problems with stationary boundaries, to inverse Stefan problems. Such problems are of great technological significance.

Introduction

Heat transfer problems with phase changes are very common in physics and engineering. Typical examples include the melting and casting processes for metals and alloys. Even when these problems involve the linear heat conduction equation, they are nonlinear owing to the presence of a moving interface.

A heat transfer problem is considered as direct when the temperature or the flux histories at the boundary of a specified domain are prescribed as functions of time. Sometimes, however, the boundary heat flux and temperature histories must be determined from transient temperature measurements at one or more interior locations of the specified domain. This is the case of a typical inverse problem (Beck et al., 1985). Another case of inverse problems, which is the subject of this paper, includes Stefan problems where the temperature, flux, and velocity are prescribed on the interface, while the temperature and the flux on the stationary boundary of the domain of interest are unknown and must be determined by the analysis. This last problem is of an inverse type since both the temperature and the flux are prescribed on one part of the boundary of the domain, while neither the temperature nor the flux is prescribed on the remaining part of it.

There are many potential applications of the latter problem to the design of casting processes. The fluxes and velocities at the solidification front determine the cast structure (Flemings, 1974). Thus, the cast structure can be controlled by determining the external boundary fluxes required to achieve certain desired fluxes and velocities at the solidification front. Also, in complex castings, where liquid feeding to the contracting solid front is essential for good quality, the time of casting can be optimized and choking of the liquid flow can be prevented by achieving desirable velocities at the freezing front.

Many numerical methods have been reported in the literature for the solution of direct heat transfer problems with phase changes. A short literature review has been given by Zabaras and Mukherjee (1987) and for more information the book by Crank (1984) is especially recommended.

It is well known that an inverse problem is much more difficult to solve numerically than a direct problem and that its solution strongly depends upon the amount of error in the prescribed data. An extensive literature review of inverse heat transfer problems without phase changes is given in a recent book by Beck et al. (1985). The limited amount of literature on the general subject of inverse heat transfer with phase changes includes Hsu et al. (1986), Frederick and Greif (1985), and Katz and Rubinsky (1984).

An extension of the sensitivity analysis procedure proposed by Beck (1968, 1970) and Beck et al. (1982), to heat transfer with phase changes, is presented in this paper. An integral formulation has been used. Such an approach considers temperature and flux as two independent variables. This procedure allows easy calculation of the sensitivity coefficients and provides certain other advantages by permitting direct calculation of the surface fluxes. It should be noted that the surface flux is considered the primary unknown of the problem in this analysis and that the boundary temperature is calculated afterward in a rather straightforward manner.

Following a precise definition of the problem of interest, a review of the integral formulation and implementation is given here. A calculation of Beck's sensitivity coefficients using the integral formulation is next. Finally, typical numerical results are reported and discussed. Even though this paper is concerned with one-dimensional geometries, extension of the proposed method to higher dimensions is rather straightforward and it will be the subject of a future publication.

Problem Definition

Consider one-dimensional heat conduction in a mold of length l occupied originally by liquid (melt) of uniform temperature T_{in} (Fig. 1). Here $h(t)$ denotes the position of the solidification front at time t and $\dot{h}(t)$ is the speed with which this front moves. It is assumed that $h(0) = 0$ and that the thermal properties of both solid and liquid phase are constant.

The governing equations with the prescribed boundary and initial conditions, for the solid and the liquid phase, are as follows (Carslaw and Jaeger, 1959):

Contributed by the Heat Transfer Division for publication in the JOURNAL OF HEAT TRANSFER. Manuscript received by the Heat Transfer Division December 12, 1986. Keywords: Modeling and Scaling, Phase-Change Phenomena.

For the solid phase:

$$\frac{\partial^2 T_s}{\partial x^2}(x, t) = \frac{1}{\alpha_s}\frac{\partial T_s}{\partial t}(x, t), \qquad 0 \le x < h(t) \tag{1}$$

$$T_s(x, t) = T_m, \qquad x = h(t) \tag{2}$$

$$\frac{\partial T_s}{\partial x}(x, t) = q_{ms}(t), \qquad x = h(t) \tag{3}$$

For the liquid phase:

$$\frac{\partial^2 T_l}{\partial x^2}(x, t) = \frac{1}{\alpha_l}\frac{\partial T_l}{\partial t}(x, t), \qquad h(t) < x \le l \tag{4}$$

$$T_l(x, t) = T_m, \qquad x = h(t) \tag{5}$$

$$\frac{\partial T_l}{\partial x}(x, t) \equiv q_{ml}(t), \qquad x = h(t) \tag{6}$$

with the initial conditions

$$T_l(x, 0) \equiv T_{in}, \qquad 0 \le x \le l \tag{7}$$

$$h(0) = 0 \tag{8}$$

where $T(x, t)$ is the temperature at time t, at position x, T_m is the constant melting temperature, and α, the thermal diffusivity, equals $k/\rho c$ in terms of the conductivity, density, and the specific heat of the material. The subscripts s and l denote the solid and liquid phases, respectively, and the symbol q_m is used to represent the known normal temperature derivatives on the moving front $x = h(t)$.

The interface velocity $\dot{h}(t)$ is related to the temperature gradients q_{ms} and q_{ml} through an energy balance at the interface, which takes the form:

$$k_s q_{ms} - k_l q_{ml} = \rho L \dot{h}, \qquad x = h(t) \tag{9}$$

where L is the latent heat of fusion.

Note that equation (9) makes it possible to have a small freezing front velocity while keeping q_{ms} and q_{ml} large. The practical significance of this observation is great, as has been reported earlier by Flemings (1974).

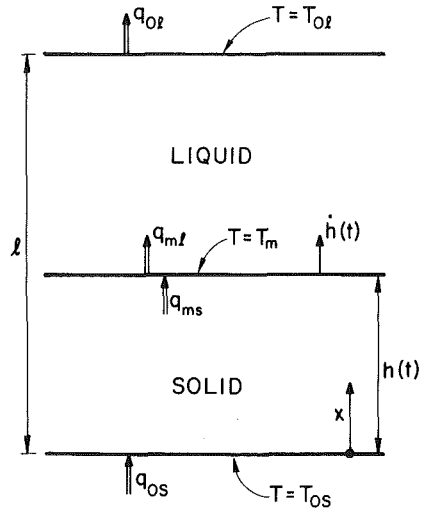

Fig. 1 Explanation of terminology used for the one-dimensional inverse solidification problem

Of interest is the following inverse problem: Given $q_{ms}(t)$, $q_{ml}(t)$, T_m, $\dot{h}$(t), T_{in}, and l, find $(\partial T_s/\partial x)\ (0, t) \equiv q_{0s}(t)$ and $(\partial T_l/\partial x)\ (l, t) \equiv q_{0l}(t)$ such that equations (1)–(8) are satisfied. The symbol q_0 is used to represent the unknown temperature gradients at the stationary boundaries. The solution of the above problem is equivalent to the solution of two separate inverse moving boundary problems, one in the solid phase ($0 \le x < h(t)$) and another in the liquid phase ($h(t) < x \le l$). The two problems will be considered separately in the following sections.

Nomenclature

$[A_i^j]$, $[B_i^j]$, $[C_i^j]$, $[D_i^j]$ = matrices defined by equations (28) and (47); subscript i denotes current time step, while the superscript j denotes the time interval during which integration is carried out
c = specific heat
$E(\bar{t}_i)$ = error given by equation (36)
erf = error function
erfc = complementary error function
$G(x, t; x_0, t_0)$ = Green's function defined in equation (21)
$h(t)$ = position of the freezing front
$\dot{h}(t)$ = speed of the freezing front
k = conductivity
l = length of the mold
L = latent heat
q_0 = temperature gradient on a stationary boundary
q_m = temperature gradient on the moving interface
$(r-1)$ = future time steps used in the sensitivity analysis
t = time
t_i = time at the end of the ith time step ($i = 1, \ldots, f, \ldots, F, \ldots$)
$\bar{t}_i$ = average time defined by equation (26) ($i = 1, \ldots, f, \ldots, F, \ldots$)
$T(x, t)$ = temperature at position x and time t
T_m = melting temperature
T_{in} = initial temperature
T_0 = temperature on a stationary boundary
$\{T^*\}$ = temperature vector defined by equation (32)
$\{T\}$, $\{q\}$ = temperature and temperature gradient vectors defined by equations (29) and (48)
$\{T^{F+i-1};\ q_{0s}^F\}$ = sensitivity coefficients defined by equation (33)
x = spatial coordinate ($x = 0$ at the lower boundary of the mold)
α = thermal diffusivity
Δt_i = $t_i - t_{i-1}$; $i = 1, \ldots, f, \ldots, F, \ldots$ (time step)
η = dimensionless coordinate = $x/h(t)$
ρ = density

Subscripts

i = indicates quantifier defined at the ith time step ($i = 1 \ldots, f, \ldots, F, \ldots$)
l = denotes liquid phase
m = denotes the moving front
0 = denotes a stationary boundary

Superscripts

i = denotes quantities defined at the ith time step ($i = 1, \ldots, f, \ldots, F, \ldots$)

Inverse Problem in the Solid Phase

The solid phase is governed by equation (1) and it is assumed that the velocity at the front $\dot{h}$, the melting temperature T_m, and the interface temperature gradient q_{ms} are given. The primary unknown is considered to be the temperature gradient $q_{0s} \equiv (\partial T/\partial x)\ (0, t)$.

Analytical Solution. By introducing a new spatial coordinate $\eta = x/h(t)$, the equations (1), (2), and (3) take the form:

$$\frac{\partial^2 T_s}{\partial \eta^2}(\eta, t) = \frac{1}{\alpha_s} h^2 \left(\frac{\partial T_s}{\partial t}(\eta, t) - \frac{\eta}{h} \dot{h} \frac{\partial T_s}{\partial \eta}(\eta, t) \right), \quad 0 \le \eta \le 1 \tag{10}$$

$$T_s(\eta, t) = T_m, \qquad \eta = 1 \tag{11}$$

$$\frac{\partial T_s}{\partial \eta}(\eta, t) = h q_{ms}(t), \qquad \eta = 1 \tag{12}$$

The unknown of this transformed problem is the temperature gradient $(\partial T_s/\partial \eta)\ (0, t)$, which is related to $q_{0s}(t)$ through the following equation:

$$\frac{\partial T_s}{\partial \eta}(0, t) = h(t) q_{0s}(t) \tag{13}$$

Using equation (11), equation (10) at $\eta = 1$ takes the form

$$\frac{\partial^2 T_s}{\partial \eta^2}(1, t) = -\frac{1}{\alpha_s} h \dot{h} \frac{\partial T_s}{\partial \eta}(1, t) \tag{14}$$

or more generally, one can derive the recursive equation

$$\frac{\partial^i T_s}{\partial \eta^i}(1, t) = -\frac{1}{\alpha_s} h \dot{h} \frac{\partial^{i-1} T_s}{\partial \eta^{i-1}}(1, t), \qquad i = 2, 3, \ldots \tag{15}$$

Using equations (11), (12), and (15) one can write a Taylor series expansion of the temperature $T(\eta, t)$ around $\eta = 1$ and thereby calculate the temperature and its spatial derivative at $\eta = 0$. These are given by the equations

$$T_{0s}(t) = \sum_{i=0}^{\infty} \frac{\partial^i T_s}{\partial \eta^i}(\eta, t) \Big|_{\eta=1} \frac{(-1)^i}{i!} \tag{16}$$

and

$$q_{0s}(t) = \frac{1}{h(t)} \sum_{i=1}^{\infty} \frac{\partial^i T}{\partial \eta^i}(\eta, t) \Big|_{\eta=1} \frac{(-1)^{i-1}}{(i-1)!} \tag{17}$$

Note that equations (16) and (17) are valid for any $h(t)$ history of the solidification front. Since they are used to determine T_s and q_s at $x = 0$ from data on the front $x = h(t)$, they are useful only if $h(t)$ is small. These equations, however, have been used for starting the solution, as will be discussed later in this paper.

It is worth mentioning that equations (16) and (17) are similar to the analytical solutions of a temperature field in a stationary boundary domain with prescribed temperature history at an internal point, as given by Burggraf (1964). More information on the limited applicability of equations like (16) and (17) is given in Beck et al. (1985).

Finally, equation (16), for the case of constant velocity $\dot{h}$, which is related to q_{ms} through equation (9) (with $q_{ml} = 0$), takes the form

$$T_{0s} = T_m + \frac{L}{c_s} \frac{1}{\alpha_s} t \dot{h}^2 - \frac{1}{2} \frac{L}{c_s} \frac{1}{\alpha_s^2} t^2 \dot{h}^4 + \ldots \tag{18}$$

Equation (18) coincides with the solution given by Stefan and reported by Carslaw and Jaeger (1959), which is

$$T_{0s} = T_m + \frac{L}{c_s}(1 - \exp(-t\dot{h}^2/\alpha_s)) \tag{19}$$

Integral Formulation. The integral equation corresponding to equation (1) is given as follows (Zabaras and Mukherjee, 1987; Chuang and Szekely, 1971; Heinlein et al. 1986):

$$T_s(x, t) = \alpha_s \int_0^t \Big[G_s(x, t; h(t_0), t_0) q_{ms}(t_0) - \frac{\partial G_s}{\partial x_0}(x, t; h(t_0), t_0) T_s(h(t_0), t_0) + \frac{1}{\alpha_s} G_s(x, t; h(t_0), t_0) T_s(h(t_0), t_0) \dot{h}(t_0) \Big] dt_0 + \alpha_s \int_0^t \Big[\frac{\partial G_s}{\partial x_0}(x, t; 0, t_0) T_{0s}(t_0) - G_s(x, t; 0, t_0) q_{0s}(t_0) \Big] dt_0 \tag{20}$$

where the Green's function is given by (Carslaw and Jaeger, 1959)

$$G_s(x, t; x_0, t_0) = \frac{\exp\left(-\frac{(x-x_0)^2}{4\alpha_s(t-t_0)}\right)}{2\sqrt{\pi \alpha_s (t-t_0)}} \tag{21}$$

By considering in turn $x = 0$ and $x = h(t)$, the following equations are obtained:

$$\frac{1}{2} T_{0s}(t) = \alpha_s \int_0^t \Big[G_s(0, t; h(t_0), t_0) q_{ms}(t_0) - \frac{\partial G_s}{\partial x_0}(0, t; h(t_0), t_0) T_m + \frac{1}{\alpha_s} G_s(0, t; h(t_0), t_0) T_m \dot{h}(t_0) \Big] dt_0 + \alpha_s \int_0^t \Big[\frac{\partial G_s}{\partial x_0}(0, t; 0, t_0) T_{0s}(t_0) - G_s(0, t; 0, t_0) q_{0s}(t_0) \Big] dt_0 \tag{22}$$

$$\frac{T_m}{2} = \alpha_s \int_0^t \Big[G_s(h(t), t; h(t_0), t_0) q_{ms}(t_0) - \frac{\partial G_s}{\partial x_0}(h(t), t; h(t_0), t_0) T_m + \frac{1}{\alpha_s} G_s(h(t), t; h(t_0), t_0) T_m \dot{h}(t_0) \Big] dt_0 + \alpha_s \int_0^t \Big[\frac{\partial G_s}{\partial x_0}(h(t), t; 0, t_0) T_{0s}(t_0) - G_s(h(t), t; 0, t_0) q_{0s}(t_0) \Big] dt_0 \tag{23}$$

Numerical Implementation. By assuming q_{0s}, T_{0s}, $\dot{h}$, and q_{ms} to be piecewise constant during every time step t_{f-1} to t_f, one can write equations (22) and (23) at time $\bar{t}_F$ as follows:

$$\frac{1}{2} T_{0s}(\bar{t}_F) = \alpha_s \sum_{f=1}^{F} \Big[q_{ms}(\bar{t}_f) \int_{t_{f-1}}^{t_f} G_s(0, t_F; h(t_0), t_0) dt_0 - T_m \int_{t_{f-1}}^{t_f} \frac{\partial G_s}{\partial x_0}(0, t_F; h(t_0), t_0) dt_0$$

$$+\frac{1}{\alpha_s}T_m\dot{h}(\bar{t}_f)\int_{t_{f-1}}^{t_f}G_s(0,\ t_F;\ h(t_0),\ t_0)dt_0\Big]$$

$$+\alpha_s\sum_{f=1}^{F}\Big[T_{0s}(\bar{t}_f)\int_{t_{f-1}}^{t_f}\frac{\partial G_s}{\partial x_0}(0,\ t_F;\ 0,\ t_0)dt_0$$

$$-q_{0s}(\bar{t}_f)\int_{t_{f-1}}^{t_f}G_s(0,\ t_F;\ 0,\ t_0)dt_0\Big] \tag{24}$$

and

$$\frac{T_m}{2}=\alpha_s\sum_{f=1}^{F}\Big[q_{ms}(\bar{t}_f)\int_{t_{f-1}}^{t_f}G_s(h(t_F),\ t_F,\ h(t_0),\ t_0)dt_0$$

$$-T_m\int_{t_{f-1}}^{t_f}\frac{\partial G_s}{\partial x_0}(h(t_F),\ t_F;\ h(t_0),\ t_0)dt_0$$

$$+\frac{1}{\alpha_s}T_m\dot{h}(\bar{t}_f)\int_{t_{f-1}}^{t_f}G_s(h(t_F),\ t_F;\ h(t_0),\ t_0)dt_0\Big]$$

$$+\alpha_s\sum_{f=1}^{F}\Big[T_{0s}(\bar{t}_f)\int_{t_{f-1}}^{t_f}\frac{\partial G_s}{\partial x_0}(h(t_F),\ t_F;\ 0,\ t_0)dt_0$$

$$-q_{0s}(\bar{t}_f)\int_{t_{f-1}}^{t_f}G_s(h(t_F),\ t_F;\ 0,\ t_0)dt_0\Big] \tag{25}$$

where

$$\bar{t}_f=\frac{t_f+t_{f-1}}{2},\qquad f=1,\ 2,\ \ldots,\ F,\ \ldots \tag{26}$$

For every time step t_{f-1} to t_f, it is assumed that

$$h(t_0)=h(t_{f-1})+\dot{h}(\bar{t}_f)\,(t_0-t_{f-1}) \tag{27}$$

The time step increment $\Delta t_f = t_f - t_{f-1}$ can vary with f. Using equation (27), one can calculate analytically all the integrals appearing in equations (24) and (25) (see the appendix).

In matrix form, equations (24) and (25) can be written as

$$[A_F^F]\{T_s^F\}=[B_F^F]\{q_s^F\}+[A_F^{F-1}]\{T_s^{F-1}\}+[B_F^{F-1}]\{q_s^{F-1}\}$$
$$+\cdots+[A_F^1]\{T_s^1\}+[B_F^1]\{q_s^1\} \tag{28}$$

where $[A_F^F]$, $[B_F^F]$, $\cdots$, etc., are 2×2 matrices that depend on the velocity $\dot{h}$ and the front position h. Subscripts in the above matrices denote current time of reference, while superscripts denote the time interval during which integration is carried out. The vectors $\{T_s^f\}$ and $\{q_s^f\}$ are defined as follows:

$$\{T_s^f\}=\begin{Bmatrix}T_m\\ T_{0s}(\bar{t}_f)\end{Bmatrix}\text{ and }\{q_s^f\}=\begin{Bmatrix}q_{ms}(\bar{t}_f)\\ q_{0s}(\bar{t}_f)\end{Bmatrix},$$
$$f=1,\ 2,\ \ldots,\ F,\ \ldots \tag{29}$$

From the recursive equation (28), one can write

$$\left[A_{F+1}^{F+1}\right]\left\{T_s^{F+1}\right\}=\left[B_{F+1}^{F+1}\right]\left\{q_s^{F+1}\right\}$$

$$+\left[A_{F+1}^{F}\right]\left\{T_s^{F}\right\}+\left[B_{F+1}^{F}\right]\left\{q_s^{F}\right\}+\left[A_{F+1}^{F-1}\right]\left\{T_s^{F-1}\right\}$$

$$+\left[B_{F+1}^{F-1}\right]\left\{q_s^{F-1}\right\}+\cdots+\left[A_{F+1}^{1}\right]\left\{T_s^{1}\right\}+\left[B_{F+1}^{1}\right]\left\{q_s^{1}\right\} \tag{30}$$

Note that $[A_{F+1}^{F+1}]\neq[A_F^F]$, so one must recalculate all the matrices from equation (20) at every new time step, using the analytical expressions given in the appendix. This situation arises because of the presence of convolution-type integrals in equation (20). Recalculation of these integrals from $t=0$ at each time step does add to the computational effort. The process has fading memory, however, so that restarting every time at $t=0$ is not essential as time increases (Brebbia et al., 1984).

Sensitivity Analysis. Following Beck's method (Beck et al., 1982, 1985; Beck 1970), it is assumed that the basic unknown of the problem, q_{0s}, changes in a piecewise constant manner as indicated in Fig. 2, where q_{0s}^F is the unknown flux during the time interval $(t_{F-1},\ t_F)$ (i.e., step F). The flux history at $t < t_{F-1}$ is considered to be known from previous calculations. To *stabilize* the solution of the inverse problem, it is assumed that q_{0s} is constant at $(r-1)$ future time steps, and has the same values as during the current time step F, i.e.,

$$q_{0s}^{F+r-1}=q_{0s}^{F+r-2}=\cdots=q_{0s}^{F+1}=q_{0s}^{F} \tag{31}$$

This assumption is used temporarily until q_{0s}^F is calculated.

At this point, for clarity, the subscript s is dropped from T_s. Let the starred temperature field vector T^* be defined as

$$\left\{T_{F+i-1}^*\right\}=\begin{Bmatrix}T^*(h(\bar{t}_{F+i-1}),\ \bar{t}_{F+i-1})\\ T^*(0,\ \bar{t}_{F+i-1})\end{Bmatrix},\qquad i=1,\ r \tag{32}$$

with $\bar{t}_{F+i-1}$ defined from an equation similar to equation (26) and with the star superscript in equation (32) indicating temperatures calculated with the flux assumption of equation (31) and the current estimate of q_{0s}^F (Fig. 2). For the first iteration, q_{0s}^F equals q_{0s}^{F-1}.

The sensitivity coefficients are defined as follows:

$$\left\{T^{F+i-1};\ q_{0s}^F\right\}\equiv\frac{\partial\left\{T^{F+i-1}\right\}}{\partial q_{0s}^F},\qquad i=1,\ r \tag{33}$$

Equation (33) expresses how the boundary temperatures during the time step $(F+i-1)$ will be affected by a unit change of q_{0s}^F. Note that the above-defined sensitivity coefficients are independent of the temperature and temperature gradient boundary conditions at $x=0$ and $x=h(t)$, but they depend upon the geometry, which changes with time. In other words, the sensitivity coefficients are functions of the velocity history $\dot{h}(t)$ as well as $h(t)$ and they have to be recalculated at each new time step.

Using a Taylor's series expansion about q_{0s}^{F-1}, one can write

$$\{T^{F+i-1}\}=\{T_{F+i-1}^*\}+(q_{0s}^F-q_{0s}^{F-1})\{T^{F+i-1};\ q_{0s}^F\} \tag{34}$$

where

$$\{T^{F+i-1}\}=\begin{Bmatrix}T(h(\bar{t}_{F+i-1}),\ \bar{t}_{F+i-1}\\ T(0,\ \bar{t}_{F+i-1})\end{Bmatrix} \tag{35}$$

is the boundary temperature vector calculated using the real flux condition at $x=0$. The higher order terms in the Taylor series (34) have been neglected here. The aim is to minimize the error $E(\bar{t}_F)$ introduced in the temperature at $x=h(t)$ when equation (34) is used, i.e.,

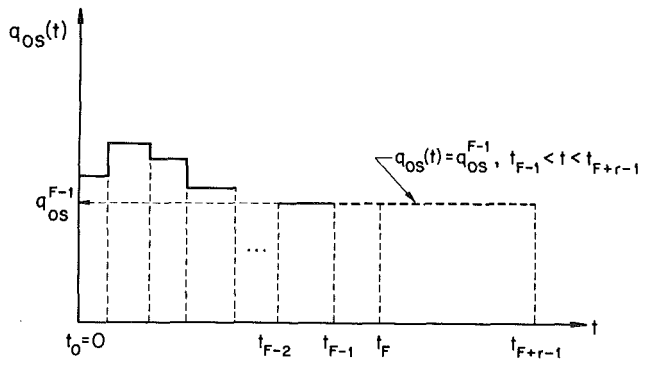

Fig. 2 Constant heat flux assumption used for calculation of the starred temperature field during the interval $t_{F-1} < t < t_{F+r-1}$; the flux at $t < t_{F-1}$ is known, while q_{0s}^F $(t_{F-1} < t < t_F)$ is the primary unknown.

$$E(\bar{t}_F) = \sum_{i=1}^{r} (T(h(\bar{t}_{F+i-1}), \bar{t}_{F+i-1}) - T_m)^2 \tag{36}$$

Equation (36) expresses the error $E(\bar{t}_F)$ not just as the step (F) but also at $(r-1)$ *future steps*. Note that equation (36) looks similar to the minimization technique reported in Beck et al. (1982, 1985) and Beck (1970), if the solidification front is considered to be the position of *a perfect* (without error) moving temperature sensor. By requiring

$$\frac{\partial E(\bar{t}_F)}{\partial q_{0s}^F} = 0 \tag{37}$$

at every time step F and by using equations (34) and (36), one can get

$$q_{0s}^F = q_{0s}^{F-1} + \frac{\sum_{i=1}^{r} (T_m - T^*(h(\bar{t}_{F+i-1}), \bar{t}_{F+i-1})) \frac{\partial T}{\partial q_{0s}^F}(h(\bar{t}_{F+i-1}), \bar{t}_{F+i-1})}{\sum_{i=1}^{r} \left(\frac{\partial T}{\partial q_{0s}^F}(h(\bar{t}_{F+i-1}), \bar{t}_{F+i-1})\right)^2} \tag{38}$$

Note that it is very simple to calculate q_{0s}^F through equation (38), if one gives a procedure to calculate $\{T^{F+i-1}; q_{0s}^F\}$ and the starred temperatures, for $i = 1, r$.

Calculation of the Sensitivity Coefficients. The integral formulation gives a great advantage with regard to direct computation of the sensitivity coefficients.

For example, consider one future step ($r = 2$). Then, using equations (28) and (30), and the definitions given by equations (29) and (33), one gets

$$\{T^F; q_{0s}^F\} = [A_F^F]^{-1}[B_F^F]\begin{Bmatrix} 0 \\ 1 \end{Bmatrix} \tag{39}$$

and

$$\{T^{F+1}; q_{0s}^F\} = \left[A_{F+1}^{F+1}\right]^{-1} \left(\left[B_{F+1}^{F+1}\right] + \left[B_{F+1}^F\right] + \left[A_{F+1}^F\right]\left[A_F^F\right]^{-1}\left[B_F^F\right]\right)\begin{Bmatrix} 0 \\ 1 \end{Bmatrix} \tag{40}$$

where the constant heat flux assumption (equation (31)) has also been taken into account. The sensitivity coefficients required in equation (38) are just the first components of the vectors in equations (39) and (40).

The starred boundary temperatures can be calculated from equation (28) using the actual $q_{ms}(t)$, $\dot{h}(t)$, and the $q_{0s}(t)$ profile of Fig. 2. Once q_{0s}^F is calculated from equation (38), one can calculate the actual $T(0, t) \equiv T_{0s}(t)$ from the following equation:

$$T(0, \bar{t}_F) = T^*(0, \bar{t}_F) + (q_{0s}^F - q_{0s}^{F-1}) \frac{\partial T(0, \bar{t}_F)}{\partial q_{0s}^F} \tag{41}$$

where the sensitivity coefficient is given by the second component of the vector $\{T^F; q_{0s}^F\}$ in equation (39).

Note that since the sensitivity coefficients, given by equations (39) and (40), are independent of q_{0s}^F, the equations (34) and (41) add no error to the errors introduced by the numerical discretization of equations (22) and (23), and the constant heat flux assumption.

Starting the Algorithm. To start the proposed algorithm presented in the last paragraph, it is required that one know q_{0s}^1 at time $(t_0 + t_1)/2$. Even though an iterative technique has been successful, it is preferable to use equation (17) (just the first three terms) to estimate the required temperature gradient at the first time step. In brief, the algorithm works as follows:

The temperature gradient q_{0s}^F is unknown. Assuming temporarily $q_{0s}^{F+i-1} = q_{0s}^{F-1}$, $i = 1, r$ (where q_{0s}^{F-1} is considered to be known), and by using the known quantity $q_{ms}(\bar{t}_{F+i-1})$, one can (by solving a direct problem) calculate the starred temperatures at the time steps $F + i - 1$, $i = 1, r$. Then, using the sensitivity coefficients and equation (38), one calculates q_{0s}^F and so from equation (41) the actual $T_{0s}(\bar{t}_F)$. Note that T_m is used only in the minimization process, *and not* in the calculation of the starred temperature field. In other words, T_m here plays the same role as that of an internal temperature measurement in the problems discussed by Beck et al. (1985).

Numerical Results. Consider the case $T_{in} = T_m = 0$, $k_s = 1$, $\rho = 1$, $c_s = 1$, $L = 1/2$, and $q_{ms} = 1$. Then $q_{ml} = 0$ and from equation (9) $\dot{h} = 2$. An analytical solution for this problem is given in equation (19) for T_{0s} and an expression for q_{0s} can be derived from equation (17). These expressions are

$$q_{0s}(t) = e^{4t} \tag{42}$$

$$T_{0s}(t) = \frac{1}{2}(1 - e^{4t}) \tag{43}$$

Physically, this case represents solidification of a liquid initially at the melting temperature, which is cooled on the boundary $x = 0$. Solidification starts at $x = 0$ and proceeds upward. The liquid portion of the mold remains at the melting temperature during the process. Even though the above example is physically an unrealistic one for large castings (since it is required eventually to have infinite flux at $x = 0$ to maintain constant velocity at the front), it is a very good way to examine the effectiveness of the present algorithm in the solid phase.

Figure 3 shows plots of the flux $q_{0s}(t)$ together with the exact solution given by equation (42) for three different time steps: $\Delta t_f = 0.1$, 0.05, and 0.005. One future time step ($r = 2$) has been used to stabilize the solution. It is expected that the comparison should be good at small times, while later, when the interface moves away from the $x = 0$ boundary, oscillations or divergence from the analytical solution should occur. In Fig. 3 only the stable region has been plotted. As can be seen, the smaller the time step, the more accurate the numerical solution, but also the sooner it starts to diverge from the exact solution. For example, using $\Delta t_f = 0.005$, the numerical solution rapidly diverges from the exact one at about $t = 0.3$ (the region $t > 0.3$ is not shown in this figure), while, if $\Delta t_f = 0.5$ is used, divergence starts only after $t = 0.9$. Similar conclusions can be drawn from Fig. 4 where the boundary temperature $T_{0s}(t)$ has been plotted together with the analytical solution from equation (43). Note that the results for temperatures are in general (as is expected) more accurate than those for the temperature gradients, but when the temperature gradient solution starts to diverge, the temperature does also. If $r > 2$ is used, the numerical solution becomes slightly more accurate and more stable.

Inverse Problem in the Liquid Phase

The liquid phase is governed by equation (4) and it is assumed that the velocity of the front $\dot{h}$ is given while the melting and initial temperatures as well as the interface temperature gradient q_{ml} are known through equations (5), (7), and (6), respectively. The primary unknown of the problem is the temperature gradient $q_{0l}(t) \equiv (\partial T_l/\partial x)(x, t)|_{x=l}$.

Analytical Solution. A solution similar to equations (16) and (17) can be written for the liquid phase but it is rather impractical, especially at small times when the distance between $x = h(t)$ and $x = l$ is quite large (assuming the worst case of

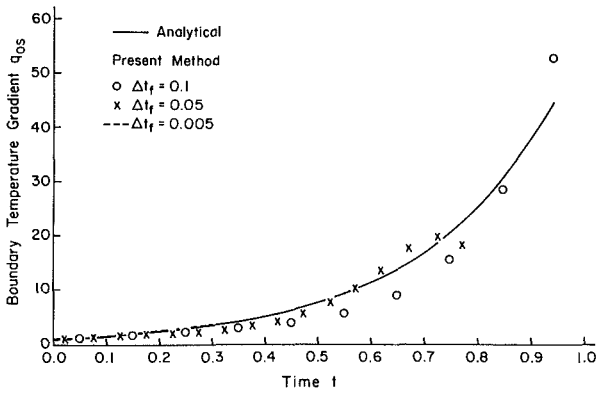

Fig. 3 Boundary temperature gradient q_{0s} as a function of time for different time steps

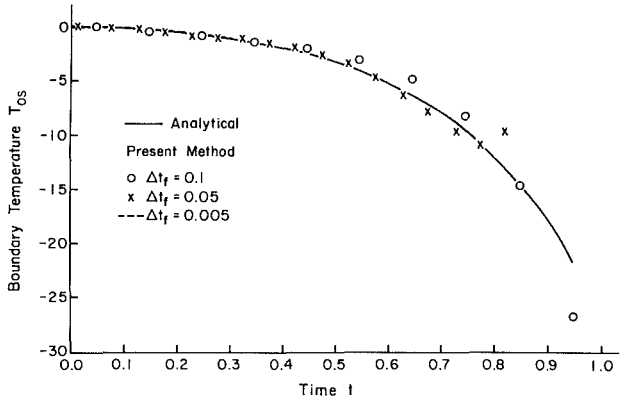

Fig. 4 Boundary temperature T_{0s} as a function of time for different time steps

large l). So this analytical solution cannot be used to start the algorithm.

Integral Formulation. The integral equation corresponding to equation (4) is given as follows (Zabaras and Mukherjee, 1987; Chuang and Szekely, 1971; Heinlein et al., 1986):

$$T_l(x,t)-T_{in}=\alpha_l\int_0^t\Big[G_l(x,\,t;\,h(t_0),\,t_0)(-q_{ml}(t_0))$$

$$+\frac{\partial G_l}{\partial x_0}(x,\,t;\,h(t_0),\,t_0)(T_l(h(t_0),\,t_0)-T_{in})$$

$$-\frac{1}{\alpha_l}\,G_l(x,\,t;\,h(t_0),\,t_0)(T_l(h(t_0),\,t_0)-T_{in})\dot{h}(t_0)\Big]dt_0$$

$$+\alpha_l\int_0^t\Big[-\frac{\partial G_l}{\partial x_0}(x,\,t;\,l,\,t_0)(T_{0l}(t_0)-T_{in})$$

$$+G_l(x,\,t;\,l,\,t_0)q_{0l}(t_0)\Big]dt_0 \qquad (44)$$

where an equation similar to equation (21) is valid for G_l.

By considering $x = h(t)$ and $x = l$, one gets the following set of equations:

$$\frac{1}{2}(T_m-T_{in})=\alpha_l\int_0^t\Big[-G_l(h(t),\,t;\,h(t_0),\,t_0)q_{ml}(t_0)$$

$$+\frac{\partial G_l}{\partial x_0}(h(t),\,t;\,h(t_0),\,t_0)(T_m-T_{in})$$

$$-\frac{1}{\alpha_l}\,G_l(h(t),\,t;\,h(t_0),\,t_0)(T_m-T_{in})\dot{h}(t_0)\Big]dt_0$$

$$+\alpha_l\int_0^t\Big[G_l(h(t),\,t;\,l,\,t_0)q_{0l}(t_0)$$

$$-\frac{\partial G_l}{\partial x_0}(h(t),\,t;\,l,\,t_0)(T_{0l}(t_0)-T_{in})\Big]dt_0 \qquad (45)$$

and

$$\frac{1}{2}(T_{0l}(t)-T_{in})=\alpha_l\int_0^t\Big[-G_l(l,\,t;\,h(t_0),\,t_0)q_{ml}(t_0)$$

$$+\frac{\partial G_l}{\partial x_0}(l,\,t;\,h(t_0),\,t_0)(T_m-T_{in})$$

$$-\frac{1}{\alpha_l}\,G_l(l,\,t;\,h(t_0),\,t_0)(T_m-T_{in})\dot{h}(t_0)\Big]dt_0$$

$$+\alpha_l\int_0^t\Big[G_l(l,\,t;\,l,\,t_0)q_{0l}(t_0)$$

$$-\frac{\partial G_l}{\partial x_0}(l,\,t;\,l,\,t_0)(T_{0l}(t_0)-T_{in})\Big]dt_0 \qquad (46)$$

Numerical Implementation. A numerical implementation similar to that for the solid phase can be applied here. Omitting the details, one finally obtains an equation similar to equation (28), which is

$$\left[C_F^F\right]\left\{T_l^F\right\}=\left[D_F^F\right]\left\{q_l^F\right\}+\left[C_F^{F-1}\right]\left\{T_l^{F-1}\right\}+\left[D_F^{F-1}\right]\left\{q_l^{F-1}\right\}$$

$$+\cdots+\left[D_F^1\right]\left\{q_l^1\right\}+\left[C_F^1\right]\left\{T_l^1\right\} \qquad (47)$$

where the same notation as before is used, together with

$$\left\{T_l^f\right\}=\begin{Bmatrix}T_m-T_{in}\\ T_{0l}(\bar{t}_f)-T_{in}\end{Bmatrix}\text{ and }\left\{q_l^f\right\}=\begin{Bmatrix}q_{ml}(\bar{t}_f)\\ q_{0l}(\bar{t}_f)\end{Bmatrix} \qquad (48)$$

with $f = 1, 2, \ldots, F, \ldots$. The sensitivity analysis applied to the solid phase remains unchanged here. The subscripts s must be replaced by l everywhere and the position $x = 0$ by the position $x = l$.

Starting the Algorithm in the Liquid Phase. No "perfect" way to start the algorithm has been found yet. It is expected that if l is large only a rough estimation of q_{0l}^1 can be achieved.

A first approximation is to estimate $T_{0l}^1 = T_{in}$ and then solve a direct problem for q_{0l}^1. Another possibility is to assume $q_{0l}^2 = q_{0l}^1$ and using equations (47) at $t = \bar{t}_1$ and $t = \bar{t}_2$, solve a 4×4 least-squares system for the three unknowns, q_{0l}^1, $T_{0l}^1 - T_{in}$, and $T_{0l}^2 - T_{in}$. The second way has been used here but the error in the initial estimated temperature gradients remains large. Fortunately, regardless of this initial error, the algorithm is forgiving and soon picks up the right values.

Numerical Results. To test this part of the algorithm, the following case is considered:

$$T_{in}=-1,\quad T_m=0,\quad \alpha_l=1,\quad k_l=1,$$

$$\rho=1,\quad c_l=1,\quad L=2,\quad l=1,$$

$$\dot{h}=\frac{0.43}{\sqrt{t}},\quad h=0.86\sqrt{t},\quad q_{ml}=-0.76178\,\frac{1}{\sqrt{t}}$$

An analytical solution of this problem has been reported by Carslaw and Jaeger (1959) and it has the following form:

$$q_{0l}=-0.9165\,\frac{1}{\sqrt{t}}\,e^{-\frac{1}{4t}} \qquad (49)$$

and

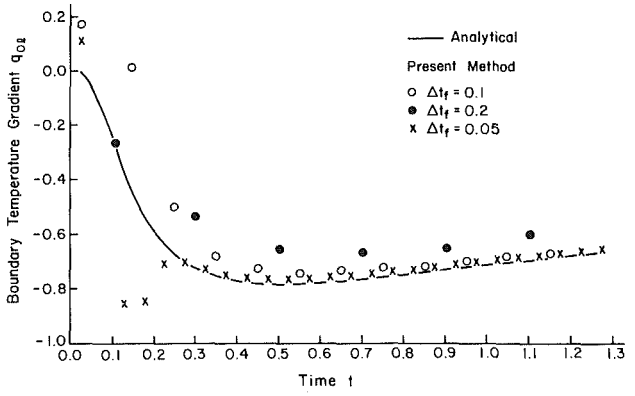

Fig. 5 Boundary temperature gradient q_{0l} as a function of time for different time steps

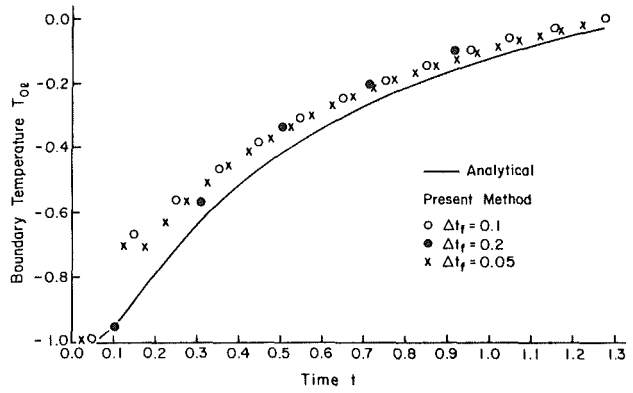

Fig. 6 Boundary temperature T_{0l} as a function of time for different time steps

$$T_{0l} = -1 + 1.833 \text{ erfc } \frac{1}{2\sqrt{t}} \tag{50}$$

where erfc is the complementary error function.

Physically this case represents solidification of a liquid that is initially supercooled. The lower boundary $x = 0$ is suddenly brought up to the melting temperature. Solidification starts from the bottom and proceeds upward. The solidified part of the mold remains at the melting temperature during this process.

The above expressions for $\dot{h}(t)$, $h(t)$, and $q_{ml}(t)$, as well as the solution given by the equations (49) and (50), are slightly approximate, in the sense that a transcendental equation has to be solved numerically (Carslaw and Jaeger, 1959) in order to estimate the solution of the associated direct problem.

Figures 5 and 6 show comparisons for q_{0l} and T_{0l} for three different time step sizes: $\Delta t_f = 0.2$, 0.1, and 0.05. Similar conclusions can be drawn as for the calculations in the solid phase. The difference here is that one starts with large errors, then the error decreases and finally divergence occurs. Obviously, when the interface approaches $x = l$ the analytical approximation can be used.

One future time step ($r = 2$) has been used to stabilize the solution in the liquid phase. If $r > 2$ is used, the solution becomes considerably more accurate at early times, while later (when the interface approaches $x = l$) the accuracy of the solution drops significantly. This last fact is naturally expected, since time steps with $h(t) > l$ are not possible.

Discussion

As shown before, the present algorithm remains more stable when large time steps are used, while for smaller time steps the algorithm is more accurate but diverges sooner (especially in the solid phase).

These observations suggest an advantage of the present method. Since the BEM formulation can use different time steps Δt_f as one proceeds forward in time, one can adjust the time step in such a way that the calculations remain both stable and accurate for longer times. For example, in the solid phase, one can start with small time steps until the flux q_{0s} starts diverging. Then the time step size can be increased until new divergence occurs, at which time the time step is increased again, etc. Obviously, there is a time step upper bound that fails to give acceptable accuracy.

Conclusions

An integral formulation has been presented in this paper for the solution of certain inverse Stefan problems, which are of special interest in the design of casting processes. Based on the results presented in this paper, the integral formulation appears to have some advantages over the finite difference method and the finite element method for the solution of inverse moving interface problems for four reasons:

(*a*) the present algorithm is clearly a boundary algorithm, so no domain calculations have to be done;

(*b*) the integral formulation considers the flux as a primary unknown;

(*c*) the calculation of the sensitivity coefficients is straightforward; and

(*d*) the matrix form of the integral representation of Stefan problems looks like that for problems with stationary boundaries.

The last observation (*d*) suggests that all the current advances in inverse heat conduction with stationary boundaries can be extended easily to inverse Stefan problems.

A disadvantage of this method is the assumption of constant material properties. Different material properties can, however, be assigned to the solid and the liquid phase, respectively.

As has been mentioned several times before in this paper, the idea here is to set desired values of front velocity and temperature gradients and then to determine the conditions on the stationary boundary that are required to achieve these desired values. Hence, random errors in the desired quantities have not been included in this work. Further investigation is necessary in order to examine the stability and accuracy of the solution of inverse problems such as these when errors are allowed in the desired data.

Acknowledgments

The research reported in this paper has been supported by NSF grant number DMC-8421258 to Cornell University. The computing has been supported by the Production Supercomputer Facility of Cornell University. The authors are grateful for the expert secretarial assistance of Mrs. Tammie Martin.

References

Beck, J. V., 1968, "Surface Heat Flux Determination Using an Integral Method," *Nuclear Engineering and Design*, Vol. 7, pp. 170–178.

Beck, J. V., 1970, "Nonlinear Estimation Applied to the Nonlinear Heat Conduction Problem," *International Journal of Heat and Mass Transfer*, Vol. 13, pp. 703–716.

Beck, J. V., Blackwell, B., and St. Clair, C. R., Jr., 1985, *Inerse Heat Conduction, Ill-Posed Problems*, Wiley-Interscience, New York.

Beck, J. V., Litkouhi, B., and St. Clair, C. R., Jr., 1982, "Efficient Sequential Solution of Nonlinear Inverse Heat Conduction Problems," *Numerical Heat Transfer*, Vol. 5, pp. 275–286.

Brebbia, C. A., Telles, J. C. F., and Wrobel, L. C., 1984, *Boundary Element Techniques—Theory and Applications in Engineering*, Springer-Verlag, Berlin.

Burggraf, O. R., 1964, "An Exact Solution of the Inverse Problem in Heat Conduction Theory and Applications," ASME JOURNAL OF HEAT TRANSFER, Vol. 86, pp. 373–382.

Carslaw, H. S., and Jaeger, J. C., 1959, *Conduction of Heat in Solids*, 2nd ed., Oxford University Press, Oxford.

Chuang, Y. K., and Szekely, J., 1971, "On the Use of Green's Function for Solving Melting and Solidification Problems," *International Journal of Heat and Mass Transfer*, Vol. 14, pp. 1285–1294.

Crank, J., 1984, *Free and Moving Boundary Problems*, Clarendon Press, Oxford.

Flemings, M. C., 1974, *Solidification Processing*, McGraw-Hill, New York.

Frederick, D., and Greif, R., 1985, "A Method for the Solution of Heat Transfer Problems With a Change of Phase," ASME JOURNAL OF HEAT TRANSFER, Vol. 107, pp. 520–526.

Heinlein, M., Mukherjee, S., and Richmond, O., 1986, "A Boundary Element Method Analysis of Temperature Fields and Stresses During Solidification," *Acta Mechanica*, Vol. 59, pp. 59–81.

Hsu, Y. F., Rubinsky, B., and Mahin, K., 1986, "An Inverse Finite Element Method for the Analysis of Stationary Arc Welding Processes," ASME JOURNAL OF HEAT TRANSFER, Vol. 108, pp. 739–741.

Katz, M. A., and Rubinsky, B., 1984, "An Inverse Finite Element Technique to Determine the Change of Phase Interface Location in One Dimensional Melting Problems," *Numerical Heat Transfer*, Vol. 7, pp. 269–283.

Zabaras, N., and Mukherjee, S., 1987, "An Analysis of Solidification Problems by the Boundary Element Method," *International Journal for Numerical Methods in Engineering*, Vol. 24, pp. 1879–1900.

APPENDIX

The integrals in equations (24) and (25) are

$$I_1 = \alpha_s \int_{t_{f-1}}^{t_f} G_s(0,\, t_F;\, 0,\, t_0)dt_0$$

$$= \sqrt{\frac{\alpha_s}{\pi}}\left(\sqrt{t_F - t_{F-1}} - \sqrt{t_F - t_f}\right)$$

$$I_2 = \alpha_s \int_{t_{f-1}}^{t_f} \frac{\partial G_s}{\partial x_0}(0,\, t_F;\, 0,\, t_0)dt_0 = 0$$

$$I_3 = \alpha_s \int_{t_{f-1}}^{t_f} G_s(h(t_F),\, t_F;\, 0,\, t_0)dt_0$$

$$= \frac{h(t_F)}{2\sqrt{\pi}}\left(\frac{e^{-a_{f-1}^2}}{a_{f-1}} - \frac{e^{-a_f^2}}{a_f} - \sqrt{\pi}(\mathrm{erf}(a_f) - \mathrm{erf}(a_{f-1}))\right]$$

where

$$a_{f-1} = \frac{h(t_F)}{\sqrt{4\alpha_s(t_F - t_{f-1})}}$$

and

$$a_f = \frac{h(t_F)}{\sqrt{4_s(t_F - t_f)}}$$

$$I_4 = \alpha_s \int_{t_{f-1}}^{t_f} \frac{\partial G_s}{\partial x_0}(h(t_F),\, t_F;\, 0,\, t_0)dt_0$$

$$= \frac{1}{2}\left\{\mathrm{erf}(a_f) - \mathrm{erf}(a_{f-1})\right\}$$

$$I_5 = \alpha_s \int_{t_{f-1}}^{t_f} \frac{\partial G_s}{\partial x_0}(h(t_F),\, t_F;\, h(t_0),\, t_0)dt_0$$

$$= \frac{1}{2}\, e^{-h(\bar{t}_f)B/\alpha_s}\left\{\mathrm{erf}\left(\frac{-(t_F - t_f)\dot{h}(\bar{t}_f) + B}{\sqrt{4\alpha_s(t_F - t_f)}}\right)\right.$$

$$\left. - \mathrm{erf}\left(\frac{-(t_F - t_{f-1})\dot{h}(\bar{t}_f) + B}{\sqrt{4\alpha_s(t_F - t_{f-1})}}\right)\right\}$$

where

$$B = h(t_F) - h(t_{f-1}) - \dot{h}(\bar{t}_f)(t_F - t_{f-1})$$

$$I_6 = \alpha_s \int_{t_{f-1}}^{t_f} G_s(h(t_F),\, t_F;\, h(t_0),\, t_0)dt_0$$

$$= -\frac{\alpha_s}{2}\,\frac{1}{\dot{h}(\bar{t}_f)}\left\{\mathrm{erf}\left(\frac{h(t_F) - h(t_{f-1}) - \dot{h}(\bar{t}_f)(t_f - t_{f-1})}{\sqrt{4\alpha_s(t_F - t_f)}}\right)\right.$$

$$\left. - \mathrm{erf}\left(\frac{h(t_F) - h(t_{f-1})}{\sqrt{4\alpha_s(t_F - t_{f-1})}}\right) - 2I_5\right\}$$

On Numerical Methods Used in Mathematical Modeling of Phase Change in Liquid Metals

D. Poirier
Department of Mechanical Engineering,
University of Ottawa,
Ottawa, Ontario, K1N 6N5, Canada

M. Salcudean
Department of Mechanical Engineering,
University of British Columbia,
Vancouver, B.C., V6T 1W5, Canada

The work presents an analysis and comparative evaluation of different methods used for the numerical solution of heat conduction with phase change problems. Both freezing (melting) water as well as solidifying liquid metal problems are examined. Emphasis is placed on weak formulations as they tend to be simple to program and easily implemented in existing single-phase codes. A new method based on the apparent capacity technique is proposed. In this technique an "effective capacity" is computed, based on the integration of temperature profiles over the nodal volumes. This method shows significantly better performance when compared with other methods for the numerical analysis of solidifying metals.

1 Introduction

With the advent of high-speed digital computers, mathematical modeling of the solidification process has become a useful tool in designing permanent molds for metal casting.

The heat transfer problem to be solved, often referred to as Stefan's problem (Stefan, 1891), involves solving the heat conduction equation with moving boundaries. The governing equations for the simple one-dimensional Stefan problem can be written as

$$\frac{\partial}{\partial x}\left[k_s\frac{\partial T_s}{\partial x}\right] = \rho_s C_s\frac{\partial T_s}{\partial t},\ 0\le x\le S(t) \tag{1}$$

$$\frac{\partial}{\partial x}\left[k_L\frac{\partial T_L}{\partial x}\right] = \rho_L C_L\frac{\partial T_L}{\partial t},\ x>S(t) \tag{2}$$

with conditions at the interface $x=S(t)$ of the type

$$T_L=T_S=T_f$$

$$k_L\frac{\partial T_L}{\partial x}-k_s\frac{\partial T_s}{\partial x}=-\rho_S L\frac{dS(t)}{dt} \tag{3}$$

In these equations, the subscript s refers to the solid phase and L to the liquid phase. Along with these equations, boundary and initial conditions have to be specified. Stefan's problem has been extensively investigated due to its practical implications. Neumann (1912) presented an analytical solution to a one-dimensional Stefan problem. Unfortunately, unless the problem geometry is very simple, analytical solutions are not available and hence most techniques for solving Stefan problems rely on some numerical scheme, usually finite difference or finite element.

One of the simplest techniques of accounting for the latent heat effect is to set up an energy budget at each node of a grid and to set the nodal temperature back to the phase change temperature after each time step until enough heat has been accumulated to account for the latent heat associated with that node. The technique was described by Dusinberre (1945) and later by Doherty (1970). Recently, Rolph and Bathe (1982) incorporated a similar technique into a finite element formulation of the Stefan problem.

A commonly used technique of accounting for the latent heat in a fixed spatial grid is to increase the heat capacity artificially near the phase change temperature. Some of the early work developing this technique was done by Hashemi and Sliepcevich (1967), who used an implicit finite difference formulation of the problem. Later, Comini et al. (1974) implemented the method with a finite element formulation. Recently, Pham (1985) presented a three-level finite difference formulation of this method.

Many of the more recent works have dealt with methods that formulate the governing equations in terms of enthalpy. Crowley (1978) used the enthalpy formulation with a finite difference scheme to solve two-dimensional problems. Bell and Wood (1983) tested the explicit finite difference formulation of the enthalpy method in the region of a singularity. Recently, Tacke (1985) presented a new formulation of the explicit enthalpy method for one-dimensional problems. He tested his technique on both ice-water and solidifying steel test cases. If an implicit scheme is used, the enthalpy method requires the solution of a system of nonlinear equations. Meyer (1973), Shamsunder and Sparrow (1975), and Jerome (1977) have all presented formulations of the implicit enthalpy method.

Some researchers have transformed the governing equations to use the freezing index as the state variable. Kikuchi and Ichikawa (1979) used this method to solve two-dimensional ice-water problems. Later Blanchard and Fremond (1984) introduced the homographic approximation (Brauner et al., 1982) along with the freezing index to solve two-dimensional freezing of soil around buried pipes.

A technique that attempts to track the phase front using the method of lines was presented by Meyer (1977). The technique can run into difficulties if the moving boundary does not vary smoothly or monotonically with time. Also, the method is not suitable for problems where a mushy range exists.

Lazaridis (1970) presented a method that solves for the front locations and solves the finite difference equations based on this location. His method is capable of handling multidimensional problems but is extremely complex. He tested his method on solidifying metal.

Duda et al. (1975) presented a technique that transforms the governing partial differential equations into a coordinate system where the phase boundaries correspond to fixed coordinate surfaces.

Several researchers have presented techniques, usually with a finite element formulation, which actually deform the spacial grid in order to track the phase front. Some recent work using this technique has been done by Lynch and O'Neil (1981) and Lynch (1982). Lynch (1982) tested his method on freezing water test cases.

Some researchers have presented fairly in-depth reviews of

Contributed by the Heat Transfer Division and presented at the ASME Winter Annual Meeting, Anaheim, California, December 7-12, 1986. Manuscript received by the Heat Transfer Division January 6, 1987. Keywords: Numerical Methods, Phase-Change Phenomena.

existing methods, but few actually have done a comparison of the performance of the various methods when applied to specific problems. An extensive review of the literature is given by Lunardini (1981). Due to the interest in this field, however, a number of important papers have been written since his review. It should be mentioned that the majority of researchers have tested their method on ice-water test cases, and the problem of solidifying metal has been primarily a beneficiary of the former.

The present work examines the performance of various techniques in solving solidifying liquid metal problems in order to determine their applicability for implementation into a general purpose metal casting algorithm. A one-dimensional freezing water problem is also examined in order to determine the difference between the numerical behavior of metals and water. A new method developed by the authors based on the apparent capacity method is presented.

2 Methods

The criteria for choosing the methods to be investigated are:

1 Ability to solve multidimensional problems

2 Ease of implementation

3 Ability to account for a "mushy" region (latent heat released in a temperature range) commonly encountered in solidifying metal alloy problems.

It was felt that in general, the so-called "weak methods" best fulfilled these criteria. Weak methods do not explicitly make use of the phase-change boundary. Because of this, they are often capable of handling problems where the phase change region is a volume and not a surface as in isothermal solidification. In multidimensional problems, the phase front can be very difficult to track, particularly if it does not vary smoothly with space and time; therefore weak methods tend to be simpler. The methods chosen for investigation are the following:

2.1 Postiterative (Isothermal). The postiterative method (Dusinberre, 1945; Doherty, 1970) of accounting for the latent heat is probably the simplest of all the methods. The first step in setting up the method is to write the usual finite difference or finite element equations. For the nodes at which phase change is occurring the temperature is set back to the phase change temperature and the equivalent amount of heat is added to an enthalpy budget for that node. Once the heat in the enthalpy budget equals the latent heat for the volume associated with that node, the temperature is allowed to fall according to heat diffusion. Both explicit and implicit finite difference as well as implicit finite element formulations have been considered in this study.

2.2 Postiterative (Mushy). This is the same as the previous technique except that a mushy range is to be accounted for (Salcudean et al., 1983, 1986). The latent heat is released (or absorbed) over a temperature range, and is assumed to be a function of the temperature in that range. For the purpose of this investigation, the latent heat is assumed to be released linearly with temperature. The procedure is as in the isothermal case except that now the temperature will be set to

$$T = T_2 - (\Delta H/L)\Delta T$$

where T_2 is the temperature at the top end of the mushy range.

Isothermal solidification problems can be solved using this method by assuming solidification to occur over a small temperature range. Again, both implicit and explicit finite difference, as well as implicit finite element formulations of this method, have been investigated in this work.

2.3 Apparent Capacity. In this technique (Hashemi et al., 1967; Comini et al., 1974; Pham, 1985), the latent heat effect is accounted for by increasing the heat capacity in the phase change temperature range. If a linear release of the latent heat across the temperature range is assumed, the apparent capacity is

$$C_a = \begin{cases} C & T < T_1 \quad \text{solid region} \\ C_M & T_1 \le T \le T_2 \quad \text{mushy region} \\ C & T > T_2 \quad \text{liquid region} \end{cases} \tag{4}$$

where

$$C_M = C + L/\Delta T$$

The apparent capacities are calculated based on the temperatures at the nodes and the resulting finite difference or

Nomenclature

C = specific heat, $Jkg^{-1}K^{-1}$
e = specific energy, Jkg^{-1}
f_t = function to calculate temperature from enthalpy
f_H = function to calculate enthalpy from temperature
F_o = Fourier moduli $= k\Delta t\rho^{-1} C^{-1}\Delta x^{-2}$
H = enthalpy, J
ΔH = heat in enthalpy budget of postiterative method, J
I = number of points used in standard deviation calculation
k = thermal conductivity, $Wm^{-1}K^{-1}$
l = characteristic length in test problems, m
L = latent heat of fusion, Jkg^{-1}
N = number of time steps used in standard deviation calculation
Q_L, Q_R = heat flux from left and right and into nodal volume, Wm^{-2}
s = standard deviation, °C
$S(t)$ = position of phase front at time t
t = time, s
T = temperature, °C
ΔT = mushy range, °C
TT = analytical or converged temperature, °C
u = freezing index: $= k\int_0^t T dt$, Jm^{-1}
V = volume, m^3
x, y = Cartesian coordinates, m
Δ = increment
η = constant in homographic approximation
μ = liquid water content
ξ = fraction of nodal volume which is solid
ρ = density, kgm^{-3}

Subscripts

1 = solidus
2 = liquidus
a = apparent
eff = effective
f = phase change
$i-1$, i, $i+1$ = grid points
L = liquid
LM = position of left element boundary
M = mushy
MR = position of right element boundary
s = solid

Superscripts

$*$ = second-order approximation
m, $m+1$, $m+2$ = time steps.

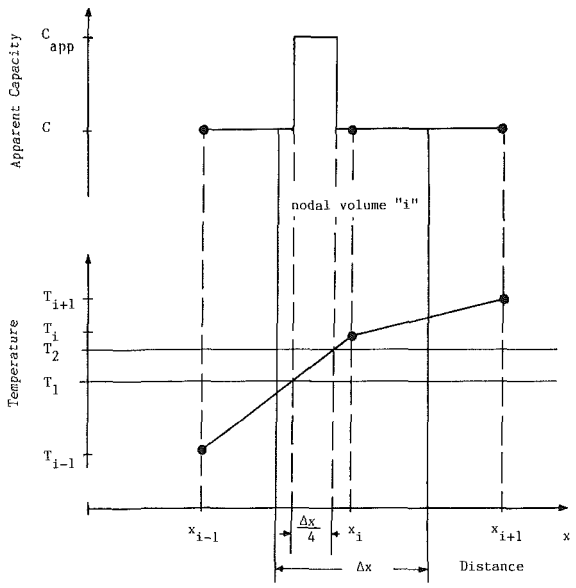

Fig. 1 One-dimensional temperature and heat capacity profile in an element

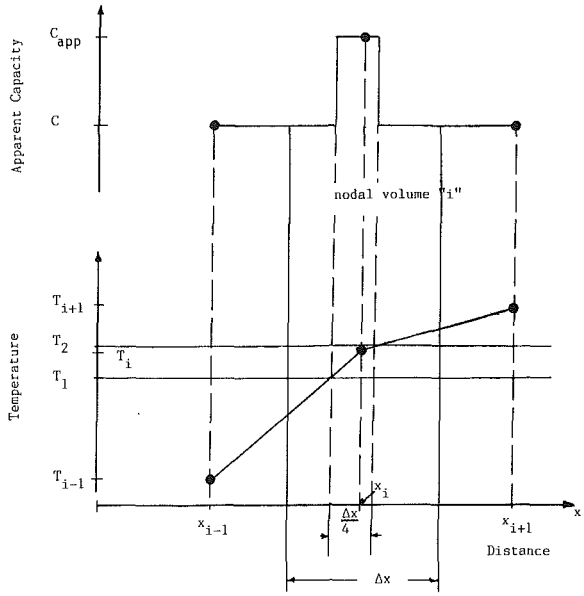

Fig. 2 One-dimensional temperature and heat capacity profile in an element

finite element equations are set up based on these apparent capacities.

Again, isothermal solidification can be modeled by assuming a small mushy range. Both implicit and explicit finite difference formulations of this method have been considered.

2.4 Enthalpy Method. In the enthalpy method (Meyer, 1973; Shamsunder and Sparrow, 1975; Crowley, 1978; Bell and Wood, 1983; Tacke, 1985), the heat conduction equation is written as

$$\rho\frac{\partial H}{\partial t}=k\left[\frac{\partial^2 T}{\partial x^2}+\frac{\partial^2 T}{\partial y^2}\right] \tag{5}$$

An enthalpy versus temperature variation is then assumed. For the case of linear latent heat release, the variation is

$$H=\begin{cases} CT & T<T_1 \quad \text{solid region} \\ CT+L(T-T_1)/(T_2-T_1) & T_1\le T\le T_2 \quad \text{mushy region} \\ CT+L & T>T_2 \quad \text{liquid region} \end{cases} \tag{6}$$

As mentioned before, in the implicit case, a set of nonlinear equations results and must be solved iteratively. Both the implicit and the explicit finite difference formulations have been investigated in this study.

2.5 Pham's Method. The technique recently published by Pham (1985) is actually a hybrid of the enthalpy and apparent capacity methods. He uses a three-time-level finite difference scheme. For the one-dimensional case, this can be written as

$$\rho C_i^{m+1}(T_i^{m+2}-T_i^m)=\frac{2\Delta tk}{3(\Delta x)^2}[T_{i+1}^{m+2}+T_{i+1}^{m+1}+T_{i+1}^m + T_{i-1}^{m+2}+T_{i-1}^{m+1}+T_{i-1}^m-2T_i^{m+2}-2T_i^{m+1}-2T_i^m] \tag{7}$$

where C_i^{m+1} is calculated as

$$\Delta H^* = \frac{2k\Delta t}{(\Delta x)^2}[T_{i+1}^{m+1}+T_{i-1}^{m+1}-2T_i^{m+1}] \tag{8}$$

$$T^* = f_T(f_H(T_i^m)+\Delta H^*) \tag{9}$$

$$C_i^{m+1} = \Delta H^*/(T^*-T_i^m) \tag{10}$$

After T_i^{m+2} has been found from equation (7), it is recalculated based on

$$T_i^{m+2}(\text{corrected})=f_T[f_H(T_i^m)+C_i^{m+1}(T_i^{m+2}-T_i^m)] \tag{11}$$

The term in the square brackets represents the calculated new enthalpy at node i. If C_i^{m+1} was underestimated causing T_i^{m+2} to "jump" past the freezing temperature, equation (11) will reset T_i^{m+2} back to the freezing range.

2.6 Effective Capacity. This is a new technique, which is being proposed in this work. A temperature profile is assumed between the nodes, and instead of calculating an apparent capacity based on the nodal temperature, an effective capacity is calculated based on an integration through the nodal volume and the assumed temperature profile. The integration to be evaluated is the following:

$$C_{eff}=\left[\int C_a dV\right]/V \tag{12}$$

For the purpose of this work, linear temperature profiles between the nodes have been assumed. Figure 1 illustrates a possible temperature profile for a one-dimensional problem, along with the apparent capacity distribution that would result assuming the apparent capacity function given by equation (4). Since node i is not within the mushy range, the apparent capacity method would set the heat capacity of nodal volume i to C, thus neglecting the latent heat effect for that time step. By evaluating equation (12), the effective capacity method sets the heat capacity of nodal volume i to $(3/4)C+(1/4)C_M$; thus accounting for the latent heat effect.

If, however, the temperature profile and apparent capacity distribution happen to be as in Fig. 2, the apparent capacity method sets the heat capacity of nodal volume i to C_M, thereby overemphasizing the latent heat effect. The effective capacity method again would set the heat capacity to $(3/4)C+(1/4)C_M$. Similar problems occur in multidimensional cases.

By evaluating equation (12) at each time step, it is ensured that the latent heat effect is accounted for at all time steps, even if the mushy range happens to fall between two nodes. Implicit and explicit finite difference as well as implicit finite element formulations have been investigated. Linear temperature profiles between the nodes have been assumed. For further details on this method, see Poirier (1986).

2.7 Tacke's Method. This is a variation of the enthalpy

method for one-dimensional isothermal solidification. The method was introduced by Tacke (1985). It is based on an explicit finite difference formulation and is identical to the enthalpy method except for the element that contains the phase front.

If an element contains the phase front, the front position is calculated using Newton's iterations based on

$$H_i = L(1-\xi) + C(T_{MR} - T_F)(1-\xi)/2 - C(T_F - T_{LM})\xi/2 \tag{13}$$

Once the front location is known, the heat flux density into and out of the element can be defined as

$$Q_L = k(T_F - T_{i-1})/(\Delta x(0.5+\xi)) \tag{14}$$

$$Q_R = k(T_{i+1} - T_m)/(\Delta x(1.5-\xi)) \tag{15}$$

If the phase front passes from one element to another in a time step, the enthalpies are corrected to account for the errors in the assumed heat flux densities.

2.8 Blanchard and Fremond's Method. This technique (Blanchard et al., 1984) uses the freezing index and the homographic approximation. The homographic approximation is simply an approximation to the variation of the liquid water content μ with temperature. It is expressed as

$$\mu = \frac{1}{2}\left(\frac{(T-T_F)}{\eta + |T-T_F|} + 1\right) \tag{16}$$

If T is greater than T_F, μ from this equation approaches unity, while if T is less than T_F, μ approaches zero.

The specific energy of the solidifying material is given by

$$e = CT + L\mu \tag{17}$$

Using this definition and expressing the freezing index by

$$u = k\int_0^t T dt \text{ or } T = \frac{1}{k}\frac{du}{dt} \tag{18}$$

the energy equation can be rewritten as

$$\rho e^t - \rho e^0 = \frac{\partial^2 u}{\partial x^2} + \frac{\partial^2 u}{\partial y^2} \tag{19}$$

In this method, equation (19) is discretized and solved instead of the original energy equation. Both implicit finite difference and finite element formulations have been considered.

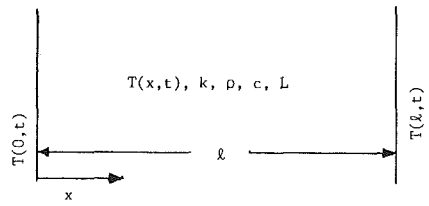

Fig. 3 Schematic of one-dimensional test problem

3 Test Problems

The first three test cases are one dimensional. Figure 3 illustrates the geometry of the problem. The problem was taken to be pure conductive heat transfer. The entire domains was assumed to be at a uniform initial temperature above the phase change temperature, with the front end ($X=0$) dropped to some temperature below the phase change temperature at time ($t=0$).

Table 1 gives the material properties and boundary conditions used for the three test cases. Typical material property values for iron (test case #1), aluminum alloy (test case #2), and water (test case #3) were assumed. The material properties were assumed constant for simplicity, neglecting temperature dependence. For test case #1 and test case #3, the well-known Neumann analytical solution (Neumann, 1912) was used for the comparison of the computed results. Although the Neumann solution is for an infinite solid, the assumption of a constant temperature $T(l, t)$ was found to be acceptable as only an advance of the front through a short distance from the boundary is considered in the computations of the test cases.

The other two test cases were two dimensional. Figure 4 illustrates the geometry of the problem. The problem corresponds to 1/4 of a long square cross-sectional solid initially at some temperature above the phase change temperature, with the surface dropped to some temperature below the phase change temperature at time $t=0$. Table 1 gives the material properties for these test cases. Again, typical material properties for iron (test case #4) and an aluminum alloy (test case #5) were assumed.

4 Results and Discussion

The five test cases were solved using the various techniques and the results were analyzed for accuracy and sensitivity to various parameters. For the two-dimensional test runs, computational costs were also examined. Cost was not examined

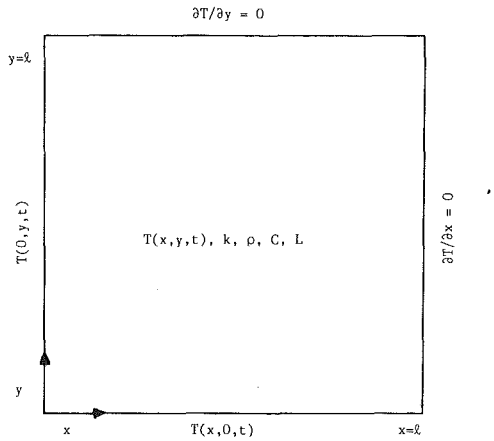

Fig. 4 Schematic of two-dimensional test problem

Table 1 Material properties and boundary conditions for the five test cases

		Test Case #1 1-D Iron	Test Case #2 1-D Aluminum	Test Case #3 1-D Water	Test Case #4 2-D Iron	Test Case #5 2-D Aluminum
Thermal Conductivity	(W/mK)	30.0	130.0	2.0	30.0	130.0
Heat Capacity	(J/kg K)	800.0	900.0	2,500.0	800.0	900.0
Density	(kg/m^3)	7,000.0	2,500.0	1,000.0	7,000.0	2,500.0
Latent Heat	(J/kg)	200,000.0	400,000.0	100,000.0	200,000.0	400,000.0
Phase Change Temperature	(°C)	0.0	-	0.0	0.0	-
Mushy Range	(°C)	-	-50.0 to +50.0	-	-	-50.0 to +50.0
ℓ	(m)	1.0	1.0	2.5	0.1	0.1
T(x,o)	(°C)	150.0	150.0	2.0	-	-
T(o,t)	(°C)	-500.0	-400.0	-10.0	-	-
T(ℓ,t)	(°C)	150.0	150.0	2.0	-	-
T(x,y,o)	(°C)	-	-	-	150.0	150.0
T(o,y,t) = T(x,o,t)	(°C)	-	-	-	-500.0	-400.0

Table 2 Conditions for test cases #1, #2, and #3

	Test Case #1 1-D Iron Explicit	Test Case #1 1-D Iron Implicit	Test Case #2 1-D Aluminum Explicit	Test Case #2 1-D Aluminum Implicit	Test Case #3 1-D Water Explicit	Test Case #3 1-D Water Implicit
Δx (m)	0.05	0.05	0.05	0.05	0.125	0.125
No. of nodes	21	21	21	21	21	21
Δt "A" (s)	70	200	7	20	2000	10000
Fourier moduli "A"	0.15	0.43	0.16	0.46	0.10	0.50
Δt "B" (s)	140	600	14	60	6000	30000
Fourier moduli "B"	0.30	1.3	0.32	1.4	0.31	1.5
Δt "C" (s)	210	1000	21	100	10000	50000
Fourier moduli "C"	0.45	2.1	0.49	2.3	0.50	2.6
Mushy Range* (°C)	10	10	100	100	0.5	0.5
Constant in Homographic Approximation* (°C)	10	10	-	-	0.5	0.5

* Either assumed or actual where applicable.

Table 3 Conditions for test cases #4 and #5

	Test Case 4A 2-D Iron	Test Case 4B 2-D Iron	Test Case 5A 2-D Aluminum	Test Case 5B 2-D Aluminum
$\Delta x = \Delta y$ (m)	0.02	0.01	0.02	0.01
Grid	6×6	11×11	6×6	11×11
Δt (s)	20	10	5.0	2.0
Mushy Range* (°C)	10	10	100	100

* Either assumed or actual where applicable.

for the one-dimensional runs as it was felt that the results for two-dimensional cases are more significant. For some of the methods, both finite difference and finite element formulations have been used. In the one-dimensional finite element cases, three-node quadratic elements were used with a lumped capacity matrix. In the two-dimensional finite element cases, three-node triangular elements were used, again with a lumped capacity matrix. For the finite difference formulations central differences were used in the spatial domain.

The time steps, spatial increments, and mushy ranges used in the computations are given in Tables 2 and 3. In the case of freezing water, the material properties, time steps, and spatial increments were taken similar to those used by Goodrich (1978), as his is a commonly used test case for ice-water modeling.

Tables 4, 5, and 6 give the results of the tests. In the two-dimensional test cases, as well as the test cases involving a mushy region, no analytical solution exists for the comparison of the computed results. For this reason, the problems were solved by a number of methods on an extremely fine grid. It was found that all methods converged to the same results if a fine enough grid and small enough time step were used. These results were used when calculating the standard deviations of the various methods. The standard deviations given in the tables were calculated from the following equation:

$$s = \left[\sum_{n=1}^{N} \left[\sum_{i=1}^{I} (T_i^n - TT_i^n)^2 / I \right]^{0.5} \right] / N \qquad (20)$$

In the two-dimensional test cases five representative points were compared, as shown in Fig. 4. These points are:

$$A = (0.02, \quad 0.02), B = (0.02, \quad 0.040), C = (0.02, \quad 0.08),$$

$$D = (0.06, \quad 0.08), E = (0.08, \quad 0.08)$$

Note: The dimensions of the spatial domain are 0.1×0.1.

For those test cases for which an analytical solution does exist, the evaluation of the solution was started at a small time after zero in order to reduce the errors associated with the stepwise variation of the initial boundary condition being approximated by an element of finite volume.

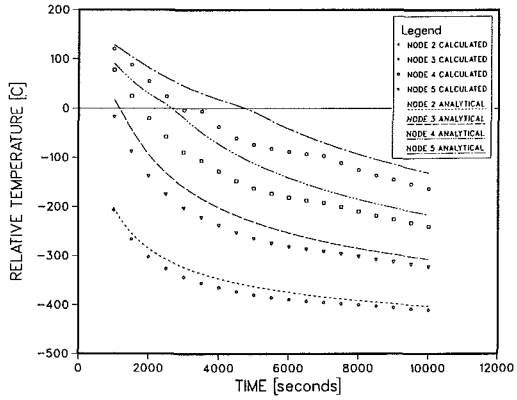

Fig. 5 Temperature histories for test case #1 by the apparent capacity method (mushy = − 5.0 to + 5.0 °C), implicit finite difference; time step is 500 s

4.1 One-Dimensional Iron and One-Dimensional Aluminum. Table 4 gives the standard deviations for the one-dimensional runs. Looking at the explicit runs of the one-dimensional solidifying iron case (test case #1), it is evident that the performance of the apparent capacity method is poor compared with the other techniques. The implicit apparent capacity standard deviations for the same test case again appear much larger than some of the other methods. Figure 5 shows the temperature history of the second to the fifth nodes for test case #1 with a time step of 500 s. Obviously, the apparent capacity method is severely underpredicting the temperatures. Referring again to Table 4, for the one-dimensional aluminum case, although the mushy range is much larger than in the first test case, the apparent capacity performs poorly, particularly in the explicit runs. Figure 6 shows the variation of the standard deviation with the time step for the one-dimensional aluminum test case. The errors are large (some >8°C), and decreasing the time step does not always result in improved accuracy. These large errors can be explained, however. If the mushy range at any time falls between two nodes, the latent heat effect is not accounted for in that time step and hence the temperatures fall unrealistically fast. It seems then that increasing the assumed mushy range in the one-dimensional iron case might help alleviate this problem. Figure 7 illustrates the effect of the assumed mushy range. As expected, increasing the assumed mushy range does

Table 4 Standard deviations for test cases #1, #2, and #3

	Test Case #1 1-D Iron (°C)			Test Case #2 1-D Aluminum (°C)			Test Case #3 1-D Water (°C)		
	A	B	C	A	B	C	A	B	C
Explicit Time Step (s)	70	140	210	7	14	21	2000	6000	10000
Post Iterative (isothermal, explicit)	4.3	4.6	5.2	-	-	-	0.17	0.17	0.17
Post Iterative (mushy, explicit)	3.8	4.1	4.7	2.6	2.6	3.0	0.16	0.16	0.17
Apparent Capacity (explicit)	12.5	17.2	19.0	2.8	6.4	9.4	0.32	0.60	0.65
Enthalpy Method (mushy, explicit)	3.8	4.1	4.5	2.4	2.3	2.2	0.17	0.16	0.17
Effective Capacity (explicit)	3.5	4.1	4.8	1.2	1.6	2.7	0.24	0.26	0.33
Tacke Method (explicit)	1.4	1.8	2.3	-	-	-	0.021	0.017	0.03
Implicit Time Step (s)	200	600	1000	20	60	100	10000	30000	50000
Post Iterative (isothermal, implicit)	7.0	11.0	14.0	-	-	-	0.45	0.75	1.0
Post Iterative F.E. (isothermal, implicit)	12.0	19.0	25.0	-	-	-	0.40	0.75	1.0
Post Iterative (mushy, implicit)	7.0	11.0	21.0	9.0	19.0	27.4	0.40	0.75	1.0
Apparent Capacity (implicit)	12.0	15.0	17.0	5.2	5.9	9.7	0.60	1.3	0.65
Enthalpy Method (mushy, implicit)	3.5	4.3	5.8	4.5	6.2	8.3	0.16	0.16	0.17
Pham Method (implicit)	5.5	17.0	32.0	4.0	6.5	>30	0.20	0.60	1.7
Effective Capacity (implicit)	2.3	3.2	5.0	1.5	3.2	4.3	0.18	0.22	0.32
Effective Capacity F.E. (implicit)	2.4	3.0	4.8	1.6	2.5	4.0	0.18	0.22	0.26
Blanchard & Fremond (implicit)	2.2	3.8	6.0	-	-	-	0.29	0.29	0.28
Blanchard & Fremond F.E. (implicit)	3.7	4.0	5.0	-	-	-	0.46	0.46	0.46

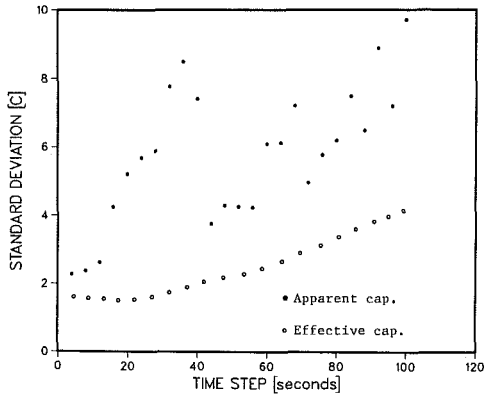

Fig. 6 Variation of standard deviation with time step for test case #2

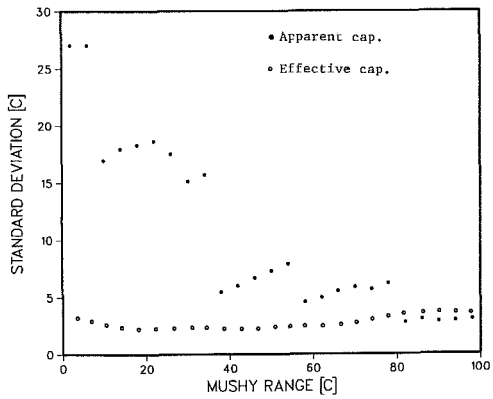

Fig. 7 Variation of standard deviation with mushy range for test case #1; time step is 500 s

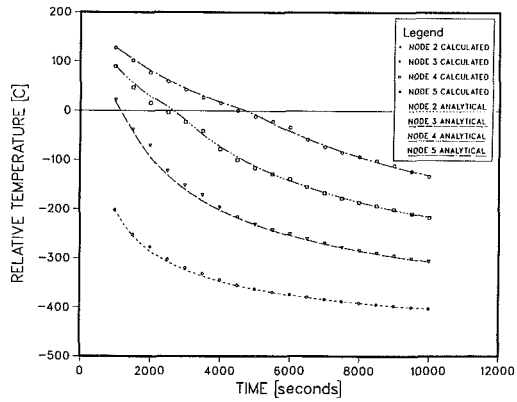

Fig. 8 Temperature histories for test case #1 by the effective capacity method (mushy = −5.0 to +5.0 °C), implicit finite element; time step is 500 s

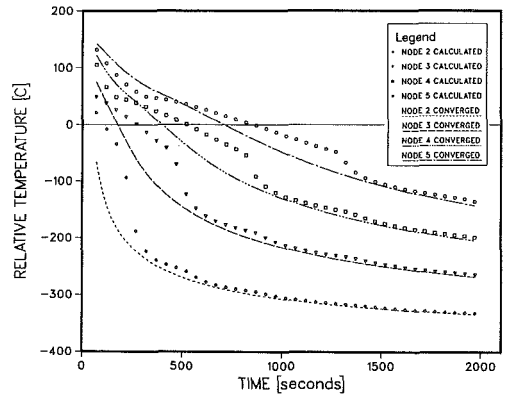

Fig. 9 Temperature histories for test case #2 by the postiterative method, implicit finite difference; time step in 50 s

improve the results, but a very large mushy range must be assumed (>80°C for standard deviation consistently below 5°C).

Referring again to the first two test cases in Table 4, Pham's method, which should reduce the errors associated with the apparent capacity method, seems to help for the smaller time steps, but for the larger time steps, the problems persist.

From Table 4, the proposed effective capacity formulation is very accurate for the first two test cases. Figure 8 shows the temperature histories for the implicit finite element formulation of the effective capacity method for the one-dimensional iron test case (#1). The accuracy is excellent, even near the phase change temperature. Figure 6 shows the effect of increasing the time step on the effective capacity solution to the one-dimensional aluminum test case. The solution is very well behaved. Figure 7 shows the effect of the assumed mushy range on the solution to the first test case using the effective capacity method. The effect is minimal for the range considered. The effective capacity formulation appears to be very good in solving the two one-dimensional solidifying metal

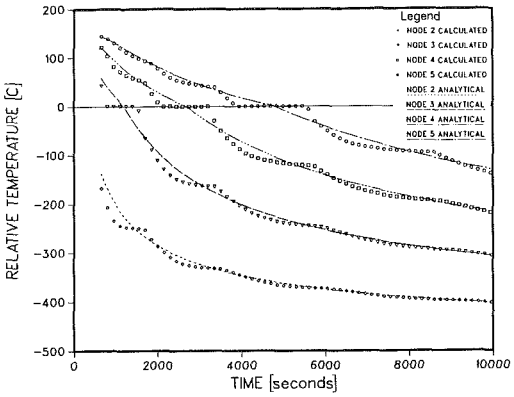

Fig. 10 Temperature histories for the test case #1 by the postiterative (isothermal) method, explicit finite difference formulation; time step is 150 s

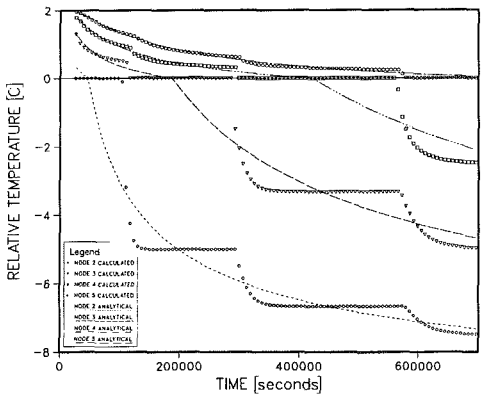

Fig. 11 Temperature histories for test case #3 by the postiterative (isothermal) method, explicit finite difference; time step is 6500 s

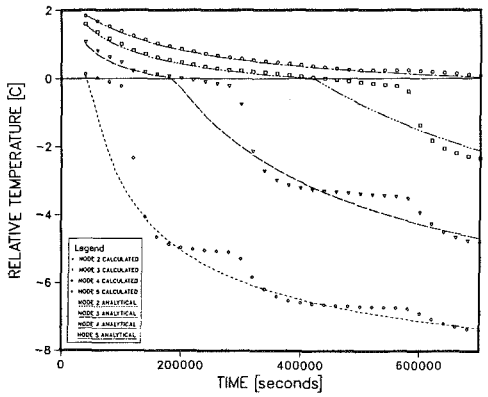

Fig. 12 Temperature histories for test #3 by the enthalpy method (mushy = −0.25 to +0.25 °C), implicit finite difference; time step is 2000 s

cases (with a mushy range or isothermal solidification by assuming a small mushy range.)

Referring to the two metal test cases in Table 4, the postiterative solutions appear acceptable for smaller time steps but not very accurate for the larger time steps. Even in the second test case, where the mushy range is large, the standard deviations are greater than 20°C for the larger time steps. Figure 9, illustrating the temperature histories calculated for the one-dimensional aluminum case using the postiterative method, reveals that the temperatures fall unrealistically while in the mushy range. Figure 10 shows the temperature histories for the one-dimensional iron test case, calculated using the postiterative method. It is evident from this figure that even though the overall errors are sometimes acceptable in the first

Table 5 Costs and standard deviations for test case #4

	Test Case #4A 2-D Iron Δt = 20s ΔX = ΔY = 0.02m		Test Case #4B 2-D Iron Δt = 10s ΔX = ΔY = 0.01m	
	Cost*	Standard Deviation (°C)	Cost*	Standard Deviation (°C)
Post Iterative (isothermal, F.D.)	0.02	10.9	0.07	7.4
Post Iterative (mushy, F.D.)	0.02	10.3	0.07	6.8
Post Iterative (mushy, F.E.)	0.11	18.6	2.08	12.2
Apparent Capacity (F.D.)	0.02	55.9	0.07	39.8
Apparent Capacity (mushy = −25 to +25, F.D.)	0.02	9.5	0.07	12.5
Effective Capacity (F.D.)	2.64	17.2	4.15	7.7
Effective Capacity (F.E.)	2.95	14.0	10.5	10.4
Effective Capacity (mushy = −25 to +25, F.D.)	0.23	10.5	0.58	3.2
Enthalpy (F.D.)	0.10	9.5	1.03	5.9

*Cost = constant (395 + virtual memory pages) CPU time

Table 6 Costs and standard deviations for test case #5

	Test Case #5A 2-D Aluminum Δt = 5s ΔX = ΔY = 0.02m		Test Case #5B 2-D Aluminum Δt = 2s ΔX = ΔY = 0.01m	
	Cost*	Standard Deviation (°C)	Cost*	Standard Deviation (°C)
Post Iterative F.D.	0.02	19.2	0.04	9.7
Post Iterative F.E.	0.05	38.7	1.04	19.0
Apparent Capacity F.D.	0.02	42.3	0.04	23.6
Effective Capacity F.D.	0.09	8.6	0.31	3.5
Effective Capacity F.E.	0.19	10.3	3.33	7.2
Enthalpy (F.D.)	0.06	12.0	0.81	5.7

*Cost = constant (395 + virtual memory pages) CPU time

test case, the errors near the phase change temperature using the postiterative method can be quite large.

Referring once again to the first two test cases in Table 4, the enthalpy method gives accurate solutions in the first two test cases, but in general, not as accurate as the effective capacity results. This is particularly true in the one-dimensional aluminum test case. Tacke's formulation of the enthalpy method gives accurate results in the one-dimensional case. Finally, Blanchard and Fremond's formulation give accurate results in the one-dimensional iron test case. It should be mentioned that this formulation is more difficult to add to existing single-phase codes than most of the others, and that the formulation is very sensitive to the chosen constant in the homographic approximation.

4.2 One-Dimensional Water. The third test case is the ice-water case. Looking at the one-dimensional water test case in Table 4, and remembering that the total temperature range of the initial condition is only 12°C, and hence a standard deviation of 1°C represents 8.3 percent of the total, one recognizes that the solutions are extremely poor except for Tacke's solution. Figures 11 and 12 show the temperature histories calculated with the explicit postiterative and the implicit enthalpy methods for the ice-water case. There are large fluctuations in the temperature histories. Figure 13 shows the solution using Tacke's formulation. The improvement is exceptional. It appears then that there are significant differences in the numerical behavior between the solidfying metal and the ice-water test cases. Examining the ratio of the latent heat to the total sensible heat that would be released if the whole domain dropped from its initial condition to the boundary temperature gives:

One-dimensional iron test case
$L/(C(150+500))\times 100 = 38$ percent
One-dimensional aluminum test case
$L/(C(150+400))\times 100 = 80$ percent
One-dimensional ice-water test case
$L/(C(\ 2+\ 10))\times 100 = 330$ percent

The difference is evident. The ratio of the latent heat to the sensible heat in the ice-water case is much higher. This means that in the ice-water test case, the effect of the latent heat is greater when the phase front is within the nodal volume and hence the nodal temperature falls unrealistically slowly. Tacke's formulation allows the temperature to fall realistically while the front is within the nodal volume and hence the

results are much better. Although Tacke has succeeded in doing this for the one-dimensional case, it is extremely difficult to extend to multidimensional cases since the phase front is no longer necessarily parallel to the element boundaries.

4.3 Two-Dimensional Iron and Two-Dimensional Aluminum. Tables 5 and 6 give the results for some of the methods applied to the two-dimensional test cases. All of these formulations use an implicit scheme. The finite difference formulations all used the well-known Alternating Direction Implicit (ADI) scheme. The finite element formulations used Gaussian elimination (taking into account the banded nature of the matrices) to solve the equations. Although this is not the most efficient method for solving the matrices, observations are made about the relative costs of the different methods. The runs were done on a 48 megabyte Amdahl 5850 computer with accelerator. The costs are based on CPU time and virtual memory usage.

In order to assess the effect of the magnitude of the assumed mushy range, the apparent capacity and the effective capacity runs for the two-dimensional iron test case were redone with a larger assumed mushy region than that given in Table 3. These results are given along with the other results for the two-dimensional iron test case in Table 5. The cost columns of Table 5 show some dramatic differences between the various formulations. The large costs and errors associated with the effective capacity method are related to the integrating subroutine attempting to locate such a small mushy range in the first few time steps, when the boundary condition temperature gradients are large. Increasing the assumed mushy range facilitates this integration and hence the cost effectiveness and accuracy are greatly enhanced. The apparent capacity method still gives poor accuracy when the mushy range is small, although for the larger assumed mushy range, the results are better. The low cost of using the postiterative method means that very fine grids can be used at competitive cost, in order to improve the accuracy of the results. The enthalpy method standard deviations are low; however, for larger problems with many grid points, the cost of the iterative solving routine is expected to be prohibitive. Finally, the cost of the ADI finite difference formulation relative to the finite element formulation is considerably less. This difference is expected to be even larger for three-dimensional problems.

Table 6 gives the results for the two-dimensional aluminum alloy test cases. In these test cases, a mushy range does exist. The standard deviation results reveal that the effective capacity and the enthalpy method results are consistently more accurate than the other methods. Although the cost is slightly greater for the effective capacity method, it should be pointed out that this is a very simplified problem. In practical problems, relatively few of the nodal points in the grid would be changing phase since the grid would include the mold as well as the casting. Also, having temperature-dependent properties would increase the cost per grid point. If grid size then is dominated by the latent heat effect, the effective capacity may offer substantial savings by reducing the size of the grid needed. Also, the large initial temperature gradients encountered in these test cases are not expected in practical problems and hence the relative cost of the effective capacity method is expected to be much less.

5 Conclusions

It has been shown that the best numerical methods for solving phase change problems for water are not necessarily the best for metals. Tacke's formulation of the enthalpy method offers significantly better performance than the other methods investigated for the one-dimensional ice-water test case. More work needs to be done in order to determine the best method for solving multidimensional isothermal solidification problems where the latent heat is large compared to the sensible heat (as for water). In this case the integrating subroutine of the effective capacity method can be made more efficient by adding a check for temperature gradients that are large compared to the mushy range. Simplifying assumptions can then be made in order to decrease the numerical effort for the integration. For solidifying metal problems where the latent heat is spread over a large temperature range, or if the phase change is isothermal but the latent heat is small compared to the sensible heat, the effective capacity method proposed by the authors performs better than other methods investigated for comparable costs. The results using this method appear good even near the phase front.

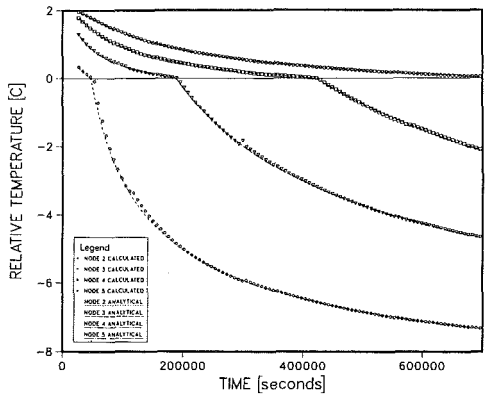

Fig. 13 Temperature histories for test case #3 by Tacke's method, explicit finite difference; time step is 6500 s

References

Bell, G. E., and Wood, A. S., 1983, "On the Performance of the Enthalpy Method in the Region of a Singularity," *Int. J. Num. Meth. Engr.*, Vol. 19, pp. 1583–1592.

Blanchard, D., and Fremond, M., 1984, "The Stefan Problem: Computing Without the Free Boundary," *Int. J. Num. Meth. Engr.*, Vol. 20. pp. 757–771.

Brauner, C. M., Fremond, M., and Nicolaenko, B., 1982, "A New Homographic Approximation to Multiphase Stefan Problems, in Free Boundary Problems," *Theory and Applications*, A. Fasano and M. Primicerio, eds., Elsevier, Amsterdam.

Comini, G., Del Guidice, S., Lewis, R. W., and Zienkiewicz, O. C., 1974, "Finite Element Solution of Non-linear Heat Conduction Problems With Special Reference to Phase Change," *Int. J. Num. Meth. Engr.*, Vol. 8, pp. 613–624.

Crowley, A. B., 1978, "Numerical Solution of Stefan Problems," *Int. J. Heat Mass Transfer*, Vol. 21, pp. 215–219.

Doherty, P. C., 1970, "Hot Pipe," *U.S. Geological Survey Computer Contribution*, No. 4.

Duda, J. L., Malone, M. F., Notter, R. H., and Vrentas, J. S., 1975, "Analysis of Two-Dimensional Diffusion—Controlled Moving Boundary Problems," *Int. J. Heat Mass Transfer*, Vol. 18, pp. 901–910.

Dusinberre, G. M., 1945, "Numerical Methods for Transient Heat Flows," *Trans. ASME*, Vol. 67, p. 703.

Goodrich, L. F., 1978, "Efficient Numerical Technique for One-Dimensional Thermal Problems With Phase Change," *Int. J. Heat Mass Transfer*, Vol. 21, pp. 615–621.

Hashemi, H. T., and Sliepcevich, C. M., 1967, "A Numerical Method for Solving Two-Dimensional Problems of Heat Conduction With Change of Phase," *Chem. Eng. Prog. Symp. Series*, No. 79, Vol. 63, pp. 34–41.

Jerome, J. W., 1977, "Nonlinear Equations of Evolution and a Generalized Stefan Problem," *Journal of Diff. Eqn.*, Vol. 26, pp. 240–261.

Kikuchi, N., and Ichikawa, Y., 1979, "Numerical Methods for a Two-Phase Stefan Problem by Variational Inequalities," *Int. J. Num. Meth. Engr.*, Vol. 14, pp. 1221–1239.

Lazaridis, A., 1970, "A Numerical Solution of the Multi-dimensional Solidification (or Melting) Problem," *Int. J. Heat Mass Transfer*, Vol. 13, pp. 1459–1477.

Lunardini, V. J., 1981, *Heat Transfer in Cold Climates*, Van Nostrand Reinhold, New York, pp. 471–532.

Lynch, D. R., 1982, "Unified Approach to Simulation on Deforming Elements With Application to Phase Change Problems," *Journal of Computational Physics*, Vol. 47, No. 3, pp. 387–411.

Lynch, D. R., and O'Neill, K., 1981, "Continuously Deforming Finite Elements for the Solution of Parabolic Problems, With and Without Phase Change," *Int. J. Num. Meth. Engr.*, Vol. 17, pp. 81–96.

Meyer, G. H., 1977, "An Application of the Method of Lines to Multi-dimensional Free Boundary Problems," *J. Inst. Maths Applics*, Vol. 20, pp. 317–329.

Meyer, G. H., 1973, "Multi-dimensional Stefan Problems," *SIAM J. Numer. Anal.*, Vol. 10, No. 3, pp. 522–538.

Neumann, F., 1912, "Die Partiellen Differentialgleichungen der Mathematischen Physik," *Riemann-Weber*, Vol. 2, p. 121.

Pham, Q. T., 1985, "A Fast Unconditionally Stable Finite-Difference Scheme for Heat Conduction With Phase Change," *Int. J. Heat Mass Transfer*, Vol. 28, No. 11, pp. 2079–2084.

Poirier, D., 1986, Master of Applied Science Thesis, University of Ottawa.

Rolph, W. D., and Bathe, D., 1982, "An Efficient Algorithm for Analysis of Nonlinear Heat Transfer With Phase Changes," *Int. J. Num. Meth. Engr.*, Vol. 18, pp. 119–134.

Salcudean, M., and Abdullah, Z., 1986, "Numerical Simulation of Casting Processes," *Proceedings of the VIII International Heat Transfer Conference and Exhibition*, San Francisco, CA, Aug. 12–22, pp. 459–464.

Salcudean, M., and Mashaie, A., 1983, "Mathematical Modelling of Heat Transfer in Permanent Molds," (Rep. II—Cylindrical—2D Coordinates), Dept. of Mechanical Engineering, University of Ottawa.

Shamsunder, N., and Sparrow, E. M., 1975, "Analysis of Multi-dimensional Conduction Phase Change Via the Enthalpy Model," ASME JOURNAL OF HEAT TRANSFER, Vol. 97, pp. 333–340.

Stefan, J., 1891, *Ann. Phys. U. Chem.*, (Wiedemann) N. F., Vol. 42, pp. 269–286.

Tacke, K. H., 1985, "Discretization of the Explicit Enthalpy Method for Planar Phase Change," *Int. J. Num. Meth. Engr.*, Vol. 21, pp. 543–554.

Forced Convection Heat Transfer in a Finitely Conducting Externally Finned Pipe

F. Moukalled

S. Acharya

Mechanical Engineering Department,
Louisiana State University,
Baton Rouge, LA 70803

A numerical study to determine the influence of axial wall conduction on forced convection heat transfer in an externally finned pipe has been made. The effects of wall conductivity, interfin spacing, and external heat transfer coefficient are examined by comparing the results with the corresponding solutions obtained assuming negligible wall conduction. Results indicate that the axial conduction in the pipe walls has a significant influence on the heat transfer behavior. The bulk temperature or the heat transferred to the fluid is underestimated when wall conduction is ignored. At high wall conductivity values, the wall temperatures and Nusselt numbers exhibit a monotonic variation in the axial direction, with the behavior becoming increasingly nonmonotonic as the wall conductivity value is decreased.

Introduction

Externally finned pipes are commonly encountered in engineering practice and are routinely used in a large number of heat exchange applications, such as residential or institutional space heating. The fins, which are generally equispaced annular or square plates on the outer pipe surface, produce a local augmentation in heat transfer between the fin base area and the surroundings. Thus, the outside surface of the pipe may be assumed to be subjected to a periodic boundary condition with low heat transfer rates along the unfinned part of the pipe and high heat transfer rates along the finned parts. This physical picture may be represented by assuming that the convection heat transfer coefficient on the outer surface of the pipe has a small value (h_1) along the unfinned part and a high value (h_2) along the finned part. A schematic of the externally finned pipe and the periodic variation of the heat transfer coefficient along the outer surface are shown in Fig. 1.

In a recent paper, Sparrow and Charmchi (1980) have studied the heat transfer behavior in an externally finned pipe, but have neglected the effects of axial wall conduction in the pipe walls. Thus, the flow in the pipe is subjected to abrupt variations of convection heat transfer through the pipe walls. In reality, the behavior is likely to be quite different since the longitudinal wall conduction will smear the abrupt variations of the convection heat transfer along the outer pipe surface, with the extent of such smearing determined by the simultaneous solution of the coupled wall conduction-convection problem. Sparrow and Charmchi (1980) recognized the importance of the conduction-convection coupling, but, in view of the computational complexity, elected to tackle a simpler problem by neglecting axial wall conduction. The present paper extends the work reported by Sparrow and Charmchi (1980), and delineates the influence of axial wall conduction on convection heat transfer in an externally finned pipe. For this purpose, results presented by Sparrow and Charmchi (1980) are used as a baseline case for comparison purposes.

Reported studies describing the effects of axial wall conduction on convection in smooth (not finned) ducts are limited, with the studies reported by Faghri and Sparrow (1980), Davis and Gill (1970), Hsu (1968), Reynolds (1963), and Mori et al. (1974, 1976) representative of the available literature. No work dealing with conjugate heat transfer (coupled conduction-convection) problems in finned ducts has been reported in the literature, and therefore results in the present paper are a first in this regard.

Since no analytical solution for this problem is possible, results have been obtained by a finite difference procedure. The thermal conditions along the inside pipe surface are required as a boundary condition for both the convection and wall conduction problem, but are not known a priori to the calculation process. In fact, these conditions are dictated by the coupling between axial conduction and pipe convection and, therefore, they have to be solution determined. Thus, unlike the problem studied by Sparrow and Charmchi (1980), consecutive solutions of the equations governing the axial wall conduction and pipe convection are necessary in order to resolve the heat transfer coupling across the inner pipe surface.

Governing Equations

A schematic of the physical situation considered is shown in Fig. 1(*a*), and the model adopted for the variation of heat transfer coefficient on the outside pipe surface is displayed in Fig. 1(*b*). Results will be obtained for laminar, hydrodynamically fully developed flow entering the finned

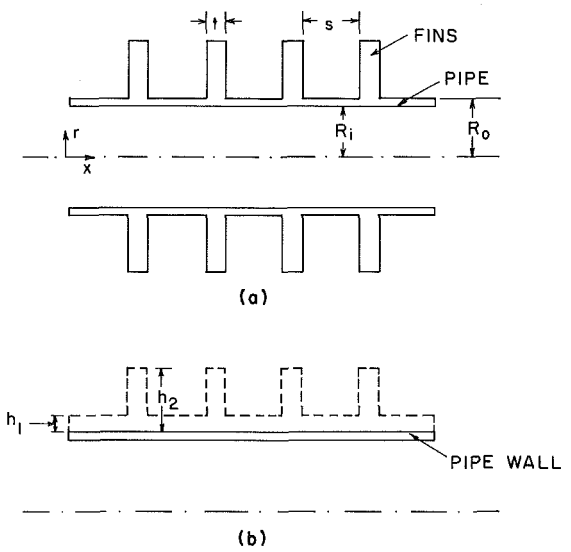

Fig. 1 (*a*) Physical situation; (*b*) adopted model for the heat transfer coefficient variation

Contributed by the Heat Transfer Division for publication in the JOURNAL OF HEAT TRANSFER. Manuscript received by the Heat Transfer Division March 21, 1986. Keywords: Conjugate Heat Transfer, Finned Surfaces, Forced Convection.

pipe at a uniform temperature of T_o. The pipe walls are assumed to be finitely conducting, and since the wall thickness is small compared to the longitudinal dimension, only axial wall conduction is considered.

To minimize the number of parameters to be considered, the following dimensionless variables are introduced:

$$X = x/R_i/\mathrm{Pe}, \quad \eta = r/R_i, \text{ and } \theta = (T - T_o)/(T_\infty - T_o) \tag{1}$$

where Pe is the Peclet number defined as $2\bar{U}R_i/\alpha$. Since the Peclet number range of interest in this paper is larger than 50, the axial diffusion of energy in the fluid is neglected. The resulting dimensionless energy equation in the flow is

$$(U/\bar{U})(\partial\theta/\partial X) = (2/\eta)\frac{\partial}{\partial\eta}(\eta\partial\theta/\partial\eta) \tag{2}$$

where $U/\bar{U}$ in the above equation, due to the hydrodynamically fully developed flow assumption, can be written as

$$U/\bar{U} = 2(1-\eta^2) \tag{3}$$

Since equation (2) is parabolic in nature, boundary conditions are needed along $X=0$ and along $\eta=0$ and $\eta=1$. These conditions can be expressed as

$$\theta = 0 \quad \text{at} \quad X = 0 \tag{4}$$

$$\partial\theta/\partial\eta = 0 \quad \text{at} \quad \eta = 0 \tag{5}$$

$$\theta = \theta_w \quad \text{at} \quad \eta = 1 \tag{6}$$

In equation (6), θ_w represents the pipe wall temperature, which is not known a priori to the calculation procedure but is solution determined. Discussion on how the correct solution for θ_w is obtained is given in the next section.

Along the pipe walls, the heat conduction equation can be determined by making a quasi one-dimensional energy balance (as for a fin). Before presenting the energy balance equation, it should be noted that along the outer pipe surface, the convection heat transfer is periodic in nature with a Biot number equal to Bi_1 along the unfinned portion and Bi_2 along the finned part. The dimensionless energy balance along the pipe walls can be expressed as

$$\partial^2\theta_w/\partial X^2 - \psi\mathrm{Bi}\theta_w + \gamma = 0 \tag{7}$$

where

$$\psi = 2\mathrm{Pe}^2/[(R_o/R_i)^2 - 1] \tag{8}$$

$$\gamma = \psi[\mathrm{Bi} - \beta(\partial\theta/\partial\eta)_{\eta=1}] \tag{9}$$

$$\beta = K_f/K \tag{10}$$

As mentioned above, the Biot number varies periodically in the axial direction, i.e.,

$$\mathrm{Bi} = \mathrm{Bi}_1 = h_1R_o/K \qquad n(\sigma+\tau) < X < n(\sigma+\tau)+\sigma \tag{11}$$

$$\mathrm{Bi} = \mathrm{Bi}_2 = h_2R_o/K \qquad n(\sigma+\tau)+\sigma < X < (n+1)(\sigma+\tau) \tag{12}$$

where σ and τ are the dimensionless interfin spacing and fin thickness, respectively, and n takes the values of 0, 1, 2, ...

To solve equation (7), thermal conditions for θ_w are needed at the inlet ($x=0$) and exit ($x=L$) of the finned pipe. Since, at $x=0$, the velocity profile is taken to be fully developed, it has been implicitly assumed that the pipe length preceding the finned section is long and therefore, it is reasonable to presume that the flow and pipe wall at $x=0$ are isothermal at T_o. Another boundary condition of interest is that corresponding to a very poorly conducting pipe upstream (e.g., a CPVC pipe) of the finned section, in which case, adiabatic conditions may be assumed at $x=0$. At the other end, $x=L$, it is assumed (for lack of better information) that the finned section is followed by a well-insulated length of a poorly conducting pipe (e.g., a CPVC pipe), so that adiabatic conditions may be considered to be approximately valid. In dimensionless terms, these conditions may be expressed as

$$\theta_w = 0, \text{ or } \partial\theta_w/\partial X = 0 \text{ at } X = 0 \tag{13}$$

and

$$\partial\theta_w/\partial X = 0 \text{ at } X = L/R_i/\mathrm{Pe} \tag{14}$$

In addition to the justification provided above for the boundary conditions expressed by equations (13) and (14), it should be mentioned that reported studies in the literature dealing with the effect of axial conduction on flow in smooth pipes and channels have used similar boundary conditions. For example, Davis and Gill (1970) and Mori et al. (1974, 1976) have considered a situation in which wall conduction effects are confined to a finite length of the heated pipe walls with an adiabatic boundary condition imposed at the upstream and downstream ends of the heated segment. In the studies reported by Aleksashenko (1968), Luikov et al. (1971),

Nomenclature

Bi = external Biot number = hR_o/K
Bi_1 = Biot number for unfinned surface = h_1R_o/K
Bi_2 = Biot number for finned surface = h_2R_o/K
h = external heat transfer coefficient
h_1 = coefficient for unfinned surface
h_2 = coefficient for finned surface
K = pipe wall thermal conductivity
K_f = fluid thermal conductivity
L = tube length
Nu_i, $\overline{\mathrm{Nu}}_i$ = local and average Nusselt numbers based on the wall to fluid temperature difference
Nu_o, $\overline{\mathrm{Nu}}_o$ = local and average Nusselt numbers based on the outside to fluid temperature difference
$\mathrm{Nu}_{i,u}$, $\overline{\mathrm{Nu}}_{i,u}$ = local and average Nu_i values for the unfinned part of the pipe
$\mathrm{Nu}_{o,u}$, $\overline{\mathrm{Nu}}_{o,u}$ = local and average Nu_o values for the unfinned part of the pipe
$\mathrm{Nu}_{i,f}$, $\overline{\mathrm{Nu}}_{i,f}$ = local and average Nu_i values for the finned part of the pipe
$\mathrm{Nu}_{o,f}$, $\overline{\mathrm{Nu}}_{o,f}$ = local and average Nu_o values for the finned part of the pipe
Pe = Peclet number
Q = rate of heat transfer between $x = 0$ and $x = x$
$Q_{\max}$ = maximum heat transfer rate
R_i = inside tube radius
R_o = outside tube radius
r = radial coordinate
s = interfin spacing
t = fin thickness
T = temperature
T_o = inlet fluid temperature
T_∞ = ambient temperature
U = axial velocity
$\bar{U}$ = mean velocity
x = axial coordinate
X = dimensionless axial coordinate = $(x/R_i)/\mathrm{Pe}$
α = thermal diffusivity = $K_f/\rho C_p$
β = ratio of fluid to wall thermal conductivity = K_f/K
η = dimensionless radial coordinate = r/R_i
θ = dimensionless temperature = $(T-T_o)/(T_\infty - T_o)$
σ = dimensionless interfin spacing = $(s/R_i)/\mathrm{Pe}$
τ = dimensionless fin thickness = $(t/R_i)/\mathrm{Pe}$

and Povarnitsyn and Yurlova (1966), a semi-infinite heated and conducting wall was considered with either a given temperature or adiabatic condition being prescribed at the upstream end of the wall.

It should be pointed out that $(-\partial\theta/\partial\eta)_{\eta=1}$ appearing in equation (9) is the dimensionless heat flux entering the pipe walls from the fluid side and, since it is not known a priori to the calculation, has to be continuously updated as the solution progresses.

Equations (1)–(14) provide a complete mathematical specification of the problem. Prescribable parameters in the problem are the conductivity ratio ($\beta = K_f/K$), the Biot numbers Bi_1 and Bi_2, the interfin spacing σ, the fin thickness τ, the radius ratio R_i/R_o, and the length of the finned pipe $L/R_i/\mathrm{Pe}$. To minimize the number of parameters to be studied, the radius ratio R_i/R_o was assigned the constant value of 0.9 while the dimensionless length of the finned pipe was taken to be 0.2 (which is approximately the value reported by Sparrow and Charmchi (1980), within which the flow attains a thermally fully developed state). For the other parameters, representative values were chosen and are presented later.

Solution Procedure

The energy equation in the fluid (equation (2)) is solved by adopting the parabolic calculation procedure of Patankar and Spalding (1970), which is a forward marching procedure starting from $X=0$. The heat conduction equation in the pipe is solved by a finite difference scheme. Since θ_w in equation (6) and $(\partial\theta/\partial\eta)_{\eta=1}$ in equation (9) are not known beforehand, a consecutive solution scheme with information exchange in each cycle of solution is necessary. To elaborate further, the boundary layer energy equation in the fluid is first solved using a guessed value for θ_w. Using this solution, the heat flux along the inner pipe surface $(\partial\theta/\partial\eta)_{\eta=1}$ is determined and these values are employed in the heat conduction equation (7) to obtain updated values for θ_w. With the updated θ_w, equation (2) is again solved and a better estimate for $(\partial\theta/\partial\eta)_{\eta=1}$ is obtained. This new estimate for the heat flux is again used in solving the heat conduction equation. The aforementioned consecutive calculations for θ_w and θ are continued until successive changes in the temperature values are less than 10^{-4}. Typically, three to six consecutive calculations are required in the parameter range considered.

As mentioned earlier, the computational task is a demanding one, partly due to the consecutive calculations required to resolve the conduction-convection coupling and partly due to the periodic boundary condition, which, for purposes of accuracy, necessitates the deployment of an excessively fine grid, particularly in the streamwise direction. In solving the boundary layer energy equation, 100 cross-stream grid points are used, with a higher concentration of grid points near the pipe walls. In the streamwise direction, the forward step size is gradually increased from 10^{-6} at $X=0$ to 5×10^{-6} at $X=0.2$. In solving the conduction equation, 6100 grid points, each at the center of a control volume, are used. Since the numbers of axial grid points in the conduction and the flow problems are different, averaging or interpolation is necessary to transfer information from one problem to the other. To facilitate this process, the forward step sizes in the boundary layer calculation are continuously monitored and, in the immediate vicinity of a conduction control volume boundary, the forward step size is adjusted so that the forward step location in the boundary layer corresponds exactly to the control volume boundary location.

To verify the numerical accuracy of the solution, results were first obtained without accounting for axial wall conduction and the solution compared with those reported by Sparrow and Charmchi (1980). The two solutions compared very well with each other, with the results computed in this work falling right on top of the plotted curves of Sparrow and Charmchi (1980). As a further test, the calculations were performed on a finer grid, with forward step sizes of the order of 10^{-8}, 200 cross-stream points in the boundary layer and 6100 grid points in the conduction problem. Results obtained with the finer grid agree to within 0.75 percent of the results reported in this paper.

Table 1 Parameter values

Case	$\beta\ (=K_f/K)\times10^3$	τ	σ	Bi_1	Bi_2
1	66	10^{-4}	3τ	1	50
2	1.65	10^{-4}	3τ	1	50
3	66	10^{-4}	7τ	1	50
4	1.65	10^{-4}	7τ	1	50
5	66	10^{-4}	3τ	5	250
6	1.65	10^{-4}	3τ	5	250

Results and Discussion

In view of the very lengthy computations required for each case, results have been obtained only for a sequence of representative cases in order to highlight the influence of the various parameters. Choices for τ, σ, Bi_1, and Bi_2 are identical to those chosen by Sparrow and Charmchi (1980). Two values of β are chosen with one corresponding to a low wall conductivity value ($\beta = 66\times10^{-3}$) and the other to a high value of wall thermal conductivity ($\beta = 1.65\times10^{-3}$). The two β values are based on a fluid thermal conductivity (K_f) of 0.66 W/m-K (corresponding to water) and wall thermal conductivity values of 10 W/m-K (corresponding to steel) and 400 W/m-K (corresponding to copper). Thus, β values used correspond to commonly encountered pipe materials. The various cases studied are listed in Table 1. In cases 1 and 2, the interfin spacing is three times the fin thickness, with the heat transfer coefficient along the finned part 50 times the heat transfer coefficient over the unfinned part of the tube. Cases 3 and 4 examine the effect of increasing the interfin spacing to seven times the fin thickness while cases 5 and 6 explore the influence of increasing the general level of the heat transfer coefficient, keeping the ratio h_2/h_1 the same (i.e., 50). As mentioned earlier, results will be compared with those presented with negligible wall conduction (Sparrow and Charmchi, 1980). Results will be primarily obtained with the $\theta_w = 0$ condition at $X = 0$, with limited calculations made using the $\partial\theta_w/\partial X = 0$ boundary condition. Representative results will also be obtained for an unfinned pipe with a constant external heat transfer coefficient.

It should be pointed out that with $\beta\to\infty$, locally adiabatic conditions will prevail along the pipe walls, and heat flux on the outer pipe surface will be transmitted entirely in the radial direction, with no longitudinal heat transfer in the walls. This situation is then identical to that of Sparrow and Charmchi (1980). Calculations were performed in this paper with a very high value (10^{20}) assigned to β. Computed results were found to be in excellent agreement with the results reported by Sparrow and Chamchi (1980).

Results presented include the bulk temperature, the local and average Nusselt numbers, and finally the pipe wall temperature distribution. The bulk temperature is defined as

$$\theta_{bx} = 2\int_0^1 (U/\bar{U})\theta\eta d\eta \tag{15}$$

Since the rate of heat transfer for the pipe length between $x = 0$ and $x = x$ can be expressed as

$$Q = \dot{m}C_p(T_{bx} - T_o) \tag{16}$$

and noting that the maximum possible heat transfer rate $Q_{\max}$ occurs as $x\to\infty$ and $T_{bx}\to T_\infty$, the ratio $Q/Q_{\max}$ is given by

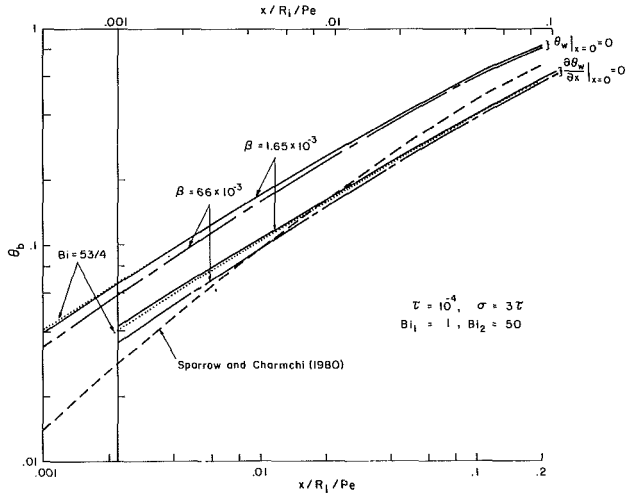

Fig. 2 Streamwise θ_b (or Q/Q_{max}) variation, $\tau = 10^{-4}$, $\sigma = 3\tau$, $Bi_1 = 1$, $Bi_2 = 50$

$$Q/Q_{\max} = (T_{bx} - T_o)/(T_\infty - T_o) = \theta_{bx} \tag{17}$$

Thus θ_{bx}, as calculated by equation (15), can be interpreted as the ratio $Q/Q_{\max}$.

The Nusselt number is defined in the conventional way

$$\mathrm{Nu} = hD/K, \quad h = [-K_f(\partial T/\partial r)_{r=R_i}]/\Delta T \tag{18}$$

where ΔT is the characteristic temperature difference. In this paper, two choices for ΔT have been made: one is the wall to bulk temperature difference $(T_w - T_{bx})$ designated by the subscript i, and the other is the temperature difference between the surroundings and the bulk fluid $(T_\infty - T_{bx})$ designated by the subscript o. The Nusselt numbers are averaged along each of the finned and unfinned sections of the pipe with these averages denoted by subscripts f and u. Thus, the Nusselt numbers presented are identified by two subscripts (either f or u and i or o).

Figures 2–4 present the bulk temperature (θ_b) or the heat transfer rate ($Q/Q_{\max}$) distributions. It can be easily seen that the heat transfer rate increases when axial conduction along the pipe wall is accounted for, with a larger value for $Q/Q_{\max}$ (or θ_b) at the higher wall conductivity. To explain this behavior, a longitudinal control volume (of length dx and thickness $(R_o - R_i)$) can be visualized in the pipe wall. The heat transfer rate to the fluid $Q/Q_{\max}$ and also the wall temperature in the control volume are determined by an energy balance over this control volume. In the absence of axial conduction, locally adiabatic conditions exist along the pipe wall, i.e., there is only transverse heat transfer through the control volume with heat transferred to the wall by external convection along the length dx being entirely transferred to the fluid along dx. In the presence of axial wall conduction, since $T_{bx} \to T_\infty$ as $x \to L$, the axial wall heat transfer (assuming $T_\infty > T_o$) is directed in the negative x direction, and therefore, it is natural to expect that T_w and hence, $Q/Q_{\max}$ (or T_{bx}) will be larger. Since axial conduction is stronger at higher wall conductivity values, T_w and $Q/Q_{\max}$ (or T_{bx}) are correspondingly higher.

The effect of assuming a poorly conducting pipe upstream of the finned section (i.e., $\partial\theta_w/\partial X = 0$ at $X = 0$) is also shown in Fig. 2. For the purposes of clarity, the horizontal axis has been shifted to the right and is shown on the top of the page. However, it can be seen that the θ_b (or $Q/Q_{\max}$) curves for both boundary conditions are nearly the same with slightly higher values obtained when the adiabatic condition is imposed. At $X = 0.0015$, the percentage difference between the two solutions in Fig. 2 is 3 percent while at $X = 0.01$ the difference is only 0.62 percent. At still higher values of X, the differences are very small. The Nusselt number curves with the two boundary conditions are also nearly the same, as shown later.

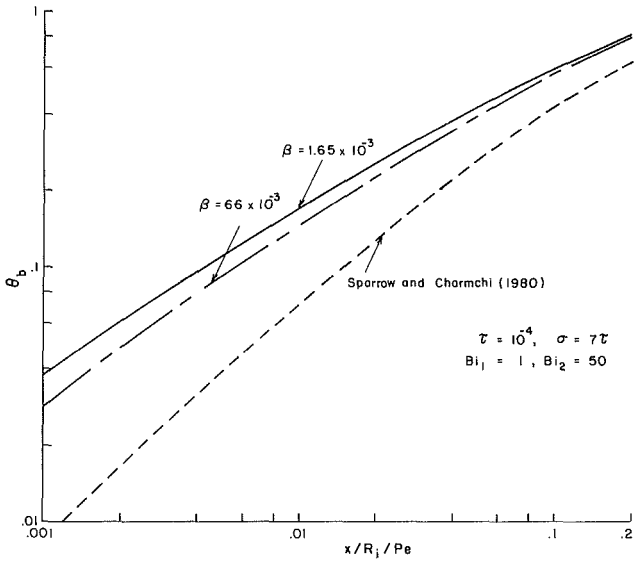

Fig. 3 Streamwise θ_b (or $Q/Q_{\max}$) variation, $\tau = 10^{-4}$, $\sigma = 7\tau$, $Bi_1 = 1$, $Bi_2 = 50$

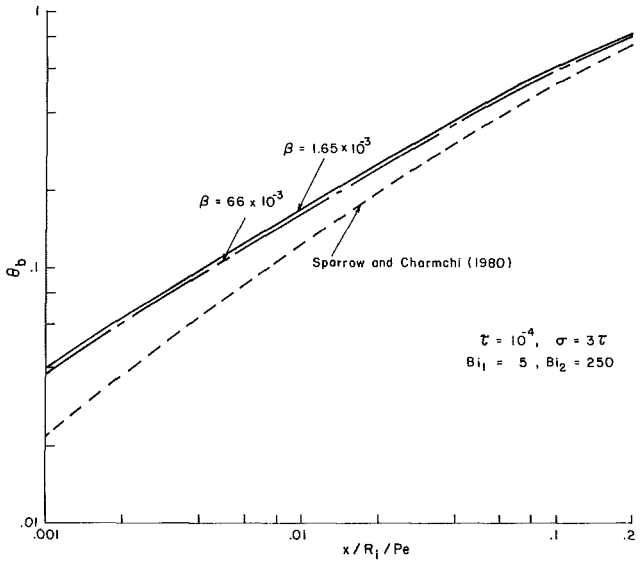

Fig. 4 Streamwise θ_b (or $Q/Q_{\max}$) variation, $\tau = 10^{-4}$, $\sigma = 3\tau$, $Bi_1 = 5$, $Bi_2 = 250$

As noted earier, limited calculations have also been made with a uniform area-averaged Biot number Bi calculated as

$$\mathrm{Bi} = (\sigma \mathrm{Bi}_1 + \tau \mathrm{Bi}_2)/(\sigma + \tau) \tag{19}$$

The corresponding θ_b (or Q/Q_{max}) curves are shown in Fig. 2 for both $\theta_w = 0$ and $\partial\theta_w/\partial X = 0$ conditions at $X = 0$. It can be clearly seen that the simpler calculations with a uniform area-averaged Biot number gives results that are in good agreement with the calculations with finned and unfinned Biot numbers Bi_1 and Bi_2. The largest difference between the two curves is at $x = 0$, and is of the order of 10–12 percent. The corresponding difference, in the absence of pipe wall axial conduction, was reported to be 20 percent (Sparrow and Charmchi, 1980).

The magnitude of error incurred by neglecting axial conduction is noteworthy. In Fig. 3, for example, the heat transfer rate is underestimated nearly four times near the pipe entrance with the degree of underestimation diminishing with increasing x. This observation is an important one since it has significant design ramifications.

Figure 3 shows the effect of increasing the interfin spacing

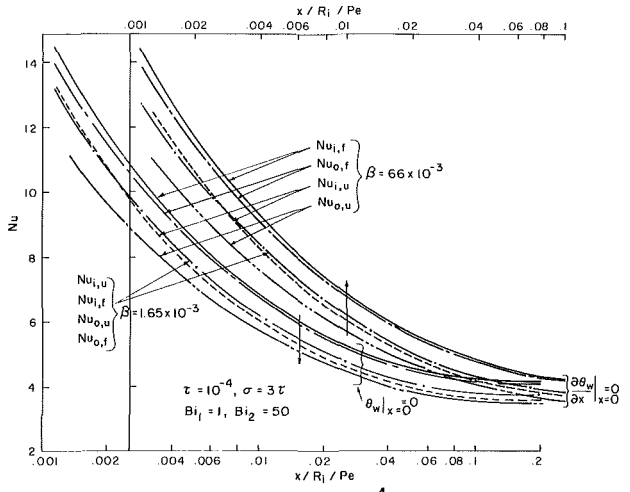

Fig. 5 Streamwise Nu variation, $\tau = 10^{-4}$, $\sigma = 3\tau$, $Bi_1 = 1$, $Bi_2 = 50$

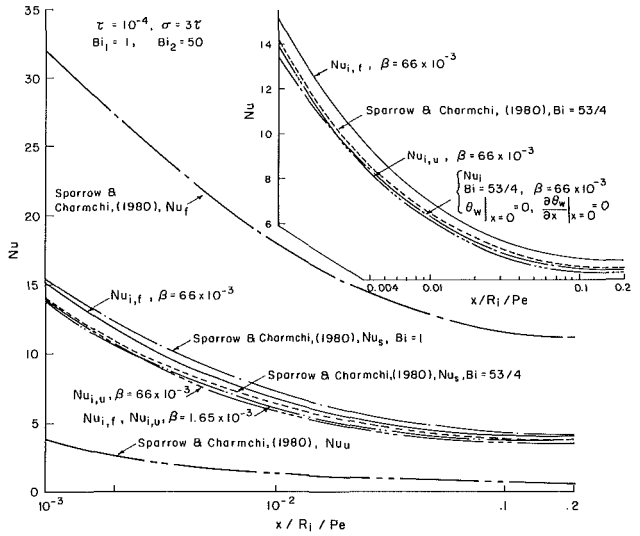

Fig. 6 Nusselt number comparisons with axial wall conduction accounted for (present predictions) and neglected, $\tau = 10^{-4}$, $\sigma = 3\tau$, $Bi_1 = 1$, $Bi_2 = 50$

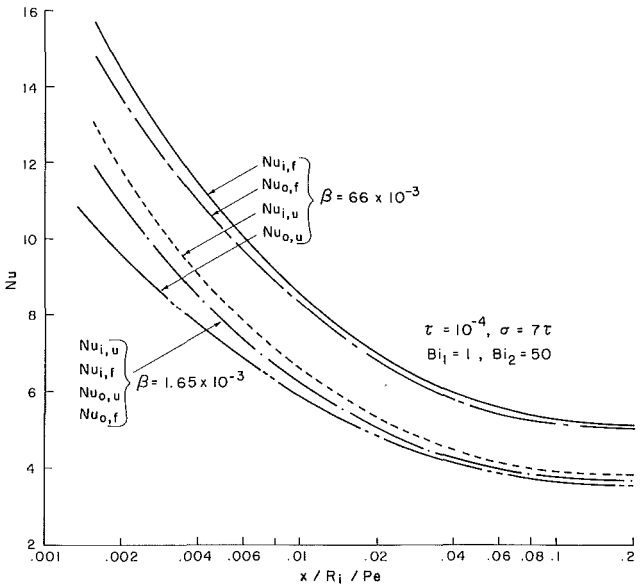

Fig. 7 Streamwise Nu variation, $\tau = 10^{-4}$, $\sigma = 7\tau$, $Bi_1 = 1$, $Bi_2 = 50$

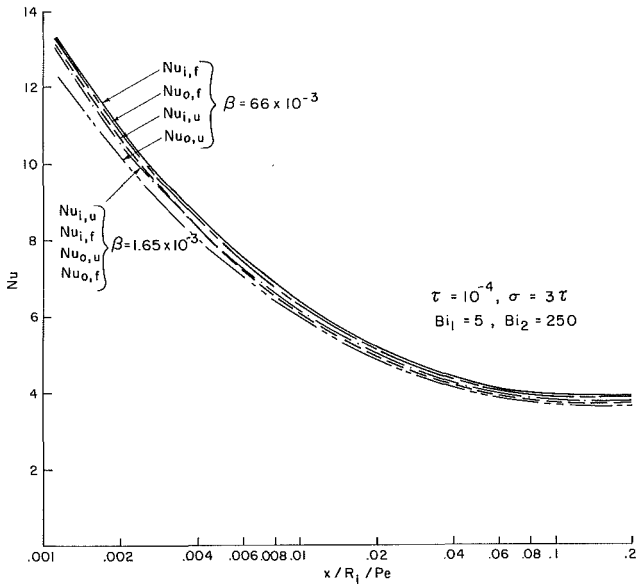

Fig. 8 Streamwise Nu variation, $\tau = 10^{-4}$, $\sigma = 3\tau$, $Bi_1 = 5$, $Bi_2 = 250$

while Fig. 4 presents the influence of increasing the level of the external heat transfer coefficients (h_1 and h_2), keeping the ratio h_1/h_2 constant. When σ is increased from 3τ (Fig. 2) to 7τ (Fig. 3), axial heat conduction becomes more important with significantly larger values obtained for θ_b (or $Q/Q_{\max}$) when the pipe walls are considered to be finitely conducting. On the other hand, when h_1 and h_2 are both increased five times (Fig. 4), the external convective thermal resistance is correspondingly reduced, and therefore, the internal convective thermal resistance becomes relatively more dominant. In view of the small external resistance, the pipe wall temperatures are close to T_∞ and are relatively uniform (see Fig. 9). Therefore, axial conduction, in comparison to the other cases presented, has a much smaller effect on the bulk temperature and heat transfer rate distributions.

Figures 5–8 present the local Nusselt number distributions. As mentioned earlier, the Nu values are identified by two subscripts with the first subscript denoting the ΔT on which Nu is based (i if $\Delta T = T_w - T_{bx}$ and o if $\Delta T = T_\infty - T_{bx}$) and the second subscript denotes either the finned portion (subscript f) or the unfinned portion (subscript u). For the higher wall thermal conductivity, since axial conduction is significant, the wall temperature (and therefore, also the heat flux along the inner pipe wall) increases monotonically from the entrance. In view of this smoothing action, for the high pipe wall conductivity, the Nusselt number curves for the finned and unfinned parts are nearly coincident, and since the pipe wall temperatures rapidly approach T_∞, the Nusselt numbers based on the two different ΔT values are also nearly identical. Thus, a single curve characterizes the Nusselt number distributions for the high wall conductivity. For the pipe with poorly conducting walls, the Nusselt numbers along the finned sections are expectedly higher.

Results with the $\partial\theta_w/\partial X = 0$ boundary condition at $X = 0$ are also shown in Fig. 5. If the same axes were used, the plotted curves would be nearly identical to the corresponding curves for $\theta_w = 0$ at $X = 0$. Therefore, the horizontal axes has been shifted, as shown on the top of the figure.

Figure 6 compares the present Nu predictions with the calculations of Sparrow and Charmchi (1980) for a finned pipe with negligible axial conduction. In view of the smoothing effect of axial conduction, the present calculations for the Nusselt number in the finned section fall below the values predicted by Sparrow and Charmchi (1980), while the Nusselt numbers along the unfinned section are higher than the corresponding values in the absence of axial conduction. The differences between the present calculations and those

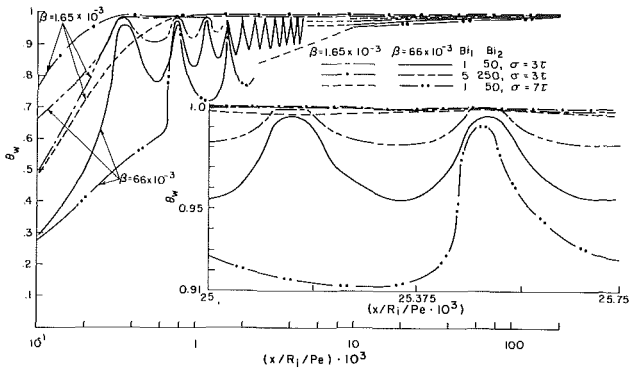

Fig. 9 Pipe wall temperature distributions

reported by Sparrow and Charmchi (1980) are significant (factor of 2 or 3) and are indicative of the importance of axial conduction in the pipe walls. Nusselt number calculations done by Sparrow and Charmchi (1980) for smooth (unfinned) pipes with uniform Biot numbers corresponding to either Bi_1 ($\simeq 1$) or the spatially averaged mean of Bi_1 and Bi_2 ($= (\sigma Bi_1 + \tau Bi_2) / (\sigma + \tau) = 53/4$), are also shown in the figure and imply that, if lengthy computations, such as those performed in this paper, are not possible, the most appropriate values to use are the smooth pipe Nusselt numbers based on the spatially averaged mean of the high and low Biot numbers. This conclusion was not evident from the calculations reported by Sparrow and Charmchi (1980). The inset of Fig. 6 plots the Nu_i distribution for the area-averaged Biot number Bi = 53/4, and with longitudinal wall conduction accounted for (as in this study) or neglected (as in Sparrow and Charmchi, 1980). Also plotted are the Nu_i distributions with finned and unfinned Biot numbers Bi_1 and Bi_2, respectively. Both area-averaged uniform Biot number estimates yield results that are within 15 percent of the longitudinally nonuniform Bi (Bi_1 and Bi_2) predictions.

The effect of increasing the interfin spacing is shown in Fig. 7. It may be seen that the Nusselt numbers along the finned portions are higher and the Nusselt number difference between the finned and unfinned sections are larger as compared to corresponding values for a pipe with smaller interfin spacing ($\sigma = 3\tau$). This is because, when the interfin spacing is large, the primary heat transfer area is the one corresponding to the unfinned sections and therefore, the preheating of the flow as it encounters a finned section is smaller compared to the pipe with smaller interfin spacing. As a consequence, the Nusselt numbers corresponding to the finned sections and the Nusselt number difference between the finned and unfinned parts increase with interfin spacing. On the other hand, these values ($Nu_{o,f}$ or $Nu_{i,f}$ and $Nu_{o,f} - Nu_{i,f}$, or $Nu_{o,u} - Nu_{i,u}$) decrease as the dimensionless external heat transfer coefficients (Bi_1 and Bi_2) are increased keeping the ratio Bi_2/Bi_1 constant. This is because as the external heat transfer coefficient, and therefore, the heat transferred to the pipe walls, is increased, the pipe wall temperature variation becomes increasingly monotonic and the wall temperatures approach those of the surroundings (Fig. 9). For $Bi_1 = 5$ and $Bi_2 = 250$, the average dimensionless wall temperature is very close to unity and therefore, the Nusselt number curves shown in Fig. 8 are very close to each other.

Dimensionless pipe wall temperatures are shown on a semilog plot in Fig. 9 and indicate that for high wall conductivity ($\beta = 1.65 \times 10^{-3}$) the wall temperature variation is monotonic due to the smoothing effect of axial conduction, while for $\beta = 66 \times 10^{-3}$ the temperatures exhibit a very nonmonotonic periodic variation, with high values in the fin region and low values in the interfin spacing. With increasing X the wall temperature differences in the fin and interfin regions progessively diminish. As expected, when the interfin spacing is large, the amplitude of the periodic variation is the most significant and exhibit the slowest decay with increasing X. Furthermore, when the level of the external heat transfer coefficient is high, the wall temperatures are closer to the ambient temperature (T_∞) and the amplitudes of the periodic temperature variations are small.

Since for $x/R_i/\mathrm{Pe} > 0.01$, wall temperatures are in the range of 0.9 to 1, the different temperature curves are not distinguishable from each other. Therefore, a local magnifying figure in the range of $0.024 \leq x/R_i/\mathrm{Pe} \leq 0.02575$ is provided as an inset, to illustrate the typical temperature variation in this region. In keeping with the trends at smaller X values, nonmonotonic, streamwise periodic temperature variations exist for the less conducting pipe. At the higher wall conductivity, strong longitudinal conduction leads to a relatively uniform and near-constant temperature profile.

Concluding Remarks

The influence of axial wall conduction on laminar, forced convection in an externally finned pipe is studied by a numerical technique. Results indicate that the axial wall conduction has a significant effect on the heat transfer characteristics. It is found that by neglecting axial wall conduction, the magnitude of heat transfer to the fluid is significantly underestimated, particularly for highly conducting pipes. Axial conduction effects become increasingly important as the interfin spacing is increased. On the other hand, the influence of conduction diminishes as the level of the external heat transfer coefficient is increased. When the pipe wall conductivity is large, both the Nusselt number and wall temperatures exhibit a smooth variation along the length of the pipe, while, for low wall conductivity, the Nusselt number values in the finned and interfin region are substantially different and the pipe wall temperatures exhibit a decaying periodic variation in the axial direction. If a quick estimate of the Nusselt number is required, the smooth pipe Nusselt number based on the spatially averaged external heat transfer coefficient appears to be the most reasonable.

References

Aleksashenko, V. A., 1968, "Conjugate Stationary Problem of Heat Transfer With a Moving Fluid in a Semi-infinite Tube Allowing for Viscous Dissipation," *Inzhenerno-Fizicheskii Zhurnal*, Vol. 14(1), pp. 100–107.

Davis, E. J., and Gill, W. N., 1970, "The Effect of Axial Conduction in the Wall on Heat Transfer With Laminar Flow," *International Journal of Heat and Mass Transfer*, Vol. 13, pp. 459–470.

Faghri, M., and Sparrow, E. M., 1980, "Simultaneous Wall and Fluid Axial Conduction in Laminar Pipe-Flow," ASME JOURNAL OF HEAT TRANSFER, Vol. 102, pp. 58–63.

Hsu, C. J., 1968, "Exact Solution to Entry-Region Laminar Heat Transfer With Axial Conduction and the Boundary Condition of the Third Kind," *Chemical Engineering Science*, Vol. 23, pp. 457–468.

Luikov, A. V., Aleksashenko, V. A., and Aleksashenko, A. A., 1971, "Analytical Methods of Solution of Conjugated Problems in Convective Heat Transfer," *International Journal of Heat and Mass Transfer*, Vol. 14, pp. 1047–1056.

Mori, S., Sakakibara, M., and Tanimoto, A., 1974, "Steady Heat Transfer to Laminar Flow in a Circular Tube with Conduction in the Tube Wall," *Heat Transfer—Jpn. Res.*, Vol. 3(2), pp. 37–46.

Mori, S., Shinke, T., Sakakibara, M., and Tanimoto, A., 1976, "Steady Heat Transfer to Laminar Flow Between Parallel Plates With Conduction in Wall," *Heat Transfer—Jpn. Res.*, Vol. 5(4), pp. 17–25.

Patankar, S. V., and Spalding, D. B., 1970, *Heat and Mass Transfer in Boundary Layers*, Intertext Books, London.

Povarnitsyn, M. S., and Yurlova, E. V., 1966, "Calculation of the Temperature Field in a Plane Channel With Nonuniform Heating of Thermally Conducting Walls," *Inzhenerno-Fizicheskii Zhurnal*, Vol. 10(1), pp. 120–126.

Reynolds, W. C., 1963, "Effect of Wall Heat Conduction on Convection in a Circular Tube With Arbitrary Circumferential Input," *International Journal of Heat and Mass Transfer*, Vol. 6, pp. 925–932.

Sparrow, E. M., and Charmchi, M., 1980, "Laminar Heat Transfer in an Externally Finned Circular Tube," ASME JOURNAL OF HEAT TRANSFER, Vol. 102, pp. 605–611.

Boundary Layer Analysis for Two-Dimensional Slot Jet Impingement on Inclined Plates

V. K. Garg[1]
Mem. ASME

S. Jayaraj[2]

Department of Mechanical Engineering,
Indian Institute of Technology,
Kanpur 208016, India

The laminar boundary layer flow when a two-dimensional slot jet impinges on a flat plate at some angle is analyzed theoretically. The conservation equations in primitive variables are solved using a finite-difference technique. The computed results at 0 and 90 deg angle of impingement are in perfect agreement with the standard solutions available in the literature. The influence of the angle of impingement on the velocity and temperature profiles is studied. The presence of a stagnation point when the plate is not parallel to the oncoming jet is found to affect considerably the local Nusselt number and skin friction coefficient. These parameters attain very large values close to the stagnation point at small angles of impingement. However, far from the stagnation point, they approach values corresponding to a flat plate at zero incidence, irrespective of the angle of jet impingement.

1 Introduction

Many practical applications in fluid mechanics involve a nonzero pressure gradient in the boundary layer over a body either due to the shape of the body or due to its orientation with respect to the main flow. As these problems are generally not amenable to similarity solutions, one has to use numerical methods for solution. Moreover, depending upon the nature of pressure distribution, different numerical methodologies have to be adopted. One such problem involving a slot jet impinging on a plate at an angle is commonly encountered in industrial applications, due to its excellent heat and mass transfer characteristics. Notable among its numerous applications are turbine blade cooling, heat treatment of nonferrous metal sheets, cooling of high energy/density electronic components, tempering of glass, drying of textiles and paper, etc. (van Heiningen et al., 1976). Martin (1977) provides a comprehensive list of the available literature on the study of jets impinging normally on a flat plate.

Experimental investigations of heat and/or mass transfer characteristics of normally impinging two-dimensional slot jets were reported by Gardon and Akfirat (1972), Sparrow and Wong (1975), and Masliyah and Nguyen (1979). The common result of these investigations is that the heat and mass transfer coefficients are maximum at the stagnation point and decrease monotonically with respect to the distance from the stagnation point along the plate. The theoretical study of normal impingement of a slot jet has also been reported by many investigators. Miyazaki and Silberman (1972) studied the effect of distance between the nozzle and the impinging plate on the local skin friction coefficient and Nusselt number. Both these parameters increase with decreasing distance between the nozzle and plate, and exhibit a maximum just beyond the half-width of the nozzle along the plate. In the study by Sparrow and Lee (1975), the nonuniform (fully developed) velocity profile of the slot jet is found to double the heat and mass transfer at the stagnation point compared to that due to the flat velocity profile. The application of suction and the presence of a confining wall parallel to the impingement wall are the new features of the finite-difference analysis of slot jet flow by van Heiningen et al. (1976). The analysis of Ero (1978) is limited to the close proximity of slot jet impingement on a plate.

All the above studies deal with a slot jet impinging normally onto a plate. Tamada (1979) has solved exactly the nonorthogonal stagnation point flow in two dimensions by combining the irrotational stagnation point flow and uniform shear flow parallel to the wall. The governing similarity solution for stream function is split into two parts; the first part satisfies exactly the familiar Hiemenz equation. Recently Dorrepaal (1986) followed a similar procedure and arrived at a universal constant (independent of the angle of impingement) for the ratio between the slopes of streamlines intersecting the plate at the viscous and potential flow stagnation points. The scope of both these studies is limited to the hydrodynamic boundary layer only. Moreover, they are confined to the calculation of stream function only, and are not applicable to the impingement of a slot jet on a plate.

Herein we present a finite-difference solution for both hydrodynamic and thermal boundary layers formed by impingement of a two-dimensional slot jet over a flat plate at various angles of attack. The pressure distribution in the boundary layer is found from the inviscid flow solution obtained from a direct impact of two unequal inviscid jets.

2 Analysis

Consider an incompressible two-dimensional slot jet of width L impinging on a flat plate at some angle as shown in Fig. 1. The origin of the coordinate system coincides with the stagnation point. Since the fluid properties are assumed constant, the hydrodynamic solution can be obtained independent of the knowledge of the temperature distribution. The applicable dimensionless continuity, momentum, and energy equations for the incompressible boundary layer flow are (Schlichting, 1979)

$$\frac{\partial U}{\partial X} + \frac{\partial V}{\partial Y} = 0 \tag{1}$$

$$U\frac{\partial U}{\partial X} + V\frac{\partial U}{\partial Y} = \frac{\partial^2 U}{\partial Y^2} - \frac{dP}{dX} \tag{2}$$

$$U\frac{\partial \theta}{\partial X} + V\frac{\partial \theta}{\partial Y} = \frac{1}{\mathrm{Pr}}\frac{\partial^2 \theta}{\partial Y^2} + \mathrm{Ec}\left(\frac{\partial U}{\partial Y}\right)^2 \tag{3}$$

[1]Present address: Department of Mechanical Engineering, The Ohio State University, Columbus, OH 43210, USA.

[2]On leave from Regional Engineering College, Calicut 673601, India.

Contributed by the Heat Transfer Division for publication in the JOURNAL OF HEAT TRANSFER. Manuscript received by the Heat Transfer Division January 7, 1986. Keywords: Forced Convection, Jets, Numerical Methods.

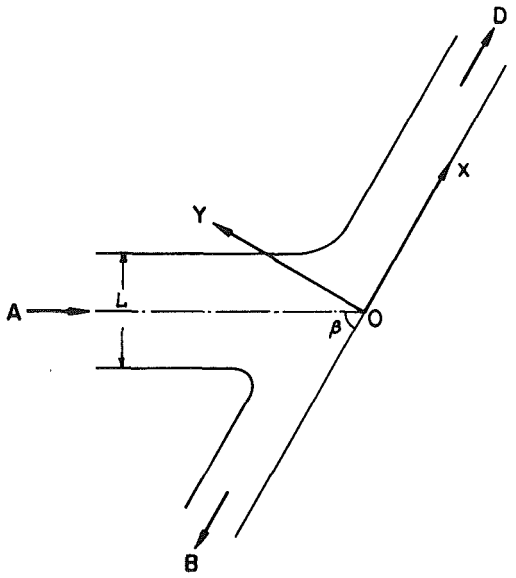

Fig. 1 Physical configuration and coordinate system

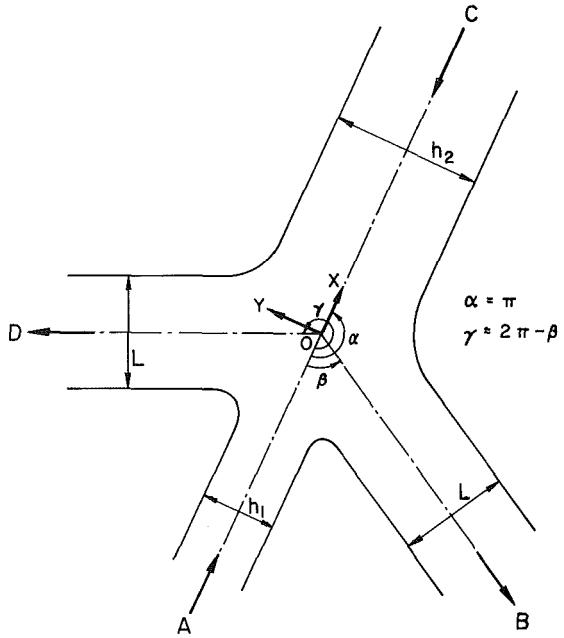

Fig. 2 Direct impact of two unequal jets

where

$X = x/L$, $Y = \mathrm{Re}^{1/2} y/L$, $\theta = (T - T_\infty)/(T_\omega - T_\infty)$,

$U = u/u_\infty$, $V = \mathrm{Re}^{1/2} v/u_\infty$, $P = (p - p_\infty)/(\rho u_\infty^2)$

The boundary conditions for an isothermal plate are

$U(X, 0) = 0$, $V(X, 0) = 0$, $\theta(X, 0) = 1$, $\theta(0, Y) = 0$,

$U(X, \infty) = U_s(X)$, $\theta(X, \infty) = 0$, $U(0, Y) = U_s(0) = 0$

It should be pointed out that the boundary layer equations are really not valid at $X = 0$. In the close vicinity of the stagnation point, the full Navier–Stokes and energy equations including the diffusion terms in the X direction must be used. Later in Section 4.3 we will look at the actual limiting values of X for which the boundary layer analysis for a laminar slot jet is valid. Numerically the effect of singularity at the stagnation point is confined to a region very close to the stagnation point by taking a very small step size initially in the X direction (Hornbeck, 1973). More details are given in Section 3.

In order to estimate the pressure gradient to be used in the momentum equation, a direct impact of two unequal inviscid jets is considered as shown in Fig. 2. It is assumed that the outgoing jets (B and D) are of equal width L. In this general case the equation relating the complex coordinate $z (= x + iy)$ with the complex velocity ξ is (Milne Thomson, 1960)

Nomenclature

a_1, a_2, b_1, b_2 = constants used in equation (4)
C_f = local skin friction coefficient
C_p = specific heat at constant pressure
Ec = Eckert number $= u_\infty^2/C_p(T_w - T_\infty)$
h = local heat transfer coefficient
h_1, h_2 = jet thicknesses
H = ratio of nozzle height from the plate to L
k = thermal conductivity of the fluid
L = width of the slot jet
Nu = local Nusselt number
Nu_m = mean Nusselt number
p = pressure
P = dimensionless pressure $= (p - p_\infty)/\rho u_\infty^2$
Pr = Prandtl number
Re = Reynolds number $= u_\infty L/\nu$
T = temperature
u, v = velocity components in x, y directions, respectively
u_s = potential flow velocity at the plate
U, V = dimensionless velocity components in X, Y directions, respectively given by u/u_∞, $\mathrm{Re}^{1/2} v/u_\infty$
U_s = dimensionless potential flow velocity at the plate $= u_s/u_\infty$
x, y = coordinates along and normal to the plate, respectively
X, Y = dimensionless coordinates along and normal to the plate, respectively, given by x/L, $\mathrm{Re}^{1/2}\, y/L$
z = complex coordinate $= x + iy$
Z = dimensionless complex coordinate $= z/L$
α, β, γ = angles between jets
δ = hydrodynamic boundary layer thickness
$\Delta X, \Delta Y$ = mesh sizes in X, Y directions, respectively
θ = dimensionless temperature defined by $(T - T_\infty)/(T_w - T_\infty)$
ν = kinematic viscosity of the fluid
ρ = density of the fluid
ξ = complex velocity in potential flow
Ξ = dimensionles complex velocity $(= \xi/u_\infty)$

Subscripts

j, k = location in X, Y directions, respectively
w = value at the plate
∞ = value in the free stream

$$z = \frac{u_\infty}{\pi}\left[\frac{h_1}{a_1}\ln(1-\xi/a_1) + \frac{h_2}{a_2}\ln(1-\xi/a_2) - \frac{L}{b_1}\ln(1-\xi/b_1) - \frac{L}{b_2}\ln(1-\xi/b_2)\right] \quad (4)$$

where

$$a_1 = -u_\infty = -a_2,\ b_1 = u_\infty e^{-i\beta},\ \text{and}\ b_2 = u_\infty e^{i\beta} \quad (5)$$

Also we have the following relations between the widths of the jets:

$$h_1 = L(1-\cos\beta),\ h_2 = L(1+\cos\beta) \quad (6)$$

Substituting equations (5) and (6) into equation (4) and simplifying leads to the following relation:

$$\pi Z + \ln(1+\Xi) - \ln(1-\Xi) - \cos\beta\ln(1-\Xi^2) + e^{i\beta}\ln(1-\Xi e^{i\beta}) + e^{-i\beta}\ln(1-\Xi e^{-i\beta}) = 0 \quad (7)$$

Without loss of generality the configuration shown in Fig. 2 can be regarded as the jet from D impinging on the plate kept along the line AC, which is at an angle β to the oncoming slot jet. Hence the dimensionless complex velocity Ξ, obtained by solving equation (7), can be used directly in order to compute the pressure distribution over the plate AC. In fact, since we are interested only in the potential flow velocity $U_s(X)$ at the plate, we set $Z = -X$ and $\Xi = U_s$ in equation (7) to obtain

$$\pi X = -\ln\left(\frac{1-U_s}{1+U_s}\right) + \cos\beta\ln\left(\frac{1+U_s^2-2U_s\cos\beta}{1-U_s^2}\right) + 2\sin\beta\tan^{-1}\left(\frac{U_s\sin\beta}{1-U_s\cos\beta}\right) \quad (8)$$

Thus for a given value of angle β, $U_s(X)$ is a solution of equation (8). The pressure distribution and pressure gradient in the boundary layer over the plate are given by

$$2P = 1 - U_s^2 \quad (9)$$

and

$$dP/dX = -U_s dU_s/dX \quad (10)$$

This pressure gradient is used in the momentum equation (2). It may be noted that equation (8) is identical to equation (3) of Miyazaki and Silberman (1972) in the limit $H \to \infty$.

3 Numerical Solution

Equations (1) to (3) are now written in finite-difference form by superposing a two-dimensional rectangular mesh on the flow field. We use the indices (j, k) to indicate the position of a point in the boundary layer. Let the plate be represented by $k = 0$ and the edge of the boundary layer by $k = n+1$. The finite difference equations are written as (Hornbeck, 1973)

$$V_{j+1,k+1} = V_{j+1,k} - \frac{\Delta Y}{\Delta X}\left[U_{j+1,k+1} - U_{j,k+1}\right] \quad (11)$$

$$U_{j+1,k}\frac{U_{j+1,k}-U_{j,k}}{\Delta X} + V_{j+1,k}\frac{U_{j+1,k+1}-U_{j+1,k-1}}{2\Delta Y} = \frac{U_{j+1,k+1}-2U_{j+1,k}+U_{j+1,k-1}}{(\Delta Y)^2} - \frac{dP}{dX} \quad (12)$$

$$U_{j+1,k}\frac{\theta_{j+1,k}-\theta_{j,k}}{\Delta X} + V_{j+1,k}\frac{\theta_{j+1,k+1}-\theta_{j+1,k-1}}{2\Delta Y} = \frac{1}{\mathrm{Pr}}\frac{\theta_{j+1,k+1}-2\theta_{j+1,k}+\theta_{j+1,k-1}}{(\Delta Y)^2} + \mathrm{Ec}\frac{(U_{j+1,k+1}-U_{j+1,k-1})^2}{4(\Delta Y)^2} \quad (13)$$

This discretization is second-order accurate in ΔY for U and θ, and is suitable for the marching procedure along the X direction in conformity with the parabolic nature of equations (2) and (3).

Table 1 Step size in X direction

$\lvert\Delta X\rvert$	No. of steps marched
10^{-5}	20
2×10^{-5}	10
5×10^{-5}	12
10^{-4}	10
2×10^{-4}	10
5×10^{-4}	12
10^{-3}	10
2×10^{-3}	10
5×10^{-3}	12
10^{-2}	90
2×10^{-2}	100

The solution for U, V, and θ is carried out in a marching procedure starting from the stagnation point ($X = 0$). The discretized momentum equation (12) written for $k = 1(1)n$ leads to a set of n nonlinear equations for n unknown values of U at the X location $(j+1)$. This set is reduced to a linear set by replacing the coefficients $U_{j+1,k}$ and $V_{j+1,k}$ on the left side of equation (12) by their known values at the previous iteration. The linearized tridiagonal set is solved iteratively using the discretized continuity equation (11) to update V at the X location $(j+1)$. Once values of U and V have been determined at $(j+1)$, the energy equation (13) written for $k = 1(1)n$ leads to a tridiagonal set of n linear equations that can be easily solved for the n unknown values of θ at the X location $(j+1)$. This completes the solution at $(j+1)$. A repetition of the above steps allows us to march in either direction from the stagnation point.

The computer program takes care of the fact that the boundary layer thickness increases as we move away from the stagnation point. Thus we increase n as we march in the X direction on either side of the stagnation point. The value of n is chosen so as to ensure that there are at least three to four points for $k \le n$ for which $U \approx U_s$ and $\theta \approx 0$. A variable grid size is used in the X direction. Table 1 gives the values of ΔX used and the number of steps marched with each ΔX. For a small enough value of the initial ΔX, such as 10^{-5} used here, it was found that the singularity at the stagnation point was confined to about $5(\Delta X)$ on either side of the stagnation point. While ΔX can be assigned any value without difficulty it is easier to keep ΔY uniform. However, due to large gradients near the plate ΔY must be quite small near the plate, and if ΔY is uniform across the boundary layer thickness, the number of simultaneous equations to be solved increases excessively. Solution of such a large number of equations not only requires excessive computer time but also involves large roundoff errors. A practical solution is to use a fine mesh size near the plate and a relatively coarse mesh size away from the plate. A self-adaptive grid (Nakahashi and Deiwert, 1986, 1987) was therefore used in the Y direction. This yields very accurate results since the large gradients in the Y direction near the plate are resolved accurately. This requires modifications to equations (12) and (13) for the k value on either side of which ΔY is different, as described by Hornbeck (1973). The minimum value of ΔY was set at 0.005 and the maximum at 0.05. The self-adaptive grid generation technique distributes values of ΔY within this range. As many as 500 steps in the Y direction were required for some values of angle β at the farthest downstream location $X = 3$. This discretization was used following considerable experimentation keeping the error incurred and reasonable computer time in view. The test case for error analysis was the Blasius solution for the flat plate at zero incidence. Our values of U and V for $\beta = 0$ were found to match exactly with the Blasius solution for all $X \ge 10^{-4}$.

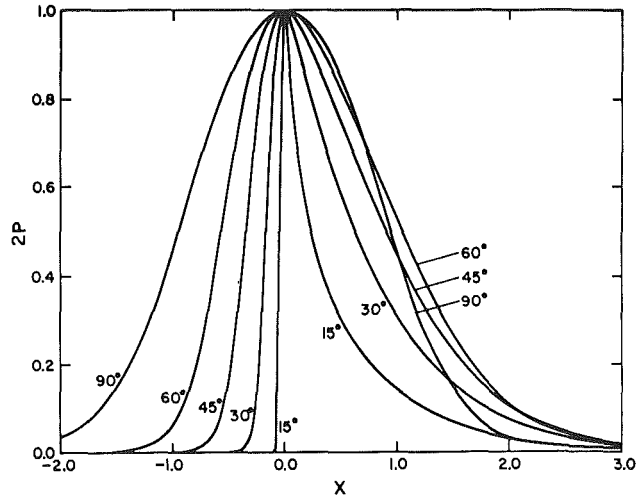

Fig. 3 Pressure distribution on the plate

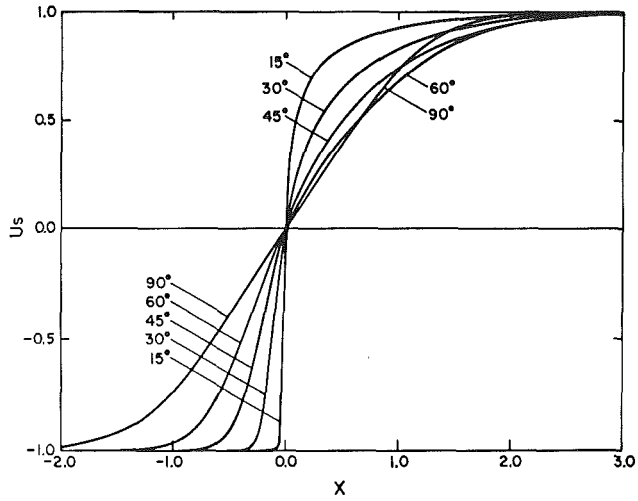

Fig. 4 Potential flow velocity at the plate

Similar results were obtained for θ for which the exact solution corresponding to $\beta = 0$ is given by Schlichting (1979). During the testing phase, values of local skin friction coefficient and Nusselt number for normal impingement of the slot jet on the plate ($\beta = 90$ deg) were also found to match exactly with those given by Miyazaki and Silberman (1972) for $H \geq 3$.

4 Results and Discussion

Results were computed for six values of $\beta = 0$, 15, 30, 45, 60, and 90 deg, five values of Pr = 0.07, 0.2, 0.7, 2.0, and 7.0, and two values of Ec = 0 and 1. The plate was assumed to be isothermal for all the cases.

4.1 Pressure Distribution. The pressure distribution in the boundary layer at various angles of slot jet impingement is shown in Fig. 3. As observed experimentally by Gardon and Akfirat (1966) in Fig. 7 of their paper, the pressure distribution on the plate for normal impingement ($\beta = 90$ deg) is symmetric about the stagnation point ($X = 0$). It is clear from Fig. 3 that except for $\beta = 90$ deg, the pressure distribution is asymmetric. Also the presence of the stagnation point for angles other than zero considerably modifies the distribution especially near the stagnation point. In the positive X direction, pressure reaches a nearly zero value at $X \approx 3.0$ for all angles, but in the negative X direction, zero pressure is obtained at different X locations depending upon the value of β. For low angles of impingement the zero value of pressure is obtained quite close to the stagnation point for $X < 0$, as seen from Fig. 3. The reason for this lies in the smaller thickness (h_1) of the outgoing stream on the ($X < 0$) side of the plate at smaller values of β (see equation (6) and Fig. 1). In the limiting case of $\beta \to 0$, $h_1 \to 0$ and we get the flow over a flat plate at zero incidence. Figure 4 illustrates the potential flow velocity at the plate as a function of distance along the plate with β as a parameter. The effect of pressure distribution on the plate is very clearly reflected in these curves.

4.2 Velocity and Temperature Profiles. Figure 5 illustrates the normalized streamwise velocity profiles in the boundary layer at various angles (β) and dimensionless distances (X) from the stagnation point. There is perfect agreement between the present results and the standard similarity solution at zero incidence (Blasius flow) denoted by "stars". This is true even close to the stagnation point ($X = 0.01$). This establishes the validity of the numerical marching technique employed in the present investigation. For Pr = 0.7 and Ec = 0, the behavior of the dimensionless temperature θ is very similar to that of $(1 - U/U_s)$, and is

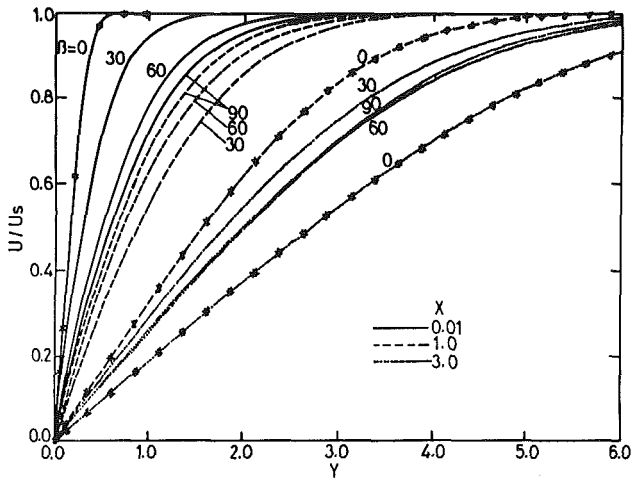

Fig. 5 Longitudinal velocity profiles

therefore not shown here. The temperature distribution for $\beta = 0$ was also found to match perfectly with the exact solution for a flat plate at zero incidence (Schlichting, 1979) at all locations along the plate, thus validating the present results. It was also found that the transverse velocity distribution for $\beta = 0$ matched exactly with the Blasius solution at all locations along the plate.

4.3 Boundary Layer Thickness. The hydrodynamic boundary layer thickness δ is shown in Fig. 6. As in Fig. 5, the stars on this figure correspond to the exact values for a flat plate at zero incidence. Clearly, the presently computed results for $\beta = 0$ are in very good agreement with the exact results. The hydrodynamic boundary layer thickness in Fig. 6 corresponds to the usual $U/U_s = 0.99$. Similar results hold for displacement, momentum, and thermal boundary layer thicknesses. Note that the boundary layer thickness is nonzero at $X = 0$ for $\beta \neq 0$ as expected. Also, for $\beta = 90$ deg, the boundary layer thickness is almost constant in the region $|X| \leq 0.5$. For other values of β, minimum value of the boundary layer thickness is reached in the $X < 0$ region, as expected. The location of this minimum shifts away from the stagnation point as β increases, except for $\beta = 90$ deg. For large values of $|X|$, the curves for different β are almost parallel except for $\beta = 90$ deg. Thus while $\delta |x|^{-1/2}$ is a constant for $\beta = 0$ for all $x > 0$, it is a constant for nonzero $\beta (\neq 90$ deg) for large $|X|$ only.

Note that close to the stagnation point, $\mathrm{Re}^{1/2}\delta/L$ is of order

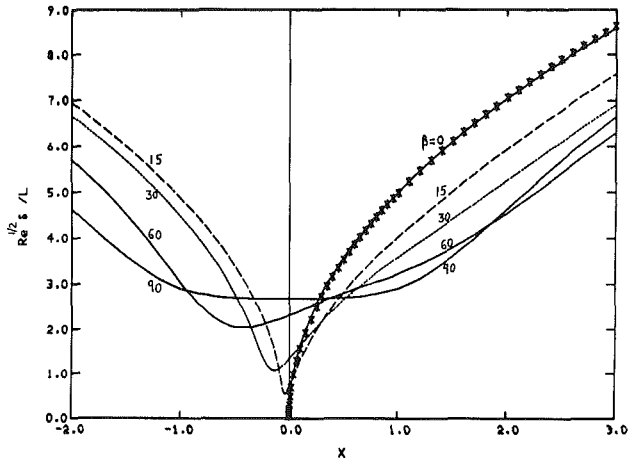

Fig. 6 Hydrodynamic boundary layer thickness versus X for various values of β

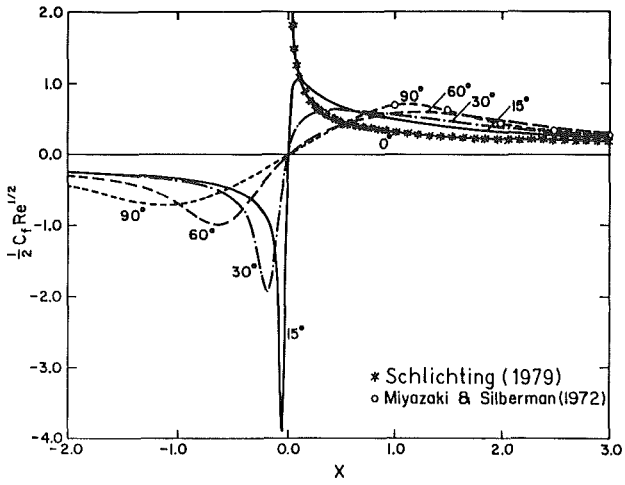

Fig. 7 Local skin friction coefficient over the plate

unity. For the boundary layer analysis to be valid, it is required that δ/x be small. Thus it appears that for $X\to 0$, the present results would be valid for $\mathrm{Re}\to\infty$. At such a high Re, the assumption that the slot jet be laminar would no longer hold. According to Hanks and Ruo (1966), the upper limit of Re for ensuring a laminar slot jet would be about 2800. Thus the present results based on the boundary layer analysis of a *laminar* slot jet are expected to hold good experimentally in the region $|X|\geq 0.1$.

4.4 Skin Friction and Heat Transfer. Values of the local skin friction coefficient and the Nusselt number are calculated using the relations

$$\frac{1}{2}C_f\mathrm{Re}^{1/2}=(\partial U/\partial Y)_{Y=0} \tag{14}$$

and

$$\mathrm{Nu}=hL/k=-\mathrm{Re}^{1/2}(\partial\theta/\partial Y)_{Y=0} \tag{15}$$

These parameters at different angles of impingement are shown in Figs. 7 and 8. At $X=0$, the friction factor is zero for $\beta\neq 0$. This obviously follows from the fact that for nonzero angles of impingement there is no velocity gradient in the transverse direction at the stagnation point. The effect of potential flow velocity distribution at the plate for different angles β, shown in Fig. 6, is very clearly reflected on the local skin friction coefficient. Far downstream from the stagnation point ($X\geq 3$) the potential flow velocity at the plate U_s approaches the free-stream velocity U_∞ so that the skin friction coefficient for any nonzero angle of impingement tends to vary as that for the flow over a flat plate at zero incidence. The latter, as computed presently, is also shown in Fig. 7, and matches perfectly with the exact curve (Schlichting, 1979) represented by stars. For nonzero angles of impingement the skin friction coefficient, starting from a zero value at the stagnation point, increases and reaches a maximum value close to the stagnation point owing to the small boundary layer thickness and large value of U_s in this region. The maximum shifts toward the stagnation point with a decrease in the angle of impingement since the potential flow velocity U_s approaches the free-stream velocity more rapidly for small values of β (see Fig. 4). Particularly striking is the shape of the curve in $X<0$ region for small values of β owing to the rapid increase in U_s for such cases. The curve for $\beta=90$ deg in Fig. 7 agrees perfectly with that corresponding to $H\geq 3$ in Fig. 3 of Miyazaki and Silberman (1972).

Figure 8 displays the local Nusselt numer (based on slot jet thickness L) or the normalized temperature gradient in the transverse direction at the plate surface obtained for $\mathrm{Pr}=0.7$,

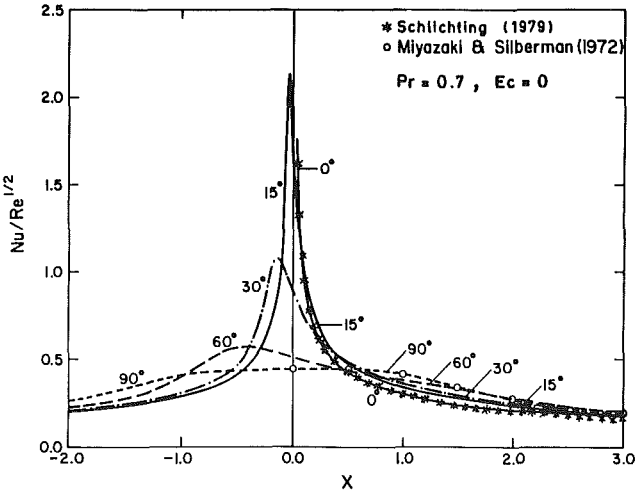

Fig. 8 Local Nusselt number over an isothermal plate ($\mathrm{Pr}=0.7$, $\mathrm{Ec}=0$)

$\mathrm{Ec}=0$, and isothermal wall conditions. Here again the curve for $\beta=90$ deg agrees exactly with that for $H\geq 3$ in Fig. 4 of Miyazaki and Silberman (1972). For $\beta=90$ deg, the Nusselt number variation is symmetric about the stagnation point, and Nu at $X=0$ is almost twice that at $X=3$. There is a substantial change in the $\mathrm{Nu}/\mathrm{Re}^{1/2}$ profiles for other values of angle β. The maximum in these profiles lies in the $X<0$ region, and shifts toward the stagnation point as β decreases. At $\beta=15$ deg, the maximum value of local Nusselt number is as much as 10 times that at $X=3$. However, this maximum lies in the region $|X|<0.1$, and is therefore not very meaningful for the laminar slot jet as per the discussion in Section 4.3. It should be noted that the large change in Nusselt number values with respect to β occurs only in the range $|X|<1$. Outside this range the Nusselt number is very close to that for the flow over a flat plate at zero incidence. The latter is also shown in Fig. 8 based on present computations, and matches perfectly with the exact curve (Schlichting, 1979) represented again by stars. The Nusselt number variation with respect to β for other Prandtl numbers is similar to that shown in Fig. 8 for $\mathrm{Pr}=0.7$.

The mean Nusselt number over a length X of the plate can be computed using the relation

$$\mathrm{Nu}_m\mathrm{Re}^{-1/2}=-\frac{1}{X}\int_0^X(\partial\theta/\partial Y)_{Y=0}dX \tag{16}$$

The variation of mean Nusselt number computed over a length of the plate equal to the slot jet thickness on either side of the

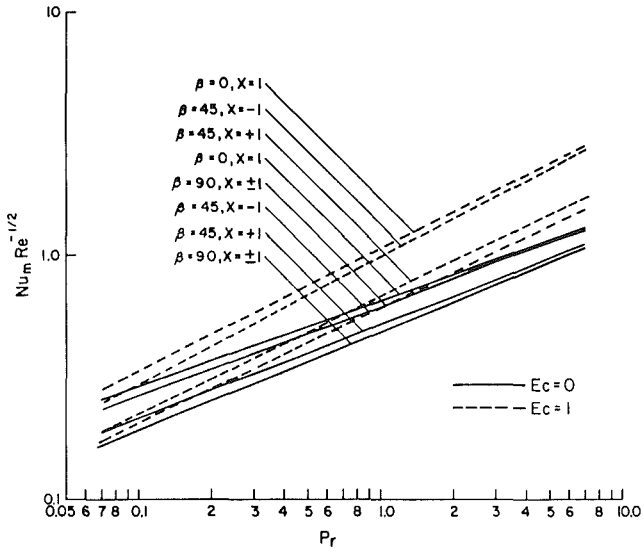

Fig. 9 Mean Nusselt number over an isothermal plate (various β and Ec)

stagnation point is shown in Fig. 9 for selected values of angle β and Eckert number. As expected the mean Nusselt number increases with the Prandtl number. The presence of viscous dissipation with Ec = 1 further increases the mean Nusselt number as shown in Fig. 9 for a jet colder than the plate. Also note that on a log-log plot $Nu_m Re^{-1/2}$ varies linearly with Pr. Thus we have

$$Nu_m Re^{-1/2} \propto Pr^m \tag{17}$$

where the exponent m depends upon β and Ec, and for the results shown in Fig. 9 varies from 1/3 to 1/2.

5 Conclusions

A finite-difference method is developed for the two-dimensional boundary layer flow resulting from the impingement of a slot jet on an inclined flat plate. The influence of the angle of impingement on the velocity and temperature profiles over an isothermal plate is studied for various Prandtl and Eckert numbers. From the results obtained the following conclusions can be drawn:

1 The presence of a stagnation point for nonzero angles of jet impingement significantly affects both the pressure distribution over the plate and the potential flow velocity U_s at the plate.

2 Near the stagnation point the hydrodynamic and thermal boundary layers are thinner for lower angles of impingement but away from the stagnation point they are thinner for higher angles of impingement except for $\beta = 90$ deg.

3 The local skin friction coefficient and the Nusselt number show a larger maximum value closer to the stagnation point at smaller angles of impingement.

4 In order for the slot jet to remain laminar, the boundary layer analysis is valid in the region $|X| \geq 0.1$.

Acknowledgments

This work was revised while the first author was on sabbatical at The Ohio State University. Use of computing facilities at The Ohio State University and helpful comments of the referees are gratefully acknowledged.

References

Dorrepaal, J. M., 1986, "An Exact Solution of the Navier-Stokes Equation Which Describes Non-orthogonal Stagnation Point Flow in Two Dimensions," *J. Fluid Mech.*, Vol. 163, pp. 141-147.

Ero, M. I. O., 1978, "Heat and Mass Transfer in Close Proximity Impinging Two-Dimensional Laminar Jets," *AIAA J.*, Vol. 16, pp. 611-613.

Gardon, R., and Akfirat, J. C., 1966, "Heat Transfer Characteristics of Impinging Two-Dimensional Air Jets," ASME JOURNAL OF HEAT TRANSFER, Vol. 88, pp. 101-108.

Hanks, R. W., and Ruo, H. C., 1966, "Laminar-Turbulent Transition in Ducts of Rectangular Cross Section," *Ind. Eng. Chem. Fund.*, Vol. 5, pp. 558-561.

Hornbeck, R. W., 1973, *Numerical Marching Techniques for Fluid Flows With Heat Transfer*, NASA SP-297.

Martin, H., 1977, "Heat and Mass Transfer Between Impinging Gas Jets and Solid Surfaces," *Adv. in Heat Transfer*, J. P. Hartnett and T. F. Irvine, Jr., eds., Academic Press, New York, Vol. 13, pp. 1-60.

Masliyah, J. H., and Nguyen, T. T., 1979, "Mass Transfer Due to an Impinging Slot Jet," *Int. J. Heat Mass Transfer*, Vol. 22, pp. 237-244.

Milne Thomson, L. M., 1960,, *Theoretical Hydrodynamics*, 4th ed., Macmillan, London.

Miyazaki, H., and Silberman, E., 1972, "Flow and Heat Transfer on a Flat Plate Normal to a Two-Dimensional Laminar Jet Issuing From a Nozzle of Finite Height," *Int. J. Heat Mass Transfer*, Vol. 15, pp. 2097-2107.

Nakahashi, K., and Deiwert, G. S., 1986, "Three-Dimensional Adaptive Grid Method," *AIAA J.*, Vol. 24, pp. 948-954.

Nakahashi, K., and Deiwert, G. S., 1987, "Self-Adaptive Grid Method With Application to Airfoil Flow," *AIAA J.*, Vol. 25, pp. 513-520.

Schlichting, H., 1979, *Boundary Layer Theory*, 7th ed., McGraw-Hill, New York.

Sparrow, E. M., and Lee, L., 1975, "Analysis of Flow Field and Impingement Heat/Mass Transfer Due to a Nonuniform Slot Jet," ASME JOURNAL OF HEAT TRANSFER, Vol. 97, pp. 191-197.

Sparrow, E. M., and Wong, T. C., 1975, "Impingement Transfer Coefficients Due to Initially Laminar Slot Jets," *Int. J. Heat Mass Transfer*, Vol. 18, pp. 597-605.

Tamada, K., 1979, "Two-Dimensional Stagnation-Point Flow Impinging Obliquely on a Plane Wall," *J. Phys. Soc. Japan*, Vol. 46, pp. 310-311.

van Heiningen, A. R. P., Mujumdar, A. S., and Douglas, W. J. M., 1976, "Numerical Prediction of the Flow Field and Impingement Heat Transfer Caused by a Laminar Slot Jet," ASME JOURNAL OF HEAT TRANSFER, Vol. 98, pp. 654-658.

A Two-Equation Model for Heat Transport in Wall Turbulent Shear Flows

Y. Nagano
Professor.
Mem. ASME

C. Kim
Graduate Student.

Department of Mechanical Engineering,
Nagoya Institute of Technology,
Gokiso-cho, Showa-ku,
Nagoya 466, Japan

A new proposal for closing the energy equation is presented at the two-equation level of turbulence modeling. The eddy diffusivity concept is used in modeling. However, just as the eddy viscosity is determined from solutions of the k *and* ϵ *equations, so the eddy diffusivity for heat is given as functions of temperature variance* $\overline{t^2}$*, and the dissipation rate of temperature fluctuations* ϵ_t*, together with* k *and* ϵ*. Thus, the proposed model does not require any questionable assumptions for the "turbulent Prandtl number." Modeled forms of the* $\overline{t^2}$ *and* ϵ_t *equations are developed to account for the physical effects of molecular Prandtl number and near-wall turbulence. The model is tested by application to a flat-plate boundary layer, the thermal entrance region of a pipe, and the turbulent heat transfer in fluids over a wide range of the Prandtl number. Agreement with the experiment is generally very satisfactory.*

1 Introduction

With the wide accessibility of high-speed computers, turbulence models have been steadily securing their position as an effective strategy for solving flow problems encountered in engineering applications. The turbulence model for the scalar field, on the other hand, is still rather primitive. By far the most common approach to the analytical studies of turbulent heat transfer problems is to solve the energy equation in which the turbulent heat flux is modeled by using the classical Boussinesq approximation. The unknown eddy diffusivity for heat α_t is expressed by the known eddy viscosity ν_t, so that $\alpha_t = \nu_t/\mathrm{Pr}_t$. Thus, in this formulation the analogy is assumed tacitly between turbulent heat and momentum transfer. Also, the turbulent Prandtl number Pr_t needs to be prescribed. However, there are so many ambiguous points in Pr_t itself, and none of the empirical formulae for Pr_t can work universally (Reynolds, 1975). Accordingly, the calculation methods based on Pr_t have inherent limitations, since the calculations of a temperature field depend largely upon Pr_t values used.

An alternative independent of an assumption of turbulent Prandtl number is to solve directly the transport equations for turbulent heat fluxes. This trial was performed by Newman et al. (1981), Elghobashi and Launder (1981, 1983), and Shih and Lumley (1986) to analyze the spread of fluctuating temperature in a homogeneous turbulence field with no mean velocity gradients. In heat flux equation modeling, correct modeling of the pressure scrambling terms is generally critical in obtaining correct heat flux values (Nagano and Hishida, 1985). Much of the modeling, however, is almost completely ad hoc (Lumley, 1983). Thus, the heat flux equation model needs further study and refinement. The development of more sophisticated new models is awaited.

The turbulence model for scalar field proposed in this study is that which solves the energy equation with the aid of the concept of eddy diffusivity for heat. However, in the present model, a value for the turbulent Prandtl number Pr_t need not be postulated. The eddy diffusivity for heat α_t is expressed in terms of the turbulent kinetic energy k, the dissipation rate of turbulence energy ϵ, the temperature variance $\overline{t^2}$, and the temperature variance dissipation rate ϵ_t. The most appropriate α_t value can be given as a function of the state of velocity and temperature fields by solving the transport equations for these turbulence quantities. Therefore, the proposed model is applicable to the problems where a value of Pr_t is not known. The verification of the validity of the proposed model is presented by application to a flat-plate boundary layer and the thermal entrance region of a pipe. The latter test case provides a critical check of the model because the relevant velocity and temperature fields are not similar, and hence the Reynolds analogy collapses. The range of satisfactory performance of the model for various kinds of fluids was tested. The tested range of the molecular Prandtl number Pr was from 0.1 to 10,000.

2 Improved Form of k-ϵ Turbulence Model for Wall Turbulent Shear Flows

A two-equation model uses the concept of eddy viscosity (turbulent diffusivity) ν_t so as to describe the magnitude of turbulence intensity and its spatial extent. In the k–ϵ model, the reference velocity of turbulence is represented by $k^{1/2}$ determined from the turbulent kinetic energy k. The characteristic length scale is given by the eddy length scale $L_\epsilon = k^{3/2}/\epsilon$.

The governing equations for the k–ϵ model, improved after consideration of the characteristic of wall turbulence (Nagano and Hishida, 1987), may be written as

k-equation

$$\frac{\partial k}{\partial \tau} + \bar{U}_j \frac{\partial k}{\partial x_j} = \frac{\partial}{\partial x_j}\left\{\left(\nu + \frac{\nu_t}{\sigma_k}\right)\frac{\partial k}{\partial x_j}\right\} - \overline{u_i u_j}\frac{\partial \bar{U}_i}{\partial x_j} - \epsilon - 2\nu\left(\frac{\partial \sqrt{k}}{\partial x_j}\right)^2 \tag{1}$$

ϵ-equation

$$\frac{\partial \epsilon}{\partial \tau} + \bar{U}_j \frac{\partial \epsilon}{\partial x_j} = \frac{\partial}{\partial x_j}\left\{\left(\nu + \frac{\nu_t}{\sigma_\epsilon}\right)\frac{\partial \epsilon}{\partial x_j}\right\} - C_{\epsilon 1} f_1 \frac{\epsilon}{k}\overline{u_i u_j}\frac{\partial \bar{U}_i}{\partial x_j} - C_{\epsilon 2} f_2 \frac{\epsilon^2}{k} + \nu\nu_t(1 - f_\mu)\left(\frac{\partial^2 \bar{U}_i}{\partial x_j \partial x_k}\right)^2 \tag{2}$$

$$-\overline{u_i u_j} = \nu_t\left(\frac{\partial \bar{U}_i}{\partial x_j} + \frac{\partial \bar{U}_j}{\partial x_i}\right) - \frac{2}{3}\delta_{ij} k \tag{3}$$

$$\nu_t = C_\mu f_\mu k^{1/2} L_\epsilon = C_\mu f_\mu k^2/\epsilon \tag{4}$$

In the above set, the values of the constants and the model

Contributed by the Heat Transfer Division for publication in the JOURNAL OF HEAT TRANSFER. Manuscript received by the Heat Transfer Division August 4, 1987. Keywords: Forced Convection, Modeling and Scaling, Turbulence.

functions which account for low-Reynolds-number and/or wall-proximity effects are

$$C_\mu = 0.09, \quad C_{\epsilon 1} = 1.45, \quad C_{\epsilon 2} = 1.9, \quad \sigma_k = 1.0, \quad \sigma_\epsilon = 1.3$$
$$f_\mu = \{1 - \exp(-R_\tau/26.5)\}^2, \quad f_1 = 1.0, \quad f_2 = 1 - 0.3\exp(-R_t^2)$$
$$R_\tau = u_* y/\nu = y^+, \quad R_t = k^2/\nu\epsilon$$

The turbulence quantities for a velocity field can be obtained from equations (1)–(4), together with the following continuity and momentum equations:

$$\partial \bar{U}_i/\partial x_i = 0 \tag{5}$$

$$\frac{\partial \bar{U}_i}{\partial \tau} + \bar{U}_j \frac{\partial \bar{U}_i}{\partial x_j} = -\frac{1}{\rho}\frac{\partial \bar{P}}{\partial x_i} + \frac{\partial}{\partial x_j}\left(\nu \frac{\partial \bar{U}_i}{\partial x_j} - \overline{u_i u_j}\right) \tag{6}$$

3 Two-Equation Model for Temperature Field

3.1 Governing Equations. When temperature is regarded as a passive scalar, the transport equation is expressed as follows:

$$\frac{\partial \bar{T}}{\partial \tau} + \bar{U}_j \frac{\partial \bar{T}}{\partial x_j} = \frac{\partial}{\partial x_j}\left(\alpha \frac{\partial \bar{T}}{\partial x_j} - \overline{u_j t}\right) \tag{7}$$

On the other hand, the temperature variance $\overline{t^2}$ and the dissipation rate of half the temperature variance ϵ_t, corresponding to k and ϵ in the velocity field, are given (Launder, 1976) by

$\overline{t^2}$-equation

$$\frac{\partial \overline{t^2}}{\partial \tau} + \bar{U}_j \frac{\partial \overline{t^2}}{\partial x_j} = \frac{\partial}{\partial x_j}\left(\alpha \frac{\partial \overline{t^2}}{\partial x_j} - \overline{u_j t^2}\right) - 2\overline{u_j t}\frac{\partial \bar{T}}{\partial x_j} - 2\epsilon_t \tag{8}$$

ϵ_t-equation

$$\frac{\partial \epsilon_t}{\partial \tau} + \bar{U}_j \frac{\partial \epsilon_t}{\partial x_j} = \frac{\partial}{\partial x_j}\left(\alpha \frac{\partial \epsilon_t}{\partial x_j} - \overline{u_j \epsilon_t'}\right) - 2\alpha \overline{\frac{\partial u_j}{\partial x_k}\frac{\partial t}{\partial x_k}\frac{\partial t}{\partial x_j}}$$
$$- 2\alpha\left(\overline{\frac{\partial u_j}{\partial x_k}\frac{\partial t}{\partial x_k}}\frac{\partial \bar{T}}{\partial x_j} + \overline{\frac{\partial t}{\partial x_j}\frac{\partial t}{\partial x_k}}\frac{\partial \bar{U}_j}{\partial x_k} + \overline{u_j \frac{\partial t}{\partial x_k}}\frac{\partial^2 \bar{T}}{\partial x_j \partial x_k}\right) - 2\left(\alpha \overline{\frac{\partial^2 t}{\partial x_j \partial x_k}}\right)^2 \tag{9}$$

where $\epsilon_t' = \alpha(\partial t/\partial x_k)(\partial t/\partial x_k)$ and $\epsilon_t = \overline{\epsilon_t}'$.

3.2 Modeling A temperature field can be analyzed from the energy equation (7). However, this equation is not closed since it contains an unknown turbulent heat flux $\overline{u_j t}$. Also, unknown higher-order moments are included in equations (8) and (9), and the equations are not closed. In what follows, the main aim is to devise a rational closure of equations (7)–(9) at the two-equation level of turbulence modeling.

Using the eddy diffusivity for heat α_t, we represent a turbulent heat flux $\overline{u_j t}$ by the following simple gradient form:

$$-\overline{u_j t} = \alpha_t \partial \bar{T}/\partial x_j \tag{10}$$

Next, we express the eddy diffusivity for heat α_t as a function of the state of velocity and temperature fields. This is a counterpart of the eddy viscosity ν_t represented as a function of the state of a velocity field by using k and ϵ as given by equation (4). Since it is interpreted that $\alpha_t \propto$ (turbulent velocity) $\times$ (spatial extent of a fluctuating temperature), α_t may be written as

$$\alpha_t \propto k^{1/2} L_m \tag{11}$$

Nomenclature

C_f = skin-friction coefficient = $\tau_w/(\rho \bar{U}_r^2/2)$
C_μ, $C_{\epsilon 1}$, $C_{\epsilon 2}$ = turbulence model constants for velocity field
C_λ, C_{P1}, C_{P2}, C_{D1}, C_{D2} = turbulence model constants for temperature field
C_p = specific heat at constant pressure
d = pipe diameter
f_μ, f_1, f_2 = turbulence model functions for velocity field
f_λ, f_{P1}, f_{P2}, f_{D1}, f_{D2} = turbulence model functions for temperature field
k = turbulent kinetic energy = $\overline{u_i u_i}/2$
Nu = Nusselt number
$\bar{P}$ = mean pressure
Pr, Pr_t = molecular and turbulent Prandtl numbers
q_w = wall heat flux
R = time-scale ratio = τ_t/τ_u
Re = Reynolds number = $\bar{U}_b d/\nu$
r_o = pipe radius
St = Stanton number = $q_w/\rho C_p \bar{U}_r(\bar{T}_w - \bar{T}_r)$
$\bar{T}$, t = mean and fluctuating temperatures
$\bar{T}_w$, $\bar{T}_r$ = wall and reference temperatures
t_* = friction temperature = $q_w/\rho C_p u_*$
$\bar{U}$ = mean streamwise velocity
$\bar{U}_r$ = reference velocity
$\bar{U}^+$ = dimensionless velocity = $\bar{U}/u_*$
$\bar{U}_i$, u_i = mean and fluctuating velocity components in x_i direction
u_* = friction velocity = $\sqrt{\tau_w/\rho}$
x, y = coordinates
x_i = coordinates in tensor notation
y^+ = dimensionless distance from wall = $u_* y/\nu$
α, α_t = molecular and eddy diffusivities for heat
ϵ = dissipation rate of k = $\nu(\partial u_i/\partial x_j)(\partial u_i/\partial x_j)$
ϵ_t = dissipation rate of $\overline{t^2}/2$ = $\alpha(\partial t/\partial x_j)(\partial t/\partial x_j)$
ν, ν_t = molecular and eddy viscosities
ρ = density
σ_k, σ_ϵ, σ_h, σ_ϕ = turbulence model constants for diffusion of k, ϵ, $\overline{t^2}$, and ϵ_t
τ, τ_w = time and wall shear stress
τ_u, τ_t = time scales of velocity and temperature fields = k/ϵ, $\overline{t^2}/2\epsilon_t$
$\overline{(\ )}$ = time mean value

Subscripts

b = bulk
e = boundary-layer edge

where L_m is the characteristic length scale. To describe L_m explicitly, we need an appropriate turbulent time scale equivalent to the relative "lifetime" of the energy-containing eddies or temperature fluctuations (Elghobashi and Launder, 1983). There may be three choices for the time scale: the dynamic time scale $\tau_u = k/\epsilon$, the scalar time scale $\tau_t = (\overline{t^2}/2)/\epsilon_t$, and the mixed time scale $\tau_m = \sqrt{\tau_u \tau_t}$. We adopt the mixed time scale τ_m, since it blends both thermal and mechanical contributions, and is almost equal to an arithmetic mean of τ_u and τ_t in simple shear layers, as evidenced experimentally by Nagano and Hishida (1985), so that $L_m = k^{1/2}\tau_m$. Thus, from equation (11), α_t may be modeled as

$$\alpha_t = C_\lambda f_\lambda k \sqrt{(k/\epsilon)\cdot(\overline{t^2}/\epsilon_t)} \tag{12}$$

where C_λ is the model constant, and f_λ is the model function, which has some properties in common with f_μ in equation (4), as will be described later.

To the turbulent diffusion terms in equations (8) and (9), we apply the gradient-type diffusion model, and write using the eddy diffusivity for heat

$$-\overline{u_j t^2} = (\alpha_t/\sigma_h)\partial\overline{t^2}/\partial x_j \tag{13}$$

$$-\overline{u_j \epsilon_t'} = (\alpha_t/\sigma_\phi)\partial\epsilon_t/\partial x_j \tag{14}$$

where σ_h and σ_ϕ are the model constants.

The direct mean-field generation terms in the ϵ_t-equation are negligible when the turbulence Reynolds number Re_t $(= k^2/\nu\epsilon)$ is large (Launder, 1976). However, they become important in the immediate neighborhood of the wall because of a sharp decrease of Re_t values. Thereupon, extending the model of Newman et al. (1981) for the generation and destruction of ϵ_t due to fine-scale turbulence interactions, we write the unknown source/sink terms in equation (9) as follows:

$$-2\alpha\overline{\frac{\partial u_j}{\partial x_k}\frac{\partial t}{\partial x_k}\frac{\partial t}{\partial x_j}} - 2\alpha\left(\overline{\frac{\partial u_j}{\partial x_k}\frac{\partial t}{\partial x_k}\frac{\partial \bar{T}}{\partial x_j}} + \overline{\frac{\partial t}{\partial x_j}\frac{\partial t}{\partial x_k}\frac{\partial \bar{U}_j}{\partial x_k}}\right) - 2\overline{\left(\alpha\frac{\partial^2 t}{\partial x_j \partial x_k}\right)^2} = -C_{P1} f_{P1}\frac{\epsilon_t}{\overline{t^2}}\overline{u_j t}\frac{\partial \bar{T}}{\partial x_j}$$

$$-C_{P2} f_{P_2}\frac{\epsilon_t}{k}\overline{u_i u_j}\frac{\partial \bar{U}_i}{\partial x_j} - C_{D1} f_{D1}\frac{\epsilon_t^2}{\overline{t^2}} - C_{D2} f_{D2}\frac{\epsilon\epsilon_t}{k} \tag{15}$$

where f_{P1} and f_{P2} correspond to f_1 in equation (2), f_{D1} and f_{D2} are equivalent to f_2 in the same equation, and all are the correction functions to account for low-Reynolds-number effects.

The other mean-field generation process in equation (9) may be modeled as

$$-2\alpha\overline{u_j\frac{\partial t}{\partial x_k}}\frac{\partial^2 \bar{T}}{\partial x_j \partial x_k} = \alpha C_{P3} f_{P3}\sqrt{\frac{k}{\epsilon}\frac{\overline{t^2}}{\epsilon_t}}\overline{u_j u_l}\left(\frac{\partial^2 \bar{T}}{\partial x_l \partial x_k}\right)\left(\frac{\partial^2 \bar{T}}{\partial x_j \partial x_k}\right) \tag{16}$$

We further approximate equation (16) at the two-equation level of modeling as

$$-2\alpha\overline{u_j\frac{\partial t}{\partial x_k}}\frac{\partial^2 \bar{T}}{\partial x_j \partial x_k} = \alpha\alpha_t(1-f_\lambda)\left(\frac{\partial^2 \bar{T}}{\partial x_j \partial x_k}\right)^2 \tag{17}$$

3.3 Wall-Proximity Effects. Viscosity and molecular conduction also become dominant in the close vicinity of the wall, and anisotropy increases due to the presence of the wall. In turbulence modeling, it is important how to account for these near-wall features. Obviously, from equations (7) and (8), the most essential factor that determines the character of a temperature field is the turbulent heat flux $\overline{u_j t}$. Accordingly, the quality of the modeling of the function f_λ in equation (12), which is introduced mainly to improve the near-wall behavior of $\overline{u_j t}$, influences the overall quality of the turbulence model. In what follows, we devise the modeling of f_λ.

Generally, the relative thickness of the conduction-dominating sublayer to that of the viscous sublayer near the wall changes with the molecular Prandtl number Pr (Townsend, 1976). Thus, even at the same distance from the wall y, the value of f_λ must change according to the corresponding thickness of the conductive sublayer if the Prandtl number changes. In view of this, we represent f_λ as a single function of the dimensionless distance $y^{++} = u_* y/\sqrt{\nu\alpha} = \sqrt{\mathrm{Pr}}\, y^+$. In this formulation, the value of f_λ depends uniquely upon y^{++}. Hence the actual location y^+ giving the same value of f_λ parts from the wall in the case that Pr is small, and approaches the wall when Pr becomes large. This corresponds exactly with the physical behavior of the conductive sublayer thickness. In addition, the relation $\delta_c/\delta_v \propto 1/\sqrt{\mathrm{Pr}}$ may hold if the ratio of the conductive sublayer thickness δ_c to the viscous sublayer thickness δ_v is regarded approximately as the ratio of the thermal and hydrodynamic boundary-layer thicknesses in laminar flows. The coordinate y^{++} also satisfies this relation. On the other hand, the effect of f_λ needs to change with the development of a thermal boundary layer, regardless of the Pr value, in such a flow field as the thermal entrance region where the Reynolds analogy does not hold. Considering these requirements, we propose the following formula for f_λ:

$$f_\lambda = \{1 - \exp(-\phi y^{++}/A)\}^2 \tag{18}$$

with

$$\phi = \sqrt{2/C_f}\cdot t_*/(\bar{T}_w - \bar{T}_r) = (2/C_f)\mathrm{St} \tag{19}$$

Here $C_f = \tau_w/(\rho\bar{U}_r^2/2)$ and $\mathrm{St} = q_w/\rho C_p \bar{U}_r(\bar{T}_w - \bar{T}_r)$ are the skin-friction coefficient and the Stanton number, respectively. The value of St varies in accordance with the thermal boundary-layer development. Thus, as seen from equations (18) and (19), ϕ is the factor controlling the effective range for f_λ to match the thermal boundary-layer development. In particular, when the Reynolds analogy holds, we get $\phi = 1$ and $y^{++} = y^+$, and hence equation (18) yields

$$f_\lambda = \{1 - \exp(-y^+/A)\}^2 \tag{20}$$

which is indeed equivalent to the model function f_μ for the velocity field. The best value for the constant A is chosen as 30.5 after computer optimization.

It should be mentioned that the influence of the decrease in turbulence Reynolds numbers near the wall is not counted directly in the formulation (18). This is because the eddy diffusivity for heat α_t is already modeled so that it decreases with decreasing turbulence Reynolds numbers, as may be readily seen by rewriting equation (12) as

$$\alpha_t/\nu = C_\lambda f_\lambda \mathrm{Re}_h \tag{21}$$

where $\mathrm{Re}_h = k\sqrt{k\overline{t^2}/\epsilon\epsilon_t}/\nu$ is the turbulence Reynolds number based on the mixed time scale.

Next, we consider the limiting behavior of the dissipation rate of temperature fluctuations ϵ_t at a wall. If the isotropy of the small-scale dissipative motion is assumed, ϵ_t is consistently zero at the heat transfer surface with a uniform wall temperature. The actual anisotropic ϵ_t, however, is not zero, so $\epsilon_t = \alpha(\overline{\partial t/\partial y})_0^2 = 0$. Nevertheless, it might be suggested that we make ϵ_t zero at the wall for computational expediency. Since this loses in the $\overline{t^2}$-equation the balancing term with the molecular diffusion $\alpha(\partial^2\overline{t^2}/\partial x_j \partial x_j)$ at the wall, we add a correction term in equation (8), as will be developed below.

In case of a uniform wall temperature, a fluctuating temperature near the wall may be expressed using the Taylor expansion as

$$t = ay + by^2 + 0(y^3) \tag{22}$$

$$\overline{t^2} = \overline{a^2}y^2 + 2\overline{ab}y^3 + 0(y^4) \tag{23}$$

The actual ϵ_t in the immediate neighborhood of the wall may be given by

$$\epsilon_t \cong \alpha\overline{(\partial t/\partial y)^2} = \alpha\overline{a^2} + 4\alpha\overline{ab}y + 0(y^2) \tag{24}$$

while from equation (23) it is easily demonstrated that

$$\alpha(\partial\sqrt{\overline{t^2}}/\partial y)^2 = \alpha\overline{a^2} + 4\alpha\overline{ab}y + 0(y^2) \tag{25}$$

We thus conclude from equations (24) and (25) that the anisotropic behavior of the true temperature-variance dissipation rate may be represented with the term $\alpha(\partial\sqrt{\overline{t^2}}/\partial y)^2$ by substituting $\epsilon_t + \alpha(\partial\sqrt{\overline{t^2}}/\partial y)^2$ for ϵ_t in equation (8), even if we make ϵ_t zero at the wall.

From these considerations, we finally obtain the governing equations of the two-equation model for scalar turbulence as follows:

$\overline{t^2}$-equation

$$\frac{\partial\overline{t^2}}{\partial\tau} + \bar{U}_j\frac{\partial\overline{t^2}}{\partial x_j} = \frac{\partial}{\partial x_j}\left\{\left(\alpha + \frac{\alpha_t}{\sigma_h}\right)\frac{\partial\overline{t^2}}{\partial x_j}\right\} - 2\overline{u_j t}\frac{\partial\bar{T}}{\partial x_j} - 2\epsilon_t - 2\alpha\left(\frac{\partial\sqrt{\overline{t^2}}}{\partial x_j}\right)^2 \tag{26}$$

ϵ_t-equation

$$\frac{\partial\epsilon_t}{\partial\tau} + \bar{U}_j\frac{\partial\epsilon_t}{\partial x_j} = \frac{\partial}{\partial x_j}\left\{\left(\alpha + \frac{\alpha_t}{\sigma_\phi}\right)\frac{\partial\epsilon_t}{\partial x_j}\right\} - C_{P1}f_{P1}\frac{\epsilon_t}{\overline{t^2}}\overline{u_j t}\frac{\partial\bar{T}}{\partial x_j} - C_{P2}f_{P2}\frac{\epsilon_t}{k}\overline{u_i u_j}\frac{\partial\bar{U}_i}{\partial x_j} - C_{D1}f_{D1}\frac{\epsilon_t^2}{\overline{t^2}} - C_{D2}f_{D2}\frac{\epsilon\epsilon_t}{k} + \alpha\alpha_t(1-f_\lambda)\left(\frac{\partial^2\bar{T}}{\partial x_j\partial x_k}\right)^2 \tag{27}$$

At high-Reynolds-number flows where the wall-proximity effects are immaterial, we may put $f_\lambda = f_{P1} = f_{P2} = f_{D1} = f_{D2} \equiv 1$.

3.4 Model Constants. The constants appearing in the two-equation model for scalar turbulence are determined in the following manner. First, we specify a value of C_λ in equation (12) defining the eddy diffusivity for heat α_t. In the log-law region where the turbulence develops sufficiently to render the molecular diffusion negligible, i.e., $f_\mu = f_\lambda = 1$, C_λ may be given from equations (4) and (12), together with the thermal/mechanical time-scale ratio $R = \tau_t/\tau_u = (\overline{t^2}/2\epsilon_t)/(k/\epsilon)$ and the turbulent Prandtl number $\mathrm{Pr}_t = \nu_t/\alpha_t$, by

$$C_\lambda = C_\mu/\mathrm{Pr}_t\sqrt{2R} \tag{28}$$

Here we have $C_\mu = 0.09$, and for air flows $\mathrm{Pr}_t = 0.87$ and $R = 0.4$–0.5 (Béguier et al., 1978; Nagano and Hishida, 1985). Thus, from equation (28) we obtain $C_\lambda = 0.11$.

The constants σ_h and σ_ϕ for the turbulent diffusion terms given by equations (13) and (14) are assigned the same value of 1.0. This is consistent with the assumption in the heat flux equation modeling by Elghobashi and Launder (1981, 1983).

We determine the constants C_{D1} and C_{D2} in the ϵ_t-equation (27) through consideration of existing data concerning decay of homogeneous scalar turbulence. In a homogeneous decaying turbulent flow, equations (1), (2), (26), and (27) become simply

$$\bar{U}dk/dx = -\epsilon \tag{29}$$

$$\bar{U}d\epsilon/dx = -C_{\epsilon 2}\epsilon^2/k \tag{30}$$

$$\bar{U}d\overline{t^2}/dx = -2\epsilon_t \tag{31}$$

$$\bar{U}d\epsilon_t/dx = -C_{D1}\epsilon_t^2/\overline{t^2} - C_{D2}\epsilon\epsilon_t/k \tag{32}$$

where the x axis is taken in the flow direction. The dissipation rate of temperature fluctuations may be written as $\epsilon_t = (\epsilon/2R)(\overline{t^2}/k)$ from the definition of the time-scale ratio $R = (\overline{t^2}/2\epsilon_t)/(k/\epsilon)$. In homogeneous grid-generated turbulence, it is known that R does not change in the flow direction (Warhaft and Lumley, 1978). From equations (29)–(31), we thus obtain:

$$\begin{aligned}\bar{U}d\epsilon_t/dx &= (\bar{U}/2R)d(\epsilon\overline{t^2}/k)/dx \\ &= (\bar{U}/2R)\{-(\epsilon\overline{t^2}/k^2)dk/dx \\ &\quad + (\overline{t^2}/k)d\epsilon/dx + (\epsilon/k)d\overline{t^2}/dx\} \\ &= (1/2R)(\epsilon^2\overline{t^2}/k^2 - C_{\epsilon 2}\epsilon^2\overline{t^2}/k^2 - 2\epsilon\epsilon_t/k) \\ &= -2R(C_{\epsilon 2}-1)\epsilon_t^2/\overline{t^2} - (1/R)\epsilon\epsilon_t/k\end{aligned} \tag{33}$$

Equations (32) and (33) give the following relations:

$$C_{D1} = 2R(C_{\epsilon 2} - 1) \tag{34}$$

$$C_{D2} = 1/R \tag{35}$$

The values of $C_{D1} = 2.03$ and $C_{D2} = 0.88$ are then specified from the above equations if we set $R = 1.13$. We also get the values of $C_{D1} = 2.25$ and $C_{D2} = 0.80$ for $R = 1.25$. Newman et al. (1981) obtained the values of $C_{D1} = 2.02$ and $C_{D2} = 0.88$, and Elghobashi and Launder (1983) the values of $C_{D1} = 2.20$ and $C_{D2} = 0.80$ by trial and error through the analysis of homogeneous scalar turbulence using the heat flux equation model. Considering these related items, the values of $C_{D1} = 2.20$ and $C_{D2} = 0.80$, which are the same as those of Elghobashi and Launder (1983), are adopted in the present study. We take accordingly the value of 1.80 for C_{P1} in equation (27) to match the value of Elghobashi and Launder (1983).

The constant C_{P2} in equation (27), on the other hand, is assigned the value of 0.72 on the basis of the present computer optimization, because there has been no research on the behavior of ϵ_t in inhomogeneous shear flows.

The modeling of the functions f_P and f_D in the ϵ_t-equation is possible from the correspondence to f_1 and f_2 in the ϵ-equation. For simplicity, however, we put: $f_{P1} = f_{P2} = f_{D1} = f_{D2} = 1.0$. The model functions and constants proposed in the present study are summarized in Table 1.

4 Numerical Scheme

The numerics sometimes affect the results of the turbulence models both in the algorithm chosen and the number and distribution of grid points. Therefore, attention was paid to the numerics so as to make the model appraisal meaningful. The coordinate for regions of very large gradients should be expanded near the heat transfer surface. Thus, for internal flows, a transformation is introduced so that $\eta = (y/r_o)^{1/2}$. For external flows, the following nonuniform grid (Bradshaw et al., 1981) across the layer is employed:

$$y_j = \Delta y_1(K^j - 1)/(K - 1) \tag{36}$$

where Δy_1, the length of the first step, and K, the ratio of two successive steps, are chosen as 10^{-5} and 1.03, respectively. For both internal and external flow cases, 201 cross-stream grid points were used to obtain grid-independent solutions. The first grid point was normally located well into the viscous

Table 1 Constants and functions in the proposed two-equation model for scalar turbulence

C_λ	C_{P1}	C_{P2}	C_{D1}	C_{D2}	σ_h	σ_ϕ	f_λ	f_{P1}	f_{P2}	f_{D1}	f_{D2}
0.11	1.80	0.72	2.20	0.80	1.0	1.0	$\{1-\exp(-\frac{\sqrt{Pr}}{30.5}\frac{2}{C_f}St\ y^+)\}^2$	1.0	1.0	1.0	1.0

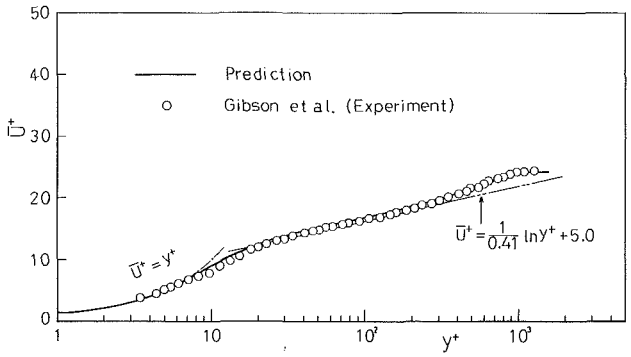

Fig. 1 Mean velocity profile in a flat-plate boundary layer

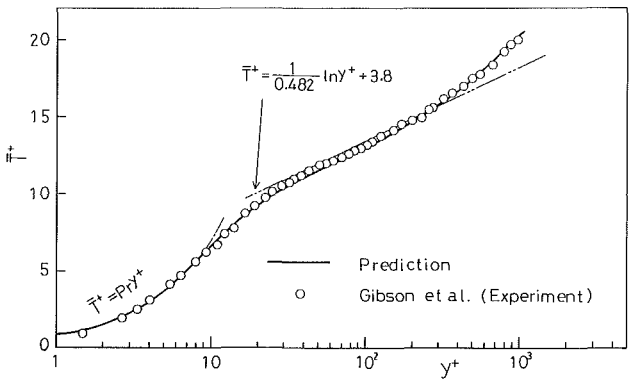

Fig. 2 Mean temperature profile in a flat-plate boundary layer

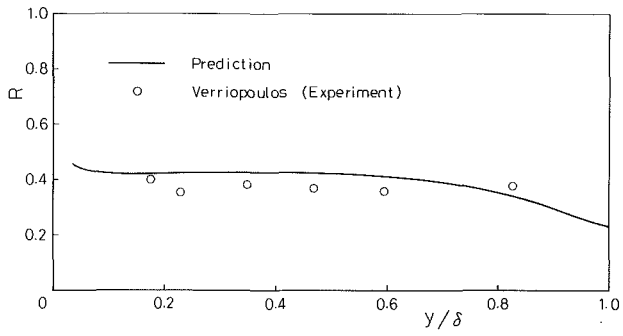

Fig. 3 Profile of thermal/mechanical time-scale ratio in a turbulent boundary layer

sublayer: e.g., less than $y^+ = 0.03$ in the case of internal flows. The numerical technique used is a well-tested Keller's Box method (Bradshaw et al., 1981). It is known that this method is unconditionally stable and the accuracy of a solution is high.

The boundary conditions are: $\bar{U} = k = \epsilon = 0$, $\bar{T} = \bar{T}_w$, and $\overline{t^2} = \epsilon_t = 0$ at the wall (nonslip and uniform wall temperature); $\partial\bar{U}/\partial y = \partial k/\partial y = \partial\epsilon/\partial y = \partial\bar{T}/\partial y = \partial\overline{t^2}/\partial y = \partial\epsilon_t/\partial y = 0$ at the axis for internal flows (symmetry); $\bar{U} = \bar{U}_e$, $\bar{T} = \bar{T}_e$, and $k = \epsilon = \overline{t^2} = \epsilon_t = 0$ at the free stream for external flows ($\bar{U}_e$ and $\bar{T}_e$ being prescribed from experiments).

The criterion for convergence is

$$\max|Y^{(i+1)} - Y^{(i)}|/\max|Y^{(i)}| < 10^{-5} \tag{37}$$

where $Y = \partial X/\partial y$ (X: $\bar{U}$, k, ϵ, $\bar{T}$, $\overline{t^2}$, and ϵ_t), and i denotes the number of iterations. The wall shear stress τ_w and wall heat flux q_w are obtained directly from the solutions as: $\tau_w/\rho = \nu(\partial\bar{U}/\partial y)_{y=0}$, and $q_w/\rho C_p = -\alpha(\partial\bar{T}/\partial y)_{y=0}$.

The local Nusselt number for internal flows, Nu(x), is regarded as a fully developed one when the following criterion is satisfied:

$$|\mathrm{Nu}(x_{i+1}) - \mathrm{Nu}(x_i)|/\mathrm{Nu}(x_i) < 10^{-5} \tag{38}$$

The computations were performed on a FACOM M-382 computer.

5 Discussion of Predictions With the Proposed Model

5.1 Flat-Plate Boundary Layer. To assess the performance of the present model for the prediction of external flows, the calculations of the flat-plate boundary layer are compared with the experimental data of Gibson et al. (1982), and Verriopoulos (1983). A flat plate had a uniform wall temperature, and air (Pr = 0.71) was used as a working fluid. The Reynolds number per unit length was $\bar{U}_e/\nu = 1.41 \times 10^6$ 1/m. The prediction of mean velocity profile in the turbulent boundary layer is presented in Fig. 1, compared with the experimental result (with streamwise location at $x = 971$ mm downstream from leading edge). The corresponding comparison of mean temperature profile is shown in Fig. 2. It is obvious from these figures that both mean velocity and mean temperature profiles are predicted almost perfectly with the proposed model. Whether or not a turbulence model is able to reproduce the "law of the wall" correctly is one important criterion to judge the quality of the model (Patel et al., 1981). As seen from Figs. 1 and 2, the present model satisfies this criterion.

The proposed model has k, ϵ, $\overline{t^2}$, and ϵ_t as the basic turbulence parameters. Thus the time-scale ratio $R = (\overline{t^2}/2\epsilon_t)/(k/\epsilon)$ may be obtained directly from these solutions. As shown in Fig. 3, the calculated time-scale ratio agrees well with actual measurements.

The predictions for the skin-friction coefficient $C_f = \tau_w/(\rho\bar{U}_e^2/2)$ and the Stanton number $\mathrm{St} = q_w/\rho C_p \bar{U}_e(\bar{T}_w - \bar{T}_e)$, are shown in Fig. 4. The calculated values are seen to be in almost complete agreement with the experimental values. It is known that the following Colburn's relation holds generally in the case that the hydrodynamic and thermal boundary layers develop simultaneously from the leading edge of a plate:

$$\mathrm{StPr}^{2/3} = C_f/2 \tag{39}$$

The present predictions of St and C_f satisfy this relation.

5.2 Thermal Entrance Region of Pipe. The thermal entrance region is taken up as a test case to examine the validity of the present model for the prediction of internal-flow heat transfer. In the thermal entrance region, where the Reynolds analogy or Colburn's relation does not hold, the eddy diffusivity for heat α_t changes in the flow direction along with

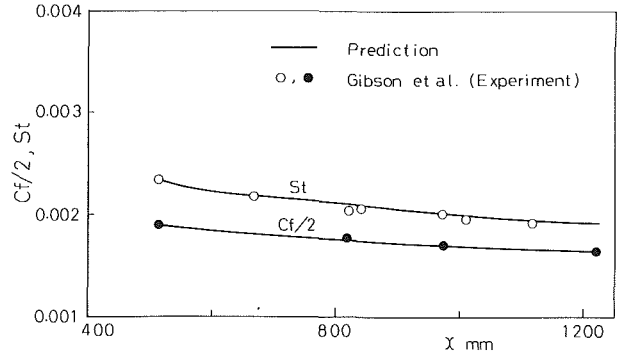

Fig. 4 Streamwise variation of skin-friction coefficient and Stanton number

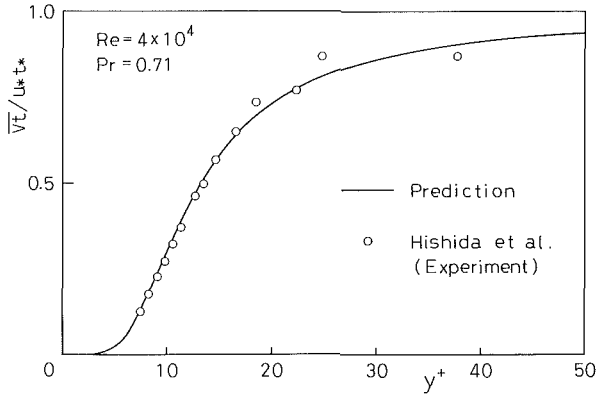

Fig. 7 Distribution of turbulent heat flux near the wall

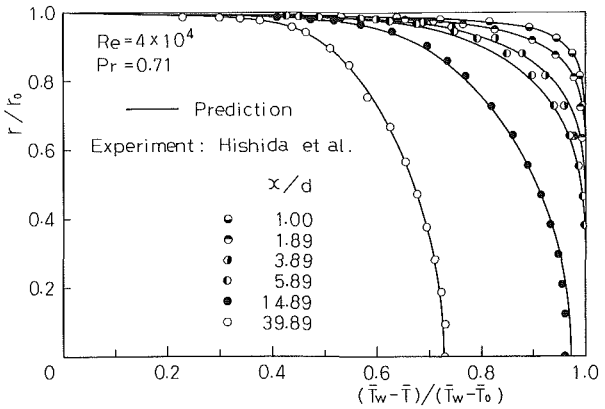

Fig. 5 Mean temperature profiles in the thermal entrance region of a pipe

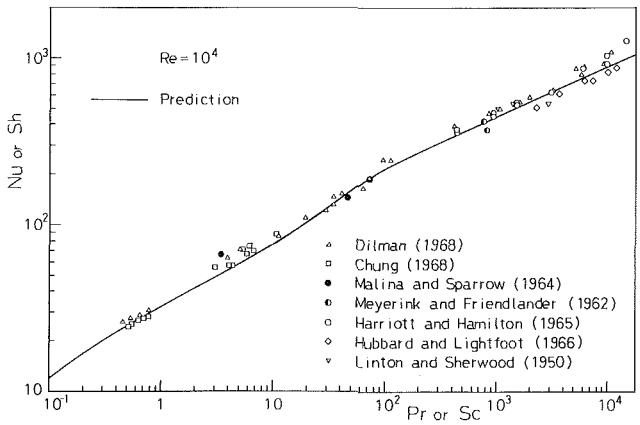

Fig. 8 Turbulent heat and mass transfer in various kinds of fluids

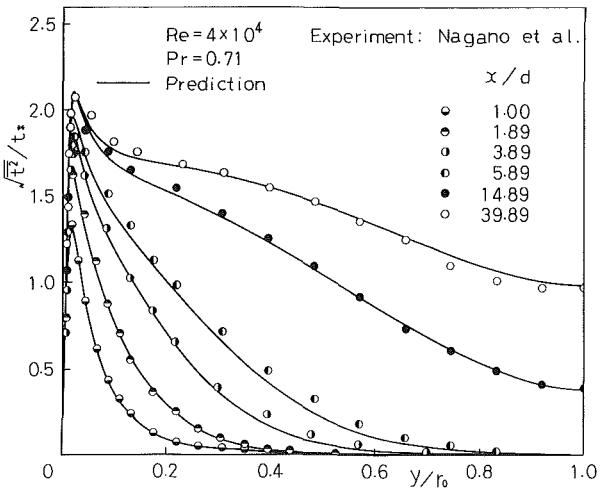

Fig. 6 Intensities of temperature fluctuations in the thermal entrance region of a pipe

the development of a thermal boundary layer, whereas the eddy viscosity ν_t remains unchanged. Accordingly, the turbulent Prandtl number, $\mathrm{Pr}_t = \nu_t/\alpha_t$, varies largely in the flow direction. As a result, it was almost impossible to analyze correctly the entry-region heat transfer with the conventional calculation method based on a prescribed Pr_t value. The present model makes it possible to analyze the temperature field where the analogy fails, because α_t is determined according to the state of the field by solving the transport equations for turbulence quantities. The predictions with the present model are compared with the experimental data of Hishida and Nagano (1978), Nagano et al. (1985), and Hishida et al. (1986) in Figs. 5–7.

The experiments were performed in an air flow in a uniformly heated pipe for a Reynolds number (based on bulk velocity and pipe diameter) of 40,000. In modeling, C_f and St in equation (19) are defined with the bulk velocity $\bar{U}_b$ and the bulk temperature $\bar{T}_b$ so that $C_f = \tau_w/(\rho \bar{U}_b^2/2)$ and $\mathrm{St} = q_w/\rho C_p \bar{U}_b(\bar{T}_w - \bar{T}_b)$. The experimental value at $x/d = 1.0$ (with x as the axial distance from the beginning of the heated section) was given as an initial profile of the calculation.

As shown in Fig. 5, the very fine results of predictions in agreement with experiments are obtained for the mean temperature profiles in the thermal entrance region. The proposed model reproduces accurately the succession of stages that occurs after the thermal boundary layer reaches the pipe centerline.

The predicted change of profiles of temperature-fluctuation intensities with the thermal boundary-layer development is shown in Fig. 6. Obviously, this too is predicted correctly with the proposed model.

The distribution of turbulent heat flux $\overline{vt}$ in the vicinity of the heat transfer surface cannot be predicted exactly, if the modeling of the eddy diffusivity for heat is inappropriate. The present prediction for $\overline{vt}$ in a fully developed region ($x/d = 39.89$) is shown in Fig. 7, compared with the experimental result of Hishida et al. (1986). Again, agreement between the two is very satisfactory when making allowance for the uncertainty that might be involved in the measurements.

5.3 Influence of Prandtl Number. As the last test case, the heat transfer in a pipe for various kinds of working fluids has been calculated to inspect the universality of the proposed model. The relative locational relations between the velocity

and temperature fields, as mentioned previously, depend upon the molecular Prandtl number. This physical action should be reflected in the turbulence model in order to assure its wide use. Figure 8 shows the prediction of turbulent heat transfer in fluids over a wide range of Prandtl number. Comparison with the experiments (Sideman and Pinczewski, 1975) substantiates that the proposed model can predict, with sufficient accuracy, the heat and mass transfer for various kinds of fluids.

6 Concluding Remarks

A closure for the energy equation to solve turbulent heat transfer problems has been developed at the two-equation level of turbulence modeling. The turbulent heat flux is expressed by using the eddy diffusivity for heat. However, in the proposed model, the prescription of a value for the "turbulent Prandtl number" is not needed, since the eddy diffusivity for heat can be determined from the solutions of transport equations for turbulence quantities. This is substantially different from conventional calculation methods for turbulent heat transfer. The validity of the present model has been verified by analyzing the temperature fields for both external and internal flows. Especially the thermal entry region is a very crucial test case, which almost all the existing models have been unable to analyze correctly. This is because the turbulent Prandtl number is too dependent upon the thermal boundary layer development for an adequate value to be prescribed. It is established that the present model is valid even for such a nonequilibrium field. Also the effects of the molecular Prandtl number on turbulent heat transfer are counted in the present model. Its effectiveness has been verified by the predictions of turbulent heat transfer in various kinds of working fluids ($Pr = 0.1$–10000).

The present model does not need any questionable empirical wall functions as boundary conditions, i.e., strict conditions for the velocity and temperature fields are imposed at a heat transfer surface. The low-Reynolds-number effects are considered in the model. Furthermore, governing equations are not complex, and thus the computing time required is usually very reasonable. From these standpoints, the proposed model may be regarded as a turbulence model of considerable accuracy, universality, and cost efficiency.

References

Béguier, C., Dekeyser, I., and Launder, B. E., 1978, "Ratio of Scalar and Velocity Dissipation Time Scales in Shear Flow Turbulence," *Phys. Fluids*, Vol. 21, pp. 307–310.

Bradshaw, P., Cebeci, T., and Whitelaw, J. H., 1981, *Engineering Calculation Methods for Turbulent Flow*, Academic Press, London.

Elghobashi, S. E., and Launder B. E., 1981, "Modelling the Dissipation Rate of Temperature Variance in a Thermal Mixing Layer," *Proceedings, 3rd Symposium on Turbulent Shear Flows*, University of California, Davis, pp. 15.13–15.17.

Elghobashi, S. E., and Launder, B. E., 1983, "Turbulent Time Scales and the Dissipation Rate of Temperature Variance in the Thermal Mixing Layer," *Phys. Fluids*, Vol. 26, pp. 2415–2419.

Hishida, M., and Nagano, Y., 1978, "Structure of Turbulent Temperature and Velocity Fluctuations in the Thermal Entrance Region of a Pipe," *Proceedings, 6th International Heat Transfer Conference*, Hemisphere, Washington, DC, Vol. 2, pp. 531–536.

Hishida, M., Nagano, Y., and Tagawa, M., 1986, "Transport Processes of Heat and Momentum in the Wall Region of Turbulent Pipe Flow," *Proceedings, 8th International Heat Transfer Conference*, C. L. Tien et al., eds., Hemisphere, Washington, DC, Vol. 3, pp. 925–930.

Gibson, M. M., Verriopoulos, C. A., and Nagano, Y., 1982, "Measurements in the Heated Turbulent Boundary Layer on a Mildly Curved Convex Surface," *Turbulent Shear Flows 3*, L. J. S. Bradbury et al., eds., Springer-Verlag, Berlin, pp. 80–89.

Launder, B. E., 1976, "Heat and Mass Transport," *Turbulence*, P. Bradshaw, ed., Springer-Verlag, Berlin, pp. 231–287.

Lumley, J. L., 1983, "Turbulence Modelling," ASME *Journal of Applied Mechanics*, Vol. 50, pp. 1097–1103.

Nagano, Y., and Hishida, M., 1985, "Production and Dissipation of Turbulent Velocity and Temperature Fluctuations in Fully Developed Pipe Flow," *Proceedings, 5th Symposium on Turbulent Shear Flows*, Cornell University, Ithaca, pp. 14.19–14.24.

Nagano, Y., Hishida, M., and Tagawa, M., 1985, "Turbulent Heat Transport Process in the Thermal Entrance Region of a Pipe," *Proceedings, 22nd National Heat Transfer Symposium of Japan*, pp. 232–234.

Nagano, Y., and Hishida, M., 1987, "Improved Form of the k–ϵ Model for Wall Turbulent Shear Flows," ASME *Journal of Fluids Engineering*, Vol. 109, pp. 156–160.

Newman, G. R., Launder, B. E., and Lumley, J. L., 1981, "Modelling the Behaviour of Homogeneous Scalar Turbulence," *Journal of Fluid Mechanics*, Vol. 111, pp. 217–232.

Patel, V. C., Rodi, W., and Scheuerer, G., 1981, "Evaluation of Turbulence Models for Near-Wall and Low-Reynolds Number Flows," *Proceedings, 3rd Symposium on Turbulent Shear Flows*, University of California, Davis, pp. 1.1–1.8.

Reynolds, A. J., 1975, "The Prediction of Turbulent Prandtl and Schmidt Numbers," *Int. J. Heat Mass Transfer*, Vol. 18, pp. 1055–1069.

Shih, T.-H., and Lumley, J. L., 1986, "Influence of Timescale Ratio on Scalar Flux Relaxation: Modelling Sirivat & Warhaft's Homogeneous Passive Scalar Fluctuations," *Journal of Fluid Mechanics*, Vol. 162, pp. 211–222.

Sideman, S., and Pinczewski, W. V., 1975, "Turbulent Heat and Mass Transfer at Interfaces: Transport Models and Mechanisms," *Topics in Transport Phenomena*, C. Gutfinger, ed., Hemisphere, Washington, DC, pp. 47–207.

Townsend, A. A., 1976, *The Structure of Turbulent Shear Flow*, 2nd ed., Cambridge University Press, Cambridge, pp. 352–360.

Verriopoulos, C. A., 1983, "Effects of Convex Surface Curvature on Heat Transfer in Turbulent Flow," Ph. D. Thesis, Imperial College, London.

Warhaft, Z., and Lumley, J. L., 1978, "An Experimental Study of the Decay of Temperature Fluctuations in Grid-Generated Turbulence," *Journal of Fluid Mechanics*, Vol. 88, pp. 659–684.

Three-Dimensional Unsteady Flow With Heat and Mass Transfer Over a Continuous Stretching Surface

K. N. Lakshmisha

S. Venkateswaran[1]

Department of Aerospace Engineering,
Indian Institute of Science,
Bangalore 560 012, India

G. Nath

Department of Applied Mathematics,
Indian Institute of Science,
Bangalore 560 012, India

A numerical solution of the unsteady boundary layer equations under similarity assumptions is obtained. The solution represents the three-dimensional unsteady fluid motion caused by the time-dependent stretching of a flat boundary. It has been shown that a self-similar solution exists when either the rate of stretching is decreasing with time or it is constant. Three different numerical techniques are applied and a comparison is made among them as well as with earlier results. Analysis is made for various situations like deceleration in stretching of the boundary, mass transfer at the surface, saddle and nodal point flows, and the effect of a magnetic field. Both the constant temperature and constant heat flux conditions at the wall have been studied.

1 Introduction

During many mechanical forming processes, such as extrusion, melt-spinning, etc., the extruded material issues through a die. The ambient fluid condition is stagnant but a flow is induced close to the material being extruded, due to the moving surface. In regions away from the slit the flow may be considered to be of boundary layer type, although this is not true just near the slit. Similar situations prevail during the manufacture of plastic and rubber sheets where it is often necessary to blow a gaseous medium through the not-yet-solidified material, and where the stretching force may be varying with time. Another example that belongs to the above class of problems is the cooling of a large metallic plate in a bath, which may be an electrolyte. In this case the fluid flow is induced due to shrinking of the plate. Glass blowing, continuous casting, and spinning of fibres also involve the flow due to a stretching surface. In all these cases, a study of the flow field and heat transfer can be of significant import since the quality of the final product depends to a large extent on the skin friction coefficient and the surface heat transfer rate. After a pioneering work by Sakiadis (1961a; 1961b) the flow field over a continuous stretching surface has drawn considerable attention and a good amount of literature has been generated on this problem (Griffin and Thorne, 1967; Vleggar, 1977; Gupta and Gupta, 1977; Abdelhafez, 1986). Most of these papers have presented analytic solutions by which only simple cases are treated. Recently, Wang (1984) has presented an exact similarity solution for the steady three-dimensional flow over the stretching flat surface. However, he has not considered the heat transfer aspect. Later, Dutta et al. (1985) analyzed the temperature field with a constant heat flux condition at the wall for steady two-dimensional flow using Crane's (1970) boundary layer solution. Practical situations cited above call for a complete analysis of the fluid dynamics that would be a three-dimensional time-dependent flow with heat and mass transfer at the boundary. It appears that an understanding of the effect of magnetic field on the temperature field is useful during the cooling process in the presence of an electrolytic bath, as mentioned earlier. A problem of this kind would involve considerable mathematical difficulties in numerically solving the governing equations, let alone obtaining a closed-form solution, as pointed out by Wang (1984). The present paper aims at a comprehensive study of the problem, taking into consideration the various complexities of the process.

Three different numerical techniques have been applied and a comparison is made among them and also with the results of Wang. The solutions show excellent agreement with each other and thus confidence in the results is established. Transient behavior is studied in the form of time-dependent stretching of the boundary. It has been shown by asymptotic analysis that a similarity solution is admissible when either the rate of stretching is decreasing or it is constant with respect to time. Thus, four independent variables x, y, z, t are collapsed into a single independent similarity variable η, and a two-point boundary value problem is formulated. It is found that the shooting method and quasilinearization are extremely sensitive to the initial guesses in cases of unlike stretching ($c<0$) and the solution does not converge for $c<-0.25$. Hence the method of parametric differentiation is applied to these cases. The analysis is made over the complete range of stretching ratios (including negative values, which have not been considered by previous workers). The effect of suction and blowing at the surface, and the effect of a magnetic field over the fluid, are included. Both the constant wall temperature (CWT) and constant heat flux (CHF) conditions at the surface are studied for a wide range of Prandtl numbers.

It may be remarked in passing that the current results for the steady case ($\lambda=0$) can be regarded as the stretching counterparts of the exact stagnation point solutions of Howarth (1951), Davey (1961), and Libby (1967), and for the unsteady case ($\lambda>0$) they are the stretching counterparts of the results of Teipel (1979).

2 Description of the Problem

We consider the laminar motion of a viscous, incompressible, electrically conducting fluid caused by the stretching of an infinite flat surface in two lateral directions x and y (see Fig. 1). The surface is assumed to be highly elastic and porous and is stretched by the action of uniform but increasing forces in the same or in opposite directions. The rate of stretching a and b in the two directions varies inversely as a linear function of time.

The fluid is assumed to have constant properties. The fluid is at rest at infinity and the no-slip condition is imposed at the stretching surface, where suction or injection can be applied. The temperature of the quiescent fluid is kept constant. In the constant wall temperature (CWT) case the surface

[1] Currently at the Institute of Hydraulic Research, The University of Iowa, Iowa City, IA 52242.

Contributed by the Heat Transfer Division for publication in the JOURNAL OF HEAT TRANSFER. Manuscript received by the Heat Transfer Division February 10, 1987. Keywords: Mass Transfer, Moving Boundaries, Transient and Unsteady Heat Transfer.

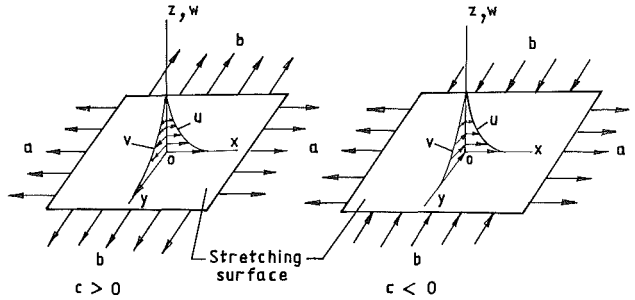

Fig. 1 The coordinate system and forces applied

temperature is kept uniform while in the constant heat flux (CHF) case the temperature gradient in the z direction at the surface is kept uniform. A magnetic field B is applied in the z direction. It is assumed that the magnetic Reynolds number is small. Hence, the induced magnetic field is small in comparison to the applied field and is therefore neglected.

3 Governing Equations and Problem Formulation

With the usual boundary layer approximations the governing equations for the situation described in the previous section are:

$$\text{continuity: } u_x + v_y + w_z = 0 \tag{1}$$

$$x\text{ momentum: } u_t + uu_x + vu_y + wu_z = \nu u_{zz} - \sigma B^2 u/\rho \tag{2}$$

$$y\text{ momentum: } v_t + uv_x + vv_y + wv_z = \nu v_{zz} - \sigma B^2 v/\rho \tag{3}$$

$$\text{energy: } T_t + uT_x + vT_y + wT_z = \alpha T_{zz} \tag{4}$$

The associated initial and boundary conditions are given by

$$u(x, y, z, 0) = u_i, \quad v(x, y, z, 0) = v_i,$$

$$w(x, y, z, 0) = w_i, \quad T(x, y, z, 0) = T_i \tag{5}$$

$$u(x, y, 0, t) = u_w, \quad v(x, y, 0, t) = v_w, \quad w(x, y, 0, t) = w_w \tag{6}$$

$$T(x, y, 0, t) = T_w \quad \text{for CWT}$$

$$-kT_z(x, y, 0, t) = q_w \quad \text{for CHF} \tag{7}$$

$$u(x, y, \infty, t) = v(x, y, \infty, t) = w(x, y, \infty, t) = 0,$$

$$T(x, y, \infty, t) = T_\infty \tag{8}$$

We apply the following similarity transformations:

$$\eta = z(a/\nu)^{1/2}(1-\lambda t^*)^{-1/2}, \quad \lambda t^* < 1, \quad c = b/a, \quad t^* = at$$

$$u = ax(1-\lambda t^*)^{-1} f'(\eta)$$

$$v = ay(1-\lambda t^*)^{-1} s'(\eta)$$

$$w = -(a\nu)^{1/2}(1-\lambda t^*)^{-1/2}(f+s) \tag{9}$$

$$(T-T_\infty)/(T_w-T_\infty) = g(\eta) \quad \text{for CWT}$$

$$T - T_\infty = (q_w/k)(\nu/a)^{1/2}(1-\lambda t^*)^{1/2} g(\eta) \quad \text{for CHF}$$

$$B = B_o(1-\lambda t^*)^{-1/2}, \quad M = H_a^2/\mathrm{Re}_x, \quad H_a^2 = \sigma B_o^2 x^2/\mu$$

$$\mathrm{Re}_x = ax^2/\nu, \quad \mathrm{Pr} = \nu/\alpha$$

to equations (1)–(8) and find that equation (1) is satisifed identically. Equations (2)–(4) reduce on substitution to

$$f''' + (f+s)f'' - (f')^2 - Mf' - \lambda(f' + f''\eta/2) = 0 \tag{10}$$

$$s''' + (f+s)s'' - (s')^2 - Ms' - \lambda(s' + s''\eta/2) = 0 \tag{11}$$

$$g'' + (f+s-\eta\lambda/2)g'\,\mathrm{Pr} = 0 \quad \text{for CWT} \tag{12a}$$

$$g'' + (f+s-\eta\lambda/2)g'\,\mathrm{Pr} + \lambda g\mathrm{Pr}/2 = 0 \quad \text{for CHF} \tag{12b}$$

The conditions at the surface ($\eta = 0$) and in the quiescent interior ($\eta \to \infty$) reduce to

$$\eta = 0: \quad f = f_w, \; s = 0, \quad f' = 1, \; s' = c$$

$$g = 1 \text{ for CWT}$$

$$g' = -1 \text{ for CHF} \tag{13}$$

$$\eta \to \infty: \quad f' = s' = g = 0 \tag{14}$$

The factor f_w represents the mass transfer at the surface with the following relationship:

$$f_w = -w_w(1-\lambda t^*)^{1/2}/(a\nu)^{1/2} \tag{15}$$

f_w will be a constant if $w_w \propto (1-\lambda t^*)^{-1/2}$ ($f_w < 0$ for blowing and $f_w > 0$ for suction at the surface).

The stretching ratio c can have values between -1 and $+1$. When $c = 1$, the problem is axisymmetric and when $c = 0$, we have a two-dimensional case. c takes negative values when the natures of the forces in the x and y axes are opposite to each other. In this situation ($c < 0$) we have a saddle point flow while for $c > 0$ it is a nodal point flow. For $c < -1$, the equations are insoluble (Davey, 1961) while for $c > +1$, we have to simply interchange the x and y axes.

Nomenclature

a, b = stretching rate in x and y directions
B, B_o = magnetic fields
c = stretching ratio
C_1, C_2 = constants
f, s, g = similarity functions
F, S, G, H = asymptotic functions
h = heat transfer coefficient
H_a = magnetic Reynolds number
k = thermal conductivity
M = nondimensional magnetic force
P = parabolic cylinder function
Pr = Prandtl number
q = heat flux
Re = Reynolds number based on distance x
t = time
t^* = nondimensional time
T = temperature
u, v, w = velocity components in x, y, and z directions
x, y = rectangular coordinates parallel to the surface
z = coordinate perpendicular to the surface
α = thermal diffusivity
β = constant
η = independent similarity coordinate
σ = electrical conductivity
μ = dynamic viscosity
ρ = fluid density
ν = kinematic viscosity
λ = parameter associated with unsteadiness
θ = nondimensional temperature
τ_{zx}, τ_{zy} = shear stresses on $x-y$ plane in x and y directions, respectively

Subscripts

i = initial conditions at $t = 0$
w = wall condition
x, y, z, t = differentiation with respect to x, y, z, and t
∞ = conditions at the interior of the fluid

Superscripts

$'$ = denotes differentiation with respect to η

For $t^*=0$ ($\lambda=0$) equations (10)–(12) reduce to those of steady flow and for $t^*>0$ ($\lambda\neq 0$) it applies to unsteady flow. Therefore, λ is a measure of unsteadiness, and $\lambda<0$ means the stretching rate decreases with time while for $\lambda>0$ it increases with time.

Expression for wall shear stresses:

$$\tau_{zx(z=0)} = -\mu ax(1-\lambda t^*)^{-3/2}(a/\nu)^{1/2} f''(0) \tag{16}$$

$$\tau_{zy(z=0)} = -\mu ay(1-\lambda t^*)^{-3/2}(a/\nu)^{1/2} s''(0) \tag{17}$$

Expression for heat transfer coefficient:

$$h = -k(a/\nu)^{1/2}(1-\lambda t^*)^{-1/2} g'(0) \text{ for CWT} \tag{18}$$

Evidently, $f''(0)$ and $s''(0)$ are measures of wall shear stresses in the x and y directions, respectively. $g'(0)$ represents the heat transfer coefficient for CWT and $g(0)$ is wall temperature for CHF.

3.1 Asymptotic Solution. In order to ascertain the admissible range of values for λ we consider the asymptotic behavior of equations (10)–(12), i.e., the behavior of the equations for large η. Consequently, we set

$$f = C_1 + F, \quad s = C_2 + S, \quad g = G, \quad \beta = C_1 + C_2 \tag{19}$$

where C_1 and C_2 are constants and F, S, and G are small. Also from the boundary conditions (14), we get

$$f \to C_1, \quad s \to C_2, \quad F \to 0, \quad S \to 0, \quad G \to 0 \text{ as } \eta \to \infty \tag{20}$$

Substituting for f, s, and g in equations (10)–(12) and linearizing we get

$$F''' + (\beta - \lambda\eta/2)F'' - (M+\lambda)F' = 0 \tag{21}$$

$$S''' + (\beta - \lambda\eta/2)S'' - (M+\lambda)S' = 0 \tag{22}$$

$$G'' + \Pr(\beta - \lambda\eta/2)G' = 0 \text{ for CWT} \tag{23}$$

$$G'' + \Pr(\beta - \lambda\eta/2)G' + (\lambda \Pr/2)G = 0 \quad \text{for CHF} \tag{24}$$

Equations (21) and (22) are identical and equation (24) is also similar to (21) or (22). Hence we consider equations (21) and (23). Applying the transformation

$$F' = \exp[-(\beta\eta - \lambda\eta^2/4)/2]H \tag{25}$$

to equation (21), we get

$$H'' - [(3\lambda/4 + M) + (\beta - \lambda\eta/2)^2/4]H = 0 \tag{26a}$$

$$H(\infty) \to 0 \tag{26b}$$

Equation (26*a*) is a Weber-type equation whose solution for large η satisfying the boundary condition (26*b*) can be expressed in terms of parabolic cylinder functions as (Whittaker and Watson, 1965)

$$H = \exp[-(\beta - \lambda\eta/2)^2/4](\beta - \lambda\eta/2)^{-(3/4\lambda + M + 1/2)} P_1(\eta) \tag{27}$$

From equations (25) and (27) we get

$$F' = \exp(-[\beta^2 + \beta(2-\lambda)\eta - \lambda(2-\lambda)\eta^2/4]/4) (\beta - \lambda\eta/2)^{-(3/4\lambda + M + 1/2)} P_1(\eta) \tag{28}$$

where

$$P_1(\eta) = 1 - 2^{-1}(3/4\lambda + M + 1/2)(3/4\lambda + M + 3/2)(\beta - \lambda\eta/2)^{-2} + 0(\beta - \lambda\eta/2)^{-4} + \ldots \tag{29}$$

The asymptotic solution of equation (22) is also given by equation (28). The asymptotic solution of equation (24) is similar to that of (21) or (22) and can be represented by

$$G = \exp(-[\beta^2 \Pr^2 + \beta \Pr(2 - \lambda \Pr)\eta - \lambda \Pr(2 - \lambda \Pr)\eta^2/4]/4]) \cdot [\Pr(\beta - \lambda\eta/2)]^{(3/4\lambda \Pr - 1/2)} P_2(\mu) \tag{30}$$

where

$$P_2(\eta) = 1 - 2^{-1}(3/4\lambda \Pr - 1/2)(3/4\lambda \Pr - 3/2) \cdot [\Pr(\beta - \lambda\eta/2)]^{-2} + 0[\Pr(\beta - \lambda\eta/2)]^{-4} \ldots \tag{31}$$

Also, the asymptotic solution of equation (23) is given by

$$G = -A_1 \int_\eta^\infty \exp\,[-\Pr(\beta\eta - \lambda\eta^2/4)]d\eta \tag{32}$$

where A_1 is a constant. It is evident from equations (28), (30), and (32) that exponential decay is possible if and only if $\lambda \leq 0$ (i.e., steady case and decelerating case). For the accelerating case ($\lambda > 0$), F, S, and G diverge. Therefore, similarity solutions are not possible for $\lambda > 0$. Consequently, we have considered only the cases when $\lambda \leq 0$. Results similar to these above have been obtained by Watson and Wang (1979) for the rotating disk problem.

4 Method of Solution

Equations (10)–(12) together with boundary conditions (13)–(14) form a nonlinear two-point boundary value problem, which has been solved by three different numerical methods. In this section we briefly describe these methods, although a complete description may be obtained from the references.

4.1 Shooting Method (Nachtsheim, 1965): The three missing initial slopes $f''(0)$, $s''(0)$, and $g'(0)$ were assumed arbitrarily and the integration was carried out from the wall to the interior ($\eta_\infty \sim 10$ typically) using an Adams-Moulton predictor-corrector algorithm. These missing slopes were given a correction before the next iteration based on the Newton method using a least-square error criterion of 10^{-6} with respect to the outer ambient fluid conditions.The iterations were stopped when these corrections themselves were less than 10^{-6}. A uniform step size of $\Delta\eta = 0.01$ was found to be optimum and a typical case took 25.5 s on a DEC 1090 system.

4.2 Quasilinearization (Radbill, 1964): The nonlinear equations (10)–(12) were expanded in Taylor series about a current iterative solution and terms with second order and higher derivatives were omitted, resulting in equations linear with respect to the next iterative solution. The well-known initial value method (Radbill and McCue, 1970) of splitting the solutions into complementary and particular solutions posed difficulties in matrix inversion for large values of η since all conditions defined there go to zero. Therefore the finite difference method was applied taking a uniform mesh size of $\Delta\eta = 0.01$. Starting from arbitrary initial profiles, the solutions rapidly converged for the CWT case (about 20 iterations, 3.5 s) while for the CHF case convergence was very slow (about 1.5 to 2.0 min). However, a proper η_∞ must be selected to satisfy the asymptotic conditions as $\eta \to \infty$.

4.3 Parameter Differentiation (Na, 1979): Equations (10)–(14) were differentiated with respect to the parameter c and the resulting linear boundary value problem was solved iteratively by finite differencing. The solutions of these equations give the rate of change of the functions f, s, g, etc., with respect to c at every η (i.e., $\partial f/\partial c$, $\partial s/\partial c$, etc.). Thus, starting from a correct initial solution at $c=0$ (which could be obtained from quasilinearization) the solutions were marched in the c direction taking a step size of Δc as follows:

$$f(\eta)|_{c+\Delta c} = f(\eta)|_c + \Delta c(\partial f/\partial c(\eta)|_c), \text{ etc.} \tag{33}$$

Repeating this procedure, solutions can be obtained for the complete range of c at every step finding $\partial f/\partial c$, $\partial s/\partial c$, $\partial g/\partial c$, etc. In the present case, a step size of $\Delta c = 0.001$ and $\Delta\eta = 0.01$ was found suitable but the computational time required to march from $c=0$ to $c=-1$ was found to be large (35 min). It may be noted that by treating λ as a parameter instead of c we can study the transient behavior of the system.

Table 1 Comparison of various results ($Pr=0.7$, $f_w=M=\lambda=0$, $\Delta\eta=0.01$)

c		Wang (1984)	Present: Shooting method	Present: Quasilinearization	Present: Parametric Differentiation ($c_o=0$, $\Delta c=0.001$)
	f"(0)	-1.000000	-1.0000000	-0.9999742	
0.00	s"(0)	0.000000	-0.0000000	0.0000000	
	g'(0)	-	-0.4544600	-0.4544605	
	f"(0)	-1.048813	-1.0488130	-1.0488033	-1.0487991
0.25	s"(0)	-0.194564	-0.1945640	-0.1945756	-0.1944022
	g'(0)	-	-0.5210561	-0.5211126	-0.5211050
	f"(0)	-1.093097	-1.0930960	-1.0931049	-1.0930968
0.50	s"(0)	-0.465205	-0.4652053	-0.4652213	-0.4649367
	g'(0)	-	-0.5757608	-0.5758181	-0.5758263
	f"(0)	-1.134485	-1.1344860	-1.1344954	-1.1345014
0.75	s"(0)	-0.794622	-0.7946185	-0.7946398	-0.7942636
	g'(0)	-	-0.6237759	-0.6238348	-0.6238532
	f"(0)	-1.173720	-1.1737230	-1.1737406	-1.1737505
1.00	s"(0)	-1.173720	-1.1737230	-1.1737406	-1.1732877
	g'(0)	-	-0.6674502	-0.6673411	-0.6673682

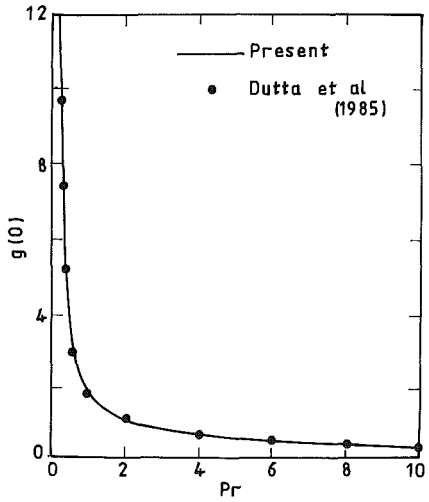

Fig. 2 Dimensionless wall temperature variation with Pr ($c=f_w=\lambda=M=0$)

5 Results and Discussion

A comparison is made among the three different methods as well as with the results of Wang (1984) (see Table 1) and of Dutta et al. (1985) (see Fig 2). The wall shear stresses, heat transfer coefficient, and wall temperature show very close agreement. Consequently, the effect of various parameters on the solutions was studied.

5.1 Effect of Stretching Ratio c. Heretofore only the positive values (0 to 1) have been considered by the previous workers, and in this range solutions were obtained without any problem by both the shooting method and quasilinearization. However, in many instances the two lateral forces acting on the sheet are of opposite kind, as for example when a polymer sheet issues from a die there is contraction in lateral direction while a tensile force acts in longitudinal direction. In an attempt to understand the flow pattern in such a case, negative values for the stretching ratio were given. It was found that both the shooting method and quasilinearization were extremely sensitive to the initial guesses for $c<0$, and for $c<-0.25$ convergence could not be obtained. Therefore for such cases the parametric differentiation was applied. Since this is not a self-starting method, initial solutions at $c_o=0$ were obtained from quasilinearization. To validate the computer program, initially solutions were marched for $c>0$ and the results agreed very well with those obtained by other methods (see Table 1). A step size of $\Delta c=0.001$ was required to obtain the initial slopes accurate up to the first four decimal places. Thus confidence in the results for $c<0$ was established.

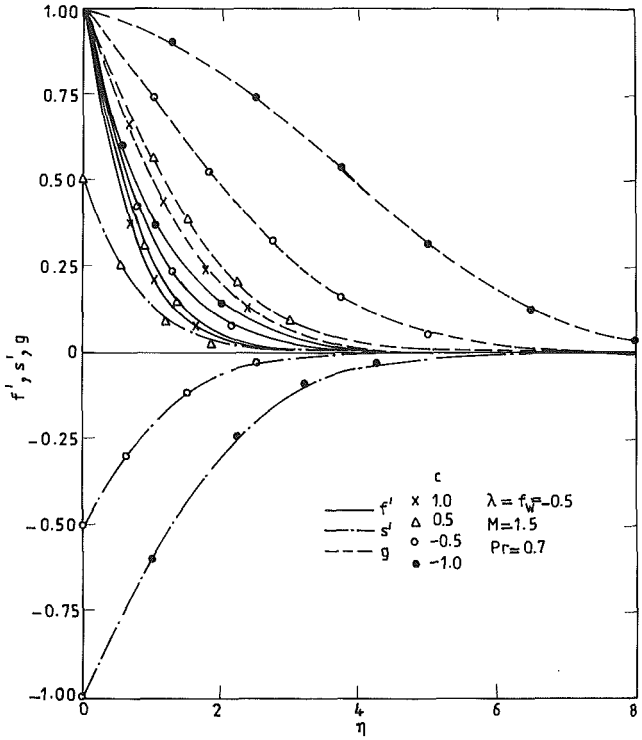

Fig. 3 Effect of stretching ratio on velocity and temperature profiles ($f_w=\lambda=-0.5$, $M=1.5$, $Pr=0.7$)

It may be remarked here that the difficulties experienced with negative values of c are not surprising. Davey (1961) has shown that, in the case of a three-dimensional incompressible flow at a stagnation point, the boundary layer equations admit nonunique solutions when $-1<c<0$. He has also found that part of the boundary layer begins to show a reversal of flow at $c=-0.4294$ for that problem. Indeed, as c is increased further in the negative direction, the tendency for the flow reversal increases due to the highly adverse pressure gradient, and there is an increased inflow in the y direction. Further research in this direction by Libby (1967) has asserted the nonunique nature of the solutions for $-1<c<0$ in the case of a compressible boundary layer. In the current problem, perhaps the solutions for $-1<c<-0.25$ latch onto a singular solution when the shooting method and quasilinearization are applied. This probably is the reason that the solutions for $c<-0.25$ do not converge when either the shooting method or quasilinearization is used. Since the method of parametric differentiation is essentially a continuation process, the solutions are marched in the direction of a particular branch and a converged solution can be obtained.

Figure 3 shows some representative velocity and temperature profiles for different stretching ratios. Also, it can be seen from Figs. 4 and 5 that increasing c on the positive

Table 2 Comparison of the techniques for unsteady flow ($c = f_w = 0.5$, $Pr = 0.7$, $\Delta\eta = 0.01$)

λ		Quasilinearization		Parametric differentiation ($\Delta\lambda = 0.025$)	
		M = 0	M = 1.0	M = 0	M = 1.0
0.00	f"(0)	-1.3791017	-1.7529570		
	s"(0)	-0.6175051	-0.8224046		
	g'(0)	-0.8039143	-0.7535454		
-0.25	f"(0)	-1.3119016	-1.6973704	-1.3119180	-1.6973995
	s"(0)	-0.5808346	-0.7929573	-0.5808372	-0.7929761
	g'(0)	-0.8702118	-0.8274119	-0.8708332	-0.8282535
-0.50	f"(0)	-1.2445297	-1.6411696	-1.2445405	-1.6412273
	s"(0)	-0.5440580	-0.7631492	-0.5440649	-0.7631876
	g'(0)	-0.9262852	-0.8878101	-0.9271618	-0.8889399
-0.75	f"(0)	-1.1769641	-1.5844207	-1.1769913	-1.5845049
	s"(0)	-0.5071910	-0.7330250	-0.5072011	-0.7330760
	g'(0)	-0.9761054	-0.9406090	-0.9771165	-0.9418685
-1.00	f"(0)	-1.1092514	-1.5271802	-1.1092886	-1.5272886
	s"(0)	-0.4702408	-0.7026060	-0.4702548	-0.7026711
	g'(0)	-1.0215186	-0.9882737	-1.0226082	-0.9895902

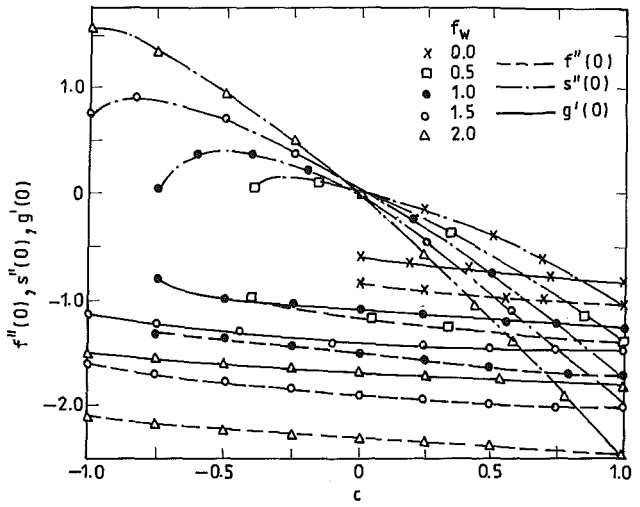

Fig. 4 Effect of mass transfer on initial slopes at different stretching ratios ($\lambda = -0.5$, $Pr = 0.7$, $M = 0$)

side increases $f''(0)$ and $g'(0)$ while increasing c on the negative side has the opposite effect. However, $s''(0)$ increases when c is increased in either direction from zero.

5.2 Effect of Unsteadiness Parameter. Since most of the practical situations involve nonuniform stretching with respect to time, transient behavior of the system is interesting and important. It has been shown in section 3.0 how a constant parameter λ may be introduced as a measure of unsteadiness in the stretching action and also that only for $\lambda \leq 0$ is self-similarity exhibited. Table 2 compares the results between two methods for different λ. It is evident from Fig. 6 that the wall shear stresses decrease with increase on λ on the negative side but the heat transfer coefficient increases. Figure 7 shows velocity and temperature profiles for different λ. We find that the temperature profile is affected to a greater extent compared to velocity profiles by variation of λ.

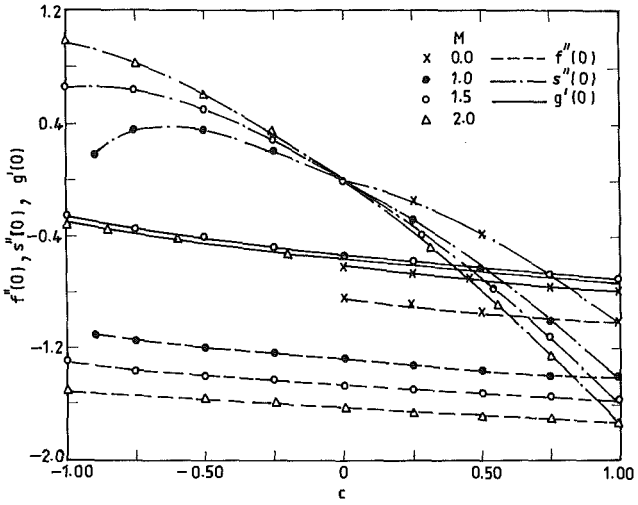

Fig. 5 Effect of magnetic force on initial slopes at different stretching ratios ($f_w = 0$, $\lambda = -0.5$, $Pr = 0.7$)

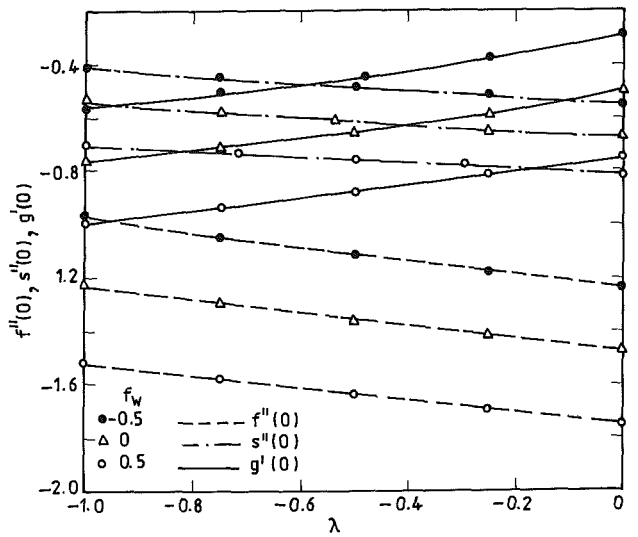

Fig. 6 Effect of mass transfer on initial slopes at different λ ($c = 0.5$, $Pr = 0.7$, $M = 1.0$)

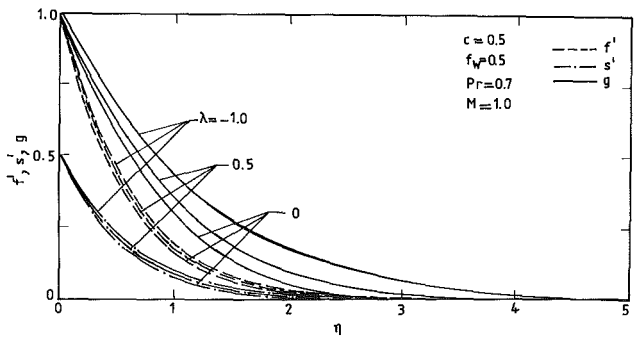

Fig.7 Effect of unsteadiness on velocity and temperature profiles ($c = f_w = 0.5$, $Pr = 0.7$, $M = 1.0$)

5.3 Effect of Magnetic Field M and Mass Transfer f_w. In general, suction ($f_w > 0$) and a magnetic field ($M > 0$) show the same effect on the wall shear stresses (see Figs. 4 and 5). Suction and magnetic field both increase $s''(0)$. Suction increases $f''(0)$ and $g'(0)$ while magnetic force increases $f''(0)$ but decreases $g'(0)$. It was found that more suction and magnetic field are needed to obtain the converged solutions at a greater negative c. Injection ($f_w < 0$) reduces the wall shear stresses

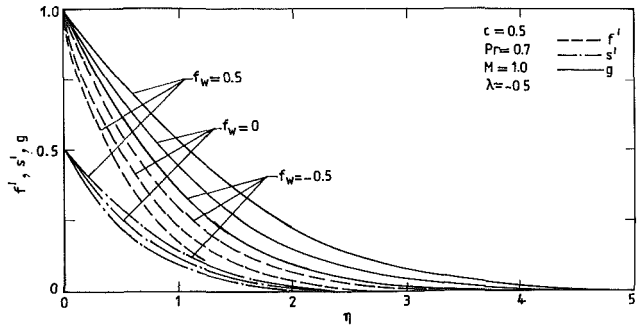

Fig. 8 Effect of mass transfer on velocity and temperature profiles ($c = 0.5$, $\lambda = -0.5$, $Pr = 0.7$, $M = 1.0$)

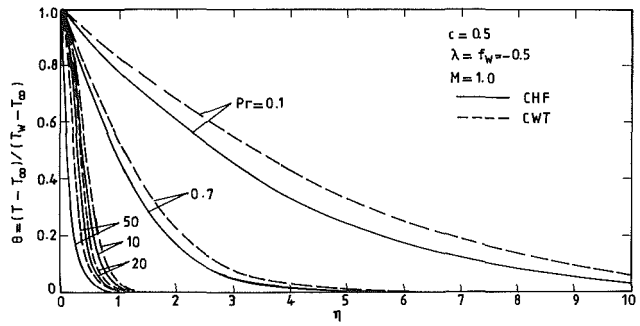

Fig. 9 Effect of Prandtl number on temperature profiles ($c = 0.5$, $\lambda = f_w = -0.5$, $M = 1.0$)

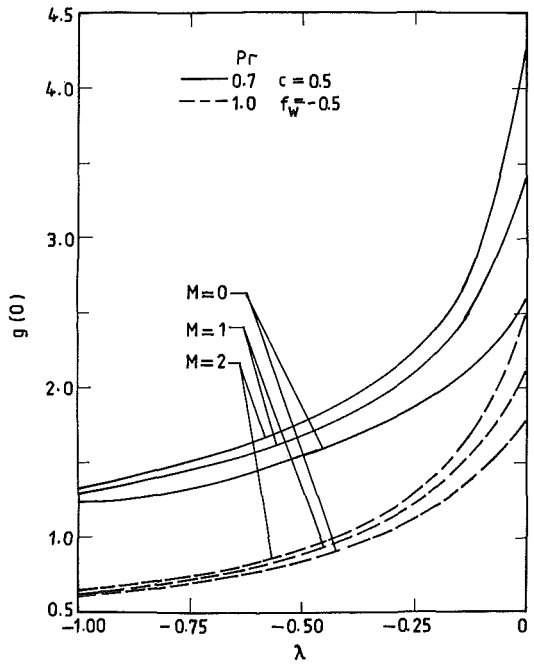

Fig. 10 Effect of λ and M on the wall temperature ($c = 0.5$, $f_w = -0.5$)

and heat transfer (see Fig 6). Velocity and temperature profiles for different f_w are shown in Fig. 8. It was found that the increase in M has a smaller efffect on temperature distribution, although it reduces the viscous boundary layer thickness.

5.4 Effect of CWT and CHF Conditions. Figure 9 shows the temperature distribution obtained for different Prandtl numbers. Temperature at any point in the flow field is found to be smaller for the CHF case as compared to the CWT case. Wall temperature (for CHF) decreases rapidly with increasing Prandtl number up to about $Pr = 1.5$ to 2, and then remains more or less constant. Similar behavior has been reported by Dutta et al. (1985) for $\lambda = M = c = 0$. It can be seen from Fig. 10 that decreasing the magnetic field or increasing the Prandtl number has a cooling effect on the surface.

6 Conclusions

Both physically and numerically the flow induced by a two-dimensionally stretching membrane behaves differently for positive and negative values of the stretching ratio, and for the latter case the usual numerical techniques do not work and parametric differentiation has to be applied. Similarity solutions can be obtained if the stretching force decreases linearly or remains constant with respect to time. Both suction and magnetic field are found to be important in obtaining a convergent solution in the saddle point region. Magnetic force and the unsteadiness factor exhibit a direct influence on the wall temperature when a constant heat flux is applied at the surface.

References

Abdelhafez, T. A., 1986, "Laminar Thermal Boundary Layer on a Continuous Accelerated Sheet Extruded in an Ambient Fluid," Acta Mechanica, Vol. 64, pp. 207–213.

Crane, L. J., 1970, "Flow Past a Stretching Plate," *Zeitschrift für angewandte Mathematic und Physik*, Vol. 21, pp. 645–647.

Davey, A., 1961, "Boundary Layer Flow at a Saddle Point of Attachment," *Journal of Fluid Mechanics*, Vol. 10, Part 4, pp. 593–610.

Dutta, B. K., Roy, P., and Gupta, A. S., 1985, "Temperature Field in Flow Over a Stretching Sheet With Uniform Heat Flux," *International Communications in Heat and Mass Transfer*. Vol. 12, No. 1, pp. 89–94.

Griffin, J. F., and Thorne, J. L., 1967, "On Thermal Boundary Layer Growth on Continuous Moving Belts," *AIChE Journal*, Vol. 13, No. 6, pp. 1210–1211.

Gupta, P. S., and Gupta, A. S., 1977, "Heat and Mass Transfer on a Stretching Sheet Wth Suction and Blowing," *Canadian Journal of Chemical Engineering*, Vol. 55, pp. 744–746.

Howarth, L., 1951, "The Boundary Layer on Three-Dimensional Flow, Part 2: The Flow Near a Stagnation Point," *Philosophical Magazine*, Series 7, Vol. 42, No. 335, pp. 1433–1440.

Libby, P. A., 1967, "Heat and Mass Transfer at a General Three-Dimensional Stagnation Point," *AIAA Journal*, Vol. 5, pp. 507–519.

Na, T. Y., 1979, *Compuational Methods in Engineering Boundary Value Problems*, Academic Press, New York.

Nachtsheim, P. R., and Swigert, P., 1965, "Satisfaction of Asymptotic Boundary Conditions in Numerical Solution of Systems of Nonlinear Equations of Boundary Layer Type," NASA Technical Note D 3004.

Radbill, J. R., 1964, "Applications of Quasilinearization to Boundary Layer Equations," *AIAA Journal*, Vol. 2, pp. 1860–1862.

Radbill, J. R., and McCue, G. A., 1970, *Quasilinearization and Nonlinear Problems in Fluid and Orbital Mechanics*, Elsevier, New York, pp. 24–27.

Sakiadis, B. C., 1961a, "Boundary Layer Behavior of Continuous Solid Surfaces: I. Boundary-Layer Equations for Two-Dimensional and Axisymmetric Flow," *AIChE Journal*, Vol. 7, No. 1, pp. 26–28.

Sakiadis, B. C., 1961b, "Boundary Layer Behavior on Continuous Solid Surfaces: II, The Boundary Layer on Continuous Flat Surface," *AIChE Journal*, Vol. 7, No. 2, pp. 221–225.

Teipel, I., 1979, "Heat Transfer in Unsteady Laminar Boundary Layers at an Incompressible Three-Dimensional Stagnation Flow," *Mechanics Research Communciations*, Vol. 6, pp. 27–32.

Vleggar, J., 1977, "Laminar Boundary Layer Behavior on Continuous Accelerating Surfaces," *Chemical Engineering Science*, Vol. 32, pp. 1517–1525.

Wang, C. Y., 1984, "The Three-Dimensional Flow Due to a Stretching Flat Surface," *The Physics of Fluids*, Vol. 27, pp. 1915–1917.

Watson, L. T., and Wang, C. Y., 1979, "Deceleration of a Rotating Disk in a Viscous Fluid," *The Physics of Fluids*, Vol. 22, pp. 2267–2269.

Whittaker, E. T., and Watson, G. N., 1965, *Modern Analysis*, Cambridge University Press, London, pp. 347–349.

Buoyancy Effects on Forced Convection Heat Transfer in the Transition Regime of a Horizontal Boundary Layer Heated From Below

K. C. Cheng
T. Obata[1]
R. R. Gilpin

Department of Mechanical Engineering,
The University of Alberta,
Edmonton, Alberta, Canada T6G 2G8

Convective instability and buoyancy effects on forced convection heat transfer in horizontal boundary layers heated from below by a constant temperature plate are studied experimentally for flow regimes with $Re_x = 2.5 \times 10^4 \sim 2.2 \times 10^6$ *and* $Gr_x = 2 \times 10^8 \sim 1.5 \times 10^{12}$. *Heat transfer results obtained by heat flux gages and temperature measurements are studied using convective instability parameters,* $Gr_x/Re_x^{1.5}$ *for laminar flow and* $Gr_x/Re_x^{2.7}$ *for turbulent flow, with emphasis on flow in the transition regime. Buoyancy effects on heat transfer are also studied by comparison with predictions from the Pohlhausen solution and the von Kármán analogy. Convective instability data, velocity and temperature profiles, and flow visualization photographs (obtained by the hydrogen bubble method) and the wall temperature field (obtained by liquid crystal visualization) are presented. Flow visualization photographs reveal the spanwise periodic vortical motion, and the fluctuating velocity and temperature fields near the wall.*

1 Introduction

In recent years the problem of buoyancy effects on forced convection heat transfer in a horizontal boundary layer heated from below has received much attention in the engineering heat transfer literature. Sparrow and Minkowycz (1962) and Mori (1961) approached the laminar mixed convection in a horizontal boundary layer over an isothermal plate by using a two-dimensional formulation and considering only the acceleration effect along the plate due to density change. In reality the vortex rolls appear even with a relatively small temperature difference between the plate and free stream and a convective instability problem arises similar to the centrifugal instability problem for Gortler vortices in the boundary layer along a concave wall.

Because of practical interest, linear stability analysis for the thermal instability of Blasius flow along a constant temperature horizontal plate has been carried out by several investigators (Wu and Cheng, 1976; Moutsoglou et al., 1981; Takimoto et al., 1978; Chen and Chen, 1984; Yoo et al., 1987) and the existing theoretical vortex instability results are well summarized in Table 4 of Yoo et al. (1987). The related experimental investigations were reported by Gilpin et al. (1978), Imura et al. (1978), Takimoto et al. (1983), Wang (1982), and Wang et al. (1983) dealing also with heat transfer in the postcritical regime.

The effects of buoyancy forces on forced convection along a horizontal constant temperature plate in the transition and turbulent flow regimes are also of considerable practical interest and have been studied experimentally by Hayashi et al. (1977), Imura et al. (1978), and Wang et al. (1983). Ali et al. (1983) reported a theoretical study on mixed convection in turbulent boundary layer flow over a horizontal plate using an extended version of the Van Driest mixing length model. Numerical results are presented for Prandtl number $Pr = 0.7$ for the buoyancy force parameter in the range $Gr_x/Re_x^{5/2} = 0 \sim 1000$ for assisting flow with local Reynolds numbers $Re_x \leq 10^7$ and local Grashof numbers $Gr_x \leq 10^{15}$. Kasagi and Hirata (1976) presented experimental investigations of the buoyancy effects on the structure of the turbulent boundary layer on a horizontal flat plate heated from below with particular emphasis on bursting phenomena.

The effects of buoyancy forces on turbulent structure and heat flux in a horizontal turbulent boundary layer were studied by Deissler (1962), Townsend (1972), Nicholl (1970), and Arya (1978) for geophysical applications, but these studies were not specifically concerned with heat transfer at the wall for engineering applications. Seban and Doughty (1956) presented experimental Nusselt number results in the transition and turbulent flow regimes without buoyancy effects.

Since the discovery of coherent flow structures in the turbulent boundary layer near the wall by Kline and co-workers (1959, 1967, 1971, 1974) using flow visualization techniques, many investigations regarding turbulence struction have been reported in recent years. Currently it is known that in the transition (buffer) layer between the viscous layer near the wall and the outer turbulent layer, relatively regular velocity fluctuations exist, and rising and falling flows caused by spanwise periodic vortical motion are observed near the wall. It is to be expected that buoyancy forces will have considerable effect on the flow structure and the heat transfer mechanism in the viscous layer with its large velocity gradient and in the transition layer.

Recently, Kasagi and co-workers (1982, 1985, 1986a, 1986b, 1987) studied experimentally heat transport mechanisms in a turbulent boundary layer using the hydrogen-bubble technique for coherent flow structure near the flat wall and liquid crystal sheet for unsteady wall temperature field visualization. They subsequently developed a structural model for streamwise pseudovortical structure in the near-wall region of a wall-bounded shear flow and carried out numerical investigations on turbulent heat transport mechanisms near the wall. The

[1]Current address: Department of Mechanical Engineering, University of Tokyo, Tokyo, Japan.

Contributed by the Heat Transfer Division for publication in the JOURNAL OF HEAT TRANSFER. Manuscript received by the Heat Transfer Division April 18, 1986. Keywords: Flow Instability, Flow Transition, Mixed Convection.

production and the diffusion of temperature fluctuations associated with the coherent turbulence structure are found to be in good agreement with the experiment.

Kuroda et al. (1987) carried out a numerical investigation of turbulent thermal fields, by coupling the energy equation for turbulent flow using the unsteady streamwise pseudovortical motion model with the unsteady heat conduction in the solid wall, and reported that the calculated rms temperature fluctuations in the near-wall region and those on the wall agree with experimental results for water for the two thermal boundary conditions of constant wall temperature and uniform wall heat flux. They show that the near-wall behavior of the temperature fluctuations, the turbulent heat flux, and the turbulent Prandtl number are influenced by the wall material and its thickness. It is of interest to observe that even with the imposition of a constant wall temperature on one side of a flat plate, wall temperature fluctuations exist on the other surface in response to the streamwise vortical motion near the wall.

The purpose of this paper is to study experimentally the effects of buoyancy forces of the flow and heat transfer characteristics of horizontal boundary layer flows over a constant temperature horizontal flat plate in the transition and turbulent flow regimes, and to present some flow visualization photographs obtained by the hydrogen-bubble method and a liquid crystal sheet attached to the plate surface. It is noted that experimental investigations on the buoyancy effects on turbulent heat transport near the wall reported in the literature are rather limited. This work was motivated by a desire to extend the earlier experimental investigations (Gilpin et al. 1978; Imura et al., 1978) for convective instability and postcritical heat transfer in the transition and turbulent flow regimes to the cases with larger Reynolds and Grashof numbers by extending a heating plate length from 1.52 m to 4.27 m. It is noted that the experimental measurements of the statistical quantities of thermal field in the region near the wall are extremely difficult. In this study, two wall heat flux gages were employed to determine the local average heat transfer coefficients in addition to the determination of local heat transfer coefficient by temperature profile measurements near the wall.

2 Experimental Apparatus and Procedure

2.1 Water Tunnel. The experiments were carried out in an existing closed-loop water tunnel (see Gilpin et al., 1978, for a schematic diagram and other general details). The circulating water can be cooled to any temperature between room temperature and about 0.2°C by a heat exchanger connected to a refrigeration system. The test section has dimensions of $45.7 \times 25.4 \times 427$ cm (width, height, length). The test section is preceded by a converging section having a contraction ratio of 5 to 1. The test section has side walls made of acrylic resin plates for the flow visualization. The steady water velocity in the test section can be controlled between 0.08 and 5 m/s.

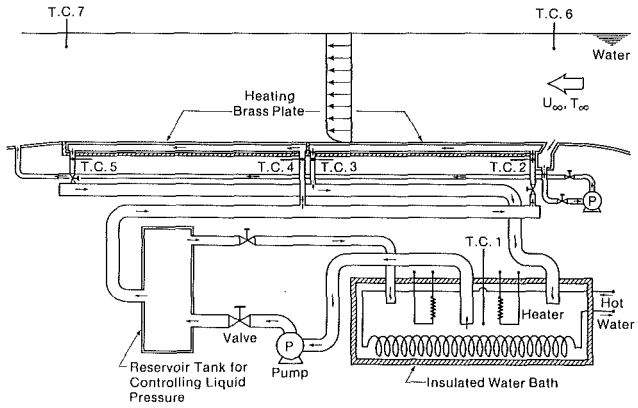

Fig. 1 Schematic diagram of the constant temperature plate with heating arrangement

2.2 Constant Temperature Heating Plate Assembly. The isothermal heating plates and the associated equipment are shown in Fig. 1. The test surface measuring 45.7×427 cm (width, length) was provided by two brass plates (thickness 6.35 mm), which were installed as the bottom surface of the test section. Each heating plate (213.5 cm in length) was designed to provide an isothermal surface for the horizontal boundary layer flow. The plate can be heated from the bottom surface by circulating hot water parallel to main flow at high speed through the heating channel with cross section 0.63×45.7 cm from a controllable, constant temperature bath. The isothermal plate can be simulated by providing a large Biot number flow between the heating fluid and the plate.

The heating fluid temperature was measured by ther-

Nomenclature

C_f = local friction coefficient $= \tau_w/(\rho u_\infty^2/2)$
C_p = specific heat at constant pressure
Gr_x = Grashof number $= g\beta(\Delta T)x^3/\nu^2$
g = gravitational acceleration
H = boundary layer shape factor $= \delta^*/\theta =$ displacement/momentum thickness
h_x = local heat transfer coefficient $= q_w/\Delta T = -K(\partial T/\partial y)_{y=0}/\Delta T$
K = $\mathrm{Re}_x^{0.8}\,\mathrm{Pr}/[1 + B\mathrm{Re}_x^{-0.1}(\mathrm{Pr}-1)]$, where B is defined in equation (1)
k = thermal conductivity
Nu_x = local Nusselt number $= h_x x/k$
Pr = Prandtl number
q_w = wall heat flux
Re_x = local Reynolds number $= u_\infty x/\nu$
St = Stanton number $= h_x/\rho_f C_p u_\infty$
T, T_w, T_∞ = fluid, wall, and free-stream temperatures
T_f = film temperature $= (T_w + T_\infty)/2$
T^+ = dimensionless temperature $= (T_w - T)u^*\rho C_p/q_w$
ΔT = temperature difference $= (T_w - T_\infty)$
u, u_∞ = fluid and free-stream velocities
u^+ = dimensionless velocity $= u/u^*$
u^* = friction velocity $= (\tau_w/\rho)^{1/2}$
x, y = distance from leading edge and normal distance from plate surface
y^+ = dimensionless distance from wall $= y/(\nu/(\tau_w/\rho)^{1/2})$
β = coefficient of thermal expansion
δ, δ_t = velocity and temperature boundary layer thicknesses
ν = kinematic viscosity
ρ_f = density evaluated at film temperature T_f
τ_w = wall shear stress

mocouples T. C. 1 to 5 (see Fig. 1) with an uncertainty of ±1.3 percent. The plate temperature was maintained in the range $T_w = 19.1 \sim 24.1°C$ with $T_2 \simeq T_4$. Throughout the experiments, the temperatures T_3 and T_5 were found to be around 4.4 percent lower than T_2. The plate surface temperatures at distances 20, 50, 70, 100, 150, and 200 cm from the leading edge were confirmed to be within 2.6 percent in the spanwise direction and 1.5 percent in the main flow direction of the wall temperature by measuring the plate contact temperature and extrapolation from the fluid temperature near plate using a 50 μm C-C thermocouple at three locations in the spanwise direction. The plate temperature measurement has an accuracy of 0.1°C. The leading edge of the isothermal plate was located right at the exit of the converging section of the tunnel. To avoid flow separation at the leading edge and to maintain flow parallel to the plate, a pump was used to suck a small amount of water through a slit near the leading and reinject it farther downstream.

2.3 Heat Flux Gage. For the purpose of obtaining heat transfer coefficients at the plate surface, two heat flux gages wer installed at distances from the leading edge of 1.98 m and 4.17 m, along the centerline. The heat flux gages were installed flush with the brass plate as shown in Fig. 2. These gages have an effective surface area of 38.4 cm^2 with 5.12 cm length in the flow direction. The size of the heat flux gage was determined considering ease of fabrication and calibration. The final design represents a compromise. The heat transfer coefficient obtained represents the local average over the length 5.12 cm. An insulated copper foil heater (MINCO 340 Ω) was attached on the top of an acrylic resin plate (adiabatic flat plate with 3 mm thickness), which was in turn fixed in a shallow groove with silicon cement in the heating plate. A thermopile (10 junctions) using copper-constantan thermocouple wires having diameters of 100 μm was installed between the upper and lower surfaces of the acrylic resin plate. Copper-constantan thermocouples (TC 8 to 10, 70 μm dia) were installed at the foil heater surface and at two locations on the brass plate to measure the wall temperature near the heat flux gage.

The downward heat loss from the heat flux gage was estimated from the output of the calibrated thermopile. The lateral heat loss was considered to be small and was neglected. The wall heat flux based on the effective gage surface area was computed from the power input to the foil heater. The direct current heating of the foil heater can be adjusted until the readings from thermocouples TC 8 to 10 are equalized. The wall heat flux thus obtained represents the average wall heat flux over the effective surface area of the heat flux meter. The uncertainty of heat flux measurement is estimated to be ±3.6 percent. The radiation loss from the heat flux meter surface is negligible. The range of uncertainty for the local heat transfer coefficient h_x is 4.8 ~ 3.7 percent for $\Delta T = 4 \sim 12°C$. The accuracy of the wall heat flux gage was also confirmed by a good agreement (within 3.5 ~ 5 percent, see Fig. 10) between the heat transfer coefficients from measurements and the predictions from the von Kármán analogy for forced convection in turbulent boundary layer flow along a flat plate with small temperature differences between the plate wall and the free steam. Within the experimental uncertainty, the heat flux gage is considered to provide a reasonable local heat transfer coefficient.

2.4 Temperature and Velocity Measurments. The temperature of the heating liquid was measured near the suction pipe of the pump in the constant temperature bath and at the inlets and outlets of the heating channel by copper-constantan thermocouples TC 1 to 5. The surface temperature of the heating plate was estimated from the outputs of the two 70 μm C-C thermocouples embedded on the heating plate near the heat flux gage, TC 9 and 10. The temperature in the free

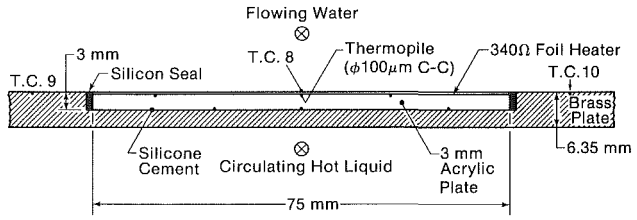

Fig. 2 Heat flux gage in the test plate and locations of thermocouples

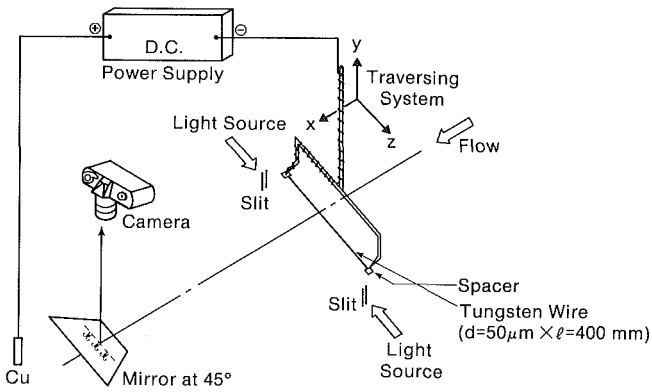

Fig. 3 Schematic diagram of the hydrogen-bubble method

stream was measured 10 cm upstream from the leading edge and also 10 cm downstream from the end of the second heating plate by C-C thermocouples TC 6 and 7, respectively.

In order to measure the temperature profile across the boundary layer, a 70 μm C-C thermocouple junction was formed at the center of a **U** probe with 9 cm span. The junction of the 70 μm thermocouple was made by butt welding the copper and constantan wires together, thus providing a very small junction volume. The span of the **U** probe was provided by a 50 μm supporting wire transverse to the main flow. The supporting frame of the **U** probe was made from 1.5 mm dia stainless steel wire. The thermocouple was positioned using a traversing mechanism with an accuracy of 1/50 mm. The heat transfer coefficient at the isothermal plate was also estimated from the temperature profile measurements near the wall in the boundary layer for axial positions different from the two heat flux meters. The heat transfer coefficient determined from the temperature gradient agreed with the value from the first heat flux meter within 3 percent for $Re_x = 2.6 \times 10^5$ and T = 7.1°C, for example.

The free-stream velocity was measured using a Pitot tube with a 3 mm outside diameter. The measurement of the velocity profile in the boundary layer was accomplished by using an impact tube with 0.7 × 4.5 mm opening area. The static pressure was obtained from a Pitot tube mounted in the free stream. The differential pressure thus obtained was measured by a manometer using carbon tetrachloride liquid with a small amount of Sudan III added to provide a red color. The coefficient of the impact tube was determined from the average value of several calibrations. It was found unnecessary to make a correction for viscosity effect.

2.5 Flow Visualization Techniques. The hydrogen bubble method was used to visualize the flow in the near-wall region of the turbulent boundary layer. A schematic diagram of the experimental setup is shown in Fig. 3. In order to obtain a cross-sectional view of the flow structure, an inclined mirror was set at an angle of 45 deg from the heating plate, 1.2 m downstream from the bubble-generating tungsten wire (50 μm

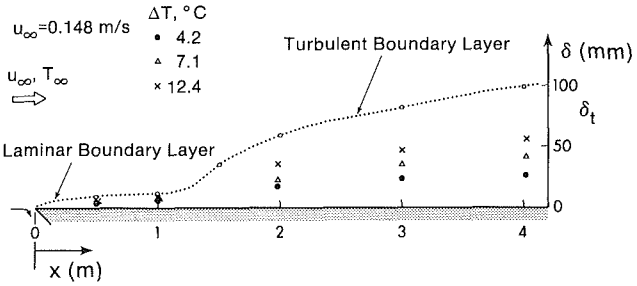

Fig. 4 Development of velocity and temperature boundary layers

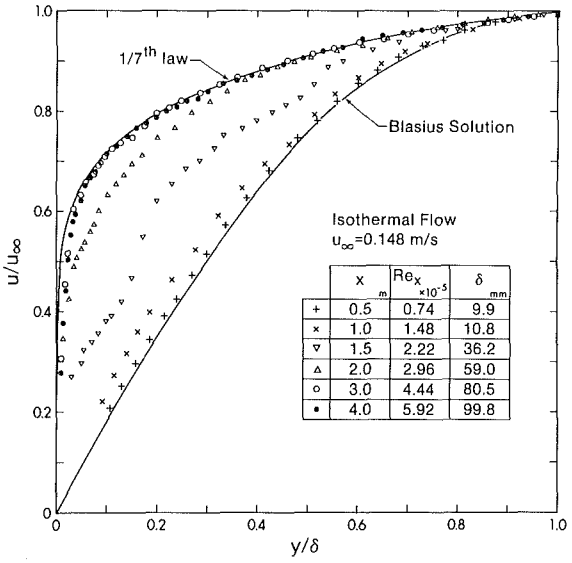

Fig. 5 Velocity profiles for the basic flow

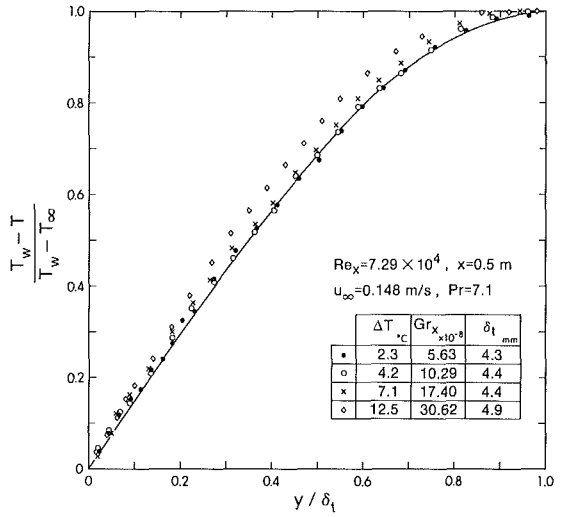

Fig. 6 Temperature profiles for the basic flow

dia and 40 cm length). This position was slightly upstream of a slit light source. The bubbles were generated continuously by a d-c power supply (Kasagi and Hirata, 1976).

A temperature-sensitive liquid crystal sheet was utilized to visualize the temperature patterns at the heat transfer surface (Kasagi, 1980; Hirata and Kasagi, 1979). The liquid crystal film displays a color change from red to dark blue over a temperature range of 5°C. The liquid crystal is enclosed in

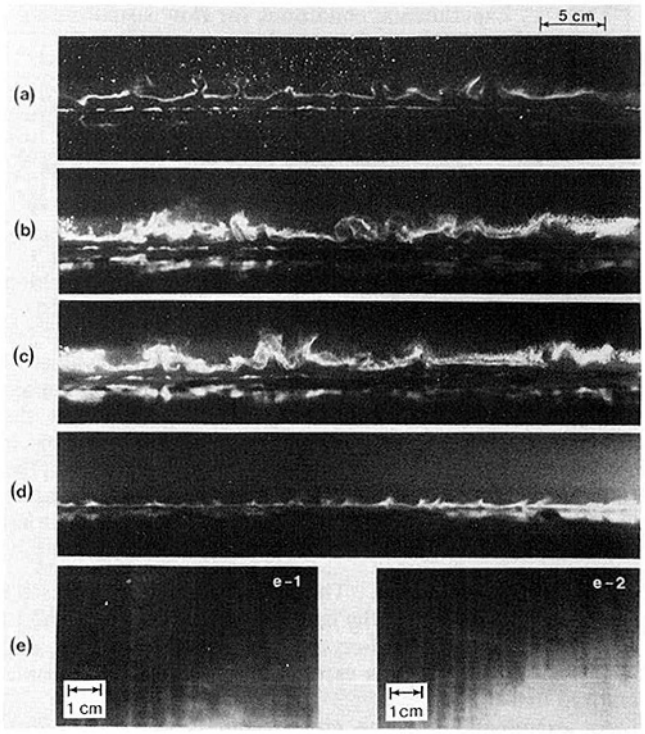

Fig. 7 Flow visualization photographs (the scale shown applies to (a-d))

capsules 5 ~ 20 μm in diameter. These capsules are pasted and fixed uniformly on a black polyester film with 100 μm thickness. The liquid crystal sheet (total thickness ≃ 180 μm) was attached flush on the heating plate surface. The wall temperature fluctuations can be visualized as a color change of liquid crystal.

3 Experimental Results and Discussion

3.1 Basic Flow and Temperature Fields. The experiments were performed under open-channel flow conditions in the test section. Measurements of the velocity profile above the plate showed that the free-stream velocity was uniform (deviations from the mean value were within 0.6 percent). Due to the development of boundary layers along the walls of the test section, the free stream accelerates slightly (about 3.6 percent) near the end of the test section. The measured free-stream turbulence level was 0.8 ~ 1.4 percent (rms velocity fluctuations). The effect of free-stream turbulence remains to be studied.

The measured velocity boundary layer development along the horizontal flat plate for the case of isothermal flow ($\Delta T = 0$), with a free-stream velocity $U_\infty = 0.148$ m/s, is shown in Fig. 4. Data points for temperature boundary layer are also plotted on the figure for reference. The velocity boundary layer thickness agrees with the values predicted from laminar boundary layer theory in the region $0 < x < 1.0$ m. The boundary layer thickness increased rapidly thereafter and the region $1.0 < x < 2.0$ m (corresponding to Reynolds numbers $1.48 \times 10^5 \sim 3 \times 10^5$) may be regarded as a transition region. The boundary layer thickness in the turbulent region ($x > 2.0$ m) agrees approximately with predictions (Schlichting, 1960).

Measured velocity profiles for isothermal flow, with $u_\infty = 0.148$ m/s, are shown in Fig. 5 for several values of x. It is seen that the velocity profile at $x = 0.5$ m agrees well with the Blasius profile and the profile at $x = 4.0$ m agrees with the 1/7th power law for a fully developed turbulent flow. Figure 5

Table 1 Experimental conditions for flow visualization

	x, m	y, mm	y^+	Re_x	Gr_x	$Gr_x/Re_x^{1.5}$
(*a*)	0.5	10		6.17×10^4	1.74×10^9	1.14×10^2
(*b*)	1.8	10		2.2×10^5	8.12×10^{10}	7.87×10^2
(*c*)	3.5	10	68.8	4.36×10^5	5.97×10^{11}	2.07×10^3
(*d*)	3.5	2.9	17.2	4.36×10^5	6.0×10^{11}	2.08×10^3
(*e*−1)	0.5			6.24×10^4	6.1×10^{11}	2.6×10^3
(*e*−2)	0.5			6.24×10^4	7.84×10^{11}	5.03×10^4

clearly shows the changing velocity profiles in the transition region.

The measured temperature profiles at $x=0.5$ m ($u_\infty=0.148$ m/s, $Re_x=7.29\times10^4$) are shown in Fig. 6 for several values of ΔT. The theoretical profile for $Pr=7.1$, from Pohlhausen (1921), is also plotted on the figure. It is seen that the Pohlhausen temperature profile for steady laminar flow is confirmed by the measurements at $\Delta T=2.3$ and 4.2°C. The fluid property values were evaluated at the film temperature T_f. For the present investigation, this level of agreement between theory and experiment is considered to be adequate.

3.2 Flow Visualization. The flow visualization results are shown in Fig. 7(*a–d*) for the hydrogen bubble method and in FIg. 7(*e*) for the liquid-crystal visualization of the wall temperature patterns. The experimental conditions are summarized in Table 1.

An examination of the cross-sectional view, Fig. 7(*a*), reveals that an array of more or less regularly spaced longitudinal vortices exists. The bubble tracer is being lifted off the plate by upflow between vortex rolls. During the experiment, it was observed from the top that the upflows of tracer hydrogen bubbles appear as parallel lines in the direction of main flow. With increasing temperature difference ΔT, these lines oscillate somewhat irregularly in the spanwise direction and become unsteady.

With further development of the boundary layer, the longitudinal vortices distort more in a complicated manner as shown in Fig. 7(*b, c*). The flow pattern shown in Fig. 7(*d*) is in the fully developed turbulent regime. In the viscous sublayer, the upward motion of the low-speed fluid and the downward motion of the high-momentum fluid can be visualized clearly. Some regularity of the secondary motion is still observed in the spanwise direction suggesting the existence of the longitudinal vortices.

The relationship between the longitudinal vortices and the heat transfer mechanism can be seen qualitatively from the instantaneous liquid crystal visualization of the wall temperature field as shown in Fig. 7(*e*). Color photographs were taken originally but black and white prints are presented here. The black zone in Fig. 7(*e*) indicates a lower temperature region with a higher heat transfer rate. The somewhat lighter lines indicate a higher temperature. These lines were observed directly below the tracer hydrogen bubbles being lifted up off the plate by upflow and were confirmed by simultaneous observation with the hydrogen bubble method.

The wall temperature fluctuations as revealed by the liquid crystal sheet are caused by the coupled effects between the plate and the streamwise vortical motion near the wall. The present result agrees with Kasagi and co-workers' recent observations and further details can be found in their works. The longitudinal vortices are unsteady and oscillate in the spanwise direction. It is clear that with vortical motion near the wall, the constant wall temperature cannot be prescribed. However, the instantaneous average of the fluctuating wall temperature is considered to be constant.

The spacing of the low-speed fluid lumps decreases with increasing temperature difference ΔT. The distance between stripes in *e*-2 for larger ΔT is seen to be smaller than that in *e*-1. The longitudinal stripes are observed to be over 10 cm

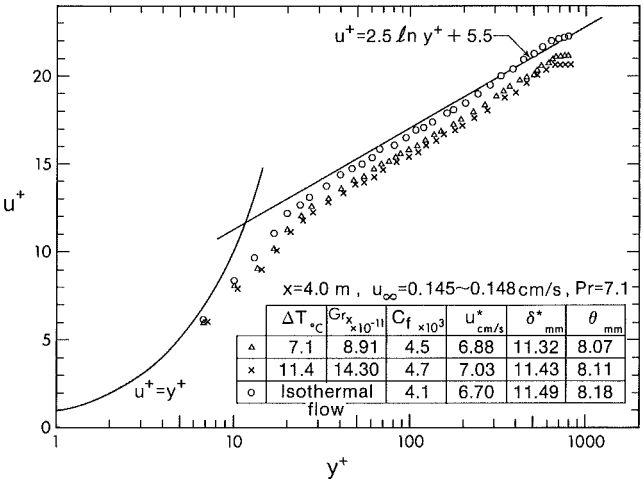

Fig. 8 Turbulent velocity profiles, u^+ versus y^+

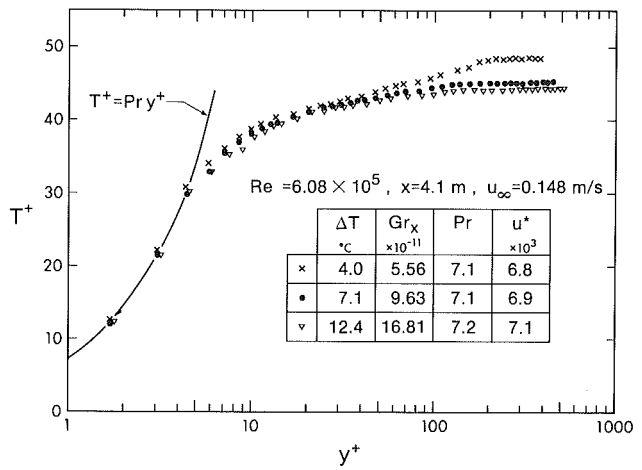

Fig. 9 Turbulent temperature profiles, T^+ versus y^+

long. Because of thermal resistance, the liquid crystal sheet does not provide accurate plate surface temperature, but it shows the pattern of temperature field. The slow hot fluid moves upward and fast cold fluid moves downward toward the hot plate. It is expected that the buoyancy force has an appreciable effect on the turbulent flow structure near the plate. The flow visualization results by Kline et al. (1967), Nychas et al. (1973), and Kasagi and Hirata (1976) show that the bursting phenomenon is characterized by a spatial length scale of order $100\nu/(\tau_w/\rho)^{1/2}$ in the spanwise direction (defined as the mean spacing between low-speed streaks in the turbulent boundary layer over a flat plate). This value agrees with the mean spacing of the vortex rolls observed in the present investigation.

3.3 Velocity and Temperature Profiles. Representative mean velocity and temperature profiles at positions along the center of the plate in the turbulent boundary layer are shown in Figs. 8 and 9. The friction velocity u^* was calculated using the friction factor predicted by Clauser's method (Clauser, 1954). For isothermal flow, the experimental data agree with the law of the wall and a shape factor $H=\delta^*/\theta=1.4$ was obtained, confirming the presence of a fully developed turbulent boundary layer. Both the velocity and temperature profiles in the buffer layer and turbulent region depend on the temperature difference between plate and free stream, ΔT. Changes in the profiles for different Grashof numbers are due to buoyancy effects.

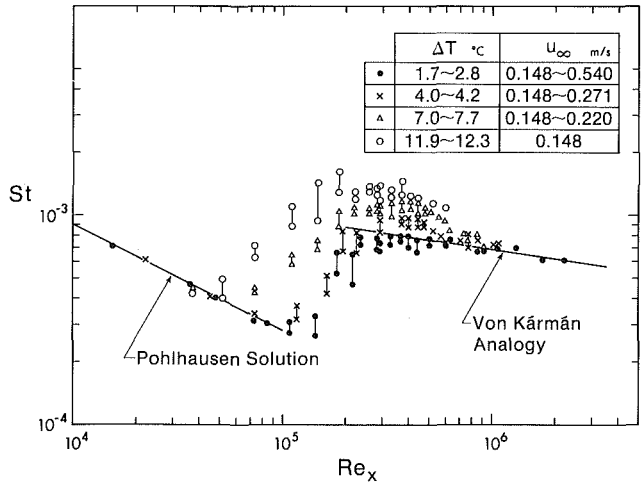

Fig. 10 Heat transfer results, St versus Re_x

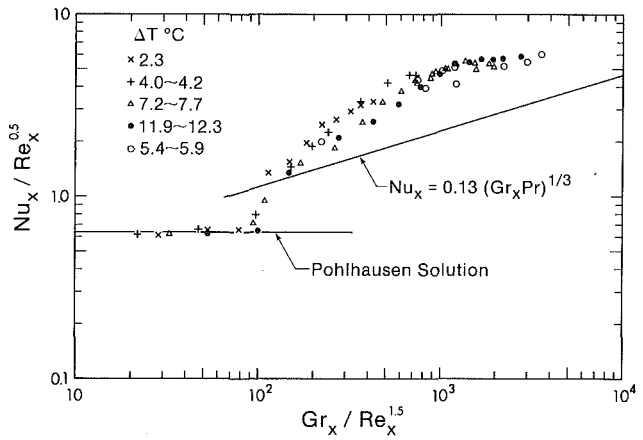

Fig. 11 Heat transfer results, $Nu_x/Re^{0.5}$ versus $Gr_x/Re_x^{1.5}$

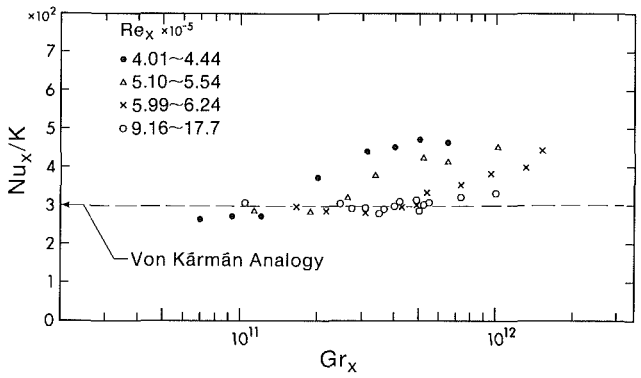

Fig. 12 Heat transfer results, Nu_x/K versus Gr_x with Re_x as parameter

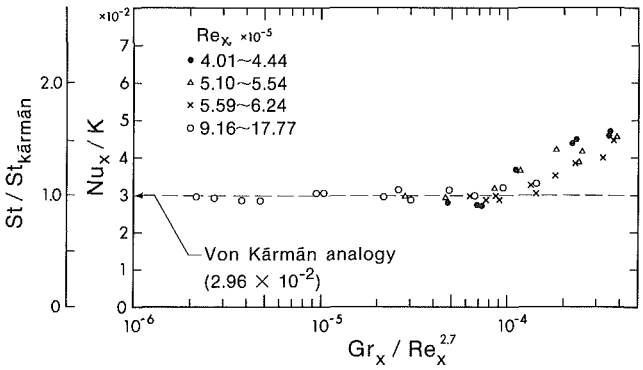

Fig. 13 Heat transfer results, St/St_{Karman} versus $Gr_x/Re_x^{2.7}$ with Re_x as parameter

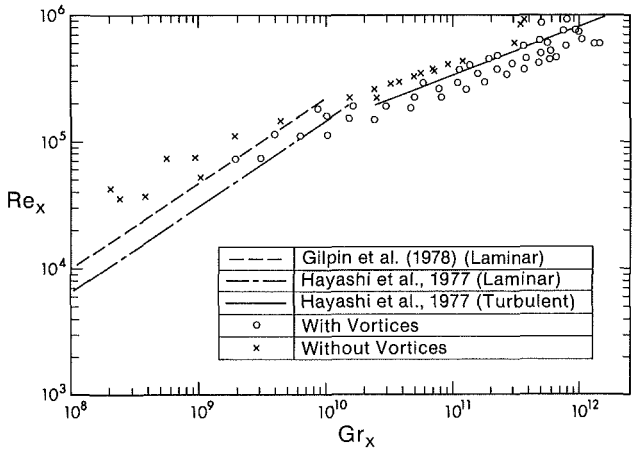

Fig. 14 Instability data, Re_x versus Gr_x

3.4 Heat Transfer Results. The heat transfer results from the present investigation are shown in Fig. 10, where the Stanton number $St = h_x/\rho_f C_p u_\infty$ is plotted as a function of Reynolds number, in the range $Re_x = 1.5 \times 10^4 \sim 2.3 \times 10^6$. For a low heating rate with small ΔT, the experimental data agree with the results from the Pohlhausen solution for pure laminar forced convection (two-dimensional flow) and from the von Kármán analogy for turbulent boundary layer heat transfer. It is seen that the deviation from pure forced convection can occur at much lower Reynolds numbers depending on the Grashof number. Within the range of Reynolds numbers in this study, the deviation of the Stanton number from pure turbulent forced convection is 19 to 59 percent. The uncertainty for St at $Re_x = 1.55 \times 10^5$ is ±4.18 percent. Within the scope of the present investigation ($\Delta T < 12.3$°C), buoyancy effects are eliminated at $Re_x \gtrsim 10^6$. At $Re_x = 8.6 \times 10^5$ and $\Delta T = 7.7$°C, for example, the Stanton number is still about 15 percent greater than the prediction from the von Kármán analogy.

The experimental data are also plotted in the form of $Nu_x/Re_x^{1/2}$ as a function of the convective instability parameter $Gr_x/Re_x^{1.5}$ in Fig. 11. The correlation equation for turbulent free convection (Fujii and Imura, 1972) is also shown for reference. Figure 11 shows clearly that the threshold value for buoyancy effects on heat transfer is $Gr_x/Re_x^{1.5} \approx 100$. For $Gr_x/Re_x^{1.5} \gtrsim 200$, the deviation from the turbulent free convection prediction is seen to be appreciable. This is in contrast to the heat transfer results obtained by Imura et al. (1978), for the low Reynolds number region ($Re_x = 3.2 \times 10^3 \sim 2 \times 10^5$), which show qualitative agreement with turbulent free convection prediction in the range $Gr_x/Re_x^{1.5} > 300$. The present results suggest that the mixed convection effect may still exist in the parametric range studied. The related flow structure near the plate is known to be very complex and the possibility of mixed convection should not be ruled out.

In order to study the effects of Grashof number on turbulent forced convection, the heat transfer data are plotted against Grashof number Gr_x, with Reynolds number Re_x as parameter in Fig. 12. The turbulent heat transfer correlation equation based on the von Kármán analogy (1939) is given as

$$\mathrm{Nu}_x = 0.0296\ \mathrm{K} = 0.0296\ \mathrm{Re}_x^{0.8}\ \mathrm{Pr}/[1 + B\ \mathrm{Re}_x^{-0.1}(\mathrm{Pr} - 1)]$$
$$\text{where } B = 0.860\ (1 + \ln[(1 + 5\mathrm{Pr})/6]/(\mathrm{Pr} - 1)) \quad (1)$$

Figure 12 shows the deviation from the von Kármán analogy but with $\mathrm{Re}_x = (9.16 \sim 17.7) \times 10^5$; the heat transfer data agree with predictions from the von Kármán analogy. For smaller Reynolds numbers, the deviation from the von Kármán analogy occurs at a certain Grashof number. Thus, the threshold value for Grashof number depends on Reynolds number as expected.

The turbulent heat transfer results are also presented in Fig. 13, using the turbulent convective instability parameter $\mathrm{Gr}_x/\mathrm{Re}_x^{2.7}$ for turbulent boundary layers derived by Hayashi et al. (1977) based on a two-layer model for turbulent boundary layer. It is seen that buoyancy effects are significant for heat transfer in turbulent boundary layer when $\mathrm{Gr}_x/\mathrm{Re}_x^{2.7} \gtrsim 10^{-4}$.

3.5 Convective Instability Data. The convective instability data from the both the flow visualization, using the hydrogen bubble method, and heat transfer coefficient measurements are plotted in Fig. 14 as Re_x versus Gr_x. The range of uncertainty is $\pm(1.2 \sim 1.6$ percent) for Re_x and $\pm(1.0 \sim 1.3$ percent) for Gr_x. The instability criteria given by the following equations are also shown for comparison.

Laminar Flow

$$\mathrm{Gr}_x/\mathrm{Re}_x^{1.5} = 100 \quad \text{(Gilpin et al., 1978)} \quad (2)$$

$$\mathrm{Gr}_x/\mathrm{Re}_x^{1.5} = 193 \quad \text{(Hayashi et al., 1977)} \quad (3)$$

Turbulent Flow

$$\mathrm{Gr}_x/\mathrm{Re}_x^{2.7} = 1.3 \times 10^{-4} \quad \text{(Hayashi et al., 1977)} \quad (4)$$

4 Concluding Remarks

Convective instability and buoyancy effects on forced convection heat transfer in horizontal boundary layers heated from below by a constant temperature plate were studied experimentally. The conditions were as follows: $u_\infty = 0.118 \sim 0.50$ m/s, $\Delta T = T_w - T_\infty = 2 \sim 12\ ^\circ\mathrm{C}$, $\mathrm{Re}_x = 2.5 \times 10^4 \sim 2.2 \times 10^6$ and $\mathrm{Gr}_x = 2 \times 10^8 \sim 1.5 \times 10^{12}$. The effects of buoyancy on heat transfer results are studied using the convective instability parameters, $\mathrm{Gr}_x/\mathrm{Re}_x^{1.5}$ for laminar flow, and $\mathrm{Gr}_x/\mathrm{Re}_x^{2.7}$ for turbulent flow, with emphasis on flow in the transition regime.

The convective instability data for the onset of longitudinal vortices were found to agree well with equation (2) for laminar flow and equation (4) for turbulent flow. The buoyancy effects on heat transfer in the turbulent flow regime were studied by comparison with predictions from the von Kármán analogy. The experimental results reveal that buoyancy effects on heat transfer are significant in the transition regime $\mathrm{Re}_x = 4 \times 10^4 \sim 5 \times 10^5$ and depend on relative magnitudes of Grashof and Reynolds numbers.

Flow visualization photographs obtained by the hydrogen bubble method show the transverse cross-sectional views of the flow with spanwise, somewhat periodic vortical motion. The liquid crystal visualization reveals the corresponding spanwise periodic wall surface temperature variation. The temperature and velocity fields near the wall are apparently coupled. Two heat flux gages installed along the centerline of the test plate were used to obtain the local average heat transfer coefficients. Velocity and temperature profiles are also presented for the flow regime, $\mathrm{Re}_x = (0.74 \sim 5.92) \times 10^5$ and $\mathrm{Gr}_x = (5.63 \sim 30.62) \times 10^8$. The present study shows clearly that the Pohlhausen solution and the von Kármán analogy for turbulent heat transfer in boundary layers are not valid when longitudinal vortices caused by convective instability occur in the flow field. In the turbulent flow regime, mixed convection effects are found to prevail in the range $\mathrm{Gr}_x/\mathrm{Re}_x^{2.7} \gtrsim 10^{-4}$.

Acknowledgments

This work, completed in 1980, was supported by an operating grant from the Natural Sciences and Engineering Research Council of Canada. The second author wishes to thank Professor M. Hirata, University of Tokyo, for his encouragement to conduct this work. This paper is dedicated to the memory of the late Professor R. R. Gilpin (1942–1982).

References

Ali, M. M., Chen, T. S., and Armaly, B. F., 1983, "Mixed Convection in Turbulent Boundary Layer Flow Over a Horizontal Plate," ASME Paper No. 83-WA/HT-5.

Arya, S. P. S., 1975, "Buoyancy Effects in a Horizontal Flat-Plate Boundary Layer," *J. Fluid Mech.*, Vol. 68, pp. 321–343.

Chen, K., and Chen, M. M., 1984, "Thermal Instability of Forced Convection Boundary Layers," ASME JOURNAL OF HEAT TRANSFER, Vol. 106, pp. 284–289.

Clauser, F. H., 1954, "Turbulent Boundary Layers in Adverse Pressure Gradients," *J. of Aeronautical Sciences*, Vol. 21, pp. 91–108.

Diessler, R. G., 1962, "Turbulence in the Presence of a Vertical Body Force and Temperature Gradient," *J. of Geophysical Research*, Vol. 67, pp. 3049–3062.

Fujii, T., and Imura, H., 1972, "Natural-Convection Heat Transfer From a Plate With Arbitrary Inclination," *Int. J. Heat Mass Transfer*, Vol. 15, pp. 755–767.

Gilpin, R. R., Imura, H., and Cheng, K. C., 1978, "Experiments on the Onset of Longitudinal Vortices in Horizontal Blasius Flow Heated From Below," ASME JOURNAL OF HEAT TRANSFER, Vol. 100, pp. 71–77.

Hayashi, Y., Takimoto, A., and Hori, K., 1977, "Buoyancy Effects on Forced Turbulent Convection Heat Transfer (the Case of Horizontal Flat Plate)," *Procs. JSME Symposium*, Hokuriku-Shinetsu Branch, pp. 155–157.

Hirata, M., and Kasagi, N., 1979, "Studies of Large-Eddy Structures in Turbulent Shear Flows With the Aid of Flow Visualization Techniques," *Studies in Heat Transfer*, A Festschrift for E.R.G. Eckert, J. P. Hartnett et al., eds., Hemisphere, Washington, DC, pp. 145–164.

Imura, H., Gilpin, R. R., and Cheng, K. C., 1978, "An Experimental Investigation of Heat Transfer and Buoyancy Induced Transition From Laminar Forced Convection to Turbulent Free Convection Over a Horizontal Isothermally Heated Plate," ASME JOURNAL OF HEAT TRANSFER, Vol. 100, pp. 429–434.

Iritani, Y., Kasagi, N., and Hirata, M., 1982, "Transport Mechanism in a Turbulent Boundary Layer (1st Report, Visualized Behaviours of Wall Temperature by Liquid Crystal)," *Trans. JSME*, Vol. 48B, No. 435, pp. 2284–2294.

Iritani, Y., Kasagi, N., and Hirata, M., 1985, "Heat Transfer Mechanism and Associated Turbulence Structure in the Near-Wall Region of a Turbulent Boundary Layer," *Turbulent Shear Flows 4*, L.J.S. Bradbury et al., eds., Springer-Verlag, New York, pp. 223–234.

Kármán, T. von, 1939, "The Analogy Between Fluid Friction and Heat Transfer," *Trans. ASME*, Vol. 61, pp. 705–710.

Kasagi, N., and Hirata, M., 1976, "Bursting Phenomena in Turbulent Boundary Layer on a Horizontal Flat Plate Heated From Below," *Heat Transfer and Turbulent Buoyant Convection*, D. B. Spalding and N. Afgan, eds., Vol. 1, Hemisphere, Washington, DC, pp. 27–38.

Kasagi, N., 1980, "Liquid Crystal Applications in Heat Transfer Experiments," Report No. IL-27, Stanford University, CA.

Kasagi, N., Hirata, M., and Nishino, K., 1986a, "Streamwise Pseudo-vortical Structures and Associated Vorticity in the Near-Wall Region of a Wall-Bounded Turbulent Shear Flow," Experiments in Fluids, Vol. 4, pp. 309–318.

Kasagi, N., Harumi, K., and Hirata, M., 1986b, "An Analysis of the Turbulent Transport Mechanism Near the Wall by Streamwise Pseudo-vortical Motion Model," *Heat Transfer 1986*, pp. 1103–1108.

Kasagi, N., Kuroda, A., and Hirata, M., 1987, "Numerical Investigation of the Turbulent Heat Transfer Near the Wall by the Unsteady Streamwise Pseudo-vortical Motion Model," *Procs. 1987 ASME-JSME Thermal Engineering Joint Conference*, Vol. 1, pp. 477–482.

Kim, H. T., Kline, S. J., and Reynolds, W. C., 1971, "The Production of Turbulence Near a Smooth Wall in a Turbulent Boundary Layer," *J. Fluid Mech.*, Vol. 50, pp. 133–160.

Kline, S. J., and Runstadler, P. W., 1959, "Some Preliminary Results of Visual Studies of the Flow Model of the Wall Layers of the Turbulent Boundary Layer," ASME *Jouranl of Applied Mechanics*, Vol. 26, pp. 166–170.

Kline, S. J., Reynolds, W. C., Schraub, F. A., and Runstadler, P. W., 1967, "The Structure of Turbulent Boundary Layers," *J. Fluid Mech.*, Vol. 30, pp. 741–774.

Kuroda, A., Kasagi, N., and Hirata, M., 1987, "Numerical Investigation of Turbulent Thermal Field Taking Into Account the Unsteady Heat Conduction in the Solid Wall," *24th National Heat Transfer Symposium of Japan*, Matsuyama, pp. 61–63.

Mori, Y., 1961, "Buoyancy Effects in Forced Laminar Convection Flow Over a Horizontal Flat Plate," ASME JOURNAL OF HEAT TRANSFER, Vol. 83, pp. 479–482.

Moutsoglou, A., Chen, T. S., and Cheng, K. C., 1981, "Vortex Instability of

Mixed Convection Flow Over a Horizontal Flat Plate," ASME JOURNAL OF HEAT TRANSFER, Vol. 103, pp. 257–261.

Nicholl, C. I. H., 1970, "Some Dynamical Effects of Heat on a Turbulent Boundary Layer," *J. Fluid Mech.*, Vol. 40, pp. 361–384.

Nychas, S. G., Hershey, H. C., and Brodkey, R. S., 1973, "A Visual Study of Turbulent Shear Flow," *J. Fluid Mech.*, Vol. 61, pp. 513–540.

Offen, G. R., and Kline, S. J., 1974, "Combined Dye-Streak and Hydrogen-Bubble Visual Observation of a Turbulent Boundary Layer," *J. Fluid Mech.*, Vol. 62, pp. 223–239.

Pohlhausen, E., 1921, "Der Warmeaustausch Zwishchen Festen Korpern und Flussigkeiten mit Kleiner Reibung und Kleiner Warmeleitung," *Zeitschrift fur Angewandte Mathematik und Mechanik*, Vol. 1, pp. 115–120.

Schlichting, H., 1960, *Boundary-Layer Theory*, 4th ed., McGraw-Hill, New York, p. 535.

Seban, R. A., and Doughty, D. L., 1956, "Heat Transfer to Turbulent Boundary Layers, With Variable Free-Stream Velocity," *Trans. ASME*, Vol. 78, pp. 217–223.

Sparrow, E. M., and Minkowycz, W. J., 1962, "Buoyancy Effects on Horizontal Boundary-Layer Flow and Heat Transfer," *Int. J. Heat Mass Transfer*, Vol. 5, pp. 505–511.

Takimoto, A., Hayashi, Y., and Matsuda, O., 1983, "Thermal Instability of Blasius Flow Over a Horizontal Plate," *Heat Transfer–Japanese Research*, Vol. 12, pp. 19–33; also Trans. *JSME*, 1982, Vol. 48B, No. 435, pp. 2295–2303.

Townsend, A. A., 1972, "Mixed Convection Over a Heated Horizontal Plane," *J. Fluid Mech.*, Vol. 55, pp. 209–227.

Wang, G. S., and Incropera, F. P., and Viskanta, R., 1983, "Mixed Convection Heat Transfer in a Horizontal Open-Channel Flow With Uniform Bottom Heat Flux," ASME JOURNAL OF HEAT TRANSFER, Vol. 105, pp. 817–822.

Wang, X. A., 1982, "An Experimental Study of Mixed, Forced, and Free Convection Heat Transfer From a Horizontal Flat Plate to Air," ASME JOURNAL OF HEAT TRANSFER, Vol. 104, pp. 139–144.

Wu, R.-S., and Cheng, K. C., 1976, "Thermal Instability of Blasius Flow Along Horizontal Plates," *Int. J. Heat Mass Transfer*, Vol. 19, pp. 907–913.

Yoo, J. Y., Park, P., Choi, C. K., and Ro, S. T., 1987, "An Analysis on the Thermal Instability of Forced Convection Flow Over Isothermal Horizontal Flat Plate," *Int. J. Heat Mass Transfer*, Vol. 30, pp. 927–935.

S. Haq

C. Kleinstreuer

J. C. Mulligan

Department of Mechanical and Aerospace Engineering, North Carolina State University, Raleigh, NC 27695-7910

Transient Free Convection of a Non-Newtonian Fluid Along a Vertical Wall

Introduction

The laminar flow behavior of a non-Newtonian fluid suddenly set into motion by temperature-induced buoyancy forces is of importance in a number of industrial applications. The transient convection heat transfer in a power-law fluid is of major interest here and a numerical solution of the appropriate unsteady boundary-layer equations is presented for the first time. Kawase and Ulbrecht (1984) employed an integral method to analyze the steady-state natural convection from an isothermal vertical wall to a power-law fluid. They assumed a very thin thermal boundary layer (see Shenoy and Ulbrecht, 1979) and employed a velocity profile taken from forced convection analysis; hence their energy and momentum equations were decoupled. Other approximate (integral) solutions for laminar free convection of a power-law fluid along an isothermal vertical wall have been reviewed by Shenoy and Mashelkar (1982). These contributions assume steady state, a non-Newtonian Prandtl number of unity, and neglect the inertia terms. Of equal relevance to this particular study are solutions to unsteady boundary layers governed by singular parabolic equations. In a series of papers discussed below, unsteady laminar boundary layers of a Newtonian fluid on a semi-infinite plate are considered. Williams et al. (1987) assumed wall temperatures that vary with time and position and found possible semisimilar solutions for a variety of classes of wall temperature distribution. Wang (1985) studied the uncoupled boundary-layer problem where a fluid on a finite heated plate is suddenly set into motion. Nanbu (1971) estimated the limit of pure conduction for unsteady free convection on a vertical flat plate. He assumed pure one-dimensional conduction everywhere until the leading edge disturbance had reached the local point. For the speed of this propagation disturbance he used the local maximum fluid velocity from the solution of the doubly infinite plate problem, the same assumption Goldstein and Briggs (1964) had made seven years earlier. Indeed, in both papers, basically the same critical times for the end of pure conduction are reported for a wide range of Prandtl number fluids. Hellums and Churchill (1962) presented a numerical solution of the coupled time-dependent boundary-layer equations considering only air as the fluid. They computed a critical time 15 percent lower than that obtained by analytical methods (see Nanbu, 1971 and Goldstein and Briggs, 1964). Rahman and Carey (1986) analyzed crossflow mixed convection over flat vertical surfaces, a problem area of which the previous contributions are special cases.

In this study the system of equations describing the transient free convection on a flat vertical surface is extended to a non-Newtonian fluid, and solved numerically.

Contributed by the Heat Transfer Division and presented at the ASME/AIChE Heat Transfer Conference, Pittsburgh, Pennsylvania, August 1987. Manuscript received by the Heat Transfer Division April 10, 1987. Keywords: Natural Convection, Non-Newtonian Flows and Systems, Transient and Unsteady Heat Transfer.

Analysis

Considering laminar free convection of a non-Newtonian fluid on an isothermal, semi-infinite vertical wall, using the Boussinesq approximation, the system may be described by

$$\frac{\partial u}{\partial x}+\frac{\partial v}{\partial y}=0 \tag{1}$$

$$\frac{\partial u}{\partial t}+u\frac{\partial u}{\partial x}+v\frac{\partial u}{\partial y}=g\beta(T-T_\infty)+\frac{1}{\rho}\frac{\partial \sigma}{\partial y} \tag{2}$$

$$\frac{\partial T}{\partial t}+u\frac{\partial T}{\partial x}+v\frac{\partial T}{\partial y}=\alpha\frac{\partial^2 T}{\partial y^2} \tag{3}$$

where

$$\sigma=K\left|\frac{\partial u}{\partial y}\right|^{n-1}\frac{\partial u}{\partial y} \tag{4}$$

is the typical power-law approximation. Here y is measured normal to the wall, β is the thermal expansion coefficient, and σ is the shear stress.

The initial and boundary conditions read:

$$\begin{aligned}
&u=0,\quad v=0,\quad T=T_\infty \text{ for } t\le 0 \text{ everywhere}\\
&u=v=0,\quad T=T_w \text{ for } t>0 \text{ at } x>0,\quad y=0;\\
&u\to 0,\quad T\to T_\infty \text{ for } t>0 \text{ when } y\to\infty, \text{ all } x;\\
&T=T_\infty,\quad u=0 \text{ and } v\to\infty \text{ at } x=0 \text{ for } t>0 \text{ and } y>0
\end{aligned} \tag{5}$$

The last boundary condition for the leading edge assumes that the fluid in this region is continually renewed from the bulk at a very high rate.

Using the nondimensional variables

$$\begin{aligned}
\theta&=\frac{T-T_\infty}{T_w-T_\infty}=\frac{\Delta T}{\Delta T_w}\\
X&=\frac{x}{(K/\rho)^{2/(n+2)}(g\beta\Delta T_w)^{(n-2)/(n+2)}}\\
Y&=\frac{y}{(K/\rho)^{2/(n+2)}(g\beta\Delta T_w)^{(n-2)/(n+2)}}\\
U&=\frac{u}{\{(K/\rho)[g\beta\Delta T_w]^n\}^{1/(n+2)}}\\
V&=\frac{v}{\{(K/\rho)[g\beta\Delta T_w]^n\}^{1/(n+2)}}\\
\tau&=\frac{t}{(K/\rho)^{1/(n+2)}[g\beta_o\Delta T_w]^{-2/(n+2)}}
\end{aligned} \tag{6}$$

and the dimensionless group

$$\mathrm{PR}^{-1}=\frac{\alpha}{\left(\frac{K}{\rho}\right)}\left[\frac{1}{\left(\frac{K}{\rho}\right)^{-1/(n+2)}[g\beta\Delta T_w]^{2/(n+2)}}\right]^{n-1}$$

$$=\frac{\mathrm{Gr}_x^{(n-1)/[2(n+1)(n+2)]}}{\mathrm{Pr}_x} \tag{7}$$

where

$$\mathrm{Gr}_x=\left(\frac{\rho}{K}\right)^2 x^{n+2}[g\beta_o\Delta T_w]^{2-n}=X^{n+2}$$

$$\mathrm{Pr}_x=\frac{\rho C_p}{k}\left(\frac{K}{\rho}\right)^{\frac{2}{n+1}} x^{\frac{(n-1)}{2(n+1)}}[g\beta\Delta T_w]^{\frac{3(n-1)}{2(n+1)}}$$

the governing equations read

$$\frac{\partial U}{\partial X}+\frac{\partial V}{\partial Y}=0 \tag{8}$$

$$\frac{\partial U}{\partial \tau}+U\frac{\partial U}{\partial X}+V\frac{\partial U}{\partial Y}=\theta+\frac{\partial}{\partial Y}\left[\left|\frac{\partial U}{\partial Y}\right|^{n-1}\frac{\partial U}{\partial Y}\right] \tag{9}$$

$$\frac{\partial \theta}{\partial \tau}+U\frac{\partial \theta}{\partial X}+V\frac{\partial \theta}{\partial Y}=\frac{1}{\mathrm{PR}}\frac{\partial^2\theta}{\partial Y^2} \tag{10}$$

Of basic interest are the velocity and temperature fields, as well as the Nusselt number in space and time. Starting with the definition of the local Nusselt number, we can derive a generalized Nusselt number and a dimensionless heat transfer group for vertical free convection of non-Newtonian fluids, $n \lesseqgtr 1$.

$$\mathrm{Nu}_x=-\frac{(\partial T/\partial y)|_{y=0}x}{\Delta T_w}=-\frac{\partial\theta}{\partial y}x\Big|_{y=0}$$

$$=-\frac{\partial\theta}{\partial Y}\Big|_{Y=0}x\left(\frac{\rho}{K}\right)^{\frac{-2}{n+2}}[g\beta_o\Delta T_w]^{(2-n)/(n+2)}$$

$$=-\frac{\partial\theta}{\partial Y}\Big|_{Y=0}X \tag{11}$$

Alternatively, a heat transfer grouping can be defined as

$$\frac{\mathrm{Nu}_x}{\mathrm{Gr}_x^{1/2(n+1)}}=-\frac{\partial\theta}{\partial Y}\Big|_{Y=0}\frac{n}{X^{2(n+1)}} \tag{12}$$

Equations (9)–(11) are approximated using an explicit finite difference method with upwind differences for the convection terms. The heat equation is actually a mixed parabolic-hyperbolic equation, i.e., initial-valued in both X and τ and boundary-valued in Y. Experience indicates (see Isenbert and DeVahl Davis, 1975) that fully explicit schemes for this type of conduction-convection process are very insensitive to singularities such as they occur at $\tau = X = 0$ and when $\partial U/\partial\tau$ and $\partial\theta/\partial\tau$ change sign. Nevertheless, especially the shear stress term in the momentum equation required careful treatment for the cases $n \leq 1.0$. The explicit finite difference approximation of

$$\delta^k_{i,j}=\left\{\frac{\partial}{\partial Y}\left[\left|\frac{\partial U}{\partial Y}\right|^{n-1}\frac{\partial U}{\partial Y}\right]\right\}^k_{i,j}$$

can be written, using the product rule, as

$$\delta^k_{i,j}=\left[\frac{|S_{i,j+}|^{n-1}-|S_{i,j-}|^{n-1}}{\Delta Y}S_{i,j+}\right.$$

$$\left.+|S_{i,j+}|^{n-1}\frac{U_{i,j+1}-2U_{i,j}+U_{i,j-1}}{\Delta Y^2}\right]^k \tag{13}$$

Table 1 Effect of power-law index n on mesh density and time step near leading edge

n and PR	No. of mesh points $N_x \times N_y$	Time step $\Delta\tau$	HTG at $X=1.0$ $\mathrm{Nu}_x/\mathrm{Gr}_y^{1/2(n+1)}$
0.8	30×40	0.005	1.37
and	30×50	0.005	1.39
100	30×60*	0.005*	1.40
0.8	30×50	0.005	1.74
and			
300	40×70*	0.004*	1.82
	15×25	0.04	2.02
1.2	20×30	0.04	2.25
and	25×35	0.04	2.25
300	30×40	0.04	unstable
	30×40*	0.03*	2.28

*Mesh density and time step selected for specific case (see Table 2).

Table 2 Values of steady-state heat transfer group $\mathrm{Nu}_x/\mathrm{Gr}^{1/2(n+1)}$ at $X = 1.0$ compared to measured data points

n	PR	This work	Shenoy and Ulbrecht (1979)
0.8	100	1.40	1.47
	300	1.82	1.81
	500	2.05	2.04
1.0	100	1.58	1.55
	300	2.05	2.11
1.2	10	0.90	0.94
	100	1.74	1.71
	300	2.28	2.28
	500	2.56	2.61

where

$$S_{i,j+}=\frac{U_{i,j+1}-U_{i,j}}{\Delta Y} \text{ and } S_{i,j-}=\frac{U_{i,j}-U_{i,j-1}}{\Delta Y}$$

Here δ is the dimensionless shear stress and S is the slope of velocity U with respect to Y.

By setting $S \equiv 1$ when U reaches the maximum or becomes zero at the boundary-layer edge, the characteristics of Newtonian fluids ($n = 1.0$) are preserved and possible computational difficulties due to singular parabolic effects are resolved.

Since an analytic approach for the nonlinear problem is not available, a trial and error procedure was required for determining the local mesh density, the number of grid points, and the maximum time step. As expected, the finite difference grid is a function of the power-law index n and the non-Newtonian Prandtl number PR, i.e., the type of power-law fluid considered (Table 1). The mesh has to be very fine near the leading edge and can gradually turn downstream into a coarser grid. The allowable time step is directly related to the local mesh size and hence to the power-law index n, in order to preserve numerical stability. To keep the program relatively simple, we selected a fine, uniform mesh which differs with n and PR for the domain $0 \leq X \leq 1.0$ and $0 \leq Y \leq 10$, and then, farther downstream, a realtively coarse, uniform mesh independent of n. The local mesh dependence on n is illustrated in Table 1 using the steady-state value of the local heat transfer group as a criterion. For the coarse mesh of extent $1 < X < 50$ and $0 \leq Y \leq 25$, 25×50 nodal points and $\Delta\tau = 0.025$ were sufficient for all types of power-law fluids. In general, further mesh refinement did not alter the results measurably. Nevertheless, for more complex studies of convection heat transfer in non-Newtonian fluids a compromise between model accuracy and computer requirements can be achieved by employing (unique) transformations for the governing equations and an implicit finite difference scheme

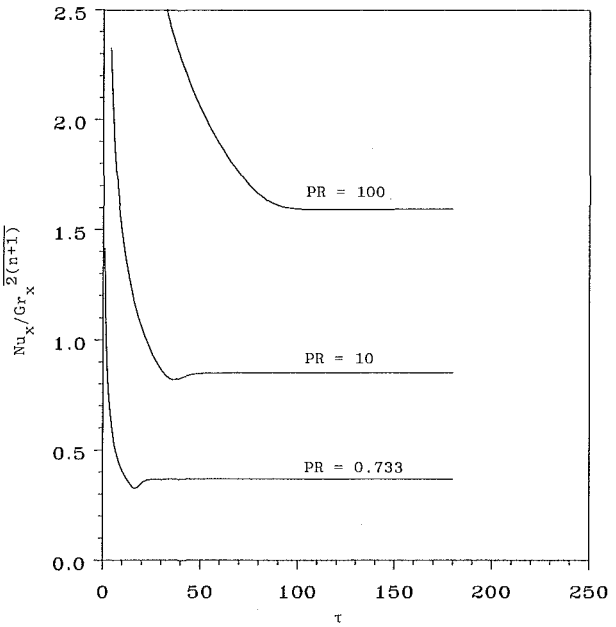

Fig. 1 Transient Nusselt number for various Newtonian fluids ($X = 50$)

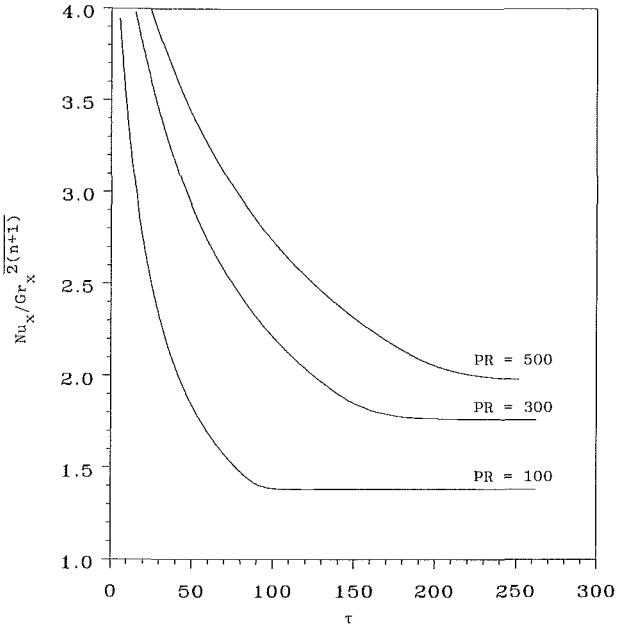

Fig. 2 Transient Nusselt number for pseudoplastic fluid ($n = 0.8$) of Prandtl numbers PR = 100, 300, and 500 ($X = 50$)

with nonuniform mesh generator for the numerical solution (see Wang and Kleinstreuer, 1987, 1988).

For the present code, the principal variables, U, V, and θ, are initialized, time is advanced one step and at this quasi-steady state, the solution front is advanced in the X-direction starting at $X = 0$. At every new X-station, all variables are computed outward from the wall.

Results and Discussion

Table 2 summarizes the steady-state computer predictions as compared with measured data sets (Shenoy and Ulbrecht, 1979) for fluids with a power-law index of $n = 0.8$, 1.0, and 1.2. In addition, the temporal changes in the local heat transfer group (HTG) were compared with accepted data for Newtonian fluids.

Figure 1 shows HTG at station $X = 50$ as a function of dimensionless time. The local steady-state value of HTG is 0.365 for air, which compares very well with numbers obtained by Ostrach (1953) or Hellums and Churchill (1962). The minimum in the transient Nusselt number distribution is directly related to the maxima in the dimensionless velocity and temperature profiles, $U(\tau)$ and $\theta(\tau)$. This minimum, here $\mathrm{Nu}_x\mathrm{Gr}^{-1/2(n+1)} = 2.4$, signals the end of the so-called initial (pure) conduction period when the transient terms in the momentum and heat transfer equations change sign. Somewhat higher values for t_{crit}, the time of occurrence of the extrema, were obtained by others, e.g., Nanbu (1971) or Goldstein and Briggs (1964), who presented approximate solutions. Indeed, we approached Nanbu's value, i.e., $t_{crit} \approx 2.916$, when we ran our program without the inertia terms, $(\mathbf{v} \cdot \nabla)\mathbf{v}$, in equation (10). When the Prandtl number is increased, the minimum point in the transient Nusselt number is delayed and the undershoot vanishes for very high Prandtl numbers, e.g., heavy oils (see Fig. 1). This trend is consistent with the expectation that t_{crit} increases for slower moving, more viscous fluids (Rahman and Carey, 1986). The local steady-state values of HTG for high Prandtl numbers (PR $\geq$ 16; $n = 1.0$) compare well with the corresponding results given, for example, by Carey (1983).

As can be seen from Table 2, predicted values and measurements (Shenoy and Ulbrecht, 1979) of the steady-state (local) heat transfer group compare quite well for power-law fluids ($n = 0.8$ and 1.2) of different non-Newtonian Prandtl

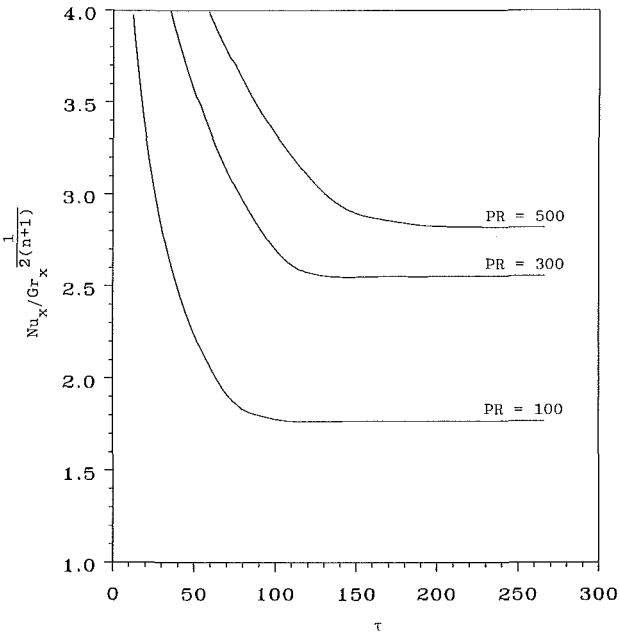

Fig. 3 Transient Nusselt number for dilatant fluid ($n = 1.2$) of Prandtl numbers PR = 100, 300, and 500 ($X = 50$)

numbers. Figures 2 and 3 show the transient Nusselt numbers for two different polymeric liquids, i.e., with a power-law index of $n = 0.8$ and $n = 1.2$, respectively. As can be expected, dilatant fluids that exhibit a shear thickening behavior generate consistently higher Nusselt numbers, especially at large Prandtl numbers. Industrial applications of different power-law fluids are discussed in Bird et al. (1977). In contrast to typical Newtonian fluids, this generalized Prandtl number of power-law fluids is much larger and hence the undershoot in $\mathrm{Nu}(\tau)$ tends to disappear for PR $>$ 100. As a result, the singular parabolic effects are less influential for most polymeric liquids.

References

Bird, R. B., Armstrong, R. C., and Hassager, O., 1977, *Dynamics of Polymeric Liquids*, Vol. 1, Wiley, New York.

Carey, V. P., 1983, "Analysis of Transient Natural Convection Flow at High Prandtl Number Using a Matched Asymptotic Expansion Technique," *Int. J. Heat and Mass Transfer*, Vol. 26, pp. 911–919.

Goldstein, R. J., and Briggs, D. G., 1964, "Transient Free Convection About Vertical Plates and Circular Cylinders," ASME JOURNAL OF HEAT TRANSFER, Vol. 86, pp. 490–500.

Hellums, J. D., and Churchill, S. W., 1962, "Transient and Steady-State Free and Natural Convection, Numerical Solutions," *AIChE J.*, Vol. 8, pp. 690–965.

Isenbert, J., and DeVahl Davis, G., 1975, "Finite Difference Methods in Heat and Mass Transfer," in: *Topics in Transport Phenomena*, C. Gutfinger, ed., Hemisphere Publ. Corp., Washington.

Kawase, Y., and Ulbrecht, J. J., 1984, "Approximate Solution to the Natural Convection Heat Transfer From a Vertical Plate," *Int. Comm. Heat Mass Transfer*, Vol. 11, pp. 143–155.

Kleinstreuer, C., Wang, T.-Y., and Haq, S., 1987, "Free Convection Heat Transfer Between a Permeable Vertical Wall and a Power-Law Fluid," 24th ASME/AIChE National Heat Transfer Conference, Pittsburgh, PA, Paper No. NH-4.

Nanbu, K., 1971, "Limit of Pure Conduction for Unsteady Free Convection on a Vertical Plate," *Int. J. Heat Mass Transfer*, Vol. 14, pp. 1531–1534.

Ostrach, S., 1953, "An Analysis of Laminar Free Convection Flow and Heat Transfer About a Flat Plate Parallel to the Direction of the Generating Body Forces," NACA Report No. 1111.

Rahman, M. M., and Carey, V. P., 1986, "Steady and Transient Mixed Convection Near a Vertical Uniformly Heated Surface Exposed to Horizontal Fluid Flow," *Num. Heat Transfer*, Vol. 10, pp. 327–347.

Shenoy, A. V., and Ulbrecht, J. J., 1979, "Temperature Profiles for Laminar Natural Convection Flow of Dilute Polymer Solutions Past an Isothermal Vertical Flat Plate," *Chem. Eng. Commun.*, Vol. 3, pp. 303–324.

Shenoy, A. V., and Mashelkar, R. A., 1982, "Thermal Convection in Non-Newtonian Fluids," *Adv. in Heat Transfer*, Vol. 15, pp. 143–225.

Wang, J. C. T., 1985, "Renewed Studies on the Unsteady Boundary Layers Governed by Singular Parabolic Equations," *J. Fluid Mech.*, Vol. 155, pp. 413–427.

Wang, T.-Y., and Kleinstreuer, C., 1987, "Free Convection Heat Transfer Between a Permeable Vertical Wall and a Power-Law Fluid," *Numerical Heat Transfer*, Vol. 12, pp. 367–379.

Wang, T.-Y., and Kleinsteuer, C., 1988, "Combined Free-Forced Convection Heat Transfer Between Vertical Slender Cylinders and Power-Law Fluids," *Int. J. Heat and Mass Transfer*, Vol. 31, No. 1, pp. 91–98.

Williams, J. C., Mulligan, J. C., and Rhyne, T. B., 1987, "Semi-similar Solutions for Unsteady Free-Convection Boundary Layer Flow on a Vertical Flat Plate," *J. Fluid Mech.*, Vol. 175, pp. 309–332.

Flow Visualization Studies on Vortex Instability of Natural Convection Flow Over Horizontal and Slightly Inclined Constant-Temperature Plates

K. C. Cheng

Y. W. Kim

Department of Mechanical Engineering,
University of Alberta,
Edmonton, Alberta, Canada T6G 2G8

Flow visualization experiments were performed in a low-speed wind tunnel to study vortex instability of laminar natural convection flow along inclined isothermally heated plates having inclination angles from the horizontal of $\theta = 0$, 5, 10, 15 and 20 deg. The temperature difference between plate surface and ambient air ranged from $\Delta T = 15.5$ to 37.5°C and the local Grashof number range was $Gr_x = 1.02 \times 10^6$ to 2.13×10^8. Three characteristic flow regimes were identified as follows: a two-dimensional laminar flow, a transition regime for developing longitudinal vortices, and a turbulent regime after the breakdown of the longitudinal vortices. Photographs are presented of side and top views of the flow and of cross-sectional views of the developing views of the developing secondary flow in the postcritical regime. Instability data of critical Grashof number and wavelength are presented and are compared with the theoretical predictions from the literature.

1 Introduction

The problem of natural convection flows along inclined plates, with thermal boundary conditions of constant wall temperature or uniform wall heat flux, has been studied both theoretically and experimentally in the past because of its importance for various technical applications. When a natural convection flow is induced by heating from below over a horizontal or slightly inclined plate having a constant wall temperature, the flow is potentially unstable because of a top-heavy situation (unstable density distribution). The convective instability occurs if the destabilization caused by buoyancy is large enough to overcome the stabilizing effects of viscous and thermal diffusion.

The occurrence of longitudinal vortices or rolls in natural convection boundary-layer flows along inclined isothermal surfaces was clearly established by Sparrow and Husar (1969) using a flow visualization technique, where the flow pattern was made visible by local changes of the fluid color due to changes in pH. Subsequently, instability data for natural convection flows on inclined isothermal plates were also obtained by Lloyd and Sparrow (1970) and Lloyd (1974). These experimental investigations have motivated a series of linear stability studies on the onset of longitudinal vortices in natural convection flow along inclined surfaces. In this connection, one may mention the linear stability analyses by Haaland and Sparrow (1973a), Hwang and Cheng (1973), and Kahawita and Meroney (1974). Wave instability analysis was also presented by Lee and Lock (1972), Haaland and Sparrow (1973b), and Pera and Gebhart (1973a). Iyer and Kelly (1974) studied both wave and vortex modes of instability for a heated inclined plate. Recently, both vortex and wave instability analysis results were presented by Chen and co-workers (1982, 1985) for natural convection flow on inclined isothermal surfaces. Hsu and Cheng (1979) also carried out vortex instability analysis for buoyancy-induced flows over inclined heated surfaces in porous media.

It is now well established that in the range of inclination angles from the horizontal, $\theta = 0$ to 73 deg, vortex instability has priority over wave instability, while the opposite is true for a vertical plate. Experimental instability data for the onset of longitudinal vortices are rather limited for the inclination angle range $\theta = 0$ to 25 deg.

Heat transfer results for free convection over inclined plates have been reported by many investigators. The pertinent literature includes recent works by Rotem and Claassen (1969a), Fujii and Imura (1972), Pera and Gebhart (1973b), Ackroyd (1976), Chen and Tzuoo (1982), and Yousef et al. (1982). The appearance of longitudinal vortices in free convection flow over inclined surfaces near the horizontal represents the first stage of the laminar-turbulent transition process. This is in contrast to Tollmien–Schlichting waves as the first stage of transition for natural convection on a vertical plate. After the onset of longitudinal vortices, the flow field becomes three dimensional, and two-dimensional free convection boundary-layer theory is not strictly applicable.

The natural convection heat transfer on horizontal or nearly horizontal surfaces has not been studied as extensively as for vertical surfaces. The Schlieren pictures of the temperature fields near various heated objects obtained by Schmidt (1932) provide considerable physical insight into the physical phenomena of natural convection. Interference photographs were used by Eckert and Soehngen (1951) to study laminar and turbulent free convection on a vertical plate. Flow visualization photographs reveal the whole flow field and provide considerable physical insight in understanding the free convection phenomena. Flow visualization was also used extensively by Prandtl (1927) in his investigations of fluid motion.

The occurrence of longitudinal vortices in the boundary layer along a concave wall was first shown by Görtler (1940). The related centrifugal instability problems have subsequently been studied by many investigators. The analogy between centrifugal and thermal instability problems is well known, and it

Contributed by the Heat Transfer Division for publication in the JOURNAL OF HEAT TRANSFER. Manuscript received by the Heat Transfer Division April 18, 1986. Paper No. 86-WA/HT-85. Keywords: Flow Instability, Flow Visualization, Natural Convection.

is interesting to compare the flow visualization results from this study with those of Görtler vortices. Chandra (1938) conducted flow visualization studies on thermal instability of a horizontal air layer heated from below, using cigarette smoke; for the case with shear longitudinal rolls were observed. The vortex instability problem also arises when a laminar boundary layer is heated from below. This problem was studied by Wu and Cheng (1976), Gilpin et al. (1978), Takimoto et al. (1983), and Moutsoglou et al. (1981), among others.

The purpose of this paper is to present flow visualization photographs for the onset and subsequent development of longitudinal vortex rolls for natural convection flow along inclined constant temperature rectangular plates at inclination angles $\theta = 0$, 5, 10, 15, and 20 deg. The flow visualization was realized by a smoke injection method. The experiments were conducted in a low-speed suction type wind tunnel specifically designed for convective heat transfer and flow visualization studies, but the fan was not used. Instability data for the critical Grashof number and wavelength were obtained and compared with the experimental and theoretical results from the literature.

2 Apparatus and Experimental Procedure

2.1 Wind Tunnel and Isothermal Heating Plate Assembly. The flow visualization experiments were performed in a wind tunnel that can be tilted at an inclination angle from the horizontal about the lateral axis located at the center of the tunnel body. The height of the tunnel body can be adjusted. Schematic diagrams of the wind tunnel, the constant-temperature plate with auxiliary equipment, and a smoke generator with its injection device, are shown in Fig. 1. The tunnel test section had a 30.6×30.6 cm cross section and was 247 cm long. The test surface was fabricated from a copper plate having a width of 24.1 cm, a length of 152.4 cm, and a thickness of 6.35 mm. The test plate was installed as the bottom surface of the test section with the leading edge of the plate placed flush with the end of the contraction section. Except for the bottom, the test section was made of acrylic resin plates in order to permit a visual investigation of the flow.

The constant wall temperature condition was provided by water from a hot water tank circulating at high speed through a channel attached to the bottom surface of the test plate. The isothermal plate condition can be approached by high-Biot-number flow between heating fluid and a flat plate. At lower temperature levels, the wall temperature remained practically constant during a complete run due to the large capacity of the hot water tank. At wall temperature levels higher than 50°C, a maximum temperature drop of 1°C was observed during the course of a complete run. It should be pointed out that for the present natural convection experiments the fan shown in Fig. 1(*a*) was not in use and the boundary-layer flow over the entrance section in the converging nozzle was not observed.

2.2 Wall Temperature Measurements. The wall temperature measurements were made by four 0.3-mm-dia copper-constantan thermocouples installed at four locations along the side edges of the test plate. The thermocouples were installed in a 1 mm deep depression and covered with aluminum epoxy. The four readings essentially agreed within

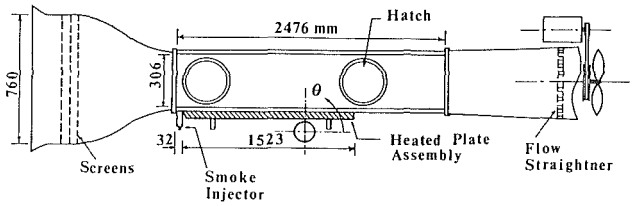

(a)

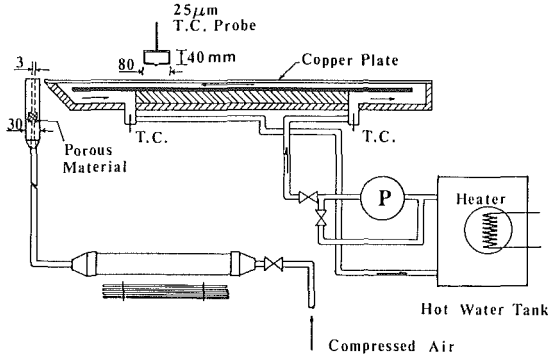

(b)

Fig. 1 Schematic diagrams for (a) wind tunnel test facility and (b) constant-temperature plate and auxiliary equipment

the calibration error of the thermocouples once steady-state conditions were reached. The inlet and outlet temperatures of the circulating hot water were also monitored by two 0.8 mm iron-constantan sheathed thermocouples (see Fig. 1). The difference between the two readings was less than 0.2°C for all temperature levels. The wall temperature was always lower than the heating water temperature, up to a maximum of 1°C, decreasing at lower water temperature levels.

The ambient air temperature was measured using a 25 μm copper-constantan thermocouple. The thermocouple junction was made by butt-welding to produce an effective junction diameter of around 50 μm. The probe was positioned within an accuracy of 1/50 mm using a traversing mechanism. All thermocouples were calibrated in a constant temperature bath against a laboratory grade digital thermometer.

2.3 Flow Visualization Technique and Photographic Arrangement. Smoke for visualization was generated by burning paper sticks in a 55 mm o.d. copper tube, which was connected to the room compressed air. The smoke was then injected through a small slot-type smoke injector along the leading edge of the heated test plate. The temperature of the injected smoke was confirmed to be close to the room temperature. The setup is shown in detail in Fig. 1.

The transverse cross-sectional views of the developing secondary flow were recorded by a camera, through a mirror placed near the end of the test plate having an angle of 45 deg to the direction of the main flow. The secondary flow was made visible by a sheet of light produced from a 1.5 kW

Nomenclature

Gr_x^* = local Grashof number $= g\beta(T_w - T_\infty)x^3/\nu^2$
Gr_x = $\cos\theta\ \mathrm{Gr}_x^*$
g = gravitational acceleration
T_w, T_∞ = constant wall temperature and ambient air temperature
x = distance from leading edge of a heated plate
x_c = critical distance x at the onset of vortex rolls
β = coefficient of thermal expansion
θ = inclination angle from horizontal direction
ν = kinematic viscosity
σ = standard deviation
$\Delta T = T_w - T_\infty$

Table 1 Ranges of experimental parameter

θ	=	0, 5, 10, 15, 20 deg
T_w	=	34.0 to 57.6°C
ΔT	=	$T_w - T_\infty = 15.5$ to 37.5°C
Gr_x	=	1.02×10^6 to 2.13×10^8

halogen slit light source. The mushroomlike counterrotating vortices were recorded by a camera pointed toward the mirror placed at 45 deg from the test plate at a downstream location.

2.4 Measurements of the Onset of Instability. The onset point of the vortex rolls was determined by carefully observing changes in the cross-sectional flow pattern as the slit light source was moved in the downstream direction. The region of two-directional laminar flow along the plate was first confirmed. Proceeding farther downstream, the critical distance x_c from the leading edge of the heated plate was recorded after detecting the onset of cellular motion. The above procedure was repeated several times to obtain a single data point. The experimental data could be reproduced within a distance of 1 cm.

3 Experimental Parameters

The experimental parameters for this investigation are an inclination angle measured from the horizontal θ, the constant wall temperature T_w, the wall-to-ambient temperature difference ΔT, and the local Grashof number Gr_x. The ranges of these parameters are given in Table 1.

4 Results and Discussion

4.1 Horizontal Plate. The experiments were conducted in a wind tunnel and the results should be interpreted in this light. The present study was mainly concerned with vortex instability phenomena in the region from the leading edge $x=0$ to 50 cm while the adjoining surfaces near both ends of the test plate (24.1 cm × 152.4 cm) can be regarded to be adiabatic. It should be pointed out that the natural convection flow is predominantly in the streamwise direction with plume rising at the center for the present rectangular plate with length/width = 6.32.

Photos depicting the side and top views of the developing longitudinal vortices in natural convection flow along the horizontal isothermal plate with $T_w = 51.8$°C and $T_\infty = 21.0$°C are shown in Fig. 2. At the distances from the leading edge $x=10$, 20, 30, 40, and 50 cm, the corresponding values for local Grashof number are $\mathrm{Gr}_x = 3.54\times10^6$, 2.83×10^7, 9.55×10^7, 2.26×10^8, and 4.42×10^8, respectively. At the onset of vortex instability at $x=7$ cm ($\mathrm{Gr}_x = 1.21\times10^6$), the longitudinal vortices develop rather quickly, and then the flow becomes turbulent in the range $x \geq 40$ cm. The corresponding top view shows the smoke tracer lines (seven lines), which represent the upwash flow in each pair of counterrotating vortex rolls. These lines also show the approximate locations of the start of formation of longitudinal vortices and the eventual breakup.

Cross-sectional views of the secondary flow at different axial positions are shown in Fig. 3 for $\theta = 0$ deg and $\Delta T = 30.8$°C. At $x=9$ cm cellular motion has already appeared and one sees clearly the embryo of the growing longitudinal vortices. The two mushroom-type vortices at both ends might be caused by disturbances due to smoke injection. At $x=15$ cm six pairs of vortices are quite stable. At $x=20$ cm, each vortex pair is seen to be of about the same size. Although not shown here, at other times three pairs of vortices are seen to be much taller than the neighboring pairs for the same run. At $x=25$ and 30 cm, the different height of each vortex pair is of interest. At $x=35$ cm, the secondary flow is seen to be unstable and the

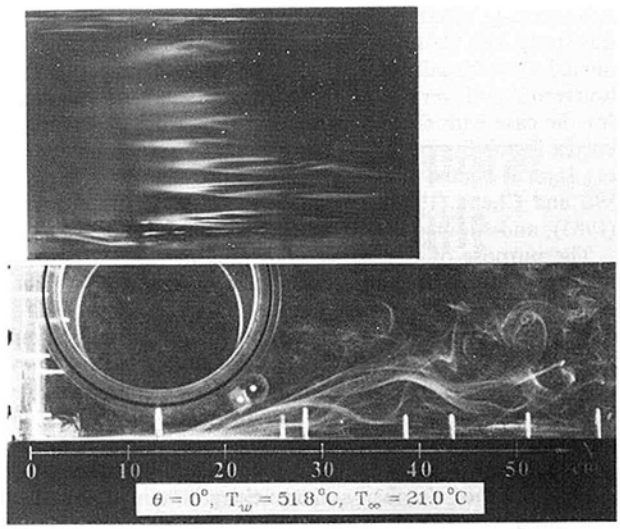

Fig. 2 Top and side views of developing longitudinal vortices for $\theta = 0$ deg, $T_w = 51.8$°C, and $T_\infty = 21.0$°C

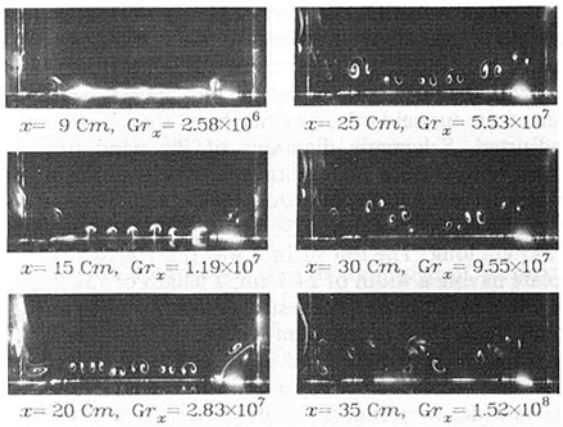

Fig. 3 Cross-sectional views of secondary flow patterns for $\theta = 0$ deg, $\Delta T = 30.8$°C

vortex pairs oscillate sidewise. Figure 3 shows the developing region of longitudinal vortices. From Figs. 2 and 3, one may distinguish three flow regimes consisting of two-dimensional laminar flow, three-dimensional developing flow for longitudinal vortices in the postcritical regime, and turbulent flow. One is impressed with the complex flow patterns for natural convection flow along a horizontal isothermal plate. Within the scope of this investigation, a flow separation phenomenon (Pera and Gebhart, 1973b) was not observed.

The effect of the temperature difference $\Delta T = T_w - T_\infty$ on developing secondary flow pattern of vortex rolls is of interest. Photos are shown in Figs. 4(*a*), 4(*b*), 4(*c*), and 4(*d*) for $\Delta T = 21.7$, 25.0, 30.8, and 37.5°C, respectively. The destabilizing effect of ΔT is clearly seen from the secondary flow patterns at $x=15$ cm. At large ΔT such as 37.5°C, a destabilizing trend due to non-Boussinesq effects may exist. The onset of vortex instability occurs at smaller values of x or Gr_x, and the average wavelength tends to decrease significantly as the value of ΔT increases. In Fig. 4, the developing secondary flow pattern is also of special interest for each ΔT. The temperature dependence of wavelength observed in this study for $\theta = 0$ deg was not as prominent as that observed by Sparrow and Husar (1969) for inclined plates using water. However, a Prandtl number effect may exist.

4.2 Inclined Plate (0 deg $< \theta \leq$ 20 deg). The overall top and side views of developing longitudinal vortices in a natural

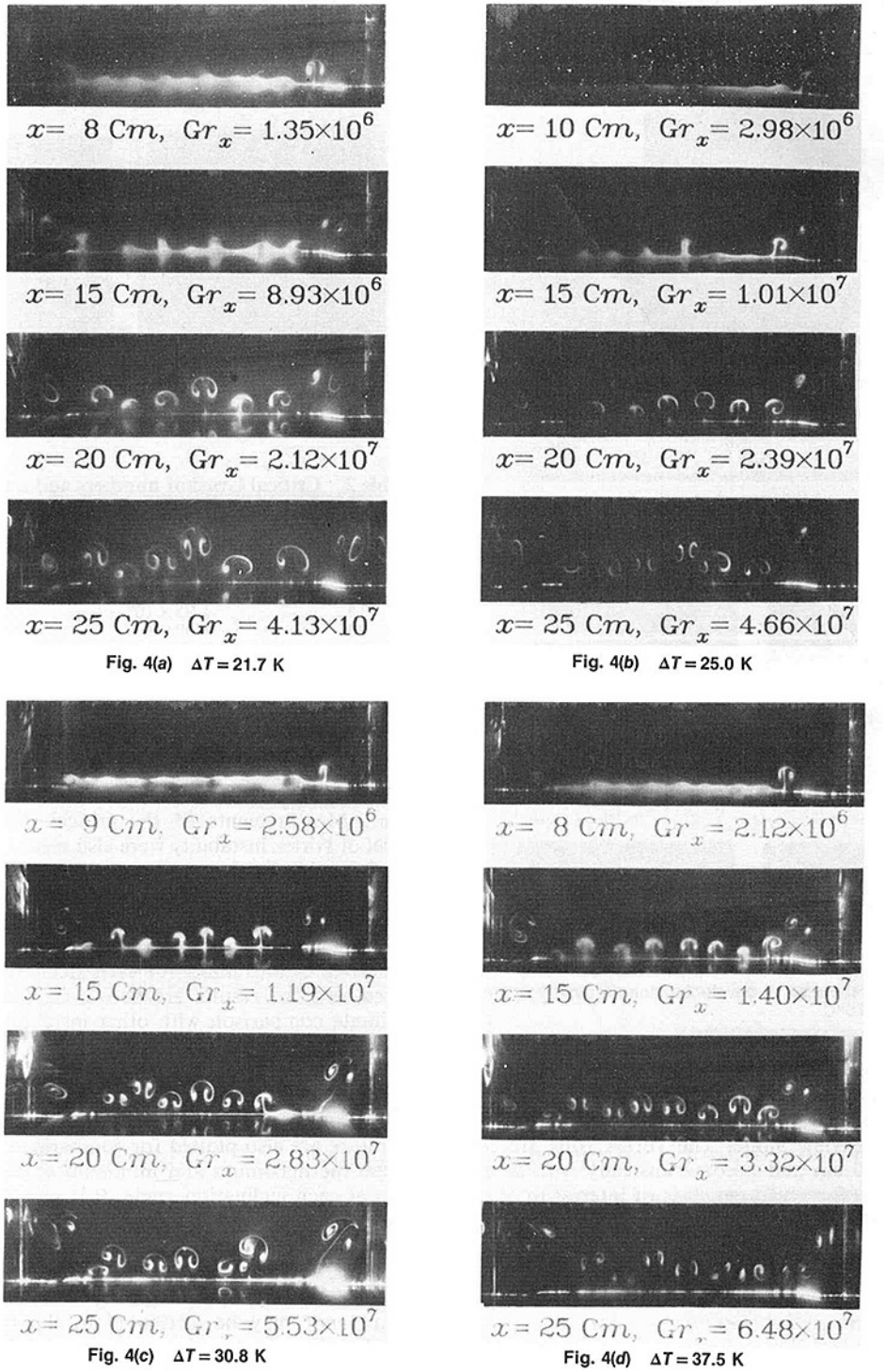

Fig. 4(a) $\Delta T = 21.7$ K

Fig. 4(b) $\Delta T = 25.0$ K

Fig. 4(c) $\Delta T = 30.8$ K

Fig. 4(d) $\Delta T = 37.5$ K

Fig. 4 Effect of ΔT on secondary flow pattern for $\theta = 0$ deg

convection flow are shown in Fig. 5 for $\theta = 15$ deg and $\Delta T = 15.5°C$. The side view shows the general flow field and one may again distinguish three flow regimes, a two-dimensional laminar flow for $x = 0$ to 10 cm, a transition regime with developing longitudinal vortices for $x = 10$ to 35 cm, and a turbulent regime with the eventual breakdown of the longitudinal vortices for $x \geq 35$ cm. For $x \geq 40$ cm, the smoke rises as plume. For the side view photo, it is of interest to note that at $x = 10$, 20, 30, 40, and 50 cm, the values for Gr_x are 1.99×10^6, 1.59×10^7, 5.36×10^7, 1.27×10^8, and 2.48×10^8, respectively. Thus, the effect of Gr_x on flow pattern can also be seen. The top view reveals seven smoke tracer lines showing the approximate locations of the beginning and the breakdown of the developing longitudinal vortices. The lines indicated meandering motion with amplification of the longitudinal vortices in the main flow direction.

Cross-sectional views of the developing longitudinal vortices in the postcritical regime for $\theta = 15$ deg and $\Delta T = 15.5°C$ are shown in Fig. 6. The beginning stage of the formation of longitudinal vortices is characterized by cellular motion. The

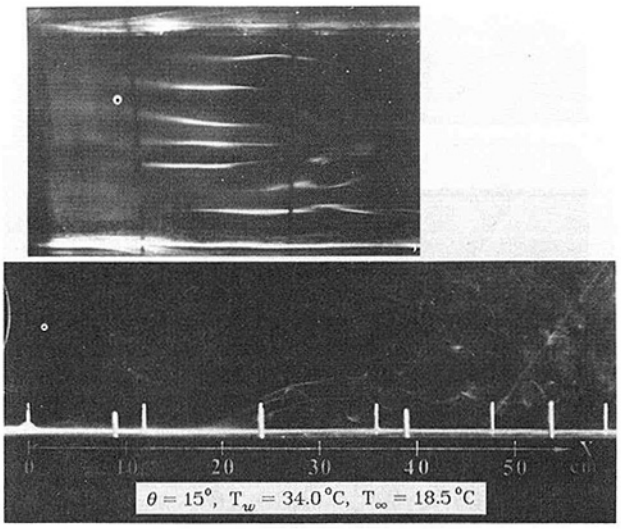

Fig. 5 Top and side views of developing longitudinal vortices for $\theta = 15$ deg and $\Delta T = 15.5°C$

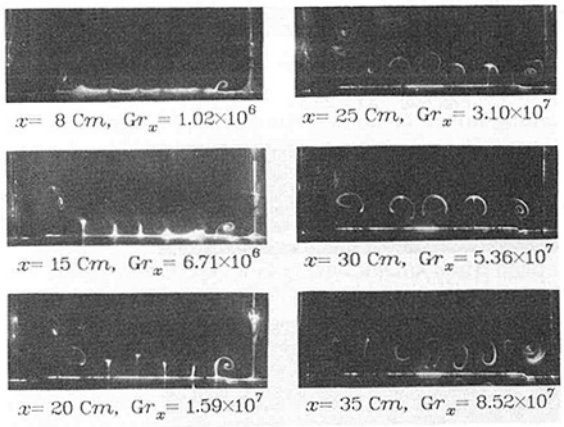

Fig. 6 Cross-sectional views of developing longitudinal vortices for $\theta = 15$ deg and $\Delta T = 15.5°C$

more or less periodic disturbances in the transverse cross section provide a fairly good indication of the onset point of the vortex instability, in contrast to some uncertainty from observations of the side view alone. The vortex rolls are fairly steady up to $x = 20$ cm and become unsteady with sidewise meandering motion for $x > 25$ cm. It is of interest to observe the varying pitch (wavelength) between two neighboring counterrotating vortex rolls with increasing distance from the leading edge. Photographic results for $\theta = 20$ deg, $\Delta T = 23.1°C$, are also shown in Fig. 7. Unsteady motion can be seen for $x > 35$ cm.

Developing secondary flow patterns at five different inclination angles are shown in Figs. 8(*a*)-(*e*) for $\theta = 0$, 5, 10, 15, and 20 deg, respectively, with $\Delta T = 18.3$–$19.4°C$ and $x = 10$, 15, 20, and 25 cm. The photos are at identical downstream locations and facilitate a direct comparison of the developing secondary flow patterns at different inclination angles. By observing the flow patterns at $x = 10$ cm, one can see clearly that the onset point of vortex instability is gradually being delayed as the inclination angle increases from the horizontal. This is due to the decreasing buoyancy force component normal to the plate as the inclination angle increases, and can also be seen from the factor $g \cos \theta$. The wavelength of the vortex rolls does not seem to vary significantly with increasing inclination angle. The photos presented provide considerable physical insight into the developing longitudinal vortices in the natural convection flows along inclined isothermal plates. Within the scope

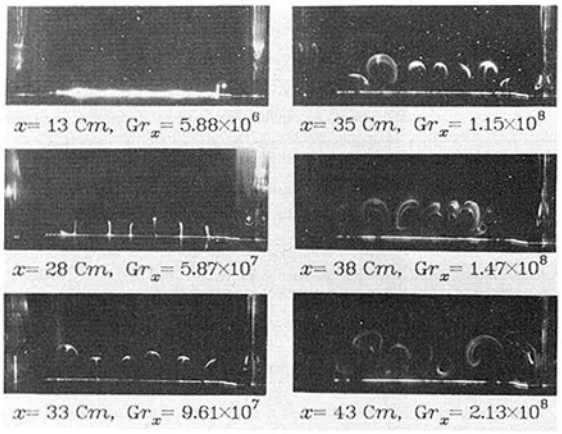

Fig. 7 Developing secondary flow patterns for $\theta = 20$ deg, $\Delta T = 23.1°C$

Table 2 Critical Grashof numbers and standard deviations

θ, deg	Gr_x^*	σ
0	8.86×10^5	2.51×10^5
5	1.03×10^6	6.45×10^5
10	1.53×10^6	7.08×10^5
15	1.95×10^6	1.13×10^6
20	1.02×10^6	1.02×10^6

of the present investigation, the effect of the inclination angle on the wavelength appears to be rather weak. This observation agrees with that of Sparrow and Husar (1969), using water.

4.3 Instability Results and Wavelength Correlation. Measurements of the critical distance marking the onset of vortex instability were also made during the course of the flow visualization study. At each inclination angle, eight or nine independent determinations of the onset point were made, with wall-to-ambient temperature difference ΔT ranging from 15 to 45°C. The mean and standard deviation of the critical Grashof number for each inclination angle were computed and the results are shown in Table 2. In order to facilitate comparison with other instability data, the critical Grashof number Gr_x^* was defined.

The instability data are presented in the form of mean critical Grashof number as a function of inclination angle in Fig. 9. Other theoretical and experimental results from literature are also plotted for comparison. The error bars indicate the maximum and minimum values of the instability data at each inclination angle. It is seen that theory predicts values of critical Grashof number for air ($Pr = 0.7$) over three orders of magnitude lower than those found by the present measurements. The same remark also applies to the instability data of Lloyd and Sparrow (1970) for water ($Pr = 7$). The large discrepancy may be attributed to the fact that the linear stability theory is based on infinitesimal disturbances and the experimental determination of the onset point requires a certain amplification of the formation process. However, the exact reasons for the large discrepancy between theory and experiment remain to be clarified. Apparently, one needs an analytic or numerical technique that can predict the growth of the first linear instabilities through nonlinear growth dynamics to developed longitudinal vortex rolls in order to compare with the present visualization photographs. It is noted that the general trend, as revealed by the slope of the present instability data, is in good agreement with that predicted by theory. The trend of the present data also appears to be in agreement with the air data obtained by Lock et al. (1967) for inclination angles $\theta > 35$ deg.

For a horizontal plate, it is possible to compare the present instability data with those of Rotem and Claassen (1969b).

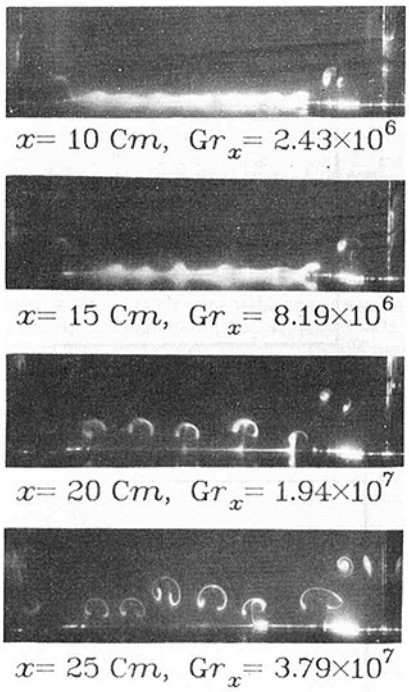

Fig. 8(a) $\theta = 0$ deg, $\Delta T = 19.4$ K

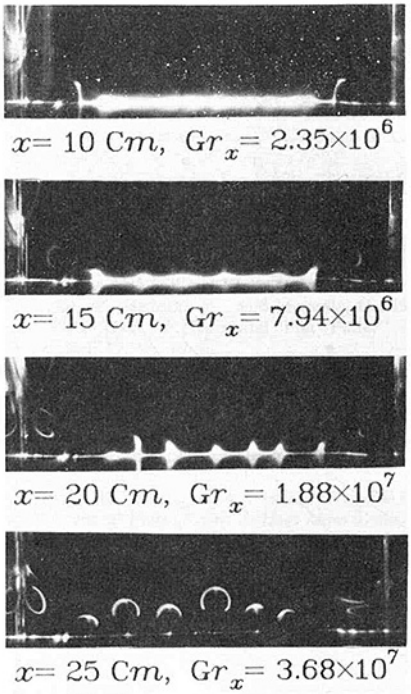

Fig. 8(b) $\theta = 5$ deg, $\Delta T = 19.4$ K

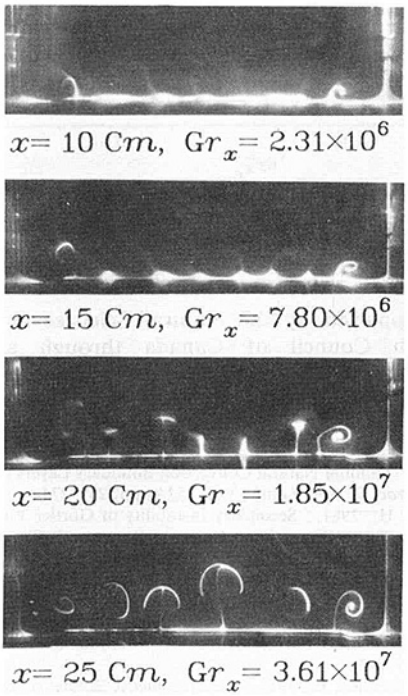

Fig. 8(c) $\theta = 10$ deg, $\Delta T = 18.3$ K

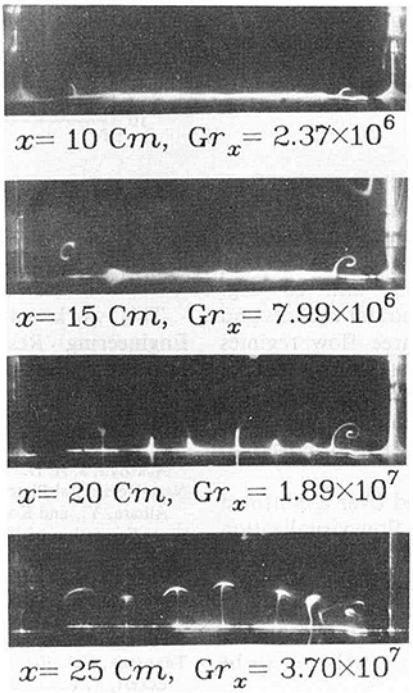

Fig. 8(d) $\theta = 15$ deg, $\Delta T = 19.2$ K

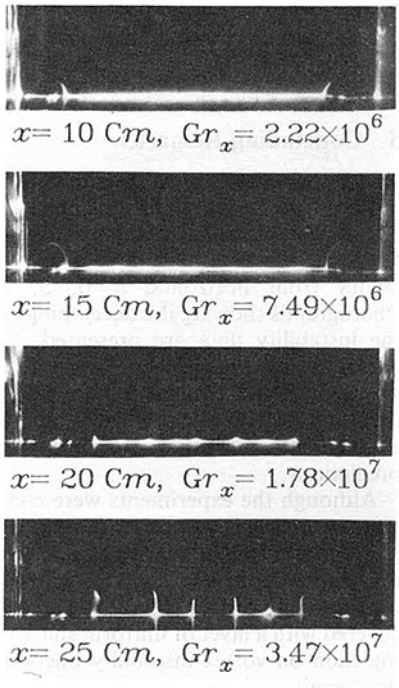

Fig. 8(e) $\theta = 20$ deg, $\Delta T = 19.4$ K

Fig. 8 Effect of inclination angle of developing secondary flow pattern

These results are shown in Fig. 10. The agreement is seen to be satisfactory.

The mean wavelength of the vortex rolls is also of particular interest. Measurements of the wavelength were made directly from photographs of the cross-sectional views using the distance between the two lines in the photos representing the inner walls of the test section as a reference. The wavelengths of vortex rolls at a particular cross section were then averaged to obtain a single data point for the mean wavelength. The results are plotted in Fig. 11 together with theoretical predictions from Chen and Tzuoo (1982). The following correlation equation for wavelength is also obtained:

$$x_c/\lambda = C\mathrm{Gr}_x^{*1/4} \tag{1}$$

where $C = 0.088$ and 0.068 for upper and lower bounds, respectively. It is noted that $\mathrm{Gr}_x^{*1/2}$ may be regarded to be a Reynolds number Re_x based on the characteristic velocity $[g\beta(T_w - T_\infty)x]^{1/2}$. This observation provides a qualitative analogy with forced convection problem, and shows that this class of convective instability phenomena is somewhat analogous.

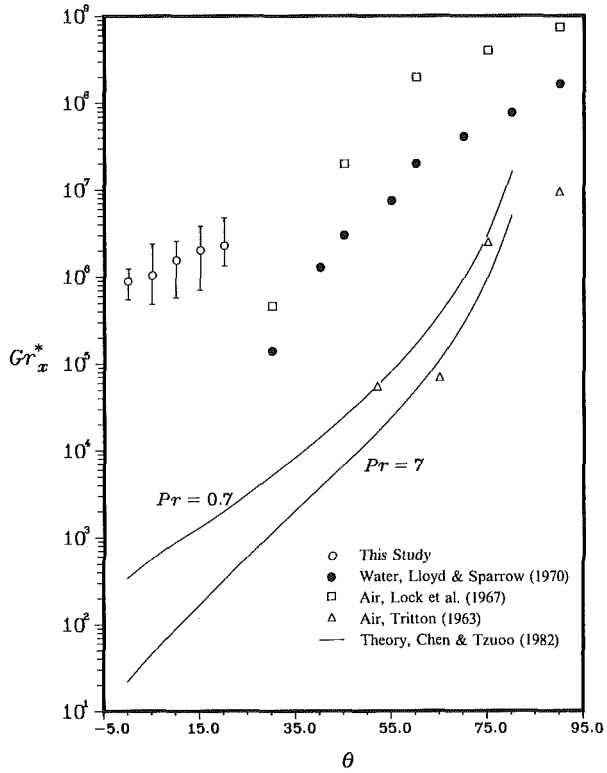

Fig. 9 Variation of critical Grashof number with angle of inclination

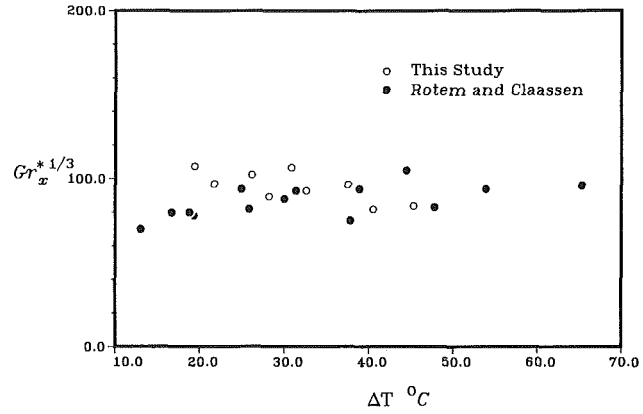

Fig. 10 Critical Grashof number for horizontal plate

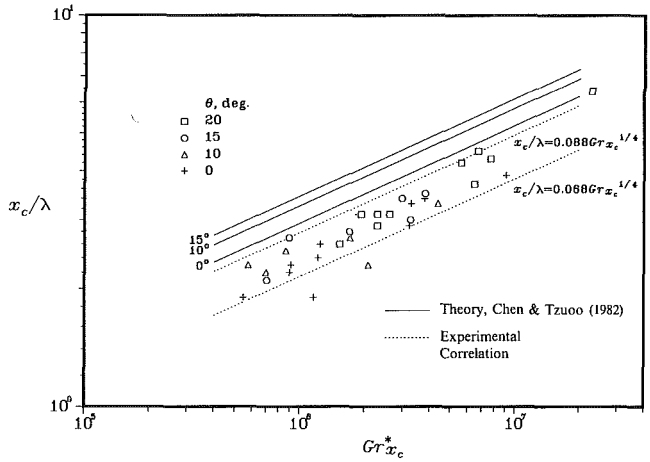

Fig. 11 Correlation for the wavelength of vortex rolls

5 Concluding Remarks

The problem of vortex instability of natural convection flow over horizontal or slightly inclined isothermally heated flat rectangular plates with length/width = 6.32 was studied by a flow visualization technique using smoke for inclination angles from horizontal $\theta = 0$, 5, 10, 15, and 20 deg. Photographs showing the developing longitudinal vortices and the instability data are presented. The three flow regimes characterizing the natural convection flow are shown to be a two-dimensional laminar flow regime, a transition regime for developing longitudinal vortices, and a turbulent regime. The experimental results are compared with theoretical predictions.

Although the experiments were conducted over a confined plate as opposed to an unconfined plate, the flow visualization photographs suggest that entrance, side wall, and edge effects are negligible in the central region of the plate. Without longitudinal vortices (small ΔT), the whole heated plate was covered with a layer of uniform smoke and the effect of smoke injection on vortex instability phenomenon is believed to be very small.

The present vortex instability problem for natural convection flow along an inclined isothermal plate is also somewhat analogous to the centrifugal instability problem for Görtler vortices in the boundary layer along a concave wall. The secondary flow pattern in a cross section normal to the main flow for Görtler vortices, shown in Fig. 4 of Aihara and Koyama (1981), for example, is strikingly similar to the flow patterns observed in this investigation dealing with vortex instability due to buoyancy forces. The flow visualization study provides considerable physical insight into the structure and nature of the developing longitudinal vortices in the transition regime for a natural convection flow heated from below. The problem of transition from laminar to turbulent flow through developing longitudinal vortices apparently needs further investigation.

Acknowledgments

This work was supported by the Natural Sciences and Engineering Research Council of Canada through an operating grant.

References

Ackroyd, J. A. D., 1979, "Laminar Natural Convection Boundary Layers on Near-Horizontal Plates," *Proc. R. Soc. Lond.*, Vol. 352A, pp. 249–274.

Aihara, Y., and Koyama, H., 1981, "Secondary Instability of Görtler Vortices: Formation of Periodic Three-Dimensional Coherent Structure," *Trans. Japan Soc. Aeronautical and Space Sciences*, Vol. 24, pp. 78–94.

Chandra, K., 1938, "Instability of Fluids Heated From Below," *Proc. Roy. Soc.*, Vol. 164A, pp. 231–242.

Chen, T. S., and Tzuoo, K. L., 1982, "Vortex Instability of Free Convection Flow Over Horizontal and Inclined Surfaces," ASME JOURNAL OF HEAT TRANSFER, Vol. 104, pp. 637–643.

Eckert, E. R. G., and Soehnghen, E., 1951, "Interferometric Studies on the Stability and Transition to Turbulence of a Free Convection Boundary Layer," *General Discussion on Heat Transfer*, Institution of Mechanical Engineers, pp. 321–323.

Fujii, T., and Imura, H., 1972, "Natural-Convection Heat Transfer From a Plate With Arbitrary Inclination," *Int. J. Heat Mass Transfer*, Vol. 15, pp. 755–767.

Gilpin, R. R., Imura, H., and Cheng, K. C., 1978, "Experiments on the Onset of Longitudinal Vortices in Horizontal Blasius Flow Heated From Below," ASME JOURNAL OF HEAT TRANSFER, Vol. 100, pp. 71–77.

Görtler, H., 1974, "Uber eine dreidimensionale Instabilitat laminarer Grenzschichten an konkaven Wander," *Nachr. Ges. Wiss. Gottingen, Math.-phys. kl.*, Vol. 2, No. 1.

Haaland, S. E., and Sparrow, E. M., 1973a, "Vortex Instability of Natural Convection Flow on Inclined Surfaces," *Int. J. Heat Mass Transfer*, Vol. 16, pp. 2355–2367.

Haaland, S. E., and Sparrow, E. M., 1973b, "Wave Instability of Natural Convection on Inclined Surfaces Accounting for Nonparallelism of the Basic Flow," ASME JOURNAL HEAT TRANSFER, pp. 405–407.

Hsu, C. T., and Cheng, P., 1979, "Vortex Instability in Buoyancy-Induced

Flow Over Inclined Heated Surfaces in Porous Media," ASME JOURNAL OF HEAT TRANSFER, Vol. 101, pp. 660–665.

Hwang, G. J., and Cheng, K. C., 1973, "Thermal Instability of Laminar Natural Convection Flow on Inclined Isothermal Plates," *Canadian J. of Chemical Engineering*, Vol. 51, pp. 659–666.

Iyer, P. A., and Kelly, R. E., 1974, "The Stability of the Laminar Free Convection Flow Induced by a Heated Inclined Plate," *Int. J. Heat Mass Transfer*, Vol. 17, pp. 517–525.

Kahawita, R. A., and Meroney, R. N., 1974, "The Vortex Mode of Instability in Natural Convection Flow Along Inclined Plates," *Int. J. Heat Mass Transfer*, Vol. 17, pp. 541–548.

Lee, J. B., and Lock, G. S. H., 1972, "Instability in Buoyancy-Layer Free Convection Along an Inclined Plate," *Trans. Canadian Soc. for Mechanical Engineering*, Vol. 1, pp. 197–203.

Lloyd, J. R., and Sparrow, E. M., 1970, "On the Instability of Natural Convection Flow on Inclined Plates," *J. Fluid Mech.*, Vol. 42, pp. 465–470.

Lloyd, J. R., 1974, "Vortex Wavelength in the Transition Flow Adjacent to Upward Facing Inclined Isothermal Surfaces," *Proc. 5th Int. Heat Transfer Conference*, Vol. 3, pp. 34–37.

Lock, G. S. H., Gort, C., and Pond, G. R., 1967, "A Study of Instability in Free Convection From an Inclined Plate," *Applied Scientific Research*, Vol. 18, pp. 171–182.

Moutsoglou, A., Chen, T. S., and Cheng, K. C., 1981, "Vortex Instability of Mixed Convection Flow Over a Horizontal Flat Plate," ASME JOURNAL OF HEAT TRANSFER, Vol. 103, pp. 257–261.

Pera, L., and Gebhart, B., 1973a, "On the Stability of Natural Convection Boundary Layer Flow Over Horizontal and Slightly Inclined Surfaces," *Int. J. Heat Mass Transfer*, Vol. 16, pp. 1147–1163.

Pera, L., and Gebhart, B., 1973b, "Natural Convection Boundary Layer Flow Over Horizontal and Slightly Inclined Surfaces," *Int. J. Heat Mass Transfer*, Vol. 16, pp. 1131–1146.

Prandtl, L., 1927, "The Generation of Vortices in Fluids of Small Viscosity," *Royal Aeronautical Soc.*, Vol. 31, pp. 720–743.

Rotem, Z., and Claassen, L., 1969a, "Free Convection Boundary-Layer Flow Over Horizontal Plates and Discs," *Canadian J. Chemical Engineering*, Vol. 47, pp. 461–468.

Rotem, Z., and Claassen, L., 1969b, "Natural Convection Above Unconfined Horizontal Surfaces," *J. Fluid Mech.*, Vol. 38, pp. 173–192.

Schmidt, E., 1932, "Schlierenaufnahmen des Temperaturfeldes in der Nahe warmeabgebender Korper," *Forsch. Geb. Ingwes.*, Vol. 3, pp. 181–189.

Sparrow, E. M., and Husar, R. B., 1969, "Longitudinal Vortices in Natural Convection Flow on Inclined Plates," *J. Fluid Mech.*, Vol. 37, pp. 251–255.

Takimoto, A., Hayashi, Y., and Matsuda, O., 1983, "Thermal Stability of Blasius Flow Over a Horizontal Flat Plate," *Heat Transfer—Japanese Research*, Vol. 12, pp. 19–33.

Tritton, D. J., 1963, "Transition to Turbulence in the Free Convection Boundary Layers on an Inclined Heated Plate," *J. Fluid Mech.*, Vol. 16, pp. 417–435.

Tzuoo, K. L., Chen, T. S., and Armaly, B. F., 1985, "Wave Instability of Natural Convection Flow on Inclined Surfaces," ASME JOURNAL OF HEAT TRANSFER, Vol. 107, pp. 107–111.

Wu, R. S., and Cheng, K. C., 1976, "Thermal Instability of Blasius Flow Along Horizontal Plates," *Int. J. Heat Mass Transfer*, Vol. 19, pp. 907–913.

Yousef, W. W., Tarasuk, J. D., and McKeen, W. J., 1982, "Free Convection Heat Transfer From Upward-Facing Isothermal Surfaces," ASME JOURNAL OF HEAT TRANSFER, Vol. 104, pp. 493–500.

An Experimental Study of Natural Convection in a Vertical Cavity With Discrete Heat Sources

M. Keyhani
Department of Mechanical and Aerospace Engineering,
The University of Tennessee,
Knoxville, TN 37996
Mem. ASME

V. Prasad
Department of Mechanical Engineering,
Columbia University,
New York, NY 10027
Mem. ASME

R. Cox
Department of Mechanical and Aerospace Engineering,
The University of Tennessee,
Knoxville, TN 37996
Student Mem. ASME

Natural convection heat transfer in a tall vertical cavity (aspect ratio = 16.5), with one isothermal vertical cold wall, and eleven alternately unheated and flush-heated sections of equal height on the opposing vertical wall, is experimentally investigated. The flow visualization pictures for the ethylene glycol–filled cavity reveal a flow pattern consisting of primary, secondary, and tertiary flows. The heat transfer data and the flow visualization photographs indicate that the stratification is the primary factor influencing the temperature of the heated sections. This behavior persists for all the runs where the secondary flow cells cover a large vertical extend of the cavity. Based on the analysis of the photographs it is suggested that the turbulent flow should be expected when the local modified Rayleigh number is in the range of 9.3×10^{11} to 1.9×10^{12}. It is found that discrete flush-mounted heating in the enclosure results in local Nusselt numbers that are nearly the same as those reported for a wide flush-mounted heater on a vertical plate. This is believed to be due to the fact that the present problem is inherently unstable, and the smallest temperature difference between a heated section and the cold wall results in the onset of convection motion.

Introduction

Effective cooling of electronic components has become increasingly important as power dissipation and component density continue to increase substantially with the fast growth of electronic technology. In many electronic cooling situations, arrays of heat-dissipating components are mounted on flat-parallel plates forming a series of passages, each having either one very rough wall and the other relatively smooth or both walls rough. The simplest method of cooling these arrays is air circulated by naturally generated buoyant forces. Natural convection provides low-cost, reliable, maintenance-free, and electromagnetic interference–free cooling (Johnson, 1986). Each pair of these vertical electronic card arrays may thus be modeled as a vertical channel or a vertical cavity depending on the end conditions.

Sparrow and Faghri (1980) numerically solved boundary layer equations for the problem of two in-line flush-mounted isothermal heaters on a vertical plate for natural convection in air. Jaluria also numerically solved this problem for multiple, wide heaters (1982a) and experimentally and numerically studied two line sources (1982b). Finite-difference solutions for more general equations for two in-line vertical heaters were reported by Jaluria in a follow-up paper (1984). Studies on free convection from a discrete heat source on a vertical plate have also been reported by Zinnes (1970), and Carey and Mollendorf (1977). Park and Bergles (1987) have experimentally studied free convection from in-line and staggered arrays of heaters with varying distances between heaters. Ortega and Moffat (1985, 1986a, 1986b) and Moffat and Ortega (1986) have experimentally investigated the buoyancy-induced convective heat transfer from an array of cubical elements that are deployed in an array on one wall of a vertical, open-ended parallel-plane channel. They have reported that the heat transfer rate is significantly affected by the variation in the ratio of the gap width to the protrusion height of up to 4.

As stated earlier, some electronics packaging problems, depending on the end conditions, may be modeled as an enclosure. Although buoyancy-driven flow and heat transfer in a differentially heated vertical cavity have been investigated extensively, most of these studies consider only fully heated vertical walls. A detailed review of literature indicates that, indeed, very few efforts have been made to study free convection from either an isolated heat source or an array of distributed heat sources on one vertical wall of an enclosure. Chu et al. (1976) might have been the first to consider free convection from a heated strip located on one side wall of a rectangular cavity. They used a finite-difference numerical scheme to study the effects of the heater size, its location, the aspect ratio of the cavity, and the endwall thermal boundary conditions on the flow structure and heat transfer. Recently Kuhn and Oosthuizen (1986) conducted a numerical study of three-dimensional transient natural convective flow in a rectangular enclosure with localized heating. The enclosure that they considered had a height-to-width ratio of 3 and depth-to-width ratio of 6. The thermal boundary conditions of the enclosure were adiabatic horizontal surfaces and vertical endwalls; one constant-temperature vertical wall; and finally the other vertical wall had one or two spanwise in-line flush-mounted two-dimensional isothermal heat sources. Their major conclusions are: (*i*) Proximity of the heater element to the horizontal walls (especially the top wall) has strong effect on heat transfer coefficient while the side walls have a weak effect; (*ii*) the three-dimensional flow increases the local heat transfer coefficient at the edges of the element resulting in a higher average Nusselt number than the corresponding two-dimensional flow. However, the difference decreases as the Rayleigh number is increased (at Rayleigh number of 10^5 the Nusselt numbers are nearly the same); (*iii*) results of the two spanwise in-line flush-mounted symmetrically placed heaters indicate that the distance between the elements has little effect on the mean heat transfer rate variation but has a significant effect on the local Nusselt number distribution.

The most recent studies of natural convection heat transfer in rectangular enclosures with heated protrusion(s) on one vertical wall are by Kelleher et al. (1987), Lee et al. (1987), and Liu et al. (1987). The first two papers report on experimental (Part I) and numerical (Part II) studies of geometric effects of

Contributed by the Heat Transfer Division and presented at the 24th AIChE/ASME National Heat Transfer Conference, Pittsburgh, Pennsylvania, August 9–12, 1987. Manuscript received by the Heat Transfer Division April 20, 1987. Keywords: Electronic Equipment, Enclosure Flows, Natural Convection.

a single two-dimensional heated protrusion mounted on one adiabatic vertical wall of an enclosure. The opposing vertical wall is insulated while the top and bottom surfaces are isothermal. The experiments were conducted with water and the heat transfer and flow visualization results confirmed their numerical work. In the third paper, Liu et al. (1987) presented the results of a numerical study of three-dimensional convection cooling of an array of heated protrusions in an enclosure filled with a dielectric fluid. In this paper an array of 3×3 isoflux heated protrusions mounted on one vertical wall was considered. The remaining boundary conditions were kept the same as in the first two papers. The results were for Fluorinert FC 75 (a dielectric fluid) at a single Rayleigh number using three different widths for the enclosure. Liu et al. (1987) point

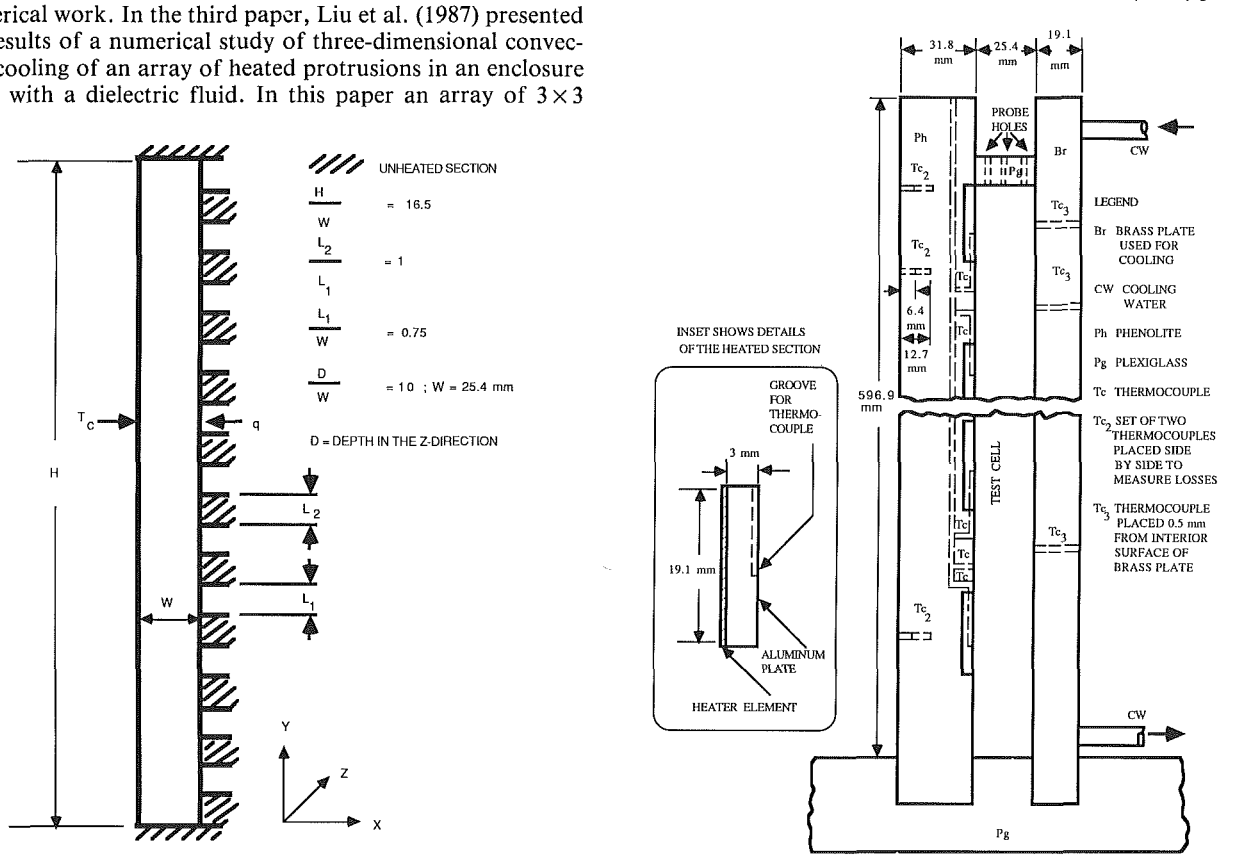

Fig. 1 Experimental apparatus: (*a*) test cell geometry and coordinate system; and (*b*) details of the apparatus

Nomenclature

A = aspect ratio $= H/W$
A_h = surface area of a heater, m^2
C = isobaric specific heat, J/kg-K
D = depth of enclosure in z direction, m
g = acceleration due to gravity, m/s^2
h = local heat transfer coefficient $= q/(T_h - T_c)$, W/m^2-K
$\bar{h}$ = average heat transfer coefficient $= q/(T_{h,m} - T_c)$, W/m^2-K
H = height of cavity, m
k = thermal conductivity, W/m-K
L = pitch for the array of heating element $= L_1 + L_2$, m
L_1 = height of the heated section, m
L_2 = height of the unheated section, m
N = heater row number (starting from the bottom)
Nu = Nusselt number $= h$ [length scale]$/k$
Pr = Prandtl number ν/α
q = convective heat flux per heated section $= (Q - Q_L - Q_{sc})/A_h$, W/m^2
Q = power input per heated section, W
Q_L = heat loss per heated section, W
Q_{sc} = substrate conduction heat transfer per heated section, W
Ra = Rayleigh number $= g\beta(T_h - T_c)$ [length scale]$^3/\alpha\nu$
Ra* = modified Rayleigh number = Nu Ra
T = temperature, K
T_{Core} = average fluid temperature at $x/W = 0.25$, 0.5, and 0.75 at a fixed y, °C
x, y, z = Cartesian coordinates, m
W = width of the cavity, m
α = thermal diffusivity $= k/\rho C$, m^2/s
ρ = density, kg/m^3
σ = standard error

Subscripts

c = cold wall
f = weighted average (equation (1))
h = heated section
H = based on cavity height
m = mean value
w = based on cavity width
y = based on local height, measured from bottom of cavity to midheight of heated section

Superscripts

$\bar{}$ = average value

out that no studies dealing with the cooling of array of chips in a closed enclosure are available for comparison. It is believed that a substantial body of experimental data is needed in order to have a complete description of heat transfer, flow field, and flow regimes in this important area of electronics packaging problems.

The purpose of the present work is to fill this gap and experimentally study the buoyancy-driven flow and heat transfer in a vertical cavity with discrete heat sources on one vertical wall while the other vertical wall is cooled at a constant temperature. Only the flush-mounted heat source has been considered for the present work. However, this should later provide a basis for examining the effects of heated protrusion (bluff bodies) on flow structure and local heat transfer behavior in a cavity.

Experimental Apparatus and Procedure

The experimental apparatus consists of an enclosure with 11 alternately unheated and flush-mounted rows of isoflux heated strips with $H/W=16.5$, $D/W=10$, $L_1/W=L_2/W=0.75$, and $W=25.4$ mm. The geometry, coordinate system, boundary conditions, and the details of the experimental apparatus are given in Fig. 1. The data that will be presented are for ethylene glycol ($\mathrm{Pr}\sim 150$) with nominal power inputs of $Q=5$, 10, 20, 30, 40, and 50 W per heater. It should be noted that it is believed that the ethylene glycol results can be applied to liquid immersion cooling (Prandtl number of dielectric fluids such as FC-77 is about 28) without a loss of accuracy. Incropera et al. (1986) experimentally investigated forced convection heat transfer from discrete heat sources in a rectangular channel. They reported that their water ($\mathrm{Pr}=5.4$, 8.3) data were in excellent agreement with their FC-77 ($\mathrm{Pr}=22.1$, 28.1) results.

The heated wall of the test cell, 596.9×254 mm, was constructed out of 31.8-mm-thick phenolite sheet ($k=0.33$ W/m-K). Twelve slots, 19.1 mm wide, 3.5 mm deep, and 254 mm long, were cut in this plate to place 19.1×254 mm thermofoil heaters with a thickness of 0.5 mm. The experiments reported in this paper were, however, conducted with only 11 heaters. Each heater was covered with a 3-mm-thick aluminum plate ($k=170$ W/m-K) with a heat sink compound filled between the heater and the aluminum strip to reduce contact resistance. Thermocouples were then placed in grooves that were milled into each of the heated and three of the unheated sections of this plate. These thermocouples were located at the midheight of their respective sections. To ascertain that the end effects of insulated side walls are negligible, two thermocouples were also located on heater number 6 (midheight) near the ends. The slots for thermocouple wires were filled with plastic steel. The phenolite plate was then sanded to obtain a smooth surface with heat sources and unheated strips arranged alternately in an array. All the thermocouples used in the instrumentation were 30 gauge copper-constantan type.

Thermocouples were also placed at different depths in the phenolite plate to estimate the conduction loss. Heater leads and thermocouple wires were taken out through the holes made in the phenolite plate, and were connected to a power panel and a digital data acquisition system, respectively. The power panel consisted of a voltage stabilizer, a step-down transformer, and four manually controlled voltage regulators. These voltage regulators were used to supply power to four circuits each consisting of a number of heaters in a series. Three of the circuits had three heaters each, and the fourth circuit consisted of two heaters. The heaters for each circuit were carefully selected such that the variations in their resistance were less than 1 percent. Voltage information for each heater circuit was fed to the data acquisition system coupled with a personal computer for data reduction and analysis.

The cold wall of the test cell was made out of two 9.6-mm-thick brass plates. A 3.2 mm circular groove was milled in each plate. The groove made in one plate was a mirror image of the other, so that when the two plates were silver-soldered, the grooves met to form a channel. Cooling water from a constant-temperature circulator bath was run through this channel to maintain the plate at a constant temperature. The circulator could maintain water within 0.1°C. Several thermocouples were placed to within 0.5 mm of the cold surface to measure temperature at various locations.

All other sides of the cavity were made out of plexiglass, 12.7 mm thick, except the base, which was 25.4 mm thick. The side walls were fitted into the slots made in the base plate and sealed with silicone rubber. The top plate was provided with an O-ring to seal the test cell, and was free to move up and down. Two threaded rods were attached to the top plate to help in insertion and removal as well as positioning of the plate.

The top plate in these experiments was positioned at the top edge of heater number 11, resulting in an inside height of 419.1 mm and an aspect ratio of 16.5 for the enclosure. Although heater number 11 is thermally active unfortunately no heat transfer data for this heater can be reported. This is due to the fact that the thermocouple circuit for this heater was broken and could not be easily repaired. The power in each heater could be varied up to 50 W, i.e., 1.03 W/cm^2 for the heated sections. The conduction losses through various walls of the cavity were also calculated to obtain net energy transported by the convective fluid. In general, the conduction loss was within 9 percent of the total power input for the present experiments.

To examine the flow structure, flow visualization experiments were conducted for several power inputs. Neutrally buoyant aluminum powder (5 to 20 μm in size) was used with the ethylene glycol as convection medium to visualize the flow. The aluminum particles were illuminated by proper lighting to obtain still and video photographs. Ilford PANF ASA 50 film was used to take the photographs with an exposure time of 30 to 90 s. Pictures were taken only when the information on the power inputs and temperatures was already collected by the data acquisition system.

Uncertainty Analysis

A Hewlett-Packard 3054A automatic data acquisition system, together with a HP 9817A personal computer, was used for data collection. The thermocouple outputs were measured to 0.1 μV, which results in 0.0025°C sensitivity. A conservative estimate of the accuracy of the temperature measurements is ±0.1°C. This includes the errors introduced by reference junction compensation (±0.01°C), temperature difference along terminals, thermal offset, voltage-to-temperature conversion error, and DVM accuracy. The voltage input to each heater circuit was measured with a sensitivity of 1 mV and an accuracy of 0.1 percent. Several runs were conducted where the voltage and current for each circuit were measured, and the calculated resistance was highly stable. These data indicated a maximum uncertainty of ±1 percent in the resistance of each circuit. The power input to each circuit was then calculated by using the measured voltage drop across the circuit and its respective resistance. This procedure resulted in an uncertainty of ±1 percent in the calculated power inputs. The uncertainty associated with the length scale used in the data reduction was ±0.25 mm. The thermophysical properties of the ethylene glycol were assigned an uncertainty of ±2 percent. This judgment was based on the observed variations in the reported values in the literature.

The overall uncertainty in the Nusselt and Rayleigh numbers varies with the power input. Smaller power input results in a larger uncertainty primarily because of a lower temperature difference across the cavity and a higher fraction of energy lost by conduction. As the power input is increased, the uncertainty in the experimental data decreases. The estimated uncertainties in Nu_w and Ra_w^* are 3.0 to 5.2, and 7.7 to 8.1 percentages, respectively. It should be noted that the uncertainty in these parameters is reduced when they are considered in terms of local values since the percent error in the length measurement is decreased.

Data Reduction

The local values of the thermophysical properties of ethylene glycol were obtained at a reference fluid temperature of

$$T_f = T_c + 0.25(T_h - T_c) \tag{1}$$

where T_h is the local temperature of the heated segment, and T_c is the cold wall temperature. Zhong et al. (1985) have shown that this form of weighted averaging (equation (1)) is more appropriate than the arithmetic mean of T_h and T_c.

The local heat transfer coefficient for a given heater was calculated as

$$h = (Q - Q_L - Q_{sc})/A_h(T_h - T_c) \tag{2}$$

where Q is the power input to the heater, Q_L is the heat loss per heater to the laboratory environment, Q_{sc} is the substrate conduction heat transfer, A_h is the surface area of the heater, and $(T_h - T_c)$ represents the temperature difference between the heater and the cold wall. The substrate conduction heat transfer (which eventually is convected to the working fluid in the unheated section) was calculated using a two-dimensional unit cell conduction heat transfer model. The unit cell represented the details of the phenolite plate from midheight of a heated section (with a line source 3 mm from the surface) to the midheight of the adjacent unheated section. The measured temperatures were used to specify the boundary conditions of the unit cell. The substrate conduction heat transfer was calculated for heaters 3, 6, and 9, where the temperature of the adjacent unheated section is known, for all power inputs. For a given power input, it was found that Q_{sc} was nearly the same (within 1 percent) for these heaters. Therefore, for each run all the heaters were assigned the average value of Q_{sc} of heaters 3, 6, and 9. The calculated substrate conduction heat transfer varied from 12 percent (at 5 W/heater) to 7 percent (at 50 W/heater) of the total convected energy.

The local Nusselt, Rayleigh, and modified Rayleigh numbers used in the presentation of the data were calculated by

$$\mathrm{Nu} = h[\text{length scale}]/k \tag{3}$$

$$\mathrm{Ra} = g\beta(T_h - T_c)[\text{length scale}]^3/\alpha\nu \tag{4}$$

$$\mathrm{Ra}^* = \mathrm{Nu}\,\mathrm{Ra} \tag{5}$$

Three length scales of local height y (Nu_y, Ra_y, Ra_y^*), cavity width W (Nu_w, Ra_w, Ra_w^*), and cavity height H (Nu_H, Ra_H, Ra_H^*) are used, where appropriate, in the presentation and discussion of the results. Furthermore, the average values are distinguished by a bar superscript (e.g., $\overline{Nu}_w$, $\overline{Ra}_H$).

Results and Discussion

As mentioned earlier, the experiments with ethylene glycol as convective medium were conducted for 5, 10, 20, 30, 40, and 50 W per heating element (approximately). This covered a local modified Rayleigh number Ra_y^* range of 8.98×10^6 to 5.09×10^{12} while the local Prandtl number varied between 161.7 and 94.3. The range of average modified Rayleigh number studied in these experiments was $5.85 \times 10^6 \le \overline{Ra}_w^* \le 1.01 \times 10^8$ (Table 1).

Table 1 Average Rayleigh and Nusselt numbers for ethylene glycol experiments ($A = 16.5$, $L_1/L_2 = 1$, $92 < Pr < 162$)

Run No.	Q (W)	$\overline{Ra}^*_w$	$\overline{Ra}_H$	$\overline{Ra}_w$	$\overline{Nu}_w$
1	5	5.85×10^6	2.87×10^9	6.40×10^5	9.14
2	10	1.25×10^7	5.04×10^9	1.12×10^6	11.14
3	20	2.91×10^7	9.73×10^9	2.16×10^6	13.47
4	30	4.85×10^7	1.42×10^{10}	3.17×10^6	15.30
5	40	7.12×10^7	1.87×10^{10}	4.17×10^6	17.07
6	50	1.01×10^8	2.36×10^{10}	5.26×10^6	19.18

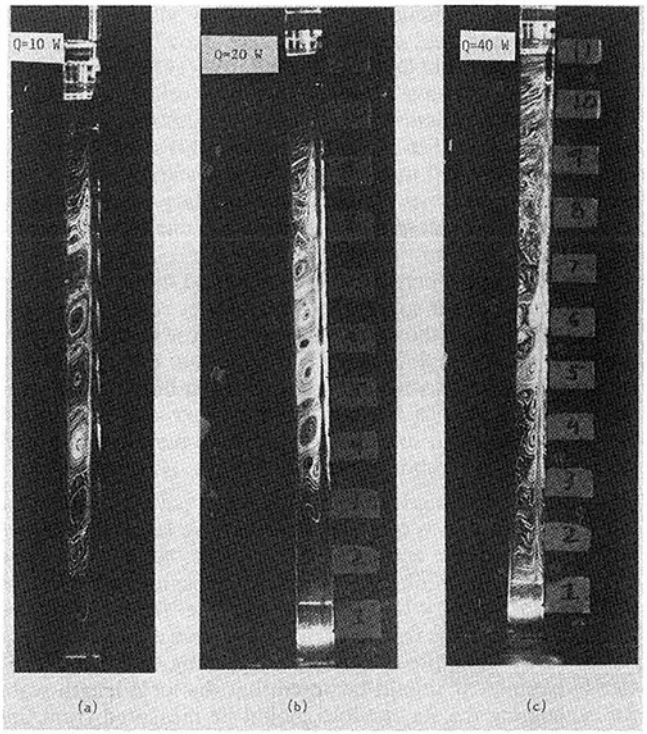

Fig. 2 Streak photographs for the entire cavity: (a) $Q = 10$ W, $\overline{Ra}_H = 5.04 \times 10^9$; (b) $Q = 20$ W, $\overline{Ra}_H = 9.73 \times 10^9$; and (c) $Q = 40$ W, $\overline{Ra}_H = 1.87 \times 10^{10}$

Flow Visualization. The typical flow patterns visualized are shown in Figs. 2–4. Figures 2(*a–c*) present photographs for the entire cavity, and the local flow patterns in the central portion of the cavity are demonstrated in Figs. 3(*a–c*). Close-ups of the above and below midheight regions of the cavity for $Q = 40$ W and 50 W are presented in Figs. 4(*a–b*), respectively. The cold wall in all the photographs is on the left side. The flow for 10 W (Fig. 2*a*, $\overline{Ra}_w^* = 1.25 \times 10^7$) is observed to be highly structured except for small regions near the end walls. Figure 2(*a*) shows primary flow circulating from the hot wall to the cold wall (counterclockwise in the figure), a secondary flow with the same sense of circulation as the primary flow, and a tertiary flow in the opposite direction of the secondary flow. A close-up that clearly shows these three kinds of convection cell is presented in Fig. 3(*a*). The photographs in Figs. 2(*a–c*) show that as Rayleigh number is increased the

wavelength of the secondary flow cells decrease (as expected). The observed number of secondary flow cells is 6, 4, and 1 at $\overline{Ra}_w^* = 1.25 \times 10^7$, 2.91×10^7, and 7.12×10^7, respectively.

A survey of literature on natural convection in a differentially heated, tall vertical cavity reveals that Elder (1965), for the first time, had observed multicellular flow patterns for an oil with Pr = 1000. Vest and Arpaci (1969) observed this for silicone oil (Pr = 900) in a cavity of aspect ratio 20. Bergholz (1978) later showed that the traveling wave solutions arise from the instability of the transition and boundary-layer regimes for low Prandtl number fluids. However, Bergholz' analysis showed that the secondary flow becomes steady at high Prandtl numbers, a situation applicable to Elder's study. Extensive numerical work by Thomas and de Vahl Davis (1970), de Vahl Davis and Mallison (1975), Lee and Korpela (1983), and others supports the existence of multicellular flow patterns in a tall cavity and reports that traveling cells may exist under certain circumstances. The flow visualizations by Elder (1965) and Seki et al. (1978) also show the presence of tertiary flow. de Vahl Davis and Mallinson (1975), and Pepper and Harris (1977) have obtained this three-cell flow structure via numerical calculations. A similar computation and further experiments by Seki et al. (1978) confirm this structure of the flow at high Prandtl numbers. They have stated that the tertiary flow that emerges between the secondary flows might be considered to be caused by the shear force due to the secondary flows.

The present flow patterns (Figs. 3*a–c*) and those reported in the literature further suggest that the tertiary cells first appear at the midheight of the cavity in a region close to the cold wall (higher viscosity region) due to the viscous effects. As the Rayleigh number increases, the velocities in both the secondary and tertiary cells increase. The tertiary cells, however, grow significantly in size with the Rayleigh number, and tend to displace the neighboring secondary cells. (Fig. 3*c*).

Another interesting feature of these flow patterns is the fact that at a given y, it is quite possible to have laminar and turbulent flows coexist across the cavity (Figs. 4*a*, *b*). The flow pattern above the midheight region of the cavity for $Q = 40$ W (Fig. 4*a*, $\overline{Ra}_w^* = 7.12 \times 10^7$) shows that the flow along the "hot" wall is going through transition from laminar to turbulent flow, while the downward flow along the cold wall is clearly laminar. It should be noted that the local length scale for calculating the Ra_y or Ra_y^* should be measured from the bottom of the cavity for upward flow, and the top of the cavity for downward flow. Therefore, the turbulent upward flow corresponds to a local Rayleigh number greater than the critical value for onset of turbulent flow. Conversely, the local Rayleigh number for laminar downward flow is sufficiently small that laminar flow condition prevails. The photograph indicating laminar upward flow and turbulent downward flow at a region below midheight of the cavity is shown in Fig. 4(*b*) ($Q = 50$ W, $\overline{Ra}_w^* = 1.01 \times 10^8$).

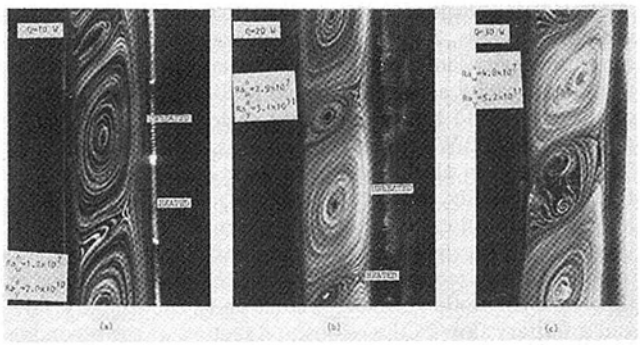

Fig. 3 Streak photographs showing primary, secondary, and tertiary flows in the central region of the cavity: (*a*) $Q = 10$ W, $\overline{Ra}_H = 5.04 \times 10^9$; (*b*) $Q = 20$ W, $\overline{Ra}_H = 9.73 \times 10^9$; and (*c*) $Q = 30$ W, $\overline{Ra}_H = 1.42 \times 10^{10}$

In order to determine the value of the critical local Rayleigh number for the onset of turbulent flow, the photographs showing the details of the flow above midheight of the cavity have been analyzed. The results of the analysis of the photographs are tabulated in Table 2. In that table, the lowest Ra_y and Ra_y^* at which unsteady or turbulent flow was first observed, as well as the maximum Ra_y and Ra_y^* at which the flow was laminar, are given. The data in Table 2 clearly indicate that the modified Rayleigh number is the appropriate parameter for specifying the critical value for onset of turbulence. Based on these data, and allowing for one L_1 error in specifying the local height, it is suggested that turbulent flow should be expected when $9.3 \times 10^{11} < Ra_y^* < < 1.9 \times 10^{12}$.

In general, the present flow patterns are similar to those observed by Seki et al. (1978) and other investigators studying natural convection in tall enclosures with two isothermal, but different, vertical walls. However, no statement can be made with respect to differences in the velocities, or for that matter, the sequence of change in flow pattern with respect to a common flow parameter. Moreover, it should be noted that the present problem is fundamentally different from the numerous studies of natural convection in enclosures where the entire "hot" wall is heated (be it isothermal or isoflux). In the case of a fully heated vertical wall, for a sufficiently small temperature difference across the cavity, the heat transfer mode will be conduction flow regime ($Nu_w \simeq 1.0$). As the temperature difference is increased, and the critical Rayleigh number is reached, the convection motion due to hydrodynamic instability is initiated ($Nu_w > 1.0$). The present problem, however, is inherently unstable. Therefore, the smallest temperature difference between the heated sections and the cold wall results in convection motion ($Nu_w > 1.0$). Consequently, it should be expected that the present heat transfer coefficients will be much higher than those of a uniformly heated wall (isothermal or isoflux) enclosure.

Temperature Distribution. The temperature distribution, $T - T_c$, across the cavity ($x/W = 0$, 0.25, 0.5, 0.75, and 1.0) at each heated section elevation for $Q = 5$ W is given in Fig. 5. A slight temperature inversion at the core (from $x/W = 0.25$ to 0.75) is observed (this behavior persists for all power inputs). This phenomenon has also been observed in the boundary layer flow regime in a vertical cavity with an isothermal heated

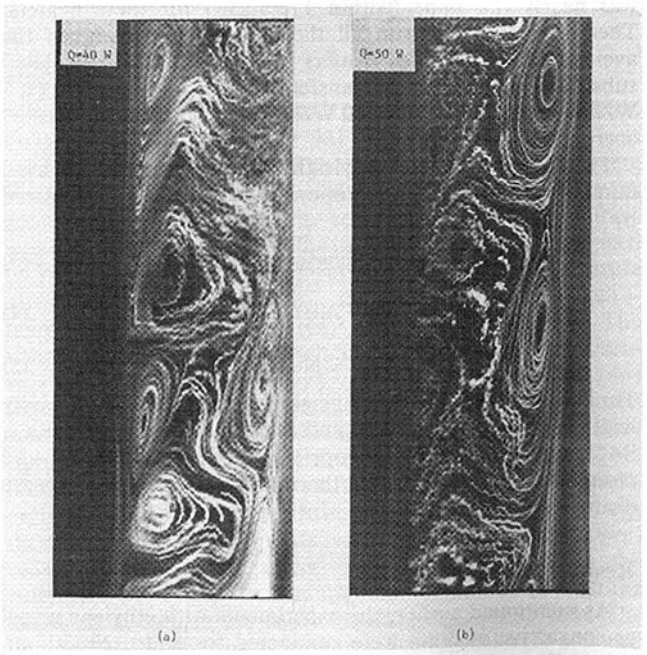

Fig. 4 Detail flow patterns for: (*a*) $Q = 40$ W, above the midheight region of the cavity; and (*b*) $Q = 50$ W, below the midheight region of the cavity

Table 2 Lowest local Rayleigh numbers (Ra_y, Ra^*_y) at which unsteady or turbulent flow was observed

Q (W)	Heater No.	Observed Flow Condition: Laminar	Unsteady or Turbulent	Laminar	Unsteady or Turbulent
		Ray		Ra*y	
20	10	1.1×10^{10}	--	1.4×10^{12}	--
30	8	6.3×10^{9}	--	9.1×10^{11}	--
	9	--	9.9×10^{10}	--	1.5×10^{12}
40	7	4.8×10^{9}	--	7.6×10^{11}	--
	8	--	8.3×10^{9}	--	1.4×10^{12}
50	6	3.8×10^{9}	--	5.8×10^{11}	--
	7	--	6.0×10^{9}	--	1.1×10^{12}

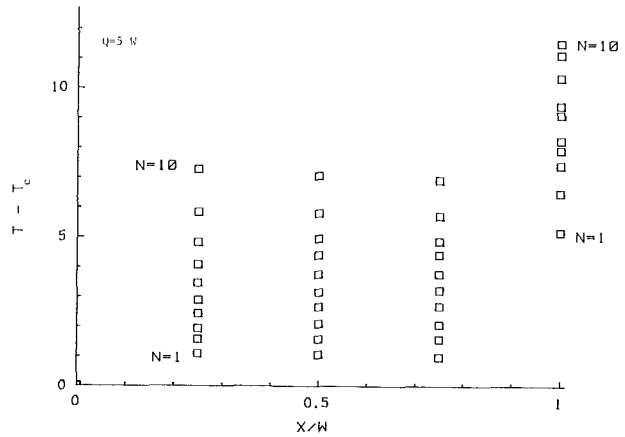

Fig. 5 Temperature distribution, $T - T_c$, across the cavity at each heated section elevation for $Q = 5$ W

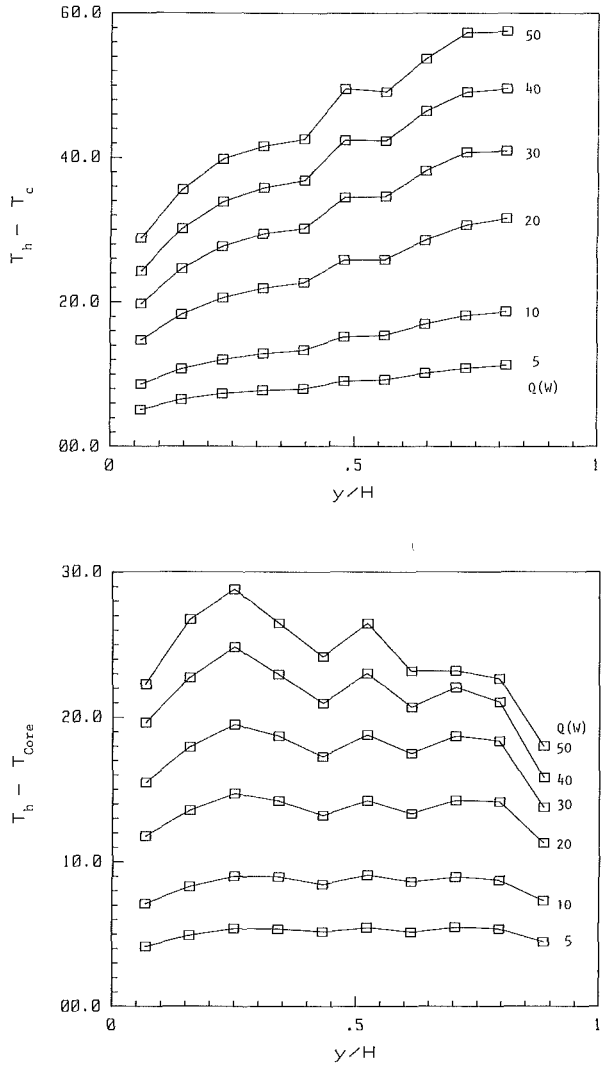

Fig. 6 Temperature of the heated sections for all the power inputs: (a) $T_h - T_c$; and (b) $T_h - T_{Core}$

wall by Korpela et al. (1982) and other investigators. The temperature profile at $x/W = 1.0$ (for the heated sections only) for all the experimental runs is presented in Fig. 6(*a*). The numerical values of $T - T_c$ for the three instrumented unheated sections along with their respective preceding and succeeding heated sections are also given in Table 3.

The temperatures of the heated sections (Fig. 6*a*) show a steady increase from heater 1 to 10 at $Q = 5$ W and 10 W. The temperatures of heaters 6 (midheight) and 7 are nearly the same for $Q = 20$ W to 50 W. The variation of surface temperature depends on changes in the flow pattern (presence of a secondary or tertiary flow cell), flow regime (laminar, transional, unsteady, turbulent) and the stratification parameter. Therefore, no single explanation can be offered for the measured profiles. The temperature of the unheated section (Table 3), $T - T_c$, is nearly the same as that of the heated section preceding it by two heaters. For example, at $Q = 50$ W, $T - T_c$ for the unheated section between heaters 9 and 10 is 48.70°C, which is equal to that of heater 7. The reader should be cautioned against interpreting the magnitude of $T - T_c$ of the unheated sections as evidence of substantial heat transfer to the fluid. The convection heat transfer is dependent on the temperature gradient near the surface, which in turn is strongly influenced by the stratification parameter. The temperature gradient is also a function of the local flow velocity, which is partially dependent on the local buoyant force.

In order to demonstrate the effect of stratification on the surface temperature distribution, $T - T_{Core}$ for the heated sections is plotted for $Q = 5$ W to 50 W and presented in Fig. 6(*b*). T_{Core} is the average of the three probe temperatures at the given heater elevation. $T - T_{Core}$ is nearly constant for all heaters (expect heaters 1 and 10), for $Q = 5$ W and 10 W. The two runs correspond to flow conditions where the secondary flow patterns cover a large vertical extent of the cavity. As mentioned earlier, as Rayleigh number increases, the portion of the cavity which is covered by secondary flow cells decreases. The secondary flow cells were observed in the midsection of the cavity for power inputs up to $Q = 30$ W. The data in Fig. 6(*b*) indicate that $T - T_{Core}$ for heaters 3 to 9 can be approximated with an average value ±6 percent for $Q = 5$ W to 30 W runs. The temperature differences for $Q = 40$ W and 50 W correspond to flow patterns where only one secondary flow cell (next to heater 5) was present. Moreover, the flow above the midheight was in transition to turbulent flow. Indeed, for $Q = 50$ W, $T - T_{Core}$ of heater 10 (fully turbulent flow) is 4.36°C (20 percent) less than that of heater 1. In summary, it can be stated that when secondary flow cells cover a large extent of the cavity, the surface temperature is essentially a function of stratification.

Heat Transfer Results. Figure 7 presents the local Nusselt number Nu_w plotted against the cavity-modified Rayleigh number Ra^*_w. Since Ra^*_w is directly proportional to power input q, the Rayleigh number in Fig. 7 is observed to be almost constant for each set of experiments; a small increase in Ra^*_w with the increasing heater number N is caused by the property

Table 3 Temperature readings ($T - T_c$, °C) at insulated segments along with preceding and succeeding heater temperatures

Heater	Power Input Per Heater (W)					
No. N	5	10	20	30	40	50
3	7.35	12.02	20.58	27.69	33.87	39.80
Ins	5.74	9.33	15.95	21.56	26.29	30.70
4	7.81	12.87	21.91	29.43	35.81	41.58
6	8.87	14.74	25.03	33.34	40.85	47.75
Ins	7.57	12.53	21.41	28.59	35.03	40.46
7	9.29	15.42	25.90	34.65	42.32	48.79
9	10.87	18.17	30.69	40.77	49.14	57.36
Ins	9.37	15.84	26.69	34.73	42.29	48.79
10	11.32	18.72	31.61	40.96	49.62	57.55

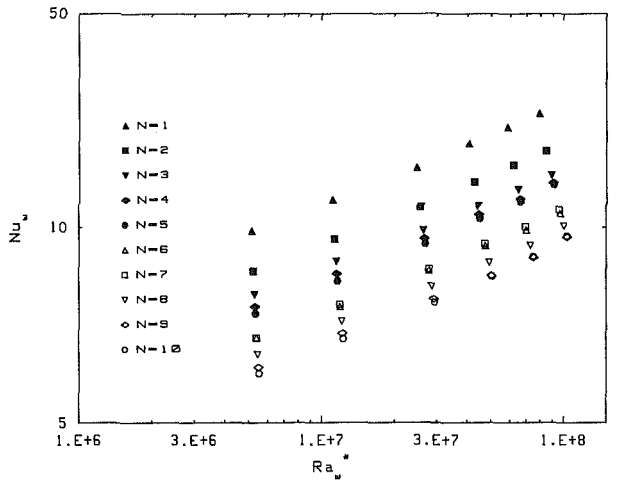

Fig. 7 Local Nusselt numbers Nu_w versus their respective local modified Rayleigh numbers Ra_w^*, for heaters 1 to 10

Table 4 Coefficients C, exponents m, and standard errors σ, for heat transfer correlations (equation (6))

N	C	m	σ
1	0.345	0.242	0.223
2	0.272	0.243	0.182
3	0.266	0.236	0.148
4	0.218	0.244	0.105
5	0.176	0.255	0.143
6	0.189	0.242	0.123
7	0.170	0.249	0.132
8	0.168	0.243	0.199
9	0.157	0.243	0.225
10	0.117	0.259	0.229

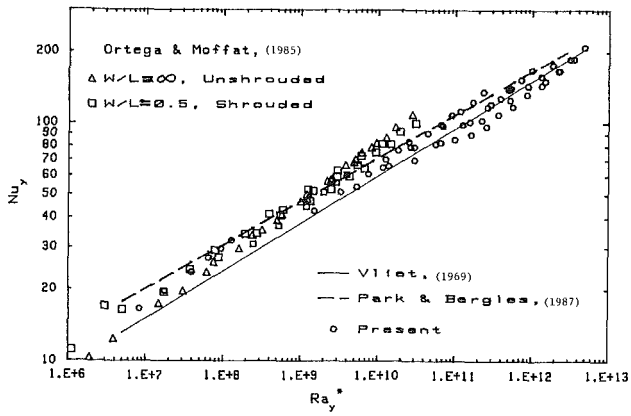

Fig. 8 Present local Nusselt numbers compared with the reported results for a smooth flat plate (Vliet, 1969), a miniature heat source on a vertical surface (Park and Bergles, 1987), and for vertical plates and channels with protruded heaters on one wall (Ortega and Moffat, 1985, 1986a); all of these studies were conducted for constant flux heating

variation. Figure 7 shows that for a fixed power input (or Ra_w^*), the heat transfer coefficient generally decreases with the increase in height (or heater). The rate at which Nu_w decreases with the increase in heater number is, however, a strong function of the heater location. The variation in Nu_w is minimal between the pairs of heaters 4 and 5, 6 and 7, and 9 and 10, whereas it is largest between the heaters 1 and 2, 2 and 3, and 5 and 6. Indeed, it is possible that the heat transfer coefficient for $N=7$ exceeds that of $N=6$. It should be noted that these heat transfer coefficients are calculated based on the temperature difference of $T_h - T_c$. Therefore, the differences among the Nu_w of the heaters is partially due to stratification (please refer to discussion of Fig. 6*b*). Nevertheless, the changes in the flow pattern and flow regime can be of sufficient impact to overcome the stratification effect, thus resulting in a slightly higher Nu_w for heater 7 than for heater 6. Park and Bergles have reported that the ratio of the heat transfer coefficient of the top heater to that of the bottom one (at a fixed modified Rayleigh number, for the case of two flush in-line heaters) reduces from an asymptotic value of 0.9 to 0.78 as L/L_1 decreases from 9.94 to 1.42. The ratio of the heat transfer coefficient of heater 2 to that of heater 1, at a fixed Ra_w^*, in the present study ($L/L_1 = 2$) is 0.79. The Nu_w of each heated section is correlated in terms of Ra_w^* in the form of

$$Nu_w = C Ra_w^{*m} \tag{6}$$

and the constants C, exponents m, and the standard errors σ, are tabulated in Table 4. These correlations represent the experimental data with maximum error of 2.7 percent.

Present values of Nu_y are compared with predicted/measured Nusselt numbers for a smooth vertical plate (Vliet, 1969), a miniature flush-mounted heating element on a vertical surface (Park and Bergles, 1987), an unshrouded vertical plate with protruded heating elements, and a vertical channel with protuberance (Ortega and Moffat, 1985) in Fig. 8. All of these studies were conducted for constant flux heating. It should be noted that Vliet's empirical correlation (for air and water)

$$Nu_y = 0.6 Ra_y^{*0.2} \tag{7}$$

predicts Nusselt numbers 3.3 percent lower than that obtained by using the Fujii and Fujii (1976) correlation of laminar boundary layer flow for $Pr = 125$ (1975). The correlation of Park and Bergles (1987) used in Fig. 8 is obtained for their widest flush-mounted heater width in the spanwise direction (width = 20 mm, water data)

$$Nu_y = 1.035\ Ra_y^{*0.184} \tag{8}$$

which takes into account the edge effects. In Fig. 8, the correlation of Park and Bergles (1987) is extended beyond the experimental range of Ra_y^* for which it was determined ($Ra_y^* \leq 10^7$).

The experimental data of Ortega and Moffat, presented in Fig. 8, are directly taken from their report (1986a). Only two extreme cases have been considered for the comparison: the unshrouded vertical plate and the vertical channel with smallest gap-width ($W/L = 0.5$). In both cases, their data for 0.2, 0.4, and 0.8 W per element have been reproduced. It should also be noted, however, that their data for the first two arrays of heaters are not plotted in Fig. 8. It is recognized that the data presented in Fig. 8 has been obtained from different geometric configurations, and are for various Prandtl numbers (air, water, ethylene glycol). Moreover, they represent different flow regimes. For example, Ortega and Moffat (1985) have reported that their air data are in turbulent flow regime over the entire Ra_y^* range, while the liquid data at the same range are in the laminar flow regime. Nonetheless, it is interesting to note that the extension of the correlation of Park and Bergles, equation (8) with ±25 percent lines drawn, will cover the present data, Vliet's correlation, equation (7), and the data of Ortega and Moffat (1986a) (except few points at $Ra_y^* < 3 \times 10^6$).

The present local Nusselt numbers for all heaters have been correlated in terms of Ra_y^* as

$$Nu_y = 1.009\ Ra_y^{*0.1805} \tag{9}$$

This correlation predicts the experimental data with an average error of 6.64 percent. The minimum and maximum errors are 0.4 percent and 19.5 percent, respectively. In the present experiments, the heater width in the spanwise direction was 254 mm. Park and Bergles (1987) have suggested that the heater edge effect vanishes at a width of 70 mm. Using the heater width effect proposed by them, equation (8) for the limiting case (water data, heater width in z direction of 70 mm) becomes

$$Nu_y = 0.91\ Ra_y^{*0.184} \tag{10}$$

The present correlation, equation (9), at $Ra_y^* = 1.0 \times 10^7$ and 5×10^{12}, predicts Nusselt numbers that are 4.8 and 0.1 percent higher than those obtained from equation (10), respectively. The agreement of the present correlation (equation (9) for $94 < Pr < 162$) with the extension of the proposed correlation by Park and Bergles (equation (10) for the limiting case of the heater width effect, $2.7 \leq Pr \leq 5.6$) is quite remarkable. This agreement is attributed to the fact that the present problem (recirculating convection) is inherently unstable (as discussed earlier) and the smallest buoyant force results in convection motion, which is exactly the case for external convection (Park and Bergles study). It should be noted that the results of Park and Bergles (equations (8) and (10)) are for a single flush-mounted heater, and y represents the distance from the leading edge of the heater to its midheight, whereas in the present work (array of flush-mounted heaters) y is measured from the bottom of the cavity to the midheight of a given heater.

At this point, it may be interesting to compare the present heat transfer results with those for a vertical cavity fully heated on one side wall. Since the relevant information on local Nusselt number is not available for the fully heated cavity, only the average Nusselt number can be compared. For this purpose, the present data are compared with those calculated from the McGregor and Emery (1969) correlation for laminar, free convection in a tall cavity

$$\overline{Nu}_w = 0.42 \overline{Ra}_w^{0.25} Pr^{0.012} A^{-0.30} \tag{11}$$

for

$$10^4 < \overline{Ra}_w < 10^7, \quad 10 < A < 40, \quad 1 < Pr < 2 \times 10^4$$

This correlation is based on the experimental data for constant flux heating and predicts Nusselt numbers, in the present range of Rayleigh number, that are higher than those predicted by their correlation for turbulent flow. The present average Nusselt numbers at $\overline{Ra}_w = 6.4 \times 10^5$ and 5.26×10^6 (tabulated in Table 1) are 68 and 108 percent higher than those predicted by equation (11) (for $A = 16.5$ and $Pr = 135$), respectively.

It is thus evident that the heat transfer coefficient in a vertical cavity can be enhanced significantly by distributing the heat sources, i.e., changing the problem from one with a stable base conduction flow regime to one that is inherently unstable. In the case of a tall cavity with equal widths of heated and unheated sections ($L_1 = L_2$), this enhancement is so great that the Nusselt numbers may exceed that for a fully heated, smooth vertical plate, and may be close to that for a surface with flush-mounted heating elements.

Final Remarks

- Discrete flush-mounted heating in an enclosure (recirculating convection, cooled from the side) results in local Nusselt numbers that are nearly the same as those reported by Park and Bergles (1987) for a wide flush-mounted heater on a vertical plate. This is believed to be due to the fact that the present problem is inherently unstable, and the smallest temperature difference between a heated section and the cold wall results in onset of the convection motion.
- The heat transfer data and the flow visualization photographs indicate that the stratification is the primary factor influencing the temperature of the heated sections. This behavior persists for all the runs where the secondary flow cells cover a large vertical extent of the cavity.
- Based on the analysis of the photographs, it is suggested that the turbulent flow should be expected when $9.3 \times 10^{11} < Ra_y^* < 1.9 \times 10^{12}$.
- It is found that at a fixed Ra_w^* the heat transfer coefficient of heater 2 is 79 percent of that of heater 1 ($L/L_1 = 2$). Park and Bergles (1987) have reported a value of 78 percent for the case of two flush in-line heaters with $L/L_1 = 1.42$.
- The results indicate that the average Nusselt number $\overline{Nu}_w$ for the discrete heating case is substantially higher than that of a fully heated vertical cavity. For the present range of $\overline{Ra}_w$, $\overline{Nu}_w$ is from 68 to 108 percent higher than that reported by McGregor and Emery (1969) for the fully heated wall.

References

Bergholz, R. F., 1978, "Instability of Steady Natural Convection in a Vertical Fluid Layer," *Journal of Fluid Mechanics*, Vol. 84, pp. 743–768.

Carey, V. P., and Mollendorf, J. C., 1977, "The Temperature Field Above a Concentrated Heat Source on a Vertical Adiabatic Surface," *International Journal of Heat and Mass Transfer*, Vol. 20, pp. 1059–1067.

Chu, H. H. S., Churchill, S. W., and Patterson, C. V. S., 1976, "The Effects of Heater Size, Location, Aspect Ratio, and Boundary Conditions on Two-Dimensional, Laminar, Natural Convection in Rectangular Channels," ASME JOURNAL OF HEAT TRANSFER, Vol. 98, pp. 194–201.

de Vahl Davis, G., and Mallinson, G. D., 1975, "A Note on Natural Convection in a Vertical Slot," *Journal of Fluid Mechanics*, Vol. 72, pp. 87–93.

Elder, J. W., 1965, "Laminar Free Convection in a Vertical Slot," *Journal of Fluid Mechanics*, Vol. 23, pp. 77–98.

Fujii, T., and Fujii, M., 1976, "The Dependence of Local Nusselt Number on Prandtl Number in the Case of Free Convection Along a Vertical Surface With Uniform Heat Flux," *International Journal of Heat and Mass Transfer*, Vol. 19, pp. 121–122.

Incropera, F. P., Kerby, J. S., Moffat, D. F., and Ramadhyani, S., 1986, "Convection Heat Transfer From Discrete Heat Sources in a Rectangular Chan-

nel," *International Journal of Heat and Mass Transfer*, Vol. 29, pp. 1051–1058.

Juluria, Y., 1982a, "Buoyancy-Induced Flow Due to Isolated Thermal Sources on a Vertical Surface," ASME JOURNAL OF HEAT TRANSFER, Vol. 104, pp. 223–227.

Juluria, Y., 1982b, "Natural Convection Flow Due to Line Thermal Sources on a Vertical Adiabatic Surface," *Heat Transfer—1982, Proceedings of the Seventh International Heat Transfer Conference*, Hemisphere Publishing Corporation, Vol. 2, pp. 147–152.

Jaluria, Y., 1984, "Interaction of Natural Convection Wakes Arising From Thermal Sources on a Vertical Surface," *Fundamentals of Natural Convection/Electronic Equipment Cooling*, ASME HTD-Vol. 32, pp. 67–76.

Johnson, C. E., 1986, "Evaluation of Correlations for Natural Convection Cooling of Electronic Equipment," *Heat Transfer in Electronic Equipment—1986*, ASME HTD-Vol. 57, pp. 103–111.

Korpela, S. A., Lee, Y., and Drummond, J. E., 1982, "Heat Transfer Through a Double Pane Window," ASME JOURNAL OF HEAT TRANSFER, Vol. 104, pp. 539–544.

Kuhn, D., and Oosthuizen, P. H., 1986, "Three-Dimensional Transient Natural Convective Flow in a Rectangular Enclosure With Localized Heating," *Natural Convection in Enclosures—1986*, ASME HTD-Vol. 63, pp. 55–62.

Kelleher, M. D., Knock, R. H., and Yang, K. T., 1987, "Laminar Natural Convection in a Rectangular Enclosure Due to a Heated Protrusion on One Vertical Wall—Part I: Experimental Investigation," *Proc. 2nd ASME/JSME Thermal Engineering Joint Conference*, Honolulu, HI, Vol. 2, pp. 169–177.

Lee, J. J., Liu, K. V., Yang, K. T., and Kelleher, M. D., 1987, "Laminar Natural Convection in a Rectangular Enclosure Due to a Heated Protrusion on One Vertical Wall—Part II: Numerical Simulations," *Proc. 2nd ASME/JSME Thermal Engineering Joint Conference*, Honolulu, HI, Vol. 2, pp. 179–185.

Lee, Y., and Korpela, S. A., 1983, "Multicellular Natural Convection a Vertical Slot," *Journal of Fluid Mechanics*, Vol. 126, pp. 91–121.

Liu, K. V., Yang, K. T., and Kelleher, M. D., 1987, "Three-Dimensional Natural Convection Cooling of an Array of Heated Protrusions in an Enclosure Filled With a Dielectric Fluid," *Proc. Int. Symposium on Cooling Technology for Electronic Equipment*, Honolulu, HI, pp. 486–497.

McGregor, R. K., and Emery, A. F., 1969, "Free Convection Through Vertical Plane Layers," ASME JOURNAL OF HEAT TRANSFER, Vol. 91, pp. 391–401.

Moffat, R. J., and Ortega, A., 1986, "Buoyancy Induced Forced Convection," *Heat Transfer in Electronic Equipment—1986*, ASME HTD-Vol. 57, pp. 135–144.

Ortega, A., and Moffat, R. J., 1985, "Heat Transfer From an Array of Simulated Electronic Components: Experimental Results for Free Convection With and Without a Shrouding Wall," *Heat Transfer in Electronic Equipment—1985*, ASME HTD-Vol. 48, pp. 5–15.

Ortega, A., and Moffat, R. J., 1986a, "Experiments on Buoyancy-Induced Convection Heat Transfer From an Array of Cubical Elements on a Vertical Channel Wall," Report No. HMT-38, Department of Mechanical Engineering, Stanford University.

Ortega, A., and Moffat, R. J., 1986b, "Buoyancy-Induced Convection in a Non-uniformly Heated Array of Cubical Elements on a Vertical Channel Wall," *Heat Transfer in Electronic Equipment–1986*, ASME HTD-Vol. 57, pp. 123–134.

Park, K. A., and Bergles, A. E., 1987, "Natural Convection Heat Transfer Characteristics of Simulated Microelectronic Chips," ASME JOURNAL OF HEAT TRANSFER, Vol. 109, pp. 90–96.

Pepper, D. A., and Harris, S. D., 1977, "Numerical Simulation of Natural Convection in Closed Containers by a Fully Implicit Method," ASME *Journal of Fluids Engineering*, Vol. 99, pp. 649–656.

Seki, N., Fukusako, S., and Inaba, H., 1978, "Visual Observation of Natural Convective Flow in a Narrow Vertical Cavity," *Journal of Fluid Mechanics*, Vol. 84, pp. 695–704.

Sparrow, E. M., and Faghri, M., 1980, "Natural Convection Heat Transfer From the Upper Plate of a Colinear, Separated Pair of Vertical Plates," ASME JOURNAL OF HEAT TRANSFER, Vol. 102, pp. 623–629.

Thomas, R. W., and de Vahl Davis, G., 1970, "Natural Convection in Annular and Rectangular Cavity—A Numerical Study," *Proceedings 4th International Heat Transfer Conference*, Vol. 4, NC 2.4, Elsevier, Amsterdam.

Vest, C. M., and Arpaci, V. S., 1969, "Stability of Natural Convection in a Vertical Slot," *Journal of Fluid Mechanics*, Vol. 36, pp. 1–15.

Vliet, G. C., 1969, "Natural Convection Local Heat Transfer on Constant Heat-Flux Inclined Surfaces," ASME JOURNAL OF HEAT TRANSFER, Vol. 91, pp. 511–516.

Zhong, Z. Y., Yang, K. T., and Lloyd, J. R., 1985, "Variable Property Effects in Laminar Natural Convection in a Square Enclosure," ASME JOURNAL OF HEAT TRANSFER, Vol. 107, pp. 133–138.

Zinnes, A. E., 1970, "The Coupling of Conduction With Laminar Natural Convection From a Vertical Flat Plate With Arbitrary Surface Heating," ASME JOURNAL OF HEAT TRANSFER, Vol. 92, pp. 528–535.

Natural Convection in Shallow Enclosures With Differentially Heated Endwalls

S. Paolucci

D. R. Chenoweth

Applied Mechanics Department,
Sandia National Laboratories,
Livermore, CA 94550

We consider a low-aspect-ratio two-dimensional rectangular cavity, differentially heated with an arbitrarily large horizontal temperature difference. Steady-state results obtained from numerical solutions of the transient Navier–Stokes equations are given for air using the ideal gas law and Sutherland law transport properties. We clarify the different flow regimes possible by using numerical results for aspect ratios $0.025 \le A \le 1$ and for Rayleigh numbers (based on height) $10^2 \le Ra \le 10^9$. We present Nusselt numbers, and temperature and velocity distributions, and compare them with existing data. At high Ra in the Boussinesq limit we show the existence of weak secondary and tertiary flows in the core of the cavity. In addition we present novel solutions in the non-Boussinesq regime. We find that the classical parallel flow solution, accurate in the core of the cavity in the Boussinesq limit, does not exist when variable properties are introduced. For higher Rayleigh numbers, we generalize the well-known analytical boundary layer solution of Gill. The non-Boussinesq solutions show greatly reduced static pressure levels and lower critical Rayleigh numbers.

1 Introduction

A natural convection flow that has numerous engineering and geophysical applications is that arising in a rectangular cavity with differentially heated endwalls. Cavities with small aspect ratios have not received as much attention as those with aspect ratios larger than unity. Furthermore, to our knowledge all analytical and experimental studies conducted to date on this problem have been in the Boussinesq or near-Boussinesq limit.

In exemplary studies, the problem was treated by Cormack et al. (1974a, 1974b) and Imberger (1974) analytically, numerically, and experimentally, respectively. Cormack et al. (1974a) presented an asymptotic solution to the laminar problem. This solution is valid in the aspect ratio limit of $A \to 0$ for fixed, though arbitrary, values of the Rayleigh and Prandtl numbers, and is assumed to consist of two distinct regions: a parallel flow in the central core (first obtained by Hart, 1972) and a nonparallel flow confined within a distance of order H from the endwalls. Cormack et al. (1974b) developed an algorithm for the numerical solution of the flow in the cavity. They found their results to be in good agreement with the parallel flow solution obtained by Cormack et al. (1974a) provided $A \le 0.1$ and $\mathrm{Ra}^2 A^3 \le 10^5$. In addition, the solutions show a parallel flow transition between the asymptotic limit of Cormack et al. (1974a) and the boundary layer limit (A fixed and $\mathrm{Ra} \to \infty$) of Gill (1966). Imberger (1974) presented experimental results for water with $A = 0.01$ and 0.019 in the range $1.31 \times 10^6 \le \mathrm{Ra} \le 1.11 \times 10^8$. Most of the flow features indicated by the numerical work were qualitatively observed in the experimental work. When $\mathrm{Ra}^2 A^3$ becomes nearly 10^{11}, experiments indicate that the midheight of the cavity becomes an isotherm and there is a slow central circulation throughout the entire shallow cavity. We note that while A can be decreased by increasing the length of the cavity without varying the Rayleigh number, often to change the aspect ratio in an experiment the height is decreased, thus forcing a large increase in temperature difference to keep the Rayleigh number fixed. Use of this experimental procedure to verify numerical Boussinesq results has limited validity since the numerical solutions do not account for property variations.

Bejan and Tien (1978) extended the asymptotic analysis of Cormack et al. (1974a) to include both $\mathrm{Ra} \to 0$, A finite, and $A \to 0$, Ra finite. They also developed a Nusselt number correlation in the boundary layer regime and an empirical correlation including both limits. Bejan et al. (1981) presented experimental results for water with $A = 0.0625$ and $2 \times 10^8 < \mathrm{Ra} < 2 \times 10^9$. They showed that, contrary to the assumption of Bejan and Tien, for $\mathrm{Ra}^{1/4} A > 1$, the core flow is nonparallel and is dominated by horizontal intrusions flowing along the two insulated horizontal walls and embracing a practically stagnant and thermally stratified fluid. In addition they observed weak counterflow. Finally, by statistically analyzing previously published experimental work, Ostrach (1982), in a recent review paper, shows that the heat transfer varies with $\mathrm{Ra}^{0.3}$ for $A < 0.1$ and $\mathrm{Ra} > 5 \times 10^5$. He notes that the variation with $\mathrm{Ra}^{0.2}$ obtained by Bejan and Tien is incorrect since they assumed that the core flow was parallel in matching with the boundary layers in the end regions.

In this work we improve the understanding of the small-aspect-ratio problem. Specifically, we study two-dimensional rectangular cavities with rigid walls and whose horizontal walls are insulated, while the vertical walls are at constant but different temperatures (the two-dimensionality assumption has been shown to be valid in a number of experiments, e.g., Ostrach et al., 1980; Kamotani et al., 1983). We emphasize non-Boussinesq effects arising from property variations due to large temperature differences. In addition, we extend the numerical solution in the Boussinesq regime to Rayleigh numbers larger than available in the literature. Numerical solutions of the transient Navier–Stokes equations are used to generate laminar steady-state results. The use of the transient form of the equations was necessary to obtain oscillatory stability results.

2 Problem Definition

Consider a two-dimensional rectangular enclosure of width L and height H filled with a gas. The gas is initially quiescent at a uniform temperature T_0 and pressure p_0. The walls of the vessel are initially at the same temperature T_0. At times larger

Contributed by the Heat Transfer Division and presented at the ASME Winter Annual Meeting, Anaheim, California, December 7–12, 1986. Manuscript received by the Heat Transfer Division February 6, 1987. Keywords: Enclosure Flows, Natural Convection.

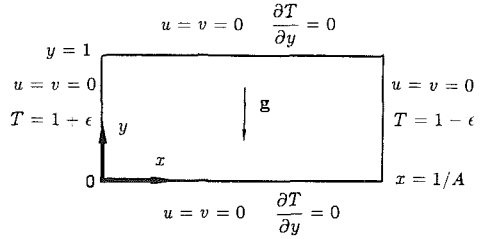

Fig. 1 Problem definition

than zero, the left and right walls are maintained at temperatures of T_h and T_c, respectively, where $T_h > T_c$. The top and bottom walls are insulated. The above problem is illustrated in Fig. 1, where we have used the following nondimensionalizations:

$$x_i^* = Hx_i, \quad t^* = \frac{H}{U}\, t, \quad v_i^* = Uv_i,$$

$$\bar{p}^* = p_0\bar{p}, \quad T^* = T_0 T, \quad \rho^* = \rho_0\rho, \quad \Pi^* = \rho_0 U^2\Pi, \tag{2.1}$$

$$\mu^* = \mu_0\mu, \quad k^* = k_0 k, \quad c_p^* = c_{p_0} c_p.$$

The independent dimensionless parameters appearing in the problem are

$$A = \frac{H}{L}, \quad \epsilon = \frac{\Delta T}{2T_0}, \quad \gamma = \frac{c_{p_0}}{c_{v_0}},$$

$$\mathrm{Pr} = \frac{\nu_0}{\alpha_0}, \quad \mathrm{Ra} = \frac{\beta_0 g H^3 \Delta T}{\nu_0 \alpha_0}, \quad \mathrm{M} = \frac{U}{c_0}. \tag{2.2}$$

The problem evolves in time t and can be described in terms of the velocity components $v_i = (u, v)$ in the $x_i = (x, y)$ directions, the density ρ, temperature T, and pressure p. The governing equations are statements of conservation of mass, momentum, and energy, with the addition of a state equation describing the gas. These equations, valid under a small Mach number approximation, have been derived by Paolucci (1982) and are given as follows:

$$\frac{\partial \rho}{\partial t} + \frac{\partial \rho v_j}{\partial x_j} = 0, \tag{2.3}$$

$$\frac{\partial \rho v_i}{\partial t} + \frac{\partial}{\partial x_j}(\rho v_j v_i) = -\frac{\partial \Pi}{\partial x_i} + \frac{\mathrm{RaPr}}{2\epsilon}\rho n_i + \mathrm{Pr}\frac{\partial}{\partial x_j}\tau_{ij}, \tag{2.4}$$

$$\rho c_p\left(\frac{\partial T}{\partial t} + v_j\frac{\partial T}{\partial x_j}\right) - \Gamma\frac{d\bar{p}}{dt} = \frac{\partial}{\partial x_j}\left(k\frac{\partial T}{\partial x_j}\right), \tag{2.5}$$

$$\rho = \rho(\bar{p}, T), \tag{2.6}$$

where $\Pi = p^{(1)}/(\gamma \mathrm{M}^2)$ is a reduced pressure that accounts for hydrostatic and dynamic effects, $p^{(1)}$ is the second term in the Mach number expansion of p and is $\mathrm{O}(\mathrm{M}^2)$, n_i is the unit vector in the direction of gravity, and the viscous stress tensor is given by

$$\tau_{ij} = \mu\left(\frac{\partial v_i}{\partial x_j} + \frac{\partial v_j}{\partial x_i}\right) - \frac{2}{3}\delta_{ij}\mu\frac{\partial v_k}{\partial x_k}. \tag{2.7}$$

The thermal conductivity, viscosity, and specific heat at constant pressure are functions of the thermodynamic variables. The Mach number only serves as a scaling for the pressure component Π, which contains both dynamic and hydrostatic effects. Γ only enters into the transient solution.

The dimensionless initial and boundary conditions are (see Fig. 1)

$$v_i(x, y, 0) = 0, \quad \bar{p}(0) = 1, \quad T(x, y, 0) = 1, \tag{2.8}$$

$$v_i(0, y, t) = v_i(1/A, y, t) = v_i(x, 0, t) = v_i(x, 1, t) = 0,$$

$$T(0, y, t) = 1 + \epsilon, \quad T(1/A, y, t) = 1 - \epsilon, \tag{2.9}$$

$$\frac{\partial T}{\partial y}(x, 0, t) = \frac{\partial T}{\partial y}(x, 1, t) = 0.$$

We note that it is difficult to maintain adiabatic boundary conditions on the horizontal walls in an experiment at $A \to 0$. This is particularly so in the non-Boussinesq range since we use a gas as the working fluid. However, we point out that the results obtained near the Boussinesq limit are valid for any Newtonian fluid.

The spatially uniform pressure $\bar{p} = p^{(0)}(t)$ appearing in the energy equation and the equation of state, which represents the first term in the expansion of p, accounts for the change of the static pressure with time. The separation of the pressure components, holding under the small Mach number approximation, is the essence of the acoustic wave "filtering" (Paolucci, 1982); however this splitting introduces $\bar{p}$ as an extra unknown. It can be shown that the differential equation for $\bar{p}$ using the ideal gas equation of state

$$\bar{p} = \rho T \tag{2.10}$$

is obtained by a statement of global mass conservation and the use of boundary conditions:

Nomenclature

A = aspect ratio $= H/L$
c_p = specific heat at constant pressure
c_v = specific heat at constant volume
C = constant
g = acceleration of gravity
H = cavity height
k = thermal conductivity
L = cavity width
M = Mach number $= U/c_0$
n_i = normal vector
Nu = Nusselt number
p = pressure
$\bar{p}$ = static pressure
Pr = Prandtl number $= \nu_0/\alpha_0$
Ra = Rayleigh number $= \beta_0 g \Delta T H^3/\alpha_0\nu_0$
S = cavity surface
S_k = constant
S_μ = constant
t = time
T = temperature
T_0 = reference temperature $= \frac{1}{2}(T_h + T_c)$
ΔT = temperature difference $= T_h - T_c$
U = reference speed $= \alpha_0/H$
v_i = velocity vector $= (u, v)$
V = cavity volume
x_i = coordinate directions $= (x, y)$
α = thermal diffusivity
β = coefficient of volume expansion $= 1/T$
γ = specific heat ratio $= c_{p_0}/c_{v_0}$
Γ = $(\gamma - 1)/\gamma$
δ = boundary layer thickness
δ_{ij} = Krönecker delta function
ϵ = wall temperature difference parameter $= \Delta T/2T_0$
Λ = constant
μ = dynamic viscosity
ν = kinematic viscosity
ξ = stretched x coordinate
Π = reduced pressure
ρ = density
τ_{ij} = viscous stress tensor
ψ = stream function
$(\ )_c$ = cold wall
$(\ )_h$ = hot wall
$(\ )_0$ = reference or initial values
$(\ )^*$ = dimensional variables
$(\ )_\infty$ = outside boundary layer

$$\frac{d\bar{p}}{dt}=\frac{1}{\int_V (c_p-\Gamma)dV}\left[\int_s k\frac{\partial T}{\partial x_j}\,dS_j+\bar{p}\int_V v_j\frac{\partial c_p}{\partial x_j}\,dV\right]. \tag{2.11}$$

If we let

$$D=\frac{\partial}{\partial x_i}(\rho v_i), \tag{2.12}$$

then it can be shown that the continuity equation (2.3) is identically satisfied if the pressure component Π is obtained from the following elliptic equation:

$$\frac{\partial^2\Pi}{\partial x_i\partial x_i}=\frac{\partial}{\partial x_i}R_i-\frac{\partial}{\partial t}D, \tag{2.13}$$

where

$$R_i=-\frac{\partial}{\partial x_j}(\rho v_j v_i)+\mathrm{Pr}\frac{\partial}{\partial x_j}\tau_{ij}+\frac{\mathrm{RaPr}}{2\epsilon}\rho n_i. \tag{2.14}$$

In this paper we only present results for an ideal diatomic gas ($c_p=1$, $\gamma=7/5$) with a reference Prandtl number $\mathrm{Pr}=0.71$. The dimensionless thermal conductivity and viscosity are obtained using the Sutherland-law forms

$$k=T^{3/2}(1+S_k)/(T+S_k), \tag{2.15}$$

$$\mu=T^{3/2}(1+S_\mu)/(T+S_\mu), \tag{2.16}$$

where White (1974) gives the dimensional values of $S^*=ST_0$ for viscosity and conductivity for a variety of gases along with their corresponding ranges of validity. Although the local Prandtl number is constant when $S_k=S_\mu$ and the specific heat at constant pressure is constant, this simplification is not justified in many cases.

Here we use the dimensionless values of $S_\mu=0.368$ and $S_k=0.648$ (local Prandtl number not constant). As an example, when $T_0=300$ K, $T_h=480$ K, and $T_c=120$ K ($\epsilon=0.6$), for air (Hilsenrath et al., 1960) the maximum viscosity error for the entire temperature range is less than 1 percent, that for c_p is approximately 2 percent (at the hot wall), and the maximum error in k is near -6 percent (at the cold wall). The accuracy of equation (2.15) degrades rapidly above $\epsilon=0.6$.

It is interesting to note that the steady-state results given here apply as well to gases other than air, although the temperature range may be somewhat different. For example, at a reference temperature of 260 K, hydrogen has a reference Prandtl number of 0.70, and $S_\mu=0.372$ and $S_k=0.641$, so that the results should be approximately the same as those for air, but for different values of L, H, and ΔT.

3 Numerical Scheme

The physical domain is discretized in the x-y plane using three interlacing meshes as shown schematically in Fig. 2: one (●) for the horizontal velocity component u, one (■) for the vertical velocity component v, and one (×) for all scalar variables. The positions of the grid points and their spacings are chosen such that the fluid boundaries lie between scalar points (×). Thus, the top and bottom boundaries go through v points (■), and the vertical boundaries go through u points (●). Note that there is one layer of grid points outside the region of interest, as indicated in Fig. 2, to facilitate the application of boundary conditions. Most of the computations were performed with an 81×41 grid network. The grid distribution was uniform in the vertical direction, while in the horizontal direction the nonuniform distribution described by Paolucci and Chenoweth (1988) was used. We note that the grid size ratio between the minimum and maximum size in the horizontal direction was varied between 0.003 for high Rayleigh numbers to 1.0 for the low Rayleigh numbers.

We have solved equations (2.4), (2.5), (2.7), (2.10), (2.11), and (2.13)–(2.16) using primitive variables on this staggered grid with an explicit predictor-corrector finite-difference method using forward differences for time derivatives and central differences for spatial derivatives, with a truncation error $O(\Delta t, \Delta x^2)$. For details and description of the computational procedure the reader is referred to Chenoweth and Paolucci (1986).

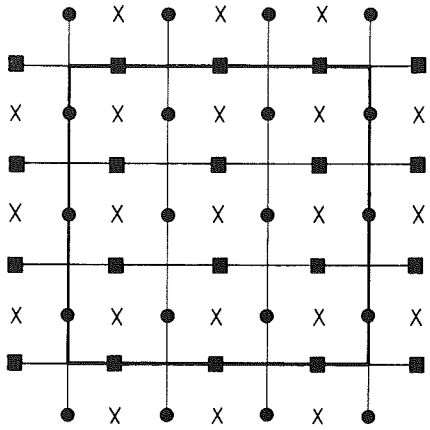

Fig. 2 Schematic structure of the discretized region in the x-y plane for the horizontal velocity u (●), the vertical velocity v (■), and all scalar variables (×). Thick full lines denote the boundaries of the rectangular region at $x=0$, $1/A$ (vertical lines) and $y=0$, 1 (horizontal lines).

The fluid velocity is prescribed on the boundaries of the cavity. This is done in two different ways: At those points lying on a boundary we fix the corresponding velocity component to the desired value, e.g., $u(\bullet)=0$ at $x=0$, $1/A$; for those components for which the computational points do not fall on a boundary, we force two interior points and the point exterior to the boundary to give the desired value at the wall by adjusting the velocity at the outside points by quadratic extrapolation. Temperature points do not lie on any boundary. Hence, we force two interior points and the point exterior to the boundary to yield a constant temperature on the vertical walls and a zero flux on the horizontal walls by quadratic extrapolations.

In solving the discretized form of the Poisson equation (2.13) knowledge of the reduced pressure gradient normal to the walls is required. A simple and popular choice is to set this gradient to zero as for boundary layer flows. For physical reasons no boundary conditions for Π ought to be prescribed at the walls. A zero gradient normal to the walls, however, is not a bad approximation as long as the Rayleigh number is high, so that a boundary layer exists, and as long as this boundary layer does not separate from the surface. Such is not the case in all wall regions of the cavity. A consistent and correct condition for the reduced pressure gradient is obtained by evaluating the momentum equations (2.4) at the walls.

All computations were perfomed within the parameter range $\mathrm{Ra}=10^2$–10^9, $A=0.025-1$, $\epsilon=0.005-0.6$, by a time-accurate integration of the equations so as to obtain the limits of steady flow presented in Section 4. All results presented in this work are at steady state. In addition, even though the computations were done using primitive variables, all velocity field results are presented in terms of the stream function defined by

$$\rho u=\frac{\partial\psi}{\partial y},\quad \rho v=-\frac{\partial\psi}{\partial x}, \tag{3.1}$$

to facilitate the display of recirculating regions. For validation and check of the accuracy of the computer program, the reader is referred to Chenoweth and Paolucci (1986).

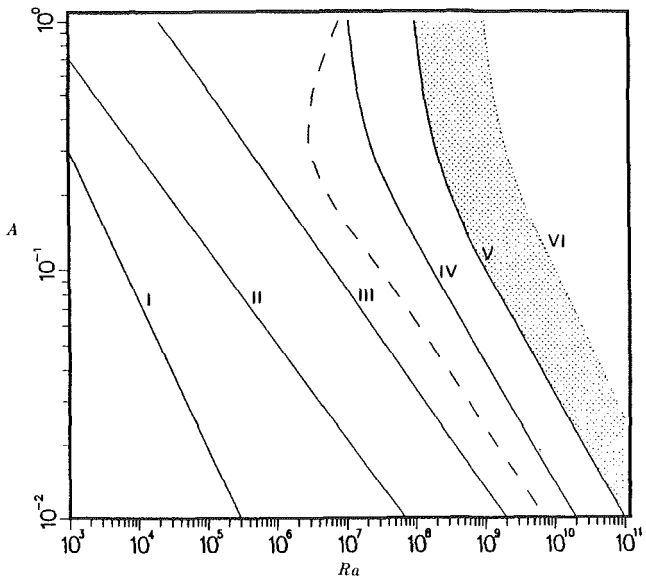

Fig. 3 Flow regions dependence on A, Ra and ϵ. Solid lines bound regions for $\epsilon = 0.005$, while the dashed line separates regions for $\epsilon = 0.6$. The shaded area represents transition to turbulence. All flow regions bounded by the numbered lines are explained in the text.

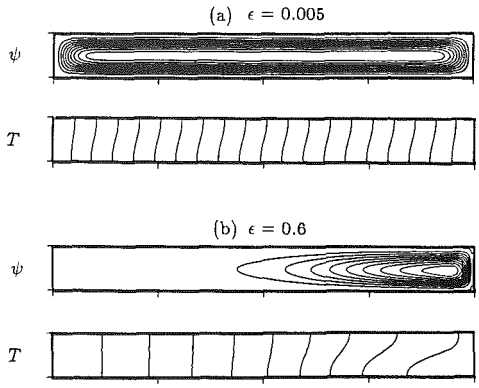

Fig. 4 Contour maps of stream function and temperature for $Ra = 10^3$, $A = 0.1$: (*a*) $\epsilon = 0.005$ with ψ contours at $-0.2645(0.2645 \times 10^{-2})0$, and T contours at $0.995(5 \times 10^{-4})1.005$, and (*b*) $\epsilon = 0.6$ with ψ contours at $-14.8(0.148)0$, and T contours at $0.4(0.12)1.6$

4 Flow Regimes

Figure 3 gives the various flow regions classified according to different velocity field behaviors. This figure is the result of many calculations and is given in A–Ra space for $\mathrm{Pr} = 0.71$ and two values of ϵ; the solid lines are for $\epsilon = 0.005$ and the dashed line is for $\epsilon = 0.6$. The numbered solid lines bound the different flow regions.

To the left of I the core flow is parallel. Cormack et al. (1974a) and Hart (1972) give the exact solution for this flow. It can be easily shown that in this region the maximum horizontal velocity is $u_m = \pm \mathrm{Ra}/72\sqrt{3}$ and its location is at $y_m = (1 \mp 1/\sqrt{3})/2$. In the region between I and II, parallel flow still exists in the core, but the magnitude of the maximum velocity decreases below u_m, even though its location remains the same. Cormack et al. (1974a) as well as Bejan and Tien (1978) give formulas for the variation of u_m that depend on aspect ratio and Rayleigh number. The flow remains unicellular between II and III, but the core flow becomes nonparallel and boundary layers exist next to the active walls. Thus all regions to the right of II are considered to be in the boundary layer regime. In the region between III and IV, secondary flows develop in the top-left and bottom-right (emerging) corner regions. These secondary flows separate and elongate as the Rayleigh number is increased and eventually grow to occupy most of the core region. The flow remains steady in the region between IV and V, but a weak tertiary flow develops in the center of the core region. The rotation of this cell is the same as to those of the primary and secondary flows. Finally to the right of V the flow becomes unsteady and eventually becomes turbulent to the right of VI. The unsteady flow is in the form of oscillations near the active walls. These oscillations, and resulting turbulence, are localized near the endwalls and emerging corners, and do not penetrate the central core region. We remark that throughout the entire boundary layer regime, the temperature in the central core region is approximately linearly stratified with horizontal isolines.

For $\epsilon = 0.6$ the flow is unicellular approximately up to line III. However, in contrast to the Boussinesq limit, no parallel flow was observed for the case, which has the character of either that to the left or right of I. Due to property variations, the flow on the cold wall enters the boundary layer regime long before II, while that at the hot wall makes that transition significantly to the right of II. Similarly, secondary flows develop near the emerging corners at the cold end significantly before III and at the hot end much later than III. A most important result is that at the dashed line the cold wall boundary layer becomes unsteady. This same transition corresponds to the line V in the Boussinesq limit. Note that there is a very large reduction in the critical Rayleigh number with increasing ϵ. In contrast, the hot wall layer remains steady well past line V. Similarly, there is a large Ra range where the flow at the cold wall end becomes turbulent, but the hot wall region and the core flow remain laminar since the turbulence is localized and does not penetrate very far into the central core.

5 Temperature, Velocity, and Stream Function

In this section we present detailed velocity, stream function, and temperature results illustrating the different regions of the parameter space shown in Fig. 3. Cormack et al. (1974a) and Hart (1972) presented an analytical solution valid in the limit $A \to 0$, and Ra and Pr arbitrary but fixed. Their solutions consisted of a parallel flow in the core of the cavity, which is valid to within $O(H)$ of the ends. In Fig. 4(*a*) we show the result of a computation for $\mathrm{Ra} = 10^3$, $A = 0.1$, and $\epsilon = 0.005$, which is within the Boussinesq limit and asymptotic limit of the analytical solution. The figure clearly shows the flow to be parallel, and furthermore the solution is in excellent quantitative agreement (within 1 percent) with the analytical solution.

The computations were repeated using the same conditions except that $\epsilon = 0.6$ was used. The resulting steady-state stream function and temperature fields are shown in Fig. 4(*b*). It is immediately apparent that in this case the flow in the core of the cavity is not parallel. Because of property variations we see that the flow is nearly stagnant in the left half of the region, while the boundary layer on the cold wall is considerably thinner than the corresponding one in the Boussinesq limit. This qualitative change in the flow is a strong function of ϵ. Indeed, computations for $\mathrm{Ra} = 100$ and $A = 0.025$ still show the flow to be very far from parallel. Thus we conclude that the classical analytical solution is only accurate in the Boussinesq limit, e.g., $\Delta T < 29°\mathrm{C}$ for air and $\Delta T < 1.3°\mathrm{C}$ for water with $T_0 = 300$ K (see Gray and Giorgini, 1976). The above result predicates that caution be used in interpretation of experimental results where ΔT is increased so as to obtain higher values of Rayleigh number. We note that the above conclusion for small A is fundamentally different than the corresponding one at large A. In that case it was shown by Chenoweth and Paolucci (1985) that the parallel flow solution valid in the

small Ra regime of the Boussinesq limit generalizes to a parallel flow solution for arbitrary ϵ.

Figures 5(a) and 5(b) for $\mathrm{Ra}=10^7$, $A=0.1$, and $\epsilon=0.005$ and 0.6, respectively, illustrate the fact that as Ra is increased to within the boundary layer regime, the flows in the core of the cavity become qualitatively similar in the two cases. This fact is further illustrated in Figs. 6(a) and 6(b), which show the horizontal velocity and temperature distributions at the mid-width of the cavity for the two cases. The relatively small asymmetry of the core flow in the case of $\epsilon=0.6$ can be traced back directly to property variations. In both cases we observe the presence of secondary flow in the emerging corners of the cavity. Although not clearly visible from Fig. 5(b), the secondary flow near the hot wall is much weaker than the Boussinesq counterpart, while near the cold wall, it is much more vigorous. This is due to the fact that the boundary layers near the hot and cold walls are much thicker and thinner, respectively, than the corresponding ones in the Boussinesq limit. (We will elaborate more on this point in the following section.) Because of the above fact, the cold wall boundary layer for $\epsilon=0.6$ and $A=0.1$ becomes unsteady for values of Ra not much greater than $\mathrm{Ra}=10^7$ (see Fig. 3). As Ra is increased further, the unsteadiness leads to turbulence. This scenario is repeated at the hot wall but for considerably larger values of Rayleigh numbers. We point out that the resulting unsteadiness and turbulence remains confined to the vicinity

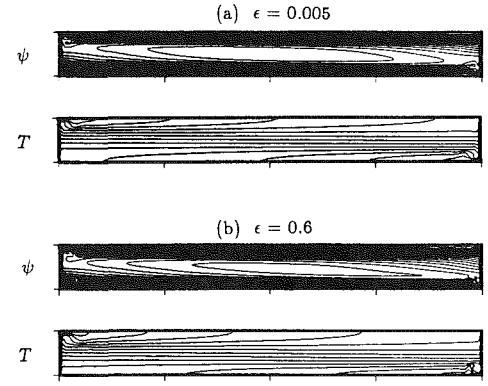

Fig. 5 Contour maps of stream function and temperature for $\mathrm{Ra}=10^7$, $A=0.1$: (a) $\epsilon=0.005$ with ψ contours at $-40.5(2.025)0$, and T contours at $0.995(5\times10^{-4})1.005$, and ($b$) $\epsilon=0.6$ with ψ contours at $-41.5(2.075)0$, and T contours at 0.4(0.06)1.6

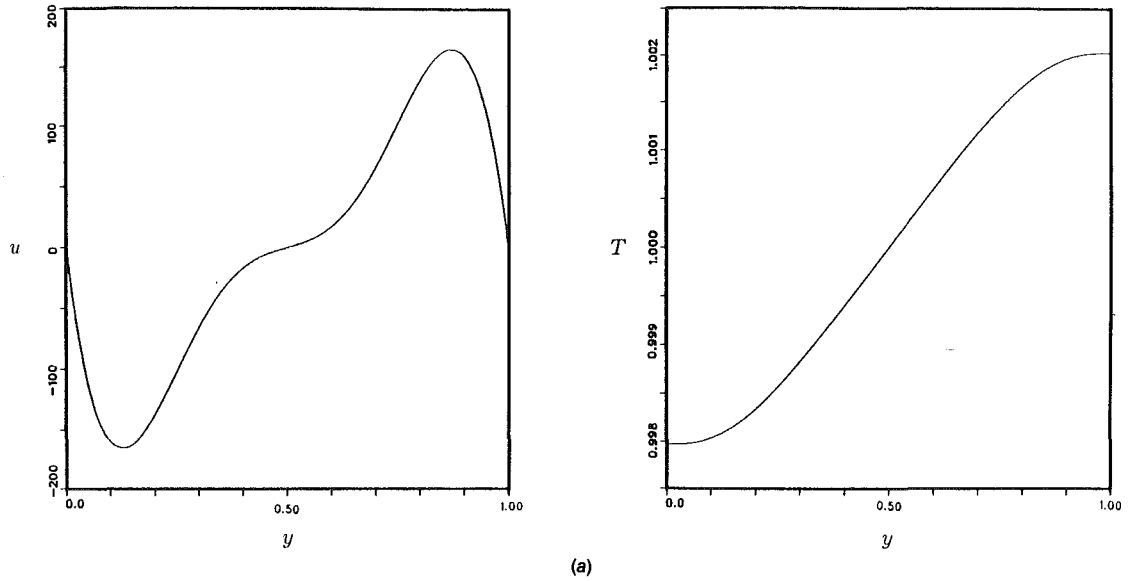

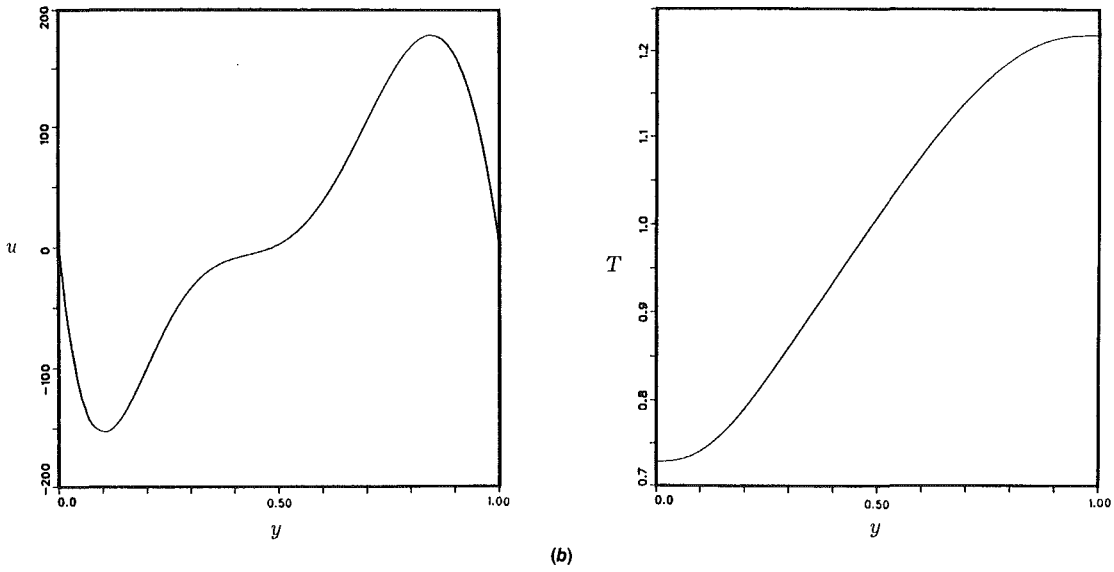

Fig. 6 Horizontal velocity and temperature profiles at $x=0.5/A$ for $\mathrm{Ra}=10^7$, $A=0.1$: (a) $\epsilon=0.005$, and (b) $\epsilon=0.6$

of the active walls and does not penetrate to the core, which remains well behaved.

For $\epsilon = 0.005$, which is near the Boussinesq limit, the flow remains steady for much higher values of Ra (see Fig. 3). In Fig. 7(*a*) we show the stream function and temperature fields for $\mathrm{Ra} = 10^8$ and $A = 0.1$. In this case we clearly see the presence of secondary flows in the core of the cavity. These secondary flows are in addition to smaller ones present near the emerging corners. The corresponding horizontal velocity and temperature distributions at the midwidth of the cavity are shown in Fig. 8(*a*). The reverse flows due to the secondary circulations are clearly apparent. We point out that the flow is antisymmetric with respect to the center but nonparallel. We also note from Figs. 7(*a*) and 8(*a*) that the temperature is approximately linearly stratified over most of the core. This fact is one of the primary indicators that a flow is within the boundary layer regime. The presence of this weak reverse flow is clearly apparent in the experimental results of Bejan et al. (1981) and Al-Homoud and Bejan (1979). We note that Shiralkar et al. (1981) were not able to reproduce this result in their numerical solutions, since we believe that their solutions contained substantial artificial diffusion due to their upwind treatment of the nonlinear convective terms. Furthermore, as they themselves noted (due to this same fictitious diffusion) the velocity boundary layers on the top and bottom walls don't decay as rapidly toward the center as experiments and

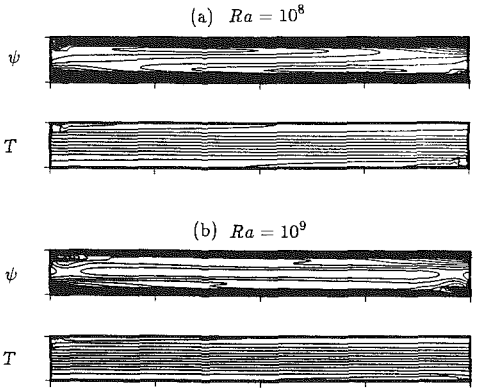

Fig. 7 Contour maps of stream function and temperature for $A = 0.1$, $\epsilon = 0.005$: (a) $\mathrm{Ra} = 10^8$ with ψ contours at $-62.8(3.14)0$, and T contours at $0.995(5 \times 10^{-4})1.005$, and (b) $\mathrm{Ra} = 10^9$ with ψ contours at $-117.7(5.89)0$, and T contours at $0.995(5 \times 10^{-4})1.005$

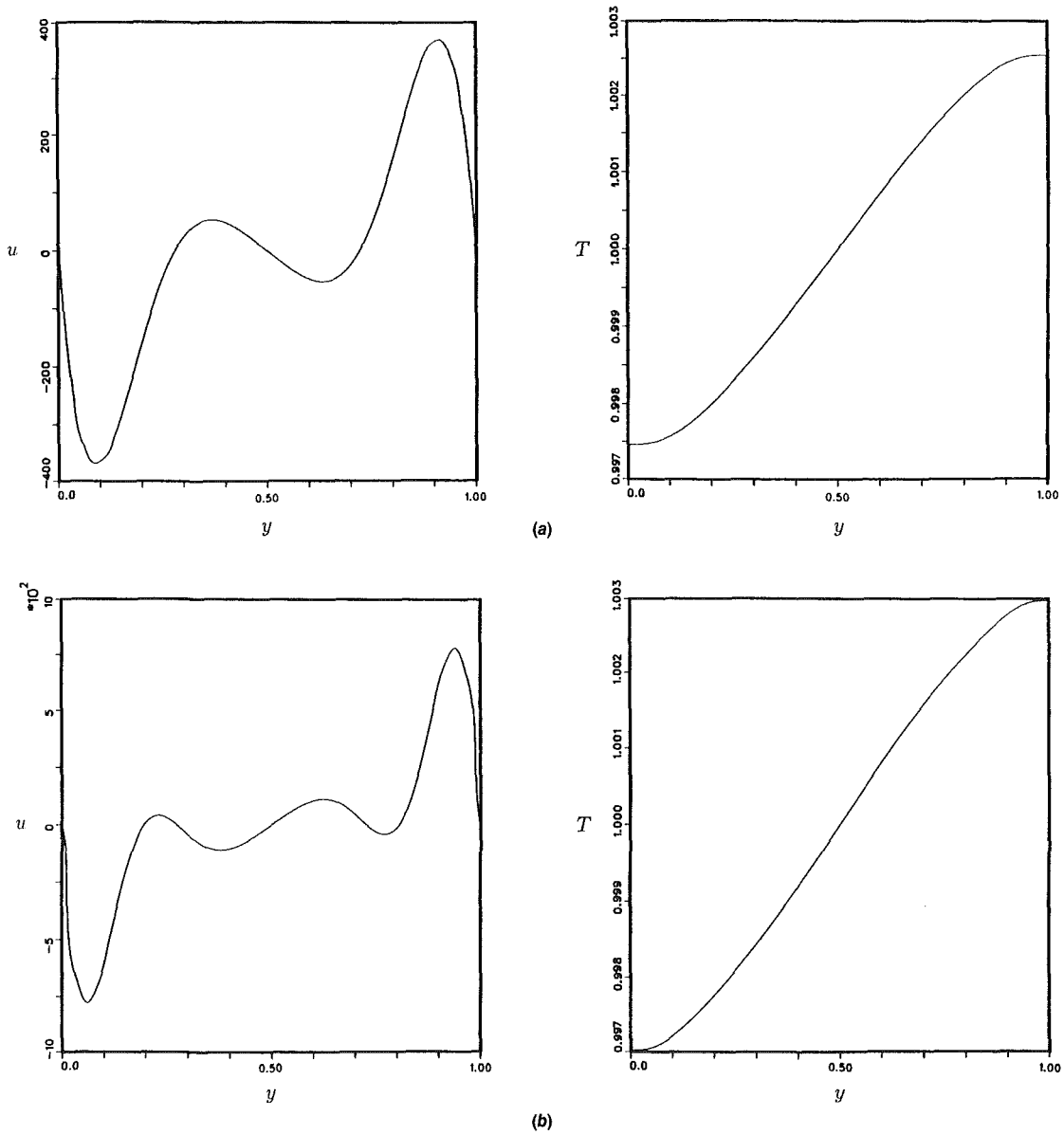

Fig. 8 Horizontal velocity and temperature profiles at $x = 0.5/A$ for $A = 0.1$, $\epsilon = 0.005$: (a) $\mathrm{Ra} = 10^8$, and (b) $\mathrm{Ra} = 10^9$

our results show. Tichy and Gadgil (1982), "using an approximate analysis based on first principles," obtained an analytical solution containing arbitrary constants purported to be valid in this high Ra regime. Furthermore, using the same scheme as Shiralkar et al. (1981), they obtain numerical solutions in the same regime, which they then use to choose the constants so that the two results are in close agreement. They also note that their resulting core velocity field is qualitatively different than the experimental results of Al-Homoud and Bejan. However, they attribute this difference to experimental heat losses on the horizontal walls. The present results very clearly indicate that the reason for the disagreement between the above works and the experimental results is due primarily to the use of the upwind scheme in their numerical solutions.

In Fig. 7(*b*) we show the stream function and temperature fields for $\mathrm{Ra}=10^9$ and at the same aspect ratio of $A=0.1$. First, the secondary flow near the corners starts to become elongated. More importantly, we observe the creation of a thin cell which occupies most of the length of the core region and is sandwiched in the center between the original secondary cells. This tertiary flow, to our knowledge, has never been previously observed experimentally or numerically. The sense of rotation of the flow in this cell is clockwise, which is the same as that of the primary and secondary cells. Note that additional shear regions now exist between the secondary and tertiary cells. The creation of the tertiary flow appears to be due to an instability arising from the strong torques applied by the secondary cells in the core. The horizontal velocity and temperature distributions at the midwidth of the cavity for this case are shown in Fig. 8(*b*). From the figure we clearly observe the double reverse flow indicated by Fig. 7(*b*). No further bifurcations in the core flow are observed before the flow becomes unsteady. To observe the above phenomena experimentally would require very good accuracy in the velocity measurements in the central region of the core flow.

6 Vertical Boundary Layers

The equations governing the fluid flow in the rectangular enclosure are given by equations (2.3)–(2.6). As the Rayleigh number is increased, the boundary layers on the active vertical walls get thinner. The region to the right of II in Fig. 3 is the boundary layer regime. In this region, the boundary layer thickness δ is much smaller than both the height H and width L. Here, the strong temperature variation is confined to the two very thin fluid layers adjacent to the vertical walls.

The structure of the boundary layer in the Boussinesq regime has been discussed by Gill (1966) and Elder (1965). Since $\delta << L$, one feature of the boundary layer is that it is driven not by the imposed temperature difference between the vertical walls, but by the difference between each wall and the thermally stratified fluid filling the core region. Another important feature is due to the centrosymmetry of this limiting problem. At the midheight of the cavity, the temperature is unity in the core, and the boundary layer exhibits no entrainment of core fluid, i.e., the horizontal velocity component u is zero across the boundary layer. Indeed, sufficiently away from the top and bottom ends, the entrainment remains relatively small. Gill further shows that the boundary layer structure is only weakly dependent on the Prandtl number. Below, we will use these observations in developing a boundary layer theory for arbitrary temperature difference between the walls and the thermally stratified core.

When $\delta << L$ and H, we can make the standard boundary layer approximation to the steady equations (2.3)–(2.5) where we neglect the $\partial^2/\partial y^2$ terms in favor of the $\partial^2/\partial x^2$ terms, to obtain

$$\frac{\partial \rho u}{\partial x}+\frac{\partial \rho v}{\partial y}=0, \tag{6.1}$$

$$\frac{\partial \Pi}{\partial x}=0, \tag{6.2}$$

$$\rho u\frac{\partial v}{\partial x}+\rho v\frac{\partial v}{\partial y}=-\frac{\partial \Pi}{\partial y}-\frac{\mathrm{RaPr}}{2\epsilon}\rho+\mathrm{Pr}\frac{\partial}{\partial x}\left(\mu\frac{\partial v}{\partial x}\right), \tag{6.3}$$

$$\rho u\frac{\partial T}{\partial x}+\rho v\frac{\partial T}{\partial y}=\frac{\partial}{\partial x}\left(k\frac{\partial T}{\partial x}\right). \tag{6.4}$$

In writing the above equations, we took the specific heats to be constant. If we eliminate II between equations (6.2) and (6.3), and integrate the resulting equation once from a value x in the boundary layer to a value of ∞ in the core, we obtain

$$\frac{1}{\mathrm{Pr}}\left[\rho u\frac{\partial v}{\partial x}+\rho v\frac{\partial v}{\partial y}\right]=\frac{\partial}{\partial x}\left(\mu\frac{\partial v}{\partial x}\right)-\frac{\mathrm{Ra}}{2\epsilon}\left[\rho-\rho_\infty(y)\right]. \tag{6.5}$$

For arbitrary temperature difference the problem does not possess the centrosymmetry property. However, we still expect (and numerical solutions show) that near $y=0.5$, the entrainment in the boundary layer is very small. In addition, at the midheight, the temperature in the core is unity to a first approximation. After setting $u\approx 0$ and $\rho_\infty\approx 1$ in equations (6.1), (6.4), and (6.5) evaluated at $y=0.5$, we find that the equations are still nonlinear, and therefore difficult to treat analytically. Following Gill (1966), we regard $\partial T/\partial y$ appearing in equation (6.4) as a known constant Λ that we later relate to the observed constant vertical temperature gradient present outside the boundary layer, in the core region. However, whereas in the Boussinesq limit $\partial v/\partial y$ is zero at the midheight (from equation (6.1)), this is clearly not the case for arbitrary ϵ. The nonlinear term $\rho v\partial v/\partial y$ appearing in (6.5) can still be neglected in the large Prandtl number limit. To make the problem amenable to analysis we will neglect this term even for $\mathrm{Pr}=\mathrm{O}(1)$. This approximation can be justified a posteriori, since the numerical solutions of the full equations show that in the boundary layer the term is negligible in comparison to the other terms retained. Thus we are left to solve the following equations valid near $y=0.5$:

$$\frac{\partial \rho v}{\partial y}=0, \tag{6.6}$$

$$\frac{\partial}{\partial x}\left(\mu\frac{\partial v}{\partial x}\right)=\frac{\mathrm{Ra}}{2\epsilon}(\rho-1), \tag{6.7}$$

$$\frac{\partial}{\partial x}\left(k\frac{\partial T}{\partial x}\right)=\Lambda\rho v, \tag{6.8}$$

$$\bar{p}=\rho T, \tag{6.9}$$

with boundary conditions

$$v(x=0)=v(x\to\infty)=0,\quad T(x=0)=1\pm\epsilon,\quad T(x\to\infty)=1. \tag{6.10}$$

We note that in the boundary conditions, $x\to\infty$ means "outside the boundary layer," and the plus and minus signs denote a heated or cooled wall, respectively, located at $x=0$.

Now let

$$\xi=\int_0^x \rho dx', \tag{6.11}$$

and assume that the thermal conductivity and viscosity vary linearly with temperature. Then, after eliminating ρ in equation (6.7) by making use of equation (6.9), it is a simple matter of algebra to show the equations (6.7) and (6.8) in the variable ξ reduce to the same form as those treated by Gill (1966).

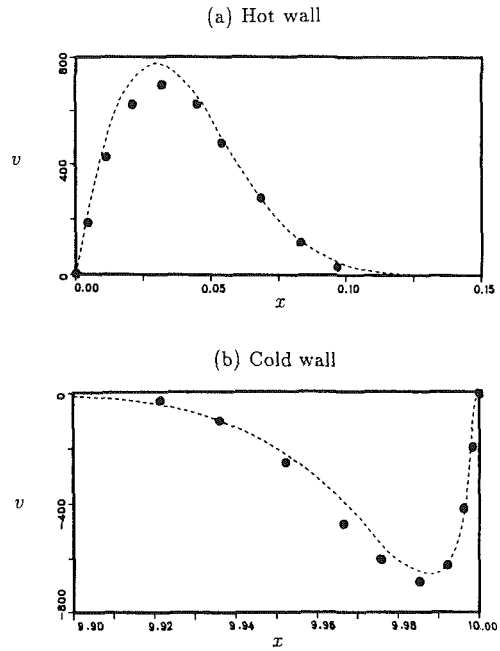

Fig. 9 Boundary layer profiles at the hot and cold wall and at $y = 0.5$ for $Ra = 10^7$, $A = 0.1$, and $\epsilon = 0.6$. The lines denote the numerical solution, while the symbols are obtained from equations (6.12) and (6.14)

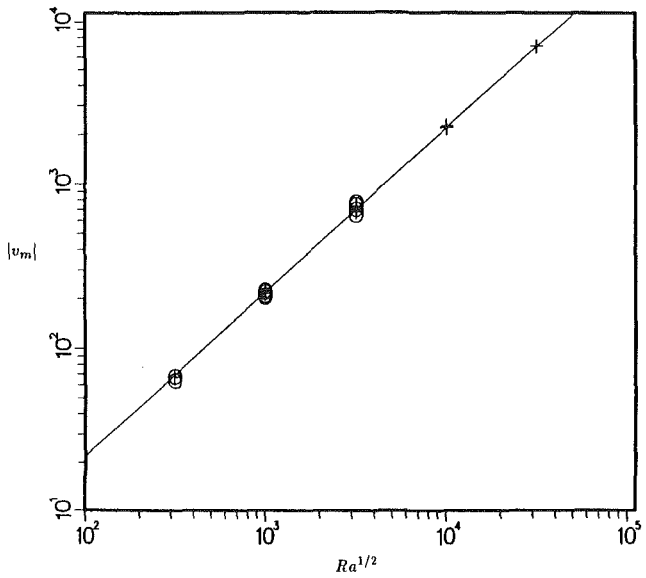

Fig. 10 Magnitude of maximum velocity in the hot and cold wall boundary layers versus $Ra^{1/2}$: ——— equation (6.16), $+\epsilon = 0.005$, $\circ\ \epsilon = 0.6$. The symbols are results of numerical solutions.

Thus, making use of Gill's solution, it can be shown that the boundary layer structure for arbitrary ϵ is given by

$$v = \frac{1}{2}\left(\frac{\mathrm{Ra}}{C\bar{p}}\right)^{1/2} e^{-b\xi/\sqrt{2}} \sin\left(\frac{b\xi}{\sqrt{2}}\right), \tag{6.12}$$

$$T = 1 \pm \epsilon e^{-b\xi/\sqrt{2}} \cos\left(\frac{b\xi}{\sqrt{2}}\right), \tag{6.13}$$

and

$$x = \frac{\pm\epsilon}{\sqrt{2}} (C\bar{p}\mathrm{Ra})^{-1/4}\left\{1 \pm \frac{2}{\epsilon}\left(\frac{b\xi}{\sqrt{2}}\right) - e^{-b\xi/\sqrt{2}}\left[\cos\left(\frac{b\xi}{\sqrt{2}}\right) - \sin\left(\frac{b\xi}{\sqrt{2}}\right)\right]\right\}, \tag{6.14}$$

where

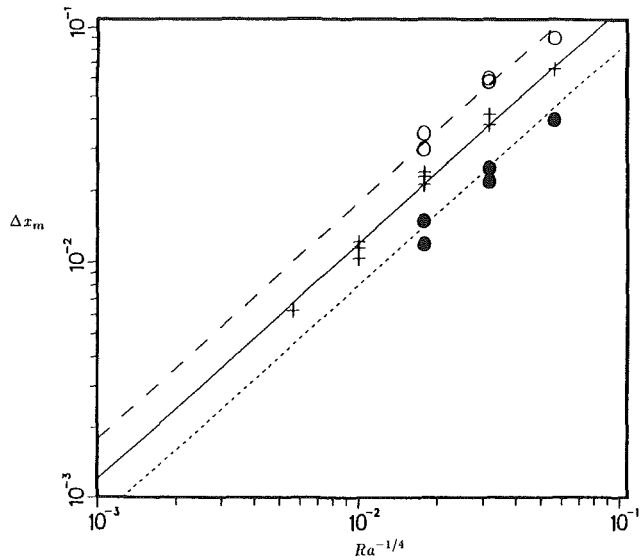

Fig. 11 Distance from wall of maximum velocity in the hot and cold wall boundary layers versus $Ra^{-1/4}$: ——— $\epsilon = 0$, — — — $\epsilon = 0.6$ (hot wall). - - - - - $\epsilon = 0.6$ (cold wall), $+\ \epsilon = 0.005$, $\circ\ \epsilon = 0.6$ (hot wall), $\bullet$ $\epsilon = 0.6$ (cold wall). The symbols are results of numerical solutions, while the lines are obtained from equation (6.17).

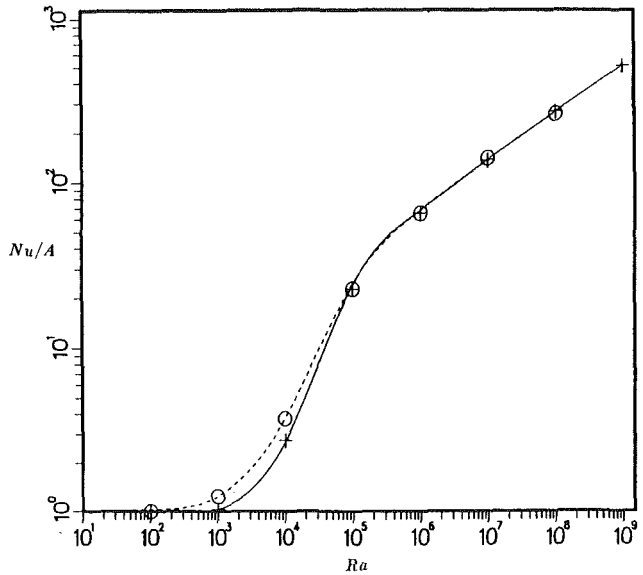

Fig. 12 Nusselt number versus Rayleigh number correlations for $A = 0.1$: ——— $\epsilon = 0.005$, - - - - - $\epsilon = 0.6$, $+\ \epsilon = 0.005$, $\circ\ \epsilon = 0.6$. The symbols are results of numerical solutions, while the lines are obtained from equation (7.1).

$$b = \frac{(C\bar{p}\mathrm{Ra})^{1/4}}{A\bar{p}}. \tag{6.15}$$

Solutions for the maximum absolute value of velocity, and its location from the wall, can be readily obtained from equations (6.12) and (6.14) resulting in

$$|v_m| = \frac{e^{-\pi/4}}{2\sqrt{2}}\left(\frac{\mathrm{Ra}}{C\bar{p}}\right)^{1/2}, \tag{6.16}$$

$$x_m = \frac{\pi}{2\sqrt{2}}\left(1 \pm \frac{2\epsilon}{\pi}\right)(C\bar{p}\mathrm{Ra})^{-1/4}. \tag{6.17}$$

In writing the above solutions, we have used the fact that in the boundary layer limit $\Lambda \approx 2\epsilon C$ (see Chenoweth and Paolucci, 1986), where C varies slightly with Ra, A, and ϵ. Here, we will take $C\bar{p} = 0.54$ to recover the constant obtained in the Boussinesq limit by Chenoweth and Paolucci (1986).

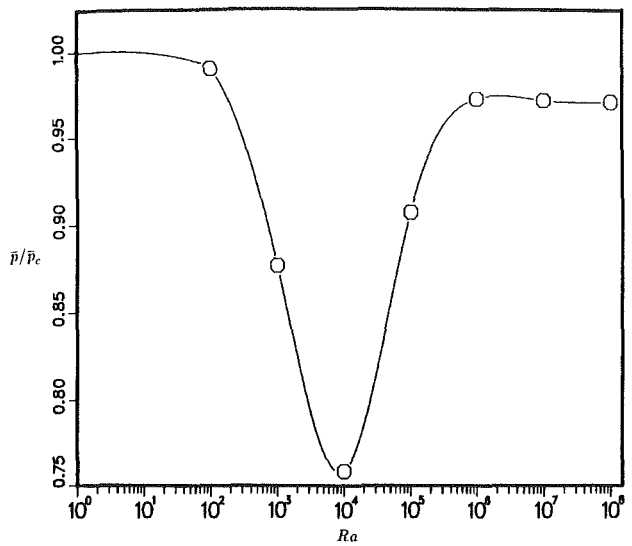

Fig. 13 Pressure versus Rayleigh number for $A = 0.1$ and $\epsilon = 0.6$. The computed points have been connected using a cubic spline interpolation.

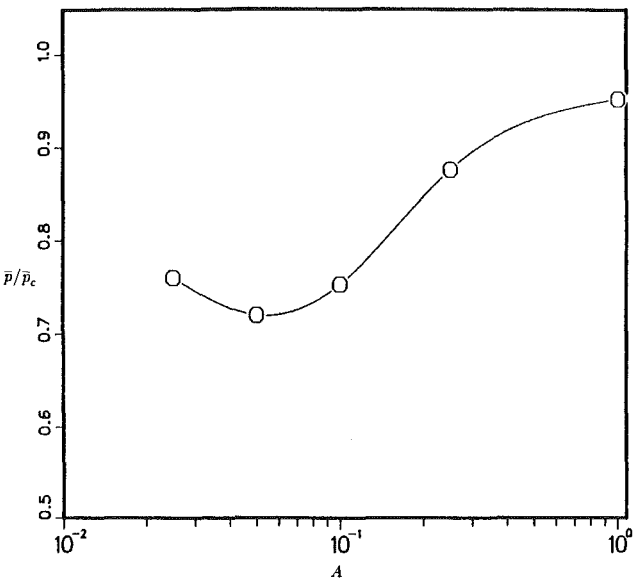

Fig. 14 Pressure versus aspect ratio for $Ra = 10^4$ and $\epsilon = 0.6$. The computed points have been connected using a cubic spline interpolation.

In Figs. 9(*a*) and 9(*b*) we show a comparison of the hot and cold wall velocity distributions, respectively, obtained from equations (6.12) and (6.14) to those obtained numerically for the specific case of $Ra = 10^7$, $A = 0.1$, and $\epsilon = 0.6$. As can be observed, the two results are in good quantitative agreement. Note that the scales are different on the two figures, and that the maximum velocity on the hot wall is located approximately three times farther from the wall than that at the cold end.

In Fig. 10 we show as a solid line the absolute value of the maximum vertical velocity $|v_m|$ versus $Ra^{1/2}$ as given by equation (6.16). The symbols represent numerical results obtained in the boundary layer range of $Ra = 10^5$–10^9, $A = 0.025$–1, and $\epsilon = 0$–0.6. We note that for any fixed ϵ we obtain two values of $|v_m|$ (from the hot and cold walls), which in the Boussinesq limit are equal. Equation (6.16) and the numerical results displayed in Fig. 10, as well as those given by Chenoweth and Paolucci (1986), show that any ϵ dependence is relatively weak, in agreement with the correlations given by Chenoweth and Paolucci (1986). Furthermore, the agreement with (6.16) is very good.

Figure 11 shows the locations of $|v_m|$ off the wall, Δx_m, versus $Ra^{-1/4}$ for $\epsilon = 0$, and 0.6, representing the Boussinesq limit, and the hot and cold wall for finite ϵ, respectively. The lines are obtained from equation (6.17) while the symbols are results of numerical computations for the same range of parameters used in Fig. 10. The agreement between the two sets of results is good. Additionally, we note that equation (6.17) is in reasonable agreement with the correlations obtained from the extensive numerical computations of Chenoweth and Paolucci (1986) for $A \geq 1$. They both display a strong linear dependence with ϵ, and the constants are within 20 percent of each other. The slight aspect ratio dependence for the location from the cold wall obtained by Chenoweth and Paolucci (1986) obviously cannot be obtained from a boundary layer analysis.

7 Pressure and Heat Transfer

When $A \geq 1$ it has been shown (see Chenoweth and Paolucci, 1986) that the Nusselt number, based on the exact conduction heat flux, has little dependence on the parameter ϵ over the entire range of $0 \leq Ra \leq 10^7$. However for $A < 1$ this is not the case. Figure 12 gives Nu/A versus Ra for $A = 0.1$ and two values of ϵ, $\epsilon = 0.005$ and $\epsilon = 0.6$. It can be seen that for $Ra > 10^5$, the power law correlation obtained in the Boussinesq limit is valid in the boundary-layer regime. Therefore, in that region we find no ϵ dependence. Below $Ra = 10^5$ there is significant ϵ dependence, and it is the direct result of the greatly different behavior near the cold and hot walls when $\epsilon = 0.6$. Here, as noted, the flow is fundamentally different from the parallel core flow found in the Boussinesq limit. For approximately $A < 0.5$ our results show that the Nusselt number is correlated by

$$Nu/A - 1 = [(2.7\epsilon\eta + \eta^2)^n + (1.05\eta^{0.288}/A^{1.188})^n]^{1/n} \qquad (7.1)$$

where $n = -0.585$ and $\eta = ARa/602.4$. Note that for low Ra, the form of the aspect ratio dependence in the first term inside the brackets is incorrect for $A > 0.5$, even in the Boussinesq limit, since a parallel core flow can never develop. In addition, Chenoweth and Paolucci (1986) show that in the boundary layer regime and for aspect ratios near unity, the correlation has a more complicated aspect ratio dependence than is given by the second term in (7.1). The correlation (7.1) includes the proper asymptotic behavior in a form given by Bejan and Tien (1978), but with different constants and an additional term describing non-Boussinesq effects. It should be noted that Shiralkar and Tien (1981) have generalized the Boussinesq correlation obtained by Bejan and Tien since they found it to have poor accuracy in the intermediate range of $10^4 \leq Ra \leq 10^6$. They introduced coefficients having a complicated aspect ratio dependence that modify both the high and low Ra limits in equation (7.1). We do not have sufficient data to verify these formulas for $\epsilon << 1$. However, it should be noted that they determined n to be -0.386 and their high Ra power law included $Ra^{0.2}$, compared to our $n = -0.585$ and $Ra^{0.288}$. Some of this difference may be due to our use of data for $Ra \leq 10^9$, which is several orders of magnitude larger than their maximum Rayleigh number. The Rayleigh number power of 0.288 is in close agreement with the value of 0.3 obtained by Ostrach (1982). We note that the correlation value of 0.288 represents an average over a very large range of Ra and A. In reality we observe that this power is a function of both Ra and A, and for $A >> 1$ it approaches 1/4 asymptotically for large Rayleigh numbers (see Chenoweth and Paolucci, 1986). Shiralkar and Tien examined a very wide range of Prandtl numbers and found that Nu was essentially independent of it for $Pr > 0.3$, but the dependence was significant below that value.

For highly non-Boussinesq convection problems, it has been

shown by Chenoweth and Paolucci (1985, 1986) that the pressure level must decrease in a closed system. In the conduction limit of $\mathrm{Ra} \to 0$, about a 1 percent pressure drop is found when $\epsilon = 0.6$. For the same value of ϵ, $A \geq 1$, and $0 < \mathrm{Ra} < 10^7$, as much as a 5 percent drop beyond the conduction pressure $\bar{p}_c$ is observed. Here, for $A < 1$ we obtain much larger decreases in pressure. The example shown in Fig. 13 for $A = 0.1$ and $\epsilon = 0.6$ indicates that the normalized pressure decreases by 25 percent near $\mathrm{Ra} = 10^4$. This large pressure drop occurs in the region $10^2 < \mathrm{Ra} < 10^4$. This corresponds to the same region where convection is increasing at the cold end, while the hot end remains essentially stagnant. This physical behavior is responsible for the nonexistence of parallel flow in non-Boussinesq problems. Subsequently, for Rayleigh numbers between 10^4 and 10^6, convection increases greatly at the hot end, causing a recovery in static pressure. For $\mathrm{Ra} > 10^6$, when both walls enter the boundary layer regime, a small pressure drop is maintained due to the asymmetry in the boundary layers. The plot of $\bar{p}/\bar{p}_c$ versus A in Fig. 14 for $\epsilon = 0.6$ and $\mathrm{Ra} = 10^4$ shows that a minimum pressure is reached near $A = 0.05$; for smaller values of aspect ratio the stagnant flow occupies most of the cavity so that the pressure must return toward the conduction pressure level $\bar{p}_c$ as $A \to 0$.

8 Conclusions

The numerical solutions to the non-Boussinesq equations presented here contribute to the physical understanding of the low-aspect-ratio convection problem for a broad range of parameters. The results are compared to existing Boussinesq solutions, which we also extend to higher Rayleigh numbers. Contrary to the recent result of Shiralkar et al. (1981) and Tichy and Gadgil (1982), we find the presence of weak reverse flows in the core region, for high Ra in the boundary layer regime, in agreement with experimental results. In addition, for still higher Ra, we observe this flow to bifurcate and lead to a tertiary flow consisting of a central cell having the same rotation as the primary and secondary cells. This last result, to our knowledge, has not been previously observed either experimentally or numerically.

In the non-Boussinesq regime, the velocity and temperature fields show significant dependence on ϵ especially near the side walls. As a result, the well-known parallel flow solution, accurate in the core of the cavity for $\epsilon << 1$, does not exist. For higher Rayleigh numbers, we generalize the well-known analytical boundary layer solution of Gill (1966) to the case of arbitrary ϵ. This solution and the numerical results show that the cold-wall boundary layer is much thinner than the corresponding layer in the Boussinesq limit. As a result, the critical Rayleigh numbers of stationary and oscillatory instabilities are lowered with increasing temperature difference and are governed by the cold wall. In contrast to the high-aspect-ratio problem, the heat transfer and pressure also depend strongly on ϵ. Although the average Nusselt number is almost independent of ϵ in the boundary layer regime, this is not the case for lower Rayleigh numbers. Furthermore, the largest pressure change occurs in this same low Rayleigh number region. Both effects are physically related to the large departures from the parallel flow solution valid in the Boussinesq limit. These results show that there can be considerable risk if results obtained from the well-established Boussinesq limit are extrapolated for use where large temperature differences exist.

Acknowledgments

This work was performed under the auspices of the U.S. Department of Energy by Sandia National Laboratories, Livermore, CA, under Contract No. DE-AC04-76DP00789.

References

Al-Homoud, A. A., and Bejan, A., 1979, "Experimental Study of High Rayleigh Number Convection in a Horizontal Cavity With Different End Temperatures," Rep. CUMER-79-1, Dept. of Mech. Eng., University of Colorado, Boulder, CO.

Bejan, A., Al-Homoud, A. A., and Imberger, J., 1981, "Experimental Study of High-Rayleigh-Number Convection in a Horizontal Cavity With Different End Temperatures," *J. Fluid Mech.*, Vol. 109, pp. 283–299.

Bejan, A., and Tien, C. L., 1978, "Laminar Natural Convection Heat Transfer in a Horizontal Cavity With Different End Temperatures," ASME JOURNAL OF HEAT TRANSFER, Vol. 100, pp. 641–647.

Chenoweth, D. R., and Paolucci, S., 1985, "Gas Flow in Vertical Slots With Large Horizontal Temperature Differences," *Phys. Fluids*, Vol. 28, pp. 2365–2374.

Chenoweth, D. R., and Paolucci, S., 1986, "Natural Convection in an Enclosed Vertical Air Layer With Large Horizontal Temperature Differences," *J. Fluid Mech.*, Vol. 169, pp. 173–210.

Cormack, D. E., Leal, L. G., and Imberger, J., 1974a, "Natural Convection in a Shallow Cavity With Differentially Heated End Walls, Pt. 1, Asymptotic Theory," *J. Fluid Mech.*, Vol. 65, pp. 209–229.

Cormack, D. E., Leal, L. G., and Seinfield, J. H., 1974b, "Natural Convection in a Shallow Cavity With Differentially Heated End Walls, Pt. 2, Numerical Solutions," *J. Fluid Mech.*, Vol. 65, pp. 231–246.

Elder, J. W., 1965, "Laminar Free Convection in a Vertical Slot," *J. Fluid Mech.*, Vol. 23, pp. 77–98.

Gill, A. E., 1966, "The Boundary Layer Regime for Convection in a Rectangular Cavity," *J. Fluid Mech.*, Vol. 26, pp. 515–536.

Gray, D. D., and Giorgini, A., 1976, "The Validity of the Boussinesq Approximation for Liquids and Gases," *Int. J. Heat Mass Transfer*, Vol. 19, pp. 545–551.

Hart, J. E., 1972, "Stability of Thin Non-rotating Hadley Circulations," *J. Atmos. Sci.*, Vol. 29, pp. 687–697.

Hilsenrath, J., Beckett, C. W., Benedict, W. S., Fano, L., Hodge, H. J., Masi, J. F., Nuttall, R. L., Touloukian, Y. S., and Woolley, H. W., 1960, *Tables of Thermodynamic and Transport Properties*, Pergamon, New York.

Imberger, J., 1974, "Natural Convection in a Shallow Cavity With Differentially Heated End Walls. Pt. 3, Experimental Results," *J. Fluid Mech.*, Vol. 65, pp. 247–260.

Kamotani, Y., Wang, L. W., and Ostrach, S., 1983, "Experiments on Natural Convection Heat Transfer in Low Aspect Ratio Enclosures," *AIAA J.*, Vol. 21, pp. 290–294.

Ostrach, S., 1982, "Natural Convection Heat Transfer in Cavities and Cells," *Heat Transfer 1982*, Vol. 1, Hemisphere Publishing Corp., pp. 365–379.

Ostrach, S., Loka, R. R., and Kumar, A., 1980, "Natural Convection in Low Aspect-Ratio Rectangular Enclosures," *Natural Convection in Enclosures*, K. E. Torrance and I. Catton, eds., ASME HTD-Vol. 8, pp. 1–10.

Paolucci, S., 1982, "On the Filtering of Sound from the Navier–Stokes Equations," Sandia National Laboratories Rep. SAND82-8257.

Paolucci, S., and Chenoweth, D. R., 1988, "Transition to Chaos in a Differentially Heated Vertical Cavity," submitted to *J. Fluid Mech.*

Shiralkar, G. S., Gadgil, A., and Tien, C. L., 1981, "High Rayleigh Number Convection in Shallow Enclosures With Different End Temperatures," *Int. J. Heat Mass Transfer*, Vol. 24, pp. 1621–1629.

Shiralkar, G. S., and Tien, C. L., 1981, "A Numerical Study of Laminar Natural Convection in Shallow Cavities," ASME JOURNAL OF HEAT TRANSFER, Vol. 103, pp. 226–231.

Tichy, J., and Gadgil, A., 1982, "High Rayleigh Number Laminar Convection in Low Aspect Ratio Enclosures With Adiabatic Horizontal Walls and Differentially Heated Vertical Walls," ASME JOURNAL OF HEAT TRANSFER, Vol. 104, pp. 103–110.

White, F. M., 1974, *Viscous Fluid Flow*, McGraw-Hill, New York, pp. 29–32.

An Effective Equation Governing Convective Transport in Porous Media

J. G. Georgiadis[1]

I. Catton

Department of Mechanical, Aerospace, and Nuclear Engineering, University of California, Los Angeles, CA 90024

The fine structure of disordered porous media (e.g., fully saturated randomly packed beds) causes microscopic velocity fluctuations. The effect of the spatial and temporal randomness of the interstitial velocity field on the convective transport of a scalar (heat or mass) is investigated analytically. For a uniform mean velocity profile, the effective heat transport equation is obtained as the equation governing the transport of the ensemble average of the scalar under conditions of steady or unsteady random fields (with given statistics). In both cases, it is shown that the effective transport coefficient is enhanced by a hydrodynamic dispersive component, which is an explicit function of the mean filtration velocity. The agreement with experiments is encouraging. The effective transport equation is then generalized to three-dimensional mean velocity fields for isotropic media.

Introduction

In recent years, the determination of the effective transport coefficients has received considerable attention from researchers who are studying the transport of heat (or a conservative solute) through fully saturated porous media by advection and diffusion. In his study of thermoconvective transport through porous media, Rubin (1977) used an effective thermal conductivity that was a linear function of the local filtration velocity. Prasad et al. (1985) demonstrated that the large-scale divergence of correlations of Nusselt as a function of Rayleigh number (which has been reported for natural convection in packed beds) can be reduced by using an "effective" value for the local thermal conductivity of the fluid-filled matrix. This "effective" conductivity was assumed to be a function of global parameters of the flow (such as the Rayleigh number) and it was adjusted so that the computed overall heat transfer (as expressed by the Nusselt number) matches with experimental results available. Little effort was made to justify this ad-hoc model and when it failed, it was postulated that the Darcy law fails. Georgiadis and Catton (1986) proved that the Forchheimer–Brinkman-extended model can explain the divergence of the Nusselt versus Rayleigh number data in terms of a new parameter that depends on the porous medium Prandtl number and the ratio d/L. The "effective" thermal conductivity of the medium was identified with its "stagnant" value obtained under no-flow conditions. In view of certain discrepancies between predicted and measured Nusselt number values for the porous Bénard problem, Georgiadis and Catton (1988) revised the constant conductivity model. They used a single energy equation with an "effective" thermal conductivity expressed as a linear function of the local Peclet number. The need to examine the validity of the above model provides the motivation for the present paper.

Convective flows in straight pipes filled with a stationary porous medium are encountered in various technological applications like heat pipes and adsorption chromatography columns, and can be also used to study the fundamental mechanisms of transport phenomena. We start here by considering heat and mass transport in a single-phase unidirectional flow through a packed bed. In this case, all measurements of the longitudinal heat transport coefficient reported in the literature have been obtained under transient conditions in pipes filled with packed beds. Levec and Carbonell (1985) delineated the basic heat transfer mechanisms and showed that, for long times in the fully developed regime, a single energy equation can be used with an effective transport coefficient that accounts for the interaction between the two phases. This effective conductivity is a sum of the stagnant porous medium conductivity and a dispersion coefficient, which has a hydrodynamic "eddy" contribution and an interfacial heat exchange contribution. For steady heat transport the interfacial heat exchange contribution is zero.

Levec and Carbonell (1985) applied the method of spatial averaging, and in order to achieve closure, they used models that can be related only to ordered porous media. The majority of packed beds are intrinsically disordered; therefore, it is not feasible to solve the exact balance equations on the fine-grain scale. Moreover, the fact that the properties of such "random" fields are known only in the statistical sense makes the use of stochastic methods very convenient for their study. In a previous work, Georgiadis and Catton (1987) derived the statistics of the steady isotropic field that is induced by the spatially random structure of a typically disordered packed bed. The next step is to examine the transport of a sclar in such a field. In the following, we will use a coarse-grain description of the field, where every point in the flow domain is occupied simultaneously by the solid and fluid phases (homogenized continuum) and the solid matrix has become "transparent."

In order to address the heat and mass transfer problem, it is necessary to examine first the validity of the various momentum transport laws, e.g., Darcy versus Forchheimer. Measurements in columnar packed beds by Fand et al. (1986) showed that the pressure drop is proportional to the filtration velocity (Darcy's law) at low filtration rates. Georgiadis and Catton (1987) supported the Forchheimer formulation for local momentum transport, based on their statistical model. In the following section, we will demonstrate that theory and experiment are not inconsistent for nonuniformly packed beds (as is the case in real systems). Since the experiments refer to averaged values of the velocity over the pipe cross section, the nonuniformity of the velocity profile has to be taken into account when we interpret such data. Next we seek to derive the (ensemble) averaged heat transport equation given the statistics of the velocity field. Finally, the general three-

[1]Present address: Department of Mechanical Engineering and Materials Science, Duke University, Durham, NC 27706.

Contributed by the Heat Transfer Division for publication in the JOURNAL OF HEAT TRANSFER. Manuscript received by the Heat Transfer Division January 26, 1987. Keywords: Geophysical Heat Transfer, Natural Convection, Porous Media.

dimensional effective transport equation is derived for an isotropic medium and fluctuation field.

Channeling Due to Velocity Nonuniformity

Fully developed flow driven by a constant pressure gradient along a cylindrical pipe, of diameter $2L$, filled with a stationary porous medium, is described by the following Darcy-Forchheimer-Brinkman momentum equation in nondimensional form:

$$\frac{d^2W}{dr^2} + \frac{1}{r}\frac{dW}{dr} = -\mathrm{Gr} + KW + \Lambda |W| W,$$

$$r \in [0, 1], \quad \frac{dW}{dr}(0) = W(1) = 0 \tag{1}$$

In all dimensionless equations in the present work, velocity is scaled with ν/L, where L is the macroscopic length scale. The presence of the solid walls causes a variation of the porosity (see Benenati and Brosilow, 1962). As in Vafai (1984), we assume the following dependence of the local porosity on distance from the wall:

$$\epsilon = \epsilon_0 \left[1 + 0.98 \exp\left(-\frac{2y}{d}\right)\right] \tag{2}$$

where ϵ_0 is the bulk porosity away from the wall. The following empirical relations are also used:

$$K = \frac{\epsilon L^2}{\gamma}, \quad \gamma = \frac{d^2\epsilon^3}{A(1-\epsilon)^2};$$

$$\Lambda = \frac{\epsilon b L}{\gamma}, \quad \frac{b}{\gamma} = B\frac{1-\epsilon}{d\epsilon^3} \tag{3}$$

By relating the average superficial velocity to the pressure gradient for flow along columnar packed beds, Ergun (1952) obtained $A = 150$, $B = 1.75$, while Fand et al. (1986) reported $A = 182$, $B = 1.92$. From equations (2) and (3), the dimensionless coefficients Gr, K, and Λ in equation (1) depend on r (since $r = 1 - y/L$).

The method of false transient is applied to the solution of the boundary value problem (1). The false transient equation for the velocity is integrated with a semi-implicit central finite-difference scheme as in Georgiadis and Catton (1985). In order to explain the deviations from the prediction of the Forchheimer model at low filtration rates, we use the thermophysical parameters given in the Table 1 of the experimental work of Fand et al. (1986). In the latter work, it was postulated that Darcy's linear law is valid for low velocities (the "flat" Darcy regime $\mathrm{Re} < 2$ in Fig. 2) and that a "pre-Darcy" region exists.

For nonuniformly packed beds, our computations show that the flow is enhanced within a few bead diameters from the solid walls, due to the high values of porosity there, as is shown in Fig. 1. As Re increases, the channeling effect becomes increasingly important and a large portion of the flow passes through the high-porosity medium near the solid walls. There, the flow is approximately of the Poiseuille type. Consequently, the dependence of the pressure gradient on the average velocity q (over the cross section) becomes close to linear. For high Re values, wall channeling is increasingly suppressed and the velocity profile becomes more uniform, so that the value at the core approaches the average velocity (the wall effect is not important).

In Fig. 2, we plot the computed dimensionless pressure gradient as a function of Reynolds number, in a form that allows direct comparison with the corresponding plot (Fig. 1) of the experimental work by Fand et al. (1986). The good qualitative agreement between predictions and experiment, for the laminar flow regime $0 < \mathrm{Re} < 80$, implies that the Forchheimer law adequately models momentum transport through pipes filled with packed beds, when the nonuniformity of porosity is taken into account. Furthermore, it can be seen that the uniformity of the velocity profile in such flows depends not only on the ratio d/L but also on the particle Reynolds

Nomenclature

a = thermal diffusivity $= k/(\rho c)$
b = inertial resistance coefficient, equation (3)
B = Ergun numerical constant, equation (3)
c = specific heat
d = spherical bead diameter
D = turbulent dispersion coefficient $= (4/\pi)[B/(1-\epsilon)](d/L)\mathrm{Pr}\,\Omega\mathrm{Re}^2$
$\mathfrak{D}$ = molecular mass transport coefficient
Gr = pressure gradient $= -(dP/dz)\epsilon_0 L^3/\rho\,\nu^2$
k_m = stagnant thermal conductivity
k^*_{zz} = effective axial conductivity
K = inverse Darcy number $= \epsilon L^2/\gamma$
L = radius of the cylindrical pipe
P = average pressure of the interstitial fluid
Pe = Peclet number $= qd/\alpha_f(1-\epsilon)$
Pr = Prandtl number of the medium $= \nu(\rho c)_f/k_m$
q = mean axial Darcy velocity
q' = interstitial velocity fluctuation
r = radial coordinate
$\mathbf{r}$ = Cartesian coordinate vector
R = mean interstitial path $= (d/L)\epsilon/(1-\epsilon)$
Re = Reynolds number $= qd/\nu$
t = time
T = temperature
w = local Darcy velocity (stochastic field)
W = local Darcy velocity (deterministic field)
$\mathbf{x}$ = position vector in the transverse direction
y = distance from the solid wall
z = longitudinal (axial) coordinate, $j = 1$
α = amplitude of random fluctuations
γ = porous medium permeability
δ = Kronecker delta, delta function
Δ = separation between fluid and solid temperature responses
ϵ = porosity
Λ = inverse Cozeny-Karman number $= \epsilon bL/\gamma$
ν = kinematic viscosity
ρ = density
ρ_{zz} = axial ensemble dispersion coefficient equation (7)
τ = correlation time
ω^2 = forcing coefficient $= 8qK^2R^2\Lambda/\pi$
Ω = heat capacity ratio $= (\rho c)_f/(\rho c)_m$

Subscripts

f = fluid
j = j component; $j = 1, 2, 3$
m = porous medium
s = solid matrix
z = axial component
0 = reference

Superscripts

$*$ = effective value
$'$ = fluctuation

Special symbols

$\langle\ \rangle$ = ensemble average
∂_j = partial derivative with respect to space j coordinate

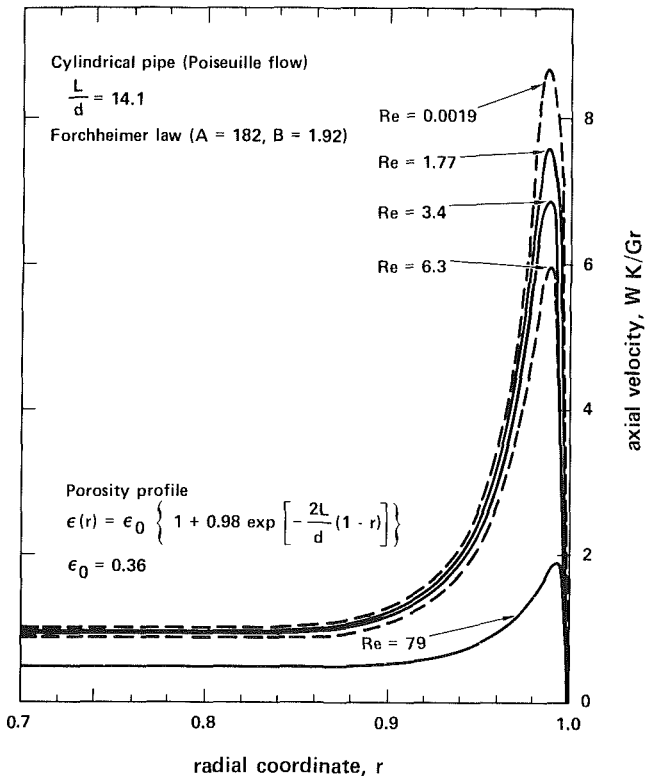

Fig. 1 Computed velocity profiles for Poiseuille flow in pipes filled with nonuniform stationary packed beds: the channeling phenomenon

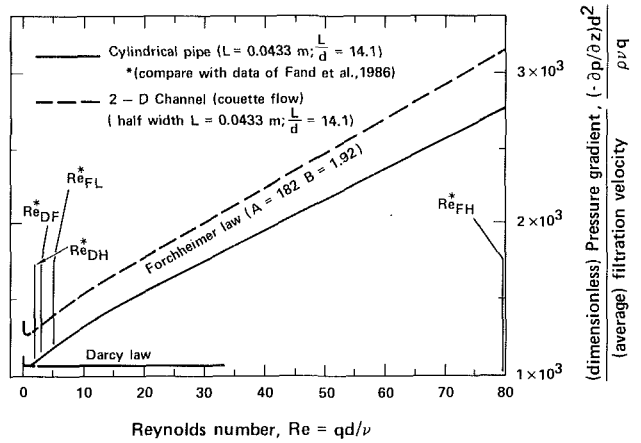

Fig. 2 Graph of pressure drop versus particle Re number for Poiseuille and Couette flow; compare with Fig. 1 of Fand et al. (1986)

number. For large Re, the boundary layer thickness decreases and the velocity profile becomes fairly uniform. A few bead diameters away from the solid boundaries, we can consider the transport of a scalar quantity in a plug flow regime (uniform mean velocity profile) and focus on the effect of local random velocity fluctuations of the interstitial fluid.

Dispersion in a Statistically Uniform and Steady Velocity Field

We represent the interstitial velocity as a stochastic function parameterized by local spatial coordinates. The fluid velocity field can be decomposed into an axial mean q (coarse) and a random fluctuating q_j' component. Using angle brackets to denote ensemble averages, we have by definition

$$\langle w_j(\mathbf{r})\rangle = \langle \delta_{1j} q + q_j'(\mathbf{r})\rangle = \delta_{1j} q$$

The axial z coordinate corresponds to $j=1$. Georgiadis and Catton (1987) described the fluctuating interstitial velocity field by a Gaussian spatial process with the following covariance function:

$$\langle q_j'(\mathbf{r}_2) q_k'(\mathbf{r}_1)\rangle \sim \delta_{jk} \frac{\omega^2}{2K} \exp\left(-\frac{K|z_2 - z_1|}{q}\right)$$

For realistic flow rates, we can show that the following is true:

$$\langle q_j'(\mathbf{r}_2) q_k'(\mathbf{r}_1)\rangle \to \delta_{jk} \frac{\omega^2 q}{K^2} \delta(z_2 - z_1)$$

$$\text{as } \frac{K}{q} \to \infty \tag{4}$$

This form of the covariance function has also been proposed by Matheron and de Marsily (1980).

We consider the convective heat transport in the above spatially varying velocity field. In the fluid phase, the microscopic energy equation for steady-state convection is

$$w_j(\mathbf{r}) \partial_j T = \frac{1}{\mathrm{Pr}} \frac{k_f}{k_m} \partial_k \partial_k T \tag{5}$$

Starting with equation (5), the index summation notation is used. Given the statistics of the fluctuating field $q_j'(\mathbf{r})$, we can derive rigorously (see Tang et al., 1982) the transport equation that the ensemble average $\langle T\rangle$ obeys,

$$q \frac{\partial \langle T\rangle}{\partial z} = \left[\frac{\delta_{jk}}{\mathrm{Pr}} \frac{k_f}{k_m} + \rho_{jk}\right] \partial_j \partial_k \langle T\rangle \tag{6}$$

Since the covariance function (4) depends only on the z coordinate, the ensemble dispersion coefficient becomes

$$\rho_{jk} = \delta_{jk} \frac{x}{2q}\left[\frac{1}{x}\int_0^x \langle q_z'(z_2) q_z'(z_1)\rangle dx\right],$$

$$x = |z_2 - z_1| \tag{7}$$

Using equation (4), the longitudinal dispersion coefficient reduces to

$$\rho_{zz} \sim \frac{\omega^2}{4K^2}\left[1 - \exp\left(-\frac{K|z_2 - z_1|}{q}\right)\right]$$

and for $x \neq 0$, the following limit is considered:

$$\rho_{zz} \to \frac{\omega^2}{4K^2} \quad \text{as } |z_2 - z_1| \frac{K}{q} \to \infty \tag{8}$$

Using equation (3) and the value for ω obtained by Georgiadis and Catton (1987), the dispersion coefficient (8) becomes in the limit of the delta-correlated velocity field

$$\rho_{zz} = \frac{2B}{\pi} \frac{1}{1-\epsilon} \frac{qd}{\nu} = \frac{2B}{\pi} \mathrm{Pe} \frac{a_f}{\nu} \tag{9}$$

Using equations (7) and (8), the dimensional form of the fluid energy equation averaged over the ensemble becomes

$$(\rho c)_f q \frac{\partial \langle T\rangle}{\partial z} = \left[k_f + \frac{2B}{\pi} \mathrm{Pe}\, k_f\right] \partial_k \partial_k \langle T\rangle \tag{10}$$

with the expression in square brackets representing an "effective" fluid conductivity, which we denote by k_f^*. The energy equation for the solid matrix is the heat conduction equation. We now assume that local thermal equilibrium prevails. Therefore, the locally averaged temperatures of the fluid and solid phase are equal. The conditions under which such an assumption is valid have been investigated by Whitaker (1986). The simplest model of heat transport that is consistent with the above assumption is the so called "parallel model": The average energy equations for the fluid and solid phase are weighted by ϵ and $(1-\epsilon)$, respectively, and added to yield an advection-diffusion transport equation that is similar in form to equation (10). The result is an "effective" equation that models heat transfer through the homogenized fluid-solid

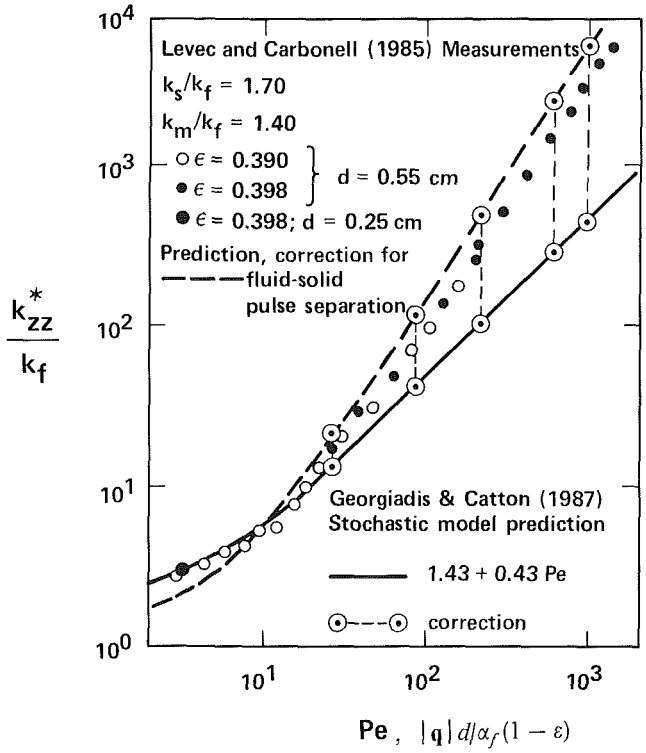

Fig. 3 Effective axial heat transport coefficient in packed beds; comparison between theory and experiments

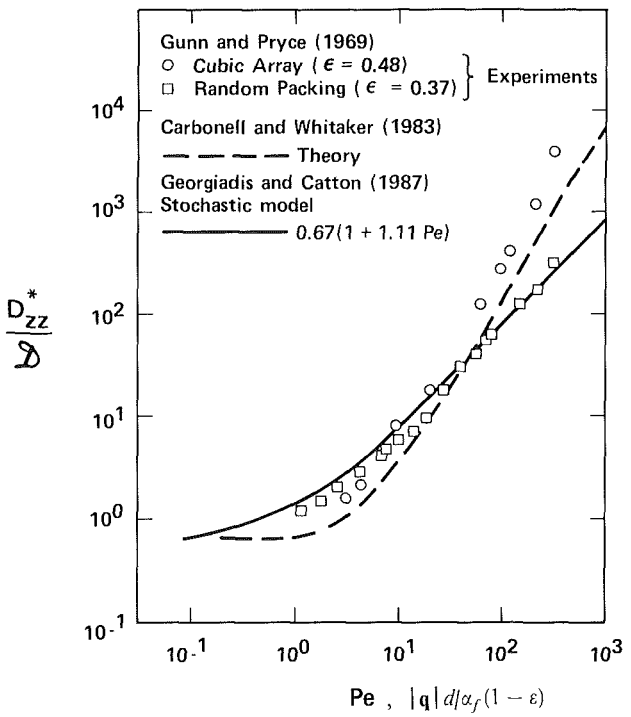

Fig. 4 Effective axial mass transport coefficient in packed beds; for the stochastic model, the tortuosity factor is 0.67

medium. The expression for the effective thermal conductivity of the fluid-saturated porous medium becomes

$$k^*_{zz} = \epsilon k^*_f + (1-\epsilon)k_s = [\epsilon k_f + (1-\epsilon)k_s] + \left[\epsilon \frac{2B}{\pi} \mathrm{Pe} k_f\right] \quad (11)$$

The first square bracket of equation (11) contains the expression for the stagnant effective conductivity according to the simple "parallel model" of heat conduction in packed beds

$$k_m = [\epsilon k_f + (1-\epsilon)k_s]$$

The second bracket is the ("eddy") hydrodynamic contribution to conductivity that was also identified by Levec and Carbonell (1985). Considering the transport of a passive conservative solute, equation (11) remains invariant if we substitute

$$D^*_{zz} \text{ for } k^*_{zz},\ \mathfrak{D} \text{ for } k_f, \text{ and } k_s = 0 \quad (12)$$

where D^*_{zz} and $\mathfrak{D}$ are the effective and molecular mass transport coefficients, respectively. In order to model mass transport, the void fraction (porosity) in equation (11) has to be replaced by another structural parameter, the tortuosity. Since the solute particles follow longer paths of diffusion in the tortuous interstitial space of the packed bed that is fully saturated with stagnant fluid, the effective mass transport coefficient is smaller than that for pure fluid. For a randomly packed bed of equal size spheres, the ratio $D^*_{zz}/\mathfrak{D}$ (tortuosity) is equal to 0.67 under the no-flow condition (Pe = 0) (see Hiby, 1962). For steady-state mass transport in a fully saturated bed of chemically inert spheres, dispersion is the only mechanism that enhances the transport coefficient, since no mass exchange takes place between the solid and fluid phases.

Plots of measured values of the ratio of effective to stagnant transport coefficients versus the particle Peclet number are available for heat transfer (Levec and Carbonell, 1985), and mass transfer (Gunn and Pryce, 1969). Levec and Carbonell (1985) measured the distance of separation Δ between fluid and solid temperature breakthrough curves and computed the axial component of the dispersion coefficient by using a two-equation model of transport in packed beds of ordered structure. Their predictions are in good agreement with experiments, as shown in Fig. 3. The theoretical model that was employed by Levec and Carbonell (1985) had been presented earlier in greater detail by Carbonell and Whitaker (1983), who have also reported mass transfer calculations for dispersion in ordered packed beds. In the latter work, good agreement is reported between predicted mass transfer coefficients for an in-line array of cylinders and measured values by Gunn and Pryce (1969) for a cubic array of spheres, as Fig. 4 shows.

Our theoretical prediction (11) gives

$$k^*_{zz}/k_f = k_m/k_f + 0.43 \text{ Pr}; \quad B = 1.75, \quad \epsilon = 0.39 \quad (13)$$

The expression above remains invariant for mass transfer after making the substitutions (12) and replacing ϵ by the tortuosity. As Fig. 4 shows, our predictions of the axial mass transport coefficient are in excellent agreement with measurements by Gunn and Pryce (1969) for random packing. The strong influence of the packing disorder on dispersivity is demonstrated very clearly. For heat transfer, the agreement between our predictions and experiments is good only in the range $0 < \mathrm{Pe} < 20$, as shown in Fig. 3. This needs an explanation. In the case of mass transfer, there is no transport through the solid phase but, in general, this is not true for heat transfer. A careful examination of the pertinent literature shows that mesurements of axial effective thermal conductivities are taken under transient conditions. As Levec and Carbonell (1985) demonstrated, the positive contribution of the heat exchange between the phases becomes dominant as the Pe number increases. This explains why the measured values in Fig. 3 are higher than our predictions (13) for large Pe numbers. Levec and Carbonell (1985) gave the following estimate for the enhancement of the effective heat conductivity due to interfacial heat exchange in terms of the separation Δ between fluid and solid temperature responses:

$$(1-\epsilon)\frac{\Delta}{d}\,\mathrm{Pe}\,\frac{(1-\epsilon)(\rho c)_s}{\epsilon(\rho c)_f + (1-\epsilon)(\rho c)_s}$$

Based on the above expression and using the measured values of Δ/d plotted in Fig. 10 of the paper by Levec and Carbonell (1985), we can compute the positive increase of the effective conductivity and add it to our prediction (11) in order to account for the interfacial heat exchange. As is evident from Fig. 3, our corrected values agree well with experiments and are almost identical to the predictions of Levec and Carbonell for unsteady heat transfer. Therefore, the expression (11) for the effective transport coefficient is valid for a wide range of Pe number values. We may note in passing that the character of the flow changes at high filtration rates from laminar to "turbulent" (Jolls and Hanratty, 1966). Consequently, the model of steady unidirectional flow becomes unrealistic above a certain critical Pe (or Re) number. For the packed bed considered by Levec and Carbonell (1985) (urea formaldehyde beads/water), this critical Pe number is approximately 600.

Dispersion in a Turbulent Velocity Field

We assume that a single energy equation can be used to model the heat transport in a turbulent interstitial velocity field with unidirectional mean velocity. The local unsteady heat transfer process is described by

$$\frac{1}{\Omega}\frac{\partial T}{\partial t} + w_j(\mathbf{r}, t)\partial_j T = \frac{1}{\mathrm{Pr}}\partial_k\partial_k T \tag{14}$$

Local measurements and observations by Jolls and Hanratty (1966) revealed transition from steady to irregular unsteady flow in a randomly packed bed of spheres over the range $110 < \mathrm{Re} < 150$. In order to model the irregularly fluctuating interstitial velocity field, we simply assume that $w_j(\mathbf{r}, t)$ is a Gaussian temporal and spatial process of the form

$$w_j(\mathbf{r}, t) = \delta_{1j} q[1 + \mu_j(\mathbf{r}, t)]; \quad \langle w_j(\mathbf{r}, t)\rangle = \delta_{1j} q \tag{15}$$

and is described by the following correlation function, which has the same spatial dependence as equation (4)

$$\langle \mu_j(\mathbf{r}_1, t)\mu_k(\mathbf{r}_2, t_1)\rangle = \delta_{jk}\frac{\omega^2}{K^2 q}\delta(z_2 - z_1)\delta(t - t_1) \tag{16}$$

Equations (14) and (15) define a multiplicative stochastic process. By using the method of ordered cumulants (as described in the Appendix), we can derive the following approximate (deterministic) equation that the solution of equations (14) and (15) obeys when averaged:

$$\frac{1}{\Omega}\frac{\partial}{\partial t}\langle T\rangle + q\frac{\partial}{\partial z}\langle T\rangle = \left[\frac{1}{\mathrm{Pr}}\partial_k\partial_k + \Omega q^2 K_2\right]\langle T\rangle \tag{17}$$

The above equation is exact when equation (16) holds because in that case $\tau \to 0$. Using equation (16) and the continuity equation ($\partial_j \mu_j = 0$), the cumulant operator in equation (17) reduces to

$$K_2 = \int_0^t \langle \mu_j(\mathbf{r}, t)\partial_j \mu_k(\mathbf{r}, t_1)\rangle \partial_k dt_1 = \frac{\omega^2}{2K^2 q}\partial_k\partial_k \tag{18}$$

We notice the augmentation of the heat conduction coefficient in front of the Laplacian operator by a dispersive positive term. This comes from the coupling between the random fluctuations of temperature and velocity. By using equation (3), we can obtain an estimate for the (nondimensional) longitudinal dispersion coefficient in equation (17)

$$\frac{\Omega\omega^2}{2K^2}q = \frac{4\Omega R^2 \Lambda q^2}{\pi} = \frac{4B}{\pi(1-\epsilon)}\frac{L}{d}\mathrm{Re}^2 \tag{19}$$

We notice the quadratic dependence of the dispersion coefficient on the velocity q. The dimensional form of the energy equation becomes

$$(\rho c)_m\frac{\partial}{\partial t}\langle T\rangle + (\rho c)_f q\frac{\partial}{\partial z}\langle T\rangle = k_m[1 + D]\partial_k\partial_k\langle T\rangle \tag{20}$$

The turbulent dispersion coefficient D (defined in the nomenclature) depends on the square of the Reynolds number, the porous medium Prandtl number, and the heat capacity ratio.

Multidimensional Effective Transport Equation

We have so far considered transport in a unidirectional mean velocity field. Such flows are encountered when one seeks to measure the transport coefficients in the longitudinal and transverse directions, k^*_{zz} and k^*_{yy}, respectively. We are now ready to generalize the transport equations (10) and (20) in a spatially varying (in a deterministic fashion) Darcy velocity field W_j ($j = 1, 2, 3,$). Consider first a two-dimensional flow field in an isotropic porous medium and imbed an orthogonal curvilinear coordinate system (y, z) in it, with z being the coordinate along a streamline and y the one normal to it. For an elementary volume $\Delta z \times \Delta y \times \Delta n$ (Δn is the thickness of the infinitesimal volume perpendicular to the plane of the flow), the law of energy conservation implies

$$\frac{\partial}{\partial t}\{(\rho c)_m \Delta z\Delta y\Delta n\ T\} + \frac{\partial}{\partial z}\{(\rho c)_f \Delta y\Delta n W_z T\}\Delta z$$

$$= \frac{\partial}{\partial z}\left\{k^*_{zz}\frac{\partial}{\partial z}\Delta y\Delta n\ T\right\}\Delta z + \frac{\partial}{\partial y}\left\{k^*_{yy}\frac{\partial}{\partial y}\Delta z\Delta n\ T\right\}\Delta y \tag{21}$$

For constant-property media and since $\Delta y\ W_z = \mathrm{const}$, equation (21) reduces to

$$(\rho c)_m\frac{\partial T}{\partial t} + (\rho c)_f W_z\frac{\partial T}{\partial z} = \frac{\partial}{\partial z}\left(k^*_{zz}\frac{\partial T}{\partial z}\right) + \frac{\partial}{\partial y}\left(k^*_{yy}\frac{\partial T}{\partial y}\right) \tag{22}$$

In a general three-dimensional Cartesian system, the transport equation (22) is transformed to

$$(\rho c)_m\frac{\partial T}{\partial t} + (\rho c)_f W_j\partial_j T = \partial_j(k^*_{jk}\partial_k T) \tag{23}$$

The expression for the transport coefficient in the Cartesian coordinates (j, k) is given by the following second-order tensor:

$$k^*_{jk} = k^*_{yy}\delta_{jk} + (k^*_{zz} - k^*_{yy})\frac{W_j W_k}{U^2} \tag{24}$$

where U is the amplitude of the velocity vector (invariant in the transformation). Recall that for unidirectional flow along z, z and y are the principal directions of the tensor.

In the case of steady (spatially varying) interstitial flow, the dispersion tensor is isotropic ($k^*_{zz} = k^*_{yy}$). Therefore, the transformation in any Cartesian coordinate system according to (24) will leave it invariant. Consequently, the generalized form of (10) becomes

$$(\rho c)_m\frac{\partial T}{\partial t} + (\rho c)_f W_j\partial_j T = \partial_j(k^*_{zz}\partial_j T) \tag{25}$$

where $j = 1, 2, 3$ correspond to the three coordinate axes.

Discussion

A general literature survey suggests that the dependence of the measured dispersion coefficient on the filtration velocity q ranges between linear and quadratic (Scheidegger, 1960). The exact functional relation depends of course on the statistics of the flow field and the medium (Greenkorn and Kessler, 1969). All measurements are obtained from single realizations of the transport process. Before any further extensive comparisons are made, one has to decide how ensemble averages given by the stochastic model will be related to measured values that are

determined in a single realization of the experiment. In this work, we tacitly made the assumption that the stochastic process is ergodic and statistically homogeneous. Therefore, we assumed that ensemble averages are equal to spatial averages.

For steady-state convective heat transport and under the assumption of local thermal equilibrium between the two phases, dimensional analysis gives the following functional dependence of the effective thermal conductivity of the medium k_{zz}^* on the thermal conductivity of the fluid and solid phases, k_f and k_s, respectively:

$$\frac{k_{zz}^*}{k_f} = f\left\{\frac{k_s}{k_f},\ \text{Pe; interstitial geometry}\right\}$$

In the function above, the Peclet number is based on a microscopic spatial scale (e.g., the sphere diameter in a packed bed), the local filtration velocity, and the thermal diffusivity of the saturating fluid. In the present work, we used a simple linear function and this resulted in a linear dependence of the effective conductivity on the Peclet number, as given in equation (11). The Peclet number dependence accounts for the dispersion due to the tortuous interstitial flow. As we have shown, this is an additional mechanism of transport that is in its phenomenological aspects very similar to diffusion. The interstitial geometry enters the formulation usually as a set of statistical parameters of the microstructure, one of which is the local void fraction (porosity) ϵ. Further work is needed in order to build more realistic transport models that will incorporate additional statistical parameters of the heterogeneous medium and to account for the coupling between dispersion and interfacial heat exchange. Levec and Carbonell (1985) argued that the interfacial heat exchange process tends to lower the magnitude of the hydrodynamic dispersion term for small Pe numbers. This can explain why our model slightly overpredicts the effective transport coefficients in Figs. 3 and 4.

Concerning the lateral dispersion coefficient, Levec and Carbonell (1985) observed that, for very low Peclet numbers, the axial and lateral conductivities become nearly equal. Our stochastic model agrees with this since it predicts an isotropic conductivity tensor. At high Peclet numbers, measured axial conductivities are much higher than the lateral ones. An explanation for this is given by Levec and Carbonell (1985) in terms of the dominant transient heat exchange contribution to the transport coefficient during the transient measurements of the axial component, while the lateral component is measured under steady-state conditions.

Conclusions

We assume that mass and energy transport in disordered heterogeneous two-phase media can be economically modeled by stochastic processes and we use a simple model of microscopic transport to achieve closure. A novel methodology is introduced that combines the physical accuracy of a microdynamic formulation with the mathematical simplicity of a stochastic phenomenological approach. By comparing with available measured values of steady-state heat and mass axial transport coefficients, we prove that this methodology is successful in providing good *a priori* estimates of effective transport coefficients. For steady convective heat transfer through a packed bed, the effective conductivity (13) is shown to depend linearly on the local Peclet number, which is based on the bead diameter, the porosity, and the thermal diffusivity of the infiltrating fluid. It can be therefore significantly larger than the stagnant value for large Prandtl numbers even for the Re <1 values that we encounter in natural convection problems, as Georgiadis and Catton (1988) have demonstrated.

Acknowledgments

This work was performed under the auspices of the U.S. Department of Energy (grant No. DE-AT03-82ER12021). The authors wish to thank Professor Stephen Whitaker for reviewing a preliminary draft of the paper.

References

Benenati, R. F., and Brosilow, C. B., 1962, "Void Fraction Distribution in Beds of Spheres," *AIChE J.*, Vol. 8, No. 3, pp. 359–361.

Carbonell, R. G., and Whitaker, S., 1983, "Heat and Mass Transport in Porous Media," *Proc. NATO Adv. Study Inst. Mechanics of Fluids in Porous Media*, J. Bear and Y. Corapcioglu, eds., Martinus Nijhoff, Brussels.

Ergun, S., 1952, "Fluid Flow Through Packed Columns," *Chem. Engng. Prog.*, Vol. 48, No. 2, pp. 89–94.

Fand, R. M., Steinberger, T. E., and Cheng, P., 1986, "Natural Convection Heat Transfer From a Horizontal Cylinder Embedded in a Porous Medium," *Int. J. Heat Mass Transfer*, Vol. 29, No. 1, pp. 119–133.

Fox, R. F., 1976, "Critique of the Generalized Cumulant Expansion Method," *J. Math. Physics*, Vol. 17, No. 7, pp. 1148–1153.

Georgiadis, J. G., and Catton, I., 1985, "Free Convective Motion in an Infinite Vertical Porous Slot: the Non-Darcian Regime," *Int. J. Heat Mass Transfer*, Vol. 28, No. 12, pp. 2389–2392.

Georgiadis, J. G., and Catton, I., 1986, "Prandtl Number Effect on Benard Convection in Porous Media," ASME JOURNAL OF HEAT TRANSFER, Vol. 108, No. 2, pp. 284–290.

Georgiadis, J. G., and Catton, I., 1987, "Stochastic Modeling of Unidirectional Fluid Transport in Uniform and Random Packed Beds," *Phys. Fluids*, Vol. 30, No. 4, pp. 1017–1022.

Georgiadis, J. G., and Catton, I., 1988, "Dispersion in Cellular Thermal Convection in Porous Layers," *Int. J. Heat Mass Transfer*, Vol. 31, No. 5, pp. 1081–1091.

Greenkorn, R. A., and Kessler, D. P., 1969, "Dispersion in Heterogeneous Nonuniform Anisotropic Porous Media," *Ind. Eng. Chemistry*, Vol. 61, No. 9, pp. 14–32.

Gunn, D. J., and Pryce, C., 1969, "Dispersion in Packed Beds," *Trans. Instr. Chem. Engrs.*, Vol. 47, pp. 341–350.

Hiby, J. W., 1962, *Proc. Symp. on Interaction Between Fluids and Particles*, Inst. Chemical Eng., London, Great Britain, p. 312.

Jolls, K. R., and Hanratty, T. J., 1966, "Transition to Turbulence for Flow Through a Dumped Bed of Spheres," *Chem. Engng. Sci.*, Vol. 28, pp. 673–682.

Levec, J., and Carbonell, R. G., 1985, "Longitudinal and Lateral Thermal Dispersion in Packed Beds, Parts I & II," *AIChE J.*, Vol. 31, No. 4, pp. 581–602.

Matheron, G., and de Marsily, G., 1980, "Is Transport in Porous Media Always Diffusive? A Counter Example," *Water Resour. Res.*, Vol. 16, No. 5, pp. 901–917.

Prasad, V., Kulacki, F. A., and Keyhani, M., 1985, "Natural Convection in Porous Media," *J. Fluid Mechanics*, Vol. 150, pp. 89–119.

Scheidegger, A. E., 1960, *The Physics of Flow Through Porous Media*, 2nd ed., MacMillan, New York.

Rubin, H., 1977, "Thermal Convection in a Cavernous Aquifer," *Water Resour. Res.*, Vol. 13, No. 1, pp. 34–40.

Tang, D. H., Schwartz, F. W., and Smith, L., 1982, "Stochastic Modeling of Mass Transport in a Random Velocity Field," *Water Resour. Res.*, Vol. 18, No. 2, pp. 231–244.

Vafai, K., 1984, "Convective Flow and Heat Transfer in Variable-Porosity Media," *J. Fluid Mech.*, Vol. 147, pp. 233–259.

van Kampen, N. G., 1974, "A Cumulant Expansion for Stochastic Linear Differential Equations, Parts I & II," *Physica*, Vol. 74, pp. 215–247.

Whitaker, S., 1986, "Local Thermal Equilibrium: An Application to Packed Bed Catalytic Reactor Design," *Chem. Engng. Sci.*, Vol. 41, No. 8, pp. 2029–2039.

APPENDIX

Multiplicative Stochastic Processes

In the following, we present an application of the theory developed by van Kampen (1974) and Fox (1976) for the approximate solution of the following stochastic equation, which describes a multiplicative random process:

$$\frac{\partial}{\partial t} u(\mathbf{r}, t) = \alpha' B(t) u(\mathbf{r}, t) \tag{A1}$$

where $B(t)$ is a differential operator (includes spatial $\mathbf{r}$ derivatives of u), which has in general sure and random parts, and α' is a parameter. Without loss of generality, this operator can be witten in the form

$$\alpha' B(t) = A + \alpha \tilde{A}(t) \tag{A2}$$

where A is deterministic and independent of time and $\tilde{A}$ is stochastic with zero mean. The above form suggests that equation (A1) could be solved with a regular perturbation method (expansion in powers of α), but this would introduce secular terms. To avoid them, the method of cumulant expansion is used.

The exact solution of (A1) can be written formally in terms of the time-ordered exponential (operator inside the braces)

$$u(\mathbf{r}, t) = \left\{1 + \alpha' \int_0^t dt_1 B(t_1) + \alpha'^2 \int_0^t dt_1 \int_0^{t_1} dt_2 B(t_2) + \ldots \right\} u(\mathbf{r},0) \tag{A3}$$

If $B(t_1)$ commutes with $B(t_2)$, the time-ordered exponential reduces to the ordinary exponential

$$\exp\left\{\int_0^t dt_1 B(t_1)\right\}$$

By taking the ensemble average of expression (A3), an equation for $\langle u(\mathbf{r}, t)\rangle$ can be obtained in terms of the following ordered-cumulant expansion:

$$\frac{\partial}{\partial t}\langle u(\mathbf{r}, t)\rangle = \{\alpha' K_1(\mathbf{r}, t) + \alpha'^2 K_2(\mathbf{r}, t) + O(\alpha'^3 \tau^2)\}\langle u(\mathbf{r}, t)\rangle \tag{A4}$$

where

$$K_1(\mathbf{r}, t) = \langle B(t)\rangle$$

$$K_2(\mathbf{r}, t) = \langle B(t)\int_0^t B(t_1)dt_1\rangle - \langle B(t)\rangle\langle\int_0^t B(t_1)dt_1\rangle \tag{A5}$$

and τ is the autocorrelation time scale of $B(t)$. The expansion in (A4) is essentially in terms of τ and remains valid as long as $t \gg \tau$. Because of the "cluster property," the higher order cumulants can be estimated by

$$\alpha'^n K_n \sim \alpha'^n \tau^{n-1} \quad \text{for } t \gg \tau$$

From equation (A2), the governing equation for the ensemble average (A4), correct to order $O(\alpha^2\tau)$, becomes

$$\frac{\partial}{\partial t}\langle u(\mathbf{r}, t)\rangle = \left\{A + \alpha^2 \int_0^t \langle \tilde{A}(\mathbf{r}, t)\tilde{A}(\mathbf{r}, t_1)\rangle dt_1\right\}\langle u(\mathbf{r}, t)\rangle \tag{A6}$$

Natural Convection Around a Heated Cylinder in a Saturated Porous Medium

B. Farouk

H. Shayer

Department of Mechanical Engineering and Mechanics,
Drexel University,
Philadelphia, PA 19104

Numerical solutions are presented for the natural convection heat transfer from a heated cylinder buried in a semi-infinite liquid-saturated porous medium. The governing equations are expressed in the stream function–temperature formulation and finite difference equations are obtained by integrating the governing equations over finite cells. The heat transfer characteristics of the heated cylinder are studied as functions of the Rayleigh number and the vertical depth of the cylinder center from a permeable surface. The numerical scheme involves the use of a cylindrical network of nodes in the vicinity of the cylinder with a Cartesian mesh covering the remainder of the flow domain. The results are of use in the design of underground electrical cables, power plant steam, and water distribution lines, among others.

Introduction

Convective fluid flow and heat and mass transport in porous media have become the subject of increased recent investigations. Problems arise in ground water systems for industrial and agricultural uses, buried electrical cable and transformer coils, and in the storage of radioactive nuclear waste materials. The existing literature on convective flows and heat transfer in porous media mostly considers a regular geometric domain, e.g., rectangular enclosures, the annulus between concentric cylinders, etc. (Buretta and Berman, 1976; Holst and Aziz, 1972; Caltazirone, 1976; Facas and Farouk, 1983). The natural convective flow induced by a heated cylinder buried in a semi-infinite porous medium has, however, received little attention in the past, in spite of its many engineering applications and the interesting flow patterns it generates. A numerical study of the above problem is considered in this paper. The buoyancy-induced flow around a heated cylinder embedded in a semi-infinite porous medium offers a challenge to analysis because of the indeterminate boundary conditions on the mass inlet flow rate and the selection of an appropriate grid system to handle the circular boundary within a rectangular flow domain.

Heat transfer from buried pipes and cables has long been of interest to engineers. The medium considered has usually been purely conductive. Approximate and exact steady-state heat loss calculations are available in the literature for pipes and cables buried in a conductive medium (Eckert and Drake, 1972; Bau and Sadhal, 1982; Thiayagarajan and Yovanovich, 1974; Martin and Sadhal, 1978). Eckert and Drake (1972) considered the problem of the buried cylinder in a semi-infinite homogeneous conducting medium by an approximate analytical model using the concept of infinite line heat sources and sinks. Bau and Sadhal (1982) recently treated the same problem analytically but considered varying surface temperature for cylinder. A bicylindrical coordinate system was considered for the analysis. Schrock et al. (1970) and Fernandez and Schrock (1982) carried out experiments and numerical calculations (using a bicylindrical coordinate system) for a cylinder buried beneath a permeable horizontal surface. A heat transfer correlation was suggested (Schrock et al., 1970), which was later replaced (Fernandez and Schrock, 1982) by a new correlation with an expanded data base. The standard deviation of data from the correlation was found to be 11.4 percent. The Rayleigh number was based on $(h^2 - D^2/4)^{1/2}$ instead of the diameter of the cylinder in the above two studies, where h is the burial depth of the cylinder. Hickox (1981) and Hickox and Watts (1980) used regular perturbation expansion to calculate a first-order solution for the flow field induced by a point heat source. Their results are of significance only for deeply buried sources. Nield and White (1982) modeled the cylinder as a line source and studied natural convection in an infinite medium. More recently Bau (1984) presented analytical solutions for steady-state, low-Rayleigh-number natural convection induced by a pipe buried in a saturated, semi-infinite, permeable medium. Both the cylinder and the medium surfaces are maintained at constant uniform surface temperatures. The uniform upper surface temperature for the medium may, however, be difficult to realize physically.

The objective of the present work was to obtain steady-state solutions to the coupled momentum and energy equations for natural convection around a heated cylinder buried in a semi-infinite porous medium, bounded above by a liquid layer. Results are obtained over a wide range of Rayleigh numbers (based on the diameter of the cylinder) (0–300). Temperature and streamline distributions as well as the heat transfer characteristics are presented. The effect on the heat transfer of the vertical depth of the cylinder from a permeable surface is also investigated for the above range of Rayleigh numbers. A finite difference numerical scheme using hybrid difference approximation is used for generating the two-dimensional transient and steady-state results. An efficient grid system (Launder and Massey, 1978), which involves a polar mesh surrounding the cylinder and a Cartesian mesh covering the remainder of the flow domain, has been chosen.

The finite difference calculations invoke problems due to the circular boundary of the cylinder as opposed to the rectangular boundary of the flow domain. A Cartesian grid could in principle be adopted, as is often the case in conduction problems. In convection studies, however, there are strong advantages to making all rigid surfaces coincide with a surface on which one of the coordinates is uniform. Body-fitted coordinate systems or finite element methods could also be employed at the expense of additional complexity in the governing equations and formulations respectively. The polar grid used here in the vicinity of the cylinder gives better control of grid location at the plume region than the body-fitted coordinate system. The main disadvantage of the grid system

Contributed by the Heat Transfer Division for publication in the JOURNAL OF HEAT TRANSFER. Manuscript received by the Heat Transfer Division May 19, 1986. Keywords: Environmental Heat Transfer, Natural Convection, Porous Media.

used here is the presence of the intersection zone between the polar and the Cartesian grids. The effects of the intersection zone was minimized by properly choosing the intersection zone for the flow domain and making the polar and Cartesian grids of similar sizes near the intersection zone. Nonuniform mesh was used in the radial direction near the surface of the cylinder.

Formulation

The system considered is a buried cylinder in a semi-infinite saturated porous medium as shown in Fig. 1, where h represents the vertical depth of the cylinder center from the permeable upper surface. A rectangular flow domain is approximated for obtaining the numerical solutions. For the finite difference solution of the elliptic equations (in space) the flow boundaries should be grid lines themselves; otherwise either an uneven boundary will result or special finite difference formulae will be needed at the boundaries. This constraint is more important at a solid boundary since any mismatch here between the grid and the boundary could lead to an erroneous flow pattern. Referring to Fig. 1, the main deterrent here is the circular boundary of the cylinder as opposed to the rectangular flow domain considered.

Close to the cylinder, the steepest gradients of flow properties are in the radial direction. Thus a cylindrical polar grid in the neighborhood of the cylinder is retained. The remaining flow region is filled with a Cartesian mesh. The cylindrical and Cartesian grids are entirely independent of one another. However, the grids overlap each other and no matching of nodes between neighboring grid regions were attempted. A line of "false" nodes was defined, for each grid, beyond the interaction line to provide a connection between the cylindrical and polar regions. Additional details of the matching region can be found elsewhere (Launder and Massey, 1978; Farouk, 1981) and are not repeated here. This system of the composite grid was chosen for the present problem as it is found to be flexible and capable of modeling any ratio of vertical depth (h) to the cylindrical diameter D.

The governing equations for transient natural convection with the Boussinesq, Darcy flow, and negligible inertia approximations are given as

$$\nabla \cdot \bar{v} = 0 \tag{1}$$

$$\frac{\mu}{K}\,\bar{v} = -[\nabla p - \rho_f \bar{g}] \tag{2}$$

$$(\rho c)' \frac{\partial T}{\partial t} = \lambda' \nabla^2 T - (\rho c)\,[\nabla \cdot \bar{v} T] \tag{3}$$

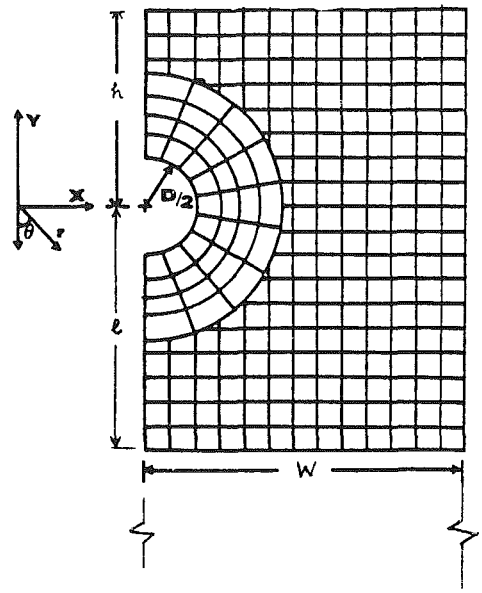

Fig. 1 Problem geometry and the composite grid used for the flow calculations

and

$$p_f = \rho_0\,[1 - \beta_f (T - T_0)] \tag{4}$$

where the primes indicate equivalent properties for the medium. By taking the curl of equation (2) and using the equation of state (4) we obtain in cylindrical coordinates

$$\nabla^2 \psi = \left(\frac{\rho_f K}{\mu}\right) g \rho_0 \beta_f \left[\sin\theta \frac{\partial T}{\partial r} + \frac{\cos\theta}{r}\frac{\partial T}{\partial \theta}\right] \tag{5}$$

$$\nabla^2 T - \frac{c_f}{\lambda' r}\left[\frac{\partial \psi}{\partial \theta}\frac{\partial T}{\partial r} - \frac{\partial \psi}{\partial r}\frac{\partial T}{\partial \theta}\right] = \frac{(\rho c)'}{\lambda'}\frac{\partial T}{\partial t} \tag{6}$$

where the stream function is defined as

$$v_r = \frac{1}{\rho_f r}\frac{\partial \psi}{\partial \theta}; \quad v_\theta = -\frac{1}{\rho_f}\frac{\partial \psi}{\partial r} \tag{7}$$

The equations above are used in the vicinity of the cylinder. The equations in Cartesian coordinates become

$$\nabla^2 \psi = \left(\frac{\rho_f K}{\mu}\right) g \rho_0 \beta_f \frac{\partial T}{\partial x} \tag{8}$$

$$\nabla^2 T - \frac{c_f}{\lambda'}\left[\frac{\partial \psi}{\partial y}\frac{\partial T}{\partial x} - \frac{\partial \psi}{\partial x}\frac{\partial T}{\partial y}\right] = \frac{(\rho c)'}{\lambda'}\frac{\partial T}{\partial t} \tag{9}$$

Nomenclature

c = specific heat
D = diameter of cylinder
h = burial depth of the cylinder
g = acceleration of gravity
K = permeability
l = vertical depth of solution domain from the cylinder center
r = radial coordinate
Ra = Rayleigh number [equation (16)]
T = temperature
t = time
$\bar{v}$ = velocity vector
v_r = radial velocity component
v_θ = angular velocity component
v_x = nondimensional velocity component in the x direction
v_y = velocity component in the y direction
W = half-width of the (symmetric) solution domain
x = Cartesian coordinate denoting horizontal distance
y = Cartesian coordinate denoting vertical distance
β_f = thermal coefficient of volume expansion of fluid
θ = circumferential (angle) coordinate, measured from the bottom vertical line, counterclockwise
λ = thermal conductivity
λ' = equivalent thermal conductivity of medium
μ = molecular viscosity
ρ = density
ϕ = porosity (void volume fraction)
ψ = stream function

Subscripts
f = fluid
s = solid
0 = reference condition (for the medium)

Superscripts
* = dimensionless parameter

where the stream function here is defined as

$$v_x = \frac{1}{\rho_f}\frac{\partial \psi}{\partial y}; \qquad v_y = -\frac{1}{\rho_f}\frac{\partial \psi}{\partial x} \tag{10}$$

Nondimensionalizing the variables as defined below

$$T^* = \frac{T - T_0}{T_w - T_0}, \quad r^* = \frac{r}{D}, \quad x^* = \frac{x}{D}, \quad y^* = \frac{y}{D} \tag{11}$$

$$\psi^* = \frac{\psi}{\alpha \rho_f} \text{ where } \alpha = \frac{\lambda'}{\rho_f c_f}, \quad t^* = \frac{\lambda'}{(\rho c)'}\frac{t}{D^2}$$

the governing equations reduce to the following:

(*a*) *Cylindrical coordinates*

$$\nabla^2 \psi^* - \mathrm{Ra} \cdot \left[\sin\theta \frac{\partial T}{\partial r^*} + \frac{\cos\theta}{r^*}\frac{\partial T^*}{\partial \theta}\right] \tag{12}$$

and

$$\nabla^2 T^* - \frac{1}{r^*}\left[\frac{\partial \psi^*}{\partial \theta}\frac{\partial T^*}{\partial r} - \frac{\partial \psi^*}{\partial x^*}\frac{\partial T^*}{\partial \theta}\right] \frac{\partial T^*}{\partial t^*} \tag{13}$$

(*b*) *Cartesian coordinates*

$$\nabla^2 \psi^* - \mathrm{Ra} \cdot \frac{\partial T^*}{\partial x^*} \tag{14}$$

and

$$\nabla^2 T^* - \frac{1}{r^*}\left[\frac{\partial \psi^*}{\partial y^*}\frac{\partial T^*}{\partial x^*} - \frac{\partial \psi^*}{\partial y^*}\frac{\partial T^*}{\partial \theta}\right] = \frac{\partial T^*}{\partial t^*} \tag{15}$$

The Rayleigh number is defined as

$$\mathrm{Ra} = \frac{g \rho_0 \beta_f c_f D \cdot \nabla T \cdot \rho_f}{\lambda'(\mu/K)} \tag{16}$$

and

$$\nabla T = (T_w - T_0) \tag{17}$$

The solutions of equations (12)–(15) with appropriate boundary conditions give the desired distribution of ψ^* and T^*. The physical properties are evaluated at the mean temperature $T_m = 1/2\,(T_w + T_0)$.

Solution Domain and Boundary Conditions

The coupled set of elliptic equations can be solved only if the conditions are specified along the entire boundary that closes the flow field. The cylinder is considered to be held at a uniform temperature T_w ($T_w > T_0$) and the upper surface is considered to be permeable. The medium initially is considered to be at T_0. The solution scheme presented here is, however, not restricted to the isothermal conditions. The necessity to limit the size of the solution domain requires that the upstream boundary be defined at finite distances from the cylinder. The boundary sections are handled as follows:

Symmetry Plane. Because of the geometry considered, a vertical symmetry plane exists and the problem is solved only for the vertical half-plane. On the symmetry plane the stream function is set equal to zero and the gradient of the temperature normal to the symmetry plane is also set to zero.

Cylinder Surface. The value of the stream function is uniform around the cylinder, corresponding to an impermeable wall. Its value is the same as that along the adjacent symmetry plane. The thermal boundary condition applied in the present case is that of uniform surface temperature around the perimeter of the cylinder. At $r^* = 0.5$, $\psi^* = 0$, $T^* = 1$.

Upper Surface. Flow or recharge through a permeable surface may occur when either a standing liquid or a second porous medium (with a larger permeability) overlies the porous layer of interest. For such cases, the least restrictive boundary condition at the permeable surface is one of constant pressure. The constant pressure assumption implies no viscous interaction between an overlying liquid and porous layer. From the vertical momentum balance and the stream function definitions, a constant pressure horizontal surface is represented by $\partial \psi^*/\partial y^* = 0$.

Specifying the thermal boundary condition for the upper permeable surface is not obvious. Bau (1984) considered an isothermal surface, which is difficult to realize in a physical sense, especially for moderate or high Rayleigh numbers. Schrock and Fernandez (1982) chose a condition similar to that used in transpiration cooling. The convective heat transfer coefficient at the upper surface was evaluated from $\mathrm{Nu} = 0.54\ (\mathrm{Gr} \cdot \mathrm{Pr})^{1/4}$. The length scales for the Grashof number was not defined and an average value of Nusselt number is obtained from the above relation. In this study, zero gradient temperature boundary conditions are used for the permeable upper surface (of the porous medium) when the Rayleigh number (based on diameter) is equal to or above 10. It is assumed that the heat transfer through the permeable upper surface to the liquid layer is primarily by convection. Such an approach has been considered for natural convection flows around cylinders in an infinite medium (Farouk and Guceri, 1983). At $y^* = h/_D$, $\partial T^*/\partial y^* = \partial \psi^*/\partial y = 0$.

Far Field Boundaries. It is assumed that if the far field boundaries are set sufficiently far away (given by l and W in Fig. 1) from the cylinder, then the velocity components in the direction parallel to the far field surfaces is negligible. The approach here is somehow to neglect the minor details of farther upstream flow and obtain realistic answers near field and downstream (Roache, 1972). The boundary conditions for the stream function at the bottom section ($y^* = -l/D$) become $\partial \psi^*/\partial y^* = 0$ and at the side ($x^* = W/D$) become $\partial \psi^* \partial x^* = 0$.

The temperature of the fluid drawn into the flow field is the same as the ambient temperature. However, for a finite far field distance from the cylinder, zero gradient temperature boundary conditions were considered, i.e., at $y^* = -l/D$, $\partial T^*/\partial y^* = 0$ and at $x^* = W/D$, $\partial T^*/\partial x^* = 0$.

Intersections Between Polar and Cartesian Grids. The values of the dependent variables on the "false" polar and Cartesian nodes are obtained by interpolation from the surrounding four Cartesian and polar nodes, respectively (Launder and Massey, 1978). These values are then used as the boundary conditions during the next cycle of iteration. The interpolation assumes a linear variation of the dependent variables between the grid nodes, which is a reasonable approximation when the grid intersections are not within the wall boundary layers and when sufficiently fine grids are used.

Local Nusselt numbers are defined for the cylinder surface as

$$\mathrm{Nu}(\theta) = -\frac{\partial T^*}{\partial r^*} \tag{18}$$

Mean or average value of Nusselt number at the cylindrical surface is given by

$$\overline{\mathrm{Nu}} = \frac{1}{\pi}\int_0^{\pi} \mathrm{Nu}(\theta)\, d\theta \tag{19}$$

Solution Procedure

For both polar and Cartesian coordinates, equations (12)–(15) are transformed in difference equations using a control volume approach. A fully implicit scheme is employed and the energy and stream function equations are solved by a point iteration scheme. A hybrid difference scheme was used for the convection-diffusion terms.

A grid is established by dividing the region close to the cylinder in the r and θ directions. For the remaining area of the flow domain considered the grid is established by dividing the region in the x and y directions. For the range of Rayleigh number and the ratio of vertical depth to diameter (h/D) considered, a polar grid of 25×25 ($r \times \theta$) and a maximum Cartesian grid of the 54×91 ($x \times y$) appeared sufficient. The extent of the cylindrical domain was chosen such that the intersection region of the polar and Cartesian grid fell halfway between the upper surface and cylinder top. Steady-state solutions were believed to have been reached when $| \mathrm{Nu}^{n+1} - \mathrm{Nu}^{n} | \leq 10^{-5}$ where n denotes the number of time increments. For different values of h/D and Rayleigh number, minimum values for l and W had to be determined such that the mean Nusselt number would be independent of these two parameters. The values of $3.5D$ for l and $6D$ for W were found to be adequate for the range of Rayleigh number and h/D investigated. Only steady-state solutions are presented in the following section.

Results and Discussion

For a horizontal heated cylinder submerged in an unbounded medium, the natural convection heat transfer characteristics are functions of the Rayleigh number only. When the cylinder is buried in a semi-infinite medium in close proximity to the upper bounding surface, the Nusselt number becomes a function of the geometry, in particular of the vertical depth of burial, as well. To study the effects of h/D ratio on the heat transfer characteristics and the flow patterns, results were obtained for a range of h/D values at specified Rayleigh numbers (based on the diameter D of the cylinder). Results were obtained for h/D values of 0.8, 1.2, 2.0, 2.8, 3.8, 4.6, 5.2, and 7.2 for Rayleigh numbers varying from 0 to 300.

For a Rayleigh number set equal to zero the problem reduces to that of a buried cylinder in a purely conductive medium. To assess the validity of the solution scheme and the approximate boundary conditions used, the above problem was investigated first. For the pure conduction problem, the temperature boundary condition of the upper surface was considered to be constant (as against the zero gradient boundary condition used for the natural convection cases.) The h/D ratio in this case was set equal to 3 and l/D and W/D ratios were equal to 5.0 and 8.0, respectively. Near the cylinder surface and in the region between the upper bounding surface and the cylinder, excellent agreements were obtained with the approximate solutions given by Eckert and Drake (1972).

For the conduction problem, no boundary layer is formed and a finite far field approximation is more severe than in a convection dominated problem. Indeed, it was found that for high Rayleigh number flows, large values of l and W (of the computational domain) had little significance for the heat transfer characteristics predicted.

Figures 2 to 4 show the local Nusselt number predictions for a wide range of Rayleigh number, for h/D equal to 2.4, 3.8, and 5.2, respectively. As shown in Fig. 3, the local Nusselt numbers are high at the bottom region of the cylinder, due to little fluid movement in this region. For all Rayleigh numbers considered, the local Nusselt number decreases continuously as the upward plume region is approached. For $h/D = 3.8$, the local Nusselt number behavior for Rayleigh numbers of 10 and 50 is almost the same as compared to the $h/D = 2.4$ case, as shown in Fig. 3. For higher Rayleigh numbers, the increased burial depth (from h/D of 2.4 to 3.8) causes a decrease of the local values of the Nusselt numbers, especially at the lower stagnation ($\theta < 60$ deg) region. A similar trend is obtained for an even higher burial depth ($h/D = 5.2$) as shown in Fig. 4. Numerical and experimental heat transfer data for the above ranges of Rayleigh number (based on cylinder diameter) and burial depth were reported earlier by Fernandez and Schrock (1982). For the numerical computations, a different thermal boundary condition for the upper surface was used. However, no local Nusselt number predictions or measurements were reported. The results presented in Figs. 2–4 thus could not be compared with the above study.

Figure 5 shows the steady-state results of the mean Nusselt numbers for various h/D ratios and for the entire Rayleigh number range (0–300) considered. At low Rayleigh numbers ($\mathrm{Ra} \simeq 10$), heat transfer from the cylinder is conduction dominated and larger values of the mean Nusselt number are observed as the h/D ratio is decreased. For computational reasons (the hybrid grid), no results were obtained below an h/D ratio of 0.8, although the minimum ratio possible is 0.5, when the cylinder is just under the permeable horizontal sur-

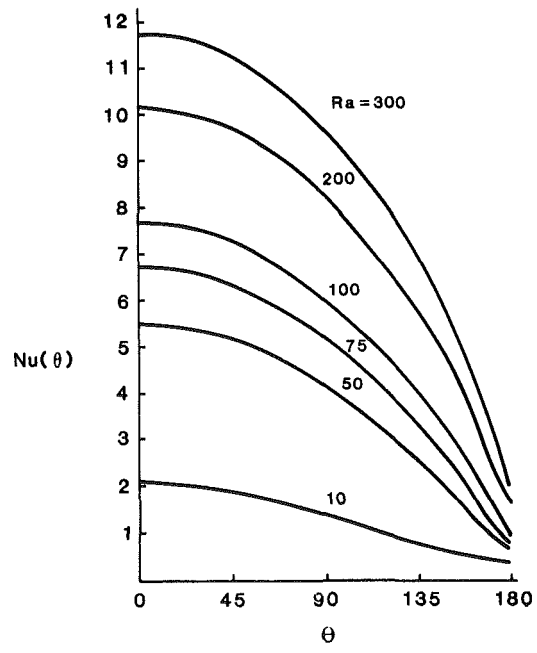

Fig. 2 Local Nusselt number distributions at various Rayleigh numbers ($h/D = 2.4$)

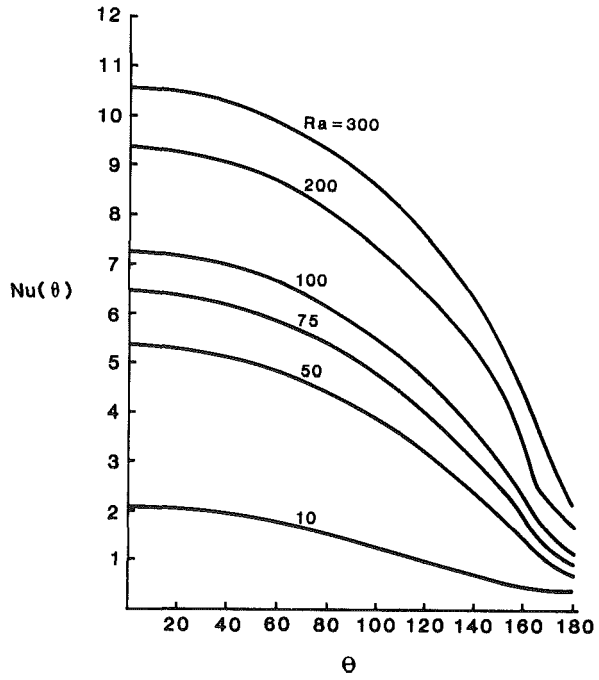

Fig. 3 Local Nusselt number distributions at various Rayleigh numbers ($h/D = 3.8$)

face. Recently, Bau (1984) has reported that on optimal burial depth exists for which heat losses from the cylinder are minimized. His results are, however, for a low Rayleigh number range (0–20) and an isothermal upper surface boundary condition was used in the analysis.

As the Rayleigh number increases, interesting trends are observed for the Nusselt numbers over varying h/D ratios. The heat transfer is enhanced by convection and a transition range is observed where conduction, convection, and burial depth have significant effects on the mean Nusselt number. This transition range may be indicated by the inflection points observed for Rayleigh number equal to 50. A minimum point is observed, but with increasing burial depth, the heat transfer increases signifying a developing flow field. After reaching a maximum point, the Nusselt number is found to level out and will ultimately reach the value for a cylinder buried in an infinite porous medium. Intermediate runs were made between Rayleigh numbers of 10 and 50 and it was found that the minimum heat transfer point shifts to a lower h/D ratio for increasing Rayleigh numbers. This agrees qualitatively with the predictions of Bau (1984).

One of the important observations from Fig. 5 is that at higher Rayleigh numbers (Ra $\geq$ 75), the heat transfer is, in fact, found to increase as the h/D ratio is increased from the value of 0.8. It is conjectured that for convection-dominated cases, the flow field is not well developed when the h/D ratio is small. As h/D is increased, a maximum heat transfer situation is observed, and then the Nusselt number gradually reaches the asymptotic value, corresponding to a cylinder buried in an infinite medium. The asymptotic values of the Nusselt number (for h/D very large) could not be found in the literature for finite diameter cylinders. The maximum heat transfer occurrence seems to shift toward smaller burial depth as the Rayleigh number increases, suggesting that a full development of flow is crucial to the maximization of the heat transfer.

The mean Nusselt number predictions of Fernandez and Schrock (1982) are now compared with the present predictions. A one-to-one comparison, however, is not possible due to the differences in considering the upper bounding thermal boundary condition as discussed earlier. In Fig. 6, we plot the Nusselt numbers predicted in Fernandez and Schrock (1982) as a function of h/D for various Rayleigh numbers (based on the cylinder diameter D). It should be noted here again that the Rayleigh number in Fernandez and Schrock (1982) is based on the length scale $[h^2 - D^2/4]^{1/2}$ and hence the predictions were converted to the cylinder diameter-based Rayleigh number. For low Rayleigh numbers ($\simeq$ 10) there is good agreement between our predictions and those given in Fernandez and Schrock (1982). Qualitatively similar results are obtained in the two studies between Rayleigh numbers of 50 and 100. In our predictions, the Nusselt number decreases at a faster rate than in Fernandez and Schrock (1982) for higher burial depths. This may be caused by the difference in the boundary conditions in Figs. 5 and 6. Significant differences are, however, observed for Rayleigh numbers of 200 and 300 between the two predictions. Data (both numerical and experimental) are presented for limited h/D values in Fernandez and Schrock (1982) for the higher Rayleigh numbers and no variation of Nusselt number with burial depth is observed. This is difficult to justify from a physical point of view. The characteristics observed in our predictions for the high Rayleigh numbers have already been explained. More investigation is recommended in this area to verify the results.

Figures 7 and 8 show computed steady-state streamlines and isotherms for Ra = 10 and h/D = 1.2. The entire computational domain is not shown in the above figures (l/D = 3.5D and W/D = 8). Due to the approximate boundary conditions used at the far fields, only the near field solutions are shown in the above figures. The boundary layer is substantially thick and for the weak convective effects, little refilling or discharge is occurring through the upper permeable surface and a large recirculating zone appears. The steady-state streamlines and isotherm patterns for an intermediate Rayleigh number of 75 and h/D = 2.4 are shown in Figs. 9 and 10. A much more vigorous convective flow is indicated by the higher values of the streamlines. The thermal boundary layer is much thinner due to increasing fluid velocity. The results shown in Figs. 7–10 are qualitatively similar to the calculated results of Fernandez and Schrock (1982). Figure 2 of Fernandez and

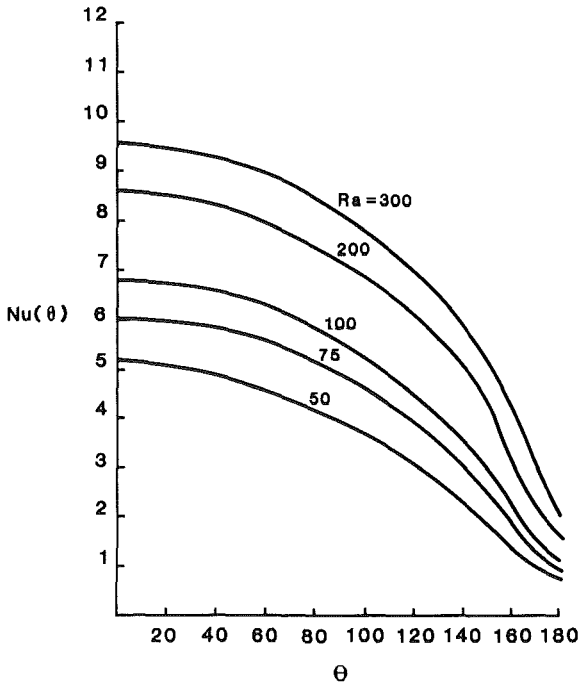

Fig. 4 Local Nusselt number distributions at various Rayleigh numbers (h/D = 5.2)

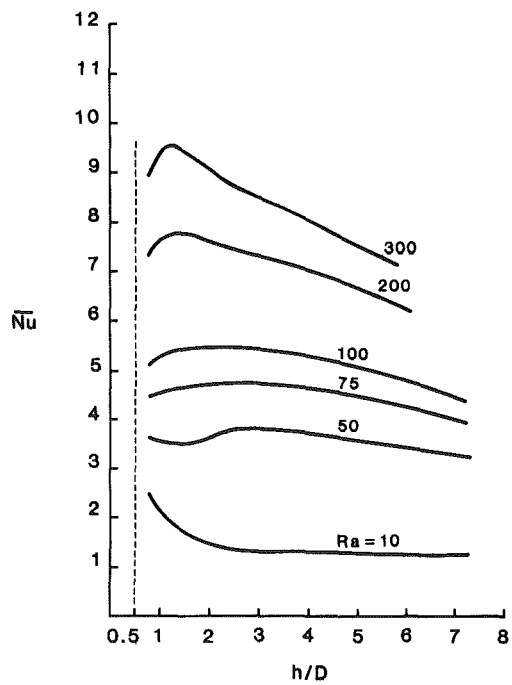

Fig. 5 Mean Nusselt number as a function of h/D for various Rayleigh numbers

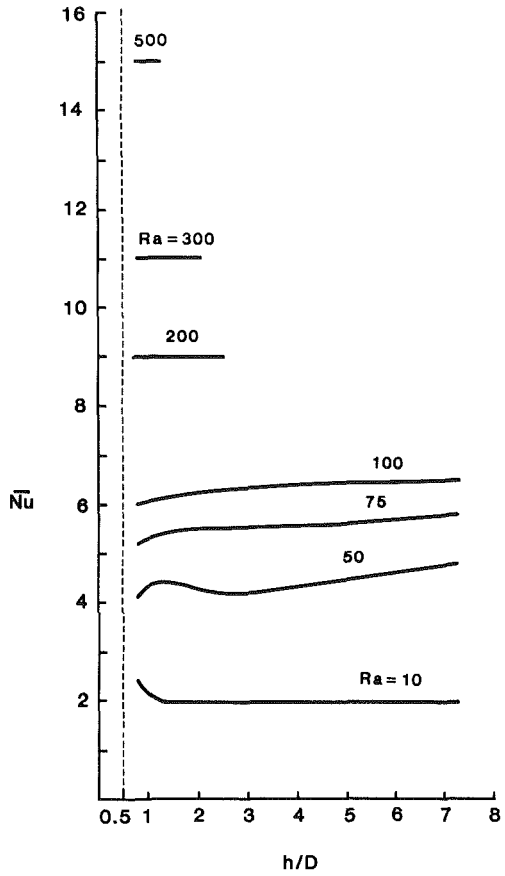

Fig. 6 Mean Nusselt number (predicted by Fernandez and Schrock [10] as a function of *h/D* for various Rayleigh numbers

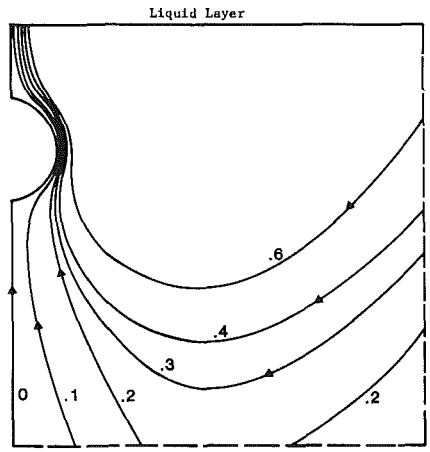

Fig. 7 Streamlines around the heated cylinder, Ra = 10, *h/D* = 1.2

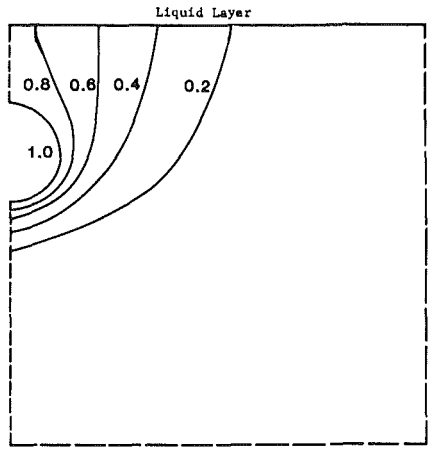

Fig. 8 Isotherms around the heated cylinder, Ra = 10, *h/D* = 1.2

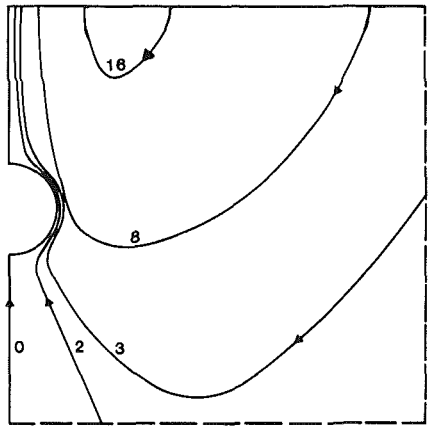

Fig. 9 Streamlines around the heated cylinder, Ra = 75, *h/D* = 2.4

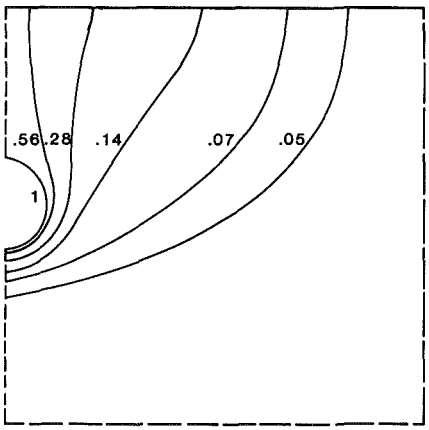

Fig. 10 Isotherms around the heated cylinder, Ra = 75, *h/D* = 2.4

Schrock (1982) give results for $h/D = 1.2$ and Ra = 9.2. The velocity fields are similar to those shown in Fig. 7 (in this paper) where the plume is a little narrow due to the higher Ra. The temperature fields predicted near the upper surface are quite different from those shown in Fernandez and Schrock (1982), which may be due to the difference in thermal boundary condition at the medium surface. However, there is good agreement between the Nusselt number predictions. For Ra > 10, the isotherms become increasingly skewed in the upward direction which results from the relatively strong convective flow.

Finally Figs. 11 and 12 depict the streamlines and isotherms for Ra = 200 and $h/D = 2.4$. At this high Rayleigh number, a thin boundary layer forms near the cylinder surface and the upward plume is narrow. The major portion of the discharge comes from the sides and top, instead of the bottom. Such trends are also obtained for natural convection flows around heated cylinders in a single-phase medium at high Rayleigh numbers (Farouk and Guceri, 1983).

As can be seen in Figs. 7, 9, and 11, the flow near the cylinder is much stronger compared to the rest of the flow domain. For a representative case (Fig. 7), solutions were obtained for larger W/D and l/D ratios, keeping the grid density in the flow domain constant. In that case the flow lines

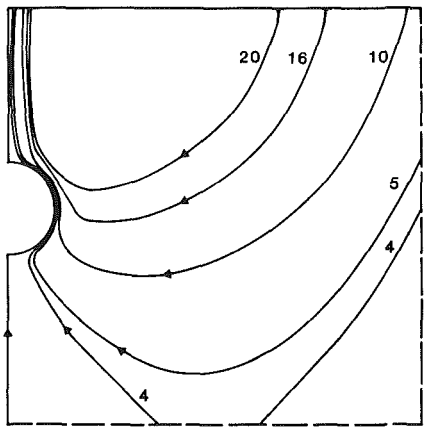

Fig. 11 Streamlines around the heated cylinder, Ra = 200, h/D = 2.4

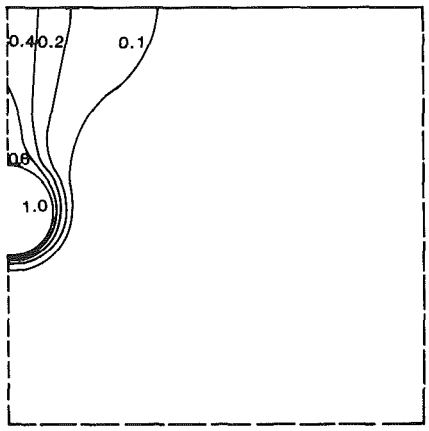

Fig. 12 Isotherms around the heated cylinder, Ra = 200, h/D = 2.4

represented the approximate far field boundary conditions much better than as shown in Fig. 7. Little change was, however, predicted for the mean Nusselt numbers. As can be seen in Figs. 8, 10, and 12, the location of the far field boundaries has less effect on the temperature solutions.

Conclusions

The natural convection from a cylinder buried in a semi-infinite porous medium, bounded above by a liquid layer, has been numerically investigated. The behavior of the mean Nusselt number as a function of the burial depth to cylinder diameter ratio is interesting and is found to be quite different for conduction and convection-dominated cases. The results presented here can be explained well from physical standpoints.

References

Buretta, R. J., and Berman, A. S., 1976, "Convective Heat Transfer in a Liquid Saturated Porous Layer," ASME *Journal of Applied Mechanics*, Vol. 43, pp. 249–253.

Holst, P. H., and Aziz, K., 1972, "Transient Three Dimensional Natural Convection in Confined Porous Media," *International Journal of Heat Mass Transfer*, Vol. 15, pp. 73–90.

Caltagirone, J. P., 1976, "Thermoconvective Instabilities in a Porous Medium Bounded by Two Concentric Horizontal Cylinders," *Journal of Fluid Mechanics*, Vol. 76, No. 2, pp. 337–362.

Facas, G. N., and Farouk, B., 1983, "Transient and Steady State Natural Convection in a Porous Medium Between Two Concentric Cylinders," ASME JOURNAL OF HEAT TRANSFER, Vol. 105, pp. 660–663.

Eckert, E. R. G., and Drake, R. M., 1972, *Analysis of Heat and Mass Transfer*, McGraw-Hill, New York, pp. 98, 340.

Bau, H. H., and Sadhal, S. S., 1982, "Heat Losses From a Fluid Flowing in a Buried Pipe," *International Journal of Heat Mass Transfer*, Vol. 25, pp. 1621–1629.

Thiayagarajan, M., and Yovanovich, M. M., 1974, "Thermal Resistance of a Buried Cylinder With Constant Flux Boundary Conditions," ASME JOURNAL OF HEAT TRANSFER, Vol. 96, pp. 249–250.

Martin, W. W., and Sadhal, S. S., 1978, "Bounds on Transient Temperature Distribution Due to a Buried Cylindrical Heat Source," *International Journal of Heat Mass Transfer*, Vol. 21, pp. 783–789.

Schrock, V. E., Fernandez, R. T., and Kesavan, K., 1970, "Heat Transfer From Cylinders Embedded in a Liquid-Filled Porous Medium," *Proc. of the Int. Heat Transfer Conf.*, Paris, Vol. VIII, p. CT 3.6.

Fernandez, R. T., and Schrock, V. E., 1982, "Natural Convection From Cylinders Buried in a Liquid-Saturated Porous Medium," *Proc. of the Int. Heat Transfer Conf.*, Munich, Vol. 2, pp. 335–340.

Hickox, C. E., 1981, "Thermal Convection at Low Rayleigh number From Concentrated Sources in Porous Media," ASME JOURNAL OF HEAT TRANSFER, Vol. 103, pp. 232–236.

Hickox, C. E., and Watts, H. A., 1980, "Steady Thermal Convection From a Concentrated Source in a Porous Medium," ASME JOURNAL OF HEAT TRANSFER, Vol. 102, pp. 248–253.

Nield, D. A., and White, S. P., 1982, "Natural Convection in an Infinite Porous Medium Produced by a Line Heat Source," *Mathematical Models in Engineering Science*, A. McNabb, R. Wooding, and M. Rosser, eds., Department of Scientific and Industrial Research, New Zealand.

Bau, H. H., 1984, "Convective Heat Losses From a Pipe Buried in a Semi-infinite Porous Medium," *International Journal of Heat Mass Transfer*, Vol. 27, No. 11, pp. 2047–2056.

Launder, B. E., and Massey, T. H., 1978, "The Numerical Prediction of Viscous Flow Heat Transfer in Tube Banks," ASME JOURNAL OF HEAT TRANSFER, Vol. 100, pp. 565–571.

Farouk, B., 1981, "Laminar and Turbulent Natural Convection Heat Transfer From Horizontal Cylinders," Ph.D. Thesis, University of Delaware, Newark, DE

Farouk, B., and Guceri, S. I., 1983, "Natural Convection From a Horizontal Cylinder – Laminar Regime," ASME JOURNAL OF HEAT TRANSFER, Vol. 103, pp. 522–527.

Roache, P. J., 1972, *Computational Fluid Dynamics*, Hermosa Publishers, Albuquerque, NM, pp. 152–161.

Thermal Convection Around a Heat Source Embedded in a Box Containing a Saturated Porous Medium

K. Himasekhar

H. H. Bau

Department of Mechanical Engineering and Applied Mechanics, University of Pennsylvania, Philadelphia, PA 19104-6315

A study of the thermal convection around a uniform flux cylinder embedded in a box containing a saturated porous medium is carried out experimentally and theoretically. The experimental work includes heat transfer and temperature field measurements. It is observed that for low Rayleigh numbers, the flow is two dimensional and time independent. Once a critical Rayleigh number is exceeded, the flow undergoes a Hopf bifurcation and becomes three dimensional and time dependent. The theoretical study involves the numerical solution of the two-dimensional Darcy–Oberbeck–Boussinesq equations. The complicated geometry is conveniently handled by mapping the physical domain onto a rectangle via the use of boundary-fitted coordinates. The numerical code can easily be extended to handle diverse geometric configurations. For low Rayleigh numbers, the theoretical results agree favorably with the experimental observations. However, the appearance of three-dimensional flow phenomena limits the range of utility of the numerical code.

1 Introduction

Thermal convection around a uniform flux pipe embedded in a box containing a saturated porous medium is studied experimentally and theoretically. The geometric configuration involved is schematically depicted in Fig. 1. The study is relevant to the estimation of heat transfer from stored nuclear fuel rods and buried nuclear waste. Additionally, the experiment simulates approximately the problems associated with hot pipes buried in saturated soils. Such problems arise, for example, in connection with underground electrical power-transmission lines, and oil or gas transmission in pipelines where the fluid is heated or cooled to reduce pumping costs.

Although the case studied in this manuscript has not attracted much attention in the literature, the related problem of heat losses from buried pipes has been considered in the heat transfer literature. In the past, some authors (Lebedev et al., 1965; Thiyarajan and Yovanovich, 1974; Bau and Sadhal, 1982; DiFelice and Bau, 1983) have assumed that heat losses may be calculated using a conduction model. Such an approach may be valid in the case of dry or low-permeability soils. However, should the medium be permeable to fluid motion, the heat transport mechanisms would include both conduction and thermal convection. Thermal convection in the porous medium around buried pipes with a variety of boundary conditions has been taken into account in experimental and theoretical works by Schrock et al. (1970), Fernandez and Schrock (1982), Farouk and Shayer (1985), Bau (1984), and Himasekhar and Bau (1986).

Our main objective in this study is to obtain correlations for the heat transfer associated with a cylindrical heat source embedded in a box. To this end, we solve the two-dimensional Darcy-Oberbeck-Boussinesq equations numerically. The complicated geometry (Fig. 1) is handled through the use of boundary-fitted coordinates (Thompson and Warsi, 1982). Experiments are conducted to verify the numerical results. The experimental observations show that for low Rayleigh numbers, the flow is, indeed, two dimensional; however, as the Rayleigh number increases beyond some critical value, which depends on the geometric dimensions of the apparatus, the two-dimensional flow undergoes a Hopf bifurcation into three-dimensional, time-dependent convection. Thus, the two-dimensional, numerical solution is valid only for Rayleigh numbers smaller than the critical one. As a secondary objective, we wish to establish whether the experimental apparatus may be used to model convection associated with a heated pipe buried in a semi-infinite medium. The difference between the model and the real-life situation is, of course, the presence of lateral boundaries in the experimental apparatus. Accordingly, we investigate numerically the effect of the location of the lateral boundaries on the heat transfer process.

We note in passing that Schrock et al. (1970) have used an experimental apparatus similar to ours though with somewhat different boundary conditions (a permeable top surface was used in their case in contrast to the impermeable top surface used in our case). In their work, Schrock et al. (1970) did not report the transition into a three-dimensional, time-dependent flow that we observed in our experiments.

2 Experimental Apparatus and Procedure

The experimental apparatus consists of a cylindrical, quartz, immersion heater 9.6 mm in diameter and 114 mm in heated length, embedded in a well-insulated plexiglass box whose schematic description and major dimensions are depicted in Fig. 1. The length of the heater spans the box's width. The top boundary of the apparatus consists of a perforated brass plate heat exchanger. A network of 6.3 mm (1/4 in.) holes was drilled inside the plate to accommodate cooling water circulation. Four thermocouples were welded to the bottom surface of the plate. The measured temperature variations were always smaller than 1 percent of the temperature difference between the heater and the top plate. The perforations in the plate were made to accommodate thermal expansion of the fluid inside the apparatus. The equivalent permeability of the plate is estimated as 3.6×10^{-11} m^2, which is about 0.2 percent of the porous medium's permeability inside the apparatus. In view of the above, the plate is assumed to be impermeable and isothermal for the purpose of the theoretical modeling (section 3). The vertical distance between the top

Contributed by the Heat Transfer Division for publication in the JOURNAL OF HEAT TRANSFER. Manuscript received by the Heat Transfer Division March 9, 1987. Keywords: Natural Convection, Numerical Methods, Porous Media.

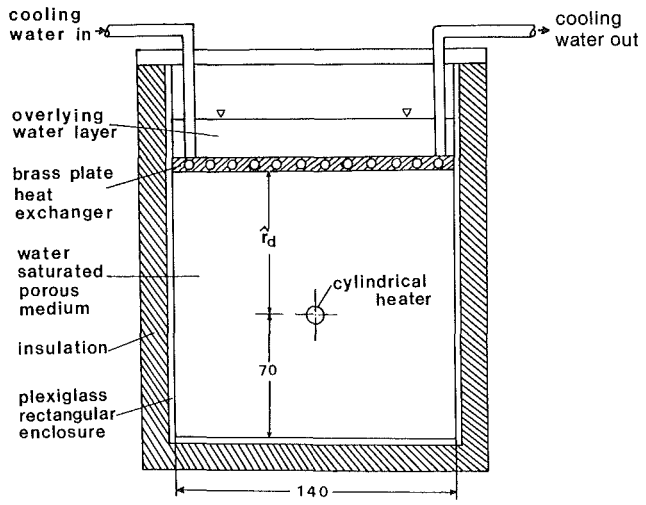

Fig. 1 Schematic description of the experiment setup (all dimensions are in mm); the third dimension of the apparatus $L = 114$ mm

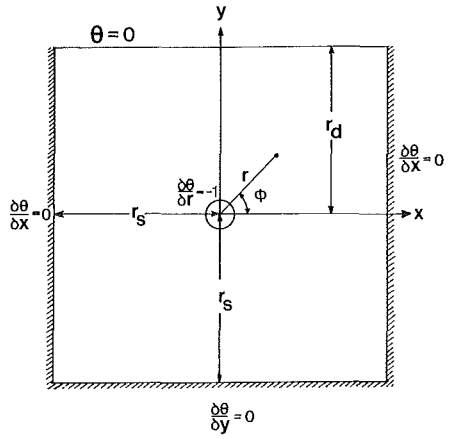

Fig. 2 Mathematical model

surface and the heater (r_d in Fig. 1) can be varied. A water pool of approximately 10 mm depth is maintained above the heat exchanger. The top of the apparatus is sealed to prevent evaporation.

The flow rate and temperature rise of the cooling water (typically around 1°C) in the top brass plate were continuously monitored with thermopiles and used to compute the rate of energy outflow from the apparatus with an estimated error smaller than 3 percent. This quantity was compared and found to be within 6 percent of the electrical power input into the heater. The above difference is attributed to heat losses through the lateral and bottom walls.

A network of forty 36-gage copper-constantan thermocouples is embedded at various locations within the porous matrix. Some of the temperatures were continuously recorded with a multichannel strip chart recorder to facilitate detection of time-dependent phenomena.

The porous medium is simulated using uniformly sized, closely packed, spherical glass beads, each of which is 4 mm in diameter. The saturating fluid is distilled, degassed water. The porosity, $\phi_p = 0.4 \pm 0.001$, is determined experimentally by displacing water as the bed is packed. The permeability, $\lambda = 1.6 \times 10^{-8}$ m^2, is obtained from Kozeny Carman's formula (Bear, 1972). The effective thermal conductivity, $k_{eq} = 0.85 \pm 0.05$ W/mK, is determined by comparing measured and computed heat flows in the region of low heat inputs when the heat transfer is conduction dominated and convective effects are negligibly small. The computed heat flow is obtained by solving a conduction problem that utilizes the measured temperature distribution on both the cylinder and box surfaces as an input. The aforementioned thermal conductivity lies between the values 0.83 and 0.90 W/mK, which were obtained from series and parallel models (Combarnous and Bories, 1975), respectively.

More details about the experimental apparatus and procedure are provided by Himasekhar (1987).

Experiments are carried out, starting from a quiescent initial state. The power input into the heater is changed in a sequence of small steps. After each step, a period of several hours is allowed in order to achieve steady state. Once the maximum allowed temperature has been achieved, the experiment is repeated by gradually reducing the input power to the heater. At each stage, the power input and output as well as the temperature distribution inside the porous medium are measured.

3 Analysis

3.1 Mathematical Model. In this study, we focus on relatively low Rayleigh numbers. Thus, we neglect inertia, dispersion, and wall channeling effects and assume that the fluid flow may adequately be described by the Darcy-Oberbeck-Boussinesq's equations (Joseph, 1976), which in nondimensional form may be written as

$$\nabla^2\psi = -R_q\,\theta_x$$
$$\nabla^2\theta = \psi_y\,\theta_x - \psi_x\,\theta_y \qquad (1)$$

Nomenclature

g = gravitational acceleration
k_{eq} = equivalent thermal conductivity of the porous medium
L = axial length of the apparatus
Nu = Nusselt number (equation 4)
Q = heat flow per unit length of the pipe $= \hat{Q}/k_{eq}\,(\hat{T}_i - \hat{T}_o)$
q_i = heat flux on pipe surface $= \hat{q}\hat{r}_i/k_{eq}\,(\hat{T}_i - \hat{T}_o)$
r, ϕ = cylindrical coordinates
$\hat{r}_i$ = radius of the cylinder
r_d = burial depth (Fig. 2)
r_s = distance between the cylinder center and the side walls (Fig. 2)
R_q = Darcy-Rayleigh number (equation (2))
R_{eff} = effective Darcy-Rayleigh number $= R_q \cdot (\hat{r}_d/\hat{r}_i)$
$\hat{T}$ = temperature
x, y = Cartesian coordinates (Fig. 2)
α_{eq} = equivalent thermal diffusivity of the porous medium
β = thermal expansion coefficient of the saturating fluid
θ = nondimensional temperature $= (\hat{T} - \hat{T}_o)k_{eq}/\hat{q}_i\hat{r}_i$
λ = permeability
ν_f = kinematic viscosity of the saturating fluid
ξ, η = body-fitted coordinates
τ = nondimensional time $= \hat{\tau}\alpha_{eq}/\hat{r}_i^2$
ϕ_p = porosity of the porous medium
ψ = streamfunction

Subscripts

1 = cylinder surface
o = surface of the top horizontal medium
c = centerline above the top of the cylinder

Superscripts

$\hat{}$ = dimensional quantities

where ψ and θ are the stream function and the temperature, respectively; x and y are Cartesian coordinates (Fig. 2); subscripts indicate partial derivatives;

$$R_q = \frac{g\beta\lambda \hat{r}_i^2 \hat{q}_i}{\nu_f \alpha_{eq} k_{eq}} \tag{2}$$

is the Rayleigh number based on the heat flux $\hat{q}_i$; $\hat{r}_i$ is the radius of the cylinder; ν_f is the kinematic viscosity of the fluid; and α_{eq} is the effective thermal diffusivity.

The length scale is $\hat{r}_i$; the temperature scale is $\hat{q}_i\,\hat{r}_i/\alpha_{eq}$, and the time scale is $\hat{r}_i^2/\alpha_{eq}$. Quantities with (without) superscript caret are dimensional (nondimensional). From here on, all the numerical values appearing in the manuscript are nondimensional.

The boundary conditions are:

$$\begin{aligned}
&\theta_r = -1, \quad \psi = 0 \quad @x^2 + y^2 = 1 \\
&\theta_X = \psi = 0 \quad x = \pm r_s, \quad -r_s \le y \le r_d \\
&\theta_y = \psi = 0 \quad -r_s \le x \le r_s \quad y = -r_s \\
&\theta = \psi = 0 \quad -r_s \le x \le r_s \quad y = r_d
\end{aligned} \tag{3}$$

The Nusselt number (Nu) is defined as the ratio between the actual heat flow and the heat flow in the absence of convection (Q_{cond}).

$$\text{Nu} = \frac{Q}{Q_{\text{cond}}} \tag{4}$$

The specification of the location of the boundary conditions using conventional coordinate systems is somewhat inconvenient. To overcome this difficulty, we map the physical domain (Fig. 2) onto a rectangle. This mapping may be accomplished by employing boundary-fitted coordinates (Thompson and Warsi, 1982).

3.2 Boundary-Fitted Coordinates. We introduce a new curvilinear coordinate system (ξ, η) such that the inner boundary (the cylinder's surface) and the outer boundary (the rectangle) coincide with fixed values of η, η_o, and η_m, say. In general ξ and η may not be orthogonal.

From the various techniques available for the generation of curvilinear coordinate systems, we chose the PDE method advocated by Thompson and co-workers. For details, interested readers are referred to Thompson and Warsi (1982) and the literature cited there. Briefly, we obtain the transformation relations for the mapping by solving the nonlinear partial differential equations

$$L^2 x = 0, \quad L^2 y = 0$$

where the operator

$$\begin{aligned}
L^2 f = \frac{1}{J^2}\,[&a_1 f_{\xi\xi} - 2a_3 f_{\xi\eta} + a_2 f_{\eta\eta} + J^2(P f_\xi + Q f_\eta)], \\
&a_1 = x_\eta^2 + y_\eta^2,\ a_2 = x_\xi^2 + y_\xi^2, \\
&a_3 = x_\xi x_\eta + y_\xi y_\eta, \text{ and } J = x_\xi y_\eta - x_\eta y_\xi
\end{aligned} \tag{5}$$

P and Q are both functions of ξ and η. Their main use is to control the physical distance between any two adjacent coordinates. Here, we set

$$P = 0$$

and

$$\begin{aligned}
Q = -A\,\{&\text{sgn}\,(\eta - \eta_o)\,\exp\,[-D(\eta - \eta_o)] \\
&+ \text{sgn}(\eta - \eta_m)\cdot\exp[-D(\eta_m - \eta)]\}
\end{aligned} \tag{6}$$

The boundary conditions consist of the specification of the location of the boundary surfaces plus a symmetry condition along the vertical axis.

Equations (5) are solved iteratively using central differences. A typical example of the resulting coordinate system is depicted in the physical plane in Fig. 3. The computational domain consists of the rectangle $\xi_o \le \xi \le \xi_m$ and $\eta_o \le \eta \le \eta_m$.

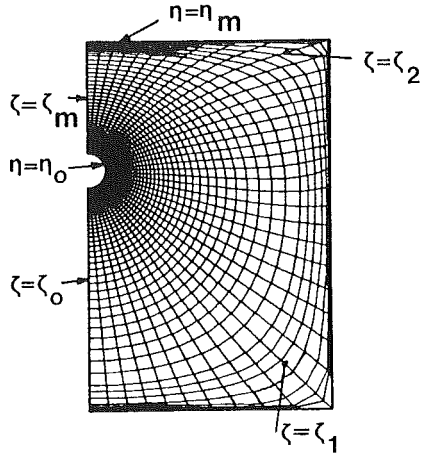

Fig. 3 A typical example of the boundary-fitted coordinates (r_d = 7.4 and r_s = 14.6; all quantities are dimensionless)

3.3 Numerical Solution. Next, the governing equation (1) with the boundary conditions (3) are transformed into the new coordinate system (ξ, η). The resulting equations are

$$\begin{aligned}
L^2\psi &= -\frac{R_q}{J}\,(y_\eta \theta_\xi - y_\xi \theta_\eta) \\
L^2\theta &= \frac{1}{J}\,(\psi_\eta \theta_\xi - \psi_\xi \theta_\eta)
\end{aligned} \tag{7}$$

with the boundary conditions

$$\begin{aligned}
&\psi = 0,\ \theta_\eta(x_\xi \sin\phi - y_\xi \cos\phi) + \theta_\xi(y_\eta \cos\phi - x_\eta \sin\phi) = -J \\
&\qquad\qquad \text{at} \quad \eta = \eta_o; \quad \xi_o \le \xi \le \xi_m \\
&\psi = y_\eta \theta_\xi - y_\xi \theta_\eta = 0 \qquad \text{at} \quad \eta = \eta_m; \quad \xi_o \le \xi \le \xi_1 \\
&\psi = x_\xi \theta_\eta - x_\eta \theta_\xi = 0 \qquad \text{at} \quad \eta = \eta_m; \quad \xi_1 \le \xi \le \xi_2 \\
&\psi = \theta = 0 \qquad \text{at} \quad \eta = \eta_m; \quad \xi_2 \le \xi \le \xi_m \\
&\psi = \theta_\xi = 0 \qquad \text{at} \quad \xi = \xi_1, \quad \xi_m; \quad \eta_o \le \eta \le \eta_m
\end{aligned}$$

where $\phi = \tan^{-1}(y/x)$ and the significance of ξ_i and η_i is depicted in Fig. 3.

The equations (7) are discretized using finite differences on a uniform grid with $\Delta\xi = \Delta\eta$. Diffusive and convective terms are approximated, respectively, with central and upwind differences (Roache, 1976). The resulting algebraic equations are solved iteratively using successive overrelaxation. The iterative procedure is terminated once the convergence criteria

$$\max_{i,j} \frac{\psi_{i,j}^{n+1} - \psi_{i,j}^n}{\psi_{i,j}^n}, \frac{\theta_{i,j}^{n+1} - \theta_{i,j}^n}{\theta_{i,j}^n} < \epsilon$$

are satisfied. $\epsilon = 10^{-4}$ is used since more stringent conditions do not lead to a significant difference in the results.

Since boundary-fitted coordinates are infrequently employed in thermal convection analysis, we decided to verify our numerical code by solving a thermal convection problem in a concentric, horizontal annulus for which solutions are available from other sources (i.e., Caltagirone, 1976; Bau, 1984). Results obtained using the present code favorably agree (as shown in Table 1) with those of others.

The next issue we address is the minimal number of grid points required to obtain solutions that are reasonably grid-independent. To this end, we solve the problem at hand (a cylindrical source in a rectangle) for various mesh sizes. In Table 2, we document the effect of mesh size on the solution for R_q = 25. Nu_i and Nu_o are the Nusselt numbers computed

Table 1 Comparison of results for Ra = 100 for a concentric annulus with radius ratio = 2

Source	Bau, 1984	Caltagirone, 1976	Present code		
Number of grid points	(30×44)	(49×49)	(17×17)	(25×25)	(33×33)
Nu	1.844	1.829	1.810	1.834	1.848
ψ_{max}	9.964	9.748	9.961	9.996	9.996

at the cylinder and top surfaces, respectively. ψ_{max} is the maximum value of the streamfunction. We estimate that for (42×42) grid points, the results should be correct within 0.2 percent. This is the mesh size employed in all our computations.

4 Results and Discussion

In this section, we describe and compare the results of the experiments and the numerical simulation. The first part of the section considers the description of the temperature and flow fields while the second part focuses on the heat transfer.

4.1 Flow and Temperature Fields. The flow (stream lines) and the temperature field (isotherms) are depicted, respectively, on the right-hand side and left-hand side of Figs. 4 and 5. In both cases, the nondimensional burial depth $r_d = 7.4$. Both isotherms and streamlines are equally spaced. The solid lines and the symbols correspond, respectively, to the theoretical and experimental results.

For low Rayleigh numbers, as in the case depicted in Fig. 4 ($R_q = 0.24$), the temperature field resembles the conductive one. This suggests that most of the heat is transported by conduction. The flow field is two dimensional and consists of two counterrotating cells, one in each half of the box. Hot fluid is rising next to the cylindrical heater and descending along the side walls.

As the Rayleigh number increases, the convective effects become more important. This is signified by the appearance of a plume region above the hot pipe (Fig. 5, $R_q = 8.8$). The computed isotherms (solid lines) agree with the measurements (symbols in Fig. 5). The flow field remains two dimensional and bicellular although the center of rotation moves upward as the Rayleigh number increases.

In Figs. 6 and 7, we depict, respectively, the temperature distribution around the pipe surface and that along the vertical axis (above the heater) for various Rayleigh numbers. The solid lines and the symbols represent, respectively, theoretical and experimental results. The agreement between the theoretical and experimental results is quite good for $R_q < 10$. For $R_q > 10$, we observe significant deviations between the theory and experiment (beyond the margins of experimental error). These deviations are attributed to the evolution of three-dimensional flow, which we describe later.

In Fig. 6, the temperature distribution on the cylinder surface is depicted. Although the actual temperature increases as R_q increases, the nondimensional temperature exhibits the reverse trend. This is due to the nondimensional scheme employed in this paper in which the temperature scale is proportional to the heat flux (or to R_q).

In Fig. 7, the temperature distribution along the plume axis is depicted as a function of the vertical location for various values of the Rayleigh number. As the Rayleigh number increases, boundary layers develop next to the cylinder and top surface; the temperature distribution between the boundary layers tends to flatten out.

As the Rayleigh number increases further, the temperature field ceases to be time independent. The recorded time traces

Table 2 Effect of grid size for a rectangular box with the heated pipe subjected to a uniform heat flux condition for dimensionless $r_d = 7.4$ and $r_s = 14.6$; $R_q = 25$

Grid points	Nu_i	Nu_o	ψ_{max}
18×18	4.142	4.756	10.06
26×26	4.284	4.647	9.97
34×34	4.425	4.463	9.83
42×42	4.436	4.446	9.62
50×50	4.442	4.444	9.61

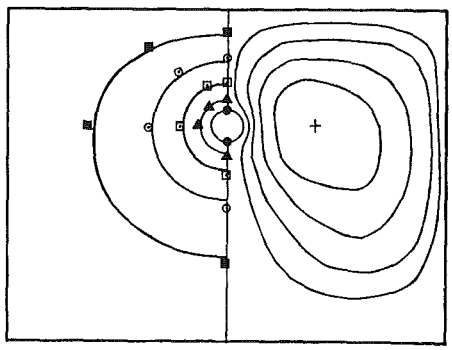

Fig. 4 The flow (RHS) and temperature fields (LHS) corresponding to $R_q = 0.24$ and $r_d = 7.4$; the symbols and the solid lines represent, respectively, the experimental and the numerical data

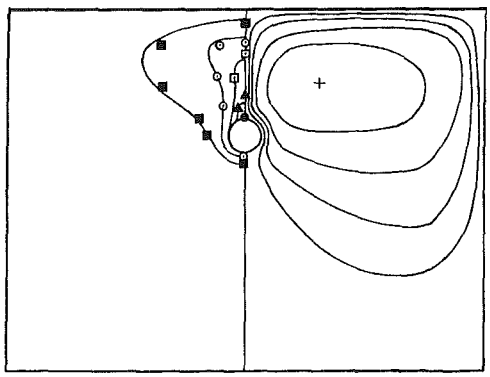

Fig. 5 The flow (RHS) and temperature fields (LHS) corresponding to $R_q = 8.8$ and $r_d = 7.4$; the symbols and the solid lines represent, respectively, the experimental and the numerical data

of the temperature at nondimensional height $y = 2$ reveal approximately periodic behavior for $R_{eff} > 50$ and $r_d = 7.4$ and for $R_{eff} > 150$ and $r_d = 13.9$. The magnitude of the critical Rayleigh number at the onset of the three-dimensional, oscillatory convection appears to be an inverse function of the ratio of the axial length of the heater to the burial depth which in our experiments had values of 3.2 and 1.7. In Fig. 8, we depict the measured average period as a function of the Rayleigh numbers for $r_d = 7.4$ (open circles) and 13.9 (solid circles). The period appears to decrease as the Rayleigh number increases.

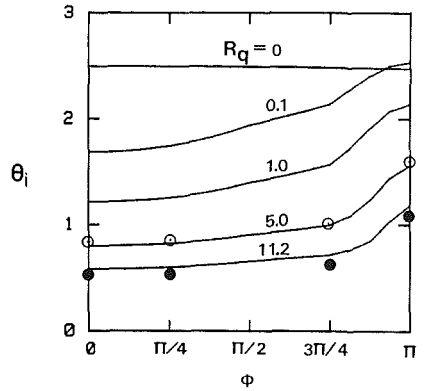

Fig. 6 The variation of the cylinder surface temperature (θ_i) is depicted as a function of angular location (ϕ) for various Rayleigh numbers R_q for r_d = 7.4; the experimental and numerical data are represented by symbols and solid lines, respectively

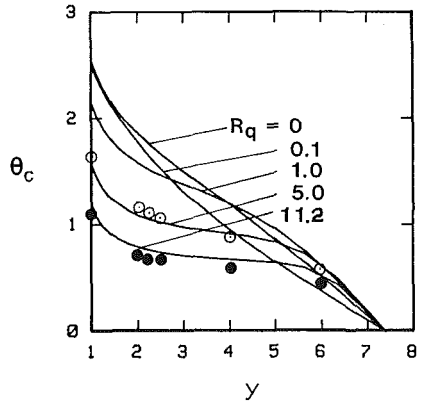

Fig. 7 The variation of the centerline temperatures (θ_c) is depicted as a function of the vertical distance (y) for several Rayleigh numbers, r_d = 7.4; the symbols and the solid lines correspond to the experimental and numerical data, respectively

Examination of the temperature field reveals that once the phenomenon becomes time dependent the temperature field is no longer two dimensional. In Fig. 9, we depict the temperature distribution along a horizontal line parallel to the heater axis (z) at a nondimensional height $y = 2$. This temperature distribution (Fig. 9) has a sinusoidal shape, which corresponds to ascending (peaks) and descending (valleys) fluid columns. Hence, the flow must have a velocity component in the z direction. That is, the convective motion has a spiral form where the ascending column above the heater is also moving axially. The spatial periodicity corresponds roughly to the burial depth r_d. Clearly, the utility of the present numerical code is limited to Rayleigh numbers smaller than the critical ones.

We note in passing that the evolution of time-dependent, three-dimensional flows also has been observed by others for different geometric configurations involving thermal convection in porous media. See, for example, Caltagirone's (1976) work concerning a horizontal concentric annulus and Bau and Torrance's (1982) work concerning a vertical cylinder heated from below.

4.2 Heat Transfer. In Fig. 10, we depict the variation of the Nusselt number (Nu) as a function of the Rayleigh number (R_q) for various burial depths r_d = 2, 7.4, and 13.9. The solid lines correspond to the theoretical results while the symbols represent experimental data. The dashed line in Fig. 10 indicates the appearance of the three-dimensional, time-dependent flow. For Rayleigh numbers smaller than the critical one, the experimental data are scattered around the

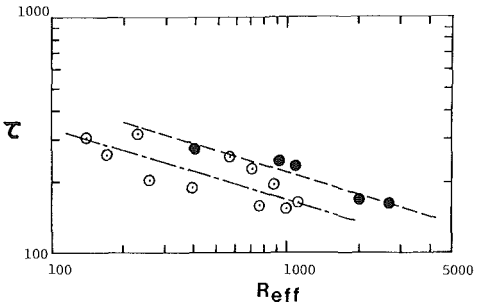

Fig. 8 The variation of the nondimensional time period (τ) is depicted as a function of R_{eff} for r_d = 7.4 (open circles) and r_d = 13.9 (solid lines)

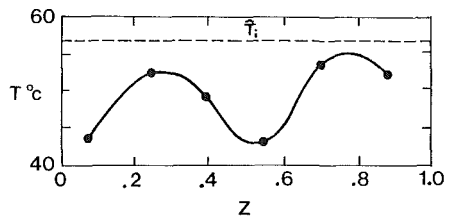

Fig. 9 The variation of the temperature at $y = 2$ and $\phi = \pi$ is depicted as a function of the nondimensional axial distance z/L, for r_d = 7.4 and R_q = 139.4

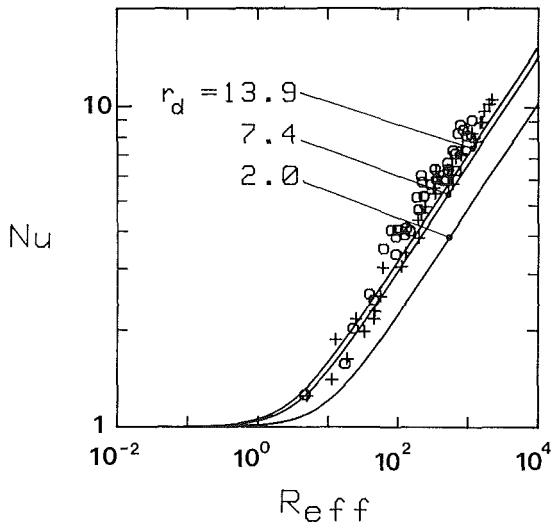

Fig. 10 The variation of the Nusselt number (Nu) is depicted as a function of the Rayleigh number R_{eff} for various burial depths; the symbols and solid lines represent, respectively, the experimental data and correlation equation (8)

theoretical predictions. However, for Rayleigh numbers larger than the critical one, once the flow becomes three dimensional and time dependent, the theoretical calculation tends to underestimate the Nusselt number; thus it may merely be used for estimating a lower bound for the heat transfer.

Based on our theoretical predictions, we construct a correlation for the Nusselt number for $r_s > 2\,r_d$ in the form

$$\mathrm{Nu} = (1 + \mathrm{Nu}_\infty^4)^{1/4} \tag{8}$$

where

$$\mathrm{Nu}_\infty = [1.52 - 1.41\, e^{-0.43(r_d - 1)}]\, R_q^{1/3}$$

Next, we consider the effect of the location of the lateral boundaries on the heat transfer. In Fig. 11, we depict the average surface temperature ($\bar{\theta}_i$) which is inversely proportional to the heat flow as a function of the distance to the lateral boundary (r_s) for various Rayleigh numbers R_q = 1, 5, and 10, and for burial depth r_d = 7.4. As Fig. 11 makes ap-

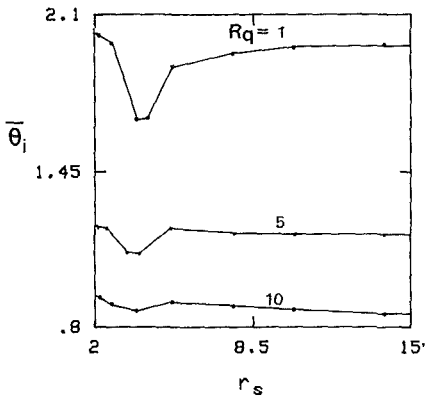

Fig. 11 The effect of boundaries on the average surface temperature $\bar{\theta}_i$, for r_d = 7.4

parent, the average temperature ($\bar{\theta}_i$) is not a monotonic function of r_s. As r_s increases, $\bar{\theta}_i$ initially decreases, attains a minimum value, and then increases again to some asymptotic value, which corresponds to the average temperature of the cylinder in the absence of lateral boundaries. The existence of a similar temperature minima has been observed by Fand et al. (1986) and by Sparrow and Pfeil (1984) and has been attributed to a chimney effect.

For any practical purpose, it appears that the asymptotic value of $\bar{\theta}_i$ (which corresponds to $r_s \to \infty$) is approximately obtained for $r_s > 2\, r_d$. Thus, if one were to construct an experiment to simulate heat losses from a buried pipe, it would suffice to set $r_s > 2\, r_d$.

5 Conclusion

An experimental and theoretical study of heat losses from a cylindrical source embedded in a box is carried out.

The experimental evidence shows that there exists a critical Rayleigh number below which the flow is two dimensional and time independent and above which the flow becomes three dimensional and time dependent. The magnitude of the critical Rayleigh number appears to be an inverse function of the ratio of the cylinder length and the burial depth.

The theoretical work consists of developing a finite difference code based on the Darcy-Oberbeck-Boussinesq equations. The complex geometry is conveniently handled through the use of boundary-fitted coordinates. The theoretical results agree favorably with experimental observations for subcritical Rayleigh numbers.

Thus, it appears that both the DOB equations and the numerical code based on the boundary-fitted coordinates can adequately predict subcritical flows. However, for supercritical Rayleigh numbers, the numerical code underestimates the heat transfer. Accordingly, it will have to be modified to enable treatment of three-dimensional and time-dependent phenomena. It is also possible that for large Rayleigh numbers, non-Darcian effects may become important, and it would be necessary to modify the equations accordingly.

The adequacy of the experimental apparatus for modeling heat losses from a buried pipe is also examined and it appears that for any practical purpose (i.e., 1 percent accuracy), it would suffice to construct an apparatus where the lateral boundaries are positioned at a distance from the pipe of about twice the burial depth.

Acknowledgments

This material is based upon work supported by the National Science Foundation under Grant No. CBT83-51658.

References

Bau, H. H., 1984, "Convective Heat Losses From a Pipe Buried in a Semi-infinite Porous Medium," *Int. Journal of Heat Mass Transfer*, Vol. 27, pp. 2047-2056.

Bau, H. H., and Sadhal, S. S., 1982, "Heat Losses From a Fluid Flowing in a Buried Pipe," *Int. Journal of Heat Mass Transfer*, Vol. 25, pp. 1621-1629.

Bau, H. H., and Torrance, K. E., 1982, "Low Rayleigh Number Thermal Convection in a Vertical Cylinder Filled With Porous Materials and Heated From Below," ASME JOURNAL OF HEAT TRANSFER, Vol. 104, pp. 166-172.

Bear, J., 1972, *Dynamics of Fluids in Porous Media*, Elsevier, Amsterdam.

Caltagirone, J. P., 1976, "Thermoconvective Instabilities in a Porous Medium Bounded by Two Concentric Horizontal Cylinders," *Journal of Fluid Mechanics*, Vol. 76, pp. 337-362.

Combarnous, M. A., and Bories, S. A., 1975, "Hydrothermal Convection in Saturated Porous Medium," *Advances in Hydro Science*, Vol. 10, pp. 237-307.

DiFelice, R. F., and Bau, H. H., 1983, "Conductive Heat Transfer Between Eccentric Cylinders With Boundary Conditions of the Third Kind," ASME JOURNAL OF HEAT TRANSFER, Vol. 105, pp. 678-680.

Fand, R. M., Steinberger, T. E., and Cheng, P., 1986, "Natural Convection Heat Transfer From a Horizontal Cylinder Embedded in a Porous Medium," *Int. Journal of Heat Mass Transfer*, Vol. 29, pp. 119-134.

Farouk, B., and Shayer, H., 1985, "Natural Convection Around a Heated Cylinder Buried in a Saturated Porous Medium," in: *Heat Transfer in Porous Media and Particulate Flows*, Proc. of the 23rd National Heat Transfer Conference, Denver, CO (ASME HTD-Vol. 46).

Fernandez, R. T., and Schrock, V. E., 1982, "Natural Convection From Cylinders Buried in a Liquid-Saturated Porous Medium," *Proc. Int. Heat Transfer Conf.*, Munich, Vol. 2, pp. 335-340.

Himasekhar, K., 1987, "Thermal Convection in a Horizontal Eccentric Annulus Filled With a Saturated Porous Medium," Ph.D. Thesis, Univ. of Pennsylvania, Philadelphia, PA.

Himasekhar, K., and Bau, H. H., 1987, "Thermal Convection Associated With Hot/Cold Pipes Buried in a Semi-Infinite Saturated Porous Medium," *Int. J. Heat Mass Transfer*, Vol. 30, pp. 263-273.

Joseph, D. D., 1976, *Stability of Fluid Motions II*, Springer-Verlag, Berlin.

Lebedev, N. N., Skalakaya, I. P., and Uflyand, Y. S., 1979, *Worked Problems in Applied Mathematics*, Dover. NY, pp. 212-214.

Roache, P. J., 1976, *Computational Fluid Dynamics*, Hermosa, Albuquerque, NM.

Schrock, V. E., Fernandez, R. T., and Kesavan, K., 1970, "Heat Transfer From Cylinders Embedded in a Liquid Filled Porous Medium," *Proc. Int. Heat Transfer Conf., Paris*, Vol. VII, Ct. 3.6.

Sparrow, E. M., and Pfeil, D. R., 1984, "Enhancement of Natural Convection Heat Transfer From a Horizontal Cylinder Due to Vertical Shrouding Surfaces," ASME JOURNAL OF HEAT TRANSFER, Vol. 106, pp. 124-130.

Thiyagarajan, R., and Yovanovich, M. M., 1974, "Thermal Resistance of Buried Cylinder With Constant Flux Boundary Condition," ASME JOURNAL OF HEAT TRANSFER, Vol. 96, pp. 249-250.

Thompson, J. F., and Warsi, Z. U. A., 1982, "Boundary-Fitted Coordinate System for Numerical Solution of Partial Differential Equations – A Review," *Journal of Comp. Physics*, Vol. 47, pp. 1-108.

Fluid Flow and Mixed Convection Transport From a Moving Plate in Rolling and Extrusion Processes

M. V. Karwe

Y. Jaluria
Mem. ASME

Department of Mechanical and Aerospace Engineering, Rutgers University, New Brunswick, NJ 08903

The heat transfer arising due to the movement of a continuous heated plate in processes such as hot rolling and hot extrusion has been studied. Of particular interest were the resulting temperature distribution in the solid and the proper imposition of the boundary conditions at the location where the material emerges from a furnace or die. These considerations are important in the simulation and design of practical systems. A numerical study of the thermal transport process has been carried out, assuming a two-dimensional steady circumstance. The boundary layer equations, as well as full governing equations including buoyancy effects, are solved employing finite difference techniques. The effect of various physical parameters, which determine the temperature and flow fields, is studied in detail. The significance of these results in actual manufacturing processes is discussed.

Introduction

Heat and momentum transfer from a heated moving surface to a quiescent ambient medium occur in many manufacturing processes such as hot rolling, hot extrusion, wire drawing, and continuous casting; see Altan et al. (1970) and Fisher (1976). When the material emerges from the die or the rollers, it is at a temperature higher than that of the surroundings. Generally, external heating is the source of these high temperatures as is the case of hot extrusion. Plastic deformation of the material and the friction between the flowing material and the die also contribute to the heating. In the case of cold extrusion, a portion of the heat generated is lost to the die and the rest is dissipated to the environment. In many practical circumstances, the extruded material passes through a cooling bath or trough. Consider, for example, the schematic representation of wire coating process, discussed by Fisher (1976), as shown in Fig. 1(*a*). The metal wire is coated with a plastic sheath from an extruder and then the insulated wire passes through a cooling system. The size of the cooling bath varies according to the volume of the plastic to be cooled. The length of the bath can be calculated depending upon properties of the materials, the conditions of extrusion, i.e., speed, temperature, etc., and the temperature of the cooling water. With increasing speeds of extrusion in recent years, the amount of time the material spends in the water has become progressively lower and, therefore, cooling troughs of the order of 30 m are common.

The transport process is time dependent at the initial stages of the process when the material emerges from the die. However, at large time, it may generally be treated as a steady-state convective circumstance. For short periods of time, after the onset of the process, the thermal field has not been established and the transient process is of interest. At large times, the process attains steady flow situation, because the end effects decrease in importance. For instance, in hot rolling, if the tip of the material is far from the rollers, then the effect of end conduction on the flow and heat transfer in the vicinity of the rollers is negligible. Therefore, a steady-state situation may be assumed over most of the material.

The essential features of the two-dimensional flow induced by a long, continuously moving plate are shown in Fig. 1(*b*). The plate moves out of the slot of an extrusion die or between the rollers, and moves steadily through an otherwise quiescent medium. Due to viscous drag at the surface of the plate, flow is induced in the vicinity of the plate surface. The plate also loses energy to the ambient fluid. If the temperature of fluid in the vicinity of the plate surface is sufficiently high, a significant effect on the flow may arise due to the thermal buoyancy. This effect will, obviously, depend upon the orientation of the plate with respect to gravity.

Assuming such a flow to be of boundary layer type, Sakiadis (1961a, 1961b) obtained a numerical solution for the flow field, using a similarity transformation. The velocity boundary layer is seen to grow in the direction of motion of the plate. Tsou et al. (1967) have shown experimentally that such a flow indeed arises. Griffin and Thorne (1967) observed the growth of the thermal boundary layer over a flat, continuously moving belt. They have also discussed the effect of

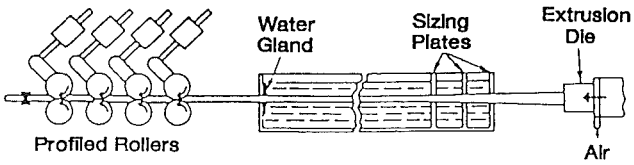

Fig. 1(*a*) Schematic of the wire plastic coating process

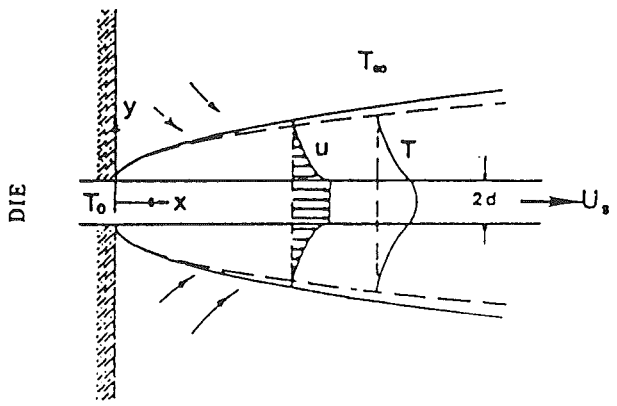

Fig. 1(*b*) Flow geometry near the die

Contributed by the Heat Transfer Division and presented at the ASME Winter Annual Meeting, Anaheim, California, December 7–12, 1986. Manuscript received by the Heat Transfer Division August 1, 1986. Keywords: Conjugate Heat Transfer, Materials Processing and Manufacturing Processes, Mixed Convection.

the presence of walls near the slot on the heat transfer near the slot. Tsou et al., as well as Griffin and Thorne, assumed the surface of the plate to be isothermal and the thickness of the plate to be small. However, in the practical problems mentioned above, the thickness of the emerging plate is obviously finite. When the material is losing energy, the temperature distribution in the material can be important from the viewpoint of molecular structure within the material, which in turn determines the properties of the material of the plate. This is particularly relevant in continuous casting and plastic extrusion, considered by Fisher (1976). Assuming a constant heat transfer coefficient at the surface, Jaluria and Singh (1983) obtained the temperature distribution in a moving plate and in a circular rod. Chida and Katto (1976) have computed the flow induced by a continuously moving plate of finite thickness, employing boundary layer assumptions, for high values of the Peclet number. They included the conjugate transport resulting from conduction within the plate. Karwe and Jaluria (1986a) have also studied the conjugate problem, using boundary layer equations.

The present work considers the conjugate heat transfer from a continuously moving heated plate. The hot plate is assumed to be at a given uniform temperature at the slot and to move at a uniform speed U_s. Thus, flow is induced in the ambient medium due to viscous effects. The plate also loses energy to the surroundings. Numerical calculations are carried out for two different formulations based upon the nature of governing equations. These are the boundary layer solutions and the solutions of the full elliptic equations. The effects of buoyancy for the vertical and horizontal cases and of heat transfer due to radiation, at the surface of the plate, on the thermal transport are also considered. Effects of various physical parameters like Peclet number Pe, the ratio K_f/K_s of thermal conductivity of the fluid K_f to that of the material K_s, physical properties parameter R, Prandtl number Pr, Grashof number Gr, and radiation parameter Rp are studied. These results are important in the mathematical modeling and the numerical simulation of manufacturing processes such as hot rolling and hot extrusion. The relevance of the results obtained in the design of the system for these processes is also outlined in the paper.

Analysis

Consider the flow situation in Fig. 1(*b*), where a continuously moving plate emerges from the slot of an extrusion die at constant velocity U_s. The temperature of the plate is assumed to be at uniform value T_0 at the slot. The governing equations for fluid flow are first obtained by employing the boundary layer approximations. In addition, the energy equation for the temperature distribution within the moving plate is employed, neglecting the axial conduction.

For a plate moving vertically upward, the equations may be generalized by using the following nondimensionalization, as outlined by Karwe and Jaluria (1986a):

$$X = x/L, \quad Y = (y/L)(\mathrm{Re})^{1/2}, \quad \mathrm{Re} = U_s L/\nu_f, \quad U = u/U_s$$
$$V = (v/U_s)(\mathrm{Re})^{1/2}, \quad \theta = (T - T_\infty)/(T_0 - T_\infty),$$
$$Y_s = y_s/d, \quad \mathrm{Gr} = g\beta(T_0 - T_\infty)L^3/\nu_f^2, \quad \mathrm{Pr} = \nu_f/\alpha_f,$$
$$R = (K_f \rho_f C_f / K_s \rho_s C_s)^{1/2} \tag{1}$$

The dimensionless boundary layer equations, thus obtained, are

For the fluid:

$$\frac{\partial U}{\partial X} + \frac{\partial V}{\partial Y} = 0 \tag{2}$$

$$U\frac{\partial U}{\partial X} + V\frac{\partial U}{\partial Y} = \frac{\partial^2 U}{\partial Y^2} + \frac{\mathrm{Gr}}{\mathrm{Re}^2}\theta \tag{3}$$

$$U\frac{\partial \theta}{\partial X} + V\frac{\partial \theta}{\partial Y} = \frac{1}{\mathrm{Pr}}\frac{\partial^2 \theta}{\partial Y^2} \tag{4}$$

For conduction within the plate:

$$\frac{\partial \theta}{\partial X} = \frac{1}{\mathrm{Pe}}\frac{\partial^2 \theta}{\partial Y_s^2} \tag{5}$$

Nomenclature

C = specific heat of the plate material
$2d$ = plate thickness
g = magnitude of gravitational acceleration
Gr, Gr* = Grashof number
K = thermal conductivity
L = length scale
Pe, Pe* = Peclet number
Pr = Prandtl number
R = physical properties parameter
Re, Re* = Reynolds number
Rp = radiation parameter
t = time
T = temperature
u = velocity component along x direction
U, U^* = nondimensional velocity component in x direction
U_s = velocity of the plate
v = velocity component along y direction
V, V^* = nondimensional velocity component in y direction
$\bar{V}$ = velocity vector
x = coordinate along the length of the plate
X, X^* = nondimensinal coordinate distance parallel to the plate
x_b = conductive upsteam penetration distance
y = coordinate perpendicular to the plate surface in the fluid
Y, Y^* = nondimensional coordinate distance y
y_s = coordinate inside the plate, normal to the plate surface
Y_s, Y_s^* = nondimensional coordinate distance y_s
α = thermal diffusivity $= K/\rho C$
β = coefficient of thermal expansion of the fluid
ϵ = emissivity of the plate surface
θ, θ^* = nondimensional temperature
$\hat{\theta}$ = nondimensional temperature when radiation effects are included
ν = kinematic viscosity of the fluid
ρ = density
σ = Stefan–Boltzmann constant
ψ = stream function
ω = vorticity
∇, ∇_s = gradient operators

Superscript

* = nondimensional quantity in the case of the elliptic formulation

Subscripts

∞ = ambient quantity
f = fluid
s = plate material
0 = at $x = 0$, or at $x = -x_b$

where the Prandtl number Pr and the Peclet number Pe are

$$\mathrm{Pr} = \nu_f/\alpha_f \qquad \mathrm{Pe} = U_s d^2/\alpha_s L \tag{6}$$

Note that the Peclet number Pe is defined in terms of the properties of the moving solid, instead of the fluid as is often the case in convective transport.

The symbol L stands for an arbitrarily chosen length scale in the boundary layer formulation. Since there is no representative length scale along the length of the plate any arbitrarily chosen value of L may be employed for nondimensionalization and for yielding results in the entire flow field. This is analogous to the self-similar circumstance for flow over a flat plate. The various boundary conditions on u, v, and T that arise from physical considerations are: the no-slip condition at the surface of the plate and at the wall adjacent to the die, zero flow in the ambient medium far from the surface, temperature and heat flux continuity at the plate surface, and symmetry about the x axis (Karwe and Jaluria, 1986a). The symmetry condition is valid when the plate is moving vertically upward. These boundary conditions, when nondimensionalized, become

$$\begin{aligned}
&\text{for } X>0, \quad Y_s=1 \text{ or } Y=0: \quad U=1, \quad V=0, \text{ and} \\
&\qquad \frac{\partial\theta}{\partial Y_s} = R\cdot(\mathrm{Pe}/\mathrm{Pr})^{1/2}\,\frac{\partial\theta}{\partial Y} \\
&\text{for } Y>0, \quad X=0: \quad U=0, \quad V=0, \quad \theta=0 \\
&\text{for } X>0, \quad Y\to\infty: \quad U\to 0, \quad \theta\to 0 \\
&\text{for } X=0, \quad 0\le Y_s\le 1: \quad \theta=1.0 \\
&\text{for } X>0, \quad Y_s=0: \quad \partial\theta/\partial Y_s=0
\end{aligned} \tag{7}$$

When radiation loss from the surface was also taken into account, the temperature was nondimensionalized by T_∞. Because of the appearance of the T^4 terms in radiation, the nondimensionalization of equation (1) is inconvenient (Jaluria, 1982), and the nondimensional temperature is denoted by $\hat{\theta} = T/T_\infty$ when radiative loss is included. Therefore the boundary condition of $T = T_0$ at $x = 0$ gives an additional parameter $\hat{\theta}_0 = T_0/T_\infty$, which is obviously taken as greater than unity. Assuming the endwall and the environment to be black at T_∞, the boundary condition at the surface of the plate then becomes

$$\begin{aligned}
&\text{for } X>0, \quad Y_s=1 \text{ or } Y=0: \quad U=1, \quad V=0, \text{ and} \\
&\qquad \frac{\partial\hat{\theta}}{\partial Y_s} = R\cdot(\mathrm{Pe}/\mathrm{Pr})^{1/2}\,\frac{\partial\hat{\theta}}{\partial Y} + Rp(\hat{\theta}^4-1)
\end{aligned} \tag{8}$$

where Rp is the radiation parameter defined as $Rp = \epsilon\sigma d\,T_\infty^3/K_s$. Since the governing equations are parabolic in nature, boundary conditions are not needed downstream. Also, the dimensionless temperature $\hat{\theta} = T/T_\infty$ is greater than 1.0 throughout the region, whereas θ varies from 0 to 1.0, according to the definitions employed for the two formulations.

When the axial conduction within the plate is to be taken into account, for instance at small values of the Peclet number and near the slot, the full governing equations, which are elliptic in nature, must be employed. The full governing equations, including the transient and buoyancy terms, are:

For the fluid:

$$\nabla\cdot\bar{V} = 0 \tag{9}$$

$$\frac{\partial\bar{V}}{\partial t} + \bar{V}\cdot\nabla\bar{V} = -\frac{\nabla P}{\rho_f} + \nu_f\nabla^2\bar{V} + \bar{g}\beta(T-T_\infty) \tag{10}$$

$$\frac{\partial T}{\partial t} + \bar{V}\cdot\nabla T = \alpha_f\nabla^2 T \tag{11}$$

For conduction within the plate:

$$\rho_s C_s\frac{\partial T}{\partial t} + \rho_s C_s U_s\frac{\partial T}{\partial x} = K_s\nabla_s^2 T \tag{12}$$

The various symbols that appear in equations (1)–(12) are given in the Nomenclature.

The pressure term in equation (10) is eliminated by transforming the equation into the vorticity equation by taking a curl of this equation. The vorticity ω and stream function ψ are defined as

$$u = \frac{\partial\psi}{\partial y}, \quad v = -\frac{\partial\psi}{\partial x}, \quad \text{and} \quad \omega = \frac{\partial v}{\partial x} - \frac{\partial u}{\partial y} \tag{13}$$

Equations (10)–(12) are nondimensionalized as

$$\begin{gathered}
X^* = x/d, \quad Y^* = y/d, \quad Y_s^* = y_s/d, \quad U^* = u/U_s, \quad V^* = v/U_s \\
\theta^* = (T-T_\infty)/(T_0-T_\infty), \quad \psi^* = \psi/U_s d, \quad \omega^* = \omega d/U_s, \\
t^* = tU_s/d, \quad \mathrm{Re}^* = U_s d/\nu_f, \quad \mathrm{Pe}^* = U_s d/\alpha_s, \\
\mathrm{Gr}^* = g\beta(T_0-T_\infty)d^3/\nu_f^2
\end{gathered} \tag{14}$$

where the asterisk indicates nondimensional variables for the elliptic formulation.

The dimensionless equations, in the vorticity-stream function formulation, for a plate that is moving vertically upward, become

$$\frac{\partial\omega^*}{\partial t^*} + \bar{V}^*\cdot\nabla^*\omega^* = \frac{1}{\mathrm{Re}^*}(\nabla^{*2}\omega^*) - \frac{\mathrm{Gr}^*}{\mathrm{Re}^{*2}}\left(\frac{\partial\theta^*}{\partial Y^*}\right) \tag{15}$$

$$\nabla^{*2}\psi^* = -\omega^* \tag{16}$$

$$\frac{\partial\theta^*}{\partial t^*} + \bar{V}^*\cdot\nabla^*\theta^* = \frac{1}{\mathrm{Re}^*\mathrm{Pr}}(\nabla^{*2}\theta^*) \tag{17}$$

For the case of a plate moving horizontally, equation (15) is changed to

$$\frac{\partial\omega^*}{\partial t^*} + \bar{V}^*\cdot\nabla^*\omega^* = \frac{1}{\mathrm{Re}^*}(\nabla^{*2}\omega^*) + \frac{\mathrm{Gr}^*}{\mathrm{Re}^{*2}}\left(\frac{\partial\theta^*}{\partial X^*}\right) \tag{18}$$

For conduction within the plate, the energy equation is

$$\frac{\partial\theta^*}{\partial t^*} + \frac{\partial\theta^*}{\partial X^*} = \frac{1}{\mathrm{Pe}^*}(\nabla_s^{*2}\theta^*) \tag{19}$$

In the case of the elliptic formulation, a boundary condition of uniform temperature, $\theta^* = 1.0$ at $X^* = 0$, may not be an accurate representation of practical circumstances, especially at small values of the Peclet number Pe*. To account for the penetration of conduction effects upstream, along the negative x direction, the boundary condition of uniform temperature was applied at a distance x_b from the origin, along the negative x axis. Within this region, no energy loss was assumed to occur at the plate surface. The corresponding boundary conditions are given as

$$\begin{aligned}
&\text{for } -X_b^*\le X^*\le 0, \quad Y_s^*=1: \quad \frac{\partial\theta^*}{\partial Y_s^*}=0 \\
&\text{for } X^*=-X_b^*, \quad 0\le Y_s^*\le 1: \quad \theta^*=1.0
\end{aligned} \tag{20}$$

The distance x_b is not known and is treated as a numerical parameter. The value of x_b is increased until the numerical results downstream are largely unaffected by a further increase, as discussed later.

The boundary conditions in terms of ω^* and ψ^* were obtained by employing the appropriate transformation (Roache, 1976) of the physical boundary conditions mentioned before and shown in Fig. 2. Note that additional boundary conditions, downstream in x, are needed. This is achieved by specifying the conditions at a numerically determined interface between the two regions as shown in Fig. 2 and discussed in the next section. When the elliptic equations were solved in conjunction with the transient parabolic boundary layer equation, a uniform length scale d was chosen in both the domains. The results from the parabolic formulation can easily be transformed into the dimensionless variables of the elliptic formulation by employing equations (1) and (14) for the given set of physical variables.

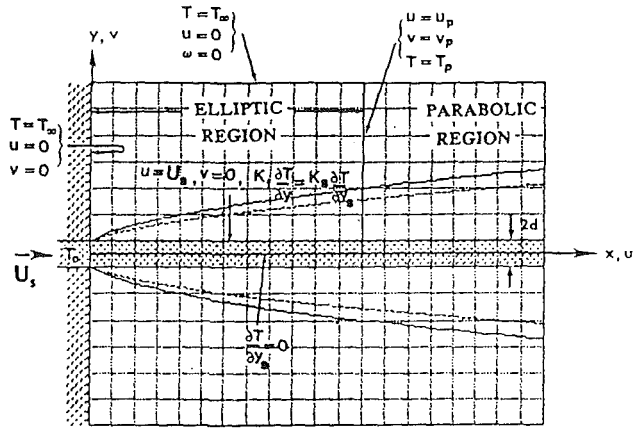

Fig. 2 Computational domain with various boundary conditions

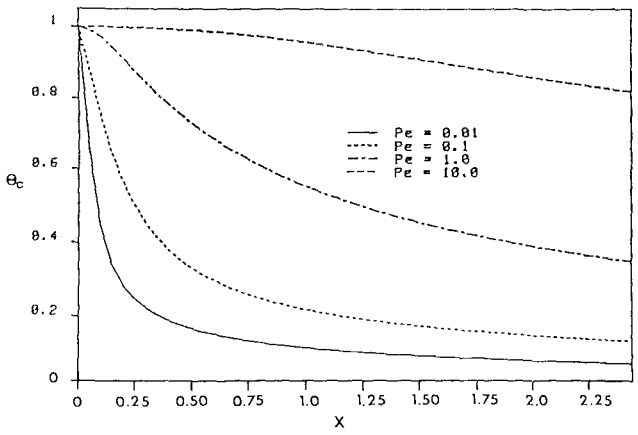

Fig. 3 Centerline temperature variation along X from the parabolic formulation, for glass-water, R = 1.092, Pr = 7.0, Gr = 0.0, at different values of Pe

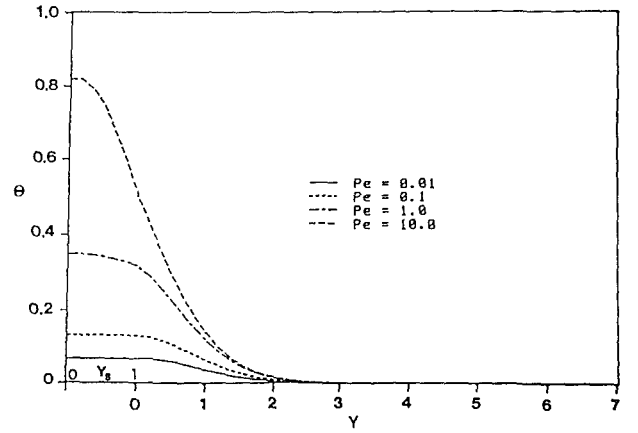

Fig. 4 Transverse temperature variation along Y from the parabolic formulation, at X = 2.45, for glass-water, R = 1.092, Pr = 7.0, Gr = 0.0, at different values of Pe

In the horizontal case, the problem is not symmetric about the x axis because the buoyancy forces are away from the plate on the upper side and toward the plate on the lower surface. Nevertheless, for the sake of limiting the complexity, we have considered only the upper half of the domain and applied the condition of symmetry at the centerline of the plate. This is appropriate when dealing with a plate that has thickness d and the bottom surface is insulated or when the buoyancy effects are small. For an arbitrary horizontally moving plate, the upper and lower regions must both be solved for. Also, it would be necessary to solve for the pressure field in the parabolic domain as well, when the buoyancy forces are significant (Jaluria, 1980). However, in our case, the elliptic domain was extended far enough so that the temperature of the plate becomes sufficiently small and forced convection effects dominate in the parabolic region. Thus, buoyancy effects are small far from the entrance region, $X^* = 0$, and the pressure may be taken as uniform across the horizontal boundary layer forced flow. The discussion on the numerical procedure is given in the next section.

Numerical Solution

In all cases, the numerical calculations were carried out in the upper half of the computational domain shown in Fig. 2.

In the case of the boundary layer formulation, equations (2)–(5) were solved using an implicit method similar to the Crank-Nicolson finite difference method (Carnahan et al., 1969). The equations were solved by marching along the x direction and solving for the flow quantities U, V, and θ implicitly at each X. The numerical scheme was tested by applying it to the isothermal case, the results of which could be compared with the similarity solution; see Karwe and Jaluria (1986a). The agreement between the two was excellent far away from the slot.

In the case of the elliptic formulation, the transient vorticity equation (15) was solved along with the energy equations (17) and (19), for the flow and the plate, respectively, using the Alternate Direction Implicit (ADI) method (Jaluria and Torrance, 1986). Poisson's equation (16), the equation for the stream function, was solved using the Successive Over-Relaxation (SOR) method; see Jaluria and Torrance (1986). For the first step in the numerical procedure, the calculations in the elliptic region were started using the ambient conditions at the interface between the two regions, as shown in Fig. 2. Using the values of U^*, V^*, and θ^* obtained at one grid location away from the interface, inside the elliptic region, the values of U^*, V^*, and θ^* at the interface were then updated. The updated values were obtained by solving the transient boundary layer equations, marching along the x direction. Time marching is continued, with numerical solution being obtained for the two regions, elliptic and parabolic, until steady state is attained. All calculations were done for $X_b^* = 4.5$. A convergence criterion of the order of 10^{-3} was applied to the temperature θ^* and U^* velocity gradients in time, to stop the computation. The calculations were stopped when $[\max\{\partial\theta^*/\partial t^*\}$ and $\max\{\partial U^*/\partial t^*\}] \leq 10^{-3}$. The location of the interface between the two regions was varied to ensure a negligible dependence of the results on the chosen location. Similarly, other numerical parameters like convergence criterion, grid size, etc., were also varied. For further details on the numerical procedure, see Karwe and Jaluria (1986b).

Results and Discussion

Numerical solutions to equations (2)–(5) were obtained for various values of Pe, Pr, R, Re, Rp, and K_f/K_s, ignoring the natural convection effects, i.e., Gr = 0. In the case of the parabolic formulation, conduction in the X direction is also neglected. The value of the temperature was specified as T_0 at $X = 0$. Figure 3 shows the computed centerline temperature variation with X, for the case when the plate material is glass and the ambient medium is water, for which $R = 1.092$. The corresponding transverse temperature distributions within the plate and the fluid are shown in Fig. 4. It may be seen that, given the value of Pe and given the fluid, the axial temperature drops gradually with increasing values of Pe. Thus, the downstream penetration of thermal effects is large. From Fig. 3, it is also clear that the temperature profiles are very steep

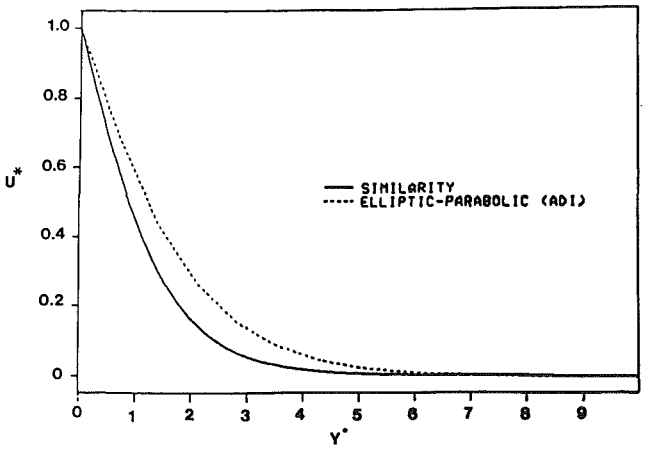

Fig. 5(*a*) Comparison between the results from the boundary layer similarity formulation and those from the elliptic formulation, in terms of the variation of U^* along Y^* at $X^* = 2.5$

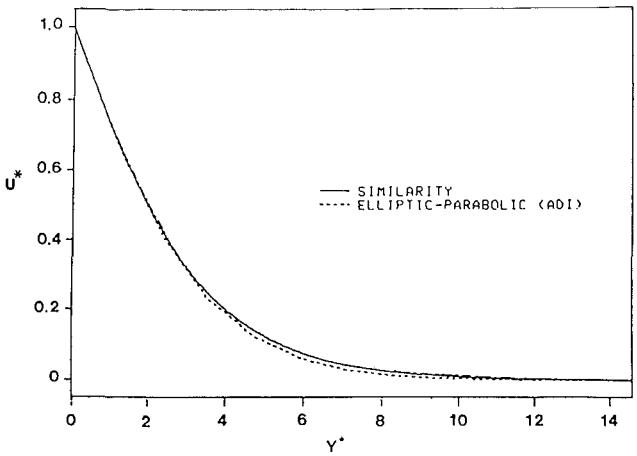

Fig. 5(*b*) Comparison between the results from the boundary layer similarity formulation and those from the elliptic formulation, in terms of the variation of U^* along Y^* at $X^* = 12.25$

near the slot, especially at very small values of Pe. Therefore, the assumption of negligible conduction along the plate length is not valid near the slot. From Fig. 4, it is seen that temperature profiles in the y direction are more or less uniform within the plate for smaller values of Pe. Therefore, the governing equation for the plate can be simplified by employing the assumption of uniform temperature across the plate.

The information on the temperature distribution, obtained for a given set of parameters, is useful for the design of the system needed for the particular manufacturing process. For example, in the rolling process, which uses multiple stations of rollers to obtain successive reduction in the thickness of the material, the distance between two stations can be adjusted to achieve the desired temperature distribution. This in turn will determine the total length required in the system. Similar considerations arise in continuous casting, wire drawing, and extrusion.

In the case of the elliptic formulation, solutions to equations (15)–(19) were obtained for various values of the governing parameters Re*, Pe*, Pr, Rp, K_f/K_s, and $\mathrm{Gr}^*/\mathrm{Re}^{*2}$. In addition, the effects of buoyancy and radiative loss at the plate surface were also considered. Figure 5(*a*) and 5(*b*) show the comparison between the results for the boundary layer and the elliptic formulations in terms of the transverse variation of U^*, along Y^*, at $X^* = 2.5$ and 12.25, respectively. The variation of U^* in the case of the boundary layer was obtained from the similarity solution of Karwe and Jaluria (1986a). It is seen that the elliptic effects are important near the slot, as expected. However, farther downstream, the flow approaches the characteristics of the boundary layer. Therefore, the boundary layer approximations are not valid near the slot of the die, though they are satisfactory far downstream. Typical streamlines and isotherms for aluminum and air are shown in Fig. 6. The boundary layer thickness is seen to grow along the direction of the motion. Also, it may be seen from the isotherms that strong temperature gradients exist near the slot. This implies strong thermal stresses and structural changes in this region.

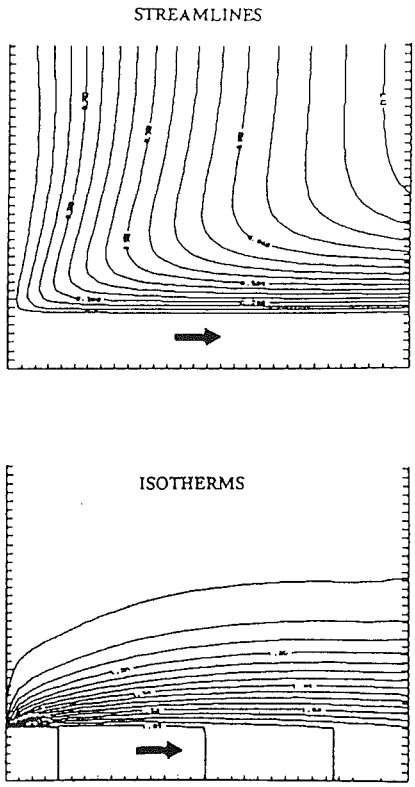

Fig. 6 Streamlines and isotherms for aluminum and air, Pe* = 0.05, Pr = 0.7, and K_f/K_s = 0.000127, using the elliptic formulation, at Re* = 20.0, Gr* = 0.0

Transverse and axial temperature distributions, with and without radiation boundary condition at the plate surface, are shown in Figs. 7 and 8, respectively. In Figs. 7 and 8, the radiation parameter $Rp = 9.2 \times 10^{-5}$ when $\epsilon = 0.5$ and $Rp = 0$ when $\epsilon = 0$. It is seen that radiation affects the temperature decay very substantially. The radiation losses are important when dealing with processes involving high temperatures, such as hot rolling of steel billets; see Altan et al. (1979). For accelerating the cooling, in order to reduce the length of the system, the surrounding may be water cooled to increase radiative loss, as is usually done in continuous casting. It must be noted that the dimensionless temperature $\hat{\theta} = T/T_\infty$ is taken as 1.75 at $x = 0$ so that the value of $\hat{\theta}$ ranges from 1.0 to 1.75 in these figures.

The parameter that determines the importance of buoyancy forces is $\mathrm{Gr}^*/\mathrm{Re}^{*2}$. In addition, the orientation of the plate motion with respect to the gravity determines whether the buoyancy aids or opposes the induced flow. Here, the two cases discussed are: (I) plate moving vertically upward (buoyancy aligned with plate motion), and (II) plate moving horizontally. As mentioned earlier, in case II, only the upper surface of the plate was considered.

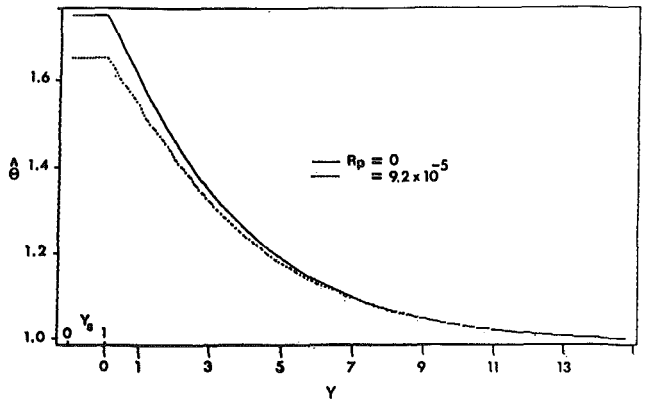

Fig. 7 Transverse temperature variation at $X^* = 2.45$ with and without radiation loss: radiation parameter $Rp = 9.2 \times 10^{-5}$, Pr = 0.7, Gr = 0.0, Pe = 0.5, $R = 3.35 \times 10^{-4}$, and $T_0/T_\infty = 1.75$ ($Rp = 0$ when $\epsilon = 0$), employing the parabolic formulation

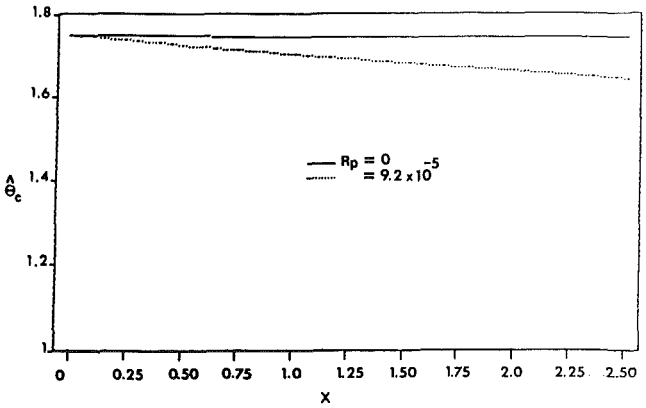

Fig. 8 Axial temperature variation with and without radiation loss: radiation parameter $Rp = 9.2 \times 10^{-5}$, Pr = 0.7, Gr = 0.0, Pe = 0.5, $R = 3.35 \times 10^{-4}$, and $T_0/T_\infty = 1.75$, employing the parabolic formulation

In both the cases mentioned above, buoyancy aids the induced flow. However, in case II, buoyancy forces are perpendicular to the plate motion. Figure 9 shows the distribution of the x component of the velocity at various values of Gr^*/Re^{*2}, for case I. Notice that the velocity level near the plate is significantly affected by buoyancy, thus enhancing the heat transfer from the plate to the environment. Therefore, the plate loses energy faster. This is shown in Fig. 10 in terms of the axial temperature variation under the same condition.

Figure 11 compares the two cases mentioned above in terms of U^* velocities at $X^* = 15.0$. It may be seen that when the plate is horizontal, the effect of buoyancy is small on the overall transport process, as compared to the case when the buoyancy is aligned with the flow. Most of the relevant manufacturing processes considered here are horizontal because of the larger cooling lengths required. However, continuous casting is often carried out vertically. These results indicate the effect of mixed convection and the importance of buoyancy effects for vertical circumstances and at large temperature levels. Again, as mentioned earlier, temperature symmetry is assumed at the x axis, i.e., $\partial\theta^*/\partial Y_s^* = 0$ at $Y_s^* = 0$. This is done to restrict the computation to only the upper region. This assumption is applicable if the lower surface is insulated or if the buoyancy effects are small. Otherwise, the two regions on either side of the plate are coupled and must be computed in conjunction.

In Figs. 9–11 radiation losses are not taken into account, i.e., $Rp = 0$. It should be pointed out that in the horizontal

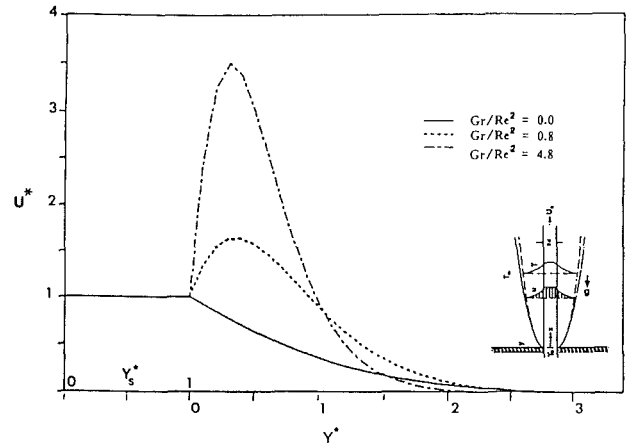

Fig. 9 Variation of U^* along Y^* at $X^* = 15.0$, with Pe* = 0.05, Pr = 7.0, Re* = 25.0, and $K_f/K_s = 0.0128$, for various values of the mixed convection parameter Gr^*/Re^{*2}: Case I—plate aligned with gravity, moving vertically upward, using the elliptic formulation

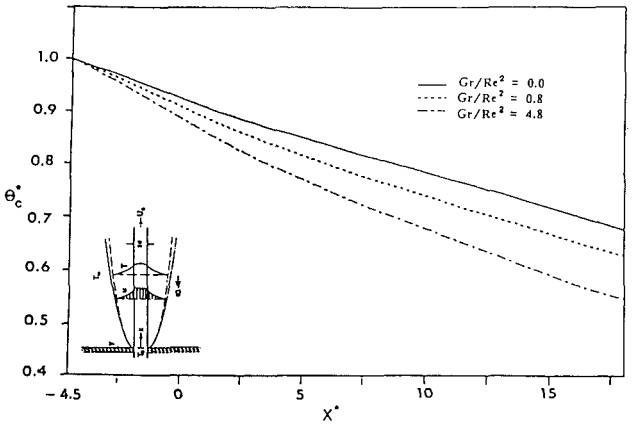

Fig. 10 Axial temperature variation at Pe* = 0.05, Pr = 7.0, Re* = 25.0, and $K_f/K_s = 0.0128$, for various values of Gr^*/Re^{*2} (Case I), using the elliptic formulation

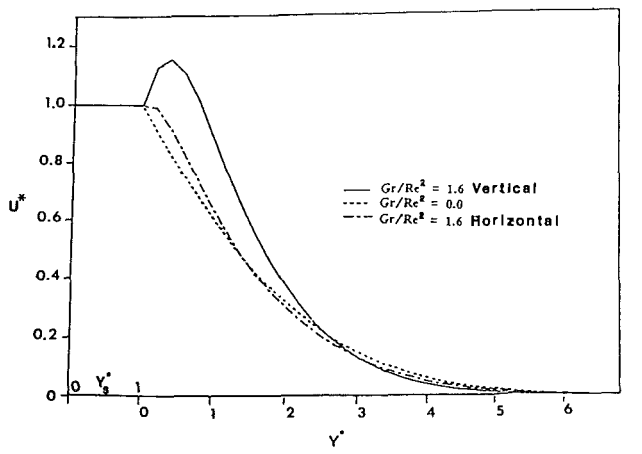

Fig. 11 Comparison between the two mixed convection cases, vertical and horizontal, in terms of the variation of U^* along Y^* at $X^* = 15.0$ for Pe* = 0.05, Pr = 7.0, Re* = 25.0, $K_f/K_s = 0.0128$. Case I—plate aligned with gravity, moving vertically upward. Case II—plate moving horizontally, with only the lower surface taken as insulated and employing the elliptic formulation.

case, no flow separation was assumed. However, due to the nature of buoyancy forces, flow separation at some distance downstream cannot be ruled out; see Jaluria (1980). In that

case further experimental inputs are needed for an appropriate analytical and numerical model.

Conclusions

An analysis and numerical simulation of heat transfer from a continuous moving plate in manufacturing processes such as hot rolling and extrusion has been carried out. The numerical solutions for the induced flow field and temperature field, after the material emerges from the die or the rollers, have been obtained. It is found that at low values of the Peclet number Pe, temperature uniformity across the moving material can be assumed. This is particularly valid for the extrusion of metals such as copper and aluminum, which are highly conducting. For plastics, the temperature variation across the plate must generally be considered. The temperature within the material is mainly governed by the ratio K_f/K_s of the conductivity of the fluid to that of the solid, or by the physical properties parameter R. The buoyancy effects on the axial temperature variation are more important when the plate moves vertically, i.e., aligned with gravity, than when it is horizontal. This can be utilized further in the design of the manufacturing system.

The numerical results obtained here indicate the temperature decay in the material as it moves away from the die. The resulting heat transfer and the characteristics of the flow are also determined. These results will be valuable in the evaluation of the importance of buoyancy and radiative effects in the thermal transport and in determining the system length needed for attaining a given temperature level. Also, if a limitation on the total distance is given, the results can be employed to determine if any additional cooling arrangement is needed or if the choice of the fluid, say water, will be adequate. Several such questions arise in the design of practical systems and this paper presents numerical results that can be used in achieving the optimized design for the relevant processes.

Acknowledgments

The authors acknowledge the partial financial support provided by the National Science Foundation, under Grant CBT-84-15364, and by the NJ Center of Advanced Food Technology for this work.

References

Altan, T., Oh., S., and Gegel, H., 1979, *Metal Forming Fundamentals and Applications*, American Society of Metals, Metals Park, OH.

Carnahan, B., Luther, H. A., and Wilkes, J. O., 1969, *Applied Numerical Methods*, Wiley, New York.

Chida, K., and Katto, Y., 1976, "Conjugate Heat Transfer of Continuously Moving Surfaces," *Int. J. Heat and Mass Transfer*, Vol. 19, pp. 461–470.

Fisher, E. G., 1976, *Extrusion of Plastics*, Wiley, New York.

Griffin, J. F., and Thorne, J. L., 1967, "On the Thermal Boundary Layer Growth on Continuous Moving Belts," *AIChE Journal*, Vol. 13, No. 6, pp. 1210–1211.

Jaluria, Y., 1982, "Mixed Convection in a Wall Plume," *Computers and Fluids*, Vol. 10, pp. 95–104.

Jaluria, Y., and Singh, A. P., 1983, "Temperature Distribution in a Moving Material Subjected to Surface Energy Transfer," *Comp. Meth. Appl. Mech. Eng.*, Vol. 41, pp. 145–157.

Jaluria, Y., and Torrance, K. E., 1986, *Computational Heat Transfer*, Hemisphere, New York, to appear.

Jaluria, Y., 1980, *Natural Convection Heat and Mass Transfer*, Pergamon Press, New York.

Karwe, M. V., and Jaluria, Y., 1986a, "Thermal Transport From Heated Moving Surfaces," ASME JOURNAL OF HEAT TRANSFER, Vol. 108, No. 4, pp. 728–733.

Karwe, M. V., and Jaluria, Y., 1986b, "Numerical Simulation of the Conjugate Heat Transfer Process From a Heated Moving Surface," *Proc. Int. Conf. on Comp. Mech.*, Tokyo, Japan, pp. VIII19–VIII24.

Roache, P. J., 1976, *Computational Fluid Dynamics*, Hermosa Publishers, New Mexico.

Sakiadis, B. C., 1961a, "Boundary Layer Behavior on Continuous Solid Surfaces: I. Boundary Layer Equations for Two-Dimensional and Axisymmetric Flow," *AIChE Journal*, Vol. 7, No. 1, pp. 26–28.

Sakiadis, B. C., 1961b, "Boundary Layer Behavior on Continuous Solid Surfaces: II. The Boundary Layer on Continuous Flat Surface," *AIChE Journal*, Vol. 7, No. 2, pp. 221–225.

Tadmor, Z., and Klein, I., 1970, *Engineering Principles of Plasticating Extrusion*, Polymer Science and Engineering Series, Van Nostrand Reinhold, New York.

Tsou, F. K., Sparrow, E. M., and Goldstein, R. J., 1967, "Flow and Heat Transfer in the Boundary Layer on a Continuous Moving Surface," *International Journal of Heat and Mass Transfer*, Vol. 10, pp. 219–235.

The Influence of Secondary Convection on Axial Segregation in a Floating Zone

J. Y. Murthy
Department of Mechanical and Aerospace Engineering,
Arizona State University,
Tempe, AZ 85287

The redistribution of impurity due to secondary convection in a cylindrical floating zone is studied using a control volume-based numerical technique. The flow is induced by differential rotation of the feed rod and crystal. Attention is focused on the transient stage of segregation. It is found that the transient length increases with the strength of secondary convection. A maximum in radial segregation is found to occur when secondary convection creates radial gradients but is not strong enough to homogenize them. The influence of cellular structure on the transient length is also examined.

Introduction

The floating zone process is often employed in the growth of high-quality semiconductor materials and in the refinement of metal alloys. In this process, a ring heater traverses the length of the rod to be purified and melts a cylindrical zone of finite length, which travels with the heater. Repartitioning of the impurity contained in the feed rod is achieved due to the difference in the equilibrium concentration of impurity in the melt and in the solid (Pfann, 1966).

Consider a floating zone composed of material for which the equilibrium concentration of impurity (or dopant) is greater in the melt than in the solid, a case usually encountered in the processing of semiconductor materials. At the melting interface, the impurity in the solid is absorbed completely into the melt, since the impurity is more soluble in the latter. At the freezing interface, however, the lower solubility of the impurity in the solid implies that the growing crystal can absorb only a fraction of impurity present in the melt; consequently, the solute accumulates at the freezing interface, increasing in concentration as the rod is traversed. An observer moving with the freezing interface would register this accumulation as an increase in impurity concentration with time. A "steady state" may be reached if the rod is long enough, so that the impurity absorbed by the melt at the melting interface is exactly balanced by the loss of impurity to the crystal at the freezing interface. Thus, zone refinement can take place only as long as "unsteady state" prevails; no net refinement of the feed rod is possible once balance is achieved.

Previous studies of the process have either concentrated almost exclusively on convectionless melts, or assumed a constant boundary layer thickness for mass transfer at the freezing interface (Pfann, 1966; Smith et al., 1955; Tiller, 1953; Wagner, 1954; Favier, 1981). The former assumption neglects radial variations induced by body/surface forces; the latter neglects the fluid flow problem either by leaving the boundary layer thickness to be experimentally determined, or in the tradition of the popular Burton-Prim-Slichter model (Burton ton et al., 1953), determines it from the flow over an infinite rotating disk. In the absence of radial gradients set up by convection, segregation is purely axial, and may be analyzed using an unsteady one-dimensional formulation, as in Tiller et al. (1953). This treatment is also expected to be valid if secondary mixing is vigorous enough to obliterate radial gradients, but cannot predict the large radial segregation noted experimentally (Keller, 1976; Jurisch et al., 1982). Many computations of flow fields set up by various driving forces in this geometry are available in the literature. The flow field induced by differential end rotation in the low Reynolds number limit has been studied by Harriott and Brown (1983) and an extension to moderate Reynolds numbers has been made using a finite element simulation (Harriott and Brown, 1984a). Numerical simulations using a control volume technique in the same geometry have been performed by Murthy (1987). The flow fields computed by Harriott and Brown (1983) have been used for the calculation of steady solute fields in Harriott and Brown (1984b); solute distributions have also been presented in Murthy (1987) and those induced by Marangoni convection in Chang and Wilcox (1976). Radial segregation of over 100 percent of the average feed rod concentration has been reported by Harriott and Brown (1984b); an inclusion of meridional flow effects appears essential if analysis is to agree with experiment. However, since steady state is assumed at the outset, these studies are incapable of predicting either radial or axial segregation during refinement.

A closely related and much analyzed problem is that of the unidirectional solidification of a finite ampoule of molten liquid, such as that employed in Bridgeman growth. Here, the finite length of the liquid ampoule makes for an inherently unsteady situation, as the process of solidification progressively enriches the molten charge. A quasi-steady finite element analysis of this system is available in Chang and Brown (1983). Transient unidirectional solidification of an aqueous NaCl solution has been studied by Wollhover et al. (1985). Here, the moving boundary problem is solved for the case when solute is rejected totally into the liquid ($k=0$); however, transport is considered to be by diffusion alone. No solution of the complete unsteady problem in the presence of fluid flow appears available.

This paper presents a numerial study of the refinement of a dilute binary alloy before the achievement of steady state. Meridional circulation is set up by the differential rotation of feed rod and crystal, although the results obtained give qualitative insight into other patterns of cellular convection as well. The influence on both radial and axial segregation is examined.

Formulation

The physical configuration is shown in Fig. 1. The floating zone is idealized as a circular cylinder of length L held between two rotating disks of radius d. The free surface may be approximated as cylindrical if the capillary number ($\mu\Omega_f d/\sigma$) is low, a situation typical of semiconductor applications. For the present study, the effects of natural and Marangoni convec-

Contributed by the Heat Transfer Division for publication in the JOURNAL OF HEAT TRANSFER. Manuscript received by the Heat Transfer Division September 1, 1987. Keywords: Materials Processing and Manufacturing Processes, Phase-Change Phenomena.

tion are neglected in order to focus on the mass transfer process; strictly speaking, the former assumption is valid for microgravity situations, and the latter for the relatively high rates of rotation where thermocapillary convection is confined to the surface by the stronger flows due to rotation (Kobayashi, 1984). The dimensionless equations governing the axisymmetric, incompressible, constant property flow of a Newtonian fluid in the zone may be written in the frame of reference of the moving zone as

$$\frac{1}{R}\frac{\partial}{\partial R}(RV_r)+\frac{\partial}{\partial Z}(V_z)=0$$

$$V\cdot\nabla V_r-\mathrm{Re}^2\frac{V_\theta^2}{R}=-\frac{\partial P}{\partial R}+\nabla^2 V_r-\frac{V_r}{R^2}$$

$$V\cdot\nabla V_\theta+\frac{V_r V_\theta}{R}=\nabla^2 V_\theta-\frac{V_\theta}{R^2} \qquad (1)$$

$$V\cdot\nabla V_z=-\frac{\partial P}{\partial Z}+\nabla^2 V_z$$

$$\frac{\partial C}{\partial \tau}+\mathrm{Sc}V\cdot\nabla C=\nabla^2 C$$

with boundary conditions

$$V_r=V_\theta=\frac{\partial V_z}{\partial R}=\frac{\partial C}{\partial R}=0 \quad (R=0,\ 0\le Z\le A)$$

$$V_r=\frac{\partial}{\partial R}\left(\frac{V_\theta}{R}\right)=\frac{\partial V_z}{\partial R}=0,\quad \frac{\partial C}{\partial R}=0 \quad (R=1,\ 0\le Z\le A) \qquad (2)$$

$$V_r=V_z=0,\ V_\theta=SR,\quad \frac{\partial C}{\partial Z}=\mathrm{Pe}[C-1] \quad (0\le R\le 1,\ Z=0)$$

$$V_r=V_z=0,\ V_\theta=R,\quad \frac{\partial C}{\partial Z}=\mathrm{Pe}[1-k]C \quad (0\le R\le 1,\ Z=A)$$

As in Tiller et al. (1953), the initial condition for impurity transport is

$$C(R, Z, 0)=1 \qquad (3)$$

In the computation of the flow field, the velocity of zone traverse is considered negligibly small with respect to the typical meridional velocities in the melt. This assumption is valid at all but the lowest rotational Reynolds numbers; in this limit, the uniform axial flow due to pure zone translation is linearly superimposed on the velocities due to rotation alone. The computation of the velocity field employs the variable (V_θ/R) rather than V_θ, since this quantity is found to be virtually constant in the core of the rotating fluid for high rates of rotation. It has been suggested by Langlois (1985) that (RV_θ) be used instead. This practice eliminates the $(V_r V_\theta/R)$ term in the azimuthal momentum equation, and thus alleviates numerical difficulties caused by a loss of diagonal dominance when V_r is negative. In this study, no such difficulties were encountered; under relaxation of the (V_θ/R) equation always yielded stable results. Computations with (RV_θ) and (V_θ/R) as dependent variables yielded virtually identical results for the grids employed here. The unsteady term is included only in the equation for impurity transport, and is neglected in the momentum equations. The implications and limitations of this assumption will be discussed in a later section. Both solid and melt have been assumed to have the same density, and diffusion of impurity in the solid has been neglected. The parameters governing impurity transport are the rotational Reynolds number Re, the aspect ratio A, the rotation ratio S, the Peclet number of zone traverse Pe, the Schmidt number Sc, and the equilibrium segregation coefficient k. This latter is the ratio of the equilibrium impurity concentration in the solid to that in the melt. Clearly, $kC(R, A, \tau)=C_s(R, X)$. The extent of radial segregation of impurity in the crystal is quantified by a dimensionless radial segregation given by

$$\gamma=\max[C_s(R, X)]-\min[C_s(R, X)] \qquad 0\le R\le 1 \qquad (4)$$

Steady state is considered to have been reached when $\bar{C}_s(X)=0.99$. The aspect ratio was assumed to be unity in all cases.

Numerical Scheme

The equations of transport are solved using the control volume scheme outlined in Patankar (1980), in conjunction

Nomenclature

A = aspect ratio $= L/d$
c_0 = solute concentration in feed rod
C = dimensionless solute concentration in melt, scaled to c_0
C_s = solute concentration in crystal scaled to c_0
$\bar{C}_s$ = radially averaged solute concentration in crystal at any axial location
d = radius of disk
D = diffusion coefficient for solute
L = length of zone
L_c = length scale associated with cell
P = dimensionless pressure, scaled to $\rho\nu^2/d^2$
Pe = Peclet number $= V_{\mathrm{zone}}d/D$
Pe_c = Peclet number associated with cell $= U_c L_c/D$
Pe_{cr} = Peclet number for maximum radial segregation
Pr = Prandtl number
r = radial coordinate, Fig. 1
R = dimensionless radial coordinate $= r/d$
Re = rotational Reynolds number $= \Omega_f d^2/\nu$
S = rotation ratio $= \Omega_s/\Omega_f$
Sc = Schmidt number $= \nu/D$
U_c = velocity scale associated with cell
V = velocity vector with components V_r, V_θ, V_z
V_r = dimensionless radial velocity, scaled to ν/d
V_θ = dimensionless radial velocity, scaled to $d\Omega_f$
V_z = dimensionless axial velocity, scaled to ν/d
V_{zone} = velocity of zone traverse
X = length traversed by zone in the laboratory frame $= \mathrm{Pe}\tau$
z = axial coordinate, Fig. 1
Z = dimensionless axial coordinate $= z/d$
γ = dimensionless radial segregation of solute (equation (4))
∇ = dimensionless gradient operator
∇^2 = dimensionless Laplacian operator
θ = azimuthal direction
μ = dynamic viscosity
ν = kinematic viscosity
σ = surface tension
τ = dimensionless time, scaled to (d^2/D)
ψ = stream function
$\psi_{\max}$ = absolute maximum value of ψ, associated with counterclockwise vortex
$\psi_{\min}$ = absolute minimum value of ψ, associated with clockwise vortex
Ω_f = angular velocity of disk at $Z=A$
Ω_s = angular velocity of disk at $Z=0$

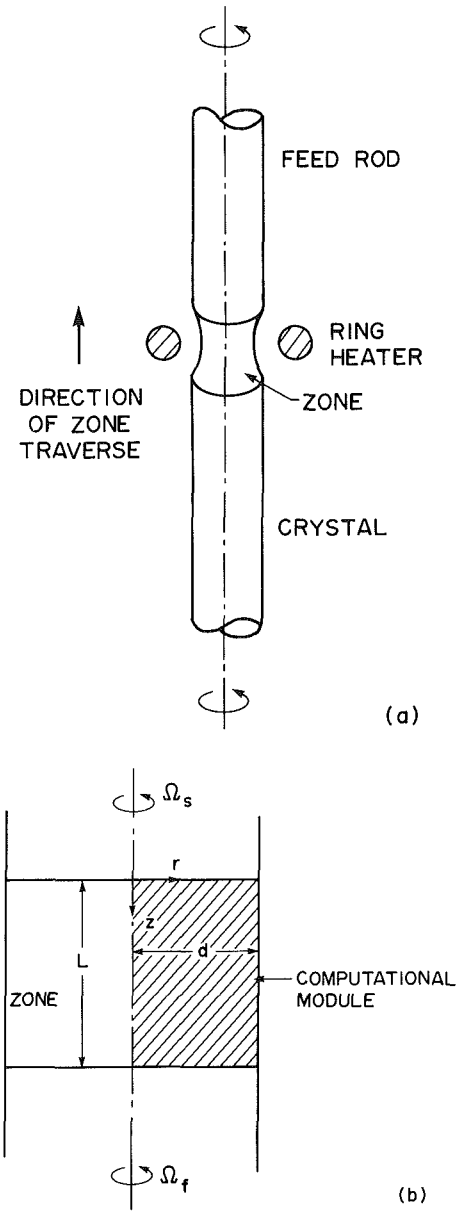

Fig. 1 The physical configuration: (a) schematic, (b) computational domain

with the SIMPLER algorithm. The computation of the steady flow field has been presented in Murthy (1987); important details will be discussed in the following section. A fully implicit scheme is used to solve the linear, unsteady equation for solute transport. The discrete equations generated by the boundary conditions on the solute are not diagonally dominant, necessitating the use of direct rather than iterative methods for the solution of the equation set for mass transfer.

A 30×30 nonuniform grid is employed for the low Reynolds numbers cases ($Re\leq100$); for these cases, the maximum value of the stream function changes by less than 1 percent when compared with asymptotic values obtained using finer grids. The same is true of steady-state values of the radial segregation γ. For high Reynolds numbers, the solute boundary layers become exceedingly thin, and a 38×38 nonuniform grid is employed. Here, the maximum stream function is accurate to 1 percent; however, the radial segregation is accurate to only 4 percent compared to computations on a 50×50 grid. Available computer facilities do not allow further grid refinement. The transient is covered in 350–650

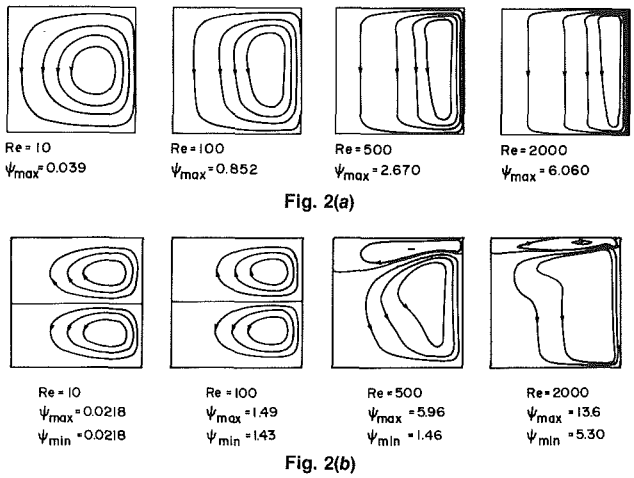

Fig. 2 Contours of the stream function for (a) $S=0.5$; (b) $S=-1.0$

nonuniform steps. Each step engenders a change of no more than 0.5 percent in the average concentration at the freezing interface; for most runs, the change is even less.

All computations were performed on an IBM 3090. One time step took 0.56 s of CPU time, so that most runs took 3–6 minutes.

Results

Flow Structure. The flow fields presented are the same as those in Murthy (1987); they are repeated here for convenience. Two values of S are considered: $S=-1.0$ and $S=0.5$. Contours of the dimensionless stream function for these configurations are presented in Fig. 2. The domain is oriented in this and subsequent contour plots in the same manner as the hatched region in Fig. 1. For $S=0.5$, the meridional flow is counterclockwise, as the faster rotating disk pushes the fluid outward toward the meniscus. As the Reynolds number is increased, the flow loses the purely viscous character exhibited at $Re=10$, and the vortex center is seen to move upward toward the slower disk. The strength of vortex motion, as indicated by the absolute maximum value of the stream function, also increases. At high Reynolds numbers, a core of nearly constant angular velocity evolves, rotating at the average speed of the ends, in keeping with the Taylor–Proudman theorem (Chandrasekhar, 1968).

For perfect counterrotation, $S=-1$, the fluid at each disk is thrown outward toward the meniscus, and a two-vortex pattern results. The horizontal midplane of the zone is a plane of reflective symmetry, and exactly symmetric flow patterns are exhibited up to $Re=100$ or so. At this point, a bifurcation takes place, and two asymmetric families evolve supercritically in the Reynolds number, each a reflection of the other about the midplane. Computations on one of these branches indicate that the flow patterns become increasingly asymmetric as Re is increased, with the smaller cell being pushed up against the upper disk. The freezing interface is always considered closest to the stronger vortex for the calculation of impurity transport. A few computations have been made for the situation when the weaker vortex occurs near the freezing interface in order to delineate the influence of cellular structure; these are referred to as the "flipped" cases in this paper.

Solute Field

Steady-State Solutions. In the absence of secondary motion, the steady-state distribution of solute in the melt is the solution of a one-dimensional convection–diffusion equation, driven by the axial flow due to zone translation (Harriott and Brown, 1984b; Murthy, 1987)

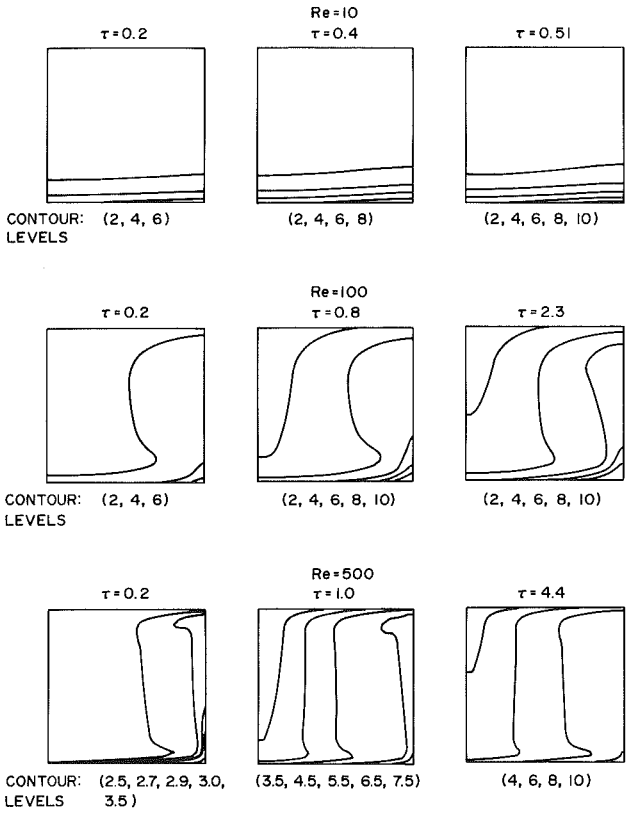

Fig. 3 Contours of solute concentration for $S=0.5$; $k=0.1$, Pe = 10.0, and Sc = 10.0

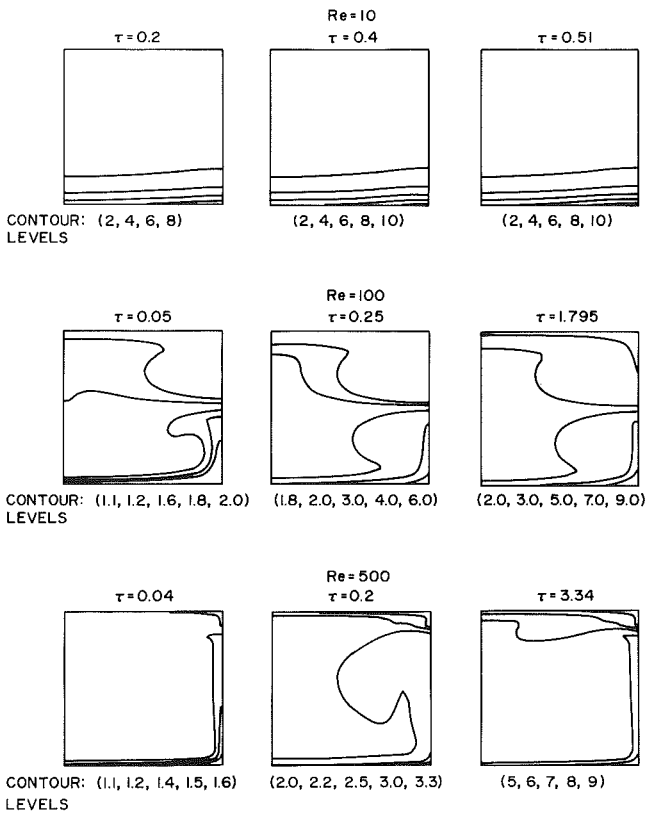

Fig. 4 Contours of solute concentration for $S=-1.0$, $k=0.1$, Pe = 10.0, and Sc = 10.0

$$C(Z)=1+\frac{(1-k)}{k}\exp[\mathrm{Pe}(Z-A)] \tag{5}$$

This solution is exact, and displays no radial segregation. The concentration at the freezing interface is $1/k$. For $\mathrm{Pe}\ll 1$, diffusion dominates the zone, and the concentration is very nearly uniform, approaching the value $1/k$ throughout the melt. For $\mathrm{Pe}\gg 1$, the uniform value $C=1$ at the melting interface is convected virtually unaugmented into the zone; at the freezing interface, a boundary layer forms to meet the imposed boundary condition. The influence of secondary motion on this basic one-dimensional pattern has been studied by Harriott and Brown (1984b) and Murthy (1987), and may be understood by examining the last columns of contours in Figs. 3 and 4, which have been drawn for steady state. The domain in these figures has the same orientation as the computational domain in Fig. 1. The highest concentration of solute occurs near the freezing interface and the lowest at the melting interface. The function of the secondary flow is to distort the one-dimensional profile of equation (5) in the direction of the flow. The lowest Re causes only minimal distortion, with a somewhat higher aggregation of dopant near the meniscus at the freezing interface. As the Reynolds number increases, very thin boundary layers are formed at the melting and freezing interfaces. The zone becomes much more homogeneous, and exhibits the sharp peaks and valleys characteristic of solute transport in the presence of vigorous mixing.

The major difference between co- and counterrotation of the ends is the profound difference in cellular structure. This difference is reflected in the concentration contours in Fig. 4. The loss of midplane symmetry displayed in Fig. 2(*b*) is also seen in Fig. 4. The perfectly counterrotated zone has a greater input of angular momentum than when the zone is co-rotated with $S=0.5$; better mixing leads to a near-uniform zone at Re = 500, with lines of constant concentration running parallel to the melting interface. For low Pe, as the Reynolds number becomes even higher, the distribution of dopant in the melt will approach $1/k$, as in Murthy (1987). A sharp variation in bulk concentration occurs between the two eddies in Fig. 4. Dopant released at the freezing interface is trapped in the adjacent eddy; transport of dopant across the dividing streamline is only by diffusion, a very weak mechanism for crystal growth applications.

Unsteady Behavior: The approach to steady state in the case of a zone with no secondary flow has been analyzed by Tiller et al. (1953). By assuming an exponential concentration in the zone, and performing a mass balance of dopant, as approximate solution to the unsteady problem is obtained

$$C_s(X)=(1-k)(1-\exp(-\beta X))+k$$

$$\beta=k\mathrm{Pe}/(1-\exp(-\mathrm{Pe})) \tag{6}$$

A perturbation solution to the original $1-D$ unsteady problem in the limit $\mathrm{Pe}\to 0$ has been presented in Harriott (1983) by expanding the concentration in powers of the Peclet number. For $\mathrm{Pe}\gg 1$, a stretching of the axial length scale is required to resolve the boundary layer, and a lengthy solution using Laplace transforms is available in Smith et al. (1955) and in Harriott (1983). The approximate solution (6) agrees quite well with these more accurate treatments, and has the advantage of mathematical simplicity; hence, it will be the basis of the following discussion.

The initial solid frozen has a dopant concentration equal to k, corresponding to the initial condition (equation (3)). The average concentration in the solid at steady state is unity, corresponding to a concentration in the melt at the freezing interface of $1/k$. The approach to steady state is governed by several competing time scales. In the absence of secondary convection, the rate of release of solute at the melting interface is set by equation (6). For $\mathrm{Pe}\ll 1$, this time scale is $0(d/V_{\mathrm{zone}}k)$ and transients are long; for $\mathrm{Pe}\gg 1$, the rate of

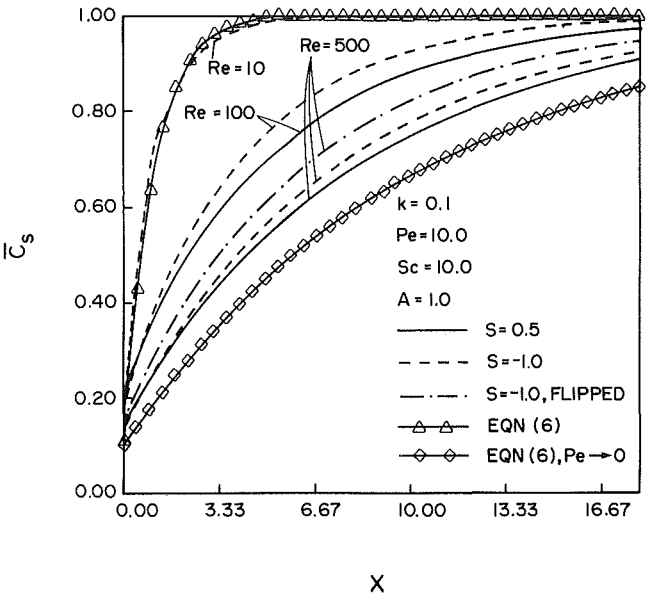

Fig. 5 Variation of average solute concentration with distance zoned for $k = 0.1$, Pe = 10.0, and Sc = 10.0

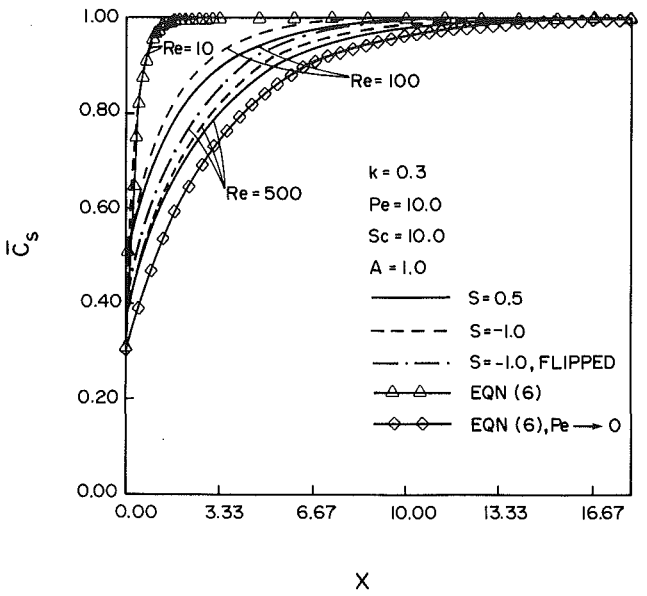

Fig. 6 Variation of average concentration with distance zoned for $k = 0.3$, Pe = 10.0, and Sc = 10.0

solute release scales as $0(d/k\mathrm{Pe}V_{\mathrm{zone}})$ and rapid transients result. The influence of secondary motion depends on the Peclet number associated with the secondary flow, Pe_c. If $\mathrm{Pe}_c \gg \mathrm{Pe}$, the time scale of solute release is $0(d/V_{\mathrm{zone}}k)$ as the zone is well mixed by convection; if $\mathrm{Pe}_c \ll \mathrm{Pe}$, zone translation dominates and the time scale is $0(d/k\mathrm{Pe}V_{\mathrm{zone}})$. Thus, secondary motion does not influence the transient in these extreme limits. For intermediate values of $\mathrm{Pe}/\mathrm{Pe}_c$, the time required to attain steady state is intermediate; increasing secondary motion removes solute from the freeze interface, preventing the buildup of solute towards the average steady-state value of $1/k$ and lengthening the transient.

The convection time scale is $0(\mathrm{Pe}_c^{1/3}L_c/U_c)$, according to Rhines and Young (1983). Thus, secondary motion homogenizes solute along the periphery of the zone over this time scale, which is rapid for crystal growth applications. The gradients so created are homogenized by diffusive transport normal to the streamlines; this takes place over $0(L_c^2/D)$, which is relatively slow. Thus the general form of the transient consists of an initial length of rapid rise of solute concentration in the crystal, followed by a slow approach to the average concentration $1/k$.

This behavior is clearly demonstrated in the concentration profiles of Figs. 3 and 4, as well as in the plots of $\bar{C}_s$ versus X in Figs. 5 and 6. The time required to attain steady state increases with the Reynolds number. The initial slopes of the curves in Figs. 5 and 6 are lower for higher Re. Both these effects are clearly related to the greater mixing associated with high Re. The curves for Re = 10 fall very close to the limit set by equation (6). The upper bound on transient length is the low Pe limit of equation (6). Solute is homogenized quickly in the direction of the flow, as for example, in Fig. 4, where the distortion of concentration contours is evident even at $\tau = 0.04$. The diffusion time scale is slow for crystal growth applications; this is demonstrated by the slow rise of core concentration, steady state being achieved at approximately $\tau = 3.34$.

Counterrotation leads to a shorter transient than corotation, except at low Re, where the flow is too weak to alter solute transport significantly. Here, influence of flow structure is clearly evident. While the convection of solute away from the freezing interface tends to increase the transient length, the trapping of solute in the adjacent eddy elevates the average solute levels in that region, and causes steady state to be attained more rapidly. This is especially the case when the "flipped" velocity field is used in Figs. 5 and 6. Here, the meridional velocity field for Re = 500, $S = -1.0$, has been reflected about the midplane, so that the smaller eddy in Fig. 2(*b*) is now adjacent to the freezing interface. As pointed out earlier, this field is also a solution to the flow equations. Steady state is approached more readily when the freezing interface is washed by the smaller eddy than by the larger one. Theoretically, the bifurcation for $S = -1.0$ is perfect, in that both solutions to the flow equations are equally realizable. However exact symmetry about the midplane is rarely achieved in practice; if one of the disks is rotated slightly faster, for example, the larger eddy would occur adjacent to the faster disk, and shorter transients would result.

The curves for $k = 0.3$ in Fig. 6 indicate that steady state is achieved more readily for higher values of k, in keeping with equation (6). The rate of rise in average solute concentration is also more rapid, again in keeping with equation (6). The envelope of the curves narrows as $\mathrm{Pe} \to 0$, so that curves for different Re are expected to fall much closer together as Pe is decreased.

Radial Segregation. Patterns of radial segregation at steady state have been studied in Murthy (1987) and Harriott and Brown (1984b), for a variety of flow configurations. For $\mathrm{Pe} \gg \mathrm{Pe}_c$, segregation is entirely axial, as indicated by equation (5). For $\mathrm{Pe} \ll \mathrm{Pe}_c$, again, complete mixing leads to the disappearance of all radial gradients. The time scale for the development of radial segregation is essentially that set by secondary convection, $0(\mathrm{Pe}_c^{1/3}L_c/U_c)$. For low Re, the convection time scale is longer than that over which solute release takes place. This is evident in the relatively slow initial rise of γ for Re = 10 in Figs. 7 and 8. This effect disappears as Re increases, and the convection time scale becomes the shortest time scale governing the problem. Thus the initial buildup of γ is extremely rapid of Re = 500. If the secondary flow creates radial gradients, but is not strong enough to obliterate them, significant solute segregation may occur; values over 100 percent of the mean concentration have been reported by Harriott and Brown (1984b). The same behavior is seen in the unsteady situation, as demonstrated in Figs. 7 and 8. At any given time, the plot for Re = 100 displays greater radial segregation than those for Re = 10 or Re = 500. For $k = 0.1$ and Re = 100, the steady-state value is 124.5 percent of the average impurity con-

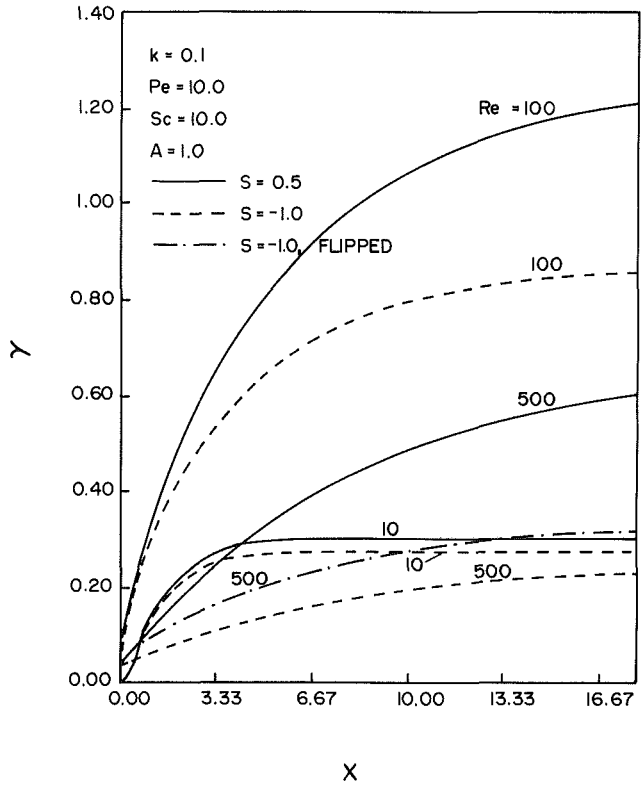

Fig. 7 Variation of radial segregation with distance zoned for $k = 0.1$, $Pe = 10.0$, and $Sc = 10.0$

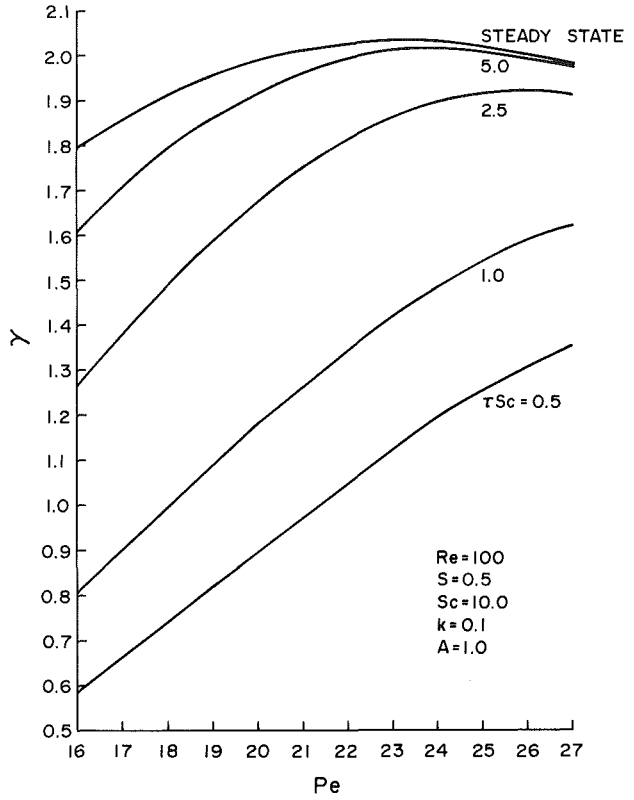

Fig. 9 Variation of radial segregation with Peclet number for $S = 0.5$, $k = 0.1$, and $Sc = 10.0$

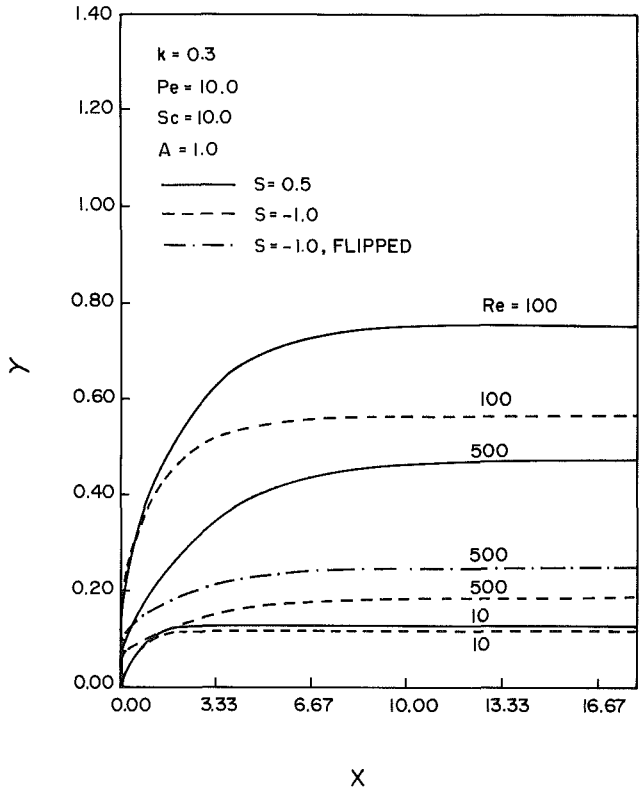

Fig. 8 Variation of radial segregation with distance zoned for $k = 0.3$, $Pe = 10.0$, and $Sc = 10.0$

centration in the feed rod. Typically, a variation of no more than 10 percent is considered desirable. Similar behavior is seen at other values of k. The greater mixing due to counterrotation manifests itself in lower values of γ; for $k = 0.1$, the mixing at $Re = 500$ is so vigorous that γ values fall below those for $Re = 10$. The crossing over of curves in Fig. 7 is evidence of the different rates of profile development at the freezing interface.

The extent of radial segregation is lower for lower k. The average concentration at the freezing interface is $1/k$ in the melt at steady state. The feed rod provides solute at $C = 1.0$. Thus, the gradients of C in the melt decrease as k increases, and result in lower radial segregation. A reversal in this trend is seen in the earlier part of the transient. An examination of Figs. 7 and 8 reveals a crossing over of the plots for $k = 0.1$ and $k = 0.3$ for any given Re for small time. This is thought to be primarily a result of the quicker development of the solute field at high values of k. This effect becomes less important as steady state is reached.

Maxima in the radial segregation are found with respect to other parameters governing the problem as well. Figures 9 and 10 show the variation of with the zone translation Peclet number. At steady state, a maximum in γ is found at approximately $Pe \simeq 23$ for corotation and $Pe \simeq 34$ for counterrotation. The concentration field develops more quickly for high Pe (see equation (6)) and attains its highest γ earlier; hence the critical value of the Peclet number shifts toward lower Pe as τSc increases. The peak is relatively wide and the maximum value of γ for co- and counterrotation is nearly the same. Qualitatively similar behavior is seen in Figs. 11 and 12 where γ has been plotted with respect to the Schmidt number Sc, with time as the parameter. Here again, a maximum in γ is seen at $Sc \simeq 4$ for corotation and $Sc \simeq 2$ for counterrotation at steady state. The solute field develops more quickly for low Sc; the Peclet number associated with the secondary flow decreases as Sc, and leads to less mixing and shorter transients. Thus, the critical Schmidt number shifts toward higher Sc with time. The maximum γ for co- and counterrotation is

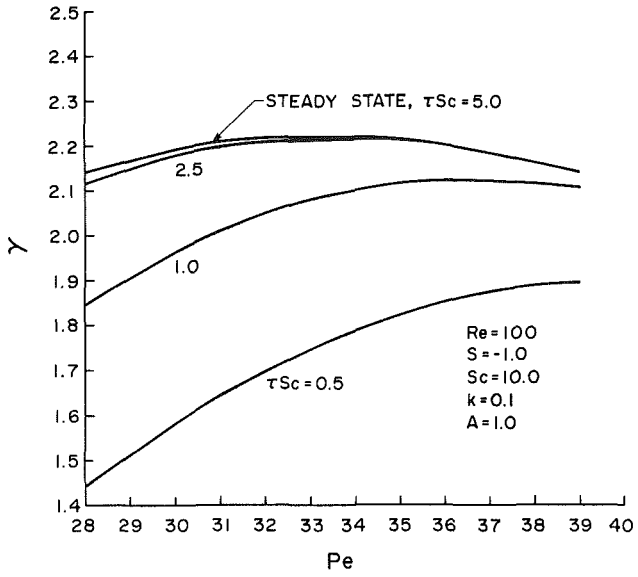

Fig. 10 Variation of radial segregation with Peclet number for $S = -1.0$, $k = 0.1$, and $Sc = 10.0$

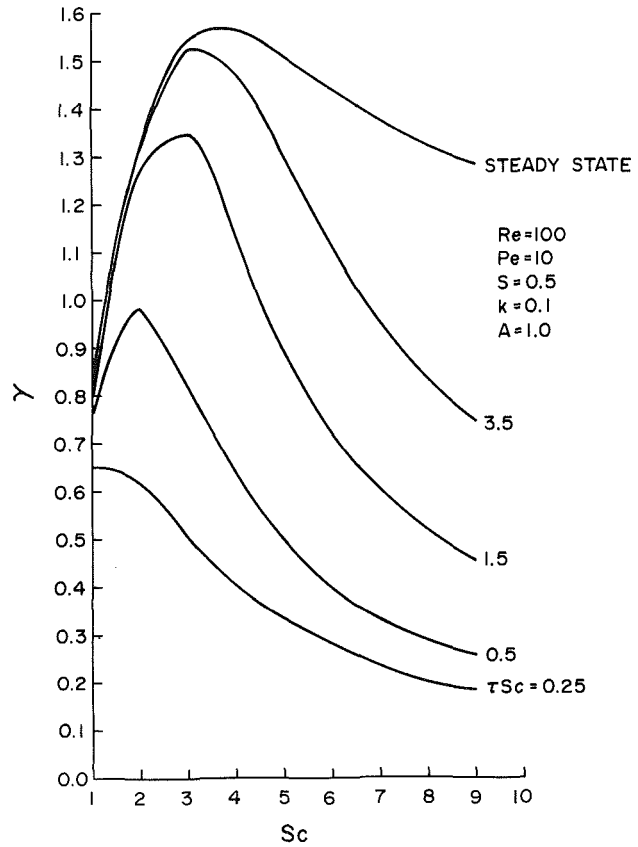

Fig. 11 Variation of radial segregation with Schmidt number for $S = 0.5$, $k = 0.1$, and $Pe = 10.0$

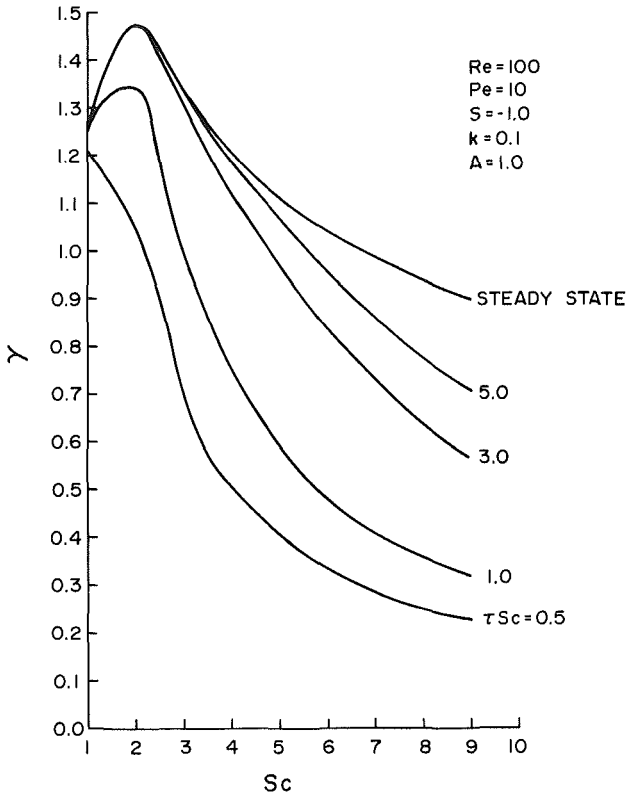

Fig. 12 Variation of radial segregation with Schmidt number for $S = -1.0$, $k = 0.1$, and $Pe = 10.0$

of approximately the same magnitude, but the peak is much sharper than in Figs. 9 and 10.

Figure 9 suggests that the preferable way to decrease radial gradients is to decrease the rate of zone traverse rather than to increase it. Suppose that the critical Peclet number for a given set of governing parameters is Pe_{cr} in steady state. Two options exist for decreasing radial segregation, either to increase Pe above Pe_{cr} in order to approximate equation (6) more closely, or to decrease Pe below Pe_{cr} in order to allow the secondary flow to mix better. Figure 9 suggests that the latter is the wiser strategy. Intermediate axial locations will always have lower radial segregation if $Pe < Pe_{cr}$. If $Pe > Pe_{cr}$ is chosen instead, there is a risk of increasing axial segregation at intermediate locations.

Conclusions

Numerical analysis of transient segregation in the floating zone yields several significant results. It is found that the transient length is bounded by two limits set by equation (6). The lower limit is that predicted by equation (6) for the specific Pe and k under consideration; the upper limit is the diffusion limit of equation (6). Mechanisms that tend to homogenize the melt increase the transient length. These include increases in the zone translation Peclet number. The initial transient response is relatively steep, as a result of the rapid buildup of solute at the freezing interface; the slope of the transient then decreases as cross-stream diffusion transports solute to the core. Flow structure is of critical importance in determining the transient length. Cellular structures that tend to trap solute near the freezing interface decrease the transient length. A maximum in the extent of radial segregation occurs when the radial flow creates concentration gradients, but is unable to homogenize them. Zone translation Peclet numbers are typically low for crystal growth applications; unsuccessful attempts to damp secondary convection may result in meridional motion of the same order as the rate of growth, actually increasing radial segregation rather than eliminating it.

The validity of using a steady velocity field in the calculation of unsteady solute segregation may now be examined. If the time scale for solute release is longer than that for mixing due to the secondary flow, the transient length for mass transfer is diffusion limited. The same is true for the velocity field if the Reynolds number of rotation is much greater than the Reynolds number associated with zone traverse. In this

limit, the treatment used in this paper is valid if $Sc > 1$. Thus, the nearly one-dimensional solute fields presented for $Re = 10$ are, strictly speaking, invalid, unless the velocity field has been allowed to develop before the partition process begins. For practical crystal growth situations, however, such a treatment is probably adequate. Typical values of the zone translation rate are low; on the other hand, Reynolds numbers of rotation are high, frequently greater than 2000 (Keller, 1976). Typical Schmidt numbers are in the range 5–50. Furthermore, the floating zone process is limited to material-impurity combinations with low values of k, since higher values do not provide adequate partitioning. All these considerations mean that the transient response of the melt is limited by a diffusion time scale of $0(L_c^2/D)$. This is further confirmed by a computation of the unsteady flow field for $Re = 500$, $S = -1.0$ by Murthy (1987), which indicates that the flow field achieves steady state at approximately $\tau = 0.154$, whereas the present study shows that the mass transfer problem in this configuration becomes steady after $\tau = 3.34$. Computation of the temperature field may similarily assume steady state. Prandtl numbers for crystal growth applications are $0(10^{-2})$, so that the temperature field evolves virtually independently of the velocity field, and far more rapidly. Thus, the heat transfer results presented in Murthy (1987) adequately describe the transient problem for high Reynolds numbers.

The results obtained here also provide guidelines for the prediction of unsteady solute segregation in other flow fields. The degree of mixing increases with the number and strength of cells washing the freezing interface. If the flow is turbulent, mixing would increase dramatically. In this limit, gradual transients would result, similar to the diffusion limit of equation (6). The specific cellular pattern also changes the transient response. If the flow pattern tends to isolate the freezing interface, a buildup of solute would shorten the response time.

It is also clear from the concentration contours of Figs. 3 and 4 that the assumption of the constant boundary layer thickness for mass transfer is valid only in well-mixed zones. For intermediate values of the Reynolds number, the turning flows near the meniscus cause significant radial segregation. Thus great care must be taken in using models based on this idea (Wagner, 1954; Favier, 1981).

Acknowledgments

This research was supported by National Science Foundation grant No. CBT-8504917.

References

Burton, J. A., Prim, R. C., and Slichter, W. P., 1953, "The Distribution of Solute in Crystals Grown From the Melt," *J. Chem. Physics*, Vol. 21, pp. 1987–1991.

Chandrasekhar, S., 1968, *Hydrodynamic and Hydromagnetic Stability*, Oxford University Press, London.

Chang, C. E., and Wilcox, W. R., 1976, "Analysis of Surface Tension Driven Flow in Floating Zone Melting," *Int. J. Heat Mass Transfer*, Vol. 19, pp. 355–366.

Chang, C. J., and Brown, R. A., 1983, "Radial Segregation Induced by Natural Convection and Melt/Solid Interface Shape in Vertical Bridgeman Growth," *J. Crystal Growth*, Vol. 63, pp. 343–364.

Favier, J. J., 1981, "Macrosegregation—I. Unified Analysis During Nonsteady State Solidification," *ACTA Metallurgica*, Vol. 29, pp. 197–204.

Harriott, G. M., 1983, "Fluid Flow and Mass Transfer in a Small Floating Zone," Ph.D. Thesis, Massachusetts Institute of Technology, Cambridge, MA.

Harriott, G. M., and Brown, R. A., 1983, "Flow in a Differentially Rotated Cylindrical Drop at Low Reynolds Number," *J. Fluid Mech.*, Vol. 126, pp. 269–285.

Harriott, G. M., and Brown, R. A., 1984a, "Flow in a Differentially Rotated Cylindrical Drop at Moderate Reynolds Number," *J. Crystal Growth*, Vol. 96, pp. 589–604.

Harriott, G. M., and Brown, R. A., 1984b, "Steady Solute Fields Induced by Differential Rotation in a Small Floating Zone," *J. Crystal Growth*, Vol. 69, pp. 589–604.

Jurisch, M., Loser, W., Lyumkis, E., Martuzans, B., and Martuzane, E., 1982, "Connection of the Thermocapillary Flow Characteristics and the Impurity Distribution Pattern in Floating Zone Molybdenum Single Crystal," *Crystal Res. Tech.*, Vol. 17, pp. 963–971.

Keller, W., 1976, "Experimental Influence of Some Growth Parameters Upon the Shape of the Melt Interfaces and the Radial Phosphorus Distribution During Float-Zone Growth of Silicon Single Crystals," *J. Crystal Growth*, Vol. 36, pp. 215–231.

Kobayashi, N., 1984, "Computer Simulation of the Steady Flow in a Cylindrical Floating Zone Under Low Gravity," *J. Crystal Growth*, Vol. 66, pp. 63–67.

Langlois, W. E., 1985, "Buoyancy-Driven Flows in Crystal-Growth Melts," *Ann. Rev. Fluid Mech.*, Vol. 17, pp. 191–215.

Murthy, J. Y., 1987, "A Numerical Simulation of Flow, Heat and Mass Transfer in a Floating Zone at High Rotational Reynolds Numbers," *J. Crystal Growth*, Vol. 83, pp. 23–34.

Patankar, S. V., 1980, *Numerical Heat Transfer and Fluid Flow*, McGraw-Hill, New York.

Pfann, W. G., 1966, *Zone Melting*, Wiley, New York.

Rhines, P. B., and Young, W. R., 1983, "How Rapidly in a Passive Scalar Mixed Within Closed Streamlines?" *J. Fluid Mech.*, Vol. 133, pp. 133–145.

Smith, V. G., Tiller, W. A., and Rutter, J. W., 1955, "Solute Redistribution During Growth of a Binary Alloy," *Can. J. Phys.*, Vol. 33, pp. 723–730.

Tiller, W. A., Jackson, K. A., Rutter, J. W., and Chalmers, B., 1953, "The Redistribution of Solute Atoms During the Solidification of Metals," *Acta Metallurgica*, Vol. 1, pp. 428–437.

Wagner, C., 1954, "Theoretical Analysis of Diffusion of Solutes During the Solidification of Alloys," *J. Metals*, Vol. 6, pp. 154–160.

Wollhover, K., Korber, Ch., Scheiwe, M. W., and Hartman, U., 1985, "Unidirectional Freezing of Binary Aqueous Solutions: An Analysis of Transient Diffusion of Heat and Mass," *Int. J. Heat Mass Transfer*, Vol. 28, pp. 761–769.

Modeling of Hot Fragment Conductive Ignition of Solid Propellants With Applications to Melting and Evaporation of Solids

K. K. Kuo

W. H. Hsieh

K. C. Hsieh

Department of Mechanical Engineering,
The Pennsylvania State University,
University Park, PA 16802

M. S. Miller

U.S. Army Ballistic Research Laboratory,
Aberdeen Proving Ground, MD 21005

A comprehensive theoretical model has been formulated for studying the degree of vulnerability of various solid propellants being heated by hot spall fragments. The model simulates the hot fragment conductive ignition (HFCI) processes caused by direct contact of hot inert particles with solid propellant samples. The model describes the heat transfer and displacement of the hot particle, the generation of the melt (or foam) layer caused by the liquefaction, pyrolysis, and decomposition of the propellant, and the regression of the propellant as well as the time variation of its temperature distributions. To validate partially the theoretical model in the absence of the necessary chemical kinetic data, an ice melting and evaporation experiment was designed and conducted. These experiments provide features of the conductive heating, melting, and evaporating processes. Calculated results compare well with experimental data in temperature-time traces, spall particle sinking velocity, and displacement.

Introduction

Ignition of solid gun propellants in go/no-go tests that employ a hot metallic element of well-defined geometry as the source of energy has been a conventional method of determining the vulnerability of propellants (Gol'dshleger, 1973), especially in the Low Vulnerability Ammunition (LOVA) development program (Wise et al., 1980; Law and Rocchio, 1981; Wise and Rocchio, 1981). Hot fragment conductive ignition (HFCI) studies help to determine the survivability of weapon systems (such as tanks, ships, etc.) containing stowed ammunition (Gol'dshleger et al., 1973; Wise et al., 1980; Law and Rocchio, 1981; Wise and Rocchio, 1981). Ignition of propellant charges by hot metallic spall fragments can be generated through such threats as shaped charges and kinetic energy penetrators.

Review of HFCI processes indicates that both experimental and theoretical investigations have been conducted. The experiments generally employ hot steel balls of known diameters and temperatures, which are suddenly brought into contact with the propellant (Gol'dshleger et al., 1973a; Wise et al., 1980; Law and Rocchio, 1981; Wise and Rocchio, 1981).

Gol'dshleger et al. (1973a) used a hot steel ball with a diameter of 0.4-2.5 mm and smooth surface finish (<0.1 μm) to ignite the propellant. They noted that ignition does not occur when the particle temperature is below a critical value, and that results are dependent upon contact between the hot particle and the propellant. They also proposed a theoretical model and obtained numerical solutions.

Wise et al. (1980, 1981) and Law and Rocchio (1981) conducted similar experiments to characterize LOVA propellants. They used hot steel balls (with diameters between 3.2 and 11.1 mm), and a cluster of propellant slabs. The ignition boundary for propellants was determined in terms of minimum temperature for a given size steel ball, using go/no-go tests. Their HFCI experiments indicated that the binder composition may be one of the most important factors in the determination of LOVA propellant vulnerability.

Kirschenbaum et al. (1983) studied the sensitivity properties of various candidate LOVA propellants using various tests, including HFCI. Their study showed that LOVA candidates are significantly less susceptible to thermal ignition than conventional propellants. Caveny et al. (1973) also investigated the effect of additives on the flammability limits of propellants, investigated the effect of additives on flammability limits of propellants, and evaluated three types of additives (including coolants, char formers, and flame inhibitors) for reducing flammability.

Prior to the present study, several attempts have been made to model the ignition process encountered in HFCI experiments (Gol'dshleger et al., 1973a; Vilyunov and Kolchin, 1966; Anderson et al., 1972; Gol'dshleger et al., 1973b; Linan and Kindelan, 1981; Tyler and Jones, 1981). However, because most of the existing models of of conductive ignition employ numerous simplifying assumptions and asymptotic solution procedures, their validity and usage are limited. Grossman and Rele (1974) obtained numerical solutions for the ignition of cellulose by impingement of hot, high-velocity spherical particles. They concluded that the total energy of the metal particle (both thermal and kinetic) is important in determining whether or not ignition occurs.

None of the theoretical models to date have attempted to describe the foam and/or melt layer that has been experimentally observed on the propellant surface in contact with hot particles. Nor has the effect of binder composition been studied in previous models. A theoretical model for simulating the ignition processes of solid propellants in HFCI tests is needed in order to evaluate new propellant formulations with respect to their ability to resist conductive ignition and thereby reduce system vulnerability.

Specific objectives of this study are: (1) to formulate a comprehensive model for simulating the ignition of solid propellants under HFCI situations; (2) to identify chemical and physical input parameters required for the model; (3) to design and conduct simplified melting and evaporation experiments to partially validate the theoretical model under special limiting conditions; and (4) to demonstrate the capability of the theoretical model to simulate ice melting and evaporation processes.

Contributed by the Heat Transfer Division and presented at the ASME Winter Annual Meeting, Anaheim, California, December 7-12, 1986. Manuscript received by the Heat Transfer Division March 27, 1987. Keywords: Combustion, Phase-Change Phenomena, Reacting Flows.

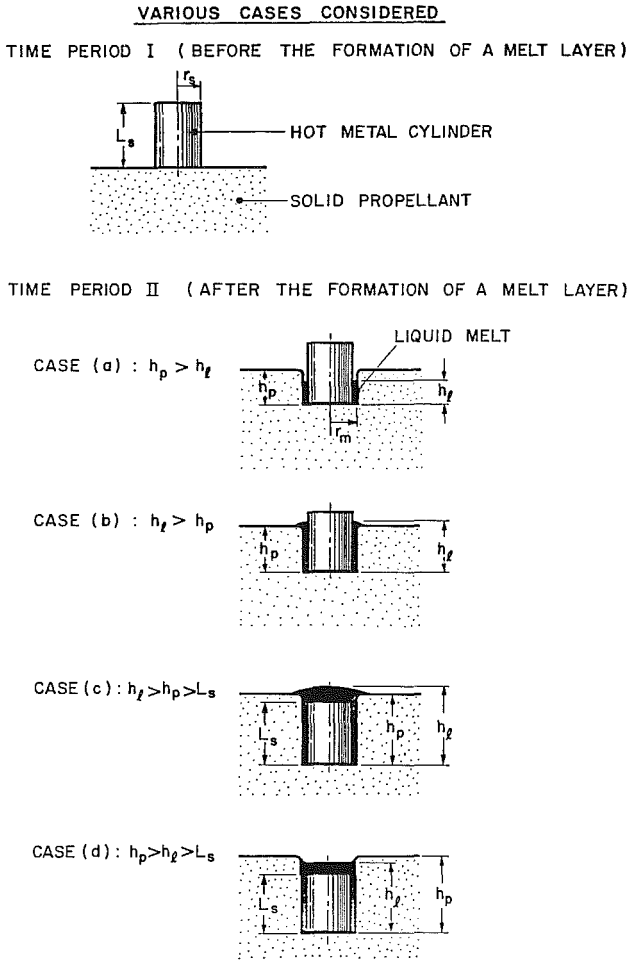

Fig. 1 Physical event of hot fragment conductive ignition (HFCI) processes represented by various cases in two different time periods

Method of Approach

Selection of Particle Geometry and Description of Physical Events. In actual HFCI processes, the hot fragments (spall particles) generated from the penetration of shaped charge jets of armor plates are in different shapes and sizes. In order to understand the physical and chemical processes, a particular particle shape has to be selected in the formulation of the theoretical model. Since no particular shape can truly represent the actual geometry of spall fragments, any particle geometry (e.g., spherical, cylindrical, cubic, parallelepiped) could be chosen. The cubic or parallelepiped particles require a three-dimensional and unsteady solution, which is more complex than the cylindrical and spherical cases. The spherical particle geometry seems simpler than cylindrical; however, the heat transfer process involved does not satisfy the point symmetry condition. Therefore, the cylindrical particle geometry has been selected. One additional advantage of the cylindrical spall particle is its flat-bottomed surface, which can easily maintain a good contact with a flat propellant surface.

Consider a typical HFCI experiment using a hot spall particle with cylindrical geometry. At time equals zero, the spall particle is placed on a cold propellant sample. In the early phase of the process (Time Period I), heat is conducted from the hot particle to the propellant without any phase change or pyrolysis (see Fig. 1). As time progresses, the temperature of the propellant increases and that of the particle decreases. Following a period of inert heating, the propellant starts to decompose, melt, and/or gasify (Time Period II). Since the density of the metal particle is much higher than the density of the decomposed propellant, it displaces the decomposed propellant and becomes imbedded in (sinks into) the propellant, as shown in Fig. 1. The amount of imbedding depends on the temperature and size of the hot particle and the composition of the propellant. The decomposed species can further react exothermically in the gas and/or condensed (solid or liquid (foam)) phase to cause ignition. Self-sustained ignition will occur only if the heat generated by the exothermic reactions ex-

Nomenclature

A = Arrhenius frequency factor of chemical reaction of melt or foam layer in Region 1, kg/m^3-s
A_i = interface area between liquid melt and gas bubbles, m^2
C_p = constant-pressure specific heat, J/kg-K
C_{pr} = specific heat of LOVA propellant, J/kg-K
C_s = specific heat of spall particle, J/kg-K
D_b = averaged diameter of bubbles generated from gasification process, m
E_a = activation energy of chemical reaction of melt or foam layer, J/mole
$h_{c1,2}$ = convective heat transfer coefficient on top and lateral surfaces of spall particle, W/m^2-K
h_{c3} = convective heat transfer coefficient on top surface of LOVA propellant, W/m^2-K
ΔH_f° = heat of formation, J/kg
h_{fg} = latent heat of liquid melt, J/kg
h_ℓ = instantaneous height of melt or foam layer in Region 2, m
h_p = instantaneous distance traveled by spall particle, m
L_m = height of melt or foam layer in Region 1, m
L_s = height of the spall particle, m
$\dot{m}_b$ = rate of conversion of reactant (R) into product (P), kg/s
$\dot{m}_{gB}$ = rate of mass generation of reactant species from the base of spall particle, kg/s
$\dot{m}_{g_{\text{net}_1}}$ = net rate of production of gaseous mass in Region 1 of foam layer, kg/s
n = order of chemical reaction in gas bubbles
p = pressure, N/m^2
$\dot{q}''_{\min}$ = critical heat flux for producing gaseous bubbles from melt of LOVA propellant on surface of spall particle, W/m^2
$\dot{q}''_{m1}$ = heat flux on submerged lateral surface of spall particle, W/m^2
$\dot{q}''_{m2}$ = heat flux from foam layer to LOVA propellant, W/m^2
$\dot{q}'''_{pr}$ = net heat generation in LOVA propellant, W/m^3
$\dot{q}''_{pr}$ = heat flux transferred to LOVA propellant from melt or foam layer in Region 1, W/m^2
$\dot{q}''_{\text{rad}}$ = net radiant heat flux, W/m^2
$\dot{q}''_{\text{spall}}$ = heat flux at base of spall particle, W/m^2

ceeds the heat losses. The entire process is strongly dependent upon the energy content of the hot particle and physicochemical properties of the propellant.

Governing Equations and Boundary Conditions. The mathematical model consists of governing equations and their associated initial and boundary conditions for the hot particle, the propellant, and the melt (or foam) layer. Figure 2 schematically shows these regions and the coordinate system. The energy equations for the hot spall particle and the propellant are as follows:

Hot Spall Particle:

$$\frac{\partial}{\partial t}(\rho_s C_s T_s) = \frac{1}{r}\frac{\partial}{\partial r}\left(\lambda_s r \frac{\partial T_s}{\partial r}\right) + \frac{\partial}{\partial z}\left(\lambda_s \frac{\partial T_s}{\partial z}\right) \tag{1}$$

Propellant:

$$\frac{\partial}{\partial t}(\rho_{pr} C_{pr} T_p) - v_s \frac{\partial}{\partial z}(\rho_{pr} C_{pr} T_p)$$

$$= \frac{1}{r}\frac{\partial}{\partial r}(\lambda_{pr} r \frac{\partial T_p}{\partial r}) + \frac{\partial}{\partial z}\left(\lambda_{pr}\frac{\partial T_p}{\partial z}\right) + \dot{q}'''_{pr} \tag{2}$$

During the HFCI tests, a foam layer could be generated, and the gases pyrolyzed from liquid melt may undergo exothermic chemical reactions to generate heat for further reactions. In order to take the above processes into consideration, the conservation equations for the foam region must be formulated. The following assumptions are adopted:

1 The liquefaction process at the interface of the propellant and liquid melt involves no gasification;

2 the gaseous mixtures are produced from the base of the spall particle or at the liquid-gas interfaces according to the Arrhenius rate law; and

3 the energy release process in the gas phase can be represented by a single-step forward reaction

$$R \rightarrow P \tag{3}$$

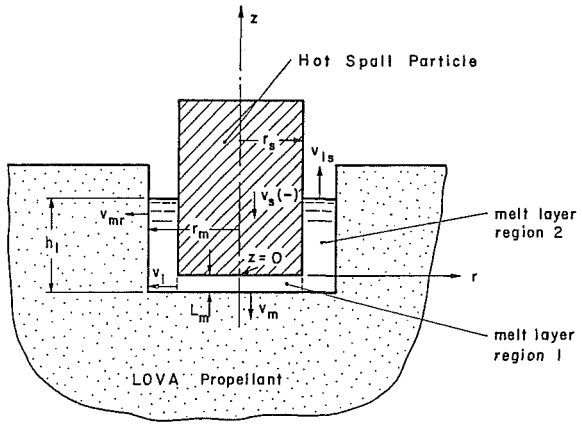

Fig. 2 Schematic diagram of the model

where R represents the gaseous reactant mixtures, and P represents the gaseous products.

The mass continuity equation for the reactant species can be derived from consideration of mass-flux balance in region 1 of the foam layer as

$$\frac{D}{DT}(Y_R \rho_{g_1} \psi L_m \pi r_s^2) = -2\pi r_s L_m Y_R \rho_{g_1} v_{lr} \psi + \dot{m}_{g_{\text{net}_1}} + \dot{m}_{g_B} - \dot{m}_b \tag{4}$$

The mass continuity equation for the product species can be written as

$$\frac{D}{Dt}[(1-Y_R)\rho_{g_1}\psi L_m \pi r_s^2] = -2\pi r_s L_m (1-Y_R)\rho_{g_1} v_{lr}\psi + \dot{m}_b \tag{5}$$

The source terms $\dot{m}_b$ and $\dot{m}_{g_{\text{net}_1}}$ can be expressed as follows according to the Arrhenius law:

$$\dot{m}_b = A_g \rho_{g_1}^n Y_R^n \exp\left(-\frac{E_{a,g}}{R_u T_{g_1}}\right) \tag{6}$$

Nomenclature (cont.)

r = radial coordinate, m
R_u = universal gas constant = 8314.4 J/kg-mole-K
r_m = outer radius of melt or foam layer in Region 2, m
r_s = radius of spall particle, m
$T_b (\equiv T_{\text{sat}})$ = boiling temperature of liquid melt, K
T_g = gas temperature, K
T_m = bulk temperature of melt or foam layer, K
T_{melt} = melting temperature of LOVA propellant, K
T_p = temperature of LOVA propellant, K
T_{ps} = average surface temperature of LOVA propellant exposed to air, K
T_s = temperature of spall particle, K
v_b = average axial velocity of bubbles in Region 1 of foam layer, m/s
v_{lr} = radial velocity of melt or foam layer in Region 1, m/s
v_m = axial velocity of boundary surface of melt or foam layer in Region 1, m/s
v_{mr} = outward radial velocity of foam layer in Region 2, m/s
v_s = sinking velocity of spall particle, m/s
z = axial distance above base of spall particle, m
z^* = axial distance below instantaneous surface of propellant under foam layer, m
α = thermal diffusivity, m^2/s
β = bubble contact angle, deg
ϵ_s = emissivity of spall particle
λ = thermal conductivity, W/m-K
μ = dynamic viscosity, kg/m-s
ρ = density, kg/m^3
σ = Stefan-Boltzmann constant $\equiv 5.6696 \times 10^{-8}$ $W/m^2\text{-}K^4$
σ_s = surface tension of liquid melt of LOVA propellant, N/m
ψ = average porosity (void fraction) of foam layer in Region 1
ψ_B = average void fraction of spall base surface in contact with gas bubbles

Subscripts

g = gas phase
i = initial condition
ℓ = liquid phase
melt = liquid melt
pr = propellant
∞ = room condition
1 = region 1 of foam layer

Superscripts

$*$ = $T^* \equiv T - T_{\text{ref}}$

$$\dot{m}_{g_{\text{net}_1}} = A_{\ell g} A_{i_1} \rho_\ell \exp\left(-\frac{E_{a,\ell g}}{R_u T_{\ell_1}}\right) \tag{7}$$

where $A_{\ell g}$ represents the Arrhenius coefficient of the reaction at the interface of the liquid and gas phases. The mass continuity equation for the liquid phase of the foam layer in region 1 can be given as

$$\frac{D}{Dt}[\rho_{\ell_1}(1-\psi)L_m \pi r_s^2] = -2\pi r_s L_m \rho_{\ell_1} v_{\ell r}(1-\psi) - \dot{m}_{g_{\text{net}_1}} - \dot{m}_{g_B} + \rho_{pr}\pi r_s^2(-v_m) \tag{8}$$

Rearranging equations (4) and (5), one can obtain the following equation:

$$\frac{DY_R}{Dt} = \frac{1}{\rho_{g_1}\psi L_m \pi r_s^2}[(1-Y_R)(\dot{m}_{g_{\text{net}_1}} + \dot{m}_{g_B}) - \dot{m}_b] \tag{9}$$

By considering the energy fluxes shown in Fig. 3(*a*), one can derive the following equation describing the rate of accumulation of the gas-phase energy:

$$\frac{D}{Dt}[\psi\rho_{g_1}\pi r_s^2 L_m (C_{vg} T_{g_1}^* + \Delta H_{f,g}^\circ)] = -(\Delta H_{f,g}^\circ + C_{Pg} T_{g_1}^*)\rho_g v_{\ell r} 2\pi r_s L_m \psi + \dot{q}''_{\text{gas}} \psi_B \pi r_s^2 + \dot{m}_{g_{\text{net}_1}}(C_{P,R} T_b^* + \Delta H_{f,R}^\circ) - p\frac{D}{Dt}(\pi r_s^2 L_m \psi) + \dot{m}_{g_B}(C_{P,R} T_b^* + \Delta H_{f,R}^\circ) - \dot{q}''_{\text{gas-liq}} A_{i_1} \tag{10}$$

For the liquid phase, the balances of energy fluxes are given in Fig. 3(*b*), and the energy equation can be written as

$$\frac{D}{Dt}[(1-\psi)\rho_\ell \pi r_s^2 L_m (C_{v\ell} T_{\ell_1}^* + \Delta H_{f,\ell}^\circ)] = -(\Delta H_{f,\ell}^\circ + C_{P\ell} T_{\ell_1}^*)\rho_\ell v_{\ell r} 2\pi r_s L_m (1-\psi) + \dot{q}''_{\text{liq}}(1-\psi_B)\pi r_s^2 - \dot{m}_{g_{\text{net}_1}}(C_{p,R} T_b^* + \Delta H_{f,R}^\circ) + (-v_m)\rho_{pr}\pi r_s^2 (C_{P\ell} T_{\text{melt}}^* + \Delta H_{f,\ell}^\circ) - \dot{q}''_{\text{liq-solid}}\pi r_s^2 - \dot{m}_{g_B}(C_{P,R} T_b^* + \Delta H_{f,R}^\circ) + \dot{q}''_{\text{gas-liq}} A_{i_1} \tag{11}$$

where

$$\Delta H_{f,g}^\circ = Y_R \Delta H_{f,R}^\circ + (1-Y_R)\Delta H_{f,P}^\circ \tag{12}$$

$$C_{vg} = Y_R C_{v,R} + (1-Y_R) C_{v,P} \tag{13}$$

$$C_{Pg} = Y_R C_{P,R} + (1-Y_R) C_{P,P} \tag{14}$$

Both $\dot{q}''_{\text{liq}}$ and $\dot{q}''_{\text{liq-solid}}$ are positive for downward heat fluxes.

Initial and Boundary Conditions. In order to solve the temperature distributions inside the spall particle and solid propellant, a set of initial and boundary conditions must be specified for equations (1) and (2). There are two sets of conditions: One corresponds to Time Period I ($t < t_{\text{melt}}$); the other corresponds to Time Period II ($t \geq t_{\text{melt}}$). The initial conditions for Time Period I are

$$T_s(0) = T_{si} \tag{15}$$

$$T_p(0) = T_{pi} \tag{16}$$

The initial conditions for Time Period II are the temperature profiles solved at the end of Time Period I.

The boundary conditions for spall particles in Time Period I can be specified readily; some of the boundary conditions are special cases of those for Time Period II. Therefore, they are omitted here. The boundary conditions for the spall particle of Case (*a*) in Fig. 1 during Time Period II are given as

at $z = L_s$:

$$-\lambda_s \frac{\partial T_s}{\partial z} = h_{c1}(T_s - T_\infty) + \epsilon_s \sigma (T_s^4 - T_\infty^4) \tag{17}$$

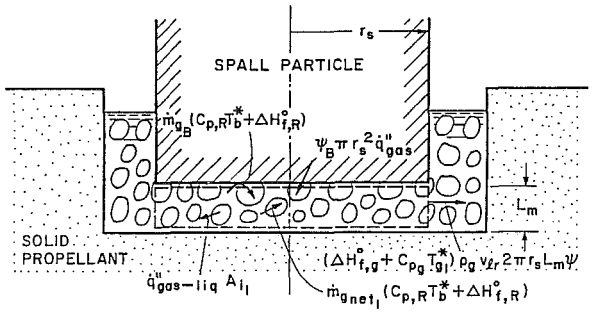

Fig. 3(*a*) Energy fluxes associated with the gas phase in region 1 (thickness of foam layer is highly exaggerated)

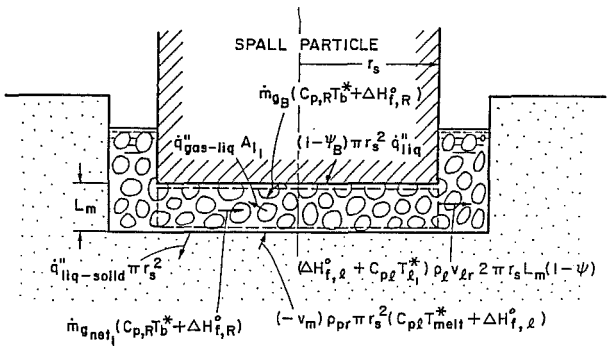

Fig. 3(*b*) Energy fluxes associated with the liquid phase in region 1 (thickness of foam layer is highly exaggerated)

at $z = 0$:

$$\lambda_s \frac{\partial T_s}{\partial z} = -\frac{1}{\pi r_s^2}\dot{m}_{g_B}(C_{P\ell} T_b^* + \Delta H_{f,\ell}^\circ) + \psi_B \dot{q}''_{\text{gas}} + (1-\psi_b)\dot{q}''_{\text{liq}} + \frac{1}{\pi r_s^2}\dot{m}_{g_B}(C_{P,R} T_b^* + \Delta H_{f,R}^\circ) \tag{18}$$

at $r = 0$:

$$\frac{\partial T}{\partial r} = 0 \tag{19}$$

at $r = r_s$:

$$\left.\frac{\partial T_s}{\partial r}\right|_{r_s} = \begin{cases} -\dfrac{1}{\lambda_s} h_{\text{eff}_{2_\ell}}(t, z)[T_s(t, r_s, z) - \bar{T}_m(t)] \\ = \dfrac{\dot{q}_{m1}}{\lambda_s} \quad (\text{for } 0 < z \leq h_\ell) \end{cases} \tag{20a}$$

$$-\frac{1}{\lambda_s} h_{\text{eff}_{2_g}}(t, z)[T_s(t, r_s, z) - T_g] \quad (\text{for } h_\ell < z \leq L_s) \tag{20b}$$

The boundary conditions for LOVA propellant in Time period II for Case (*a*) can be written as follows:

at $z = -\infty$:

$$T_p = T_{pi} \tag{21}$$

at $z = -L_m$ *and* $r \leq r_m$:

$$T_p = T_{\text{melt}} \tag{22}$$

at $r = \infty$:

$$T_p = T_{pi} \tag{23}$$

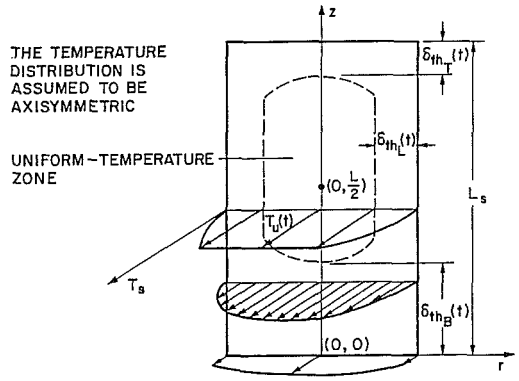

Fig. 4 Temperature distributions in a cylindrical shaped spall particle

at $r = r_m$ *and* $z \le h_\ell$:

$$-\lambda_{pr}\frac{\partial T_p}{\partial r} = \dot{q}''_{m2} \quad (\text{if } v_{mr} = 0)$$
$$T_p = T_{\text{melt}} \quad (\text{if } v_{mr} > 0) \tag{24}$$

at $r = r_m$ *and* $h_\ell < z$:

$$-\lambda_{pr}\frac{\partial T_p}{\partial r} = \dot{q}''_{\text{rad}_p} + h_{c2}(T_g - T_{ps}) \quad (\text{if } v_{mr} = 0) \tag{25}$$
$$T_p = T_{\text{melt}} \quad (\text{if } v_{mr} > 0)$$

at $z = h_p$ *and* $r > r_m$:

$$-\lambda_{pr}\frac{\partial T_p}{\partial z} = h_{c3}(T_{ps} - T_\infty) - \dot{q}''_{\text{rad}_p} \tag{26}$$

The boundary conditions for the spall particle and LOVA propellant in Time Period II for Cases (*b*), (*c*), and (*d*) can be written in a similar manner and are omitted here to save space.

Simplifications of the Mathematical Model. Although the above set of governing equations can be solved with their boundary and initial conditions, together with a set of adequate heat transfer correlations, the calculation of the above PDE model is extremely time-consuming. In order to bypass this difficulty in solving many coupled partial differential equations (PDEs) and intricate boundary conditions, the theoretical model has been recast into a set of ordinary differential equations (ODEs) using Goodman's (1964) integral method.

In general, the instantaneous temperature distribution inside the spall particle with a cylindrical shape is a function of radial and axial positions. During the interval of contact with the LOVA propellant, the heat fluxes across the boundaries of the spall particle are high enough to generate nonnegligible temperature gradients inside the particle. Therefore, lumped-parameter analysis cannot be used for this situation. To obtain approximate solution of the HFCI model based upon PDE formulation, the temperature profile is assumed to obey the following polynomial form (see Fig. 4):

$$\frac{T_s(t, r, z)}{T_u(t)} = [1 + C_1(t)r^2 + C_2(t)r^3] \cdot [1 + C_3(t)(z - z_m) + C_4(t)(z - z_m)^2 + C_5(t)(z - z_m)^3 + C_6(t)(z - z_m)^4] \tag{27}$$

where $T_u(t)$ represents either the temperature of the uniform-temperature zone in the spall or the maximum instantaneous temperature when the uniform-temperature zone shrinks to zero. The height z_m represents either that of the midpoint of the uniform-temperature zone or that of the maximum temperature point. Z_m can be calculated from the following equations:

$$z_m = \begin{cases} \frac{1}{2}[\delta_{th_B} + (L_s - \delta_{th_T})] & \text{for finite uniform-temperature zone} \quad (28a) \\ \delta_{th_B} & \text{after uniform-temperature zone disappears} \quad (28b) \end{cases}$$

$C_1(t)$ through $C_6(t)$ are time-dependent coefficients to be determined by various boundary and smooth conditions discussed later.

Following Goodman's (1964) integral method, by integrating equation (1) twice with respect to z and r and applying the polynomial form of equation (27), the PDE for the spall particle is reduced to

$$\frac{dP(t)}{dt} = r_s^2 \alpha_s T_u(t) S(t) \tag{29}$$

where the parameters $P(t)$ and $S(t)$ are defined as

$$P(t) \equiv \frac{1}{\pi C_s \rho_s}[\theta_B(t) + \theta_T(t) + \theta_L(t) + \theta_u(t)] \tag{30}$$

$$S(t) \equiv \frac{1}{r_s^2}\{r_s^2 + \frac{C_1}{2}[r_s^4 - (r_s - \delta_{th_L})^4] + \frac{2}{5}C_2 \cdot [r_s^5 - (r_s - \delta_{th_L})^5]\} \cdot \{2C_4 L_s + 3C_5[(L_s - z_m)^2 - z_m^2] + 4C_6[(L_s - z_m)^3 + z_m^3]\} + 2(2C_1 + 3C_2 r_s) \cdot \{L_s + \frac{C_3}{2}[(L_s - z_m)^2 - z_m^2] + \frac{C_4}{3}[(L_s - z_m)^3 - z_m^3] + \frac{C_5}{4}[(L_s - z_m)^4 - z_m^4] + \frac{C_6}{5}[(L_s - z_m)^5 - z_m^5]\} \tag{31}$$

In equation (30), θ_B, θ_T, and θ_L represent the thermal energy content in the bottom, top, and lateral thermal penetrated zone of the spall particle; their mathematical definitions are as follows:

$$\theta_B(t) = \int_0^{\delta_{th_B}(t)} \int_0^{r_s} C_s \rho_s T_s 2\pi r dr dz \tag{32}$$

$$\theta_T(t) = \int_{L_s - \delta_{th_T}(t)}^{L_s} \int_0^{r_s} C_s \rho_s T_s 2\pi r dr dz \tag{33}$$

$$\theta_L(t) = \int_{\delta_{th_B}(t)}^{L_s - \delta_{th_T}(t)} \int_{r_s - \delta_{th_L}(t)}^{r_s} C_s \rho_s T_s 2\pi r dr dz \tag{34}$$

The thermal energy storage in the uniform temperature zone, $\theta_u(t)$, can be expressed as

$$\theta_u(t) = \int_{\delta_{th_B}(t)}^{L_s - \delta_{th_T}(t)} \int_{r_s - \delta_{th_L}(t)}^{r_s} C_s \rho_s T_s 2\pi r dr dz \tag{35}$$

The above four θs are expressed in terms of thermal wave penetration depths and constants C_1 through C_6. These six constants are solved from a set of coupled linear algebraic equations obtained from the boundary and smooth conditions. Their explicit forms are given by Kuo et al. (1985).

To evaluate the thicknesses of the thermal waves near the top and bottom of the spall particle, the following equations, deduced from the expression obtained by Goodman (1964), can be used:

$$\delta_{th_T}(t) = \sqrt{6\alpha}\left\{\frac{1}{h_{\text{eff}_{1C}}(t)(T_{s_{TC}} - T_g)} \cdot \int_0^t h_{\text{eff}_{1C}}(t)(T_{s_{TC}} - T_g)dt\right\}^{1/2} \tag{36a}$$

$$\delta_{th_B}(t) = \sqrt{6\alpha}\left[\frac{1}{\dot{q}''_{\text{spall}_1}(t)}\int_0^t \dot{q}''_{\text{spall}_1}(t)dt\right]^{1/2} \tag{36b}$$

where the subscript TC stands for top center location of the spall particle. The thickness of the thermal wave penetration depth in the lateral direction can also be given in a similar form.

Using a third-degree polynomial in z^* to represent the temperature profile in the solid propellant and integrating equation (2) with respect to z^*, the time variation of the thermal wave penetration depth (the thickness of the heated zone), δ_{pr}, can be determined from

$$\frac{d\delta_{pr}^2(t)}{dt} = 6\alpha_{pr} + 2v_m(t)\delta_{pr}(t) \tag{37}$$

The initial condition for δ_{pr} is

$$\delta_{pr}(0) = 0 \tag{38}$$

After $\delta_{pr}(t)$ is solved, $\dot{q}''_{pr}(t)$ can be calculated from

$$\dot{q}''_{pr}(t) = 3\lambda_p \frac{(T_{\text{melt}} - T_{pi})}{\delta_{pr}(t)} \tag{39}$$

Heat Transfer Correlations Employed in the Theoretical Model. To complete the model formulation, the following heat transfer correlations are presented as a part of physical input to the model.

a. Heat Transfer at the Base of Spall Particle. The rates of heat transfer from the spall particle base to the liquid and gas bubbles in the foam layer ($\dot{q}''_{\text{liq}}$ and $\dot{q}''_{\text{gas}}$) can be evaluated from

$$\dot{q}''_{\text{liq}} = h_{\text{base}}(\bar{T}_{SB} - T_{\ell_1}) \tag{40}$$

$$\dot{q}''_{\text{gas}} = h_{\text{base}}(\bar{T}_{SB} - T_{g_1}) \tag{41}$$

When the average temperature at the base of the spall particle ($\bar{T}_{SB}$) is higher than the saturation temperature of the liquid melt, the boiling heat transfer correlation should be used. According to the empirical correlations of Jakob and Hawkins (1957) and Holman (1977), h_{base} is related to the temperature difference between $\bar{T}_{SB}$ and saturation temperature T_{sat} by the following equation:

$$h_{\text{base}} = \begin{cases} 1042(\bar{T}_{SB} - T_{\text{sat}})^{1/3} & \text{if } \dot{q}''_{\text{spall}} < 15{,}770 \\ 5.56(\bar{T}_{SB} - T_{\text{sat}})^3 & \text{if } 15{,}770 < \dot{q}''_{\text{spall}} < 2.365 \times 10^5 \end{cases} \tag{42}$$

This equation was developed from boiling heat transfer data of water at one atmospheric pressure on a horizontal plate. Strictly speaking, this correlation is not completely suitable for the downward heating from the spall particle base to the foam layer, but in the absence of better correlations, it is temporarily adopted and used with caution. According to Cheung (1985), the boiling heat transfer for the downward-heating case may follow the same temperature-difference dependence, but the constants could be approximately two to three times higher than the upward heating. In view of the confined space available between the base of the spall particle and the solid propellant, the gas bubble may be trapped momentarily in this foam layer region. If this happens, the material in the foam layer could accumulate thermal energy and reduce the rate of boiling heat transfer. Because the downward-heating effect may compensate for the confined-space effect, equation (42) is used at present for the simulation of melting and evaporation of ice to be discussed in a later section.

After the base temperature of the spall particle has dropped below the boiling temperature, gas bubbles could still be generated from the spall surface (due to transient heating of the foam layer) until $\dot{q}''_{\text{spall}}$ decreases to the level of $\dot{q}''_{\text{min}}$. $\dot{q}''_{\text{min}}$ can be calculated from the following equation based upon the studies of Chang (1959), Zuber (1959), and Lienhard and Dhir (1980):

$$\dot{q}''_{\text{min}} = 0.177\rho_g h_{fg}\left[\frac{\sigma_s g(\rho_\ell - \rho_g)}{(\rho_\ell - \rho_g)^2}\right]^{1/4} \tag{43}$$

where g is the gravitational acceleration. The average velocity of bubbles leaving the heated surface area is

$$v_b = 0.59[g\sigma_s(\rho_\ell - \rho_g)/\rho_\ell^2]^{1/4} \tag{44}$$

which is based upon the relationship reported by Rohsenow and Choi (1969). The average bubble diameter at detachment from the heating surface, based upon the empirical formula of Fritz (1935), is

$$D_b = C_d\beta\sqrt{\frac{2\sigma_s}{g(\rho_\ell - \rho_g)}} \tag{45}$$

where β is approximately 40 deg and $C_d = 0.0148$ for water in the ice melting and evaporation simulation.

The void fraction at the base of the spall particle, ψ_B, can be evaluated from the following approximation:

$$\psi_B = \frac{1}{\pi}\tan^{-1}\left[a\left(\frac{\dot{q}''_{\text{spall}}}{\dot{q}''_{\text{min}}}\right) - b\right] + \frac{1}{2} \tag{46}$$

where a is a stretching constant in the order of one, and b is a specific heat-flux ratio at which ψ_B versus $\dot{q}''_{\text{spall}}/\dot{q}''_{\text{min}}$ has a point of inflection. This equation is formulated based upon the fact that it satisfies the limiting case of film boiling, which requires that $\psi_B \to 1$ when $\dot{q}''_{\text{spall}} >> \dot{q}''_{\text{min}}$. It also satisfies the condition that when $\dot{q}''_{\text{spall}} \cong \dot{q}''_{\text{min}}$, ψ_B should approach zero.

When $\bar{T}_{SB}$ is lower than the saturation temperature of the liquid melt, the heat transfer coefficient between the fluid in the foam layer and the bottom surface of the spall particle can be evaluated from the following Kercher's empirical correlation, taken from the General Electric Heat Transfer Data Book (1979):

$$h_{\text{base}} = \frac{C\phi_1\phi_2\lambda_{\text{mixture}}}{D_b}\left(\frac{\rho_g v_b D_b}{\mu_g}\right)^m \left(\frac{L_m}{D_b}\right)^{0.091} (\text{Pr}_g)^{1/3} \tag{47}$$

where λ_{mixture} is calculated from

$$\lambda_{\text{mixture}} = \psi_B\lambda_{\text{vapor}} + (1 - \psi_B)\lambda_{\text{liq}} \tag{48}$$

ϕ_1 and ϕ_2 of equation (47) are correlation factors that depend upon the ratio of bubble separation distance (X_n), bubble diameter, and the Reynolds number ($\equiv \rho_g v_b D_b/\mu_g$). The above equation was initially developed for gases flowing through an array of circular holes of a porous plate, located at the top of a horizontal gap. Numerous jets impinge on a bottom horizontal plate located a small distance from the top porous plate. The bubbles generated at the base of the spall can be regarded as gases injected downward through a horizontal porous plate. Even though the locations of bubbles vary from time to time, as long as the bubble sizes and separation distances are properly calculated, the flow agitation and heat transfer processes are quite similar to those of a porous plate. The average separation distance between bubbles is calculated from the bubble size and the void fraction in the foam layer by the following equation:

$$X_n = 0.5\sqrt{\frac{\pi}{\psi_B}}D_b \tag{49}$$

The heat transfer coefficient given in equation (47) is used to determine the energy fluxes, $\dot{q}''_{\text{gas}}$ and $\dot{q}''_{\text{liq}}$, until $\bar{T}_{SB}$ decreases to T_{melt}.

b. Heat Transfer at the Interface Between Liquid Melt and Solid Material. The heat transfer process in the foam layer at the interface with solid material is governed by the condensation of bubbles at the interface. Levenspiel's correlation of steam-bubble condensation (Soo, 1967) has been adopted to calculate the instantaneous heat transfer coefficient and the heat flux $\dot{q}''_{\text{liq-solid}}$. The heat transfer coefficient can be written as

$$h_c(t) = 3.54D_{b_{\text{eff}}}(t)\rho_g(t)h_{fg} \tag{50}$$

To calculate adequately the values of $h_c(t)$, the effective bub-

ble diameter is used in the above equation to replace the instantaneous diameter of a single bubble. During the condensation process, the rate of decrease of bubble diameter can be described by the followng equation (Soo, 1967):

$$\frac{d\ln D_b(t)}{Dt} = 7.08[T_{pr}(t, 0) - T_{g_1}(t)] \tag{51}$$

Both the propellant or ice surface temperature and the bulk temperature of the gas bubble are functions of time. However, experimental evidence indicates that the bubble lifetime is much shorter than the foam-layer action time; hence, T_{g_1} can be treated as a constant in estimating single bubble lifetime. Setting the propellent surface temperature equal to T_{melt}, equation (51) can be integrated with respect to time to give

$$D_b(t) = D_b(0)\exp[-7.08(T_{g_1} - T_{\text{melt}})t] \tag{52}$$

Using the same functional form, the effective bubble diameter can be expressed as

$$D_{b_{\text{eff}}}(t) = D_b \exp[-kt] \tag{53}$$

where D_b (the average diameter at detachment) is calculated from equation (45) and k^{-1} represents the characteristic decay time. The physical meaning of the effective bubble diameter is associated with the averaged void fraction of the surface area due to bubble impingement on the propellant surface. As the spall particle sinks into the ice block, the particle is cooled by transferring the heat to its adjacent material. The boiling process becomes less intense and generates fewer gas bubbles to impinge on the ice block. Therefore, the effective diameter decreases with respect to time. The k value used in equation (53) is on the order of 0.2 s^{-1}. To account for the above effect caused by the reduction of bubble number density in terms of effective bubble diameter, the decay time (k^{-1}) used in the computation is considerably longer than the bubble lifetime.

c. Heat Transfer at the Top and Lateral Surfaces of the Spall Particle. The top surface of a spall particle can be considered as a horizontal plate where the heat transfer mechanism is due mainly to natural convection (McAdams, 1954; Goldstein et al., 1973). The Nusselt number is expressed as a function of the Rayleigh number in the commonly used McAdams' (1954) correlation.

The lateral surface of the spall particle in contact with the foam layer experiences natural convection or conduction since the velocity of the melt layer is quite small. On the other hand, the lateral surface of the spall particle that is exposed to the air experiences forced convection due to the flow of pyrolyzing gaseous species above the melt layer. In order to consider these two different mechanisms, it is necessary to determine the different heat transfer coefficients caused by forced and free convection.

For laminar flow, the conventional correlation for parallel external flow, along the axis of a cylinder, is used to relate the local Nusselt number to the local Reynolds and Prandtl numbers (Holman, 1972). For turbulent flows, Schlichting's (1968) local friction coefficient is used to relate Reynolds numbers to the local Nusselt number.

Application of the HFCI Model for Simulating the Melting and Evaporation of Ice Upon Direct Contact With a Hot Element. In order to verify the theoretical model developed for predicting HFCI phenomena, a set of input parameters and functions is required. At present, although some measurements are being conducted by Miller (1986), many critical parameters for LOVA propellants are not fully characterized. In view of this situation, experiments must be conducted in a simpler system to simulate HFCI phenomena.

One obvious way to simulate the conductive heating, melting, and evaporating processes of HFCI tests is to heat an ice block with a hot metal rod. In such an experiment, uncertainties in chemical kinetics in the melt layer are avoided, and data from experiments can be used to validate the theoretical model under the limiting condition without involving chemical reactions. The reason ice was selected for melting and evaporation simulation is due to the well-known boiling heat transfer characteristics of water, as well as its thermal properties. The ice cube is also readily available for experiments.

The regression velocity of the ice surface, v_m, is computed from the heat-flux balance at the interface between the foam layer and ice by the following equation:

$$v_m = \frac{\dot{q}''_{\text{liq-solid}} - \dot{q}''_{pr}}{\rho_{pr}[(C_{pr} - C_{p\ell})T^*_{\text{melt}} + \Delta H^\circ_{f,pr} - \Delta H^\circ_{f,\ell}]} \tag{54}$$

Major and minor unknowns, together with the numbers of equations for their determination, are listed in Tables 1 and 2.

Table 1 Major unknowns and equations

Region	Unknown	Equation
Spall	T_S	(27)
Particle	P	(29)
	T_u	(30),(31-35)
Foam	Y_R	=0
Layer	T_{g1}	(10)
	T_{ℓ_1}	(11)
	v_m	(54)
	Ψ	(4)
Ice	δ_{pr}	(37)

Table 2 Minor unknowns and equations

Region	Unknown	Equation	Unknown	Equation
Spall Particle	Θ_B	(32)	Θ_L	(34)
	Θ_T	(33)	Θ_u	(35)
	δ_{thT}	$(36)_a$	δ_{thB}	$(36)_b$
	δ_{thL}	$(36)_a$ & $(36)_b$	z_m	$(28)_a$ or $(28)_b$
Foam Layer	$\Delta H^\circ_{f,g}$	(12)	D_b	(45)
	C_{vg}	(13)	C_{pg}	(14)
	h_{base}	(42) or (47)	$\dot{q}''_{liq}$	(40)
	h_c	(50)	$\dot{q}''_{gas}$	(41)
			Ψ_B	(46)
Ice	$\dot{q}''_{pr}$	(39)	----	----

Test Setup and Results for Ice Melting and Evaporation Experiments

An ice-melting and evaporating experiment has been devised and conducted. To be compatible with the theoretical model, a steel cylindrical rod with a diameter of 1.27 cm and a length of 2.54 cm is connected at one end to a 10.16-cm-long guiding steel rod with a diameter of 0.3175 cm. Four copper-constantan thermocouples with bead sizes of 0.025 cm and wire diameters of 0.0075 cm were soldered to different locations of the heating element (shown in Fig. 5). In these tests,

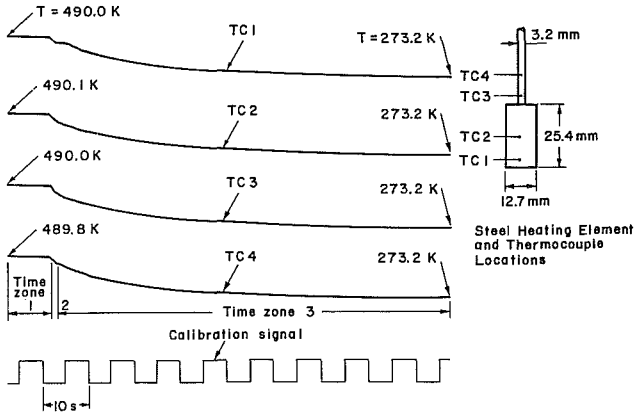

Fig. 5 Measured temperature-time traces from ice melting and evaporating experiments

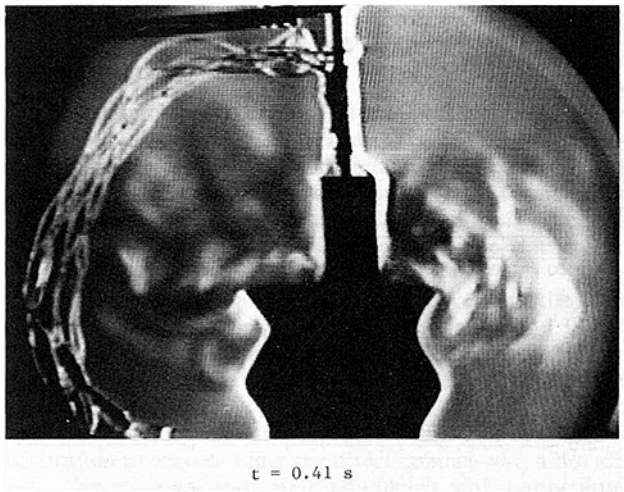

Fig. 6 A color Schlieren photograph of ice-melting and evaporating experiment

the heating element was heated inside an oven with preselected temperature. The heating element was placed on top of an ice cube, and the temperature–time variations at different locations were recorded. A typical set of recorded temperature–time traces is shown in Fig. 5.

In addition to temperature–time measurements, a video movie camera was used to record the ice melting and evaporating phenomena. The instantaneous position of the heating element was recorded on the video camera. The displacement and velocity of the heating element were determined by reading the instantaneous top surface location of the heating element against a stationary scale and the digital time counter on the video screen. Time variations of the measured velocity of the heating element are compared with theoretical results in a later section.

In order to observe the flow pattern of the gas and steam surrounding the heating element, a Schlieren optical system (Settles, 1970; Kuo et al., 1985) was used. A typical color Schlieren photograph obtained from an ice-melting and evaporating experiment is shown in Fig. 6. Several interesting observations are made from the video and temperature records of these experiments:

1 Although all four temperature–time traces in Fig. 5 showed similar variations, there are some differences among these traces. The temperatures on the main body of the heating element decay at a slower rate than those on the guiding rod. This is due to the fact that the surface area per unit volume is much larger on the guiding rod than that of the main body.

2 Based upon the slope changes of the temperature decay, the overall process can be divided into the three time zones shown in Fig. 5. In the initial time zone, the temperature of the heating element decays slowly with time since the element was taken from the oven and cooled by natural convection in air and radiation to the surrounding. A small amount of energy is lost from the guiding rod to a room-temperature clamp by conduction. In the second time zone, a significant amount of steam was generated at the contact zone of the heating element and the ice. The flow around the cylindrical rod was highly turbulent. Associated with steam generation, the temperatures at all thermocouple locations decrease drastically in 1.2 s, as shown in Fig. 5. In the last time zone, steam generation is gradually replaced by ice melting and slow sinking of the heating element into the ice block. Eventually, the heating element stopped at a terminal position inside the ice block.

3 The downward velocity of the heating element was highest upon initial contact with the ice block, and then decayed monotonically to zero velocity.

4 From the color Schlieren photographs, one can see clearly that the steam-jet velocity is mostly in the radial direction at the initial time interval. The steam jet then changed from radial outward direction to vertical upward direction. Associated with steam-jet action, the flow field surrounding the cylinder is highly turbulent. Following the decay of steam generation, the flow became laminar at the later stage.

Table 3 Input data used in the ice-melting and evaporation simulation

Region	Parameter	Value	Parameter	Value
Spall Particle	r_s	0.635×10^{-2}	λ_s	6.39×10^{-1}
	L_s	2.54×10^{-2}	C_s	4.34×10^{2}
	ρ_s	7.83×10^{3}	T_{si}	4.90×10^{2}
	ρ_ℓ	9.87×10^{2}	λ_ℓ	4.52×10^{-2}
Foam Layer	$C_{p\ell}$	4.18×10^{3}	$\Delta H^\circ_{f,\ell}$	-1.59×10^{7}
	C_{pg}	1.87×10^{3}	$\Delta H^\circ_{f,g}$	-1.34×10^{7}
	C_{vg}	1.41×10^{3}		
Ice	C_{pr}	2.04×10^{3}	λ_{pr}	2.21
	ρ_{pr}	9.13×10^{2}	$\Delta H^\circ_{f,pr}$	-1.55×10^{7}

Comparison of Numerical Results With Test Data of Ice Melting and Evaporation

To verify partially the HFCI model, numerical solutions were compared with experimental data obtained from an ice-melting and evaporating experiment. Input data for this numerical simulation are given in Table 3. Figure 7 presents a comparison of the calculated sinking velocity of the spall particle with the measured data. It is quite obvious that agreement between calculated results and measured data is reasonably close. The trend of sharp decline followed by a much slower rate of sinking is exhibited in both theoretical and experimental results. Figure 8 shows the comparison of calculated spall particle trajectory with experimental data. The agreement is

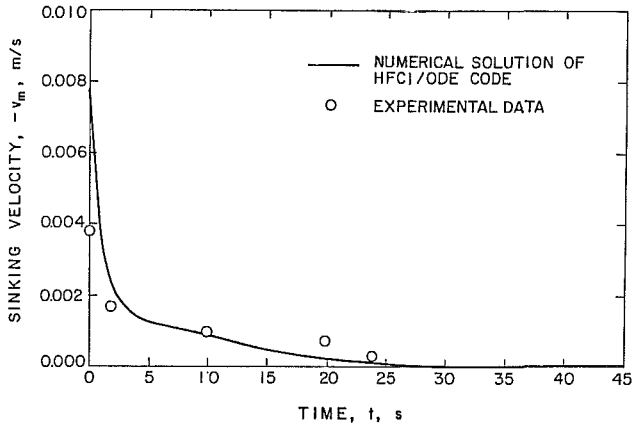

Fig. 7 Comparison of calculated sinking velocity of the spall particle with the measured data obtained from ice-melting and evaporating experiment

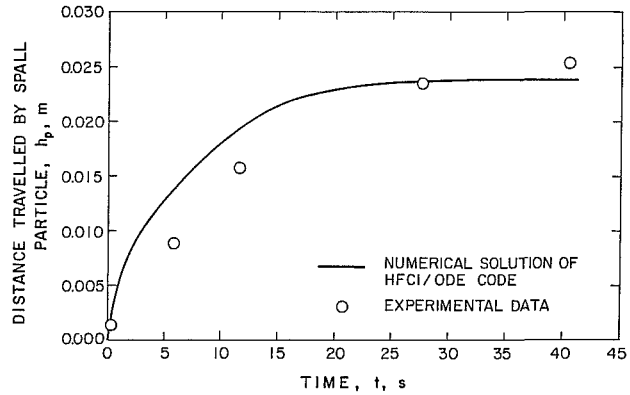

Fig. 8 Comparison of calculated spall particle trajectory with data obtained from ice-melting and evaporating experiment

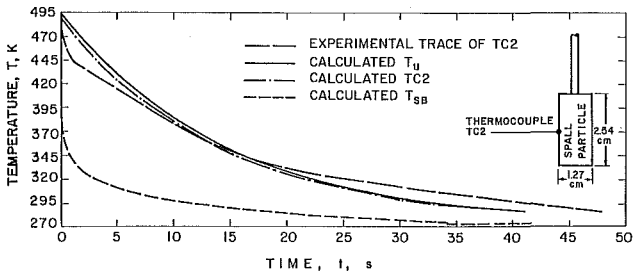

Fig. 9 Comparison of the measured temperature-time trace of *TC2* with calculated temperature—time traces at the spall-particle base, *TC2*, and maximum temperature locations of the spall particle

not extremely close; however, the calculated trend of traveling distance variation with time and the magnitude of h_p are not far from the measured data.

From the comparison of the calculated and measured temperature–time traces at the thermocouple *TC2* location shown in Fig. 9, it is evident that the two traces are very close. In the same figure, calculated traces for the average temperature at the base of the spall particle ($\bar{T}_{SB}$) and the maximum spall particle temperature (T_u) are plotted. It is interesting to note that the temperature difference between T_u and $\bar{T}_{SB}$ is much larger than that between T_u and *TC2*. This implies that a significant temperature gradient exists near the base of the spall particle because of the high heat flux leaving the spall particle base region. The temperature gradient in the radial direction in the middle of the cylindrical spall particle is nearly negligible due to relatively low radial heat fluxes and high thermal conductivity of the material.

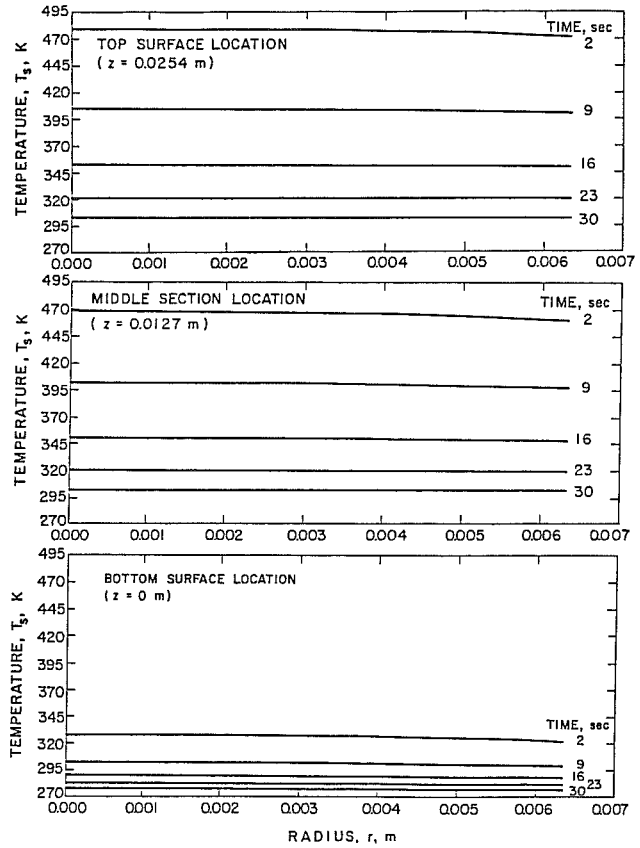

Fig. 10 Calculated radial temperature profiles at the top surface, middle section, and bottom surface locations of the spall particle for various times

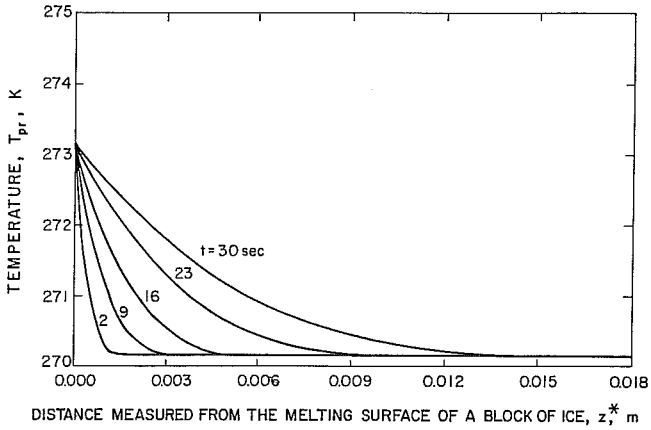

Fig. 11 Calculated temperature profiles in the ice block at various times

Figure 10 shows the calculated radial temperature profiles at the top surface, middle section, and bottom surface of the spall particle for various times. Most of the profiles are quite flat, but there is some gradient in the radial direction, especially during the early part of the event. Calculated temperature profiles in the ice are shown in Fig. 11. It is clear that the thermal penetration depth increases monotonically with respect to time, while the surface temperature is maintained at a fixed value.

The calculated time variations of $\dot{q}''_{\text{spall}}$ and $\dot{q}''_{pr}$ are shown in Fig. 12. It is useful to point out that $\dot{q}''_{\text{spall}}$ is significantly higher than $\dot{q}''_{pr}$ for a long period of time. This indicates that a substantial amount of energy is carried away by evaporation of liquid melt in the foam layer. The sharp declines of $\dot{q}''_{\text{spall}}$

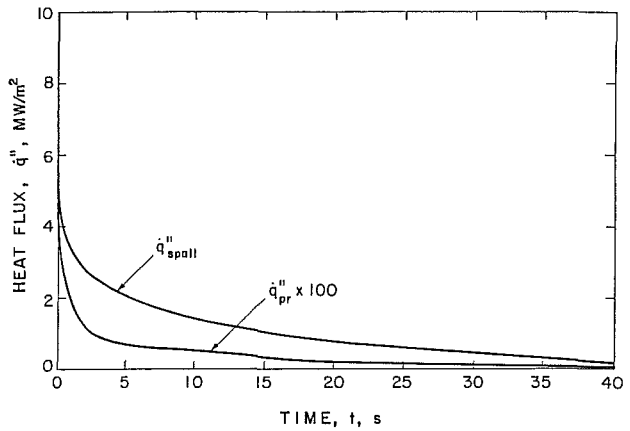

Fig. 12 Calculated time variation of heat fluxes $\dot{q}''_{spall}$ and $\dot{q}''_{pr}$

and $\dot{q}''_{pr}$ in the initial time period dictate the rapid decrease of sinking velocity with respect to time.

Summary and Conclusions

1 A comprehensive theoretical model for simulating hot fragment conductive ignition processes of LOVA propellants has been formulated. This model simulates: heat transfer processes between the spall particle and propellant; formation of the liquid-melt or foam layer, propellant pyrolysis processes; displacement of the hot spall particle; and propellant ignition or quenching of the spall particle.

2 The partial differential equations governing the transient heat transfer processes in the spall particle and LOVA propellant have been successfully converted to a set of ordinary differential equations. This leads to a major reduction in computational time.

3 The HFCI model has been applied to the ice melting and evaporation processes under the direct contact with a hot element. Experimental tests were conducted with temperature measurements and flow visualization using a color Schlieren system.

4 Good agreement between calculated results and test data of ice-melting and evaporation experiments shows that the HFCI model is capable of predicting the major heat- and mass-transfer characteristics in the melting and evaporation of a solid with known thermal properties and boiling characteristics of its liquid melt.

5 During the initial contact between the spall particle and ice block, a strong steam jet in the radial direction is generated. As time progresses, the steam jet changes from the radial to the vertical direction as its strength decays. A substantial amount of energy is carried away by the steam jet generated from evaporation of liquid melt in the foam layer.

6 The input parameters and types of correlations required for studying the HFCI processes of a given solid propellant can be identified from the theoretical model presented in this paper. The full validation of the HFCI model cannot be performed until a set of input parameters and correlations become available.

Acknowledgments

This work was performed under Contract No. DAAK11-83-C-0015, sponsored by the Applied Ballistics Branch of the U. S. Army Ballistic Research Laboratory under the support and encouragement of Dr. Joseph J. Rocchio and Mr. Norman Gerri. The authors would like to thank Dr. M. Kumar for his participation in the early stage of this research.

References

Anderson, W. H., Brown, R. E., and Louie, N. A., 1972, *Proceedings of the 9th JANNAF Combustion Meeting*, CPIA Publication 231, pp. 67–82.

Caveny, L. H., Summerfield, M., Strittmater, R. C., and Barrows, A. W., 1973, "Solid Propellant Flammability Including Ignitability and Combustion Limits," CPIA Publication 243, Vol. III, pp. 133–155.

Chang, Y. P., 1959, "A Theoretical Analysis of Heat Transfer in Natural Convection and in Boiling," *Trans. ASME*, Vol. 79, p. 1501.

Cheung, F. B., 1985, The Pennsylvania State University, University Park, PA, Private Communication.

Fritz, H. K., 1935, *Physik*, pp. 36, 379.

General Electric Heat Transfer Data Book, 1979.

Gol'dshleger, U. I., Barzykin, V. V., and Ivleva, T. P., 1973, *Combustion, Explosion and Shock Waves*, Vol. 9, No. 5, pp. 642–647.

Gol'dshleger, U. I., Pribytkova, K. V., and Barzykin, V. V., 1973, *Combustion, Explosion and Shock Waves*, Vol. 9, No. 1, pp. 99–102.

Goldstein, R. J., Sparrow, E. M., and Jones, D. C., 1973, "Natural Convection Mass Transfer Adjacent to Horizontal Plates," *International Journal of Heat and Mass Transfer*, Vol. 16, p. 1025.

Goodman, T. R., 1964, "Application of Integral Methods to Transient Nonlinear Heat Transfer," *Advances in Heat Transfer*, T. F. Irvine and J. P. Hartnett, Jr., eds., Vol. 1.

Grossman, E. D., and Rele, P. J., 1974, "Ignition of Cellulose Nitrate by High Velocity Particles," *Combustion Science and Technology*, Vol. 9, pp. 55–60.

Holman, J. P., 1972, *Heat Transfer*, 3rd ed., McGraw-Hill, New York, Chap. 5.

Holman, J. P., 1977, *Heat Transfer*, 4th ed., McGraw-Hill, New York, Chap. 9.

Jakob, M., and Hawkins, G., 1957, *Elements of Heat Transfer*, 3rd ed., Wiley, New York.

Kirshenbaum, M. S., Avrami, L., and Strauss, B., 1983, "Sensitivity Characterization of Low Vulnerability (LOVA) Propellants," U.S. Army AR-RADCOM Technical Report, ARLCD-TR-83005.

Kuo, K. K., Hsieh, W. H., and Hsieh, K. C., 1985, *Eighth Quarterly Progress Report* to Army Ballistic Research Laboratory, Contract No. DAAK11-83-C-0015.

Kuo, K. K., Hsieh, W. H., Hsieh, K. C., and Kumar, M., 1985, "A Comprehensive Model for Simulating Hot Fragment Conductive Ignition of Low Vulnerability Ammunition Propellant," Scientific Report, Contract No. DAAK-11-83-C-0015.

Law, H. C., and Rocchio, J. J., 1981, *Proceedings of the 18th JANNAF Combustion Meeting*, CPIA Publication No. 347, Vol. 2, pp. 321–334.

Lienhard, J. H., and Dhir, V. K., 1980, "On the Prediction of the Minimum Pool Boiling Heat Flux," ASME JOURNAL OF HEAT TRANSFER, Vol. 102, pp. 457–460.

Linan, A., and Kindelan, M., 1981, *Combustion in Reactive Systems*, J. Ray Bowen et al., eds., Progress in Astronautics and Aeronautics, Vol. 76, pp. 412–426.

McAdams, W. H., 1954, *Heat Transmission*, 3rd ed., McGraw-Hill, New York, Chap. 7.

Miller, M. S., 1986, Army Ballistic Research Laboratory, Aberdeen Proving Ground, MD, Private Communication.

Rohsenow, W. M., and Choi, H. Y., 1969, *Heat Mass and Momentum Transfer*, Prentice-Hall, New York, Chap. 9.

Schlichting, H., 1968, *Boundary Layer Theory*, 6th ed., McGraw-Hill, New York, Chap. 5.

Settles, G. S., 1970, "A Direction-Indicating Color Schlieren System," *AIAA Journal*, Vol. 8, No. 12.

Soo, S. L., 1967, *Fluid Dynamics of Multiphase Systems*, Blaisdell Publishing Company, Waltham, MA, p. 113.

Tyler, B. J., and Jones, D. R., 1981, *Combustion and Flame*, Vol. 42, pp. 147–156.

Vilyunov, V. N., and Kolchin, A. K., *Combustion, Explosion and Shock Waves*, 1966, Vol. 2, No. 3, pp. 61–65.

Wise, S., and Rocchio, J. J., 1981, *Proceedings of the 18th JANNAF Combustion Meeting*, CPIA Publication No. 347, Vol. 2, pp. 305–320.

Wise, S., Rocchio, J. J., and Reeves, H. J., 1980, *Proceedings of the 17th JANNAF Combustion Meeting*, CPIA Publication 329, Vol. 3, pp. 457–475.

Zuber, N., 1959, "Hydrodynamic Aspects of Boiling Heat Transfer," *Physics and Mathematics*, AEC Report No. AECU-4439.

Measurements of the Spectral and Directional Emission From Microgrooved Silicon Surfaces

P. J. Hesketh[1]

B. Gebhart

J. N. Zemel

University of Pennsylvania,
Philadelphia, PA 19104-6390

This paper reports measurements of both the spectral and specular thermal radiation emission characteristics of very regularly microconfigured grooved surfaces in a silicon substrate at 300 and 400°C. The resulting surfaces were phosphorus-doped, to assure the dominance of the emission from the material near the sample surface. The samples had groove depths H *of zero for a reference, to 42 μm, and widths* L = *12.6 to 14 μm. The geometry repeat distance was 22 μm, or 455 grooves per cm. The grooves correspond directly in size to the band of principle emission wavelengths* λ *that arises at these temperature levels. The measurements show strong spectral effects for normal emission, including highly favored frequencies, for* H > λ. *This suggests a cavity "organ pipe" mode of emission. Similar, though modified, effects were found in directional emission, away from the normal. There also were strong polarization effects, with the cross-groove polarization mode dominant. The spectral and specular measurements are compared with calculations of the classical kind, which tacitly assume that* λ << H = *0*(L).

I Introduction

Radiant emission from regular microstructures has, to the best of our knowledge, not been measured before. Radiant emission is just one aspect of the largely unexplored area of the transport of heat from microstructures. In general, the nature of the interaction is often not fully understood when the characteristic length governing the heat transfer process is comparable to the local surface geometry. In radiant emission, when the wavelength λ is the order of the scale of the surface geometry S noncontinuum effects arise.

Radiant emissions from smooth surfaces and macroscopic black bodies are well understood (Planck, 1959; Siegel and Howell, 1981). Measurements and calculations for surfaces with regular geometries, where λ is much less than S, are in close agreement. A recent review is given by Demont et al. (1982). In this region, geometric optics applies. A simplified conventional geometric model will also be developed in this paper, for the microgrooves, as the asymptotic limit of $\lambda/S \to 0$. A model based on interference is inappropriate here as the source is thermally incoherent.

The electromagnetic interactions at a surface with $\lambda \approx S$ is receiving considerable attention and some of the most recent results will be discussed here. Measurements carried out by the authors indicate the presence of anomalies in the normal spectral polarized emittance of deep gratings (Hesketh et al., 1986). Measurements of the directional spectral polarized absorptance at a grating and silvered bi-grating, where the grating depth H is much less than Λ, show other directional anomalies (Inagaki et al., 1983, 1985).

The remainder of previous relevant studies fall into two areas. These are emission from metal surfaces with irregular surface asperities (Lofving, 1980; Edwards, 1965; Kanayama, 1972; Rolling, 1967) and calculations of absorption with deep regular grooves (Glass et al., 1982; Wirgin and Maradudin, 1986, 1987). The irregular surfaces show increased emittance, with more energy at smaller polar angles. The theory of Baltes et al. (1976), for radiation from finite blackbodies, is also relevant to these mechanisms.

II The Present Measurements

The experiments employed (110) crystallographically oriented silicon wafers on which "square wave" gratings were etched to a common repeat distance of 22 μm, see Fig. 1(*A*). Groove depths of 7, 14, and 42 μm were etched using standard photolithography, and a 40 percent wt. solution of KOH at 52°C. The etching duration was chosen to obtain different depths, with an etch rate of roughly 0.3 μm/min. After etching, the microconfigured wafers were spin-coated with a phosphorus-based dopant and heated at 1250°C for 10 h. The resulting peak phosphorus surface concentration was 0.4–0.6 $\times$ $10^{20}/cm^3$, as determined from sheet resistance measurements. This carrier concentration yields an effective radiative skin depth of 1 μm or less, for λ > 5 μm. Auger measurements gave surface phosphorus concentrations of ~ 1 $\times$ $10^{20}/cm^3$. This is in good agreement with the sheet resistance measurements. The heavily doped back surface of the silicon wafers was used as a plane electrical heater element. A schematic drawing of the grating is shown in Fig. 1(*A*), along with the polarizations s and p studied. In Fig. 1(*B*), a scanning electron micrograph of a grating with Λ = 22 μm is shown. The white markers are 10 μm long.

The emissivity measurement system is shown in Fig. 2. The signal-to-noise ratio of the infrared measurements was 100:1 or better. The data were processed with a small data logging system based on a single board Z-80 computer.

The 1.27 × 1.27 cm microconfigured chips were mounted in a specially designed low-thermal-loss holder. More energy was required to reach operating temperature for microconfigured surfaced samples, compared to a similarly treated smooth surface. The blackbody source was constructed from a copper cylinder. Peak blackbody emission at 400°C occurs at 4.3 μm.

The temperature of the source and the temperature difference between it and the sample were monitored throughout each measurement sequence. The 400°C blackbody source, controlled to better than 10m°C, was used as a reference for controlling the silicon sample temperature. Temperature differences between the back of the silicon sample and the blackbody did not exceed 0.5°C. The temperature fluctuations of the sample were typically less than 0.2°C during the course of a measurement.

Measurements were made of the normal spectral emission, at $\theta = 0$. This consisted of logging the normal polarized spec-

[1]Present address: SRI International, Menlo Park, CA 94025.

Contributed by the Heat Transfer Division for publication in the JOURNAL OF HEAT TRANSFER. Manuscript received by the Heat Transfer Division January 6, 1987. Keywords: Radiation, Radiation Interactions.

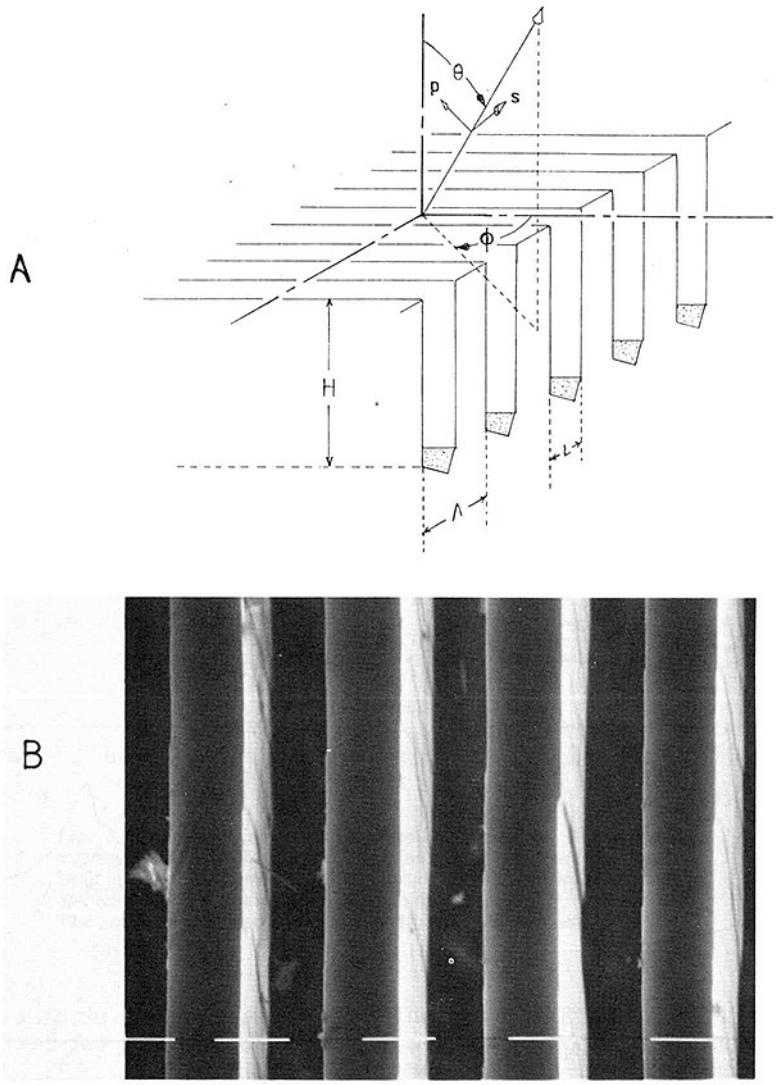

Fig. 1 *(A)* **Schematic drawing of the microgrooves showing: repeat distance Λ; slot width *L*; depth *H*. The direction of emission is given in terms of azimuthal angle ϕ, and polar angle θ. The direction of polarization is indicated by the arrows labeled *s* and *p*. *(B)* Electron micrograph of the microgrooves; Λ – 22, $H = 44\ \mu$m. The marker shown in white is 10 μm wide. The lighter grey areas are the side walls of the silicon and the almost black areas are the bottom of the microgrooves.**

Nomenclature

A = ratio of H to L
f = fraction of rays incident on base
F = diffuse geometric angle factor
H = depth of microgrooves
$I(\overset{S}{p}, \lambda, T, \theta, \phi)$ = specular polarized intensity
N = number of reflections of a ray with the side wall
L = width of microgrooves
M, P, Q, m = integers
R = specular reflectance of cavity excluding diffuse part
T = temperature
S = scale of surface geometry
α_λ = hemispherical spectral absorptance
ϵ = emittance/emissivity
ϵ_λ = hemispherical spectral emissivity
$\epsilon(\overset{S}{p}, \lambda, T)$ = normal spectral emissivity
$\epsilon(\overset{S}{p}, \lambda, T, \theta, \phi)$ = directional spectral polarized emittance
ζ = angle of incidence of a ray with the side wall
θ = polar angle of emittance measurement
λ = wavelength
Λ = repeat distance of microgrooves
ρ = reflectance
ϕ = azimuthal angle of emittance measurement

Subscripts

D = diffuse model
S = specular model

tral intensity of both the 400°C blackbody and silicon sample at normal incidence. The s and p polarized normal spectral emittances $\epsilon(\overset{s}{p}, \lambda, T)$ at 400°C are defined as the ratio of these spectral intensities.

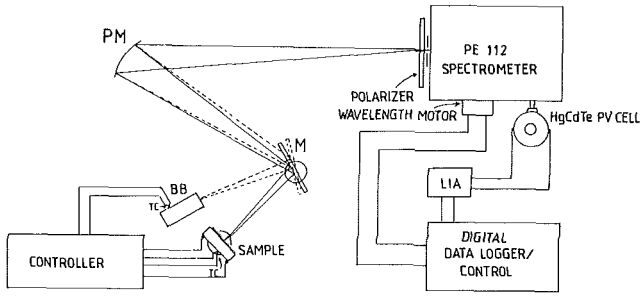

Fig. 2 Schematic layout of the emittance measuring equipment: TC = thermocouple, BB = blackbody, LIA = lock-in amplifier, PE = Perkin-Elmer spectrometer, M = plane mirror, and PM = parabolic mirror

Measurements of the directional spectral emission, at both azimuthal angles $\phi = 0$ deg and 90 deg were made by logging the sample polarized directional spectral intensity $I(\overset{s}{p}, \lambda, T, \theta, \phi)$ as a function of polar angle θ between 0 and 75 deg. The directional emittance was then calculated as the ratio of the measured intensities at θ and $\theta = 0$ deg, and multiplied by the normal spectral emittance. This directional spectral polarized emittance (DSPE) is

$$\epsilon(\overset{s}{p}, \lambda, T, \theta, \phi) = \frac{I(\overset{s}{p}, \lambda, T, \theta, \phi)}{I(\overset{s}{p}, \lambda, T, 0, \phi)} \epsilon(\overset{s}{p}, \lambda, T) = \text{DSPE} \quad (1)$$

The normal spectral polarized emittance corresponds to a polar angle, $\theta = 0$ deg, and an azimuthal angle, $\phi = 90$ deg, as defined in Fig. 1(*A*). For this orientation, the s polarization vector is parallel to the grooves and the p polarization is

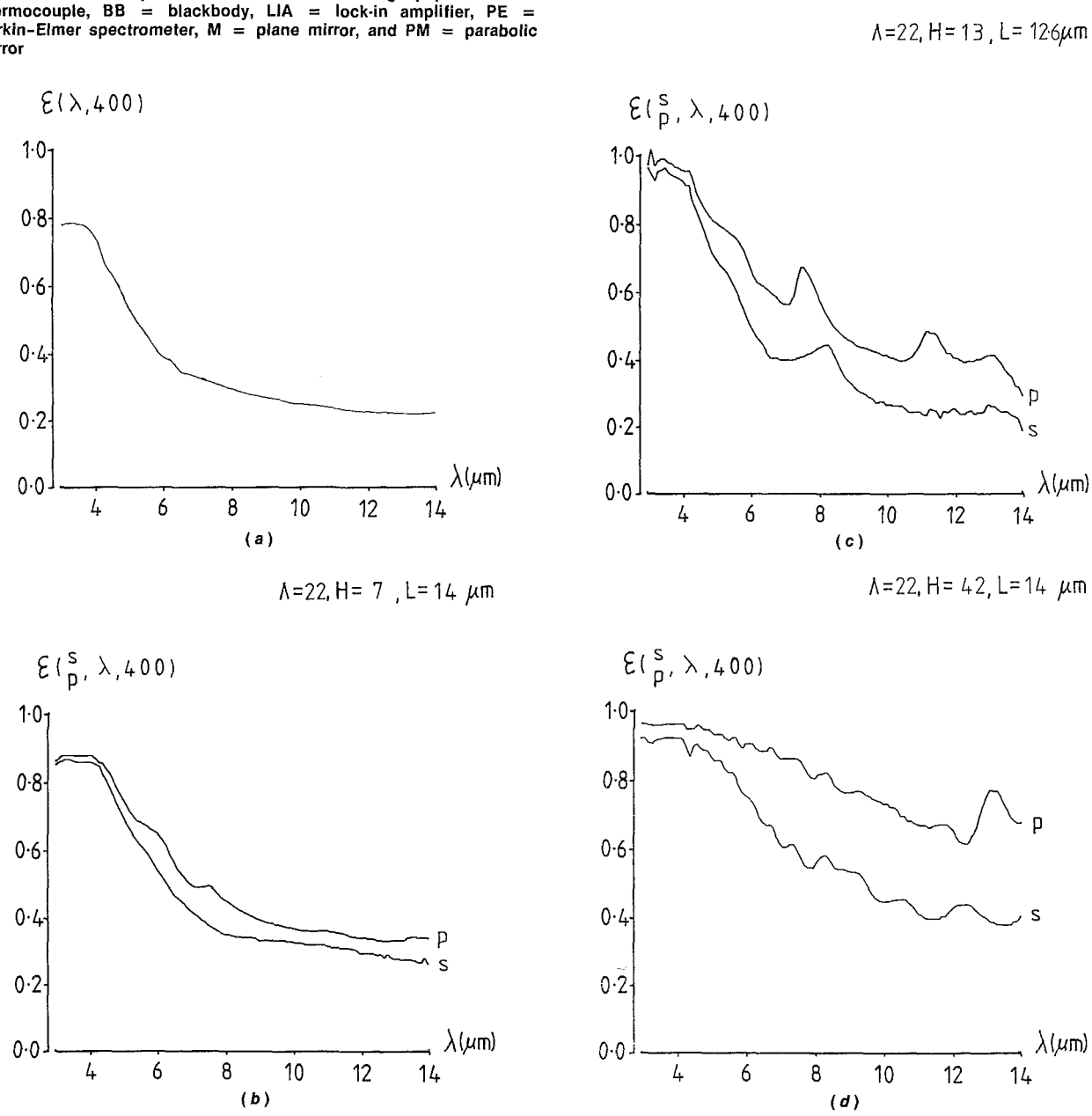

Fig. 3 Normal spectral polarized emittance as a function of wavelength with polarization as a parameter, at 400°C. The smooth surface emissivity is shown in (*A*). All microgrooves had a repeat distance Λ = 22 μm. For (*B*) $H = 7$ μm and $L = 14$ μm, for (*C*) $H = 14$ μm and $L = 12.6$ μm, and for (*D*) $H = 42$ μm and $L = 14$ μm.

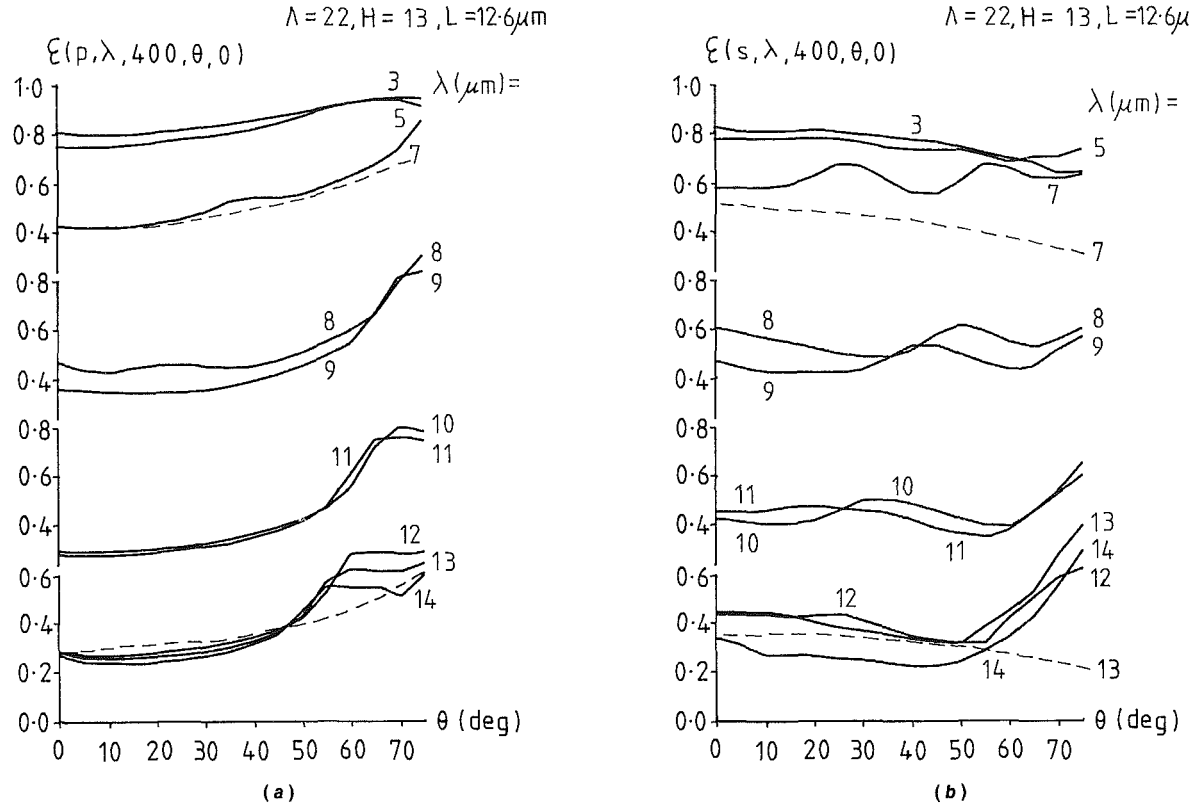

Fig. 4 Directional spectral polarized emittance of doped silicon microgrooves, at 400C and ϕ = 0 deg, as a function of wavelength. The solid lines are experimental data. The dashed lines shown are from the specular geometric calculation. (A) p-polarized Λ = 22, H = 13, and L = 12.6 μm; (B) s-polarized Λ = 22, H = 13, and L = 12.6 μm.

perpendicular to them. Rotating the sample to ϕ = 0 deg reverses the definitions of the s and p polarization vectors, relative to the grooves. The reproducibility of $\epsilon(\overset{s}{p}, \lambda, T, \theta, \phi)$ in these comparable measurements was 2–4 percent from run to run.

The emissivity of a smooth equally doped silicon surface is shown in Fig. 3(*A*). Multiple maxima were found in both $\epsilon(p; \lambda; 400°C)$ and $\epsilon(s; \lambda; 400°C)$ from gratings with H = 7, 14, and 42 μm, as seen in Fig. 3(*B–D*). These peak results from the noncontinuum behavior of the emittance. Other measurements, at 300°C, indicated that temperature had little effect on the magnitude of ϵ and essentially no effect on the position or amplitude of the observed maxima.

The number of maxima is seen to increase as the groove depth increased. These peaks are thought to be due to "organ pipe" like electromagnetic modes, which arise in the microgrooves. (Hesketh et al., 1986). Fewer maxima are seen in the polarized emittance for H = 7 and 13 μm. For all the data the emittance polarized across the grooves exceeds that polarized along the grooves.

The directional spectral polarized emittance data are shown in Figs. 4 and 5, plotted against polar angle θ, with wavelength as the parameter. These four figures are for the s- and p-polarized emission at both azimuthal angles ϕ = 0 and 90 deg. These two angles result in the plane containing the angle θ and the surface normal being parallel and perpendicular to the microgrooves in Figs. 4 and 5, respectively.

For ϕ = 0 the results are shown in Fig. 4. The p-polarized DSPE increases with wavelength and a peak is discerned near θ = 60 deg, for the sample shown. The polar angle at which the peak occurs decreases as the wavelength increases. This is typical of the behavior of the DSPE for these microgrooves. The s-polarized DSPE, in Fig. 4(*B*), increases with angle and several maxima occur at the shorter wavelengths. These are associated with the noncontinuum effects in the electromagnetic radiation (Hesketh, 1987).

In Fig. 5(*A*), for ϕ = 90 deg, the p-polarized DSPE generally increases with polar angle. The s-polarized DSPE, in Fig. 5(*B*) show a broad maximum at roughly θ = 40 deg. In general, the position of this maximum has virtually no dependence on H, Λ, or wavelength.

III Modeling of Emission

The emission was calculated from a purely classical model, that is for the wavelength range much less than H, Λ, and L. This asymptotic limit excludes any quantum or noncontinuum effects. However, it provides a base of comparison for the experimental data. A model based on interference was not available for incoherent thermally excited grating. Therefore, the conventional geometric model of Sparrow and Jonsson (1963) was used.

The model considers the microgrooves as alternating flat surfaces and grooves. The emission properties of the flat material are known from measurements on smooth silicon, as in Fig. 3(*A*). Hence, cavity models developed here need only apply to the grooves. Two kinds of model are used. The first model assumes that all surfaces are diffuse reflectors and was used for the normal emittance calculation only. Here a collimated set of rays normal to the structure was considered to determine the normal absorptance. Some of the incident energy is absorbed at the base. The remainder is either reflected out of the cavity or interacts further with the sides,

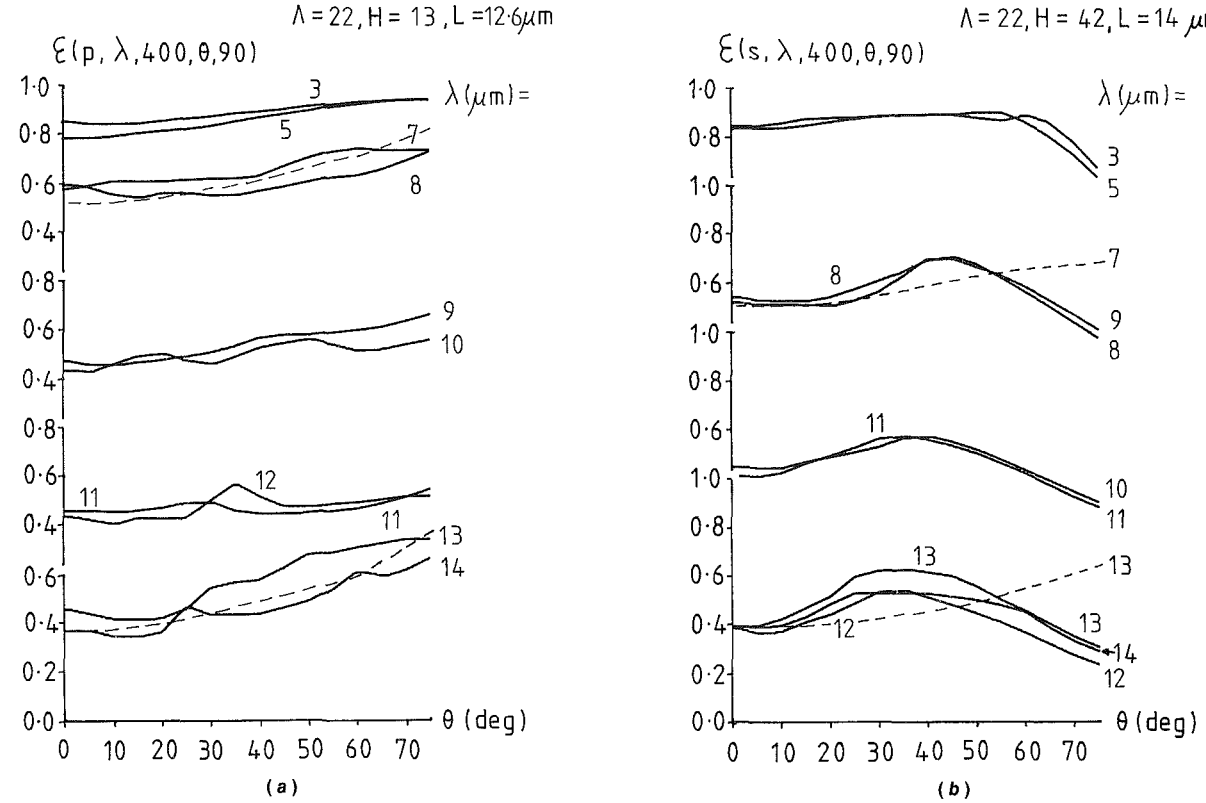

Fig. 5 Directional spectral polarized emittance of doped silicon microgrooves, at 400C and ϕ = 90 deg, as a function of wavelength. The solid lines are experimental data. The dashed lines shown are from the specular geometric calculation. (*A*) *p*-polarized, $\Lambda = 22$, $H = 13$, $L = 12.6$ μm; (*B*) s-polarized, $\Lambda = 22$, $H = 42$, $L = 14$ μm.

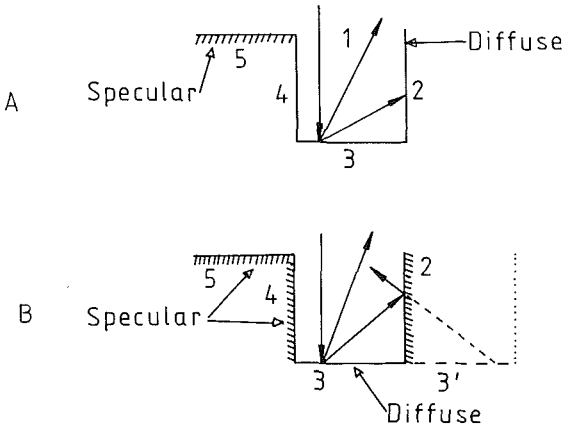

Fig. 6 Schematic of the geometric models for the microgrooves: (*A*) diffuse model; (*B*) specular model indicating image of base, 3′

see Fig. 6(*A*). Subsequent diffuse absorptances, $\alpha_{2,D}$, occur at the side walls. The emittance of the cavity is

$$\epsilon_{1,D}(\overset{S}{p}, \lambda, T) = \alpha_{3,S} + \frac{2\rho_{3,S}F_{32}[\alpha_{2,D} + \alpha_{3,D}\rho_{2,D}F_{32}]}{[1 - \rho_{2,D}(F_{24} + 2F_{23}F_{32}\rho_{3,D})]} \quad (2)$$

The subscripts refer to the walls of the cavity and F is a uniform diffuse irradiation angle factor (shown in Fig. 6*A*).

The emittance of the grooved surface is then determined by summing in the emissivity of the flat surface and cavity in proportion to their projected areas, as follows:

$$\epsilon_D(\overset{S}{p}, \lambda, T) = \frac{(\Lambda - L)}{\Lambda}\epsilon_5(\overset{S}{p}, \lambda, T) + \frac{L}{\Lambda}\epsilon_{1,D}(\overset{S}{p}, \lambda, T) \quad (3)$$

Table 1 Calculated and measured normal emittance

H, μm	L, μm	λ, μm	Polarization	ϵ_D	ϵ_S	Measured emittance
7	14	7	*s*	0.427	0.420	0.42
			p	0.465	0.447	0.50
		13	*s*	0.301	0.301	0.28
			p	0.347	0.326	0.33
13	12.6	7	*s*	0.467	0.429	0.43
			p	0.517	0.488	0.59
		13	*s*	0.340	0.304	0.29
			p	0.405	0.364	0.43
42	14	7	*s*	0.590	0.501	0.63
			p	0.648	0.625	0.88
		13	*s*	0.470	0.373	0.40
			P	0.558	0.521	0.65

The second model assumes that the reflectance of the base is diffuse and that of the side walls is specular (shown in Fig. 6*B*). This model was used for both the normal and directional calculations. The simplified conventional specular model is derived from a method used by Sparrow and Jonsson (1963) for a set of parallel rays incident on the structure. Since the diffuse reflectance at the base is hemispherical, the calculation must include the angular variation. Details of the model are given by Hesketh (1987). The specular reflectance of the cavity is given by the following expression, which includes the direct diffuse reflectance from the base out of the cavity, $\rho_{3,S}F_{31}$:

$$R = 4\rho_{3,S}\Sigma M\Sigma Q\Sigma P\frac{2H^2}{\pi L^2}\frac{\left[\rho_{2,S}(\overset{S}{p}, \lambda, T, \xi)\right]^N}{\left[(M+Q-1)^2 + (P-0.5)^2 + 4A^2\right]} + \rho_{3,S}F_{31} \quad (4)$$

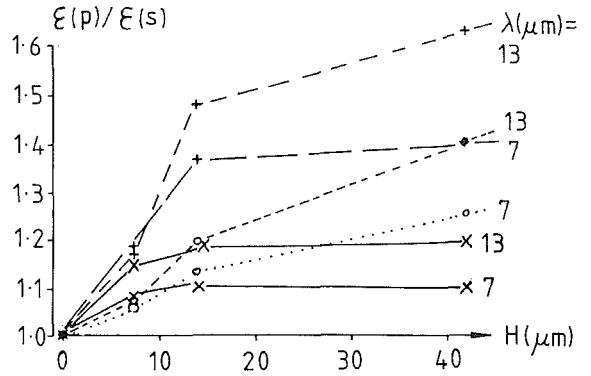

Fig. 7 Ratio of *p* to *s* normal spectral polarized emittance against *H* with wavelength as a parameter: × diffuse model; ○ specular model; * measurements

where ζ is the angle of incidence on the side wall, M and $P = 1$ to ∞, $Q = 1, 2$, $N = M/2$ for M even, $N = (M + 1)/2$ for M odd, and N is an integer equal to the number of times a ray is reflected from the side wall. The asymptotic limits of this equation are physically correct. For example $\rho_s \to \rho_{3,S}$ as $H \to 0$. Also as $H \to \infty$ then $\rho_s \to 0$. That is, the cavity is so deep that no energy is reflected out of it.

The emittance of the surface is again determined by summing the emissivity of the flat surface and cavity in proportion to their projected areas, as follows:

$$\epsilon_S(\overset{S}{p}, \lambda, T) = \frac{(\Lambda - L)}{\Lambda}\epsilon_5(\overset{S}{p}, \lambda, T) + \frac{L}{\Lambda}[1 - R(\overset{S}{p}, \lambda, T)] \quad (5)$$

These expressions were evaluated with a Fortran program to $M, P = 50$. The calculated emittances at wavelengths of 7 and 13 μm are given in Table 1.

The specular model was extended to include polar angular (θ) variation. The reflectance of an incoming set of parallel rays, inclined at an angle θ to the surface, was calculated. Two situations arise, $\phi = 0$ and $\phi = 90$ deg. First, the $\phi = 90$ deg case is considered. The $(\overset{S}{p}, \lambda, T)$ functional dependence will be omitted from the following discussion for brevity.

Azimuthal Angle $\phi = 90$ deg. The fraction of the rays incident on the side wall at an angle $(90 - \theta)$ are specularly reflected toward the base and the intensity is reduced by a factor $\rho_{2,S}(90 - \theta)$. This fraction f is a function of θ and is given by

$$f = \frac{H\tan\theta}{L} - \mathrm{INT}\left(\frac{H\tan\theta}{L}\right) \quad (6)$$

where INT means take the integer value, m, of the expression in brackets. In a manner similar to equation (5) the emittance of the cavity is given by

$$\epsilon_{1,S}(\theta, 90) = 1 - R(\theta)\rho_{2,S}^{m}(90-\theta)(1 - f\epsilon_{2,S}(90-\theta)) \quad (7)$$

These two terms account for the rays diffusely reflected directly out of the cavity and those multiply reflected.

$$\epsilon_s(\theta, 90) = \frac{L}{\Lambda}\epsilon_{1,S}(\theta, 90) + \frac{\Lambda - L}{L}\epsilon_5(\theta, 90) \quad (8)$$

This was evaluated using a Fortran program and the results are plotted as a dashed line on Fig. 4 at wavelengths of 7 and 13 μm.

Azimuthal Angle $\phi = 0$ deg. The s and p polarizations have switched direction, with respect to the grooves, see Fig. 1(A). This means that on the side wall the direction has been rotated through 90 deg so the s and p indices must be exchanged. Therefore, the reflectance of the side wall, surface 2, is $\rho_{2,S}(\overset{S}{p}, \lambda, T, \phi, 0)$. This modifies the expression for R, equation (4). However, the direction of polarization is not affected for the smooth flat surface and base of the cavity.

IV Discussion and Conclusions

This comparison of the data and calculations shows a strong departure from simple geometric behavior, in both the normal and directional spectral emittance of highly doped silicon microgrooves. First consider the directional behavior. The calculated DSPE for both $\phi = 0$ and 90 deg predict a monotonic variation with polar angle. The DSPE data at $\phi = 90$ deg show an increase with polar angle. This increase is in agreement with calculations for a similar shaped cavity with specular reflecting walls, by Demont et al. (1982) and Sparrow and Jonsson (1963). The s-polarized data deviate more strongly from the calculation than do the p.

The DSPE of microgrooves at $\phi = 0$ has apparently not been measured or calculated before. The variation as a function of polar angle is governed by the directional characteristics of both the base and the smooth unetched lands of the microgrooves. The s-polarized emittance decreases with angle and the p-polarized increases. Again, the s-polarized emittance shows a more pronounced deviation from geometric behavior than the p. The maxima in the DSPE, with θ, are related to a coupling of the radiation to a vertical "organ pipe" standing wave in the microgroove (Hesketh et al., 1986). The maxima in the p-polarized DSPE have been related to a quantization of the electromagnetic field across the grooves (Hesketh, 1987; Hesketh et al., 1987). This corresponds to the dimension equal to L in Fig. 1(A). In addition, the calculations do not show the wavelength maxima, in the normal emittance, which were measured at all microgroove depths.

The model correctly predicts that the p-polarized emission is larger than the s-polarized. In Fig. 7 the ratio of the p and s-polarized normal emittance is plotted. The specular model is seen to be a much better predictor of the measured ratio of polarized emission, since these values are much closer than those for the diffuse model. The additional p-polarized emission arises from emission from the side walls. Data for the smooth samples indicate that the p-polarized emission increases with polar angle rapidly, whereas the s-polarized decreases (see also Siegel and Howell, 1981).

The tabulated values indicate that both the diffuse and specular models more closely predict the normal emittance for the shallower grooves than for the deep grooves. However, the diffuse calculation is in closer agreement with the data for larger depths H.

Neither of the geometric models account for the noncontinuum effects that have been measured. It is clear that additional important physical mechanisms arise in these structures.

V Acknowledgments

The authors wish to acknowledge the contribution of an HgCdTe infrared detector by Judson Infrared, Montgomeryville, PA; thanks to Dr. A. Ipri for supplying the photomasks. The partial support of the EEMS Program of NSF, D. Silversmith, Program Manager, under Grant No. ECSS-84-12241 (P.J.H., J.N.Z.) and partial support from NSF Grant No. CBT 84-18517 (B.G.) is also acknowledged. Further, thanks go to Professors H. Baltes and A. Maradudin for useful discussions (J.N.Z., P.J.H.)

References

Baltes, H. P., and Kneubuhl, F. K., 1976, "Thermal Radiation in Finite Cavities," *Helvetica Physica Acta*, Vol. 45, pp. 481–529.

Baltes, H. P., and Hilf, E. R., 1976, *Spectra of Finite Systems*, Bibliographisches Institute-Wissenschaftsverlag, Zurich.

Demont, P., Hvetz-Aubert, M., and Trann'guyen, H., 1982, "Experimental and Theoretical Studies of the Influence of Surface Conditions on Radiative Properties of Opaque Metals," *Int. J. Thermophysics*, Vol. 3, pp. 335-364.

Edwards, D. K., 1965, "Radiation Characteristics of Rough and Oxidized Metals," *Advances in Thermophysical Properties at Extreme Temperatures and Pressures*, 3rd Internatioanl Symposium, ASME, New York, p. 189.

Glass, N. E., Maradudin, A. A., and Celli, V., 1982, "Surface Plasmons on a Large-Amplitude Doubly Periodically Corrugated Surface," *Phys. Rev.*, Vol. B26, pp. 5357-5365.

Hesketh, P. J., 1987, "The Emittance of Heavily Doped Microconfigured Silicon Surfaces," Ph.D. Dissertation, Electrical Engineering, University of Pennsylvania, Philadelphia, PA.

Hesketh, P. J., Zemel, J. N., and Gebhart, B., 1986, " 'Organ Pipe' Radiant Modes of Micromachined Silicon Surfaces," *Nature*, Vol. 352, pp. 549-551.

Hesketh, P. J., Zemel, J. N., and Gebhart, B., 1987, "Polarized Spectral Emittance From Periodic Micromachined Surfaces: I. Doped Silicon: the Normal Direction; II. Doped Silicon: Angular Variation," submitted to *Phys. Rev.*

Inagaki, T., Motosuga, M., Kamamori, K., and Arakawa, E. T., 1983, "Photoacoustic Study of Plasmon Resonance Absorption in a Diffraction Grating," *Phys. Rev.*, Vol. B28, pp. 1740-1744.

Inagaki, T., Goudennet, J. P., Little, J. W., and Arakawa, E. T., 1985, "Photoacoustic Study of Plasmon-Resonance Absorption in a Bi-grating," *J. Opt. Soc. Am.*, Vol. 2B, p. 433.

Kanayama, K., 1972, "Total Emittance and Monochromatic Emittance of Metals and Nonmetals," *Heat Transfer—Japanese Res.*, Vol. 1, p. 11.

Lofving, S., 1980, "Hemispherical Emittance of Rough Metal Surfaces," *Applied Physics Letters*, Vol. 36, pp. 632-633.

Planck, M., 1959, *Theory of Heat Radiation*, English translation of *Theorie der Warmestrahlung*, 2nd ed., 1913, Dover, New York.

Rolling, R. E., 1967, *Progress in Astronautics and Aeronautics: Thermophysical Properties of Spacecraft and Planetary Bodies*, G. B. Heller, ed., Academic Press, New York.

Siegel, R., and Howell, J. R., 1981, *Thermal Radiation Heat Transfer*, 2nd ed., McGraw-Hill, New York.

Sparrow, E. M., and Jonsson, V. K., 1963, "Thermal Radiation Absorption in Rectangular-Groove Cavities," *J. Appl. Mechanics*, Vol. 85E, pp. 237-244.

Wirgin, A., and Maradudin, A. A., 1986, "Resonant Enhancement of the Electric Field in the Grooves of Bare Metallic Grating Exposed to *s*-Polarized Light," *Phys. Rev.*, Vol. B31, pp. 5573-5576.

Wirgin, A., and Maradudin, A. A., 1987, "Resonant Response of a Bare Metallic Grating to *s*-Polarized Light," submitted to *Applied Surface Science*, by permission of the authors.

Heat Transfer Characteristics From a Flat Plate to a Gas-Solid Two-Phase Flow Downstream of a Slit Injection

S. Obi
Ph.D. Candidate.

K. Hishida
Assistant Professor.

M. Maeda
Professor.

Department of Mechanical Engineering,
Keio Univeristy,
3-14-1 Hiyoshi Kohoku-ku Yokohama 223
Japan

The behavior of fine glass particles and their influence on fluid motion are investigated in a flow over a flat plate downstream of a two-dimensional slit injection. Heat transfer characteristics are examined in terms of the mass loading ratio of the particles ranging up to 0.8 and particle size varying from 68.6 to 148 μm in mean diameter. The particles promote turbulence of the fluid in a weakly turbulent flow, but suppress turbulence in a strongly turbulent flow. The heat transfer characteristics along the wall are well correlated to the variation of turbulent flow field due to the effect of the particles.

Introduction

As an augmenting technique for heat transfer in industrial applications, the utilization of a liquid-air two-phase mist flow has been proposed that makes use of the latent heat transfer due to the evaporation of small liquid particles. Its advantages were clarified by an experimental study in a laminar boundary layer flow (Hishida et al., 1980), which indicated that the heat transfer rate became several times larger than the single-phase flow under equivalent conditions of the free-stream velocity and the wall temperature. Apart from this latent heat transport, the heat transfer enhancement in two-phase flows is generally achieved by a combination of many other fluid dynamic effects due to the existence of particles or droplets in the fluid, all of which should be taken into account for the optimum operation of two-phase flow systems. For instance, the particles collide with the pipe walls in a heat exchanger and disturb the viscous sublayer, increasing heat transfer coefficients as a result. On the other hand, the added particles also play an important role in increasing the total specific heat of the operational fluid.

Among these many unique characteristics, the authors have been interested in the behavior of fine particles and their influence on the fluid motion in connection with heat transfer, and have performed an experimental investigation of heat transfer characteristics in a gas-solid two-phase flow over a flat plate (Maeda et al., 1976). As a consequence, they have clarified that, even at a low particle concentration up to about 0.4 percent by volume, loading of particles into a weakly turbulent flow caused an increase in the turbulence intensity of the free stream and consequently promoted heat transfer. Maeda et al. (1980) pointed out that the free-stream turbulence increased due to the particle loading during turbulent flow through pipes.

To extend knowledge concerning the relation between free-stream turbulence and heat transfer, Maeda et al. (1982) performed measurements on velocity and heat transfer in a two-phase backward-facing step flow. The results indicated that the local heat transfer rates along the wall were remarkably reduced behind the step in comparison to the single-phase flow, especially at the flow reattaching region, and the turbulence intensity in the free shear layer was reduced accordingly. The particle trajectory was observed by a flow visualization, which confirmed that the particles rarely came directly into the flow recirculating region. Therefore, the effect of the particles in the vicinity of the wall was considered to be small in this case, and the particle existence in the shear flow primarily varied the free-stream turbulence and heat transfer from the wall.

As outlined above, the particles either promote or suppress turbulence, which results in a change in the heat transfer rate. It is also found that the role of the added particles, whether they induce or reduce the turbulence, depends on the original state of the flow field without particles. In the present study, the dependency of the above-mentioned effect of the particles added to the original state of the free stream is examined further. In order to control the initial turbulence level in the flow field, a plane boundary layer flow with two-dimensional injection is adopted and the turbulence and heat transfer are compared with the results about the backward-facing step flow. For instance, by varying the rate of injection, various types of flow are reproduced on the wall, such as a laminar boundary layer and turbulent recirculating flows. This kind of flow field is widely applied in the film cooling technique and its characteristics and effectiveness are summarized by Goldstein (1971). In comparison with the separted flow behind the backward-facing step, the effect of particles on the fluid motion in the recirculating region will be investigated. The measurements of heat transfer coefficients in two-phase flows from an isothermal heated plate are made considering the injection flow rate, the mass loading ratio of the particles in the free stream, and the effect of particle size. Together with the heat transfer measurements, detailed velocity measurements of the fluid and the particles are undertaken using a modified laser-Doppler velocimeter for two-phase flows proposed by Hishida et al. (1984).

Experimental Setup and Procedure

The test section, shown in Fig. 1, is set in the gravitational direction so that the particles do not accumulate on the wall. An air suction type experimental duct was adopted in this study, in order to minimize free-stream turbulence and to keep the air temperature constant, and for the convenience of particle loading. A two-dimensional injection slit 3 mm wide was cut across the plate at 70 mm from the leading edge of a flat plate. Its blowing direction was set normal to the free stream. An auxiliary plate in front of the leading edge and a louver at the exit of the test section provided a uniform velocity condition at the leading edge. A uniform velocity distribution at the exit of the slit injection was also obtained by a nozzle and a

Contributed by the Heat Transfer Division for publication in the JOURNAL OF HEAT TRANSFER. Manuscript received by the Heat Transfer Division June 23, 1987. Keywords: Forced Convection, Multiphase Flows, Turbulence.

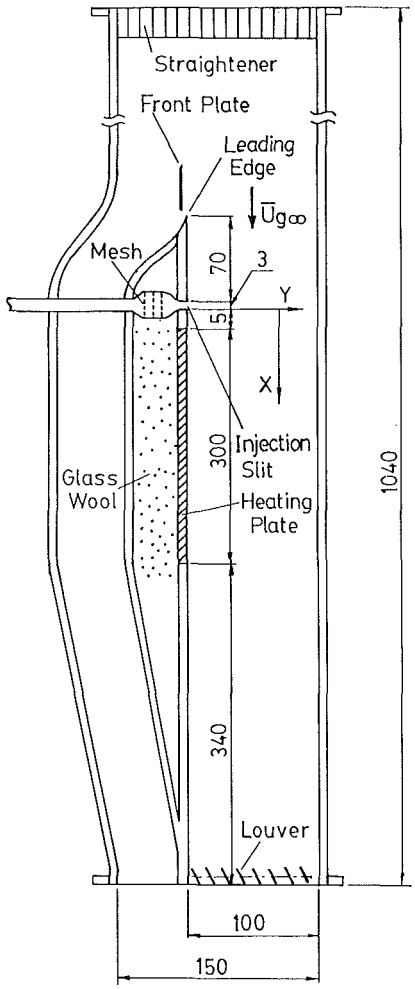

Fig. 1 Test section

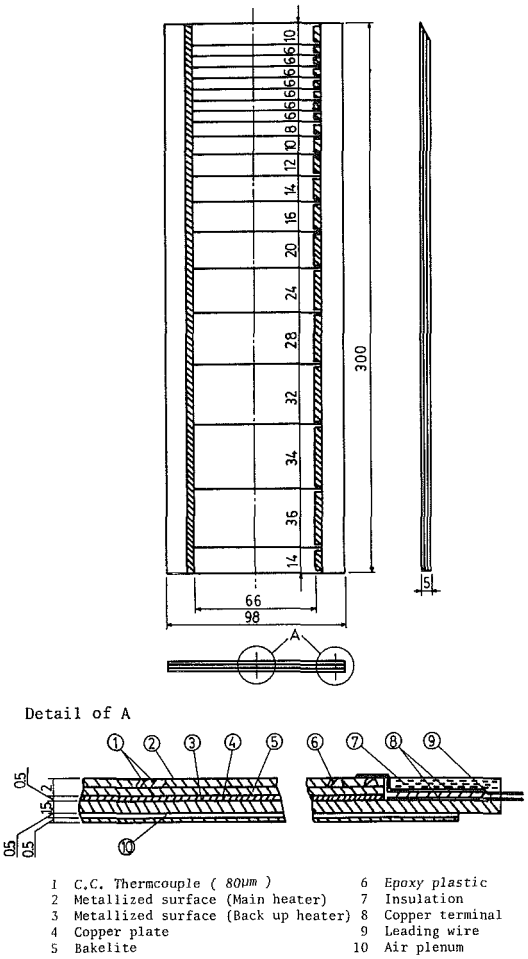

Fig. 2 Heating plate

grid, which were set upstream of the outlet. Fine powder of aluminum oxide (approximately 1 μm in diameter) was added to the flow at the inlet of the duct and to the injection flow as the tracer for the LDV measurements.

An orthogonal coordinate system was adopted here as shown by the X and Y axes in the streamwise and transverse directions, respectively, originating from the edge of the injector exit. A 300-mm-long, 98-mm-wide isothermal heating plate was located 5 mm downstream of the slit, where local heat transfer coefficients were obtained in the same manner as Maeda et al. (1982). The heating plate was made of a nickel-plated bakelite as shown in Fig. 2. Its plated surface was divided into 20 sections in the flow direction, and each section was heated individually by controlling the supply power, so that the wall temperature was maintained constant everywhere. The plate was heated from behind by an auxiliary backup heater, in order to avoid heat loss by conduction to the back side wall. Hence, the heat transferred from the wall to the flow was estimated in terms of the power supplied to the heating plate. Local heat transfer coefficients were then obtained from the following relations:

$$h_x = q_x/(T_w - T_0) \tag{1}$$

$$q_x = W_x/S_x \tag{2}$$

where h_x is the local heat transfer coefficient and q_x is the

Nomenclature

d_p = mean particle diameter
h_x = local heat transfer coefficient
h_{x0} = local heat transfer coefficient of single phase
M = mass loading ratio (mass of particles per unit mass flow rate)
Nu_x = local Nusselt number based on the local heat transfer coefficient and the distance from the injection slit
q_x = local heat flux
Re_x = local Reynolds number based on distance from the injection slit
S_x = area of each section of heating plate
T_0 = free-stream temperature
T_w = wall temperature
$U_{g\infty}$ = free-stream velocity
U_j = injection velocity
W_x = electric power per section of heating plate
β = injection ratio = U_j/U_g
ρ_p = density of particles
σ = standard deviation of the particle diameter

Subscripts

l = laminar flow
t = turbulent flow

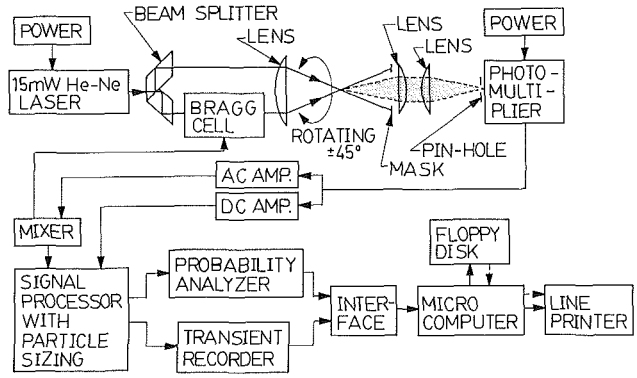

Fig. 3 Schematic view of the LDV system for two-phase flow measurements

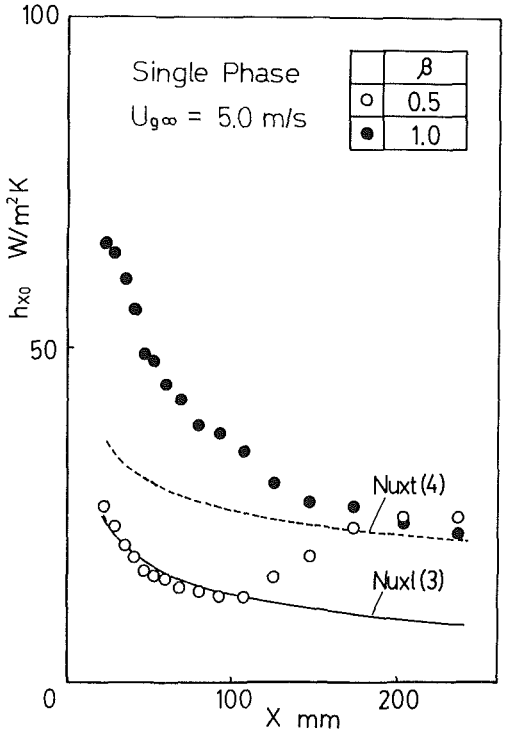

Fig. 4 Variation of the local heat transfer coefficients along the heating plate on single-phase flows for $\beta = 0.5$ and 1.0

local heat flux. S_x is the area of each heating section and W_x is the electric power supplied to it. The wall temperature was monitored by copper/constantan thermocouples of 80 μm diameter, buried just under the wall surface. All the heating section temperatures were maintained within 0.2 K. The heat loss due to the radiation was estimated at about 3 percent of the total heat flux. The uncertainty of the heat transfer coefficient that was estimated by the "Root Sum Square Method" (Abernethy, 1985) was ± 5 percent with a 95 percent confidence interval for the heat flux, free-stream temperature, and other factors.

The LDV system applied in these measurements is shown schematically in Fig. 3. The optics were a conventional differential mode type which consisted of a 15-mW He-Ne laser source, a beam splitter, a Bragg cell for measuring the reverse flow region, and a focusing lens of 250 mm focal length. The control volume was approximately $200 \times 200 \times 2000$ μm. At each measuring point, over 3000 signals were sampled to calculate the local mean value and its deviation. The sampling was repeated three times at every location, setting the transmitting optics at 0, +45, and −45 deg with respect to the

Table 1 Experimental condition

Free-stream velocity	$U_{g\infty}$(m/s)	5.0 ± 0.1
Injection velocity	U_j(m/s)	$2.5\text{–}15.0 \pm 0.1$
Injection ratio		0.5–3.0
Wall temperature	T_w(°C)	50 ± 0.2
Air temperature	T_0(°C)	20–23

Table 2 Loaded particles

Shape: sphere	Material: Sodium glass			
Density	p(kg/m^3)	2590		
Mean diameter	d_p(μm)	68.6	91.7	148
Standard deviation	(μm)	12.4	12.6	18.0
Mass loading ratio	$M = m_p/m_a$	$0 - 0.8 \pm 0.06$		

X axis. The local mean velocity, fluctuating components in two directions, and the Reynolds shear stress were calculated from these three sets of measurements by means of a vector analysis (e.g., Hishida et al., 1985). The signal processing unit consisted of basically the same logic circuits used by Hishida et al. (1984), which could measure both the air and particle velocities in a two-phase flow, where the discrimination of particle sizes was made by a specially designed discriminating circuit (Hishida et al., 1984) based on the scattering intensity difference. The location of the particle path in the control volume has been determined by counting the number of Doppler cycles in the burst signal. The weak scattering lights from large particles flying from the edge of the control volume could be eliminated in this way. This method has been applied also for measurements of a turbulent free jet (Fleckhaus et al., 1987) and its performance has been confirmed. The sampling number for the particles was also 3000 for each point. It took about 20 min to finish the sampling for each set of profiles, which was long enough to yield time-independent results even at a location where a highly turbulent flow was found in the present measurements. The experimental conditions are summarized in Table 1, and possible fixed errors are also shown within the uncertainty bands.

Spherical glass particles were added to the air at the inlet of the duct. The properties of the particles are shown in Table 2. The particle diameter was calculated from the optical measurement of over 1000 samples. The particle seeder was made of a plastic bucket that had uniformly distributed small holes on the bottom, and mounded above the inlet of the duct. The number of particles falling through the holes was controlled by gradually opening/closing all the apertures simultaneously. The resultant flow rate of the particles was measured by an isokinetic sampling probe at typically nine points traversed across the test section at the inlet plane. The uniformity of the particle concentration was within 10 percent of overall value at the inlet cross section.

Results and Discussion

Single Phase Flow. The flow field on the flat plate varies with the injection flow rate from the slit. It is meaningful to study the profiles of the local heat transfer coefficients along the wall, since they directly express the time-averaged features of the flow field adjacent to the wall. Figure 4 presents the measured distribution of the local heat transfer coefficients downstream of the injection slit, for injection ratios of $\beta = 0.5$ and 1.0. The solid line and the broken line indicate the results from theoretical analysis for laminar and turbulent boundary layers on the flat plate without injection, respectively. Equation (4) was obtained from von Kármán (1939).

$$\mathrm{Nu}_{xl} = 0.332\,\mathrm{Re}_x^{0.5}\mathrm{Pr}^{0.33} \tag{3}$$

$$\mathrm{Nu}_{xt} = 0.0296\,\mathrm{Re}_x^{0.8}\,\mathrm{Pr}/\{1 + B\,\mathrm{Re}_x^{-0.1}(\mathrm{Pr} - 1)\} \tag{4}$$

$$B = 0.860[1 + \ln\{(1 + 5\mathrm{Pr})/6\}(\mathrm{Pr} - 1)]$$

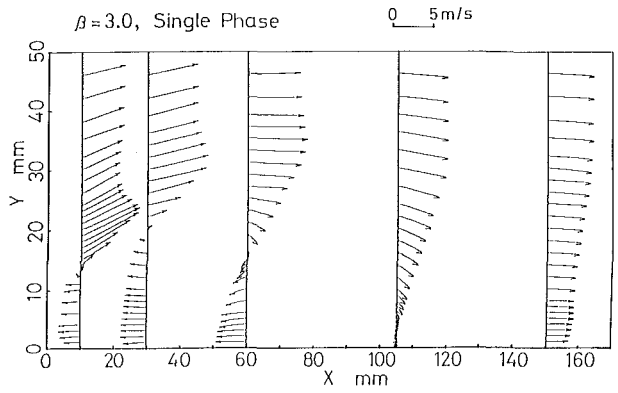

Fig. 5 Mean velocity vector distribution downstream of the slit in single-phase flow for $\beta = 3.0$

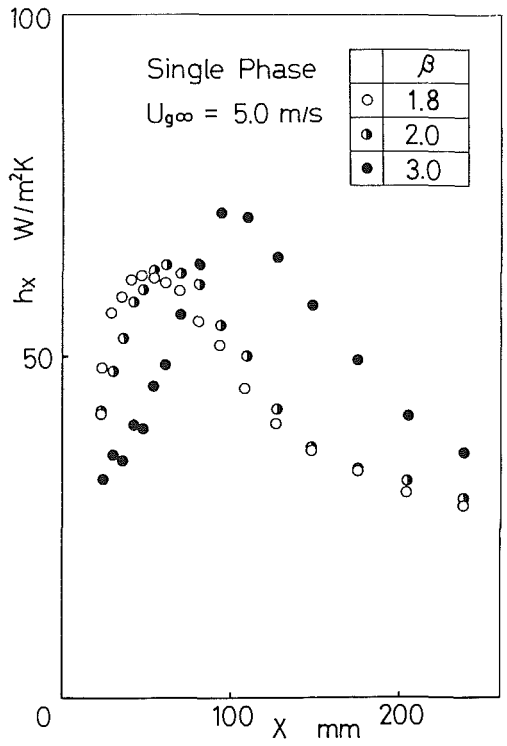

Fig. 6 Variation of the local heat transfer coefficients along the heating plate in single-phase flows for $\beta = 1.8$, 2.0, and 3.0

The distance from the slit to the position in question was taken as the length for nondimensional quantities, such as the local Nusselt number and Reynolds number, assuming that the boundary layer develops from the edge of the injection slit. The results show that, for an injection ratio of $\beta = 0.5$, the heat transfer coefficients decrease with an increasing distance from the injection slit up to about $X = 100$ mm along the solid line, which denotes the analytical solution for a laminar boundary layer. Farther downstream, the experimental results approach the turbulent boundary layer solution, implying that a transition from a laminar to a turbulent boundary layer occurred around $X = 100$ to 200 mm. The local Reynolds number corresponding to the transition is approximately $Re_x = 3.3 \times 10^4$, which is one order of magnitude smaller than the critical Reynolds number for an ordinary boundary layer flow. On the other hand the measured heat transfer coefficients for $\beta = 1.0$ exceed the analytical solution for turbulent boundary layers up to about $X = 100$ mm, and tend to approach the analytical solution farther downstream. The heat

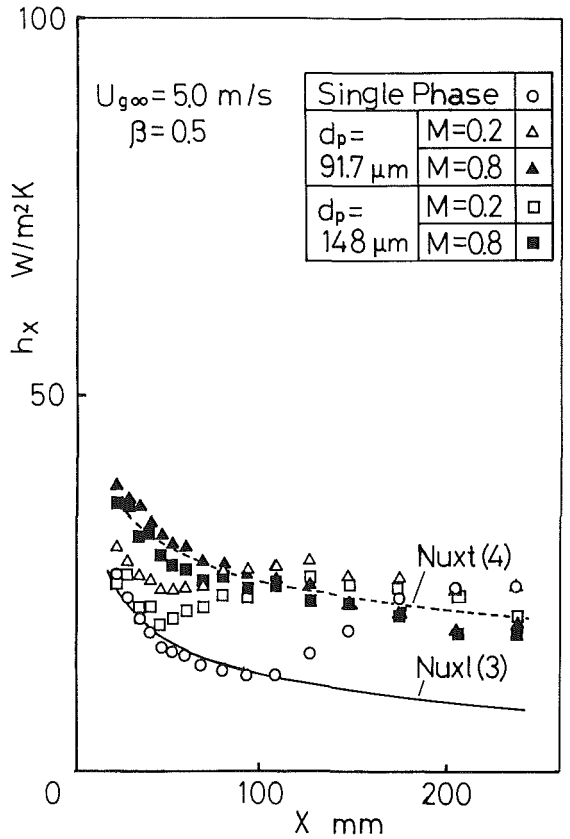

Fig. 7 Variation of the local heat transfer coefficients in two-phase flows at $\beta = 0.5$, $d_p = 91.7$ and 148 μm

transfer coefficients in this case become much higher than the values for a usual turbulent boundary layer because the flow slightly detached just behind the injection slit, as confirmed by the corresponding velocity field measurements (not presented).

When the injection ratio exceeds a certain value, i.e., for the strong injection flow, the mainstream is curved outward and separates from the wall. Figure 5 shows the mean velocity vector distribution for $\beta = 3.0$, which demonstrates a recirculating eddy downstream of the injection slit. The distribution of the heat transfer coefficients in the same flow field is shown in Fig. 6 together with the results for the injection ratios of $\beta = 1.8$ and 2.0. The location of the maximum heat transfer coefficients for $\beta = 3.0$, that is around $X = 100$ mm, coincides with the reattachment region of the separated flow shown in Fig. 5. Thus, the maximum value of each profile is situated near the reattachment point of the separated flow, which is common for heat transfer in impinging and/or wall reattaching flows (e.g., Aung 1983). It is recognized that a higher injection ratio makes the recirculating region larger and results in a shift of the reattachment of the mainstream in the downstream direction, and in addition, causes an increase of the maximum value of the heat transfer coefficient at reattachment.

As described above, the variation of the flow field is roughly divided into two groups according to the injection ratio. Namely, one consists of boundary layer type flows and the other includes separation followed by a recirculating region on the wall. The latter condition is thought to be more turbulent, since it has much higher heat transfer coefficients. Therefore, by controlling the injection ratio, various initial conditions can be prepared in terms of the turbulence level, to allow study of the effect of particle loading. For each condition, particle loading ratio and size were changed so that their effects could be considered.

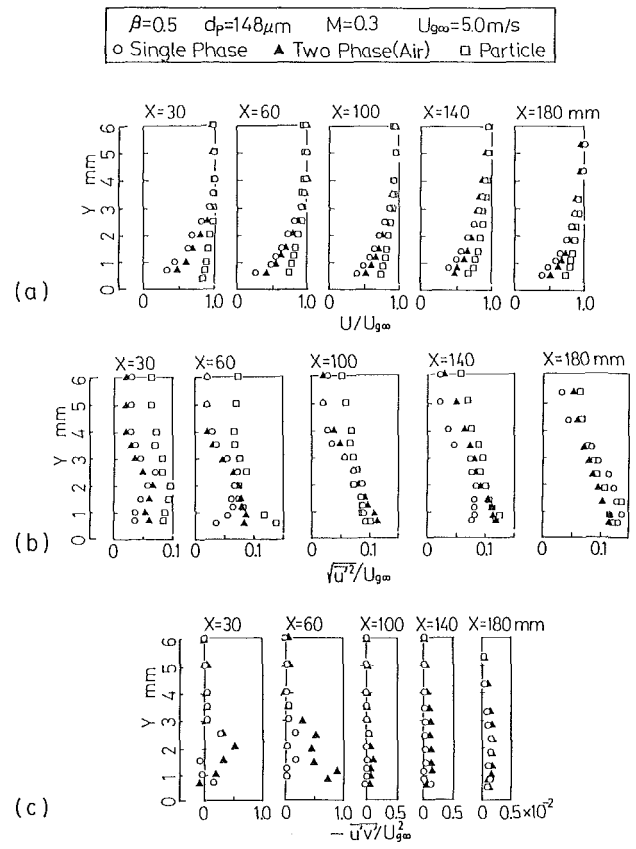

Fig. 8 Velocity profiles in single- and two-phase flows along the wall for $\beta = 0.5$: (a) local mean velocity, (b) turbulence intensity, and (c) profiles of Reynolds stress

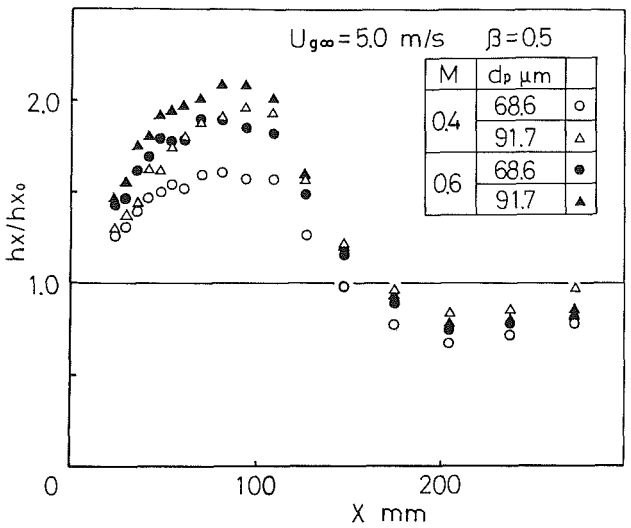

Fig. 9 Comparison of the normalized heat transfer coefficients in terms of the mass loading ratio and the mean particle diameter variations for $\beta = 0.5$

Two Phase Flow

Heat Transfer at Lower Injection Ratio. Figure 7 shows the distribution of the local heat transfer coefficients in the single- and two-phase flows along the heating plate for an injection ratio of $\beta = 0.5$. Results are illustrated for various particle sizes and mass loading ratios. It is seen that the heat transfer coefficients are increased by the particle loading at locations of X less than 150 mm, where a quasi-laminar boundary layer flow develops. The influence of the particles does not seem to depend on the particle size. At the lower mass loading ratio, $M = 0.2$, it is thought from the profile of local heat transfer coefficients that the laminar boundary layer undergoes an earlier transition due to disturbances by particles. At the higher mass loading ratio, $M = 0.8$, the experimental results coincide well with the analytical result for a fully turbulent boundary layer, which indicates that a higher particle concentration promotes turbulence generation.

The results of the velocity measurements for $\beta = 0.5$ are summarized in Figs. 8*a*, *b*, *c* at $M = 0.3$, confirming the relation between heat transfer enhancement and turbulence promotion mentioned above. That is, the mean velocity gradient at the wall is larger for the two-phase flow than for the single-phase flow, as shown in Fig. 8(*a*). Particles mostly have larger velocities than the air due to gravity and accelerate the gas phase in the boundary layer. Meanwhile a fluid flow with low velocity impedes the particle motion, which results in a boundary-layer-like shape of particle velocity profiles. Both turbulence intensity and Reynolds stress increase in two-phase flow as shown in Figs. 8(*b*, *c*), in accordance with the rapid increase of heat transfer coefficients found in Fig. 7. A remarkable increase of Reynolds stress at $x = 30$ and 60 mm is thought to be typical of the effect of particle in the flow developing region, which has been also found in the measurement of two-phase wall jet (Hishida et al., 1986). It should be noted that the measured turbulence intensity of the particles does not stand for the velocity fluctuation of a single particle, since it is calculated statistically using values for a number of particles that have different velocities.

In the weakly turbulent flow, the larger velocity difference between the air and the particles induces a more intensive mixing of the air and hence a more active momentum exchange. Thus, larger particles are capable of producing a higher heat transfer enhancement. On the other hand, under the fixed mass loading ratio, the total number of the particles decreases as the diameter of the particle increases. Hence, the variation of particle size and mass loading ratio cannot be considered independently from each other. Figure 9 is an illustration of results for different particle diameters, $d_p = 68.6$ and 91.7 μm, in terms of the normalized heat transfer coefficients referred to that of single-phase flow. Although the diameter difference is smaller between two particles in this figure, the difference in the effect of heat transfer enhancement is larger than the former case, Fig. 7, for particles with $d_p = 91.7$ and 148 μm. At a mass loading ratio of $M = 0.4$, larger particles with $d_p = 91.7$ μm provide a larger heat transfer rate than smaller particles with $d_p = 68.6$ μm, while the difference in heat transfer enhancement by particle size becomes smaller for a larger mass loading ratio. In addition, it is also indicated that the rate of heat transfer enhancement becomes smaller with an increasing mass loading ratio. Maeda et al. (1976) made it clear that turbulence intensity approaches a certain value with an increasing mas loading ratio. Taking account of these facts, it is supposed that there exists an equilbrium state of momentum exchange between the air and the particles, and hence the contribution of the particle loading to the turbulence generation eventually diminishes regardless of the particle size.

Heat Transfer at Higher Injection Ratio. A higher injection ratio provides a highly turbulent flow. As stated already, the influence of the particle loading on a flow field of this kind is expected to be different from the case of a lower injection ratio. The distribution of the local heat transfer coefficients along the heating plate confirms this matter, as shown in Fig. 10. The injection ratio β is 2.0 and the particles of d_p = 91.7 μm are mixed with the fluid with mass loading ratios ranging up to M = 0.6. In contrast to the lower injection ratio case, the heat transfer rate decreases in the entire region with

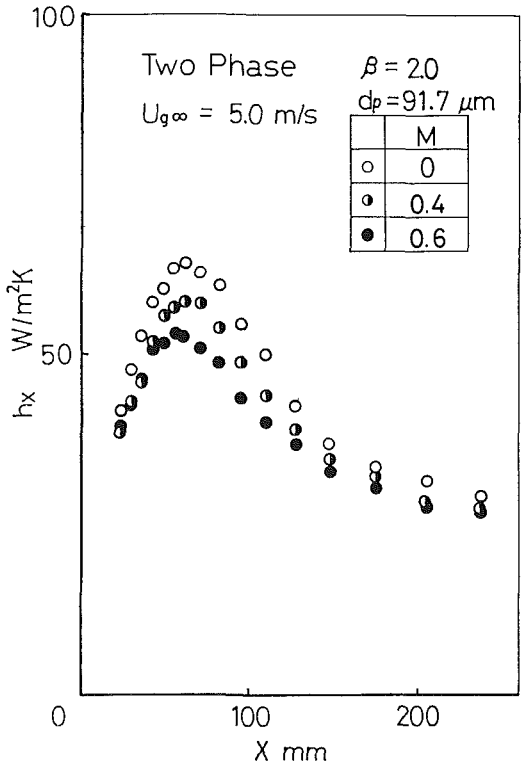

Fig. 10 Variation of the local heat transfer coefficients in two-phase flows for $\beta = 2.0$ and $d_p = 91.7$ μm

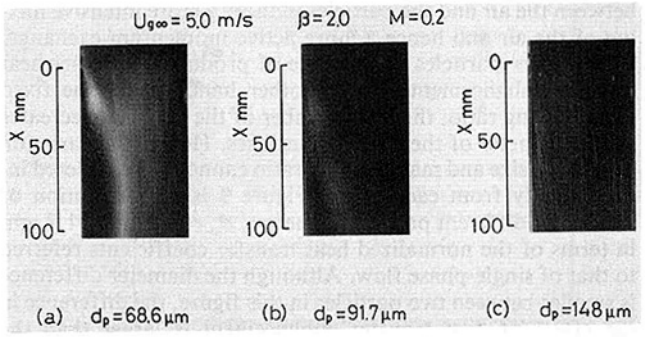

Fig. 11 Difference of the particle trajectory for injection ratio = 2.0: (a) $d_p = 68.6$ μm, (b) $d_p = 91.7$ μm, and (c) $d_p = 148$ μm

an increasing particle concentration. A similar tendency was observed in the previous study for the backward-facing step flow (Maeda et al., 1982), and the decrease of the heat transfer rate was well correlated with the reduction of the turbulence intensity in the flow field due to the presence of particles. It is therefore pointed out that the particles will also damp the highly turbulent motion for the separated flow in the present case. The corresponding velocity results of the velocity measurements will be shown later. In accordance with the entire reduction of turbulence, the location of the maximum heat transfer coefficient shifts slightly upstream. This may be caused by the increase in the momentum of the mainstream against the injection flow, which is due to acceleration of the gas phase by the particles, which have larger velocity by gravity.

Figure 11 demonstrates the trajectory of particles for $\beta = 2.0$, comparing the results of three different particle sizes. The mass loading ratio was fixed at $M = 0.2$ for each particle size. As observed in the photographs, the trajectories of the $d_p = 68.6$ μm particles are mostly curved near the injected flow and indicate an extremely high concentration along the shear

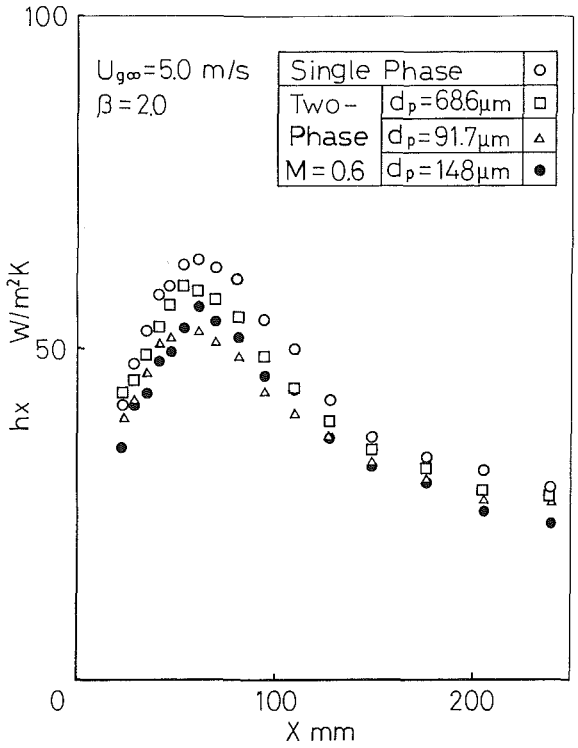

Fig. 12 Comparison of the heat transfer coefficients in terms of the mean particle diameter variations for $\beta = 2.0$ and $M = 0.6$

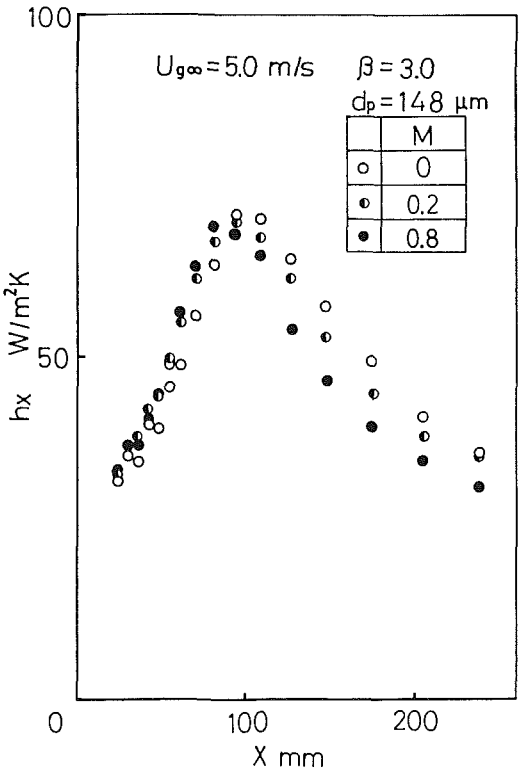

Fig. 13 Variation of the local heat transfer coefficients in two-phase flows for $\beta = 3.0$ and $d_p = 148$ μm

layer, while the $d_p = 148$ μm particles penetrate the injection flow and fly straight into the recirculating region. The pictures also show that the particles of these three groups collide with the wall in the recirculating region. Therefore, a certain degree of direct heat transfer from the wall to the particles is present

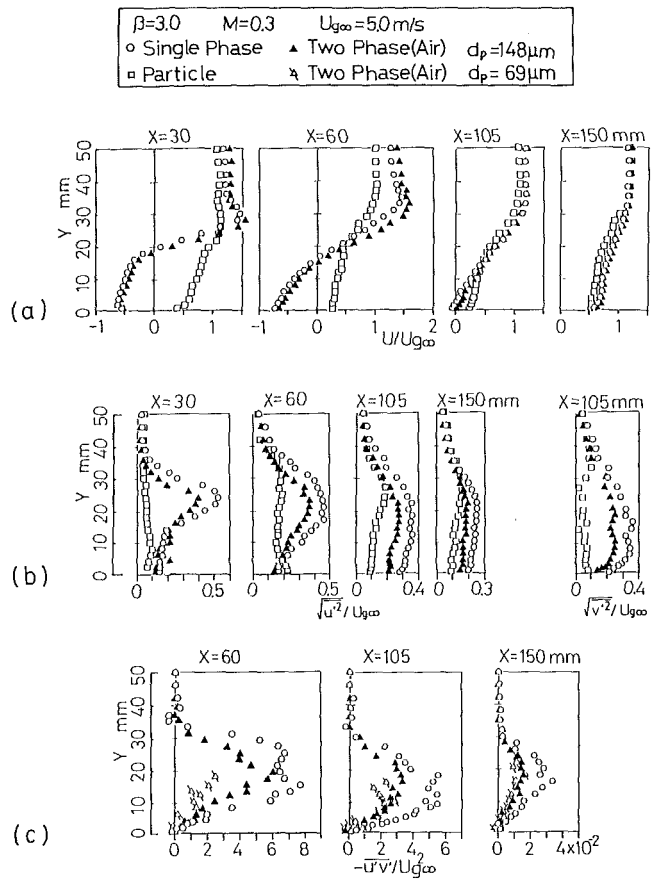

Fig. 14 **Velocity profiles in single- and two-phase flows along the wall for $\beta = 3.0$: (a) local mean velocity, (b) turbulence intensity, and (c) profiles of Reynolds stress**

in that region. The effect of the particle size difference is indicated in Fig. 12 in terms of the heat transfer coefficient for $\beta = 2.0$ and $M = 0.6$. In general, the smallest particles yield the least heat transfer reduction, although the number of the particles is more than 10 times that of the largest particles for the same mass loading ratio.

The distribution of the heat transfer coefficients for $\beta = 3.0$ is shown in Fig. 13, which indicates that the particles of $d_p = 148$ μm reduce the heat transfer coefficient as a whole and that the location of the maximum point shifts upstream, which is similar to the case of $\beta = 2.0$. The extent of the reduction is relatively large in the region from $X = 105$ mm to 200 mm. Figures 14(*a, b, c*) present the results of velocity measurements under similar conditions, $\beta = 3.0$, $d_p = 148$ μm, and $M = 0.3$, which show the profiles of the local mean velocity, turbulence intensity and Reynolds stress, respectively. As observed in Fig. 11(*c*), the mean velocity profiles, Fig. 14(*a*), indicate that the particles, having a large inertia, move downward against the air in the recirculating region around $X = 30$ to 60 mm. As a consequence, the reverse flow is impeded by particles and the size of the recirculating region is reduced, which has been observed also in the heat transfer results. Figure 14(*b*) indicates that the existence of the particles reduces the turbulence intensity. This is likely to reduce turbulent diffusion during scalar transport in the flow field. Figure 14(*c*) shows that Reynolds stress is decreased at $X = 105$ and 150 mm, where the boundary layer redevelops after the separated flow reattaches to the wall. The reduction of heat transfer in the corresponding region, which is indicated in Fig. 13, is qualitatively confirmed by this result.

In general, heat transfer phenomena in turbulent flows are under the subject of turbulent motion of the fluid, whose activity is determined by both length and velocity scale of the energy-containing eddy in the field. In gas-solid two-phase flows, the turbulent structure is changed by the existence of the particles. For instance, the fact that the effect of the particle loading becomes weaker with increasing mass loading ratio implies that the state of turbulent field reaches the equilibrium state as particles yield the uniform size of eddies. In a strong shear flow, provided by a high injection in the present study, both the fluctuating velocity and length scale are much larger than those of a weakly turbulent flow, the flow field of a low injection rate, and they strongly vary in the flow field. Hence, the effect of added particles is a combination of many factors. From the present experiment, however, it is implied that the particles tend to smooth the flow characteristics and the effect appearing alternatively, i.e., either enhance or reduce the turbulent intensity depending on the initial state, confirms this matter.

Concluding Remarks

The characteristics of the gas–solid two-phase flow were investigated for two types of flow fields, one a transitional boundary layer flow and the other a turbulent separated flow. The variation of the flow field was achieved by changing the velocity of the injection flow from 2.5 to 15 m/s while the mainstream velocity was fixed at 5.0 m/s. The particles were spherical glass beads of three groups, which had mean diameters of 68.6, 91.7, and 148 μm. The mass loading ratio of the particles to the air flow ranged up to 0.8. The following conclusions are obtained from the present study:

The transition of the boundary layer came earlier than in single-phase flow, as a consequence of particle loading, causing an increase in turbulence intensity and Reynolds stress and a related increase in heat transfer coefficients.

A heat transfer reduction occurred in the highly turbulent flow due to the addition of particles, corresponding to the suppression of turbulent motion of the gas phase by the particles. The heat transfer coefficients in the recirculating region were reduced with an increasing particle loading ratio. The general trend was similar to that of the backward-facing step flow.

In addition to these observations, it was confirmed that the effect of the particle loading on the fluid motion became apparent even at quite a low volume concentration. It was also clear that particles promote the turbulence in weakly turbulent flow and suppress turbulence in strongly turbulent flow, yielding either heat transfer enhancement or reduction. The enhancement and/or reduction rate became lower with the increasing mass loading ratio. These findings were considered as the consequence of the effect that the particles smooth the original characteristics of the flow field as the concentration increases.

Acknowledgments

The authors would like to thank Messrs. H. Watanabe, M. Ono, M. Ohsato, and K. Satoh for performing the experiments.

References

Abernethy, R. B., Benedict, R. P., and Dowdell, R. B., "ASME Measurement Uncertainty," ASME *J. Fluids Engineering*, Vol. 107, pp. 161–164.

Aung, W., 1983, "Separated Forced Convection," *Proceedings of ASME-JSME Thermal Engineering Joint Conference*, Honolulu, Hawaii, Y. Mori and W. J. Yang, eds., ASME, New York, Vol. 2, pp. 499–515.

Fleckhaus, D., Hishida, K., and Maeda, M., 1987, "Effect of Laden Solid Particles on the Turbulent Flow Structure of a Round Free Jet," *Experiments in Fluids*, Vol. 5, pp. 323–333.

Goldstein, R. J., 1971, "Film Cooling," *Advances in Heat Transfer*, Vol. 7, Academic Press, p. 321.

Hishida, K., Maeda, M., and Ikai, S., 1980, "Heat Transfer From a Flat Plate in Two-Component Mist Flow," ASME JOURNAL OF HEAT TRANSFER, Vol. 102, pp. 513–518.

Hishida, K., Maeda, M., Imaru, J., Hironaga, K., and Kano, H., 1984, "Measurements of Size and Velocity of Particle in Two-Phase Flow by a Three Beam LDA System," *Laser Anemometry in Fluid Mechanics*, LADOAN-Instituto Superior Tecnico, Lisbon, Portugal, pp. 121–136.

Hishida, K., Wanajo, H., and Maeda, M., 1985, "Characteristics of Gas–Solids Two-Phase Flow and Heat Transfer Downstream of the Backward-Facing Step" [in Japanese], *Trans. JSME*, Ser. B, Vol. 51, No. 467, pp. 2176–2183.

Hishida, K., Umemura, K., and Maeda, M., 1986, "Heat Transfer to Plane Wall Jet in Gas–Solids Two-Phase Flow," *Proceedings of the 8th International Heat Transfer Conference*, San Francisco, CA, Hemisphere Publishing Corp., Washington, Vol. 5, pp. 2385–2390.

Maeda, M., Saigusa, T., and Ikai, S., 1976, "Study on Heat Transfer to Gas–Solids Suspension, Part 1, Influence of Free Stream Turbulence on Heat Transfer," *Bulletin of the JSME*, Vol. 19, No. 137, pp. 1317–1325.

Maeda, M., Hishida, K., and Furutani, T., 1980, "Optical Measurements of Local Gas and Particle Velocity in an Upward Flowing Gas-Solids Suspension," *Proceedings of the Symposium on Polyphase Flow and Transport Technology*, San Francisco, CA, R. A. Bajura, ed., ASME, New York, pp. 211–216.

Maeda, M., Kiyota, H., and Hishida, K., 1982, "Heat Transfer to Gas–Solids Two-Phase Flow in Separated, Reattached and Redevelopment Regions," *Proceedings of the 7th International Heat Transfer Conference*, Munich, Germany, U. Grigull, ed., Hemisphere Publishing Corp., Washington, Vol. 5, pp. 249–254.

Von Kármán, T., 1939, "The Analogy Between Fluid Friction and Heat Transfer," *Trans. ASME*, Vol. 61, pp. 705–710.

N. Kaji
Associate Professor,
Division of Mechanical Engineering,
The Institute of Vocational and Technical Education,
Sagamihara 229, Japan

Y. H. Mori
Associate Professor,
Department of Mechanical Engineering,
Keio University,
Yokohama 223, Japan
Mem. ASME

Y. Tochitani
Associate Professor,
Department of Mechanical Engineering,
Kanazawa Institute of Technology,
Nonoichi 921, Japan

Electrically Induced Shape Oscillation of Drops as a Means of Direct-Contact Heat Transfer Enhancement: Part 1—Drop Dynamics

The shape oscillation of liquid drops passing through an immiscible liquid medium subject to a low-frequency (1 ~ 16 Hz) alternating electric field having a sinusoidal waveform has been studied experimentally with the intention of investigating the enhancement of the direct-contact heat exchange between the two liquids. We have found that the field can induce, depending on its frequency, not only the resonant oscillation of the second mode of the drops, but also another peculiar oscillation that is related to the resonant oscillation of the third mode superposed on the second-mode oscillation.

Introduction

Heat transfer to or from liquid drops passing through an immiscible liquid can be enhanced effectively by applying an electric field whose strength changes periodically, so that the drop shapes oscillate following changes in the field strength (Mori et al., 1977; Kaji et al., 1978, 1980, 1985). In the latest work (Kaji et al., 1985) we succeeded in making water drops, which were rising in a medium of denser methylphenyl silicone oil confined by vertically oriented parallel-plate electrodes (Fig. 1), undergo a resonant oscillation of the second mode causing an intensive heat transfer enhancement. The waveform of the fields we used in the work was the one illustrated in Fig. 2: The magnitude of the field strength $|E|$ changed sinusoidally with time between two limiting values, $|E|=0$ and $|E|=E_0>0$, and the direction of the field was alternated in order to prevent the drops from possibly migrating toward either electrode plate. The drops oscillated, responding to the change in $|E|$, at a frequency f', which was twice as high as the frequency f of the field. A resonant oscillation was observed as f was controlled to f_{r2}, half the resonance frequency f'_{r2} of the second-mode oscillation of the drops.

The present work was motivated, however, by a suspicion that the abovementioned waveform—which we call hereafter "modified sinusoidal waveform"—is not the most favorable for causing a shape oscillation in drops. Since the electric stress at the drop surface is in proportion to the square of the field strength, E^2, the most favorable waveform may be one such that E^2 instead of $|E|$ varies with time as illustrated in Fig. 3(*a*) or expressed as

$$\left(\frac{E}{E_0}\right)^2 = \frac{1}{2}\left[\sin\left(2\pi f' t-\frac{\pi}{2}\right)+1\right] = \frac{1}{2}(1-\cos 2\pi f' t) = \sin^2\pi f' t \qquad (1)$$

Accordingly $|E|/E_0$ has the waveform illustrated in Fig. 3(*b*). If the direction of the field is to be alternated because of the same reason as stated before, E/E_0 should be

$$E/E_0=\sin\pi f' t=\sin 2\pi f t \qquad (2)$$

which is illustrated in Fig. 3(*c*). Thus, we find that the waveform of the field possibly ideal for inducing a shape oscillation of frequency f' is no more than a simple sine wave with a frequency just half of f'.

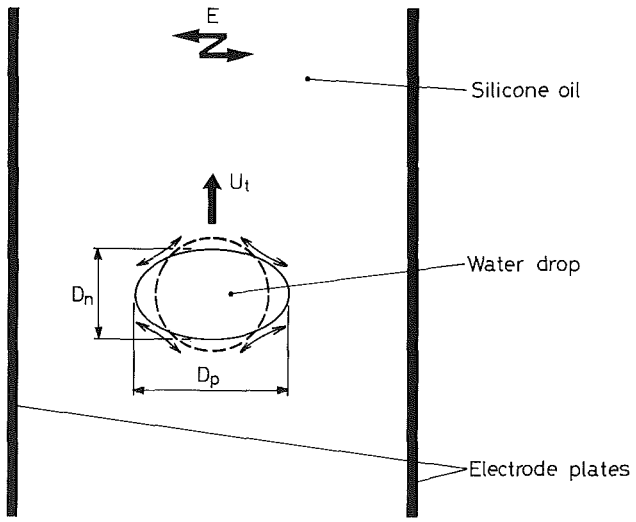

Fig. 1 Schematic of a water drop undergoing shape oscillation while rising in denser silicone oil across which a periodically changing electric field is applied

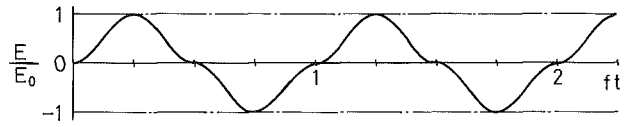

Fig. 2 Modified sinusoidal waveform of electric fields used in the preceding study (Kaji et al., 1985)

Contributed by the Heat Transfer Division for publication in the JOURNAL OF HEAT TRANSFER. Manuscript received by the Heat Transfer Division February 17, 1987. Keywords: Augmentation and Enhancement, Direct-Contact Heat Transfer, Sprays/Droplets.

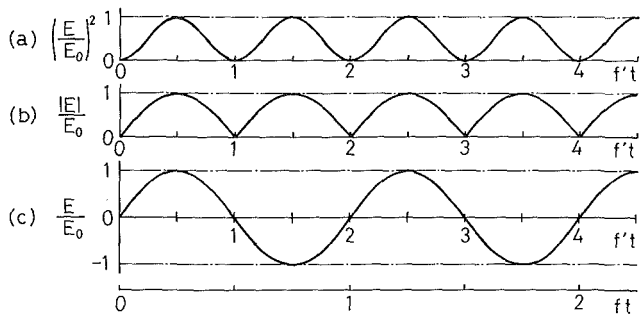

Fig. 3 Waveforms of $(E/E_0)^2$ (a) and $|E|/E_0$ (b), which are considered the most favorable for giving drops a shape oscillation of frequency f', and the waveform of an alternating field (c), which is consistent with the former two

Based on the above consideration we have repeated some of our former experiments (Kaji et al., 1985) using electric fields with a simple sinusoidal waveform. The obtained results are presented and discussed in two papers, Part 1 and Part 2 of this series. The aspect of drop dynamics is dealt with in this paper, Part 1; and that of heat transfer augmentation is dealt with in Part 2 (Kaji et al., 1988).

Experimental

The scheme of the experiments was the same as that employed in our preceding single-drop studies on the electrohydrodynamic heat transfer augmentation (Kaji et al., 1978, 1980, 1982, 1985; Kaji and Mori, 1986), and is described here only briefly. Isolated distilled-water drops of a specified volume were released, under no electric field, to rise in a stagnant, hotter medium of methylphenyl silicone oil (KF 54 fluid prepared by Shin-Etsu Chemical Co., Tokyo) contained in a space between a pair of vertical brass-plate electrodes set parallel to each other. The distance between the electrodes l was 38 mm. As each drop arrived at a certain elevation, an electric field was applied across the electrodes, possibly causing shape oscillation of the drop (Fig. 1). The undisturbed temperature of the medium was maintained at 50.0 ± 0.4 °C. (Some physical properties of the water/KF 54 system at 50 °C are listed in the paper by Kaji and Mori, 1986.) The drops in the course of free rise in the presence or absence of electric fields were photographed with a Locam Model 51 16-mm cinecamera at 30 ~ 320 fps, and their images on the films were analyzed later on an NAC Model 16-S analysis projector. The drop temperatures were measured at several different elevations in the medium under each condition of the applied electric field. The method of the measurements and the temperature-data processing will be explained briefly in Part 2.

The power supply specially designed by Tochitani (1985) for our previous work (Kaji et al., 1985) was used again after a little modification had been made on it so that it could supply electrode voltages, which changed sinusoidally with time, while maintaining a phase lag of π rad between them. Since these voltages were equal to each other in magnitude and opposite in sign at each instant, we can assume that the voltage at the midplane between the electrodes from which rising drops deviated little was maintained nearly at the ground level. Concerning the evaluation of field strengths based on the voltage data, see the Appendix.

Results

Shape Oscillation—Description of Experimental Results. In the absence of an electric field, water drops rising in the medium of silicone oil took on an almost spherical shape. To be more exact, the distortion ratio, defined as $\delta \equiv (D_p - D_n)/(D_p + D_n)$, was -0.014 ± 0.014 irrespective of D_0, the equivalent spherical diameter, which ranged from 4.4 to 6.0 mm, where D_p and D_n denote the drop axes as indicated in Fig. 1. No shape oscillation was recognized.

The shape oscillations of drops observed under fields with the sinusoidal waveform as shown in Fig. 3(*c*) were generally the same in appearance as those observed in the previous studies (Kaji et al., 1978, 1980, 1985) under electric fields with a pulsed quasi-square waveform or the modified sinusoidal waveform shown in Fig. 2. The instantaneous shape of each drop was approximated by a prolate spheroid whose axis of rotation was parallel to the field. Every drop rose rectilinearly in the medium, whether it was subjected to an electric field or not.

As for drops subjected to an electric field, we measured, by frame-by-frame analysis of the cinefilms, D_p and D_n, both varying with time with a frequency $f'(=2f)$, and then determined the maximum and the minimum of D_p/D_n or of δ in each period f'^{-1}. The uncertainties of the determined values of $(D_p/D_n)_{max}$ and $(D_p/D_n)_{min}$ are estimated, based on the root sum square method (Abernethy et al., 1985), to be within ± 0.01, and those for δ_{max} and δ_{min} within ± 0.005. Figure 4 shows the dependencies of $(D_p/D_n)_{max}$ and $(D_p/D_n)_{min}$ on the field frequency f. This figure corresponds to Fig. 4 in our latest paper (Kaji et al., 1985), which shows the results obtained in the presence of electric fields having the modified sinusoidal waveform (Fig. 2), and also to Fig. 4(*a*) in the earlier paper (Kaji et al., 1980) in which we dealt with the effects of intermittent fields having a pulsed quasi-square waveform. In comparing the present and the previous results,

Nomenclature

A_L, A_R = areas of drop image illustrated in Fig. 5
A_0 = half area of such an ellipse as illustrated in Fig. 5
D_n, D_p = axes of drop normal and parallel to electric field
D_0 = equivalent spherical diameter of drop
E, E_0 = strength of electric field and its amplitude
E_b, E_{b0} = E in the bulk region between the electrodes and its amplitude
E_n, E_{n0} = E evaluated as $\Delta V/l$ and its amplitude
f = frequency of electric field
f_{cr} = critical field frequency shown in Fig. 4
f_{r2} = field frequency yielding the second-mode resonant oscillation of drop
f_{r3} = field frequency shown in Fig. 4
f_{r2}, f'_{r3} = frequencies of the second and third-mode resonant oscillations of drop
l = electrode spacing
K = mobility of charge carrier
t_T = time required for charge carrier to transit half of the electrode spacing
U_t, U_{t0} = translational velocity of drop and its value in the absence of electric field
V_0 = amplitude of ΔV
ΔV = voltage difference between the electrodes
δ = $(D_p - D_n)/(D_p + D_n)$
ζ = E_b/E_n

Subscripts

max, min = maximum and minimum in each period of drop oscillation

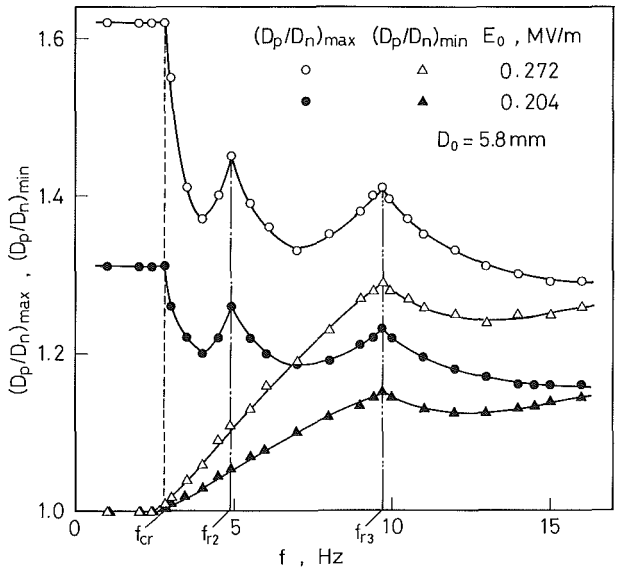

Fig. 4 Dependencies of $(D_p/D_n)_{max}$ and $(D_p/D_n)_{min}$ on the field frequency

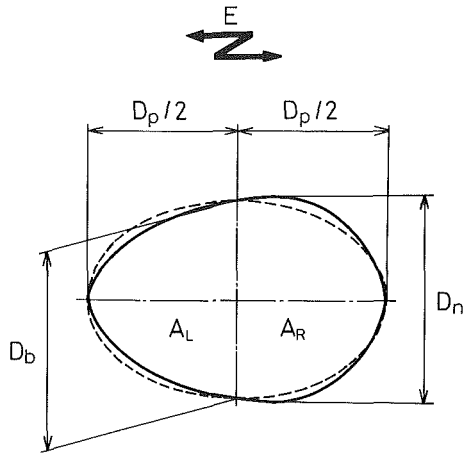

Fig. 5 Schematic illustrating the contour of a drop (solid line) and an ideal ellipse (dashed line) sharing the major axis D_p and the bisector of the major axis D_b

given in those figures, with each other, one should double the magnitudes of the field-strength amplitude indicated in the previous results because of the difference in evaluation of field strengths, which is described in the Appendix.

The results given in Fig. 4 show some conspicuous features partially in common with the previous results obtained with the different waveforms. First, the existence of the critical frequency, f_{cr}, where $(D_p/D_n)_{max}$ and hence the amplitude of oscillation starts to decrease with an increasing f, is common to all the results obtained with the three different waveforms. In the case of the sinusoidal and the modified sinusoidal waveforms, the frequency f_{cr} may be regarded as the maximum frequency permitting the shape of each drop to vary, well following the change of the field strength, or in other words, holding an instantaneous balance between the electric stress and the capillary force on the drop. In case of the pulsed quasi-square waveform, f_{cr} can be interpreted in some different way (see Kaji et al., 1980). The second feature, which is common only to the results obtained with the sinusoidal and the modified sinusoidal waveforms, is that $(D_p/D_n)_{max}$ reaches a peak at the frequency f_{r2} because of the resonant oscillation of the second mode of drops (Kaji et al., 1985). The third feature, which distinguishes the present results obtained with the sinusoidal waveform from the previous results obtained with either of the other waveforms, is that as f exceeds f_{cr}, $(D_p/D_n)_{min}$ starts to rise, exceeding unity, and continues to increase with an increasing f until it reaches a peak, in synchronism with the second peak of $(D_p/D_n)_{max}$, at a frequency that we denote by f_{r3}. For the present time we cannot give a satisfactory interpretation of the drop dynamics at the frequency f_{r3}. Nevertheless, it seems reasonable to assume that f_{r3} is just a half of f'_{r3}, the resonance frequency of the third mode of drops, and the oscillation observed at f_{r3} involves the resonant oscillation of the third mode being superposed on the second-mode oscillation, which is much more prominent. This idea is supported in part by an agreement, within a deviation of 10 percent, between experimentally determined f_{r3} and the prediction of $f'_{r3}/2$ based on the theory (see, for example, Trinh et al., 1982) for driven oscillating drops. (The abovementioned deviation can be ascribed to the assumption, employed in the theory, of a small-amplitude oscillation of spherical drops and more probably to uncertainties of the properties—densities, viscosities, and interfacial tension—of the water/KF 54 system.) The idea is also supported by the findings concerning drop configurations, which are described below in some detail.

The oscillation of the third mode of a drop is characterized by its instantaneous configurations, which are asymmetric about the plane that bisects the drop axis D_p at right angles to it (see, for example, Sample et al., 1970). In order to detect such a feature in drop configurations, which may be quite inconspicuous, we made a detailed analysis of configurations, taken on cinefilms, of drops undergoing oscillations at the frequency f_{r3} and some other frequencies. For each frame of the cinefilms, we traced, at a high magnification, the contour of the image of a drop as illustrated in Fig. 5 with a solid line, and measured, with the aid of a TCOM video image analyzing system (Model COM-9210 #002), the area A_R of the image on the right of the bisector of D_p, and A_L, the area on the left of the bisector. At the same time we calculated a half-area A_0 of an ideal ellipse, illustrated in Fig. 5 with a dashed line, whose major and minor axes coincide with D_p and D_b, the length of the bisector of D_p, of the drop, respectively. (The ellipse represents the projection, on a vertical plane set parallel to the electric field, of a prolate spheroid whose volume coincides with that of the drop within ±2 percent.) Exemplified in Fig. 6 are the variations with the time of (D_p/D_n), $(A_R/A_0 - 0.986)$, and $(A_L/A_0 - 0.986)$ for a particular drop when $f=f_{r3}$. Each point for the latter two indices has an uncertainty of ±0.002 at the most, which was inevitable in the abovementioned drop-image analysis process. The numeral 0.986 is an empirically determined time-averaged value of either A_R/A_0 or A_L/A_0. [The average value of either A_R/A_0 or A_L/A_0 being less than unity probably results from a finite deviation of the drop shape from a prolate spheroid (Sample et al., 1970).] It can be recognized that both $(A_R/A_0 - 0.986)$ and $(A_L/A_0 - 0.986)$ oscillate at the frequency $2f_{r3}$ with phase angles shifted by approximately $\pi/2$ rad in opposite directions to each other from that of D_p/D_n. This finding is consistent with the expected appearance of the third-mode oscillation. Figure 7 shows the variation of $[(A_L/A_0)_{max} - (A_L/A_0)_{min}]/2$, the amplitude of A_L/A_0, with the field frequency f. The amplitude is largest at $f=f_{r3}$, and hence we believe that the third-mode resonant oscillation arises at this frequency. Further, we presume that it is the very third-mode resonant oscillation that causes such maximization at $f=f_{cr}$ of the drop distortion, measured with the index of D_p/D_n, as shown in Fig. 4, though we have no satisfactory explanation on the possible mechanism that the third-mode oscillation affects the level of D_p/D_n.

Shape Oscillation—Comparison With Theory. Torza et al.

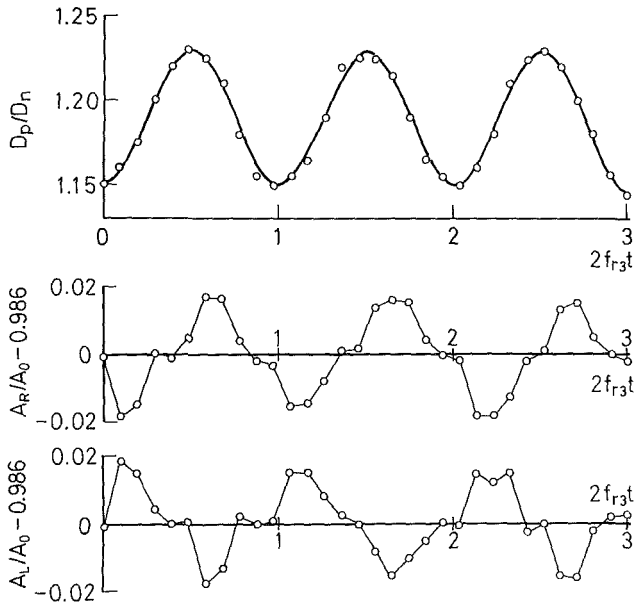

Fig. 6 Simultaneous variations with time of D_p/D_n, $(A_R/A_0-0.986)$, and $(A_L/A_0-0.986)$ for the same drop ($D_0 \simeq 5.8$ mm) undergoing oscillation at the field frequency $f_{r3}(\simeq 9.7$ Hz)

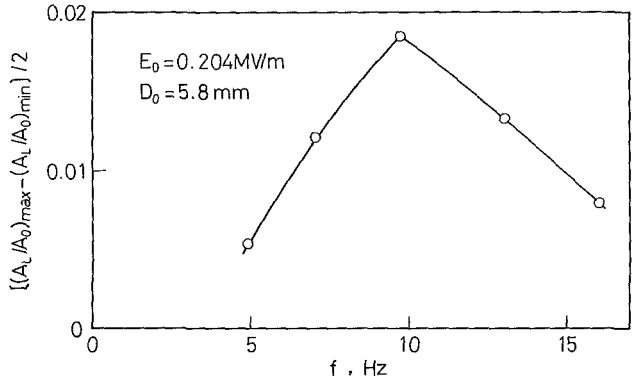

Fig. 7 Dependency of the amplitude of A_L/A_0 on the field frequency

(1971) developed an electrohydrodynamic theory on the deformation of an isolated liquid drop suspended in a neutrally buoyant condition in an immiscible fluid subject to a uniform electric field whose strength varies sinusoidally with time, as illustrated in Fig. 3(*c*). The theory assumed a small deformation of the drop from a spherical shape and negligible inertial effects. Here we attempt to compare our experimental results with the predictions by the above theory.

Figure 8 shows the experimental results and the theoretical predictions both in the form of frequency dependencies of the maximum and the minimum of the drop distortion ratio δ during each period of oscillation. The experimental values of δ_{max} and δ_{min} are normalized by the constant value of δ_{max} in the range of $f \leq f_{cr}$, while the theoretical values are normalized by the asymptotic value of δ_{max} at $f \to 0$, which means the steady distortion ratio available under a steady field whose strength is maintained at E_0. The experimental results agree with the theoretical prediction only in that δ_{max} and δ_{min} tend to approach, with an increasing f, half of the level of δ_{max} at $f \to 0$. The rate of the fractional decay of the difference between δ_{max} and δ_{min} with increasing f is much higher in the experimental results. The theory fails to predict the peculiar variations of δ_{max} and δ_{min} with f near f_{r2} and f_{r3}, because it neglects the inertial effects. The theory also fails to predict that δ_{max} and δ_{min} take constant values in the range of $f \leq f_{cr}$ probably for the same reason. Another discrepancy between the experimental

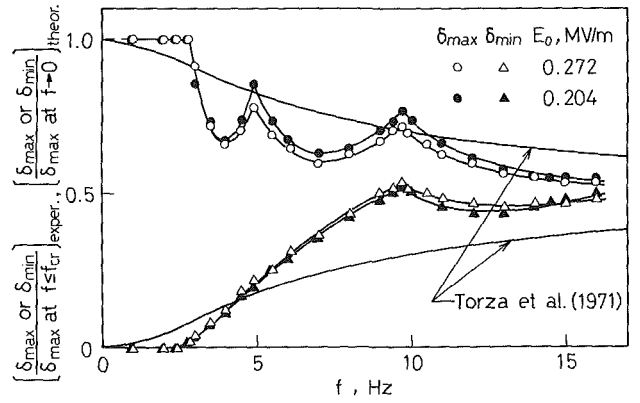

Fig. 8 Dependencies of δ_{max} and δ_{min} on the field frequency: comparison of the experimental results with the theory of Torza et al. (1971)

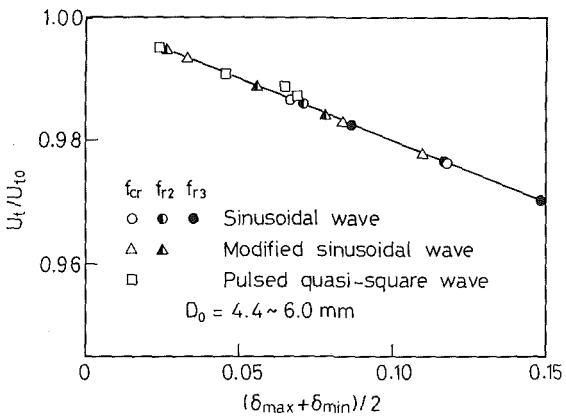

Fig. 9 Relative change in rise velocity of drops with their mean distortion ratio

and the theoretical results, which is masked in the comparison shown in Fig. 8, is in the magnitudes of δ_{max} and δ_{min}. For example, at each level of E_0 the experimental value of δ_{max} in the range of $f \leq f_{cr}$ is approximately 2.1 times as large as the asymptotic value of δ_{max} at $f \to 0$ predicted by the theory. This discrepancy is essentially the same as the one that Torza et al. themselves found in their experiments using steady and 60 Hz electric fields, and no satisfactory explanation has been presented so far in spite of some efforts having been made (Ajayi, 1978).

Translational Motion. The translational motion of drops experiences some effect of the applied electric field. Figure 9 summarizes the data of the rise velocity at $f=f_{cr}$, f_{r2}, and f_{r3} obtained in the present experiments, and also those obtained in the previous experiments in which were applied electric fields having the modified sinusoidal waveform shown in Fig. 2 (Kaji et al., 1985) and the pulsed quasi-square waveform (Kaji et al., 1980). The data are shown in the form of reduced velocity versus the arithmetic mean of the maximum and the minimum drop distortion ratios. Each point in Fig. 9 involves an uncertainty in U_t/U_{t0} within ± 0.01. It is noted that the rise velocity of drops subjected to the periodically changing fields decreases, with an increase in the average distortion ratio, at a constant rate that is practically dependent neither on the waveform nor on the frequency of the fields. This fact suggests that the reduction of rise velocity U_t from U_{t0} is primarily ascribed to the time-averaged deformation of drops rather than some dynamic effect of their shape oscillation, although more detailed examinations are needed to settle this matter. In any case, the reduction of rise velocity is no more than a few percent in the range of the experiments, and thus its effect on heat transfer will possibly be limited.

Conclusions

The motions of drops subject to oscillatory forcing electric fields have been examined with the intention of investigating the heat transfer enhancement caused by the fields. Particular attention has been paid to showing the nature of the shape oscillation of drops forced by alternating fields having a sinusoidal waveform. With this waveform we have found three particular field frequencies—f_{cr}, f_{r2}, and f_{r3}, indicated in Fig. 4—which are of interest in considering the heat transfer enhancement. The findings of the former two are not essentially new, since their existences were found before in the presence of electric fields having different waveforms (Kaji et al., 1978, 1985). The existence of f_{r3}, at which the resonant oscillation of the third mode is presumably superposed on the second-mode oscillation, is a new finding with the fields having the sinusoidal waveform.

Concerning the second-mode resonant oscillation at $f=f_{r2}$, no significant difference has been found between the sinusoidal and the modified sinusoidal waveforms. The amplitude of the oscillation is increased only a little by replacing the latter waveform with the former.

Acknowledgments

We are indebted to Dr. Kazuo Yoshida of Department of Mechanical Engineering, Keio University, for his helpful comments concerning the interpretation of the observed drop oscillations. We are also grateful to Ng Buck Hwa and H. Yamada, students at the Division of Mechanical Engineering, The Institute of Vocational and Technical Education, for their assistance in the laborious work of drop-image analysis. This study was performed within the framework of the Special Project Research on Energy under a Grant-in-Aid of Scientific Research on the Ministry of Education, Science and Culture of Japan.

References

Abernethy, R. B., Benedict, R. P., and Dowdell, R. B., 1985, "ASME Measurement Uncertainty," ASME *Journal of Fluids Engineering*, Vol. 107, pp. 161–164.

Ajayi, O. O., 1978, "A Note on Taylor's Electrohydrodynamic Theory," *Proceedings of the Royal Society of London*, Series A, Vol. 364, pp. 499–507.

Kaji, N., and Mori, Y. H., 1986, "Direct Contact Heat Transfer to a Drop Translating in a Transverse Electric Field," *Wärme- und Stoffübertragung*, Vol. 20, pp. 11–18.

Kaji, N., Mori, Y. H., and Tochitani, Y., 1985, "Heat Transfer Enhancement Due to Electrically Induced Resonant Oscillation of Drops," ASME JOURNAL OF HEAT TRANSFER, Vol. 107, pp. 788–793.

Kaji, N., Mori, Y. H., and Tochitani, Y., 1988, "Electrically Induced Shape Oscillation of Drops as a Means of Direct Contact Heat Transfer Enhancement: Part 2—Heat Transfer," ASME JOURNAL OF HEAT TRANSFER, Vol. 110, this issue.

Kaji, N., Mori, Y. H., Tochitani, Y., and Komotori, K., 1978, "Direct-Contact Heat Transfer to Drops in an Intermittent Electric Field," *Proceedings of the 6th International Heat Transfer Conference*, Hemisphere Publishing Corp., Washington, DC, Vol. 3, pp. 165–170.

Kaji, N., Mori, Y. H., Tochitani, Y., and Komotori, K., 1980, "Augmentation of Direct-Contact Heat Transfer to Drops With an Intermittent Electric Field," ASME JOURNAL OF HEAT TRANSFER, Vol. 102, pp. 32–37.

Kaji, N., Mori, Y. H., Tochitani, Y., and Komotori, K., 1982, "Electrohydrodynamic Augmentation of Direct-Contact Heat Transfer to Drops Passing Through an Immiscible Dielectric Liquid: Effect of Field-Induced Shuttle Migration Between Parallel Plane Electrodes of Drops," *Proceedings of the 7th International Heat Transfer Conference*, Hemisphere Publishing Corp., Washington, DC, Vol. 5, pp. 231–236.

Mori, Y. H., Kaji, N., and Tochitani, Y., 1977, "An Augmentation Method of Heat or Mass Transfer With an Intermittent Electric Field," Japanese Patent Application No. SHO 52-9488; Patent No. 1043731, 1981.

Sample, S. B., Raghupathy, B., and Hendricks, C. D., 1970, "Quiescent Distortion and Resonant Oscillation of a Liquid Drop in an Electric Field," *International Journal of Engineering Science*, Vol. 8, pp. 97–109.

Tochitani, Y., 1985, "High Voltage ac Power Supply With Variable Frequency Output from 0.5 to 10 Hz." *Review of Scientific Instruments*, Vol. 56, pp. 321–325.

Torza, S., Cox, R. G., and Mason, S. G., 1971, "Electrohydrodynamic Deformation and Burst of Liquid Drops," *Philosophical Transactions of the Royal Society of London*, Series A, Vol. 269, pp. 295–319.

Trinh, E., Zwern, A., and Wang, T. G., 1982, "An Experimental Study of Small-Amplitude Drop Oscillations in Immiscible Liquid Systems," *Journal of Fluid Mechanics*, Vol. 115, pp. 453–474.

Yasufuku, S., Umemura, T., and Tanii T., 1979, "Electric Conduction Phenomena and Carrier Mobility Behavior in Dielectric Fluids," *IEEE Transactions of Electric Insulation*, Vol. EI-14, pp. 28–35.

APPENDIX

Evaluation of Field Strengths

The voltage difference between the electrodes ΔV changes according to

$$\Delta V = V_0 \sin 2\pi f t \tag{A1}$$

If we define the nominal field strength E_n and its amplitude E_{n0} as

$$E_n = \Delta V/l, \quad E_{n0} = V_0/l \tag{A2}$$

E_n/E_{n0} changes with time following the desirable mode of change in E/E_0 given by equation (2). However, E_n is not always equal to the local strength of the field on the path of drops unless the medium between the electrodes is free from space charge. In fact, our previous measurements of the potential profiles in the electrode spacing while steady voltages were applied to the electrodes showed a bulk region where the profiles were almost linear and two space-charge regions, one near each electrode, where the potential gradients were steeper (Kaji et al., 1978, 1982). (The measurements were performed by traversing a Langmuir electrostatic probe in the water-saturated but droplet-free silicone oil in place.) The ratio ζ of the field strength in the bulk region E_b to the nominal field strength E_n was very close to 0.5, irrespective of the levels of the steady voltages at the electrodes. When the voltages at the electrodes varied periodically with time providing alternating fields (Kaji et al, 1978, 1980, 1985), we had no means to reveal instantaneous potential profiles, and hence we assumed that the amplitude of the field strength in the bulk region E_{b0} could be evaluated as

$$E_{b0} = \zeta V_0/l \tag{A3}$$

by assigning to ζ the same value as the one obtained in case of the steady voltages having been applied. At present, however, we have a rather negative view on the above assumption because of the reason explained below.

The carrier mobility K in the silicone oil, whose viscosity is as high as 147 mPa•s (Kaji and Mori, 1986), is assumed to be as low as 1×10^{-10} m^2/V – s based on the data by Yasufuku et al. (1979). Hence, the time t_T required for each charge carrier to transit a half of the electrode spacing, which is given by $(l/2)/KE_n$, is evaluated to be well over 10^2s, even if we substitute into E_n the highest value of E_{n0} used in the present experiments, 0.277 MV/m. Evidently, the order of t_T is much larger than that of a half-period of the field, $1/2f$. This fact means that the carriers in the electrode spacing hardly migrate along the field in each half period, and hence the potential profile at any instant is rather linear throughout the electrode spacing. Based on the above consideration, we assume that the instantaneous field strength E_b and its amplitude E_{b0} in the bulk region are essentially the same as E_n and E_{n0}, respectively, and denote them simply by E and E_0 in this paper.

N. Kaji
Associate Professor,
Division of Mechanical Engineering,
The Institute of Vocational and
Technical Education,
Sagamihara 229, Japan

Y. H. Mori
Associate Professor,
Department of Mechanical Engineering,
Keio University,
Yokohama 223, Japan
Mem. ASME

Y. Tochitani
Associate Professor,
Department of Mechanical Engineering,
Kanazawa Institute of Technology,
Nonoichi 921, Japan

Electrically Induced Shape Oscillation of Drops as a Means of Direct-Contact Heat Transfer Enhancement: Part 2—Heat Transfer

The heat transfer enhancement caused by the application of a low-frequency (1 ~ 16 Hz) alternating field having the sinusoidal waveform has been studied experimentally with water drops in a medium of silicone oil. The heat transfer coefficient has been found to peak at three particular frequencies. The data newly obtained with the sinusoidal waveform are compared with earlier results obtained with electric fields having other waveforms. The waveform and the frequency that yield the largest enhancement of heat transfer are sought.

Introduction

This paper reports on some experimental examinations of the effects of electrically forced shape oscillation of drops on the heat transfer to the drops while they are passing through the medium of another immiscible liquid. The basic idea of using the electrically forced oscillation of drops as a means of heat transfer enhancement was originated by Mori et al. (1977), and was first tested by applying an intermittent electric field having a pulsed quasi-square waveform (Fig. 1*a*) to water drops rising in creeping motion in a denser methylphenyl silicone oil (Kaji et al., 1978, 1980). A particular field frequency at which the quasi-steady heat transfer coefficient reaches a maximum, while the field amplitude is held constant, was found, and it was identified as the critical frequency f_{cr} bordering the lower frequency range in which the amplitude of drop oscillation is maintained constant and the higher frequency range in which the amplitude decreases with an increasing frequency. Typically $f_{cr} = 3 \sim 4$ Hz for drops of $3 \sim 6$ mm diameter. Later Mori et al. (1985) examined the same matter in two different drop/medium systems, other than the water/methylphenyl silicone oil system, each consisting of two immiscible oils. They found that f_{cr} in those oil/oil systems are significantly lower than those in the water/oil systems because the oil/oil interfacial tensions are very low, and hence the heat transfer enhancements in those oil/oil systems are much less extensive. Thus, we can assume that the electrically forced drop oscillation as a means of heat transfer enhancement can be applied most effectively to systems that consist of some aqueous drops and an oil medium and accordingly have an interfacial tension of the order of 10 mN/m or higher.

In the latest work (Kaji et al., 1985) we applied to the water/methylphenyl silicone oil system electric fields having a specially designed waveform: The magnitude of the field strength $|E|$ changes sinusoidally with time between two limiting values, $|E| = 0$ and $|E| = E_0 > 0$, at the very frequency f' to which the drop oscillation is to respond, and the field direction is alternated at the frequency $f = f'/2$ so that the variation of the field strength is expressed as

$$\frac{E}{E_0} = (-1)^{[2ft]} \frac{1}{2}\left[\sin\left(4\pi ft - \frac{\pi}{2}\right) + 1\right] = (-1)^{[2ft]} \sin^2 2\pi ft \qquad (1)$$

where the brackets in the exponent of (-1) denote Gauss' notation; i.e., $[2ft]$ means the maximum integer that does not exceed $2ft$. The waveform is illustrated in Fig. 1(*b*). With this "modified sinusoidal waveform" we successfully made water drops undergo a resonant oscillation of the second mode by controlling the field frequency f to f_{r2}, a half of the resonance frequency f'_{r2} of the drops. The coefficient α of the quasi-steady heat transfer to each drop was found to have two maxima at $f = f_{cr}$ and $f = f_{r2}$ when we vary f, keeping E_0 at a constant level.

In the preceding paper, Part 1 of this series (Kaji et al., 1988), we showed the drop dynamics in the presence of electric fields having another waveform illustrated in Fig. 1(*c*): E changes sinusoidally with time as

$$E/E_0 = \sin 2\pi ft \qquad (2)$$

This simple sinusoidal waveform resulted in the amplitude of drop oscillation having two peaks at two different frequencies: f_{r2}, the same frequency as the one found in case of the modified sinusoidal waveform, and f_{r3}, which is presumably half of the resonance frequency of the third-mode oscillation. In this paper we first show experimental results on heat transfer, which were obtained simultaneously with those on drop dynamics shown in the preceding paper. Then, the results are compared with those obtained in the previous works (Kaji

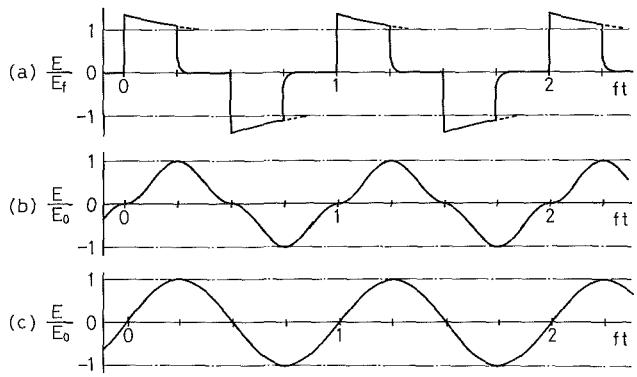

Fig. 1 Three waveforms tested in the previous and the present studies: (*a*) pulsed quasi-square, (*b*) modified sinusoidal, and (*c*) sinusoidal waveforms

Contributed by the Heat Transfer Division for publication in the JOURNAL OF HEAT TRANSFER. Manuscript received by the Heat Transfer Division February 17, 1987. Keywords: Augmentation and Enhancement, Direct-Contact Heat Transfer, Sprays/Droplets.

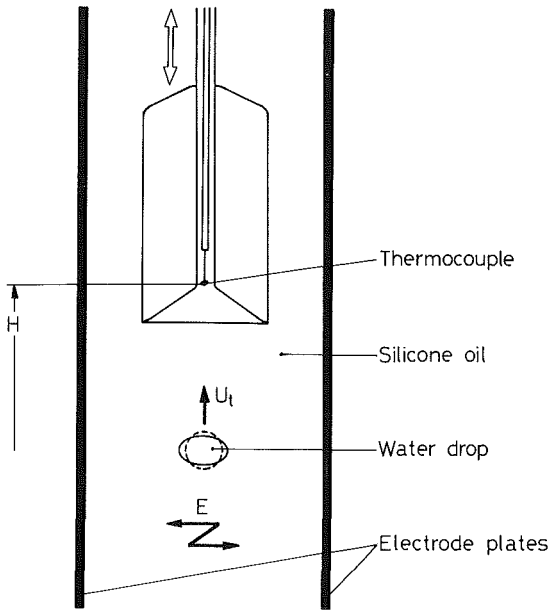

Fig. 2 Schematic illustration of drop-collecting funnel inserted in the space between the electrodes for measuring drop temperature

et al., 1980, 1985) in the presence of electric fields with the other waveforms, and the selection of the waveform and the frequency for obtaining the largest heat transfer enhancement is considered.

Experimental

The scheme of the present experiments is described in Part 1 except for the drop-temperature measurement and the temperature-data processing. The procedure of measuring temperature of each drop and deducing the quasi-steady heat transfer coefficient is common throughout our single-drop studies of electrohydrodynamic heat transfer augmentation and is described fully in the earliest paper (Kaji et al., 1978). In the following we describe the procedure only briefly.

A vacuum-jacketed glass funnel with a long capillary stem is inserted, as illustrated in Fig. 2, into the medium of uniformly heated methylphenyl silicone oil (KF 54 fluid prepared by Shin-Etsu Chemical Co., Tokyo) along the possible trajectory of oncoming cooler water drops. Each drop is swallowed into the funnel, passing slowly over the junction of a thermocouple located at the entrance of the capillary stem of the funnel. The lowest temperature that the thermocouple shows while the drop passes over its junction is regarded as the reference drop temperature T_d. By traversing the funnel vertically we get the dependency of T_d on the elevation H, from which we can deduce the quasi-steady overall heat transfer coefficient α related to the equivalent spherical surface area of each drop and to the difference between the undisturbed medium temperature, T_c, and T_d. Some uncertainties in the measurements of T_d and T_c and also in the determination of dT_d/dH provide each deduced value of α with an uncertainty that is estimated, based on the root sum square method (Abernethy et al., 1985), to be ± 3.5 percent or less.

Hydrodynamic and electrical properties of the water/KF 54 system are given in the paper by Kaji and Mori (1986). For thermal properties and the heat transfer data obtained in the absence of electric field, consult the paper by Kaji et al. (1980). It may be worthwile to note here that the major resistance to heat flow in the water/KF 54 system is considered to be in the medium side at least in the absence of electric field (Kaji et al., 1980).

Results and Discussion

The heat transfer data obtained in the present experiments are shown in Fig. 3 in the form of the relative increase in the heat transfer coefficient α depending on the field frequency. This figure is the counterpart of Fig. 4 in Part 1 (Kaji et al., 1988) in which the dependency of the oscillatory deformation of drops on the field frequency is shown. At the same time, Fig. 3 is to be compared with some figures given in our earlier papers (e.g., Fig. 4(*b*) in Kaji et al., 1980; Figs. 6(*a*) and 6(*b*) in Kaji et al., 1985) where shown in the same form are frequency dependencies of α obtained with the pulsed quasi-square and the modified sinusoidal waveforms, respectively.

Figure 3 clearly shows that α peaks at three different frequencies: f_{cr}, f_{r2}, and f_{r3}. This fact should be related to the fre-

Nomenclature

D_n, D_p = axes of drop normal and parallel to electric field

D_0 = equivalent spherical diameter of drop

E; E_f, E_0 = strength of electric field; its amplitudes shown in Fig. 1

f; f_{cr}, f_{r2}, f_{r3} = frequency of electric field; particular frequencies at which α peaks, as shown in Fig. 3

f' = frequency of drop oscillation

H = elevation in the medium

Nu; Nu_0, Nu_s = Nusselt number defined as $\alpha D_0/\lambda_c$; its values available in the absence of electric field and in a completely quiescent system, respectively

Nu^+ = reduced Nusselt number defined by equation (3)

S = Strouhal number defined as U_D/U_t

T_c, T_d = undisturbed temperature in the medium and reference temperature of drop

U_D = oscillatory radial velocity given by equation (4)

U_t = translational velocity of drop

α, α_0 = heat transfer coefficient based on surface area of spherical drop and its value in the absence of electric field

δ, δ_{cr} = distortion ratio of drop defined as $(D_p - D_n)/(D_p + D_n)$ and its critical value for drop burst

λ_c = thermal conductivity of medium liquid

Subscripts

max, min = maximum and minimum in each period of drop oscillation

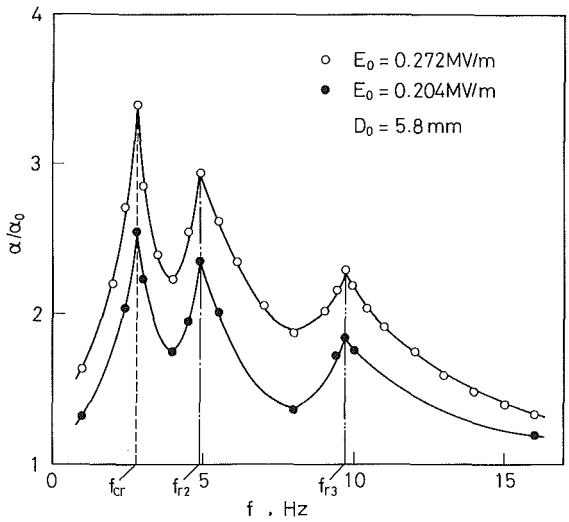

Fig. 3 Dependency of relative increase of heat transfer coefficient on the field frequency

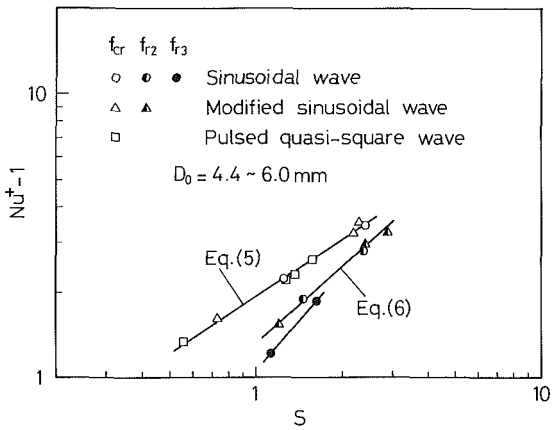

Fig. 4 Heat transfer data, for $f=f_{cr}$, f_{r2}, and f_{r3}, correlated with oscillatory-to-translational velocity ratio

quency dependency of the drop oscillation shown in Fig. 4 in Part 1. The first frequency f_{cr} is the upper limit of a frequency range wherein the amplitude of oscillation is held constant at the highest level, while at either of the latter two higher frequencies the amplitude peaks. Thus, the rate of oscillatory displacement of drop surface takes the maximum at each of these three frequencies. The most distinct deviation of the present results shown in Fig. 3 from the former results obtained with the modified sinusoidal waveform (Kaji et al., 1985) is that α exhibits a third peak at $f=f_{r3}$.

Irrespective of the waveform and the frequency of the applied field, any appreciable increase in α must result from oscillatory flows, both inside and outside of each drop, driven by the oscillatory displacement of the drop surface. (Note that the fractional increase, due to the shape oscillation, in the instantaneous surface area of each drop over the surface area that the drop would take in the course of rise under no field is no more than 3.8 percent at most in the range of our experiments, while the fractional increase of the latter area due to steady deformation of the drop from the spherical form is estimated to be as low as 0.01 percent. Hence, the drop oscillation can have little effect on α via an increase in the surface area.) In this respect, the phenomenon of the present interest may be quite similar to the evaporation of drops suspended in an oscillatory gas flow, which was studied earlier by some researchers (Mori et al., 1969; Larsen et al., 1978). Based on the above view, we suppose that our data of α obtained not only in the present experiments but also in the previous experiments (Kaji et al., 1980, 1985) can be correlated in terms of some factor relevant to the rate of oscillatory displacement of the drop surface, provided that the induced oscillatory flows were approximately similar in those experiments. In an earlier paper (Mori et al., 1985) we made an attempt at correlating only the data for $f=f_{cr}$ obtained with the pulsed quasi-square waveform. Here we extend and modify the attempt to include the data obtained with each of the three different waveforms. The parameters we selected for correlating the data are Nusselt number normalized as

$$\mathrm{Nu}^+ \equiv (\mathrm{Nu}-\mathrm{Nu}_s)/(\mathrm{Nu}_0-\mathrm{Nu}_s) \tag{3}$$

and the Strouhal number S defined as the ratio of a radial velocity U_D due to the drop oscillation to the translational velocity U_t. In equation (3), Nu is the Nusselt number related to α, D_0, and thermal conductivity of the medium; Nu_0 denotes Nu in the absence of electric field; and Nu_s means the Nu that would be available in a completely quiescent system due to conduction only, which is determined to be 1.87 for the water/KF 54 system (Kaji et al., 1982). The radial velocity U_D is given by

$$U_D = f'(D_{p,\max}-D_{p,\min}) = 2fD_0[(D_p/D_n)^{2/3}_{\max}-(D_p/D_n)^{2/3}_{\min}] \tag{4}$$

The data for $f=f_{cr}$, f_{r2}, and f_{r3} obtained with the three waveforms are shown in Fig. 4 in the form of a (Nu^+-1) versus S relation. The uncertainty that each deduced value of (Nu^+-1) bears is evaluated, based on the root sum square method (Abernethy et al., 1985), to be ± 0.06, and that for S ± 0.005. It is recognized that the data for $f=f_{cr}$ and $f=f_{r2}$ are correlated by the following equations irrespective of the field waveforms and of drop diameters in the range of our experiments:

$$\text{at } f=f_{cr}: \mathrm{Nu}^+ = 1+1.95\,\mathrm{S}^{2/3} \tag{5}$$

$$\text{at } f=f_{r2}: \mathrm{Nu}^+ = 1+1.33\,\mathrm{S}^{8/9} \tag{6}$$

As for $f=f_{r3}$, the data that we have obtained are too limited to establish a reliable correlation between Nu^+ and S. The data for frequencies other than f_{cr}, f_{r2}, and f_{r3}—which are omitted from Fig. 4 for the sake of clarity—are scattered over a wide region with an upper boundary given by equation (5). In the range of our experiments the critical frequency f_{cr} gives the highest value of Nu^+ at each level of S.

Although the Nu^+ versus S correlation presented above may be instrumental in understanding how the heat transfer is governed by the oscillatory motions, it is of little practical use unless we can predict S a priori. In Figs. 5 and 6 the same heat transfer data as those used in Fig. 4 are plotted against the amplitudes of the field strength, E_f and E_0[1], and the maximum of the drop distortion ratio during each period of oscillation, $\delta_{\max}$, respectively, instead of S. The possible utilities of these alternative data arrangements are discussed below.

In general, the amplitude of the field strength that we can apply may be limited by either of two different restrictions: One is the upper limit of the output voltage of a given power supply, and the other is one imposed by the fact that a drop becomes unstable resulting in its burst as $\delta_{\max}$ increases up to a critical level, $\delta_{cr}=0.47$ (Kaji and Mori, 1986). (The burst of each drop produces a large number of tiny drops, yielding a difficulty in separating the two liquids, and hence it should be avoided.) If the voltage available by a given power supply is

[1]Because of the reason described in Part 1 of this series (Kaji et al., 1988), the values of E_f and E_0 used in preparing Fig. 5 are those evaluated by simply dividing the voltage differences between the electrodes by the electrode spacing. These values are two times as large as those according to the former evaluation used in the first papers (Kaji et al., 1980, 1985) to cite the data concerning the pulsed quasi-square and the modified sinusoidal waveforms.

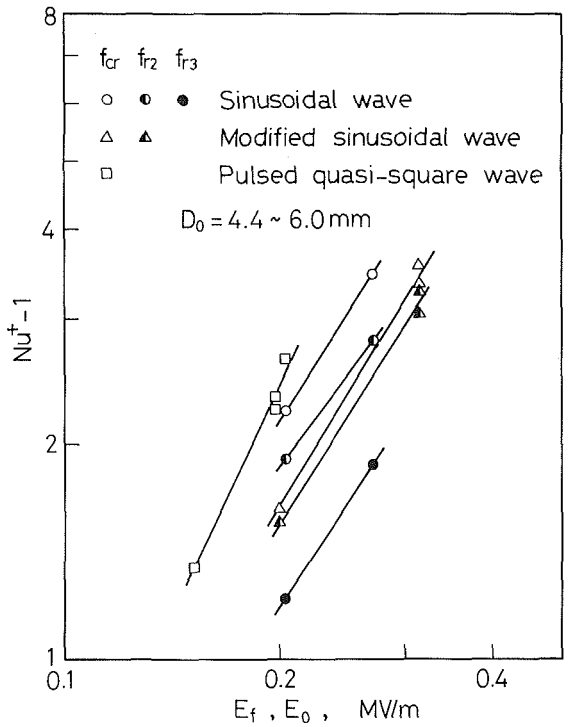

Fig. 5 Heat transfer data plotted against the amplitude of electric field strength

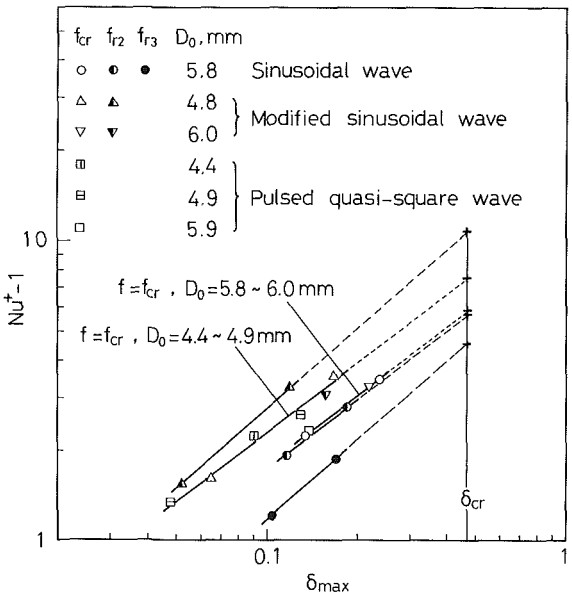

Fig. 6 Heat transfer data plotted against the maximum distortion ratio of drops

not so high as to yield a risk of drop burst, the problem that we should consider may be to find out the waveform and the frequency that will result in the largest enhancement at a specified level of the amplitude of the field strength. Figure 5 shows that for each waveform the critical frequency f_{cr} gives the largest enhancement. The sinusoidal waveform is superior to the modified sinusoidal waveform in the extent of enhancement at either $f=f_{cr}$ or $f=f_{r2}$, but it may fall behind the pulsed quasi-square waveform in the extent of enhancement at $f=f_{cr}$. (The latter comparison should probably be accepted with some reservation because of the incomplete consistency in the definition of the field-strength amplitude between the two waveforms in question. See Fig. 1.)

When a given power supply can afford output voltage high enough to cause the burst of drops, we will be interested in determining the waveform and the frequency that will yield the largest enhancement without making the drops burst. Since the range of δ_{max} covered by our experimental data is far below δ_{cr} because of the limitations of the output voltages of the power supplies that we used in the experiments, we can predict the enhancements at $\delta_{max} \to \delta_{cr}$ only by extensive extrapolations of the data as shown in Fig. 6. Despite the uncertainties involved in the extrapolations, it is very likely that the modified sinusoidal waveform with the frequency f_{r2} yields the largest enhancement at $\delta_{max} \to \delta_{cr}$. The superiority of the sinusoidal waveform to the modified sinusoidal waveform noted in the $(Nu^+ - 1)$ versus E_0 correlation vanishes at $f=f_{cr}$, and is even reversed at $f=f_{r2}$ in the $(Nu^+ - 1)$ versus δ_{max} correlation. In this correlation the extent of enhancement at f_{cr} seems to depend on the drop size but hardly on the waveform. These facts are quite consistent with the following facts, which we have shown in Part 1 of this series (Kaji et al., 1988): The range of drop deformation limited by δ_{max} and δ_{min} (or $(D_p/D_n)_{max}$ and $(D_p/D_n)_{min}$) is higher in the case of the sinusoidal waveform than in the case of the modified sinusoidal waveform at any level of E_0 over the frequency range above f_{cr}, while at f_{cr} and lower frequencies $\delta_{min} \simeq 0$ (i.e., $(D_p/D_n)_{min} \simeq 1$) irrespective of the waveform.

Conclusions

The heat transfer enhancement caused by alternating electric fields having the sinusoidal waveform has been studied experimentally. It has been found that the heat transfer coefficient peaks at three particular frequencies, which have been discussed in Part 1 of this series from the aspect of drop dynamics: the critical frequency f_{cr} beyond which the oscillation amplitude exhibits a sudden drop, f_{r2}, which yields the resonant oscillation of the second mode, and f_{r3} at which the resonant oscillation of the third mode is presumably superposed on the second-mode oscillation.

The experimental data newly obtained with the sinusoidal waveform have been compared with earlier data obtained with the quasi-square waveform (Fig. 1*a*) and the modified sinusoidal waveform (Fig. 1*b*). The comparison has provided some useful knowledge such as: (1) The heat transfer enhancements at each of f_{cr} and f_{r2} are represented by the same Nu^+ versus S relation irrespective of the waveform and the drop size (Fig. 4); (2) the largest enhancement at a specified level of field-strength amplitude is available at $f=f_{cr}$ with the pulsed quasi-square or sinusoidal waveform; and (3) the largest enhancement at the critical condition for the drop burst will be available at $f=f_{r2}$ with the modified sinusoidal waveform.

Acknowledgments

This study was performed within the framework of the Special Project Research on Energy under a Grant-in-Aid of Scientific Research of the Ministry of Education, Science and Culture of Japan.

References

Abernethy, R. B., Benedict, R. P., and Dowdell, R. B., 1985, "ASME Measurement Uncertainty," ASME *Journal of Fluids Engineering*, Vol. 107, pp. 161-164.

Kaji, N., and Mori, Y. H., 1986, "Direct Contact Heat Transfer to a Drop Translating in a Transverse Electric Field," *Wärme- und Stoffübertragung*, Vol. 20, pp. 11-18.

Kaji, N., Mori, Y. H., and Tochitani, Y., 1985, "Heat Transfer Enhancement Due to Electrically Induced Resonant Oscillation of Drops," ASME JOURNAL OF HEAT TRANSFER, Vol. 107, pp. 788–793.

Kaji, N., Mori, Y. H., and Tochitani, Y., 1988, "Electrically Induced Shape Oscillation of Drops as a Means of Direct-Contact Heat Transfer Enhancement: Part 1—Drop Dynamics," ASME JOURNAL OF HEAT TRANSFER, Vol. 110, this issue.

Kaji, N., Mori, Y. H., Tochitani, Y., and Komotori, K., 1978, "Direct-Contact Heat Transfer to Drops in an Intermittent Electric Field," *Proceedings of the 6th International Heat Transfer Conference*, Hemisphere Publishing Corp., Washington, DC, Vol. 3, pp. 165–170.

Kaji, N., Mori, Y. H., Tochitani, Y., and Komotori, K., 1980, "Augmentation of Direct-Contact Heat Transfer to Drops With an Intermittent Electric Field," ASME JOURNAL OF HEAT TRANSFER, Vol. 102, pp. 32–37.

Kaji, N., Mori, Y. H., Tochitani, Y., and Komotori, K., 1982, "Electrohydrodynamic Augmentation of Direct-Contact Heat Transfer to Drops Passing Through an Immiscible Dielectric Liquid: Effect of Field-Induced Shuttle Migration Between Parallel Plane Electrodes of Drops," *Proceedings of the 7th International Heat Transfer Conference*, Hemisphere Publishing Corp., Washington, DC, Vol. 5, pp. 231–236.

Larsen, P. S., and Jensen, J. W., 1978, "Evaporation Rates of Drops in Forced Convection With Superposed Transverse Sound Field," *International Journal of Heat and Mass Transfer*, Vol. 21, pp. 511–517.

Mori, Y., Imabayashi, M., Hijikata, K., and Yoshida, Y., 1969, "Unsteady Heat and Mass Transfer From Spheres," *International Journal of Heat and Mass Transfer*, Vol. 12, pp. 571–585.

Mori, Y. H., Kaji, N., and Nagashima, A., 1985, "Augmentation of Direct-Contact Liquid/Liquid Heat Transfer by the Application of an Electric Field," *Reports of Special Project Research on Energy Under Grant in Aid of Scientific Research of the Ministry of Education, Science and Culture, Japan*, Series No. SPEY 14, pp. 75–82.

Mori, Y. H., Kaji, N., and Tochitani, Y., 1977, "An Augmentation Method of Heat or Mass Transfer With an Intermittent Electric Field," Japanese Patent Application No. SHO 52-9488; Patent No. 1043731, 1981.

D. M. France

S. K. Shin

M. Azimi

A. Shafiei

University of Illinois at Chicago,
Department of Mechanical Engineering,
Chicago, IL 60680

Transition Boiling Models in Heat Exchangers

Models are presented for the inclusion of transition boiling heat transfer in the thermal analysis of liquid-heated boiling water heat exchangers. A relation was developed from experimental data for the prediction of the quality change in the transition boiling region. This quality relation was used alone and in conjunction with a transition boiling heat transfer coefficient to formulate two successful models. Predictions of heat exchanger heat transfer, including the transition boiling models, were compared with experimental results for high-pressure water in the range 7–15.3 MPa over a mass flux of 0.7–3.2 Mg/m²s.

Introduction

The thermal analysis of shell and tube heat exchangers in which one of the fluids is boiling and the other is single phase is often addressed in a manner similar to heat exchangers in which both fluids are single phase. One-dimensional energy equations are used for each fluid, and the heat transfer between them is governed by the thermal resistances of the fluids and the tube wall. Heat transfer coefficients are supplied to such analyses, and when these coefficients may be taken as constant along the tube length, integration of the energy equations results in the familiar analytical relation for overall heat transfer in terms of the log-mean temperature difference. In the case of one fluid boiling, the heat transfer coefficient is not constant and is supplied by flow regime. The energy equations are put into finite difference form and a numerical solution is obtained for the heat transfer. An analysis of this type was presented in [1] and is typical of analyses in general use for nuclear steam generators. The analysis of [1] neglected heat transfer in the transition boiling region; this omission is also typical of such analyses.

There are limited results available in the engineering literature for transition boiling heat transfer inside tubes. The relations presented in [2–4] represent extensive data for boiling water at low, intermediate, and high pressures, respectively. The general method of incorporating such results into a heat exchanger thermal analysis is to invoke a transition boiling heat transfer coefficient downstream of the critical heat flux (CHF) point. Farther downstream, this coefficient is replaced by a relation related to post-CHF heat transfer in the liquid deficient region, often referred to as the film boiling region. The flow regime boundary between transition boiling and film boiling can be a troublesome division to define due to the independent development of heat transfer relationships in each region. Consequently, the heat exchanger thermal analysis can be adversely affected. The subject of this investigation is methods of incorporating transition boiling heat transfer into the thermal analysis of heat exchangers that do not suffer from the transition boiling/film boiling boundary definition problem of the conventional method.

Transition Boiling Quality Formulation

The approach used to predict transition boiling heat transfer involved the development of a relationship for the quality change ΔX in this region. Measurements from 242 high-pressure (7–15.3 MPa) experiments described in [5] were used for this purpose. The test facility is a 1 MW system employing liquid sodium to boil water. Maximum facility operating parameters are: sodium volumetric flow rate = 0.0044 m³/s at 650°C, water pressure = 16.5 MPa, and water volumetric flow rate = 0.0082 m²/s at 500°C. The test section employed in the experiments consisted of a single straight water tube vertically oriented in a sodium shell. The water tube material was 2¼Cr–1 Mo steel with i.d. = 10 mm, o.d. = 15.8 mm, and heated length = 13.1m. The test section was well instrumented with over 100 shell thermocouples, a turbine flow meter in the water, and an electromagnetic flow meter in the sodium. All instrument calibrations were traceable to the National Bureau of Standards. Test results included the axial heat flux, water tube wall temperature, water bulk temperature, and steam quality, which were used in this study to determine transition boiling heat transfer parameters.

Over 400 test results were reported in [5], the majority of which were performed at combinations of four values of water pressure and four values of water mass flux. The results of 242 tests were used in this study at the 16 combinations of the following water parameters:

pressure = 7, 10, 13, 15.3 MPa
mass flux = 0.7, 1.4, 2.4, 3.2 Mg/m²s.

All the tests of [5] were conducted with subcooled water entering the test section, but the exit quality varied considerably among the tests. The 242 tests selected from the total for use in this study met the criterion that the transition boiling region was followed by a clear post-CHF region such that test section end effects did not influence the heat transfer in transition boiling. The tests thus selected included results at all 16 combinations of water pressure and mass flux.

The liquid-heating aspect of the experiments of [5] produced stable transition boiling regions in the test section. In the water parameter range used, the test section length over which transition boiling occurred was generally small, which is typical of the relatively high pressure and mass fluxes of this investigation. This condition along with the unstable nature of the transition boiling region in directly heated experiments have been the major contributors to experimental difficulties in transition boiling heat transfer. The liquid heating aspect of the current experimental results eliminated the instability problem, and the heat flux, temperature, and quality were obtained at three to six discrete locations in the transition boiling region in each test. However, the relatively large parameter range covered by the experiments required a somewhat elaborate mathematical form to represent all the data. Several empirical relations were investigated relating the quality change in the transition boiling region to various flow parameters. The following relation, relating ΔX to the water pressure, water mass flux (through Re), and quality at CHF, was found to represent the functional form of the data well:

Contributed by the Heat Transfer Division for publication in the JOURNAL OF HEAT TRANSFER. Manuscript received by the Heat Transfer Division January 2, 1986. Keywords: Flow Transition, Modeling and Scaling, Multiphase Flows.

Table 1 Constants for equation (1)

i	A_i	B_i
1	0.029005	1.3526
2	7.1266×10^{5}	0.1108
3	6.7126×10^{6}	2.3928×10^{-8}
4	-1.9617×10^{7}	1.7872
5	1.4442×10^{7}	
6	−4.3307	
7	2.4810	
8	−11.601	
9	10.473	
10	−0.099956	

$$\Delta X = A_1 + \frac{A_2 + A_3\mathrm{Pr} + A_4\mathrm{Pr}^2 + A_5\mathrm{Pr}^3}{\mathrm{Re}^{B_1}} + \left[\frac{A_6 + A_7\mathrm{Pr} + A_8\mathrm{Pr}^2 + A_9\mathrm{Pr}^3}{\mathrm{Re}^{B_2} + B_3\mathrm{Re}^{B_4}} + A_{10}\right] X_{\mathrm{CHF}} \quad (1)$$

The values of the A's and B's in equation (1) were optimized to best fit the experimental data using a multidimensional minimization computer code. The resulting values are given in Table 1.

The predictions of equation (1) are compared in Fig. 1 with typical measurements chosen at one of the 16 water parameter groups of the data. The comparison is considered to be good for this relatively difficult experimental region.

The transition boiling quality change as predicted by equation (1) is shown in Fig. 2 over the water pressure and mass flux range of the data for a typical value of CHF quality. The quality change is seen to be the largest at the lower pressures and mass flux. It is important to note that negative quality changes can be predicted by equation (1). To be consistent with the data, a prediction of $\Delta X < 0.02$ should be set to $\Delta X = 0.02$.

Heat Transfer Using ΔX

A typical heat flux distribution is shown as a solid line in Fig. 3 for liquid-heated boiling water in a tube. Point A marks CHF; point C marks the start of the post-CHF (film boiling) region, and transition boiling is defined as the region between points A and C. When transition boiling is neglected in a thermal analysis of a system of this type, curve A-B-C is followed. This procedure effectively extends film boiling over the entire transition boiling region. As a consequence, the heat transferred in this region of the heat exchanger is underpredicted by the analysis. An alternative approach would be to extend nucleate boiling over the entire transition boiling region. The result would be an overprediction of the heat transfer, and a criterion would be required to mark the beginning of film boiling. The quality change result given by equation (1) can be used for such a criterion. That is, nucleate boiling could be extended in an analysis beyond CHF for a quality change of ΔX after which film boiling would be assumed. However, overprediction of the heat transfer is no more desirable than underprediction.

A simplified but more accurate approach to the inclusion of transition boiling heat transfer in the thermal analysis of a boiling tube is to extend nucleate boiling beyond CHF for some fraction of ΔX after which film boiling is assumed to exist. This approach would follow curve A-D-E-C in Fig. 3. Heat transfer would be alternately overpredicted and underpedicted through the transition boiling region, but the net heat transfer calculated would be correct. In comparing this approach with the data of [5], a value of $\Delta X/2$ was found to be a good choice for the change from nucleate to film boiling.

A thermal analysis computer code, similar to the one described in [1], was adapted to the conditions and geometry of the test section of [5]. Five parameters from an experiment were supplied to the code: water pressure, mass flow rate and

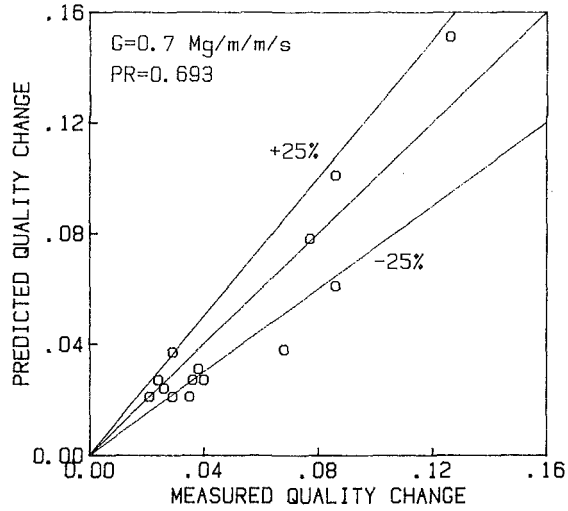

Fig. 1 Quality change in transition boiling

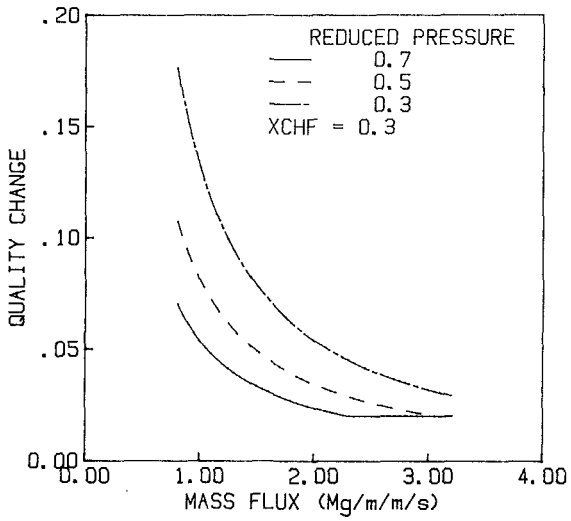

Fig. 2 Quality change trends

Nomenclature

A, B = dimensionless constants in equation (1)
D = water tube diameter, m
G = water mass flux, $\mathrm{Mg/m^2s}$
h = heat transfer coefficient, $\mathrm{kW/m^2C}$
Pr = reduced pressure
Re = liquid Reynolds number $= GD/\mu$
ΔT = (heated surface temperature) − (saturation temperature), °C
X = flow quality
ΔX = quality change in transition boiling
μ = dynamic viscosity of liquid, kg/m s

Subscripts

CHF = condition at the critical heat flux (CHF)

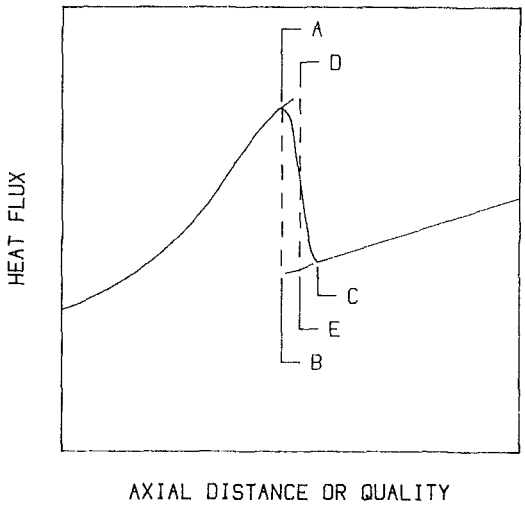

Fig. 3 Heat flux distribution for liquid-heated boiling

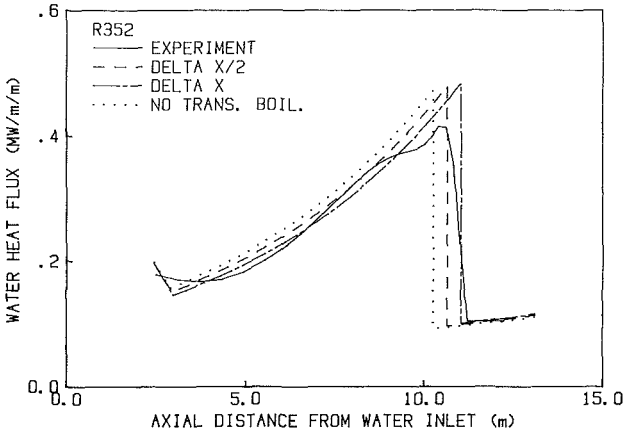

Fig. 4 Heat flux comparisons: ΔX relation

inlet temperature, and sodium mass flow rate and inlet temperature. (The sodium and water flowed in a countercurrent configuration.) The code predicted the axial heat flux, water quality, and temperature distributions of the water, sodium, and tube wall along the length of the test section. Typical results are shown in Fig. 4 for Test R352 from [5]. The water mass flux was 0.7 Mg/m^{2}s and the pressure was 7 MPa.

Three calculated results are shown in Fig. 4. When transition boiling was neglected and film boiling was assumed to exist in this region, the predicted heat flux decreased from a maximum at CHF to the film boiling level upstream of the measurements, and the heat transferred was underpredicted compared to the experiment curve as described for the general case with respect to Fig. 3. The curve marked "DELTA X" in Fig. 4 represents the results obtained when nucleate boiling was assumed to persist over the entire transition boiling region (over a quality change of ΔX calculated from equation (1)). As expected, the heat transfer was overpredicted compared to the experiment curve. The heat flux results marked "DELTA X/2" in Fig. 4 produced the best representation of the experiment for the three predictions shown in this figure. In this case, nucleate boiling was forced to extend beyond CHF for a quality of $\Delta X/2$ calculated from equation (1).

Heat Transfer Using Coefficient

The use of a heat transfer coefficient in the transition boiling region eliminates the need for the approximation of the

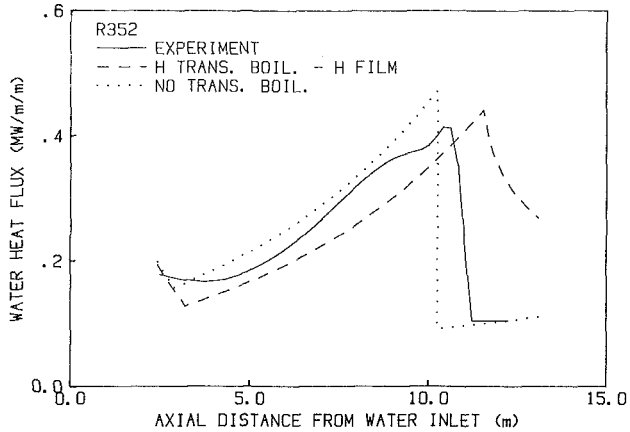

Fig. 5 Heat flux comparison: heat transfer coefficient

simplified approach using the ΔX result alone. However, some difficulty occurs in marking the change from transition boiling to film boiling. A technique suggested in [6] for coiled tubes is to assume a linear heat flux distribution in the transition boiling region. This technique amounts to connecting points A and C in Fig. 3 with a straight line. The same problem exists in knowing the location of point C, or the slope of the straight line. This problem is evident in the following results of the direct application of a transition boiling heat transfer coefficient in a thermal analysis computer code.

The thermal analysis code discussed previously was modified to include a water heat transfer coefficient in the transition boiling region. Downstream of CHF this coefficient was employed for some distance beyond which a film boiling heat transfer coefficient was introduced. The change from transition boiling to film boiling was made in the same manner in which codes of this type change from single-phase forced convection to nucleate boiling. After CHF, a transition boiling heat transfer coefficient was applied, and a film boiling heat transfer coefficient was also calculated from a correlation equation. When the film boiling coefficient exceeded the transition boiling coefficient, the regime was changed from transition to film boiling.

The transition boiling heat transfer coefficient of [4] was used in this investigation because it was developed for the high-pressure range of the experimental data. That relation is

$$\frac{h}{h_{\mathrm{CHF}}}=\frac{\Delta T_{\mathrm{CHF}}}{\Delta T}\exp([-C[\Delta T-\Delta T_{\mathrm{CHF}})] \tag{2}$$

where $C=0.0279-0.00556G$, and the range of the water mass flux G was 0.7–3.2 Mg/m^{2}s in equation (2), and C has the units °C^{-1}. Several equilibrium film boiling correlation equations were used, including those of [7–9], with similar results.

The prediction of heat flux, using this heat transfer coefficient approach with the use of a film boiling coefficient to mark the end of the transition boiling region, is compared in Fig. 5 with the same experimental data of Fig. 4. The prediction is denoted "H TRANS. BOIL.—H FILM" in Fig. 5, and the case where transition boiling was neglected is shown for reference. The heat transfer coefficient result significantly overpredicts the heat transfer, and the predicted transition boiling region extends far beyond the measured region. This unsatisfactory result is a consequence of the procedure used to change from transition to film boiling. All of the transition boiling heat transfer coefficients in [2–4] decrease exponentially in the flow direction while the film boiling coefficients of [7–9] increase slowly. The intersection marking the change from transition boiling can occur well beyond the measured point, as occurred in Fig. 5. This situation is a result of the independent development of the transition boiling and film boil-

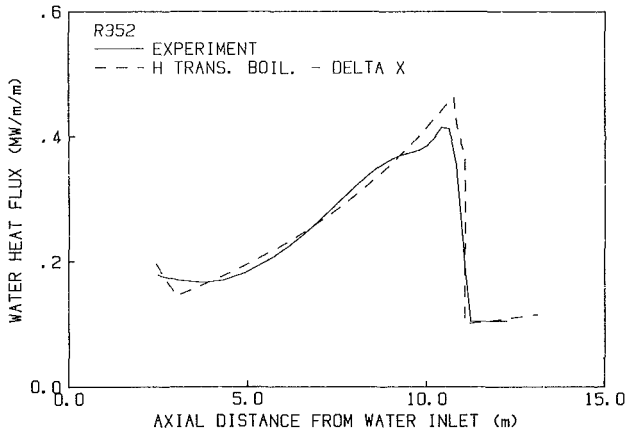

Fig. 6 Heat flux comparison: combined model

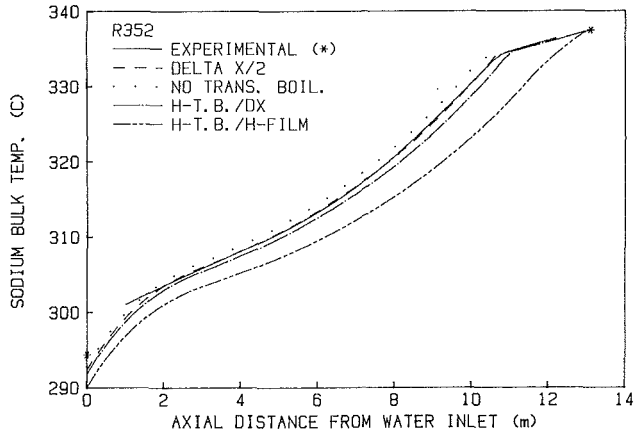

Fig. 7 Sodium bulk temperature: four models

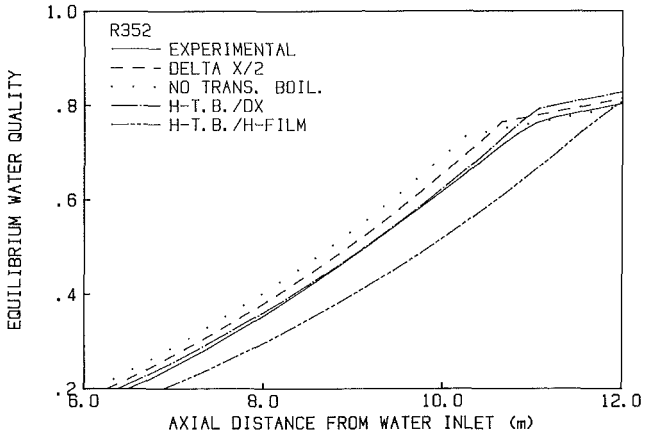

Fig. 8 Water quality: four models

ing relations and the almost asymptotic way in which the transition boiling heat transfer coefficient can decrease toward the film boiling coefficient in some parameter ranges.

Heat Transfer Using Coefficient and ΔX

The problem with using the transition boiling heat transfer coefficient from equation (2) in the thermal analysis, the results of which are given in Fig. 5, was with the way in which the transition boiling region was mathematically terminated. (The method applied is the same as used for forced convection to nucleate boiling transition.) This conventional approach produced poor results, similar to those of Fig. 5, in nearly all 16 parameter groups of the data. Thus, a technique was employed wherein the transition boiling heat transfer coefficient was applied, and the region was terminated via the ΔX relation of equation (1). This technique is a combination of the two previously discussed techniques, and the results were the most satisfactory.

The predicted heat flux, denoted "H TRANS. BOIL—DELTA X," is shown in Fig. 6 compared with the same data as in Figs. 4 and 5. Transition boiling was included through the use of equation (2), and it was terminated at a quality obtained from equation (1) after which a film boiling coefficient was employed. The local results shown in Fig. 6 represent the physical shape of the measurements well; the heat transfer predicted is in good agreement with the experimental results in all the boiling regions shown.

Comparisons and Discussion

Predicted and experimental results are given in Figs. 7–10 for the same test as shown in Figs. 4–6. These results were typical of all 16 parameter groups investigated. The four transition boiling models shown in these figures are denoted as:

"NO TRANS. BOIL" = film boiling extending over the entire transition boiling region

"DELTA $X/2$" = nucleate boiling extending into the transition boiling region for a quality change of $\Delta X/2$ from equation (1)

"H-T.B./H-FILM" = transition boiling heat transfer coefficient from equation (2) with termination based on the film boiling coefficient

"H-T.B./DX" = transition boiling heat transfer coefficient from equation (2) with termination at ΔX from equation (1)

The sodium bulk temperature distributions predicted from use of these four models are compared to experimental results in Fig. 7. All results compare well with the data except for the H-T.B./H-FILM case, and the best local results were obtained from the DELTA $X/2$ analysis.

All models represented in Fig. 7, except for the H-T.B./H-FILM case, predicted approximately the same value of the sodium outlet temperature, i.e., the temperature at 0.0 m in Fig. 7. This result indicates that prediction errors occurring in the transition boiling region can be offset by prediction errors elsewhere in the heat exchanger. Consider, for example, the case in which transition boiling heat transfer is omitted from the analysis. The local heat flux distribution shown in Figs. 4 and 5 displays a significant underprediction of the experimental values in the region of transition boiling, but there is compensating overprediction upstream. Integrating the heat flux over the transition boiling region and the adjacent portion of the bulk boiling region from 7 to 12 m produced a net underprediction of 5 percent in heat transfer when transition boiling was omitted from the analysis. On a similar basis, the integrated heat transfer results for the DELTA $X/2$ and the H-T.B./DX models were overpredictions of 0.5 and 6 percent, respectively. The H-T.B./H-FILM model predicted integrated heat transfer 12 percent above the experimental value even though the transition boiling prediction was significantly above this percentage. These comparisons serve to accentuate the importance of considering the local results when assessing model accuracy to avoid the effects of compensating errors.

The equilibrium water qualities predicted from the four models of Fig. 7 are compared to experimental results in Fig. 8. Clearly, the inclusion of the transition boiling region in the analysis by either the DELTA $X/2$ or the H-T.B./DX models produced better results than neglecting transition boiling. The

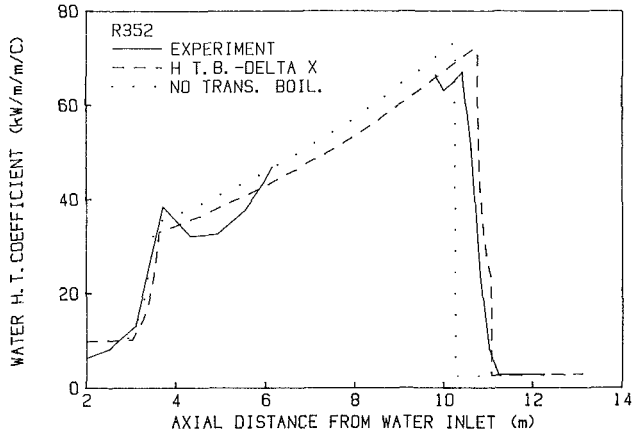

Fig. 9 Water heat transfer coefficients: combined model

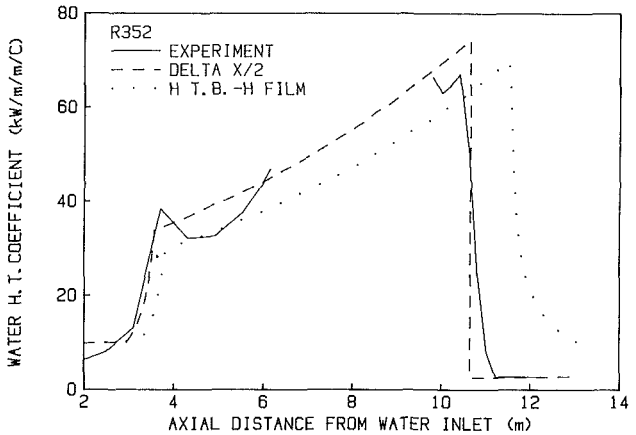

Fig. 10 Water heat transfer coefficient: simplified model

predictions of the combined method, H-T.B./DX, are nearly coincident with the data over most of the test section length.

The water heat transfer coefficient predicted by the combined method came very close to the experimental coefficient. A comparison is shown in Fig. 9 over the entire test section length and includes the flow regimes of single-phase forced convection, nucleate boiling, transition boiling, and film boiling. The case where transition boiling was neglected is shown for comparison. (Experimental values for the water heat transfer coefficient could not be obtained accurately in the very high heat flux range upstream of CHF due to the very small wall-to-fluid temperature differences.)

Water heat transfer coefficients are shown in Fig. 10 for the simplified transition boiling model, DELTA $X/2$, and the conventional application of the transition boiling heat transfer coefficient. The latter compared poorly with experimental results for reasons discussed previously. Although the best predictions are from the combined model as shown in Fig. 9, the simplified method approximated the heat transfer coefficient well as shown in Fig. 10.

Conclusions

Of all the methods investigated for representing transition boiling heat transfer in a liquid-heated system, the combined model produced the best overall results. This model utilized a heat transfer coefficient in the transition boiling region in a thermal analysis code. The change from transition boiling to film boiling was calculated from the relation for quality change in transition boiling developed in this study from extensive experimental data. The predictions matched experimental values well, and predicted trends and parametric forms were closest to the experiments.

The simplified approach to the prediction of transition boiling heat transfer developed in this study utilized the quality change result alone. Although predictions from this method did not represent the physical form of the data well, the overall predictions were good. The simplicity of this method makes it an attractive alternative.

Both the combined and simplified models for including transition boiling heat transfer in the thermal analysis of liquid-heated boiling systems were shown to be more accurate than the common practice of neglecting transition boiling entirely. That practice actually assumes that film boiling persists over the transition boiling region, and it underpredicts the heat transferred in that region of the system. The available data at high pressure [4] used in this study covered large ranges of mass flux, 0.7–3.2 Mg/m^{2}s and pressure 7–15.3 MPa. The models performed equally well throughout these parameter ranges.

Acknowledgments

This study was sponsored by a U.S. Department of Energy Award.

References

1 Oberjohn, W. J., Carter, H. R., and Schluderberg, D. C., "Thermal-Hydraulic Performance of a Consolidated Nuclear Steam Generator (CNSG) Module," ASME Paper No. 77-JPGC-NE2, 1977.

2 Weisman, J., Kao, Y. K., and Rahrooh, G., "Transition Boiling Heat Transfer in a Vertical Round Tube," ASME Paper No. 79-HT-47, 1979.

3 Tong, L. S., and Young, J. D., "A Phenomenological Transition and Film Boiling Heat Transfer Correlation," *Proceedings of the Fifth International Heat Transfer Conference*, Vol. IV, Tokyo, 1974.

4 France, D. M., Chan, I. S., and Shin, S. K., "High-Pressure Transition Boiling in Internal Flows," ASME JOURNAL OF HEAT TRANSFER, Vol. 109, 1987, pp. 498–502.

5 France, D. M., Carlson, R. D., Chiang, T., and Minkowycz, W. J., "Critical Heat Flux Experiments and Correlation in a Long, Sodium-Heated Tube," ASME JOURNAL OF HEAT TRANSFER, Vol. *103*, No. *1*, *1981*, pp. 74–80.

6 Bailey, N. A., and Holland, E., "High Pressure Heat Transfer and Pressure Drop Tests on a Helical Coil in Support of CFR Boiler Design," AEEW-R-1008, 1975.

7 Groeneveld, D. C., "The Thermal Behavior of a Heated Surface at and Beyond Dryout," AECL-4309, 1972.

8 Bishop, A. A., Sandberg, R. O., and Tong, L. S., "Forced Convection Heat Transfer at High Pressure After the Critical Heat Flux," ASME Paper No. 65-HT-31, 1965.

9 Miropol'skiy, Z. L., "Heat Transfer in Film Boiling of a Steam Water Mixture in Steam Generating Tubes," *Teploenergetika*, Vol. 10, 1963, pp. 49–53.

Application of a Multifield Model to Reflooding of a Hot Vertical Tube: Part II—Analysis of Experimental Results

M. Kawaji
Department of Chemical Engineering and Applied Chemistry, University of Toronto, Toronto, Ontario, Canada

S. Banerjee
Department of Chemical and Nuclear Engineering, University of California, Santa Barbara, CA 93106

The two-fluid model equations developed for reflood calculations and discussed in Part I (Kawaji and Banerjee, 1987) are solved numerically with appropriately formulated constitutive relations to analyze the Inconel tube reflood experiments involving inverted annular and dispersed flow regimes downstream of the quench front. Constitutive relations are formulated separately for individual transfer mechanisms that are considered to be phenomenologically significant. For inverted annular flow, phasic pressure difference is incorporated into the momentum equations to predict the interfacial waves which enhance film boiling heat transfer. For dispersed flow, a size distribution of drops is considered and both single and multifield equations of motion are solved to calculate the droplet transport. Most of the important heat transfer and hydrodynamic aspects of the experimental results are predicted reasonably well, indicating the adequateness of the mechanisms considered. In particular, a wall-drop interaction heat transfer mechanism is determined to be essential in explaining the experimentally observed strong dependence of heat transfer rate on liquid volume fraction in the dispersed flow region. A sensitivity study is made to identify the weaknesses in the constitutive relations, but no single relation could be accounted for areas in need of further improvement. In comparison with the predictions of the single-field model, those of the multifield model showed improvement for some but not all experiments.

Introduction

Reflooding of a vertical flow channel involves complicated thermal hydraulic phenomena. Although the macroscopic aspects of many of these phenomena are already known (e.g., flow patterns, modes of heat transfer, parametric effects on quench speed, and so on), understanding of the details of the physical phenomena is far from satisfactory due to the lack of local measurements. Local measurements are difficult to achieve, but are valuable in understanding the basic mechanisms and formulating mechanistic models. In recent years, measurements have been reported on local void fraction histories (Kawaji et al., 1985), vapor film thickness (Edelman et al., 1983), and liquid column breakup (De Jarlais, 1983) in an inverted annular flow regime that exists just above the quench front. For the dispersed flow regime farther downstream, droplet size distribution and velocity measurements have been reported by Lee et al. (1982) and Ardron and Hall (1983).

To be able to predict the reflooding phenomena under a wide range of conditions, a mechanistic model is preferred that contains little empiricism in constitutive relations. Among the various two-phase flow models available, a two-fluid model should be used when mechanical and thermal nonequilibrium effects are present. The structure of two-fluid models for the inverted annular and dispersed flows has been described in Part I of this paper (Kawaji and Banerjee, 1987). Incorporation of the phasic pressure difference term into the momentum equations was shown to render stability to the model while allowing descriptions of the long-wavelength interfacial waves. In the present paper, the two-fluid models are solved numerically in conjunction with constitutive relations described below to analyze the Inconel-tube reflood experiments reported previously (Kawaji et al., 1985).

The dispersed flow equations actually solved in the present work differ from those of the six-equation model described in Part I. Thus, the multifield model equations are developed for dispersed droplet flow and described first, followed by the constitutive relations, thermal equations, and the calculated results.

Multifield Dispersed Flow Model

Hydrodynamic calculations are important in prediction of dispersed flow heat transfer, because the local heat transfer rate depends strongly on the local liquid volume fraction, which is determined by the rate of drop entrainment and transport, as evident in the experimental data (Kawaji et al., 1985). Thus, a mechanistic model was developed to calculate the drop transport in the dispersed flow regime and two sets of calculations were performed treating the droplets as either one group with group average properties (single-field model) or multiple groups with size dependent properties (multifield model).

The present multifield dispersed flow model differs considerably from other mechanistic models such as those developed by Thurgood and Kelly (1980) and Whalley et al. (1982). To analyze reflooding phenomena, Thurgood and Kelly (1980) divided the liquid into a continuous field corresponding to a liquid column in inverted annular flow or a liquid film in annular flow, and a dispersed field representing the droplets entrained into the vapor stream and solved the conconservation equations separately for each field. In the absence of a continuous liquid field in the dispersed flow regime, their model corresponds to our single-field model.

Contributed by the Heat Transfer Division for publication in the JOURNAL OF HEAT TRANSFER. Manuscript received by the Heat Transfer Division May 9, 1986. Keywords: Phase-Change Phenomena, Sprays/Droplets, Transient and Unsteady Heat Transfer.

On the other hand, the present multifield model is similar in basic concept to the steady-state model of Whalley et al. (1982) used to calculate droplet transport in the analysis of post-dryout heat transfer. In their model, a droplet size spectrum was automatically calculated at the dryout point due to the entrainment of drops differing in size at various positions upstream of the dryout point. The droplet transport downstrean of the dryout point was then calculated for each size separately. This treatment of droplet transport in the post-dryout region apparently improved the accuracy of vapor-to-drop convective heat transfer calculation.

In vertical reflooding, droplets of various sizes are generated at the top of the inverted annular flow regime as the liquid column disintegrates due to instability. Once the droplets are entrained by vapor, the subsequent transport depends strongly on their size distribution.

In the present model, assumptions of constant pressure and incompressible vapor and liquid are made, and a one-dimensional, two-fluid model with five conservation equations is used to describe the motion and energy of vapor and liquid phases. The time and volume-averaged equations previously described in Part I were simplified and modified as given below.

$$\frac{\partial}{\partial t}(\rho_l \alpha_l) + \frac{\partial}{\partial z}(\eta_l \rho_l \alpha_l U_d) = -m_l''' \tag{1}$$

$$\frac{\partial}{\partial t}(\rho_v \alpha_v) + \frac{\partial}{\partial z}(\rho_v \alpha_v U_v) = m_l''' \tag{2}$$

$$\frac{\partial}{\partial t}(\eta_l \rho_l \alpha_l U_d) + \frac{\partial}{\partial z}(\eta_l \rho_l \alpha_l U_d U_d) = \tau_d''' - \eta_l \rho_l \alpha_l g - \eta_l m_l''' U_d \tag{3}$$

$$\frac{\partial}{\partial t}(\rho_l \alpha_l h_l) + \frac{\partial}{\partial z}(\eta_l \rho_l \alpha_l U_d h_l) = q_{dH}''' - m_l''' h_{l,\text{sat}} \tag{4}$$

$$\frac{\partial}{\partial t}(\rho_v \alpha_v h_v) + \frac{\partial}{\partial z}(\rho_v \alpha_v U_v h_v) = q_v''' + m_l''' h_{v,\text{sat}} \tag{5}$$

The convective terms in the drop continuity, momentum, and energy equations contain η_l, which is defined as the carryover fraction and represents the fraction of drops that can be carried downstream by vapor. For the mass and energy equations, we consider the entire droplet population in the control volume. Only a fraction of the droplet population is convected in and out and so η_l is included only in the convective terms. For the momentum equation, only the droplets that are carried over by the vapor are considered. One then requires, of course, a constitutive relationship for the carryover fraction, which will be discussed shortly. Also, to simplify the calculation, the vapor flow rate is assumed to be given by the vapor flux at the top of the inverted annular flow region and the vaporization from the drops. Such a scheme is, of course, only accurate if the flow is relatively steady and pressure variation is small. The constant injection reflood experiments analyzed (Kawaji et al., 1985) satisfied these conditions. To analyze more realistic reflood situations involving steam binding and flow oscillation phenomena, the vapor momentum equation also has to be solved.

Although a population of drops has a size distribution, the drop velocity U_d appearing in the equations above is assumed to represent a population-mean velocity. Thus, the model described above is referred to as the single-field (mean droplet) model and appropriate population-mean diameters are used to calculate the interfacial area and various interfacial transfer terms. Uncertainty remains, however, as to whether the nonlinear velocity terms appearing in the liquid momentum equation and in drag force correlations can be calculated correctly by assuming a population-mean velocity.

To answer this question, a simple extension was made from the single-field model to a multifield model by modifying only the liquid momentum equation as follows. First, the drop size

Nomenclature

A_i = interfacial area
C_D = drag coefficient
C_p = specific heat capacity
D = diameter
$D_{\max}$ = maximum droplet diameter
D_{20}, D_{30}, D_{32} = area, volume, or Sauter mean diameter
F_1, F_2 = liquid heat flux correlating function
F_D = drag force
F_{red} = interfacial friction reduction factor
Nu = Nusselt number
R = radius
Pr = Prandtl number
Re = Reynolds number
T = temperature
U = velocity
V = volume fraction of drop size distribution
We_{cr} = critical Weber number
ΔZ = distance between axial nodes
a = drop size distribution parameter
f = friction factor
g = gravity constant
h = enthalpy, heat transfer coefficient
h_{fg} = heat of vaporization
k = thermal conductivity
m_l = interfacial mass transfer rate
q'' = heat flux
r = radial coordinate
t = time
Δt = time step size
z = axial coordinate
α_v = void fraction
α_l = volume fraction of liquid
β = drop size distribution parameter
δ = vapor film thickness
ϵ = emissivity
η_l = droplet carryover fraction
θ = $(T_{\text{sat}} - T_l)/(T_{\text{sat}} - T_0)$ = dimensionless bulk liquid temperature
μ = viscosity
ρ = density
σ' = Stefan–Boltzmann constant
τ'' = shear stress

Subscripts

d = drops
f = film
i = vapor–liquid interface, ith group of drops
j = axial node
l = liquid
rad = radiation
sat = saturation
t = tube
v = vapor
w = wall

Superscripts

R = radiative heat transfer
$'''$ = quantity per unit volume

Table 1 Summary of constitutive relations for the inverted annular flow

Relations	Equations	Reference
Wall heat flux	$\dot{q}''_w = \dot{q}''_{wv} + \dot{q}''_{\text{rad}}$	
Wall to vapor convection	$\dot{q}''_{wv} = \dfrac{k_v \text{Nu}_1}{2\delta}(T_w - T_v)$	
Wall to liquid radiation	$\dot{q}''_{\text{rad}} = \dfrac{\sigma'(T_w^4 - T_{\text{sat}}^4)}{\dfrac{1}{\epsilon_w} - \dfrac{1}{\epsilon_l\sqrt{\alpha_l}} - 1}$	Siegel and Howell (1972)
Vapor to liquid convection	$\dot{q}''_{vl} = \dfrac{k_v \text{Nu}_2}{2\delta}(T_v - T_l)$	
	where Nu_1 and Nu_2 are for annulus	Kays (1966)
Liquid heating flux	$q'''_{lH} = A_i''' \dfrac{k_l}{D\sqrt{\alpha_l}}(T_{\text{sat}} - T_o)F_1$	
Vaporization heat flux	$\dot{q}''_{\text{evap}} = \dot{q}''_{vl} + \dot{q}''_{\text{rad}} - \dot{q}''_{lH}$	
Vapor heating flux	$q'''_v = \dfrac{4}{D}(q''_{wv} - \sqrt{\alpha_l} q''_{vl})$	Kawaji (1984)
Interfacial mass transfer	$\dot{m}'''_l = A_i'''(q''_{\text{evap}}/h_{fg})$	
Interfacial area concentration	$A_i''' = \dfrac{4\sqrt{\alpha_l}}{D}$	
Wall–vapor shear	Laminar: $\tau'''_{wv} = \dfrac{16\mu_v}{D^2}\left[\dfrac{-u_l}{2\xi} + \dfrac{u_v(2\xi+\alpha_v) + u_l(1 + 2\alpha_l\xi/\alpha_v + \alpha_l + \alpha_v/(2\xi))}{\alpha_v + (1+\alpha_l)\xi}\right]$	Kawaji (1984)
	where $\xi = \ln\sqrt{\alpha_l}$	
	Turbulent: $\tau'''_{wv} = \dfrac{4}{D}\dfrac{f_w}{2}\rho_v \lvert u_v \rvert u_v$	
	$f_w = \dfrac{0.085}{\text{Re}^{1/4}}$; $\text{Re} = \dfrac{\rho_v \lvert u_v \rvert 2\delta}{\mu_v}$	
Interfacial shear	Laminar: $\tau_i''' = \dfrac{16\mu_v}{D^2}\left[\dfrac{u_l}{2\xi} - \dfrac{u_v(2\alpha_l\xi+\alpha_v) + u_l(2\alpha_l + 2\alpha_l^2\xi/\alpha_v + \alpha_v/(2\xi))}{\alpha_v + (1+\alpha_l)\xi}\right]$	Kawaji (1984)
	Turbulent: $\tau_i''' = A_i''' \dfrac{f_i}{2}\rho_v \lvert u_v - u_l \rvert (u_v - u_l)$	
	$f_i = \dfrac{0.085}{\text{Re}^{1/4}}$, $\text{Re} = \dfrac{\rho_v \lvert u_v - u_l \rvert 2\delta}{\mu_v}$	
	Reduction factor: $F_{\text{red}} = e^{-(0.5189 + 0.0974x)\cdot x}$	Jeromin (1970)
	where $x = \dfrac{1}{2f_i}\left(\dfrac{m_l''' D}{\rho_v u_v}\right)$	
Transition to dispersed flow	$\alpha_{l_j} < 0.5$ or	Kawaji (1984)
	$\dfrac{\alpha_{l_{j-1}} - \alpha_{l_j}}{\Delta Z} > 0.15$ and $\alpha_{l_{j+1}} > 0.6$	

distribution, which will be described in the next section, is divided into a number of groups, each having a different mean diameter D_i. The volume fraction of each group is then given by $\eta_i \alpha_l$, where the sum of η_i over all groups with diameters less than the maximum carryover diameter defined in the next section equals the carryover fraction η_l.

The equation of motion for each group is now given by

$$\frac{\partial}{\partial t}(\eta_i \rho_l \alpha_l U_{di}) + \frac{\partial}{\partial z}(\eta_i \rho_l \alpha_l U_{di} U_{di}) = \tau_{di}''' - \eta_i \rho_l \alpha_l g - \eta_i m_l''' U_{di} \tag{6}$$

with the interfacial drag term calculated using the group diameter and velocity.

The population-mean droplet velocity is calculated from the following relation:

$$U_d = \frac{1}{\eta_l} \sum_{i=1}^{I_{\max}} \eta_i U_{di} \tag{7}$$

where $I_{\max}$ is the group number of the maximum carryover diameter. The population-mean velocity is used in the liquid continuity and energy equations, as well as in vapor-to-drop heat transfer calculations. In this multifield dispersed flow model, terms describing the intragroup transfer of mass, momentum, and energy due to droplet collision, breakup, and coalescence are not considered explicitly. However, it is assumed that the shape of the droplet size distribution is maintained, i.e., if it starts off as log normal, it remains log normal.

Both the single-field and multifield equations are solved numerically with a log-normal size distribution assumed for the droplet size.

Constitutive Relations

Formulation of each constitutive relation is discussed in detail by Kawaji (1984), so only a brief description is given in this paper.

(a) Inverted Annular Flow. Constitutive relations for the inverted annular flow regime are summarized in Table 1. The heat transfer mechanisms considered for the inverted annular flow regime are wall-to-vapor convection, wall-to-liquid radiation, and vapor-to-liquid convection.

The temperature at the surface of the subcooled liquid column is assumed to be at saturation and vapor generation is occurring at the interface at all axial locations above the quench front. Thus, out of the total energy received by the subcooled liquid column, some is used for vaporization at the interface, and the rest for heating the liquid column until it becomes saturated. The liquid heating flux is clearly dependent on the local subcooling of the bulk liquid and the thickness of the thermal boundary layer near the interface. In order to estimate the liquid heating flux, the following laminar thermal entry problem was considered. A liquid column of uniform temperature T_o, and with a flat velocity profile U_l, enters the film boiling region where the surface temperature is kept at saturation.

The assumption of radially uniform temperature and velocity profiles at entry into the film boiling region is based on the possible mixing of liquid near the quench front due to rapid and frequent growth and collapse of bubbles on the wetted surface below the quench front. Furthermore, the radial velocity profile is expected to remain relatively uniform above the quench front because of the free surface of the liquid core.

The analytical solutions for the temperature profile, bulk temperature, and local Nusselt number are readily available for various Peclet numbers (Singh, 1958). The actual correlation for the liquid heating flux was expressed as follows and is valid for Pe > 100 where axial conduction is negligible:

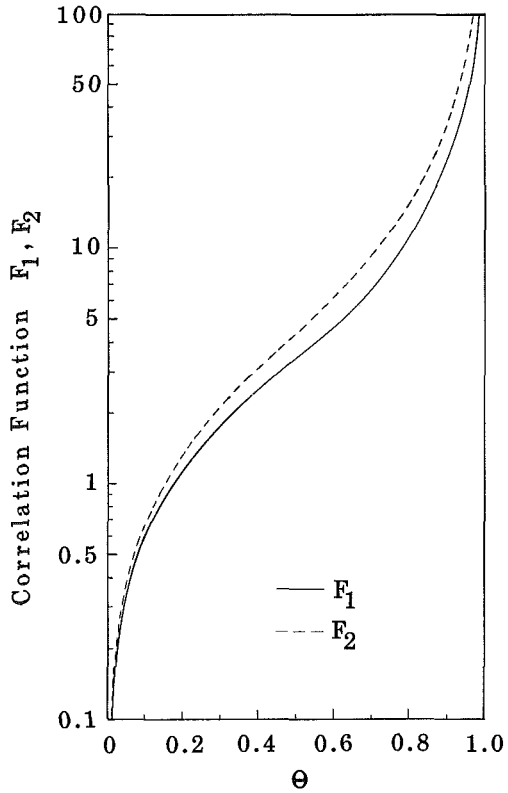

Fig. 1 Liquid heat flux correlating functions F_1 and F_2

$$q_{lH}'' = \frac{k_l}{D\sqrt{\alpha_l}}(T_{\text{sat}} - T_o)F_1 \tag{8}$$

The correlating function F_1 is shown in Fig. 1 and is specified in terms of the dimensionless bulk liquid temperature θ. The ratio F_1/θ corresponds to the local Nusselt number. Under all situations, the maximum value of the liquid heating flux is limited to that of the total heat flux received.

The shear stress terms are evaluated with either empirical correlations or approximate analytical expressions for turbulent or laminar vapor flow, respectively. The effect of vaporization on interfacial friction is considered by including a reduction factor derived from the experimental data discussed by Jeromin (1970).

(b) Transition to Dispersed Flow. Transition from an inverted annular to a dispersed flow regime is believed to be related to the instabilities that develop at the liquid–vapor interface. These instabilities have been discussed in Part I (Kawaji and Banerjee, 1987) of this paper. The transition criterion used in this model results directly from the numerically predicted Kelvin–Helmholtz instabilities, which consequently lead to necking of the liquid column. When the variation in wave amplitude expressed in terms of the liquid volume fraction, meets the criterion given in Table 1, the liquid column is assumed to undergo necking there. The liquid above the point of necking is assumed to detach from the liquid column and to be entrained into the dispersed flow region as a population of drops with a size distribution described below.

(c) Dispersed Flow. The constitutive relations for the dispersed flow regime are summarized in Table 2.

A log-normal drop size distribution was used based on the data obtained by Ardron and Hall (1983) for reflooding of a quartz tube. Values of the distribution parameters in the equilibrium size distribution function were selected to fit the description of their data.

Table 2 Summary of constitutive relations for the dispersed flow model

Relations	Equations	Reference
Drop size distribution	Volume distribution: $\frac{dV}{dy}=\frac{\beta}{\sqrt{\pi}}e^{-\beta^2 y^2}$	Mugele and Evans (1951)
	where $y=\ln\left(\frac{a\,D_d}{D_t-D_d}\right)$, $\beta=0.6474$	
	$a=\begin{cases}0.4923 & \text{Flow transition}\\ 1.1212 & \text{Dispersed flow}\end{cases}$	Kawaji (1984)
Maximum drop size (D_{max})	Smaller of	
	(*a*) Maximum stable diameter	
	$D^s_{max}=\frac{\sigma\,We_{cr}}{\rho_v u_v^2}$	
	where $We_{cr}=22$	Hinze (1955)
	(*b*) Maximum carryover diameter	
	$D^c_{max}=\frac{3}{4}\frac{C_D\rho_v u_v^2}{g(\rho_l-\rho_v)}$	
Carryover fraction	where $\eta_l=\eta_l^c/\eta_l^*$	Kawaji (1984)
	$\eta_l^c=\frac{1}{\sqrt{\pi}}\int_{-\infty}^{\beta y^c_{max}} e^{-U^2}dU$	
	$y^c_{max}=\ln\left(\frac{a\,D^c_{max}}{D_t-D^c_{max}}\right)$	
	and $\eta_l^*=\frac{1}{\sqrt{\pi}}\int_{-\infty}^{\beta y_{max}} e^{-U^2}dU$	
	$y_{max}=\ln\left(\frac{a\,D_{max}}{D_t-D_{max}}\right)$	
Interfacial drag	$\tau'''_d=\frac{6\alpha_l F_D}{\pi D_{30}^3}$	
	where	
	$F_D=\frac{C_D}{2}\rho_v\lvert u_v-u_d\rvert(u_v-u_d)\frac{\pi}{4}D_{20}^2$	
	$C_D=\frac{24}{Re_d}(1+0.15\,Re_d^{0.687})$	Rowe (1961)
	and $Re_d=\frac{\rho_v\lvert u_v-u_d\rvert D_{20}}{\mu_v}$	
Wall-to-vapor convection	$\dot q''_{wv}=0.023\frac{k_f}{D_t}Re^{0.8}Pr^{0.33}(T_w-T_v)$	Dittus-Boelter
Wall-drop interaction	$q''_{wd}=0.2552\left[\frac{k_f^3 h^*_{fg} g\rho_v\rho_l}{\mu_v D_{30}}\right]^{1/4}\alpha_l^{2/3}(T_w-T_{sat})^{3/4}\left(\frac{D_{30}}{D_{32}}\right)$	Forslund and Rohsenow (1968)
Radiation heat transfer	Wall vapor : $q''^R_{wv}=F_{wv}\sigma'(T_w^4-T_v^4)$	Sun et al. (1976)
	Wall drop : $q''^R_{wd}=F_{wd}\sigma'(T_w^4-T_d^4)$	
	Vapor drop : $q''^R_{vd}=F_{vd}\sigma'(T_v^4-T_d^4)$	
	with $\epsilon_v=0.1$, $\epsilon_w=0.7$, $\epsilon_l=1-e^{-(1.11\alpha_l D_t/D_{32})}$	

Vapor-to-drop convection	$q'''_{vd} = A_i''' \dfrac{k_f}{D_{20}}(2 + 0.74\ \mathrm{Re}_d^{0.5}\mathrm{Pr}_f^{0.33})(T_v - T_d)$	Lee and Ryley (1968)
Energy partition	Droplet heating flux: $q'''_{dH} = A_i''' \dfrac{k_l}{D_{30}}(T_{\mathrm{sat}} - T_o)F_2$ Vaporization heat flux: $q'''_{\mathrm{evap}} = q'''_d - q'''_{dH}$ where $q'''_d = q'''_{vd} + \dfrac{4}{D}(q''^R_{vd} + q''^R_{wd} + q''_{wd})$	Kawaji (1984)
Interfacial mass transfer	$m_i''' = \dfrac{q'''_{\mathrm{evap}}}{h_{fg}}$	
Interfacial area concentration	$A_i''' = \dfrac{6\alpha_l}{D_{32}}$	

In the flow transition region between the inverted annular and dispersed flow regions, liquid is expected to exist in larger sizes than in the fully developed dispersed flow regime. According to the linear stability analysis of the two-fluid equations for the inverted annular flow described in Part I, the wavelength of maximum growth rate was calculated to be at most about 4.5 times the diameter of the liquid column. Therefore, the liquid in the flow transition regime was considered to be an ellipsoidal rather than spherical shape with the length of a semimajor axis larger than that of the semiminor axis by a factor of 4.5. In order to incorporate the significantly larger volume of the ellipsoidal drops into the present model, the value of one of the size distribution parameters was changed for the flow transition regime. The volume distributions for the drops in flow transition and dispersed flow regimes are shown in Fig. 2.

At a given elevation, the actual size distribution is cut off at a maximum diameter, which is equal to the smaller of the maximum stable diameter $D^s_{\max}$ calculated at that elevation and the smallest maximum carryover diameter $D^c_{\max}$, calculated in regions upstream. The maximum stable size of drops is specified by a critical Weber number. The maximum size of drops that can be carried upward for a given local vapor velocity is determined from the balance of gravity and drag forces.

The liquid momentum equation in the present model thus describes the motion of the drops carried upward by vapor. The carryover fraction is computed from the ratio of the integrals of the size distribution function as shown in Table 2.

For use in calculating the interfacial transfer terms, the area-weighted, volume-weighted, and Sauter mean diameters are computed using the log-normal size distribution function and either $D_{\max}$ or $D^c_{\max}$ for the entire population or only the carryover fraction, respectively.

In the multifield model, the size distribution is divided into eleven discrete groups of varying diameters, and the drag force is calculated for each group using the diameter and velocity of each group. The equation of motion is, thus, solved for each group and the total droplet momentum is given by the sum of the momentum of all groups. Consequently, the mass-average velocity can be computed from the total momentum in a straightforward manner to be used in calculating the vapor-to-droplet convection heat transfer rate. This approach is expected to be more demanding in computational efforts but superior in accuracy. In the present work, both the single and multifield modeling approaches were used to determine how significant differences can be obtained in the calculated results.

The heat transfer mechanisms incorporated into the present dispersed flow model include convection from wall to vapor and from vapor to drops, radiation among wall, vapor, and drops, and wall-drop interaction. The heat transfer due to wall-drop interaction is calculated using a model developed by Forslund and Rohsenow (1968), which accounts for heat transfer from the hot wall to a single layer of droplets next to the surface of the tube. It consists of a heat transfer coefficient for a droplet undergoing film boiling on a horizontal hot surface in a gravity field multiplied by the effective surface area of the droplets dispersed around the tube wall. Their correlation contains a parameter whose value was chosen based on their nitrogen data and may not be applicable to a water system. In the present work, the value recommended by Forslund and Rohsenow (1968) was used for reference calculations and the effect of varying this parameter was investigated in the sensitivity study. The total wall heat flux is given by the sum of the wall-to-vapor convection, wall-to-vapor and wall-to-liquid radiation, and wall-drop interaction heat transfer rates.

The droplet surface is assumed to be at saturation and generating vapor even though the drops may be subcooled. The energy received is used partially for vaporization and partially to raise the sensible heat. In a manner similar to that used for the inverted annular flow model, a transient heat conduction problem for a sphere of radius R_d, initially at T_o and the surface raised to T_{sat} for $t > 0$, is solved to derive a droplet heating flux correlation. The correlating function F_2 is shown in Fig. 1. The initial temperature is taken to be the temperature of the drops most recently formed from the liquid column in the inverted annular flow regime.

Thermal Equations and Quench Front Propagation

(a) Heat Conduction in Flow Channel Wall. The flow channel in the experiments (Kawaji et al., 1985) was a thin-walled tube, and a two-dimensional heat conduction equation was solved with fine mesh nodalization in the quench front

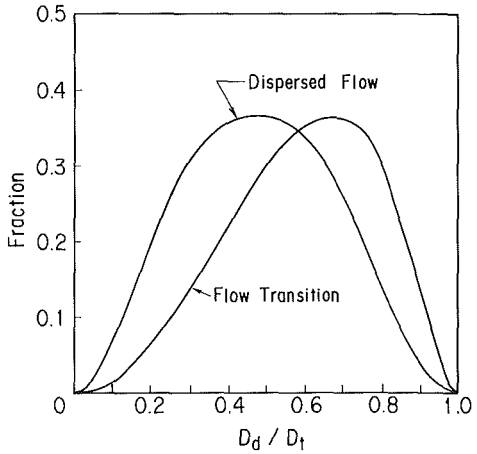

Fig. 2 Volume distributions of drops in flow transition and dispersed flow regimes

region where severe axial and radial temperature gradients exist. In regions far from the quench front, a lumped parameter technique was used and a one-dimensional heat conduction equation was solved. The wall temperatures were matched at the boundaries between the two regions.

(b) Quench Speed. The exact mechanism of rewetting of a hot metal surface, i.e., how and why the vapor film collapses, is not well understood at present, and a common approach adopted in many reflood models is to employ a rewetting criterion based on quench temperature correlations. When the wall temperature drops to a specified quench temperature, the heat transfer mode is assumed to change from film boiling to nucleate boiling. The apparent quench temperatures reported in the literature are, however, scattered in value ranging from slightly above saturation to well above critical temperatures.

If the quench temperature is not correctly specified, the quench speed would be poorly predicted and comparison of hydrodynamic and heat transfer calculations with the experimental data becomes quite difficult. Thus, instead of using a quench temperature correlation, the quench speeds extracted from the experimental data were used in the present work to decouple the heat transfer and hydrodynamic aspects of reflood from the rewetting problem and analyze them independently.

(c) Heat Transfer and Vapor Generation in the Quench Front Region. To calculate heat transfer rates in regions below the quench front, the Dittus-Boelter equation and a correlation by Chen (1963) were used for convection and subcooled nucleate boiling, respectively. The heat transfer coefficient predicted by Chen's correlation is unrealistically large if the wall superheat is very high. Such a condition exists at the instant liquid rewets the metal surface. Therefore, an upper limit of 2.3×10^5 W/m^2 was placed on the value of the heat transfer rate at the quench front. This particular value was obtained from the CHF values measured by Cheng and Ragheb (1979) for an Inconel-copper composite test section at atmospheric pressure.

A significant source of vapor exists at the quench front during reflood. The heat flux shows a peak during quenching and a fraction of this heat transferred from the wall to the subcooled liquid is likely used in generation of vapor bubbles, which escape into the vapor film in the inverted annular flow regime. Elias and Chambré (1981) explicitly considered this source of vapor as the major contributor to the vapor film in the entrance region of their inverted annular flow model. In the present work, net generation of vapor at the quench front

Table 3 Nodal cells used in numerical calculation

Region	Hydrodynamic cell	Wall conduction cell
Single-phase liquid	2.5 cm	17.5 cm
Quench front	2.5 cm	0.36 cm (axial) 0.27 cm (radial)
Inverted annular flow	2.5 cm	2.5 cm
Transition flow	33 cm	17.5 cm
Dispersed flow	33 cm	17.5 cm

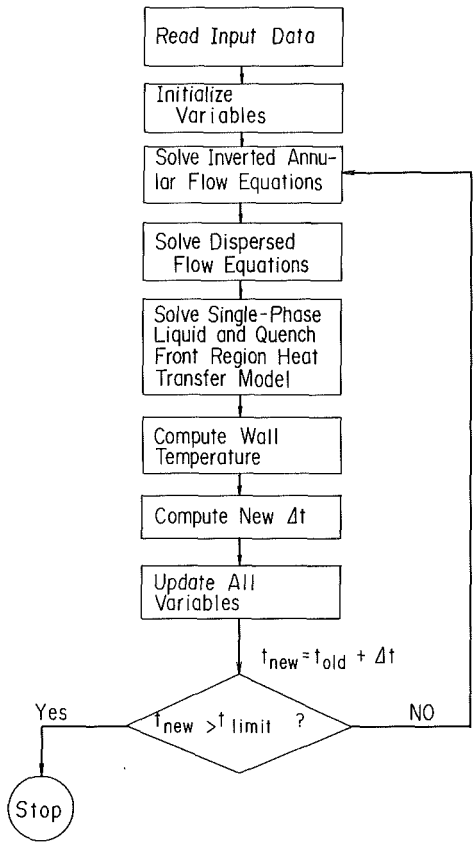

Fig. 3 Overall computational scheme

was assumed to occur immediately below the quench front based on observations from the quartz tube quench experiments (Kawaji, 1984). The fraction of heat transferred from the wall to the liquid and used for net vapor generation is expected to change with the liquid subcooling, but was assumed to be constant at 5 percent of the total wall heat flux. Since the vapor generated in this region was used as a boundary condition in the vapor conservation equations of the inverted annular flow model, the use of values larger than 5 percent resulted in thicker vapor film, lower heat transfer rates, and a shorter liquid column due to premature instability in the inverted annular flow regime. As shown later, the use of 5 percent gave reasonable predictions of the liquid column height in the early part of all the experiments simulated.

Numerical Solution Scheme

As the linear stability analysis described in Part I showed, incorporation of the phasic pressure difference has a stabilizing effect against short-wavelength perturbations and permits the use of numerical schemes with less implicitness and greater computational efficiency. Further simplification in the solution scheme is provided by the fact that the system pressure varied little during forced reflooding of a single tube (Kawaji

Table 4 Experiments analyzed for model verification

Run number	Initial wall temperature (°C)	Coolant injection rate (cm/s)	Coolant temperature at inlet (°C)
560-7.6-25	560	7.6	25
560-12.7-25	560	12.7	25
730-12.7-25	730	12.7	25
730-17.8-25	730	17.8	25

et al., 1985), and at atmospheric pressure, only the vapor properties are strongly dependent on temperature.

The numerical solution method adopted in this study is a semi-implicit, finite-difference scheme for the inverted annular flow equations and an explicit scheme for the dispersed flow equations. Numerical stability is enhanced by adopting a donor-cell, upwind differencing scheme for convective terms. Details of the finite differencing scheme are given by Kawaji (1984).

A computer program was written to perform the numerical solution of the finite difference equations with the constitutive relations given in Tables 1 and 2.

In the calculations described below, the flow channel was divided into a number of nodal cells for hydrodynamic calculations. The nodal cells for heat conduction calculations in the channel wall were also specified separately from the hydrodynamic cells. The nodal cell sizes used in the calculations presented in this paper are listed in Table 3. Near the quench front, a two-dimensional fine mesh is placed in the flow channel wall in order to resolve the two-dimensional wall temperature gradients. As the quench front moves upward in time, the fine mesh is moved along as well by creating and destroying the fine mesh nodes downstream and upstream, respectively.

The size of the axial fine mesh used in the present analysis of the fast reflooding data was adequate to resolve the large temperature gradient in the quench front region. For slow reflooding cases in which the axial conduction controls the quench speed, the use of a much finer mesh size may be necessary to obtain more accurate wall temperature profiles at the quench front.

The overall computation scheme is represented by a flow chart shown in Fig. 3. At every time step, the hydrodynamic and heat transfer calculations are performed for each cell. The time increment for the next time step is computed from the hydrodynamic node size and the maximum fluid velocity obtained in the previous time step, such that the Courant condition given below is not violated.

$$\frac{U_{\max}\Delta t}{\Delta Z} < 1 \tag{9}$$

Comparison of Model Predictions With Data

Several of the Inconel tube reflood experiments reported previously (Kawaji et al., 1985) were simulated using the two-fluid model and constitutive relations described in Parts I and II of this paper. The initial and boundary conditions of the tests shown in Table 4, and selected for model verification, were such that the inverted annular flow regime was believed to have existed near the quench front at nearly all axial locations.

The wall temperature histories predicted for two of the tests with the single-field and multifield models are compared with the experimental data in Figs. 4 and 5. In both of these tests, the wall temperature predictions are in fair agreement with the experimental data. Slight underprediction of wall-to-fluid heat transfer rate and overprediction of wall temperature is evident for the test involving a higher initial wall temperature (Run 730-17.8-25).

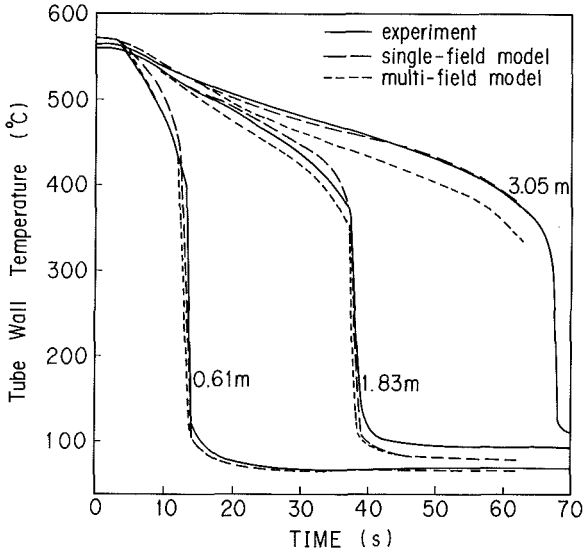

Fig. 4 Multifield model prediction of wall temperature histories (Run 560-12.7-25)

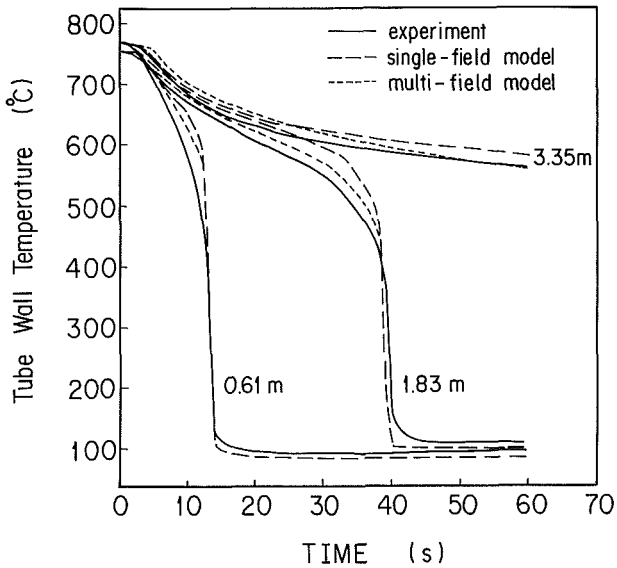

Fig. 5 Multifield model prediction of wall temperature histories (Run 730-17.8-25)

In the film boiling region, the interfacial waves were predicted as described in Part I and contributed to the increased heat transfer rates in this region. However, in Run 730-17.8-25, the wall temperatures are still overpredicted due probably to the limitation of the present one-dimensional model in predicting the possibly two-dimensional motion of the liquid column. The eccentricity of the liquid core and random motion in radial and circumferential directions can lead to an extremely thin vapor film locally, giving rise to sharp increases in the rate of heat transfer especially in regions close to the quench front.

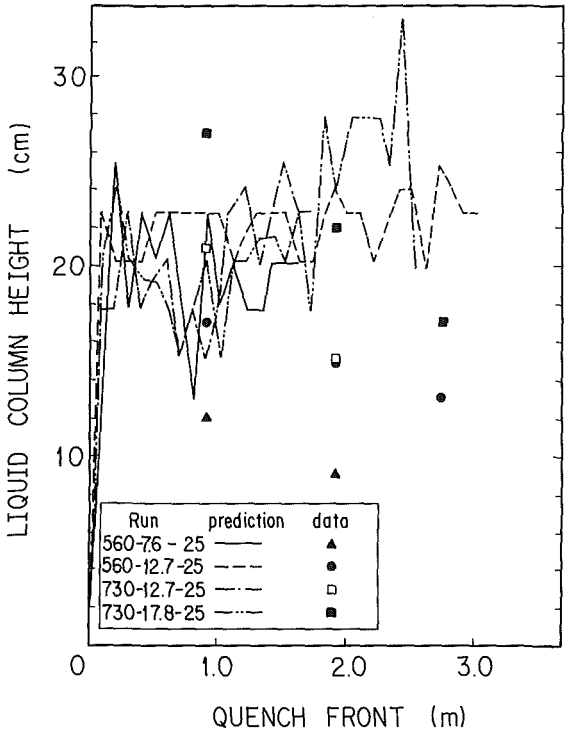

Fig. 6 *Comparison of predicted and measured liquid column height in inverted annular flow regime*

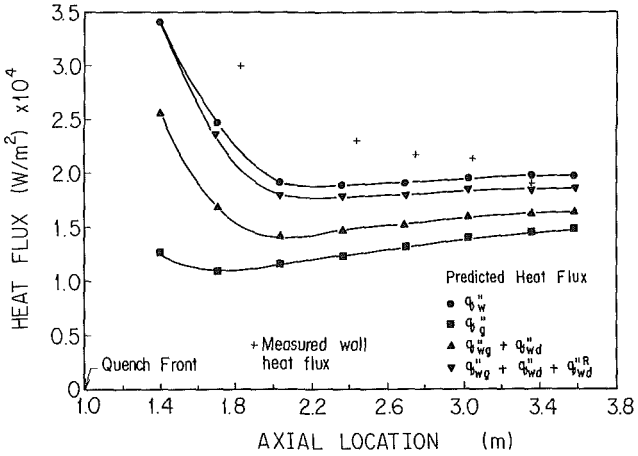

Fig. 7 *Predicted contributions of various heat transfer mechanisms in the dispersed flow regime (Run 730-17.8-25)*

The height of the liquid column in the inverted annular flow regime was determined based on interfacial wave growth. The predictions are compared with the heights estimated from the void fraction measurements in Fig. 6. Although the calculated breakup lengths are in fair agreement with the data in the early part of the transients, they do not decrease with the quench front elevation as observed in the data. This may be attributed to the use of a constant fraction of heat flux at the quench front for the generation of vapor that enters the vapor film in the inverted annular flow regime. As the liquid loses subcooling at higher quench front locations, more vapor is expected to enter into the film boiling region and a larger vapor velocity in the vapor film would lead to instability of the liquid column at shorter distances above the quench front.

In the dispersed flow regime, the wall temperature predictions were overpredicted in experiments with higher initial wall temperature (730°C) for both the single and multifield dispersed flow models (Fig. 5). For Run 730-17.8-25, the underprediction of wall heat flux was noted in the flow transition region and the entrance region of the dispersed flow regime as shown in Fig. 7. The calculations indicated the presence of vapor superheat but a direct comparison of predicted values with the data could not be made due to the lack of such measurements in the experiment. On the other hand, the mass balance calculations shown in Fig. 8 indicate that there is a consistent relationship between the hydrodynamic and heat transfer calculations.

The relative contributions of individual heat transfer mechanisms calculated by the single-field model as shown in Fig. 7 indicate that wall-to-vapor convection is the most dominant heat transfer mechanism in the fully developed region of the dispersed flow regime. However, the radiative heat transfer from the wall to drops and wall-drop interaction are calculated to be equally important and together exceed the wall-to-vapor convective heat transfer rate in the flow transition region. The contribution of drops is gradually reduced as the liquid volume fraction decreases along the flow channel. The wall-to-vapor radiation is relatively unimportant compared to the other mechanisms.

The axial variation of the predicted wall heat flux in the fully developed region of the dispersed flow regime is in reasonable agreement with the experimental results. However, the present model still underpredicts the heat transfer rates in the flow transition region despite inclusion of a wall-droplet interaction mechanism. The prediction can be improved by increasing the contribution of the wall-droplet interaction component as discussed in the next section. Nevertheless, the above result gives strong support for the existence of an additional heat transfer mechanism besides convection and radiation in the entrance region of the dispersed flow regime, where the liquid volume fraction and drop sizes are both significantly larger than those further downstream.

The mass balance comparisons for Run 730-17.8-25 are shown in Fig. 8. For this run, the multifield model predictions showed better agreement with the experimental data than those of the single-field model. However, for other runs with a lower initial temperature, opposite results were obtained.

As shown above, mixed results have been obtained with the present multifield approach. Predictions have been improved for runs involving a higher initial wall temperature; however, the single-field model showed better agreement with the data for runs with a lower initial wall temperature.

The drop velocities calculated by the single and multifield models are compared in Fig. 9. Drops with smaller diameters are strongly accelerated by the vapor phase and approach their terminal velocities downstream. Although the velocities of drops in many of the smaller size groups calculated by the multifield model exceeded the population-mean velocity of drops in the single-field model, the multifield model predictions of the population-mean velocities are lower than those of the single-field model for both of these tests. This is because the smaller size groups contribute little to the overall liquid volume fraction. The larger size groups may contain fewer drops, but account for the major part of the liquid volume.

The differences noted above apparently led to the mixed results obtained when drops were divided into multiple groups. The factors that contributed to the lowering of the population-mean velocity in the multifield model calculations are not clear at present, but may be related, for example, to the correlation used to evaluate the drag coefficient. Factors such as deformation of relatively larger droplets, which were not considered here, may have a considerable effect on the actual drag force. It should also be noted here that the present multifield model does not account for the intragroup transfer of mass, momentum, and energy, due to the lack of

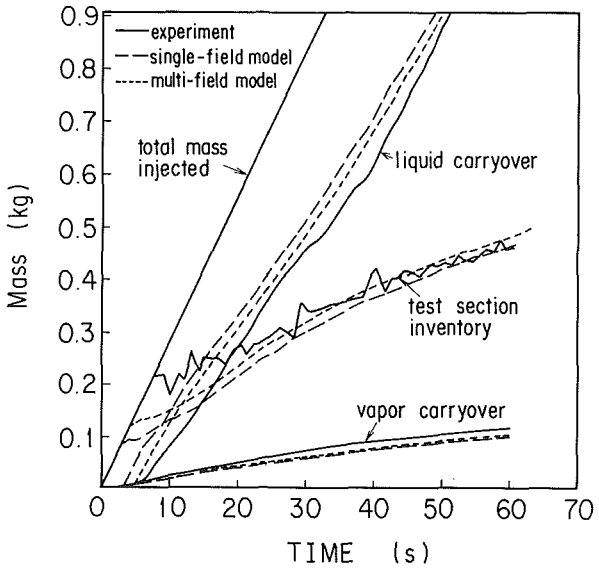

Fig. 8 Multifield model prediction of mass balance data (Run 730-17.8-25)

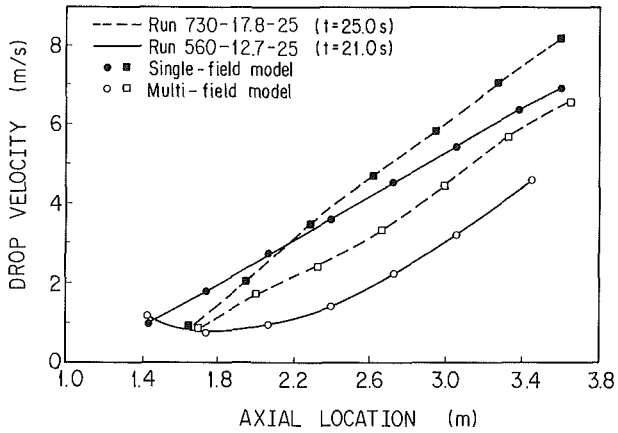

Fig. 9 Comparison of population-mean drop velocities calculated by single and multifield models

understanding of the interaction among the drops of different sizes. This aspect of the multifield model needs further investigation as it may have a significant effect on the evolution of droplet size distribution above the inverted annular flow regime.

Sensitivity Study

Values of several parameters in the dispersed flow model were varied in order to appraise the sensitivity of the predictions to the particular values used in the single-field model calculations. The study consisted of three cases, in which the critical Weber number, flow transition regime length, and wall-to-droplet heat transfer rate were varied one at a time, and the results compared with the reference single-field model predictions described above.

Case 1: Critical Weber Number. To determine the maximum stable size of drops, a value of 22 was used for the critical Weber number, assuming that the drops are slowly accelerated (Hinze, 1955). Adoption of a value larger than 22 lacks a physical basis and was not considered in this study. Decreasing the Weber number, on the other hand, would seem to lead to a smaller maximum droplet diameter; however, this was not always the case in our model because the maximum drop size is determined by the lesser of the maximum stable and maximum carryover diameters.

In tests with a lower initial wall temperature (560°C), vapor velocities in the flow transition and part of the dispersed flow regime were predicted to be sufficiently low, so that at a given axial location, the maximum carryover diameter in the upstream region was found to be limiting the maximum droplet size rather than the critical Weber number.

On the other hand, in tests involving a higher initial wall temperature (730°C), significantly higher vapor velocities were calculated in the dispersed flow regime, making the maximum stable diameter more limiting than the maximum entrainable diameter. For this case, decreasing the value of the critical Weber number affected the model predictions but only slightly as shown in Fig. 10.

Case 2: Flow Transition Regime Length. The larger droplet size distribution is used in the flow transition regime, and the length of the flow transition regime equal to 33 cm was used in the reference calculations based on observation of the size of drops reaching an equilibrium distribution at about this distance above the point of droplet generation in reflooding experiments by Ardron and Hall (1983). The actual length of the flow transition regime is, however, difficult to determine precisely or to model analytically, since it is likely dependent on many factors including the local vapor velocity and liquid breakup time. Thus, simulations were made with the length of the flow transition regime doubled as shown in Fig. 11. The predictions are not overly sensitive to the length selected. Similar results have been obtained for other tests.

Case 3: Wall-to-Drop Heat Transfer Rate. A correlation of the film boiling component of the dispersed flow heat transfer mechanisms, developed by Forslund and Rohsenow (1968), contains an empirical constant that strictly applies to the post-CHF heat transfer data for nitrogen. However, the same value has been used in the reference calculations described earlier despite physical differences in fluid properties between nitrogen and water. In order to assess the effect of this constant, simulations were performed with the constant multiplied by a factor of two, as shown in Figs. 10 and 11. For runs involving a higher initial wall temperature, better agreement was found for the dispersed flow heat transfer with an increase in the value of the wall-drop interaction heat transfer rate. However, for tests with a lower initial wall temperature, poorer agreement with the experimental data was obtained.

The model predictions were found to be rather insensitive to any of the parameters discussed above and that no single parameter could be modified to universally improve the predictions.

Conclusions

A mechanistic multifield model was developed and used to analyze the reflooding of a hot vertical tube. Constitutive relations were developed based on the present understanding of the mechanisms involved in inverted annular and dispersed flow hydrodynamics and heat transfer. The inverted annular flow model incorporates the phasic pressure difference, which assures numerical stability while allowing prediction of interfacial waves due to Kelvin-Helmholtz instabilities. The dispersed flow model was solved with both single and multifield equations for droplet motion in order to account for the effect of droplet size distribution.

Simulations of a number of reflood experiments involving a vertical Inconel tube showed that the model predictions are in fair agreement with the data, indicating that many of the constitutive relations used in the model properly account for the physical mechanisms. The results, however, also point out

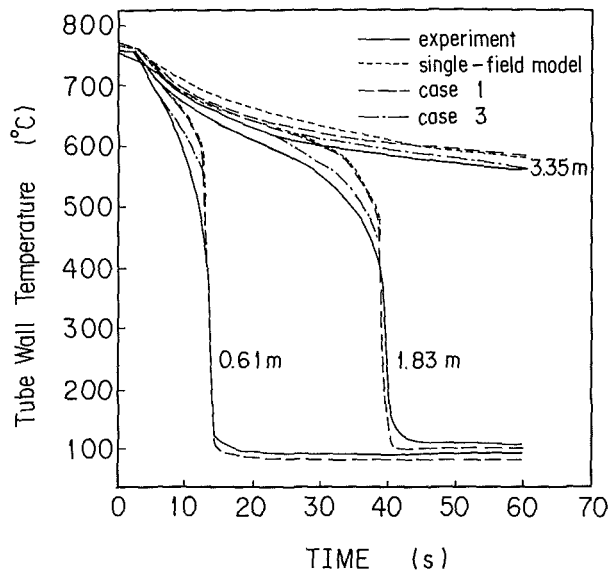

Fig. 10 Comparison of wall temperature predictions for Run 730-17.8-25 (Case 1: We_{cr} = 15, Case 3: wall-to-droplet heat transfer doubled)

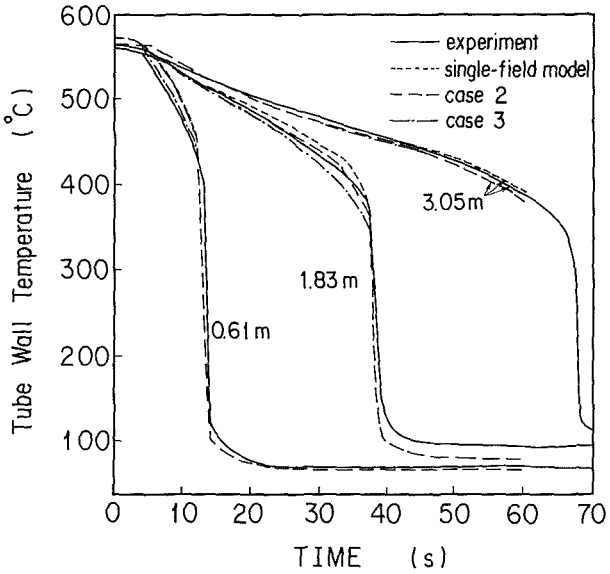

Fig. 11 Comparison of wall temperature predictions for Run 560-12.7-25 (Case 2: transition flow regime length doubled, Case 3: wall-to-drop heat transfer doubled)

areas where further investigation of the physical mechanism is still needed to improve the model predictions.

For the inverted annular flow regime, heat transfer rates were somewhat underpredicted for experiments with high initial wall temperatures (730°C), despite the appearance of interfacial waves in the calculated results. Causes of underprediction are postulated to be related to the two-dimensional motion of the liquid column, which cannot be predicted by the present one-dimensional model.

For the dispersed flow regime downstream, the wall-droplet interaction heat transfer was found to be an important factor in explaining the strong dependence of heat transfer rate on local liquid volume fraction, which had been experimentally observed. To improve the wall-to-droplet heat transfer predictions, a more detailed study on the interactions of large drops with the flow channel wall is recommended. Finally, a comparison of the single and multifield model predictions for the droplet velocities showed differences that significantly affected the heat transfer and overall mass balance calculations. The effect of intragroup transfer terms, which were neglected in the present multifield model, should be evaluated in order to determine the relative accuracies of both modeling approaches.

References

Ardron, K. H., and Hall, P. C., 1983, "Droplet Hydrodynamics and Heat Transfer in the Dispersed Flow Regime in Bottom Flooding," in: *Transient Two-Phase Flow, Proc. of the Third Specialist Meeting*, M. S. Plesset, N. Zuber, and I. Catton, eds., Hemisphere Publishing Corporation, Washington, DC.

Chen, J. C., 1963, "A Correlation for Boiling Heat Transfer to Saturated Fluids in Convective Flow," ASME Paper No. 63-HT-34.

Cheng, S. C., and Ragheb, H., 1979, "Transition Boiling Data of Water on Inconel Surface Under Forced Convective Conditions," *Int. J. Multiphase Flow*, Vol. 5, No. 4, pp. 281–291.

De Jarlais, G., 1983, "An Experimental Study of Inverted Annular Flow Hydrodynamics Utilizing an Adiabatic Simulation," NUREG/CR-3339, ANL-83-44.

Edelman, Z., Elias, E., and Naot, D., 1983, "Optical Illustration of Liquid Penetration to the Vapour Film in Inverted Annular Boiling," *Int. J. Heat Mass Transfer*, Vol. 25, No. 11, pp. 1715–1717.

Elias, E., and Chambré, P., 1981, "Inverted Annular Film Boiling Heat Transfer From Vertical Surfaces," *Nuclear Engineering and Design*, Vol. 64, pp. 249–257.

Forslund, R. P., and Rohsenow, W. M., 1968, "Dispersed Flow Film Boiling," ASME JOURNAL OF HEAT TRANSFER, Vol. 90, pp. 399–407.

Hinze, J. O., 1955, "Fundamentals of the Hydrodynamic Mechanism of Splitting in Dispersion Process," *AIChE Journal*, Vol. 1, pp. 289–295.

Jeromin, L. O. F., 1970, "The Status of Research in Turbulent Boundary Layers With Fluid Injection," *Progress in Aeronautical Science*, Vol. 10, Pergamon Press.

Kawaji, M., 1984, "Transient Non-equilibrium Two-Phase Flow: Reflooding of a Vertical Flow Channel," Ph.D. Thesis, Dept. of Nuclear Engineering, University of California, Berkeley, CA.

Kawaji, M., and Banerjee, S., 1987, "Application of a Multifield Model to Reflooding of a Hot Vertical Tube: Part I—Model Structure and Interfacial Phenomena," ASME JOURNAL OF HEAT TRANSFER, Vol. 109, pp. 204–211.

Kawaji, M., and Banerjee, S., 1983, "Two-Phase Flow Characteristics During Reflooding of a Hot Vertical Tube," EPRI Report NP-2620.

Kawaji, M., Ng, Y. S., Banerjee, S., and Yadigaroglu, G., 1985, "Reflooding With Steady and Oscillatory Injection: Part I—Flow Regimes, Void Fraction, and Heat Transfer," ASME JOURNAL OF HEAT TRANSFER, Vol. 107, pp. 670–678.

Kays, W. M., 1966, *Convective Heat and Mass Transfer*, McGraw-Hill, New York.

Lee, K., and Ryley, D. J., 1968, "The Evaporation of Water Droplets in Superheated Steam," ASME JOURNAL OF HEAT TRANSFER, Vol. 90, pp. 445–451.

Lee, N., Wong, S., Yeh, H. C., and Hochreiter, L. E., 1982, "PWR FLECHT SEASET Unblocked Bundle Forced and Gravity Feed Reflood Task Data Evaluation and Analysis Report," EPRI Report NP-2013 (also NUREG/CR-2256).

Mugele, R. A., and Evans, H. D., 1951, "Droplet Size Distribution in Sprays," *Industrial and Engineering Chemistry*, Vol. 43, No. 6, pp. 1317–1324.

Rowe, R. N., 1961, *Trans. Inst. Chem. Eng.*, Vol. 39, p. 175.

Siegel, R., and Howell, J. R., 1972, *Thermal Radiation Heat Transfer*, McGraw-Hill, New York.

Singh, S. N., 1958, "Heat Transfer by Laminar Flow in a Cylindrical Tube," *Appl. Sci. Res.*, Vol. A7, p. 325.

Sun, K. H., Gonzales, J. M., and Tien, C. L., 1976, "Calculations of Combined Radiation and Convection Heat Transfer in Rod Bundles Under Emergency Cooling Conditions," ASME JOURNAL OF HEAT TRANSFER, Vol. 98, pp. 414–420.

Thurgood, M. J., and Kelly, J. M., 1980, "COBRA-TF, a Three-Field Two-Fluid Model for Reactor Safety Analysis," presented at the ASME/AIChE National Heat Transfer Conference, Orlando, FL.

Whalley, P. B., Azzopardi, B. J., Hewitt, G. F., and Owen, R. G., 1982, "A Physical Model for Two Phase Flows With Thermodynamic and Hydrodynamic Non-equilibrium," *7th Int. Heat Transfer Conf.*, Munich, Vol. 5, pp. 181–188.

Parametric Trends for Post-CHF Heat Transfer in Rod Bundles

C. Unal[1]
K. Tuzla
O. Badr[2]
S. Neti
J. Chen

Institute of Thermo-Fluids Engineering and Science, Lehigh University, Bethlehem, PA 18015

A 3 × 3 rod bundle with a heated shroud was developed to study post-critical-heat-flux (post-CHF) dispersed-flow boiling. The hot-patch technique was applied to a rod bundle, which successfully arrested the quench front at the test section inlet. Measurements included mass flux, wall heat flux, inlet equilibrium quality, wall temperatures along the bundle axis, and actual vapor temperatures upstream and downstream of a spacer grid. The vapor superheat (up to 600°C) increased with increasing wall heat flux and decreasing mass flux and vapor quality. The heat partition ratio (fraction of total heat input that goes toward evaporation) was found to increase with increasing mass flux and decreasing inlet quality but remained essentially independent of heat flux. The results for the rod bundle were found to be in good agreement with trends previously reported for post-CHF heat transfer in single tubes.

Introduction

In flow boiling systems, drastic changes in flow pattern and heat transfer mechanisms occur at the critical heat flux (CHF) point, beyond which the liquid becomes depleted at the heated surface, resulting in low heat transfer coefficients with correspondingly high surface temperatures (Chen et al., 1979). Depending on the vapor quality at the CHF point, the post-CHF flow may exhibit the inverse annular flow pattern or the dispersed flow pattern. Convective film boiling with this type of flow pattern is encountered in such applications as cryogenic systems, metallurgical processing, steam generators, and nuclear reactor loss-of-coolant accidents. Post-CHF heat transfer was often modeled assuming thermodynamic equilibrium between vapor and liquid droplets, until Parker and Grosh (1962) observed some liquid droplets at equilibrium qualities exceeding unity. Obviously, in this nonequilibrium situation, actual and equilibrium qualities are not equal. Laverty and Rohsenow (1967), Forslund and Rohsenow (1968), and Hynek et al. (1969) published early attempts to analyze such nonequilibrium dispersed flow boiling. More recently, models incorporating nonequilibrium concepts were proposed by Plummer et al. (1976), Saha et al. (1977), Jones and Zuber (1977), Tong and Young (1974), Groeneveld and Delorme (1976), Chen et al. (1979), and Webb et al. (1982). Verifications and improvements of such models are greatly hampered by the lack of experimental data regarding the degree of thermodynamic nonequilibrium in convective boiling in rod bundles.

Successful measurements of nonequilibrium vapor temperatures in convective film boiling experiments are very limited due to quenching of the measuring probes by the entrained liquid droplets. Mueller (1967) and Polomik (1967) obtained some limited data at high vapor qualities for internal flows in tubes. Nijhawan et al. (1980), Gottula et al. (1983), and Evans et al. (1983) successfully measured vapor superheats for internal flows in tubes. Hochreiter (1977) and Loftus et al. (1981) obtained indication of vapor superheats in rod bundles for high vapor qualities, but to date, there are only very limited data for nonequilibrium flow film boiling in rod bundle geometries.

In many of the tube experiments, attempts were made to stabilize post-CHF conditions in the test section and permit measurements of vapor temperature at fixed distances from the CHF location. Groeneveld and Gardiner (1978) proposed the use of a large thermal mass (hot patch) at the test section inlet. When such a hot patch was preheated to a temperature well above Leidenfrost wetting temperature, its thermal inertia would arrest the quench front, giving an opportunity to adjust the test section power to maintain post-CHF conditions. Such a technique was applied successfully for single tube experiments by Nijhawan et al. (1980) and Gottula et al. (1983).

The objective of the present investigation was to study the post-CHF heat transfer phenomena experimentally in a 3×3 rod bundle array. The experiment provided simultaneous measurements of wall heat flux, nonequilibrium vapor temperature, wall temperatures, flow rate, inlet equilibrium quality, and system pressure. The hot-patch technique to obtain stabilized conditions was applied successfully to the rod bundle geometry. This paper describes the test facility and presents the data as a set of parametric plots in an attempt to delineate the influence of various system parameters on post-CHF heat transfer phenomena in rod bundles. The parametric trends are also compared with observations from earlier experiments in a single vertical tube (Nijhawan, 1980).

Experimental Approach

A circulating flow boiling loop, shown in Fig. 1, was used for the present study. Subcooled water was pumped to a vertical boiler tube of 14.3 mm i.d. and 3.66 m length. Direct resistive heating of the Inconel 600 alloy tube was used to heat and partially vaporize the inlet water, and the two-phase mixture was then passed vertically upward through the test section. The two-phase mixture exiting the test section was throttled to the condenser pressure (~1 atm). A separation tank was used upstream of the throttling valve to minimize two-phase flow oscillations during throttling. The condensate flowed to a surge tank and then returned to the pump.

A 3×3 rod bundle, simulating pressurized water reactors, was selected for the test section. The test section was designed to obtain equal pressure drops in all flow subchannels by requiring equal hydraulic diameters, leading to the dimensions shown in Fig. 2. It was also important to provide equal rates of heat addition per unit length per unit mass of flow in each subchannel in order to obtain equal vapor qualities in all subchannels at a given axial level. This required equal heat fluxes from all heated rods and the heated shroud. The shroud, made of 2-mm-thick Inconel 625 alloy, was heated by radiation from a tubular furnace with three independently controlled

[1]Presently with Chemical and Nuclear Engineering Department, University of Maryland, College Park, MD.

[2]Presently with Mechanical Engineering Department, UAE University, United Arab Emirates.

Contributed by the Heat Transfer Division for publication in the JOURNAL OF HEAT TRANSFER. Manuscript received by the Heat Transfer Division April 28, 1986. Keywords: Boiling, Heat Exchangers, Multiphase Flows.

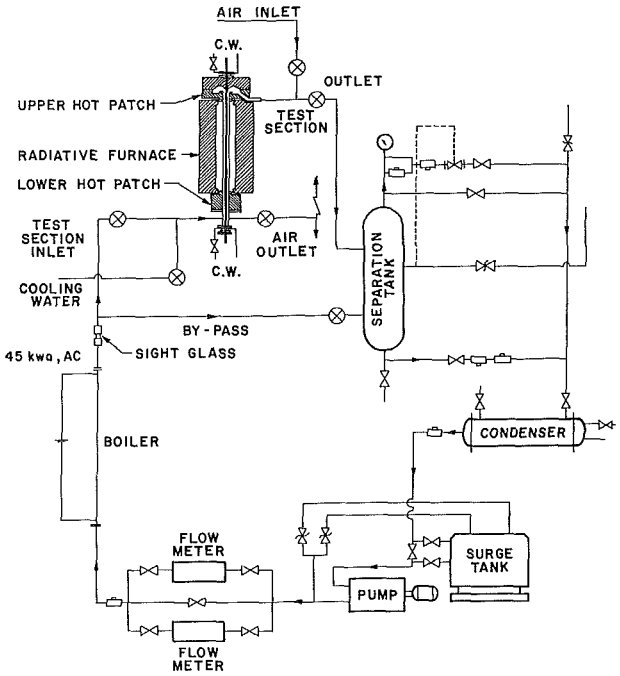

Fig. 1 Schematic diagram of the rod bundle test loop

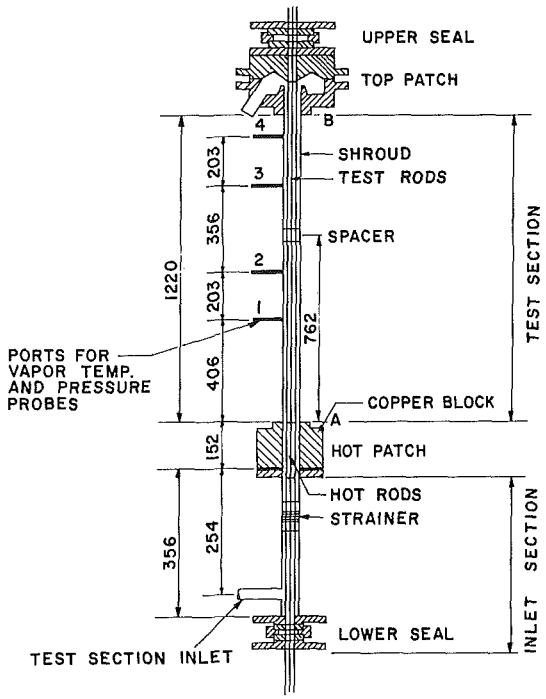

Fig. 3 Schematic diagram of the test bundle

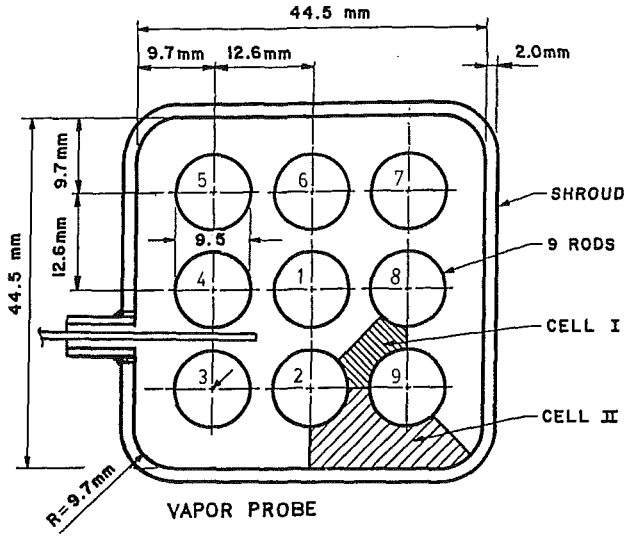

Fig. 2 Cross-sectional view of the test bundle

zones. Twelve chromel-alumel thermocouples were brazed onto the outside surface of the shroud at different axial locations.

A side view of the test bundle, as given in Fig. 3, shows a 1.22-m-long test section with a grid spacer located 76 cm from the inlet (point A in Fig. 3), and four instrumentation ports located on one side of the shroud for vapor temperature and pressure measurements. The inlet to the test section contained a strainer to provide uniform flow across the bundle cross section. The test rods (9.5 mm o.d.) were heated internally by electrical resistance ribbons embedded in boron nitride. Each rod was equipped with 12 thermocouples placed in groves to measure the wall temperatures at different axial elevations.

The hot-patch technique introduced by Groeneveld and Gardiner (1978) was modified and utilized in this apparatus to prevent both upward and downward propagation of quench fronts into the test section. As shown in Fig. 4, the inlet hot patch consisted of an outer copper block surrounding the shroud, and nine short hot rods each acting as an individual hot patch for one of the nine test rods of the bundle. The hot rods were similar to test rods in construction but provided higher heat fluxes and were individually temperature controlled. The exit hot patch consisted of extensions of the test

Nomenclature

A = area, m^2
CHF = critical heat flux
D = hydraulic diameter, m
G = mass flux, kg/m^2s
h = convective heat transfer coefficient, $W/m^2°C$
H = enthalpy, kJ/kg
H_{fg} = latent heat of vaporization, kJ/kg
L = axial distance between CHF location and the vapor probe, m
p = pressure, kPa
R_e = evaporation ratio
q = heat flux, W/cm^2
Q = average heat flux, W/cm^2
T = temperature, °C
x = vapor mass quality

Subscripts

a = actual
e = equilibrium
ev = evaporative
in = inlet
l = liquid
L = distance from CHF
r = test rod
s = saturation
t = total
v = vapor
vl = vapor-to-liquid
w = wall
wv = wall-to-vapor

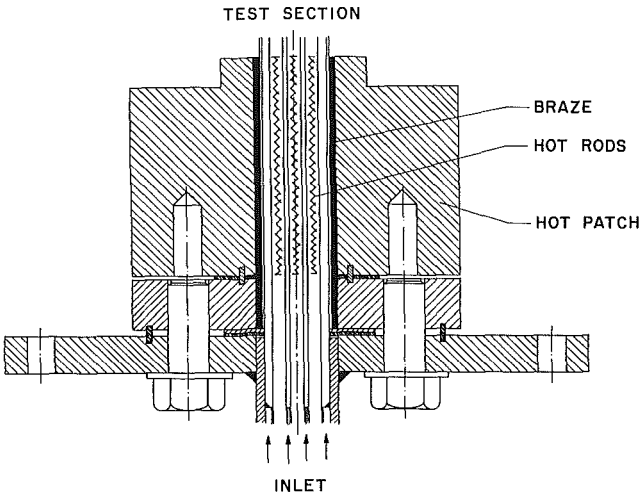

Fig. 4 Lower hot-patch assembly

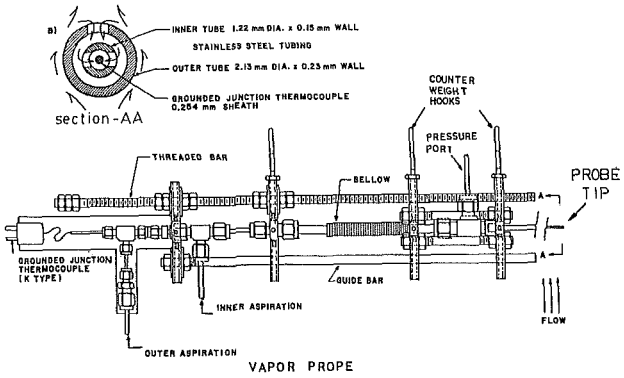

Fig. 5 Schematic diagram of the traversable vapor superheat probe

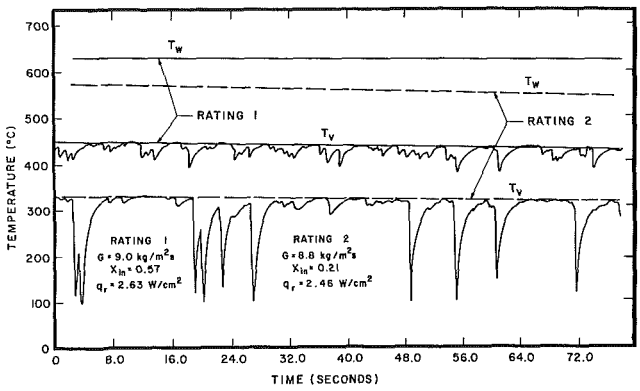

Fig. 6 Vapor superheat probe traces with low measurement uncertainties

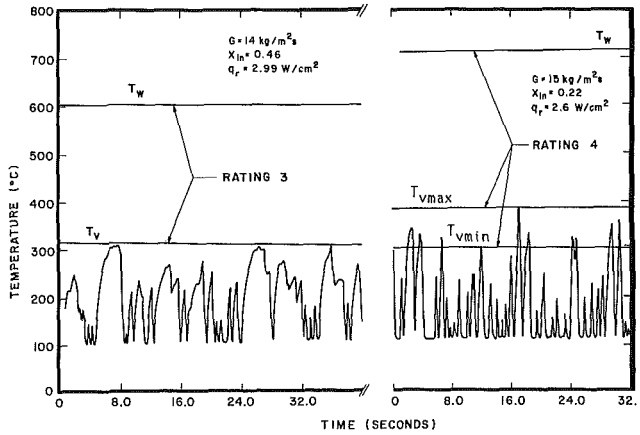

Fig. 7 Vapor superheat probe traces with higher measurement uncertainties

rods surrounded by two heated copper blocks. The upper block with a conical base was superheated to avoid quenching due to the impingement of liquid droplets in the two-phase fluid. The conical shape of the block reduced the likelihood of liquid droplets falling back onto the test section wall. The lower block was also superheated to avoid quenching by the liquid collected in the plenum before discharging from the test section.

The vapor temperature probe shown schematically in Fig. 5 was a modified version of the one developed by Nijhawan (1980) and used by Gottula et al. (1983) and Evans et al. (1983). The probe diameter was made small enough to pass through the clearance gap (3.1 mm) between rods. The bellow contained in the probe allowed the traversing measurement of lateral variations of vapor superheat within a subchannel. Two probes were located upstream and downstream of the grid spacer in the test section. Each vapor temperature probe consisted of a microthermocouple with its hot junction placed within the inner of two concentric capillary tubes. The ends of both tubes were sealed closed. Access holes to both tubes were drilled at 90 deg displacement as shown in section AA of Fig. 5. The probe assembly was inserted into the test section so that the sampled mixture had to traverse through a 180 deg change of direction and then a second 90 deg change of direction before passing over the sensing thermocouple junction. Inertial separation of the phase drawn into the probe allowed the liquid droplets to be collected and drawn off by aspiration through the outer annulus. Aspiration through the inner tube ideally caused liquid-free vapor to be drawn past the sensing thermocouple junction. Practically, however, some liquid droplets were drawn into the inner tube causing some periodic quenching of the thermocouple. Due to the small dimensions involved, residence time of the sample within the probe was minimal, thus preventing any significant equilibration between the two phases before the vapor passed over the thermocouple junction. The double tube arrangement also provided radiation shielding. For this design, the error caused by radiation from hot walls at operating conditions was calculated to be less than 2°C. Judicious control of the differential aspiration between the inner tube and the outer annulus of the probe permitted adjustment of the liquid quenching frequency. Time-history plots of the vapor temperature, shown in Figs. 6 and 7, were classified according to the frequency of liquid quenching as rating 1 through 4. The trace corresponding to rating 1 (Fig. 6) indicated very few droplets in the probe, and thus the vapor temperature could be read right off the chart as the mean corresponding to the top of the line indicated. The dips in the temperature trace of rating 2 (Fig. 6) were indicative of liquid droplets reaching the probe thermocouple as well as the subsequent complete recovery of the thermocouple temperature. Figure 7 shows two types of traces (rating 3 and 4) that result when larger amounts of liquid existed in the test section. At rating 4, the probe thermocouple had no opportunity to recover to the vapor temperature. In such cases the vapor superheat was interpreted as shown on the plot.

Instrumentation of these tests consisted primarily of thermocouples, pressure transducers, power metering devices, and flow meters. Standard K type thermocouples were used for temperature measurements. The thermocouples that measured the saturation temperature and the fluid temperature at the boiler inlet were calibrated by a Platinum Resistance

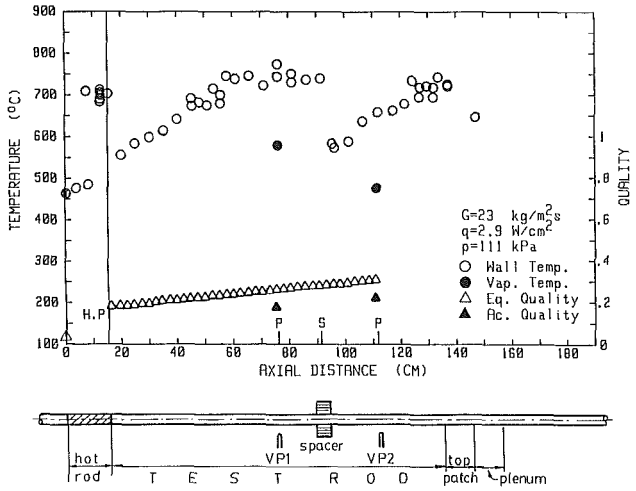

Fig. 8 Axial variation of temperatures and vapor qualities for a typical post-CHF run with high mass flux

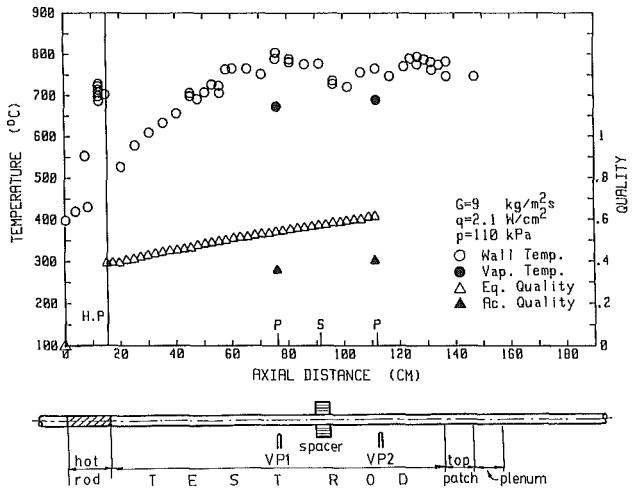

Fig. 9 Axial variation of temperatures and vapor qualities for a typical post-CHF run with low mass flux

Reference Thermometer with estimated uncertainty of $\mp 0.4°C$. The wall thermocouples were then calibrated with reference to the thermocouple that measured the saturation temperature. Maximum uncertainty on wall temperature measurements was $\mp 2°C$. (Unal, 1986). Vapor temperature measurements included additional uncertainties due to chart reading and the characteristic of vapor probe response. These uncertainties, as discussed by Unal (1986), ranged from $\mp 5°C$ to $\mp 30°C$. Vapor superheat data used in this parametric study were limited to rating 1, having a $\mp 5°C$ uncertainty (Unal, 1986). The power inputs to all components were measured by power transducers. Total uncertainties of power metering were as follows (Tuzla, 1984):

Test rod power	0–15 kW range	∓ 159 W
	15–28 kW range	∓ 297 W
Hot rod power	0–5.8 kW	∓ 60 W
Boiler power	0–10 kW range	∓ 65 W
	10–14 kW range	∓ 233 W
Hot patch power	0–5.8 kW	∓ 22 W
Shroud furnace power	0–16.5 kW	∓ 130 W

Flow rates were measured with variable area flow meters, having uncertainties of:

0–68 kg/h range	∓ 0.41 kg/h
68–136 kg/h range	∓ 0.82 kg/h

Results and Discussion

A typical experiment was started by preheating the hot rods and hot patches while the two-phase fluid bypassed the test section. When the temperatures in the test section reached the desired values, the fluid was sent into the test section. With such a technique, the hot patches were successful in arresting quench fronts and sustaining film boiling with almost constant wall temperatures. Data were obtained over the following parametric ranges:

Mass flux	7–26 kg/m²s
Pressure	105 to 120 kPa
Inlet equilibrium vapor quality	40°C subcooled to 0.50
Heat flux	7–50 kW/m²

The data of a typical run included measurements of mass flux, equilibrium vapor quality at test section inlet, pressure, average wall heat flux, wall temperature distribution along the test section, and vapor temperatures at the axial positions located upstream and downstraam of the spacer grid.

Figures 8 and 9 illustrate results in two typical runs, including vapor superheat at two locations and wall temperature distribution along the test section. The figures also show the equilibrium qualities along the test section axis and the actual qualities at the probe locations, calculated from the following equation:

$$x_{aL} = x_{e,L} \frac{h_{fg}}{H_v(T_v, p_s) - H_l} \tag{1}$$

The wall superheat temperatures were mainly obtained from three representative rods, which are indicated as 1, 2, and 3 in Fig. 2. Within the test section length, each of the above rods had nine wall thermocouples, with a 150-mm distance between them. The indicated vapor superheat temperatures were measured at elevations of 150 mm upstream and 200 mm downstream of the grid spacer. Axial locations of the spacer and the two vapor probes are indicated in the figure by "S" and "P," respectively. Radially, both vapor-probe-sensing tips were located at the center of the flow subchannel surrounded by rods 1–4. Wall and vapor superheats, in the range of 400–800°C and 300–600°C, respectively, were typical for these experiments. Such high values of vapor nonequilibrium $(T_v - T_s)$, relative to the wall-to-vapor heat transfer driving force $(T_w - T_v)$, indicate the inefficiency of vapor-to-liquid heat transfer. Also shown in the figures are the desuperheating effects of the spacer on wall and vapor temperatures. A comparison between Figs. 8 and 9 shows that the spacer effects are less apparent for lower mass fluxes. Although many data sets similar to those shown in Figs. 8 and 9 were obtained, the present paper emphasizes the thermohydraulic characteristics between the test section inlet (CHF point) and the location of the first vapor probe. A detailed study of the effects of grid spacer will be considered in a subsequent article.

Figure 10 is an illustration of the variation of vapor superheat, measured by the first probe, with mass flux for a range of equilibrium qualities. For a given wall heat flux and quality, there is a significant decrease in vapor superheat with an increase in mass flux. In addition, vapor superheat decreases with an increase in equilibrium quality for a given mass flux. The driving force for wall-to-vapor heat transfer, $(T_w - T_v)$, is also shown in Fig. 10. For lower qualities, there is a noticeable increase in this driving force with an increase in mass flux. For high qualities, however, the increase in driving force $(T_w - T_v)$ with increased mass flux is insignificant.

Figure 11 illustrates the variation of vapor and wall superheats with wall heat flux, at two different mass fluxes. For a given mass flux, the vapor superheat increases with increasing wall heat flux, but the driving force for wall-to-vapor

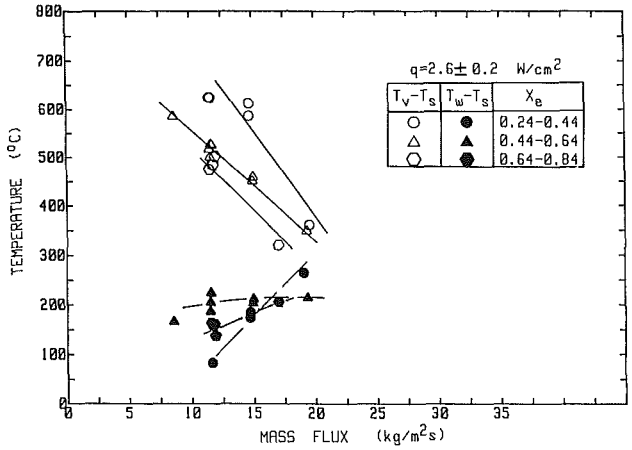

Fig. 10 Variation of vapor superheat and wall-to-vapor driving force with mass flux, for various equilibrium qualities at the vapor probe location

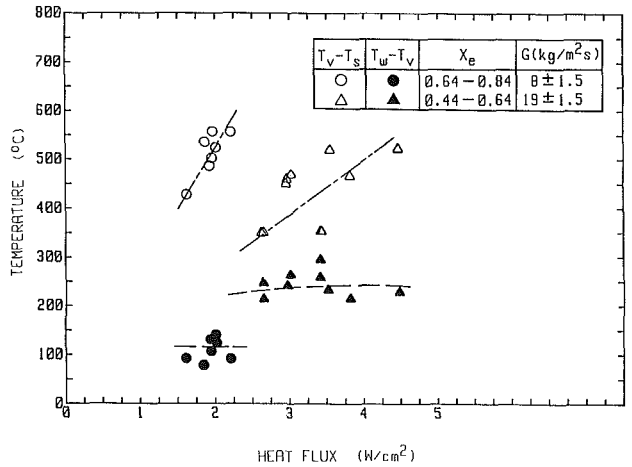

Fig. 11 Variation of vapor superheat and wall-to-vapor driving force with total heat flux for different mass fluxes

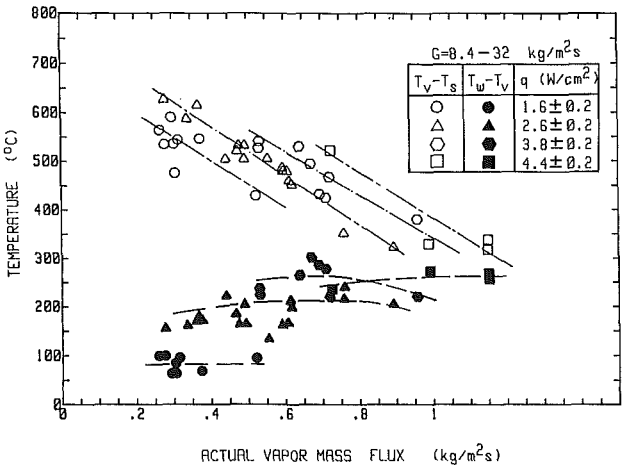

Fig. 12 Variation of vapor superheat and wall-to-vapor driving force with actual vapor mass flux

heat transfer, $(T_w - T_v)$, remains about constant with increasing wall heat flux. These two observations indicate that inefficiency of vapor-to-liquid heat transfer, as compared to wall-to-vapor heat transfer, becomes more important at higher heat fluxes.

Figure 12 is an illustration of combined effect of mass flux and actual vapor quality, Gx_a (the actual vapor mass flux at the probe location), on the vapor superheat and the driving force for wall-to-vapor heat transfer. For a given wall heat flux, the vapor superheat decreases with increasing actual vapor mass flux. It is again evident that for a given actual vapor mass flux, the vapor superheat increases with wall heat flux. It is also clear from Fig. 12 that while the driving force for vapor-to-liquid heat transfer is decreasing with increasing vapor flux, the driving force for wall-to-vapor heat transfer stays approximately constant. This observation indicates that the inefficiency of vapor-to-liquid heat transfer becomes more important at lower vapor fluxes.

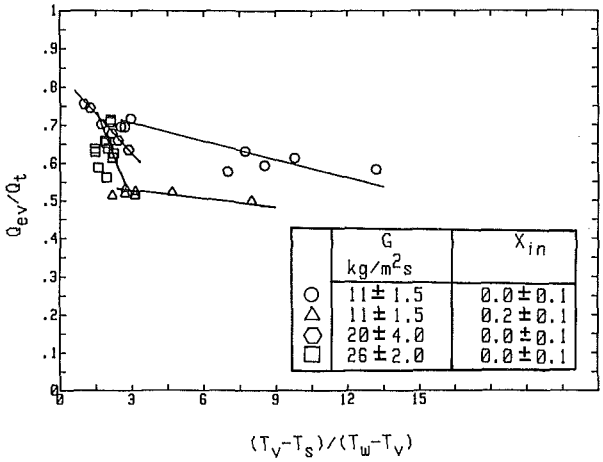

Fig. 13 Heat partition ratio as a function of the ratio of driving forces for heat transfer

The heat partition ratio (Q_{ev}/Q_t), an important feature of the post-CHF heat transfer phenomenon, is defined as the length-averaged fraction of total heat input that goes into evaporation of the liquid phase

$$R_e = \frac{Q_{ev}}{Q_t} \equiv \left[\frac{\text{Latent heat of vaporization}}{\text{Time}\cdot\text{Volume}}\right] \div \left[\frac{\text{Total heat input}}{\text{Time}\cdot\text{Volume}}\right]$$

or

$$R_e = \left[\frac{(x_{aL} - x_{e,\text{CHF}})H_{fg}G\pi D^2/4}{\pi DL}\right] \Bigg/ \left[\frac{(x_{e,L} - x_{e,\text{CHF}})H_{fg}G\pi D^2/4}{\pi DL}\right] \tag{2}$$

This parameter also can be expressed as

$$R_e = \frac{x_{a,L} - x_{e,\text{CHF}}}{x_{e,L} - x_{e,\text{CHF}}} \tag{3}$$

which represents the ratio of the increase in the actual vapor quality past dryout, to the increase in equilibrium quality. Moreover, when radiation and liquid-wall contact heat transfer are neglected, Q_{ev} and Q_t could be expressed as

$$Q_{ev} = (hA)_{vl}(T_v - T_s) \tag{4}$$

$$Q_t = (hA)_{wv}(T_w - T_v) \tag{5}$$

and the evaporation ratio would be

$$R_e = \frac{Q_{ev}}{Q_t} = \left[\frac{(hA)_{vl}}{(hA)_{wv}}\right] \times \left[\frac{T_v - T_s}{T_w - T_v}\right] \tag{6}$$

Figure 13 shows the variation of the heat partition ratio as a function of the ratio of the driving forces, $(T_v - T_s)/(T_w - T_v)$, Each subset represents data points at constant

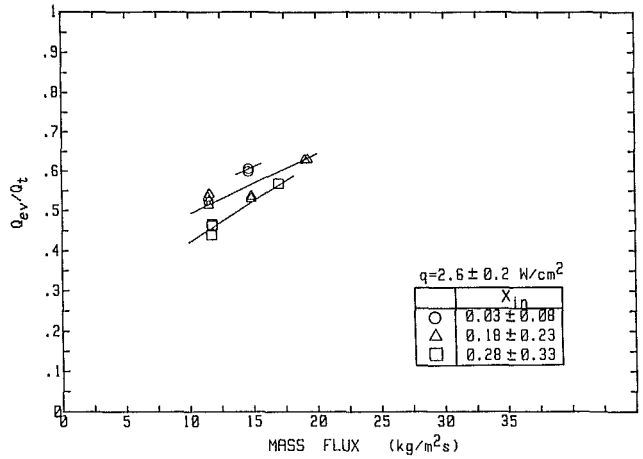

Fig. 14 Variation of the heat partition ratio with mass flux for different inlet equilibrium qualities

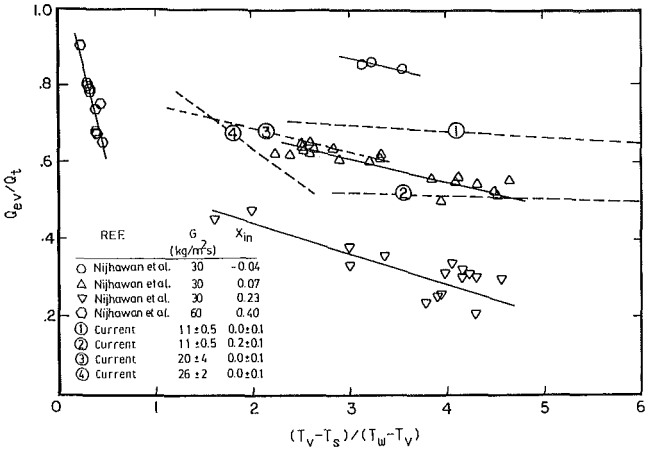

Fig. 16 Comparison of heat partition ratios for single tube and rod bundle tests

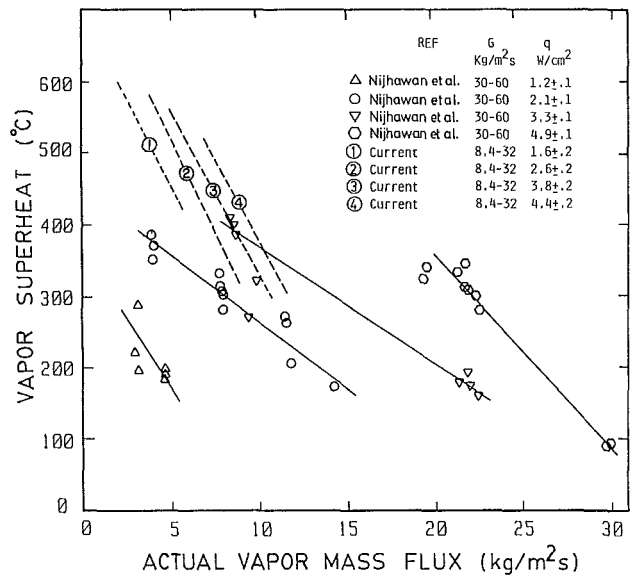

Fig. 15 Comparison of experimental vapor superheat data for single tube and bundle geometries

mass flux and constant vapor quality at the inlet of the test section. When radiation heat transfer and liquid-wall contact heat transfer are neglected, the slope of each line is the ratio of corresponding heat transfer coefficients multiplied by the heat transfer surfaces, $(hA)_{vl}/(hA)_{wv}$ (see equation (6)). For the same mass flux but different inlet qualities, the slopes are almost the same, indicating similar ratios of $(hA)_{vl}/(hA)_{wv}$. The slope increases with increasing mass flux, which shows that $(hA)_{vl}$ increases faster than $(hA)_{wv}$ with increasing mass flux. It is also shown in Fig. 13 that the heat partition ratio increases with decreasing inlet quality for a given value of the ratio of the driving forces. This is explained by noting that at low inlet qualities, the wall and vapor superheats are expected to be higher due to the low actual vapor mass flux in the channel, and thus the evaporative heat flux is higher due to the high vapor-to-liquid heat transfer driving force, $(T_v - T_s)$.

The effect of mass flux is further isolated and presented in Fig. 14, for a range of inlet qualities. For a given inlet quality the heat partition ratio increases with increasing mass flux. This observation supports one of the conclusions from Fig. 13, that $(hA)_{vl}$ increases faster than $(hA)_{wv}$ with increasing mass flux. It is again evident that for a given mass flux, the heat partition ratio increases with decreasing inlet quality due to reasons explained above.

The present results are compared to those obtained by Nijhawan (1980) in a single vertical tube. Figure 15 is an illustration of the variation of vapor superheat for both the single tube and the rod bundle with the actual vapor mass flux. Symbols and solid lines are used for the Nijhawan's tube data, and dotted lines represent the present rod bundle data. It is seen that the vapor superheat decreases with increasing actual vapor mass flux for both geometries. However, the decrease for the rod bundle is slightly faster. It is also evident that for both geometries, the vapor superheat increases with increasing wall heat flux for a given actual vapor mass flux. Figure 15 also shows that for a given vapor mass flux and wall heat flux, the magnitude of the vapor superheat in the rod bundle experiments is significantly higher than that in the tube experiments. Such significant differences in superheats may be due to the differences in heated surface to volume ratios. Figure 15 indicates that, although vapor superheats are relatively high in magnitude for the rod bundle geometry, the parametric trend of the vapor superheat is consistent with that obtained for a single tube geometry. It decreases with increasing actual vapor mass flux (consequently with increasing mass flux for a given quality, or with increasing quality for a given mass flux), and increases with increasing total wall heat flux.

Figure 16 compares the heat partition ratio as a function of the ratio of the driving forces for heat transfer $(T_v - T_s)/(T_w - T_v)$, for the rod bundle and tube experiments. Figure 16 is similar to Fig. 13 with the addition of the single-tube results obtained from Nijhawan (1980). Each line represents data for given mass flux and inlet vapor quality. In spite of differences in heated surface-to-volume ratios for the two geometries, the following common conclusions can be drawn. For a given inlet quality, the slopes of the lines, corresponding to $(hA)_{vl}/(hA)_{wv}$, increase with increasing mass flux. Moreover, the slopes of the lines do not change with inlet quality. Furthermore, for the same ratio of the temperature differences, the heat partition ratio increases with decreasing inlet quality. In conclusion, Fig. 16 indicates that the behaviors obtained for the rod bundle are in agreement with that observed earlier on single tube.

Conclusions

Experimental data for post-CHF heat transfer are reported for a nine-rod bundle.

Vapor superheats up to 600°C, indicating high levels of thermodynamic nonequilibrium between phases, were measured. Such vapor superheats were found to increase with

increasing total wall heat flux and to decrease with increasing mass flux and vapor quality. The wall-to-vapor heat transfer driving force, $(T_w - T_v)$, was found to be essentially independent of vapor mass flux, total mass flux, and total wall heat flux.

Distributions of wall temperatures showed that the desuperheating effects of spacers on wall and vapor temperatures were functions of inlet quality and mass flux.

The heat partition ratio, Q_{ev}/Q_t, was found to increase with increasing mass flux. This implied an increase in the ratio $(hA)_{vl}/(hA)_{wv}$ with increasing mass flux. The heat partition ratio was also found to increase with decreasing inlet quality, due to an increase in vapor-to-liquid heat transfer driving force, $(T_v - T_s)$. Finally, the heat partition ratio appeared to be independent of the total wall heat flux.

These parametric trends for the rod bundle were found to be in good agreement with those reported for single tubes.

Acknowledgments

This research was sponsored by the US Nuclear Regulatory Commission under Contract No. NRC-04-81-183. The authors acknowledge with gratitude the continued interest, encouragement, and technical participation provided by Drs. Yih-Yun Hsu, Michael Young, Richard Lee, and Jose N. Reyes, Program Managers at USNRC, throughout the course of this work. The technical discussions with Dr. Ralph Nelson of Los Alamos National Laboratory were also very helpful to the research effort.

References

Chen, J. C., Ozkaynak, F. T., and Sundaram, R. K., 1979, "Vapor Heat Transfer in Post-CHF Region Including the Effect of Thermodynamic Nonequilibrium," *Nuclear Engineering and Design*, Vol. 51, pp. 143–155.

Evans, D. G., Webb, S. W., and Chen, J. C., 1983, "Measurement of Axially Varying Nonequilibrium in Post-Critical-Heat-Flux Boiling in a Vertical Tube," NUREG/CR-3363, TS-831-I, Vol. 1.

Forslund, R. P., and Rohsenow, W. M., 1968, "Dispersed Flow Film Boiling," ASME JOURNAL OF HEAT TRANSFER, Vol. 90, pp. 399–407.

Gottula, R. C., Nelson, R. A., Chen, J. C., Neti, S., and Sundaram, R. K., 1983, "Forced Convective Nonequilibrium Post-CHF Heat Transfer Experiments in a Vertical Tube," ASME–JSME Thermal Engineering Conference, Honolulu, Mar.

Groeneveld, D. C., and Delorme, G. G. J., 1976, "Prediction of Thermal Nonequilibrium in the Post-dryout Regime," *Nuclear Engineering and Design*, Vol. 36, pp. 17–26.

Groeneveld, D. C., and Gardiner, S. R. M., 1978, "A Method of Obtaining Flow Film Boiling Data for Subcooled Water," *International Journal of Heat and Mass Transfer*, Vol. 21, pp. 664–665.

Hochreiter, L. E., 1977, "NRC/Westinghouse/EPRI FLECHT Low Flooding Rate Skew Axial Profile Results," presented at the 5th Water Reactor Safety Information Meeting, Washington, DC.

Hynek, S. J., Rohsenow, W. M., and Bergles, A. E., 1969, "Forced Convection Dispersed Flow Film Boiling," MIT Heat Transfer Lab, Report DSR 70586-63.

Jones, O. C., and Zuber, N., 1977, "Post CHF Heat Transfer: A Non-equilibrium, Relaxation Model," presented at the 17th National Heat Transfer Conference, Salt Lake City, UT.

Loftus, M. J., Hochreiter, L. E., Conway, C. E., Rosal, E. R., and Wenzel, A. H., 1981, "Non-equilibrium Vapor Temperature Measurements in Rod Bundle and Steam Generator Two-Phase Flows," *Proceedings OECD (NEA) CSNI Third Special Meeting on Trans. Two-Phase Flow*, Pasadena, CA, CSNI Report No. 61.

Laverty, W. F., and Rohsenow, W. M., 1967, "Film Boiling of Saturated Nitrogen Flowing in a Vertical Tube," ASME JOURNAL OF HEAT TRANSFER, Vol. 89, pp. 90–98.

Mueller, R. E., 1967, "Film Boiling Heat Transfer Measurements in a Tubular Test Section," EURAEC-1871/GEAP-5423.

Nijhawan, S., 1980, "Experimental Investigation of Thermal Non-equilibrium in Post-dryout Steam-Water Flow," Dissertation, ME & Mech. Dept., Lehigh University, Bethlehem, PA.

Nijhawan, S., Chen, J. C., Sundaram, R. K., and London, E. J., 1980, "Measurements of Vapor Superheat in Post-Critical-Heat-Flux Boiling," ASME JOURNAL OF HEAT TRANSFER, Vol. 102, pp. 465–470.

Parker, J. D., and Grosh, R. J., 1962, "Heat Transfer to a Mist Flow," ANL-6291.

Plummer, D. N., Griffith, P., and Rohsenow, W. M., 1976, "Post-Critical Heat Transfer to Flowing Liquid in a Vertical Tube," 16th National Heat Transfer Conference, St. Louis, MO, Paper No. 76-CSME/CS ChE-13.

Polomik, E. E., 1967, "Transition Boiling Heat Transfer Program—Final Summary Report for Feb. 1973–Oct. 1967," GEAP-5563, Oct.

Saha, P., Shiralkar, B. S., and Dix, G. E., 1977, "A Post-dryout Heat Transfer Model Based on Actual Vapor Generating Rate in Dispersed Droplet Regime," ASME Paper No. 77-HT-80.

Tong, L. S., and Young, J. D., 1974, "A Phenomenological Transition and Film Boiling Correlations," *Proceedings of the 5th International Heat Transfer Conference*, Vol. IV, B3.9, Tokyo, Japan.

Tuzla, K., Unal, C., Badr, O., Neti, S., and Chen, J. C., 1984, "Two-Phase 3×3 Rod Bundle Test Facility for Post-Critical-Heat Flux Boiling," NUREG/CR-3869.

Unal, C., Tuzla, K., Badr, O., Neti, S., and Chen, J. C., 1985, "Application of the Hot Patch Technique for Stabilized Post-CHF Test in Rod Bundle," presented at the ASME Winter Annual Meeting, Miami, FL, Paper No. 85-WA/HT-27.

Unal, C., 1986, "An Experimental Study of Thermal Nonequilibrium Convective Boiling in Post-Critical-Heat-Flux Region in Rod Bundle," Ph.D. Thesis, Lehigh University, Bethlehem, PA.

Webb, S. W., Chen, J. C., and Sundaram, R. K., 1982, "Vapor Generation Rate in Nonequilibrium Convective Film Boiling," 7th International Heat Transfer Conference, Munich, Federal Republic of Germany.

Effects of Size of Simulated Microelectronic Chips on Boiling and Critical Heat Flux

K.-A. Park
Korea Standards Research Institute,
Taejon, Chungnam 300-31,
Korea

A. E. Bergles
Rensselaer Polytechnic Institute,
Troy, NY 12180-3590

Microelectronic chips were simulated with thin foil heaters supplied with d-c power and arranged in two vertical configurations: flush mounted on a circuit board substrate or protruding from the substrate about 1 mm. Heat transfer characteristics (midpoint) were obtained with varying height (1 mm to 80 mm) and width (2.5 mm to 70 mm) in R-113. Two types of incipient boiling temperature overshoot were observed with saturated boiling. The inception of boiling depended greatly on the location of the active boiling sites on the heater. For arrays, the inception of boiling for the top heater took place at lower superheat than for the bottom heater. Heater size had no effect on established boiling, in contrast to results reported previously in the literature. The critical heat flux for wide heaters increased with decreasing heater height, as expected. The critical heat flux also increased with decreasing width. Correlations are presented that describe these effects.

Introduction

Extreme miniaturization of electronic devices has required the development of sophisticated cooling technology because the failure of microelectronic chips increases exponentially as the junction temperature increases. Direct immersion cooling in inert, dielectric liquids offers the possibility of providing cooling for all devices in an array, reducing device temperatures, and minimizing variations in device temperatures. It is important in the development of immersion cooling systems, for both normal operation and testing of microelectronic chips, to predict the heat transfer characteristics accurately for nucleate boiling as well as critical heat flux (CHF).

Few boiling curves for small vertical heaters are available. Baker (1972, 1973) reported the heat transfer characteristics of thin film resistors, flush-mounted on a substrate, which were twice as wide as they were high: 4.6 mm × 2.3 mm, 9.8 mm × 4.9 mm, and 20 mm × 10 mm. The surfaces were placed vertically in liquid Freon-113 (R-113). A single thermocouple monitored the midpoint chip temperature. Baker's boiling curves with R-113, shown in Fig. 1, exhibit pronounced shifts in the established boiling behavior as chip size decreases. He suggested qualitatively that the increases were due to leading edge and side flow effects, a contention that has not been substantiated.

Prediction of CHF is of considerable importance for estimating the maximum power of electronic components. Pool boiling CHF has been studied extensively with experimental and analytical methods, as surveyed by Efimov (1972) and Bergles (1975). The work done on CHF is divided into hydrodynamic and nonhydrodynamic aspects. The hydrodynamic instability concept suggested by Kutateladze (1948) was analytically clarified with instability theory, for a large horizontal plate, by Zuber (1958). This theory, which has some flexibility in the form of an empirical lead constant, provides a reasonable prediction of CHF for many situations of practical interest. It was recognized shortly thereafter, however, that modifications to the theory were required for other heater configurations (Bobrovich et al., 1964). As summarized by Lienhard and Dhir (1973), significant increases of CHF are observed as the diameter of a sphere, diameter of a horizontal cylinder, or height of wide vertical ribbon is decreased.

Of particular interest to the present study is the latter situations with one face insulated. Using the hydrodynamic instability model with several empirical constants, Lienhard and Dhir (1973) proposed the following correlation of their data and those of Adams (1962):

$$\frac{q''_{chf}}{q''_{chf,z}} = 1.4/(H')^{0.25} \text{ for } H' < 6 \tag{1}$$

and

$$\frac{q''_{chf}}{q''_{chf,z}} = 0.9 \text{ for } H' > 6 \tag{2}$$

where

$$H' = H[g(\rho_f - \rho_v)/\sigma]^{0.5}$$

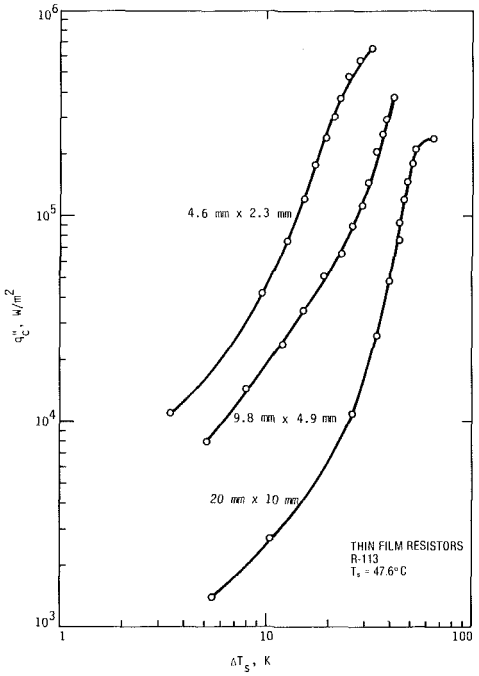

Fig. 1 Baker's boiling curves (1972)

Contributed by the Heat Transfer Division for publication in the JOURNAL OF HEAT TRANSFER. Manuscript received by the Heat Transfer Division July 18, 1986. Keywords: Boiling, Electronic Equipment, Thermal Packaging.

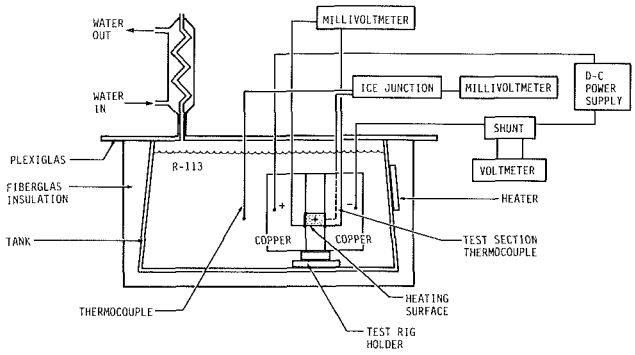

Fig. 2 Experimental apparatus

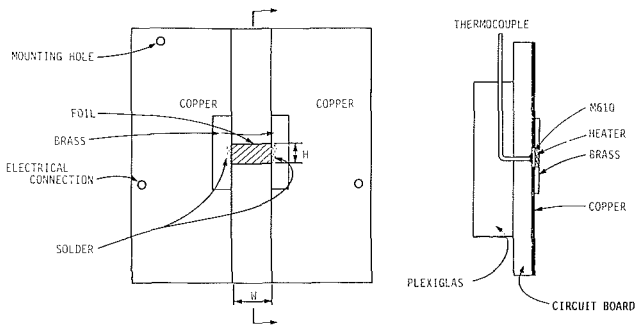

Fig. 3 Test section details

and

$$q''_{chf,z} = 0.131 h_{fg}\rho_v[\sigma(\rho_f - \rho_v)g/\rho_v^2]^{0.25}$$

which is the CHF prediction of Zuber (1958). An intrinsic variability of ±15 percent was noted for ribbon heaters in general.

Nonhydrodynamic aspects have been discussed by many investigators, e.g., Bernath (1960); Carne and Charlesworth (1966); Tachibana et al. (1967). It has been reported that CHF depends on the properties, thickness, and surface condition of the heaters as well as the type of power (Bergles, 1975). The Carne and Charlesworth (1966) study of CHF for vertical surfaces was carried out with *n*-propanol at atmospheric pressure using five different heater metals. For the tests with one face insulated, critical heat flux increased by as much as 76 percent as the product of thermal conductivity and thickness of the strips increased.

The existing data for CHF were obtained primarily from heating surfaces that were large in at least one dimension (the width). The heat dissipation area of typical microelectronic chips is very small in two dimensions (about 5 mm × 5 mm). Very few data for CHF are available for such small heat sources.

The purpose of the present study was to clarify the dependence of boiling heat transfer performance on heater size through a systematic experimental investigation. The experimental study was extended to boiling for arrays of small heaters. Of particular interest were incipient boiling, the established boiling curve, and CHF.

Experimental Apparatus and Procedure

Experimental Apparatus. The experiments were carried out with Freon-TF (R-113) in an insulated tank 273 mm × 127 mm × 152 mm high with a plexiglass cover as shown in Fig. 2. R-113 was selected because it is inexpensive and easy to handle at room temperature. Its properties are similar to those of dielectric liquids commonly used for direct immersion cooling of microelectronic components.

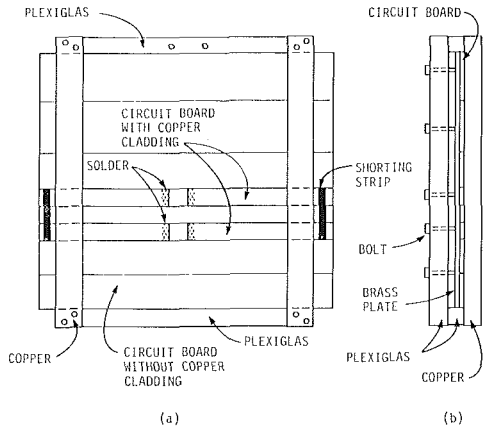

Fig. 4 Test-section assembly for multiple heaters: (*a*) front view, (*b*) view from left

A circuit board (glass epoxy G-10) clad with copper on one side was the basis of the test section, as shown in Fig. 3. The copper cladding in the center was removed by a razor blade to make room for the foil heater. Three kinds of foil were used in this study: 25.4-μm-thick steel, 10 μm-thick constantan, and 12.7-μm-thick nichrome. M610 epoxy resin (Measurements Group, Inc.) was used to bond the foil to the circuit board. The foil and copper cladding were then soldered to the 25.4-μm brass foil for the electrical connections. Direct-current power to the test section was supplied by a 50-A power supply. The surface was left in the original polished condition and cleaned with Freon-TF. Plexiglass was added on the back side of the circuit board for insulation and to guide the thermocouple wires.

A single thermocouple (36-gage copper-constantan) was placed at the back center of each foil, and the junction was electrically insulated from the heater. The midpoint of the

Nomenclature

C_p = specific heat at constant pressure
G = vertical pitch between heaters
g = gravitational acceleration
Gr_c^* = modified Grashof number at center of heater $= g\beta q''_c(H/2)^4/k\nu^2$
H = height of heater
H' = nondimensional height of the heater $= H[g(\rho_f - \rho_v)/\sigma]^{0.5}$
h = heat transfer coefficient
h_{fg} = latent heat of vaporization
I = induced-convection parameter $= (\rho_f W\sigma/\mu^2)^{0.5}$
k = thermal conductivity
Nu_c = Nusselt number at center of heater $= hH/2k$
Pr = Prandtl number $= C_p\mu/k$
q''_c = heat flux at center of heater
q''_{chf} = critical heat flux
Ra_c^* = Rayleigh number at center of heater $= \mathrm{Gr}_c^*\mathrm{Pr}$
T_b = bulk liquid temperature
T_s = saturation temperature
T_w = wall temperature
ΔT_s = wall superheat $= T_w - T_s$
W = width of test section
β = coefficient of thermal expansion
μ = dynamic viscosity of liquid
ν = kinematic viscosity of liquid
ρ_f = density of liquid
ρ_v = density of vapor
σ = surface tension

All properties were evaluated at the film temperature, $(T_w + T_b)/2$, unless otherwise noted.

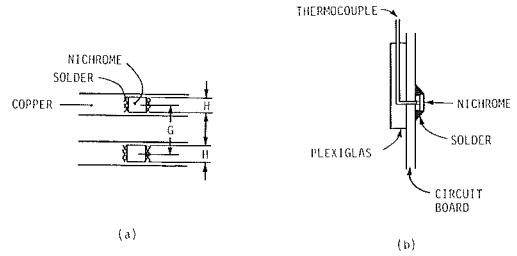

Fig. 5 (*a*) Schematic layout of in-line heaters; (*b*) protruding heater details—top view

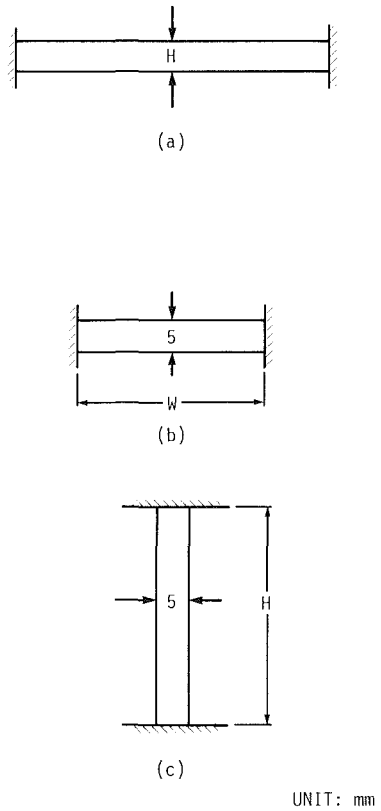

Fig. 6 Test section for variations of: (a) height, (*b*) width with fixed height, and (c) height with fixed width

heater was chosen as being representative of the thermal performance of a microelectronic chip.

The pool was thoroughly degassed prior to operation. When generating boiling curves and obtaining CHF data, the pool was maintained at saturation temperature by the tank heater and the test section. This was confirmed by a thermocouple located near the test section.

Boiling Experiment. Only nichrome foil heaters were used in the original polished condition. The main variable for the single flush heaters was the width of the heated surface (5 mm or 10 mm high and 5 mm to 60 mm wide). Array heaters (5 mm × 5 mm) were installed on strips of circuit board. These strips were then stacked on plain circuit boards and sandwiched with copper bus bars and plexiglass retainers as shown in Fig. 4. To avoid contact-resistance problems, the heaters were joined at both ends with soldered shorting strips. Arrays of in-line flush surfaces are shown in Fig. 5(*a*).

Microelectronic chips normally protrude from the substrate. To simulate this real situation, experiments were also carried out with single, protruding, simulated chips and an array of such chips. Small pieces of the bare circuit board were added to simulate the shape of the microelectronic chips as shown in Fig. 5(*b*). The chip model (4.9 mm × 5.3 mm

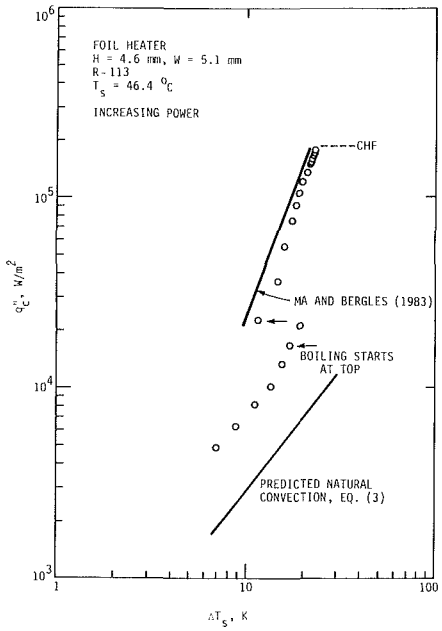

Fig. 7 Typical boiling curves

wide) was built out so that the face of the heating foil was 1.1 mm from the substrate. This is comparable to silicon thermal chips studied previously (Hwang and Moran, 1981; Oktay, 1982).

CHF Experiments. Foil heaters of the three different materials were used in these tests. The main variables for the CHF experiments were the width and height of the heaters as shown in Fig. 6. A variation in the height of the heaters from 1 to 5 mm was tested for wide test sections. The width varied from 2.5 to 70 mm for a fixed height of about 5 mm. Tall heaters with a fixed width of about 5 mm were tested with a variation of the height from 5 to 80 mm. The electrical bus connections are also indicated in Fig. 6.

The vapor formation was observed visually near CHF. Still photographs were obtained with a Canon AE-1 camera to which was attached a zoom lens 85 mm to 205 mm or a 135 mm telephoto lens with close-up rings (Nos. 1, 2, 3). The shutter speed was 1/1000 second and the aperture was about f/4. Two 100-W frosted lights from the top and two 200-W flood lights from the bottom were used. With this arrangement, good pictures were obtained with Ektachrome 160 slide film.

Each test section was used only one time to measure CHF. The power was shut off as soon as possible to prevent R-113 decomposition at high temperature after CHF occurred. After about four CHF tests were conducted with approximately one-half gallon of R-113, fresh R-113 was used.

Data Reduction. The nominal heat flux, calculated from the voltage drop across the heater and current across a calibrated shunt, was corrected for the back side heat loss and heat loss to the electrical connections. These heat loss corrections, evaluated at the midpoint of the test section, totaled about 10 to 15 percent for natural convection (5 mm × 5 mm surface) and were negligible for boiling and CHF. The main correction was heat loss to the back side. The very small temperature drop between the thermocouple junction and the outer foil surface was neglected. It was confirmed by calculation and experiment that the conduction loss through the thermocouple leads was negligible.

Experimental Results and Discussion

Pool Boiling for Single Heaters. Typical boiling curves for

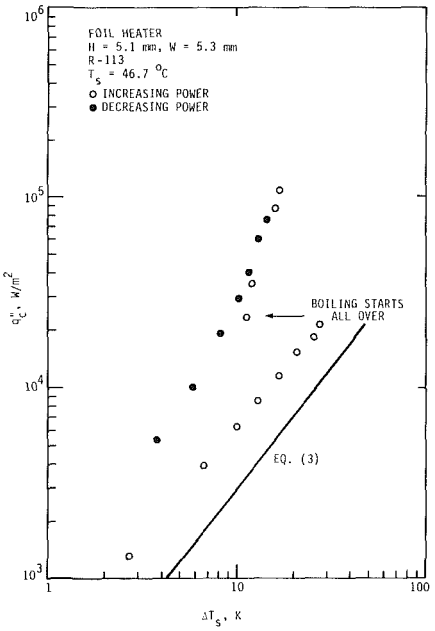

Fig. 8 Boiling data displaying large temperature overshoot

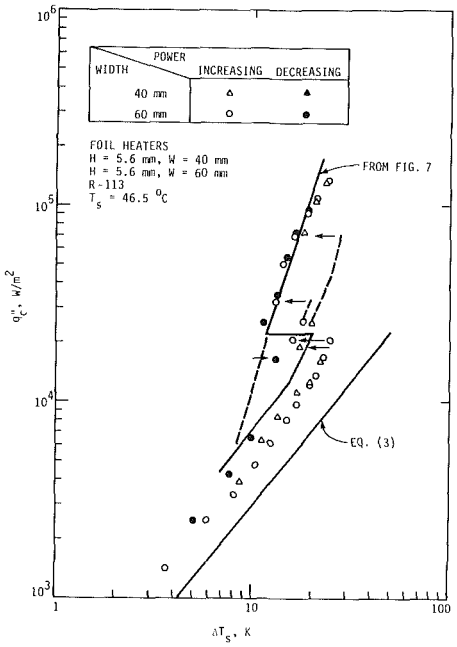

Fig. 9 Comparison of boiling curves for heaters of different width

chip-size heaters are shown in Figs. 7 and 8. The natural-convection base line is the Fujii and Fujii (1976) correlation of laminar boundary layer solutions for a vertical surface with constant heat flux

$$\mathrm{Nu}_c = \left(\frac{\mathrm{Pr}}{4+9\sqrt{\mathrm{Pr}}+10\ \mathrm{Pr}}\right)^{0.2} (\mathrm{Gr}_c^*\mathrm{Pr})^{0.2} \qquad (3)$$

The deviation of the data from predicted values is due to width and leading edge effects (Park and Bergles, 1987).

As shown in Fig. 7, the fully developed boiling curve is in good agreement with other data of the present research program. Also, the boiling curves of the present studies are in good agreement with data for fluorocarbon liquids and surface-independent correlations based on these data (Armstrong, 1966; Stephan and Abdelsalam, 1980).

A main point of interest is the thermal response at low applied heat flux. As the heat flux was increased, boiling was generally observed first at the top of the heater, and nucleation propagated from top to bottom as the heat flux was gradually increased. Then, as shown in Fig. 7, a relatively small temperature decrease (9 K) took place when boiling propagated to the location of the thermocouple junction. Sometimes the superheat was increased without early nucleation occurring at the top; then, the boiling took place suddenly over the entire heating surface with a decrease of about 19 K, as shown in Fig. 8. On other occasions, a double overshoot was observed, as shown in Fig. 9. The overshoots are characteristic of R-113 and other fluorochlorocarbons or fluorocarbons, which tend to deactivate nucleation sites when the pool is subcooled because of the near-zero contact angle. The occasional two-step overshoot could be due to irregular distribution of active boiling sites near the location of the thermocouple junction. It is speculated that the first overshoot took place when there were a few boiling sites below the location of thermocouple. The second overshoot occurred when the boling sites near the location of thermocouple finally became active. While power was decreased, sometimes the temperature increased as shown in Fig. 9. This unusual behavior was observed only a few times and was apparently due to deactivation of some nucleation sites. There is no obvious explanation why the temperature overshoots were always observed in the present study while Baker (Fig. 1) reported no such behavior.

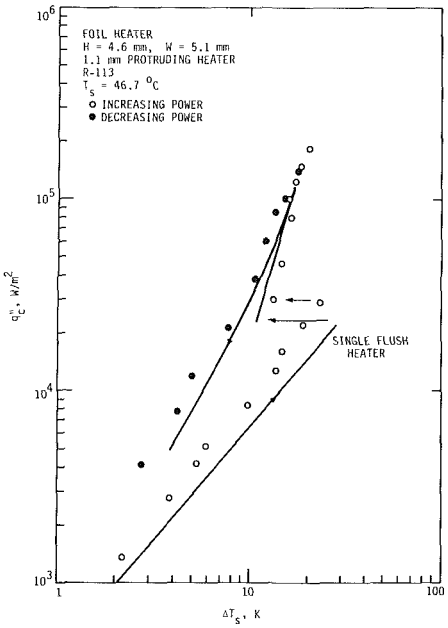

Fig. 10 Boiling data for single protruding heater compared with single flush heater

The boiling curves with wider heaters (60 mm wide × 5.6 mm high and 40 mm wide × 5.6 mm high) are presented in Fig. 9. The difference in the developed boiling curves for these two heaters is negligible, and the data are in excellent agreement with the data for the 5-mm-wide heater (Figs. 7 and 8). Similar results were obtained for a 5-mm-wide × 10-mm-high heater. This insensitivity to heater size is also contrary to the results of Baker shown in Fig. 1.

The boiling curve for the single protruding surface is in good agreement with that for the single flush surface, as shown in Fig. 10.

Pool Boiling for Array of Heaters. Boiling tests were carried out with two in-line surfaces (flush or protruding) with fixed spacing. Heat transfer characteristics for natural convection in arrays of heaters have been discussed in detail by Park

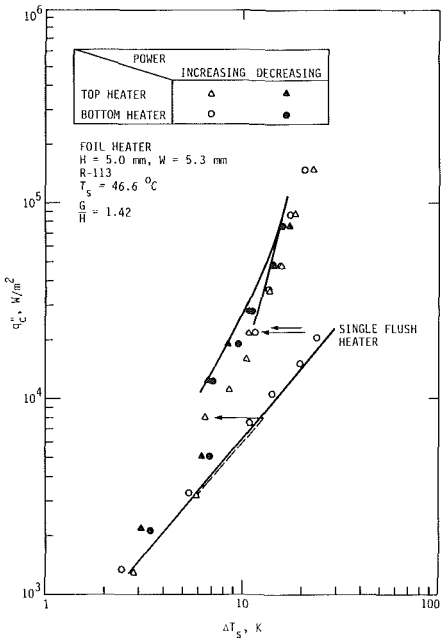

Fig. 11 Boiling data for two flush in-line heaters

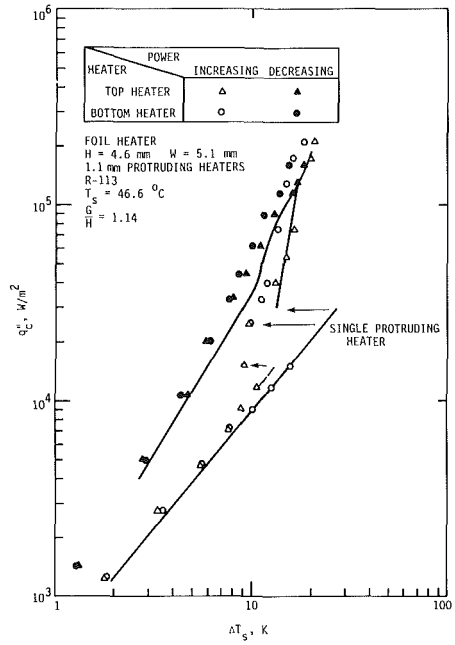

Fig. 12 Boiling data for two protruding in-line heaters

and Bergles (1987). Boiling inception occurred earlier with the top surface than with the bottom surfaces, as shown in Fig. 11 for the flush surfaces and in Fig. 12 for the protruding surfaces. Thus, the top heaters had smaller temperature overshoots than the bottom heaters. These smaller overshoots could be due to the plume from the bottom heater. The established boiling curves for either heater in an array were essentially the same for the flush and smooth surfaces.

Critical Heat Flux. The photographic observations yielded some insight into the boiling process near CHF. For the standard 5-mm-high test section, as heater width was reduced, fewer vapor columns were observed. There were four vapor columns when the width was 40 mm, two vapor columns when the width was 20 mm, and one vapor column when the width was less than 10 mm. The number of columns agreed generally

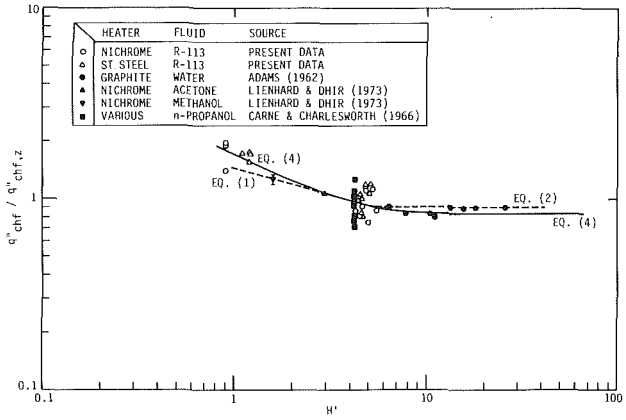

Fig. 13 Comparison between all available CHF data and correlations for the wide heaters

with the hydrodynamic model of Lienhard and Dhir except that columns were discontinuous and sometimes it was difficult to determine the number of columns. Close to CHF, large vapor masses appeared first at the top surface and then propagated toward the bottom. Nucleate boiling took place at the bottom even after the CHF condition had occurred at the top.

Carbon deposits appeared above the center on the nichrome of constantan foil test sections after the CHF was exceeded. These deposits resulted from high-temperature decomposition of the R-113. The test sections were not physically destroyed except for the 1-mm and 2-mm-high test sections. With these heaters, the wall temperature increased suddenly by more than 100 K and the foil was separated from the substrate due to deterioration of the epoxy bond. All stainless steel heaters were physically burned through.

Data for the short, but wide ($W \geq 20$ mm) heaters are plotted in Fig. 13 according to the coordinates of equation (1). Included are all of the data that seem to be available for this configuration. The present data and the data of Lienhard and Dhir (1973) exhibit the usual scatter resulting from the stochastic nature of CHF. Both studies suggest that this scatter is larger as the heater height is reduced.

The wide variation in the data of Carne and Charlesworth (1966) was attributed by these investigators to the variations in thermal conductance. By changing material and thickness, the value of kt was varied by almost three orders of magnitude and the CHF increased by nearly a factor of ten. A conduction analysis qualitatively supported this trend. According to these results, the present data as well as those of Lienhard and Dhir (1973) could reflect reduced CHF because of kt values lower than the lowest values considered by Carne and Charlesworth. However, both sets of data exhibit the expected increase in CHF ratio as H' is reduced. Furthermore, the present data do not exhibit a definitive change in CHF as kt is changed from 1.6×10^{-4} W/K (nichrome) to 10.9×10^{-4} W/K (stainless steel). Further work seems necessary to confirm whether kt really has a significant effect at low H'. It should be noted that the heaters used by Adams (1962) were relatively massive so that no complications due to thermal conductance are expected. Another potential problem is that the inflow conditions to the heaters vary from the larger substrate in the present tests to a simple insulated backing covering only the heater as apparently used in the Lienhard and Dhir tests.

In view of the uncertain effects of heater thermal conductance and test section construction, these effects were ignored and all of the data were included in a correlation. The correlation (Churchill-Usagi type (1972)) was obtained using the Statistical Analysis System (SAS) package. The Marquart nonlinear regression method was used with 10^{-4} convergence

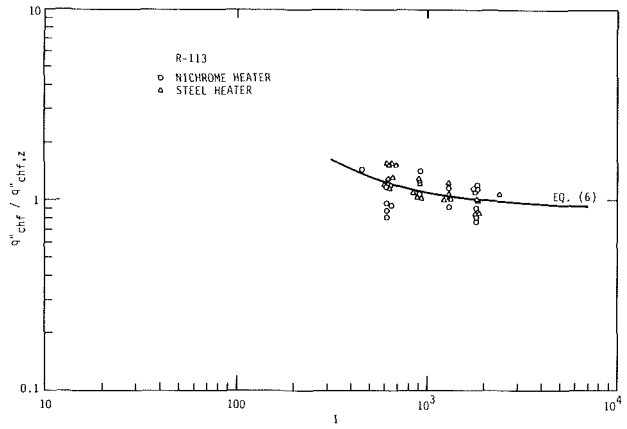

Fig. 14 Width effect for CHF for about 5 mm height

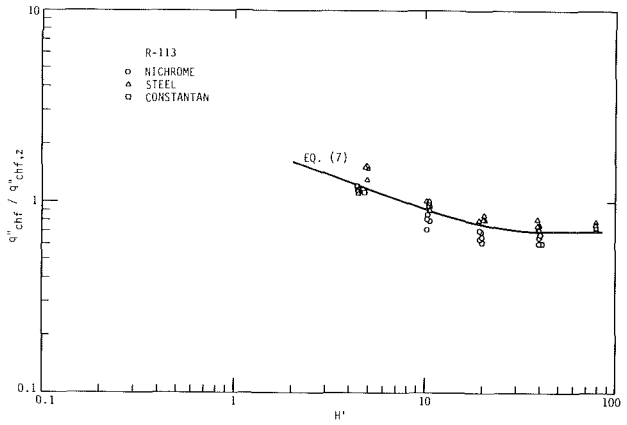

Fig. 16 Height effect for CHF for about 5 mm width

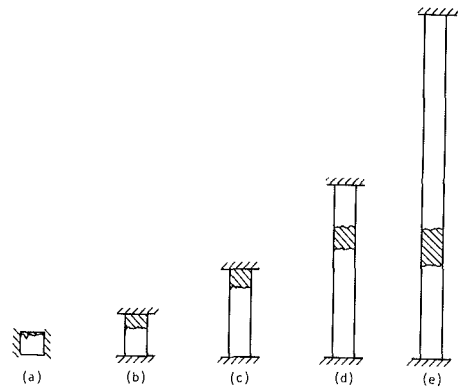

Fig. 15 Relative burnout position: (*a*) 5 mm × 5 mm high, (*b*) 5 mm × 10 mm high, (*c*) 5 mm × 20 mm high, (*d*) 5 mm × 40 mm high, and (*e*) 5 mm × 80 mm high

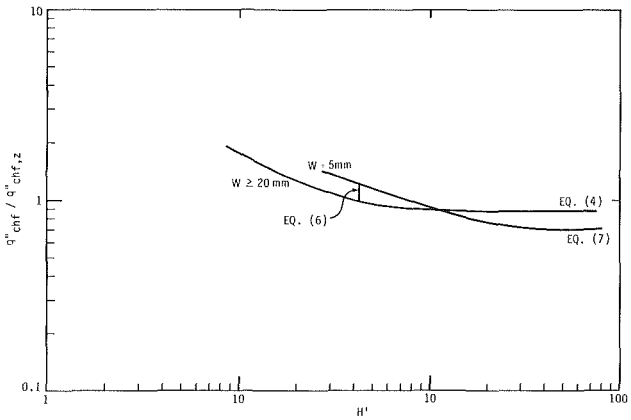

Fig. 17 Composite plot for height and width effects on CHF

criteria. The correlation of all the available data shown in Fig. 13 is

$$\frac{q''_{chf}}{q''_{chf,z}} = 0.86\left[1+\frac{152}{H'^{3.29}}\right]^{0.14} \tag{4}$$

Given the few data at large H', the difference between the present asymptote (0.86) and that of Lienhard and Dhir (0.90) is not significant. More data are also required in this region to refine the correlation.

CHF data for the 5-mm-high heaters were collected to determine the effects of variation of the width. The induced-convection parameter (Kutateladze, 1959)

$$I = (\rho_f W\sigma/\mu^2)^{0.5} \tag{5}$$

was chosen to nondimensionalize the width. CHF increased significantly as the width of the test section decreased, as shown in Fig. 14. The scatter in the data is greater than that observed with the wide heaters but again there is no particular effect of the thermal conductance. Increased randomness in the CHF process is expected as the test section size decreases because smaller heat transfer surfaces are more sensitive to local increases in nucleation site density and small imperfections in the surface, which give rise to local hot spots.

Induced flow from sides due to the Bernoulli effect is a possible reason for increasing CHF when there is only one vapor jet. Statistical methods were again used to obtain a correlation for the width effect of the heater. In equation (6) the asymptote for wide heaters (0.93) was calculated from equation (4) for the 5-mm height.

$$\frac{q''_{chf}}{q''_{chf,z}} = 0.93\left[1+\frac{52}{I^{1.02}}\right]^{3.7} \tag{6}$$

The CHF locations for the shorter 5-mm-wide test sections were at the top, but the CHF locations for the taller test sections were closer to the middle, as depicted in Fig. 15. CHF decreased as the height (5 mm width) increased, reaching an asymptotic value of approximately 0.7 $q''_{chf,z}$ as shown in Fig. 16. CHF data for the tall heater are thus about 20 percent lower than data for the wide heater. The statistical correlations for the height effect (5 mm width) is

$$\frac{q''_{chf}}{q''_{chf,z}} = 0.7\left[1+\frac{241{,}300}{H'^{4.03}}\right]^{0.087} \tag{7}$$

It is significant that the CHF occurs at approximately the same height for the two taller test sections (Fig. 15*d*, *e*). This behavior suggests a critical height for the onset of hydrodynamic instability associated with formation of the vapor jet along the heater. Although the jets for vertical ribbon heaters are assumed to be found above the heaters (Lienhard and Dhir, 1973), the present heaters are much higher than any that have been tested in the past. The present visual observations were limited so that the presence of such jets could not be confirmed. The actual CHF data (Fig. 16) then suggest that if the heater is below the critical height, a higher CHF can be tolerated (Fig. 15*a*, *b*, *c*) while if the critical height is exceeded, the CHF is reduced (Fig. 15*d*, *e*) and stays essentially constant.

The heater thermal conductance does affect these data. As shown in Fig. 16, the lower conductance nichrome data are distinctly below the stainless steel data. This is consistent with the above interpretation because an instability on the heated surface is likely to be delayed if temporary local overheating can be mitigated by conduction within the heater.

The height and width correlations for CHF are plotted in

Fig. 17. As the height and width increase, CHF decreases. For a specific size of the heater, CHF can be estimated from this figure.

Conclusions

This study has clarified a number of the unique phenomena associated with boiling on small heaters simulating microelectronic chips. While increasing power during boiling of R-113, the temperature overshoot prior to incipient boiling depends strongly on the location of the boiling sites on the heating surface, and two types of overshoot were observed. An increase in wall superheat was observed with decreasing power at low heat flux as nucleation sites were deactivated. The boiling curves for different widths agree very well and it is concluded that the size effect reported by Baker (1972) is incorrect.

In boiling from two in-line flush or protruding heaters, the inception of boiling for the top surfaces took place at lower superheat than for the bottom surfaces. There is very little difference in the established boiling behavior for the top and bottom surfaces, for either flush or protruding surfaces.

Critical heat flux data were obtained with considerable variation of the width and height for these vertical heaters with one side insulated. As the height or width become small, CHF increases. By statistical methods, nondimensionalized critical heat fluxes were correlated as a function of the nondimensionalized height and width. The maximum nucleate boiling heat flux for microelectronic chips can be estimated from the correlations.

Acknowledgments

This study was supported by IBM Corporation, Data Systems Division, Poughkeepsie, New York. The assistance of Mr. R. C. Chu and Dr. P. W. Ing of IBM is appreciated.

References

Adams, J. M., 1962, "A Study of the Critical Heat Flux in an Accelerating Pool Boiling System," Ph.D. Dissertation and Department of Mechanical Engineering Report, University of Washington, Seattle, WA.

Armstrong, R. J., 1966, "The Temperature Difference in Nucleate Boiling," *International Journal of Heat and Mass Transfer*, Vol. 9, pp. 1148–1149.

Baker, E., 1972, "Liquid Cooling of Microelectronic Devices by Free and Forced Convection," *Microelectronics and Reliability*, Vol. 11, pp. 213–222.

Baker, E., 1973, "Liquid Immersion Cooling of Small Electronic Devices," *Microelectronics and Reliability*, Vol. 12, pp. 163–193.

Bergles, A. E., 1975, "Burnout in Boiling Heat Transfer. Part 1: Pool Boiling Systems," *Nuclear Safety*, Vol. 16, No. 1, pp. 28–42.

Bernath, L., 1960, "A Theory of Local-Boiling Burnout and Its Application to Existing Data," *Chemical Engineering Progress Symposium Series*, Vol. 56, No. 30, pp. 95–116.

Bobrovich, G. I., Gogonin, I. I., and Kutateladze, S. S., 1964, "Influence of Size of Heater Surface on the Peak Boiling Heat Flux," *Journal of Applied Mechanics and Technical Physics*, No. 4, pp. 137–138.

Carne, M., and Charlesworth, D. H., 1966, "Thermal Conduction Effects on the Critical Heat Flux in Pool Boiling," *Chemical Engineering Progress Symposium Series*, Vol. 62, No. 64, pp. 24–34.

Churchill, S. W., and Usagi, R., 1972, "A General Expression for the Correlation of Rates of Transfer and Other Phenomena," *AIChE Journal*, Vol. 18, pp. 1121–1128.

Efimov, V. A., 1972, "Survey of Experimental Research on the Mechanism of the Heat Transfer Crisis During Boiling," *Heat Transfer—Soviet Research*, Vol. 4, pp. 27–38.

Fujii, T., and Fujii, M., 1976, "The Dependence of Local Nusselt Number on Prandtl Number in the Case of Free Convection Along a Vertical Surface With Uniform Heat Flux," *International Journal of Heat and Mass Transfer*, Vol. 19, pp. 121–122.

Hwang, U. P., and Moran, K. P., 1981, "Boiling Heat Transfer of Silicon Integrated Circuits Chip Mounted on a Substrate," *Heat Transfer in Electronic Equipment*, ASME HTD-Vol. 20, pp. 53–59.

Kutateladze, S. S., 1959, "Heat Transfer in Condensation and Boiling," AEC-tr-3770.

Lienhard, J. H., and Dhir, V. K., 1973, "Hydrodynamic Prediction of Peak Pool-Boiling Heat Fluxes From Finite Bodies," ASME JOURNAL OF HEAT TRANSFER, Vol. 95, pp. 152–158.

Ma, C.-F., and Bergles, A. E., 1983, "Boiling Jet Impingement Cooling of Simulated Microelectronic Chips," *Heat Transfer in Electronic Equipment*, ASME HTD-Vol. 28, pp. 3–10.

Oktay, S., 1982, "Departure From Natural Convection (DNC) in Low-Temperature Boiling Heat Transfer Encountered in Cooling Micro-electronic LSI Devices," *Heat Transfer 1982*, Proceedings of the 7th International Heat Transfer Conference, Hemisphere, Washington, DC, Vol. 4, pp. 113–118.

Park, K.-A., and Bergles, A. E., 1987, "Natural Convection Heat Transfer Characteristics of Simulated Microelectronic Chips," ASME JOURNAL OF HEAT TRANSFER, Vol. 109, pp. 90–96.

Stephan, K., and Abdelsalam, M., 1980, "Heat-Transfer Correlations for Natural Convection Boiling," *International Journal of Heat and Mass Transfer*, Vol. 23, pp. 73–87.

Tachibana, F., Akiyama, M., and Kawamura, H., 1967, "Non-hydrodynamic Aspects of Pool Boiling Burnout," *Journal of Nuclear Science and Technology*, Vol. 4, pp. 121–130.

Zuber, N., 1958, "On the Stability of Boiling Heat Transfer," *Transactions of ASME*, Vol. 80, pp. 711–720.

Stability of Single-Phase Natural Circulation With Inverted U-Tube Steam Generators

J. Sanders
Commission of the European Communities,
Joint Research Centre,
Thermodynamics Division,
LOBI Project,
Ispra, Italy

For natural circulation it is shown that parallel flow in the tubes of an inverted U-tube steam generator can be, at certain power levels, unstable. A mathematical model, based on one-dimensional Oberbeck–Boussinesq equations, shows that stability can be attained if in some tubes the water flows backward, opposite to the normal flow direction. The results are compared to measurements obtained from the natural circulation test A2-77A in the LOBI-MOD2 integral system test facility.

1 Introduction

Natural circulation in a pressurized water reactor (PWR) cooling system affects the transport of decay heat from the core to the steam generators when the main coolant pumps are stopped. A usual assumption for calculation of single-phase natural circulation is that the same flow exists in all **U**-tubes of the steam generator. It will be shown that this situation can be unstable for a range of decay heat power levels. Instead, stability can be attained when flow is parallel in most of the **U**-tubes, while in some other tubes flow is directed backward, returning from the tube outlet to the inlet plenum.

The phenomenon was observed in the LOBI-MOD2 thermohydraulic integral system test facility (a scaled model of a PWR system) during the natural circulation test A2-77A. De Santi et al. (1986) have shown that in one of the instrumented **U**-tubes fluid temperatures were measured identical to the secondary side temperature, indicating that no hot fluid was entering this tube, i.e., flow is either stalled or reverse. That flow is actually reverse can be experimentally deduced from the pressure difference of the inlet to outlet plenums and from the tube inlet plenum temperature, which results from mixing hot leg fluid from the core with colder water returning through other tubes in the steam generator. In an earlier natural circulation experiment at the Semiscale facility, nonuniform flow distribution between **U**-tubes also was observed. The data showed that in a repetition of the test the distribution of the flow regimes among tubes changed (Loomis and Soda, 1982), indicating a phenomenon of flow instability.

A physical explanation for the instability can be derived from the fluid temperature distribution within a **U**-tube, leading to a buoyancy force in the flow direction. This buoyancy can, for natural circulation, exceed friction and creates a pressure increase over the steam generator; i.e. the pressure in the outlet plenum is higher than in the inlet plenum. This can drive flow in some tubes in the reverse direction.

In the first part of this study a mathematical model for natural circulation flow is developed. This shows the conditions for which parallel flow in all **U**-tubes is an unstable solution of the equations. In the next part, the stability of flow is investigated for the case in which water flows backward in some of the tubes. The results of the calculations are then compared with measurements from the LOBI experiment.

2 Mathematical Model of the PWR Circuit

Natural circulation flow in a PWR primary circuit is driven by density differences in the cooling water. The (decay) heat, supplied by the fuel rods, heats the coolant (water), bringing it to a lower density. This causes the water to rise from the pressure vessel into the steam generator **U**-tubes, where the heat is removed by the secondary circuit. A simplified schematic of the circuit is shown in Fig. 1.

Density-driven flow can be mathematically described by the Oberbeck–Boussinesq equations. In these equations the fluid is assumed to have a uniform density; density differences are recognized only in those terms that drive the motion. A discussion of the equations is given by Joseph (1976). Here it will be sufficient to consider only one-dimensional flow. The following assumptions are made to derive the flow equations:

1 Density differences are considered only in the gravity body force term.

2 Density changes are induced by changes of temperature (T) and not by pressure (p).

3 The equation of state for the density $\rho = \rho(T)$ is linearized relative to secondary temperature (T_s) and the density at that temperature (ρ_o)

$$\rho(T) = \rho_o(1 - \alpha(T - T_s)) \tag{1}$$

where

$$\alpha = -\left(\frac{1}{\rho}\frac{\partial \rho(T, p)}{\partial T}\right)\Big|_{T_s}$$

4 Heat conduction in the liquid is neglected since heat transport is effected by convection in the water and conduction in the tube walls.

5 Temperature changes along the flow path are not considered for friction or heat transfer coefficients.

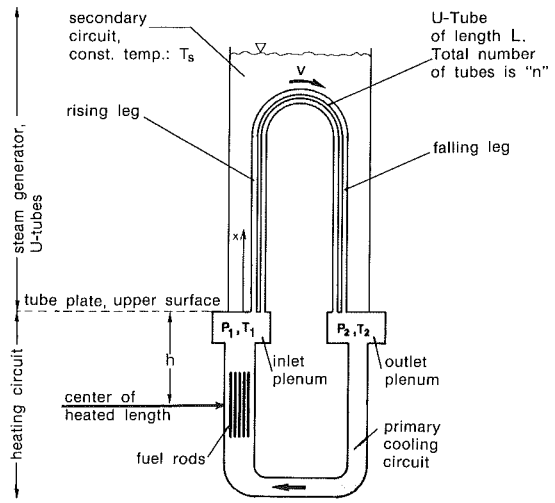

Fig. 1 Simplified schematic of PWR cooling circuit to identify principal variables used in the calculation

Contributed by the Heat Transfer Division for publication in the JOURNAL OF HEAT TRANSFER. Manuscript received by the Heat Transfer Division December 10, 1986. Keywords: Boiling, Multiphase Flows.

6 The flow is sufficiently slow to neglect heat generated by friction.

Flow in U-tubes. A direct consequence of the above assumptions is that the velocity v is constant over the length of a U-tube. Here the flow shall be assumed to be directed in the normal direction of circulation flow. The equations for momentum and energy are:

$$\rho_o \frac{dv}{dt} = -\frac{\partial p}{\partial x} (\mp)\rho_o(1-\alpha(T-T_s))g - \frac{\xi}{D}\frac{\rho_o}{2}v^2 \tag{2}$$

and

$$\frac{\partial T}{\partial t} + v\frac{\partial T}{\partial x} = -\lambda(T-T_s) \tag{3}$$

The coordinate x is in the normal flow direction, as indicated in Fig. 1, and D is the inner diameter of the U-tubes. For the influence of gravity (g) the negative sign in equation (2) stands for the rising leg and the "+" sign for the falling leg of the tube. The radius of the upper bend is small and not explicitly considered. Friction is characterized by a velocity-dependent friction coefficient $\xi = \xi(v)$, which contains a contribution for the tube inlet and outlet pressure loss. The influence of momentum, resulting from flow in the plenums and from mixing of parallel tubes with different velocities is neglected because, due to the large cross-sectional area, flow in the plenums is very slow (at LOBI about six times slower than within the U-tubes). The coefficient $\lambda = \lambda(v)$ in the energy equation (3) describes the heat transfer through the tube wall into the water and is discussed in the Appendix.

Steady-state temperature and pressure in the U-tubes are calculated with the inlet conditions p_1 and T_1. The temperature along the tube of length L, $0 \le x \le L$, is solved from equation (3)

$$T(x) = T_s + (T_1 - T_s)e^{-\frac{\lambda}{v}x} \tag{4}$$

This allows us to calculate the pressure, which is for the rising leg, $0 \le x \le \le L/2$,

$$p(x) = p_1 - \rho_o g x + \frac{\rho_o g\alpha}{\lambda} v(T_1 - T_s)\left[1 - e^{-\frac{\lambda}{v}x}\right] - \frac{\xi}{D}\frac{\rho_o}{2}v^2 x \tag{5}$$

and for the falling leg, $\frac{L}{2} \le x \le L$,

$$p(x) = p_1 + \rho_o g(x-L) + \frac{\rho_o g\alpha}{\lambda} v(T_1 - T_s)\left[1 - 2e^{-\frac{\lambda}{v}\frac{L}{2}} + e^{-\frac{\lambda}{v}x}\right] - \frac{\xi}{D}\frac{\rho_o}{2}v^2 x \tag{6}$$

The pressure difference over the tube (p_2 = outlet pressure) is

$$p_2 - p_1 = \frac{\rho_o g\alpha}{\lambda} v(T_1 - T_s)\left(1 - e^{-\frac{\lambda L}{2v}}\right)^2 - \frac{\xi L}{D}\frac{\rho_o}{2}v^2 \tag{7}$$

and the outlet temperature $T_2 = T(L)$ is

$$T_2 = T_s + (T_1 - T_s)e^{-\frac{\lambda}{v}L} \tag{8}$$

Flow in the Heating Circuit. The "heating circuit" shall comprise the whole primary circuit, modeled as one circuit only, excluding the U-tubes. The goal of the following calculations is to represent the tube inlet temperature as a function of tube flow velocity v, and the velocity v as a function of core heating power W. The tube inlet pressure p_1 is a boundary condition, imposed by the pressurizer.

For the model, the core bundle heats the coolant at the geometric center of the heated length, height h below the inlet of the U-tubes. Only steady state is modeled because the transient terms are not used in the following derivation. With a core mass flow $\dot{m}$ and the specific heat capacity of water c_p we have

$$W = c_p \dot{m}(T_1 - T_2) \tag{9}$$

The flow is again density driven

Nomenclature

A = cross-sectional flow area in the U-tube
c_p = specific heat capacity of water in the primary circuit
D = inner diameter of U-tube
f = dimensional friction coefficient for heating circuit (see equation (10))
F = friction coefficient for total primary circuit (see equation (15))
g = gravity
h = distance between center of core heat input and upper surface of tube plate, see Fig. 1
L = length of U-tube (average)
$\dot{m}$ = mass flow in primary circuit (core mass flow)
n = number of U-tubes
p = pressure
p_1 = pressure at steam generator inlet (primary)
p_2 = pressure at steam generator outlet (primary)
$\tilde{p}$ = disturbance pressure (see equation (16))
P = average perimeter of U-tube
T = temperature
T_s = temperature of secondary side
T_1 = hot leg temperature (core exit)
$\tilde{T}$ = disturbance temperature (see equation (16))
u = velocity of flow in U-tubes, reverse direction
v = velocity of flow in U-tubes, forward direction
$\tilde{v}$ = disturbance velocity (see equation (16))
W = core heating power
x = position in U-tube (see Fig. 1)
z = $\lambda L/2v$
α = coefficient of thermal expansion
α_i = inner heat transfer coefficient at U-tube surface
α_o = outer heat transfer coefficient at U-tube surface
δ = U-tube wall thickness
λ = ratio of U-tube wall heat transfer to heat capacity of water

$$= \frac{P}{A}\frac{1}{\rho_o c_p}\frac{1}{\frac{1}{\alpha_i} + \frac{\delta}{\lambda_{\text{wall}}} + \frac{1}{\alpha_o}}$$

λ_{wall} = heat conduction coefficient of U-tube
ξ = friction coefficient in U-tube
ρ = density of water
ρ_o = density at primary loop pressure and secondary side temperature
σ = stability coefficient (stable: $\sigma < 0$; unstable: $\sigma > 0$)
ϕ = fraction of tubes with flow in forward direction

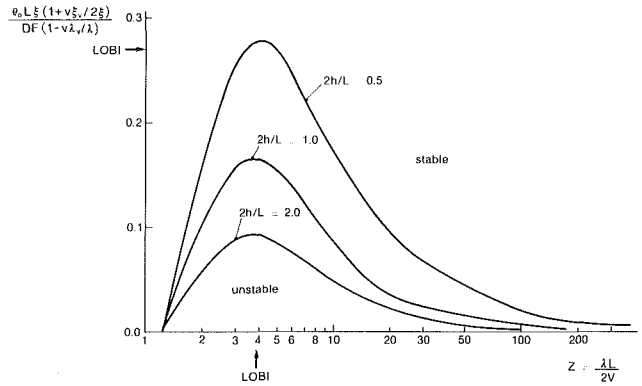

Fig. 2 Conditions for criticality and zones of stability for parallel flow in U-tubes (equation (23)). Values indicated for LOBI are calculated for the boundary conditions of Test A2-77A: $W = 143$ kW, $p = 14.0$ MPa, $T_s = 299.7°C$, and $2h/L = 1.0$.

$$p_1 - p_2 = (\rho(T_2) - \rho(T_1))gh - f\dot{m}^2 \tag{10}$$

The overall friction coefficient (f) for the heating circuit can be measured from experiments. It is not dimensionless. Using equation (1) for the density we can write

$$p_1 - p_2 = \frac{\alpha \rho_o W g h}{c_p \dot{m}} - f\dot{m}^2 \tag{11}$$

Mass flow ($\dot{m}$) is related to tube flow velocity (v), tube cross-sectional flow area (A), and the total number of tubes (n) by

$$\dot{m} = nA\rho_o v \tag{12}$$

Combining equations (7), (8), (9), (11), and (12) to calculate the total energy input as function of tube velocity, $W = W(v)$, and the tube inlet temperature T_1;

$$W = \frac{c_p nAFv^3}{\alpha g\left[h + \frac{v}{\lambda}\tanh\left(\frac{\lambda L}{4v}\right)\right]} \tag{13}$$

$$T_1 - T_s = \frac{Fv^2}{\alpha g \rho_o \left(1 - e^{-\frac{\lambda L}{v}}\right)\left[h + \frac{v}{\lambda}\tanh\left(\frac{\lambda L}{4v}\right)\right]} \tag{14}$$

The overall friction coefficient F was introduced for easier notation

$$F = f(nA\rho_o)^2 + \xi \frac{L}{D}\frac{\rho_o}{2} \tag{15}$$

These equations describe the solution of the equations when the velocity in all tubes is the same. The total energy input W leads to a unique velocity v in the tubes and circulation mass flow. An increased total energy input leads to an increased velocity.

2.1 Stability of Parallel Flow in U-Tubes. To study stability, a small disturbance of the basic solution is considered. Linearizing the differential flow equations (equations (2) and (3)) for disturbances of the basic solution leads to an exponential time dependence. The disturbed solution is therefore:

$$\begin{aligned} &\text{velocity} && = v + \tilde{v}e^{\sigma t} \\ &\text{pressure} && = p + \tilde{p}e^{\sigma t} \\ &\text{temperature} && = T + \tilde{T}e^{\sigma t} \end{aligned} \tag{16}$$

The sign of σ in the disturbance terms controls stability. The linearized momentum and energy equations (2) and (3) are

$$\sigma\rho_o\tilde{v} = -\frac{d\tilde{p}}{dx}(\pm)\rho_o g\alpha\tilde{T} - \frac{\xi}{D}\rho_o v\tilde{v} - \frac{d\xi}{dv}\frac{\rho_o}{2D}v^2\tilde{v} \tag{17}$$

and

$$\sigma\tilde{T} + v\frac{d\tilde{T}}{dx} + \tilde{v}\frac{dT}{dx} = -\lambda\tilde{T} - \frac{d\lambda}{dv}(T - T_s)\tilde{v} \tag{18}$$

With $\tilde{T}_1 \equiv \tilde{T}(x=0)$, the temperature disturbance becomes

$$\tilde{T} = \tilde{T}_1 e^{-\frac{\sigma+\lambda}{v}x} + \tilde{v}\frac{1}{\sigma}\left(\frac{\lambda}{v} - \lambda_v\right)(T_1 - T_s)\left[e^{-\frac{\lambda}{v}x} - e^{-\frac{\sigma+\lambda}{v}x}\right] \tag{19}$$

Integrating pressure along the **U**-tube, with $\tilde{p}_1 = \tilde{p}(0)$, we have at the tube outlet

$$\tilde{p}(L) = \tilde{p}_1 + \rho_o\tilde{v}\left(-\sigma L - \frac{\left(\xi + \frac{v}{2}\xi_v\right)}{D}vL + \frac{g\alpha}{\sigma}\left(\frac{\lambda}{v} - \lambda_v\right)\right.$$

$$\left.(T_1 - T_S)\left[\frac{v}{\lambda}\left(1 - e^{-\frac{\lambda L}{2v}}\right)^2 - \frac{v}{\sigma+\lambda}\left(1 - e^{-\frac{(\sigma+\lambda)L}{2v}}\right)^2\right]\right)$$

$$+ \rho_o g\alpha\frac{v}{\sigma+\lambda}\left(1 - e^{-\frac{(\sigma+\lambda)L}{2v}}\right)^2\tilde{T}_1 \tag{20}$$

Now, instability is found by dropping the assumption of parallel flow in all tubes; i.e., tubes with different flow velocity are allowed to exist simultaneously.

Looking at two tubes, which shall be called "tube A" and "tube B," the pressure at the tube exit ($x = L$) must be the same for both, i.e., $\tilde{p}_A(L) = \tilde{p}_B(L)$. This is also true for pressure and temperature at the inlet ($x = 0$). To find a nonzero solution we must have $\tilde{v}_A \neq \tilde{v}_B$ and the coefficient of $\tilde{v}$ in equation (20) must be zero, i.e.,

$$-\sigma L - \frac{\xi + \frac{v}{2}\xi_v}{D}vL + \frac{g\alpha}{\sigma}\left(\frac{\lambda}{v} - \lambda_v\right)(T_1 - T_s)$$

$$\left[\frac{v}{\lambda}\left(1 - e^{-\frac{\lambda L}{2v}}\right)^2 - \frac{v}{\sigma+\lambda}\left(1 - e^{-\frac{(\sigma+\lambda)L}{2v}}\right)^2\right] = 0 \tag{21}$$

The eigenvalue σ can be directly calculated for a given flow. Flow is stable for $\sigma < 0$ and unstable for $\sigma > 0$. Criticality (change of stability) is given for $\sigma = 0$. From equation (21) we have

$$\frac{(\xi + v\xi_v/2)vL}{D} + \frac{g\alpha}{\lambda}(1 - v\lambda_v/\lambda)(1 - e^{-z})(2ze^{-z} - 1 + e^{-z})(T_1 - T_s) = 0 \tag{22}$$

with $z = \lambda L/2v$. Substituting for the temperature with equation (14) it follows

$$\frac{\rho_o L(\xi + v\xi_v/2)}{\mathrm{DF}(1 - v\lambda_v/\lambda)} = \frac{1 - e^{-z}(1+2z)}{\frac{2h}{L}z(1 + e^{-z}) + 1 - e^{-z}} \tag{23}$$

Zones of stability are easily calculated from equation (21). Criticality and zones of stability are shown in Fig. 2.

This result shows that stability of parallel flow depends on the height of the steam generators and the ratio of friction in **U**-tubes to friction in the whole circuit. A steam generator positioned high above the core and little friction in the circuit lead to stability. Low steam generators and high friction in the circuit lead to instability. For a reactor plant, with given friction coefficients and given elevation of the steam generator,

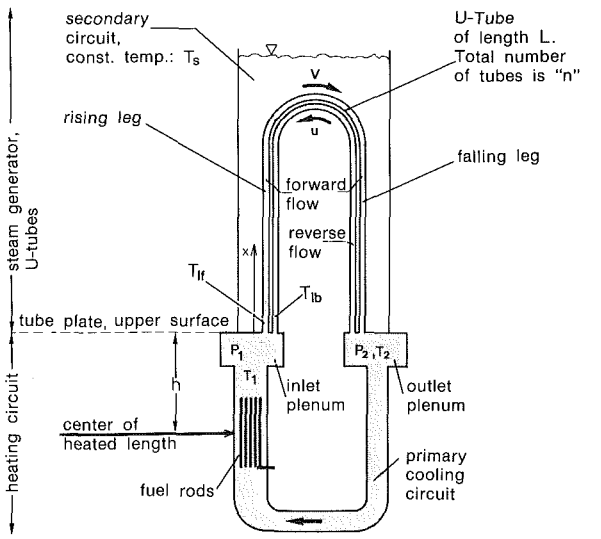

Fig. 3 Schematic with reserve flow; the fraction of tubes with forward flow is ϕ

whether flow is stable or not depends on the heat input W. The heat input W is related to the velocity v, which is used in equation (23), by equation (13).

Remark: At criticality it follows from equation (11) that

$$P_2 > P_1 \text{ when } \left| \frac{1 - v\lambda_v/\lambda}{1 + v\xi_v/2\xi} \right| < 2.$$

The latter condition holds for the usual flow models. It also follows from equation (7) that

$$\frac{\partial p_2(v, T_1)}{\partial v} = 0.$$

A physical explanation for the instability follows from the density difference of liquid in the rising and falling legs of the **U**-tubes, caused by the different temperatures. This drives the flow within the tubes leading to a pressure increase in the normal flow direction, so that $P_2 > P_1$. This also explains the growth of a disturbance of slightly higher velocity in one of the tubes: Higher velocity leads by convection to warmer liquid in the rising leg of this tube, a higher density difference between rising and falling leg, and increased gravity-driven acceleration in this tube. This could cause even faster flow, and thus lead to instability, when the increment in acceleration supersedes the increment in friction. The effect is reduced by an improved heat transfer coefficient at higher velocity.

The same mechanism explains that parallel tubes with two different velocities may solve the equations. Different velocities in two **U**-tubes can lead to the same pressure increase over these tubes by different balances of gravity and friction forces. These solutions cross the parallel flow solutions at criticality. Whether they are stable or not remains to be studied, for example using the methods shown by Ioss and Joseph (1980). Probably, they are all unstable, indicating subcritical bifurcation.

A different situation can occur as consequence of the instability, when some tubes have flow in the reverse direction. Such tubes would have practically no heat exchange with the secondary side. Their flow is driven by the higher pressure in the outlet plenum. Reverse flowing tubes would lead to stability because: (1) The tube inlet temperature of the forward flowing tubes is reduced, due to mixing of reversed and hot leg flows in the inlet plenum, and causes less-gravity driven acceleration, and (2) the increased velocity in forward flowing tubes will eventually lead to a dominance of friction forces. The calculation for stability for the case of reverse flow in some tubes is shown in the next chapter, with the main result in equation (33).

A third possible flow pattern would be to have stalled flow in some tubes. This would require that in forward-flowing tubes the velocity is sufficiently high to balance acceleration forces with friction, so that $P_2 = P_1$.

2.2 Stability With Reverse Flow in Some U-Tubes. Flow in the negative direction for some of the **U**-tubes is possible when the pressure at the tube outlet is higher than at the inlet ($P_2 > P_1$). This is the case when parallel flow in the tubes becomes unstable.

The calculation performed for stability for the case that some tubes have reverse flow is similar to the parallel flow case. First, the flow equations are solved for steady-state flow, considering that a fraction of the tubes has reverse flow. For the tubes with forward flow, the inlet temperature results from mixing the water heated in the core with the cooled water coming from the tubes with reverse flow. The instability is again found for the tubes with forward flow. Equations (21) and (22) hold with the correct tube inlet temperature replacing T_1. We introduce the following notations, as shown also in Fig. 3:

- ϕ = fraction of tubes with flow in forward direction ($(1-\phi)$ is the fraction of tubes with reverse flow)
- v = velocity in tubes with forward flow
- u = velocity in tubes with reverse flow
- T_1 = hot leg temperature (= temperature of water heated in the core)
- T_{1f} = inlet temperature in tubes with forward flow (mixing temperature of hot leg flow (T_1) and cooled water from tubes with reverse flow (T_{1b}).
- T_{1b} = temperature of water in tubes with reverse flow when it has returned to the inlet plenum.

Mixing of water in the inlet plenum relates for the mass flow through the core, m, and the mixing temperature T_{1f} to conditions in the tubes,

$$\dot{m} = [\phi v - (1-\phi)u] n \rho_o A \tag{24}$$

$$\phi v T_{1f} = [\phi v - (1-\phi)u] T_1 + (1-\phi) u T_{1b} \tag{25}$$

The temperatures at the outlets of the respective **U**-tubes are calculated as before

$$T_2 = T_s + (T_{1f} - T_s) e^{-\frac{\lambda(v)L}{v}} \tag{26}$$

$$T_{1b} = T_s + (T_2 - T_s) e^{-\frac{\lambda(u)L}{u}} \tag{27}$$

and the pressure increase is

$$p_2 - p_1 = \frac{\rho_o g \alpha}{\lambda(v)} v (T_{1f} - T_s) \left(1 - e^{-\frac{\lambda(v)L}{2v}}\right)^2 - \frac{\xi(v)L}{D} \frac{\rho_o}{2} v^2 \tag{28}$$

Combining (9), (11), and (24)–(28) leads to the calculation of the heating power and inlet (mixing) temperature T_{1f} as a function of the velocities

$$W = \frac{c_p \dot{m}\left(f\dot{m}^2 + \dfrac{\xi(v)L}{D}\dfrac{\rho_0 v^2}{2}\right)}{g\alpha\rho_o\left[h + \dfrac{v}{\lambda(v)}\dfrac{(\phi v-(1-\phi)u)\left(1-e^{-\frac{\lambda(v)L}{2v}}\right)^2}{\phi v\left(1-e^{-\frac{\lambda(v)L}{v}}\right)+(1-\phi)ue^{-\frac{\lambda(v)L}{v}}\left(1-e^{-\frac{\lambda(u)L}{u}}\right)}\right]} \tag{29}$$

$$T_{1f}-T_s = \frac{(\phi v-(1-\phi)u)\left(f\dot{m}^2 + \dfrac{\xi(v)L}{D}\dfrac{\rho_o}{2}v^2\right)}{h\alpha\rho_o g\left[\phi v\left(1-e^{-\frac{\lambda(v)L}{v}}\right)+(1-\phi)ue^{-\frac{\lambda(v)L}{v}}e^{-\frac{\lambda(u)L}{u}}+\dfrac{v}{h\lambda(v)}(\phi v-(1-\phi)u)\left(1-e^{-\frac{\lambda(v)L}{2v}}\right)^2\right]} \tag{30}$$

These equations are of the same form as (13) and (14), except that they depend, for a given ϕ, on the two velocities u and v. The two velocities are related to each other by the pressure drop over the tube. For backward flow

$$p_2-p_1 = -\frac{\rho_o g\alpha}{\lambda(u)}u(T_2-T_s)\left(1-e^{-\frac{\lambda(u)L}{2u}}\right)^2 + \xi(u)\frac{L}{D}\frac{\rho_o}{2}u^2 \tag{31}$$

With equations (26) and (28) this leads to

$$\frac{\rho_o g\alpha}{\lambda(v)}(T_{1f}-T_s)\left[v\left(1-e^{-\frac{\lambda(v)L}{2v}}\right)^2 + ue^{-\frac{\lambda(v)L}{v}}\left(1-e^{-\frac{\lambda(u)L}{2u}}\right)^2\right] - \xi(v)\frac{L}{D}\frac{\rho_o}{2}v^2 - \xi(u)\frac{L}{D}\frac{\rho_o}{2}u^2 = 0 \tag{32}$$

where $(T_{1f}-T_s)$ can be introduced from equation (30).

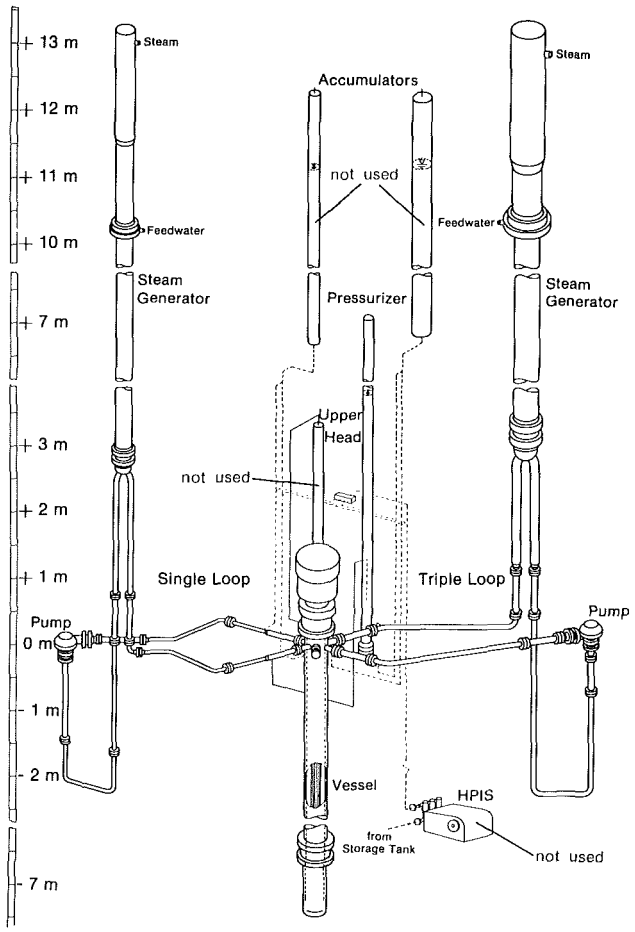

Fig. 4 LOBI-MOD2 primary system configuration for test A2-77A

Solving equation (32), it is possible to calculate the velocities u and v for any given heating power W in equation (29) (solved numerically).

The instability for this solution is again found from a disturbance of the flow in the tubes with forward direction; i.e., by equations (21) and (22) with "T_{1f}" instead of of "T_1" and $T_{1f}-T_s$ calculated from equation (30). For criticality $(z=\lambda(v)L/2v)$,

$$\frac{(\xi+v\xi_v/2)vL}{D} + \frac{g\alpha(1-v\lambda_v/\lambda)}{\lambda(v)}(1-e^{-z})(2ze^{-z} - 1+e^{-z})(T_{1f}-T_s) = 0 \tag{33}$$

Solving simultaneously equations (32) and (33), we find the fraction of tubes with forward flow yielding criticality at a given heating power.

The result indicates a set of possible reverse flow conditions. Stable reverse flow is only possible if the number of tubes with forward flow does not exceed a maximum value. It can be possible that even less than the maximum number of tubes have forward flow. This could be caused by some larger disturbance or the history of the experiment. Since the pressure increase from tubes with forward flow drives reverse flow in other tubes, it is not possible that all tubes have flow in reverse. The situation of stalled tubes would be a limiting case.

3 Comparison With Experimental Results

Reverse or stagnant flow in steam generator U-tubes was observed in the natural circulation experiment, Test A2-77A, at the LOBI-MOD2 integral system PWR test facility. The following chapters first describe briefly the facility and the test. Then the measurements are described, which lead to the interpretation of the phenomenon. At the end measurements are compared to the calculations.

3.1 The LOBI-MOD2 Experimental Facility.[1] The LOBI-MOD2 facility, see Fig. 4, is a scaled model of a nuclear pressurized water reactor cooling system. The reference reactor is of the KWU type, with 1300 MW. It is similar to plants built by Westinghouse, Framatome, etc. The facility is scaled 1:712 in volume and 1:1 for elevations, to conserve gravity influence during natural circulation. The nuclear fuel of the reference plant is simulated by 64 directly heated electrical heater rods with a fixed axial heating profile similar to the nuclear profile. Heating power can be continuously controlled up to 5.3 MW (1:1 power to volume scaling).

The test facility has two loops. The "triple loop" represents three of the four reactor loops and has three times the volume

[1]The LOBI test facility is operated at the Joint Research Centre (JRC), Ispra, of the Commission of the European Communities (CEC). It serves PWR thermohydraulic safety studies of the EC member countries for computer code validation and experimental investigations of system behavior. In addition the data contribute to the OECD-CSNI Code Validation Matrix (CCVM) and International Standard Problem (ISP) exercises. A description of the LOBI facility and the test program is given by Ohlmer et al. (1985) and Riebold (1985).

of the "single loop." Both loops have active components as steam generators and centrifugal pumps. The two steam generators have 8 and 24 U-tubes, respectively, of about the same shape as in the reactor plant (Addabbo et al., 1984). The main coolant pumps were not used for the natural circulation test. Pump rotors were in locked condition and no seal water was injected into the circuit. The primary loop volume for this test was 0.522 m^3 (not counting the pressurizer) containing about 370 kg of water at 14.0 MPa pressure.

Measurements. Over 700 measurement channels are instilled in the facility to record the thermohydraulic events during a test. Relevant for the following analysis are:

(*a*) Differential pressure from inlet to outlet plenums of the steam generators ($p_2 - p_1$).

(*b*) About 60 temperature measurements in each steam generator for secondary fluid in downcomer and riser, primary fluid in U-tubes, and on the outer tube surface. U-tube temperature measurements are installed in the longest tube in each of the steam generators. The first and last thermocouple within the U-tube flow path are positioned 50 mm (single loop) and 55 mm (triple loop) above the tube plate.

(*c*) Mass flow (fluid velocity) is measured in both loops by full flow turbometers, which are mounted at the steam generator and the pump entrances.

(*d*) General measurements such as pressures of primary and secondary sides, temperatures, heating power, etc.

3.2 Test Conditions at Single-Phase Natural Circulation. Single-phase natural circulation was part of the LOBI-MOD2 Test A2-77A on natural circulation. The experimental data and a description of the test boundary conditions are given by Sanders and Ohlmer (1985). A first analysis of the test is given by De Santi and Leva (1985).

The loop was brought to steady-state natural circulation conditions allowing sufficient time to stabilize prior to the measurement. Secondary conditions were set constant: (1) by the relief valve pressure at 8.65 MPa, leading to a secondary loop temperature of ~300°C, and (2) feedwater level control. Primary pressure was set to 14.0 MPa by use of the pressurizer (pressurizer temperature = 336°C) and core heating power (minus heat losses) was set at 143 kW, about 2.8 percent of the nominal value.

Following the measurement at single-phase subcooled natural circulation, which is considered here, the test continued with measurements at lower primary inventory, leading to single-phase saturated and two-phase natural circulation, and reflux condenser mode. The nonuniform steady flow distribution studied here ceased at the onset of two-phase circulation.

3.3 Measurements and Interpretation of Flow. Fluid temperatures were measured in one U-tube with forward flow and one tube with reverse flow. These two tubes are not in the same steam generator, so that each of them needs a separate interpretation. The measured values and measurement positions are indicated in Fig. 5.

The tube with reverse flow in the single loop steam generator produced fluid temperatures very close to those of the secondary side, even 50 mm behind the tube inlet. The possibility of forward flow with heated water entering the tube must therefore be excluded. An indication that flow is reverse could be inferred from the measurement of differential pressure; pressure at the tube outlet (P_2) is higher than at the inlet (P_1). Due to the measurement uncertainty of the instrument used, however, a zero pressure difference, and therefore stalled flow, cannot be excluded. A measured positive mass flow in the single loop shows that in other tubes of that steam generator flow must have been in the normal forward direction.

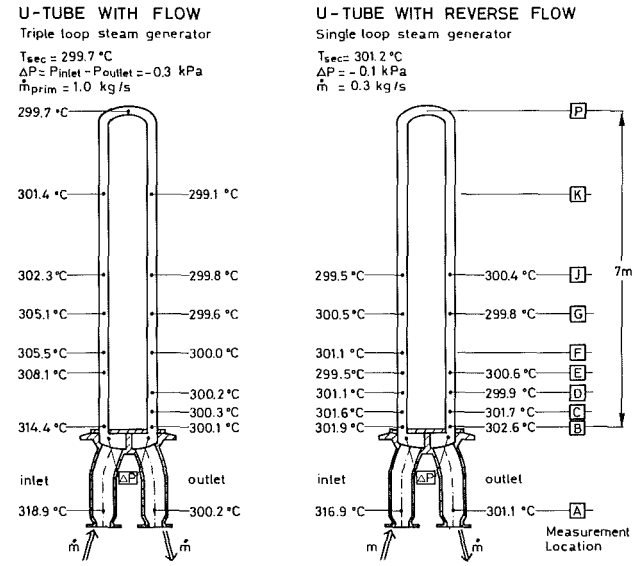

Fig. 5 Measured temperature distribution in steam generator U-tubes during single-phase, subcooled natural circulation: primary loop pressure = 14.0 MPa; secondary loop pressure = 8.6 MPa

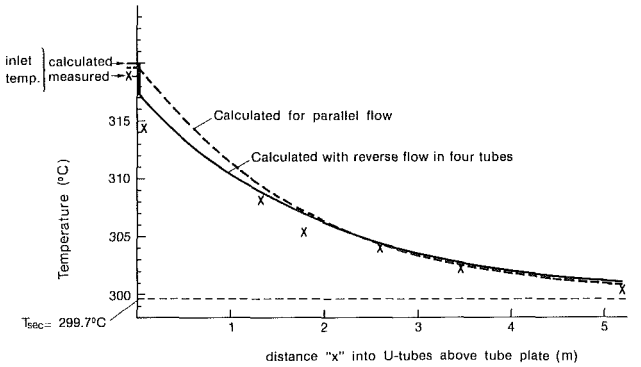

Fig. 6 Comparison of calculated and measured temperatures in the instrumented tube with flow in the normal direction:
x = measured temperature (see Fig. 5)
—— = calculated temperature when flow is backwards in four tubes (ϕ = 87.5 percent)
----- = calculated temperature for solution with all tubes having forward flow (ϕ = 100 percent)

The tube with forward flow in the triple loop steam geneator shows a sharp drop of fluid temperature from the hot leg to the tube inlet, also shown in Fig. 6. This drop in temperature supports the conclusion that other tubes in that steam generator had reverse flow mixing with the hot leg flow. Also this steam generator shows a pressure increase from the inlet to the outlet plenum which could drive the reverse flow. (Heat conduction from the inlet to the outlet plenum is less than 0.6 kW and also local heat losses are not sufficient to explain the temperature drop. They are neglected for the analysis.)

All measurements shown were taken with the standard instrumentation of the LOBI integral system test facility. Since the effect of reverse flow had not been expected, no additional instrumentation was installed specifically to monitor this effect. For all measurements the uncertainty bands must be considered for interpretation. Further conclusions than the above do not seem possible, as would be an attempt to calculate the exact number of tubes with reverse flow from the limited temperature and differential pressure data provided. The measurement uncertainties indicated in Table 1 are taken from the experimental data report (Sanders and Ohlmer, 1985). Favorable conditions (steady single-phase flow at low velocities) and good instrument performances (consistency

Table 1 Measured data during natural circulation at LOBI-MOD2 test A2-77A and calculated values for the case of four U-tubes with reverse flow and no tube with reverse flow

	Measured data (TL = triple loop; SL = single loop)	Calculated values	
		Four tubes with reverse flow, $\phi = 28/32$	parallel flow
Pressure difference $p_1 - p_2$	-0.3 ± 1.1 kPa (TL) -0.1 ± 1.1 kPa (SL)	-0.385 kPa	-0.57 kPa
Loop mass flow $\dot{m}$	~1.29 kg/s (0.99 kg/s-TL, 0.3 kg/s-SL)	1.23 kg/s	1.25 kg/s
Hot leg temperature T_1	318.9 ± 1.0°C (TL) 316.9 ± 1.0°C (SL)	320.1°C	319.8°C
Tube inlet temperature T_{1f}	~315°C (TL)	317.1°C	319.8°C
Temperature drop at tube inlet $T_1 - T_{1f}$	~3.9 K (TL)	3.0 K	0.0 K
Velocity of forward flow v	---	0.236 m/s	0.179 m/s
λ/v	~0.47 1/m	0.50 1/m	0.550 1/m
Velocity of reverse flow	---	0.244 m/s	---
$\frac{\xi\rho L(1+v\xi_v/2\xi)}{DF(1-v\lambda_v/\lambda)}$	---	---	0.275

checks) should lead to smaller uncertainty bands for the differential pressures.

It seems to be a coincidence that temperatures for both types of flow were measured in the experiment, since only 2 of the 32 tubes are instrumented. However, in a repeat measurement at different secondary pressure, forward and reverse flow were measured in the same two tubes as before. A similar experiment performed at the Semiscale facility showed that in repeat measurements reverse flow occurred not always in the same tubes, reported by Loomis and Soda (1982).

3.4 Comparison of Measured Data With Theory. The theory predicts a mechanism that would lead to the reverse flow observed in the experiment; however, it does not predict instability of parallel flow, as indicated in Fig. 2. A parameter that greatly influences the stability behavior of the model is the velocity dependence of the heat transfer coefficient $\lambda_v = d\lambda/dv$. Instability would be clearly indicated if constant heat transfer and friction coefficients were assumed, as for parallel flow $\xi\rho_o L/DF = 0.11$. In this case the stability of flow would only be possible for a maximum number of tubes with forwarded flow of $\phi = 92.5$ percent, calculated using equation (33). Parameters used for the calculations are listed in the Appendix.

Measured values are compared to calculated results for a case of parallel flow and a case where four tubes have reverse flow (one in the single and three in the triple-loop steam generator). The calculated temperature distribution in a tube with forward flow is compared to measurements in Fig. 6.

The reverse flow case better fits the data, showing a temperature drop at the tube inlet and, due to higher velocity v, matching the temperature decay along the length of the tube (given by λ/v in equation (26)). Some results of the calculations are shown in Table 1. Both, calculations and measurements, show a pressure increase over the tubes, $P_2 > P_1$.

The comparison of experimental and calculated data can lead to the conclusion that a flow pattern with reverse flow describes the measurements. Due to measurement uncertainties and the simple calculation model it is not possible, however, to draw further conclusions as to the exact number of tubes affected in the experiment.

Limits of the calculation model regarding effects that could influence the instability include simple models for friction and heat transfer, different friction in U-tubes of different length (the calculation assumes an average length for all tubes), the influence of the position of different U-tubes within the plenums, mixing in the plenums of flow coming from neighboring tubes with different velocity, the representation of two loops as one, and lack of geometric details in the heating circuit and the distribution of its heat losses.

4 Conclusions

The theory shows that parallel flow in steam generator U-tubes for natural circulation can be unstable and that stability can be attained if flow in some tubes is in reverse direction. For the conditions of single phase natural circulation at LOBI-MOD2 test A2-77A the theory does not predict that instability must have necessarily occurred; however, the mechanism is believed to have caused the reverse flow that was observed. The most important physical parameter for reverse flow is the pressure increase in the normal flow direction, $P_2 > P_1$.

Improvements in the calculation model could be made by better representation of the circuit geometry, and for friction and heat transfer coefficients. Experimentally the phenomenon could be better studied in a facility with simpler geometry, easier boundary conditions (e.g., one loop), and dedicated instrumentation. In an experiment designed to observe the effect, the influence of varying geometric and thermal parameters could be studied, also to observe the onset of instability. Theoretically interesting would be the stability of bifurcating solutions, possibly related problems of stability with tubes of different velocities in forward direction, and the case when more than the minimum number of tubes required for stability have reverse flow.

Whether for a real-sized pressurized water reactor, the instability of parallel flow occurs, depends mainly on the exact value of the overall friction coefficient F. Direct consequences for reactor safety should not be derived from the phenomenon. It could serve as a test case for computer models (reactor safety codes) for describing tube-to-tube flow variations and flow instability behavior. Different types of tube-to-tube variations of flow also occur in the more complicated case of two-phase natural circulations, as reported by Calia and Griffith (1982), De Santi and Leva (1985), and De Santi et al. (1986).

References

Addabbo, C., *et al.*, 1984, "Adequacy of LOBI-MOD2 U-Tube Steam Generators for Simulating NPP-SG Transient Behaviour," presented at the NEA/CSNI-UNIPEDE Specialist Meeting on Steam Generator Problems, Stockholm.

Becker, E., 1974, "Technische Stroemungslehre," Teubner Studienbuecher, Mechanik.

Calia, C., and Griffith, P., 1982, "Modes of Circulation in an Inverted U-Tube Array With Condensation," ASME JOURNAL HEAT TRANSFER, Vol. 104, pp. 769–773.

De Santi, G. F., and Leva, G., 1985, "Quick Look Report on LOBI-MOD2 Test A2-77A," Communication No. 4024, JRC Ispra, Italy.

De Santi, G. F., Piplies, L., and Sanders, J., 1986, "Mass Flow Instabilities in LOBI Steam Generator U-Tubes Array Under Natural Circulation Conditions," *Proceedings of Second International Topical Meeting on Nuclear Power Plant Thermal Hydraulics and Operations*, Tokyo, pp. 2-158 to 2-165.

Dubbel, 1981, *Taschenbuch für den Maschinenbau*, Vol. 14, Springer, Berlin.

Ioss, G., and Joseph, D. D., 1980, *Elementary Stability and Bifurcation Theory*, Undergraduate Texts in Mathematics, Springer.

Joseph, D. D., 1976, *Stability of Fluid Motion II*, Springer Tracts in Natural Philosophy, Vol. 28.

Loomis, G. G., and Soda, K., 1982, "Results of Semiscale MOD-2A Natural Circulation Experiments," NUREG/CR-2335, EGG-2200.

Ohlmer, E., et al., 1985, "The LOBI-MOD2 Integral System Test Facility," *Proceedings of Specialists Meeting on Small Break LOCA Analyses in LWRs*, Vol. 1, Pisa, Italy, pp. 455–469.

Riebold, W. L., 1985, "LOBI-MOD2 Programme, Status and Plans," *Proceedings of Specialists Meeting on Small Break LOCA Analyses in LWRs*, Vol. 1, Pisa, Italy, pp. 685–699.

Sanders, J., and Ohlmer, E., 1985, "Experimental Data Report on LOBI-MOD2 Test A2-77A (Natural Circulation)," Communication No. 4024, JRC Ispra, Italy.

Sanders, J., 1986, "Heat Loss Tests for the LOBI-MOD2 Facility," EUR 6539 EN, JRC Ispra, Italy.

Worth, B., and Staedtke, H., 1985, "RELAP5 Base Input Data for LOBI-MOD2," Communication No. 4030, JRC Ispra, Italy.

APPENDIX

Measurement Data, Fluid Properties, and Loop Parameters at the LOBI Natural Circulation Test A2-77A

The calculations model a circuit with only one loop. Strictly, this would be correct only for the PWR case where, due to the large number of tubes, symmetry can be assumed. For the LOBI calculations, average parameters were taken for both loops when measurements had slight differences between them. A complete set of measured data is documented in the experimental data report (Sanders and Ohlmer, 1985). Note: "TL" = triple loop, "SL" = single loop.

Measured Data

Secondary loop temperature	$T_s = 299.7°C$ (TL $\approx 299.7 \pm 1.0°C$, SL $\approx 301.2 \pm 1.0°C$)
primary loop pressure	$p_o = 14.0$ MPa
pressure difference over steam generators	$p_2 - p_1 = -0.3 \pm 1.1$ kPa (TL) $p_2 - P_1 = -0.1 \pm 1.1$ kPa (SL)
total loop mass flow	$\dot{m} = 1.29$ kg/s (TL ≈ 0.99 kg/s, SL ≈ 0.30 kg/s)
heater rod power	$W = 143$ kW

The measured heater rod power was 183 kW. Of this value 40 kW was subtracted for heat losses in the primary loop, based on the loop heat loss measurements (Sanders, 1986).

Fluid Properties at 14.0 MPa and 300°C

Density	$\rho_o = 724$ kg/m^3
dynamic viscosity	$\eta = 88 \times 10^{-6}$ kg/sm
coefficient for thermal expansion	$\alpha = 0.0032 \frac{1}{K}$
specific heat	$c_p = 5.7$ kJ/kg K
Prandtl number	Pr = 0.88
heat conduction coefficient	$\lambda_{water} = 0.56$ W/mK
gravity	$g = 9.81$ m/s^2

Loop Geometry

Length of U-tubes	$L = 14$ m (approx.)
inner tube diameter	$D = 0.0196$ m
height of steam generator upper surface of tube plate to center of core heated length	$h = 7.0$ m
flow area	$A = \pi D^2/4$
tube thickness	$\delta = 0.0012$ m
mean tube perimeter	$P = \pi(D + \delta)$
heat conduction coefficient in tube wall	$\lambda_{wall} = 16.3$ W/mK

Friction in U-Tubes: $\xi(v)$. The friction coefficient ξ is defined in equations (2) and (7). ξ shall be divided for smooth pipe friction ξ_{SP} and inlet/outlet friction ξ_{IO}, such that $\xi = \xi_{SP} + \xi_{IO}$. For the given Reynolds numbers ($Re = vD\rho/\eta$) ξ_{SP} can be calculated by Blasius' Law (for example (Becker, 1974), p. 107):

$$\xi_{SP} = 0.316\,Re^{-1/4}, \quad \text{for } 5 \times 10^3 \le Re \le 10^5$$

The coefficient for inlet/outlet friction is small and is taken from a computer model of the facility (Worth and Staedtke, 1985), $\xi_{IO} = 0.0052$. For given fluid conditions we obtain

$$\xi(v) = 0.0158 v^{-1/4} + 0.00252$$

with v in m/s (valid for 0.03 m/s $\le v \le$ 0.6 m/s).

Friction of the Heating Circuit f. The heating circuit shall be all of the primary circuit, excluding the steam generators. The friction coefficient f is taken from measurements at the circuit for the measured mass flow and heating power, using equation (11)

$$f = \frac{1}{\dot{m}^2}(p_2 - p_1 + \alpha\rho_o W g h/c_p m) = 2400\,\frac{1}{\text{mkg}}$$

Using a measured coefficient was preferred over a calculated one because of the complexity of the circuit.

Heat Transfer in U-Tubes: $\lambda(v)$. The coefficient λ, as introduced in equation (3), defines the ratio of heat transfer to the fluid heat capacity. It is calculated by

$$\lambda = \frac{P}{A}\,\frac{1}{\rho c_p}\,\frac{1}{\frac{1}{\alpha_i} + \frac{\delta}{\lambda_{wall}} + \frac{1}{\alpha_o}}$$

α_i and α_o are the heat transfer coefficients on the inner and outer tube walls. α_i is calculated by the formula of Kraussold (Dubbel, 1981, p. 245)

$$\alpha_i = 0.032\frac{\lambda_{water}}{D} Re^{0.8} Pr^{0.37} \left(\frac{2D}{L}\right)^{0.054}$$

For heat transfer on the secondary side an average value was taken, $\alpha_o = 30{,}000$ W/m^{2}K. The resulting coefficient λ is

$$\lambda = \frac{0.4907 v^{0.8}}{v^{0.8} + 1.005}\,\frac{1}{\text{s}} \quad (v \text{ in m/s})$$

Gas-Concentration Measurements and Analysis for Gas-Loaded Thermosyphons

P. F. Peterson
Assoc. Mem. ASME

C. L. Tien
A. Martin Berlin Professor.
Fellow ASME

Department of Mechanical Engineering,
University of California,
Berkeley, CA 94720

Using a miniature wet-bulb/dry-bulb probe, detailed measurements of noncondensable-gas-concentration profiles were made in a gas-loaded two-phase reflux thermosyphon to investigate the effects of orientation and gas/vapor molecular weight combinations. Natural convection and radial diffusion were found to have a large influence on the noncondensable-gas distribution, even when the gas and vapor molecular weights are equal. An axisymmetric two-dimensional diffusion model is presented to allow evaluation of the relative effects of natural convection versus diffusion. Gas recirculation, axial stratification, regions of unstable flow, and their effects on performance are discussed.

Introduction

With proper design, adding noncondensable gases to variable-conductance thermosyphons and heat pipes can help to maintain a constant evaporator temperature over a wide range of power levels by effectively and completely blocking off a varying portion of the condenser. Natural convection, axial diffusion, radial diffusion, instabilities, and other effects control the distribution of the noncondensable gas. The primary effect of natural convection is to stratify the gas and vapor axially inside the condenser. The axial stratification results from gas convection down one side of the condenser due to buoyancy forces. The gas diffuses across the stratified region into the vapor, which carries the gas back, causing gas recirculation.

The gas distribution in the condenser, along with axial conduction along the condenser wall, determines the heat transfer performance of the thermosyphon or heat pipe. Experimental evidence presented here suggests that the effects of radial diffusion and natural convection are important. These effects, however, are commonly neglected in design applications, which use one-dimensional diffusion models such as the one developed by Edwards and Marcus (1972). This model underpredicts their experimental shut-off lengths by up to two pipe diameters. Subsequent numerical investigation by Rohani and Tien (1973) suggested that the two-dimensional effect of radial diffusion could explain the increased shut-off length. Recently, Hijikata et al. (1984) established a relatively simple axisymmetric diffusion model. Kelleher (1976) recognized the potential for natural convection. The temperature profiles he measured on the surfaces of vertical and horizontal heat pipes using gas–vapor combinations with widely different molecular weights indicated that axial stratification and instabilities do occur, with the effects becoming more pronounced for larger pipe diameters. Galaktionov and Trukhanova (1985) also observed axial stratification when measuring temperatures and velocities in a rectangular water–air heat pipe with adiabatic quartz side walls.

The potential pitfalls in neglecting natural convection are perhaps greatest for space systems that are ground tested. Eninger et al. (1976) reported ground and space test results for a horizontal 1.0 cm i-d helium–methanol heat pipe. During gound testing the heat pipe experienced "heat leaks" at low power levels, causing evaporator temperatures lower than predicted with a one-dimensional model, a phenomenon consistent with stratification occurring due to natural convection. The data received during space flight could only be correlated when a gas inventory reduction of 2–10 percent was assumed, which is consistent with removal of natural convection.

Given the concern over the validity of the one and two-dimensional diffusion models and the potential for three-dimensional natural convection and instabilities, experimental measurements in the condenser vapor space were needed. Thus in this work a miniature wet-bulb/dry-bulb probe, developed earlier (Peterson and Tien, 1987), was used to make detailed measurements of noncondensable-gas-concentration profiles in a gas-loaded reflux thermosyphon. The rapid response of the miniature wet bulb to gas-concentration changes allows observation of instabilities and transient phenomena. The experimental results are compared to an axisymmetric two-dimensional diffusion model which allows evaluation of the relative effects of natural convection and diffusion. Natural convection and radial diffusion are shown to be important for most applications and help explain previously observed deviations from the one-dimensional model.

Diffusion Model

To assess the relative importance of natural convection, the experimental results are compared to an axisymmetric two-dimensional diffusion model, which predicts noncondensable gas distributions in the absence of gas recirculation. The model is based on work by Hijikata et al. (1984). Since the gas and vapor molecular weights studied here are often widely different, their assumption of constant mass density is not justified. Instead the molar density is assumed constant. Since the noncondensable gas in the shutoff region is at the cooling-water temperature, the gas inventory is calculated based on this temperature rather than the pure-vapor saturation temperature. Additional assumptions include constant heat transfer coefficient, h_w, between the wall and cooling medium, with the condensate film resistance neglected; steady-state diffusion, such that the noncondensable gas remains stationary; no axial conduction along the condenser wall; and negligible energy transport due to vapor-temperature gradients.

Application of Fick's law of diffusion to the gas-molar-flow vector $\dot{\mathbf{c}}_g$ yields

$$\dot{\mathbf{c}}_g = cx_g\mathbf{V} - cD\nabla x_g \tag{1}$$

where $\mathbf{V}$ is the average-molar-velocity vector, x_g the gas mole fraction, c the molar density, and D the mass diffusivity. If the gas is assumed to remain stationary, $\dot{\mathbf{c}}_g = 0$ and equation (1) becomes

$$\mathbf{V} = D\nabla(\ln x_g) \tag{2}$$

Contributed by the Heat Transfer Division and presented at the ASME Winter Annual Meeting. Boston, Massachusetts, December 14–18, 1987. Manuscript received by the Heat Transfer Division July 27, 1987. Keywords: Heat Pipes and Thermosyphons, Mass Transfer, Measurement Techniques.

Table 1 Thermosyphon design details

Pipe:	Material: pyrex glass
	Inside diameter: 41.3 mm
	Wall thickness: 4.76 mm
	Overall length: 1.19 m
	Condenser length: 0.63 m
	Evaporator length: 0.50 m
	Adiabatic section length: 0.06 m
Probe:	Rod material: stainless steel
	Rod diameter: 6.4 mm
	Wet bulb material: urethane foam
	Wet bulb diameter: 1.5 mm
	Thermocouple mateirals: copper/constantan
	Thermocouple diameter: 0.08 mm

For steady state and constant molar density, $\nabla \cdot \mathbf{V} = 0$, there follows

$$\nabla^2(\ln x_g) = 0 \tag{3}$$

The associated boundary conditions are

$$\text{at } z = 0 : v = 0 \text{ or } \partial(\ln x_g)/\partial z = 0 \tag{4}$$

$$\text{at } z = \infty : x_g = 0 \tag{5}$$

$$\text{at } r = 0 : u = 0 \text{ or } \partial(\ln x_g)/\partial r = 0 \tag{6}$$

$$\text{at } r = r_i : x_g = 1 - \exp(T_*(1 - T_s/T_i)) \tag{7}$$

$$M_v c D \partial(\ln x_g)/\partial r = h_w(T_i - T_c)/h_{fg} \tag{8}$$

where T_s is the saturation temperature of the pure vapor, T_i the interface temperature, T_c the cooling-medium temperature, M_v the vapor molecular weight, h_w the wall heat transfer coefficient, h_{fg} the latent heat of evaporation, r the radial coordinate, and z the axial coordinate measured from the top of the condenser. Equation (7) follows from application of the Clausius-Clapeyron equation with $T_* = (1 - T_s/T_c)^{-1} \ln(P_c/P_s)$, where P_c and P_s are the saturation pressures at T_c and T_s, respectively. Equation (8) is an energy balance. The amount of noncondensable gas in the heat pipe is

$$N_g = \int_0^\infty \int_0^{r_i} c_g 2\pi r \, dr \, dz \tag{9}$$

Dividing by $c\pi r_i^2$, it becomes

$$0.5 \, L_g = \int_0^\infty \int_0^{r_i} x_g(r/r_i) d(r/r_i) dz \tag{10}$$

where L_g is the length the gas would occupy if all the gas were restricted to the top of the condenser.

Nondimensionalization and solution of the above equations is performed in the same manner as that of Hijikata et al. (1984). The solutions were calculated for a condenser of length $(z/r_i)_{\max} = 10$. Because the gas concentration only varies in the area near the diffusion region, the solution for the shorter condenser is used for the experiment's longer condenser by adjusting the location of the gas front with the coordinate transformation

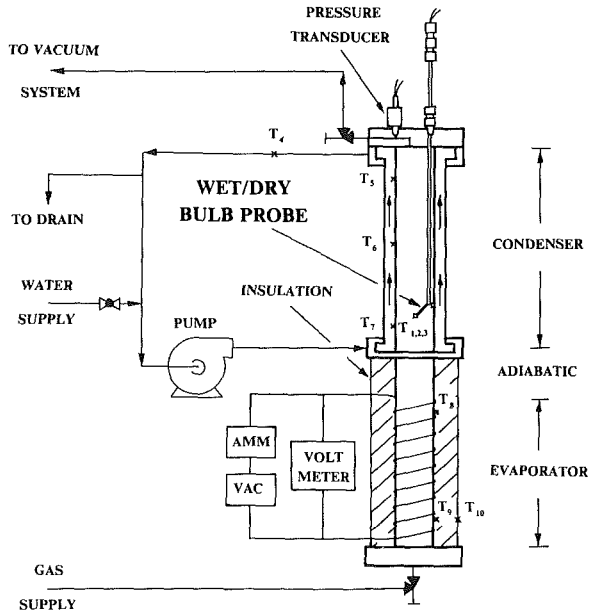

Fig. 1 Schematic of experimental apparatus

$$z_{\text{actual}} = z_{\text{calc}} + (L_{g,\text{actual}} - L_{g,\text{calc}})/x_{g,\max} \tag{11}$$

This method greatly simplified the calculation by decreasing the number of nodes and eliminating the need to iterate to find the proper value of L_g.

Experiment Description

The experimental apparatus consists of a glass thermosyphon, capped at both ends and mounted on a frame that can be positioned at any angle between vertical and horizontal (Fig. 1, Table 1). The evaporator section is heated by nichrome wire with a variable power supply. The condenser section is cooled by the circulation of water through a narrow annulus between the condenser and a glass jacket pipe. The evaporator and adiabatic sections are insulated with 8 cm of glass fiber around the circumference and 1.3-cm-thick acrylic plugs at the ends. Two-hundred-mesh stainless-steel screen is wrapped against the inside wall of the evaporator section to insure uniform wetting. Thermocouples are provided to measure the bottom, middle, and top condenser and evaporator outside wall temperatures and the cooling-water outlet temperature. The system pressure is measured with an absolute mercury manometer.

The wet-bulb/dry-bulb probe is mounted at the end of a stainless-steel tube. A fine-gage thermocouple is threaded through the 1.5-mm-dia. wet-bulb sphere. Another fine-gage thermocouple located 2.0 mm from the bulb measures the dry-bulb temperature and a third is pressed against the inside of the condenser to measure the wall temperature. The probe

Nomenclature

c = molar density, kmol/m^3
D = mass diffusivity, m^2/s
h_w = heat transfer coefficient, W/m^{2}K
h_{fg} = latent heat of vaporization, J/kg
L_g = gas inventory length, m
M = molecular weight, kg/kmol
N_g = mole inventory of noncondensable gas, kmol
P = saturation pressure, Pa
r = radial coordinate, m
Ra = Rayleigh number
T = absolute temperature, K
T^* = const $= (1 - T_s/T_c)^{-1} \ln (P_c/P_s)$
u = radial molar velocity, m/s
v = axial molar velocity, m/s
$\mathbf{V}$ = average molar velocity vector, m/s
x = mole fraction
z = axial coordinate, m
μ = viscosity, Ns/m^2
ρ = mass density, kg/m^3

Subscripts

c = cooling medium
e = evaporator
g = noncondensable gas
i = interface between vapor and wall/liquid
s = pure-vapor saturation
v = vapor

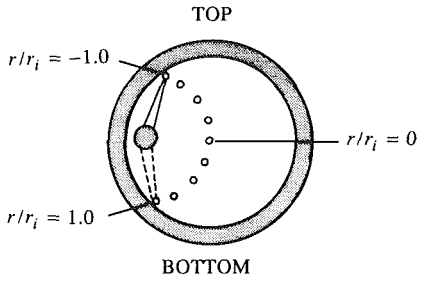

Fig. 2 Cross section, to scale, of condenser showing radial wet-bulb measurement positions

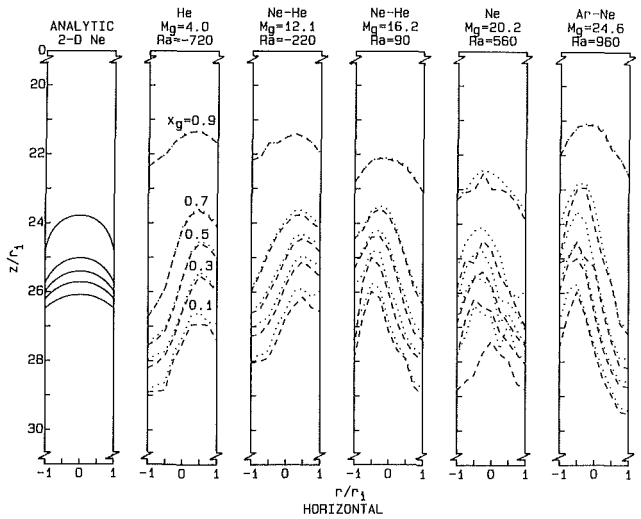

Fig. 3 Experimental and analytical gas isoconcentration profiles for *horizontal thermosyphon (right is bottom)*

tube is effectively sealed with double O-rings and vacuum grease. The finely polished tube is mounted offset from the thermosyphon centerline so it can be rotated and moved axially to make gas-concentration measurements in an arc from the centerline to the walls (Fig. 2).

The heat transfer resistance of the glass wall is much larger than that of the cooling-water and the condensate film, as was demonstrated by measurements of the cooling water, inside and outside wall, and vapor temperatures, which showed that over 98 percent of the temperature drop occurs in the wall. Thus the condenser wall heat transfer coefficient h_w is effectively constant, and also axial conduction through the glass is relatively small. Both these facts match the boundary conditions assumed by the axisymmetric diffusion model.

The experimental procedure consists of filling the thermosyphon with enough distilled water so the wet bulb can be dipped in the fluid and wetted. The thermosyphon is drained until a measured quantity of fluid is left. A vacuum is pulled on the thermosyphon to remove most of the air and it is then filled with noncondensable gas. This procedure is repeated six times to insure that all the air has been flushed out. The total pressure is adjusted to give the desired noncondensable-gas partial pressure. If required a second noncondensable gas is then added to obtain the needed average gas molecular weight. The gas inventory is calculated based on the total pressure, vapor partial pressure, temperature, and thermosyphon volume, assuming ideal-gas behavior. Heat is applied and after equilibrium is attained (3 h) minimum and maximum gas-concentration measurements are made by observing minimum and maximum wet-bulb temperatures at intervals of $r/r_i = 0.25$ and $z/r_i = 1.0$. The thermosyphon is moved and the measurements repeated to obtain profiles at 0, 45, and 90 deg orientations. The thermosyphon is allowed to cool and equilibrate (12 h) and the pressure is measured to confirm that no gas leakage occurred during the run. The entire procedure is repeated for several different average gas molecular weights at similar power levels and gas molar inventories.

Experimental Results

The glass thermosyphon gives conclusive visual evidence of the effectiveness of noncondensable gases in shutting off the condenser. The condenser can be divided into three regions: the top shut-off region, where no condensation occurs and the glass remains clear; the middle diffusion and mixing region, where a gradient of very small to large droplets forms on the wall; and the bottom active region, where full condensation occurs.

To facilitate understanding of the mass-transfer mechanisms, the experimental data measured at the points shown in Fig. 2 have been interpolated to produce gas isoconcentration profiles. Both the maximum (dashed curves) and minimum (dotted curves) axial positions at which a given concentration was measured are shown, with the magnitude of local instability indicated by the distance between these curves. Given temperature and pressure measurement accuracies of $\pm 0.3°C$ and ± 0.5 mm Hg, the maximum error of the gas fraction measurement is ± 0.005. The accuracy of the probe position measurement is $\pm$ 1.5 mm.

The primary driving force for natural convection is the difference between the pure vapor density and the gas/vapor mixture density in the shutoff region. Since velocities are low in the mixing region, inertial effects are relatively small and the proper scaling parameter is the Rayleigh number based on the mass diffusivity, which, assuming ideal gas behavior, can be expressed as

$$\mathrm{Ra} = \frac{(\rho(T_c)-\rho_v)gr_i^3}{\mu D}$$

$$= \frac{\rho_v g r_i^3}{\mu D}\left(\frac{T_v}{T_c}\left(1+x_{g,b}\left(\frac{M_g}{M_v}-1\right)\right)-1\right) \qquad (12)$$

where $\rho(T_c)$ is the density of the gas/vapor mixture at the coolant temperature T_c, ρ_v the density of the pure vapor, μ the viscosity, D the mass diffusivity, $x_{g,b}$ the maximum gas molar fraction, and M the molecular weight.

In Fig. 3 experimental isoconcentration profiles for a horizontal thermosyphon are plotted for several values of the Rayleigh number. The thermosyphon is oriented 2 deg from horizontal to allow condensate to return to the evaporator. For all cases the power level and mole inventory are similar, while the gas molecular weight varies. Effective gas molecular weights of 16.2 and 12.1 are achieved with mixtures of neon ($M=20.2$) and helium ($M=4.0$), and 24.6 with neon and argon ($M = 40.0$). The vapor molecular weight is $M_v = 18$. Also shown are the results predicted by the two-dimensional axisymmetric diffusion model for neon with water as the working fluid. The axial stratification increases slightly as Ra departs from zero. For comparison, in the experiments of Edwards and Marcus (1972), the Rayleigh number ranged from 320 to 23,000. Departure from their one-dimensional model increased with increasing Rayleigh number. In the ground tests of the Ames Heat Pipe Experiment reported by Eninger et al. (1976), the Rayleigh number is -1200. In both cases natural convection may explain deviations from predicted behavior; however, neither group reports whether their temperature measurements were made on the top, bottom, or side of the heat pipes.

Figure 4 shows experimental profiles for the thermosyphon operated at a 45 deg angle. Also shown are analytical one-dimensional diffusion predictions for helium with water as the working fluid. The flow is more stable in this orientation than

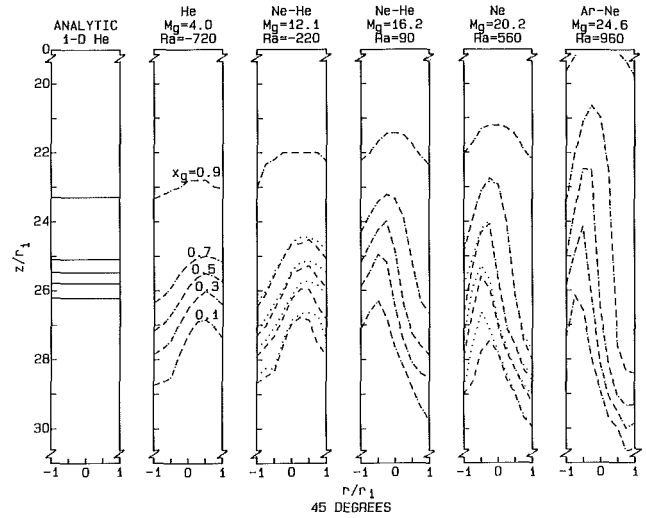

Fig. 4 Experimental and analytical gas isoconcentration profiles for 45 deg thermosyphon (right is bottom)

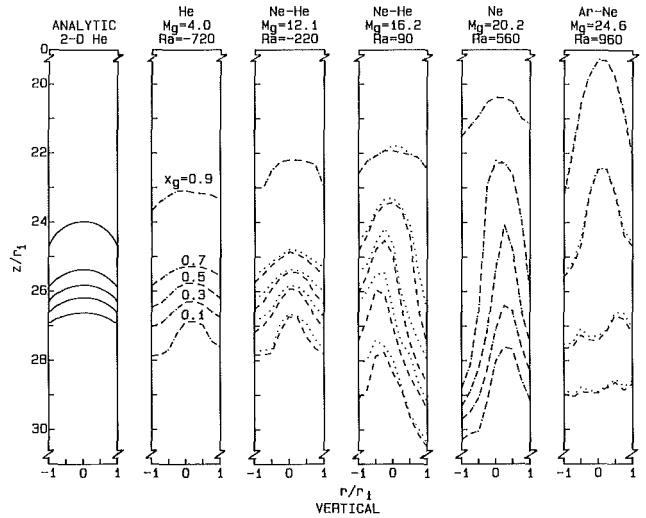

Fig. 5 Experimental and analytical gas isoconcentration profiles for vertical thermosyphon

in the horizontal orientation. The stratified region is longer than in the horizontal orientation for Ra > 0 and shorter for Ra < 0. This occurs because the gravity vector acts both to stratify the flow and to assist axial convection for Ra > 0 or retard it for Ra < 0.

Figure 5 shows experimental results for the vertical orientation and analytical results from the two-dimensional axisymmetric diffusion model for a helium/water mixture. The thermosyphon is positioned 2 deg from vertical to provide a preferred orientation for the natural convection. It is seen that this preferred orientation switches at a small value of the Rayleigh number, where the gas density in the shutoff region and the vapor density in the evaporator are approximately equal. The trend observed at the 45 deg orientation continues, with the diffusion region growing still shorter for Ra < 0 and longer for Ra > 0. For Ra << 0 the diffusion region is stable, little natural convection occurs, and the axisymmetric diffusion model does a good job of predicting the isoconcentration profiles. As Ra increases, so does axial stratification. The gas recirculation is still relatively stable for gas molecular weights of 25, but becomes very unstable at higher molecular weights. When air ($M_g = 29$) is used as the noncondensable gas, large transient fluctuations occur with the cooler air

Table 2 Experiment summary

Gases		He	Ne–He	Ne–He	Ne	Ar–Ne
M_g		4.0	12.1	16.2	20.2	24.6
Ra		−720	−220	90	560	960
Power level, W		154	154	165	158	154
	H	12.8	12.6	12.6	12.1	12.4
T_c, °C	45	13.2	12.6	12.7	12.1	12.5
	V	13.2	12.5	13.3	12.2	12.6
	H	55.2	53.9	56.4	55.8	56.6
T_e, °C	45	55.0	53.7	56.1	55.7	56.3
	V	55.0	53.6	56.6	55.9	56.7
N_g, gmole × 10^3		3.90	3.92	4.15	4.10	4.31
Screen/liquid vol, cm^3				69		
h_w, $kW/m^2 °C$				0.278		

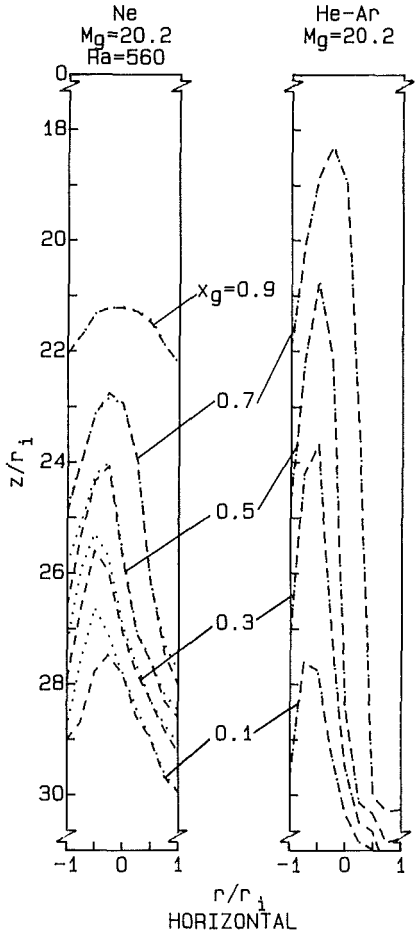

Fig. 6 Gas isoconcentration profiles for neon and equivalent helium/argon mixture

periodically slipping down beside the rising water vapor, at approximately 30-s intervals. The vapor, encountering the subcooled wall, condenses rapidly, resulting in pressure fluctuations. This moving region of intense condensation is easily observed through the glass wall. The resulting mixed region extends well down into the adiabatic section.

Table 2 summarizes the important parameters for the runs. It is interesting that for each gas molecular weight the evaporator temperature remains relatively constant for different orientations, even though the gas distribution may change radically.

The results obtained using mixtures of dissimilar noncondensable gases are different from those obtained with a single gas. This is illustrated in Fig. 6, which compares results for the thermosyphon operated at a 45 deg orientation with

pure neon and with an equivalent mixture of argon and helium. Because the diffusion rate for helium is much greater than for argon, the helium is transferred preferentially across the gas–vapor interface, and being light, the helium promotes recirculation and increases the length of the stratified zone. In Figs. 3 and 4 this effect explains the greater stability of the neon/helium mixture ($M_g = 16.0$) compared to pure neon ($M_g = 20.2$).

Other potential sources of mixing in the diffusion region were discovered in other runs of the experiment with different evaporator designs and liquid fill volumes. Evaporator wall dryout and rewetting may generate bursts of vapor and mixing. The geysering effect of rising vapor bubbles in vertical thermosyphons with large liquid fill volumes can also cause mixing.

Conclusions

Use of the miniature-wet-bulb technique permitted for the first time measurements of the noncondensable-gas concentrations in the condenser of a reflux thermosyphon. The wet-bulb probe allowed detection of natural convection and unstable phenomena. With the glass thermosyphon used in this experiment, the three regions in the condenser are readily seen: the clear shutoff region at the top, the middle diffusion and mixing region with a gradient of drop sizes, and the bottom active region with full condensation. Systems with different gas molecular weights but similar noncondensable mole inventories and power inputs behave differently because of natural convection due to temperature and concentration gradients. This natural convection results in gas recirculation and axial stratification and the proper scaling parameter for it is the Rayleigh number.

Natural convection effects have three major impacts on the performance of gas-loaded thermosyphons and heat pipes. At low power levels axial stratification will result in "heat leaks" and lower than desired evaporator temperatures since stratification permits vapor to leak into the condenser. With vertical or near-vertical orientations and high Rayleigh numbers large transient fluctuations of the gas–vapor interface can occur, resulting in pressure fluctuations and degraded performance. Finally natural convection can change the performance of ground-tested heat pipes intended for space flight.

The axisymmetric thermosyphon model does a good job of predicting gas-concentration profiles for a vertical helium/water thermosyphon and provides a reference to evaluate the effects of natural convection. To do this the assumption of constant mass density throughout the thermosyphon used in the model of Hijikata et al. (1984) was modified to constant molar density, and the calculation of the shutoff length L_g from the gas mole inventory was based on the cooling medium temperature T_c, rather than the saturation temperature T_s. A simplified method of calculation that reduces the number of nodes and iterations was also introduced.

Acknowledgments

The support of the Electric Power Research Institute through Grant No. RP-1160-3 is appreciated.

References

Edwards, D. K., and Marcus, B. D., 1972, "Heat and Mass Transfer in the Vicinity of the Vapor-Gas Front in a Gas-Loaded Heat Pipe," ASME JOURNAL OF HEAT TRANSFER, Vol. 94, pp. 155–162.

Eninger, J. E, Luedke, E. E., and Wanous, D. J., 1976, "Flight Data Analysis and Further Development of Variable-Conductance Heat Pipes," NASA CR-137782.

Galaktionov, V. V., and Trukhanova, L. P., 1985, "Study of the Process of Heat and Mass Transfer in the Region of the Vapor-Gas Front in a Gas-Regulable Heat Pipe," *Journal of Engineering Physics*, Vol. 48, pp. 296–300.

Hijikata, K., Chen, S. J., and Tien, C. L., 1984, "Non-condensable Gas Effect on Condensation in a Two-Phase Closed Thermosyphon," *International Journal of Heat and Mass Transfer*, Vol. 27, pp. 1319–1325.

Kelleher, M. D., 1976, "Effects of Gravity on Gas-Loaded Variable Conductance Heat Pipes," *Proceedings of the 2nd International Heat Pipe Conference*, Bologna, Italy, pp. 225–234.

Peterson, P. F., and Tien, C. L., 1987, "A Miniature Wet-Bulb Technique for Measuring Gas Concentrations in Condensing or Evaporating Systems," *Experimental Heat Transfer*, Vol. 1, pp. 1–15.

Rohani, A. R., and Tien, C. L., 1973, "Steady Two-Dimensional Heat and Mass Transfer in the Vapor-Gas Region of a Gas-Loaded Heat Pipe," ASME JOURNAL OF HEAT TRANSFER, Vol. 95, pp. 377–382.

D. Peterson

D. Glasser

D. Williams

University of Witwatersrand,
Dept. of Chemical Engineering,
Wits, 2050, Republic of South Africa

R. Ramsden

Chamber of Mines Research Organization,
Johannesburg 2000,
Republic of South Africa

Predicting the Performance of an Evaporative Condenser

A simple analytical method, based on the method of Parker and Treybal (1961) for evaporative coolers, was developed to predict the performance of evaporative condensers. The transfer coefficients of the model were predicted from standard correlations in the literature or those determined by Parker and Treybal for evaporative coolers. Field tests were performed on an evaporative condenser and the measured and predicted heat loads and recirculating water temperature were compared. It was found that the heat load was underpredicted by about 30 percent and the water temperature by 3°C. A change in U_o of a factor of 1.9 adequately predicts both the heat load and sump temperature.

1 Introduction

As yet no generally accepted method for predicting the performance of evaporative coolers or condensers exists, although a number of mathematical models have been developed. Most of the models given in the literature prior to 1960 were derived by assuming that the water temperature was constant (Goodman, 1938; Thomsen, 1946) or by defining a theoretical water temperature that could be assumed constant (Wile, 1950). Parker and Treybal (1961) realized that the assumption of constant water temperature caused the mathematical equations of the model to become inconsistent, thus giving a meaningless answer, unless the equations were solved in a specific order.

Parker and Treybal modeled an evaporative cooler. The main assumptions made in the derivation of the model are that:

(*i*) The Lewis relation applies. By this we mean that ($h_g \hat{C}p_g/k_y$) is unity. This relation cannot be analytically proved (Peterson, 1984) but has been experimentally verified for air–water systems.

(*ii*) The enthalpy of saturated moist air is a linear function of temperature over the whole range of bulk water and air–water interface temperatures in the unit.

(*iii*) The recirculation water flow rate is so large that changes in it due to evaporation can be neglected.

The final equations of this model are consistent and can be solved to give a simple analytical solution.

Mizushina et al. (1967) determined the various transfer coefficients in an evaporative cooler. The coefficients were not well defined and were determined by fitting test data to empirical log mean differences that used average water and tube wall temperatures. The coefficients determined in this manner differ from those determined by Parker and Treybal and this is not surprising as the transfer coefficients were defined differently in the two cases. Mizushina et al. (1968) developed two different rating methods for evaporative coolers, one a numerical technique and the other a simpler analytic model based on the assumption of constant water temperature. Finlay and Grant (1974) showed that this assumption may lead to errors in excess of 30 percent under certain conditions, for example large tube banks.

A rating method based on cooling tower rating procedures was proposed by Tezuka et al. (1976). The assumptions made in this model are not as accurate as those used in the model of Parker and Treybal nor is the model as simple.

Finlay and Grant (1972) simplified the equations describing the mass transfer in an evaporative cooler by assuming that the vapor pressure of saturated moist air is a linear function of temperature. The model can be expected to be very accurate as this is the only major assumption made in the derivation. The final design equations are very complicated however and require a numerical solution. The model of Parker and Treybal is discussed in this paper and it is said that the equations can be integrated but that the integration does not yield an explicit solution. It is also said that iteration is required to obtain a solution, which is not generally true. In a later report (Finlay and Grant, 1974) the authors compared the predictions using their model and that of Parker and Treybal and found that the results were ". . . in good agreement for most engineering purposes." There are some puzzling points in this comparison, e.g., an extra heat transfer coefficient is used in the model of Parker and Treybal, and it is not clear from the report what value was used in the comparison.

Leidenfrost and Korenic (1982) followed a development in their model similar to that of Parker and Treybal but stopped short of making three assumptions used by the latter, namely:

- The Lewis number is 1. Although Leidenfrost and Korenic did not use this in their model, they assumed it in the numerical solution of the equations in order to save computing time.
- The water flow rate is constant. This assumption is a reasonable one; for example, in the tests conducted by the authors, the water flow rate changed by less than 2.5 percent.
- The enthalpy of saturated moist air is a linear function of temperature. This assumption is used over the range of water temperatures in the condenser. If the water temperature varied by 10°C, which is probably far more than would ever be found in practice, this would introduce an error of about 3 percent in the value of the enthalpy.

The resulting model requires a numerical solution with iteration to determine the recirculating water temperature. If however the three assumptions listed above are made, a much simpler analytical model based on that of Parker and Treybal can be derived, without much loss of accuracy.

Leidenfrost and Korenic used the air heat transfer coefficient for dry tubes in the model, presumably assuming that it would be the same as the air heat transfer coefficient at the water–air interface of wet tubes. Parker and Treybal showed that this was not true. Another error in the method was the definition of the Reynolds number of the water, which according to the definition given is not dimensionless.

To summarize, there is no generally accepted means to model and predict the behavior of evaporative condensers.

Contributed by the Heat Transfer Division for publication in the JOURNAL OF HEAT TRANSFER. Manuscript received by the Heat Transfer Division June 2, 1986. Keywords: Condensation, Evaporation, Modeling and Scaling.

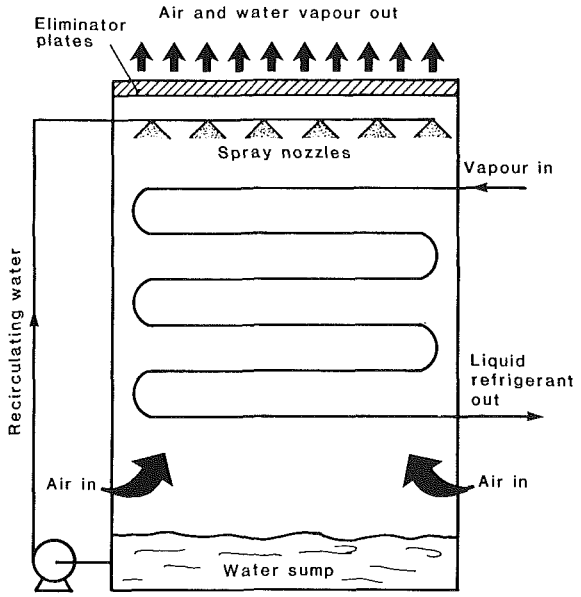

Fig. 1 Cross-sectional view of evaporative condenser

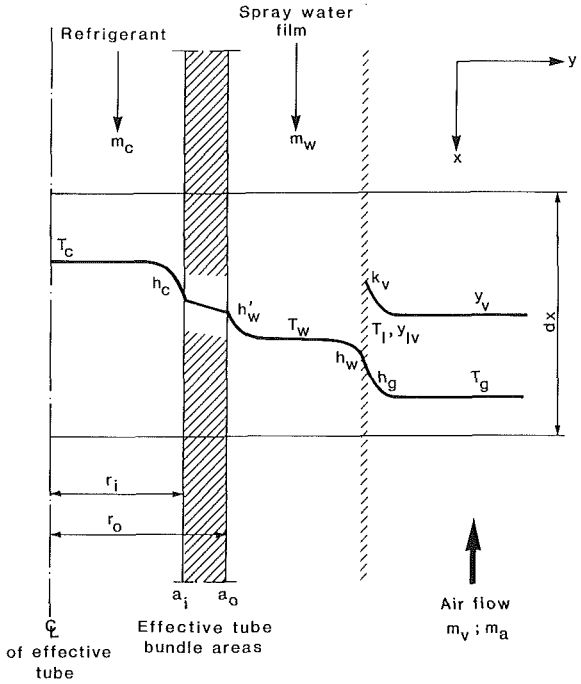

Fig. 2 Indication of parameters used in model

Most of the recent research has been on evaporative coolers, which differ from condensers firstly in that the tube-side fluid temperature varies in the cooler while remaining constant in the condenser, and secondly in that the units operate under very different conditions, i.e., tube-side fluid temperature and water and air flow rates.

The models for evaporative coolers usually require a numerical solution or give an analytic solution based on the erroneous assumption of constant water temperature. As discussed, this assumption can lead to large inaccuracies in the prediction.

The model of Parker and Treybal gives a simple analytic answer based on assumptions that are fairly accurate. The model is derived using the energy balances for all three fluids and the experimentally determined transfer coefficients are correlated for the typical range of operating conditions of evaporative coolers.

2 Description of an Evaporative Condenser

The evaporative condenser may be regarded as a cooling tower in which the packing is replaced by a bank of tubes. The process fluid, the vapor to be condensed, flows inside the tubes. Air is drawn up through the bank of tubes while water is sprayed downward over the tubes. Some of this spray water is evaporated into the air while the remainder falls back into the sump and is recirculated. A diagram of an evaporative condenser is given in Fig. 1.

Energy is transferred from the process fluid through the tube wall and into the water. From here the energy is transferred into the air due to temperature gradients and evaporation.

3 Theoretical Development

In the subsequent development it will be assumed that:

(*i*) The distribution of air and water is uniform at the inlets and this uniformity is maintained. Thus the temperatures in

Nomenclature

a_i = total inside area of tubes, m^2
a_o = total outside area of tubes, m^2
a_1 = constant used in model
$\hat{C}p$ = specific heat at constant pressure, J kg^{-1} K^{-1}
$\hat{C}p_g$ = specific heat at constant pressure for wet air, defined by $\hat{C}p_g = \hat{C}p_a + w_v\hat{C}p_v$, J kg^{-1} K^{-1}
d_i = inside diameter of tubes, m
d_o = outside diameter of tubes, m
G = mass velocity of air based on minimum cross-sectional area, kg m^{-2} s^{-1}
$\hat{H}_g$ = specific enthalpy of wet air, defined by $\hat{H}_g = (\hat{H}_a + w_v\hat{H}_v)$, J kg^{-1}
$\hat{H}'_g$ = specific enthalpy of saturated wet air at the water temperature, J kg^{-1}
$\hat{H}_{Iw}$ = specific enthalpy of water at interface temperature, J kg^{-1}
$\bar{H}_{Iv}$ = partial molar enthalpy of water vapor at interface temperature, J mol^{-1}
h_c = local heat transfer coefficient for the refrigerant side of the tube–refrigerant interface, W m^{-2} K^{-1}
h_g = local heat transfer coefficient for the air side of the water–air interface, W m^{-2} K^{-1}
h_w = local heat transfer coefficient for the water side of the water–air interface, W m^{-2} K^{-1}
h'_w = local heat transfer coefficient for the water side of the water–tube interface, W m^{-2} K^{-1}
K_0 = defined by $-1/K_0 = (m'/h_w + 1/k_y)$, kg m^{-2} s^{-1}
k = thermal conductivity of tube wall, W m^{-1} K^{-1}
k_y = local mass transfer coefficient for the air side of the water–air interface, kg m^{-2} s^{-1}
L_t = length of tube, m
M_v = molecular mass of water (vapor), kg mol^{-1}
m' = defined by $m' = d\hat{H}'_g/dT_w$, assumed constant, J kg^{-1} K^{-1}

the unit will only depend on the vertical position in the unit, which implies that the model need only be one dimensional.

(*ii*) The water may be modeled as a continuous film flowing countercurrent to the air and cocurrent to the tube-side fluid as shown in Fig. 2. This is probably not all that good an assumption but has been extensively used and is the simplest one that appears to be reasonable.

(*iii*) Transfer between the air leaving the unit and the water spraying onto the tubes and also between the air entering the unit and the water dropping into the sump will be ignored. (These effects can be incorporated into the model if desired, however.)

In the actual process the heat and mass transfer between the water and air occurs around pipes and not a plane wall as shown in Fig. 2; this is taken into account in the mathematics by using the appropriate definition for the overall heat transfer coefficient U_o. The tube-side fluid actually condenses in a horizontal tube and not on a vertical wall as shown in the diagram but this can again be taken into account by using the correct correlation for the condensing coefficient.

The transfer coefficients are defined with respect to the mole average velocities and are assumed to be independent of mass transfer rate. This is in accordance with the definition given by Bird et al. (1960). The mass transfer coefficient has been defined for a dilute water vapor–air mixture. The definitions are given below:

$$-dm_v = k_y a_o (w_{Iv} - w_v)dx$$

$$dQ_c = h_c a_i (T_i - T_c)dx$$

$$dQ_w = h_w a_o (T_I - T_w)dx + \hat{H}_{Iw} dm_w \quad (1)$$

$$dQ'_w = h'_w a_o (T_o - T_w)dx \quad (2)$$

$$dQ_g = h_g a_o (T_I - T_g)dx - (\hat{H}_{Iv}/M_v)dm_v \quad (3)$$

The steady-state mass and energy balances can be written for each fluid and simplified using the assumptions listed in the introduction as well as assuming that the fluid and transport properties and the tube-side fluid temperature are constant to give

$$-U_o a_o (T_c - T_w)dx = m_c \lambda_c dw_c \quad (4)$$

$$U_o a_o (T_c - T_w)dx + K_o a_o (\hat{H}'_g - \hat{H}_g)dx = m_w \hat{C}p_w dT_w \quad (5)$$

$$m_a d\hat{H}_g = K_o a_o (\hat{H}'_g - \hat{H}_g)dx \quad (6)$$

where

$$-1/K_o = m'/h_w + 1/k_g \quad (7)$$

$$1/U_o = a_o/(h_c a_i) + d_o \ln(d_o/d_i)/2k + 1/h'_w \quad (8)$$

The tube-side energy balance equation (4) differs from that for an evaporative cooler and, unlike the development for evaporative coolers, is not actually used in the subsequent development. If the condensing temperature T_c is constant, equation (5) becomes

$$U_o a_o (T_c - T_w)dx + K_o a_o (\hat{H}'_g - \hat{H}_g)dx = m_w \hat{C}p_w d(T_w - T_c) \quad (9)$$

Equation (6) can be rearranged to give

$$m_a d(\hat{H}'_g - \hat{H}_g) = -K_o a_o (\hat{H}'_g - \hat{H}_g)dx + m_a m' d(T_w - T_c) \quad (10)$$

These two equations are of the same form as those derived by Parker and Treybal for evaporative coolers. The coefficient a_1 of equation (11) of this reference ($a_1 = U_o a_o/m_w \hat{C}p_w + U_o a_o/m_c \hat{C}p_c$) must be modified for an evaporative condenser such that $a_1 = U_o a_o/m_w \hat{C}p_w$. (This is equivalent to assuming $\hat{C}p_c$ is infinite.) The system of equations can be solved in the same manner as described by Parker and Treybal and more fully by Peterson (1984), to give expressions that allow one to calculate the condenser load and recirculating water temperature directly.

4 Experimental Procedure

The model described above uses two overall transfer coefficients: U_o and K_o. The value of these coefficients should be such that the predicted recirculating water temperature T_{wr} and load Q fit the experimental data obtained while running the condenser conventionally.

U_o is a function of k, h_c, and h'_w. Values for k and h_c can be found in the literature. The tube–water heat transfer coefficient h'_w cannot be measured directly and the only correlation reported in the literature is by Parker and Treybal for evaporative coolers, which operate at different conditions from evaporative condensers. As these were the only reported data on this coefficient they were used to predict the overall heat transfer coefficient U_o. The overall mass transfer coefficient K_o is a function of h_w and k_y. The value of k_y can be determined separately from experimental data obtained from running the condenser as a cooling tower, i.e., with no flow through the condensing coil, while water recirculates and air blows through the coils. The water–air heat transfer coeffi-

Nomenclature (cont.)

m = mass flow rate, kg s^{-1}
N_t = number of tubes per pass
Q_c = rate of energy transfer across the tube–refrigerant interface, into the refrigerant at x, W
Q_g = rate of energy transfer across the water–air interface into the air at x, W
Q_w = rate of energy transfer across the water–air interface into the water at x, W
Q'_w = rate of energy transfer across the water–tube interface into the water at x, W
T = temperature, K
T_i = inside tube wall temperature, K
T_o = outside tube wall temperature, K
T_{wr} = recirculating water temperature, K
U_o = defined by $1/U_o = (a_o/(h_c a_i) + d_o \ln(d_o/d_i)/2k + 1/h'_w)$, W m^{-2} K^{-1}
W_t = width of tube bank, m
w_c = mass fraction of condensate in tube-side fluid
w_{Iv} = mass fraction of vapor in air at interface, assumed saturated
w_v = mass fraction of vapor in bulk air
w_{vav} = average mass fraction of vapor in bulk air
x = length dimension
Γ = mass rate of spray water per tube per unit length, kg s^{-1} m^{-1}
λ = latent heat of vaporization, J kg^{-1}

Subscripts

a = refers to dry air
c = refers to tube-side fluid, i.e., refrigerant
g = refers to wet air or an air–vapor mixture
I = refers to water–air interface
in = refers to property at the inlet conditions
v = refers to water vapor
w = refers to water film
out = refers to property at the outlet conditions
pred = refers to value calculated using standard correlations

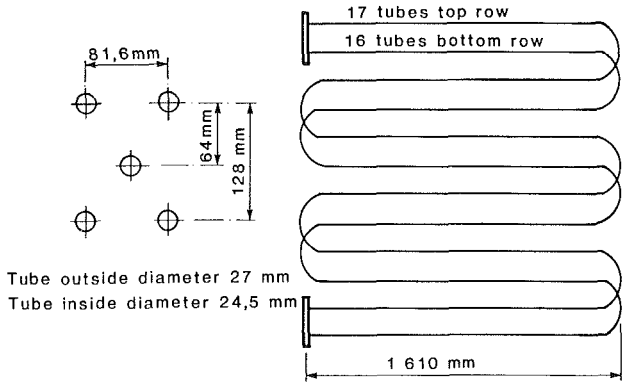

Fig. 3 Side view of condensing coil

cient h'_w has again only been measured by Parker and Treybal for evaporative coolers and was thus used to predict K_o.

(a) **Experimental Apparatus.** The evaporative condenser tested was part of an experimental plant designed to produce 24 tons of ice per day. This plant was situated outside and so subject to prevailing weather conditions. The condenser was used as the heat rejection system of the refrigeration cycle. Freon-22 was used as the refrigerant. The condenser tested was a Reco model RC 66, which has a nominal rating capacity of 250 kW. The design water flow rate is around 6 kg/s and the air flow rate is about 3.5 kg/s. Details of the coil configuration are shown in Fig. 3.

The refrigerant inlet temperature, pressure, and flow rate were measured. The refrigerant was delivered to the condenser by a six-cylinder reciprocating compressor and was always superheated. This superheating (less than 10 percent of the total heat load of the condenser) was ignored in the analysis and the refrigerant was assumed to be at the condensing temperature. The pressure and temperature at the outlet of the coil were also measured. A U bend with a sight glass in the bend was fitted to the condenser outlet line to check the flow from the condenser. In normal practice this flow would be liquid but due to a problem in the refrigeration plant piping, the flow from the condenser was never fully condensed. This meant that the heat load on the condenser could not be cross checked and only the air-side measurements could be used to determine the duty of the condenser Q. The measurements taken on the air side were the inlet and outlet wet- and dry-bulb temperatures (using Assmann psychrometers) and the outlet air velocity (using a rotating vane anemometer). The recirculating, makeup and bleed flow rates and temperatures were also measured. Turbine flow meters were used to measure the flow rates and the differences in the flow rates due to the evaporation of the water could not be detected with these meters.

The experimental data were fairly inaccurate. This will almost always be the case when testing a field unit that is part of a refrigeration or other similar plant. The range of testing conditions was limited by the plant operation. Furthermore refrigeration plant instabilities, sudden gusts of wind, entrainment of water in the air leaving the unit, etc., were all practical problems associated with field tests.

The measured heat load is very sensitive to inaccuracies in the measured inlet and outlet wet bulb temperatures and air velocity. The wet bulb temperature could be read to an accuracy of $\pm$ 0.1°C and the calibration accuracy of the anemometer was about 5 percent. The resultant error in the measured heat load is then of the order of 20 kW. The recirculating water temperature was measured to the accuracy of $\pm$ 0.1°C. The accuracy of the measured condensing pressure is the most sensitive experimental input in the predicted heat load and recirculating water temperature. It is estimated that the condensing pressure, taking into account the errors in the calibration of the gage and in the reading, was measured within $\pm$ 20 kPa. This resulted in an accuracy of $\pm$ 10 kW of the predicted heat load and of $\pm$ 0.5°C of the predicted recirculating water temperature.

(b) **Numerical Analysis of k_y.** Assuming the Lewis relationship applies, a mass balance across the unit when operating in the cooling tower mode gives

$$k_y dx = \frac{-m_a dw_v}{a_o (w_{Iv} - w_v)} \tag{10}$$

Integrating this, assuming the transfer coefficient is constant, gives

$$k_y = (m_a/a_o)\ln\{(w_{Iv} - w_v|_{in})/(w_{Iv} - w_v|_{out})\} \tag{11}$$

As a consequence of the assumption that the Lewis relationship applies, the water temperature through the condenser is equal to the air wet-bulb temperature and thus w_{Iv} is also constant, and can be determined from psychrometric data. The above equation can be used to calculate k_y.

(c) **Numerical Analysis of U_o and K_o.** The overall heat transfer coefficient U_o is a function of h_c, k, and h'_w. The value of the thermal conductivity of the tube can be found in the literature and a value of 52 W m^{-1} K^{-1} (based on stainless steel) was used. The condensing coefficient h_c presents a problem as the current methods of predicting condensing coefficients are not all that reliable. The value of the coefficient depends on the flow regime in the tubes, which in turn varies along the tube. The gas velocity in the tubes is fairly low (about 1.7 m s^{-1}), even though the Reynolds number is fairly high (about 1.8 $\times$ 10^5) and it would seem that the flow in the coil would be more stratified than annular. The Chato correlation (Collier, 1972) for stratified flow was therefore used to estimate the condensing coefficient. The correlation for h'_w as given by Parker and Treybal is

$$h'_w = (982 + 15.58\ T_{wr})(\Gamma/d_o)^{1/3}$$

where $\Gamma = m_w/N_t L_t$ and $1.36 < \Gamma/d_o < 3$.

The operating conditions of the evaporative condenser covered the following range:

$$1.3 < \Gamma/d_o < 3.36$$

Parker and Treybal found that the value of h_w was high and nonlimiting and suggested a value of 11,600 W m^{-2} K^{-1}. The following method of comparing the model and the experimental data was used:

(i) Calculate the load from the air-side measurements.

(ii) Calculate K_o using the correlation for k_y determined in the previous experiments and a value for h_w of 11,600 W m^{-2} K^{-1}.

(iii) Determine U_o using the Chato correlation for h_c, the Parker and Treybal correlation for h'_w, and a value of 52 W m^{-1} K^{-1} for k.

(iv) Calculate the load and the recirculating water temperature from the model.

(v) Check the accuracy of the transfer coefficients by comparing the measured and calculated Q and T_{wr}.

5 Experimental Results

The local mass transfer coefficient k_y is plotted versus mass flow rate of air in Fig. 4. Parker and Treybal found the following correlation to apply to the data for evaporative coolers:

$$k_y = 0.0493\{G(1 + w_{vav})\}^{0.905}$$

for $0.68 < G < 5$ where $G = m_a/\{W_t - N_t d_o/2)L_t\}$, and

$$1.36 < \Gamma/d_o < 3$$

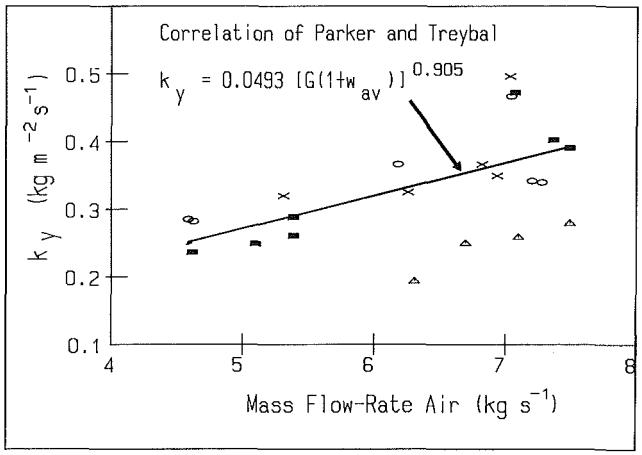

Fig. 4 Plot of k_y versus mass flow-rate air; the following ranges of water flow rates m_w are indicated: ▲ $m_w < 1.75$ kg/s; ■ $1.75 < m_w < 3$ kg/s; × $3 < m_w < 4$ kg/s; ○ $m_w > 4$ kg/s

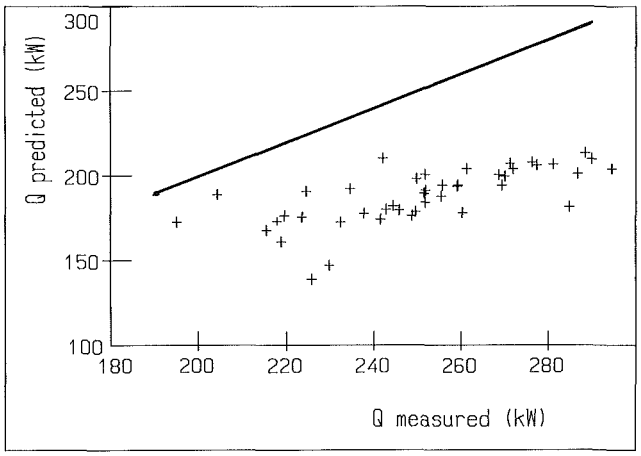

Fig. 5 Plot of measured versus predicted load when $U_o = U_{o\ pred}$

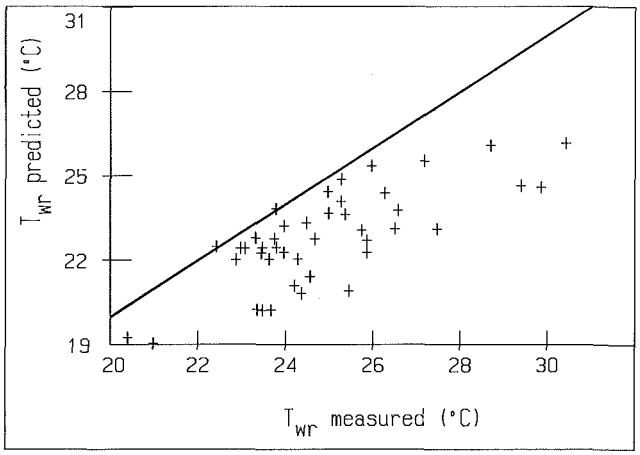

Fig. 6 Plot of measured versus predicted water temperature when $U_o = U_{o\ pred}$

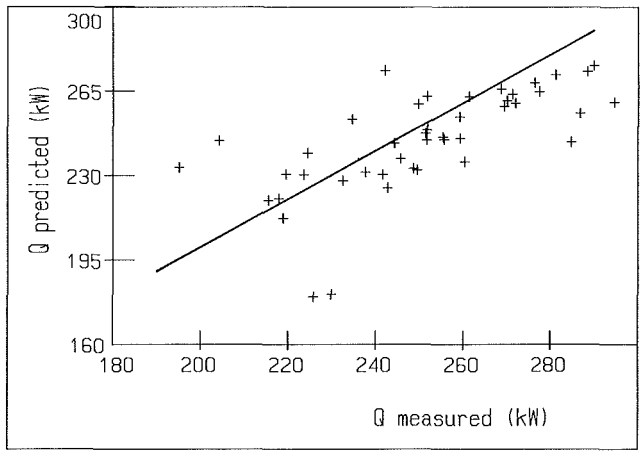

Fig. 7 Plot of measured versus predicted load when $U_o = 1.9\ U_{o\ pred}$

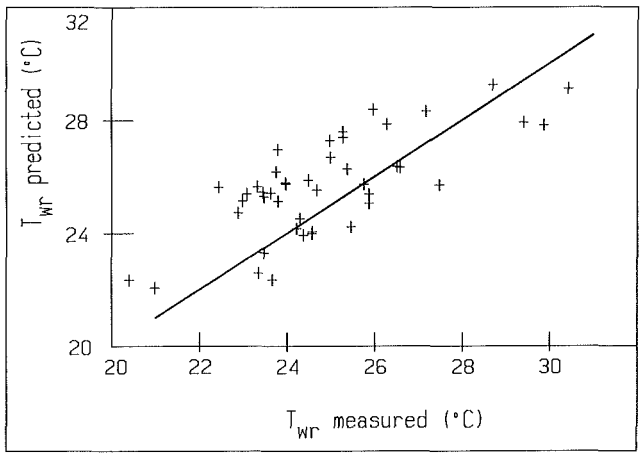

Fig. 8 Plot of measured versus predicted water temperature when $U_o = 1.9\ U_{o\ pred}$

where $\Gamma = m_w/N_t L_t$. The correlation of Parker and Treybal has been extrapolated and is shown on Fig. 4; it appears to be consistent with these results.

The range over which these experiments were performed is: $5.87 < G < 9.78$ where $G = 1.308\ m_a$; and $1.30 < \Gamma/d_o < 4.33$ where $\Gamma/d_o = 0.729\ m_w$; and this therefore extends the range over which the correlation of Parker and Treybal may be used.

The authors found that the coefficient was largely independent of the water flow rate, which agrees with the findings of Parker and Treybal.

The water flow rate only affects the coefficients at low flow rates when the tubes are incompletely wetted. The four points that fall well beneath the curve are all values where the water flow rate was less than 1.75 kg/s.

The predicted versus measured Q and T_{wr} are shown in Figs. 5 and 6. In both cases the predicted value is lower than the measured. The condenser load is underpredicted by about 30 percent and the water temperature by about 3°C. This would seem to suggest that the predicted value of the overall heat transfer coefficient is too low.

Increasing the value of U_o improves both predictions and a constant factor of 1.9 (i.e., $U_o = 1.9\ U_{o\ pred}$) gives a fairly good correlation between the measured and predicted values for the load and recirculating water temperature, as can be seen from Figs. 7 and 8. This would seem to indicate that one or both of the local heat transfer coefficients h'_w and h_c are underpredicted by the correlations. It is not clear which of the coefficients are underpredicted. If it is assumed that all the error lies in the condensing coefficient this would imply a value of about 8800 Wm^{-2}K^{-1}, which is usually only feasible in the annular flow regime at much higher gas velocities. The superheating of the vapor could also enhance the condensing coefficient as the superheating seems to promote a type of

dropwise condensation (Altman et al., 1960) with the associated high coefficients.

6 Discussion

The model of Parker and Treybal has been modified and applied to evaporative condensers. The model is very simple and straightforward to apply in practice, merely involving the solution of algebraic equations. The correlation for the water–air mass transfer coefficient (k_y) given by Parker and Treybal has been verified and the range over which this correlation has been tested has been extended. The predicted value of the overall heat transfer coefficient U_o, using the Chato correlation for the condensing coefficient h_c and the Parker and Treybal correlation for the tube–water heat transfer coefficient (h_w'), would seem to be too low as the duty of the evaporative condenser is underpredicted by about 30 percent.

Both the load and the recirculating water temperature can be predicted if the value of U_o is increased by a factor of 1.9. Further tests on a variety of evaporative condensers and coolers could be performed in order to confirm these findings and to refine the correlations. It would also be desirable to measure the various profiles through the condenser in order to verify that the predicted profiles fitted the measured ones.

Acknowledgments

This work was carried out as part of the research program of the Research Organization of the Chamber of Mines of South Africa and was submitted as an M.Sc. dissertation to the University of the Witwatersrand.

One of the authors (D. Peterson) would like to thank the University of Potchefstroom for providing time to write this manuscript.

References

Altman, M., Staub, F. W., and Norris, R. H., 1960, "Local Heat Transfer and Pressure Drop for Refrigerant-22 Condensing in Horizontal Tubes," *AIChE Chemical Engineering Progress Symposium Series*, No. 30, Vol. 56, pp. 151–159.

Bird, R. B., Stewart, W. E., and Lightfoot, E. N., 1960, *Transport Phenomena*, Wiley, New York, pp. 636–680.

Collier, J. G., 1972, *Convective Boiling and Condensation*, McGraw-Hill, London.

Finlay, I. C., and Grant, W. D., 1972, "Air Coolers, Cooling Towers and Evaporative Coolers," Report No. 534, National Engineering Laboratory, East Kilbride, Glasgow, pp. 17–22.

Finlay, I. C., and Grant, W. D., 1974, "The Accuracy of Some Simple Methods of Rating Evaporative Coolers," Report No. 584, National Engineering Laboratory, East Kilbride, Glasgow.

Goodman, W., 1938, "The Evaporative Condenser," *Heating, Piping and Air Conditioning*, Vol. 10, pp. 165–328.

Leidenfrost, W., and Korenic, B., 1982, "Evaporative Cooling and Heat Transfer Augmentation Related to Reduced Condenser Temperatures," *Heat Transfer Engineering*, Vol. 3, Nos. 3–4, pp. 38–59.

Mizushina, T., Ito, R., and Miyashita, H., 1967, "Experimental Study of an Evaporative Cooler," *International Chemical Engineering*, Vol. 7, No. 4, pp. 727–732.

Mizushina, T., Ito, R., and Miyashita, H., 1968, "Characteristics and Methods of Thermal Design of Evaporative Coolers," *International Chemical Engineering*, Vol. 8, No. 3, pp. 532–538.

Parker, R. O., and Treybal, R. E., 1961, "The Heat, Mass Transfer Characteristics of Evaporative Coolers," *AIChE Chemical Engineering Progress Symposium Series*, No. 32, Vol. 57, pp. 138–149.

Peterson, D., 1984, "Development of a Method to Predict the Performance of an Evaporative Condenser," M.Sc. Thesis, University of the Witwatersrand, Rep. of South Africa.

Tezuka, S., Takada, T., and Kasai, S., 1976, "Performance of an Evaporative Cooler," *Heat Transfer—Japanese Research*, Vol. 6, No. 1, pp. 1–18.

Thomsen, E. G., 1946, "Heat Transfer in an Evaporative Condenser," *Refrigeration Engineering*, Vol. 51, No. 5, pp. 425–431.

Wile, D. D., 1950, "Evaporative Condenser Performance Factors," *Refrigeration Engineering*, Vol. 58, No. 1, pp. 55–63.

Similarity Analysis of Condensing Flow in a Fluid-Driven Fracture

S. K. Griffiths
Sandia National Laboratories,
Livermore, CA 94550

R. H. Nilson
S-CUBED,
A Division of Maxwell Laboratories, Inc.
La Jolla, CA 92038

Similarity solutions are derived for some fundamental problems of condensing flow in a hydraulically driven fracture. The governing equations describe one-dimensional homogeneous turbulent flow along a wedge-shaped hydraulic fracture in an elastic medium. The instantaneous fracture speed is determined as an analytical function of fracture length, material properties, process parameters, and a single eigenvalue, which is calculated by solving a system of ordinary differential equations for the variation of pressure, energy, velocity, and opening displacement along the fracture. Results are presented for abrupt condensation of a pure substance and for gradual condensation of air/water mixtures. The rate of condensation is controlled by the rate of heat transfer to the fracture wall, which depends upon a single dimensionless parameter. For small and large values of this parameter the present multiphase solutions are in agreement with previous solutions for single-phase flows of vapors and liquids. Although most of the results are presented in dimensionless form, some numerical examples are given for steam-driven fractures emanating from the cavity resulting from an underground nuclear explosion.

Introduction

In underground nuclear tests conducted at the Nevada Test Site, the very rapid energy release and the associated vaporization, melting, and deformation of the surrounding rock typically results in a large spherical cavity ($R \sim 30$ m) filled with superheated steam and air at pressures and temperatures on the order of 3-10 MPa and 1000-2500 K (Teller et al., 1968). The early plastic deformation and the subsequent elastic rebound of the surrounding rock usually induce a residual confining stress around the cavity, which is greater than the internal gas pressure, thus prohibiting the growth of fractures. However, some time is required to establish the residual stress field and its effectiveness may sometimes be degraded by decoupling of the explosion, low rock strength, or the presence of nearby lithologic interfaces. Thus, it is important to estimate the speed and extent of steam-driven fractures, which might carry radioactive gases from the cavity toward the surface.

The phenomenology of steam-driven fracture propagation is sufficiently complex that comprehensive numerical models are generally required to simulate the overall process, as illustrated by the work of Keller et al. (1974), Pitts and Brandt (1977), Nilson and Griffiths (1983), and Griffiths and Nilson (1986a). However, to gain a better understanding of the controlling physics and as a check on the more comprehensive models, it is useful to investigate separately some of the important mechanisms that limit fracture growth, such as pressure decay of the cavity fluid, seepage losses from the crack into the host material, heat loss to the fracture walls, and condensation of fluid within the crack. The present paper is devoted to this last consideration.

This paper is the fourth in a sequence of studies that use similarity transformations to solve fundamental problems of fluid-driven fracture propagation. The first paper (Nilson, 1981) addressed isothermal flow of an ideal gas. The second (Nilson and Griffiths, 1986) included heat transfer to the fracture walls, but was still restricted to ideal gases. The third (Griffiths and Nilson, 1986b) dealt with two-phase gas/liquid flows under isothermal conditions. Here we investigate the more general and more realistic case of multiphase, multicomponent flows in which the rate of condensation and re-evaporation is controlled by convective and/or conductive heat transfer to the fracture walls.

Beyond the intended application to hydrofracture processes, the present analysis of transient condensing flow may be of general interest to engineers who deal with two-phase flows in narrow channels. Past comparisons between flows in pre-existing channels and flows in hydrofractures suggest that the same methodology is applicable and that there is a strong similarity of behavior (Nilson and Morrison, 1986). Indeed, the present solutions for condensing flows in fractures are even somewhat comparable to Morrison's (1973) solutions for condensing flows in permeable media.

Governing Equations

The wedge-shaped fracture geometry of Fig. 1 is typical of hydrofracture applications. The propagation velocity of the fracture is often considerably less than the wave speed in the surrounding solid, so that the aperture profile $w(\theta)$ of the fracture depends on the instantaneous fluid pressure distribution $p(\theta)$, as described by the following integral formula from linear elastic fracture mechanics (Barenblatt, 1962):

$$w(\theta) = \frac{4(1-\nu)\ell}{\pi G} \int_\theta^1 \int_0^\xi \frac{(p(\zeta)-\sigma)d\zeta}{\sqrt{\xi^2-\zeta^2}} \frac{\xi d\xi}{\sqrt{\xi^2-\theta^2}} \tag{1}$$

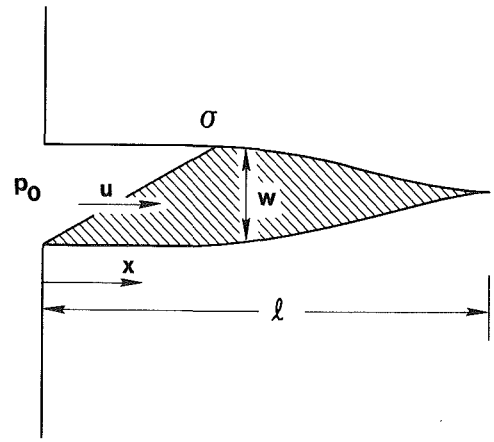

Fig. 1 Schematic of a wedge-shaped fracture in a semi-infinite medium

Contributed by the Heat Transfer Division and presented at the ASME Winter Annual Meeting, Anaheim, California, December 7-12, 1986. Manuscript received by the Heat Transfer Division January 12, 1987. Keywords: Condensation, Moving Boundaries.

Here, G and ν are the shear modulus and Poisson ratio, respectively, σ is the in situ compressive stress acting normal to the plane of the fracture, ℓ is the fracture length, and $\theta = x/\ell\,(t)$ is the normalized position along the fracture.

Rock fracturing processes are very generally described by the theory of linear elastic fracture mechanics in which the influence of the stress singularity and the inelastic zone surrounding the crack tip are accounted for by the fracture toughness K, which is a routinely measured property of rocks. In mobile-equilibrium fracturing the stress intensity at the fracture tip is continuously maintained at the critical level, as described by the balance (Barenblatt, 1962)

$$\int_0^l \frac{p(\theta)-\sigma}{\sqrt{1-\theta^2}}\,d\theta = \frac{K}{\sqrt{2\ell}} \tag{2}$$

which again applies to the geometry of Fig. 1.

The one-dimensional two-phase flow along the fracture is governed by conservation of mass, momentum, and energy for a homogeneous mixture of liquid and vapor (Shapiro, 1954; Wallis, 1969)

$$\frac{\partial}{\partial t}(\rho w)+\frac{\partial}{\partial x}(\rho w u)=0 \tag{3}$$

$$\frac{\partial}{\partial t}(\rho w u)+\frac{\partial}{\partial x}(\rho w u^2)=-\rho w\left[\frac{1}{\rho}\frac{\partial p}{\partial x}+\frac{\psi}{2}\frac{u^2}{w}\right] \tag{4}$$

$$\frac{\partial}{\partial t}(\rho w e)+\frac{\partial}{\partial x}\left[\rho w u\left(e+\frac{p}{\rho}\right)\right]=-p\frac{\partial w}{\partial t}-2q \tag{5}$$

where ρ is the mixture density, u is the fluid speed, and e is the internal energy, each averaged over the fracture cross section. In adopting a homogeneous model of the two-phase flow, we have assumed that the vapor and liquid are well mixed and, hence, share the same velocity at any axial position along the fracture. This formulation was chosen, rather than a "two-fluid" (e.g., stratified) alternative, because a layer of condensate forming on the cold walls of the crack would be subject to the Kelvin–Helmholtz instability and would not be stabilized by either surface tension (Gater and L'Ecuyer, 1970; Saric et al., 1977) or gravity (Ardon, 1980) for gas velocities in excess of a few meters per second.

In accordance with the order of magnitude estimates derived by Griffiths and Nilson (1986b), the inertial terms $u\partial u/\partial x$ and $\partial u/\partial t$ can be neglected in the momentum equation, leaving a balance between pressure forces and frictional or drag forces. The drag is incorporated through a friction factor ψ, which can be expressed in the simple analytical form

$$\psi = 2a\left(\frac{\epsilon}{w}\right)^b \tag{7}$$

This relation is based on Huitt's (1956) experimental data ($a \sim 0.1$, $b \sim 0.5$) for fully rough turbulent flows in simulated geologic fractures having roughness heights ϵ. The constants in this model might also be adjusted to fit any other set of data, such as the high Reynolds number asymptotes of a Moody chart. Moreover, with $b=0$ and $a=0.005$ the model reduces to a constant friction factor of $C_f = \psi/2 = 0.005$, which Wallis (1969) suggests as a useful rule-of-thumb estimate for homogeneous two-phase mixtures. Although the present results are limited to flows that are turbulent everywhere along the fracture, it is shown by Griffiths and Nilson (1985a) that these asymptotic solutions and their smooth-turbulent counterparts provide a good indication of the overall behavior in many applications of interest.

The lateral heat flux q from the fluid to the fracture wall is given by

$$q = h(T-T_w) \tag{7}$$

where T is the bulk temperature of the fluid at any axial location, T_w is the fracture wall temperature, and h is the convective heat transfer coefficient, which can be related to the friction factor (Kays, 1966) by way of the Reynolds/Prandtl analogy between momentum transport and energy transport in turbulent flow

$$h = \frac{1}{8}\psi\rho u C_p \mathrm{Pr}^{-2/3} \tag{8}$$

The lateral flux q is carried from the fracture wall into the surrounding solid by heat conduction

$$q = -k\frac{\partial T}{\partial y} \tag{9}$$

where k is the thermal conductivity of the wall material and y is distance into the wall. The temperature field within the wall is governed by the transient diffusion equation

$$\frac{\partial T}{\partial t} = D\,\nabla^2 T \simeq D\frac{\partial^2 T}{\partial y^2} \tag{10}$$

in which D is the thermal diffusivity and the longitudinal conduction term, $\partial^2 T/\partial x^2$, is neglected because the thermal boundary layer is very thin compared to the fracture length.

Nomenclature

a = turbulent drag constant
b = exponent in turbulent drag relation
e = internal energy
G = shear modulus
K = fracture toughness
ℓ = fracture length
N = driving pressure ratio = p_0/σ
p = fluid pressure
p_0 = fluid pressure at inlet
q = heat flux
Q^* = heat transfer parameter
R = density ratio = $(\rho_v/\rho_\ell)_0$
t = time
T = fluid temperature
u = fluid speed
U = reference speed
V = speed of evaporation interface
w = local fracture aperture
W = mass fraction of water
X = steam quality
δ = jump change across interface
Δ = overall change along fracture
ϵ = fracture surface roughness
θ = normalized position = x/ℓ
λ = normalized fracture speed = $\dot{\ell}/U$
μ = dynamic viscosity
ν = Poisson ratio
ρ = fluid density
σ = far-field confining stress
ψ = fluid friction factor

Subscripts

f = evaporation front
ℓ = liquid phase
v = vapor phase
w = wetting front
0 = inlet
+ = downstream side of interface
− = upstream side of interface

Superscripts

* = normalized or dimensionless quantity
• = overdot indicates time derivative

In general, both the convective and the conductive resistances to heat flow may be important, and the local wall temperature is controlled by their relative magnitude. Here we will consider the two limiting cases in which one mechanism, either convection or conduction, is the dominant resistance. In the convection-controlled limit the fracture wall temperature is nearly the same as the ambient temperature T_∞, so the wall is assumed to be isothermal. Conversely, in the conduction-controlled extreme, the wall temperature is nearly the same as the fluid temperature, and hence varies with position along the fracture.

To complete the problem statement it is only necessary to provide an equation of state and appropriate boundary conditions. The present paper treats a succession of problems in which the equation of state becomes progressively more complex: first, isothermal flow of an ideal gas or an incompressible liquid; then, two-phase flows separated by a sharp interface; and finally, gradual condensation of a steam/water/air mixture. In every case, however, the boundary conditions of pressure and energy at the fracture inlet are held constant in time, so that the resulting flows will have a self-similar character.

Similarity Transformation

Similarity solutions to the coupled fluid/solid governing equations are possible in situations when the following restrictions are met: (1) The confining stress σ is uniform in the far field; (2) the driving pressure is constant; (3) the flow is either isothermal or adiabatic; (4) the flow is either laminar or turbulent; and (5) the fracture toughness K is negligible. The last restriction implies that the work done in opening the fracture against the confining stress is large compared to the energy consumed at the crack tip ($\sigma >> K/\sqrt{\ell}$, as appropriate for relatively long fractures at large depths). It is shown by Nilson and Griffiths (1986) that the opposite extreme ($\sigma << K/\sqrt{\ell}$, as appropriate for surface blasting of strong rocks) is described by a closely related family of local similarity solutions in which $K/\sqrt{\ell}$ plays the role of σ.

Under the restrictions stated above, the partial differential equations in x and t can be converted to ordinary differential equations (ODEs) in $\theta = x/\ell\,(t)$. The dependent variables are first normalized as follows:

$$p^* = \frac{p}{p_0}, \quad T^* = \frac{T}{T_0}, \quad e^* = \frac{e}{e_0}, \quad \rho^* = \frac{\rho}{\rho_0},$$

$$w^* = \frac{w}{\ell}\left[\frac{\pi G}{4(1-\nu)p_0}\right], \quad u^* = \frac{u}{U} \tag{11}$$

in which the subscript "0" refers to inlet conditions and fluid velocity is scaled by a length-dependent function

$$U = \left(\frac{\ell}{\epsilon}\right)^{b/2}\left(\frac{p_0}{\rho_0 a}\right)^{1/2}\left(\frac{4(1-\nu)p_0}{\pi G}\right)^{(1+b)/2} \tag{12}$$

Then, by introduction of these transformations, the equations for the normalized opening displacement w^* and stress intensity become

$$w^* = \int_\theta^1 \int_0^\xi \frac{p^*(\zeta) - N^{-1}}{\sqrt{\xi^2 - \zeta^2}} d\zeta \frac{\xi d\xi}{\sqrt{\xi^2 - \theta^2}} \tag{13}$$

$$\int_0^1 \frac{p^*(\theta) - N^{-1}}{\sqrt{1-\theta^2}} d\theta = 0 \tag{14}$$

in which $N = p_0/\sigma$ is the ratio of driving pressure to confining stress. The relationship between pressure gradient and fluid velocity can now be written as

$$-\frac{\partial p^*}{\partial \theta} = \frac{\rho^* u^{*2}}{w^{*1+b}} \tag{15}$$

The continuity equation (3) takes the form

$$\lambda\rho^* w^* - \lambda\theta\frac{\partial}{\partial\theta}(\rho^* w^*) + \frac{\partial}{\partial\theta}(\rho^* w^* u^*) = 0 \tag{16}$$

and there can be no flow through the tip of the fracture, requiring that

$$\rho^*(u^* - \lambda\theta) = 0 \text{ at } \theta = 1 \tag{17}$$

The eigenvalue λ represents the dimensionless fracture speed

$$\lambda = \dot{\ell}^* = \dot{\ell}/U \tag{18}$$

which can be determined only by solving the system ODEs that has resulted from the transformation. Once λ is known, the fracture speed can be calculated readily from equation (18) along with the definition in (12). Note that the fracture speed is not constant; it increases with fracture length according to (12).

The energy equation must generally be solved in conjunction with the above equations, as explained in a later section. For the moment, however, we will restrict attention to isothermal flows that are governed by equations (13)–(17) alone.

Numerical solutions to (13)–(17) are calculated by the iterative method outlined below. Starting from some initial guess of λ, $p^*(\theta)$, and $T^*(\theta)$, the procedure is to:

1 calculate $w^*(\theta)$ from the integral equation (13); averaging of successive iterates affords advantageous damping;

2 calculate $u^*(\theta)$ by integration of ODE (16) starting from the leading edge of the flow where $u^* = \lambda\theta$, as generally required by (17), and integrating backward in θ to the mouth of the fracture;

3 calculate $p^*(\theta)$ and $e^*(\theta)$ by integration of ODE (15) and later the energy equation forward in θ from the mouth of the fracture, where $p^* = e^* = 1$, to the tip;

4 sequentially repeat steps 1, 2, and 3 to convergence, always using the most recent values of w^*, p^*, e^*, and u^*;

5 check to see if the integral constraint (14) is satisfied by the current $p^*(\theta)$;

6 make a better guess of λ, based on the error observed in step 5 and repeat, starting at step 1.

The aim is iteratively to adjust λ until the integral constraint is satisfied for a prescribed value of N. Alternatively, the value of λ (i.e., the fracture speed) can be prescribed and held fixed during the iterations; the integral constraint can then be used to directly calculate the corresponding value of N. Either way, convergence is fast. The double-sweep integration procedure in steps 2 and 3 is more efficient and more stable than the alternative single-sweep shooting procedures, since the double-sweep makes direct use of the known conditions at both ends of the fracture.

The ODE integrations and iterative adjustments of λ are performed using DEBDF and ZEROIN, respectively. Both of these are explained and listed by Haskell et al. (1980) and are widely available in system libraries. The reported calculations were run with 100 output stations along the fracture length, but the integrator takes intermediate steps to maintain a relative and absolute error tolerance of 10^{-4}. Quadratures are done by the trapezoidal rule.

Single-Phase Flows: Gas or Liquid

Some single-phase solutions are first presented to provide a frame of reference for later comparison with two-phase results. The only parameter that appears in the normalized equations (13)–(17) is the pressure ratio $N = p_0/\sigma$. The pressure profiles shown in Fig. 2 for incompressible liquids ($\rho^* = 1$) and ideal gas ($\rho^* = p^*$) are remarkably similar, despite the difference in equation of state. When the pressure ratio N is large, a shallow penetration is sufficient to drive the fracture ahead, i.e., to satisfy the stress intensity criterion of equation (14). For smaller N, deeper penetration is required.

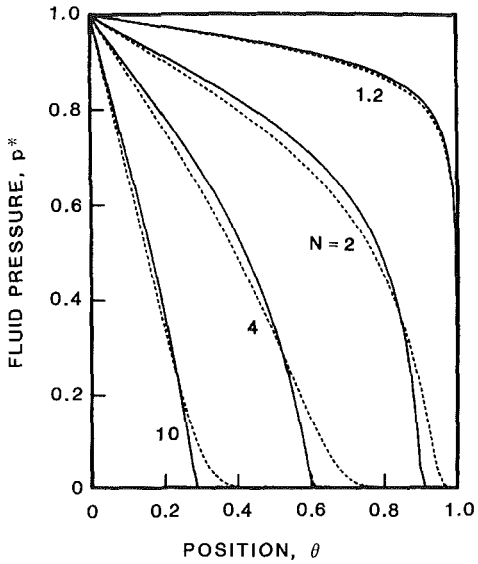

Fig. 2 Pressure distribution along fracture for turbulent flow of a gas (dotted) or liquid (solid) at various pressure ratios, $N = p_0/\sigma$

The eigenvalue or dimensionless speed, $\dot{\ell}^*$ in equation (18), is of comparable magnitude for gas and liquid flows. A reasonable approximation for fully rough turbulent flows is (Nilson and Griffiths, 1986)

$$\dot{\ell}^* \sim \text{const} \times (N \ln(N))^{3/4} \tag{19}$$

where the constant is about 0.38 for gas flows versus 0.16 for liquid flows. The gas-driven fractures run about two times faster as a result of gas expansion within the fracture. This does not imply that the dimensional speed is nearly the same for air and water, but rather that scaling fluid speeds with $U \sim (p_0/\rho_0)^{1/2}$ works for gases and liquids alike.

Conditions at the leading edge of the single-phase flows are also instructive as a prelude to the two-phase cases. In gas flows, the fluid pressure and density go exponentially to zero in the frontal portion of the fracture, and the fluid speed approaches the tip speed (Nilson, 1981)

$$u \to \dot{\ell} \text{ or } u^* \to \dot{\ell}^* \text{ as } \theta \to 1 \tag{20}$$

in order that there be no flow through the tip. In liquid flows, however, there is a distinct leading edge or wetting front θ_w, at which the trailing fluid velocity is the same as the velocity of the wetting front (Griffiths and Nilson, 1986b)

$$u = \theta_w \dot{\ell} \text{ or } u^* = \theta_w \dot{\ell}^* \text{ at } \theta = \theta_w \tag{21}$$

The fluid pressure goes to zero at this wetting front, and there is a vacuum ahead. However, the void in the tip is a mathematical consequence of assuming that the fluid is incompressible. In reality, there will be a transition from liquid to vapor as the pressure falls below the saturation pressure, as described by the two-phase solutions of the next section.

Abrupt Phase Change at a Sharp Interface

To illustrate some fundamental features of condensing and evaporating flows we first consider a simple, albeit somewhat artificial, situation in which the liquid/vapor transition occurs very abruptly at a fixed position, $\theta_f = x_f/\ell$. Such a process would occur in an isothermal flow that entered the fracture as a liquid and then flashed to vapor at the point θ_f, where the fluid pressure fell below the vapor pressure, as discussed previously by Griffiths and Nilson (1986b). Here, we briefly review those results for evaporating flow and then make a comparison with the opposite case of a condensing flow with a sharp interface.

Since the fluid is either a liquid or a vapor (not a mixture) at any position along the fracture, the equation of state can be constructed in a piecewise fashion. Assuming that the liquid is incompressible ($\rho = \rho_0$), the vapor is ideal ($\rho = p/RT$), and the temperature is everywhere uniform,

$$\rho^* = 1 \qquad \text{(liquid)} \tag{22}$$

$$\rho^* = \left(\frac{\rho_v}{\rho_\ell}\right)_0 p^* \qquad \text{(vapor)} \tag{23}$$

in which all densities are normalized to the inlet density ρ_0, and $(\rho_v/\rho_\ell)_0$ is the ratio between the vapor density (at the inlet pressure p_0) and the liquid density.

The mass balance at the evaporation front requires that

$$\rho_- (u_- - V) = \rho_+ (u_+ - V) \tag{24}$$

in which V is the interface velocity. Upon transformation to the scaled variables, noting that $V = \theta_f \dot{\ell}$ where $\theta_f = x_f/\ell$ is the normalized evaporation front location

$$u^*_- - \lambda\theta_f = \left(\frac{\rho_v}{\rho_\ell}\right)_0 p^*_f (u^*_+ - \theta_f \dot{\ell}^*) \tag{25}$$

in which $p^*_f = p_f/p_0$ is the normalized pressure at the front. Under our previous supposition that inertial forces are much smaller than pressure or drag forces, the pressure is constant across the front. That is, the pressure jump is small compared to the overall pressure drop. Finally, the isothermal supposition eliminates the need for an energy balance at the front.

Typical results for evaporating and condensing flows are shown in Figs. 3 and 4, respectively. In both cases the three dimensionless parameters that characterize the solution are chosen as follows:

$$N = \frac{p_0}{\sigma} = 2, \quad R = \left(\frac{\rho_v}{\rho_\ell}\right)_0 = \frac{1}{100}, \quad p^*_f = \frac{p_f}{p_0} = \frac{1}{2} \tag{26}$$

To obtain these sharp-front solutions, the equations were first integrated from the inlet to the point where $p^* = p^*_f$, the jump balance equation (25) was then used to cross the interface, after which forward integration was resumed. Thus the position of the phase interface was determined as a part of the solution.

It is surprising to see that the phase interface happens to reside near the middle of the fracture in both of these flows. This implies that the mean pressure gradient across the vapor is roughly the same as the mean pressure gradient across the liquid, regardless of whether the flow is evaporating or condensing.

The gas velocity is generally greater than the liquid velocity, in both evaporating and condensing flows, as seen in the curves labeled u^* in Figs. 3 and 4. The velocity contrast is even greater when measured relative to the moving θ coordinate system, that is, in terms of the curve labeled

$$\frac{u - \theta\dot{\ell}}{U} = u^* - \theta\dot{\ell}^* \tag{27}$$

At $\theta = 0$ this is simply the velocity of the liquid as it passes through the entrance plane. At θ_f^- and θ_f^+ this is the speed of the liquid and the vapor, respectively, relative to the moving evaporation front. So, in view of the mass balance (25), the relative velocity must increase by a factor of $(Rp^*_f)^{-1}$ in crossing the front. Finally, as the gas approaches the tip, its relative velocity goes to zero in order that there be no flow through the tip.

It is interesting to observe that the flow field adjusts itself such that the liquid flux passing through the phase interface is always very small. This can be seen in both Fig. 3 and Fig. 4 where $u^* - \theta\dot{\ell}^*$ is very small on the liquid side of the interface. Otherwise, there would be an enormous volume of vapor flow on the opposite side and, hence, a very steep pressure gradient.

The fracture propagation speed is generally equal to the fluid velocity at the crack tip. Thus, in an evaporating flow the

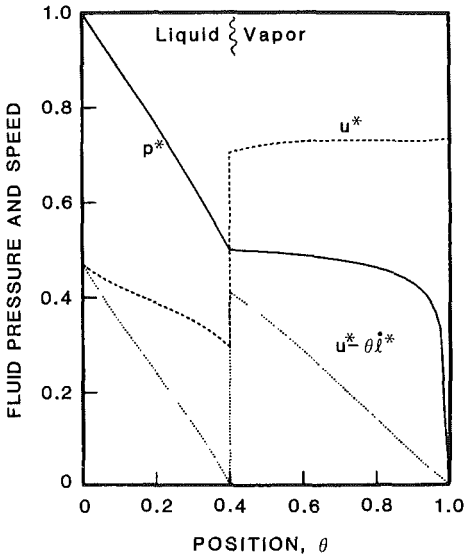

Fig. 3 Evaporation of a pure substance at a sharp interface

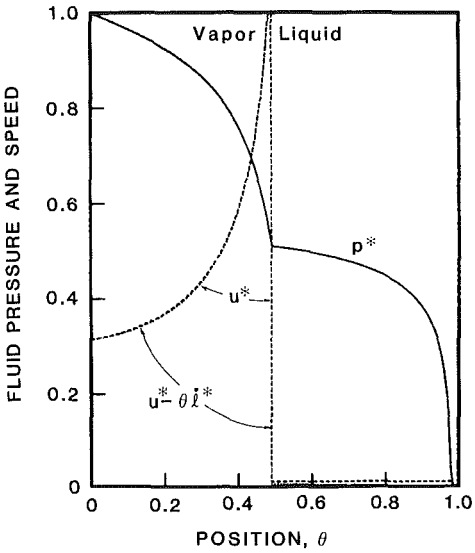

Fig. 4 Condensation of a pure substance at a sharp interface

propagation speed is comparable to the gas velocity and the liquid speed is somewhat slower. Conversely, in a condensing flow the propagation speed is comparable to the liquid velocity and the gas velocity is considerably faster. Indeed, the gas velocity is so much greater than the propagation speed, $u^* - \theta \ell^*$ is almost indistinguishable from u^* in the vapor region of Fig. 4.

Further results for evaporating flows are presented by Griffiths and Nilson (1986b) where it is shown that these two-phase flows revert to the degenerate gas-only or liquid-only solutions of Fig. 2 in the limits as $p_f^* \to 0$ or 1. In that previous work we also investigated the isothermal flow of air/water mixtures in which gradual evaporation occurs as a result of the pressure decrease along the fracture. Those flows served as a testing ground for numerically solving the self-similar transport equations in conjunction with a generalized air/water/steam equation of state. When the mass fraction of air was relatively large, the evaporation zone was spread over a large segment of the crack length. For smaller amounts of air, however, the thickness of the evaporation zone became smaller and smaller, approaching the abupt evaporation solution of Fig. 3 in the limit as the air fraction was reduced to zero. Those solutions tested the accuracy of the numerical integration procedure, including the air/water/steam equation of state, in a very severe, nearly discontinuous, case. In the next section we apply that same methodology, further supplemented by the energy equation, to investigate some more general condensing flow situations.

Gradual Condensation Controlled by Heat Transfer

The rate of condensation or evaporation is usally controlled by the rate of heat transfer between the fluid and the surrounding rock. Thus, it is generally necessary to solve the energy equation along with the other self-similar transport equations. In normalized form this is

$$\rho^* w^* (u^* - \lambda\theta) \frac{\partial e^*}{\partial \theta} + \frac{p_0}{\rho_0 e_0} \left[\frac{\partial}{\partial \theta} (u^* w^* p^*) + \lambda p^* \left(w^* - \theta \frac{\partial w^*}{\partial \theta} \right) \right]$$

$$= -Q^*_{\text{conv}} \frac{\rho^* u^*}{w^{*b}} (T^* - T_w^*) \qquad \text{(convection limited)}$$

or

$$= Q^*_{\text{cond}} \frac{\partial T^*}{\partial \eta} \qquad \text{(conduction limited)} \qquad (28)$$

where the dimensionless parameter Q^* is defined as follows for the two limiting cases of interest:

$$Q^*_{\text{conv}} = \frac{a}{2} \left[\frac{\epsilon}{\ell} \right]^b \left[\frac{\pi G}{4(1-\nu)p_0} \right]^{1+b} \left[\frac{C_p T_0}{e_0} \right] \text{Pr}^{-2/3} \qquad (29)$$

$$Q^*_{\text{cond}} = \frac{2k}{\sqrt{D}} \frac{T_0}{\rho_0 e_0} \left(\frac{p_0 a}{\rho_0} \right)^{1/4} \left(\frac{\lambda}{\ell} \frac{2-b}{2} \right)^{1/2} \left(\frac{\epsilon}{\ell} \right)^{b/4} \left(\frac{\pi G}{4(1-\nu)p_0} \right)^{(5+b)/4} \qquad (30)$$

In the convection-limited regime, the dimensionless wall temperature $T_w^* = T_w/T_0$ is prescribed and the equations can be solved without any additional information. In the conduction-limited regime, however, it is necessary to solve simultaneously the parabolic partial differential equation

$$-\left(\frac{2}{2-b} \right) \theta \frac{\partial T^*}{\partial \theta} - \frac{1}{2} \eta \frac{\partial T^*}{\partial \eta} = \frac{\partial^2 T^*}{\partial \eta^2} \qquad (31)$$

which is derived from Fourier's Law by introducing the longitudinal variable $\theta = x/\ell(t)$ along with the transverse variable $\eta = y/\sqrt{Dt}$.

The numerical solution procedure is essentially the same as before, except that the third step now includes a coupled integration of the momentum equation and the energy equation to determine $p^*(\theta)$ and $e^*(\theta)$ along the fracture. During this step the equation of state is frequently called upon to generate the corresponding values of $T^*(\theta)$ and $\rho^*(\theta)$ as well as the thermodynamic derivatives, which are needed in solving the coupled equations in terms of p^* and e^*. Also, in the case of conduction-limited heat transfer, there is one additional step in the numerical procedure wherein a marching integration algorithm is used to solve the finite-difference form of the parabolic conduction equation (31), as described by Nilson (1980).

The primary purpose of these numerical solutions is to learn how the fracture speed is influenced by cooling and condensation of the air/steam driver gas. The dimensionless parameter Q^* is a measure of the rate of energy loss to the fracture walls compared to the total rate of energy input. Note that Q^* always decreases as the fracture grows longer, so the heat transfer process becomes progressively less effective in limiting the fracture speed. Also, since Q^* decreases gradually the behavior is not truly self-similar. However, the actual behavior can be closely approximated by a sequence of local-similarity solutions for successively smaller values of Q^*, par-

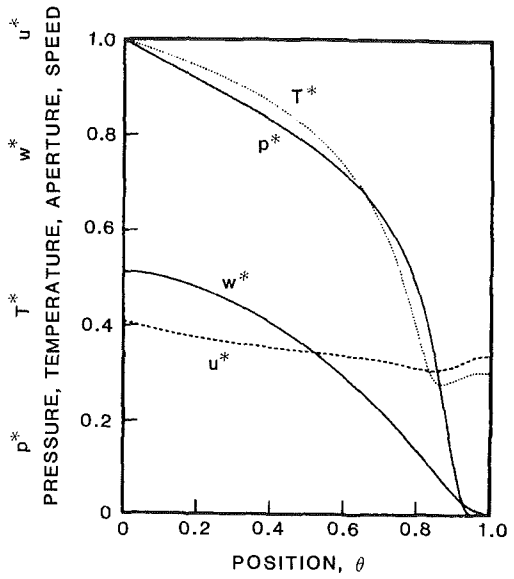

Fig. 5 Condensing flow of air/steam/water for $Q^* = 0.2$

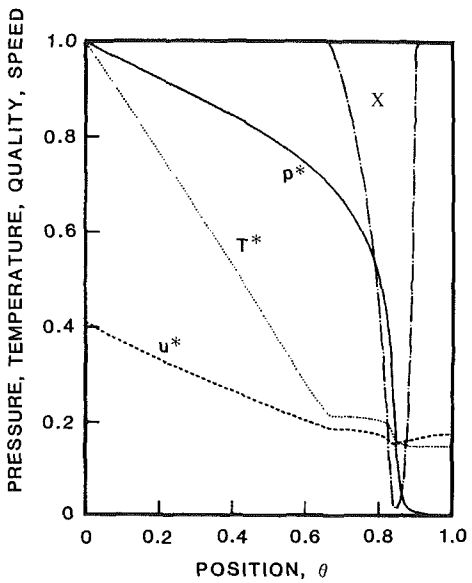

Fig. 6 Condensing flow of air/steam/water for $Q^* = 1.0$

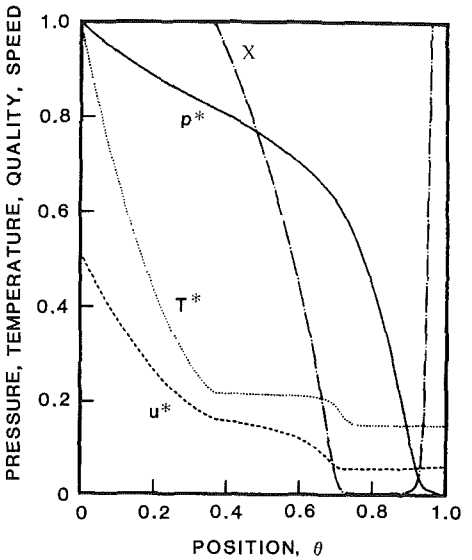

Fig. 7 Condensing flow of air/steam/water for $Q^* = 3.0$

ticularly since the behavior is truly self-similar in the limits as Q^* tends to zero (adiabatic) or infinity (isothermal and fully condensed). This local similarity approach has been applied to many problems in the fluid/thermal sciences and the results generally compare favorably with higher-order approximations.

The principal advantage of the local-similarity approach is that the influence of heat transfer is described by a single parameter Q^*, which can be readily estimated for any configuration. In formulating the problem, we have allowed for solutions that are either convection limited or conduction limited. In either instance Q^* has the same physical significance in terms of fractional heat extraction. Thus, as demonstrated for ideal gas flows by Nilson and Griffiths (1986), the dependence of the solutions on the parameter Q^* is essentially the same regardless of whether the heat transfer process is convection limited or conduction limited. For that reason we will present numerical results only for the convection-limited case, with the understanding that these should provide reasonable estimates for conduction-limited cases and even for intermediate circumstances described by the composite parameter

$$Q^*_{\text{total}} = \frac{Q^*_{\text{cond}} Q^*_{\text{conv}}}{Q^*_{\text{cond}} + Q^*_{\text{conv}}} \tag{32}$$

which recognizes that the lesser of the two thermal conductances, Q^*_{cond} from (30) and Q^*_{conv} from (29), is the controlling consideration in the heat transfer process.

The influence of steam condensation will be illustrated by a sequence of solutions for progressively larger values of Q^*. The parameters of the sample problem are chosen to be representative of the nuclear testing application while, at the same time, comparable to previously reported results for ideal gas flow. The inlet conditions are taken as $p_0 = 4$ MPa, $T_0 = 2345$ K, and $W = 0.9$ where the last indicates that the driver gas is 90 percent water by mass. The equation of state then returns the following values for the energy and density at the inlet: $e_0 = 6$ MJ/kg and $\rho_0 = 3.8$ kg/m^3. Finally, the ambient values of confining stress and temperature are defined by choosing a pressure ratio of $N = p_0/\sigma_\infty = 2$ and a temperature ratio of $T_w/T_0 = 0.15$. Note that the normalized saturation temperature corresponding to the inlet conditions is roughly $T_{\text{sat}}/T_0 = 0.25$, so considerable cooling will be required to produce condensation.

For small enough values of the heat transfer parameter there is no condensation of the water vapor, as shown in Fig. 5 where $Q^* = 0.2$. Thus, the profiles of pressure, temperature, and velocity are comparable to those presented in ideal gas flows (Nilson and Griffiths, 1986). Near the tip of the fracture, the fluid velocity approaches the propagation speed as the pressure decreases exponentially to zero. The fluid temperature at the tip is controlled by the balance between frictional heating and cooling to the wall. Thus, as apparent in Fig. 5, the fluid temperature may remain well above the wall temperature everywhere along the fracture.

Condensate begins to form near the tip of the fracture when Q^* is of order unity, as seen in Fig. 6 where the quality (X = mass water vapor/mass water total) dives sharply from unity to very near zero and then rises even more abruptly back to unity just behind the fracture tip. Thus, there is a narrow band of condensate that spans only 10 percent of the fracture length. The tip region must always be gas filled because the pressure goes to zero there and the temperature is always finite, so the tip pressure is necessarily less than the local saturation pressure. The pressure, temperature, and velocity profiles still remain quite similar to those in Fig. 5 for single-phase gas flow.

The crack is half filled with condensate for Q^* of around 3, as apparent in Fig. 7. The temperature profile now exhibits a

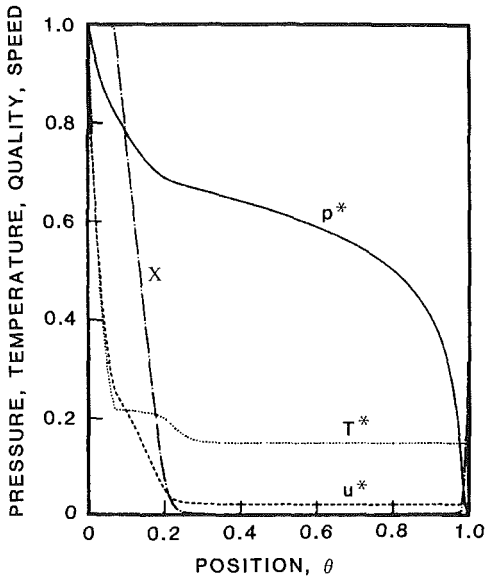

Fig. 8 Condensing flow of air/steam/water for $Q^* = 10.0$

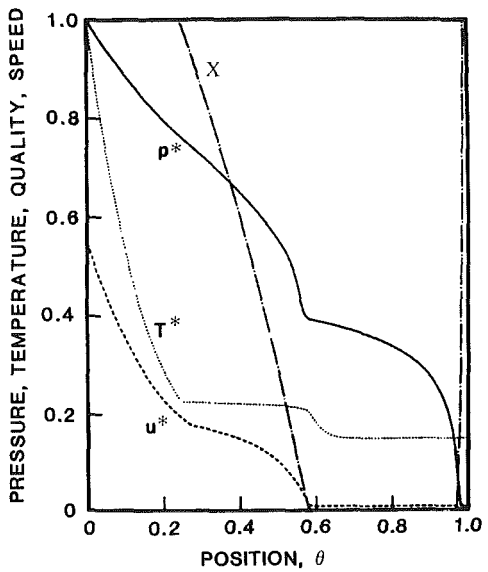

Fig. 9 Condensing flow of air/steam/water for $W = 0.999$ and $Q^* = 3$

plateaulike structure with four distinct regions: the entry region where the gas cools to the saturation condition, an intermediate plateau region where all of the water vapor is condensed, a short subcooling zone where the mixture of air and liquid water is cooled to the wall temperature, and the tip region where the fluid is in thermal equilibrium with the surroundings. The pressure profile is still surprisingly similar to the previous cases. This is because the pressure must always satisfy the integral constraint, equation (14), which ensures that the pressure loading on the walls is just sufficient to maintain a slight tensile stress at the tip.

At sufficiently large heat transfer rates there is hardly any steam in the crack, as illustrated in Fig. 8 for $Q^* = 10$. The quality is zero over the entire midsection, leaving only the narrow condensation and evaporation zones at the inlet and the tip, respectively. The character of the temperature profile is basically unchanged, but the velocity profile is tending toward the sharp-interface solution in which the gas velocity is much greater than the liquid velocity. Throughout the earlier sequence of calculations for $Q^* = 0.2$–3.0, the inlet velocity had only increased from $u^* = 0.4$ to $u^* = 0.5$, but now it is about twice that large. More importantly, the fluid speed near the tip is much smaller now, resulting in a smaller fracture speed.

At very large Q^*, the condensation and evaporation layers at the ends of the fracture become even narrower, but there is no further reduction in the fracture speed, since the fluid is already fully condensed and cooled, for all practical purposes.

Since volumetric contraction is the primary effect of condensation, the results should be sensitive to the overall density change which, in turn, depends very strongly on the mass fraction of noncondensible gas. This point is illustrated by the calculation in Fig. 9 with $W = 0.999$ and, hence, a cold fully condensed density that is essentially equal to the liquid density. Although $Q^* = 3$, the same as in Fig. 7, the amount of condensation is somewhat greater and, more importantly, the propagation speed is a few times smaller.

Fracture Propagation Speed

The primary feature of interest in these solutions is the propagation speed of the fracture, $\lambda = \dot{\ell}^*$, which is identical to the fluid velocity u^* at the tip. In the absence of condensation $\dot{\ell}^*$ was around 0.35, which is the value indicated for u^* at the crack tip in Fig. 5. However, in the nearly condensed flow of Fig. 8, the propagation speed is reduced by more than an order of magnitude to $\dot{\ell}^* \sim 0.025$.

The propagation speed of a fully condensed flow can be estimated from the scaling of velocity in equation (12) and the results of previous single-phase calculations, like those in Fig. 2, which all suggest that

$$\dot{\ell} \sim (p_0/\rho_0)^{1/2} \tag{33}$$

to a rough approximation. Thus, with a liquid density of $\rho_\ell \sim 10^3$ kg/m^3, a cold air density of $\rho_a \sim 40$ kg/m^3, and a condensible mass fraction of $W = 0.9$, the fully cooled and fully condensed inlet density is around

$$\rho_c \sim \frac{\rho_a \rho_\ell}{\rho_a W + \rho_\ell (1 - W)} \sim 300 \text{ kg/m}^3 \tag{34}$$

which is about 80 times greater than the hot inlet vapor density of 3.8 kg/m^3. Thus a crack driven by a fully cooled and condensed flow should run slower than its hot-gas counterpart by a factor of $\sqrt{80} \sim 9$ owing to the difference in density. Further, recalling that incompressible liquid flows generally run about half as fast as their ideal gas counterparts, these scaling estimates appear to be in good agreement with the numerical outcome recounted in the first paragraph of this section.

Since the limiting solutions for small and large Q^* are available, it seems reasonable to interpolate between these limits to obtain speed estimates for intermediate Q^*. The simple interpolation formula given below is in reasonable agreement with all of the previous results for ideal gas flows as well as the present results for condensing flow

$$\frac{\dot{\ell} - \dot{\ell}_{\text{cold}}}{\dot{\ell}_{\text{hot}} - \dot{\ell}_{\text{cold}}} = \exp(-Q^*) \tag{35}$$

Here, $\dot{\ell}_{\text{hot}}$ is the gas-only solution with the actual inlet density and $\dot{\ell}_{\text{cold}}$ is the fully cooled and condensed solution, which can often be approximated as liquid-only. Such a procedure is only approximate, but it does provide factor-of-two guidance for a minimal effort, and the numerical solution procedures can be used in cases where the input data are fairly well known and more accuracy is required.

Sample Calculations

The primary motivation for the present work is to estimate the speed and extent of steam-driven fractures following an underground nuclear explosion, as explained in the introduction. As an example, let us consider a rather severe case in which the cavity temperature is 2300 K, the driving fluid is 90

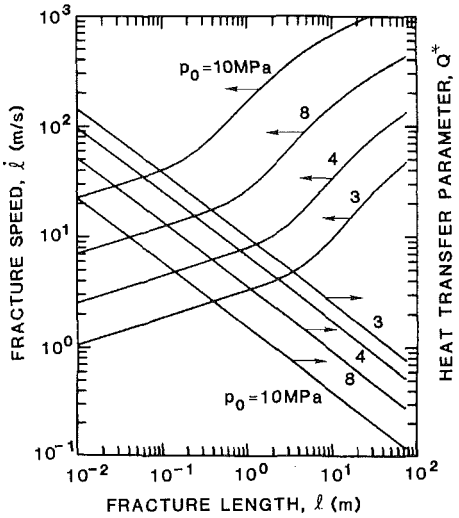

Fig. 10 Fracture speed and Q^* versus length for different choices of the driving pressure p_0

percent water (vapor), and the confining stress acting against the fracture plane is only 2 MPa. The values of Q^* and ℓ^* can then be calculated as functions of the fracture length using the algebraic approximations in equations (19) and (35) along with the definitions in equations (12), (18), (29), (30), and (32). Results are presented in Fig. 10 for four choices of driving pressure: $p_0 = 3$, 4, 8, and 10 MPa.

The decrease of Q^* with increasing fracture length is illustrated in Fig. 10 by the nearly straight lines, which fall to the right with a slope of roughly 1/2. Physically, the heat transfer process becomes less effective as the fracture grows longer because the rate of energy flow into the system is increasing faster than the rate of heat loss to the walls. As noted in the previous discussion, the transition from fully condensed cold flow to superheated gas flow is centered around $Q^* \sim 1$. Thus, the flow driven by 10 MPa will begin transition at a fracture length of around 0.5 m, and the flow will be fully dried out and unaffected by heat transfer once the fracture reaches a length of around 5.0 m. When the driving pressure is smaller, heat transfer plays a more prominent role, as in the flow driven by 3 MPa (overpressure of $p_0 - \sigma \sim 1$ MPa), which undergoes wet/dry transition at lengths ranging from 5 to 50 m.

The increase in fracture speed with increasing length is illustrated in Fig. 10 by the family of lines that rise to the right. The slope is $b/2 = 1/4$ in both the early fully condensed regime and in the late fully dry regime. However, the speed increases much more rapidly in the transition regime when dryout is occurring. The speed is very sensitive to the driving pressure, increasing from 10 m/s to 1000 m/s for pressures of 3 MPa to 10 MPa.

The implication of these results is that short fractures driven by moderate pressures will grow very slowly because of fluid condensation. But once they reach a critical length, typically around 10 m, condensation will no longer be a controlling consideration. This suggests that small-scale experiments may tend to exaggerate the effectiveness of condensation in limiting fracture growth. Also, at the nuclear testing scale where the cavity radius is measured in tens of meters, it is possible that fractures might reach beyond the critical length during the "dynamic" phase of the rock motion when the compressive stresses around the cavity are relatively small. This does not, however, imply that containment will be threatened, but rather that other mechanisms such as rebound, cavity depletion, and seepage losses into the permeable fracture walls will then be the primary mechanisms that limit the fracture growth, as discussed by Griffiths and Nilson (1985b).

Summary and Discussion

Similarity solutions have been presented for some fundamental problems of steam-driven fracture propagation. The flow in the fracture was assumed to be one dimensional, homogeneous, and fully turbulent. The response of the solid was modeled using two-dimensional integral solutions from linear elastic fracture mechanics.

The rate of condensation within the crack was controlled by the rate of heat loss to the walls, which is characterized by the dimensionless parameter Q^*. For small values of Q^*, heat transfer is unimportant and the present solutions reduce to previous results for superheated gas flow. For large Q^*, the flow is fully cooled and condensed and is, again, comparable to previous single-phase flows. The behavior at intermediate Q^* lies between these extremes.

The structure of the condensing flows is characterized by very steep gradients in the regions of condensation and reevaporation at opposite ends of the crack. It is easy to imagine that a finite-difference grid might entirely overlook or seriously smear these boundary layers. Moreover, the transport equations are very strongly coupled and sometimes degenerate within the two-phase zones. In such severe circumstances, the self-similar transformation to ordinary differential equations is particularly helpful in resolving the boundary layers and obtaining reliable benchmark solutions.

Despite the complexity of the flow structure, the propagation speed was found to be a simple monotonically decreasing function of Q^*. Thus, it is possible to estimate the speed of steam-driven fractures based on simple algebraic relationships.

Sample calculations show that the influence of condensation generally decreases as the fracture grows longer. Thus, a flow which begins with fully condensed water in the crack will gradually dry out and progressively accelerate until it is essentially unaffected by the cold fracture walls. This transition is centered around $Q^* \sim 1$, which corresponds to a fracture length of 0.5–5.0 m for parameters typical of underground nuclear tests.

Although the present analysis of condensing flow has not yet been tested against experimental data, many other features of the mathematical model have been validated by comparison of numerical calculations with the results of air-driven (Griffiths et al., 1984) and propellant-driven (Nilson et al., 1985) fracturing experiments. The present similarity solutions will serve as a guideline for the future implementation of condensing flow in a generalized method-of-lines fracture simulator (Griffiths and Nilson, 1986a), which can then be tested against the results of some steam-driven fracturing experiments which have already been conducted at the Nevada Test Site (Lagus et al., 1983).

Acknowledgments

This work was performed by the U.S. Department of Energy at Sandia National Laboratories under Contract No. DE-AC041-76DP00789.

References

Ardon, K.H., 1980, "One-Dimensional Two-Fluid Equations for Horizontal Stratified Two-Phase Flow," *Int. J. Multiphase Flow*, Vol. 6, pp. 295–304.

Barenblatt, G. I., 1962, "The Mathematical Theory of Equilibrium Cracks in Brittle Materials," *Adv. Appl. Mech.*, pp. 55–129.

Gater, R. A., and L'Ecuyer, M. R., 1970, "A Fundamental Investigation of

the Phenomena That Characterize Liquid-Film Cooling," *Int. J. Heat Mass Transfer*, Vol. 13, pp. 1925–1939.

Griffiths, S. K., Smith, C. W., and Nilson, R. H., 1984, "Gas Fracturing: Numerical Calculations and Field Experiments," *Proc. 25th Symp. on Rock Mech.*, Northwestern Univ., pp. 157–164.

Griffiths, S. K., and Nilson, R. H., 1985a, "Analysis of Fluid/Solid Interaction in Hydraulic Fracturing: Transition Between Laminar and Turbulent Flow," in: *Fluid Transients in Fluid-Structure Interactions,* ASME FED–Vol. 30, pp. 31–40.

Griffiths, S. K., and Nilson, R. H., 1985b, "Gas-Driven Fractures in Nuclear Test Containment," *Proc. 3rd Symposium on Containment of Underground Nuclear Explosions*, Lawrence Livermore National Laboratories, CONF-850953, Vol. 1, pp. 355–371.

Griffiths, S. K., and Nilson, R. H., 1986a, "Hybrid Analytical/Numerical Computation of Heat Transfer in a Gas-Driven Fracture," ASME JOURNAL OF HEAT TRANSFER, Vol. 108, pp. 585–590.

Griffiths, S. K., and Nilson, R. H., 1986b, "Transient Evaporating Flow in a Fluid-Driven Fracture," in: *First Intl. Multiphase Fluids Transients Symp.*, ASME FED-Vol. 14, pp. 75–84.

Haskell, K. H., Vandevender, W. H., and Walton, E. L., 1980, "The SLATEC Mathematical Subprogram Library: SNLA Implementation," SAND80-2792, Sandia National Laboratories, Albuquerque, NM.

Huitt, J. L., 1956, "Fluid Flow in Simulated Hydraulic Fractures," *AIChE Journal*, Vol. 2, pp. 259–264.

Kays, W. M., 1966, *Convective Heat and Mass Transfer*, McGraw-Hill, New York.

Keller, C. E., Davis, A. H., and Stewart, J. N., 1974, "The Calculation of Steam Flow and Hydraulic Fracturing in a Porous Medium With the KRAK Code," Los Alamos Scientific Laboratories, LA-5602, MS.

Lagus, P. L., Peterson, E. W., and Wu, H. E., 1983, "In Situ Steam Fracturing Experiments," *Proc. 2nd Symp. on Containment of Underground Nuclear Explosions*, Lawrence Livermore National Laboratories CONF-830882, Vol. 2, pp. 197–230.

Morrison, F. A., Jr., 1973, "Transient Multiphase Multicomponent Flow in Porous Media," *Int. J. Heat Mass Transfer*, Vol. 16, pp. 2331–2342.

Nilson, R. H., 1980, "Transient Two-Dimensional Diffusion Along a High Diffusivity Lamina Which Bisects a Half-Space," *Journal of Eng. Math.*, Vol. 14, pp. 263–282.

Nilson, R. H., 1981, "Gas-Driven Fracture Propagation," ASME *Journal of Applied Mechanics*, Vol. 48, pp. 757–762.

Nilson, R. H., and Griffiths, S. K., 1983, "Numerical Analysis of Hydraulically-Driven Fractures," *Journal of Computer Meth. Appl. Mech. Eng.*, Vol. 36, pp. 359–370.

Nilson, R. H., Proffer, W., J., and Duff, R. E., 1985, "Modelling of Gas-Driven Fractures Induced by Propellant Combustion in a Borehole," *Int. Journal of Rock Mech. Min. Sci.*, Vol. 22, pp. 3–19.

Nilson, R. H., and Griffiths, S. K., 1986, "Similarity Analysis of Energy Transport in Gas-Driven Fractures," *Int. J. Fracture*, Vol. 30, pp. 115–134.

Nilson, R. H., and Morrison, F.A., 1986, "Transient Gas or Liquid Flow Along a Preexisting or Hydraulically-Induced Fracture in a Permeable Medium," ASME *Journal of Applied Mechanics*, Vol. 53, pp. 157–165.

Pitts, J. H., and Brandt, H., 1977, "Gas Flow in a Permeable Earth Formation Containing a Crack," ASME *Journal of Applied Mechanics*, Vol. 44, pp. 553–558.

Saric, W. S., Touryan, K. J., and Scott, M. R., 1977, "Stability of Slag in Turbulent MHD Boundary Layers," *AIAA Journal of Energy*, Vol. 1, pp. 108–114.

Shapiro, A. H., 1954, *The Dynamics and Thermodynamics of Compressible Fluid Flow*, Vol. II, Ronald Press, New York.

Teller, E., Talley, W. K., Higgins, G. H., and Johnnson, G. W., 1968, *The Constructive Uses of Nuclear Explosives*, McGraw-Hill, New York.

Wallis, G. B., 1969, *One-Dimensional Two-Phase Flow*, McGraw-Hill, New York.

The Properties of Steam: Current Status

P. G. Hill

R. D. C. MacMillan

Department of Mechanical Engineering,
University of British Columbia,
Vancouver, British Columbia V6T 1W5,
Canada

A review has been made of progress in the past two decades on measurement and correlation of the properties of steam. Data bases available in 1966 and 1986 for formulation and evaluation of equations of state are described and contrasted. Progress in the formulation of wide-ranging fundamental equations is outlined with particular reference to refinement in understanding of the critical region. Consistency of data sets is discussed and attention is drawn to areas where further work is needed. The results of continuing work on correlation of viscosity and thermal conductivity are cited.

1 Introduction

In the past two decades substantial advances have been made in knowledge of the thermodynamic and transport properties of steam, and in the representation of these properties by wide-ranging algebraic formulations.

A large number of highly accurate data have been reported on density, speed of sound, specific heats, and throttling coefficients. The thermodynamic consistency of different kinds of data in different regions has been closely examined, with the help of (local or global) fundamental equations of state.

The compressed liquid states are defined experimentally with high-precision density data at pressures up to 100 MPa and at temperatures up to 500°C, and there is an abundance of data of greater uncertainty to nearly 1000 MPa and nearly 1000°C. At low temperatures (less than 200°C) density data have been reported for pressures up to 2000 MPa. Speed of sound and isobaric specific heat data are also abundantly available for the compressed liquid states. The lines of maximum density of saturated liquid states have been quite precisely defined from these data.

The vapor states are defined to some extent by density data (which, particularly at temperatures much less than the critical temperature, and in near-saturation states, tend to have considerable uncertainty), and to some extent by a small number of specific heat and speed of sound data. However, the throttling data (Joule–Thomson and isothermal coefficients) provide a valuable description of the departure of vapor states (up to 5 MPa and 800°C) from the ideal gas behavior.

The critical parameters for H_2O have recently been redetermined in light of abundant new data of different kinds in the critical region and with the benefit of improved understanding of the critical point singularity.

The saturation states of H_2O have been redetermined with the help of new data on liquid densities and vapor pressure (although still with heavy reliance on the classical work of Osborne et al., 1937, 1939) and the results are available in equations that are continuous between triple point and critical temperatures, and that give vapor pressure and equilibrium saturated liquid and vapor densities, and enthalpies all as functions of temperature.

In recent years numerous data have been reported on densities and speeds of sound for the metastable states, both liquid and vapor.

Although limited-range equations have been shown to be very useful, the major emphasis in the past two decades on thermodynamic property formulations has been in canonical equations that cover the entire range between triple point pressure and temperature to perhaps 1000 MPa and 1000°C. Although these equations, in which the Helmholtz free energy is written as a function of density and temperature, may not be as convenient as those that have pressure and temperature as the independent variables, they have the great advantage of avoiding the not-always-smooth patching together of the piecewise valid equations of, e.g., the 1967 IFC (International Formulating Committee) equations. The former have, in addition, the merit of guaranteeing thermodynamic consistency of all thermodynamic properties over the entire range of validity of the fundamental equations.

The progressive development of the four principal examples of this equation (Keenan et al., 1969; Pollak, 1974; Haar et al., 1984; Hill, 1987) will be described in this paper. The principal achievements have been in extending the range and accuracy of the representation of data and, most recently, in the inclusion of the full implications of the critical point singularity into a single wide-range fundamental equation, which represents all data within what is believed to be the experimental uncertainty.

As with thermodynamic properties, so with the transport properties. There have been substantial improvements in recent years in the accuracy and extent of the data base and in the development of formulations that properly represent the important influence of the critical region singularity.

2 Thermodynamic Property Data

To formulate an accurate wide-ranging equation of state the data base must be selected with careful attention to tests of consistency between data sets of the same kind, and tests of compatibility of data sets of different kinds. Since its formation in 1968 (and previously by predecessor working groups) Working Group A (Equilibrium Thermodynamic Properties) of the International Association for the Properties of Steam has devoted much effort to assessment of the data base, using various fundamental equations of state as common bases for comparison of data sets.

The growth in the size of the data base that has survived such critical scrutiny can be appreciated by comparing two sets of data on the thermodynamic properties of steam. The first of these, termed the 1966 data base, was that used in the formulation of the Keenan et al. (1969) equation, which first demonstrated the feasibility of a single fundamental formulation continuously valid over all single-phase liquid and vapor states over a wide range of temperatures and pressures. The second data set here referred to as the 1986 data base replaces much of the 1966 data base with data of higher accuracy, wider range, and with data of additional kinds, e.g., speed of sound.

Each of these data bases is divided into two sections: the

Contributed by the Heat Transfer Division and presented at the ASME Winter Annual Meeting, Anaheim, California, December 7–12, 1986. Manuscript received by the Heat Transfer Division January 9, 1987. Keywords: Thermophysical Properties.

Table 1 1966 correlation data base

Reference	Property	Range of t, °C	P, MPa
Friedman and Haar (1954)	C_{po}	0–1300	
Bridgeman and Aldrich (1965)	t_{crit}, v_{crit}		
Bridgeman and Aldrich (1964)	P_{sat}		
Osborne et al. (1937, 1939)	v_f, v_g, h_f, h_g	0– 374	
Kell and Whalley (1965)	pvT	0– 150	1–100
Keyes and Smith (1934)	pvT	30– 374	1– 35
Holser and Kennedy (1958)	pvT	120– 400	10–140
Holser and Kennedy (1959)	pvT	400–1000	10–140
Juza et al. (1966a)	pvT	100– 350	30–150
Rivkin and Akhundov (1962)	pvT	360– 420	5– 38
Rivkin and Akhundov (1963)	pvT	370– 500	5– 60
Vukalovich et al. (1961)	pvT	400– 650	5–120
Vukalovich et al. (1962)	pvT	700– 900	5–120

Table 2 1966 evaluation data base

Reference	Property	Range of t, °C	P, MPa
Keyes et al. (1936)	pvT	300–460	6–40
Keyes (1962),(1949)	B		
Goff and Gratch (1945)	B		
Havelick and Miskowsky (1936)	h	150–550	
Egerton and Callendar (1960)	h	200–600	
Angus and Newitt (1966)	h	400–700	
Davis and Keenan (1929)	$(\partial t/\partial p)_h$	125–350	
Juza et al. (1966b)	$(\partial t/\partial p)_h$	130–190	
Knoblauch and Winkhaus (1915a, b)	C_p	258–500	
Knoblauch and Koch (1928)	C_p		
Koch (1932a, b)	C_p	340–500	
Sirota and Mal'tsev (1962a)	C_p	300–500	
Sirota et al. (1963)	C_p	340–600	
Sirota and Grishkov (1966)	C_p	200–700	

Table 3 1986 correlation data base

Reference	Property	Region	Range of t, °C	P, MPa
Woolley (1980)	C_{p0}		50–2000 K	
Osborne et al. (1933)	P_{sat}		100–t_{crit}	
Stimson (1969)	P_{sat}		25–100	
Guildner et al. (1976)	P_{sat}		0.01	
Kell (1977)	v_f		0–150	
Kell et al. (1985)	v_f		150–350	
Osborne et al. (1937)	v_f		350–t_{crit}	
	h_f, v_g, h_g		100–t_{crit}	
Osborne et al. (1939)	h_f, v_g, h_g		0–100	
Kell and Whalley (1975)	PvT	liq	0–150	0–100
Kell et al. (1978)	PvT	liq	150–350	P_{sat}–100
Kell et al. (1985)	PvT	liq	150–350	P_{sat}–100
	PvT	vap	250–350	2.7–P_{sat}
	PvT	supercrit	375–500	2.7–100
Kell and McLaurin (1977)	PvT	vap	150–275	0.2–P_{sat}
Rivkin et al. (1966)	PvT	critical region		
Rivkin and Akhundov (1963)	PvT	critical region		
Vukalovich et al. (1961)	PvT	supercrit	400–650	5–120
Vukalovich et al. (1962)	PvT	supercrit	700–900	5–120
Grindley and Lind (1971)	PvT	high press	30–150	100–800
Hilbert (1979)	PvT	high press	150–600	100–400
Maier and Franck (1968)	PvT	high press	200–850	100–600
Koster and Franck (1969)	PvT	high press	0–600	600–1000
Bridgman (1942)	PvT	high press	25–175	500–5000

first used in formulation of the equation of state and the second typically used for independent evaluation of the equation.

The Keenan et al. (1969) equation and its successors referred to above all express the Helmholtz free energy as a function of density and temperature and are formulated with property data, e.g., pressure, enthalpy, and isochoric specific heat, which can be used in a linear least-squares fit of such data, duly weighted. Other data, e.g., speed of sound and isopiestic specific heat, are reserved for independent evaluation of the equations. This is why the 1966 and 1986 data bases described below are divided into "formulation" and "evaluation" groups.

2.1 1966 Data Base. Table 1 provides the temperature

Nomenclature

a = speed of sound
B = second virial coefficient
C_p = isopiestic specific heat
C_v = isochoric specific heat
h = specific enthalpy
P = pressure
P_{sat}, P_s = saturation vapor pressure
s = entropy
T = thermodynamic temperature
u = specific internal energy
v = specific volume
δ = uncertainty
μ = chemical potential
ρ = density
ψ = Helmholtz free energy $= u - Ts$

Subscripts

0 = zero pressure
crit, c = critical point
f = saturated liquid
g = saturated vapour

Table 4 1986 evaluation data base

Reference	Property	Region	Range of t, °C	P, MPa
Gildseth et al. (1972)	PvT	liq	0–80	0.1
Kell (1977)	PvT	liq	−30–150	0.1
Grigor'ev et al. (1974)	PvT	liq	20–360	16–80
Zubarev et al. (1977a, b)	PvT	supercrit	400–900	0–200
Aleksandrov and Larkin (1974)	PvT	critical	340–380	3–100
Hanafusa et al. (1983)	PvT	critical	370–380	21–40
	P_{sat}	critical	370–373.5	
Del Grosso and Mader (1972)	a	liq	0–95	0.1
Aleksandrov and Larkin (1976)	a	liq	−3–374	0.1–70
Aleksandrov and Kochetov (1979)	a	liq	−7–150	5–100
Aleksandrov and Kochetov (1980)	a	liq	200–400	50–100
Erokhin and Kal'yanov (1980)	a	supercrit	374–500	0–50
Novikov and Avdonin (1968)	a	vap	150–330	0–P_{sat}
Holton et al. (1968)	a	liq	0–80	0.1–1000
Petitet et al. (1985)	a	supercrit	200–700	50–300
Petitet et al. (1983)	a	liq	−20–20	0.1–460
Evstefeev et al. (1979)	a	liq(meta)	150–300	0.1–10
Sirota and Mal'tsev (1962a)	c_p	liq	300–370	12–22
		supercrit	375–500	22–27
Sirota and Timrot (1956)	c_p	vap	200–375	2–12
Sirota and Mal'tsev (1962b)	c_p	vap	350–375	6–20
Sirota and Mal'tsev (1959)	c_p	supercrit	12–500	2.5–49
Sirota and Mal'tsev (1960)	c_p	supercrit	450–600	30–50
Sirota et al. (1963)	c_p	supercrit	340–600	60–80
Sirota and Grishkov (1966)	c_p	supercrit	220–700	40–100
Sirota et al. (1970)	c_p	supercrit	−2–35	29–98
Angell et al. (1982)	c_p	liq(meta)	−40–10	0.1
Baehr and Schomacher (1975)	c_v	liq, vap	280–t_{crit}	
		supercrit	t_{crit}–420	
Ertle et al. (1980)	$(\partial t/\partial p)_h$	vap	155–800	0–5
LeFevre et al. (1975)	virial	vap	0–1250	
Wormald (1964)	$(\partial h/\partial p)_t$	vap	40–140	
Osborne et al. (beta)	$T_{vf}(dp_{sat}/dt)$		0–100	P_{sat}
(1939)(alpha)	$h_f - h_{fg}(v_f/v_{fg})$			
(gamma)	$Tv_g(dp_{sat}/dt)$			
Osborne et al. (1937)	α, β, γ		100–374	P_{sat}
Rogener and Soll (1980)	$(\partial t/\partial p)_s$	liq	3–100	0–80
Aleksandrov et al. (1981)	ρ_{max},	liq	−3–4	0.1–30
	PvT	liq	0–100	0.1–100

and pressure ranges available for pvT property measurements and cites the values used in definition of the saturation states, as well as the zero-pressure specific heat calculations of Friedman and Haar (1954). At that time the best available determinations of the critical parameters were those of Bridgeman and Aldrich (1965).

It should be noted that the values of Osborne et al. (1939) are themselves calculated from correlations of their data. In addition, only the data at 300°C of Holser and Kennedy (1958) were included in the correlation, and similarly only the high-pressure data of Juza et al. (1966) were included.

Table 2 shows the corresponding evaluation data base.

2.2 1986 Data Base. The 1986 correlation data base is presented in Table 3; it may be regarded as typical of the data used in recent formulations.

It is important to note that the v_f values presented in Kell (1977) are calculated from a correlation of relative density measurements at 0.1 MPa in combination with a saturation pressure correlation. While ordinarily unsmoothed data are to be preferred as input to a correlation procedure, these values benefit from the exceptional accuracy of numerous density observations at atmospheric pressure. Similarly, the h_g and h_f values of Osborne et al. (1937, 1939) are obtained from directly measured quantities plus a correlated function; the calculation of v_f and v_g requires the use of a saturation pressure correlation in combination with h_f and h_g.

The corresponding evaluation data base is shown in Table 4.

The 1986 correlation data base contains data that extend to much higher pressures than do those available in the 1966 correlation data base. In addition, the current evaluation data base allows an extremely comprehensive test of a particular correlation, as compared to that available in 1966. A comparison of the consistency of some of the data in the correlation data base will follow a review of the selected correlations of a number of authors in the field.

2.3 Skeleton Tables. The 1985 Skeleton Tables released by the International Association for the Properties of Steam contain two tables of the thermodynamic properties of the single-phase states of ordinary water substance. The first table gives the most probable specific volumes and associated tolerances for temperatures in the range 273.15 K to 1073.15 K and pressures up to 1000 MPa. The second table gives the most probable specific enthalpy values with their associated tolerances for the same range of temperatures and pressures. The third table provides the most probable thermodynamic property values for the coexisting vapor–liquid phases between the triple point and the critical point. With this release the IAPS has withdrawn its authorization of the 1963 Skeleton Tables.

The methods of deducing the values shown in the volume and enthalpy skeleton tables are described by Sato et al. (1981) who estimated most probable volume values by considering PvT only. The methods used in formulating algebraic relationships for the saturation liquid and vapor volumes, saturation liquid and vapor enthalpies, and saturation pressures are given by Saul and Wagner (1987) (see also Wagner and Sengers, 1986). In contrast to the procedures employed in formulating wide-ranging fundamental equations of state, the methods for constructing the skeleton tables do not in general allow for simultaneous treatment of different kinds of data. Insofar as the volume and enthalpy tables may be taken as the definitions of continuous thermodynamic surfaces, there is no guarantee that the volume and enthalpy surfaces are thermodynamically consistent. The skeleton tables of volume and enthalpy may therefore be used as representative of property values and

uncertainties but are not recommended as the data for formulation of an equation of state.

3 Saturation States

Because the saturation vapor pressure is known to high accuracy (e.g., 20 to 40 ppm below 100°C, 200 ppm above) it is convenient to have a formulation that represents the vapor pressure data within experimental uncertainty in a single function continuously valid between the triple point and the critical point temperature. An equation that meets these criteria has been provided by Saul and Wagner (1987)

$$\ln\left(\frac{P_s}{P_c}\right)=\frac{T_c}{T}(a_1\tau+a_2\tau^{1.5}+a_3\tau^3+a_4\tau^{3.5}+a_5\tau^4+a_6\tau^{7.5})$$

where $\tau=1-T/T_c$, $T_c=647.14$ K, $P_c=22.064$ MPa, and

$a_1 = -7.85823$ $\quad a_4 = +22.6705$

$a_2 = 1.83991$ $\quad a_5 = -15.9393$

$a_3 = -11.7811$ $\quad a_6 = 1.77516$

Saul and Wagner (1987) have also provided formulations for the saturation liquid density ρ_f and the saturated vapor density ρ_g. These supersede coefficients set out in Wagner and Saul (1984), are continuously valid between triple point and critical temperatures, and are given by

$$\frac{\rho_f}{\rho_c}=1+b_1\tau^{1/3}+b_2\tau^{2/3}+b_3\tau^{5/3}+b_4\tau^{16/3}+b_5\tau^{43/3}+b_6\tau^{110/3}$$

with

$$\tau=1-T/T_c,\quad T_c=647.14\ \text{K},\quad \rho_c=322\ \text{kg/m}^3 \qquad (2)$$

and

$b_1 = 1.99206$ $\quad b_4 = -1.75263$

$b_2 = 1.10123$ $\quad b_5 = -45.4485$

$b_3 = -0.512506$ $\quad b_6 = -675615.$

and

$$\ln\left(\frac{\rho_g}{\rho_c}\right)=c_1\tau^{2/6}+c_2\tau^{4/6}+c_3\tau^{8/6}+c_4\tau^{18/6}+c_5\tau^{37/6}+c_6\tau^{71/6} \qquad (3)$$

where $\tau=1-T/T_c$, $T_c=647.14$ K, $\rho_c=322$ kg/m^3, and

$c_1 = -2.02957$ $\quad c_4 = -17.3151$

$c_2 = -2.68781$ $\quad c_5 = -44.6384$

$c_3 = -5.38107$ $\quad c_6 = -64.3486$

Saul and Wagner (1987) have also provided equations for obtaining the saturation liquid enthalpy h_f and the saturation vapor enthalpy h_g. These are

$$\frac{h_f}{\text{J/g}}=\frac{\alpha}{\text{J/g}}+10^3\frac{(T/K)}{(\rho_f/\text{kg m}^{-3})}\left(\frac{dp_s}{dT}\right)\Big/\left(\frac{\text{MPa}}{\text{K}}\right)$$

and

$$\frac{h_g}{\text{J/g}}=\frac{\alpha}{\text{J/g}}+10^3\frac{(T/K)}{(\rho_g/\text{kg m}^{-3})}\left(\frac{dp_s}{dT}\right)\Big/\left(\frac{\text{MPa}}{\text{K}}\right)$$

in which

$$\frac{\alpha}{\text{J/g}}=\frac{d_0}{\text{J/g}}+d_1\theta^{-19}+d_2\theta+d_3\theta^{4.5}+d_4\theta^5+d_5\theta^{54.5}$$

where $\theta = T/T_c$

$d_1 = -0.571756\times10^{-7}$ $\quad d_4 = -137.181$

$d_2 = 2689.81$ $\quad d_5 = 0.968874$

$d_3 = 129.889$ $\quad d_0 = -1135.481615639$ J/g

4 Critical Point

Levelt Sengers et al. (1985) have reviewed critical region thermodynamic data, reassessed experimental uncertainty, and deduced the critical point parameters in the light of new knowledge of the critical point singularity (see Section 5). Their results are

$$T_c=(647.14+\delta)\text{K}$$

$$P_c=(22.064+0.276\delta\pm0.005)\text{MPa}$$

$$P_c=(322\pm3)\text{kg/m}^3$$

in which $\delta=0.00\pm0.10$.

The International Association for the Properties of Steam has issued a release recommending these values.

5 Critical Region

It has been shown (see Levelt Sengers et al., 1976, for example) that steam has singular behavior near the critical point, which cannot be represented adequately by any nonsingular equation of state. Any equation of state that is analytic, i.e., has zero or finite derivatives with respect to density or temperature at the critical point, is unable to represent the actual behavior of the isochoric specific heat (which goes to infinity at the critical point), the shape of the saturation curve on the density-temperature plane, the shape of the critical isotherm, and the shape of the saturation pressure curve close to the critical point. Very close to the critical point all fluids manifest the same behavior, which is represented accurately by results of the theory of critical phenomena. Taking these factors into account Levelt Sengers et al. (1983) have developed a new equation of state for steam in the critical region. The equation has the form of a potential function

$$\bar{P}=\bar{P}(\bar{\mu},\ \bar{T})$$

in which

$$\bar{P}=\frac{P\ T_c}{P_c T},\quad \bar{\mu}=\frac{\mu\ \rho_c T_c}{P_c T},\quad \text{and}\quad \bar{T}=-\frac{T_c}{T}$$

and in which P is the pressure, μ the chemical potential, T the temperature, ρ the density, and the subscript c denotes the critical state.

This fundamental relationship can be shown to be equivalent to the dependence of a dimensionless Helmholtz free energy on dimensionless density and temperature

$$\bar{\psi}_n=\bar{\psi}_n(\bar{\rho},\ \bar{T})$$

in which $\bar{\psi}=\psi/RT$, ψ being the Helmholtz free energy and R the gas constant, and $\bar{\rho}=\rho/\rho_c$, $\bar{T}$ being the same as given above. The subscript n denotes "near" the critical point; this includes the region 644–693 K in temperature and 200–420 kg/m^3 in density. The potential function is expressed as

$$\bar{P}=\bar{P}_0(\bar{T})+\Delta\bar{\mu}+\bar{P}_{11}\Delta\bar{\mu}\Delta\bar{T}+\Delta\bar{P}$$

in which

$$\Delta\bar{T}=\bar{T}+1$$

$$\Delta\bar{\mu}=\bar{\mu}-\bar{\mu}_0(\bar{T})$$

and

$$\bar{\mu}_0(\bar{T}) = \bar{\mu}_c + \sum_{j=1}^{3} \bar{\mu}_j (\Delta\bar{T})^j$$

$$\bar{P}_0(\bar{T}) = 1 + \sum_{j=1}^{3} \bar{P}_j (\Delta\bar{T})^j$$

$$\Delta\bar{P} = \sum_{i=0}^{1} r^{2-\alpha_i} a k_i p_i(\theta)$$

The dimensionless density $\bar{\rho}$ is obtained from the potential function by differentiation

$$\bar{\rho} = 1 + P_{11}\Delta\bar{T} + \left(\frac{\partial\Delta\bar{P}}{\partial\Delta\bar{\mu}}\right)_{\Delta\bar{T}}$$

With given values of density and temperature it is necessary first to solve iteratively for $\Delta\bar{\mu}$ using this equation and the parametric relationships

$$\Delta\bar{\mu} = r^{\beta\delta} a\theta(1-\theta^2)$$

$$\Delta\bar{T} = r(1-b^2\theta^2) - c\Delta\bar{\mu}$$

in which r and θ are the arguments of the $\Delta\bar{P}$ term alone. From the potential function the dimensionless density $\bar{\rho}$, energy $\bar{U} = \rho U/P_c$, specific heats $\bar{C}_v = C_v\,\rho T_c/P_c$ and $\bar{C}_p = C_p\,\rho T/P_c$, and compressibility $\bar{X}_T = (\partial\bar{P}/\partial\bar{\mu})_{\bar{T}}$ can be obtained as follows:

$$\bar{\rho} = 1 + \bar{P}_{11}\Delta\bar{T} + \left(\frac{\partial\Delta\bar{P}}{\partial\Delta\bar{\mu}}\right)_{\Delta\bar{T}}$$

$$\bar{U} = \frac{d\bar{P}_0}{dT} - \bar{\rho}\frac{d\bar{\mu}_0}{dT} + \bar{P}_{11}\Delta\bar{\mu} + \left(\frac{\partial\Delta\bar{P}}{\partial\Delta T}\right)_{\Delta\bar{\mu}}$$

$$\bar{X}_T = \left(\frac{\partial^2\Delta\bar{\rho}}{\partial\Delta\bar{\mu}^2}\right)_{\Delta\bar{T}}$$

$$\left(\frac{\partial\bar{P}}{\partial\bar{T}}\right)_{\bar{\rho}} = \frac{d\bar{P}_0}{dT} + \bar{P}_{11}\left[\Delta\bar{\mu} - \frac{\bar{\rho}}{\bar{X}_T}\right] + \left(\frac{\partial\Delta\bar{P}}{\partial\Delta\bar{T}}\right)_{\Delta\bar{\mu}} - \frac{\bar{\rho}}{\bar{X}_T}\frac{\partial^2\Delta\bar{P}}{\partial\Delta\bar{\mu}\partial\Delta\bar{T}}$$

$$\frac{\bar{C}_v}{\bar{T}^2} = \frac{d^2\bar{P}_0}{d\bar{T}^2} - \bar{\rho}\frac{d^2\bar{\mu}_0}{d\bar{T}^2} - \frac{\bar{P}_{11}^2}{\bar{X}_T} + \left(\frac{\partial^2\Delta\bar{P}}{\partial\Delta\bar{T}^2}\right)_{\Delta\bar{\mu}} - \frac{2\bar{P}_{11}}{\bar{X}_T}\frac{\partial^2\Delta\bar{P}}{\partial\Delta\bar{\mu}\partial\Delta\bar{T}} - \frac{1}{\bar{X}_T}\left(\frac{\partial^2\Delta\bar{P}}{\partial\Delta\bar{\mu}\partial\Delta\bar{T}}\right)^2$$

$$\bar{C}_P = \bar{C}_v + \frac{\bar{X}_T}{\bar{\rho}^2}\left[\bar{P} - \bar{T}\left(\frac{\partial\bar{P}}{\partial\bar{T}}\right)_{\bar{\rho}}\right]^2$$

The coefficients $\bar{\mu}_c$, $\bar{\mu}_j$, $\bar{P}_{11}$, $\bar{P}_j$, α_i, a, k_i, b, c, β, δ, and the coefficients for the series $P_i(\theta)$ are given in Levelt Sengers et al. (1976) along with tables of thermodynamic properties in the critical region and the listing of a computer program for calculation of property values.

Also given in Levelt Sengers et al. (1976), and Sengers et al. (1985) are comparisons of the critical region equation with data on specific heats (C_p and C_v), speed of sound, pressure, and vapor pressure. It may be said that this new formulation provides for the first time a demonstration of the compatibility of diverse, abundant, and accurate thermodynamic data in the critical region, in an area where the traditional analytical equation has not been able to represent all data within experimental uncertainty. More will be said later about the incorporation of this formulation into a continuous, wide-ranging, and fundamental equation of state.

6 Wide-Ranging Fundamental Equations for Thermodynamic Properties

In what follows a comparison is made of four fundamental equations, all of which may be expressed in the form

$$\bar{\psi} = \ln\bar{\rho} + \bar{\psi}_0(\bar{T}) + \bar{\psi}_1(\bar{\rho}, \bar{T})$$

in which the first two terms pertain to the ideal gas state and $\psi_1(\bar{\rho}, T)$ represents all the effects of departure from that ideality. Here the dimensionless variables are defined as

$$\bar{\psi} = \frac{\psi}{RT}$$

$$\bar{T} = -\frac{T_c}{T}$$

$$\bar{\rho} = \frac{\rho}{\rho_c}$$

in which ψ is the Helmholtz free energy per unit mass, T and T_c are the temperature and critical temperature, and ρ and ρ_c are the density and critical density. Using the molecular weight of 18.015242 for standard mean ocean water (SMOW) as given by Kell (1977) with the universal gas constant $\bar{R} = 8.3143$ we obtain $R = 0.46151$ kJ/kg K. Although some authors use $R = 0.46152$ the difference is generally inconsequential.

All of the above equations are adjusted so that at the triple point in the liquid state $u = s = \psi = 0$. With the above common form for the Helmholtz function the following thermodynamic properties can be obtained by differentiation:

Pressure

$$\bar{P} = \frac{P}{\rho_c RT} = \bar{\rho}^2\frac{\partial\bar{\psi}}{\partial\rho}$$

Entropy

$$\bar{s} = \frac{s}{R} = \bar{T}\frac{\partial\bar{\psi}}{\partial\bar{T}} - \bar{\psi}$$

Internal Energy

$$\bar{u} = \frac{u}{RT_c} = -\frac{\partial\bar{\psi}}{\partial\bar{T}}$$

Enthalpy

$$\bar{h} = \frac{h}{RT_c} = \bar{u} - \frac{\bar{P}}{\bar{\rho}\bar{T}}$$

Isochoric Specific Heat

$$\bar{C}_v = \frac{C_v}{R} = -\bar{T}^2\frac{\partial^2\bar{\psi}}{\partial\bar{T}^2}$$

Isopiestic Specific Heat

$$\bar{C}_p = \frac{C_p}{R} = \bar{C}_v + \left[\bar{T}\left(\frac{\partial\bar{P}}{\partial T}\right)_{\bar{\rho}} - \bar{P}\right]^2 \Big/ \left[\rho^2\left(\frac{\partial\bar{P}}{\partial\bar{\rho}}\right)_{\bar{T}}\right]$$

Speed of Sound

$$\bar{a} = a/\sqrt{RT_c} = \sqrt{-\frac{C_p}{\bar{C}_v}\frac{1}{\bar{T}}\left(\frac{\partial\bar{P}}{\partial\bar{\rho}}\right)_{\bar{T}}}$$

For comparison of the various equations the following subscripts will be used: KKHM = Keenan, Keyes, Hill, and Moore (1969); P = Pollak (1974); HGK = Haar, Gallagher, and Kell (1984); H = Hill (1987).

For the ideal gas function we may write

$$\psi_{0\mathrm{KKHM}} = \sum_{i=1}^{6} C_i(-\bar{T})^{2-i} + (C_7\bar{T} + C_8)\ln(-\bar{T})$$

It may be shown that ψ_{0P} and ψ_{0H} have exactly the same form as ψ_{0KKHM} while ψ_{0HGK} is given by

$$\psi_{0HGK} = \sum_{i=1}^{16} C_i(-\bar{T})^{4-i} + (C_{17} + C_{18}) \ln(-\bar{T})$$

It may be noted that these expressions have been formulated to match the C_{p0} values of Friedman and Haar (1954) or the more recent C_{p0} determinations of Woolley (1980).

Cooper (1981) has formulated a simplified and accurate representation of the Woolley values using a series of harmonic oscillator functions to provide the equivalent of $\psi_0(T)$. The two constants arising during integration from C_{p0} to ψ_0 are used to adjust the complete ψ function to satisfy the two liquid triple point boundary conditions.

For the relatively large and complicated part of the Helmholtz function associated with departure from the ideal gas state, the terms from the various equations may be written

$$\psi_{1KKHM} = \sum_{i=1}^{8} \sum_{j=1}^{7} C_{ij}\bar{\rho}(\bar{\rho} - \bar{\rho}_i)^{i-1}(\bar{T} - \bar{T}_j)^{j-2}(\bar{T} + 1)$$

$$+ e^{-a\bar{\rho}} \sum_{i=1}^{2} \sum_{j=1}^{7} D_{ij}\bar{\rho}^i(\bar{T} - \bar{T}_i)^{j-2}$$

in which C_{ij}, D_{ij}, $\bar{\rho}_i$, $\bar{T}_j$, and a are constants for a total of 55 nonzero coefficients.

$$\bar{\psi}_{1P} = \sum_{i=1}^{25} C_i\bar{\rho}^{r_i}\bar{T}^{\,t_i} + e^{-a\bar{\rho}^2} \sum_{i=26}^{40} C_i\bar{\rho}^{r_i}\bar{T}^{\,t_i}$$

in which C_i, a are constants. The r_i are integers that depend on i and are as large as 12. The t_i are also integers, with maximum value 7.

$$\bar{\psi}_{1HGK} = -\ln(1 - C_1\bar{\rho}) + \frac{C_2}{1 - C_1\bar{\rho}} + \frac{C_3}{(1 - C_1\bar{\rho})^2} + C_4$$

$$+ \ln(-\bar{T}) + 4C_1\bar{\rho}\left[\frac{\sum_j B_j\bar{T}^j}{b_1\ln(-\bar{T}) + \sum_j b_j\bar{T}^j} - C_5\right]$$

$$+ \sum_{i=1}^{36} d_i\bar{T}^{t_i}(1 - e^{-a\bar{\rho}})^{k_i} + \sum_{i=37}^{40} d_i(\bar{\rho} - \bar{\rho}_i)^{l_i}$$

$$e - \left\{\alpha_i(\bar{\rho} - \bar{\rho}_i)^{F_i} + B_i\left(\frac{\bar{T} - \bar{T}_i}{\bar{T}}\right)^2\right\}$$

with a total of 82 constants. It may be noted that the Haar–Gallagher–Kell equation, which is the basis of the NBS/NRC Steam Tables, has been recommended by the International Association for the Properties of Steam as "The IAPS Formulation 1984 for the Thermodynamic Properties of Ordinary Water Substance for Scientific and General Use." The equation in an alternative dimensionless form is given by Kestin et al. (1984) with the values of all constants (see also Kestin and Sengers, 1986).

The range of the KKHM equation is limited to about 100 MPa and 1000°C, whereas the HGK equation has been recommended by IAPS for use in the region

$P \le 1500$ MPa for $423.15 \le T \le 1273.15$ K

$$P \le 100\left[5 + \frac{T - 273.15\ \text{K}}{15\ \text{K}}\right]\text{MPa for } 273.15 \le T < 423.15\ \text{K}$$

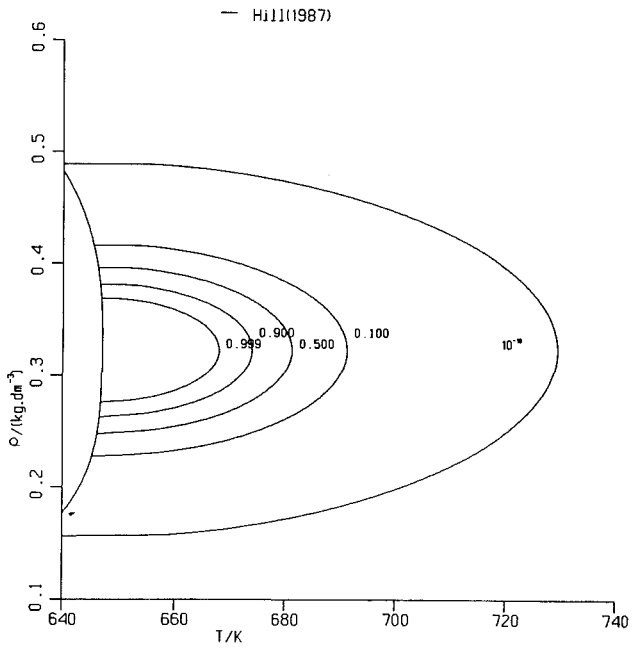

Fig. 1 Contours of constant *F* values

The region around the critical point is excluded from the recommended region of validity because the HGK equation (like the KKHM and Pollak equations) is analytic and therefore incapable of correctly representing critical point anomalies, and critical region behavior.

This has led to the development of a unified fundamental equation by Hill (1987), who has incorporated the critical region formulation of Levelt Sengers et al. (1983) into a single formulation that provides a smooth transition from critical region to far-field behavior and is continuously valid over all single-phase states between triple point temperature and pressure and the melting line or 1000 MPa and 1000°C. The equation of state is

$$\bar{\psi} = \bar{\psi}_f + F(\bar{\psi}_n - \bar{\psi}_f) \tag{2}$$

in which $\bar{\psi}_n$ is the near-critical Helmholtz function of Levelt Sengers et al. (1983); $\bar{\psi}_f = \bar{\psi}_f(\bar{\rho}, \bar{T})$ is the "far-field" function ($\bar{\psi}_f = \psi_f/RT$); the function $F(\bar{\rho}, \bar{T})$ is unity at the critical point, where all its derivatives are zero; it descends to zero inside the region of validity of $\bar{\psi}_n$ and is zero everywhere outside the critical region. Its definition is

$$F = 1 - \exp(-1/S)$$

in which

$$S = \exp[(s/\delta)^4] - 1$$

and

$$s = \sqrt{(\Delta\bar{\rho}/\Delta\bar{\rho}_0)^2 + (\Delta\bar{T}/\Delta\bar{T}_0)^2}$$

with $\delta = 1.028667$, $\Delta\bar{\rho}_0 = 0.23$, and $\Delta\bar{T}_0 = 0.05$.

Figure 1 shows contours of constant F on the density–temperature plane near the critical point. The far-field equation is in the form

$$\bar{\psi}_f = \ln\bar{\rho} + \bar{\psi}_0 + \bar{\psi}_1(\bar{\rho}, \bar{T}) \tag{4}$$

in which the first two terms pertain to the ideal gas and $\bar{\psi}_0$ has been previously defined. The function $\bar{\psi}_1(\bar{\rho}, \bar{T})$ is specified by

Table 5 Definitions of E_k

k	E_k
1	$(1-e^{-\bar{\rho}^2})/\bar{\rho}$
2	$\bar{\rho}e^{-\bar{\rho}^2}$
3	$\bar{\rho}^2\bar{T}^2\exp[-\alpha\Delta\bar{T}-\beta\Delta\bar{\rho}-\lambda\Delta\bar{T}^2-\delta\Delta\bar{\rho}^2]$
4	$E_1 e^{-\nu(\bar{T}+3)}$

α, β, γ, δ, and ν are constants. The number of nonzero coefficients selected from the $\bar{\psi}$ function "term bank" is 68.

$$\bar{\psi}_1 = \sum_i \sum_j \sum_{k=1}^{4} A_{ijk} E_k \bar{\rho}^{i-1} \bar{T}^{j-1} \tag{5}$$

except that when $i=2$ and $k=1$, $\bar{\rho}^{i-1}$ is replaced by

$$\bar{\rho}\ln\bar{\rho} - \bar{\rho}^3(\ln\bar{\rho} - 1/2)/(1-e^{-\bar{\rho}^2})$$

The values of E_k are obtained from Table 5.

7 Correlation of Experimental Data

7.1 Introduction. The IAPS working group review of data, referred to earlier, constituted a major contribution to the ongoing process of evaluating the accuracy of reported data on the properties of water (see for example Sato et al., 1975, and Straub and Rosner, 1977). There are a number of factors to be taken into account in this process, starting with the accuracy estimates provided by those who made the measurements. Similar kinds of data (for example, P-v-T observations) may be usefully compared using a common reference correlation for presentation of differences. Often these data are presented along isotherms at regular intervals, and where two or more sets of data are presented for nearly identical locations, the comparison is relatively unambiguous. Repeated measurements at the same point provide assistance in estimating the random errors affecting accuracy. However, some laboratories provide only data that have been "smoothed"; the removal of the original scatter of the data may make evaluation of those data more difficult. Consistency between results of two or more laboratories tends to confirm the accuracy of the data. A significant discrepancy between the mean values of different data sets (i.e., a discrepancy greater than that expected as a result of the random measurement errors), suggests the existence of some systematic error in one or more of the data sets. Observations of different quantities may also be compared for consistency using a reference correlation as a basis. However, for such comparisons the existence of a discrepancy may be caused not only by systematic error in the data, but may also be the result of an inadequacy of the functional form used, or as a result of "overfitting," where more terms are included in the correlation function than are warranted by the accuracy of the data. Unfortunately, it may be difficult to determine the cause of the discrepancy, and additional measurements may be the only means of resolving the inconsistency.

Plotting comparisons between the various data and correlations is an effective visual means of indicating the degree of consistency that has been obtained. The following plots of selected regions use the correlation of Hill (1987) as a basis (unless otherwise noted).

7.2 1986 Correlation Data Base. The observations of Kell and Whalley (1965) of liquid water in the range 0 to 150°C were subsequently compared with speed of sound observations, and the P-v-T data were found to be about 100 ppm lower, a discrepancy greater than the 20 ppm accuracy assigned to each data set. A re-analysis of the P-v-T data in Kell and Whalley (1975) resulted in a redetermination of the

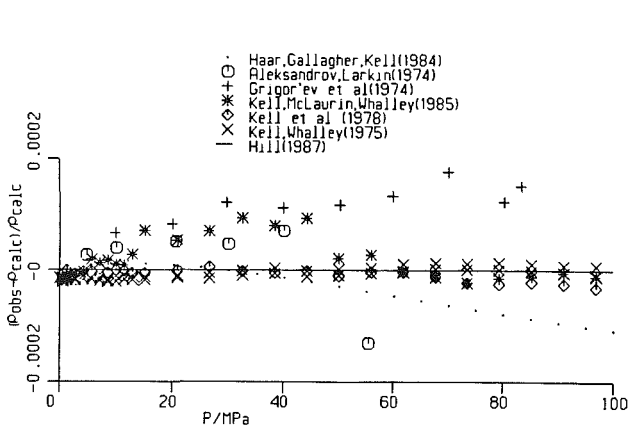

Fig. 2 Density of the compressed liquid, 150°C

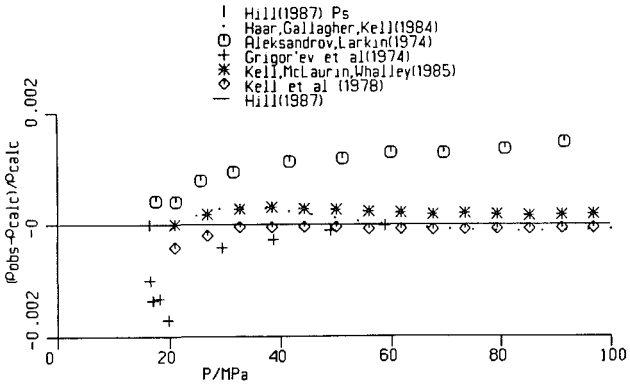

Fig. 3 Density of the compressed liquid, 350°C

measurements to bring them into accord with the values determined from measurements of the speed of sound. There remains a difference of about 20 ppm between the Kell and Whalley (1975) values, and the values of Fine and Millero (1973), which can only be resolved by more measurements in this region. Observations along the 150°C liquid isotherm are provided in each of Kell and Whalley (1975), Kell et al. (1978), and Kell et al. (1985) with systematic differences of up to 40 ppm between the various measurements, and differences of 100 ppm or more with the observations of Aleksandrov and Larkin (1974) and Grigor'ev et al. (1974) as indicated in Fig. 2. Of the three experimenters, only Kell provides repeated runs of observations along the same isotherm, to indicate random error. No two pairs of the three data sets are mutually consistent to within each other's scatter, with the exception of the consistency of Grigor'ev et al. (1974) and Kell (1985, 1978) at 350°C as indicated in Fig. 3.

On the vapor side, at 150°C, the data of Kell and McLaurin (1977) show an increasing systematic error with an increase in pressure to saturation, up to 3000 ppm, as indicated in Fig. 4, as compared to the correlations, which rely on the values of Osborne (1937) at saturation. However, a comparison of the second virial coefficient values corresponding to the Kell and McLaurin (1977) observations, and the values calculated from the correlation of LeFevre et al. (1975) indicate that the Kell and McLaurin (1977) values are significantly outside the correlation tolerance, and thus are also inconsistent with the data

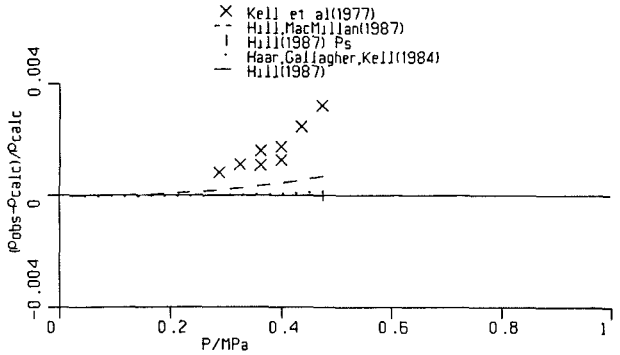

Fig. 4 Density of the vapor, 150°C

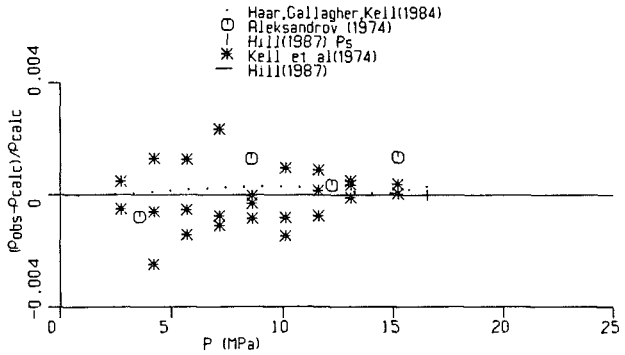

Fig. 5 Density of the vapor, 350°C

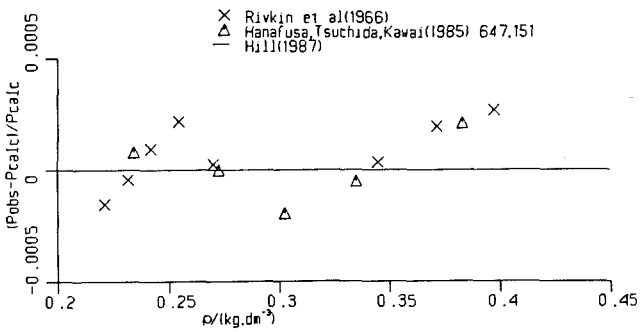

Fig. 6 Pressure close to the critical point

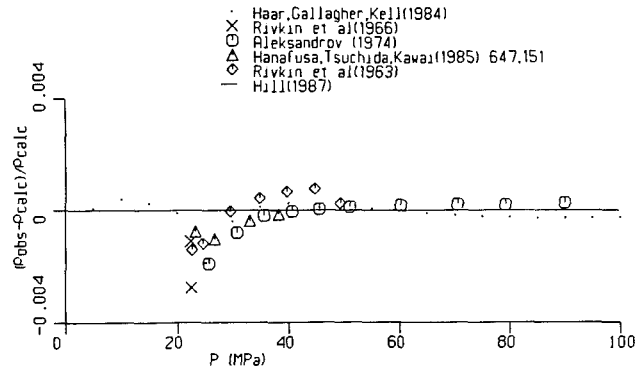

Fig. 7 Density of the fluid, 374°C

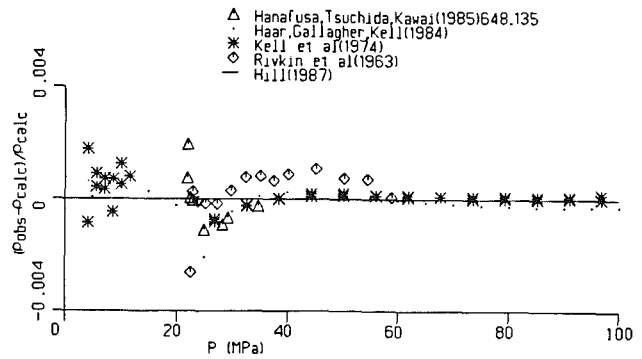

Fig. 8 Density of the fluid, 375°C

of Wormald (1964), on which the correlation depends in that temperature region.

At 350°C Kell and McLaurin (1977) and Aleksandrov and Larkin (1974) are consistent to within their scatter, which is up to ±3000 ppm, as indicated in Fig. 5.

Near the critical point, the data of Rivkin et al. (1966) supersede earlier data of the same author, based on the conclusion that insufficient time had been allowed for equilibrium to be reached within the required degree of accuracy. Hanafusa et al. (1983) report observations that are quite consistent with Rivkin et al. (1966) up to a density of about 500 kg/m^3 (see Fig. 6). Above that density, the Rivkin et al. (1966) data diverge, while those of Hanafusa et al. (1983), Aleksandrov et al. (1974), and Kell et al. (1985) remain quite consistent one with the other (see Figs. 7, 8, and 10). Observations at pressures below the critical pressure along the 375°C isotherm are shown in Fig. 9.

The value of repeated measurements as an indication of random error is indicated in Fig. 10, which shows the 500°C data of Kell et al. (1985), the data of Vukalovich et al. (1961), and also the data of Zubarev et al. (1977), with a scatter of about ±2000 ppm.

Similarly, at 400°C, the high-pressure data of Koster and Frank (1969) and Maier and Frank (1968) are consistent one with the other, with a scatter of about ±10,000 ppm, as shown in Fig. 11.

7.3 1986 Evaluation Data Base. The comparisons set out in Haar et al. (1984), Levelt Sengers et al. (1983) (in the critical region), and in Sato et al. (1982) (in the high-density region), demonstrate the good agreement between the most recent correlations and the data base. However, there remain a number of areas where there is sufficient disagreement to require further investigation. As indicated previously, while a discrepancy between the values calculated from a correlation and evaluation data may indicate a problem either with the evaluation data or the correlation data (on which the correlation is based), it can also be caused by problems inherent in a par-

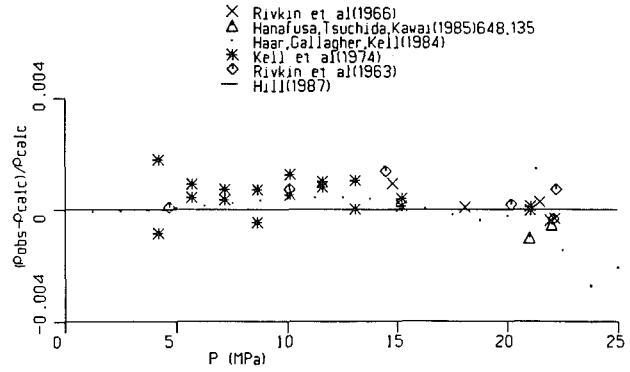

Fig. 9 Density of the fluid at subcritical pressures, 375°C

H_2O 500 C (773.15 K)

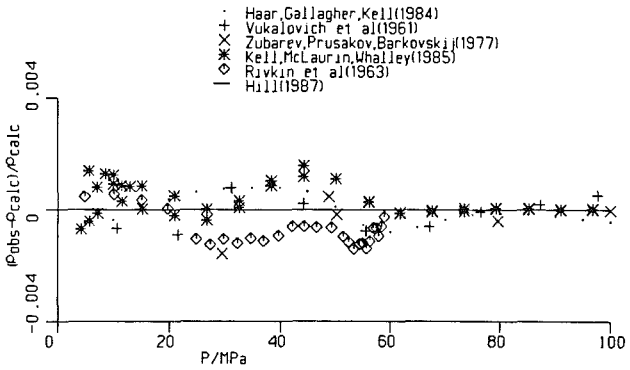

Fig. 10 Density of the fluid, 500°C

H_2O 400 C Very High Pressure

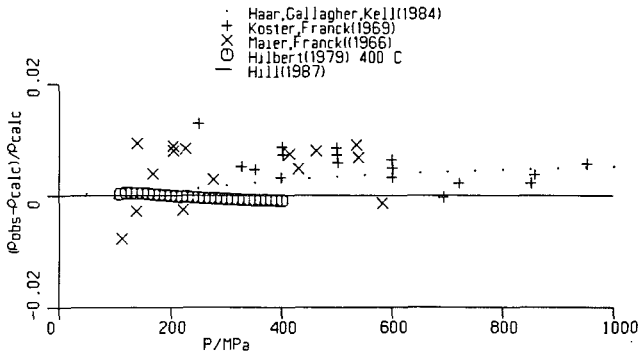

Fig. 11 Density of the fluid, 400°C, at high pressures

ticular correlation functional form. For example, there is a noticeable inconsistency between the correlations and the vapor speed of sound values of Novikov and Avdonin (1968) along the saturation line. However, since the experimenters themselves assign an error of ±1 percent (or 10,000 ppm) to their saturation measurements, and this is approximately the size of the discrepancy (as indicated in Fig. 12), it is possible that the problem arises with the speed of sound data, rather than elsewhere. Haar et al. (1984) indicate that the differences

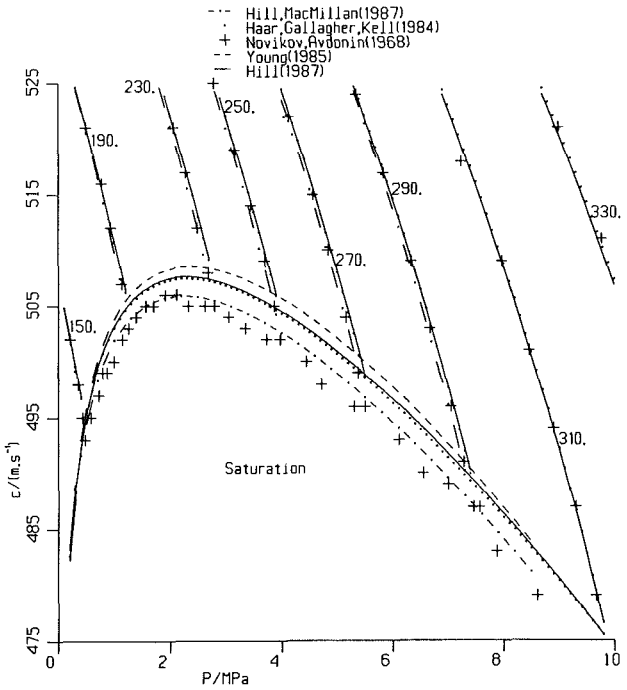

Fig. 12 Speed of sound for the vapor, 150 ≤ t ≤ 330°C

H_2O Vapour Isopiestic Specific Heat (Cp) 2 - 6 (P/MPa)

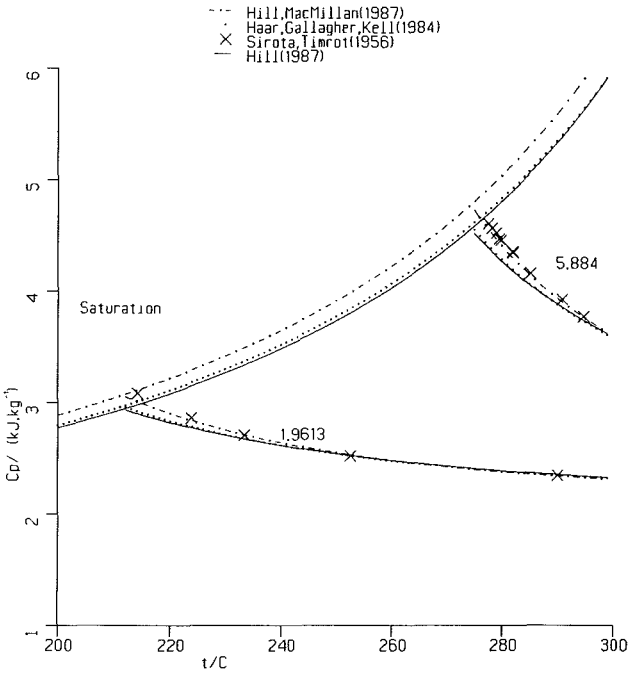

Fig. 13 Specific heat capacity at constant pressure for the vapor, 1.961 ≤ P ≤ 19.60 MPa

are in quantitative accord with the results of recent studies of experimental errors caused by precondensation.

Unfortunately, there is an additional problem of inconsistency between the calculated correlation values and the

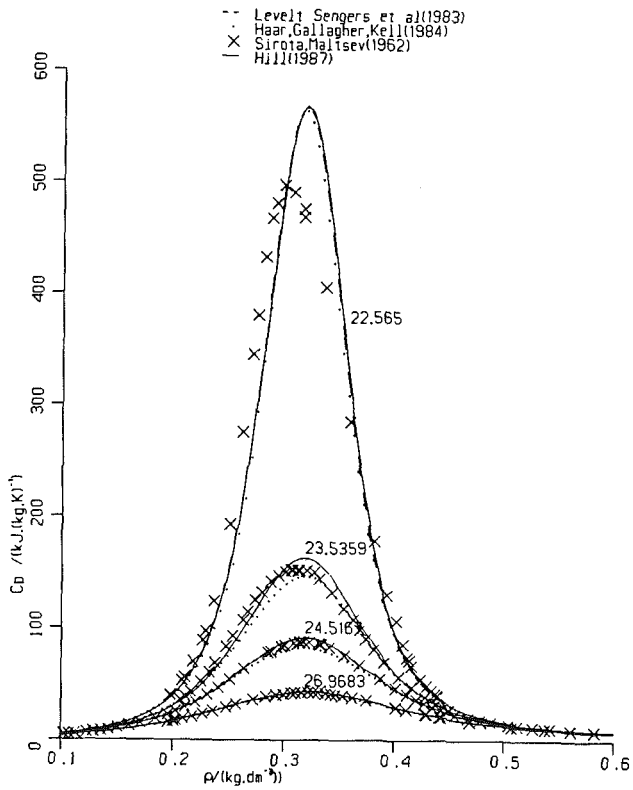

Fig. 14 Specific heat (isopiestic), isobars at supercritical pressure

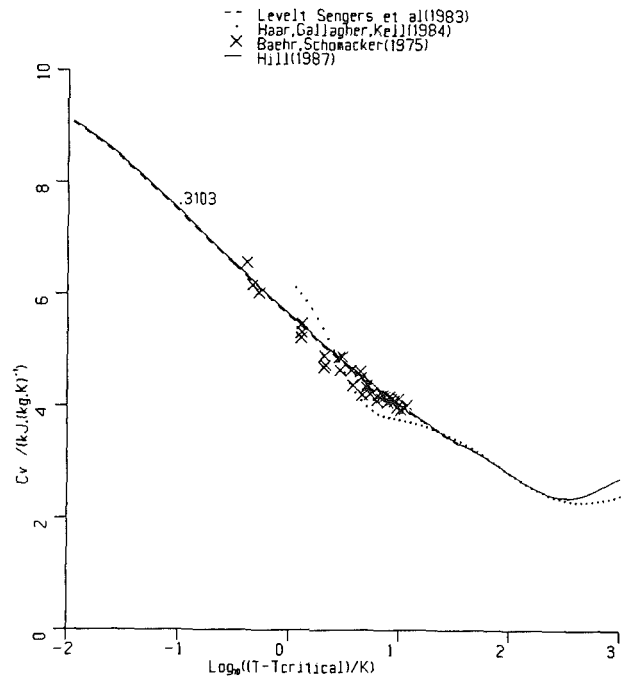

Fig. 15 Specific heat capacity (isometric), isochores near the critical density

observed values of Sirota and Timrot (1956) and Sirota and Mal'tsev (1962b), of C_p along the vapor saturation line (from 200 to 350°C) amounting to about 0.2 J out of 4 J, or 5 percent. This discrepancy is largest near the saturation line, and decreases away from saturation (see Fig. 13). Haar (1981) indicates that the Osborne et al. (1937) enthalpy values would have to be adjusted by up to 3 J to bring them into accord with the C_p values, but it is significant that an uncertainty of a similar magnitude has been assigned to the enthalpy values by Saul and Wagner (1987). Haar (1981) suggests that the discrepancy is between the data, rather than inherent in the correlation, but this is clearly a region where more accurate measurements could help to resolve relatively significant inconsistencies. (Later in this paper it will be suggested that the data of Osborne et al., 1937, and the data of Wormald, 1964, can be shown to be consistent to within about 0.8 J.)

Near the critical region, the correlations also differ from the C_p data of Sirota and Mal'tsev (1962a), both in regard to location of the maxima, and size of the maxima (see Fig. 14). As indicated earlier, there is significant uncertainty with regard to the critical parameters, and with regard to data near the critical point. The correlation of Levelt Sengers et al. (1983) (which relies on the observations of Osborne et al., 1937) results in calculated values that differ from some of the other data in the region. However, the authors demonstrate that small adjustments in temperature (0.06°C for Erohkin and Kal'yanov, 1980, 0.05°C for Sirota and Mal'tsev, 1962a), result in values which are consistent. (A similar adjustment in temperature for the C_p data is suggested in Sirota et al., 1963.)

The correlation of Haar et al. (1984) excludes a small region within one degree of the critical temperature, near the critical density. However, for some isotherms above the critical temperature (380°, 410°C) the correlation of Levelt Sengers et al. (1983) demonstrates better agreement with the observations of Rivkin et al. (1966) and Hanafusa et al. (1983), as indicated in Sengers et al. (1985). In addition, the Levelt Sengers et al. (1983) correlation results in calculated C_v values, which are also in better accord with the data of Baehr and Schomacher (1975) (see Fig. 15).

In the low-temperature region on the vapor side, additional comparisons may be made between the Osborne et al. (1939) values, the Wormald (1964) measurements, and the values calculated from correlations.

There are a number of formulations that may be used to calculate H_2O vapor values. These formulations are primarily based on the latent heat measurements of Osborne et al. (1937, 1939), which result in h_g values, and from which V_g values may be calculated using a P_s formulation. Saul and Wagner (1987) have provided separate correlations for P_s, and for v_g and h_g (see also Wagner and Sengers, 1986). The equation of state of Haar et al. (1984) is a unified correlation, which provides values for P_s, v_g and h_g. Presented here are the values of these quantities calculated from a preliminary virial equation, which adopts the Saul and Wagner (1987) P_s correlation at saturation. An improved virial formulation (set out in Hill and MacMillan, 1987) results from a least-squares fit in which all the h_g values derived from the Osborne et al. (1937, 1939) data have been multiplied by a factor of 0.9997, corresponding to 0.7 J reduction in h_g at 0.01°C, and in which also are included the data of Wormald (1964). The preliminary virial correlation included only Osborne et al. (1939) data in the low-temperature region. The values calculated at 0.01°C must be consistent with the relationship

$$h_g = h_f + (T\ dP_s/dT\ v_g) - (T\ dP/dT\ v_f) \qquad (6)$$

The values from these correlations at the initialization temperature of 0.01°C are set out in Table 6. The value of h_f at this temperature is close to zero, and v_g values are easily calculated from h_g and dP_s/dT values, using equation (6).

Table 6 Comparison of h_g values at 0.01°C

Source of h_g value	dP_s/dT (Saul and Wagner, 1987) kPa/K	dP_s/dT (Haar et al., 1984) kPa/K	h_g, abs J	v_g m^3/kg	h_g-h_g (Osborne-Calc)
Osborne et al. (1939)	0.0444266		2501.2	206.245	-
Osborne et al. (1939)		0.0444402	2501.2	206.039	
Saul and Wagner (1987)	0.0444266		2500.3	206.031	0.9
Haar et al. (1984)		0.0444402	2500.5	205.986	0.7
Virial	0.0444266		2500.0	206.004	1.2
Preliminary virial	0.0444266		2500.1	206.018	1.1

Table 7 Comparison of second virial values at 0.01°C

Source of B_2 value	R	P_s, kPa	B_2, m^3/kg	v_g, m^3/kg
Saul and Wagner (1987)	0.46151	0.611659	−0.0772	206.031
Haar et al. (1984)	0.46152	0.61173	−0.0989	205.986
Virial	0.46152	0.61173	−0.0128	206.005
LeFevre et al. (1975) (Saul and Wagner (1987) P_s)	0.46151	0.611659	−0.0977	206.013
LeFevre et al. (1975) (Haar et al. (1964) P_s)	0.46152	0.61173	−0.0977	205.991

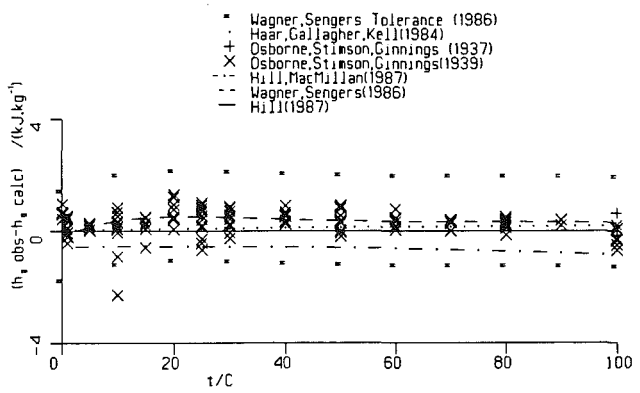

Fig. 16 Enthalpy of the saturated vapor $0 \le t \le 100$°C: comparison of experimental values and calculated correlation values.

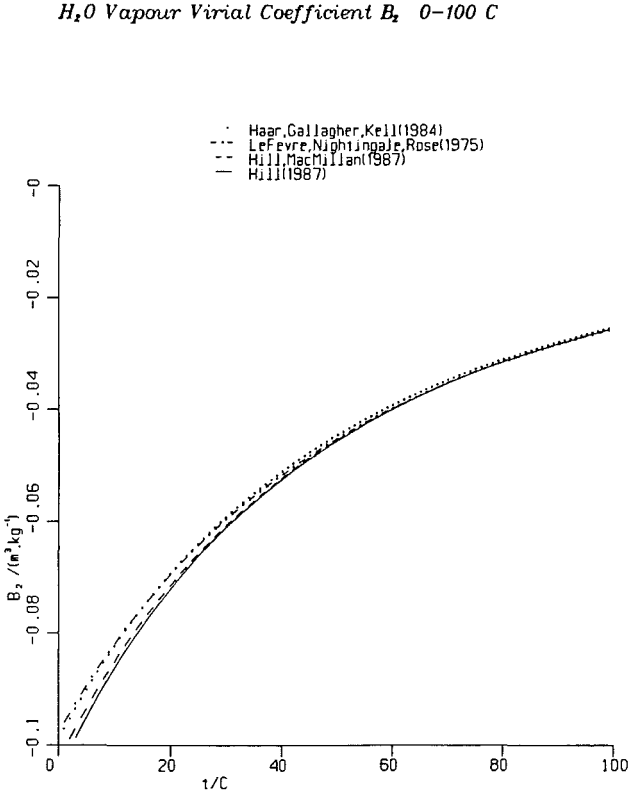

Fig. 17 Second virial coefficient, $0 \le t \le 100$°C

A comparison of the values in Table 6 indicates that combining the Osborne et al. (1939) h_g mean value with the different values of dP_s/dT of Haar et al. (1984) and Saul and Wagner (1987) results in significantly different values of v_g. In addition, the values of h_g calculated from each of the various formulations are not in accord with the Osborne et al. (1939) h_g value.

The Haar et al. (1984) values may also be considered in conjunction with the values of the second virial coefficient (B_2) correlation of LeFevre et al. (1975), and the values of v_g that those values imply. (The LeFevre et al., 1975, virial values are consistent with their own steady flow measurements, as well as those of Wormald, 1964, which were used as a basis for the correlation.) Table 7 sets out a comparison of those values, with the third and higher virial coefficients assumed zero, using the relationship

$$Pv/RT = 1.0 + B_2/v_g \tag{7}$$

LeFevre et al. (1975) suggests a tolerance of ±10 percent in his B_2 values, which results in a range in v_g of 206.022–206.004 m^3/kg (using the Saul and Wagner, 1987, P_s), and a range of 206.000–205. 981 m^3/kg (using the Haar et al., 1984, P_s). The Saul and Wagner (1987) v_g value lies outside of this range.

The variation in the values set out in Tables 6 and 7 may be due to the following factors. First, the Saul and Wagner (1987) correlation has a discrepancy with the Osborne et al. (1939) 0°C value of 0.9 J, but this function rapidly comes into close agreement above 5°C, as indicated by Fig. 16. The functional form of Saul and Wagner (1987) requires that the values of h_g and v_g be consistent, but does not require consistency with the well-known values of C_{p0}. In addition, while his P_s correlation corresponds well with the data of Guildner et al. (1976) and Stimson (1969), his value of v_g was not required to be consistent with the B_2 values of LeFevre et al. (1975).

The Haar et al. (1984) correlation has a discrepancy with Osborne et al. (1939) of 0.7 J, which is the smallest of the values in Table 1. His values in the range 5–100°C show a smaller though systematic deviation of about 0.3 J from Osborne et al. (1939) (Fig. 16). His agreement with the B_2 of LeFevre et al. (1975) is shown in Fig. 17, but obtaining the agreement requires P_s values that deviate significantly from the Guildner et al. (1976) and Stimson (1969) values (Fig. 18). The significance of the higher dP_s/dT of Haar et al. (1984) is that it allows a higher value of h_g, closer to Osborne et al. (1939), while allowing a lower value of v_g consistent with LeFevre et al. (1975), with respect to equation (6).

The values set out in Table 6 from a preliminary virial func-

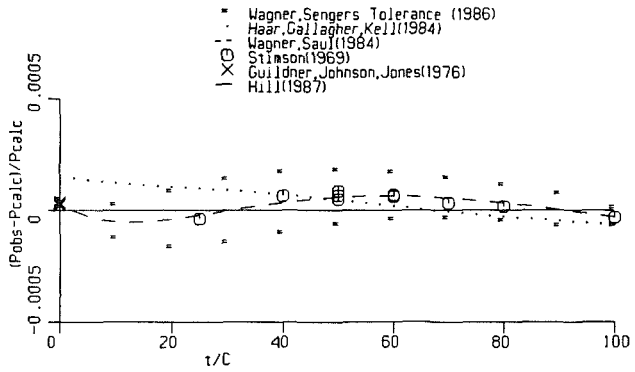

Fig. 18 Vapor pressure at saturation $0 \leq t \leq 100°C$

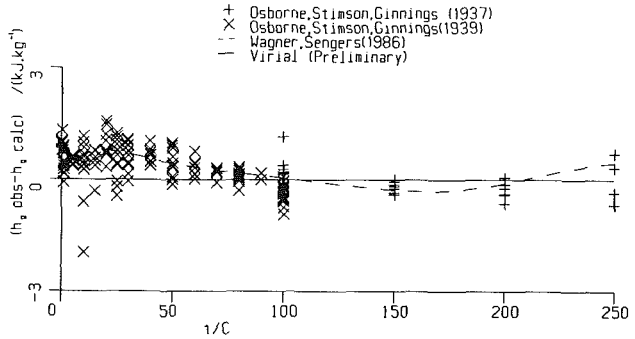

Fig. 19 Enthalpy of the saturated vapor, $0 \leq t \leq 250°C$; comparison of experimental values with the calculated values of the preliminary virial correlation of the unshifted data of Osborne et al. (1937, 1939).

tional form correlation resulted in calculated values for h_g that differed from Osborne et al. (1975) by 1.1 J at 0.01°C, but shifted into general agreement with those values at about 100°C, as indicated by Fig. 19. The values of B_2 resulting from this correlation lie just within the tolerance suggested by LeFevre et al. (1975) for his B_2 values, but differed systematically from those values up to about 140°C, and similarly differed systematically from the steady flow data of Wormald (1964), upon which the LeFevre et al. (1975) correlation is dependent in that temperature range (Fig. 20). This preliminary correlation represented the available data to within estimated tolerances, but the systematic nature of the deviations indicated the probability of inconsistency between the various data sets.

The disagreement between the preliminary virial formulation and the Wormald (1964) data suggested that closer consistency might be obtained if the Osborne et al. (1937, 1939) values were lowered by a factor of 0.9997, as demonstrated in Fig. 21. The virial correlation (Hill and MacMillan, 1987), which made use of the repositioned Osborne et al. (1937, 1939) data, shows good agreement with the B_2 of LeFevre et al. (1975) (Fig. 17), the data of Wormald (1964) (Fig. 21), the speed of sound data (Fig. 12), the specific heat data (Fig. 13), and incorporated the P_s of Saul and Wagner (1987), which shows good agreement with Guildner et al. (1976), and Stimson (1969) (Fig. 18).

Except for the possibility of inadequacy of the virial functional form used here, or inaccuracy in the value of the gas

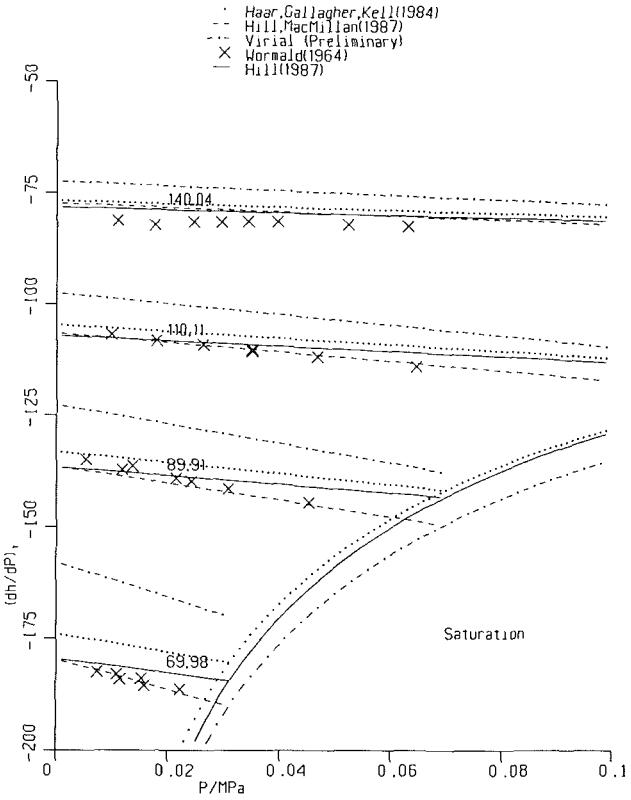

Fig. 20 Isothermal throttling coefficient, $70 \leq t \leq 140°C$

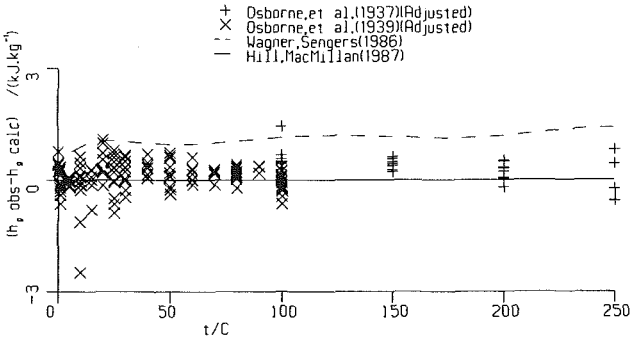

Fig. 21 Enthalpy of the saturated vapor, $0 \leq t \leq 250°C$: comparison of experimental values and calculated values of Hill and MacMillan (1987)

constant, or the C_{p0} correlation, or the P_s values of Saul and Wagner (1987), it can be said that the Haar et al. (1984) values differ significantly, especially from the Saul and Wagner (1987) P_s values. In addition, the Saul and Wagner (1987) v_g values differ from the value of B_2 of LeFevre et al. (1975). However, the shifted virial formulation demonstrates good agreement with all of the data, including agreement with the repositioned Osborne et al. (1939) data.

With regard to the Osborne et al. (1939) data, there are several factors that suggest that this adjustment is reasonable. First, there is the persistent disagreement between each formulation and the Osborne et al. (1939) mean h_g value at

0.01°C (see Table 6). It is significant that the Osborne et al. (1939) values demonstrate a scatter of ±0.5 J, disregarding any systematic error. However, it is more significant to consider the mean values of h_g obtained from the measurements of Osborne et al. (1937, 1939), which overlap at 100°C and which disagree by 0.5 J.

The deviation indicated by the preliminary virial correlation may be due to some imprecision of the measuring apparatus used in the Osborne et al. (1937, 1939) data, which introduced a systematic error only at low temperatures. However, the disagreement is also consistent with a systematic error in all the data which the least-squares procedure is able to fit at high temperatures only, but unable to replicate at low temperatures because of closeness to the perfect gas.

However, there still remains the deviation of the preliminary correlation from the Wormald (1964) data, and the corresponding virial formulation of LeFevre et al. (1975). It is significant that the magnitude and direction of the persistent discrepancy between the Osborne et al. (1939) data with a virial least-squares fit at 0.01°C should be consistent with the magnitude and direction of a similar systematic discrepancy with all the Wormald (1964) data.

As a result, the evidence suggests that a probable means of reconciling all the data is to reposition the Osborne et al. (1937, 1939) data by reducing h_g by a factor of 0.9997. A virial functional form fit to an adjusted Osborne data set and to the Wormald (1964) data results in a correlation with better agreement to both data sets. This shift is of the same order as the difference of 0.5 J in the means of the two sets of data (Osborne et al., 1937, 1939), where they overlap at 100°C.

7.4 Summary. In the liquid region, only Kell et al. (1985, 1978, 1975) provide results of repeated measurements; additional measurements could assist in assessing more confidently whether the scatter of that data represents its accuracy. On the vapor side along the saturation line, there are significant, systematic discrepancies among the data. Near the critical region, the discrepancies that exist can be related to small adjustments of temperature in the data. The data of Hanafusa et al. (1983) appear to be more consistent with other data than those of Rivkin et al. (1966), and thus may be eligible to replace those data in the current correlation data base. The continuing process of refining the accuracy of measurements and the resulting correlations will undoubtedly result in further evolution of the correlation and evaluation data bases.

8 Transport Properties

The International Association for the Properties of Steam has issued a release entitled "The IAPS Formulation 1985 for the Viscosity of Ordinary Water Substance" and one entitled "The IAPS Formulation 1985 for the Thermal Conductivity of Ordinary Water Substance." These releases supersede the releases on the transport properties issued in 1975 and 1977 and amended in 1982. Sengers and Watson (1986) have explained the revisions leading to the most recent releases, which are based on research documented in Sengers and Kamgar-Parsi (1984), Sengers et al. (1984), and Watson et al. (1980).

Conclusions

1 In the past 20 years many valuable data have been obtained on the density, specific heat, speed of sound, and throttling coefficients of steam. The major discrepancies between, or incompatibilities of, the best data sets are mainly in the "small uncertainty" range.

2 Much progress has been made in quantitative descriptions of the critical region, compressed liquid states, and vapor states.

3 Accurate, wide-ranging fundamental equations of state are available, which in single continuous functions represent the thermodynamic properties of single-phase states over a range of pressures and temperatures from the triple point pressure and temperature to 1000 MPa or the melting line, and 1000°C.

4 Corresponding progress has been made in the formulation of accurate wide-ranging equations for the transport properties.

Note

Releases of the International Association for the Properties of Steam can be obtained from

Dr. Howard White, Jr.
Executive Secretary
International Association for the Properties of Steam
c/o Office of Standard Reference Data
National Bureau of Standards
Gaithersburg, MD 20899 USA

References

Aleksandrov, A. A., and Larkin, D. K., 1974, "An Investigation of the Specific Volumes of Water at Near-Critical Temperatures and Pressures up to 1000 Bar," *Teploenergetika*, Vol. 21, No. 8, pp. 80–81.

Aleksandrov, A. A., and Larkin, D. K., 1976, "An Experimental Determination of Ultrasonic Velocity in Water in a Wide Range of Temperature and Pressures," *Teploenergetika*, Vol. 23, No. 2, pp. 75–78.

Aleksandrov, A. A., and Kochetov, A. I., 1979, "The Experimental Determination of Ultrasonic Velocity in Water at Temperatures 266–423 K and at Pressures up to 100 MPa," *Teploenergetika*, Vol. 26, No. 9, pp. 65–66.

Aleksandrov, A. A., and Kochetov, A. I., 1980, "The Investigation of Sound Velocity in Water at High Pressures," in: *Water and Steam*, J. Straub and K. Scheffler, eds., Pergamon, Oxford, pp. 221–224.

Aleksandrov, A. A., Okhotin, V. S., and Ershova, Z. A., 1981, "Calculation of the Thermodynamic Properties of Water Based on Data on the Velocity of Sound," *Teploenergetika*, Vol. 28, No. 4, pp. 74–77.

Angell, C. A., Oguni, M., and Sichina, W. J., 1982, "Heat Capacity of Water at Extremes of Supercooling and Superheating," *J. Phys. Chem.*, Vol. 86, pp. 998–1002.

Angus, S., and Newitt, D. M., 1966, "The Measurements of the Specific Enthalpy of Steam at Pressures of 60 to 1000 Bar and Temperature of 400 to 700°C," *Phil. Trans. Roy. Soc. (London)*, Vol. 259A, pp. 107–132.

Baehr, H. D., and Schomacker, H., 1975, "Messungen der spezifischen isochoren Wärmekapazität in der Umgebung des kritischen Zustands von Wasser," *Forsch. Ing.-Wes.* Vol. 41, No. 2, pp. 43–51.

Bridgeman, P. W., 1942, "Freezing Parameters and Compressions of Twenty-one Substances to 50,000 kg/cm^2," *Proc. Am. Acad. Arts & Sci.*, Vol. 74, pp. 399–424.

Bridgeman, O. C., and Aldrich, E. W., 1964, "Vapor Pressure Tables for Water," ASME Journal Heat Transfer, Vol. 86, pp. 279–286.

Bridgeman, O. C., and Aldrich, E. W., 1965, "A Reappraisal of the Critical Constants for Water," ASME Journal Heat Transfer, Vol. 87, pp. 266–274.

Cooper, J. R., 1981, "Expressions for the Thermodynamic Properties of Water in the Ideal-Gas Limit," Memorandum submitted to WGI International Association of the Properties of Steam, June.

Davis, H. N., and Keenan, J. H., 1929, World Eng. Conference Rept. No. 455, Tokyo.

Del Grosso, V. A., and Mader, C. W., 1972, "Speed of Sound in Pure Water," *J. Acoust. Soc. Amer.*, Vol. 52, No. 5, pp. 1442–1446.

Egerton, A., and Callender, G. S., 1960, "An Experimental Study of the Enthalpy of Steam," *Phil. Trans. Roy. Soc. (London)*, Vol. 252, pp. 133–164.

Erokhin, N. F., and Kal'yanov, B. I., 1980, "Experimental Behavior of Ultrasonic Velocity and Some Other Quantities in the Supercritical Region of Water," *Teploenergetika*, Vol. 27, No. 11, pp. 50–52.

Ertle, S., Grigull, U., and Straub, J., 1980, "Measurements of the Adiabatic and Isothermal Joule-Thomson Coefficients for Water Vapour," in: *Water and Steam*, J. Straub and K. Scheffler, eds., Pergamon, Oxford, pp. 191–196.

Evstefeev, V. N., Skripov, V. P., and Chukanov, V. N., 1979, "Experimental Determiniation of the Speed of Ultrasound in Superheated Ordinary and Heavy Water," *Teplo. Vys. Temp.*, Vol. 17, No. 2, pp. 299–305.

Fine, R. A., and Millero, F. J., 1973, "Compressibility of Water as a Function of Temperature and Pressure," *J. Chem. Phys.*, Vol. 59, pp. 5529–5536.

Friedman, A. S., and Haar, L., 1954, "High-Speed Machine Computation of Ideal Gas Thermodynamic Functions. I. Isotopic Water Molecules," *J. Chem. Phys.*, Vol. 22, pp. 2051–2058.

Gildseth, W., Habenschuss, A., and Spedding, F. H., 1972, "Precision Measurements of Densities and Thermal Dilation of Water Between 5° and 80°C," *J. Chem. Eng. Data*, Vol. 17, No. 4, pp. 402–409.

Goff, J., and Gratch, S., 1945, "Low Pressure Properties of Water From −160 to 212°F," *Trans. A.S.H.V.E.*, Vol. 51, pp. 125–158.

Grigor'ev, B. A., Murdaev, R. M., and Rastorguev, Y. L., 1974, "Experimental Investigation of the *P–V–T* Relation for Water," *Teplo. Vys. Temp.*, Vol. 12, pp. 83–91.

Grindley, T., and Lind, J. E., Jr., 1971, "PVT Properties of Water and Mercury," *J. Chem. Phys.*, Vol. 54, pp. 3983–3989.

Guildner, L. A., Johnson, D. P., and Jones, F. E., 1976, "Vapor Pressure of Water at Its Triple Point," *J. Res. Nat. Bur. Stds. Phys. and Chem.*, Vol. 80A, pp. 505–521.

Haar, L., Gallagher, J. S., and Kell, G. S., 1984, *NBS/NRC Steam Tables*, Hemisphere, Washington, D.C.

Haar, L., 1981, "Supplementary Information Relating to the HGK Thermodynamic Surface," Report to IAPS WG1 (available from H.J. White, Secretary, International Association for the Properties of Steam, National Bureau of Standards, Washington, D.C.).

Hanafusa, H., Tsuchida, T., Araki, A., Sato, S., Uematsu, K., and Wanatabe, X., 1983, "Volumetric Properties of Water in the Critical Region," *High Temp.-High Press*, Vol. 15, pp. 311–320.

Havlícek, J., and Miskowsky, L., 1936, "Versuche der Masaryk—Akademie der Arbeit in Prag uber die Physikalischen Eigenschaften des Wassers und des Wasserdampfes," *Hel. Phys. Acta.*, Vol. 9, pp. 161–207.

Hilbert, R., 1979, "PVT Values of Water and With 25 Weight Percent Sodium Chloride to 873 K and 4000 Bar," Ph.D. Thesis, Univ. Karlsruhe, Federal Republic of Germany.

Hill, P. G., 1987, "A Unified Equation of State for H_2O," Report to IAPS W.G. 1.

Hill, P. G., and MacMillan, R. D. C., 1987, "Virial Equations for Light and Heavy Water," submitted to *I. & E.C. Research*.

Holser, W. T., and Kennedy, G. C., 1958, "Properties of Water. Part IV. Pressure–Volume–Temperature Relations of Water in the Range 100–400°C and 100–1400 Bars," *Am. J. Sci.*, Vol. 256, pp. 744–753.

Holser, W. T., and Kennedy, G. C., 1959, "Properties of Water. Part V. Pressure–Volume–Temperature Relations of Water in the Range 400–1000°C and 100–1400 Bars," *Am. J. Sci*, Vol. 257, pp. 71–77.

Holton, G., Hagelberg, M. P., Kao, S., and Johnson, W. H., Jr., 1968, "Ultrasonic-Velocity Measurements in Water at Pressure to 10,000 kg/cm^2," *J. Acoust. Soc. Amer.*, Vol. 43, No. 1, pp. 102–107.

Juza, J., Kmonicek, V., and Sifner, O., 1966a, Appendix to Juza, J., "An Equation of State for Water and Steam," *Acad. Naklad. Cesk. Acad. Ved. Prague*, pp. 131–142.

Juza, J., Kmonicek, V., Sifner, O., and Schovanec, K., 1966b, "A Contribution to the Problem of Thermodynamic Similarity of H_2O and D_2O," *Physica*, Vol. 32, pp. 362–384.

Keenan, J. H., Keyes, F. G., Hill, P. G., and Moore, J. G., 1969, *Steam Tables*, Wiley, New York.

Kell, G. S., 1977, "Effects of Isotopic Composition, Temperature, Pressure, and Dissolved Gases on the Density of Liquid Water," *J. Phys. Chem. Ref. Data*, Vol. 6, No. 4, pp. 1109–1131.

Kell, G. S., and McLaurin, G. E., 1977, "PVT Values for Isotherms in the Vapor $150° \leq t \leq 350°C$," National Research Council, Ottawa (unpublished data).

Kell, G. S., McLaurin, G. E., and Whalley, E., 1978, "The PVT Properties of Water. IV. Liquid Water in the Range 150–350°C, From Saturation to 1 kbar," *Phil. Trans. Roy. Soc. A (London)*, Vol. 360, pp. 389–402.

Kell, G. S., McLaurin, G. E., and Whalley, E., 1985, "The PVT Properties of Fluid Water in the Range 350 to 500°C and Along the Saturation Line From 150 to 350°C," *Phil. Trans. Roy. Soc. A (London)*, Vol. 315, pp. 235–246.

Kell, G. S., and Whalley, E., 1965, "The PVT Properties of Water. I. Liquid Water in Temperature Range 0–150°C and at Pressures up to 1 kbar," *Phil. Trans. Roy. Soc. A (London)*, Vol. 258, pp. 565–617.

Kell, G. S., and Whalley, E., 1975, "Reanalysis of the Density of Liquid Water in the Range 0–150°C and 0–1 kbar," *J. Chem. Phys.*, Vol. 62, pp. 3496–3503.

Kestin, J., and Sengers, J. V., 1986, "New International Formulations for the Thermodynamic Properties of Light and Heavy Water," *J. Phys. Chem., Ref. Data*, Vol. 15, No. 1, pp. 305–320.

Kestin, J., Sengers, J. V., Kamgar-Parsi, B., and Levelt Sengers, J. M. H., 1984, "Thermophysical Properties of Fluid H_2O," *J. Phys. Chem. Ref. Data*, Vol. 13, No. 1, pp. 175–183.

Keyes, F. G., and Smith, L. B., 1934, "The Volumes of Unit Mass of Liquid Water and Their Correlation as a Function of Pressure and Temperature," *Proc. Am. Acad. Arts Sci.*, Vol. 69, pp. 285–314.

Keyes, F. G., Smith, L. B., and Gerry, H. T., 1936, "The Specific Volume of Steam in the Saturated and Superheated Condition Together With Derived Values of the Enthalpy, Entropy, Heat Capacity and Joule Thomson Coefficients," *Proc. Am. Acad. Arts Sci.*, Vol. 70, pp. 319–364.

Keyes, F. G., 1949, "The Consistency of the Thermodynamic Data for Water Substance Vapor Phase to 550°C. Part VII," *J. Chem. Phys.*, Vol. 17, pp. 923–934.

Keyes, F. G., 1962, "The Second Virial Coefficient for Steam," *Int. J. Heat Mass Transfer*, Vol. 5, pp. 137–142.

Knoblauch, O., and Winkhaus, A., 1915a, "Die Spezifische Wärme C_p des Uberhitzten Wasserdampfes für Drücke von 8 bis 20 at und von Sattigungstemperatur bis 380°C," *Z. Ver. Deutsch. Ingeniere*, Vol. 59, pp. 376–379.

Knoblauch, O., and Winkhaus, A., 1915b, "Die Spezifische Wärme C_p des Uberhitzten Wasserdampfes für Drücke von 8 bis 20 at und von Sattigungstemperatur bis 380°C," *Z. Ver. Deutsch. Ingeniere*, Vol. 59, pp. 400–405.

Knoblauch, O., and Koch, W., 1928, "Specific Heat of Superheated Steam," *Z. Ver. Deutsch. Ingeniere*, Vol. 72, No. 48, pp. 1733–1739.

Koch, W., 1932a, "Die Spezifische Wärme des überhitzten Wasserdampfes für Drücke von 120 bis 200 at und von der Sättigungstemperatur bis 450°C," *Forsch. Gebiete Ingenieurw.*, Vol. 3, pp. 1–10.

Koch, W., 1932b, "Behaviour of Water in the Critical Zone," *Forsch. Gebiete Ingenieurw.*, Vol. 3, No. 4, pp. 189–192.

Koster, H., and Franck, E. U., 1969, "The Specific Volume of Water to High Pressure, to 600°C and 10 kbar," *Ber. Buns. Physik. Chem.*, Vol. 73, pp. 716–722.

LeFevre, E. J., Nightingale, M. R., and Rose, J. W., 1975, "The Second Virial Coefficient of Ordinary Water Substance: A New Correlation," *J. Mech. Eng. Sci.*, Vol. 17, pp. 243–251.

Levelt Sengers, J. M. H., Greer, W. L., and Sengers, J. V., 1976, "Scaled Equation of State Parameters for Gases in the Critical Region," *J. Phys. Chem. Ref. Data*, Vol. 5, No. 1, pp. 1–48.

Levelt Sengers, J. M. H., Straub, J., Watanabe, K., and Hill, P. G., 1985, "Assessment of Critical Parameter Values for H_2O and D_2O," *J. Phys. Chem. Ref. Data*, Vol. 14, No. 1, pp. 193–207.

Levelt Sengers, J. M. H., Kamgar-Parsi, R., Balfour, F. W., and Sengers, J. V., 1983, "Thermodynamic Properties of Steam in the Critical Region," *J. Phys. Chem. Ref. Data*, Vol. 12, No. 1, pp. 1–28.

Maier, S., and Franck, E. U., 1968, "The Density of Water from 200 to 850°C and from 1000–6000 bar," *Ber. Buns. Physik. Chem.*, Vol. 70, pp. 639–645.

Novikov, I. I., and Avdonin, V. I., 1968, "Velocity of Sound in Saturated and Superheated Steam," Report to 7th International Conference Properties of Water and Steam, Tokyo.

Osborne, N. S., Stimson, H. G., Fiock, E. F., and Ginnings, D. C., 1933, "The Pressure of Saturated Water Vapour in the Range 100°C to 374°C," *J. Res. Nat. Bur. Stand.*, Vol. 10, pp. 155–188.

Osborne, N. S., Stimson, H. G., and Ginnings, D. C., 1937, "Calorimetric Determination of the Thermodynamic Properties of Saturated Water in Both the Liquid and Gaseous States from 100° to 374°C," *J. Res. Nat. Bur. Stand.*, Vol. 18, pp. 389–447.

Osborne, N. S., Stimson, H. G., and Ginnings, D. C., 1939, "Measurements of Heat Capacity and Heat of Vaporization of Water in the Range 0° to 100°C," *J. Res. Nat. Bur. Stand.*, Vol. 23, pp. 197–261.

Petitet, J. P., Denielou, L., Tufeu, R., and Le Neindre, B., 1985, "Velocity of Sound in Supercritical Water up to 700°C and 300 MPa," in preparation.

Petitet, J. P., Tufeu, R., and Le Neindre, B., 1983, "Determination of the Thermodynamic Properties of Water From Measurements of the Speed of Sound in the Temperature Range 251.15–293.15 K and the Pressure Range 0.1–350 MPa," *International Journal of Thermophysics*, Vol. 4, No. 1, pp. 35–50.

Pollak, R., 1974, "Die Thermodynamischen Eigenschaften von Wasser," Dissertation, Ruhr University Bochum.

Rivkin, S. L., and Akhundov, T. S., 1962, "The Specific Volume of Water Close to the Critical Point," *Teploenergetika*, Vol. 9, No. 1, pp. 57–65.

Rivkin, S. L., and Akhundov, T. S., 1963, "Experimental Determination of Specific Volumes of Water in the Range 374.15–500°C and Pressures up to 600 kg/cm^2," *Teploenergetika*, Vol. 10, No. 9, pp. 66–71.

Rivkin, S. L., Akhundov, T. S., Kremenevskaya, E. A., and Asadullaeva, N. N., 1966, "A Study of Specific Volumes of Water in the Region Close to the Critical Point," *Teploenergetika*, Vol. 13, No. 4, pp. 59–62.

Rogener, H., and Soll, P., 1980, "Contribution to Thermodynamic Measurement of the Isentropic Temperature–Pressure Coefficient of Water," *Brennst.-Warme-Kraft*, Vol. 32, No. 10, pp. 472–478.

Sato, H., Uematsu, M., and Watanabe, K., 1975, "Comparison of the Experimental PVT Property Data and Equations of State for Ordinary Water Substance," Report to IAPS WG1, Ottawa, Canada.

Sato, H., Uematsu, M., and Watanabe, K., 1981, "Determination of the PVT-Surface of Water Based on Measured Values up to 1123 K and 1 kPa," *JSME Bulletin*, Vol. 24, No. 190, pp. 691–699.

Sato, H., Uematsu, M., and Watanabe, K., 1982, "An Equation of State for Water in the High Density Region," *Proceedings of the Eighth Symposium on Thermophysical Properties*, Vol. II, ASME, New York, pp. 287–293.

Saul, A., and Wagner, W., 1987, "Correlation Equations for the Thermodynamic Properties on the Saturation Line of Ordinary Water Substance," submitted to *J. Phys. Chem. Ref. Data*.

Sengers, J. V., Levelt Sengers, J. M. H., and Kamgar-Parsi, B., 1985, "A Scaled Fundamental Equation for the Thermodynamic Properties of Steam Near the Critical Point," *Strojnicky Casopis*, Vol. 36, pp. 277–290.

Sengers, J. V., and Watson, J. T. R., 1986, "Improved International Formulations for the Viscosity and Thermal Conductivity of Water Substance," *J. Phys. Chem. Ref. Data*, Vol. 15, No. 4, pp. 1291–1214.

Sengers, J. V., and Kamgar-Parsi, B., 1984, "Representive Equations for the Viscosity of Water Substance," *J. Phys. Chem. Ref. Data*, Vol. 13, No. 1, pp. 185–206.

Sengers, J. V., Watson, J. T. R., Basu, R., Kamgar-Parsi, B., and Hendricks, R. C., 1984, "Representative Equations for the Thermal Conductivity of Water Substance," *J. Phys. Chem. Ref. Data*, Vol. 13, No. 3, pp. 893–933.

Sirota, A. M., and Grishkov, A. S., 1966, "Experimental Investigation of the Heat Capacity of Water at High Pressure," *Teploenergetika*, Vol. 13, No. 8, pp. 61–64.

Sirota, A. M., Grishkov, A. S., and Tomishko, A. G., 1970, "Experimental

Investigation of the Heat Capacity of Water Near the Melting Curve," *Teploenergetika*, Vol. 17, No. 9, pp. 60–63.

Sirota, A. M., and Mal'tsev, B. K., 1959, "Experimental Investigation of the Heat Capacity of Water at 10–500°C and to pressures of 500 kbar/cm^3," *Teploenergetika*, Vol. 6, No. 9, p. 7.

Sirota, A. M., and Mal'tsev, B. K., 1960, "Experimental Data on the Heat Capacity of Steam at 300–500 atmospheres and 500–600°C," *Teploenergetika*, Vol. 7, No. 10, p. 67.

Sirota, A. M., and Mal'tsev, B. K., 1962a, "Experimental Determination of the Specific Heat of Water in the Critical Region," *Teploenergetika*, Vol. 9, No. 1, pp. 52–57.

Sirota, A. M., and Mal'tsev, B. K., 1962b, "Experimental Investigation of the Heat Capacity of Steam," *Teploenergetika*, Vol. 9, No. 7, pp. 70–73.

Sirota, A. M., Mal'tsev, B. K., and Grishkov, A. S., 1963, "Experimental Investigation of the Heat Capacity of Steam," *Teploenergetika*, Vol. 10, No. 9, pp. 57–60.

Sirota, A. M., Maltsev, B. K., and Belyakova, P. E., 1963, "Tables of Reference Values for the Specific Heat C_p and the Enthalpy of Water and Steam," *Teploenergetika*, Vol. 10, No. 5, pp. 64–69.

Sirota, A. M., and Timrot, T. L., 1956, "Experimental Investigation of the Heat Capacity of Superheated Steam," *Teploenergetika*, Vol. 3, No. 7, pp. 16–23.

Stimson, H. F., 1969, "Some Precise Measurements of the Vapor Pressure of Water in the Range From 25 to 100°C," *J. Res. Nat. Bur. Stand.*, Vol. 73A, pp. 493–496.

Straub, J., and Rosner, N., 1977, "Classification of P-V-T Data of Water and Steam," Report to IAPS WG 1.

Vukalovich, M. P., Zubarev, V. N., and Alexandrov, A. A., 1961, "Experimental Determination of Specific Volumes of Water at Temperatures 400–650°C and Pressures to 1200 kg/cm^2," *Teploenergetika*, Vol. 8, No. 10, pp. 79–85.

Vukalovich, M. P., Zubarev, V. N., and Alexandrov, A. A., 1962, "Experimental Determination of Specific Volumes of Water at Temperatures 700–900°C and pressures to 1200 kg/cm^2," *Teploenergetika*, Vol. 9, No. 1, pp. 49–51.

Wagner, W., and Saul, A., 1984, "Correlation Equations for the Vapour Pressure and for the Orthobaric Densities of Water Substance," *Proceedings of the Tenth International Conference on the Properties of Steam*, Moscow, USSR, pp. 199–209.

Wagner, W., and Sengers, J. V., 1986, "Draft Release on Saturation Properties of Ordinary Water Substance," IAPS Technical Report BN 1051.

Watson, J. T. R., Basu, R., and Sengers, J. V., 1980, "An Improved Representative Equation for the Dynamic Viscosity of Water Substance," *J. Phys. Chem. Ref. Data*, Vol. 9, No. 4, pp. 1255–1290.

Woolley, H. W., 1980, "Thermodynamic Properties for H_2O in the Ideal Gas State," in: *Water and Steam*, J. Straub and K. Scheffler, eds., Pergamon, Oxford, pp. 166–175.

Wormald, C. J., 1964, "Thermodynamics of Vapours," Ph.D. Thesis, University of Reading.

Zubarev, V. N., Prusakov, P. G., and Barkovskij, V. V., 1977a, "Experimental Determination of Specific Volumes of Steam at Temperatures of 673.15–873.15 K and Pressures up to 200 MPa," *Teploenergetika*, Vol. 24, No. 8, pp. 77–80.

Zubarev, V. N., Prusakov, P. G., and Barkovskij, V. V., 1977b, "Experimental Determinations of Specific Volumes of Steam at Temperatures of 923.15–1123.15 K and Pressures up to 200 MPa," *Teploenergetika*, Vol. 24, No. 10, pp. 80–82.

Journal of Heat Transfer

Technical Notes

This section contains shorter technical papers. These shorter papers will be subjected to the same review process as that for full papers.

Steady Conduction With Space-Dependent Conductivity

A. V. Munoz[1] and L. C. Burmeister[2]

Introduction

The steady diffusion equation has long been used to describe heat conduction and the flow of an incompressible fluid through a porous medium. Unfortunately, even for regions of simple shape and simple boundary conditions, practical interest is not limited to the case of constant properties for which exact solutions are available. For example, if the temperature inside a manufactured part is to be accurately determined, the variation of thermal conductivity with position should be taken into account. Accurate determination of the hydraulic head at the site of a water well in a water resources problem requires accounting for the spatial variation of the permeability of the porous medium. In many cases, it is the spatial variation of thermal conductivity or permeability that causes the difficulty. However, lumped problem formulations with constant properties in which temperature variation across the thickness of a plate or velocity variation across the thickness of a confined porous medium is ignored can have the same sort of difficulty when the thickness varies with position.

Luikov (1971) surveys solution possibilities for spatially varying thermal conductivity. Except for a few fortuitous cases, either one-dimensional or with thermal conductivity being constant in convenient zones, generally applicable exact solutions do not seem to exist.

There are many approximate methods of solution, spectral (Shaughnessy and McMurray, 1979) and weighted residual (Finlayson, 1972) methods being among them. While approximate methods compactly show essential features of a solution, they can lack precision and can be defeated by awkward geometries. Thus, the diffusion equation usually must be solved by numerical methods to obtain accurate results.

The accuracy of numerical solutions obtained by finite difference and finite element methods can be improved by employing increasingly finer grids or finite elements, of course. Still, exact solutions against which the numerical results can be compared are advantageous to evaluate the accuracy of both the numerical results and the programming that implements the algorithms that lead to them. In the following, exact solutions for steady heat conduction are developed for this purpose for a class of continuous thermal conductivity variations in space.

Formulation

The equation that describes steady heat conduction is

$$\nabla \cdot (k \nabla T) + S = 0 \tag{1}$$

where k is thermal conductivity, T is temperature, and S is a distributed source. The transformation

$$y = k^{1/2} T \tag{2}$$

inserted into equation (1) gives

$$\nabla \cdot [Z^2 \nabla (Z^{-1} y)] + S = 0 \tag{3}$$

where $Z = k^{1/2}$. Since the gradient of the product of two scalars f_1 and f_2 satisfies the relationship $\nabla (f_1 f_2) = f_1 \nabla f_2 + f_2 \nabla f_1$, equation (3) can be rewritten as

$$\nabla \cdot [Z \nabla y - y \nabla Z] + S = 0 \tag{4}$$

The divergence of the product of a scalar f_3 and a vector F_4 satisfies the relationship $\nabla \cdot (f_3 F_4) = f_3 \nabla \cdot F_4 + F_4 \cdot \nabla f_3$. Hence, equation (4) can be rewritten as

$$Z \nabla \cdot \nabla y - y \nabla \cdot \nabla Z + S = 0 \tag{5}$$

or

$$\nabla^2 y - f y + S/Z = 0 \tag{6}$$

where

$$f = \nabla^2 Z / Z \tag{7}$$

Although Bellman (1953) suggested the transformation of equation (2) some years ago as reported by Ozisik (1980, p. 75), the utility of putting the result into the forms of equations (6) and (7) was apparently not fully realized. The more general form $y = k^n T$ in place of equation (2) gives a result that is substantially simplified by setting $n = 1/2$ to get equation (6).

Boundary conditions imposed on the steady heat conduction equation (1) are transformed similarly. The case of a specified boundary temperature T_B is seen from equation (2) to be equivalent to a specified boundary value of

$$y = y_B \tag{8}$$

The transformed heat conduction equation (6), subject to the appropriate boundary conditions, can be exactly solved by standard methods for simple geometries if the conductivity varies in a convenient manner. For the sake of brevity, the convective and imposed heat flux boundary conditions that this method also handles are not discussed here.

Two-Dimensional Cylindrical Geometry

The cylinder of outer radius R with a specified surface

[1]AT&T Technologies, Lee's Summit, MO 64063.
[2]Professor, Mechanical Engineering Department, University of Kansas, Lawrence, KS 66045; Mem. ASME.

Contributed by the Heat Transfer Division for publication in the JOURNAL OF HEAT TRANSFER. Manuscript received by the Heat Transfer Division June 15, 1987. Keywords: Computer Codes, Conduction, Numerical Methods.

temperature $T_R(\theta)$ is a convenient geometry for the construction of an exact two-dimensional solution if it is assumed that f is solely a function of radius r. Equation (6) with $S = 0$ can then be written as

$$r^{-1}\partial(r\partial y/\partial r)/\partial r + r^{-2}\partial^2 y/\partial\theta^2 - f(r)y = 0 \quad (9)$$

subject to $y(R, \theta) = y_R(\theta)$.

Integrating equation (9) with respect to θ gives

$$r^{-1}d(rd\bar{y}/dr)/dr - f(r)\bar{y} = 0 \quad (10)$$

where

$$(\bar{\ }) = \int_0^{2\pi} (\ )d\theta/2\pi$$

The solution to equation (10) can be represented in terms of a function $F(r)$ as $\bar{y}(r) = AF(r)$. The constant A is determined from the boundary condition $\bar{y}(R) = \bar{y}_R$ to be $A = \bar{y}_R/F(R)$. Hence the solution to equation (10) is

$$\bar{y}(r) = \bar{y}_R F(r)/F(R) \quad (11)$$

Note that $\bar{y}$ and $\bar{Z}$ have solutions of the same form since, from equation (7),

$$\nabla^2 Z - f(r)Z = 0 \quad (12)$$

which is identical in form to equation (9). Hence $\bar{Z} = aF(r)$.

The constant a is evaluated as was done for equation (11) to obtain

$$\bar{Z}(r) = \bar{Z}_R F(r)/F(R) \quad (13)$$

Combining equations (11) and (13) yields

$$\bar{y}(r) = \bar{y}_R \bar{Z}(r)/\bar{Z}_R \quad (14)$$

The temperature at the center of the cylinder is obtained from equation (14) for $r = 0$ as

$$\int_0^{2\pi} k_0^{1/2} T(0, \theta)d\theta =$$

$$\left[\int_0^{2\pi} k_R^{1/2}(\theta)T_R(\theta)d\theta\right]\int_0^{2\pi} k_0^{1/2}d\theta / \int_0^{2\pi} k_R^{1/2}d\theta$$

where k_0 and $k_R(\theta)$ are thermal conductivities evaluated at the center and periphery, respectively. Since the center temperature T_0 cannot be a function of the angle θ, it is the weighted average of the boundary temperatures

$$T_0 = \int_0^{2\pi} \left[k_R^{1/2}(\theta)/\overline{k_R^{1/2}}\right] T_R(\theta)d\theta/2\pi \quad (15)$$

The thermal conductivity variations that are admissible in equation (15) are specified by equation (12). The case in which $f(r)$ is a constant C yields

$$A_0 I_0(cr) + \sum_{n=1}^{\infty} I_n(cr)(A_n \cos n\theta + B_n \sin n\theta), \quad C > 0 \quad (16a)$$

$$Z = k^{1/2} = A_0 + \sum_{n=1}^{\infty} r^n (A_n \cos n\theta + B_n \sin n\theta), \quad C = 0 \quad (16b)$$

$$A_0 J_0(cr) + \sum_{n=1}^{\infty} J_n(cr)(A_n \cos n\theta + B_n \sin n\theta), \quad C < 0 \quad (16c)$$

where $c = |C|^{1/2}$, $I_n(x)$ is the nth order modified Bessel function of the first kind, and $J_n(x)$ is the nth order Bessel function of the first kind (Ozisik, 1980). A variation described by equation (16a) is shown in Fig. 1.

The exact central temperature of a cylinder given by equation (15) with the continuous thermal conductivity of equation (16b) was used by Munoz (1984) to evaluate the performance of two finite difference methods. In one method the effective conductivity k_{eff} between nodes was the harmonic mean (Patankar, 1978) in which $k_{\text{eff},i} = 2/(1/k_{i+1/2} + 1/k_{i-1/2})$ with central finite differences applied to equation (1) with $S = 0$. In the other, the so-called square root representation, $k_{\text{eff},i} = k_i^{1/2}$ as determined by applying central finite differences to equations (6) and (7) with $S = 0$.

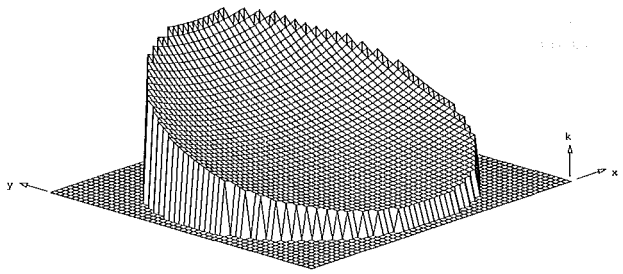

Fig. 1 Isometric representation of $k = [I_0(r) + I_1(r) \sin\theta]^2$

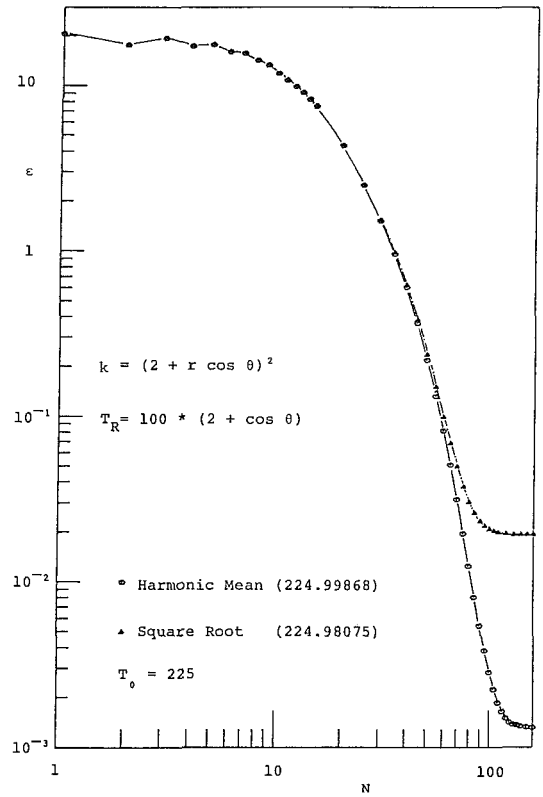

Fig. 2 Central cylinder temperature absolute error versus number of finite difference iterations for a linear radial $k^{1/2}$ variation and sinusoidal peripheral temperature

Results and Discussion

The central temperatures T_0 of the cylinder predicted by the two finite difference formulations were compared with the exact answers. To do this ϵ, the absolute value of the difference between the exact and finite difference answers, was plotted versus the number N of iterations as shown in Fig. 2. That the harmonic mean representation of thermal conductivity is of superior accuracy is readily seen because the exact value is known to be 225.

The exact temperature at the center of a cylinder is easily computed subject only to the restriction $\nabla^2 k^{1/2}/k^{1/2} = f(r)$. In other multidimensional geometries exact answers at any interior position are easily obtained by solving equation (6) with $f = C$ and can be used to evaluate the performance of numerical approximations. If f is not constant, the corresponding conductivity variation might still be expressible in terms of known functions. For example in a cylindrical geometry, if $f(r) = -\lambda_n^2 (R^2 - r^2)$ one could employ the

functions that have been determined for the Graetz problem of evaluating the temperature distribution in fully developed laminar flow in a round duct (Sellars et al., 1956; Jakob, 1949; Siegel et al., 1958). Likewise in a rectangular geometry, functions for the Graetz problem in a rectangular duct (Dennis et al., 1959) could be used if f is of the appropriate form. These exact answers could be used to establish the accuracy of predictions obtained by numerical methods.

References

Bellman, R., 1953, *Stability Theory of Differential Equations*, McGraw-Hill, New York, p. 109.

Dennis, S. C. R., Mercer, A. McD., and Poots, G., 1959, "Forced Heat Convection in Laminar Flow Through Rectangular Ducts," *Quarterly of Applied Mathematics*, Vol. 17, pp. 285–297.

Finlayson, B. A., 1972, *The Method of Weighted Residuals and Variational Principles*, Academic Press, New York.

Jakob, M., 1949, *Heat Transfer*, Vol. 1, Wiley, New York, pp. 451–455.

Luikov, A. V., 1971, "Methods of Solving the Nonlinear Equations of Unsteady-State Heat Conduction," *Heat Transfer—Soviet Research*, Vol. 3, pp. 1–51.

Munoz, Alberto V., 1984, "Variable Thermal Conductivity and the Monte Carlo Floating Random Walk," Master of Science Thesis, University of Kansas, Lawrence, KS.

Ozisik, M. N., 1980, *Heat Conduction*, Wiley-Interscience, New York.

Patankar, S. V., 1978, "A Numerical Method for Conduction in Composite Materials, Flow in Irregular Geometries and Conjugate Heat Transfer," *Proceedings of the Sixth International Heat Transfer Conference*, Toronto, Canada, Vol. 3, Paper No. CO-14, pp. 297–302.

Sellars, J. R., Tribus, M., and Klein, J. S., 1956, "Heat Transfer to Laminar Flow in a Round Tube or Flat Conduit—The Graetz Problem Extended," *Trans. ASME*, Vol. 78, pp. 441–448.

Shaughnessy, E. J., and McMurray, J. T., 1979, "Chebyshev Matrix Methods for the Heat Equation: Convergence and Accuracy," ASME Paper No. 79-HT-62.

Siegel, R., Sparrow, E. M., and Hallman, T. M., 1958, "Steady Laminar Heat Transfer in a Circular Tube With Prescribed Wall Heat Flux," *Applied Scientific Research 7A*, pp. 386–392.

Two-Dimensional Fin Performance: Bi (top surface) ≥ Bi (bottom surface)

D. C. Look, Jr.[1]

Nomenclature

- Bi = Biot number = hl/k
- h = convection coefficient
- k = thermal conductivity
- l = one half fin thickness
- L' = fin length
- L = L'/l
- P = fin perimeter = $2(2l + z)$
- Q = power lost by the fin per length along root under steady-state conditions, W/m
- T = fin temperature, °C
- x' = along the fin variable (root to tip) $\leq L$
- x = x'/l
- y' = across the fin variable $\leq |\pm l|$
- y = y'/l
- ϵ = thermal asymmetry factor = $[B_1 - B_2]/B_1$
- θ = adjusted fin temperature excess = $T - T_\infty$
- θ_o = $T_w - T_\infty$
- λ' = eigenfunction
- λ = $\lambda' l$

Subscripts

- 1 = one dimensional or, if two dimensional, top fin surface
- 2 = two dimensional or bottom fin surface
- 3 = fin tip surface
- w = wall or root
- ∞ = ambient

Introduction

A common simplification that is made when analyzing an extended surface is to assume that the temperature within the fin varies only in the dimension directly away from the root (x'). Avrami and Little (1942), Burmeister (1979), Irey (1968), Keller and Sommers (1959), Lau and Tan (1963), and Snider and Kraus (1983) have shown that this one-dimensional approach is convenient but may be in error when the physical conditions are such that the one-dimensional analysis is not valid (e.g., when the convection coefficient h is large compared to the fin material thermal conductivity). Typically this information is described by the root Biot number.

Another situation where the usual one-dimensional assumption is particularly in error is when the convection coefficients of all the heat transfer surfaces are not the same. That is, even though examples are presented where the magnitudes of the convection coefficients at the fin tip and the other heat transfer surfaces are different, the one-dimension restriction does not allow the convection coefficient to be different for those other surfaces. Further, perusal of any heat transfer book will yield experimental correlations that represent different behavior for a hot surface facing up and a hot surface facing down (Ozisik, 1985). This difference may be greater than a factor of 2 when all other parameters are equal. Thus even though the convection coefficient h is not truly constant from the root to the tip in the real case (Stachiewicz, 1969), h (top surface) is greater than or, at the best, equal to h (bottom surface).

This note presents the results of an investigation of unequal convection coefficient effects on the heat lost from a fin. Heat balance integral approaches have been applied to this two-dimensional problem with useful results for the heat transfer but only approximate results for the temperature distribution (Steir, 1976). Thus the purpose of this note is to provide additional insight into the effects of unequal top, bottom, and tip surface convection coefficients. This difference will be denoted by the Biot numbers Bi rather than the convection coefficients.

Two-Dimensional Analysis

In the case of a two-dimensional rectangular fin, the governing equation and boundary conditions are

$$\frac{\partial^2\theta}{\partial x^2}+\frac{\partial^2\theta}{\partial y^2}=0 \tag{1}$$

$$x=0,\quad \theta=\theta_o \tag{2}$$

$$x=L,\quad k\frac{\partial\theta}{\partial x}+h_3\theta=0 \tag{3}$$

$$-l\leq y\leq l$$

$$y=l,\quad k\frac{\partial\theta}{\partial y}+h_1\theta=0 \tag{4}$$

$$y=-l,\quad k\frac{\partial\theta}{\partial y}-h_2\theta=0 \tag{5}$$

$$0\leq x\leq L$$

[1]Mechanical and Aerospace Engineering Department, University of Missouri—Rolla, Rolla, MO 65401.

Contributed by the Heat Transfer Division for publication in the JOURNAL OF HEAT TRANSFER. Manuscript received by the Heat Transfer Division April 16, 1987. Keywords: Finned Surfaces, Modeling and Scaling.

functions that have been determined for the Graetz problem of evaluating the temperature distribution in fully developed laminar flow in a round duct (Sellars et al., 1956; Jakob, 1949; Siegel et al., 1958). Likewise in a rectangular geometry, functions for the Graetz problem in a rectangular duct (Dennis et al., 1959) could be used if f is of the appropriate form. These exact answers could be used to establish the accuracy of predictions obtained by numerical methods.

References

Bellman, R., 1953, *Stability Theory of Differential Equations*, McGraw-Hill, New York, p. 109.

Dennis, S. C. R., Mercer, A. McD., and Poots, G., 1959, "Forced Heat Convection in Laminar Flow Through Rectangular Ducts," *Quarterly of Applied Mathematics*, Vol. 17, pp. 285–297.

Finlayson, B. A., 1972, *The Method of Weighted Residuals and Variational Principles*, Academic Press, New York.

Jakob, M., 1949, *Heat Transfer*, Vol. 1, Wiley, New York, pp. 451–455.

Luikov, A. V., 1971, "Methods of Solving the Nonlinear Equations of Unsteady-State Heat Conduction," *Heat Transfer—Soviet Research*, Vol. 3, pp. 1–51.

Munoz, Alberto V., 1984, "Variable Thermal Conductivity and the Monte Carlo Floating Random Walk," Master of Science Thesis, University of Kansas, Lawrence, KS.

Ozisik, M. N., 1980, *Heat Conduction*, Wiley-Interscience, New York.

Patankar, S. V., 1978, "A Numerical Method for Conduction in Composite Materials, Flow in Irregular Geometries and Conjugate Heat Transfer," *Proceedings of the Sixth International Heat Transfer Conference*, Toronto, Canada, Vol. 3, Paper No. CO-14, pp. 297–302.

Sellars, J. R., Tribus, M., and Klein, J. S., 1956, "Heat Transfer to Laminar Flow in a Round Tube or Flat Conduit—The Graetz Problem Extended," *Trans. ASME*, Vol. 78, pp. 441–448.

Shaughnessy, E. J., and McMurray, J. T., 1979, "Chebyshev Matrix Methods for the Heat Equation: Convergence and Accuracy," ASME Paper No. 79-HT-62.

Siegel, R., Sparrow, E. M., and Hallman, T. M., 1958, "Steady Laminar Heat Transfer in a Circular Tube With Prescribed Wall Heat Flux," *Applied Scientific Research 7A*, pp. 386–392.

Two-Dimensional Fin Performance: Bi (top surface) ≥ Bi (bottom surface)

D. C. Look, Jr.[1]

Nomenclature

- Bi = Biot number = hl/k
- h = convection coefficient
- k = thermal conductivity
- l = one half fin thickness
- L' = fin length
- L = L'/l
- P = fin perimeter = $2(2l + z)$
- Q = power lost by the fin per length along root under steady-state conditions, W/m
- T = fin temperature, °C
- x' = along the fin variable (root to tip) $\leq L$
- x = x'/l
- y' = across the fin variable $\leq |\pm l|$
- y = y'/l
- ϵ = thermal asymmetry factor = $[B_1 - B_2]/B_1$
- θ = adjusted fin temperature excess = $T - T_\infty$
- θ_o = $T_w - T_\infty$
- λ' = eigenfunction
- λ = $\lambda' l$

Subscripts

- 1 = one dimensional or, if two dimensional, top fin surface
- 2 = two dimensional or bottom fin surface
- 3 = fin tip surface
- w = wall or root
- ∞ = ambient

Introduction

A common simplification that is made when analyzing an extended surface is to assume that the temperature within the fin varies only in the dimension directly away from the root (x'). Avrami and Little (1942), Burmeister (1979), Irey (1968), Keller and Sommers (1959), Lau and Tan (1963), and Snider and Kraus (1983) have shown that this one-dimensional approach is convenient but may be in error when the physical conditions are such that the one-dimensional analysis is not valid (e.g., when the convection coefficient h is large compared to the fin material thermal conductivity). Typically this information is described by the root Biot number.

Another situation where the usual one-dimensional assumption is particularly in error is when the convection coefficients of all the heat transfer surfaces are not the same. That is, even though examples are presented where the magnitudes of the convection coefficients at the fin tip and the other heat transfer surfaces are different, the one-dimension restriction does not allow the convection coefficient to be different for those other surfaces. Further, perusal of any heat transfer book will yield experimental correlations that represent different behavior for a hot surface facing up and a hot surface facing down (Ozisik, 1985). This difference may be greater than a factor of 2 when all other parameters are equal. Thus even though the convection coefficient h is not truly constant from the root to the tip in the real case (Stachiewicz, 1969), h (top surface) is greater than or, at the best, equal to h (bottom surface).

This note presents the results of an investigation of unequal convection coefficient effects on the heat lost from a fin. Heat balance integral approaches have been applied to this two-dimensional problem with useful results for the heat transfer but only approximate results for the temperature distribution (Steir, 1976). Thus the purpose of this note is to provide additional insight into the effects of unequal top, bottom, and tip surface convection coefficients. This difference will be denoted by the Biot numbers Bi rather than the convection coefficients.

Two-Dimensional Analysis

In the case of a two-dimensional rectangular fin, the governing equation and boundary conditions are

$$\frac{\partial^2\theta}{\partial x^2}+\frac{\partial^2\theta}{\partial y^2}=0 \tag{1}$$

$$x=0,\quad \theta=\theta_o \tag{2}$$

$$x=L,\quad k\frac{\partial\theta}{\partial x}+h_3\theta=0 \tag{3}$$

$$-l\leq y\leq l$$

$$y=l,\quad k\frac{\partial\theta}{\partial y}+h_1\theta=0 \tag{4}$$

$$y=-l,\quad k\frac{\partial\theta}{\partial y}-h_2\theta=0 \tag{5}$$

$$0\leq x\leq L$$

[1]Mechanical and Aerospace Engineering Department, University of Missouri—Rolla, Rolla, MO 65401.

Contributed by the Heat Transfer Division for publication in the JOURNAL OF HEAT TRANSFER. Manuscript received by the Heat Transfer Division April 16, 1987. Keywords: Finned Surfaces, Modeling and Scaling.

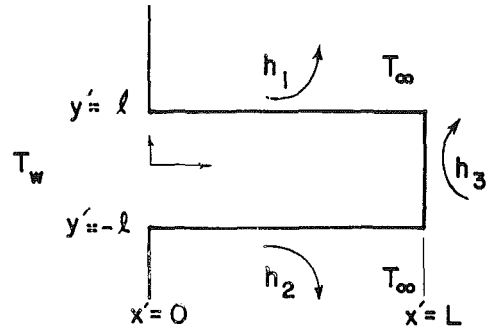

Fig. 1 Geometry of a thermally asymmetric, constant cross sectional area, rectangular fin

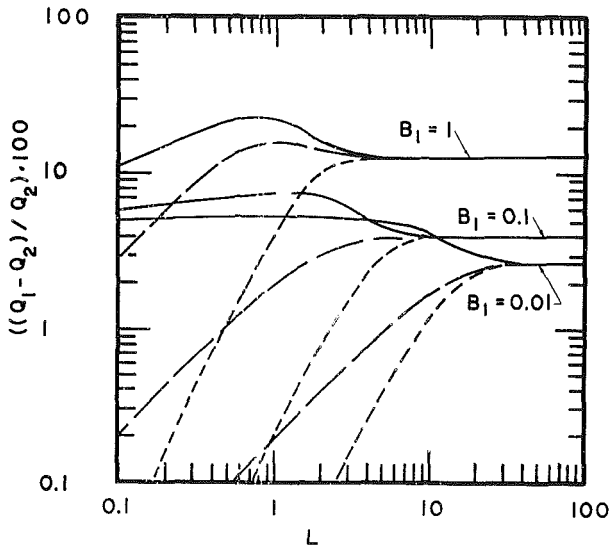

Fig. 2 Percent relative difference between the one-dimensional and two-dimensional heat losses from the fin when Bi_1/Bi_2 = 1/0.9; (——— Bi_3 = 0, — — — Bi_3 = 0.25, ----- $Bi_3 \to \infty$)

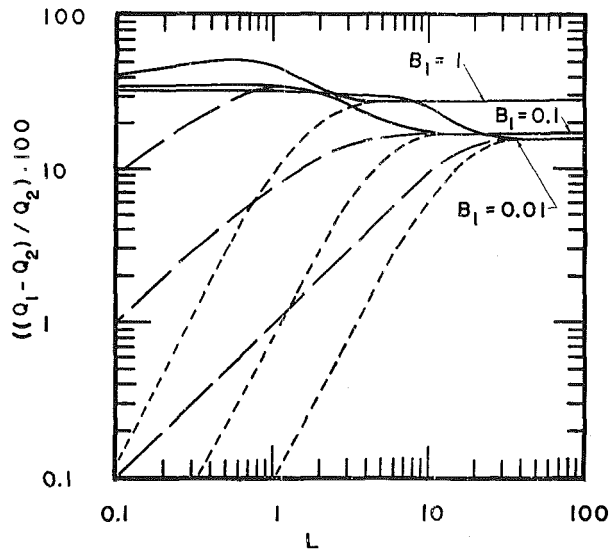

Fig. 3 Percent relative difference between the one-dimensional and two-dimensional heat losses from the fin when Bi_1/Bi_2 = 1/0.5; (——— Bi_3 = 0, — — — Bi_3 = 0.25, ----- $Bi_3 \to \infty$)

Figure 1 illustrates the geometry of this problem. The solution of equation (1) using the boundary conditions of equations (2)–(5) is

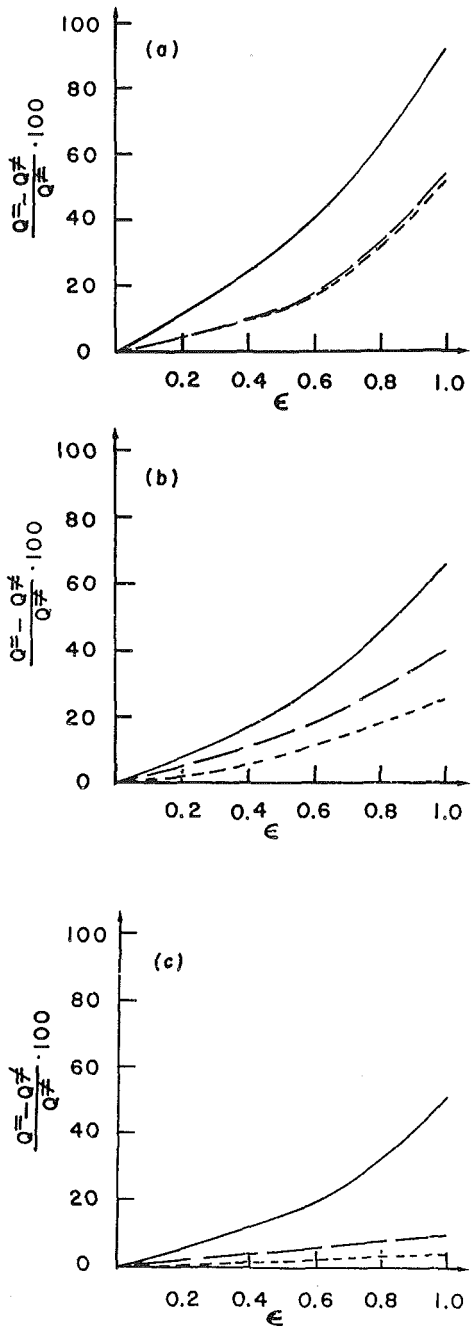

Fig. 4 Percent relative difference between the heat lost from a two-dimensional fin with equal Biot numbers ($Q^{=}$) and unequal Biot numbers ($Q^{\neq}$) versus the asymmetry factor ϵ when $L = 5$, and
(*a*) Bi_1 = 1 (——— Bi_3 = 0, — — — Bi_3 = 0.25, --- $Bi_3 \to \infty$)
(*b*) Bi_1 = 0.1 (——— Bi_3 = 0, — — — Bi_3 = 0.25, --- $Bi_3 \to \infty$)
(*c*) Bi_1 = 0.01 (——— Bi_3 = 0, — — — Bi_3 = 0.25, --- $Bi_3 \to \infty$)

$$\theta = 2\theta_o \sum_{n=1}^{\infty} \frac{\sin(\lambda_n) f_1(y) f_2(x)}{\lambda_n f_2(x=0) f_3} \tag{6}$$

and the heat lost per fin length in this two-dimensional case is

$$Q_2 = \int_{-\ell}^{\ell} \left[-k \frac{\partial T}{\partial x} \right]_{x=0} dy = 4k\theta_o \sum_{n=1}^{\infty} \frac{\sin^2(\lambda_n) f_4}{\lambda_n f_2(x=0) f_3} \tag{7}$$

where

$$f_1(y) = \cos(\lambda_n y) + C_n \sin(\lambda_n y) \tag{8}$$

$$f_2(x) = \cosh[\lambda_n (L-x)] + (\mathrm{Bi}_3/\lambda_n) \sinh[\lambda_n (L-x)] \tag{9}$$

$$f_3 = 1 + \sin(2\lambda_n)/2\lambda_n + C_n^2[1 - \sin(2\lambda_n)/2\lambda_n] \quad (10)$$

$$f_4 = \sinh(\lambda_n L) + (\mathrm{Bi}_3/\lambda_n)\cosh(\lambda_n L) \quad (11)$$

and

$$C_n = \frac{(\lambda_n)\tan(\lambda_n) - \mathrm{Bi}_1}{(\lambda_n) + \mathrm{Bi}_1\tan(\lambda_n)} = \frac{-(\lambda_n)\tan(\lambda_n) + \mathrm{Bi}_2}{(\lambda_n) + \mathrm{Bi}_2\tan(\lambda_n)} \quad (12)$$

The values of λ_n come from the roots of the last two expressions of equation (12).

Results

A personal computer was used to determine the eigenfunctions of equation (12) using a Newton–Raphson method. The results obtained when $Bi_1 = Bi_2$ were in exact agreement with the values tabulated in Ozisik (1985) for the first six values. Further, equations (6) and (7) were used to compute the temperature profiles and heat transfer per fin length. In each case the summing process was terminated when the last term computed contributed less than 0.00001.

Figures 2 and 3 may be used to compare the tip effects for various asymmetric conditions. The parameter in these two figures is the Biot number of the tip, Bi_3. The situations selected for comparison in these figures are (1) an insulated tip, denoted by $Bi_3 = 0$; (2) $Bi_3 = 0.25$, a convenient but arbitrarily selected value; and (3) the tip temperature the same as the ambient temperature. This last situation is represented as $Bi_3 \to \infty$ (i.e., $Bi_3\,(T(x = L) - T_\infty)$ must be finite). In each case the tip effects are obscured for L greater than 30, 10, or 5 depending upon Bi_1 and not the Biot number ratio.[2] Figure 4 may be used to compare the effect of asymmetry produced by different top and bottom surfaces Biot numbers (i.e., ϵ). Note, the relative error resulting when the heat lost by the fin with $Bi_1 = Bi_2$ is used instead of actual case ($Bi_1 > Bi_2$) increases as the difference becomes larger and as the top surface Biot number increases.

Conclusions

Study of the figures of this presentation indicates that the fin tip condition is a lesser parameter in its effects on the thermal characteristics of a fin than the unequal surface Biot numbers.

References

Avrami, M., and Little, J. B., 1942, "Diffusion of Heat Through a Rectangular Bar and the Cooling and Insulating Effects of Fins," *Journal of Applied Physics*, Vol. 13, pp. 255–264.

Burmeister, L. C., 1979, "Triangular Fin Performance by the Heat Balance Integral Method," ASME JOURNAL OF HEAT TRANSFER, Vol. 101, pp. 565–564.

Irey, R. K., 1968, "Errors in the One-Dimensional Fin Solution," ASME JOURNAL OF HEAT TRANSFER, Vol. 90, pp. 175–176.

Keller, H. H., and Somers, E. V., 1959, "Heat Transfer From an Annular Fin of Constant Thickness," ASME JOURNAL OF HEAT TRANSFER, Vol. 81, pp. 151–156.

Lau, W., and Tan, C. W., 1963, "Errors in One-Dimensional Heat Transfer Analyses in Straight and Annular Fins," ASME JOURNAL OF HEAT TRANSFER, Vol. 95, pp. 549–551.

Ozisik, M. N., 1985, *Heat Transfer—A Basic Approach*, McGraw-Hill, New York.

Snider, A. D., and Kraus, A. D., 1983, "Recent Developments in the Analyses and Design of Extended Surfaces," ASME JOURNAL OF HEAT TRANSFER, Vol. 105, pp. 302–306.

Stachiewicz, J. W., 1969, "Effect of Variation of Local Film Coefficients on Fin Performance," ASME JOURNAL OF HEAT TRANSFER, Vol. 91, pp. 21–26.

Steir, A. A., 1976, "The Heat Balance Integral in Steady-State Conduction," ASME JOURNAL OF HEAT TRANSFER, Vol. 98, pp. 466–470.

[2] Each curve of Figs. 2 and 3 may be linearly extrapolated on log–log paper to very small L values.

Multipass Heat Exchangers With a Single Well-Mixed Shell Pass

R. A. Seban[1]

Nomenclature

- a = constant in equation (14), unity for odd number of passes, zero for even
- A = group, equation (14)
- B = group, equation (14)
- C = group, equation (14)
- C_c = tube side (cold fluid) capacity rate, W/C
- C_H = shell side (hot fluid) capacity rate, W/C
- D = group, equation (14)
- F = group, equation (21)
- H = exp $(-2S\,\eta_L)$
- L = exchanger shell side length
- $l-r$ = tube side (cold fluid) flow is left to right
- $L-\mathrm{R}$ = shell side (hot fluid) flow is right to left
- M = constant, equation (10)
- N = number of double passes
- P = perimeter of all of the tubes in a pass
- R = ratio of capacity rates $= C_H/C_c$
- $r-l$ = tube side (cold fluid) flow is right to left
- $R-L$ = shell side (hot fluid) flow is right to left
- S = $R/(2N)$ for even number of passes, $R/(2N+1)$ for odd
- t = tube side (cold fluid) temperature
- T = shell side (hot fluid) temperature
- U = overall heat transfer coefficient, based on area associated with P, W/m^{2}C
- x = $2S$, as in equation (24)
- z = distance along exchanger length; $z=0$ on the left
- η = UP (number of passes) z/C_H, number of transfer units, η_L for $z=L$

Introduction

Analytical expressions for the performance of a shell and tube heat exchanger with a single, well-mixed shell pass and for two, three, or four tube passes have long been available. When the number of tube passes becomes very large, the shell fluid acts as though it was well mixed laterally with a single pass normal to that of the shell side fluid; this is the case of the crossflow exchanger with both fluids well mixed and expressions for the performance of this exchanger are available also. The analysis for all of these cases is reviewed in Jakob (1957). Noted there is the early comparison of the performance of the two-pass system with that of the cross flow exchanger, typical of a very large number of passes, to indicate that for normal values of the number of transfer units the effectiveness is in both cases almost the same. Because of this, the performance

[1] Professor Emeritus, Department of Mechanical Engineering, University of California at Berkeley, Berkeley, CA 94720; Hon. Mem. ASME.

Contributed by the Heat Transfer Division for publication in the JOURNAL OF HEAT TRANSFER. Manuscript received by the Heat Transfer Division May 10, 1987. Keywords: Heat Exchangers, Modeling and Scaling.

$$f_3 = 1 + \sin(2\lambda_n)/2\lambda_n + C_n^2[1 - \sin(2\lambda_n)/2\lambda_n] \quad (10)$$

$$f_4 = \sinh(\lambda_n L) + (\mathrm{Bi}_3/\lambda_n)\cosh(\lambda_n L) \quad (11)$$

and

$$C_n = \frac{(\lambda_n)\tan(\lambda_n) - \mathrm{Bi}_1}{(\lambda_n) + \mathrm{Bi}_1\tan(\lambda_n)} = \frac{-(\lambda_n)\tan(\lambda_n) + \mathrm{Bi}_2}{(\lambda_n) + \mathrm{Bi}_2\tan(\lambda_n)} \quad (12)$$

The values of λ_n come from the roots of the last two expressions of equation (12).

Results

A personal computer was used to determine the eigenfunctions of equation (12) using a Newton–Raphson method. The results obtained when $Bi_1 = Bi_2$ were in exact agreement with the values tabulated in Ozisik (1985) for the first six values. Further, equations (6) and (7) were used to compute the temperature profiles and heat transfer per fin length. In each case the summing process was terminated when the last term computed contributed less than 0.00001.

Figures 2 and 3 may be used to compare the tip effects for various asymmetric conditions. The parameter in these two figures is the Biot number of the tip, Bi_3. The situations selected for comparison in these figures are (1) an insulated tip, denoted by $Bi_3 = 0$; (2) $Bi_3 = 0.25$, a convenient but arbitrarily selected value; and (3) the tip temperature the same as the ambient temperature. This last situation is represented as $Bi_3 \to \infty$ (i.e., $Bi_3\,(T(x = L) - T_\infty)$ must be finite). In each case the tip effects are obscured for L greater than 30, 10, or 5 depending upon Bi_1 and not the Biot number ratio.[2] Figure 4 may be used to compare the effect of asymmetry produced by different top and bottom surfaces Biot numbers (i.e., ϵ). Note, the relative error resulting when the heat lost by the fin with $Bi_1 = Bi_2$ is used instead of actual case ($Bi_1 > Bi_2$) increases as the difference becomes larger and as the top surface Biot number increases.

Conclusions

Study of the figures of this presentation indicates that the fin tip condition is a lesser parameter in its effects on the thermal characteristics of a fin than the unequal surface Biot numbers.

References

Avrami, M., and Little, J. B., 1942, "Diffusion of Heat Through a Rectangular Bar and the Cooling and Insulating Effects of Fins," *Journal of Applied Physics*, Vol. 13, pp. 255–264.

Burmeister, L. C., 1979, "Triangular Fin Performance by the Heat Balance Integral Method," ASME JOURNAL OF HEAT TRANSFER, Vol. 101, pp. 565–564.

Irey, R. K., 1968, "Errors in the One-Dimensional Fin Solution," ASME JOURNAL OF HEAT TRANSFER, Vol. 90, pp. 175–176.

Keller, H. H., and Somers, E. V., 1959, "Heat Transfer From an Annular Fin of Constant Thickness," ASME JOURNAL OF HEAT TRANSFER, Vol. 81, pp. 151–156.

Lau, W., and Tan, C. W., 1963, "Errors in One-Dimensional Heat Transfer Analyses in Straight and Annular Fins," ASME JOURNAL OF HEAT TRANSFER, Vol. 95, pp. 549–551.

Ozisik, M. N., 1985, *Heat Transfer—A Basic Approach*, McGraw-Hill, New York.

Snider, A. D., and Kraus, A. D., 1983, "Recent Developments in the Analyses and Design of Extended Surfaces," ASME JOURNAL OF HEAT TRANSFER, Vol. 105, pp. 302–306.

Stachiewicz, J. W., 1969, "Effect of Variation of Local Film Coefficients on Fin Performance," ASME JOURNAL OF HEAT TRANSFER, Vol. 91, pp. 21–26.

Steir, A. A., 1976, "The Heat Balance Integral in Steady-State Conduction," ASME JOURNAL OF HEAT TRANSFER, Vol. 98, pp. 466–470.

[2] Each curve of Figs. 2 and 3 may be linearly extrapolated on log–log paper to very small L values.

Multipass Heat Exchangers With a Single Well-Mixed Shell Pass

R. A. Seban[1]

Nomenclature

- a = constant in equation (14), unity for odd number of passes, zero for even
- A = group, equation (14)
- B = group, equation (14)
- C = group, equation (14)
- C_c = tube side (cold fluid) capacity rate, W/C
- C_H = shell side (hot fluid) capacity rate, W/C
- D = group, equation (14)
- F = group, equation (21)
- H = exp $(-2S\,\eta_L)$
- L = exchanger shell side length
- $l-r$ = tube side (cold fluid) flow is left to right
- $L-\mathrm{R}$ = shell side (hot fluid) flow is right to left
- M = constant, equation (10)
- N = number of double passes
- P = perimeter of all of the tubes in a pass
- R = ratio of capacity rates $= C_H/C_c$
- $r-l$ = tube side (cold fluid) flow is right to left
- $R-L$ = shell side (hot fluid) flow is right to left
- S = $R/(2N)$ for even number of passes, $R/(2N+1)$ for odd
- t = tube side (cold fluid) temperature
- T = shell side (hot fluid) temperature
- U = overall heat transfer coefficient, based on area associated with P, W/m^{2}C
- x = $2S$, as in equation (24)
- z = distance along exchanger length; $z=0$ on the left
- η = UP (number of passes) z/C_H, number of transfer units, η_L for $z=L$

Introduction

Analytical expressions for the performance of a shell and tube heat exchanger with a single, well-mixed shell pass and for two, three, or four tube passes have long been available. When the number of tube passes becomes very large, the shell fluid acts as though it was well mixed laterally with a single pass normal to that of the shell side fluid; this is the case of the crossflow exchanger with both fluids well mixed and expressions for the performance of this exchanger are available also. The analysis for all of these cases is reviewed in Jakob (1957). Noted there is the early comparison of the performance of the two-pass system with that of the cross flow exchanger, typical of a very large number of passes, to indicate that for normal values of the number of transfer units the effectiveness is in both cases almost the same. Because of this, the performance

[1] Professor Emeritus, Department of Mechanical Engineering, University of California at Berkeley, Berkeley, CA 94720; Hon. Mem. ASME.

Contributed by the Heat Transfer Division for publication in the JOURNAL OF HEAT TRANSFER. Manuscript received by the Heat Transfer Division May 10, 1987. Keywords: Heat Exchangers, Modeling and Scaling.

Table 1

Cold (tube)

$$\text{L-R} + \frac{dt}{dz} = \frac{UP}{C_c}(T-t) \qquad (1)\quad \text{L-R} + \frac{dt}{d\eta} = S\,(T-t) \qquad S = \frac{C_H/C_L}{(\text{passes})}$$

Hot (shell)

$$\text{L-R} - \frac{dT}{dz} = \frac{UP\ (\text{passes})}{C_H}(T - t_{AVG}) \qquad (2)\quad \text{L-R} - \frac{dT}{d\eta} = (T - t_{AVG}) \qquad \eta = \frac{UP\ (\text{passes})\,z}{C_H}$$

$$R = C_H/C_c$$

Average cold fluid temperature

EVEN, 2N passes

$$t_{AVG} = \frac{1}{2N}\left(\underset{L-R}{N}\,t + \underset{R-L}{N}\,t\right)$$

ODD, (2N + 1) passes

$$(3)\quad t_{AVG} = \frac{1}{(2N+1)}\left(\underset{L-R}{N+1}\,t + \underset{R-L}{N}\,t\right)$$

Differentiate (3) and use (1)

$$\frac{d\,t_{AVG}}{d\eta} = \frac{S}{2N}\left(-\underset{L-R}{N}\,t + \underset{R-L}{N}\,t\right)$$

$$(4)\quad \frac{d\,t_{AVG}}{d\eta} = \frac{S}{(2N+1)}\left(T - \underset{L-R}{N+1}\,t + \underset{R-L}{N}\,t\right)$$

Local energy balance

$$\text{R-L} + R\frac{dT}{d\eta} = \underset{L-R}{N}\frac{dt}{d\eta} - \underset{R-L}{N}\frac{dt}{d\eta}$$

$$(5)\quad \text{R-L} + R\frac{dT}{d\eta} = \underset{L-R}{N+1}\frac{dt}{d\eta} - \underset{R-L}{N}\frac{dt}{d\eta}$$

Integrate (5) from zero to η

$$\text{R-L} + \frac{C_H}{C_c}(T-T_0) = \underset{L-R}{N}\,t - \underset{R-L}{N}\,t - t_{in} + t_{out}$$

$$(6)\quad \text{R-L} + R\,(T - T_0) = \underset{L-R}{N+1}\,t - \underset{R-L}{N}\,t - t_{in}$$

Combine (4) and (6)

$$\frac{d\,t_{AVG}}{d\eta} = \frac{S}{2N}\left((t_{out} - t_{in}) \underset{L-R}{\overset{R-L}{\pm}} R\,(T - T_0)\right)$$

$$(7)\quad \frac{d\,t_{AVG}}{d\eta} = \frac{S}{(2N+1)}\left((T - t_{in}) \underset{L-R}{\overset{R-L}{\pm}} R\,(T - T_0)\right)$$

$$\frac{d\,t_{AVG}}{d\eta} = \frac{S}{2N}\left((R\,(T_{in} - T_{out}) \underset{L-R}{\overset{R-L}{\pm}} R\,(T - T_0)\right)$$

for L-R $T_{in} = T_0$ $T_{out} = T_L$

R-L $T_{in} = T_L$ $T_{out} = T_0$

$$\frac{d\,t_{AVG}}{d\eta} = \underset{L-R}{\overset{R-L}{\pm}} S^2\,(T - T_L)$$

$$(8)\quad \frac{d\,t_{AVG}}{d\eta} = \frac{1}{(2N+1)}\left((T - T_0)\left(1 \underset{L-R}{\overset{R-L}{\pm}} R\right) - (t_{in} - T_0)\right)$$

Hot fluid temperature distribution

Differentiate (2)

$$\text{L-R} + \frac{d^2T}{d\eta^2} + \frac{dT}{d\eta} - \frac{d\,t_{AVG}}{d\eta} = 0$$

same

Use (8) with T_L as datum

$$\text{L-R} + \frac{d^2T}{d\eta^2} + \frac{dT}{d\eta} \underset{L-R}{\overset{R-L}{\pm}} S^2 T = 0$$

Use (8) with T_0 as datum

$$(9)\quad \text{L-R}\ \frac{d^2T}{d\eta^2} + \frac{dT}{d\eta} - S^2\left(1 + \frac{1}{R}\right)T = -\frac{S}{2N+1}\,t_{in}$$

$$\text{R-L}\ \frac{d^2T}{d\eta^2} - \frac{dT}{d\eta} - S^2\left(1 - \frac{1}{R}\right)T = \frac{S}{2N+1}\,t_{in}$$

Solution

$$\frac{T}{M} = c_1 e^{r_1\eta} + c_2 e^{r_2\eta}, \quad M = T_0$$

$$(10)\quad \frac{T}{M} = 1 + c_1 e^{r_1\eta} + c_2 e^{r_2\eta}$$

$M = t_{in}/(1+R)$ for hot fluid L-R

$M = t_{in}/(1-R)$ for hot fluid R-L

$$\text{L-R}\ \ r_{1,2} = \frac{1}{2}\left[-1 \pm \sqrt{1 + 4S^2}\,\right]$$

$$(11)\quad \text{L-R}\ \ r_{1,2} = \frac{1}{2}\left[-1 \pm \sqrt{1 + 4S^2\,(1 + 1/R)}\,\right]$$

$$\text{R-L}\ \ r_{1,2} = \frac{1}{2}\left[1 \pm \sqrt{1 + 4S^2}\,\right]$$

$$\text{R-L}\ \ r_{1,2} = \frac{1}{2}\left[1 \pm \sqrt{1 + 4S^2\,(1 - 1/R)}\,\right]$$

$$c_1 = \frac{1}{1 - e^{(r_2 - r_1)\eta_L}}, \qquad c_2 = 1 - c_1$$

$$(12)\quad c_1 = \frac{(T_L/M) - 1 + e^{r_2\eta_L}}{e^{r_1\eta_L} - e^{r_2\eta_L}}, \qquad c_2 = -(1 + c_1)$$

Cold Fluid Temperature Distribution

Cold L-R

Solution of (1)

$$t = e^{-S\eta}\left[\int e^{+S\eta}\,(ST)\,d\eta + c_{Lr}\right]$$

Cold R-L

$$(13)\quad t = e^{S\eta}\left[\int e^{-S\eta}\,(-ST)\,d\eta + c_{Rt}\right]$$

From (10) $\frac{T}{M} = a + c_1 e^{r_1\eta} + c_2 e^{r_2\eta}$ where a = 0 for an even number of passes and a = 1 for an odd number

Substitution into (13) gives:

$$t/M = a + \underbrace{\frac{c_1 e^{r_1\eta}}{(1 + r_1/S)} + \frac{c_2 e^{r_2\eta}}{(1 + r_2/S)}}_{I} + c_{Lr}e^{-S\eta}$$

$$(14)\quad t/M = a + \underbrace{\frac{c_1 e^{r_1\eta}}{(1 - r_1/S)} + \frac{c_2 e^{r_2\eta}}{(1 - r_2/S)}}_{II} + c_{Rt}e^{+S\eta}$$

	I	II
for $\eta = 0$	A	C
$\eta = \eta_L$	B	D

$$(C-A) = c_1\frac{2(r_1/S)}{1 - (r_1/S)^2} + c_2\frac{2(r_2/S)}{1 - (r_2/S)^2}$$

$$(D-B) = c_1 e^{r_1\eta_L}\frac{2(r_1/S)}{1 - (r_1/S)^2} + c_2 e^{r_2\eta_L}\frac{2(r_2/S)}{1 - (r_2/S)^2}$$

as specified for the two-pass exchanger is taken to apply also for any number of even passes, a recommendation made in all heat transfer books. With an odd number of passes simple algebraic relations for the effectiveness cannot be obtained so that in Jakob (1957) there is no comparison of the three-pass exchanger with one of many passes. Recently O'Hare et al. (1986) have given some results for the effectiveness of three and five-pass exchangers obtained from numerical solutions for these systems.

Here this exchanger problem is considered again and in view of its history, and of the substantial idealization involved in the well-mixed fluid assumption that is associated with the shell side fluid, some justification is needed for this further examination. This is based on a more unified presentation for all of the cases for both even and odd numbers of tube passes, which gives explicit expressions for the outlet temperature of the tube side fluid. A simple algebric result for the effectiveness is obtained for an even number of passes. One is not obtainable for an odd number of passes so that for this case the determination of the effectiveness involves a sequence of arithmetic equations, simpler however than a finite difference solution for the whole exchanger.

Analysis

The exchanger shell extends from $z=0$ to $z=L$ and within the shell there are tube passes into which one fluid, here called the cold fluid, enters at $z=0$ with inlet temperature t_{in} and capacity C_c. The shell side fluid temperatures are T_0 at $z=0$ and T_L at $z=L$; this fluid is called the hot fluid and its capacity rate is C_H. The hot fluid can flow either from $z=0$ to $z=L$ (left to right, designated as $L-R$) or from $z=L$ to $z=0$ (right to left, designated $R-L$). With P the total perimeter of all the parallel tubes in any pass and U the overall heat transfer coefficient based on the area associated with the perimeter definition, the rate equations for the cold and hot fluids are equations (1) and (2) of Table 1. For the cold fluid the flow directions are left to right, $l-r$, in the odd numbered passes, and right to left, $r-l$, in the even. These equations are given on the left in dimensional form and on the right in nondimensional form, with the generalized distance being $[UP(\text{passes})z/C_H]$, the transfer units; the ratio of capacity rates C_H/C_c being R; and the parameter S being $R/(\text{passes})$. The number of passes is $2N$ for an even number of passes and $(2N+1)$ for an odd number of passes, Equations (1) and (2), together with the overall energy balance, lead ultimately to the cold fluid temperature distribution as indicated by the tabulated algebra.

The words hot and cold fluid are adopted here as a convenient designation, rather than shell side fluid and tube side fluid, but it is the latter that is really referred to and the results are to be considered on the basis that, when for instance the hot fluid temperature distribution is obtained, it is actually the shell side fluid temperature distribution.

Equation (3) defines the average cold fluid temperature t_{AVG}, on the left side of Table 1 for an even number of passes and on the right side for an odd number. This expression is differentiated to give equation (4), which is ultimately combined with the energy balance to produce equation (7). In this balance, equation (5), the sign of the derivative of the hot fluid temperature depends on the flow direction of the hot fluid, $L-R$ or $R-L$, and this dependence is continued in all subsequent relations. Equation (7), for the derivative of the average cold fluid temperature for an even number of passes, is altered in form by the introduction of the overall energy balance to produce equation (8). For an odd number of passes the form is a rearrangement of equation (7). Next equation (2) is differentiated and equation (8) is used to eliminate the derivative of the average cold fluid temperature to produce equation (9), a differential equation for the hot fluid temperature distribu-

Table 2

	datum	M	t_{out}	$(T_{in} - T_{out})/(T_{in} - t_{in})$
even (2N)	T_L			
L-R	T_{out}	T_{in}	$t_{in} + RT_{in}$	$1/(1 - t_{in}/T_{out})$
R-L	T_{in}	T_{out}	$t_{in} - RT_{out}$	T_{out}/t_{in}
odd (2N + 1)	T_o			
L-R	T_{in}	$t_{in}/(1 + R)$	$t_{in} - RT_{out}$	T_{out}/t_{in}
R-L	T_{out}	$t_{in}/(1 - R)$	$t_{in} + RT_{in}$	$1/(1 - t_{in}/T_{in})$

tion. In this operation the hot fluid temperature at $z=L$, T_L, is chosen as datum when there is an even number of passes and the hot fluid temperature at $z=0$, T_0, is chosen as datum for an odd number of passes. Equations (10), in which M is defined as indicated, are the solutions of equation (9), $r_{1,2}$ are the roots of the differential operator in equations (9), and the constants c_1 and c_2 are defined as in equation (12). With the hot fluid temperature distribution determined, the cold fluid distribution is found from the formal solution of equation (1) which, as equation (13), depends on the direction of the cold fluid flow. The use of the hot fluid temperature distribution, equation (10), in equation (13) produces the final form for the cold fluid temperature distribution, equation (14). Quantities A, B, C, and D define three terms of this result evaluated for $\eta = 0$ and for $\eta = \eta_L$ and at the end of Table 1, two combinations of these quantities are defined for convenience.

The combination of these solutions for the distribution of the cold fluid temperature distribution for flow from left to right and for flow from right to left ultimately relates the cold fluid outlet temperature t_{out} to the inlet temperature t_{in}.

For the first pass, a left-right pass, which begins at $\eta=0$, equation (14) gives

$$\frac{t_{in}}{M}=\frac{t_{01}}{M}=A+[c_{lr}(1)] \tag{15}$$

At $\eta=\eta_L$ the temperature for this first pass is the temperature for the second pass ($a\ r-l$ pass)

$$\frac{t_{L1}}{M}=\frac{t_{L2}}{M}\ ;\ B+[c_{lr}(1)]e^{-S\eta_L}=D+[c_{rl}(2)]e^{S\eta_L} \tag{16}$$

At $\eta=0$, the end of this $r-l$ pass, the temperature is also the temperature for the next, $l-r$ pass

$$C+[c_{rl}(2)]=A+[c_{lr}(3)] \tag{17}$$

The elimination of constant $c_{rl}(2)$ from equations (16) and (17) gives

$$[c_{lr}(3)]=[(C-A)-(D-B)e^{-S\eta_L}]+[c_{lr}(1)]e^{-2S\eta_L} \tag{18}$$

Defining the first two bracketed terms on the right by Y and also defining $\exp(-2S\eta_L)$ as H makes this

$$[c_{lr}(3)]=Y+[c_{rl}(1)]H$$

In a general form equation (18) is

$$c_{lr}(i+2)=Y+H[c_{lr}(i)]$$

For example

$$c_{lr}(1)=\frac{t_{in}}{M}-A$$

$$c_{lr}(3)=Y+H[c_{lr}(1)]$$

$$c_{lr}(5)=Y+H[c_{lr}(3)]=Y+HY+[c_{lr}(1)]H^2$$

$$c_{lr}(7)=Y+H[c_{lr}(5)]=Y+HY+H^2Y+[c_{lr}(1)]H^3$$

Then generally

$$c_{lr}(2N+1)=Y\left(\frac{1-H^N}{1-H}\right)+\left(\frac{t_{in}}{M}-A\right)H^N \tag{19}$$

For an odd number, $(2N+1)$, of passes, the cold fluid outlet temperature is t_L for the last pass

$$\frac{t_{out}}{M}=\frac{t_L}{M}=B+[c_{lr}(2N+1)]e^{-S\eta_L} \tag{20}$$

or using equation (19)

$$\frac{t_{out}}{M}=B+\underbrace{\left[Y\left(\frac{1-H^N}{1-H}\right)-AH^N\right]e^{-S\eta_L}}_{\text{F}}+\frac{t_{in}}{M}\,e^{-(2N+1)S\eta_L} \tag{21}$$

For an even number $(2N)$ of passes, the outlet temperature is t_0 for the $(2N)$ pass. It is also t_0 for the (fictive), $(2N+1)$ pass

$$\frac{t_{out}}{M}=A+[c_{lr}(2N+1)] \tag{22}$$

Thus the cold fluid outlet temperature is given by either equation (20) or (22), with $[c_{lr}(2N+1)]$ obtained from equation (19). Table 2 gives, for the various flow arrangements, the datum for the temperature, the value of M, the value of the cold fluid outlet temperature in terms of the datum, and the ratio $(T_{in}-T_{out})/(T_{in}-t_{in})$, when the temperature datum is as indicated. For $R<1$ the effectiveness is defiend as

$$\frac{t_{out}-t_{in}}{T_{in}-t_{in}}\ \text{and this is}\ \frac{C_H}{C_c}\left(\frac{T_{in}-T_{out}}{T_{in}-t_{in}}\right) \tag{23}$$

Even Number of Passes

For an even number of passes, the roots $r_{1,2}$ given by equation (11) depend only on $2S$, now defined further as x, which is R/N. Then the relations become relatively simple, as partially illustrated here for the hot fluid as $L-R$

$$r_{1,2}=\frac{1}{2}\left[-1\pm\sqrt{1+x^2}\right];\quad \frac{r_{1,2}}{S}=\frac{-1\pm\sqrt{1+x^2}}{x}$$

$$1-\left(\frac{r_1}{S}\right)^2=\frac{-2+2\sqrt{1+x^2}}{x^2};\quad \frac{2r_1}{S}=\frac{-2+2\sqrt{1+x^2}}{x}$$

$$2\left(\frac{r_1}{S}\right)\Big/\left(1-\left(\frac{r_1}{S}\right)^2\right)=x;\ 2\left(\frac{r_2}{S}\right)\Big/\left(1-\left(\frac{r_2}{S}\right)^2\right)=x$$

$$(C-A)=(c_1+c_2)x=x;\quad (D-B)=x(c_1e^{r_1\eta_L}+c_2e^{r_2\eta_L})=0$$

$$Y=C-A)-(D-B)e^{-S\eta}=(C-A)=x$$

$$A=\frac{c_1}{1+r_1/S}+\frac{c_2}{1+r_2/S}=-1/2\Bigg[(x-1)+\sqrt{1+x^2}\left(\frac{1+e^{-(\sqrt{1+x^2})\eta_L}}{1-e^{-(\sqrt{1+x^2})\eta_L}}\right)\Bigg]$$

$$\frac{T_{in}-t_{in}}{T_{in}-T_{out}}=1-\frac{t_{in}}{T_{in}}=\frac{1}{2}\Bigg[(1+x)+\sqrt{1+x^2}\left(\frac{1+e^{-(\sqrt{1+x^2})\eta_L}}{1-e^{-(\sqrt{1+x^2})\eta_L}}\right)\Bigg]-\frac{x}{1-e^{-2S\eta_L}}+\frac{R}{1-e^{-R\eta_L}} \tag{24}$$

Equation (24) is the reciprocal of the effectiveness as defined for $R<1$. For $R>1$ the reciprocal of the effectiveness is obtained by multiplying equation (24) by C_c/C_H.

For a two-pass exchanger ($N=1$, $x=R$) the last two terms in equation (24) add to zero. This is the expression that is given

Table 3 Effectiveness values

CH/C_c	η_L	L-R (26)	R-L (25)	$N \to \infty$ (24)	O'Hare (1986) R-L (Polynomial)	Fig. 2 L-R	Fig. 2 R-L
1	1.5	.478	.527	.530	.530		
0.5	1.5	.618	.638	.638	.639	.62	.64
2.	.75	.628	.644	.638			

[as in for instance Holman (1986)] and then said to be applicable for any number of passes. This expression, for $N=1$, can be used as indicated to obtain the effectiveness for $R>1$. The form turns out to be the same as for $R<1$ if R is then defined as C_c/C_H, or, more specifically, as $C_{\min}/C_{\max}$ and the number of transfer units as $2UPL/C_{\min}$.

All of the above conclusions are the same if the hot fluid flow direction is $R-L$.

For $N>1$ the performance is given by equation (24). In the limit $N\to\infty$, the performance is that of the crossflow exchanger with both fluids well mixed laterally, which is

$$\frac{T_{in}-t_{in}}{T_{in}-T_{out}}=\left[\frac{R}{1-e^{-R\eta_L}}+\frac{1}{1-e^{-\eta_L}}+\frac{1}{\eta_L}\right] \tag{25}$$

A comparison of the values given by equations (24) and (25) shows that the ratio of the effectiveness for an infinite number of passes to the effectiveness for two passes is between 1.00 and 0.97 for $\eta_L<3$ when $R=1$; $\eta_L<4$ when $R=0.75$; $\eta_L<5$ when $R=0.5$; and $\eta_L<17$ when $R=0.25$. The ratio is lower for higher values of η_L, and for $\eta_L\to\infty$ the ratio is

$$\frac{1}{2}\left((1+R)+\sqrt{1+R^2}\right)/(1+R)$$

The ratio, is, for $R=0.5$ as an example, is equal to 0.872; the insensitivity of the effectiveness to the number of passes is true only for values of η_L less than those cited above, but those do include most of the critical values of η_L.

Odd Number of Passes

With an odd number of passes the roots, $r_{1,2}$ are given by equation (11), for $R-L$; they are

$$r_{1,2}=\frac{1}{2}\left[-1\pm\sqrt{1+x^2\left(1-\frac{1}{R}\right)}\right],\ R-L$$

The factor $(1-1/R)$ associated with x^2 precludes the simple relations by which equation (24) was attained for an even number of passes. Now equation (20) must be evaluated as it stands. Because the constants $c_{1,2}$ given by equation (12) each are the sum of a term that contains T_L/M as a factor and a second term, the quantity F in equation (21) is linear in T_L/M and it can be written in a form more convenient for calculation, as

$$\frac{t_{out}}{M}=\frac{T_L}{M}F_0+F_1+\frac{t_{in}}{M}e^{-R\eta_L},\ \text{since}\ (2N+1)S=R$$

Then, for the hot fluid as $R-L$, for which the datum is T_{out} and $M=t_{in}/(1+R)$, we obtain

$$\frac{T_{in}}{t_{in}}=\frac{F_1-(1-R)(1-e^{-R\eta_L})}{(1-R)(R-F_0)} \tag{26}$$

When $R=1$ the roots are such as to make F_1 equal to zero and thus equation (25) remains determinate.

For the hot fluid as $L-R$, for which the datum is T_{in} and $M=t_{in}/(1+R)$, we obtain

$$\frac{T_{out}}{t_{in}}=\frac{(1+R)(1-e^{-R\eta_L})-F_1}{(1+R)(R+F_0)} \tag{27}$$

No general comparison is possible, since the evaluation must be made for chosen values of R, $(2N+1)$, and η_L. As an example, values of the effectiveness for $N=1$ have been calculated for $\eta_L=1.5$, with C_H/C_0 equal to 1 and 0.5, for both hot fluid flow directions, $L-R$ to make the flow in two of the three passes parallel to that of the hot fluid, and $R-L$, to make this flow counter. Table 3 gives the values of the effectiveness from equations (26) and (27). Values from equation (25), the mixed fluids cross flow case, are included as are some from O'Hare et al. (1986).

With $C_H/C_c=1.5$ and 1.0 for the hot fluid $R-L$, in counterflow with two of the three tube passes, the effectiveness is practically the same as it is for an infinite number of tube passes. For the hot fluid $L-R$, in parallel with two of the tube passes, the effectiveness is slightly lower.

For $C_H/C_c=2$, for which the effectiveness is defined by equation (23), the value of η_L is taken as 0.75, so that with $A=P(2N+1)L$, $(UA/C_c)(C_c/C_H)=0.75$, to give $UA/C_H=UA/C_{\min}=1.5$ the same value that is associated with $C_H/C_0=0.5$. On this basis equation (25) gives the same effectiveness but the values from equations (26) and (27) for $C_H/C_c=0.5$, $UA/C_H=1.5$, and $C_c/C_H=0.5$, $UA/C_c=1.5$ are not quite the same so that even for $N=1$, the effectiveness is not a function of $(C_{\min}/C_{\max}, UA/C_{\min})$.

Conclusions

The classic problem of the shell and tube heat exchanger with a single well-mixed shell pass and a number of tube passes has been reconsidered to obtain algebraic expressions that lead to the effectiveness for any number of tube passes, where as the prior algebraic results were limited to four or fewer passes. Evaluation of the results for an even number of passes confirms the existing specification that the results for two passes are usable for any number of passes, with some limitation on the number of transfer units. Evaluation of the results for an odd number of passes predicts agreement with the numerical result of O'Hare (1986) to the extent of them, but with an indication that for the odd number of passes the effectiveness is not a general function of $C_{\min}/C_{\max}$ and of the transfer units calculated on the basis of $C_{\min}$.

References

Holman, J. B., 1986, *Heat Transfer*, 6th ed., McGraw-Hill, New York.

Jakob, M., 1957, *Heat Transfer*, Vol. II, Wiley, New York.

O'Hare, M. S., Hess, L., and Kraus, A. D., 1986, "The Effectiveness of Heat Exchangers With One Shell Pass and an Odd Number of Tube Passes," *Proceedings of the Eighth International Heat Transfer Conference*, Hemisphere Publishing Co., New York, Vol. 6, pp. 2691-2696.

Methods for Rapid Calculation of the Operation of Asymmetric Counterflow Regenerators

F. E. Romie[1] and B. S. Baclic[2]

Nomenclature

hA = thermal conductance, W/K
t = time, s
$t_{a,b}$ = duration of flow period, s
wc = capacitance rate of gas, W/K
WC = thermal capacitance of matrix, J/K

[1]Palos Verdes Estates, CA 90274.

[2]Tehnicki fakultet "Mihajlo Pupin," University of Novi Sad, 23000 Zrenjanin, Yugoslavia.

Contributed by the Heat Transfer Division for publication in the JOURNAL OF HEAT TRANSFER. Manuscript received by the Heat Transfer Division July 1, 1987. Keywords: Heat Exchangers, Modeling and Scaling.

Table 3 Effectiveness values

CH/C_c	η_L	L-R (26)	R-L (25)	$N \to \infty$ (24)	O'Hare (1986) R-L (Polynomial)	Fig. 2 L-R	Fig. 2 R-L
1	1.5	.478	.527	.530	.530		
0.5	1.5	.618	.638	.638	.639	.62	.64
2.	.75	.628	.644	.638			

[as in for instance Holman (1986)] and then said to be applicable for any number of passes. This expression, for $N=1$, can be used as indicated to obtain the effectiveness for $R>1$. The form turns out to be the same as for $R<1$ if R is then defined as C_c/C_H, or, more specifically, as $C_{\min}/C_{\max}$ and the number of transfer units as $2UPL/C_{\min}$.

All of the above conclusions are the same if the hot fluid flow direction is $R-L$.

For $N>1$ the performance is given by equation (24). In the limit $N\to\infty$, the performance is that of the crossflow exchanger with both fluids well mixed laterally, which is

$$\frac{T_{in}-t_{in}}{T_{in}-T_{out}}=\left[\frac{R}{1-e^{-R\eta_L}}+\frac{1}{1-e^{-\eta_L}}+\frac{1}{\eta_L}\right] \tag{25}$$

A comparison of the values given by equations (24) and (25) shows that the ratio of the effectiveness for an infinite number of passes to the effectiveness for two passes is between 1.00 and 0.97 for $\eta_L<3$ when $R=1$; $\eta_L<4$ when $R=0.75$; $\eta_L<5$ when $R=0.5$; and $\eta_L<17$ when $R=0.25$. The ratio is lower for higher values of η_L, and for $\eta_L\to\infty$ the ratio is

$$\frac{1}{2}\left((1+R)+\sqrt{1+R^2}\right)/(1+R)$$

The ratio, is, for $R=0.5$ as an example, is equal to 0.872; the insensitivity of the effectiveness to the number of passes is true only for values of η_L less than those cited above, but those do include most of the critical values of η_L.

Odd Number of Passes

With an odd number of passes the roots, $r_{1,2}$ are given by equation (11), for $R-L$; they are

$$r_{1,2}=\frac{1}{2}\left[-1\pm\sqrt{1+x^2\left(1-\frac{1}{R}\right)}\right],\ R-L$$

The factor $(1-1/R)$ associated with x^2 precludes the simple relations by which equation (24) was attained for an even number of passes. Now equation (20) must be evaluated as it stands. Because the constants $c_{1,2}$ given by equation (12) each are the sum of a term that contains T_L/M as a factor and a second term, the quantity F in equation (21) is linear in T_L/M and it can be written in a form more convenient for calculation, as

$$\frac{t_{out}}{M}=\frac{T_L}{M}F_0+F_1+\frac{t_{in}}{M}e^{-R\eta_L},\ \text{since}\ (2N+1)S=R$$

Then, for the hot fluid as $R-L$, for which the datum is T_{out} and $M=t_{in}/(1+R)$, we obtain

$$\frac{T_{in}}{t_{in}}=\frac{F_1-(1-R)(1-e^{-R\eta_L})}{(1-R)(R-F_0)} \tag{26}$$

When $R=1$ the roots are such as to make F_1 equal to zero and thus equation (25) remains determinate.

For the hot fluid as $L-R$, for which the datum is T_{in} and $M=t_{in}/(1+R)$, we obtain

$$\frac{T_{out}}{t_{in}}=\frac{(1+R)(1-e^{-R\eta_L})-F_1}{(1+R)(R+F_0)} \tag{27}$$

No general comparison is possible, since the evaluation must be made for chosen values of R, $(2N+1)$, and η_L. As an example, values of the effectiveness for $N=1$ have been calculated for $\eta_L=1.5$, with C_H/C_0 equal to 1 and 0.5, for both hot fluid flow directions, $L-R$ to make the flow in two of the three passes parallel to that of the hot fluid, and $R-L$, to make this flow counter. Table 3 gives the values of the effectiveness from equations (26) and (27). Values from equation (25), the mixed fluids cross flow case, are included as are some from O'Hare et al. (1986).

With $C_H/C_c=1.5$ and 1.0 for the hot fluid $R-L$, in counterflow with two of the three tube passes, the effectiveness is practically the same as it is for an infinite number of tube passes. For the hot fluid $L-R$, in parallel with two of the tube passes, the effectiveness is slightly lower.

For $C_H/C_c=2$, for which the effectiveness is defined by equation (23), the value of η_L is taken as 0.75, so that with $A=P(2N+1)L$, $(UA/C_c)(C_c/C_H)=0.75$, to give $UA/C_H=UA/C_{\min}=1.5$ the same value that is associated with $C_H/C_0=0.5$. On this basis equation (25) gives the same effectiveness but the values from equations (26) and (27) for $C_H/C_c=0.5$, $UA/C_H=1.5$, and $C_c/C_H=0.5$, $UA/C_c=1.5$ are not quite the same so that even for $N=1$, the effectiveness is not a function of $(C_{\min}/C_{\max}, UA/C_{\min})$.

Conclusions

The classic problem of the shell and tube heat exchanger with a single well-mixed shell pass and a number of tube passes has been reconsidered to obtain algebraic expressions that lead to the effectiveness for any number of tube passes, where as the prior algebraic results were limited to four or fewer passes. Evaluation of the results for an even number of passes confirms the existing specification that the results for two passes are usable for any number of passes, with some limitation on the number of transfer units. Evaluation of the results for an odd number of passes predicts agreement with the numerical result of O'Hare (1986) to the extent of them, but with an indication that for the odd number of passes the effectiveness is not a general function of $C_{\min}/C_{\max}$ and of the transfer units calculated on the basis of $C_{\min}$.

References

Holman, J. B., 1986, *Heat Transfer*, 6th ed., McGraw-Hill, New York.

Jakob, M., 1957, *Heat Transfer*, Vol. II, Wiley, New York.

O'Hare, M. S., Hess, L., and Kraus, A. D., 1986, "The Effectiveness of Heat Exchangers With One Shell Pass and an Odd Number of Tube Passes," *Proceedings of the Eighth International Heat Transfer Conference*, Hemisphere Publishing Co., New York, Vol. 6, pp. 2691-2696.

Methods for Rapid Calculation of the Operation of Asymmetric Counterflow Regenerators

F. E. Romie[1] and B. S. Baclic[2]

Nomenclature

hA = thermal conductance, W/K
t = time, s
$t_{a,b}$ = duration of flow period, s
wc = capacitance rate of gas, W/K
WC = thermal capacitance of matrix, J/K

[1]Palos Verdes Estates, CA 90274.

[2]Tehnicki fakultet "Mihajlo Pupin," University of Novi Sad, 23000 Zrenjanin, Yugoslavia.

Contributed by the Heat Transfer Division for publication in the JOURNAL OF HEAT TRANSFER. Manuscript received by the Heat Transfer Division July 1, 1987. Keywords: Heat Exchangers, Modeling and Scaling.

Subscripts

a = refers to conditions during period t_a
b = refers to conditions during period t_b

Introduction

The regenerator is characterized by the thermal capacitance of its matrix, which alternately supplies or accepts heat from two fluids, a and b, that enter at different but constant temperatures and flow countercurrently but alternately through the same flow passages for time periods t_a and t_b. Steady-state periodic operation is attained after a sufficient number of alternating periods following startup.

The purpose of this note is twofold. First, it is desired to show a new method of evaluating the coefficients that arise in the analysis of steady-state periodic operation of counterflow regenerators. The second purpose is to express the solution of the regenerator problem in terms of the functions $F_n(u, v)$ and $G_n(u, v)$ (Romie, 1987) that permit, particularly with the new method of coefficient evaluation, a very rapid numerical description of regenerator operation. The method of analysis generally follows that described by Nusselt (1927) and first put into use by Nahavandi and Weinstein (1961), and, later, by Romie (1979), Willmott and Duggan (1980), Baclic (1985), and Hill and Willmott (1987).

The Differential Equations

The regenerator analyzed is defined by the following idealizations: (1) The capacitance rates, $(wc)_a$ and $(wc)_b$, of the fluids and the thermal conductances, $(hA)_a$ and $(hA)_b$, for transfer of heat between the fluid and matrix are uniform and constant as is the thermal capacitance, WC, of the regenerator matrix. (2) No heat is conducted axially in the matrix and the matrix material offers no resistance to heat flow in the direction normal to fluid flow. (3) The ratios of the thermal capacitances of the fluids contained at any instant in the matrix to the thermal capacitance of the matrix are negligibly small and are treated as zero. This latter idealization means, in effect, that the two fluids must be gases and that transit times required for particles of gas to flow through the regenerator must be negligibly small compared to the flow periods t_a and t_b.

With these idealizations, energy balances give two equations applicable during period a

$$\frac{\partial \tau_a}{\partial(\Lambda_a y)} = T_a - \tau_a = -\frac{\partial T_a}{\partial(\Pi_a x)} \tag{1}$$

With counterflow the two equations during period b are

$$-\frac{\partial \tau_b}{\partial(\Lambda_b y)} = T_b - \tau_b = -\frac{\partial T_b}{\partial(\Pi_b x)} \tag{2}$$

In these equations, x is the fractional completion of a period ($x = t/t_a$ during period a and $x = t/t_b$ during period b), and y is the fractional distance along the flow path in the matrix of length L and is always measured from the entrance plane of gas a. The parameters Π and Λ are $\Pi_a = (hAt)_a/WC$, $\Pi_b = (hAt)_b/WC$, $\Lambda_a = (hA)_a/(wc)_a$, and $\Lambda_b = (hA)_b/(wc)_b$. The subscript a is assigned such that the term $\Lambda_b\Pi_a/(\Lambda_a\Pi_b) \equiv (wct)_a/(wct)_b$ is not greater than unity.

If τ_h is the temperature of the hotter gas with inlet temperature τ_{hin} and τ_c is the temperature of the colder gas with inlet temperature τ_{cin}, then $\tau_a = (\tau_c - \tau_{cin})/(\tau_{hin} - \tau_{cin})$, $\tau_b = (\tau_h - \tau_{cin})/(\tau_{hin} - \tau_{cin})$ and $T = (T_m - \tau_{cin})/(\tau_{hin} - \tau_{cin})$ where T_m is the matrix temperature. Alternate definitions can be used: $\tau_a = (\tau_h - \tau_{hin})/(\tau_{cin} - \tau_{hin})$, $\tau_b = (\tau_c - \tau_{hin})/(\tau_{cin} - \tau_{hin})$ and $T = (T_m - \tau_{hin})/(\tau_{cin} - \tau_{hin})$. Thus τ_a represents the temperature of the hotter or colder gas as appropriate. The temperature variables τ_a, τ_b, and T will be referred to as temperatures.

Functions Used

Two closely related families of functions, $F_n(u, v)$ and $G_n(u, v)$ (Romie, 1987), are used to express the solutions of equations (1) and (2). The functions satisfy two equations

$$\frac{\partial G_n(u, v)}{\partial v} = F_n - G_n = -\frac{\partial F_n(u, v)}{\partial u} \tag{3}$$

For $n \geq 0$, $F_n(0, v) = v^n/n!$ and $G_n(u, 0) = 0$. Two integrals used in this note are

$$\int_0^v F_n(u, z)dz = F_{n+1}(u, v), \qquad n \geq 0 \tag{4}$$

$$\int_0^u G_n(z, v)dz = -F_{n+1}(u, v) + v^{n+1}/(n+1)!, \qquad n \geq -1 \tag{5}$$

Numerical values for F_n and G_n, $n = 0,1,2, \ldots$, can be found by evaluating just three functions and then using two recurrence equations. The three functions to be evaluated are

$$G_{-1}(u, v) = \exp(-u-v)I_0(2\sqrt{uv}) \tag{6}$$

$$F_{-1}(u, v) = \exp(-u-v)(u/v)^{1/2}I_1(2\sqrt{uv}) \tag{7}$$

$$G_0(u, v) = \exp(-u-v)\sum_{r=0}^{\infty}(v/u)^{(r+1)/2}I_{r+1}(2\sqrt{uv}) \tag{8}$$

I_r is the modified Bessel function of the first kind, rth order, and u and v are positive. The two recurrence equations are

$$F_n(u, v) = G_n(u,v) + G_{n-1}(u, v), \qquad \pm \text{ integer } n \tag{9}$$

$$G_{n+1}(u, v) = \frac{1}{n+1}\Big((v-u-1-2n)G_n + (2v-n)G_{n-1} + vG_{n-2}\Big), \qquad n \geq 0 \tag{10}$$

Series expansions for G_{-1}, F_{-1}, and G_0 are given by Romie (1987).

Solution of Equations

The solution of equations (1) must satisfy two conditions: gas a enters ($y = 0$) at zero temperature, $\tau_a(x, 0) = 0$, and the temperature distribution of the matrix at the beginning ($x = 0$) of period a must be the matrix temperature distribution at the end ($x = 1$) of period b, $T_a(0, y) = T_b(1, y)$. The solutions for the temperatures are

$$T_a(x, y) = \sum_{n=0}^{N} A_n F_n(\Pi_a x, \Lambda_a y) \tag{11}$$

$$\tau_a(x, y) = \sum_{n=0}^{N} A_n G_n(\Pi_a x, \Lambda_a y) \tag{12}$$

Note that the governing equations (1) as well as the first condition ($\tau_a(x, 0) = 0$) are identically satisfied for arbitrary expansion coefficients A_n ($n = 0,1,2, \ldots, N < \infty$). Also note that, due to the properties of the F_n functions, the matrix temperature distribution at the beginning ($x = 0$) of period a is expressible as an Nth degree polynomial of $\Lambda_a y$

$$T_a(0, y) = \sum_{n=0}^{N} A_n(\Lambda_a y)^n/n! \tag{13}$$

During period b, gas b enters ($y = 1$) at unity temperature, $\tau_b(x, 1) = 1$, and the matrix temperature distribution at the beginning ($x = 0$) of period b must be the matrix temperature distribution at the end ($x = 1$) of period a, $T_b(0, y) = T_a(1, y)$. The matrix and fluid temperatures during period b are

$$T_b(x, y) = 1 - \sum_{n=0}^{N} B_n F_n(\Pi_b x, \Lambda_b(1-y)) \tag{14}$$

$$\tau_b(x, y) = 1 - \sum_{n=0}^{N} B_n G_n(\Pi_b x, \Lambda_b(1-y)) \quad (15)$$

These expansions satisfy the governing equations of period b and the condition $\tau_b(x, 1) = 1$ for arbitrary B_n ($n = 0,1,2, \ldots, N < \infty$). Also equation (14) makes the matrix temperature distribution at the beginning of period b expressible as an Nth degree polynomial of $\Lambda_b(1-y)$

$$T_b(0, y) = 1 - \sum_{n=0}^{N} B_n(\Lambda_b(1-y))^n/n! \quad (16)$$

The coefficients A_n and B_n are evaluated in a following section.

Thermal Effectiveness

With adoption of the convention regarding assignment of the subscript a, the thermal effectiveness $\bar{\tau}_a$ of the regenerator is the time-mean temperature of gas exiting ($y = 1$) the regenerator during period a

$$\bar{\tau}_a = \int_0^1 \tau_a(x, 1)dx \quad (17)$$

Carrying out the integration using equations (5) and (12) gives the thermal effectiveness

$$\bar{\tau}_a = \frac{1}{\Pi_a} \sum_{n=0}^{N} A_n \left(\Lambda_a^{n+1}/(n+1)! - F_{n+1}(\Pi_a, \Lambda_a) \right) \quad (18)$$

For an alternative method of computing the thermal effectiveness note that the product $(wct)_a \bar{\tau}_a$ is the change in enthalpy of the mass of gas that passes through the regenerator during period a. This change in enthalpy must equal the change in internal energy of the regenerator matrix during period a

$$(wct)_a \bar{\tau}_a = WC\left(\int_0^1 T_a(0, y)dy - \int_0^1 T_b(0, y)dy \right) \quad (19)$$

(The matrix temperature distribution at the end of period a is the matrix temperature distribution at the beginning of period b.) Using equations (13) and (16) for the integrations gives the alternative expression for $\bar{\tau}_a$

$$\bar{\tau}_a = \frac{\Lambda_a}{\Pi_a} \left(-1 + \sum_{n=0}^{N} (A_n \Lambda_a^n + B_n \Lambda_b^n)/(n+1)! \right) \quad (20)$$

Coefficient Evaluation

The equations used to find values of the coefficients are found by noting that the matrix temperature distribution at the end of a period must be the matrix temperature distribution at the beginning of the succeeding period: $T_a(0, y) = T_b(1, y)$ and $T_a(1, y) = T_b(0, y)$. Substituting equations (11), (13), (14), and (16) into these two relations gives two equations

$$\sum_{n=0}^{N} \{A_n(\Lambda_a y)^n/n! + B_n F_n(\Pi_b, (1-y)\Lambda_b)\} = 1 \quad (21)$$

$$\sum_{n=0}^{N} \{A_n F_n(\Pi_a, y\Lambda_a) + B_n((1-y)\Lambda_b)^n/n!\} = 1 \quad (22)$$

The $2(N+1)$ values of A_n and B_n can be found by satisfying these two equations at $N+1$ points, y_m, along the flow path.

Table 1 Gas a exit temperatures for $\Lambda_a = 286$, $\Lambda_b = 220$, $\Pi_a = 200$, $\Pi_b = 162$

Method	N	Initial temperature	Average temperature	Final temperature
Equal	1	0.998103	0.808414	0.618725
Chebyshev	1	0.998103	0.808414	0.618725
SIM	1	1.154760	0.953318	0.751877
Equal	2	1.002453	1.012171	0.789764
Chebyshev	2	1.002453	1.012171	0.789764
SIM	2	0.909124	0.993969	0.853971
Equal	3	0.998166	0.985661	0.901632
Chebyshev	3	0.999339	0.989885	0.906392
SIM	3	1.035396	0.996871	0.921728
Equal	4	1.000973	1.000075	0.974715
Chebyshev	4	1.000326	0.994997	0.959135
SIM	4	1.004268	0.995655	0.936621
Equal	5	0.970991	1.035788	1.840665
Chebyshev	5	1.000684	0.997887	0.919978
SIM	5	0.992523	0.996039	0.948847
Equal	6	1.000827	1.009082	1.068527
Chebyshev	6	0.999736	0.995228	0.947480
SIM	6	1.005521	0.995991	0.952070
Equal	7	0.999218	0.993112	0.930150
Chebyshev	7	1.000081	0.996541	0.958667
SIM	7	0.999944	0.995896	0.951429
Equal	8	1.007747	0.990141	0.862835
Chebyshev	8	1.000026	0.995817	0.950614
SIM	8	0.999908	0.995897	0.951513

Note: The four values of Λ and Π correspond (Shah, 1981) to Ntu = 128, $C^* = 0.95$, $1/Cr^* = 0.7$, $(hA)^* = 1.23$.

This procedure is termed the collocation method. Coefficient evaluation requires the solution of a $2(N+1)\times 2(N+1)$ array with a unit vector.

Nahavandi and Weinstein (1961) used equally spaced points, $y_m = m/N$, $m = 0,1,2, \ldots, N$. Romie (1979) and Willmott and Duggan (1980) used Chebyshev points; $y_m = (1-\cos(\pi m/N))/2$. (Willmott and Duggan first proposed use of the Chebyshev points in 1975.) In either case $2N$ nontrivial sets of values of the three functions, F_{-1}, G_{-1}, and G_0, must be evaluated. A trivial set is one for which at least one argument is zero.

A new method of finding values for the coefficients will be termed the Successive Integral Method (SIM). The basis of the method is that if two functions are equal over an interval then their successive integrals over the interval will be equal. The method thus reduces to finding successive integrals, 0 to y, of both sides of equation (22) ($T_a(1, y) = T_b(0, y)$), and after discerning the general form of the kth integration, setting $y = 1$. Using equation (4) for the integrations produces the first set of $N+1$ equations

$$\sum_{n=0}^{N}\left(A_n k! F_{n+k}(\Pi_a, \Lambda_a)/\Lambda_a^k + B_n \frac{k}{k+n}\Lambda_b^n/n!\right) = 1, \qquad (23)$$

$$k = 1,2, \ldots, N+1$$

For the second set of $N+1$ equations the same procedure is used on equation (21) but with substitution of $\eta = 1-y$ and setting $\eta = 1$ after discerning the general form of the kth integration with respect to η:

$$\sum_{n=0}^{N}\left(A_n \frac{k}{k+n}\Lambda_a^n/n! + B_n k! F_{n+k}(\Pi_b, \Lambda_b)/\Lambda_b^k\right) = 1, \qquad (24)$$

$$k = 1,2, \ldots, N+1$$

Each equation for each value of k produces a row in a $2(N+1)\times 2(N+1)$ array and, cumulatively, a unit vector.

The advantage of the method is twofold. First, only two sets rather than $2N$ sets of values of the three functions, F_{-1}, G_{-1}, and G_0, are required. Second, the value of N for attainment of a given accuracy in $\bar{\tau}_a$ is less than that required with use of the collocation method. Generally, $N=2$ will give an accuracy in $\bar{\tau}_a$ sufficient for most requirements when SIM is used.

The second advantage is illustrated in Table 1, which shows the initial, time-mean, and final temperatures, $\tau_a(0, 1)$, $\bar{\tau}_a$, and $\tau_a(1, 1)$, computed for the exiting gas a. If an accuracy of 0.1 percent is arbitrarily specified for $\bar{\tau}_a$, then $N=3$ is sufficient with SIM and $N=6$ if Chebyshev points are used. Equally spaced points do not provide the specified accuracy even for $N=8$. It should be pointed out that the values of Λ and Π used in Table 1 were selected to provide a severe test of the three methods. As stated, $N=2$ is generally adequate for use with the SIM method of determining the coefficients when computing $\bar{\tau}_a$. However, for the parameters used in Table 1, a larger value of N is required when computing the initial and final exiting temperatures to the accuracy specified for $\bar{\tau}_a$.

For the symmetric regenerator ($\Lambda_a = \Lambda_b = \Lambda$ and $\Pi_a = \Pi_b = \Pi$) the coefficients are equal ($A_n = B_n$) and equations (23) and (24) reduce to a single equation

$$\sum_{n=0}^{N} A_n\left(\frac{k}{k+n}\Lambda^n/n! + k! F_{n+k}(\Pi, \Lambda)/\Lambda^k\right) = 1, \qquad (25)$$

$$k = 1, 2, \ldots, N+1$$

Table 2 Comparison of coefficients found using SIM and Galerkin methods for $\Lambda = 15.5$, $\Pi/\Lambda = 5/6$

	SIM	Galerkin
$N=1$		
$\bar{\tau}_a =$	.8121465774	.8121465774
n	Coefficients	
0	.5619699238	.5619699238
1	.0356676753	.0356676753
$N=2$		
$\bar{\tau}_a =$	.8196202710	.8196202710
n	Coefficients	
0	.4355477952	.4355477953
1	.0857580835	.0857580835
2	−.0064598834	−.0064598834
$N=3$		
$\bar{\tau}_a =$	.8196268928	.8196268928
n	Coefficients	
0	.4402233435	.4402233434
1	.0822727225	.0822727226
2	−.0053523750	−.0053523751
3	−.0001418375	−.0001418375
$N=4$		
$\bar{\tau}_a =$	.8197045909	.8197045909
n	Coefficients	
0	.4570317525	.4570317499
1	.0605382352	.0605382386
2	.0073233305	.0073233285
3	−.0039701816	−.0039701810
4	.0004950542	.0004950541
$N=5$		
$\bar{\tau}_a =$	.8197045949	.8197045949
n	Coefficients	
0	.4568970453	.4568970371
1	.0608010421	.0608010569
2	.0070856437	.0070856310
3	−.0038475153	−.0038475090
4	.0004594559	.0004594541
5	.0000045913	.0000045915

For the symmetric regenerator only one set of values of the three functions is required to compute the coefficients, $\bar{\tau}_a$ and the final exiting temperature $\tau_a(1, 1)$.

The successive integral method (SIM) and the Galerkin method of determining coefficients (Baclic, 1985) share the advantages noted above and produce coefficients that are, for all practical purposes, identical as shown in Table 2 for a symmetric regenerator. The advantages of SIM are the ease of derivation and simplicity of equations (23) and (24) and a slightly shorter computation time.

References

Baclic, B. S., 1985, "The Application of the Galerkin Method to the Solution of the Symmetric and Balanced Counterflow Regenerator Problem," ASME JOURNAL OF HEAT TRANSFER, Vol. 107, pp. 214–221.

Hill, A., and Willmott, J. A., 1987, "A Robust Method for Regenerative Heat Exchanger Calculations," *International Journal of Heat and Mass Transfer*, Vol. 30, pp. 241–249.

Nahavandi, A. N., and Weinstein, A. S., 1961, "A Solution to the Periodic-Flow Regenerative Heat Exchanger Problem," *Applied Science Research*, Vol. 10, pp. 335–348.

Nusselt, W., 1927, "Die Theorie des Winderhitzers," *Zeitschrift des Vereines deutscher Ingenieure*, Vol. 71, pp. 85–91.

Romie, F. E., 1979, "Periodic Thermal Storage: The Regenerator," ASME JOURNAL OF HEAT TRANSFER, Vol. 101, pp. 726–731.

Romie, F. E., 1987, "Two Functions Used in the Analysis of Crossflow Exchangers, Regenerators and Related Equipment," ASME JOURNAL OF HEAT TRANSFER, Vol. 109, pp. 518–521.

Shah, R. K., 1981, "Thermal Design Theory for Regenerators," *Heat Exchangers: Thermal-Hydraulic Fundamentals and Design*, S. Kakac, A. E., Bergles, and F. Mayinger, eds., Hemisphere Publishing Corp., Washington, DC, pp. 712–763.

Willmott, A. J., and Duggan, R. C., 1980, "Refined Closed Methods for the Contra-Flow Thermal Regenerator Problem," *International Journal of Heat and Mass Transfer*, Vol. 23, pp. 655–662.

Heat Transport Along an Oscillating Flat Plate

U. H. Kurzweg[1] and J. Chen[1,2]

Introduction

Several recent papers (Kurzweg and Zhao, 1984; Kurzweg 1985a, 1985b, 1986; Kaviany, 1986) have examined the transport of heat between a hot and cold fluid reservoir when the two reservoirs are connected to each other by an array of open-ended pipes and when the fluid within these pipes is set into sinusoidal axial oscillations. This new heat transfer mode involves the periodic interaction of axial convection with radial heat conduction between the fluid core and Stokes boundary layer formed by the oscillations (Kurzweg, 1986) and can lead to effective axial conductivities orders of magnitude larger (Kurzweg and Zhao, 1984; Zhao, 1985) than achievable by axial conduction in the absence of oscillations. An interesting property of this heat transfer method is that there is no convective mass exchange between the fluid in the two reservoirs, whenever the maximum fluid displacement within the tubes is less than the tube length and the flow remains laminar. Such conditions can readily be met in experiments using capillaries (Kurzweg and Zhao, 1984) and can lead to heat transfer rates considerably higher than achievable with heat pipes (Dunn and Reay, 1978).

In the above studies the oscillations responsible for the enhanced heat transfer are due to a periodic pressure gradient produced by moving pistons or membranes located within the fluid reservoirs. It is the purpose of the present note to show that the same enhanced heat transfer process can occur along rigid walls bounded by a viscous fluid when such walls execute a periodic motion parallel to the fluid-solid interface, and a longitudinal temperature gradient is present. In particular, we examine the problem of thermal pumping existing in the classical Stokes problem of a sinusoidally oscillating flat plate immersed within a viscous fluid of infinite extent (Schlichting, 1978). A constant-temperature gradient is superimposed on the fluid parallel to the plate surface and in the direction of plate motion. As will be seen, this leads to a large longitudinal heat flux within a relatively narrow boundary layer region next to the plate. The thickness of this layer, containing 99 percent of the time-averaged thermal flux, is found to be no more than 3.754 of the Stokes viscous boundary layer thickness and for low Prandtl number fluids, such as liquid metals, can become considerably less than one Stokes layer thickness.

Formulation and Solution

Consider a very thin plate oscillating sinusoidally within an unbounded viscous fluid, as shown in Fig. 1. The plate movements are parallel to the fluid-solid interface and the oscillation amplitude is A_0. A constant temperature gradient $\gamma = \partial T/\partial x$ is superimposed on the fluid in the oscillation direction x. Using the nondimensional transverse coordinate $\eta = y/\delta$, where $\delta = \sqrt{2\nu/\omega}$ is the Stokes layer thickness, with ω the angular oscillation frequency, ν the fluid kinematic viscosity, and $\tau = \omega t$ the nondimensional time, the assumed laminar velocity field within the bounding fluid for $\eta > 0$ is (Schlichting, 1978)

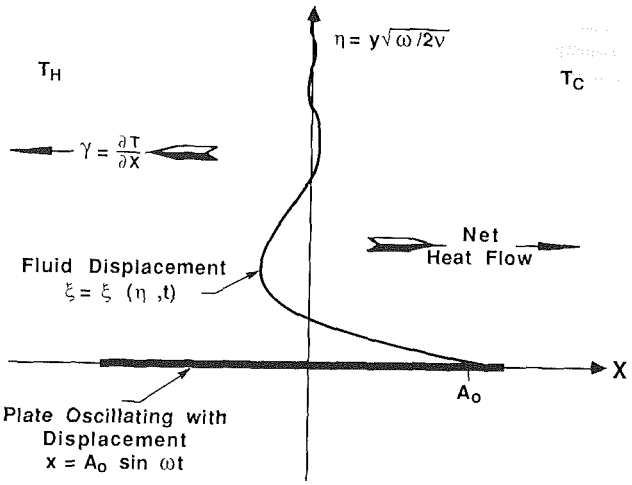

Fig. 1 Schematic of oscillating plate problem

$$U(\eta, \tau) = \omega A_0 \cos(\tau - \eta) e^{-\eta} \tag{1}$$

The corresponding temperature field can be derived from the energy equation and, upon neglecting viscous heating effects and assuming a temperature variation of the form (Chatwin, 1975)

$$T(x, \eta, \tau) = \gamma[x + \delta g(\eta) e^{i\tau}]_R \tag{2}$$

where the subscript R refers to the real part of the function shown within the bracket, leads to the equation

$$g'' - 2i\,\mathrm{Pr}\, g = \mathrm{Pe}\, e^{-(1+i)\eta} \tag{3}$$

Here the prime denotes differentiation with respect to η, $\mathrm{Pr} = \nu/\kappa$, $\mathrm{Pe} = \omega A_0 \delta/\kappa$ is the Peclet number, and κ the fluid thermal diffusivity. On solving this last equation, subject to the physically relevant boundary conditions that $g'(0) = g'(\infty) = 0$, leads to

$$g(\eta) = \frac{\mathrm{Pe}}{2i(1-\mathrm{Pr})}\left[e^{-\sqrt{2i}\eta} - \frac{1}{\sqrt{\mathrm{Pr}}} e^{-\sqrt{2i\mathrm{Pr}}\eta}\right] \tag{4}$$

The longitudinal heat flow caused by the interaction of the temperature and velocity field consists of a time-dependent convective part and an x-direction conductive part. The latter is negligibly small for most cases of physical interest. On neglecting such direct longitudinal conduction, one is left with that part produced by the interaction of longitudinal convection with conduction in the transverse direction across the Stokes layer. As already shown in an earlier study (Kurzweg, 1986), this latter quantity can be appreciable because of the very large temperature gradients that are established in the η direction by the plate oscillation. Mathematically this latter heat transport, expressed as a longitudinal thermal flux (in $\mathrm{W/m^2}$), can be written at $x = 0$, with aid of equation (1), as

$$\dot{\phi} = \rho c U T_R$$

$$= \rho c \gamma A_0 \delta \omega [g_R \cos\tau - g_I \sin\tau] \cos(\tau - \eta) e^{-\eta} \tag{5}$$

where ρc is the product of the fluid density and its specific heat and the subscript I refers to the imaginary part of the function shown. On time averaging this result over one period of the sinusoidal oscillations, we find that

$$\hat{\dot{\phi}} = -\rho \frac{c}{2} \gamma \left[\frac{\sqrt{\mathrm{Pr}}}{(1-\mathrm{Pr})}\right] \omega A_0^2 \sin(1 - \sqrt{\mathrm{Pr}})\eta e^{-(1+\sqrt{\mathrm{Pr}})\eta} \tag{6}$$

This result clearly shows that the total thermal flux is confined to a relatively thin layer near the plate of the order of the Stokes boundary layer thickness and that the flux is directly proportional to the product $\rho c \gamma A_0^2$.

One can integrate equation (6) over the entire range of η to

[1]Department of Engineering Sciences, University of Florida, Gainesville, FL 32611.

[2]Permanent address: Department of Civil and Environmental Engineering, Taiyuan University, Taiyuan, Shanxi Province, The People's Republic of China.

Contributed by the Heat Transfer Division for publication in the JOURNAL OF HEAT TRANSFER. Manuscript received by the Heat Transfer Division September 10, 1987. Keywords: Forced Convection, Moving Boundaries, Transient and Unsteady Heat Transfer.

Table 1 Flux boundary layer thickness as a function of Prandtl number; the thickness n containing 99 percent of the heat flux is given in multiples of the Stokes layer

Pr	0	0.01	0.1	0.36	1	10	100
n	2.287	2.605	3.336	3.754	3.319	1.055	0.261

obtain the total time-averaged heat transport in watts for a w wide plate of

$$Q = -\rho c w \gamma \frac{\sqrt{\omega\nu}}{2\sqrt{2}} A_0^2 \left[\frac{\sqrt{\mathrm{Pr}} - \mathrm{Pr}}{1 - \mathrm{Pr}^2}\right] \tag{7}$$

This last result shows that the total heat flow also increases with $\rho c \gamma A_0^2$ and in addition goes as the square root of the oscillation frequency and is a function of fluid Prandtl number. The Prandtl number function within the square bracket of this last expression has a maximum value of 0.277 at $\mathrm{Pr} = 0.432$. The square root frequency dependence has also been found for contaminant dispersion (Watson, 1983) and for heat transport (Kurzweg and Zhao, 1984) in pipes under high-frequency conditions. The heat flow predicted by equation (7) can become appreciable. For example, for a plate of width $w = 1$ m oscillating at $\omega = 8\pi$ r/s in water for which $\rho c = 4.18 \times 10^6$ J/m^{3}K, $\mathrm{Pr} = 7$, and $\nu = 10^{-6}$ m^2/s yields 67.2 kW along one side of the plate when $A_0 = 1$ m and $\gamma = 100°$C/m. This figure becomes particularly interesting when it is realized that in a practical regenerator (Walker, 1982) many such plates would be stacked on top of each other with just enough space left between them to accommodate the relatively thin fluid layers within which the flux transport occurs. With counter-oscillating plates, this could lead to very high heat flux densities but would also require considerable external energy input to oscillate the plates because of the large viscous shear forces existing under such conditions.

As a final calculation, we have examined the fraction F of the time-averaged flux $\hat{\phi}$ passing through thickness η of fluid near the plate. Using equation (6), it readily follows that this fraction is given by

$$F(\eta) = 1 - \frac{e^{-b\eta}}{a}[a \cos a\eta + b \sin a\eta] \tag{8}$$

where $a = 1 - \sqrt{\mathrm{Pr}}$ and $b = 1 + \sqrt{\mathrm{Pr}}$. Defining the flux boundary layer as the thickness within which 99 percent of the flux is transported, one finds the Prandtl number dependence shown in Table 1. We see there that the flux boundary layer thickness ranges from 2.287δ for very small Pr fluids to a maximum thickness of 3.754δ near $\mathrm{Pr} = 0.36$ to values that go to zero as Pr approaches infinity. These thicknesses are all quite small. For the above-discussed case involving water, the flux boundary layer thickness would be 0.282 mm.

Discussion and Concluding Remarks

It has been shown that the oscillation of a flat plate immersed in a viscous fluid and subjected to a longitudinal temperature gradient can lead to the establishment of a large heat flux within a relatively narrow region along the plate in the direction from hot to cold. The mechanism responsible for this transport is the interaction of a transverse conduction flux with periodic longitudinal convection. The process works only as long as there exists an η dependent phase difference between the fluid velocity and temperature field. As seen from equation (7), the transport would not occur if the fluid were either an ideal conductor ($\mathrm{Pr} = 0$) or an insulator ($\mathrm{Pr} = \infty$). Also it is clear that liquids will allow considerably higher heat flux than gases at the same oscillation amplitude and frequency due to the much higher heat capacity of the former. Some modification of the present results can be expected if one deals with several counteroscillating plates when these are spaced closer than several Stokes boundary layer thicknesses. Also plates of finite thickness with heat storage capability should receive future consideration. Such plates would modify the simple boundary conditions used in the present analysis and could be expected to modify the present results especially when dealing with low Prandtl number fluids such as liquid metals.

Acknowledgments

Partial support by the National Science Foundation (Grant No. CBT-86112544) is gratefully acknowledged.

References

Chatwin, P.C., 1975, "On the Longitudinal Dispersion of Passive Contaminant in Oscillating Flow in Tubes," *J. Fluid Mech.*, Vol. 71, pp. 513-527.

Dunn, P. D., and Reay, D. A., 1978, *Heat Pipes*, Pergamon Press, Oxford, pp. 3-11.

Kaviany, M., 1986, "Some Aspects of Heat Diffusion in Fluids by Oscillation," *Int. J. Heat and Mass Transfer*, Vol. 29, pp. 2002-2006.

Kurzweg, U. H., and Zhao, L. D., 1984, "Heat Transfer by High-Frequency Oscillations: A New Hydrodynamic Technique for Achieving Large Effective Thermal Conductivities," *Phys. Fluids*, Vol. 27, pp. 2624-2627.

Kurzweg, U. H., 1985a, "Enhanced Heat Conduction in Flows Subjected to Sinusoidal Oscillations,"ASME JOURNAL OF HEAT TRANSFER, Vol. 107, pp. 459-482.

Kurzweg, U. H., 1985b, "Enhanced Heat Conduction in Oscillating Viscous Flow Within Parallel-Plate Channels," *J. Fluid Mech.*, Vol. 156, pp. 291-300.

Kurzweg, U. H., 1986, "Temporal and Spatial Distribution of Heat Flux in Oscillating Flow Subjected to an Axial Temperature Gradient," *Int. J. Heat and Mass Transfer*, Vol. 29, pp. 1969-1977.

Schlichting, H., *1978, Boundary Layer Theory*, McGraw-Hill, New York, p. 93.

Walker, G., 1982, *Industrial Heat Exchangers; A Basic Guide*, McGraw-Hill, New York, pp. 311-321.

Watson, E., 1983, "Diffusion in Oscillating Flow," *J. Fluid Mech.*, Vol. 133, pp. 233-244.

Zhao, L. D., 1985, "Heat Transfer by High Frequency Oscillations," 5th Session of the Chinese Society of Engineering Thermophysics, Peking, People's Republic of China.

Transient Forced Convection in Fluids With Vanishing Prandtl Number

R. W. Lycans[1] and B. T. F. Chung[2]

Introduction

The analytical solution of transient heat transfer from incompressible laminar boundary layer flows over a curved surface when the Prandtl number is zero was attempted by Soliman and Chambre (1969) using Fourier transforms and the method of characteristics. The same problem was addressed by Biasi (1971) using the von Karman-Pohlhausen integral method. A conceptual error in both papers was first detected by Sucec (1978) and was found to cause significant error in the formulation of the response function for wall heat flux and wall temperature, as well as the temperature distribution in the fluid. In correcting the earlier works, Sucec unfortunately, due to a slight oversight, obtained an erroneous solution for the time-varying wall heat flux. Because the papers considered by those investigators represent a class of important transient forced convective heat transfer problems involving liquid metals, it is believed that the problem warrants further investigation and rectification.

In this work the problem attempted by Soliman and Cham-

[1]Development Engineer, Goodyear Aerospace Corporation, Akron, OH 44315.

[2]Professor, The University of Akron, Akron, OH 44325.

Contributed by the Heat Transfer Division for publication in the JOURNAL OF HEAT TRANSFER. Manuscript received by the Heat Transfer Division July 1, 1987. Keywords: Forced Convection, Modeling and Scaling, Transient and Unsteady Heat Transfer.

Table 1 Flux boundary layer thickness as a function of Prandtl number; the thickness n containing 99 percent of the heat flux is given in multiples of the Stokes layer

Pr	0	0.01	0.1	0.36	1	10	100
n	2.287	2.605	3.336	3.754	3.319	1.055	0.261

obtain the total time-averaged heat transport in watts for a w wide plate of

$$Q = -\rho c w \gamma \frac{\sqrt{\omega\nu}}{2\sqrt{2}} A_0^2 \left[\frac{\sqrt{\mathrm{Pr}} - \mathrm{Pr}}{1 - \mathrm{Pr}^2}\right] \tag{7}$$

This last result shows that the total heat flow also increases with $\rho c \gamma A_0^2$ and in addition goes as the square root of the oscillation frequency and is a function of fluid Prandtl number. The Prandtl number function within the square bracket of this last expression has a maximum value of 0.277 at $\mathrm{Pr} = 0.432$. The square root frequency dependence has also been found for contaminant dispersion (Watson, 1983) and for heat transport (Kurzweg and Zhao, 1984) in pipes under high-frequency conditions. The heat flow predicted by equation (7) can become appreciable. For example, for a plate of width $w = 1$ m oscillating at $\omega = 8\pi$ r/s in water for which $\rho c = 4.18 \times 10^6$ J/m^{3}K, $\mathrm{Pr} = 7$, and $\nu = 10^{-6}$ m^2/s yields 67.2 kW along one side of the plate when $A_0 = 1$ m and $\gamma = 100°$C/m. This figure becomes particularly interesting when it is realized that in a practical regenerator (Walker, 1982) many such plates would be stacked on top of each other with just enough space left between them to accommodate the relatively thin fluid layers within which the flux transport occurs. With counter-oscillating plates, this could lead to very high heat flux densities but would also require considerable external energy input to oscillate the plates because of the large viscous shear forces existing under such conditions.

As a final calculation, we have examined the fraction F of the time-averaged flux $\hat{\phi}$ passing through thickness η of fluid near the plate. Using equation (6), it readily follows that this fraction is given by

$$F(\eta) = 1 - \frac{e^{-b\eta}}{a}[a \cos a\eta + b \sin a\eta] \tag{8}$$

where $a = 1 - \sqrt{\mathrm{Pr}}$ and $b = 1 + \sqrt{\mathrm{Pr}}$. Defining the flux boundary layer as the thickness within which 99 percent of the flux is transported, one finds the Prandtl number dependence shown in Table 1. We see there that the flux boundary layer thickness ranges from 2.287δ for very small Pr fluids to a maximum thickness of 3.754δ near $\mathrm{Pr} = 0.36$ to values that go to zero as Pr approaches infinity. These thicknesses are all quite small. For the above-discussed case involving water, the flux boundary layer thickness would be 0.282 mm.

Discussion and Concluding Remarks

It has been shown that the oscillation of a flat plate immersed in a viscous fluid and subjected to a longitudinal temperature gradient can lead to the establishment of a large heat flux within a relatively narrow region along the plate in the direction from hot to cold. The mechanism responsible for this transport is the interaction of a transverse conduction flux with periodic longitudinal convection. The process works only as long as there exists an η dependent phase difference between the fluid velocity and temperature field. As seen from equation (7), the transport would not occur if the fluid were either an ideal conductor ($\mathrm{Pr} = 0$) or an insulator ($\mathrm{Pr} = \infty$). Also it is clear that liquids will allow considerably higher heat flux than gases at the same oscillation amplitude and frequency due to the much higher heat capacity of the former. Some modification of the present results can be expected if one deals with several counteroscillating plates when these are spaced closer than several Stokes boundary layer thicknesses. Also plates of finite thickness with heat storage capability should receive future consideration. Such plates would modify the simple boundary conditions used in the present analysis and could be expected to modify the present results especially when dealing with low Prandtl number fluids such as liquid metals.

Acknowledgments

Partial support by the National Science Foundation (Grant No. CBT-86112544) is gratefully acknowledged.

References

Chatwin, P.C., 1975, "On the Longitudinal Dispersion of Passive Contaminant in Oscillating Flow in Tubes," *J. Fluid Mech.*, Vol. 71, pp. 513-527.

Dunn, P. D., and Reay, D. A., 1978, *Heat Pipes*, Pergamon Press, Oxford, pp. 3-11.

Kaviany, M., 1986, "Some Aspects of Heat Diffusion in Fluids by Oscillation," *Int. J. Heat and Mass Transfer*, Vol. 29, pp. 2002-2006.

Kurzweg, U. H., and Zhao, L. D., 1984, "Heat Transfer by High-Frequency Oscillations: A New Hydrodynamic Technique for Achieving Large Effective Thermal Conductivities," *Phys. Fluids*, Vol. 27, pp. 2624-2627.

Kurzweg, U. H., 1985a, "Enhanced Heat Conduction in Flows Subjected to Sinusoidal Oscillations," ASME JOURNAL OF HEAT TRANSFER, Vol. 107, pp. 459-482.

Kurzweg, U. H., 1985b, "Enhanced Heat Conduction in Oscillating Viscous Flow Within Parallel-Plate Channels," *J. Fluid Mech.*, Vol. 156, pp. 291-300.

Kurzweg, U. H., 1986, "Temporal and Spatial Distribution of Heat Flux in Oscillating Flow Subjected to an Axial Temperature Gradient," *Int. J. Heat and Mass Transfer*, Vol. 29, pp. 1969-1977.

Schlichting, H., 1978, *Boundary Layer Theory*, McGraw-Hill, New York, p. 93.

Walker, G., 1982, *Industrial Heat Exchangers; A Basic Guide*, McGraw-Hill, New York, pp. 311-321.

Watson, E., 1983, "Diffusion in Oscillating Flow," *J. Fluid Mech.*, Vol. 133, pp. 233-244.

Zhao, L. D., 1985, "Heat Transfer by High Frequency Oscillations," 5th Session of the Chinese Society of Engineering Thermophysics, Peking, People's Republic of China.

Transient Forced Convection in Fluids With Vanishing Prandtl Number

R. W. Lycans[1] and B. T. F. Chung[2]

Introduction

The analytical solution of transient heat transfer from incompressible laminar boundary layer flows over a curved surface when the Prandtl number is zero was attempted by Soliman and Chambre (1969) using Fourier transforms and the method of characteristics. The same problem was addressed by Biasi (1971) using the von Karman-Pohlhausen integral method. A conceptual error in both papers was first detected by Sucec (1978) and was found to cause significant error in the formulation of the response function for wall heat flux and wall temperature, as well as the temperature distribution in the fluid. In correcting the earlier works, Sucec unfortunately, due to a slight oversight, obtained an erroneous solution for the time-varying wall heat flux. Because the papers considered by those investigators represent a class of important transient forced convective heat transfer problems involving liquid metals, it is believed that the problem warrants further investigation and rectification.

In this work the problem attempted by Soliman and Cham-

[1]Development Engineer, Goodyear Aerospace Corporation, Akron, OH 44315.

[2]Professor, The University of Akron, Akron, OH 44325.

Contributed by the Heat Transfer Division for publication in the JOURNAL OF HEAT TRANSFER. Manuscript received by the Heat Transfer Division July 1, 1987. Keywords: Forced Convection, Modeling and Scaling, Transient and Unsteady Heat Transfer.

bre, Biasi, and Sucec is re-examined and resolved; the correct solutions for the temperature distribution in the fluid and transient responses for wall heat flux and wall temperature are presented for laminar wedge flow. The solution is further extended to include a power law variation in wall temperature or heat flux. For comparison purposes, a direct numerical scheme using a finite difference marching technique is employed to attack the same problem. It is found that the agreement between the numerical solution and the present analytical solution is excellent, even for near stagnation and impending separation flows.

Analysis

Consideration is given to the transient forced convection of a plane laminar incompressible boundary layer flow. Consistent with the usual boundary layer approximations, we neglect viscous dissipation and conduction in the axial direction; the fluid properties are assumed to be constant, and the velocity field is taken to be steady. With the assumption of zero Prandtl number, the hydrodynamic boundary layer thickness approaches zero, and the flow throughout the thermal boundary layer is potential. Using the same notations as Soliman and Chambre (1969), we repeat their dimensionless governing equation as

$$\frac{\partial T}{\partial t}+u_p(x)\frac{\partial T}{\partial x}+v_p(x)\frac{\partial T}{\partial \zeta}=\frac{\partial^2 T}{\partial \zeta^5},\quad t>0,\ x>0,\ \zeta>0 \tag{1}$$

with $T(0, x, \zeta)=T(t, 0, \zeta)=T(t, x, \infty)=0$, $T(t, x, 0)=f(x)$ or $-\partial T_q/\partial \zeta\ (t, x, 0)=g(x)$, where $T_q=T_1\ k\sqrt{\mathrm{Pe}}/(q_0 L)$. The functions $f(x)$ and $g(x)$ describe either a variation in the wall temperature, or a variation in the wall heat flux.

Analytical Solution – Prescribed Wall Temperature. To begin the solution procedure, we employ the von Mises transformation and the Fourier sine transform to equation (1). The resulting equation is then solved using the method of characteristics. After transforming back to the (t, x, y) domain, we obtain temperature distributions for both small time and large time or steady-state solution. Details were presented in an earlier paper by these authors (1986). The wall heat flux can be easily obtained by differentiating temperature with respect to y, then letting y approach zero.

For the case of power law free-stream velocity variation, $u_p(x)=x^m$, and a step change in the surface temperature, we obtained the ratio of the time-dependent wall heat flux, $q_{1,w}$ to the steady-state value, $q_{1,w,ss}$ of the form

$$\frac{q_{1,w}}{q_{1,w,ss}}=\frac{1}{\sqrt{1-r}},\quad \tau\le\frac{1}{1-m} \tag{2}$$

$$\frac{q_{1,w}}{q_{1,w,ss}}=1,\quad \tau\ge\frac{1}{1-m} \tag{3}$$

where

$$r=[1-\tau(1-m)]^{(m+1)/(1-m)} \tag{4}$$

and

$$\tau=tu_p(x)/x=tx^{m-1} \tag{5}$$

The steady state wall heat flux is given by

$$q_{1,w,ss}=\frac{kT_w}{L}\sqrt{\mathrm{Pe}(1+m)/\pi}\left(\frac{x_1}{L}\right)^{(m-1)/2} \tag{6}$$

For computation purposes, we take the reference length L as a typical distance in the x_1 or dimensional direction. The reference velocity U corresponds to the velocity at $x_1=L$.

Soliman and Chambre (1969) mistakenly developed the following expression for the wall heat flux ratio:

$$\frac{q_{1,w}}{q_{1,w,ss}}=\frac{1}{(1-\{1-[\tau(1-m)]^{1/(1-m)}\}^{m+1})^{1/2}},\quad \tau\le\frac{1}{1-m} \tag{7}$$

The "corrected" result claimed by Sucec (1978) for the wall heat flux ratio was

$$\frac{q_{1,w}}{q_{1,w,ss}}=\frac{1}{\left\{1-\left[1-\dfrac{\tau(1-m)}{(1+m)}\right]^{(m+1)/(1-m)}\right\}^{1/2}},\quad \tau\le\frac{1}{1-m} \tag{8}$$

Unfortunately this result is only valid for the case of flow over a flat plate. However, his predicted wall temperature for the uniform wall heat flux boundary condition was correct.

We have further extended the solution to a power law variation in the wall temperature. The boundary temperature in this case becomes $f(x)=x^n$. The solution is written in terms of the incomplete Beta function $B_x(a, b)$, which is defined by Abramowitz and Stegun (1964)

$$B_x(a,b)=\int_0^x t^{a-1}(1-t)^{b-1}dt \tag{9}$$

The wall heat flux ratio is given by

$$\frac{q_{1,w}}{q_{1,w,ss}}=1+\frac{\Gamma((2n+m+1)/(2m+2))}{\sqrt{\pi}n/(m+1)\Gamma(n/(m+1))}\Big\{r^{n/(1+m)}(1-r)^{-1/2}-(n/(m+1))B_r(n/(m+1),\ 1/2)\Big\},\quad \tau\le\frac{1}{1-m} \tag{10}$$

$$\frac{q_{1,w}}{q_{1,w,ss}}=1,\quad \tau\ge\frac{1}{1-m} \tag{11}$$

The steady-state wall heat flux is

$$q_{1,w,ss}=\frac{T_w kn\sqrt{\mathrm{Pe}}\Gamma(n/(m+1))}{L\sqrt{1+m}\Gamma((2n+m+1)/(2m+2))}\left(\frac{x_1}{L}\right)^{(2n+m-1)/2} \tag{12}$$

Analytical Solution – Prescribed Wall Heat Flux. The analysis for the prescribed wall heat flux is very similar to that of prescribed wall temperature. The primary difference is the use of the Fourier cosine transform rather than the Fourier sine transform to operate on equation (1).

The boundary condition for a power law variation in the wall heat flux is $g(x)=x^n$. Assuming a power law free-stream velocity variation, $u_p=x^m$, the resulting wall temperature ratio becomes

$$\frac{T_{1,w}}{T_{1,w,ss}}=1-\frac{B_r((n+1)/(m+1),\ 1/2)\Gamma((2n+m+3)/(2m+2))}{\sqrt{\pi}\Gamma((n+1)/(m+1))},\quad \tau\le\frac{1}{1-m} \tag{13}$$

$$\frac{T_{1,w}}{T_{1,w,ss}}=1,\quad \tau\ge\frac{1}{1-m} \tag{14}$$

The steady-state wall temperature is

$$T_{1,w,ss}=\frac{q_0 L\Gamma((n+1)/(m+1))}{k\sqrt{\mathrm{Pe}(m+1)}\Gamma((2n+m+3)/(2m+2))}\left(\frac{x_1}{L}\right)^{(2n-m+1)/2} \tag{15}$$

When $n=0$, the above expressions reduce to the corrected

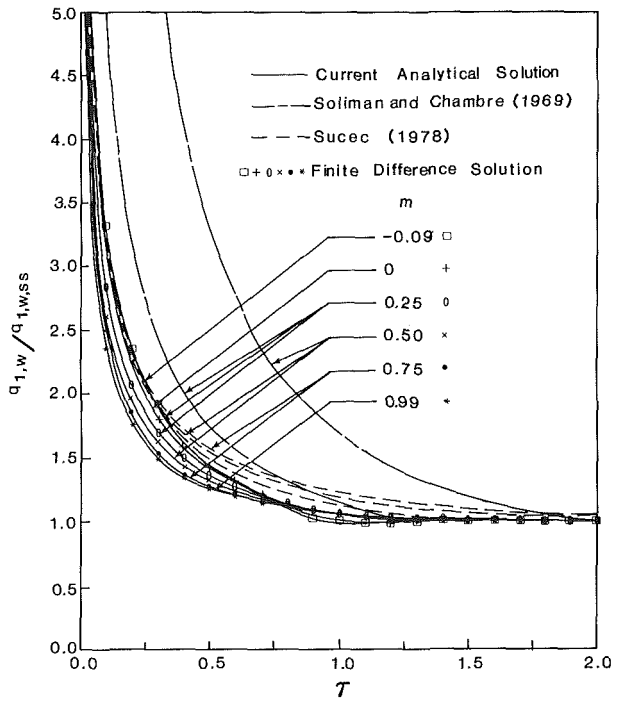

Fig. 1 Wall heat flux response to step change in wall temperature for wedge flows

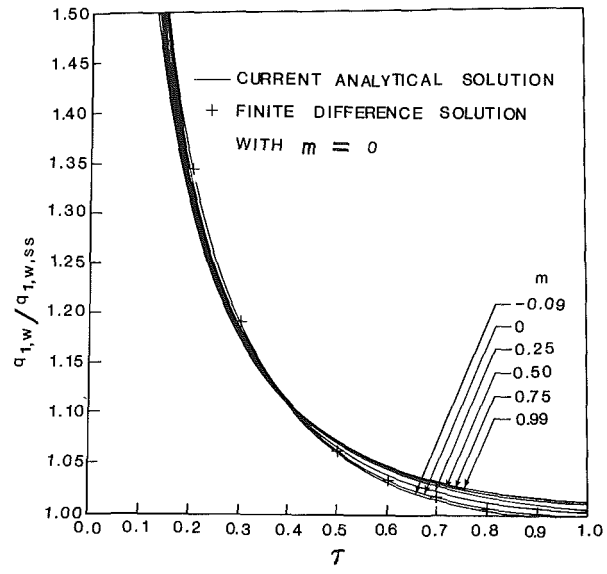

Fig. 2 Wall heat flux response to a power law variation in wall temperature. $f(x) = x$ for wedge flows

solution for the case of uniform wall heat flux derived directly by Sucec (1978).

Numerical Solution. A finite difference solution is developed for comparison with the closed-form solution derived in this paper. Both cases of prescribed wall temperature and prescribed wall heat flux boundary condition are considered. The transient energy equation is rewritten in finite difference form with a fully implicit representation. The resulting system equations for temperature distribution are in terms of a tridiagonal matrix, which is then solved using Gaussian elimination method. Details of numerical scheme can be found in an earlier work of the present authors (1986).

Results and Discussion

A large variation in the wedge angle was considered in this analysis. Results were determined for values of m ranging from 0.99 to -0.09. Thus, the results of the present analysis are demonstrated for flows varying from near stagnation to impending separation.

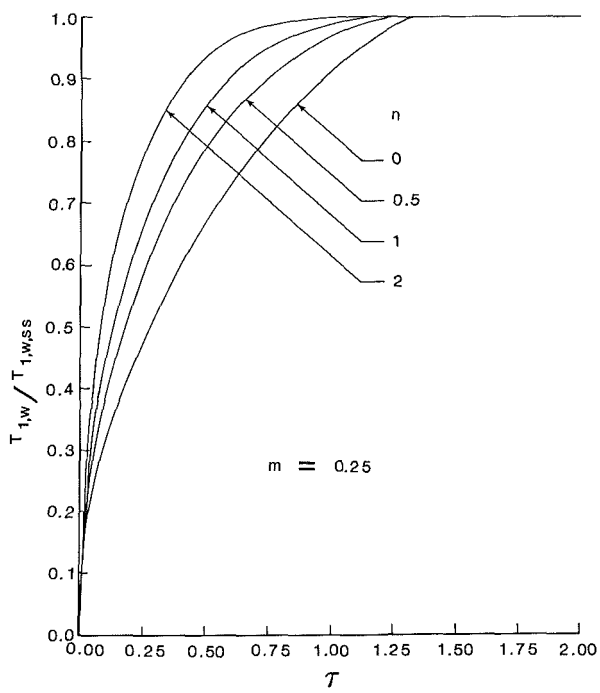

Fig. 3 Wall temperature response to power law variation in wall heat flux, constant wedge angle ($m = 0.25$)

Figure 1 shows the wall heat flux ratio plotted against the dimensionless time variable τ for the constant wall temperature boundary condition and several values of the exponent m. This figure shows our analytical solution, the results of Soliman and Chambre (1969), the results of Sucec (1978), and our finite difference solution. The agreement between the current analytical and finite difference solutions is excellent, even for impending separation flows ($m = -0.09$) and near stagnation flows ($m = 0.99$). The curve of $m = 0$ for both the Soliman-Chambre and the Sucec solutions overlay our result.

Figure 2 shows the wall heat flux ratio versus τ for $n = 1.0$ and different values of m. Included in this figure are present analytical and finite difference solutions. The curves shown in Fig. 2 indicate a smooth change from the transient solution to steady state for all values of the exponent m. The power law wall temperature variation boundary condition appears to overpower the abrupt transition observed in the constant wall temperature case for small values of m.

While the present analysis was developed for the case of zero Prandtl number fluids, the results presented by Morgan et al. (1958) suggest that an analysis of this type should give good results for cases where the Prandtl number is slightly larger than zero (liquid metals).

The numerical marching solution results, which were generated using mesh increments of $\Delta x = 0.005$, $\Delta y = 0.01$, and $\Delta t = 0.001$, required several hours of CPU time on a UNIVAC 1100/82 processor for each wedge angle investigated. This is in stark contrast to the analytical solution, which required only 3 s of CPU time for each wedge angle investigated using the same computer.

Figure 3 illustrates the variation in the wall temperature ratio with the power law boundary condition exponent n for a single value of the velocity exponent m ($m = 0.25$). These curves illustrate the current analytical solution of equations (13) and (14).

References

Abramowitz, M., and Stegun, I., 1964, *Handbook of Mathematical Functions*, National Bureau of Standards Applied Mathematics Series, Vol. 55, pp. 258–297.

Biasi, L., 1971, "Transient Convective Heat Transfer in Fluids With Vanishing Prandtl Number: An Application of the Integral Method," *International Journal of Heat and Mass Transfer*, Vol. 14, pp. 639–642.

Lycans, R., 1985, "Analytical and Numerical Solutions for Transient Forced Convection in Fluids With Vanishing Prandtl Number," M.S. Thesis, Department of Mechanical Engineering, The University of Akron, Akron, OH.

Morgan, G. W., Pipkin, A. C., and Warner, V. H., 1958, "On Heat Transfer in Laminar Boundary Layer Flows of Liquids Having a Very Small Prandtl Number," *Journal of Aeronautical Science*, Vol. 25, pp. 173–180.

Soliman, M., and Chambre, P., 1969, "On the Time-Dependent Convective Heat Transfer in Fluids With Vanishing Prandtl Number," *International Journal of Heat and Mass Transfer*, Vol. 12, pp. 1221–1230.

Sucec, J., 1978, Comment on "On the Time-Dependent Convective Heat Transfer in Fluids With Vanishing Prandtl Number," *International Journal of Heat and Mass Transfer*, Vol. 21, pp. 667–668.

Free Convection on a Horizontal Plate With Blowing and Suction

Hsiao-Tsung Lin[1] and Wen-Shing Yu[1]

Introduction

The effects of blowing and suction on forced convection (Koh and Hartnett, 1961) and those on free convection over a vertical plate (Vedhanayagam et al., 1980) have been studied extensively. On the other hand, the problem of free convection above a horizontal plate with blowing or suction has received substantially less attention. Gill et al. (1965) presented a local similarity solution for an isothermal horizontal plate with finite transverse velocity. Clarke and Riley (1975), allowing for variable density, obtained a similarity solution for the special case of a plate with constant temperature and a particular distribution of blowing rate. The data available are quite restrictive. There is still a shortage of accurate data for a wide range of both suction and blowing rate.

In this analysis of free convection over a semi-infinite horizontal plate, both the wall temperature and transpiration rate are assumed to be power-law variations. Finite-difference solutions and local similarity and nonsimilarity solutions are obtained over a wide range of transpiration rate from very strong suction to very strong blowing. Special considerations are given to the most practical cases of an isothermal plate under the condition of uniform blowing or suction.

Analysis

Consider the buoyancy-induced laminar boundary-layer flow over a semi-infinite horizontal porous plate in a uniform ambient fluid at constant temperature T_∞. The buoyancy results from a hot plate facing upward or, equivalently, from a cold plate facing downward. It is assumed that the porous plate is subjected to blowing or suction in the fashion of a power-law variation with distance x along the plate from the leading edge, i.e., $v_w(x) = Mx^m$, where M is a constant of uniform transpiration rate. The constant M is positive for the case of blowing, and negative for suction. For an impermeable surface, $M = 0$. The special case of $m = 0$ represents uniform blowing or suction. For the steady incompressible laminar free convection flow over a horizontal plate, the boundary-layer equations, with Boussinesq approximation, are

$$\frac{\partial u}{\partial x} + \frac{\partial v}{\partial y} = 0 \tag{1}$$

$$u\frac{\partial u}{\partial x} + v\frac{\partial u}{\partial y} = -\frac{1}{\rho}\frac{\partial p}{\partial x} + \nu\frac{\partial^2 u}{\partial y^2} \tag{2}$$

$$0 = -\frac{1}{\rho}\frac{\partial p}{\partial y} + g\beta(T - T_\infty) \tag{3}$$

$$u\frac{\partial T}{\partial x} + v\frac{\partial T}{\partial y} = \alpha\frac{\partial^2 T}{\partial y^2} \tag{4}$$

where u and v are, respectively, the horizontal and vertical velocity components; p is the dynamic pressure, g the gravitational acceleration, β the coefficient of thermal expansion, ν the kinematic viscosity, and α the thermal diffusivity. The boundary conditions are given by

$$u = 0, \quad v = v_w(x) = Mx^m, \quad T = T_w(x) \qquad \text{at} \quad y = 0 \tag{5}$$

$$u = 0, \quad p = 0, \quad T = T_\infty \qquad \text{as} \quad y \to \infty \tag{6}$$

The wall temperature T_w varies with x as $T_w - T_\infty = Nx^n$, where the constant N bears a positive or negative sign depending on the condition of heating or cooling, respectively. The exponent n is restricted by $-1/2 \le n \le 2$ (Gill et al., 1965). For the special case of an isothermal plate, we have $n = 0$.

Equations (1)–(5) can be transformed into the following set of nonsimilar equations:

$$f''' + aff'' - (2n+1)f'f' - (n-2)\eta\omega' - (4n+2)\omega = b\xi(f'F' - f''F + G) \tag{7}$$

$$5\omega' - \theta = 0 \tag{8}$$

$$\mathrm{Pr}^{-1}\theta'' + af\theta' - 5nf'\theta = b\xi(f'\phi - \theta' F) \tag{9}$$

$$f(\xi, 0) = -\xi(1 + bF)/a \tag{10a}$$

$$f'(\xi, 0) = 0 \tag{10b}$$

$$\theta(\xi, 0) = 1 \tag{10c}$$

$$f'(\xi, \infty) = \omega(\xi, \infty) = \theta(\xi, \infty) = 0 \tag{11a,b,c}$$

where $a = n + 3$, $b = 5m - n + 2$ and $F = \partial f/\partial\xi$, $G = \partial\omega/\partial\xi$, $\Phi = \partial\theta/\partial\xi$.

In this transformation, we have utilized the new coordinates

$$\xi = (v_w x/\nu)\lambda, \quad \eta = (y/x)\lambda \tag{12}$$

and the dimensionless quantities of stream function, dynamic pressure, and temperature as

$$f = (\Psi/5\nu)/\lambda, \quad \omega = (px^2/25\rho\nu^2)/\lambda^4,$$

and

$$\theta = (T - T_\infty)/(T_w - T_\infty) \tag{13}$$

respectively, where $\lambda = (\mathrm{Gr}/5)^{1/5}$ and $\mathrm{Gr} = g\beta(T_w - T_\infty)x^3/\nu^2$. The stream function $\Psi(x, y)$ satisfies the continuity equation (1), and

$$u = \partial\Psi/\partial y = (5v_w/\xi^2)f'(\xi, \eta) \tag{14a}$$

$$v = -\partial\Psi/\partial x = -(v_w/\xi)[(n+3)f + (n-2)\eta f' + b\xi\partial f/\partial\xi] \tag{14b}$$

The nonsimilar equations (7)–(11) were solved by an implicit finite-difference scheme known as the box method (Cebeci and Bradshaw, 1984). In the computations, a variable grid of η, $(\Delta\eta)_i = \gamma^i(\Delta\eta)_0$, was used to maintain the accuracy. However, a uniform spacing of $\Delta\xi = 0.1$ is sufficient to give results of satisfactory accuracy. The length of the first $\Delta\eta$ step, $(\Delta\eta)_0$, was chosen as 0.005, and the ratio of two successive steps γ as 1.05. In order to check the accuracy, the calculations were repeated with various values of $(\Delta\eta)_0$, γ, and $\Delta\xi$.

Nonsimilar equations were also solved by the local similarity and local nonsimilarity methods for the purpose of comparison. The sets of equations for the local similarity and local nonsimilarity models were solved by the Runge-Kutta-Gill in-

[1]Department of Chemical Engineering, National Central University, Chungli, Taiwan 32054.

Contributed by the Heat Transfer Division for publication in the JOURNAL OF HEAT TRANSFER. Manuscript received by the Heat Transfer Division October 24, 1985. Keywords: Natural Convection.

References

Abramowitz, M., and Stegun, I., 1964, *Handbook of Mathematical Functions*, National Bureau of Standards Applied Mathematics Series, Vol. 55, pp. 258–297.

Biasi, L., 1971, "Transient Convective Heat Transfer in Fluids With Vanishing Prandtl Number: An Application of the Integral Method," *International Journal of Heat and Mass Transfer*, Vol. 14, pp. 639–642.

Lycans, R., 1985, "Analytical and Numerical Solutions for Transient Forced Convection in Fluids With Vanishing Prandtl Number," M.S. Thesis, Department of Mechanical Engineering, The University of Akron, Akron, OH.

Morgan, G. W., Pipkin, A. C., and Warner, V. H., 1958, "On Heat Transfer in Laminar Boundary Layer Flows of Liquids Having a Very Small Prandtl Number," *Journal of Aeronautical Science*, Vol. 25, pp. 173–180.

Soliman, M., and Chambre, P., 1969, "On the Time-Dependent Convective Heat Transfer in Fluids With Vanishing Prandtl Number," *International Journal of Heat and Mass Transfer*, Vol. 12, pp. 1221–1230.

Sucec, J., 1978, Comment on "On the Time-Dependent Convective Heat Transfer in Fluids With Vanishing Prandtl Number," *International Journal of Heat and Mass Transfer*, Vol. 21, pp. 667–668.

Free Convection on a Horizontal Plate With Blowing and Suction

Hsiao-Tsung Lin[1] and Wen-Shing Yu[1]

Introduction

The effects of blowing and suction on forced convection (Koh and Hartnett, 1961) and those on free convection over a vertical plate (Vedhanayagam et al., 1980) have been studied extensively. On the other hand, the problem of free convection above a horizontal plate with blowing or suction has received substantially less attention. Gill et al. (1965) presented a local similarity solution for an isothermal horizontal plate with finite transverse velocity. Clarke and Riley (1975), allowing for variable density, obtained a similarity solution for the special case of a plate with constant temperature and a particular distribution of blowing rate. The data available are quite restrictive. There is still a shortage of accurate data for a wide range of both suction and blowing rate.

In this analysis of free convection over a semi-infinite horizontal plate, both the wall temperature and transpiration rate are assumed to be power-law variations. Finite-difference solutions and local similarity and nonsimilarity solutions are obtained over a wide range of transpiration rate from very strong suction to very strong blowing. Special considerations are given to the most practical cases of an isothermal plate under the condition of uniform blowing or suction.

Analysis

Consider the buoyancy-induced laminar boundary-layer flow over a semi-infinite horizontal porous plate in a uniform ambient fluid at constant temperature T_∞. The buoyancy results from a hot plate facing upward or, equivalently, from a cold plate facing downward. It is assumed that the porous plate is subjected to blowing or suction in the fashion of a power-law variation with distance x along the plate from the leading edge, i.e., $v_w(x) = Mx^m$, where M is a constant of uniform transpiration rate. The constant M is positive for the case of blowing, and negative for suction. For an impermeable surface, $M = 0$. The special case of $m = 0$ represents uniform blowing or suction. For the steady incompressible laminar free convection flow over a horizontal plate, the boundary-layer equations, with Boussinesq approximation, are

$$\frac{\partial u}{\partial x} + \frac{\partial v}{\partial y} = 0 \tag{1}$$

$$u\frac{\partial u}{\partial x} + v\frac{\partial u}{\partial y} = -\frac{1}{\rho}\frac{\partial p}{\partial x} + \nu\frac{\partial^2 u}{\partial y^2} \tag{2}$$

$$0 = -\frac{1}{\rho}\frac{\partial p}{\partial y} + g\beta(T - T_\infty) \tag{3}$$

$$u\frac{\partial T}{\partial x} + v\frac{\partial T}{\partial y} = \alpha\frac{\partial^2 T}{\partial y^2} \tag{4}$$

where u and v are, respectively, the horizontal and vertical velocity components; p is the dynamic pressure, g the gravitational acceleration, β the coefficient of thermal expansion, ν the kinematic viscosity, and α the thermal diffusivity. The boundary conditions are given by

$$u = 0, \quad v = v_w(x) = Mx^m, \quad T = T_w(x) \qquad \text{at} \quad y = 0 \tag{5}$$

$$u = 0, \quad p = 0, \quad T = T_\infty \qquad \text{as} \quad y \to \infty \tag{6}$$

The wall temperature T_w varies with x as $T_w - T_\infty = Nx^n$, where the constant N bears a positive or negative sign depending on the condition of heating or cooling, respectively. The exponent n is restricted by $-1/2 \le n \le 2$ (Gill et al., 1965). For the special case of an isothermal plate, we have $n = 0$.

Equations (1)–(5) can be transformed into the following set of nonsimilar equations:

$$f''' + aff'' - (2n+1)f'f' - (n-2)\eta\omega' - (4n+2)\omega = b\xi(f'F' - f''F + G) \tag{7}$$

$$5\omega' - \theta = 0 \tag{8}$$

$$\mathrm{Pr}^{-1}\theta'' + af\theta' - 5nf'\theta = b\xi(f'\phi - \theta' F) \tag{9}$$

$$f(\xi, 0) = -\xi(1 + bF)/a \tag{10a}$$

$$f'(\xi, 0) = 0 \tag{10b}$$

$$\theta(\xi, 0) = 1 \tag{10c}$$

$$f'(\xi, \infty) = \omega(\xi, \infty) = \theta(\xi, \infty) = 0 \tag{11a,b,c}$$

where $a = n + 3$, $b = 5m - n + 2$ and $F = \partial f/\partial\xi$, $G = \partial\omega/\partial\xi$, $\Phi = \partial\theta/\partial\xi$.

In this transformation, we have utilized the new coordinates

$$\xi = (v_w x/\nu)\lambda, \quad \eta = (y/x)\lambda \tag{12}$$

and the dimensionless quantities of stream function, dynamic pressure, and temperature as

$$f = (\Psi/5\nu)/\lambda, \quad \omega = (px^2/25\rho\nu^2)/\lambda^4,$$

and

$$\theta = (T - T_\infty)/(T_w - T_\infty) \tag{13}$$

respectively, where $\lambda = (\mathrm{Gr}/5)^{1/5}$ and $\mathrm{Gr} = g\beta(T_w - T_\infty)x^3/\nu^2$. The stream function $\Psi(x, y)$ satisfies the continuity equation (1), and

$$u = \partial\Psi/\partial y = (5v_w/\xi^2)f'(\xi, \eta) \tag{14a}$$

$$v = -\partial\Psi/\partial x = -(v_w/\xi)[(n+3)f + (n-2)\eta f' + b\xi\partial f/\partial\xi] \tag{14b}$$

The nonsimilar equations (7)–(11) were solved by an implicit finite-difference scheme known as the box method (Cebeci and Bradshaw, 1984). In the computations, a variable grid of η, $(\Delta\eta)_i = \gamma^i(\Delta\eta)_0$, was used to maintain the accuracy. However, a uniform spacing of $\Delta\xi = 0.1$ is sufficient to give results of satisfactory accuracy. The length of the first $\Delta\eta$ step, $(\Delta\eta)_0$, was chosen as 0.005, and the ratio of two successive steps γ as 1.05. In order to check the accuracy, the calculations were repeated with various values of $(\Delta\eta)_0$, γ, and $\Delta\xi$.

Nonsimilar equations were also solved by the local similarity and local nonsimilarity methods for the purpose of comparison. The sets of equations for the local similarity and local nonsimilarity models were solved by the Runge-Kutta-Gill in-

[1]Department of Chemical Engineering, National Central University, Chungli, Taiwan 32054.

Contributed by the Heat Transfer Division for publication in the JOURNAL OF HEAT TRANSFER. Manuscript received by the Heat Transfer Division October 24, 1985. Keywords: Natural Convection.

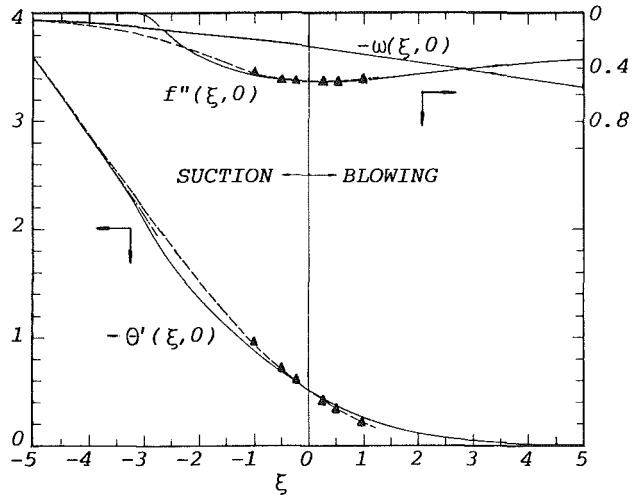

Fig. 1 Results of $\theta'(\xi, 0)$, $f''(\xi, 0)$, and $\omega(\xi, 0)$ for an isothermal plate with uniform blowing and suction, Pr = 0.72

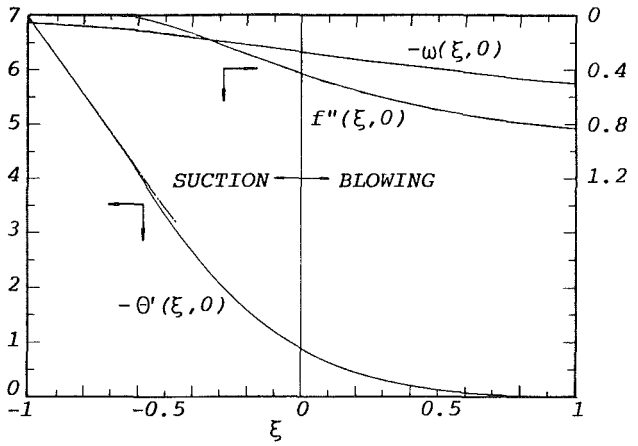

Fig. 2 Results of $\theta'(\xi, 0)$, $f''(\xi, 0)$, and $\omega(\xi, 0)$ for an isothermal plate with uniform blowing and suction, Pr = 7

tegration program in conjunction with the Newton-Raphson shooting method.

Asymptotic Solutions for Very Strong Suction

In the condition of very strong suction, the horizontal velocity component of the convective flow is small and negligible when compared with the vertical velocity component. In this case, $f'(\xi, \eta) = 0$ and $f(\xi, \eta) = -\xi/(a+b)$. Consequently, the energy equation can be decoupled from the momentum equations and reduced to

$$\theta'' - \Pr\xi\theta' = 0 \tag{15}$$

with the boundary conditions (10*c*) and (11*c*). Equation (15) admits the analytical solution

$$\theta(\xi, \eta) = \exp(\Pr\xi\eta) \tag{16}$$

Therefore, the asymptotic heat transfer rate is obtained as

$$\mathrm{Nu}/\lambda = -\theta'(\xi, 0) = -\Pr\xi \tag{17}$$

Analytical Solution for the Case of $m = n = -1/2$

For the specific distribution of $m = n = -1/2$, it is obvious that $b = 0$ and ξ is independent of x. Consequently, the energy equation becomes

$$2\theta'' + 5\Pr(f\theta)' = 0 \tag{18}$$

By integrating equation (18) from $\eta = 0$ to ∞ and utilizing the boundary conditions

$$f(\xi, 0) = -2\xi/5, \quad \theta(\xi, 0) = 1, \quad f(\xi, \infty) = \text{const},$$
$$\theta(\xi, \infty) = 0, \quad \theta'(\xi, \infty) = 0 \tag{19}$$

we obtain

$$\theta'(\xi, 0) = \Pr\xi \tag{20}$$

Results and Discussion

The primary physical quantity of interest is the heat transfer rate in terms of the local Nusselt number as $\mathrm{Nu}/\lambda = -\theta'(\xi, 0)$. In addition, the friction coefficient, $C_f = \tau_w/[5\rho(\nu/x)^2\lambda^3] = f''(\xi, 0)$, and the dimensionless dynamic pressure at the wall, $\omega(\xi, 0)$, are also of theoretical interest. Numerical results of $\theta'(\xi, 0)$, $f''(\xi, 0)$, and $\omega(\xi, 0)$ for the most practical case of an isothermal plate ($n = 0$) under uniform transpiration ($m = 0$) are presented in Figs. 1 and 2 for Pr = 0.72 and 7, respectively. For the special case of $\xi = 0$, our solutions are identical with the results of conventional free convection over a horizontal plate. In addition, the data of Gill et al. (1965) for an isothermal plate with finite transverse velocity are shown in close agreement with the dashed curves of Fig. 1, which represent the local similarity solutions.

The accuracy of the numerical results can be verified by comparing the solutions from different numerical methods. It was found (Yu, 1986) that the local nonsimilarity and finite-difference solutions are in excellent agreement for small and moderate transpiration rate. However, the convergence and accuracy of the local nonsimilarity solutions are better than those of the finite-difference solutions for a large suction rate. On the other hand, for a large blowing rate, the finite-difference solutions are convergent and accurate, while the local similarity and nonsimilarity solutions are divergent. Therefore, in the preparation of Figs. 1-4, the finite-difference solutions are presented for the cases of blowing, while the local nonsimilarity solutions are provided for suction.

As expected, the local similarity solutions are accurate in the immediate neighborhood of $\xi = 0$. It can be seen from Fig. 1 that the local similarity solutions are in agreement with the local nonsimilarity solutions (and finite-difference solutions as well) for small values of ξ. In addition, excellent agreement between the two sets of solutions is found in the regime of large negative ξ. These solutions also coincide with the asymptotic solution at $\xi < -4$ for Pr = 0.72 and $\xi < -0.8$ for Pr = 7. Therefore, any ξ in these regimes can be regarded as large negative ξ, which corresponds to the case of very strong suction.

An inspection of Figs. 1 and 2 reveals that suction increases the heat transfer rate greatly, while blowing decreases it slightly. It is evident that the effect of suction is to suck away the warm fluid on the plate and thus decrease the thermal boundary-layer thickness and increase the heat transfer rate. On the other hand, the reduction in heat transfer rate results physically from the resistance of a thick buffer layer formed by the ejected fluid. For very strong blowing, the finite-difference solutions of $\theta'(\xi, 0)$ approach zero. The variations of thermal boundary layer with ξ can be seen from Fig. 3.

The variations of $f''(\xi, 0)$ and $\omega(\xi, 0)$ with ξ are also shown in Figs. 1 and 2. As can be seen in these figures, the value of $\omega(\xi, 0)$ decreases slightly with increasing ξ from very strong suction to very strong blowing for both the cases of Pr = 0.72 and 7. The variations of wall friction, $f''(\xi, 0)$, with ξ are more complicated. For Pr = 0.72, both blowing and suction reduce shear stress, as shown in Fig. 1. This is similar to the case of a vertical plate (Eichhorn, 1961). However, for Pr = 7, suction reduces while blowing increases the wall friction, as indicated in Fig. 2. The different behavior of the wall shear stress, or $f''(\xi, 0)$, with ξ for the two fluids can be explained by the differences between the velocity profiles, $(u/v_w)\lambda^2/5 = f'(\xi, \eta)$,

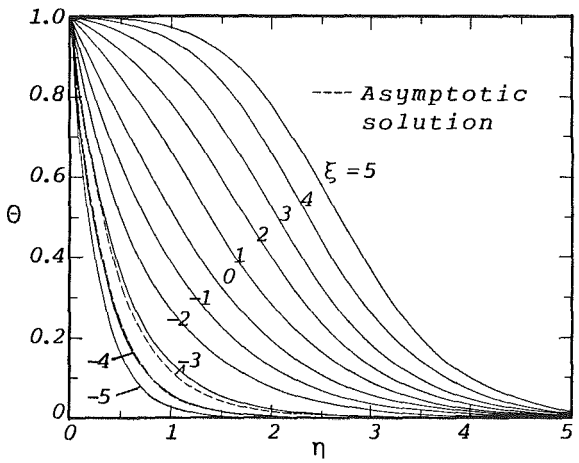

Fig. 3 Representative temperature profiles for an isothermal plate with uniform blowing and suction, Pr = 0.72

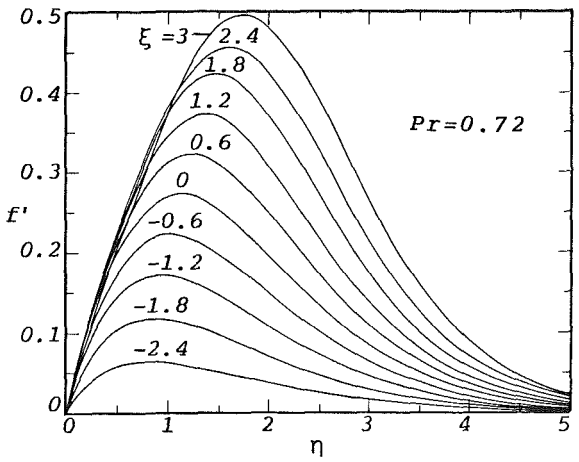

Fig. 4(a)

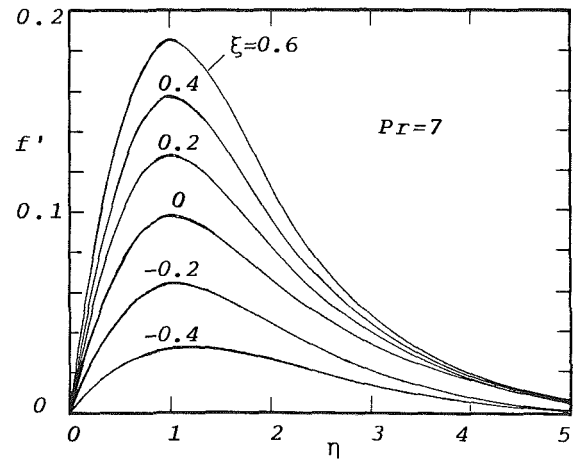

Fig. 4(b)

Fig. 4 Representative horizontal velocity profiles for isothermal plate with uniform blowing and suction: (a) Pr = 0.72; (b) Pr = 7

for Pr = 0.72 and 7 shown in Figs. 4(*a*) and 4(*b*), respectively. As can be seen from these figures, the maximum velocities for both fluids are increased with increasing ξ. As blowing rate is increased, more warm fluid is ejected from the plate. Consequently, the maximum velocity is increased with increasing buoyancy due to the energy input. An increase in maximum velocity will increase the wall shear stress, as shown in Fig. 4(*b*) for the case of Pr = 7. However, for the case of Pr = 0.72, blowing also causes the position of the maximum velocity to move away from the wall (as shown in Fig. 4*a*) and this will result in a decrease in the wall shear stress. The increase or decrease in the wall shear stress for the case of Pr = 0.72 is a net result from the competition of these two reverse effects. For the case of Pr = 7, the maximum velocities for various ξ are nearly at the same position (at $\eta \approx 1$).

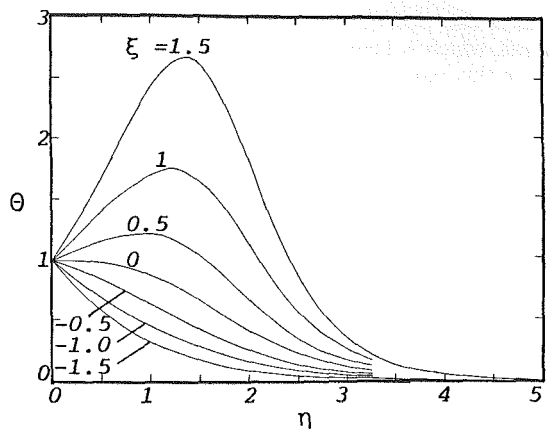

Fig. 5 Temperature profiles for the case of $m = n = -1/2$, Pr = 0.72

The variation of heat transfer rate with ξ for the case of $m = n = -1/2$ is quite different from that for the case of uniform wall temperature ($n = 0$), especially for $\xi > 0$. It is very interesting to note, from $\mathrm{Nu}/\lambda = -\theta'(\xi, 0) = -\mathrm{Pr}\xi$, that the wall heat flux is negative for the case of blowing ($\xi > 0$). Negative wall heat flux means that heat is transferred to the plate rather than from it. Physically, this occurs when the wall temperature and blowing rate decrease so rapidly in the flow direction that the fluid convected along the plate is at a higher temperature than the wall at the downstream position (Vedhanayagam et al., 1980). This is rational. Since the wall temperature and blowing rate vary with $x^{-1/2}$, we can imagine that a warm stream is ejected near the leading edge of the plate and releases its energy to the wall at the downstream side. To illustrate this, a finite-difference solution of the temperature profiles, $\theta(\xi, \eta)$, for $m = n - 1/2$ is presented in Fig. 5. The evident changes of the temperature profile with ξ for $\xi > 0$ are the sharp rise in the profile near the wall and the overshoot of fluid temperature beyond the wall temperature, especially for larger positive ξ. These particular temperature distributions are quite different from the typical profiles shown in Fig. 3. Further study of Fig. 5 reveals that, as ξ increases from negative values to positive ones, the temperature gradient at the wall increases from negative to positive, as predicted by equation (20). This corresponds to the physical situation in which heat is transferred from the plate for the suction case but to the plate for the blowing case.

Conclusion

We have presented a nonsimilar transformation for the laminar free convection above a heated upward-facing horizontal porous plate with power-law variations of both wall temperature and transpiration rate. The nonsimilar boundary-layer equations are reducible to the self-similar equations for the case of no surface transpiration ($\xi = 0$). In addition, analytical solutions can be derived for the very strong suction case and for the particular distribution of $m = n = -1/2$. For cases other than those mentioned, numerical results from the local similarity, local nonsimilarity, and finite-difference methods were obtained for an isothermal plate with uniform transpiration and for Pr = 0.72 and 7. The

finite-difference solution for the case of $m=n=-1/2$ is also presented, which is identical with the derived analytical solution. For this particular distribution of surface temperature and blowing rate, the heat transfer and temperature profiles are found to be quite special.

Acknowledgments

This work was supported by the National Science Council of R.O.C. under Grant No. NSC 75-0402-E008-01.

References

Cebeci, T., and Bradshaw, P., 1984, *Physical and Computational Aspects of Convective Heat Transfer*, Springer-Verlag, New York, pp. 385–455.

Clark, J. F., and Riley, N., 1975, "Natural Convection Induced in a Gas by the Presence of a Hot Porous Horizontal Surface," *Q. J. Mech. Appl. Math.*, Vol. 28, Part 4, pp. 373–396.

Eichhorn, R., 1961, "The Effect of Mass Transfer on Free Convection," ASME JOURNAL OF HEAT TRANSFER, Vol. 83, pp. 387–389.

Gill, W. N., Zeh, D. W., and Casal, E. D., 1965, "Free Convection on a Horizontal Plate," *Z. Angew. Math. Phys.*, Vol. 16, pp. 539–541.

Koh, J. C. Y., and Hartnett, J. P., 1961, "Skin Friction and Heat Transfer for Incompressible Laminar Flow Over Porous Wedges With Suction and Variable Wall Temperature," *Int. J. Heat Mass Transfer*, Vol. 2, pp. 185–198.

Vedhanayagam, M., Altenkirch, R. A., and Eichhorn, R., 1980, "A Transformation of the Boundary Layer Equations for Free Convection Past a Vertical Flat Plate With Arbitrary Blowing and Wall Temperature Variation," *Int. J. Heat Mass Transfer*, Vol. 23, pp. 1286–1288.

Low Peclet Number Heat Transfer in a Laminar Tube Flow Subjected to Axially Varying Wall Heat Flux

A. J. Pearlstein[1] and B. P. Dempsey[2]

Nomenclature

- $b(\eta)$ = nondimensional heat flux in $[0, \sigma]$
- c_p = specific heat of fluid at constant pressure
- k = thermal conductivity of fluid
- L = length of variably heated section
- Pe = Peclet number $=2\rho c_p V_0 r_0/k$
- q = dimensional heat flux
- r = radial coordinate
- T = temperature of fluid
- V_0 = average velocity of fluid
- z = axial coordinate
- γ = nondimensional heat flux in $[\sigma, \infty)$
- η = nondimensional axial variable $=z/(r_0\text{Pe})$
- θ = nondimensional temperature $=k(T-T_0)/(q_{\max}r_0)$
- ξ = nondimensional radial variable $=r/r_0$
- ρ = dimensional fluid density
- σ = nondimensional length of variably heated section $=L/(r_0\text{Pe})$

Since the analysis of Schneider (1957) demonstrating the importance of axial conduction in the thermal entry region for low Peclet number flows, there have been several attempts to account for both axial conduction and axially varying wall boundary conditions in hydrodynamically developed laminar flows. Nagasue (1981) obtained a closed-form solution by representing the axial flux distribution with a power series. Solutions were found for monomial (i.e., z^k) heating, with the total solution obtained by superposition. This representation is computationally impractical for sinusoidal, exponential, and other practically important axial flux distributions having slowly convergent power series. Several investigators have also used purely numerical methods to solve this problem (Lee and Hwang, 1981; McMordie and Emergy, 1967; Pearson and Wolf, 1970; Verhoff and Fisher, 1973). Unfortunately, these methods are inefficient due to the need to recompute the whole solution each time the axial heat flux distribution at the wall is changed, as in an iterative design.

Thus, there do not appear to be any general methods available for the solution of the important problem of hydrodynamically developed low Peclet number flow in a tube with axially varying wall heat flux. We have recently developed such a method (Dempsey, 1986). The purpose of the present work is to demonstrate its usefulness by presenting results for several wall heat flux distributions of interest.

We begin with the constant property energy equation

$$2\rho c_p V_0[1-(r/r_0)^2]\frac{\partial T}{\partial z} = k\left[\frac{1}{r}\frac{\partial}{\partial r}\left(r\frac{\partial T}{\partial r}\right)+\frac{\partial^2 T}{\partial z^2}\right] \tag{1a}$$

for laminar flow of a constant-property Newtonian fluid in a circular tube. The viscous dissipation term has been neglected. We consider equation (1*a*) with the Neumann boundary conditions

$$k\frac{\partial T(z, r_0)}{\partial r} = \begin{cases} 0 & -\infty < z < 0 \\ q(z) & 0 \le z \le L \\ q_\infty & L < z < \infty \end{cases} \tag{1b}$$

and the upstream condition

$$\lim_{z\to-\infty} T(z, r) = T_0 \tag{1c}$$

Equations (1*a–c*) are nondimensionalized by $\sigma=L/(r_0\text{Pe})$, $\eta=z/(r_0\text{Pe})$, $\xi=r/r_0$, $\gamma=q_\infty/q_{\max}$, $b(\eta)=q(z)/q_{\max}$, and $\theta(\eta, \xi) = k(T-T_0)/(q_{\max}r_0)$, where $q_{\max}$ is the maximum of $|q(z)|$ in the interval $[0, L]$. After substitution, (1*a–c*) become

$$(1-\xi^2)\frac{\partial\theta}{\partial\eta} = \frac{1}{\xi}\frac{\partial}{\partial\xi}\left(\xi\frac{\partial\theta}{\partial\xi}\right)+\frac{1}{\text{Pe}^2}\frac{\partial^2\theta}{\partial\eta^2} \tag{2a}$$

$$\frac{\partial\theta(\eta, 1)}{\partial\xi} = \begin{cases} 0 & -\infty < \eta < 0 \\ b(\eta) & 0 \le \eta \le \sigma \\ \gamma & \sigma < \eta < \infty \end{cases} \tag{2b}$$

and

$$\lim_{\eta\to-\infty}\theta(\eta, \xi) = 0 \tag{2c}$$

The other boundary condition is that the solution becomes fully developed at large η. We assume that in $[0, \sigma]$, b has a finite number of discontinuities, say m. We let $b^+(\eta_j)$ and $b^-(\eta_j)$ be the right and left limits of b at the jth discontinuity and write

$$b(\eta) = b_1(\eta)+\sum_{j=1}^{m}[b^+(\eta_j)-b^-(\eta_j)]U(\eta-\eta_j)$$
$$= b_1(\eta)+b_2(\eta)$$

[1]Assistant Professor, Department of Aerospace and Mechanical Engineering, University of Arizona, Tucson, AZ 85721; Assoc. Mem. ASME.

[2]Graduate Student, Department of Aerospace and Mechanical Engineering, University of Arizona, Tucson, AZ 85721; present address: TRW Space and Technology Group, One Space Park, Redondo Beach, CA 90278.

Contributed by the Heat Transfer Division and presented at the Second ASME-JSME Thermal Engineering Joint Conference, Honolulu, HI, March 22–27, 1987. Manuscript received by the Heat Transfer Division April 16, 1987. Keywords: Forced Convection, Liquid Metals.

finite-difference solution for the case of $m=n=-1/2$ is also presented, which is identical with the derived analytical solution. For this particular distribution of surface temperature and blowing rate, the heat transfer and temperature profiles are found to be quite special.

Acknowledgments

This work was supported by the National Science Council of R.O.C. under Grant No. NSC 75-0402-E008-01.

References

Cebeci, T., and Bradshaw, P., 1984, *Physical and Computational Aspects of Convective Heat Transfer*, Springer-Verlag, New York, pp. 385–455.

Clark, J. F., and Riley, N., 1975, "Natural Convection Induced in a Gas by the Presence of a Hot Porous Horizontal Surface," *Q. J. Mech. Appl. Math.*, Vol. 28, Part 4, pp. 373–396.

Eichhorn, R., 1961, "The Effect of Mass Transfer on Free Convection," ASME JOURNAL OF HEAT TRANSFER, Vol. 83, pp. 387–389.

Gill, W. N., Zeh, D. W., and Casal, E. D., 1965, "Free Convection on a Horizontal Plate," *Z. Angew. Math. Phys.*, Vol. 16, pp. 539–541.

Koh, J. C. Y., and Hartnett, J. P., 1961, "Skin Friction and Heat Transfer for Incompressible Laminar Flow Over Porous Wedges With Suction and Variable Wall Temperature," *Int. J. Heat Mass Transfer*, Vol. 2, pp. 185–198.

Vedhanayagam, M., Altenkirch, R. A., and Eichhorn, R., 1980, "A Transformation of the Boundary Layer Equations for Free Convection Past a Vertical Flat Plate With Arbitrary Blowing and Wall Temperature Variation," *Int. J. Heat Mass Transfer*, Vol. 23, pp. 1286–1288.

Low Peclet Number Heat Transfer in a Laminar Tube Flow Subjected to Axially Varying Wall Heat Flux

A. J. Pearlstein[1] and B. P. Dempsey[2]

Nomenclature

- $b(\eta)$ = nondimensional heat flux in $[0, \sigma]$
- c_p = specific heat of fluid at constant pressure
- k = thermal conductivity of fluid
- L = length of variably heated section
- Pe = Peclet number $=2\rho c_p V_0 r_0/k$
- q = dimensional heat flux
- r = radial coordinate
- T = temperature of fluid
- V_0 = average velocity of fluid
- z = axial coordinate
- γ = nondimensional heat flux in $[\sigma, \infty)$
- η = nondimensional axial variable $=z/(r_0\text{Pe})$
- θ = nondimensional temperature $=k(T-T_0)/(q_{\max}r_0)$
- ξ = nondimensional radial variable $=r/r_0$
- ρ = dimensional fluid density
- σ = nondimensional length of variably heated section $=L/(r_0\text{Pe})$

Since the analysis of Schneider (1957) demonstrating the importance of axial conduction in the thermal entry region for low Peclet number flows, there have been several attempts to account for both axial conduction and axially varying wall boundary conditions in hydrodynamically developed laminar flows. Nagasue (1981) obtained a closed-form solution by representing the axial flux distribution with a power series. Solutions were found for monomial (i.e., z^k) heating, with the total solution obtained by superposition. This representation is computationally impractical for sinusoidal, exponential, and other practically important axial flux distributions having slowly convergent power series. Several investigators have also used purely numerical methods to solve this problem (Lee and Hwang, 1981; McMordie and Emergy, 1967; Pearson and Wolf, 1970; Verhoff and Fisher, 1973). Unfortunately, these methods are inefficient due to the need to recompute the whole solution each time the axial heat flux distribution at the wall is changed, as in an iterative design.

Thus, there do not appear to be any general methods available for the solution of the important problem of hydrodynamically developed low Peclet number flow in a tube with axially varying wall heat flux. We have recently developed such a method (Dempsey, 1986). The purpose of the present work is to demonstrate its usefulness by presenting results for several wall heat flux distributions of interest.

We begin with the constant property energy equation

$$2\rho c_p V_0[1-(r/r_0)^2]\frac{\partial T}{\partial z} = k\left[\frac{1}{r}\frac{\partial}{\partial r}\left(r\frac{\partial T}{\partial r}\right)+\frac{\partial^2 T}{\partial z^2}\right] \tag{1a}$$

for laminar flow of a constant-property Newtonian fluid in a circular tube. The viscous dissipation term has been neglected. We consider equation (1*a*) with the Neumann boundary conditions

$$k\frac{\partial T(z, r_0)}{\partial r} = \begin{cases} 0 & -\infty < z < 0 \\ q(z) & 0 \le z \le L \\ q_\infty & L < z < \infty \end{cases} \tag{1b}$$

and the upstream condition

$$\lim_{z\to-\infty} T(z, r) = T_0 \tag{1c}$$

Equations (1*a–c*) are nondimensionalized by $\sigma=L/(r_0\text{Pe})$, $\eta=z/(r_0\text{Pe})$, $\xi=r/r_0$, $\gamma=q_\infty/q_{\max}$, $b(\eta)=q(z)/q_{\max}$, and $\theta(\eta, \xi) = k(T-T_0)/(q_{\max}r_0)$, where $q_{\max}$ is the maximum of $|q(z)|$ in the interval $[0, L]$. After substitution, (1*a–c*) become

$$(1-\xi^2)\frac{\partial\theta}{\partial\eta} = \frac{1}{\xi}\frac{\partial}{\partial\xi}\left(\xi\frac{\partial\theta}{\partial\xi}\right)+\frac{1}{\text{Pe}^2}\frac{\partial^2\theta}{\partial\eta^2} \tag{2a}$$

$$\frac{\partial\theta(\eta, 1)}{\partial\xi} = \begin{cases} 0 & -\infty < \eta < 0 \\ b(\eta) & 0 \le \eta \le \sigma \\ \gamma & \sigma < \eta < \infty \end{cases} \tag{2b}$$

and

$$\lim_{\eta\to-\infty}\theta(\eta, \xi) = 0 \tag{2c}$$

The other boundary condition is that the solution becomes fully developed at large η. We assume that in $[0, \sigma]$, b has a finite number of discontinuities, say m. We let $b^+(\eta_j)$ and $b^-(\eta_j)$ be the right and left limits of b at the jth discontinuity and write

$$b(\eta) = b_1(\eta)+\sum_{j=1}^{m}[b^+(\eta_j)-b^-(\eta_j)]U(\eta-\eta_j)$$
$$= b_1(\eta)+b_2(\eta)$$

[1]Assistant Professor, Department of Aerospace and Mechanical Engineering, University of Arizona, Tucson, AZ 85721; Assoc. Mem. ASME.

[2]Graduate Student, Department of Aerospace and Mechanical Engineering, University of Arizona, Tucson, AZ 85721; present address: TRW Space and Technology Group, One Space Park, Redondo Beach, CA 90278.

Contributed by the Heat Transfer Division and presented at the Second ASME-JSME Thermal Engineering Joint Conference, Honolulu, HI, March 22–27, 1987. Manuscript received by the Heat Transfer Division April 16, 1987. Keywords: Forced Convection, Liquid Metals.

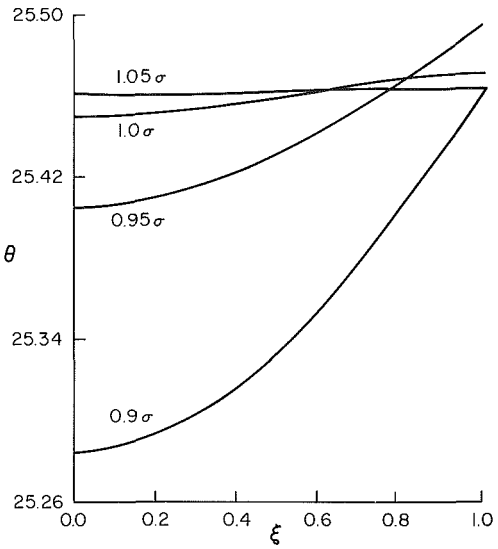

Fig. 1 Radial temperature profiles for various η with $q=0$, $\eta<0$; $q=q_{max}\sin(\pi\eta/\sigma)$, $0<\eta<\sigma$; $q=0$, $\sigma<\eta$; Pe = 1, $\sigma=10$

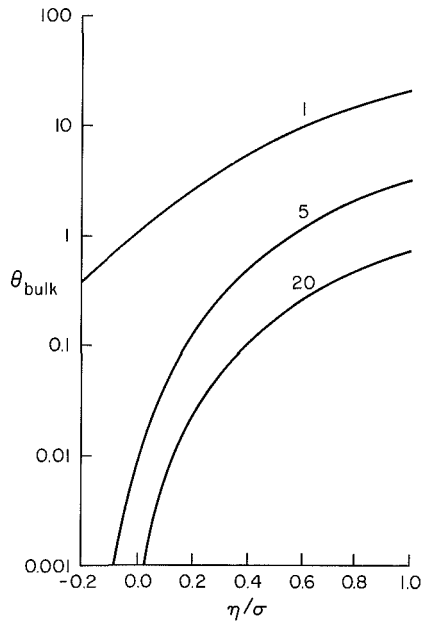

Fig. 2 Bulk temperature for various Pe with $q=0$, $\eta<0$; $q=q_{max}[\tanh(2\eta/\sigma-1)+\tanh 1]/2$, $0<\eta<\sigma$; $q=q_{max}\tanh 1$, $\sigma<\eta$, σPe = 10

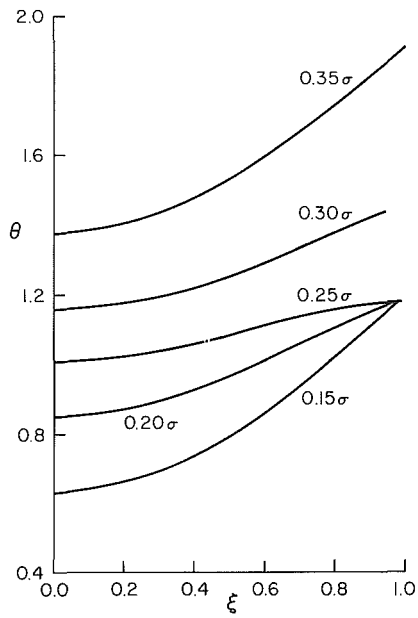

Fig. 3 Radial temperature profiles for various η with $q=0$, $\eta<0$; $q=q_{max}\sin^2(4\pi\eta/\sigma)$, $0<\eta<\sigma$; $q=0$, $\sigma<\eta$; Pe = 5, $\sigma=2$

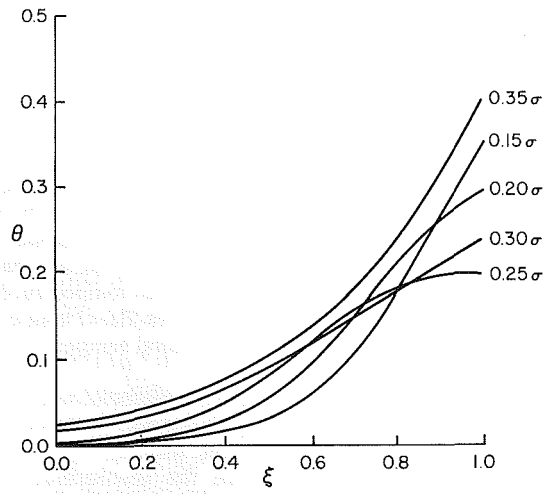

Fig. 4 Radial temperature profiles for various η with $q=0$, $\eta<0$; $q=q_{max}\sin^2(4\pi\eta/\sigma)$, $0<\eta<\sigma$; $q=0$, $\sigma<\eta$; Pe = 50, $\sigma=0.2$

where U is the unit step function. Thus, b_1 is continuous, piecewise differentiable, and $b_1(0)=0$.

The solution of equations (2*a–c*) is effected by a combined analytical and numerical procedure employing a new superposition principle. [Note that when axial conduction can be neglected, the problem is of parabolic type and the standard Duhamel superposition principle can be used (Sparrow and Siegel, 1958). In the present case, the problem is elliptic, so that Duhamel's principle is inapplicable.] A brief description of the present method is given in the following paragraph. The details of the procedure are described elsewhere (Dempsey, 1986).

We first note that equations (2*a–c*) form a linear system and decompose $\theta(\eta, \xi)$ into three parts, each of which is defined on $-\infty<\eta<\infty$. The first (θ_1) and second (θ_2) parts are the dimensionless temperature fields corresponding to heating by the flux distributions $b_1(\eta)$ and $b_2(\eta)$, respectively. The third (θ_3) part is the temperature field resulting from the uniform wall heat flux γ downstream of $\eta=\sigma$ and can be obtained by conventional techniques (e.g., Papoutsakis et al., 1980). The distributions $\theta_1(\eta, \xi)$ and $\theta_2(\eta, \xi)$ are found by linear superposition of solutions to a problem consisting of equations (2*a–c*) subject to a dimensionless wall heat flux of unity in the region $\eta^*\le\eta\le\sigma$ and insulated everywhere else, where $0\le\eta^*\le\sigma$. Each constituent dimensionless temperature distribution $\theta_i(\eta, \xi)$ is defined piecewise on the intervals $-\infty<\eta\le 0$, $0\le\eta\le\sigma$, and $\sigma\le\eta<\infty$. This is due to the fact that, in this elliptic problem, heating a finite length of the tube gives a contribution to the solution *upstream* (in addition to downstream) of the heated section. The piecewise-defined functions $\theta_i(\eta, \xi)$ and their η derivatives are made continuous at $\eta=0$ and σ by a matching procedure employing an orthogonality relationship first introduced by Smith et al. (1975).

Results have been obtained for a variety of wall heat flux distributions. The constant flux case has been included to allow comparison to results of other investigators. The axially varying cases were selected to show that the present method

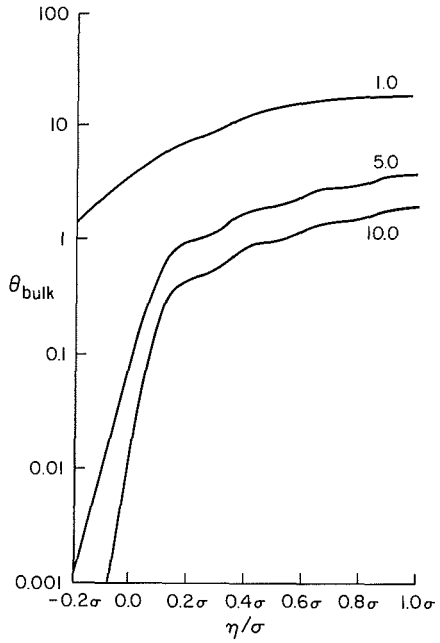

Fig. 5 Bulk temperature for various Pe with $q=0$, $\eta<0$; $q=q_{max}\sin^2(4\pi\eta/\sigma)$, $0<\eta<\sigma$; $q=0$, $\sigma<\eta$; $\sigma Pe=10$

can handle many physical situations and to show the importance of axial conduction in certain problems.

Radial temperature profiles and Nusslet numbers were computed for a unit step in heat flux at $\eta=0$ with $Pe=5$ and 10, and $\sigma Pe=10$. The results agree with those of Hsu (1971) to within 1 percent. Results for $Pe=5$ are virtually identical to those of Papoutsakis et al. (1980).

The first axially varying wall heat flux considered is $\sin(\pi\eta/\sigma)$, chosen because of its application to nuclear reactors (Burchill et al., 1968). Figure 1 shows radial temperature profiles near the end of the heated section for $Pe=1$ and $\sigma=10$. We note the rapid approach to a flat radial temperature profile at the exit as η approaches σ.

The second axially varying case is a hyperbolic tangent flux distribution, which is a better approximation to the wall flux distribution for "conjugated" heat transfer problems including wall conduction than are the discontinuous flux distributions used in previous analyses (see, e.g., Faghri and Sparrow, 1980). Figure 2 shows the bulk temperatures for Peclet numbers 1, 5, and 20 for a hyperbolic tangent distribution that slowly changes from 0 to $(1+\tanh 1)/2$. If the fully developed solution is integrated to determine the fully developed bulk temperature, we find $\theta_{bulk}=2(\eta-\sigma)+7/32+4/Pe^2$; thus, we expect to see the large difference between bulk temperatures for $Pe=1$ and $Pe=5$ shown in Fig. 2. [We note here that unlike the case with no axial conduction, $\theta_{bulk}(\eta)$ cannot be obtained by direct integration (in ξ and then η) of equation (2*a*).]

The final case considered is $\sin^2(4\pi\eta/\sigma)$. Figures 3 and 4 show radial temperature profiles for Peclet numbers 5 and 50, indicating the importance of the axial conduction term near $\eta=\sigma/4$. Note that the case $Pe=50$ roughly corresponds to no axial conduction. Figure 5 shows a plot of the bulk temperature for the $\sin^2(4\pi\eta/\sigma)$ distribution for Peclet numbers 1, 5, and 10. We note that the oscillations become less pronounced at smaller Pe due to the effect of axial conduction.

References

Burchill, W. E., Jones, B. G., and Stein, R. P., 1968, "Influence of Axial Heat Diffusion in Liquid Metal-Cooled Ducts With Specified Heat Flux," ASME JOURNAL OF HEAT TRANSFER, Vol. 90, pp. 283–290.

Dempsey, B. P., 1986, "Low Peclet Number Heat Transfer in a Laminar Tube Flow Subjected to Axially Varying Wall Heat Flux," M.S. Thesis, University of Arizona, Tucson, AZ.

Faghri, M., and Sparrow, E. M., 1980, "Simultaneous Wall and Fluid Axial Conduction in Laminar Pipe-Flow Heat Transfer," ASME JOURNAL OF HEAT TRANSFER, Vol. 102, pp. 58–63.

Hsu, C.-J., 1971, "An Exact Analysis of Low Peclet Number Thermal Entry Region Heat Transfer in Transversely Nonuniform Velocity Fields," *AIChE Journal*, Vol. 17, pp. 732–740.

Lee, S. L., and Hwang, G. J., 1981, "Finite Element Solution of Low Peclet Number Fluid Flow in a Round Pipe With the Cauchy Boundary Condition," *Can. J. Ch. E.*, Vol. 59, pp. 760–765.

McMordie, R. K., and Emery, A. F., 1967, "A Numerical Solution for Laminar-Flow Heat Transfer in Circular Tubes With Axial Conduction and Developing Thermal and Velocity Fields," ASME JOURNAL OF HEAT TRANSFER, Vol. 89, pp. 11–16.

Nagasue, H., 1981, "Steady-State Heat Transfer With Axial Conduction in Laminar Flow in a Circular Tube With a Specified Temperature or Heat Flux Wall," *Int. J. Heat Mass Transfer*, Vol. 24, pp. 1823–1832.

Papoutsakis, E., Ramkrishna, D., and Lim, H. C., 1980, "The Extended Graetz Problem With Prescribed Wall Flux," *AIChE Journal*, Vol. 26, pp. 779–787.

Pearson, S. W., and Wolf, H., 1970, "A Numerical Evaluation of the Effects of Axial Conduction and Arbitrary Axial Flux Distributions Upon Heat Transfer at Low Peclet Numbers," *Proc. Sixth Southeastern Seminar on Thermal Sciences*, J. K. Ferrell, M. N. Ozisik, and J. E. Sunderland, eds., pp. 135–156.

Schneider, P. J., 1957, "Effect of Axial Fluid Conduction on Heat Transfer in the Entrance Regions of Parallel Plats and Tubes," *Trans. ASME*, Vol. 79, pp. 765–773.

Smith, C. E., Faghri, M., and Welty, J. R., 1975, "On the Determination of Temperature Distribution in Laminar Pipe Flow With a Step Change in Wall Heat Flux," ASME JOURNAL OF HEAT TRANSFER, Vol. 97, pp. 137–139.

Sparrow, E. M., and Siegel, R., 1958, "Laminar Tube Flow With Arbitrary Internal Heat Sources and Wall Heat Transfer," *Nucl. Sci. Eng.*, Vol. 4, pp. 239–254.

Verhoff, F. H., and Fisher, D. P., 1973, "A Numerical Solution of the Graetz Problem With Axial Conduction Included," ASME JOURNAL OF HEAT TRANSFER, Vol. 95, pp. 132–134.

Convective Heat Transfer in a Circular Annulus With Variable Heat Generation

M. A. Ebadian,[1] H. C. Topakoglu,[2] and O. A. Arnas[3]

Introduction

Earlier studies by Arnas et al. (1979, 1985a), Arnas and Ebadian (1985b), and Ebadian et al. (1984, 1985) have shown that the nonuniform heat generation distribution considerably modifies convective heat transfer properties of fluid flows. The results presented here are for convective heat transfer in a circular annulus with a variable internal heat generation increasing linearly along the radial direction from a value of zero at the inner periphery to a maximum value at the outer periphery. Along the length of the pipe, flow is assumed hydrodynamically and thermally fully developed and the inner and outer surfaces are maintained under uniform but different heat flux conditions.

To improve the safety and to minimize the possibility of an accidental meltdown, future core clusters may be designed in an annular form. This configuration allows the inlet water to enter the reactor vessel in a downward direction along both inside and outside surfaces and leave the reactor in a vertically upward direction through the annular-shaped core. In such

[1]Mechanical Engineering Department, Florida International University, Miami, FL 33199.

[2]Mechanical Engineering Department, Southern University, Baton Rouge, LA 70813.

[3]Mechanical Engineering Department, California State University—Sacramento, Sacramento, CA 95819; Fellow ASME.

Contributed by the Heat Transfer Division for publication in the JOURNAL OF HEAT TRANSFER. Manuscript received by the Heat Transfer Division October 15, 1985. Keywords: Forced Convection, Numerical Methods.

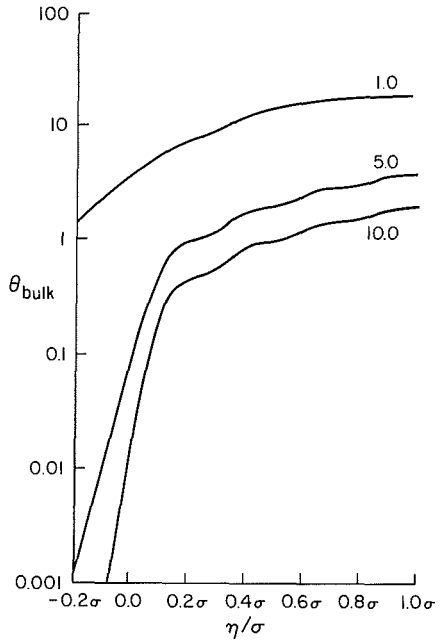

Fig. 5 Bulk temperature for various Pe with $q=0$, $\eta<0$; $q=q_{max}\sin^2(4\pi\eta/\sigma)$, $0<\eta<\sigma$; $q=0$, $\sigma<\eta$; $\sigma Pe=10$

can handle many physical situations and to show the importance of axial conduction in certain problems.

Radial temperature profiles and Nusslet numbers were computed for a unit step in heat flux at $\eta=0$ with $Pe=5$ and 10, and $\sigma Pe=10$. The results agree with those of Hsu (1971) to within 1 percent. Results for $Pe=5$ are virtually identical to those of Papoutsakis et al. (1980).

The first axially varying wall heat flux considered is $\sin(\pi\eta/\sigma)$, chosen because of its application to nuclear reactors (Burchill et al., 1968). Figure 1 shows radial temperature profiles near the end of the heated section for $Pe=1$ and $\sigma=10$. We note the rapid approach to a flat radial temperature profile at the exit as η approaches σ.

The second axially varying case is a hyperbolic tangent flux distribution, which is a better approximation to the wall flux distribution for "conjugated" heat transfer problems including wall conduction than are the discontinuous flux distributions used in previous analyses (see, e.g., Faghri and Sparrow, 1980). Figure 2 shows the bulk temperatures for Peclet numbers 1, 5, and 20 for a hyperbolic tangent distribution that slowly changes from 0 to $(1+\tanh 1)/2$. If the fully developed solution is integrated to determine the fully developed bulk temperature, we find $\theta_{bulk}=2(\eta-\sigma)+7/32+4/Pe^2$; thus, we expect to see the large difference between bulk temperatures for $Pe=1$ and $Pe=5$ shown in Fig. 2. [We note here that unlike the case with no axial conduction, $\theta_{bulk}(\eta)$ cannot be obtained by direct integration (in ξ and then η) of equation (2*a*).]

The final case considered is $\sin^2(4\pi\eta/\sigma)$. Figures 3 and 4 show radial temperature profiles for Peclet numbers 5 and 50, indicating the importance of the axial conduction term near $\eta=\sigma/4$. Note that the case $Pe=50$ roughly corresponds to no axial conduction. Figure 5 shows a plot of the bulk temperature for the $\sin^2(4\pi\eta/\sigma)$ distribution for Peclet numbers 1, 5, and 10. We note that the oscillations become less pronounced at smaller Pe due to the effect of axial conduction.

References

Burchill, W. E., Jones, B. G., and Stein, R. P., 1968, "Influence of Axial Heat Diffusion in Liquid Metal-Cooled Ducts With Specified Heat Flux," ASME JOURNAL OF HEAT TRANSFER, Vol. 90, pp. 283–290.

Dempsey, B. P., 1986, "Low Peclet Number Heat Transfer in a Laminar Tube Flow Subjected to Axially Varying Wall Heat Flux," M.S. Thesis, University of Arizona, Tucson, AZ.

Faghri, M., and Sparrow, E. M., 1980, "Simultaneous Wall and Fluid Axial Conduction in Laminar Pipe-Flow Heat Transfer," ASME JOURNAL OF HEAT TRANSFER, Vol. 102, pp. 58–63.

Hsu, C.-J., 1971, "An Exact Analysis of Low Peclet Number Thermal Entry Region Heat Transfer in Transversely Nonuniform Velocity Fields," *AIChE Journal*, Vol. 17, pp. 732–740.

Lee, S. L., and Hwang, G. J., 1981, "Finite Element Solution of Low Peclet Number Fluid Flow in a Round Pipe With the Cauchy Boundary Condition," *Can. J. Ch. E.*, Vol. 59, pp. 760–765.

McMordie, R. K., and Emery, A. F., 1967, "A Numerical Solution for Laminar-Flow Heat Transfer in Circular Tubes With Axial Conduction and Developing Thermal and Velocity Fields," ASME JOURNAL OF HEAT TRANSFER, Vol. 89, pp. 11–16.

Nagasue, H., 1981, "Steady-State Heat Transfer With Axial Conduction in Laminar Flow in a Circular Tube With a Specified Temperature or Heat Flux Wall," *Int. J. Heat Mass Transfer*, Vol. 24, pp. 1823–1832.

Papoutsakis, E., Ramkrishna, D., and Lim, H. C., 1980, "The Extended Graetz Problem With Prescribed Wall Flux," *AIChE Journal*, Vol. 26, pp. 779–787.

Pearson, S. W., and Wolf, H., 1970, "A Numerical Evaluation of the Effects of Axial Conduction and Arbitrary Axial Flux Distributions Upon Heat Transfer at Low Peclet Numbers," *Proc. Sixth Southeastern Seminar on Thermal Sciences*, J. K. Ferrell, M. N. Ozisik, and J. E. Sunderland, eds., pp. 135–156.

Schneider, P. J., 1957, "Effect of Axial Fluid Conduction on Heat Transfer in the Entrance Regions of Parallel Plats and Tubes," *Trans. ASME*, Vol. 79, pp. 765–773.

Smith, C. E., Faghri, M., and Welty, J. R., 1975, "On the Determination of Temperature Distribution in Laminar Pipe Flow With a Step Change in Wall Heat Flux," ASME JOURNAL OF HEAT TRANSFER, Vol. 97, pp. 137–139.

Sparrow, E. M., and Siegel, R., 1958, "Laminar Tube Flow With Arbitrary Internal Heat Sources and Wall Heat Transfer," *Nucl. Sci. Eng.*, Vol. 4, pp. 239–254.

Verhoff, F. H., and Fisher, D. P., 1973, "A Numerical Solution of the Graetz Problem With Axial Conduction Included," ASME JOURNAL OF HEAT TRANSFER, Vol. 95, pp. 132–134.

Convective Heat Transfer in a Circular Annulus With Variable Heat Generation

M. A. Ebadian,[1] H. C. Topakoglu,[2] and O. A. Arnas[3]

Introduction

Earlier studies by Arnas et al. (1979, 1985a), Arnas and Ebadian (1985b), and Ebadian et al. (1984, 1985) have shown that the nonuniform heat generation distribution considerably modifies convective heat transfer properties of fluid flows. The results presented here are for convective heat transfer in a circular annulus with a variable internal heat generation increasing linearly along the radial direction from a value of zero at the inner periphery to a maximum value at the outer periphery. Along the length of the pipe, flow is assumed hydrodynamically and thermally fully developed and the inner and outer surfaces are maintained under uniform but different heat flux conditions.

To improve the safety and to minimize the possibility of an accidental meltdown, future core clusters may be designed in an annular form. This configuration allows the inlet water to enter the reactor vessel in a downward direction along both inside and outside surfaces and leave the reactor in a vertically upward direction through the annular-shaped core. In such

[1]Mechanical Engineering Department, Florida International University, Miami, FL 33199.

[2]Mechanical Engineering Department, Southern University, Baton Rouge, LA 70813.

[3]Mechanical Engineering Department, California State University—Sacramento, Sacramento, CA 95819; Fellow ASME.

Contributed by the Heat Transfer Division for publication in the JOURNAL OF HEAT TRANSFER. Manuscript received by the Heat Transfer Division October 15, 1985. Keywords: Forced Convection, Numerical Methods.

designs and in the inner entrance flow region, the internal heat generation induced by the attenuation of gamma rays gains importance.

Temperature Distribution and Heat Fluxes Through the Walls

Including an arbitrary heat generation and neglecting viscous dissipation, the energy equation to be satisfied for the temperature distribution in a flow between two concentric boundaries is (Topakoglu and Arnas, 1974)

$$\mathbf{V}\ \text{grad}\ T=\alpha(\nabla^2 T+H/k) \tag{1}$$

where $\mathbf{V}$ is the velocity vector, α is the thermal diffusivity, H is the heat generation, and k is the thermal conductivity. The dimensionless excess temperature e satisfies

$$d^2e/dt^2=r^2(G\ w_0-h) \tag{2}$$

where $t = \ln r$ with r as the dimensionless radial coordinate, $G = c$ Pe with c as the uniform temperature gradient and Pe the Peclet number, w_0 the velocity, and h the dimensionless heat generation. Expressing the dimensionless velocity in an annular pipe of outer periphery of radius L and inner periphery radius ωL as $w = \text{Re}\ w_0$, where Re is a reference Reynolds number defined by Arnas and Ebadian (1985b), the solution from Topakoglu and Arnas (1974) is

$$w_0=1-r^2+\mu\ \ln r \tag{3}$$

where $\mu = -(1-\omega^2)/\ln\omega$. Due to the linear form of equation (2), the excess temperature can be separated into three parts as

$$e=e_{in}g+G\ e_0+e_h \tag{4}$$

where e_{in} is the dimensionless excess temperature on the inner wall and the functions $g(r)$, $e_o(r)$ and $e_h(r)$ are subject to boundary conditions

$$g=0,\quad e_o=0,\quad e_h=0 \qquad \text{at } t=0$$

$$g=1,\quad e_o=0,\quad e_h=0 \qquad \text{at } t=\ln\omega$$

The functions involved in the first two terms of equation (4) are independent of heat generation distribution. The equation to be satisfied by the part of e that is dependent on heat generation is

$$d/dr(r\ de_h/dr)=-r\ h \tag{5}$$

The solution for e_h under the boundary conditions stated above is

$$e_h=K_1+K_2\ \ln r-\int[(1/r)\int r\ h\ dr]dr \tag{6}$$

since h is linear and where K_1 and K_2 must be determined from the conditions $e_h=0$ for $r=1$ and $r=\omega$. Letting $e_h=h_o\ e_{ho}$, where h_o is the maximum dimensionless value of the variable heat generation density at the outer periphery, the solutions for $g(r)$, $e_o(r)$ and $e_{ho}(r)$ are obtained as

$$g = \ln r/\ln\omega \tag{7}$$

$$e_o = e_{01}+e_{02}+e_{03}+e_{04}+e_{05} \tag{8}$$

$$e_{01} = -(1-r^2+\mu\ \ln r)/4 \tag{9}$$

$$e_{02} = 0^{(4)} \tag{10}$$

$$e_{03} = \mu\ r^2\ \ln r(1-\omega^2/r^2)/4 \tag{11}$$

$$e_{04} = [1-r^4+\mu(1+\omega^2)\ln r]/16 \tag{12}$$

$$e_{05} = \mu(1-r^2+\mu\ \ln r)/4 \tag{13}$$

$$e_{ho} = [a-b\ \ln r-r^2(4r-9\omega)/(1-\omega)]/36 \tag{14}$$

[4]This term vanishes for circular peripheries. However, it is included here in order to maintain the same notations used in Topakoglu and Arnas (1974).

where

$$a=(4-9\omega)/(1-\omega)\ \text{and}\ b=(4-5\omega-5\omega^2)/\ln\omega \tag{15}$$

It is useful to define an alternate dimensionless inner wall temperature $\beta = e_{in}/G$ and a dimensionless heat generation number $\gamma = h_o/G = (H_oL)/(C\,k\,\text{Pe})$. It must be noted that the parameter β is a factor that controls the ratio of the heat fluxes from the inner, U_i, and outer periphery, U_o (Topakoglu and Arnas, 1974). Two special values of β are physically significant:

(*i*) The case of insulated outer wall ($U_o = 0$) for which

$$\beta=\beta_i=-[e_o'(1)+\gamma e_{ho}'(1)]\ln\omega \tag{16}$$

(*ii*) The case of insulated inner wall ($U_i = 0$) for which

$$\beta=\beta_o=-[e_o'(\omega)+ge_{ho}'(\omega)]\omega\ \ln\omega \tag{17}$$

The difference of these two special β values is

$$\beta_o-\beta_i=[I_{00}-\gamma(1-\omega)(2+\omega)/6]\ \ln\omega \tag{18}$$

with $I_{00} = (1-\omega^2)(1+\omega^2-\mu)/4$. Another physically significant parameter is the ratio of the heat gain rates from the outer wall to the total heat gain from both walls

$$\lambda=U_o/(U_o+U_i)=(\beta-\beta_i)/(\beta_o-\beta_i) \tag{19}$$

A third physically significant special case is that of equal wall temperatures, $T_o = T_i$, for which $\beta = 0$. The value of λ corresponding to this case is

$$\lambda_o=[e_o'(1)+\gamma e_{ho}'(1)]/[I_{00}-\gamma(1-\omega)(2+\omega)/6] \tag{20}$$

where

$$e_o'(1) = (1-\mu+\mu^2)/4-3\mu(1+\omega^2)/16 \tag{21}$$

$$e_{ho}'(1) = -b/36-(2-3\omega)/[6(1-\omega)] \tag{22}$$

Introducing a ratio $\bar{\mu} = \lambda/\lambda_o$, β changes to give

$$\beta=-(1-\bar{\mu})[e_o'(1)+\gamma e_{ho}'(1)]\ \ln\omega \tag{23}$$

which permits us to write the heat fluxes through the walls as

$$U_o=2\pi\ \text{LFG}\ \bar{\mu}[e_o'(1)+\gamma e_{ho}'(1)] \tag{24}$$

$$U_i=2\pi\ \text{LFG}\{I_{00}-\bar{\mu}\ e_o'(1)-\gamma[(1-\omega)(2+\omega)/6+\bar{\mu}\ e_{ho}'(1)]\} \tag{25}$$

The cases of equidirectional heat fluxes can be identified by the following values of $\bar{\mu}$:

(*i*) $\bar{\mu}>\bar{\mu}_o$: $\quad -1<U_i/U_o<0$ for which $\lambda>1$ (26)

(*ii*) $\bar{\mu}=-n^2\bar{\mu}_o$: $\quad U_i/U_o<-1$ for which $\lambda<0$ (27)

where n^2 represents a positive number.

Convective Heat Transfer Coefficients

The mixed mean excess temperature, E_m, must be calculated, in dimensional form, as

$$E_m=(T_m-T_o)=\rho/Q\int_S W\ E\ dS \tag{28}$$

where T_m is the mixed mean temperature, ρ is the fluid density, Q is the flow rate, and S and dS are full and elemental cross-sectional areas, respectively.

The convective heat transfer coefficients, $\tilde{h}_o$ and $\tilde{h}_i$, at the outer and inner walls, respectively, are defined in conventional manner by the equations $U_o = -E_m\ P_o\ \tilde{h}_o$, and $(U_i=-(E_i-E_{in})\ P_i\ \tilde{h}_i$.) The Nusselt numbers, at the outer and inner walls based on the hydraulic diameter D and the circumference P of the annulus, are given by

$$\text{Nu}_o=-(D/P_o)(U_o/k\ E_m)\ \text{and}$$

$$\text{Nu}_i=-(D/P_i)\{U_i/[k(E_m-E_{in})]\} \tag{29}$$

where $D = 2(1-\omega)L$, $P_o = 2\pi L$, $P_i = 2\pi\omega L$. These expressions may be reduced to

$$\mathrm{Nu}_o = 2\bar{\mu}(1-\omega)I_{00}[e_o'(1)+\gamma e_{ho}'(1)]/\mathrm{DENO} \tag{30}$$

$$\mathrm{Nu}_i = 2(1-\omega)I_{00}\{I_{00}-\bar{\mu}e_o'(1)-\gamma[(1-\omega)(2+\omega)/6 + \bar{\mu}e_{ho}'(1)]\}/(\omega\,\mathrm{DENI}) \tag{31}$$

where

$$\mathrm{DENO} = (1-\bar{\mu})[e_o'(1)+\gamma e_{ho}'(1)]I_{01} + J_o + \gamma J_h \tag{32}$$

$$\mathrm{DENI} = \mathrm{DENO} - (1-\bar{\mu})[e_o'(1)+\gamma e_{ho}'(1)]I_{00}\ln\omega \tag{33}$$

$$I_{01} = -3(1-\omega^4)/16 - \omega^2(1-\omega^2)/4 + \mu(1-\omega^2)/4 - \omega^4(\ln\omega)/4 \tag{34}$$

$$J_o = [11(1-\omega^8)/8 - 19\mu(1-\omega^6)/6 - 27\mu(1+\omega^2)/16 + 51\mu^2(1-\omega^4)/8 - 3\mu^3(1-\omega^2)]/48 \tag{35}$$

$$\begin{aligned} J_h = -\{&a(1-\omega^2)^2/4 + [b\omega^2(2-\omega^2/)/4]\ln\omega \\ &+ b(1-\omega^2)(3-\omega^2)/16 \\ &- 4(1-\omega^5)/[5(1-\omega)] + 4(1-\omega^7)/[7(1-\omega)] \\ &+ 9\omega(1-\omega^4)/[4(1-\omega)] - 3\omega(1-\omega^6)/[2(1-\omega)] \\ &+ \mu[-(a\omega^2\ln\omega)/2 - a(1-\omega^2)/4 - b\omega^2\ln\omega(1-\ln\omega)/2 \\ &- b(1-\omega^2)/4 + 4\omega^5\ln\omega/\{5(1-\omega)\} \\ &+ 4(1-\omega^5)/\{25(1-\omega)\} - 9\omega^5\ln\omega/\{4(1-\omega)\} \\ &- 9\omega(1-\omega^4)/\{16(1-\omega)\}]\}/36 \end{aligned} \tag{36}$$

Discussion of Results

The Nusselt numbers depend, besides the relative size of inner periphery ω, on two parameters: (*a*) the surface heating condition factor $\bar{\mu}$, and (*b*) the dimensionless heat generation number γ. For numerical calculations, $\gamma = 3.01$ is used, which corresponds to many common applications in engineering (Duderstadt and Hamilton, 1976). The five special surface heating conditions are:

1 Insulated inner wall
$$\bar{\mu} = \bar{\mu}_o = [I_{00} - (1-\omega^2)/3]/[e_o'(1)+\gamma e_{ho}'(1)]$$
2 Equal wall temperatures $\bar{\mu} = 1$
3 Insulated outer wall $\bar{\mu} = 0$
4 A selected case of equidirectional heat fluxes (case *a*)
$$U_i/U_o = -1/2 \quad \lambda = 2 \quad \bar{\mu} = 2\bar{\mu}_o$$
5 A selected case of equidirectional heat fluxes (case *b*)
$$U_i/U_o = -2 \quad \lambda = -1 \quad \bar{\mu} = -\bar{\mu}_o$$

In Fig. 1, the curves show the variation of Nusselt number with the dimensionless inner diameter for each surface heating condition and are compared with the corresponding case of no heat generation, $\gamma = 0$. The Nusselt numbers on the outer periphery for all values of ω and for the first three special heating conditions are higher than those values without heat generation. The physical interpretation of this can be obtained from the inspection of equation (29) where one can see that the Nusselt numbers are essentially ratios between the heat fluxes and the magnitudes of excess bulk temperatures. Therefore, a linear heat generation variation in the radial direction modifies the outer surface heat flux (or the radial temperature at the surface) more than the changes for the magnitude of excess temperature. The amount of increase caused by the heat generation considered here is decreasing gradually if one considers the special cases in the following order: case 02, case 01, case 03, and case 04.

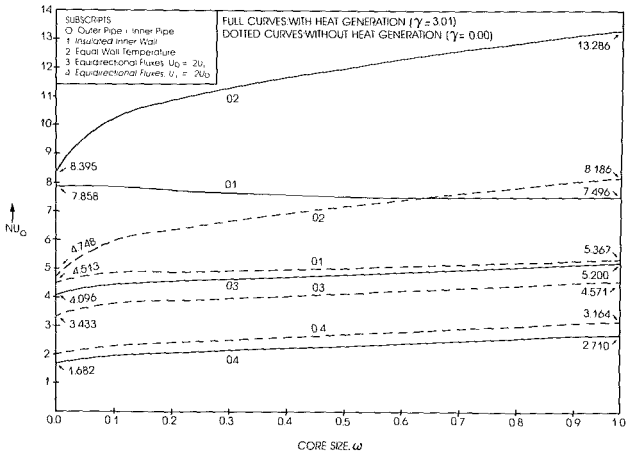

Fig. 1 Comparison of Nu_o with and without heat generation

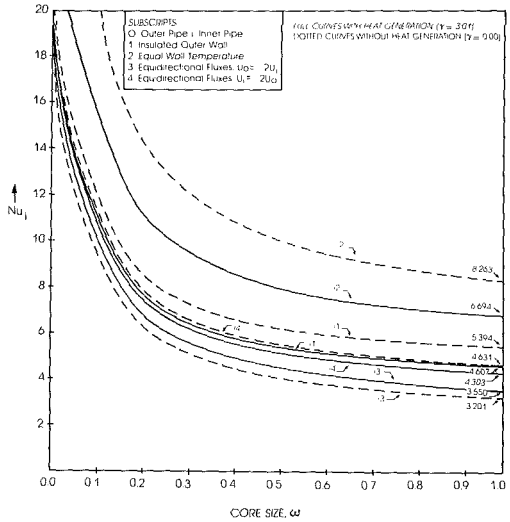

Fig. 2 Comparison of Nu_i with and without heat generation

In Fig. 2, the Nusselt numbers on the inner surface (the solid lines) for radial linear heat generation are compared to the corresponding values (the dotted lines) for no heat generation. It is found that for the first special surface heating condition, the addition of heat generation is reducing the values of the Nusselt number on the inner surface. This property is attributed to the fact that the radial linear heat generation is modifying the temperature distribution near the inner surface less than that area near the outer surface. However, for the special case of *i*4, the property is changing its direction. Therefore, the effect of heat generation considered in this paper on the radial temperature gradient near the inner surface is higher than the effect produced on the magnitude of the excess bulk temperature. The limiting values of both Nusselt numbers at $\omega = 0$ and $\omega = 1$ are also included in Figs. 1 and 2.

Acknowledgments

The results presented in this paper were obtained in the course of research sponsored by the National Science Foundation, Washington, DC, under Grant No. R11-8305297 to Southern University and its precursors. The authors appreciate the contributions made by Mr. Chiang Lee for the numerical calculations.

References

Arnas, O. A., Atam, M. K., and Topakoglu, H. C., 1979, "Heat Transfer for Laminar, Uniform Heat Generating Fluid Flow in a Curved Pipe," ASME Paper No. 79-HT-93.

Arnas, O. A., Ebadian, M. A., and Topakoglu, H. C., 1985a, "Convective Heat Transfer in Annular Tubes Carrying Radioactive Slurry," *Heat and Technology*, Vol. 3, No. 2, pp. 47-63.

Arnas, O. A., and Ebadian, M. A., 1985b, "Convective Heat Transfer in a Circular Annulus With Heat Generation," ASME JOURNAL OF HEAT TRANSFER, Vol.107, pp. 334-338.

Duderstadt, J. J., and Hamilton, L. J., 1976, *Nuclear Reactor Analysis*, Wiley, New York.

Ebadian, M. A., Topakoglu, H. C., and Arnas, O. A., 1984, "Convective Heat Transfer in Inlet Flow of a Reactor Vessel," *Southeastern Conference of Theoretical and Applied Mechanics—SECTAM XII*, Vol. I, pp. 391-396.

Ebadian, M. A., Topakoglu, H. C., and Arnas, O. A., 1985, "Convective Heat Transfer in Circular Annulus With Variable Heat Generation," *Proceedings, Tenth Canadian Congress of Applied Mechanics*, Vol. 2, pp. C9-C10.

Topakoglu, H. C., and Arnas, O. A., 1974, "Convective Heat Transfer for Steady Laminar Flow Between Two Confocal Elliptic Pipes With Longitudinal Uniform Wall Temperature Gradient," *International Journal of Heat and Mass Transfer*, Vol. 17, pp. 1487-1498.

Heat Transfer Correlation for Flow in a Parallel-Plate Channel With Staggered Fins

A. Lazaridis[1]

Introduction

In a recent paper, Kelkar and Patankar (1987) presented a mathematical analysis of the laminar flow heat transfer in a parallel-plate channel whose walls were fitted with a series of equidistant staggered fins placed transversely to the flow direction. Figure 1 shows the details of the configuration used in that analysis, which was reported to be motivated by the increasing use of compact heat exchangers in industry. The latter consist of small flow passages through which the fluid frequently flows at low velocities. Under such "laminar" flow conditions, the relatively low heat transfer coefficients observed with smooth channel walls are augmented by means of fins that are attached to the heat transfer surfaces. The arrangement of fins is important if heat transfer at these surfaces is to be increased, and the extent to which this is accomplished depends on several flow, thermal, and geometric parameters.

Assuming steady, laminar, periodically fully developed flow of a fluid with constant properties, Kelkar and Patankar obtained a numerical solution of the governing equations and determined the effects of the pertinent parameters on the flow field and the rate of heat transfer. Although vortex shedding may occur at the fin tips, their assumption of steady laminar flow was justified based on photographs obtained in an experimental investigation by Berner et al. (1984) for a flow with Reynolds number of 600. The results of that study indicated that the entrance region is very short and the flow becomes periodically fully developed quickly.

Kelkar and Patankar presented their results in a combined graphic and tabular form, and discussed the flow behavior and heat transfer characteristics on the basis of how they were affected by each of the pertinent parameters. Specifically, the effect of each parameter on the overall Nusselt number was discussed based on the changes observed as the parameter was varied through a range of numbers while all the other variables were kept constant. Although this is a perfect way to evaluate the relative importance of these parameters on the Nusselt number, graphic results such as these are hardly useful to a designer, who expects to have a correlation between the Nusselt number and all the other parameters in one expression. This note fulfills that need.

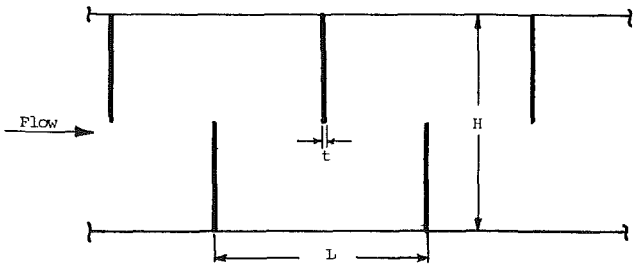

Fig. 1 Finned channel configuration

Table 1 Comparison of values from correlation with Kelkar and Patankar's (1987) data for Pr = 0.7

			Nu/Nu_o		
λ	L/H	Re	Calculated	Kelkar and Patankar (1987)	Percent difference
0	1	500	4.347	4.347	0
0.1	1	500	4.405	4.432	−0.61
1.0	1	500	4.585	4.584	0.02
10.0	1	500	5.405	5.486	−1.48
100.0	1	500	6.168	6.118	0.82
∞	1	500	6.292	6.233	0.95
0	1	400	3.72	3.75	−0.8
0	1	300	3.04	3.1	−1.9
0	1	200	2.29	2.4	−4.6
0	1	100	1.41	1.5	−6
∞	1	400	5.38	5.3	1.5
∞	1	300	4.40	4.4	0
∞	1	200	3.31	3.3	0
∞	1	100	2.04	2.25	−9.3
0	0.5	200	3.14	3.2	−1.7
0	1.5	200	1.62	1.8	−10
0	2.0	200	1.12	1.25	−10
∞	0.5	200	6.02	6.3	−4.4
∞	1.5	200	2.18	2.2	−1
∞	2.0	200	1.47	1.6	−8

Table 2 Comparison of values from correlation with Kelkar and Patankar's (1987) data for Pr = 4

			Nu/Nu_o		
λ	L/H	Re	Calculated	Kelkar and Patankar (1987)	Percent difference
0	1	500	8.729	8.716	0.15
0.1	1	500	8.845	8.782	0.72
1	1	500	9.208	9.208	0
10	1	500	10.851	10.913	−0.51
100	1	500	12.994	12.940	0.42
∞	1	500	13.256	13.441	1.38
0	1	100	2.83	2.9	2.4
0	1	200	4.60	4.7	2.1
0	1	300	6.10	6.2	1.6
0	1	400	7.47	7.5	0.4
∞	1	100	4.30	3.9	10.2
∞	1	200	6.98	6.8	2.6
∞	1	300	9.27	9.4	−1.4
∞	1	400	11.34	11.7	−3.1
0	0.5	200	6.32	6.3	0
0	1.5	200	3.25	3.4	−4.4
0	2.0	200	2.25	2.3	−2
0	2.5	200	1.54	1.6	−3.8
∞	0.5	200	12.69	13.0	−2.4
∞	1.5	200	4.59	4.5	1.9
∞	2.0	200	3.10	3.0	3.4
∞	2.5	200	2.10	1.9	10.3

[1]Assistant Professor, Department of Mechanical Engineering, Widener University, Chester, PA 19013.

Contributed by the Heat Transfer Division for publication in the JOURNAL OF HEAT TRANSFER. Manuscript received by the Heat Transfer Division August 4, 1987. Keywords: Augmentation and Enhancement, Finned Surfaces, Forced Convection.

References

Arnas, O. A., Atam, M. K., and Topakoglu, H. C., 1979, "Heat Transfer for Laminar, Uniform Heat Generating Fluid Flow in a Curved Pipe," ASME Paper No. 79-HT-93.

Arnas, O. A., Ebadian, M. A., and Topakoglu, H. C., 1985a, "Convective Heat Transfer in Annular Tubes Carrying Radioactive Slurry," *Heat and Technology*, Vol. 3, No. 2, pp. 47-63.

Arnas, O. A., and Ebadian, M. A., 1985b, "Convective Heat Transfer in a Circular Annulus With Heat Generation," ASME JOURNAL OF HEAT TRANSFER, Vol.107, pp. 334-338.

Duderstadt, J. J., and Hamilton, L. J., 1976, *Nuclear Reactor Analysis*, Wiley, New York.

Ebadian, M. A., Topakoglu, H. C., and Arnas, O. A., 1984, "Convective Heat Transfer in Inlet Flow of a Reactor Vessel," *Southeastern Conference of Theoretical and Applied Mechanics—SECTAM XII*, Vol. I, pp. 391-396.

Ebadian, M. A., Topakoglu, H. C., and Arnas, O. A., 1985, "Convective Heat Transfer in Circular Annulus With Variable Heat Generation," *Proceedings, Tenth Canadian Congress of Applied Mechanics*, Vol. 2, pp. C9-C10.

Topakoglu, H. C., and Arnas, O. A., 1974, "Convective Heat Transfer for Steady Laminar Flow Between Two Confocal Elliptic Pipes With Longitudinal Uniform Wall Temperature Gradient," *International Journal of Heat and Mass Transfer*, Vol. 17, pp. 1487-1498.

Heat Transfer Correlation for Flow in a Parallel-Plate Channel With Staggered Fins

A. Lazaridis[1]

Introduction

In a recent paper, Kelkar and Patankar (1987) presented a mathematical analysis of the laminar flow heat transfer in a parallel-plate channel whose walls were fitted with a series of equidistant staggered fins placed transversely to the flow direction. Figure 1 shows the details of the configuration used in that analysis, which was reported to be motivated by the increasing use of compact heat exchangers in industry. The latter consist of small flow passages through which the fluid frequently flows at low velocities. Under such "laminar" flow conditions, the relatively low heat transfer coefficients observed with smooth channel walls are augmented by means of fins that are attached to the heat transfer surfaces. The arrangement of fins is important if heat transfer at these surfaces is to be increased, and the extent to which this is accomplished depends on several flow, thermal, and geometric parameters.

Assuming steady, laminar, periodically fully developed flow of a fluid with constant properties, Kelkar and Patankar obtained a numerical solution of the governing equations and determined the effects of the pertinent parameters on the flow field and the rate of heat transfer. Although vortex shedding may occur at the fin tips, their assumption of steady laminar flow was justified based on photographs obtained in an experimental investigation by Berner et al. (1984) for a flow with Reynolds number of 600. The results of that study indicated that the entrance region is very short and the flow becomes periodically fully developed quickly.

Kelkar and Patankar presented their results in a combined graphic and tabular form, and discussed the flow behavior and heat transfer characteristics on the basis of how they were affected by each of the pertinent parameters. Specifically, the effect of each parameter on the overall Nusselt number was discussed based on the changes observed as the parameter was varied through a range of numbers while all the other variables were kept constant. Although this is a perfect way to evaluate the relative importance of these parameters on the Nusselt number, graphic results such as these are hardly useful to a designer, who expects to have a correlation between the Nusselt number and all the other parameters in one expression. This note fulfills that need.

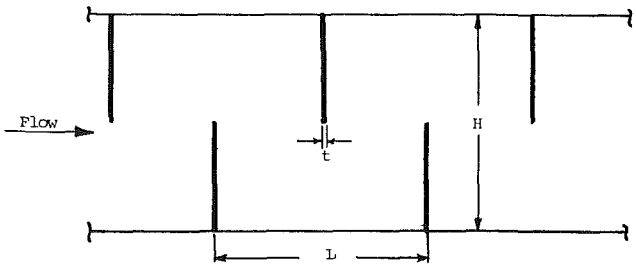

Fig. 1 Finned channel configuration

Table 1 Comparison of values from correlation with Kelkar and Patankar's (1987) data for Pr = 0.7

			Nu/Nu_o		
λ	L/H	Re	Calculated	Kelkar and Patankar (1987)	Percent difference
0	1	500	4.347	4.347	0
0.1	1	500	4.405	4.432	−0.61
1.0	1	500	4.585	4.584	0.02
10.0	1	500	5.405	5.486	−1.48
100.0	1	500	6.168	6.118	0.82
∞	1	500	6.292	6.233	0.95
0	1	400	3.72	3.75	−0.8
0	1	300	3.04	3.1	−1.9
0	1	200	2.29	2.4	−4.6
0	1	100	1.41	1.5	−6
∞	1	400	5.38	5.3	1.5
∞	1	300	4.40	4.4	0
∞	1	200	3.31	3.3	0
∞	1	100	2.04	2.25	−9.3
0	0.5	200	3.14	3.2	−1.7
0	1.5	200	1.62	1.8	−10
0	2.0	200	1.12	1.25	−10
∞	0.5	200	6.02	6.3	−4.4
∞	1.5	200	2.18	2.2	−1
∞	2.0	200	1.47	1.6	−8

Table 2 Comparison of values from correlation with Kelkar and Patankar's (1987) data for Pr = 4

			Nu/Nu_o		
λ	L/H	Re	Calculated	Kelkar and Patankar (1987)	Percent difference
0	1	500	8.729	8.716	0.15
0.1	1	500	8.845	8.782	0.72
1	1	500	9.208	9.208	0
10	1	500	10.851	10.913	−0.51
100	1	500	12.994	12.940	0.42
∞	1	500	13.256	13.441	1.38
0	1	100	2.83	2.9	2.4
0	1	200	4.60	4.7	2.1
0	1	300	6.10	6.2	1.6
0	1	400	7.47	7.5	0.4
∞	1	100	4.30	3.9	10.2
∞	1	200	6.98	6.8	2.6
∞	1	300	9.27	9.4	−1.4
∞	1	400	11.34	11.7	−3.1
0	0.5	200	6.32	6.3	0
0	1.5	200	3.25	3.4	−4.4
0	2.0	200	2.25	2.3	−2
0	2.5	200	1.54	1.6	−3.8
∞	0.5	200	12.69	13.0	−2.4
∞	1.5	200	4.59	4.5	1.9
∞	2.0	200	3.10	3.0	3.4
∞	2.5	200	2.10	1.9	10.3

[1]Assistant Professor, Department of Mechanical Engineering, Widener University, Chester, PA 19013.

Contributed by the Heat Transfer Division for publication in the JOURNAL OF HEAT TRANSFER. Manuscript received by the Heat Transfer Division August 4, 1987. Keywords: Augmentation and Enhancement, Finned Surfaces, Forced Convection.

Results

The overall Nusselt number is a function of the Reynolds number, the Prandtl number, the ratios of the fin height and distance between consecutive fins to the channel width, and the fin conductance parameter as discussed by Kelkar and Patankar (1987). Their data lead to the correlation

$$\mathrm{Nu}/\mathrm{Nu}_o = 0.36 f(\lambda, \mathrm{Pr}) g(\lambda, L/H) \mathrm{Re}^{0.7} \mathrm{Pr}^{0.4} \quad (1)$$

where

$$g(\lambda, L/H) = \{(2 + L/H) + [1 - \exp(-\lambda)] [\exp(-L/H)]/(L/H)\} \exp(1 - L/H) \quad (2)$$

$$f(\lambda, \mathrm{Pr}) = 0.05990(1 + 0.0210\lambda - 0.0421\lambda^2) \text{ for } 0 \le \lambda \le 1 \quad (3)$$

$$f(\lambda, \mathrm{Pr}) = 0.05745(1 + 0.0212\lambda - 0.00058\lambda^2) \text{ for } 1 < \lambda \le 10 \quad (4)$$

$$f(\lambda, \mathrm{Pr}) = 0.078 \mathrm{Pr}^{0.0275} \{1 - 2[\exp(-0.0001\lambda)]/\lambda\} + \lambda^2 \exp(-\lambda) \text{ for } \lambda > 10 \quad (5)$$

and $\mathrm{Nu} = hD/k$ is the overall Nusselt number, Nu_o is the Nusselt number of the unfinned channel, $\mathrm{Re} = \rho u D/\mu$ is the Reynolds number, $\mathrm{Pr} = \mu c_p/k$ is the Prandtl number, $D = 2H$ is the hydraulic diameter, H is the width of the channel, L is the distance between consecutive fins, h is the average heat transfer coefficient, u is the average velocity of the fluid, ρ is the fluid density, μ is the fluid viscosity, c_p is the fluid specific heat at constant pressure, $\lambda = k_f t/kL$ is the fin conductance parameter, k_f is the fin conductivity, k is the fluid conductivity, and t is the fin thickness.

The correlation given above has some inherent limitations that need to be discussed. Equation (1) is valid for a fin height of exactly ½ the width of the channel in the range of Reynolds numbers up to 500 and may be extended to Reynolds number of 600 based on the experimental evidence given by Berner et al. (1984). The value of ½ chosen for the ratio of fin height to channel width does not pose an unnecessary restriction on the practical use of the correlation because augmentation of heat transfer is either too small or nonexistent when this ratio falls below that value, while frictional losses become excessive when it is exceeded (see Fig. 7 of Kelkar and Patankar, 1987). Of the three expressions for $f(\lambda, \mathrm{Pr})$ only equation (4) was developed from an interpolation of $\mathrm{Nu}/\mathrm{Nu}_o$ values obtained at the limits of the indicated range of λ values since data in the middle of that range were not given. Equations (1)–(5) were generated from data with Prandtl numbers of 0.7 and 4, and they are strictly valid only for these two values of the Prandtl number. It appears, however, that their validity may be extended to the range between these two limits, especially for λ values less than 10. Tables 1 and 2 list values of $\mathrm{Nu}/\mathrm{Nu}_o$ calculated from equation (1) for Prandtl numbers of 0.7 and 4, respectively, and present a comparison with the data of Kelkar and Patankar. The accuracy of the correlation is ±10 percent with respect to the available data. Although this level of accuracy is well within the uncertainty limits of practical design criteria, as a matter of caution, it is noted that more data are needed to establish the full range of validity for this correlation.

References

Berner, C., Durst, F., and McEligot, D. M., 1984, "Flow Around Baffles," ASME Journal of Heat Transfer, Vol. 106, pp. 743–749.

Kelkar, K. M., and Patankar, S. V., 1987, "Numerical Prediction of Flow and Heat Transfer in a Parallel Plate Channel With Staggered Fins," ASME Journal of Heat Transfer, Vol. 109, pp. 25–30.

Predicting Temperatures of Stacked Heat Sinks With a Shroud

T. W. Petrie,[1] A. A. Bajabir,[2] D. J. Petrie,[3] and J. W. Kroll[4]

Introduction

Air cooling of enclosed electrical and electronic equipment is a common application for natural convection heat sinks. Space restrictions lead to stacking of the sinks into vertical arrays. A need for mechanical and electrical isolation leads to placement of a shroud over the array. The result is a complicated heat transfer situation.

The primary heat transfer mechanism is the natural convection between the fins of the sinks and the cooling air. Bar-Cohen and Rohsenow (1984) provide composite correlations over the range of conditions encountered in practice, from narrowly spaced fins to isolated plates. Temperature of the fins or heat flux from them can be specified to match known conditions. Net radiation heat transfer from the sinks to the shroud or other objects at different temperatures is a secondary mechanism, which can be handled by graybody exchange if radiation properties are known.

A further complication is the effect on free convection of stacking the heat sinks in a vertical array with open gaps between horizontal rows. Various authors have addressed this effect. For example, Sparrow and Faghri (1980) studied two flat plates. They calculated the effect of varying the gap-to-plate length ratio and changing the size of the upper plate relative to that of the lower plate.

Yet another complication is the effect of convection in the gap between the shroud and the sinks on the sink temperature. Among the relevant studies is one by Karki and Patankar (1984). They vary the ratio of space between fins to fin height and the ratio of the shroud gap to fin height. The geometry analyzed is a single sink covered by a shroud adiabatic to both convection and radiation.

To avoid costly and time-consuming tests of proposed heat sink arrays to dissipate specific heat requirements, a model is sought to generalize test data for typical arrays. The model is to predict sink temperatures, including any influence of stacking and a shroud, of candidate heat sink arrays. The separate studies of the effect of stacking and of the shroud suggest that enhanced convection occurs in certain circumstances. Generally, enhancement requires very short upper sinks located relatively far from the lower sinks or fins very closely spaced relative to the shroud gap. Neither condition seems true for the test data, but calculations are being done using a multidimensional finite element approach, including radiation effects, to see when enhancements may occur.

This paper reports on the first step toward development of analytical design procedures for stacked heat sink arrays with a shroud. It explores the use of a one-dimensional model based on available semi-empirical free convection correlations. These correlations do not yield air temperatures within the sink array. To generate predictions of sink temperatures

[1]Associate Professor, Department of Mechanical Engineering, Marquette University, Milwaukee, WI 53233; Mem. ASME.

[2]Graduate Student, Department of Mechanical Engineering, Marquette University, Milwaukee, WI 53233.

[3]Engineering Supervisor, Electronic Packaging, Electromechanical Research Department, Eaton Corporation, Operations and Technical Center, Milwaukee, WI 53216; Mem. ASME.

[4]Director, Electromechanical Technology, Eaton Corporation, Operations and Technical Center, Milwaukee, WI 53216.

Contributed by the Heat Transfer Division for publication in the Journal of Heat Transfer. Manuscript received by the Heat Transfer Division January 21, 1987. Keywords: Electronic Equipment, Natural Convection, Radiating Interactions.

Results

The overall Nusselt number is a function of the Reynolds number, the Prandtl number, the ratios of the fin height and distance between consecutive fins to the channel width, and the fin conductance parameter as discussed by Kelkar and Patankar (1987). Their data lead to the correlation

$$\mathrm{Nu}/\mathrm{Nu}_o = 0.36 f(\lambda, \mathrm{Pr}) g(\lambda, L/H) \mathrm{Re}^{0.7} \mathrm{Pr}^{0.4} \quad (1)$$

where

$$g(\lambda, L/H) = \{(2 + L/H) + [1 - \exp(-\lambda)] [\exp(-L/H)]/(L/H)\} \exp(1 - L/H) \quad (2)$$

$$f(\lambda, \mathrm{Pr}) = 0.05990(1 + 0.0210\lambda - 0.0421\lambda^2) \text{ for } 0 \le \lambda \le 1 \quad (3)$$

$$f(\lambda, \mathrm{Pr}) = 0.05745(1 + 0.0212\lambda - 0.00058\lambda^2) \text{ for } 1 < \lambda \le 10 \quad (4)$$

$$f(\lambda, \mathrm{Pr}) = 0.078 \mathrm{Pr}^{0.0275} \{1 - 2[\exp(-0.0001\lambda)]/\lambda + \lambda^2 \exp(-\lambda)\} \text{ for } \lambda > 10 \quad (5)$$

and $\mathrm{Nu} = hD/k$ is the overall Nusselt number, Nu_o is the Nusselt number of the unfinned channel, $\mathrm{Re} = \rho u D/\mu$ is the Reynolds number, $\mathrm{Pr} = \mu c_p/k$ is the Prandtl number, $D = 2H$ is the hydraulic diameter, H is the width of the channel, L is the distance between consecutive fins, h is the average heat transfer coefficient, u is the average velocity of the fluid, ρ is the fluid density, μ is the fluid viscosity, c_p is the fluid specific heat at constant pressure, $\lambda = k_f t/kL$ is the fin conductance parameter, k_f is the fin conductivity, k is the fluid conductivity, and t is the fin thickness.

The correlation given above has some inherent limitations that need to be discussed. Equation (1) is valid for a fin height of exactly ½ the width of the channel in the range of Reynolds numbers up to 500 and may be extended to Reynolds number of 600 based on the experimental evidence given by Berner et al. (1984). The value of ½ chosen for the ratio of fin height to channel width does not pose an unnecessary restriction on the practical use of the correlation because augmentation of heat transfer is either too small or nonexistent when this ratio falls below that value, while frictional losses become excessive when it is exceeded (see Fig. 7 of Kelkar and Patankar, 1987). Of the three expressions for $f(\lambda, \mathrm{Pr})$ only equation (4) was developed from an interpolation of $\mathrm{Nu}/\mathrm{Nu}_o$ values obtained at the limits of the indicated range of λ values since data in the middle of that range were not given. Equations (1)–(5) were generated from data with Prandtl numbers of 0.7 and 4, and they are strictly valid only for these two values of the Prandtl number. It appears, however, that their validity may be extended to the range between these two limits, especially for λ values less than 10. Tables 1 and 2 list values of $\mathrm{Nu}/\mathrm{Nu}_o$ calculated from equation (1) for Prandtl numbers of 0.7 and 4, respectively, and present a comparison with the data of Kelkar and Patankar. The accuracy of the correlation is ±10 percent with respect to the available data. Although this level of accuracy is well within the uncertainty limits of practical design criteria, as a matter of caution, it is noted that more data are needed to establish the full range of validity for this correlation.

References

Berner, C., Durst, F., and McEligot, D. M., 1984, "Flow Around Baffles," ASME Journal of Heat Transfer, Vol. 106, pp. 743–749.

Kelkar, K. M., and Patankar, S. V., 1987, "Numerical Prediction of Flow and Heat Transfer in a Parallel Plate Channel With Staggered Fins," ASME Journal of Heat Transfer, Vol. 109, pp. 25–30.

Predicting Temperatures of Stacked Heat Sinks With a Shroud

T. W. Petrie,[1] A. A. Bajabir,[2] D. J. Petrie,[3] and J. W. Kroll[4]

Introduction

Air cooling of enclosed electrical and electronic equipment is a common application for natural convection heat sinks. Space restrictions lead to stacking of the sinks into vertical arrays. A need for mechanical and electrical isolation leads to placement of a shroud over the array. The result is a complicated heat transfer situation.

The primary heat transfer mechanism is the natural convection between the fins of the sinks and the cooling air. Bar-Cohen and Rohsenow (1984) provide composite correlations over the range of conditions encountered in practice, from narrowly spaced fins to isolated plates. Temperature of the fins or heat flux from them can be specified to match known conditions. Net radiation heat transfer from the sinks to the shroud or other objects at different temperatures is a secondary mechanism, which can be handled by graybody exchange if radiation properties are known.

A further complication is the effect on free convection of stacking the heat sinks in a vertical array with open gaps between horizontal rows. Various authors have addressed this effect. For example, Sparrow and Faghri (1980) studied two flat plates. They calculated the effect of varying the gap-to-plate length ratio and changing the size of the upper plate relative to that of the lower plate.

Yet another complication is the effect of convection in the gap between the shroud and the sinks on the sink temperature. Among the relevant studies is one by Karki and Patankar (1984). They vary the ratio of space between fins to fin height and the ratio of the shroud gap to fin height. The geometry analyzed is a single sink covered by a shroud adiabatic to both convection and radiation.

To avoid costly and time-consuming tests of proposed heat sink arrays to dissipate specific heat requirements, a model is sought to generalize test data for typical arrays. The model is to predict sink temperatures, including any influence of stacking and a shroud, of candidate heat sink arrays. The separate studies of the effect of stacking and of the shroud suggest that enhanced convection occurs in certain circumstances. Generally, enhancement requires very short upper sinks located relatively far from the lower sinks or fins very closely spaced relative to the shroud gap. Neither condition seems true for the test data, but calculations are being done using a multidimensional finite element approach, including radiation effects, to see when enhancements may occur.

This paper reports on the first step toward development of analytical design procedures for stacked heat sink arrays with a shroud. It explores the use of a one-dimensional model based on available semi-empirical free convection correlations. These correlations do not yield air temperatures within the sink array. To generate predictions of sink temperatures

[1]Associate Professor, Department of Mechanical Engineering, Marquette University, Milwaukee, WI 53233; Mem. ASME.

[2]Graduate Student, Department of Mechanical Engineering, Marquette University, Milwaukee, WI 53233.

[3]Engineering Supervisor, Electronic Packaging, Electromechanical Research Department, Eaton Corporation, Operations and Technical Center, Milwaukee, WI 53216; Mem. ASME.

[4]Director, Electromechanical Technology, Eaton Corporation, Operations and Technical Center, Milwaukee, WI 53216.

Contributed by the Heat Transfer Division for publication in the Journal of Heat Transfer. Manuscript received by the Heat Transfer Division January 21, 1987. Keywords: Electronic Equipment, Natural Convection, Radiating Interactions.

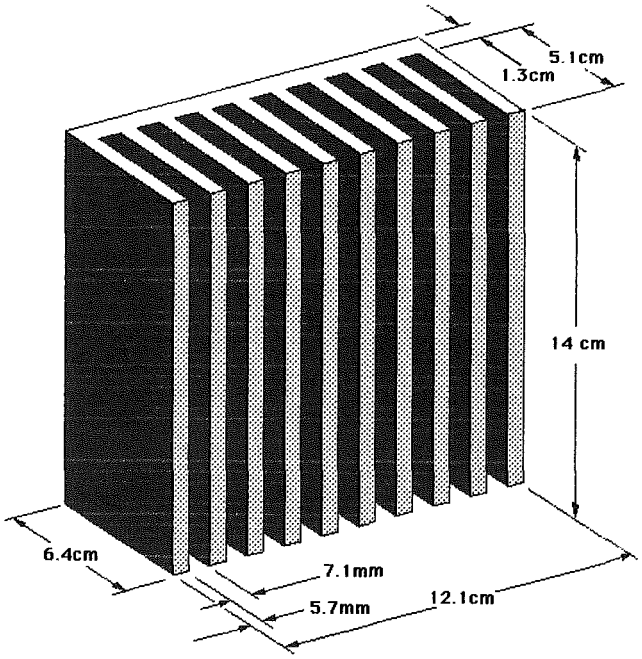

Fig. 1 Geometry of a single sink

Table 1 Steady-state conditions in the constant-power case

Row	q(W)	T_{sink}(°C)	T_{air}(°C)	T_{shroud}(°C)
			25.6±0.8	
			(25.46,24.86,26.83,25.19)	
1	64.8	77.7±0.9		
		(77.44,78.33,78.35,76.58)		
			60.8±4.8	33.2±0.8
			(55.40,58.87,66.48,62.49)	
2	65.1	95.7±1.0		
		(96.39,95.60,96.48,94.27)		
			84.1±2.5	43.6±0.6
			(83.68,81.47,87.40,83.82)	
3	64.8	110.6±1.4		
		(108.54,111.95,111.83,108.04)		
			102.9±1.9	64.3±1.5
			(102.70,103.83,104.66,100.33)	

Table 2 Steady-state conditions in the decreasing-power case

Row	q(W)	T_{sink}(°C)	T_{air}(°C)	T_{shroud}(°C)
			26.4±1.1	
			(28.04,25.82,27.87,25.87)	
1	82.0	89.2±0.9		
		(88.29,88.88,89.86,87.94)		
			66.1±6.0	35.1±0.8
			(58.50,63.48,73.58,67.75)	
2	67.4	101.0±1.1		
		(101.88,100.85,101.78,98.48)		
			89.4±3.6	46.2±0.6
			(80.18,84.25,92.58,90.58)	
3	46.6	102.7±1.5		
		(101.73,104.09,103.78,101.08)		
			97.0±1.8	63.0±1.5
			(98.78,97.98,98.71,94.68)	

independently of internal air temperatures, it is assumed that the free convection throughout the array occurs with respect to the temperature of the air that flows into both the bottom row and the gap between the sinks and the shroud. In addition, the sinks in each row exchange radiation with the sinks in other rows or with the surroundings including the shroud. The shroud does not affect the convection from the sinks directly.

Apparatus and Procedure

The geometry chosen for the tests has been used successfully to cool electrical controls enclosed in cabinets. Cast aluminum heat sinks with all exposed surfaces covered by a 1 mm coating of epoxy are arranged in an array with six sinks horizontally per row and three rows in the vertical direction. Figure 1 shows one sink in the array. Each sink is 12.1 cm wide by 6.4 cm deep by 14 cm high. It consists of ten plates, each 5.7 mm thick on the average by 14 cm high, separated by gaps each 7.1 mm wide on the average. The plates protrude 5.1 cm from a 1.3 cm base. For ease of casting, the gap between fins is slightly narrower at the base than at the tip. Also, the bottom and top edges of each fin are rounded. The base of each sink is drilled and tapped in the center to receive an electrical resistance element that simulates the heat load on the sink due to a stud-mount type semiconductor device. Each sink is attached to a phenolic mounting plate by four screws through the plate into the base of the sink. The backs of the sinks and mounting plate are insulated in the experiments to force heat out through the sink surface.

Each sink is separated from its neighbor in the row by 3.8 cm. There is a gap of 7.6 cm between rows in the vertical direction. The painted steel shroud used for mechanical and electrical isolation is bolted over the fin array and a 4.5 cm gap exists from fin tip to shroud surface. The bottom and top of the shroud contain open grilles to admit and discharge cooling air. The bottom grille is located about 5.1 cm below the bottom row of sinks. The top grille is the same distance above the top row.

The horizontal top and bottom surfaces of the sinks are assumed ineffective for convection. Based on the average fin and gap dimensions shown in Fig. 1, the total area of each sink for convection is 1630 cm^2. The 18 internal fin surfaces forming the 9 gaps make up 78½ percent of this area, the base between fins and the fin tips make up 10½ percent, and the two outside edges make up 11 percent. Actual exposed area totals about 1680 cm^2, including 90 cm^2 of horizontal surface at the top and bottom of each sink and tapered fins with 9.0 mm wide gaps at the fin tips and 5.2 mm wide gaps at the base. The free convection boundary layers in the gaps can grow at most to half the gap width. Including the base, tip and outside edge areas in the convection area implies that the convection mechanism for all these areas is the same as that on the vertical fin surfaces. Only the fin tips, comprising less than 5 percent of the total area, and the outside edges could be characterized as isolated plates relative to the fins.

The temperature of each of the 18 sinks is detected by a single iron-constantan thermocouple imbedded in its base. The most severe temperature gradient in the sinks is estimated to be a 0.5°C drop across the epoxy coating, using handbook data for the thermal conductivity of 39 percent silica-filled epoxy. Air temperatures are sensed by iron-constantan thermocouples grounded to the tip of 1.6-mm-dia stainless-steel probes. The 22 probes (only four were used ahead of the first row of sinks) are inserted in holes drilled in the mounting plate for the sinks at positions in the middle of the gaps between sink rows. Selected measurements with a radiation-shielded thermocouple verified that radiation does not affect the measurement of air temperatures with the small-diameter, low-emittance probes.

Heater voltages are adjusted to settings that cause the desired amount of heat to be generated in each sink by the resistance heating elements. Two relevant cases are selected: a constant power case in which 65 W are dissipated in each sink in each row; and a decreasing power case in which 82 W, 67½ W, and 46½ W are dissipated per sink in the bottom, middle, and top rows, respectively. The constant power case is to correspond to a constant convection flux case. The decreasing power case is to correspond to a constant wall temperature case. Following the setting of voltages, several hours are allowed for steady-state conditions to be achieved. An automated data acquisition system scans the array of thermocouples and records the temperatures they indicate. Steady state is judged to be achieved when the temperatures no longer rise, but begin to fluctuate from recording to recording.

From data after 1¼ h at steady state, averages with stand-

ard deviations for the center four sinks of the six sinks in a row are shown in Tables 1 and 2. Temperatures for the outer two sinks fell off significantly from values for the center four sinks so they were not included in the averages. Data below the averages show the values from left to right across the row. They prove that dominant changes occur vertically rather then horizontally.

Average air temperatures and values from left to right across the row are also shown into and out of each row. They were measured at locations in the middle of the gaps before, after, and between rows, halfway between the base and the tips of the fins. The data acquisition system recorded them. Shroud temperatures after each row were obtained by touching the shroud with the air temperature probes between scans of the data logging system. The shroud is made of light-gage steel, painted gray, and could support a vertical temperature gradient.

In general, the standard deviations of temperatures in Tables 1 and 2 are at most $\pm 1.5°C$. This is judged to be a reasonable experimental uncertainty to assign to temperatures measured by many different thermocouples being scanned automatically. The standard deviations of the air temperatures after each row are larger. This is due to the existence of a slightly hot air channel to the right of center in the array, possibly because of unequal heat dissipation by sinks in row 1 or local flow asymmetries. The sink temperatures do not show a similar anomaly. The experiments were run in a large, closed laboratory space within a conditioned building. A floor-to-ceiling temperature rise of 1°C was measured in the room used for the tests. Therefore, ambient temperature in the space is assumed the same as the air temperature into row 1: $26 \pm 1°C$.

Model

The model is based on available correlations, which require either isothermal or isoflux conditions. Due to the stacking of identical sinks, it is observed that the sink temperatures increase significantly up the stack if equal power is dissipated by each sink. Achieving constant sink temperatures requires much less power to a sink in row 2 or 3 than to one in row 1, such as is approximated in the decreasing-power case. Thus, the use of isothermal correlations seems justified only for the decreasing-power case. However, radiation increases with sink temperature, making convection less for row 2 or 3 than for row 1 of the constant-power case. Hence, use of isothermal correlations may be better for the constant-power case, too.

For a channel of length L formed by two plates a distance b apart, Bar-Cohen and Rohsenow (1984) give, for constant surface temperature in laminar, natural convection

$$\mathrm{Nu} = \left[\frac{576}{(\mathrm{Ra}_T)^2} + \frac{2.873}{(\mathrm{Ra}_T)^{1/2}}\right]^{-1/2} \tag{1}$$

where the Nusselt number and Rayleigh number are defined by

$$\mathrm{Nu} = \frac{q_c}{A_c(T_s - T_0)} \cdot \frac{b}{k} \quad \text{and} \quad \mathrm{Ra}_T = \mathrm{Pr} \cdot \frac{g\beta b^4 (T_s - T_0)}{\nu^2 L} \tag{1a}$$

In addition to L and b, the parameters are q_c/A_c, the convection heat transfer rate divided by area for convection; T_s, the surface temperature; T_0, the ambient temperature; g, gravitational acceleration; and k, Pr, β, and ν, the thermal conductivity, Prandtl number, isobaric volume expansion coefficient, and kinematic viscosity, respectively, evaluated at T_0. Here, the ambient temperature is taken as the air temperature into the bottom of the array. Equation (1), with equation (1*a*) for definitions, is solved for the value of T_s that yields a particular q_c.

Net thermal radiation exchange between the front of the sink in any row, sf_i, and the shroud next to it, sh_i, is given, for example, by Incropera and DeWitt (1985), as

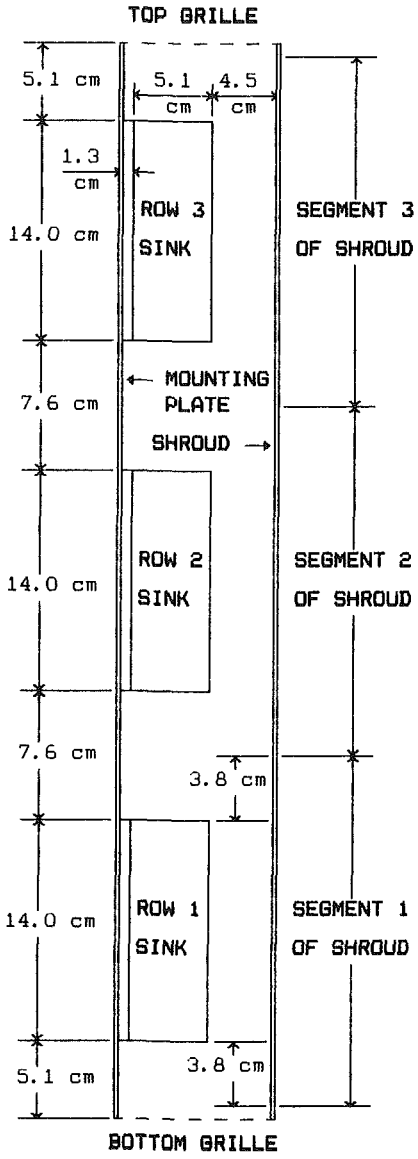

Fig. 2 Side view of heat sink array geometry

$$q_{r_{sf_i - sh_i}} = \frac{\sigma(T_{s_i}^4 - T_{sh_i}^4)}{\dfrac{1-\epsilon_{sf}}{\epsilon_{sf} A_{sf}} + \dfrac{1}{A_{sf} F_{sf-sh}} + \dfrac{1-\epsilon_{sh}}{\epsilon_{sh} A_{sh}}} \tag{2a}$$

where σ, the Stefan-Boltzmann constant, is multiplied by the difference in absolute temperatures of the sink and shroud to the fourth power and is divided by a radiation resistance. In the resistance, the graybody emittances are taken to be $\epsilon_s = 0.9$ for the epoxy-coated sinks and $\epsilon_{sh} = 0.9$ for the enamel-painted shroud. These values are judged typical for nonmetallic surfaces. Because of reflections among the fin surfaces, the gaps appear black and the effective emittance for the fin tips and the black gaps is $\epsilon_{sf} = 0.953$. For the radiation model, the shroud is taken to be three segments of a vertical plate extending from 3.8 cm below the first row of sinks to 3.8 cm above the third row. Figure 2 shows a side view of the array geometry. Each shroud segment presents an area of 261 cm^2 to incoming radiation. In equation (2*a*), A_{sh} is the area

necessary to form a two-body enclosure with the sink front, i.e., $A_{sh} = A_{sf}$. The viewfactor F_{sf-sh} is taken to be 1.00, consistent with the two-body radiation assumption. It is actually 0.89 because the front of each sink sees other segments of the shroud and the grilles. This is judged to be close enough to 1.00 to justify the two-body simplification. The projected area of each sink front for radiation toward the shroud is $A_{sf} = 169\ \text{cm}^2$. Note that this about ten times smaller than the convection area.

The sinks also radiate through their top and bottom ends. The projected area of each end is $A_{se} = 77\ \text{cm}^2$. All ends see the plate to which the sinks are attached. In addition, the bottoms of the sinks in row 1 see the bottom grille and a bit of the shroud; the tops of the sinks in row 3 see the top grille and a bit of the shroud. Any other sink end sees, besides the mounting plate, the sink end opposite it and the shroud. Refer to Fig. 2.

For the bottoms of the sinks in row 1 and the tops of the sinks in row 3, graybody radiation analysis with an adiabatic mounting plate and an enclosure consisting of the sink end, the mounting plate, and the grille yields the following:

$$q_{r_{se_i-g}} = \frac{\sigma(T_{s_i}^4 - T_g^4)}{\dfrac{1-\epsilon_{se}}{\epsilon_{se}A_{se}} + \dfrac{C}{A_{se}F_{se-g}} + \dfrac{1-\epsilon_g}{\epsilon_g A_g}} \tag{2b}$$

where $C = (1/F_{se-p} + A_{se}/A_p \cdot 1/F_{p-g}) / (1/F_{se-g} + 1/F_{se-p} + A_{se}/A_p \cdot 1/F_{p-g})$ accounts for the parallel paths for radiation from these sink ends: directly to the grille, g, or indirectly via reflection off the plate, p. Assuming that the sink surfaces have emittance $\epsilon_s = 0.9$, the effective emittance of the sink ends and black gaps is $\epsilon_{se} = 0.942$. The effective emittance of the open grilles is assumed to be $\epsilon_g = 1.00$. The low thermal conductivity of phenolic and the insulation used in the tests justifies treating the mounting plate as adiabatic. Using two-dimensional viewfactor relations, $F_{se-g} = 0.741$, $F_{se-p} = 0.259$, and $F_{p-g} = 0.675$. The shroud as modeled in Fig. 2 comprises less than 6 percent of the direct view from the bottom of a sink in row 1 or the top of one in row 3. The value of F_{se-g} includes this small fraction. The area A_g corresponds to a grille extended to include the part of the shroud actually seen by the sink end. Since $\epsilon_g = 1.00$, the value of A_g does not affect $q_{r_{se-g}}$.

For any sink end se_i, except a bottom in row 1 or a top in row 3, the two-dimensional viewfactor to the opposite sink end se_j is $F_{se_i-se_j} = 0.365$ while $F_{se_i-p} = 0.3175$. Thus, $F_{se_i-sh} = 0.3175$ and the shroud is a significant radiation target. An enclosure is formed by se_i, se_j, the adiabatic mounting plate between them, and the shroud. The shroud area in this radiation network is the value needed to complete the enclosure. Due to the symmetry of the array, half of the radiation from se_i and se_j to the shroud is assigned to the shroud segment sh_i adjacent to the sink i; the other half is assigned to sh_j adjacent to sink j. The temperature of the shroud in the enclosure is the arithmetic mean of the temperatures of sh_i and sh_j. Heat flows to the nonadiabatic surfaces of this enclosure are not easily expressed in symbols. With nominal values for the areas, emittances and viewfactors, radiation from se_i and se_j to sh_{i+j} is given by the following:

$$\left.\begin{aligned} q_{r_{se_i}} &= A_{se}\sigma(+0.8381\ T_{s_i}^4 - 0.4211\ T_{s_j}^4 - 0.4170\ T_{sh_{i+j}}^4) \\ q_{r_{se_j}} &= A_{se}\sigma(-0.4211\ T_{s_i}^4 + 0.8381\ T_{s_j}^4 - 0.4170\ T_{sh_{i+j}}^4) \\ q_{r_{sh_{i+j}}} &= A_{se}\sigma(+0.4170\ T_{s_i}^4 + 0.4170\ T_{s_j}^4 - 0.8340\ T_{sh_{i+j}}^4) \end{aligned}\right\} \tag{2c}$$

The sign convention is such that $q_{r_{se_i}} + q_{r_{se_j}} = q_{r_{sh_{i+j}}}$. The total radiation from the ends of the sinks in row 2 is $q_{r_{se_i}}$ with $i = 2$ and $j = 3$ plus $q_{r_{se_j}}$ with $i = 1$ and $j = 2$. Radiation from the ends of the sinks in row 1 and row 3 involves equations (2*a*) and (2*c*).

The temperature of the shroud segment in any row is determined by a balance between the radiation to it, from the ends and fronts of the sinks that see it, and the convection and radiation from it. Air at ambient temperature is assumed to cool both the inside and the outside of the shroud by natural convection. The laboratory at ambient temperature is modeled as a blackbody for shroud radiation. Iteration with candidate sink and shroud temperatures continues until the sink and shroud dissipate their respective heat inputs to achieve an energy balance within 0.1 W.

For the model to predict sink temperatures without specification of any temperature except the ambient temperature T_0, a simplifying assumption is needed. It makes the reference temperature for convection in row 2 and row 3 independent of the temperature of air heated by the convection in row 1 and row 2, respectively. All convection is assumed to occur relative to the ambient temperature T_0. This means that the stacked rows of sinks act as continuous channels for convection, even though there is a gap between each row and each sink reaches its own temperature peculiar to its location in the stack. In effect, this assumes that there is no regrowth of boundary layers on the fins from row to row and that the sink-to-shroud gap provides an ample supply of air at the ambient temperature T_0 to allow this reference temperature for convection in the entire stack. This assumption is consistent with convection cooling of the inside of the shroud. It will be checked by using the measured air temperatures into each row as the reference temperature for that row and a channel height L equal to one fin height H in equation (1) for each row. In effect, this restarts the convection model at the inlet to each row of sinks without changing the radiation model or the shroud cooling.

With the assumption of continuous channels for convection, convection heat transfer is evaluated for a channel height L in equation (1) equal to one fin height H only for the first row of sinks. Iteration with equations (1) and (2*a*) yields predicted sink and shroud temperatures, at first neglecting the effects of equations (2*b*) and (2*c*), so that the resulting convection plus radiation agrees with the specified heat input into row 1.

Continuing with the assumption of continuous channels for convection and remembering the convection for row 1, the convection for row 2 is again evaluated using equation (1), but with a channel height $L = 2 \cdot H$. The model finds the value for the temperature of the second row of sinks, which is required to dissipate the convection of the first and second rows over $L = 2 \cdot H$. Without radiation, this would yield a higher sink temperature for row 2 than for row 1 because convection is less effective at the end of long channels than at the beginning. Radiation is then included for the second row, at first using only equation (2*a*). Radiation loss is greater because of the higher temperature of the second row. Iteration produces sink and shroud temperatures for the second row that dissipate the total heat input to the second row over the second fin height in $L = 2 \cdot H$. Sink and shroud temperatures for the third row are calculated similarly, with a channel height $L = 3 \cdot H$ used in equation (1) and the total heat input to the third row dissipated over the third fin height.

After an initial pass over all three rows, subsequent passes include the effects of equations (2*b*) and (2*c*) in the radiation calculations. Sink and shroud segment temperatures from the previous pass are used in a given pass to correct for radiation from the ends of the sinks in each row. When the sink temperature in row 3 changes by less than 0.05°C from pass to pass, the calculations stop. Generally, only three or four

Table 3 Results of the model for the constant-power case ($T_{ambient}$ = 25.6°C)

Row	q(W)	q_c(W)	q_r(W)	T_{shroud}(°C) model vs. (in+out)/2		T_{sink}(°C) model vs.	meas
1	64.8	56.0	8.8	42.0	29.4	82.1	77.7
	(Ra_T=82.3; Nu=1.85)						
2	65.1	56.0	9.1	50.4	38.4	95.4	95.7
	(Ra_T=57.0; Nu=1.38)						
3	64.8	50.3	14.5	52.8	54.0	104.1	110.6
	(Ra_T=42.7; Nu=1.15						

Table 4 Results of the model for the decreasing-power case ($T_{ambient}$ = 26.4°C)

Row	q(W)	q_c(W)	q_r(W)	T_{shroud}(°C) model vs. (in+out)/2		T_{sink}(°C) model vs.	meas
1	82.0	70.6	11.4	46.2	30.8	93.5	89.2
	(Ra_T=108.; Nu=1.75)						
2	67.4	56.9	10.5	54.2	40.6	102.8	101.0
	(Ra_T=81.5; Nu=1.38)						
3	46.6	32.6	14.0	54.2	54.6	104.5	102.7
	(Ra_T=41.8; Nu=1.14)						

Table 5 Sensitivity of shroud temperature to changes: (*a*) convection from shroud to ambient decreased by factor of 2; (*b*) emittance of shroud decreased to ϵ_{sh} = 0.3 in equations (2a) and (2c)

Constant Power Case

Row	T_{sink}(°C) a. vs.	b. vs.	measured	T_{shroud}(°C) a. vs.	b. vs.	(in+out)/2
1	82.5	84.6	77.7	46.4	33.8	29.4
2	96.0	98.9	95.7	56.0	38.6	38.4
3	104.7	108.0	110.6	58.4	39.6	54.0

Decreasing Power Case

Row	T_{sink}(°C) a. vs.	b. vs.	measured	T_{shroud}(°C) a. vs.	b. vs.	(in+out)/2
1	93.9	96.4	89.2	51.4	36.4	30.8
2	103.4	106.8	101.0	60.2	41.0	40.6
3	105.1	108.8	102.7	59.6	40.8	54.6

passes are needed. The first pass establishes shroud temperatures for the full radiation model. The second pass refines the sink and shroud temperatures within 0.1°C of the final values.

Results and Discussion

Table 3 shows results from the model compared to measurements for the constant power case. Table 4 shows the decreasing power case. Final Rayleigh and predicted Nusselt numbers for the sink convection are shown below the convection heat loss. The total radiation from the sinks varies directly with the sink temperatures except for row 2. Radiation from the fronts of the sinks is about 50 percent of the total radiation loss from the sinks in row 1 and row 3. It increases to more than 65 percent in row 2 because sinks in row 2 do not see the open grilles.

Also in Tables 3 and 4 is a comparison between predicted shroud temperatures and the averages of the measured values before and after each row given in Tables 1 and 2. Shroud temperature into row 1 is assumed to be the ambient temperature. Except for row 3, predicted shroud temperatures are much higher than the average of the measured values. The predicted sink temperatures agree well with the measured values except for row 3 of the constant power case. Agreement of this isothermal model with the decreasing-power results is more uniform because the decreasing-power case is closer to isothermal conditions.

Use of an isoflux instead of an isothermal correlation yields, for the constant-power case, sink temperatures of 80.1°C, 105.9°C, and 121.0°C for rows 1, 2, and 3, respectively. Corresponding shroud temperatures are 39.8°C, 54.2°C, and 59.6°C. There is a slight improvement for row 1 compared to the 82.1°C and 42.0°C predicted in Table 3, but the row 2 and row 3 results are unacceptably high. Similar trends are noted if an isoflux correlation is used for the decreasing-power case.

Besides use of an isothermal correlation, the major assumption made in the convection model is that the stacked sinks present a continuous channel for convection. To test the validity of this continuous channel assumption, the measured air temperatures into each row are used as the ambient temperature for that row. Also, the length L in equation (1) is taken equal to one fin height H for each row. This, in effect, allows the boundary layers to restart in each sink, enhancing the convection. On the other hand, the higher air temperatures decrease the driving force for convection. It turns out that the net effect keeps the Rayleigh numbers essentially unchanged from the values in Tables 3 and 4. Recall from equation (1*a*) that Ra_T is proportional to $(T_s - T_0)/L$. Therefore, the higher ambient temperatures drive up the sink temperatures. The restart model yields row 1, 2, and 3 sink temperatures of 82.8°C, 118.8°C, and 137.7°C, respectively, for the constant-power case, and 94.2°C, 125.3°C and 130.5°C for the decreasing-power case. Such high sink temperatures for row 2 and row 3 justify the continuous channel model, used to generate the results in Tables 3 and 4.

One result remains puzzling in Tables 3 and 4: the high values of the predicted shroud temperatures for row 1 and row 2 compared to the mean of the measured values into and out of these rows. The radiation model for the sink end areas sends some radiation to the bottom grille, which actually goes to the row 1 shroud segment. This should be offset by the sink front in row 1 sending all its radiation to this shroud segment. Radiation to the row 2 shroud segment should be modeled correctly.

Since the model does well in predicting sink temperatures, tests were run of the sensitivity of shroud temperature to shroud parameters. Table 5 shows results using the isothermal, continuous channel model for two changes. In change (*a*), the area used for the convection cooling of the shroud is decreased by a factor of 2, corresponding to no convection cooling of the shroud by the air in the gap between the sinks and the shroud. The decreased shroud convection increases the sink temperatures a bit, but drives all shroud temperatures up by another 5°C. In change (*b*), the emittance of the shroud surface facing the sinks is decreased to 0.3 from 0.9, corresponding to an unpainted, shiny surface rather than a gray enamel surface. Decreased emittance means decreased absorptance, but increased reflectance. This change increases sink temperatures more than the decreased convection does. The increased reflectance of the shroud makes it more difficult to cool the sinks. However, the lower absorptance causes the shroud temperatures to go down significantly, to acceptable agreement with the measured values for row 1 and row 2, but below the values for row 3. Thus, predicted shroud temperatures are very sensitive to the shroud emittance. Fortunately, shroud characteristics are not critical to the model's accuracy in predicting sink temperatures. Bajabir (1986) presents other sensitivity studies of interest for heat sink array design.

Concluding Remarks

For a slightly high estimate of sink temperatures to dissipate heat by natural convection and radiation, a one-dimensional model based on isothermal correlations and graybody radiation networks is acceptable. It can be applied for conservative design of heat sinks in stacked configurations and a decreasing power situation (uniform sink temperatures throughout the array). Comparison of sink temperatures predicted by the model to measured values indicates that heat transfer is slightly better than the model predicts. This is despite the use of the ambient temperature into the stack as the reference temperature for convection in all heat sinks. Such enhancement is possible according to theoretical considerations of the

effect of the gap between sink rows and the effect of the sink-to-shroud gap. An extension of the model uses measured air temperatures between sink rows to change the reference temperature for each row and allow boundary layer development to start over in each row. It shows that any enhancement due to regrowth of boundary layers is more than offset by the inhibiting effect of the increased ambient temperature of the cooling air. Quantifying the enhancement is a complex task beyond the scope of a one-dimensional analysis. For the geometries under consideration in this study, such effects are not of major consequence for proper deployment of heat sinks.

References

Bajabir, A. A., 1986, "Computer Model to Predict Temperatures of Stacked Heat Sinks Cooled by Natural Convection," M.S. Thesis, Marquette University, Milwaukee, WI.

Bar-Cohen, A., and Rohsenow, W. M., 1984, "Thermally Optimum Spacing of Vertical, Natural Convection Cooled, Parallel Plates," ASME JOURNAL OF HEAT TRANSFER, Vol. 106, pp. 116–123.

Incropera, F. P., and DeWitt, D. P., 1985, *Introduction to Heat Transfer*, Wiley, New York, Section 13.3.3.

Karki, K. C., and Patankar, S. V., 1984, "Cooling of a Vertical Shrouded Fin Array by Natural Convection," presented at the ASME Heat Transfer Conference, Niagara Falls, NY.

Sparrow, E. M., and Faghri, M., 1980, "Natural Convection Heat Transfer From the Upper Plate of a Colinear, Separated Pair of Vertical Plates," ASME JOURNAL OF HEAT TRANSFER, Vol. 102, pp. 623–629.

A Coordinate Transformation Method for Radiation Heat Transfer Prediction in Soot-Laden Combustion Products

S. L. Chang[1] and K. T. Rhee[2]

Nomenclature

- e = Plank's emissive power
- F = species distribution function
- f = soot volume fraction or transformation function
- I = radiation intensity
- R = radius of the nozzle hole
- t = time
- v = velocity
- α = constant for plume injection speed
- θ = angle of spray plume with respect to x_1
- κ = volumetric absorption coefficient
- λ = wavelength
- Φ = transformation function
- Ω = angular speed or solid angle

Subscripts

- b = blackbody
- d = detector
- in = inclined
- o = constant or foot of optical path
- s = specified
- u = unparallel
- λ = spectral

[1]Argonne National Laboratory, EES 362, Argonne, IL 60439.

[2]Department of Mechanical and Aerospace Engineering, Rutgers University, New Brunswick, NJ 08903.

Contributed by the Heat Transfer Division for publication in the JOURNAL OF HEAT TRANSFER. Manuscript received by the Heat Transfer Division September 24, 1986. Keywords: Combustion, Fire/Flames, Radiation.

Introduction

To solve the governing equation of radiation heat transfer shown below for analysis of thermal load in a combustor having soot-laden flames, we assume that the distribution of its optically participating species is given with respect to a reference location (in-combustor distribution)

$$I_\lambda(r) = \int_r^{r_o} \frac{\kappa_\lambda(r')}{\pi} e_{b\lambda} \exp\left(-\int_r^{r'} \kappa_\lambda(r'')dr''\right)dr' \qquad (1)$$

In finding the solution to this equation, difficulties are faced including those stemming from determination of the species distribution along the individual optical paths (in-optical path distribution) and use of such transformed information for implementing equation (1). Due to the complexity of the problem, several approximation methods were employed in the previous studies, namely the Monte-Carlo method (Steward and Cannon, 1971); the zonal method (Hottel and Sarofim, 1967); geometric factors (Chang and Rhee, 1983), etc. An additional difficulty of the problem may be the lack of proper mathematical form to express the in-combustor distribution that facilitates its transformation into in-optical path distribution. Literature reveals (Takekuchi and Senda, 1983; Kuo et al., 1985) that the nonaxisymmetric plumes may be described by the following equation:

$$F = f \exp(-a\rho - b\phi^2 - cz^2) \qquad (2)$$

where F may represent either fuel/air ratio or soot and gaseous species, e.g., CO_2 or H_2O; and f, a, b, c are constants to be determined by either experimental or computational means. In spite of its macroscopic form, the equation shows to a great extent in a simple form the hitherto-found physical phenomena of the spray plume (Chang and Rhee, 1986). Note that the distribution terms in equation (2) may be replaced by either a normal (also a skewed normal) distribution or an exponential term. The present paper reports a new coordinate transformation method of the in-combustor species distribution into in-optical path distributions.

Method

The new transformation is carried out by employing two sets of coordinate systems, i.e., a cylindrical coordinate (ρ, ϕ, z) centered at the reference location, such as injection nozzle hole, 0, for describing the plume and a spherical coordinate (r, θ, ζ) for expressing the same plume with respect to the location through which the radiation heat transfer is considered, which is hereafter called a detector D (Fig. 1). In reporting the method, two cases of transformation are discussed: point-to-point and distribution equation-to-distribution equation transformations. The former is considered for use when some discrete point data are available to find the distribution with respect to the detector. The latter method is thought out for transforming the plume equation in a nozzle coordinate, e.g., equation (2), into in-optical path distributions within the hemispherical volume faced by the detector.

(1) Point-to-Point Transformation. Two cases are separately considered, as follows:

Mutually Parallel Coordinates. Referring to Fig. 1(A) and identifying the location of a detector in X coordinates at (x_{1d}, x_{2d}, x_{3d}), and in C coordinates at (ρ_d, ϕ_d, z_d), a series of transformations are performed to obtain

$$\rho^2 = r^2 \sin^2\theta + 2\, r\, \rho_d \sin\theta \cos(\phi_d + \zeta) + \rho_d^2$$

$$\phi = \tan^{-1}[(\rho_d \sin\phi_d - r \sin\theta \sin\zeta)/(\rho_d \cos\phi_d + r \sin\theta \cos\zeta)], \quad z = z_d - r\cos\theta \qquad (3)$$

where $\rho_d^2 = x_{1d}^2 + x_{2d}^2$, $\phi_d = \tan^{-1}(x_{2d}/x_{1d})$, and $z_d = x_{3d}$. Note that $\phi = \tan^{-1}(x_2/x_1)$ if $x_1 \geq 0$, $\phi = \tan^{-1}(x_2/x_1) + \pi$

effect of the gap between sink rows and the effect of the sink-to-shroud gap. An extension of the model uses measured air temperatures between sink rows to change the reference temperature for each row and allow boundary layer development to start over in each row. It shows that any enhancement due to regrowth of boundary layers is more than offset by the inhibiting effect of the increased ambient temperature of the cooling air. Quantifying the enhancement is a complex task beyond the scope of a one-dimensional analysis. For the geometries under consideration in this study, such effects are not of major consequence for proper deployment of heat sinks.

References

Bajabir, A. A., 1986, "Computer Model to Predict Temperatures of Stacked Heat Sinks Cooled by Natural Convection," M.S. Thesis, Marquette University, Milwaukee, WI.

Bar-Cohen, A., and Rohsenow, W. M., 1984, "Thermally Optimum Spacing of Vertical, Natural Convection Cooled, Parallel Plates," ASME JOURNAL OF HEAT TRANSFER, Vol. 106, pp. 116–123.

Incropera, F. P., and DeWitt, D. P., 1985, *Introduction to Heat Transfer*, Wiley, New York, Section 13.3.3.

Karki, K. C., and Patankar, S. V., 1984, "Cooling of a Vertical Shrouded Fin Array by Natural Convection," presented at the ASME Heat Transfer Conference, Niagara Falls, NY.

Sparrow, E. M., and Faghri, M., 1980, "Natural Convection Heat Transfer From the Upper Plate of a Colinear, Separated Pair of Vertical Plates," ASME JOURNAL OF HEAT TRANSFER, Vol. 102, pp. 623–629.

A Coordinate Transformation Method for Radiation Heat Transfer Prediction in Soot-Laden Combustion Products

S. L. Chang[1] and K. T. Rhee[2]

Nomenclature

- e = Plank's emissive power
- F = species distribution function
- f = soot volume fraction or transformation function
- I = radiation intensity
- R = radius of the nozzle hole
- t = time
- v = velocity
- α = constant for plume injection speed
- θ = angle of spray plume with respect to x_1
- κ = volumetric absorption coefficient
- λ = wavelength
- Φ = transformation function
- Ω = angular speed or solid angle

Subscripts

- b = blackbody
- d = detector
- in = inclined
- o = constant or foot of optical path
- s = specified
- u = unparallel
- λ = spectral

[1]Argonne National Laboratory, EES 362, Argonne, IL 60439.

[2]Department of Mechanical and Aerospace Engineering, Rutgers University, New Brunswick, NJ 08903.

Contributed by the Heat Transfer Division for publication in the JOURNAL OF HEAT TRANSFER. Manuscript received by the Heat Transfer Division September 24, 1986. Keywords: Combustion, Fire/Flames, Radiation.

Introduction

To solve the governing equation of radiation heat transfer shown below for analysis of thermal load in a combustor having soot-laden flames, we assume that the distribution of its optically participating species is given with respect to a reference location (in-combustor distribution)

$$I_\lambda(r) = \int_r^{r_o} \frac{\kappa_\lambda(r')}{\pi} e_{b\lambda} \exp\left(-\int_r^{r'} \kappa_\lambda(r'')dr''\right)dr' \qquad (1)$$

In finding the solution to this equation, difficulties are faced including those stemming from determination of the species distribution along the individual optical paths (in-optical path distribution) and use of such transformed information for implementing equation (1). Due to the complexity of the problem, several approximation methods were employed in the previous studies, namely the Monte-Carlo method (Steward and Cannon, 1971); the zonal method (Hottel and Sarofim, 1967); geometric factors (Chang and Rhee, 1983), etc. An additional difficulty of the problem may be the lack of proper mathematical form to express the in-combustor distribution that facilitates its transformation into in-optical path distribution. Literature reveals (Takekuchi and Senda, 1983; Kuo et al., 1985) that the nonaxisymmetric plumes may be described by the following equation:

$$F = f \exp(-a\rho - b\phi^2 - cz^2) \qquad (2)$$

where F may represent either fuel/air ratio or soot and gaseous species, e.g., CO_2 or H_2O; and f, a, b, c are constants to be determined by either experimental or computational means. In spite of its macroscopic form, the equation shows to a great extent in a simple form the hitherto-found physical phenomena of the spray plume (Chang and Rhee, 1986). Note that the distribution terms in equation (2) may be replaced by either a normal (also a skewed normal) distribution or an exponential term. The present paper reports a new coordinate transformation method of the in-combustor species distribution into in-optical path distributions.

Method

The new transformation is carried out by employing two sets of coordinate systems, i.e., a cylindrical coordinate (ρ, ϕ, z) centered at the reference location, such as injection nozzle hole, 0, for describing the plume and a spherical coordinate (r, θ, ζ) for expressing the same plume with respect to the location through which the radiation heat transfer is considered, which is hereafter called a detector D (Fig. 1). In reporting the method, two cases of transformation are discussed: point-to-point and distribution equation-to-distribution equation transformations. The former is considered for use when some discrete point data are available to find the distribution with respect to the detector. The latter method is thought out for transforming the plume equation in a nozzle coordinate, e.g., equation (2), into in-optical path distributions within the hemispherical volume faced by the detector.

(1) Point-to-Point Transformation. Two cases are separately considered, as follows:

Mutually Parallel Coordinates. Referring to Fig. 1(A) and identifying the location of a detector in X coordinates at (x_{1d}, x_{2d}, x_{3d}), and in C coordinates at (ρ_d, ϕ_d, z_d), a series of transformations are performed to obtain

$$\rho^2 = r^2 \sin^2\theta + 2\, r\, \rho_d \sin\theta \cos(\phi_d + \zeta) + \rho_d^2$$

$$\phi = \tan^{-1}[(\rho_d \sin\phi_d - r \sin\theta \sin\zeta)/(\rho_d \cos\phi_d + r \sin\theta \cos\zeta)], \quad z = z_d - r\cos\theta \qquad (3)$$

where $\rho_d^2 = x_{1d}^2 + x_{2d}^2$, $\phi_d = \tan^{-1}(x_{2d}/x_{1d})$, and $z_d = x_{3d}$. Note that $\phi = \tan^{-1}(x_2/x_1)$ if $x_1 \geq 0$, $\phi = \tan^{-1}(x_2/x_1) + \pi$

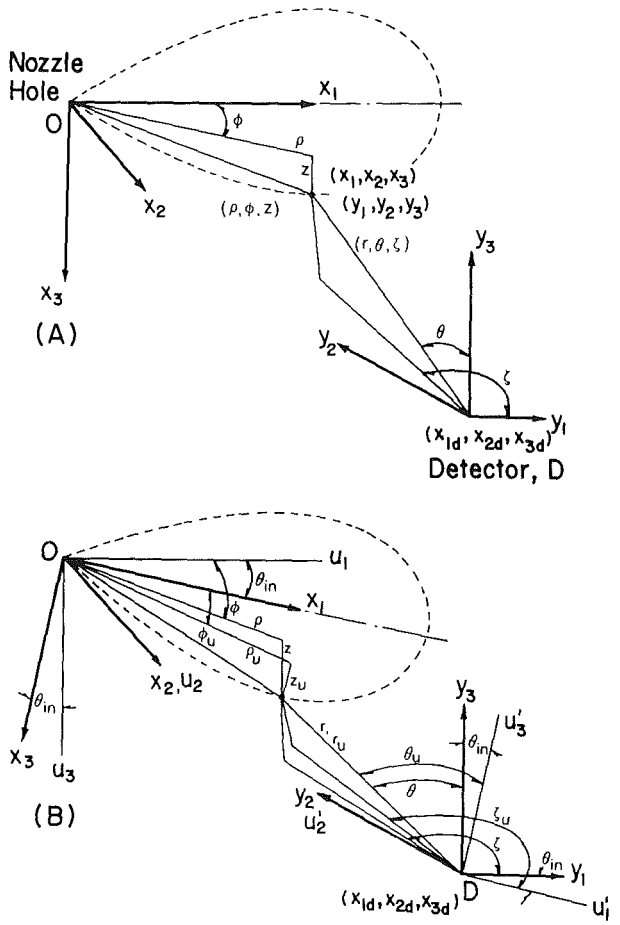

Fig. 1 Location of detectors with respect to flame plume: (A) parallel coordinate and (B) unparallel coordinate

if $x_1 < 0$ and $x_2 > 0$, and $\phi = \tan^{-1}(x_2/x_1) - \pi$ if $x_1 < 0$ and $x_2 < 0$.

Mutually Unparallel Coordinates. Since in many practical systems, the fuel is injected into the combustion chamber at an angle θ_{in}, equation (3) is not directly applicable for the purpose; an additional coordinate having an angle of θ_{in} with respect to the X coordinate is introduced, i.e., $U(u_1, u_2, u_3)$. This leads to an expression of the detector's location, initially shown by unparallel coordinate system, i.e., $D(\rho_{ud}, \theta_{ud}, z_{ud})$, in terms of the parallel coordinate system $D(\rho_d, \theta_d, z_d)$ as

$$\rho_d^2 = (\rho_{ud}\cos\theta_{in}\cos\phi_{ud} - z_{ud}\sin\theta_{in})^2 + \rho_{ud}^2 + \sin^2\phi_{ud}$$

$$\phi_d = \tan^{-1}[(\rho_{ud}\sin\phi_{ud})/(\rho_{ud}\cos\theta_{in}\cos\phi_{ud} - z_{ud}\sin\theta_{in})]$$

and

$$z_d = \rho_{ud}\sin\theta_{in}\cos\phi_{ud} + z_{ud}\cos\theta_{in} \tag{4}$$

Another look at Fig. 1(*B*) suggests that for the expression of the plume, a transformation of X coordinate to U coordinate can be made in the same way as that of Y coordinate to U' coordinate having elements (u_1', u_2', u_3'). Consequently, point information along a path r, identified by using the parallel coordinate $S(r, \theta, \zeta)$, can be expressed for the unparallel coordinate $S_u(r_u, \theta_u, \zeta_u)$:

$$\theta = \cos^{-1}[-\sin\theta_u\cos\zeta_u\sin\theta_{in} + \cos\theta_u\cos\theta_{in}]$$

$$\zeta = \tan^{-1}[\sin\theta_u\sin\zeta_u/(\sin\theta_u\cos\zeta_u\cos\theta_{in} + \cos\theta_u\sin\theta_{in})] \tag{5}$$

In summary, the result is obtained by introducing equations (4) and (5) into equation (3).

2 Distribution-to-Distribution Transformation. In order to transform an in-combustor distribution into in-optical path distributions, the Taylor method was used, since it facilitates the solution of equation (1), and the accuracy for the cases analyzed in the present work was found to be within a few percent upon truncation of terms beyond the second order of the series. Note that the present method approximates only the mathematical maneuvering, unlike the methods that approximated the physical phenomena, e.g., the zonal method. This method is applied at first to a case without swirl motion in the combustion chamber:

ρ terms:

Defining $x \equiv r\sin\theta/\rho_d$, $A \equiv \cos(\phi_d + \zeta)$ and $f \equiv \rho/\rho_d$, ρ in equation (3) can be expressed by using the series expansion, for $x = x_i + \epsilon$ and $\epsilon \ll 1$, as

$$f(x) = f(x_i) + f'(x_i)\epsilon + f''\epsilon^2/2$$

where $f(x_i) = (1 + 2Ax_i + x_i^2)^{1/2}$, $f'(x_i) = (A + x_i)/f$, and $f''(x_i) = [f^2(x_i) - (A + x_i)^2]/f^3$. Since $\epsilon = x - x_i$, $f(x)$ may be expressed as

$$f(x) = \rho/\rho_d = f_0 + f_1 x + f_2 x^2 \tag{6}$$

where $f_0 = f(x_i) - f'(x_i)\,x_i + f''(x_i)\,x_i^2/2$, $f_1 = f'(x_i) - f''(x_i)\,x_i$, and $f_2 = f''(x_i)/2$. Note that for $x \gg 1$, $f = \rho/\rho_d = x + A$.

ϕ terms:

In equation (3), putting $f(x) = \tan(\phi) = (\sin\phi_d - x\sin\zeta)/(\cos\phi_d + x\cos\zeta)$, one obtains

$$f'(x) = -\sin(\phi_d + \zeta)/(\cos\phi_d + x\cos\zeta)^2$$

$$f''(x) = -2f'(x)\cos\zeta/(\cos\phi_d + x\cos\zeta)$$

$$\phi(x) = \tan^{-1} f,$$

$$\phi'(x) = f'/(1 + f^2), \text{ and}$$

$$\phi''(x) = [-2ff'^2 + (1 + f^2)f'']/(1 + f^2)^2$$

Note that for $\cos\phi_d + x\cos\zeta = 0$, $\phi(x) = \pm\pi/2$, $\phi'(x) = -\cos^2\zeta/\sin(\phi_d + \zeta)$, and $\phi'' = 0$. For $x = x_i + \epsilon$ and $\epsilon \ll 1$, $\phi(x)$ may be written as $\phi(x) = \phi(x_i) + \phi'(x_i)\,\epsilon + \phi''(x_i)\,\epsilon^2/2$.

In view of equation (2), one defines $\Phi(x) = \phi^2(x)$ to rewrite

$$\Phi(x) = \Phi(x_i) + \Phi'(x_i) + \Phi''(x_i)\epsilon^2/2$$

where $\Phi'(x) = 2\phi(x_i)\,\phi'(x_i)$ and $\Phi''(x) = 2\phi(x_i)\,\phi''(x_i) + 2\phi'^2(x_i)$. Further, since $\epsilon = x - x_i$, Φ may be expressed as

$$\Phi(x) = \phi^2(x) = \Phi_0 + \phi_1 x + \Phi_2 x^2 \tag{7}$$

where $\Phi_0 = \Phi(x_i) - \Phi'(x_i)\,x_i + \Phi''(x_i)\,x_i^2/2$, $\Phi_1 = \Phi(x_i) - \Phi''(x_i)\,x_i$, and $\Phi_2 = \Phi''(x_i)/2$. Note that for $x \gg 1$, $\phi(x) = -\zeta$, or $\Phi(x) = \zeta^2$.

z terms:

The following is obtained for z terms from equation (3):

$$z^2 = z_d^2 = 2z_d r\cos\theta + r^2\cos^2\theta \tag{8}$$

By substituting terms in equation (2) with equations (6), (7), and (8), one obtains

$$F = f_d \exp\{-[(r - r_0)/r_w]^2\} \tag{9}$$

where $f_d = f\exp[-(a_1 - b_1^2/4c_1)]$, $r_0 = b_1/2c_1$, $r_w = (c_1)^{-1/2}$, $a_1 = a\rho_0 + b\Phi_0 + cz_d^2$, $b_1 = -[a\rho_1 + b\phi_1]\sin\theta/\rho_d + 2cz_d\cos\theta$, and $c_1 = [a\rho_2 + b\Phi_2]\sin^2\theta/\rho_d^2 + c\cos^2\theta$.

When the above results are used in solving equation (1), an exact analytical solution was obtainable for both optically thin and optically thick media; one for the optically medially thin medium, however, was accessible by using a numerical method (Chang and Rhee, 1986; Chang et al., 1985).

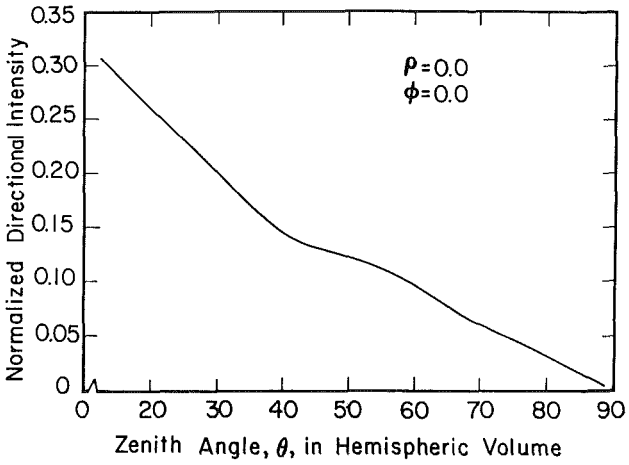

Fig. 2 Directional radiation intensity at injection nozzle, computed for varied zenith angles

In a combustor having gas swirl, the plume is accordingly bent. In order to take into account the bending of spray in the analysis of radiation heat transfer, the two cases that were proposed in the literature are considered: When the droplets move at constant axial velocity and angular speed in swirl, a point information at a location (ρ, ϕ, z) of no-swirl condition is located at $(\rho, \phi + \phi_s, z)$, due to the swirl during a period of time Δt, according to $\phi_s = (\Omega/v_f)\rho$.

The transformation of such a bent plume is exactly the same as in the no-swirl case except for a new set of equations in ϕ terms. They are

$$\Phi(x_i) = \psi^2(x_i)$$

$$\Phi'(x_i) = 2\psi(x_i)\psi'(x_i), \text{ and}$$

$$\Phi''(x_i) = 2\psi(x_i)\psi''(x_i) + 2\psi'^2(x_i) \tag{10}$$

where $(\psi(x_i) = \phi(x_i) - \phi_s(x_i)$, $\psi'(x_i) = \phi'(x_i) - \phi_s'(x_i)$, $\psi''(x_i) = \phi''(x_i) - \phi_s''(x_i)$, $\phi_s' = (\rho_1 + 2\rho_2 x)(\Omega/v_f)$, and $\phi_s'' = 2\rho_2(\Omega/v_f)$.

When the droplets move at a specified axial speed (Melton, 1981), e.g., $v_f = v_s/(1 + \alpha\rho)$ where v_s is the exit velocity of the fuel droplet at the nozzle, α is about $0.085/R_s$, and R_s is the radius of the nozzle hole, a result can be obtained as

$$\phi_s = (\Omega\rho/v_s)(1 + \alpha\rho/2)$$

$$\phi_2' = \left(\frac{\Omega}{v_s}\right)(1 + \alpha\rho)\rho'$$

$$\phi_s'' = \left(\frac{\Omega}{v_s}\right)[\alpha\rho'^2 + (1 + \alpha\rho)\rho''] \tag{11}$$

Substituting the respective terms in equation (11) into equation (10), the coordinate transformation of the above bending flame plume can be achieved.

An Example of Application

The present technique can be employed to compute the individual directional radiation intensity, $I(\rho, \phi, z)$, as reported here (Fig. 2) in terms of a normalized form I/I_b, where $I_b = \sigma T_r^4/\pi$, $\sigma = 5.670 \times 10^{-8}$ W/m^{2}K^4, and $T_r = 2400$ K. The computation was made for a spray plume having species distribution in equation (8) with f for soot, H_2O, CO_2, and burned fuel $(C_{10}H_{34})$/air ratio, 8×10^{-16}, 0.01, 0.001, and 1.0, respectively; the distribution constants, a, b, and c are 0.6, 2.36, and 2.0, respectively. Among the significance of results in Fig. 2 is that they may be used for evaluating a radiation measurement method that employs a recessed mount (at either the square angle or inclined angle) of heat flux probe with a quartz window in front to eliminate convective heat transfer (Ebersole et al., 1963). When the species distribution in the combustion chamber is not uniform as in the present case, it was considered that the measurement could, by even some inclined mounting of probe (or optical path with respect to the normal of the surface), i.e., variation in θ at the detector D, be significantly affected.

Acknowledgments

The authors would like to thank Professor R. Viskanta for his helpful suggestions on the manuscript. The present work has been supported by the U.S. Army Research Office, Contract No. DAAG29-83-K-0042 (Scientific Program Officer, Dr. David M. Mann).

References

Chang, S. L., and Rhee, K. T., 1983, "Computation of Radiation Heat Transfer in Diesel Combustion," SAE Paper No. 831332; also in *SAE Transactions*.

Chang, S. L., Yang, X. L., and Rhee, K. T., 1985, "A Parametric Analysis of Radiation Heat Transfer in Direct Injection Diesel Combustion," presented at the International Symposium on Diagnostics and Modeling of Combustion in Reciprocating Engines, Tokyo, Sept. 4-6.

Chang, S. L., and Rhee, K. T., 1986, "An Analytical Method of Non-gray Three-Dimensional Radiation Heat Transfer in Spray Combustion," ASME Paper No. 86-WA/HT-17.

Ebersole, G. D., Myers, P. S., and Uyehara, U. A., 1963, "The Radiative and Convective Components of Diesel Heat Transfer," SAE Paper No. 7016.

Hottel, H. C., and Sarofim, A. F., 1967, *Radiative Transfer*, McGraw-Hill, New York.

Kuo, T. W., Yu, R. C., and Shahed, S. M., 1983, "A Numerical Study of the Transient Evaporating Spray Mixing Process in the Diesel Environment," SAE Paper No. 831735.

Melton, R. B., Jr., 1971, "Diesel Fuel Injection Viewed as a Jet Phenomenon," SAE Paper No. 710132.

Steward, F. R., and Cannon, P., 1971, "The Calculation of Radiation Heat Flux in a Cylindrical Furnace Using the Monte Carlo Method," *Int. J. Heat Mass Transfer*, Vol. 14, No. 2, pp. 245-262.

Takekuchi, K., Senda, J., and Shikuja, M., 1983, "Transient Characteristics of Fuel Atomization and Droplet Size Distribution in Diesel Fuel Spray," SAE Paper No. 830449.